Well Logging for Earth Scientists

Well Logging for Earth Scientists

2nd Edition

By

Darwin V. Ellis
Schlumberger-Doll Research,
Ridgefield, CT, USA

and

Julian M. Singer
Richmond, UK

Springer

A C.I.P. Catalogue record for this book is available from the Library of Congress.

ISBN 978-1-4020-3738-2 (HB)
ISBN 978-1-4020-4602-5 (e-book)

Published by Springer,
P.O. Box 17, 3300 AA Dordrecht, The Netherlands.

www.springer.com

Cover illustration: First recorded electric log, Pechelbronn field, Sept. 5, 1927, reproduced courtesy of Schlumberger.

A Manual of Solutions for the end-of-chapter problems can be found at the book's homepage at www.springer .com

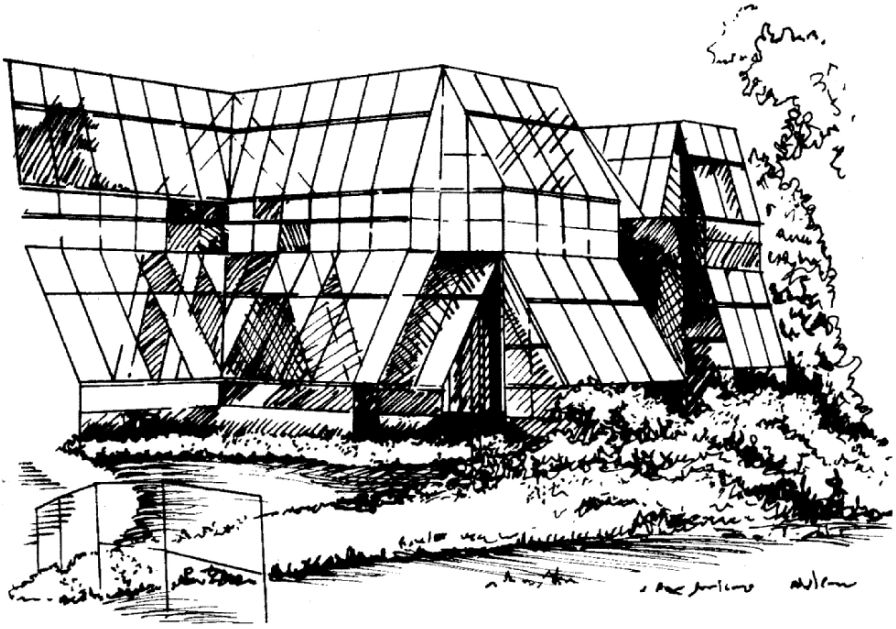
This is a second revised and enlarged edition of the first edition published by Elsevier NY, 1987.

Printed on acid-free paper

© 2007 Springer
No part of this work may be reproduced, stored in a retrieval system, or transmitted in any form or by any means, electronic, mechanical, photocopying, microfilming, recording or otherwise, without written permission from the Publisher, with the exception of any material supplied specifically for the purpose of being entered and executed on a computer system, for exclusive use by the purchaser of the work.

Dedication

To a place where much of this was invented, elaborated, or pondered and where a friendship developed that even the writing of a book could not spoil.



Contents

Preface **xvii**

Acknowledgments **xix**

1 An Overview of Well Logging **1**
1.1 Introduction 1
1.2 What is Logging? 2
1.2.1 What is Wireline Logging? 2
1.2.2 What is LWD? 5
1.3 Properties of Reservoir Rocks 7
1.4 Well Logging: The Narrow View 8
1.5 Measurement Techniques 10
1.6 How is Logging Viewed by Others? 11
References 15

2 Introduction to Well Log Interpretation: Finding the Hydrocarbon **17**
2.1 Introduction 17
2.2 Rudimentary Interpretation Principles 17
2.3 The Borehole Environment 21
2.4 Reading a Log 25
2.5 Examples of Curve Behavior and Log Display 29
2.6 A Sample Rapid Interpretation 33
References 37
Problems 38

3 Basic Resistivity and Spontaneous Potential **41**
3.1 Introduction 41
3.2 The Concept of Bulk Resistivity 42
3.3 Electrical Properties of Rocks and Brines 46
3.4 Spontaneous Potential 49
3.5 Log Example of the SP 56
References 58
Problems 59

4 Empiricism: The Cornerstone of Interpretation 63
4.1 Introduction 63
4.2 Early Electric Log Interpretation 64
4.3 Empirical Approaches to Interpretation 66
4.3.1 Formation Factor 66
4.3.2 Archie's Synthesis 69
4.4 A Note of Caution 71
4.4.1 The Porosity Exponent, m 71
4.4.2 The Saturation Exponent, n 72
4.4.3 Effect of Clay 74
4.4.4 Alternative Models 75
4.5 A Review of Electrostatics 77
4.6 A Thought Experiment for a Logging Application 78
4.7 Anisotropy 82
References 85
Problems 87

5 Resistivity: Electrode Devices and How They Evolved 91
5.1 Introduction 91
5.2 Unfocused Devices 91
5.2.1 The Short Normal 91
5.2.2 Estimating the Borehole Size Effect 94
5.3 Focused Devices 99
5.3.1 Laterolog Principle 99
5.3.2 Spherical Focusing 104
5.3.3 The Dual Laterolog 107
5.3.4 Dual Laterolog Example 110
5.4 Further Developments 114
5.4.1 Reference Electrodes 114
5.4.2 Thin Beds and Invasion 117
5.4.3 Array Tools 118
References 121
Problems 122

6 Other Electrode and Toroid Devices 125
6.1 Introduction 125
6.2 Microelectrode Devices 126
6.3 Uses for R_{xo} 129

6.4 Azimuthal Measurements 133
6.5 Resistivity Measurements While Drilling 135
6.5.1 Resistivity at the Bit 135
6.5.2 Ring and Button Measurements 138
6.5.3 RAB Response 140
6.5.4 Azimuthal Measurements 142
6.6 Cased-Hole Resistivity Measurements 142
References 145
Problems 147

7 Resistivity: Induction Devices 149
7.1 Introduction 149
7.2 Review of Magnetostatics and Induction 150
7.2.1 Magnetic Field from a Current Loop 150
7.2.2 Vertical Magnetic Field from a Small Current Loop 152
7.2.3 Voltage Induced in a Coil by a Magnetic Field 154
7.3 The Two-Coil Induction Device 155
7.4 Geometric Factor for the Two-coil Sonde 157
7.5 Focusing the Two-coil Sonde 161
7.6 Skin Effect 164
7.7 Two-Coil Sonde with Skin Effect 166
7.8 Multicoil Induction Devices 167
7.9 Induction or Electrode? 171
7.10 Induction Log Example 174
References 176
Problems 177

8 Multi-Array and Triaxial Induction Devices 179
8.1 Introduction 179
8.2 Phasor Induction 180
8.2.1 Inverse Filtering 183
8.3 High Resolution Induction 185
8.4 Multi-Array Inductions 186
8.4.1 Multi-Array Devices 188
8.4.2 Multi-Array Processing 189
8.4.3 Limitations of Resolution Enhancement 192
8.4.4 Radial and 2D Inversion 194
8.4.5 Dipping Beds 197

8.5 Multicomponent Induction Tools and Anisotropy 200
8.5.1 Response of Coplanar Coils 200
8.5.2 Multicomponent Devices 205
References 208
Problems 211

9 Propagation Measurements 213
9.1 Introduction 213
9.2 Characterizing Dielectrics 214
9.2.1 Microscopic Properties 216
9.2.2 Interfacial Polarization and the Dielectric Properties of Rocks 219
9.3 Propagation in Conductive Dielectric Materials 222
9.4 Dielectric Mixing Laws 224
9.5 The Measurement of Formation Dielectric Properties 228
9.6 2 MHz Measurements 231
9.6.1 Derivation of the Field Logs 231
9.6.2 General Environmental Factors 234
9.6.3 Vertical and Radial Response 235
9.6.4 Dip and Anisotropy 236
9.6.5 Array Propagation Measurements and their Interpretation 238
References 242
Problems 244

10 Basic Nuclear Physics for Logging Applications: Gamma Rays 247
10.1 Introduction 247
10.2 Nuclear Radiation 248
10.3 Radioactive Decay and Statistics 249
10.4 Radiation Interactions 251
10.5 Fundamentals of Gamma Ray Interactions 253
10.6 Attenuation of Gamma Rays 257
10.7 Gamma Ray Detectors 259
10.7.1 Gas-Discharge Counters 259
10.7.2 Scintillation Detectors 260
10.7.3 Semiconductor Detectors 264
References 264
Problems 265

11 Gamma Ray Devices **267**
11.1 Introduction 267
11.2 Sources of Natural Radioactivity 268
11.3 Gamma Ray Devices 271
11.4 Uses of the Gamma Ray Measurement 273
11.5 Spectral Gamma Ray Logging 275
11.5.1 Spectral Stripping 280
11.6 Developments in Spectral Gamma Ray Logging 283
11.7 A Note on Depth of Investigation 285
References 286
Problems 288

12 Gamma Ray Scattering and Absorption Measurements **289**
12.1 Introduction 289
12.2 Density and Gamma Ray Attenuation 290
12.2.1 Density Measurement Technique 293
12.2.2 Density Compensation 296
12.3 Lithology Logging 300
12.3.1 Photoelectric Absorption and Lithology 300
12.3.2 P_e Measurement Technique 304
12.3.3 Interpretation of P_e 307
12.4 Inversion of Forward Models with Multidetector Tools 312
12.5 LWD Density Devices 312
12.6 Environmental Effects 314
12.7 Estimating Porosity from Density Measurements 317
12.7.1 Interpretation Parameters 318
References 321
Problems 322

13 Basic Neutron Physics for Logging Applications **325**
13.1 Introduction 325
13.2 Fundamental Neutron Interactions 326
13.3 Nuclear Reactions and Neutron Sources 332
13.4 Useful Bulk Parameters 333
13.4.1 Macroscopic Cross Sections 333
13.4.2 Lethargy and Average Energy Loss 335
13.4.3 Number of Collisions to Slow Down 336
13.4.4 Characteristic Lengths 337
13.4.5 Characteristic Times 344

13.5 Neutron Detectors 345
References 347
Problems 348

14 Neutron Porosity Devices 351
14.1 Introduction 351
14.2 Use of Neutron Porosity Devices 353
14.3 Types of Neutron Tools 353
14.4 Basis of Measurement 354
14.5 Historical Measurement Technique 358
14.6 A Generic Thermal Neutron Tool 361
14.7 Typical Log Presentation 364
14.8 Environmental Effects 366
14.8.1 Introduction to Correction Charts 367
14.9 Major Perturbations of Neutron Porosity 370
14.9.1 Lithology Effect 370
14.9.2 Shale Effect 372
14.9.3 Gas Effect 373
14.10 Depth of Investigation 374
14.11 LWD Neutron Porosity Devices 378
14.12 Summary 379
References 379
Problems 381

15 Pulsed Neutron Devices and Spectroscopy 383
15.1 Introduction 383
15.2 Thermal Neutron Die-Away Logging 384
15.2.1 Thermal Neutron Capture 384
15.2.2 Measurement Technique 386
15.2.3 Instrumentation 390
15.2.4 Interpretation 392
15.3 Pulsed Neutron Spectroscopy 395
15.3.1 Evolution of Measurement Technique 400
15.4 Pulsed Neutron Porosity 405
15.5 Spectroscopy 408
References 410
Problems 413

16 Nuclear Magnetic Logging **415**
16.1 Introduction 415
16.1.1 Nuclear Resonance Magnetometers 416
16.1.2 Why Nuclear Magnetic Logging? 417
16.2 A Look at Magnetic Gyroscopes 418
16.2.1 The Precession of Atomic Magnets 419
16.2.2 Paramagnetism of Bulk Materials 421
16.3 Some Details of Nuclear Induction 423
16.3.1 Longitudinal Relaxation, T_1 424
16.3.2 Rotating Frame 427
16.3.3 Pulsing 429
16.3.4 Transverse Relaxation, T_2, and Spin Dephasing 430
16.3.5 Spin Echoes 431
16.3.6 Relaxation and Diffusion in Magnetic Gradients 432
16.3.7 Measurement Sensitivity 434
16.4 NMR Properties of Bulk Fluids 436
16.4.1 Hydrogen Index 436
16.4.2 Bulk Relaxation in Water and Hydrocarbons 437
16.4.3 Viscosity Correlations for Crude Oils 440
16.5 NMR Relaxation in Porous Media 442
16.5.1 Surface Interactions 443
16.5.2 Pore Size Distribution 446
16.5.3 Diffusion Restriction 448
16.5.4 Internal Magnetic Gradients 449
16.6 Operation of a First Generation Nuclear Magnetic Logging Tool 449
16.7 The NMR Renaissance of "Inside-Out" Devices 452
16.7.1 A New Approach 452
16.7.2 Numar/Halliburton MRIL 454
16.7.3 Schlumberger CMR and Subsequent Developments 455
16.7.4 LWD Devices 458
16.8 Applications and Log Examples 459
16.8.1 Tool Planners 459
16.8.2 Porosity and Free-Fluid Porosity 460
16.8.3 Pore Size Distribution and Permeability Estimation 463
16.8.4 Fluid Typing 465
16.9 Summary 471

16.10 Appendix A: Diffusion 472
References 473
Problems 477

17 Introduction to Acoustic Logging 479
17.1 Introduction to Acoustic Logging 479
17.2 Short History of Acoustic Measurements in Boreholes 480
17.3 Applications of Borehole Acoustic Logging 482
17.4 Review of Elastic Properties 483
17.5 Wave Propagation 489
17.6 Rudimentary Acoustic Logging 493
17.7 Rudimentary Acoustic Interpretation 494
References 496
Problems 497

18 Acoustic Waves in Porous Rocks and Boreholes 499
18.1 Introduction 499
18.2 A Review of Laboratory Measurements 500
18.3 Porolelastic Models of Rocks 509
18.4 The Promise of V_p/V_s 513
18.4.1 Lithology 513
18.4.2 Gas Detection and Quantification 515
18.4.3 Mechanical Properties 517
18.4.4 Seismic Applications (AVO) 518
18.5 Acoustic Waves in Boreholes 519
18.5.1 Borehole Flexural Waves 524
18.5.2 Stoneley Waves 525
References 527
Problems 529

19 Acoustic Logging Methods 531
19.1 Introduction 531
19.2 Transducers – Transmitters and Receivers 532
19.3 Traditional Sonic Logging 534
19.3.1 Some Typical Problems 540
19.3.2 Long Spacing Sonic 541
19.4 Evolution of Acoustic Devices 544
19.4.1 Arrays of Detectors 546

19.4.2 Dipole Tools 547
19.4.3 Shear Wave Anisotropy and Crossed Dipole Tools 549
19.4.4 LWD 553
19.4.5 Modeling-driven Tool Design 553
19.5 Acoustic Logging Applications 554
19.5.1 Formation Fluid Pressure 555
19.5.2 Mechanical Properties and Fractures 557
19.5.3 Permeability 559
19.5.4 Cement Bond Log 561
19.6 Ultrasonic Devices 562
19.6.1 Pulse-Echo Imaging 563
19.6.2 Cement Evaluation 565
References 566
Problems 568

20 High Angle and Horizontal Wells 573
20.1 Introduction 573
20.2 Why are HA/HZ Wells Different? 574
20.3 Measurement Response 576
20.3.1 Resistivity 577
20.3.2 Density 580
20.3.3 Neutron 582
20.3.4 Other Measurements 584
20.4 Geosteering 585
20.4.1 Deep Reading Devices for Geosteering 589
References 593
Problems 594

21 Clay Quantification 597
21.1 Introduction 597
21.2 What is Clay/Shale? 598
21.2.1 Physical Properties of Clays 599
21.2.2 Total Porosity and Effective Porosity 601
21.2.3 Shale Distribution 604
21.2.4 Influence on Logging Measurements 606
21.3 Shale Determination from Single Measurements 609
21.3.1 Interpretation of P_e in Shaly Sands 610
21.3.2 Neutron Response to Shale 613

21.3.3 Response of Σ to Clay Minerals 616
21.4 Neutron–Density Plots 617
21.5 Elemental Analysis 621
21.6 Clay Typing 624
References 624
Problems 626

22 Lithology and Porosity Estimation 629
22.1 Introduction 629
22.2 Graphical Approach for Binary Mixtures 630
22.3 Combining Three Porosity Logs 636
22.3.1 Lithology Logging: Incorporating P_e 640
22.3.2 Other Methods 643
22.4 Numerical Approaches to Lithology Determination 644
22.4.1 Quantitative Evaluation 647
22.5 General Evaluation Methods 648
References 650
Problems 651

23 Saturation and Permeability Estimation 653
23.1 Introduction 653
23.2 Clean Formations 654
23.3 Shaly Formations 658
23.3.1 Early Models 661
23.3.2 Double Layer Models 662
23.3.3 Saturation Equations 665
23.3.4 Laminated Sands 668
23.4 Carbonates and Heterogeneous Rocks 671
23.5 Permeability from Logs 674
23.5.1 Resistivity and Porosity 675
23.5.2 Petrophysical Models 676
References 681
Problems 684

Index 687

Preface

Twenty years ago, the objectives of the first edition of this book were numerous and ambitious: to demystify the process of well log analysis; to examine the physical basis of the multitude of geophysical measurements known collectively as well logging; to clearly lay out the assumptions and approximations routinely used to extract petrophysical information from these geophysical measurements; to expose the vast range of well logging instrumentation and techniques to the larger geophysical community. Finally, there was the important goal of providing a textbook for university and graduate students in Geophysics and Petroleum Engineering, where none suitable had been available before.

What's different twenty years later? First of all, *Well Logging for Earth Scientists* is long out of print. The petroleum industry, the major consumer of the geophysical information known as well logging, has changed enormously: technical staffs have been slashed, and hydrocarbons have become increasingly harder to locate, quantify, and produce. In addition, new techniques of drilling high deviation or horizontal wells have engendered a whole new family of measurement devices incorporated into the drilling string that may be used routinely or in situations where access by traditional "wireline" instruments is difficult or impossible. Petroleum deposits are becoming scarce and demand is steadily increasing. Massive corporate restructuring and the "graying" of the workforce have caused the technical competence involved in the search and exploitation of petroleum to become scarce. Although we are only attempting to address this latter scarcity with our textbook, the objectives are still ambitious.

In this thorough updating of the text, we have attempted to include all of the new logging measurement technology developed in the last twenty years and to expand the petrophysical applications of the measurements. As in the first edition, we are primarily concerned with logging techniques that lead to formation evaluation, but mention a few other applications where appropriate. We also trace the historical development of the technology as a means of better understanding it. Throughout, large sections of the text have been set in italics, which may be skipped by the casual reader. These detailed sections may be of more interest to researchers. The goals of providing a graduate level textbook as well as a useful handbook for any practicing earth scientist (geophysicist, geologist, petroleum engineer, petrophysicist) remain.

Darwin Ellis
Julian Singer

Acknowledgments

The authors would like to acknowledge the special help received from a number of individuals, without which this tome could not have been achieved.

Therefore we owe our thanks to:

Chuck Fulton, Charlie Flaum, Richard Woodhouse, and Austin Boyd for log examples;

Tom Plona, Lalitha Venkataramanan, Drew Pomerantz, Tancredi Botto, Alan Sibbit, Jacques Tabanou, Jack LaVigne, Barbara Anderson, Nikita Seleznev, and Nick Bennett for critically reviewing early versions of various chapters;

John Hsu, David Johnson, Tarek Habashy, Chris Straley, and Pabitra Sen for helpful discussions;

Charlie Case, Joe Chiaramonte, Laurent Mossé and especially to Mehdi Hizem for substantial contributions to the form and content of several chapters;

George Stewart for the drafting of the figures;

and Frank Shray, Tarek Habashy, Mark Andersen, Martin Issacs and Vicki King for help in innumerable ways with the multitude of figures.

For the deficiencies, errors, and omissions, both in the text and in these acknowledgements, the blame rests with us.

Darwin Ellis & Julian Singer

The authors also are grateful for the use of a number of figures, in this new edition, drawn from Schlumberger's Oilfield Review. The following figures are copyright Schlumberger Ltd. Used with permission.

Fig. 6.6
Fig. 12.20
Fig. 12.21
Fig. 15.9
Fig. 15.10
Fig. 15.12
Fig. 15.13
Fig. 15.14
Fig. 15.15
Fig. 15.17
Fig 15.18
Fig. 15.19
Fig. 16.9
Fig. 16.22
Fig. 16.24
Fig. 16.27
Fig. 16.32
Fig. 16.34
Fig. 16.36
Fig. 16.37
Fig 18.15
Fig. 18.16
Fig. 18.24
Fig.19.19
Fig. 19.20
Fig. 19.21
Fig. 19.26
Fig. 19.27

4 Dec. 2006

1

An Overview of Well Logging

1.1 INTRODUCTION

The French translation of the term *well logging* is *carottage électrique,** literally "electrical coring," a fairly exact description of this geophysical prospecting technique when it was invented in 1927 [1, 2]. A less literal translation might be "a record of characteristics of rock formations traversed by a measurement device in the well bore." However, well logging means different things to different people. For a geologist, it is primarily a mapping technique for exploring the subsurface. For a petrophysicist, it is a means to evaluate the hydrocarbon production potential of a reservoir. For a geophysicist, it is a source of complementary data for surface seismic analysis. For a reservoir engineer, it may simply supply values for use in a simulator.

The initial uses of well logging were for correlating similar patterns of electrical conductivity from one well to another, sometimes over large distances. As the measuring techniques improved and multiplied, applications began to be directed to the quantitative evaluation of hydrocarbon-bearing formations. Much of the following text is directed toward the understanding of the measurement devices and interpretation techniques developed for this type of formation evaluation.

Although well logging grew from the specific need of the petroleum industry to evaluate hydrocarbon accumulations, it is relevant to a number of other areas of interest to earth scientists. New measurements useful for subsurface mapping have evolved which have applications for structural mapping, reservoir description, and

*The French definition is mentioned for two reasons: as an acknowledgment of the national origin of well logging and as one of the rare cases in which Anglo-Saxon compactness is outdone by the French.

sedimentological identification. The measurements can be used to identify fractures or provide the formation mineralogy. A detailed analysis of the measurement principles precedes the discussion of these applications. In this process, well logging is seen to require the synthesis of a number of diverse physical sciences: physics, chemistry, electrochemistry, geochemistry, acoustics, and geology.

The goal of this first chapter is to discuss well logging in terms of its traditional application to formation hydrocarbon evaluation and to describe the wide variety of physical measurements which address the relevant petrophysical parameters. We begin with a description of the logging process, to provide an idea of the experimental environment in which the measurements must be made.

1.2 WHAT IS LOGGING?

The birth of logging can be dated to the first recorded event [1] at Pechelbronn on September 5, 1927 where H. Doll and the Schlumberger brothers (and a few others) made a semicontinuous resistivity measurement in that tired old field in Alsace. The operation was performed with a rudimentary device (a sonde) consisting of a bakelite cylinder with a couple of metallic electrodes on its exterior. Connecting the device to the surface was a cable/wire, thus providing us with the term wireline logging. Wireline refers to the armored cable by which the measuring devices are lowered and retrieved from the well and, by a number of shielded insulated wires in the interior of the cable, provide for the electrical power of the device and a means for the transmission of data to the surface. More recently, the devices have been encapsulated in a drill collar, and the transmission effected through the mud column. This procedure is known as logging while drilling (LWD).

1.2.1 What is Wireline Logging?

The process of logging involves a number of elements, which are schematically illustrated in Fig. 1.1. Our primary interest is the measurement device, or *sonde.* Currently, over fifty different types of these logging tools exist in order to meet various information needs and functions. Some of them are passive measurement devices; others exert some influence on the formation being traversed. Their measurements are transmitted to the surface by means of the wire line.

Much of what follows in succeeding chapters is devoted to the basic principles exploited by the measurement sondes, without much regard to details of the actual devices. It is worthwhile to mention a few general points regarding the construction of the measurement sondes. Superficially, they all resemble one another. They are generally cylindrical devices with an outside diameter on the order of 4 in. or less; this is to accommodate operation in boreholes as small as 6 in. in diameter. Their length varies depending on the sensor array used and the complexity of associated electronics required. It is possible to connect a number of devices concurrently, forming tool strings as long as 100 ft.

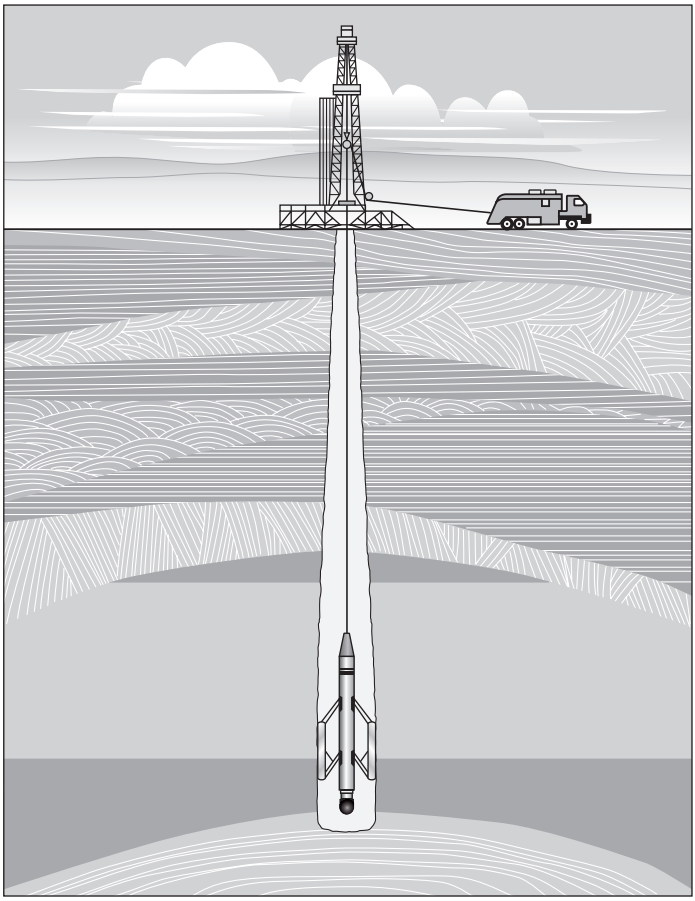


Fig. 1.1 The elements of well logging: a measurement sonde in a borehole, the wireline, and a mobile laboratory. Courtesy of Schlumberger.

Some sondes are designed to be operated in a centralized position in the borehole. This operation is achieved by the use of bow-springs attached to the exterior, or by more sophisticated hydraulically actuated "arms." Some measurements require that the sensor package (in this case called a pad) be in intimate contact with the formation. This is also achieved by the use of a hydraulically actuated back-up arm. Figure 1.2 illustrates the measurement portion of four different sondes. On the right is an example of a centralized device which uses four actuated arms. There is a measurement pad at the extremity of each arm. Second from the right is a more sophisticated pad device, showing the actuated back-up arm in its fully extended position. Third from the right is an example of a tool which is generally kept centered in the borehole by external bow-springs, which are not shown in the photo. The tool on the left is similar to the

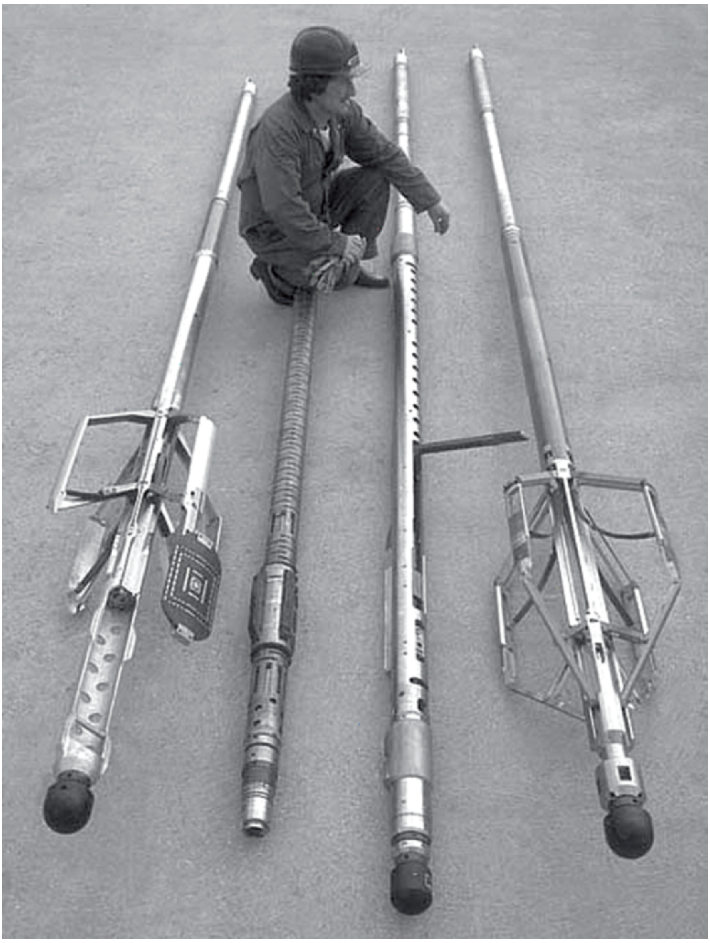


Fig. 1.2 Examples of four logging tools. The dipmeter, on the left, has sensors on four actuated arms, which are shown in their fully extended position. Attached to the bottom of one of its four arms is an additional electrode array embedded in a rubber "pad." It is followed by a sonic logging tool, characterized by a slotted housing, and then a density device with its hydraulically activated back-up arm fully extended. The tool on the extreme right is another version of a dipmeter with multiple electrodes on each pad. Courtesy of Schlumberger.

first device but has an additional sensor pad which is kept in close contact with the formation being measured.

These specially designed instruments, which are sensitive to one or more formation parameters of interest, are lowered into a borehole by a surface instrumentation truck. This mobile laboratory provides the downhole power to the instrument package. It provides the cable and winch for the lowering and raising of the sonde, and is equipped

with computers for data processing, interpretation of measurements, and permanent storage of the data.

Most of the measurements which will be discussed in succeeding chapters are continuous measurements. They are made as the tool is slowly raised toward the surface. The actual logging speeds vary depending on the nature of the device. Measurements which are subject to statistical precision errors or require mechanical contact between sensor and formation tend to be run more slowly, between 600 ft and 1,800 ft/h – newer tools run as fast as 3,600 ft/h. Some acoustic and electrical devices can be withdrawn from the well, while recording their measurements, at much greater speeds. The traditional sampling provides one averaged measurement for every 6 in. of tool travel. For some devices that have good vertical resolution, the sampling interval is 1.2 in. There are special devices with geological applications (such as the determination of depositional environment) which have a much smaller vertical resolution; their data are sampled so as to resolve details on the scale of millimeters.

In the narrowest sense, logging is an alternate or supplement to the analysis of cores, side-wall samples, and cuttings. Although often preferred because of the possibility of continuous analysis of the rock formation over a given interval, economic and technical problems limit the use of cores.* Side-wall cores obtained from another phase of wireline operations give the possibility of obtaining samples at discrete depths after drilling has been completed. Side-wall cores have the disadvantage of returning small sample sizes, as well as the problem of discontinuous sampling. Cuttings, extracted from the drilling mud return, are one of the largest sources of subsurface sampling. However, the reconstitution of the lithological sequence from cuttings is imprecise due to the problem of associating a depth with any given sample.

Although well logging techniques (with the exception of side-wall sampling) do not give direct access to the physical rock specimens, they do, through indirect means, supplement the knowledge gained from the three preceding techniques. Well logs provide continuous, in situ measurements of parameters related to porosity, lithology, presence of hydrocarbons, and other rock properties of interest.

1.2.2 What is LWD?

The crucial element in logging that has so far been glossed over, is the wellbore and the drilling process that creates it. Although it is beyond the scope of this volume to discuss drilling, there are several aspects that merit mention in their relationship to logging. To assist drillers in the complex task of a rotary drilling operation, a number of types of information like the downhole weight on bit and the downhole torque at bit are desirable in real time. To respond to this need, a type of service known as measurement while drilling (MWD) began to develop in the late 1970s [3]. A typical MWD system consisted of a downhole sensor unit close to the drill bit, a power source, a telemetry system, and equipment on the surface to receive and display data. The

*Coring takes time, and is therefore expensive. In many soft and friable rocks, it is only possible to recover part of the interval cored.

telemetry system was often a mud pulse system that used coded mud pressure pulses to transmit (at a very slow rate of a few bits per second) the measurements from the downhole subassembly. The power source was a combination of a generating turbine, deriving its power from the mud flow, and batteries. The measurement subassembly evolved in complexity from measurements of the weight and torque on bit to include the borehole pressure and temperature, mud flow rate, a natural gamma ray (GR) measurement, and a rudimentary resistivity measurement.

For wells that are primarily drilled vertically, wireline logging, which relies on gravity for the descent of the tool package, is well adapted to obtaining the measurements used in formation evaluation. However, vertical wells are not always the norm. There are a number of reasons why one might wish to drill a well with some deviation from the vertical. A short list might include: drilling multiple wells from a single surface location as in the case of offshore platforms, avoiding a geologic feature such as a salt dome, or to maximize the lateral extent of the wellbore in a reservoir by drilling parallel to the reservoir boundaries. Although a number of so-called conveyance systems (for example, coiled tubing) were innovated to "convey" wireline logging tools through the complex geometry of the nonvertical well, another technology has arisen to deal with the situation. It is referred to as LWD and provides, in addition to drilling-specific MWD measurements, a family of measurements entirely analogous to the measurements of traditional wireline logging.

The LWD tools are all built into heavy thick-walled drill collars – the special portion of the drill string used to counter buoyancy and provide stiffness to the lower segments of the drill string. Thus, like the wireline tools all the LWD resemble one another. In Fig. 1.3 one particular version is shown that contains several sensors. The sensors are built into the wall of the drill collar with some protrusions. However, an adequate channel is provided to accommodate the mud flow. As shown in the two versions of the figure, the device can be run either "slick" or with an attached clamped-on external "stabilizer." This latter device centralizes the drill collar and its contained sensors. When the unit is run in the "slick" mode it can, in the case of a horizontal well, certainly ride on the bottom of the hole. Figure 1.3 also illustrates an interesting feature of LWD. As the drill collar is rotated, data can be acquired from multiple azimuths around the borehole, something not often achievable with a wireline.

Unlike wireline tools that are generally of a standard diameter, many of the LWD tools come in families of sizes (e.g., 4, 6, and 8 in.). This is to accommodate popular drilling bit sizes and collar sizes since the LWD device must conform to the drilling string.

Another difference between LWD and wireline logging arises from the rate of drilling which is not an entirely controllable parameter. Since there is no simple way to record depth as the data are acquired, they are instead acquired in a time-driven mode. This results in an uneven sampling rate of the data when put on a depth scale. Surface software has been developed to redistribute the time-sampled data into equally spaced data along the length of the well.

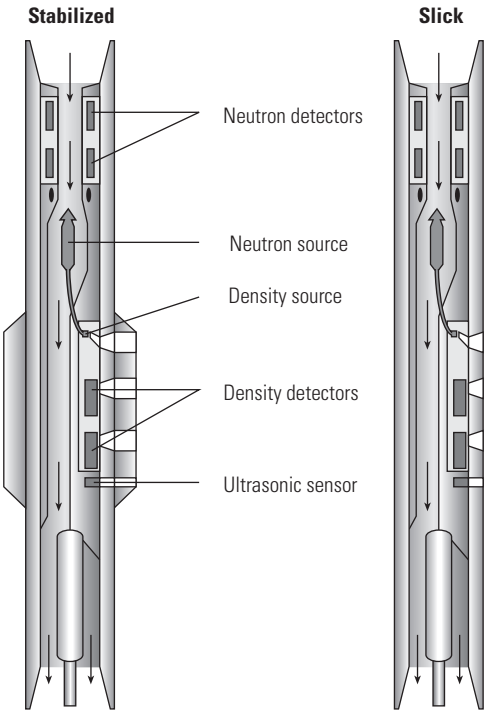


Fig. 1.3 An LWD device containing a neutron and density measurement. The panel on the left shows the tool with clamp-on wear bands so that the diameter is close to that of the drill bit. In the right panel the tool is shown in the "slick" mode. Courtesy of Schlumberger.

1.3 PROPERTIES OF RESERVOIR ROCKS

Before discussing the logging measurements which are used to extract information concerning the rock formations encountered in the borehole, let us briefly consider some of the properties of reservoir rocks, in order to identify parameters of interest and to gain some insight into the reasons for the indirect logging measurements which will be described later. The following description could be modified or augmented depending on the application [4,5]. It would be different when prepared by a geologist, a reservoir engineer, a geophysicist, or a petrophysicist.

The intergranular nature of the porous medium which constitutes the reservoir rock is fundamental. Above all, the rock must be porous. A measurement of its porosity is of primary consideration.

The rock may be clean or it may contain clays. The clean rock is of a given lithological type which in itself is an important parameter. The presence of clays can affect log readings as well as have a very important impact on the permeability which is a measure of the ease of extraction of fluids from the pore space.

The rock may be consolidated or unconsolidated. This mechanical property will influence the acoustic measurements made and have an impact on the stability of the borehole walls as well as on the ability of the formation to produce flowing fluids.

The formation may be homogeneous, fractured, or layered. The existence of fractures, natural or induced, alter the permeability significantly. Thus the detection of fractures and the prediction of the possibility of fracturing is of some importance. In layered rocks the individual layers can have widely varying permeabilities and thicknesses that range from a fraction of an inch to tens of feet. Identifying thin-layered rocks is a challenge.

The internal surface area of the reservoir rock is used to evaluate the possibilities of producing fluids from the pore space. It is related to the granular nature, which can be described by the grain size and distribution.

Although we have concentrated, so far, on the properties of the rock, it is usually the contained fluid which is of commercial interest. It is crucial to distinguish between hydrocarbons and brine which normally occupy the pore space. A term frequently used to describe the partitioning of the hydrocarbon and the brine is the "saturation"; the water saturation is the percentage of the porosity occupied by brine rather than hydrocarbons.

In the case of hydrocarbons, it important to distinguish between liquid and gas. This can be of considerable importance not only for the ultimate production procedure but also for the interpretation of seismic measurements, since gas-filled formations often produce distinct reflections.

Although the nature of the fluid is generally inferred from indirect logging measurements, there are wireline devices which are specifically designed to take samples of the formation fluids and measure the fluid pressure at interesting zones. The pressure and temperature of the contained fluids are important for both the drilling and production phases. Overpressured regions must be identified and taken into account to avoid blowouts. Temperature may have a large effect on the fluid viscosity: below a certain temperature fluids may be too viscous to flow. However, the description of these devices is beyond the scope of this book.

The contained fluids are closely linked to the structural shape of the rock body. It is of importance to know whether the rock body corresponds, for example, to a small river bar of a minor meandering stream or a vast limestone plain. This will have an important impact on the estimates of reserves and the subsequent drilling for production.

1.4 WELL LOGGING: THE NARROW VIEW

Well logging plays a central role in the successful development of a hydrocarbon reservoir. Its measurements occupy a position of central importance in the life of a well, between two milestones: the surface seismic survey, which has influenced the decision for the well location, and the production testing. The traditional role of wireline logging has been limited to participation primarily in two general domains: formation evaluation and completion evaluation.

The goals of formation evaluation can be summarized by a statement of four questions of primary interest in the production of hydrocarbons:

- Are there any hydrocarbons, and if so are they oil or gas?

  First, it is necessary to identify or infer the presence of hydrocarbons in formations traversed by the wellbore.

- Where are the hydrocarbons?

  The depth of formations which contain accumulations of hydrocarbons must be identified.

- How much hydrocarbon is contained in the formation?

  An initial approach is to quantify the fractional volume available for hydrocarbon in the formation. This quantity, porosity, is of utmost importance. A second aspect is to quantify the hydrocarbon fraction of the fluids within the rock matrix. The third concerns the areal extent of the bed, or geological body, which contains the hydrocarbon. This last item falls largely beyond the range of traditional well logging.

- How producible are the hydrocarbons?

  In fact, all the questions really come down to just this one practical concern. Unfortunately, it is the most difficult to answer from inferred formation properties. The most important input is a determination of permeability. Many empirical methods are used to extract this parameter from log measurements with varying degrees of success. Another key factor is oil viscosity, often loosely referred to by its weight, as in heavy or light oil.

Formation evaluation is essentially performed on a well-by-well basis. A number of measurement devices and interpretation techniques have been developed. They provide, principally, values of porosity and hydrocarbon saturation, as a function of depth, using the knowledge of local geology and fluid properties that is accumulated as a reservoir is developed. Because of the wide variety of subsurface geological formations, many different logging tools are needed to give the best possible combination of measurements for the rock type anticipated. Despite the availability of this rather large number of devices, each providing complementary information, the final answers derived are mainly three: the location of oil-bearing and gas-bearing formations, an estimate of their producibility, and an assessment of the quantity of hydrocarbon in place in the reservoir.

The second domain of traditional wireline logging is completion evaluation. This area is comprised of a diverse group of measurements concerning cement quality, pipe and tubing corrosion, and pressure measurements, as well as a whole range of production logging services. Although completion evaluation is not the primary focus of this book, some of the measurement techniques used for this purpose, such as clay mineral identification and estimation of rock mechanical properties, are discussed.

1.5 MEASUREMENT TECHNIQUES

In the most straightforward application, the purpose of well logging is to provide measurements which can be related to the volume fraction and type of hydrocarbon present in porous formations. Measurement techniques are used from three broad disciplines: electrical, nuclear, and acoustic. Usually a measurement is sensitive either to the properties of the rock or to the pore-filling fluid.

The first technique developed was a measurement of electrical conductivity. A porous formation has an electrical conductivity which depends upon the nature of the electrolyte filling the pore space. Quite simply, the rock matrix is nonconducting, and the usual saturating fluid is a conductive brine. Therefore, contrasts of conductivity are produced when the brine is replaced with nonconductive hydrocarbon. Electrical conductivity measurements are usually made at low frequencies. A d.c. measurement of spontaneous potential is made to determine the conductivity of the brine.

Another factor which affects the conductivity of a porous formation is its porosity. Brine-saturated rocks of different porosity will have quite different conductivities; at low porosity the conductivity will be very low, and at high porosity it can be much larger. Thus in order to correctly interpret conductivity measurements as well as to establish the importance of a possible hydrocarbon show, the porosity of the formation must be known.

A number of nuclear measurements are sensitive to the porosity of the formation. The first attempt at measuring formation porosity was based on the fact that interactions between high-energy neutrons and hydrogen reduce the neutron energy much more efficiently than other formation elements. However, it will be seen later that a neutron-based porosity tool is sensitive to all sources of hydrogen in a formation, not just that contained in the pore spaces. This leads to complications in the presence of clay-bearing formations, since the hydrogen associated with the clay minerals is seen by the tool in the same way as the hydrogen in the pore space. As an alternative, gamma ray attenuation is used to determine the bulk density of the formation. With a knowledge of the rock type, more specifically the grain density, it is simple to convert this measurement to a fluid-filled porosity value.

The capture of low-energy neutrons by elements in the formation produces gamma rays of characteristic energies. By analyzing the energy of these gamma rays, a selective chemical analysis of the formation can be made. This is especially useful for identifying the minerals present in the rock. Interaction of higher energy neutrons with the formation permit a direct determination of the presence of hydrocarbons through the ratio of C to O atoms.

Nuclear magnetic resonance, essentially an electrical measurement, is sensitive to the quantity and distribution of free protons in the formation. Free protons occur uniquely in the fluids, so that their quantity provides another value for porosity. Their distribution, in small pores or large pores, leads to the determination of an average pore size and hence, through various empirical transforms, to the prediction of permeability. The viscosity of the fluid also affects the movement of the protons during a resonance measurement, so that the data can be interpreted to give viscosity.

Acoustic measurements of compressional and shear velocity can be related to formation porosity and lithology. In reflection mode, acoustic measurements can yield images of the borehole shape and formation impedance; analysis of the casing flexural wave can be used to measure the integrity of casing and cement. Using low-frequency monopole transmitters, the excitation of the Stoneley wave is one way to detect fractures or to generate a log related to formation permeability. Techniques of analyzing shear waves and their dispersion provide important geomechanical inputs regarding the near borehole stress field. These are used in drilling programs to avoid borehole break-outs or drilling-induced fractures.

The one impression that should be gleaned from the above description is that logging tools measure parameters related to but not the same as those actually desired. It is for this reason that there exists a separate domain associated with well logging known as interpretation. Interpretation is the process which attempts to combine a knowledge of tool response with geology, to provide a comprehensive picture of the variation of the important petrophysical parameters with depth in a well.

1.6 HOW IS LOGGING VIEWED BY OTHERS?

As the first exhibit, refer to Table 1.1, taken from Serra [6]. It is an abbreviated genealogy of the geological parameters of interest concerning the depositional environment. Bed composition is the only item which is considered in any detail here. It is broken down into the framework and the fluid. The framework must be identified in terms of its mineralogical family. The clay, if present, needs to be quantified. Notice that the common term *matrix* refers, in logging, to the rock formation. Clay, or shale, is treated separately. The fluid content must be separated into water and hydrocarbon. A variety of logging measurements provide quantitative information regarding the final items of the table. In the original table, dozens of logging measurements are shown to be linked to the geological parameters [6].

The second exhibit, from Pickett [7] is shown in Table 1.2. It indicates some of the applications for borehole measurements in petroleum engineering. The thirteen different applications fall into three fairly distinct categories: identification, estimation, and production. Identification concerns subsurface mapping or correlation. Estimation is the more quantitative aspect of well logging, in which physical parameters such as water saturation or pressure are needed with some precision. The final category consists of well logging measurements which are used to monitor changes in a reservoir during its production phase.

The third and final exhibit, Table 1.3, is a list of well log uses prepared by a commercial education firm. If taken literally, it demonstrates that everyone needs well logs. To test the validity of this hypothesis, we need to look at the measurements in more detail. To start this analysis, we turn to the historical origins of logging to discover why it was called electrical coring.

Table 1.1 Geological parameters of interest concerning depositional environment. Only the compositional family is shown in any detail. The final categories are accessible by a wide variety of logging measurements. Adapted from Serra [6].

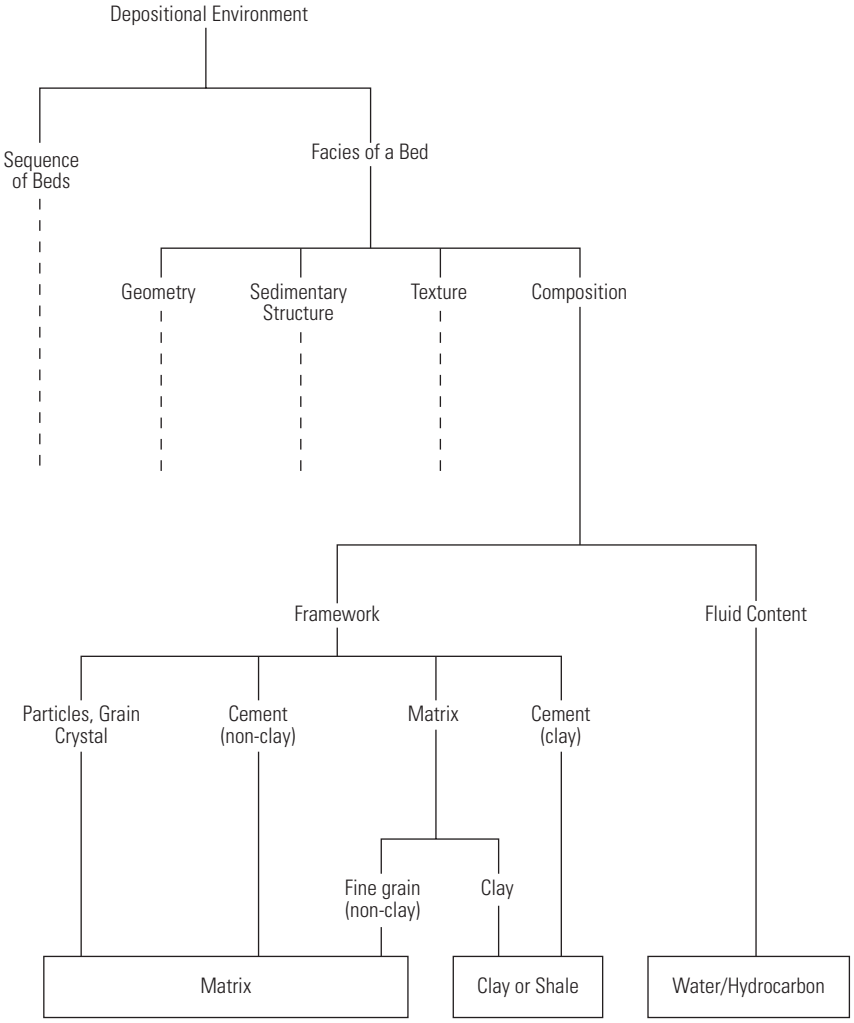


Table 1.2 Uses of well logging in petroleum engineering. Adapted from Pickett [7].

Logging applications for petroleum engineering
Rock typing
Identification of geological environment
Reservoir fluid contact location
Fracture detection
Estimate of hydrocarbon in place
Estimate of recoverable hydrocarbon
Determination of water salinity
Reservoir pressure determination
Porosity/pore size distribution determination
Water flood feasibility
Reservoir quality mapping
Interzone fluid communication probability
Reservoir fluid movement monitoring

Table 1.3 Questions answered by well logs, according to someone trying to sell a well log interpretation course.

USES OF LOGS

A set of logs run on a well will usually mean different things to different people. Let us examine the questions asked–and/or answers sought by a variety of people.

The Geophysicist:

As a Geophysicist what do you look for?

'' Are the tops where you predicted?
'' Are the potential zones porous as you have assumed from seismic data?
'' What does a synthetic seismic section show?

The Geologist:

The Geologist may ask:

'' What depths are the formation tops?
'' Is the environment suitable for accumulation of Hydrocarbons?
'' Is there evidence of Hydrocarbon in this well?
'' What type of Hydrocarbon?
'' Are Hydrocarbons present in commercial quantities?
'' How good a well is ti?
'' What are the reserves?
'' Could the formation be commercial in an offset well?

The Drilling Engineer:

" What is the hole volume for cementing?
" Are there any Key-Seats or severe Dog-legs in the well?
" Where can you get a good packer seat for testing?
" Where is the best place to set a Whipstock?

The Reservoir Engineer:

The Reservoir Engineer needs to know:

" How thick is the pay zone?
" How Homogeneous is the section?
" What is the volume of Hydrocarbon per cubic metre?
" Will the well pay-out?
" How long will it take?

The Production Engineer:

The Production Engineer is more concerned with:

" Where should the well be completed (in what zone(s))?
" What kind of production rate can be expected?
" Will there be any water production?
" How should the well be completed?
" Is the potential pay zone hydraulically isolated?

REFERENCES

1. Allaud L, Martin M (1977) Schlumberger: the history of a technique. Wiley, New York
2. Segesman FF (1980) Well logging method. Geophysics 45(11):1667–1684
3. Segesman FF (1995) Measurement while drilling. Reprint No 40, SPE Reprint Series, SPE, Dallas, TX
4. Jordan JR, Campbell F (1984) Well logging I – borehole environment, rock properties, and temperature logging. SPE Monograph Series, SPE, Dallas, TX
5. Collins RE (1961) Flow of fluids through porous materials. Reinhold, New York
6. Serra O (1984) Fundamentals of well-log interpretation. Elsevier, Amsterdam, The Netherlands
7. Pickett GR (1974) Formation evaluation. Unpublished lecture notes, Colorado School of Mines, Golden, CO

2

Introduction to Well Log Interpretation: Finding the Hydrocarbon

2.1 INTRODUCTION

This chapter presents a general overview of the problem of log interpretation and examines the basic questions concerning a formation's potential hydrocarbon production that are addressed by well logs. The borehole environment is described in terms of its impact on the electrical logging measurements, and all of the qualitative concepts necessary for simple log interpretation are presented.

Without going into the specifics of the logging measurements, the log format conventions are presented, and an example is given that indicates the process of locating possible hydrocarbon zones from log measurements. Although the interpretation example is an exercise in the qualitative art of well log analysis, it raises a number of issues. These relate to the extraction of quantitative petrophysical parameters from the logging measurements. This extraction process is the subject of subsequent chapters. Once these relationships are established, more quantitative procedures of interpretation will be described.

2.2 RUDIMENTARY INTERPRETATION PRINCIPLES

Log interpretation, or formation evaluation, requires the synthesis of logging tool response physics, geological knowledge, and auxiliary measurements or information to extract the maximum petrophysical information concerning subsurface formations. In this section, a subset of this procedure is considered: wellsite interpretation. This subset refers to the rapid and somewhat cursory approach to scanning an available set

of logging measurements, and the ability to identify and draw some conclusion about zones of possible interest. These zones, probably hydrocarbon-bearing, will warrant a closer and more quantitative analysis, which is possible only by the inclusion of additional knowledge and measurements.

The three most important questions to be answered by wellsite interpretation are:

1. Does the formation contain hydrocarbons, and if so at what depth and are they oil or gas?
2. If so, what is the quantity present?
3. Are the hydrocarbons recoverable?

In order to see how logging measurements can provide answers to these questions, a few definitions must first be set out. *Porosity* is that fraction of the volume of a rock which is not matrix material and may be filled with fluids. Figure 2.1 illustrates a unit volume of rock. The pore space has a fractional volume denoted by ϕ, and the matrix material occupies the remaining fraction of the volume, $1 - \phi$.

In addition to these fractional volumes, it is useful to use fractions in describing the contained pore fluids. *Water saturation*, S_w, is the fraction of the porosity ϕ which contains water. This fractional volume is also indicated in Fig. 2.1. In an oil/water mixture, the oil saturation, S_o, is given by $1 - S_w$. Note that the fractional volume occupied by the water is given by the product $\phi \times S_w$, and the total fraction of formation occupied by the oil by $\phi \times S_o$. The *irreducible water saturation*, S_{wirr}, corresponds to water that cannot be removed from a rock without applying undue pressure or temperature. The *residual oil saturation*, S_{or}, corresponds to oil that cannot be moved without resorting to special recovery techniques.

Since one of the principal logging measurements used for the quantification of hydrocarbon saturation is electrical in nature, it is necessary to mention some of the terminology used to describe these measurements. Electrical measurements are natural for this determination, since current can be induced to flow in a porous rock which contains a conductive electrolyte. The resistivity of a formation is a measure

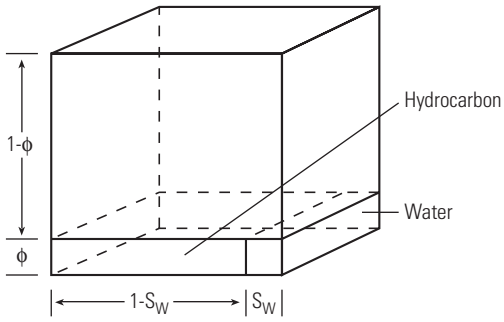


Fig. 2.1 A unit volume of formation showing the porosity ϕ and the fractional pore volume of water S_w. The fractional volume of hydrocarbons is $\phi \times (1 - S_w)$.

of the ease of electric conduction. Resistivity, a characteristic akin to resistance, is discussed in much more detail later. Replacing the conductive brine of a porous medium with essentially nonconducting hydrocarbons can be expected to impede the flow of current and thus increase its resistivity.

The resistivity of the undisturbed region of formation, somewhat removed from the borehole, is denoted by R_t, or true resistivity. As is implied, the formation resistivity R_t is derived from measurements that yield an apparent resistivity. These measurements can then be corrected, when necessary, to yield the true formation resistivity. In the region surrounding the wellbore, where the formation has been disturbed by the invasion of drilling fluids, the resistivity can be quite different from R_t. This zone is called the flushed zone, and its resistivity is denoted by R_{xo}.

Two other resistivities will be of interest: the resistivity of the brine, R_w, which may be present in the pore space, and the resistivity of the filtrate of the drilling fluid, R_{mf}, which can invade the formation near the wellbore and displace the original fluids.

Returning to the three questions that must be addressed by wellsite interpretation, refer to Fig. 2.2, which attempts to show the interrelationships implicit in the questions. Regarding question 1, the selection of an appropriate zone must be addressed. It is known that formations with low shale content are much more likely to produce accumulated hydrocarbons. Thus the first task is to identify the zones with a low-volume

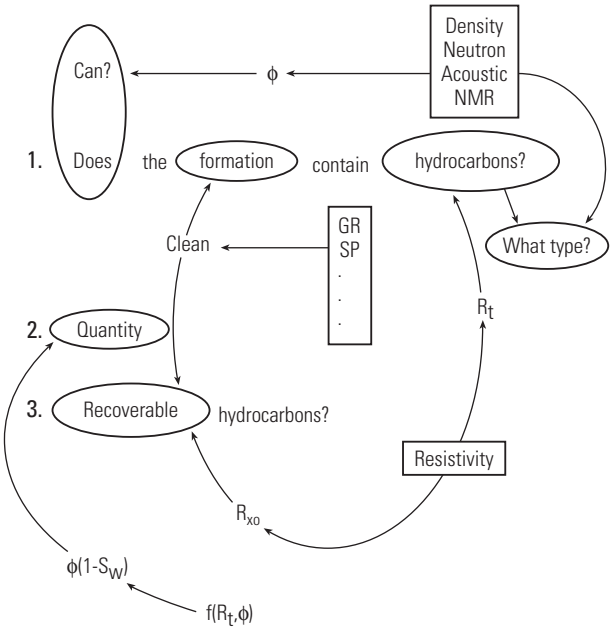


Fig. 2.2 A schematic representation of the logging measurements used and the petrophysical parameters determined for answering the basic questions of wellsite interpretation.

fraction of shale (V_{shale}), also known as clean zones. This task has traditionally been accomplished through two measurements: the gamma ray, and the spontaneous potential (SP). The qualitative behavior of the SP (a voltage measurement reported in mV) is to become less negative with increases in formation shale content. The gamma ray signal will generally increase in magnitude according to the increase in shale content. Other techniques have been used recently, for example the separation between the neutron and density measurements, the nuclear magnetic resonance (NMR) distribution, and elemental spectroscopy analysis.

The second step is to answer the question: "Can the formation contain hydrocarbons?" This condition will be possible only if the formation is porous. Four logging devices yield estimates of porosity. In the case of the *density tool*, the measured parameter is the formation bulk density ρ_b. As porosity increases, the bulk density ρ_b decreases. The *neutron tool* is sensitive to the presence of hydrogen. Its reported measurement is the neutron porosity ϕ_n, which reflects the value of the formation hydrogen content. The *acoustic tool* measures the compressional wave slowness or, interval transit time Δt (reported in μs/ft). It will increase with porosity. The total NMR signal depends on the amount of hydrogen and therefore increases with porosity.

Once a porous, clean formation is identified, the analyst is faced with deciding whether it contains hydrocarbons or not. This analysis is done in quite an indirect way, using the resistivity R_t of the formation. Basically, if the porous formation contains conductive brine, its resistivity will be low. If, instead, it contains a sizable fraction of nonconducting hydrocarbon, then the formation resistivity will be rather large. However, there is also an effect of porosity on the resistivity. As porosity increases, the value of R_t will decrease if the water saturation remains constant. The hydrocarbons may be oil or gas. The distinction is most easily made by comparing the formation density and neutron porosity measurement, as discussed in Section 2.6.

In order to answer question 2 and determine the quantity of hydrocarbon present in the formation, the product of porosity and saturation ($\phi \times S_w$) must be obtained. For the moment, all that need be known is that the water saturation S_w is a function of both formation resistivity R_t and porosity ϕ.

Another common resistivity measurement, R_{xo}, corresponds to the resistivity of the flushed zone, a region of formation close to the borehole, where drilling fluids may have invaded and displaced the original formation fluids. The measurement of R_{xo} is used to get some idea of the recoverability of hydrocarbons in the following way. If the value of R_{xo} is found to be the same as the value of R_t, then it is most likely that the original formation fluids are present in the flushed zone, indicating that no formation fluid displacement has taken place. However, if R_{xo} is different than R_t, then some invasion has taken place, and the fluids are movable. This can be taken one step further. If the ratio of R_{xo} to R_t is the same as the ratio of the water resistivities in the two zones (R_{mf} and R_w), then the flushed and non-flushed zones have either the same quantity of hydrocarbons or none. Any hydrocarbons are unlikely to be producible in this case. If the ratio of R_{xo} to R_t is less than that of R_{mf} to R_w, then some hydrocarbons have been moved by the drilling fluid and will probably be producible.

A summary of these relations is found in Table 2.1.

Table 2.1 A summary of phenomenological interpretation.

Descriptor	Measurement	Functional behavior		
Clean/shaley	SP	$V_{shale} \uparrow$	$\rightarrow$	SP $\uparrow$
	GR	$V_{shale} \uparrow$	$\rightarrow$	GR $\uparrow$
Porosity (ϕ)	Density	$\phi \uparrow$	$\rightarrow$	$\rho_b \downarrow$
	Neutron	$\phi \uparrow$	$\rightarrow$	$\phi_n \uparrow$
	Acoustic	$\phi \uparrow$	$\rightarrow$	$\Delta t \uparrow$
Hydrocarbon	R_t	$S_w \uparrow$	$\rightarrow$	$R_t \downarrow$
		$(S_o \uparrow$	$\rightarrow$	$R_t \uparrow)$
		$\phi \downarrow$	$\rightarrow$	$R_t \uparrow$
Recoverable/ movable	R_{xo}vs.R_t (shallow vs. deep)	$R_{xo} = R_t$	$\rightarrow$	No invasion
		$R_{xo} = R_t$	$\rightarrow$	If $R_{mf} = R_w$, no movable hydrocarbon
		$\frac{R_{xo}}{R_t} \neq \frac{R_{mf}}{R_w}$	$\rightarrow$	Moved fluid

2.3 THE BOREHOLE ENVIRONMENT

The borehole environment in which logging measurements are made, is of some interest from the standpoint of logging tool designs and the operating limitations placed upon them. Furthermore, it is important in terms of the disturbance it causes in the surrounding formation in which properties are being measured.

Some characterization of the borehole environment can be made using the following set of generalizations. Well depths are ordinarily between 1,000 and 20,000 ft, with diameters ranging from 5 to 15 in. Of course, larger ones can exist. A truly vertical hole is rarely encountered, and generally the deviation of the borehole is between 0° and 5°. More deviated wells, between 20° and 60° are often encountered offshore. The temperature, at full depth, ranges between 100°F and 300°F.

Since the early 1990s an increasing number of horizontal wells have been drilled. These are drilled at a suitable deviation down to near the top of the reservoir, at which point the deviation is increased until they penetrate the reservoir within a few degrees of horizontal. They are then maintained within 5° of horizontal between 1,000 and 5,000 ft.

The drilling fluid, or mud, ranges in density between 9 and 16 lb/gal; weighting additives such as barite ($BaSO_4$) or hematite are added to ensure that the hydrostatic pressure in the wellbore exceeds the fluid pressure in the formation pore space to prevent disasters such as blowouts. The salinity of the drilling mud ranges between 1,000 and 200,000 ppm of NaCl. The generally overpressured wellbore causes invasion of a porous and permeable formation by the drilling fluid. The result of the invasion process is conveyed by Fig. 2.3. In the permeable zones, due to the imbalance

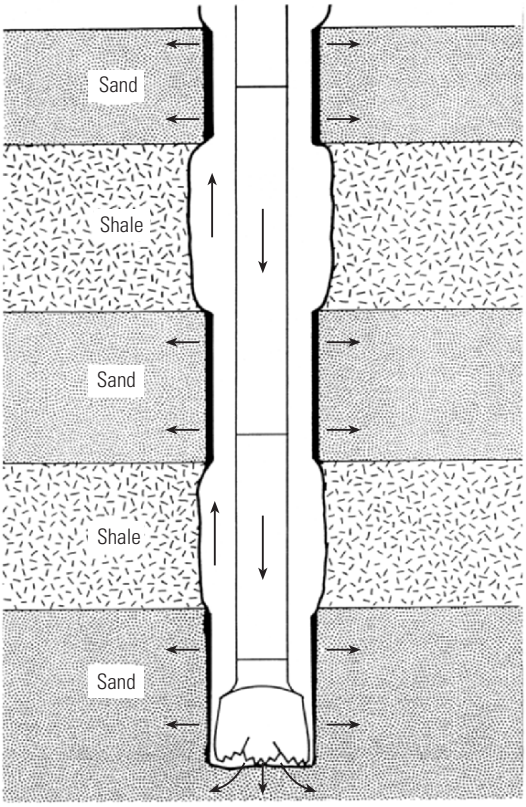


Fig. 2.3 Degradation of the formation during and after drilling. Overpressured mud is indicated to be invading porous and permeable sand formations with the formation of a mudcake. The mud circulation also causes borehole washout in the shale zones. From Dewan [2].

in hydrostatic pressure, the mud begins to enter the formation but is normally rapidly stopped by the buildup of a mudcake of the clay particles in the drilling fluid.

This initial invasion is known as the spurt loss. As the well is drilled deeper, further invasion occurs slowly through the mudcake, either dynamically, while mud is being circulated, or statically when the mud is stationary. In addition, the movement of the drill string can remove some mudcake, causing the process to be restarted. Thus, while a typical depth of invasion at the time of wireline logging is 20 in., the depth can reach 10 ft or more in certain conditions.

To account for the distortion which is frequently present with electrical measurements, a simplified model of the borehole/formation in vertical wells with horizontal beds has evolved. It considers the invaded formation of interest, of resistivity R_t, to be surrounded by "shoulder" beds of resistivity R_s. The invasion is represented by the profile shown schematically in Fig. 2.4, along with the regions and parameters of interest, starting with the mudcake of thickness h_{mc} and resistivity R_{mc}. The next

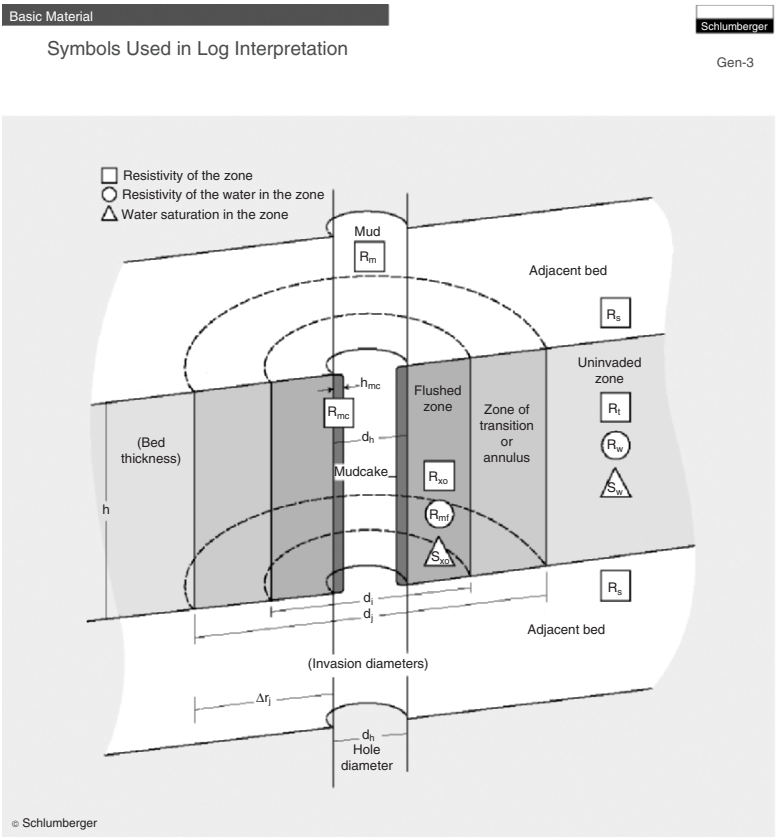


Fig. 2.4 Schematic model of the borehole and formation used to describe electric-logging measurements and corrections. Courtesy of Schlumberger.

annular region of diameter d_i is the flushed zone whose resistivity is denoted by R_{xo}, determined principally by the resistivity of the mud filtrate. Beyond the invaded zone lies the uninvaded or virgin zone with resistivity R_t. A transition zone separates the flushed zone from the virgin zone.* The transition may be smooth, but when hydrocarbons are present its resistivity can be significantly lower than either R_{xo} or R_t. This condition is known as an annulus and occurs mainly when the oil or gas is more mobile than the formation water, so that the formation water displaced from the flushed zone accumulates in the transition zone while the oil or gas is displaced beyond it. The annulus disappears with time, but can still exist at the time of logging.

*The invaded zone was originally described as a succession of radial layers starting with R_{x0}, and followed by R_{x1}, R_{x2}, etc. The numerical portion of the subscript was originally supposed to indicate the distance from the borehole wall, e.g., R_{x1} indicated 1 in. into the formation. R_{x0} was the resistivity at the borehole wall, but over time this became R_{xo} and the other distances fell out of use [1].

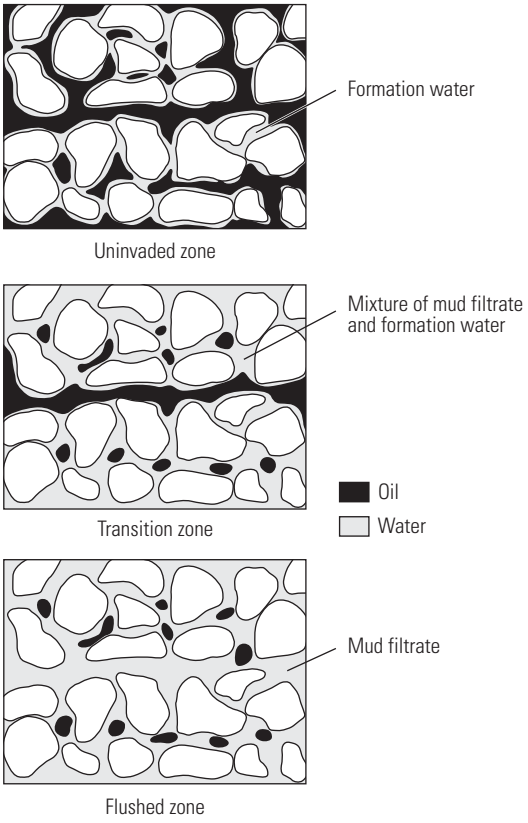


Fig. 2.5 Distribution of pore fluids in zones around a well which initially contained hydrocarbons. From Dewan [2].

The simplest model, known as the step-profile model, ignores the transition zone and describes the invaded zone in terms of just two parameters, the resistivity R_{xo} and the diameter d_i. Figure 2.5 indicates schematically the distribution of pore fluids in the uninvaded, transition, and flushed zones. This model also assumes azimuthal symmetry around the borehole. In a horizontal well gravity can cause the heavier mud filtrate to sink below the well, leaving more of the lighter oil or gas above it. Gravity effects can also affect the fluid distribution around deviated wells or in highly dipping beds.

Figure 2.5 is valid for both wireline and LWD logs. LWD logs are normally recorded a few hours after a formation is drilled, and therefore encounter less invasion than that seen by the wireline logs, which may be recorded several days after drilling. However this is not always the case: some LWD logs are recorded later while the drill string is being run out of the hole from a deeper total depth.

2.4 READING A LOG

Reading a log with ease requires familiarity with some of the standard log formats. The formats for traditional logs and most field logs are shown in Fig. 2.6 and can be seen to contain three tracks. A narrow column containing the depth is found between track 1 and tracks 2 and 3. The latter are contiguous.

The top illustration shows the normal linear presentation, with the grid lines in all three tracks having linear scales each with ten divisions. The middle figure shows the logarithmic presentation for tracks 2 and 3. Four decades are drawn to accommodate

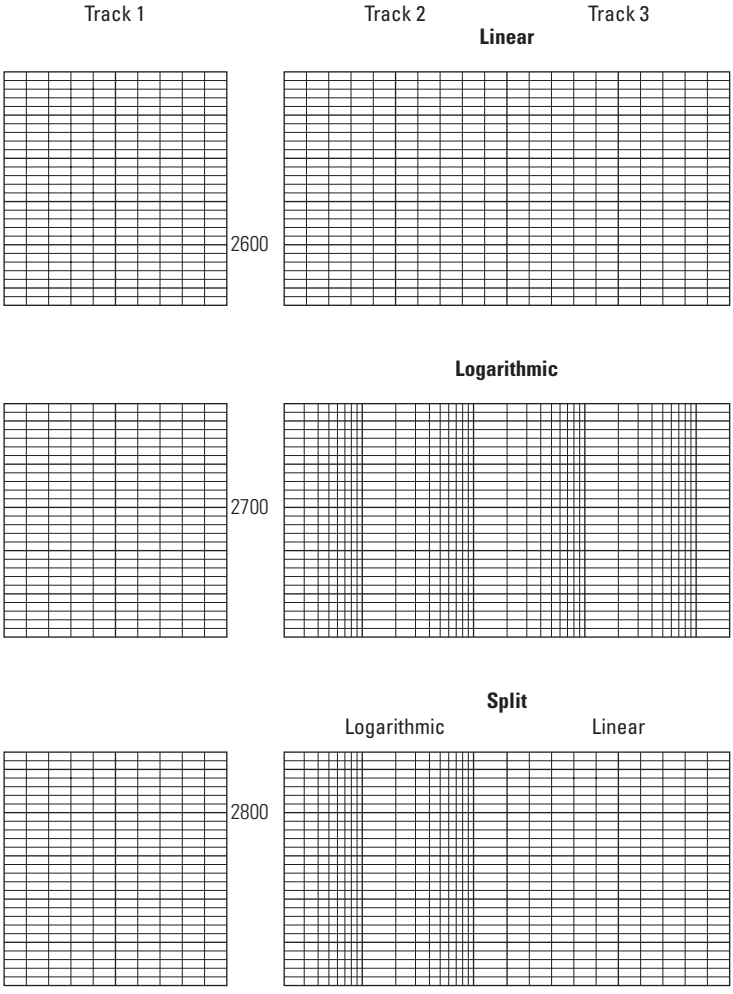


Fig. 2.6 Standard log presentation formats.

the electrical measurements, which can have large dynamic ranges. Note that the scale begins and ends on a multiple of two rather than unity. The bottom illustration is a hybrid scale with a logarithmic grid on track 2 and a linear one in track 3. Electrical measurements that may spill over from track 2 into track 3 will still be logarithmic even though the indicated scale is linear.

The depth is shown by the numbers in the center track and the horizontal lines. In Fig. 2.6 the depth scale is 1/240, or 1 ft of log for 240 ft of formation. The logs have a thin horizontal line every 2 ft, a medium thick line every 10 ft, and a thick line every 50 ft.

Figure 2.7 shows the typical log-heading presentation for several of the basic logs that will be used shortly. The upper two presentations show two variations for the SP, which is always presented in track 1. The bottom presentation shows the caliper, a one-axis measurement of the borehole diameter, and the gamma ray, which are also generally presented in track 1. Note that the SP decreases to the left. The rule given

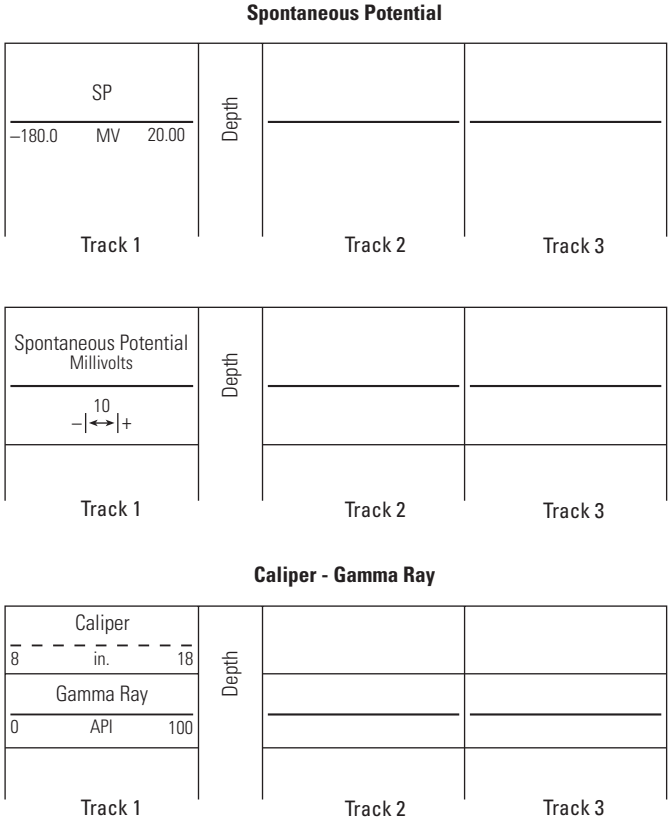


Fig. 2.7 Presentation of SP and GR log headings used for clean formation determination.

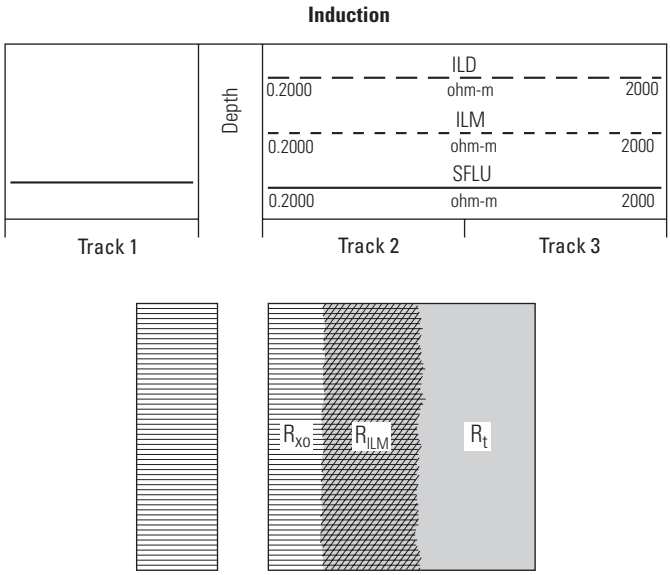


Fig. 2.8 The induction log heading and schematic of the formation, with three zones corresponding approximately to the simultaneous electrical measurements of different depths of investigation.

for finding clean sections was that the SP becomes less negative for increasing shale, so that deflections of the SP trace to the right will correspond to increasing shale content. The GR curve, as it is scaled in increasing activity (in American Petroleum Institute (API) units) to the right, will also produce curve deflections to the right for increasing shale content. Thus the two shale indicators can be expected to follow one another as the shale content varies.

Although modern tools have a larger selection of curves with different depths of investigation, the displays are similar. A traditional resistivity log heading is shown in Fig. 2.8, along with a schematic indication of the zones of investigation. The particular tool associated with this format is referred to as the dual induction-SFL and will normally show three resistivity traces (the units of which are ohm-m; see Chapter 3). The trace coded ILD (induction log deep; see Chapter 7) corresponds to the deepest resistivity measurement and will correspond to the value of R_t when invasion is not severe. The curve marked ILM (induction log medium) is an auxiliary measurement of intermediate depth of penetration and is highly influenced by the depth of invasion. The third curve, in this case marked SFLU (spherically focused log; see Chapter 5), is a measurement of shallow depth of investigation and reads closest to the resistivity of the invaded zone R_{xo}. By combining the three resistivity measurements, it is possible, in many cases, to compensate for the effect of invasion on the ILD reading.

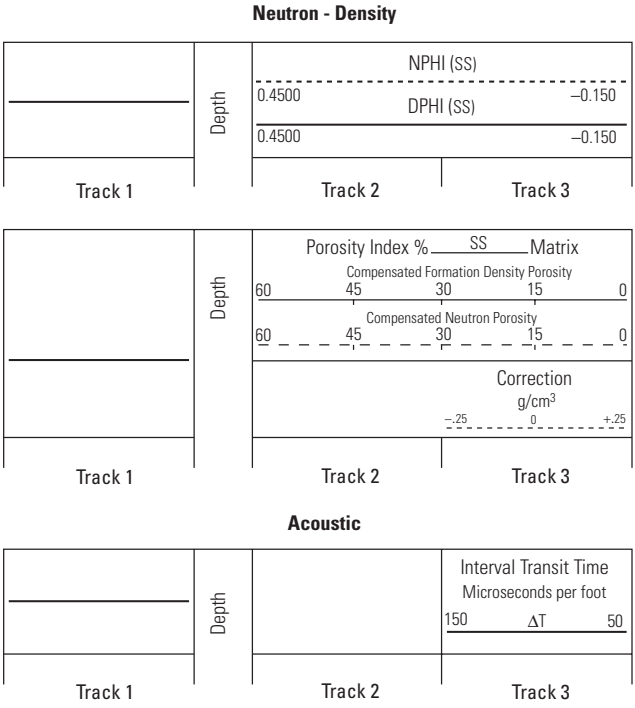


Fig. 2.9 Log headings for three porosity devices. The top two correspond to two possible formats for simultaneous density and neutron logs. The bottom is the sonic log format.

In Fig. 2.9, three typical headings for the three types of porosity devices are indicated. The porosity is expressed as a decimal (v/v) or in porosity units (p.u.), each of which corresponds to 1% porosity. The top heading shows the format for porosities derived from neutron and density measurements simultaneously. In this example, although the scale may vary depending upon local usage, porosity is shown from −0.15 to 0.45 v/v. The middle example shows an additional correction curve for the density log, which can be used to get some idea of the mudcake and rugosity of the borehole encountered during the density measurement.

It is also common practice to present the density measurement in g/cm^3 with a dynamic range of 1 g/cm^3 on the density trace across the full track (or sometimes two tracks), as is done in Fig. 2.17 below. It is easy to show that a change in bulk density of 1 g/cm^3 in a water-filled formation corresponds to a porosity change of about 60 p.u. Consequently the neutron trace is usually shown with a dynamic range of 60 p.u. across the density track. The density trace is then shifted so that the zero point on the neutron trace corresponds to the density of the matrix. Two such compatible scales are in common use: one for sandstone, in which case the zero porosity point is 2.65 g/cm^3 as in Fig. 2.17; the other for limestone, in which case the zero porosity point is 2.7 g/cm^3.

The bottom heading of Fig. 2.9 is for the traditional sonic log with the apparent transit time Δt increasing to the left. In all three presentations, the format is such that increasing porosity produces curve deflections to the left.

For the neutron and density logs, another point to be aware of is the matrix setting. This setting corresponds to a rock type assumed in a convenient pre-interpretation that establishes the porosity from the neutron and density device measurements. In both examples shown in Fig. 2.9, the matrix setting is listed as SS, which means that the rock type is taken to be sandstone. If the formations being logged are indeed sandstone, then the porosity values recorded on the logs will correspond closely to the actual porosity of the formation. However, if the actual formation matrix is different, say limestone, then the porosity values will need to be shifted or corrected in order to obtain the true porosity in this particular matrix.

2.5 EXAMPLES OF CURVE BEHAVIOR AND LOG DISPLAY

In this section, each of the primary curves to be used in a later section is shown individually, to provide more familiarity with their presentation and behavior with expected changes in lithology and porosity. The first example is the SP, which is shown over a 150 ft interval in Fig. 2.10. The intervals of high SP above 8,500 ft and

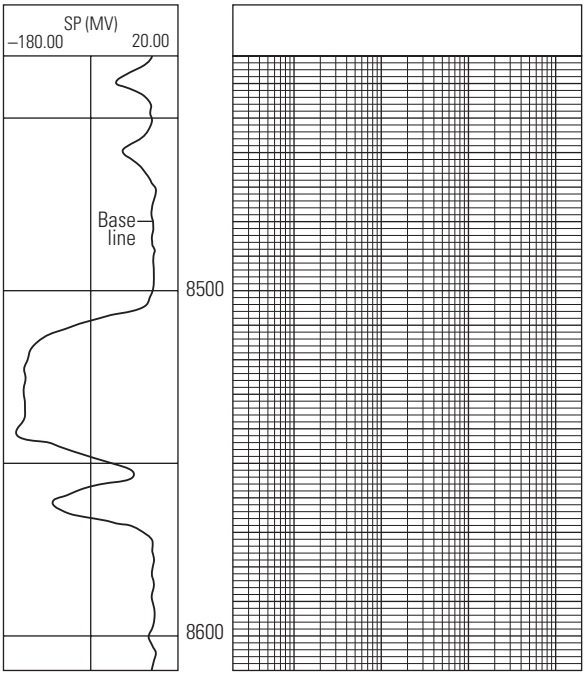


Fig. 2.10 An SP log over a clean section bounded by shales.

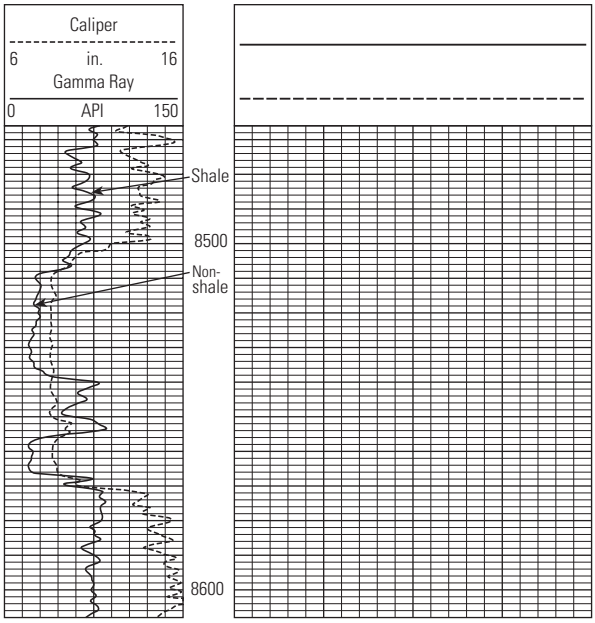


Fig. 2.11 A GR and caliper log over the same section as Fig. 2.10.

below 8,580 ft are generally identified with shale sections. The value of the typical flat response is called the shale base line, as indicated on the figure. Sections of log with greater SP deflection (i.e., with a more negative value than the shale base line) are taken as clean, or at least cleaner, zones. One clean section is the zone between 8,510 and 8,550 ft.

In Fig. 2.11, the caliper (broken) and GR (solid) traces are shown for the same section of the well. Note the similarity between the GR trace of Fig. 2.11 and the SP trace of Fig. 2.10. In the clean sections, the gammy ray reading is on the order of 15 to 30 API units, while the shale sections may read as high as 75 API units. Note also that the caliper, in this example, follows much of the same trend. This trend results from the fact that the shale sections can "wash out," increasing the borehole size compared to the cleaner sand sections that retain their structural integrity.

Figure 2.12 shows a 150 ft section of an induction log. The shallow, deep, and medium depth resistivity curves are indicated. The zone below 5,300 ft is possibly water, because of a number of tacit assumptions. First, it has been assumed that the resistivity of the formation water is much less (i.e., the water is much more saline) than the resistivity of the mud. The effect of the resistivity of the mud can be seen by sighting along the shallow resistivity curve, which for the most part stays around 2 ohm-m. At a depth of 5,275 ft, a possible hydrocarbon zone is noted. It is clear that the deep-resistivity reading (ILD) is much greater than in the supposed water zone. However, this increase in resistivity may not be the result of hydrocarbon

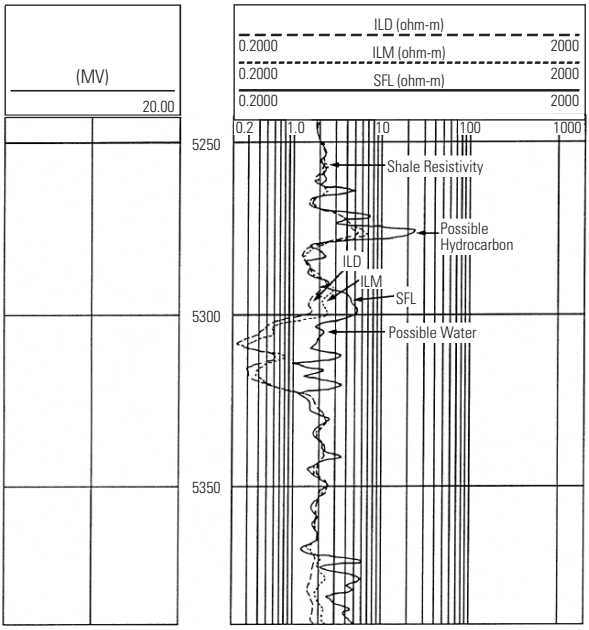


Fig. 2.12 An induction log over a section which might be interpreted as a water zone with a hydrocarbon zone above it.

presence. A decrease in porosity could produce the same effect for a formation saturated only with water. The real clue here is that even though the R_{xo} reading has also increased (this indicates that the porosity has decreased), there is less of a separation between the R_{xo} and R_t curves than in the water zone. This means that the value of R_t is higher than should be expected from the porosity change alone. By this plausible chain of reasoning, we are led to expect that this zone may contain hydrocarbons.

Figure 2.13 shows a typical log of a neutron and density device in combination. In addition to the density-porosity estimate (ϕ_d, or DPHI, on the log heading), in solid, and the dotted neutron porosity, the compensation curve $\Delta\rho$ (or DRHO) is also shown. This latter curve is the correction which was applied to the density measurement in order to correct for mudcake and borehole irregularities. It can generally be ignored if it hovers about zero, as is the case in Fig. 2.13 at certain depths. Note, once again, the built-in assumption that the matrix is sandstone. Where the density and neutron-derived porosity values are equal, the presence of liquid-filled sandstone is confirmed. This is the case for the 20 ft section below 700 ft. Separation of the two curves can be caused by an error in the assumed matrix or by the presence of clay or gas.

The presence of gas may be extremely easy to spot from a comparison of the neutron and density logs. With gas in the pores the formation density is less

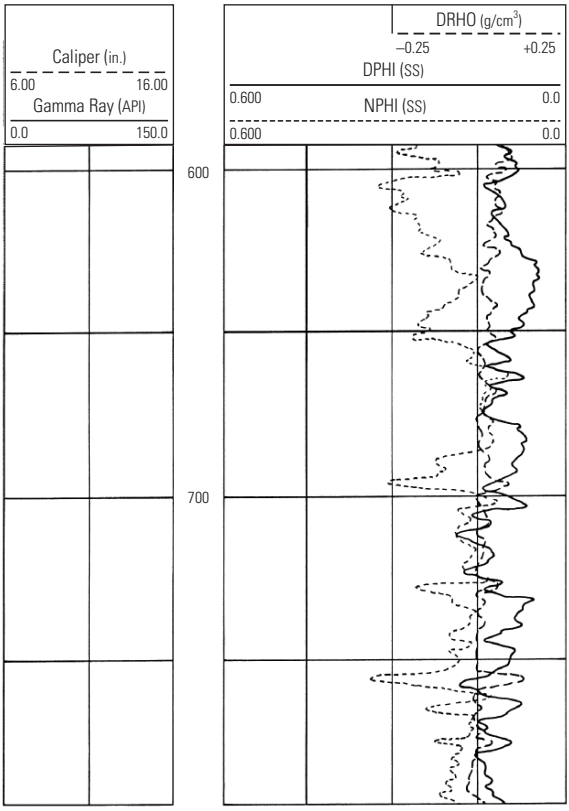


Fig. 2.13 Sample neutron and density logs which have been converted to sandstone porosity. The auxiliary curve $\Delta\rho$ indicates little borehole irregularity.

than with oil or water, so that the apparent density porosity is higher. At the same time the hydrogen content of gas is less than oil or water so the neutron porosity is lower. Thus, in the simplest of cases, gas is indicated in any zone in which the neutron porosity is less than the density porosity. Figure 2.14 shows sections which exhibit this behavior. Shale produces the opposite effect; the neutron porosity may far exceed the density porosity, as can be seen in the behavior in Fig. 2.15.

All of these generalities are true only if the principal matrix corresponds to the matrix setting on the log. The effect of having the wrong matrix setting on the log (or having the matrix change as a function of depth) is shown in Fig. 2.16. Several sections show negative density porosity. These are probably due to anhydrite streaks, which, because of their much higher density, are misinterpreted as a negative porosity.

Figure 2.17 is an example of an LWD log recorded in a horizontal well. The basic presentation is similar to wireline logs, but some other useful curves may be

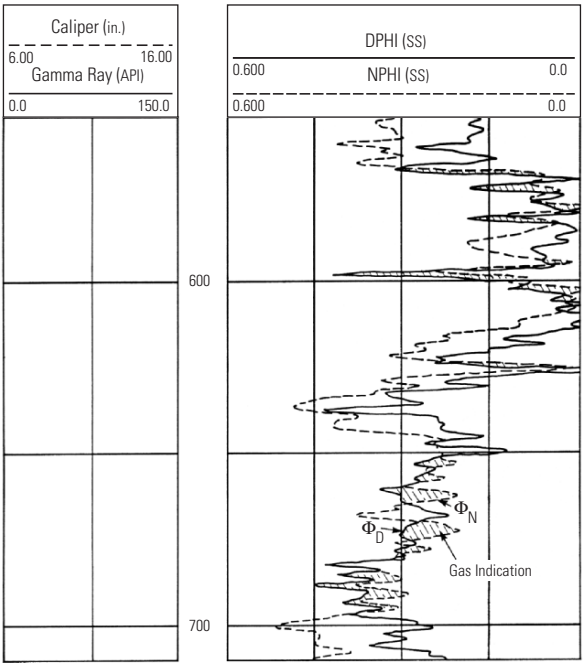


Fig. 2.14 A neutron and density log exhibiting the characteristic crossover attributed to the presence of gas in the formation.

included. LWD measurements are taken at regular time intervals, so that the sampling rate, in depth, depends on the rate of penetration of the drill bit. Sometimes tick marks in the depth track indicate the depth at which samples were taken for the different measurements. In this case some indication of the variable sampling density and rate of penetration is conveyed in track 1 by the three curves that show by how many seconds each measurement lags the bit position. In this example, the drilling rotation rate is shown in the depth track; for some oriented tools rotation is required for meaningful results.

2.6 A SAMPLE RAPID INTERPRETATION

In this section the step-by-step process of identifying interesting zones for possible hydrocarbon production is traced. In analyzing the set of basic logs available, the first step is to identify the clean and possibly permeable zones. This is done by an inspection of the SP and GR curves. In Fig. 2.18, the SP curve has been used to delineate four clean, permeable zones which have been labeled A through D. For further confirmation that these zones are relatively clean, an inspection of the GR curve also shows a minimum of natural radioactivity associated with them.

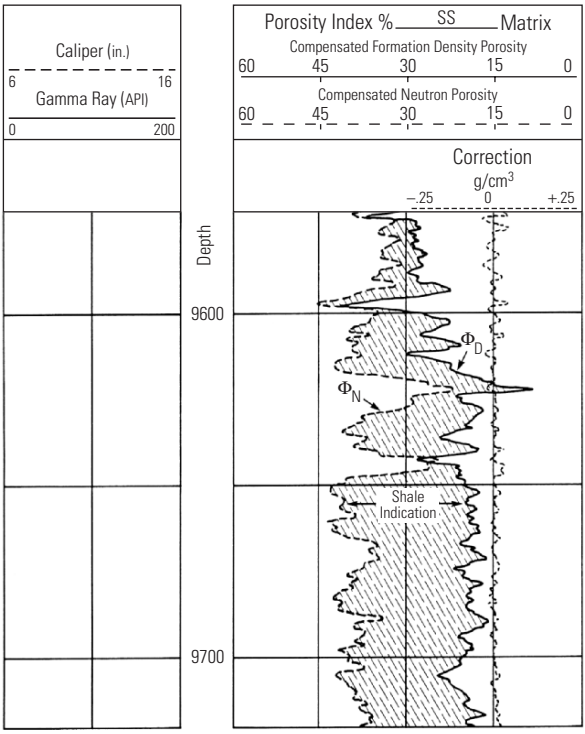


Fig. 2.15 The signature of shale on a neutron and density combination log.

In the next step, the resistivity readings in the four selected zones are examined. These curves are contained in the second track of Fig. 2.18. The first thing that is obvious is that the resistivity readings are roughly constant within the delineated zones, except in zones C and D, where a difference occurs between the lower and upper portions. For this reason, zone C is further subdivided into a zone of very low resistivity ($\approx$0.2 ohm-m on the deep resistivity ILD) at the bottom and about 4.0 ohm-m in the upper portion. A similar delineation can be made for zone D.

A first estimate of fluid content can be established by looking at the lowest resistivity values and identifying them as water, as has been done in the figure. Then the zones such as A, B, C, and D may be suspected to be hydrocarbon-bearing. For the case of zone C, compared to C′, this seems clear. With reference to the porosity values in track 3, it is seen that the porosity over these two zones is approximately constant. In this case, the increase in resistivity in the upper zone, compared to the lower, suggests the presence of hydrocarbons. The case for zone D is not quite so clear. According to the neutron and density curves, the porosity has been considerably reduced in the transition between zone D′ and D. Perhaps the

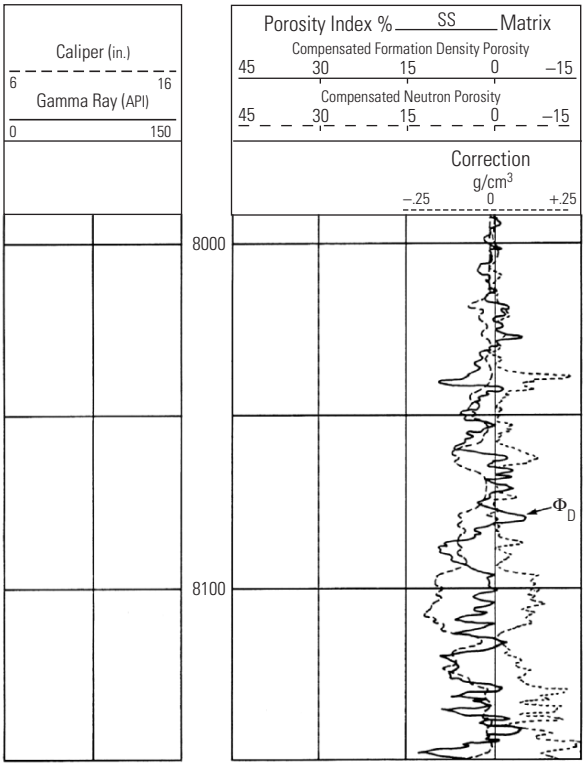


Fig. 2.16 Neutron and density crossover caused by changes in lithology.

increased resistivity is due to a purely water-saturated low porosity formation and not hydrocarbon.

A careful look at the neutron and density curves in track 3 can yield some additional information. Notice the crossover between the neutron and density curves in zone C, with neutron porosity less than density porosity. This is indicative of the presence of light hydrocarbon or gas. From this, it is now quite certain that the high resistivity in this zone is indeed the result of the presence of light hydrocarbon, or possibly gas. The same conclusion can be drawn for zone B, which shows an even greater neutron-density separation, most likely resulting from gas. The high-resistivity streaks of zone D are still questionable. There is no evidence of gas from the neutron/density presentation in this zone, and thus the high-resistivity value may simply be due to the reduced porosity. Any further speculation will depend on the ability to be more quantitative in the analysis.

A more quantitative approach to interpretation is developed through the next few chapters. One of the first questions which occurs to the observant analyst is how the porosity was actually determined in this example. For this quantity to be determined,

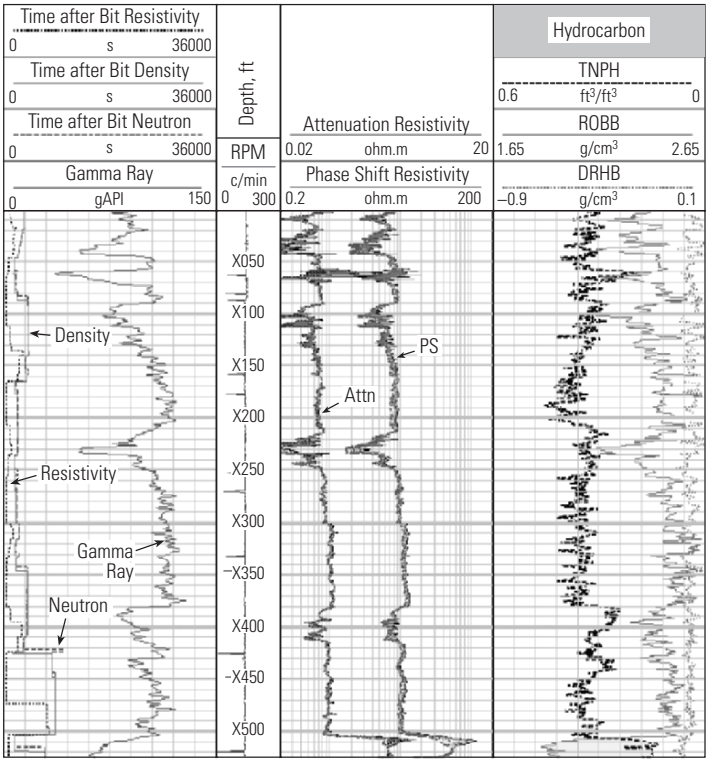


Fig. 2.17 An example of an LWD log in a horizontal well. In track 1 is the familiar GR along with three curves indicating the time delay between drilling and the three types of measurements made; the tool rotation rate appears in the depth track. Track 2 contains two types of resistivity measurements, each with multiple depths of investigation that overlay in this example. The third track contains the LWD versions of the neutron measurement (TNPH), the density measurement (ROBB), and the density correction (DRHB).

some information is needed to identify the lithology. In the example just given, the matrix was specified as sandstone, from some prior knowledge perhaps. However, what would have been the conclusions if in fact the rock were mainly dolomite?

Another question which needs to be explored is the relationship between the resistivity of a water-saturated rock and its porosity. It has been noted that the resistivity of a porous rock sample can increase if the water is replaced by hydrocarbon or if the porosity is reduced. This relationship must be quantified in order to unscramble the effects of changing these two variables simultaneously.

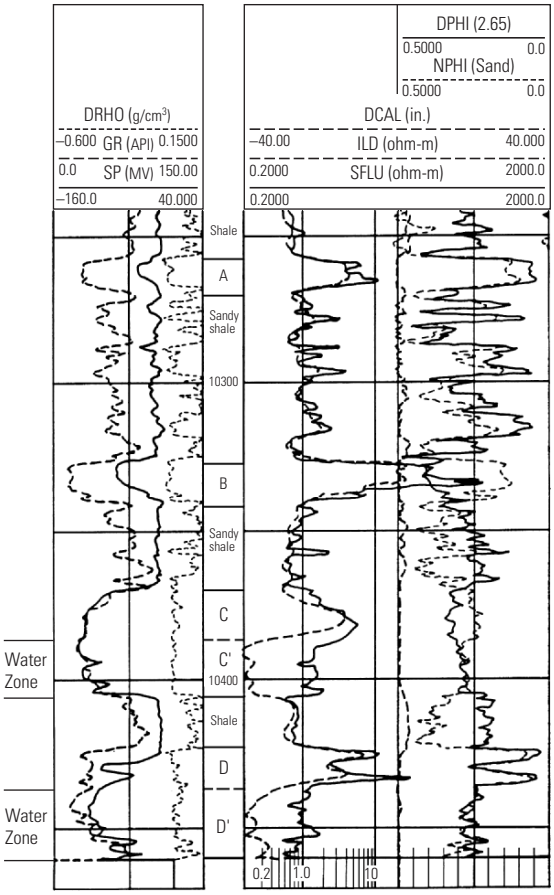


Fig. 2.18 A basic set of logs for performing a wellsite interpretation.

REFERENCES

1. Doll HG (1950) The microlog – a new electrical logging method for detailed determination of permeable beds. Pet Trans AIME 189:155–164

2. Dewan JT (1983) Essentials of modern open-hole log interpretation. PennWell Publishing, Tulsa, OK

3. Scholle PA, Bebout DG, Moore CH (eds)(1983) Carbonate depositional environments. AAPG Memoir 33, AAPG, Tulsa, OK

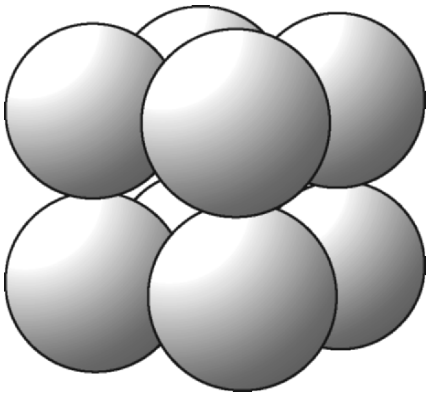


Fig. 2.19 Cubic or open packing of uniform-sized spherical particles.

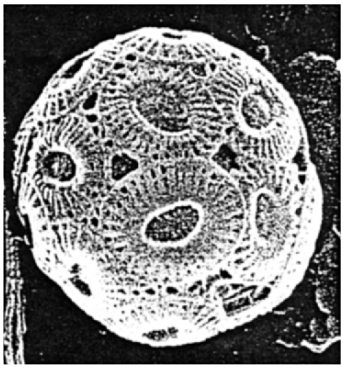


Fig. 2.20 Photomicrograph of spherical plankton which contain a nearly spherical void. From Scholle et al. [3].

Problems

2.1 Compute the porosity of a formation composed of uniform spherical grains of radius r arranged in the most "open" cubic packing. (The unit cube with side of length $2r$ spans eight grains; see Fig. 2.19.)

2.1.1 If the formation were composed of the nearly spherical plankton of Fig. 2.20, what would the porosity be for cubic packing? The spherical void at the center of each plankton seems to have a radius which is $\approx \frac{9}{10}$ of the total particle radius.

2.1.2 Most sandstone formations have porosities well below 30%. Can you suggest several reasons why this is the case?

2.2 What is the porosity (or liquid volume fraction) of an 11 lb/gal mud, assuming that it consists of water and clay particles of density 2.65 g/cm^3? The density of water is 8.3 lb/gal (1.00 g/cm^3).

2.3 In the formation of a mudcake, an annulus of lower porosity mud is formed by expelling some of the water in the mud into the formation. A typical mudcake density is 2.0 g/cm^3. What is its porosity, assuming that it was formed from the 11 lb/gal mud from the previous example?

2.4 The volume of water expelled from the mud, during the creation of the mudcake, will displace the formation fluid, creating the so-called invasion zone. The thickness of this zone, in which the formation fluid has been displaced by mud filtrate, will depend on the formation porosity. Show that the radius of invasion r_i is given by:

$$r_i^2 = \frac{1}{\pi}\left(\frac{dV}{\phi} + \pi {r_{bh}}^2\right), \tag{2.1}$$

where dV is the volume of mud filtrate/unit length displaced into the formation, ϕ is the porosity, and r_{bh} is the borehole radius.

2.5 Suppose that a mudcake of 40% porosity has been formed on the inside of a 6 in. borehole, from a mud of 80% porosity. If the mudcake thickness is 1/2 in., what is the diameter of invasion in a 20% porous formation? What is the diameter of invasion in a 2% porosity formation? [Note: The mudcake is generally scraped off by drilling and logging operations and reformed. Thus, in practice its thickness at any particular time cannot be used to estimate invasion]

2.6 Suppose a horizontal well is dipping at 91° and is passing though a horizontal boundary between a shale and a sand. The GR measurement responds to the formation within 1 ft of the center of the borehole in all azimuths. What length of borehole is needed for the gamma ray to transit from reading only shale to reading only sand?

3

Basic Resistivity and Spontaneous Potential

3.1 INTRODUCTION

The preceding chapter showed through example that an important component of the well logging suite is the measurement of electrical properties of the formation. These measurements deal with the resistivity of the formation or the measurement of spontaneously generated voltages. These voltages are the result of an interaction between the borehole fluid and the formation with its contained fluids.

Historically, the first logging measurements were electrical in nature. The first log was a recording of the resistivity of formations as a function of depth and was drawn painstakingly by hand. Unexpectedly, in the course of attempting to make other formation resistivity measurements, "noise" was repeatedly noted and was finally attributed to a spontaneous potential. It seemed most notable in front of permeable formations. Both of these measurements are still performed on a routine basis today, and their physical basis will be explored in this chapter.

Also in this chapter the concept of a bulk property of materials, known as resistivity, is examined. It is a quantity related to the more familiar resistance. The contrast in resistivity between relatively insulating hydrocarbons and the conductive formation brines is the basis for hydrocarbon detection. The quantitative relationships between resistivity and hydrocarbon saturation are taken up in the next chapter. Here, the electrical characteristics of rocks and brines are reviewed, including the temperature and salinity dependence of electrolytic conduction, which is of great importance in hydrocarbon saturation determination. The final section of the chapter is an elementary presentation of the physical mechanisms responsible for the generation of the spontaneous potential observed in boreholes.

3.2 THE CONCEPT OF BULK RESISTIVITY

In order to understand the basic resistivity measurements used in standard logging procedures, the notion of resistivity is reviewed. It is a general property of materials, as opposed to resistance, which is associated with the geometric form of the material.

The familiar expression of Ohm's law:

$$V = I\,R \tag{3.1}$$

indicates that a current I flowing through a material with resistance R is associated with a voltage drop V. The more general form of this equation, used as an additional relationship in Maxwell's equations, is:

$$\overline{J} = \sigma\,\overline{E}, \tag{3.2}$$

where $\overline{J}$ is the current density, a vector quantity; $\overline{E}$, is the electric field; and the constant of proportionality σ is the conductivity of the material. Resistivity,* a commonly measured formation parameter, is defined as the inverse of conductivity:

$$Resistivity \equiv \rho = \frac{1}{\sigma} \tag{3.3}$$

and is an inherent property of the material.

To comprehend the concept of resistivity, consider the case of a very dilute ionized gas contained between two plates of area A, as illustrated in Fig. 3.1. The charge carriers are indicated to be moving under the influence of an applied electric field E, at an average drift velocity v_{drift} *. The drift velocity can be estimated from the fact that the charge carriers are accelerated in the applied electric field until they collide with another particle, at which time they are brought to rest and begin the process again. The mean time between collisions,* τ *, is the parameter of interest, since the drift velocity can be seen to be:*

$$v_{drift} = \frac{F}{m}\,\tau\,, \tag{3.4}$$

where the term F/m *represents the acceleration of the charge carriers of mass m, subject to a force F. In this case the force applied, F, is equal to the product of the charge and the electric field (qE).*

A general expression for the drift velocity of a particle under the influence of an outside force F is:

$$v_{drift} = \mu\,F, \tag{3.5}$$

where the constant of proportionality μ *is referred to as the mobility of the particle in question in a specified medium. By reference to Eq. 3.4 it can be seen that for the case of a dilute gas the mobility is given by:*

$$\mu = \frac{\tau}{m}\,. \tag{3.6}$$

*In this chapter, resistivity is denoted by ρ, and resistance by R. In later chapters, R will frequently be used to denote resistivity, as is done in most logging publications.

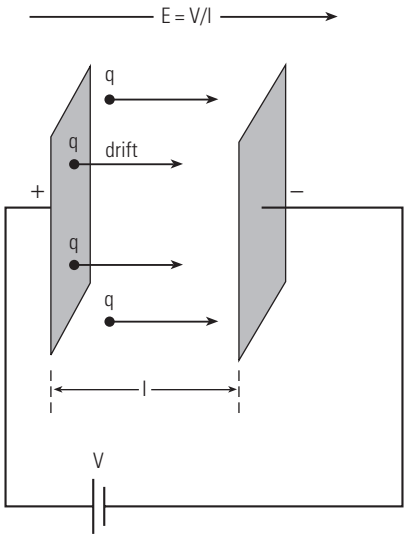


Fig. 3.1 A dilute gas with particles of charge q, drifting under the influence of the electric field.

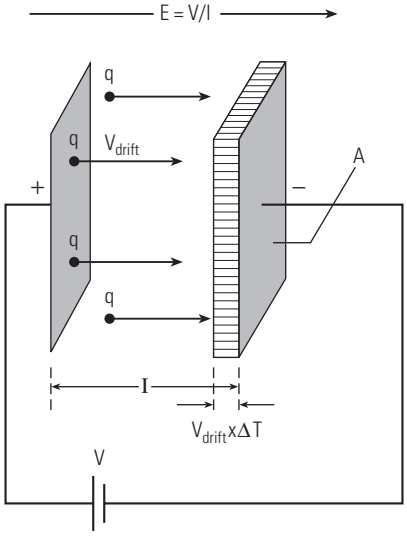


Fig. 3.2 The region of space with indicated thickness $v_{drift} \times \Delta t$ is swept of charged particles in a time Δt, contributing to the current.

To illustrate the relationship between resistivity and resistance, an expression will be written for the current flowing in the system of Fig. 3.1, in a form that resembles Ohm's law. To compute the current, note that it is the charge collected per unit time. Figure 3.2 illustrates the region of space containing charges that will reach the plate

on the right during a time Δt; the thickness of this region is $v_{drift} \times \Delta t$. The number collected during the time interval Δt is $n_i v_{drift} \Delta t A$, where n_i is the particle density (number of charge carriers per unit volume) and A is the surface area of the electrode. The current is given by:

$$I = \frac{n_i v_{drift} \Delta t A}{\Delta t} q \ . \tag{3.7}$$

The relation for drift velocity is:

$$v_{drift} = \mu F = \mu q \frac{V}{l}, \tag{3.8}$$

since the electric field strength is given by the voltage drop per unit length and the separation of the two plates is l.

Combining these two relations results in the following expression for the current:

$$I = \frac{n_i \mu q \frac{V}{l} \Delta t A}{\Delta t} q \ , \tag{3.9}$$

which, when compared with Ohm's law, $I = \frac{1}{R} V$, indicates that the resistance of the geometry illustrated in Fig. 3.2 is given by:

$$R = \frac{1}{n_i \mu q^2} \frac{l}{A} \ . \tag{3.10}$$

From this expression it is clear that the resistance R is composed of two parts, one which is material dependent $\left(\frac{1}{n_i \mu q^2}\right)$ and a second which is purely geometric (the length of the sample divided by the surface area of the contact plates). Resistivity, ρ, is in fact, this first factor:

$$R = \frac{1}{n_i \mu q^2} \frac{l}{A} = \rho \frac{l}{A} \ . \tag{3.11}$$

It follows that the dimensions of resistivity are ohms-m^2/m, or ohm-m.* As the illustration of Fig. 3.3 indicates, a material of resistivity 1 ohm-m with dimensions of 1 m on each side will have a total resistance, face-to-face, of 1 ohm. Thus a system to measure resistivity would consist of a sample of the material to be measured contained in a simple fixed geometry. If the resistance of the sample is measured, the resistivity can be obtained from the relation:

$$\rho = R \times \frac{A}{l} \ , \tag{3.12}$$

*The units of its reciprocal, conductivity, are Siemens per meter. In well-logging, to accommodate the usual range of conductivities, milliSiemens per meter (mS/m) are used, where 1,000 mS/m = 1 S/m.

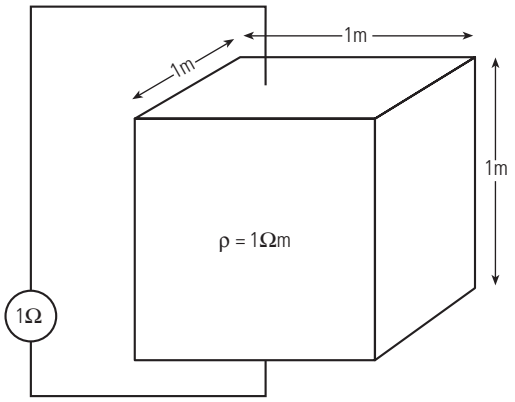


Fig. 3.3 A 1 m cube of characteristic resistivity 1 ohm-m has a resistance of 1 ohm face-to-face.

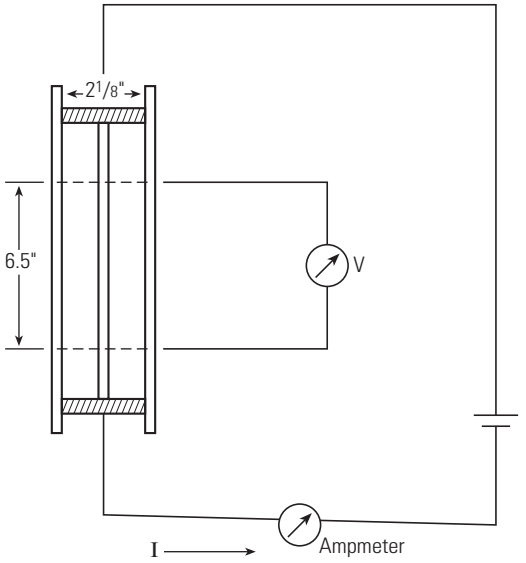


Fig. 3.4 A schematic diagram of a mud cup, used for determining the resistivity of a mud sample. A current, I, is passed through the sample and the corresponding voltage, V, is measured.

which becomes, using Ohm's law:

$$\rho = \frac{V}{I}\frac{A}{l} = k\frac{V}{I}. \tag{3.13}$$

This constant k, referred to as the system constant, converts the measurement of a voltage drop V, for a given current I, into the resistivity of the material.

The practical exploitation of such a system is shown in Fig. 3.4, which shows the so-called mud cup into which a sample of drilling fluid can be placed for the

determination of its resistivity. From the dimensions given in the figure, the system constant can be calculated to be 0.012 m. The resistivity, ρ, in ohm-m, is then obtained from the measured resistance R by:

$$\rho = R\frac{A}{l} = R \times 0.012\,. \tag{3.14}$$

For this particular measuring device, a sample of salt water with a resistivity of 2 ohm-m in the chamber would yield a total resistance of 166 ohms.

3.3 ELECTRICAL PROPERTIES OF ROCKS AND BRINES

There are two general types of conduction: electrolytic and electronic. In electrolytic conduction, the mechanism is dependent upon the presence of dissolved salts in a liquid such as water. Examples of electronic conduction are provided by metals, which are not covered here.

Table 3.1 illustrates the resistivity of some typical materials. Notice the range of resistivity variation for salt water, which depends on the concentration of NaCl. Typical rock materials are in essence insulators. The fact that reservoir rocks have any detectable conductivity is usually the result of the presence of electrolytic conductors in the pore space. The conductivity of clay minerals is also greatly increased by the presence of an electrolyte. In some cases, the resistivity of a rock may result from the presence of metal, graphite, or metal sulfides. The table shows that the resistivity of formations of interest may range from 0.5 to 10^3 ohm-m, nearly four orders of magnitude.

The conductivity of sedimentary rocks is primarily of electrolytic origin. It is the result of the presence of water or a combination of water and hydrocarbons in the pore space as a continuous phase. The actual conductivity will depend on the resistivity of the water in the pores and the quantity of water present. To a lesser extent, it will depend on the lithology of the rock matrix, its clay content, and its texture (grain size and the distribution of pores, clay, and conductive minerals). Finally, the conductivity of a sedimentary formation will depend strongly on temperature.

Figure 3.5 graphically presents the resistivity of saltwater (NaCl) solutions as a function of the electrolyte concentration and temperature. According to the preceding analysis, the resistivity is expected to depend inversely on the charge carrier concentration:

$$\rho \propto \frac{1}{nq^2\mu}\,. \tag{3.15}$$

To see that this is nearly the case, look at the figure to determine resistivity for concentrations of 4,000 and 40,000 ppm. At a temperature of 100°F , the resistivities are 0.12 and 1.0 ohm-m, or nearly in the ratio expected. However, the temperature dependence, which is seen from the chart to be rather substantial, is not explicitly given by the simple expression for resistivity in Eq. 3.11. It was derived for the case of a dilute gas, a medium which is rather different from a saline solution. In the latter

Table 3.1 Resistivity values. Adapted from Tittman [3]

Material	Resistivity (ohm-m)
Marble	$5 \times 10^7 - 10^9$
Quartz	$10^{12} - 3 \times 10^{14}$
Petroleum	2×10^{14}
Distilled water	2×10^{14}
Saltwater (15°C):	
2 kppm	3.4
10	0.72
20	0.38
100	0.09
200	0.06
Typical formations	
Clay/shale	2–10
Saltwater sand	0.5–10
Oil sand	5–10^3
"Tight" limestone	10^3

case, the interactions of the charge carriers with one another and with the medium in which they are found cannot be ignored.

An explanation for the temperature dependence comes from a consideration of viscosity. Figure 3.6 shows a setup to measure the effects of viscosity. A film of liquid of thickness t is contained between two plates of surface area A. The bottom plate is fixed, and a force is applied to the top plate in order to move it parallel to the bottom plate. Experimentally it is found that for a given liquid film, the force F necessary to achieve the velocity v_o is directly proportional to the velocity, the surface area of the plate being dragged, A, and inversely to the thickness of the film, t. The constant of proportionality η is the viscosity, and the experimental relationship is expressed as:

$$F = \eta \frac{v_o A}{t}, \tag{3.16}$$

or

$$\frac{F}{A} = \eta \frac{v_o}{t}. \tag{3.17}$$

A practical application of this concept, known as Stokes's law, predicts that the viscous force on a spherical object of radius a is given by:

$$F = 6\pi \eta a v, \tag{3.18}$$

where v is the velocity of the object. In this case, it refers to the electrolytic particles in solution. For future reference, note that Eq. 3.18 *implies that the mobility of an electrolytic particle, or ion, will vary inversely with its size.*

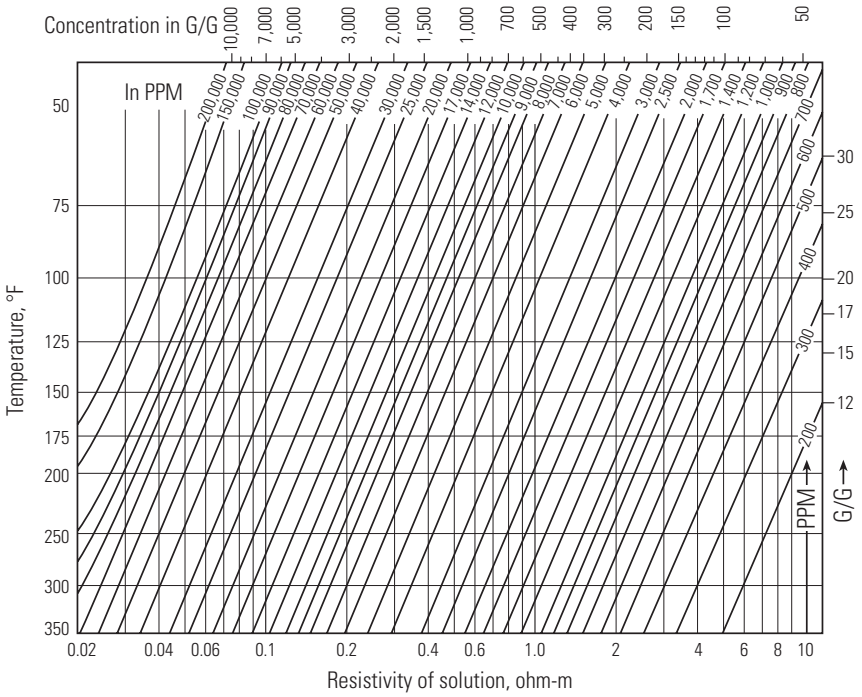


Fig. 3.5 A nomogram for determining the resistivity of an NaCl solution as a function of the NaCl concentration and temperature. G/G is grains per gallon. Courtesy of Schlumberger [1].

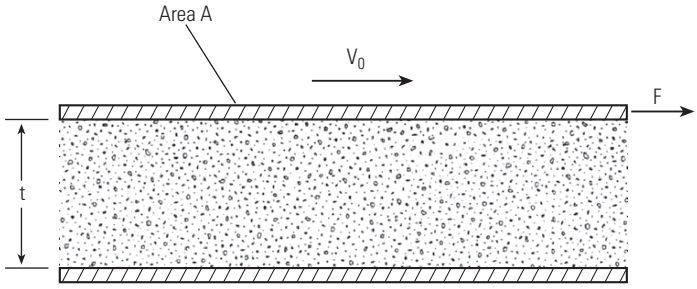


Fig. 3.6 Relative motion between two parallel plates separated by a liquid film will require overcoming a drag force determined by the viscosity of the liquid. Adapted from Feynman [2].

From the analysis of the ionized gas resistivity, it was seen how the mobility, μ, entered into the final expression:

$$v_{drift} = \mu F \rightarrow R = \frac{1}{n\mu q^2}\frac{l}{A}. \tag{3.19}$$

If the electrolytic particle is considered to be a sphere of radius a, then from Stokes's law the drift velocity would be given by:

$$v_{drift} = \frac{1}{6\pi\eta a} F, \tag{3.20}$$

and the resistivity should be given by:

$$R = \frac{6\pi\eta a}{nq^2} \frac{l}{A}. \tag{3.21}$$

The temperature dependence of resistivity for an electrolytic conductor comes from the viscosity factor in Eq. 3.21. The liquid's viscosity has a strong temperature dependence; unlike the case of ionized gas, it decreases with increasing temperature. In the case of a liquid, viscosity is the result of strong intermolecular forces which impede the relative motion of fluid layers. As the temperature increases, the kinetic energy of the molecules helps to overcome the molecular forces so that viscosity decreases. One simple model [4] relates the probability of moving a molecule (of the somewhat structured fluid) by viscous flow, to its vibrational energy. It predicts an exponential dependence of viscosity on temperature. Not surprisingly, the experimental temperature dependence of viscosity for many liquids, such as water, can be described by an expression like:

$$\eta = \eta_o e^{\frac{C}{T}}, \tag{3.22}$$

where C is characteristic of a given liquid.

3.4 SPONTANEOUS POTENTIAL

Spontaneous potential was shown in the last chapter to be of considerable practical use in the identification of permeable zones. The origins of the spontaneous potential in wellbores involve both electrochemical potentials and the cation selectivity of shales. However, the underlying basis for the spontaneous potential is the fundamental process of diffusion – the self-diffusion of the dissolved ions in the fluids in the borehole and in the formation.

Electrochemical potentials of interest to the generation of the spontaneous potential are the *liquid junction potential* and the *membrane potential*. Figure 3.7 schematically illustrates the situation for the generation of the liquid-junction potential. To the left is a saline solution of low NaCl concentration. To the right is one of a higher ionic concentration, as indicated by the sketch of electrolyte number densities $n_+(x)$ and n_-(x) as a function of position. To add a note of realism, imagine the borehole, filled with a fluid of low salinity, to the far left of the figure. The first zone will then correspond to a permeable invaded zone, and the second region, to the undisturbed formation with water of greater salinity.

Because of the particle concentration gradient, dn/dx, where $n = n_+ + n_-$, there will be a diffusion of both Na^+ and Cl^- ions from the region of higher concentration

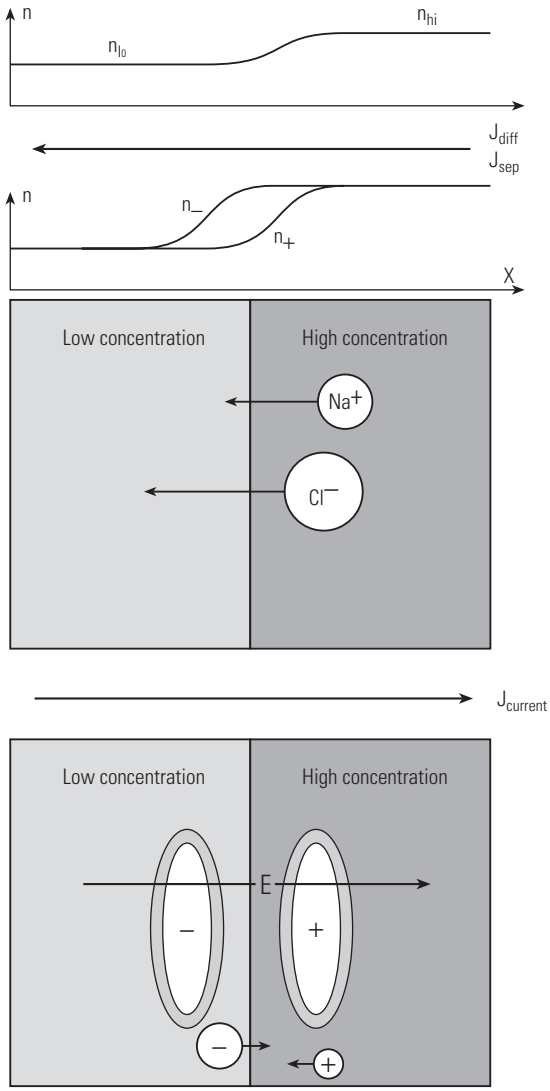


Fig. 3.7 Schematic representation of the mechanism responsible for the generation of the liquid-junction potential. A concentration gradient, as indicated in the upper panel, results in diffusion. The higher mobility of Cl^- causes a charge separation as indicated by the sketch of the Cl^- and Na^+ concentrations.

to that of lower concentration. An approximation of the diffusion process, known as Fick's law, is given by:

$$J_{diff} = -D\frac{dn}{dx}, \tag{3.23}$$

where the current density of diffusing *particles* is J_{diff}. The diffusion constant D can be shown [2] to be related to the mobility of the ions and the temperature, so that one can write:

$$J_{diff} = -\mu kT \frac{dn}{dx} . \tag{3.24}$$

This connection between mobility and diffusion is called the Nernst–Einstein relation.

Although Eq. 3.20 would lead us to believe that the smallest ions should have the largest mobilities, this is not the case for ions dissolved in water. Confining ourselves to the case of NaCl, a common salt found in formation waters, the cation Na^+ is considerably smaller than the anion Cl^-. Since water is dipolar, both anions and cations in solution tend to loosely attach a sphere of water molecules around them through electrostatic attraction. However the much smaller size of the cation causes a much stronger binding of water molecules simply due to the surface charge distribution. The solvation number is the average number of H_2O molecules that remain attached during diffusion. For Na^+ the solvation number is 4.5, but it is only 2.2 for Cl^- [5]. Consequently, the apparent size of the hydrated Na^+ cation ion is much larger than the hydrated Cl^- anion, resulting in a mobility difference between the two ions in accordance with Eq. 3.20.

Because the Na and Cl ions have different mobilities, with $\mu_{Cl} > \mu_{Na}$, the diffusion will tend to produce a charge separation. The higher mobility Cl ions will more readily migrate to the region of lower concentration and tend to create an excess negative charge to the left and a net excess positive charge to the right, as indicated in the lower half of Fig. 3.7. The diffusion ionic *current* that produces this charge separation with the excess negative charge on the left of the figure can be written as:

$$J_{sep} = -(\mu_{Cl} - \mu_{Na})kT \frac{dn}{dx} . \tag{3.25}$$

The diffusion current, by itself, would continue to accumulate excess negative charge in the region of low ionic concentration and positive charge in the region of high concentration were it not for the electric field that results from the charge separation. With accumulating charge separation, an electric field, $\overline{E}$, grows with the orientation shown in the lower panel of the figure. The effect of the electric field is to impose a drift velocity on the ions, speeding up cations to the left and slowing down anions diffusing to the left. The magnitude of the electric field will increase until the diffusion of the anions and cations is the same, resulting in an equilibrium consisting of a constant electric field and no additional charge separation. However, diffusion, although modified, continues.

To quantify this effect it is simpler to consider the electric field $\overline{E}$ as producing an ionic current flowing to the right, as seen in the lower panel of Fig. 3.7, which will balance the separation current flowing to the left as indicated in the upper panel of the figure. This ionic current can be expressed as:

$$\overline{J}_{current} = \sigma_{Cl}\overline{E} + \sigma_{Na}\overline{E}. \tag{3.26}$$

The conductivities in Eq. 3.26 are proportional (κ is the constant of proportionality) to the number density of charge carriers and their mobilities. Thus the electrical current,

dropping the vector notation, is:

$$J_{current} = \kappa n(\mu_{Cl} + \mu_{Na})E \, . \tag{3.27}$$

For the charge separation and electric field to remain stable, the two currents (the separation portion of the diffusion current, J_{sep}, and oppositely directed current flow produced by the electric field) must balance. This leads to the following relation:

$$(\mu_{Cl} - \mu_{Na})kT\frac{dn}{dx} = \kappa \, n \, (\mu_{Cl} + \mu_{Na})E \, . \tag{3.28}$$

This expression can be rearranged and integrated to get a voltage drop from the electric field term:

$$\frac{(\mu_{Cl} - \mu_{Na})}{\kappa(\mu_{Cl} + \mu_{Na})} \, kT \int \frac{dn}{n} = \int E \, dx, \tag{3.29}$$

where the integration is performed over a dimension consistent with the particle density gradient. The liquid junction potential V_{l-j} is the expression on the right side of Eq. 3.29.

The integration results in the liquid junction potential being a logarithmic ratio of the particle concentrations n_{hi} and n_{lo} in the two regions:

$$V_{l-j} = c \, T \, \ln\frac{n_{hi}}{n_{lo}} \, . \tag{3.30}$$

As is often the case, the resistivity of the drilling mud filtrate (R_{mf}) is greater than the resistivity of the formation water (R_w), so that the above equation can be written, with the help of Eq. 3.11, in the form:

$$V_{l-j} = -c' \, \log_{10} \frac{R_{mf}}{R_w}. \tag{3.31}$$

Figure 3.8 is a schematic representation of the circuit producing the SP. The cell marked E_d corresponds to the liquid junction potential just discussed and is sketched with the polarity corresponding to a higher electrolyte concentration in the formation water than in the mud filtrate. As can be seen from the figure, an additional source of the spontaneous potential is associated with the shale. This second component of the SP is the result of the membrane potential generated in the presence of the shale that contains clay minerals which have large negative surface charge.

Now what does that mean? First, we define shale to be a conglomeration of fine grained particles, many of which are clay minerals, as seen in the left-hand panel of Fig. 3.9. We will assume that it is nearly impermeable to fluid flow, but that it is still capable of ionic transport, although considerably altered by the presence of clay minerals. The shale acts like a cation-selective membrane. This property is related to the sheet-like structure of the alumino-silicates that form the basic structure of clay minerals. At the surface of the clay minerals there is a strong negative charge related to unpaired Si and O bonds. When the clay mineral particles are exposed to an ionic solution, one containing Na^+ and Cl^- for example, the anions will be repulsed by their surfaces while the cations will be attracted to the surface charge, forming the

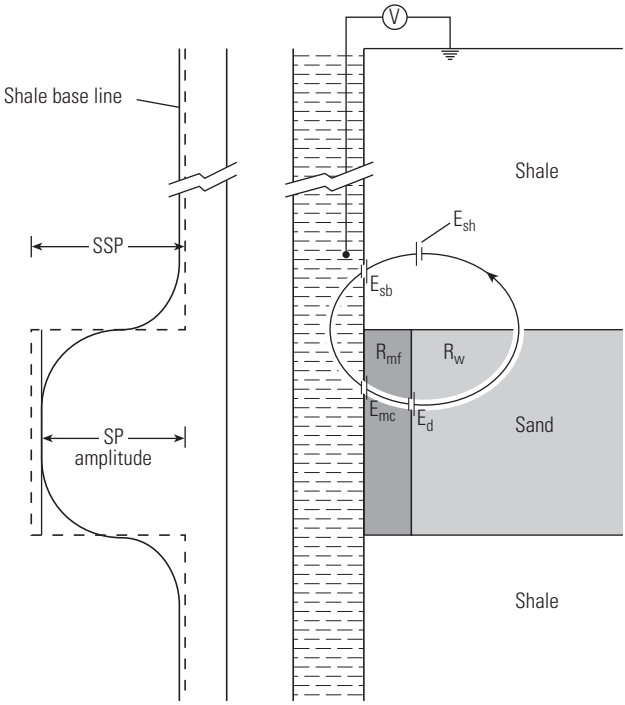


Fig. 3.8 A schematic representation of the development of the spontaneous potential in a borehole. Adapted from Dewan [6].

so-called electrical double layer as shown in the right-hand portion of Fig. 3.9. Close to the clay layers, the fluid will be dominated by cations since the anions are excluded by electrostatic repulsion. In this manner, in a complex mixture of clay minerals and other small mineral particles, with pore spaces even too small to permit the hydraulic flow of water, the cations will be able to diffuse along the charged surfaces, from high concentration to low concentration while the negative Cl ions will tend to be excluded. Such a diffusion process will tend to accumulate a positive charge on the low ionic concentration side of the shale barrier, producing an attendant electric field. In the practical situation of Fig. 3.8, the cations from the fluid saturating the porous sand zone diffuse through the shale to the borehole with the lower cation concentration.

To aid a quantitative description, Fig. 3.10 shows a simplified setup for evaluating the membrane potential when a semipermeable shale barrier separates the solutions of two different salinities. The natural diffusion process is impeded because of the negative surface charge of the shale. The Cl ions which otherwise would diffuse more readily are prevented from traversing the shale membrane, whereas the less mobile Na ions can pass through it readily. The result is that the effective mobility of the chlorine in this case is reduced to nearly zero. An experimental study to simulate the development of the SP in a borehole in front of a permeable sand and

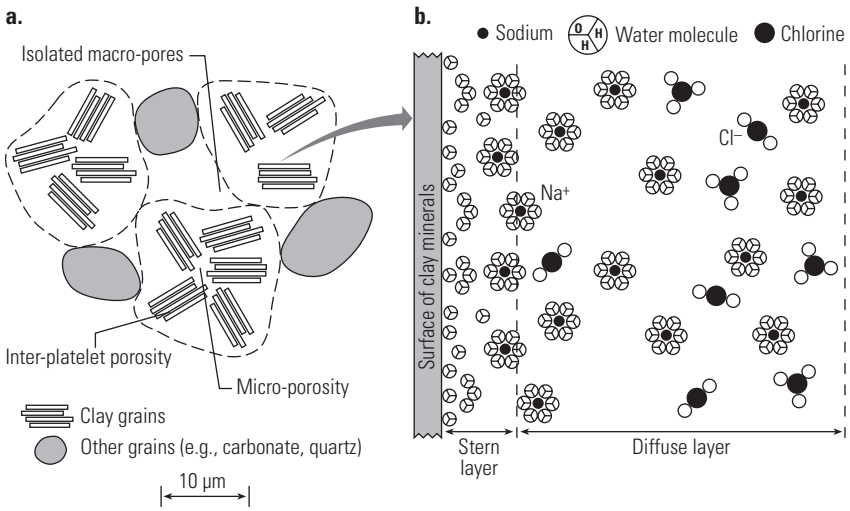


Fig. 3.9 A representation of a shale on the left, consisting of rock mineral grains and small platy clay particles. On the right the distributions of ions close to the face of one of the clay minerals is shown, which illustrates the so-called electrical double-layer. Adapted from Revil and Leroy [7].

an impervious shale, using cation- and anion-selective membranes, is described in Taherian et al. [8].

The diffusion ionic current across the membrane in Fig. 3.8 can thus be expressed as:

$$J_{mem} = -D\frac{dn}{dx} = -\mu_{Na}kT\frac{dn}{dx}, \tag{3.32}$$

where only the Na concentration and mobility figure in the expression. As in the case of the liquid-junction potential, there will be a charge separation. However, this time there will be a positive charge accumulation to the left or low concentration side, which will tend to cause the Na ions to flow back to the region of higher concentration. The electric field causes a current that can be written as:

$$J_{current} = \kappa n(\mu_{Na})E\ . \tag{3.33}$$

Equating the two currents results in an equation similar to Eq. 3.29 that results in the magnitude of the membrane potential V_m:

$$\frac{-\mu_{Na}}{\kappa(\mu_{Na})}\,kT\int\frac{dn}{n} = \int E\,dx = V_m. \tag{3.34}$$

The negative sign indicates that the electric field points out of the formation in front of the shale which is opposite of the electric field in front of the clean water (salty) sand. As indicated in Fig. 3.8, drawn for the case of lower NaCl concentration in the mud, the voltages add, resulting in a more negative voltage in front of the sand than in front of

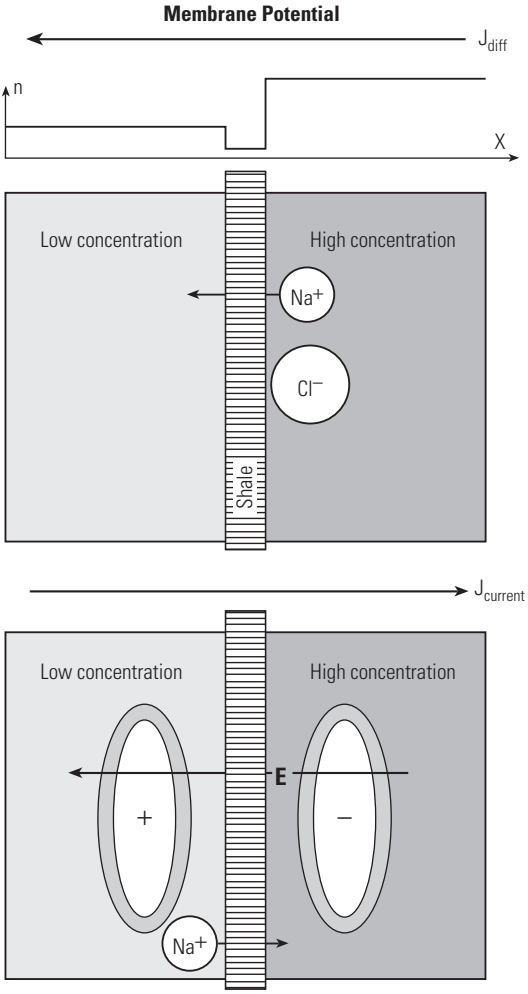


Fig. 3.10 A schematic representation of the mechanism responsible for the generation of the membrane potential. The diffusion process is altered by the selective passage of Na^+ through the shale membrane.

the shale zone. The membrane potential provides about 4/5 of the SP amplitude, since the absolute value of mobilities enters in its potential, rather than the difference as in the liquid-junction potential. Figure 3.8 also shows how the SP is measured, between an electrode in the borehole and a distant reference. The shale baseline represents the natural potential between the two electrodes, without electrochemical effects, and is ideally a straight line from top to bottom. The static spontaneous potential (SSP), is the ideal SP generated by electrochemical effects when passing from the shale to a thick porous clean (shale-free) sand if no current flowed. In practice the electrode can

only measure the potential change in the borehole. Although the mud is usually less resistive than the formation, the area for current flow is much smaller in the borehole than in the formation, so that the borehole resistance is usually much higher than the formation resistance. Most of the potential drop therefore takes place in the borehole with the result that the measured SP amplitude in the center of the bed is close to the SSP.

In the best of cases, the measurement of the SP allows the identification of permeable zones and the determination of formation water resistivity. A deflection indicates that a zone is porous and permeable and has water with a different ionic concentration than the mud. The determination of R_w can be seen from Eq. 3.31. Since the mud filtrate resistivity can be measured, the formation water resistivity can be calculated using factors that are well known for NaCl solutions. In practice the electrochemical potential is often written in terms of effective water resistivities (R_{mfe}) and (R_{we}) rather than actual resistivities. These are equal to R_{mf} and R_w except for concentrated or dilute solutions. In concentrated solutions, below about 0.1 ohm- m at 75° F, the conductivity is no longer proportional to the number density of charge carriers and their mobilities, and Eq. 3.27 is no longer exact. At high concentrations the proximity of the ions to one another is increased; their mutual attractions begin to compete with the solvation to reduce their mobilities. In dilute solutions of most oilfield waters, other ions than Na^+ Cl^- become increasingly important. Numerous charts exist for the determination of R_w from the SP, knowing R_{mf} and temperature.

The SP is also used to indicate the amount of clay in a reservoir. The presence of clay coating the grains and throats of the formation will impede the mobility of the Cl anions because of the negative surface charge, and thus spoil the development of the liquid-junction potential. The ideal SP generated opposite a shaley sand when no current flows is known as the pseudo static potential (PSP). Further information on the development of SP in permeable formations can be found in Revil et al. [9]. In addition to these quantitative interpretations, elaborate connections have been established between the shape of the SP over depth and geologically significant events. Some examples of using the SP curve to determine patterns of sedimentation are given in Pirson [10].

3.5 LOG EXAMPLE OF THE SP

The measurement of the SP is probably the antithesis of the high-tech image of many of the logging techniques to be considered in subsequent chapters. The sensor is simply an electrode (often mounted on an insulated cable, known as the "bridle," some tens of feet above any other measurement sondes) which is referenced to ground at the surface, as indicated in Fig. 3.8. The measurement is essentially a dc voltage measurement in which it is assumed that unwanted sources of dc voltage are constant or only slowly varying with time and depth.

To illustrate some of the characteristic behavior to be anticipated by the SP measurement on logs, refer to Fig. 3.11. In the left panel of this figure, a sequence of shale and clean sand beds is represented, along with the idealized response. The shale

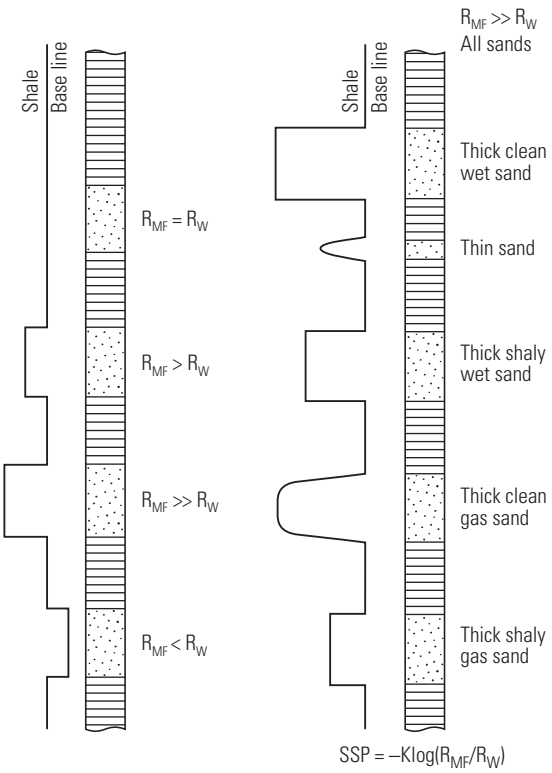


Fig. 3.11 Schematic summary SP curve behavior under a variety of different logging circumstances commonly encountered. From Asquith [11].

baseline is indicated, and deflections to the left correspond to increasingly negative values. In the first sand zone, there is no SP deflection since this case represents equal salinity in the formation water and in the mud filtrate. The next two zones show a development of the SP which is largest for the largest contrast in mud filtrate and formation water resistivity. In the last zone, the deflection is seen to be to the right of the shale baseline and corresponds to the case of a mud filtrate which is saltier than the original formation fluid.

The second panel of Fig. 3.11 illustrates several cases, for a given contrast in mud filtrate salinity and formation water salinity, where the SP deflection will not attain the full value seen in a thick, clean sand. The first point is that the deflection will be reduced if the sand bed is not thick enough because not enough of the potential drop occurs in the borehole. The transition at the bed boundary is much slower for the same reason. Depending mainly on the depth of invasion and the contrast between invaded zone and mud resistivity, the bed thickness needs to be more than 20 times the borehole diameter to attain its full value. A full modeling effort to quantify these relations is reported by Tabanou et al. [12].

The second point is the effect of clay in reducing the SP, as already discussed. The third point is the effect of oil or gas. In a clean sand the electrochemical potentials are not affected by oil or gas, but the formation resistivities are higher so that the transition at bed boundaries may be slower and a thicker bed may be needed for full SP development. However, the effect of oil or gas is stronger in a shaley sand. The electrochemical potentials are reduced compared to a water-bearing sand because there is less water in the pore space, so that the effect of the surface-charged clay particles is proportionately higher.

Other effects not illustrated in Fig. 3.11 can also upset the SP. There can be electrical noise, and bimetallic currents between the different metal parts of a logging tool that can create an unwanted potential at the SP electrode. Another culprit is the electrokinetic, or streaming, potential caused by the higher pressure in the borehole moving cations through a cation-selective membrane. The membrane may be a shale that has some very small permeability (E_{sh} in Fig. 3.8), or the mudcake which contains a large percentage of clay particles and also has some very small permeability (E_{mc}). Normally these effects are small and balance each other out. However, when the pressure differential is high, or the mud and other resistivities are high enough that even a small current produces a large potential, the electrokinetic effect can be comparable to the electrochemical effect.

The baseline often drifts slowly with time and depth. Sharper shifts occur when the membrane potential at the top of a sand is different to that at the bottom. This happens when the top and bottom shales have different cation selection properties, and also when the formation water or hydrocarbon saturation changes within the sand. Finally, the symmetric responses of Fig. 3.11 can be upset by vertical movement of mud filtrate in high permeability sands: upwards in the presence of heavier saline formation water, and downwards in the presence of gas and light oil.

REFERENCES

1. Schlumberger (2005) Log interpretation charts. Schlumberger, Houston, TX

2. Feynman RP, Leighton RB, Sands ML (1965) Feynman lectures on physics, vol 1, Ch 43. Addison-Wesley, Reading, MA

3. Tittman J (1986) Geophysical well logging. Academic Press, Orlando, FL

4. Adamson AW (1979) A textbook of physical chemistry, second international edition. Academic Press, New York, San Francisco, London, p 291

5. Lest AM (1982) Introduction to physical chemistry. Prentice-Hall, Englewood Cliffs, NJ p 605

6. Dewan JT (1983) Essentials of modern open-hole log interpretation. PennWell Publishing, Tulsa, OK

7. Revil A, Leroy P (2004) Constitutive equations for ionic transport in porous shales. J Geophys Res 109(B3):B03208

8. Taherian MR, Habashy TM, Schroeder RJ, Mariani DR, Chen M-Y (1995) Laboratory study of the spontaneous potential – experimental and modeling results. The Log Analyst 36(5):34–48

9. Revil A, Pezard PA, Darot M (1997) Electrical conductivity, spontaneous potential and ionic diffusion in porous media. In: Lovell MA, Harvey PK (eds) Developments in petrophysics. Geological Society (London) special publication no 122, pp 253–275

10. Pirson SJ (1977) Geologic well log analysis. Gulf Publishing, Houston, TX

11. Asquith G, Gibson C (1982) Basic well log analysis for geologists. AAPG, Tulsa, OK

12. Tabanou JR, Rouault GF, Glowinski R (1987) SP deconvolution and quantitative interpretation in shaly sands. Trans SPWLA 28th Annual Logging Symposium, paper SS

13. Hearst JR, Nelson P (1985) Well logging for physical properties. McGraw-Hill, New York

Problems

3.1 In the log example of Fig. 3.12, indicate the shale baseline and zone the log into three major units; label the shale and the two reservoir units.

Using the qualitative log interpretation guides of Chapter 2, assuming that the lower reservoir is water-filled, answer the following questions.

3.1.1 Is the mud filtrate more or less saline than the formation water?

3.1.2 Is the average porosity of the upper reservoir greater or less than that of the lower reservoir?

3.1.3 In the upper reservoir, which curve(s) indicate(s) why the neutron porosity is greater than the density porosity?

3.1.4 On the basis of the resistivity curves alone, the upper reservoir may be split into two portions. Do they both contain hydrocarbons? Why?

3.1.5 Which of the two zones do you expect to be more permeable?

3.2 From the log of Fig. 3.13, determine the corrected value of the SP deflection in the one clean zone. Using the information alongside the log, and bed thickness correction chart SP− 4 in the chartbook [1]. Note that the scale for the SP is 10 mV per division.

3.3 Using the corrected deflection of the SP from Problem 3.2, estimate the water resistivity using the relation:

$$SSP = -70.7\, log_{10} \frac{R_{mf}}{R_w} . \tag{3.35}$$

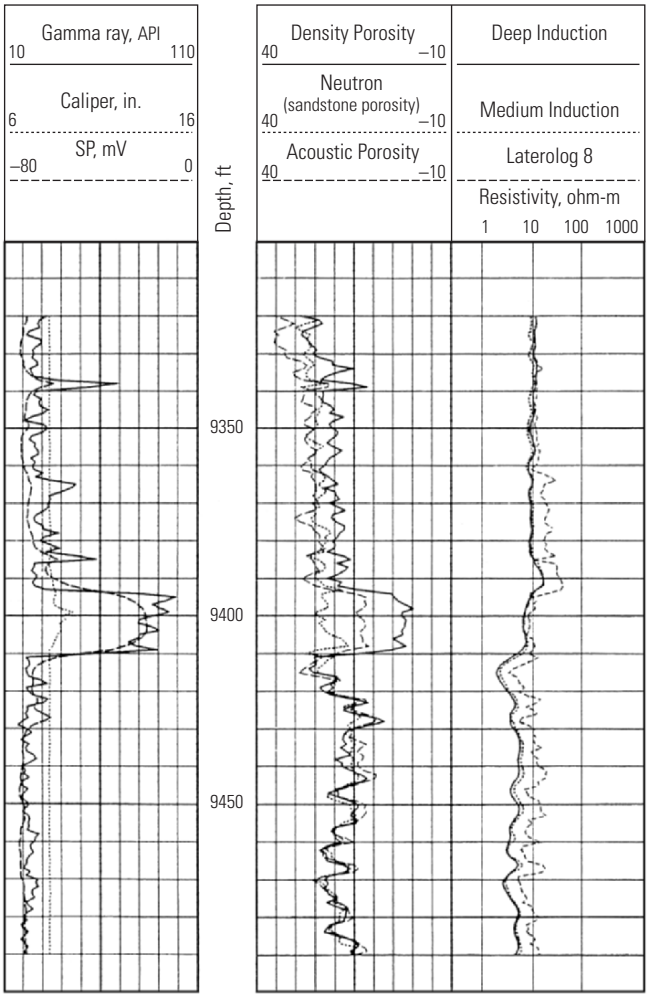


Fig. 3.12 Log example for Problem 3.1. From Hearst and Nelson [13].

What is the value of R_w if you use the uncorrected value of SP?

3.4 A 9 in. borehole is filled with mud at a constant temperature of 100° F. The resistivity of the mud is 0.9 ohm-m at 100°F.

3.4.1 What is the resistance of the mud column from surface to 7,000 ft?

3.4.2 What is the resistance if the temperature is raised to 200°F?

3.4.3 In the latter case, what would be the resistance if the diameter of the borehole were increased to 1 m?

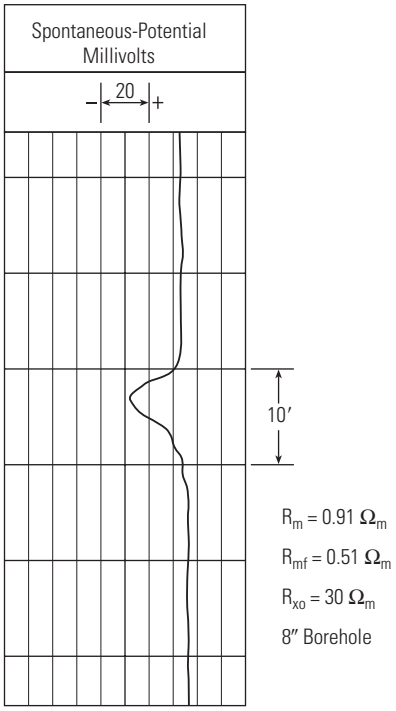


Fig. 3.13 SP log for Problems 3.2 and 3.3, showing effects of bed thickness.

3.5 The log of Fig. 3.14 shows a measurement of the mud resistivity (in ohm-m) as a function of depth. Ignore the SP curve since it was measured 9 months prior to the mud measurements.

3.5.1 Assuming constant mud salinity for the bottom 300 ft of log, what temperature variation would be required to produce such a resistivity change? Sketch a log of it in track 3.

3.5.2 What salinity variation could produce a similar change in resistivity in accordance with the temperature over this zone? Plot a few points of the concentration of NaCl as a function of depth in track 3.

3.5.3 What is a good explanation for the resistivity behavior in this example?

3.6 From the data of Fig. 3.5 verify the expected exponential dependence of resistivity on the inverse of temperature (°K). Taking points from the curve for a concentration of 4,000 kppm, how far does the resistivity at 350°F deviate from the model of Eq. 3.22?

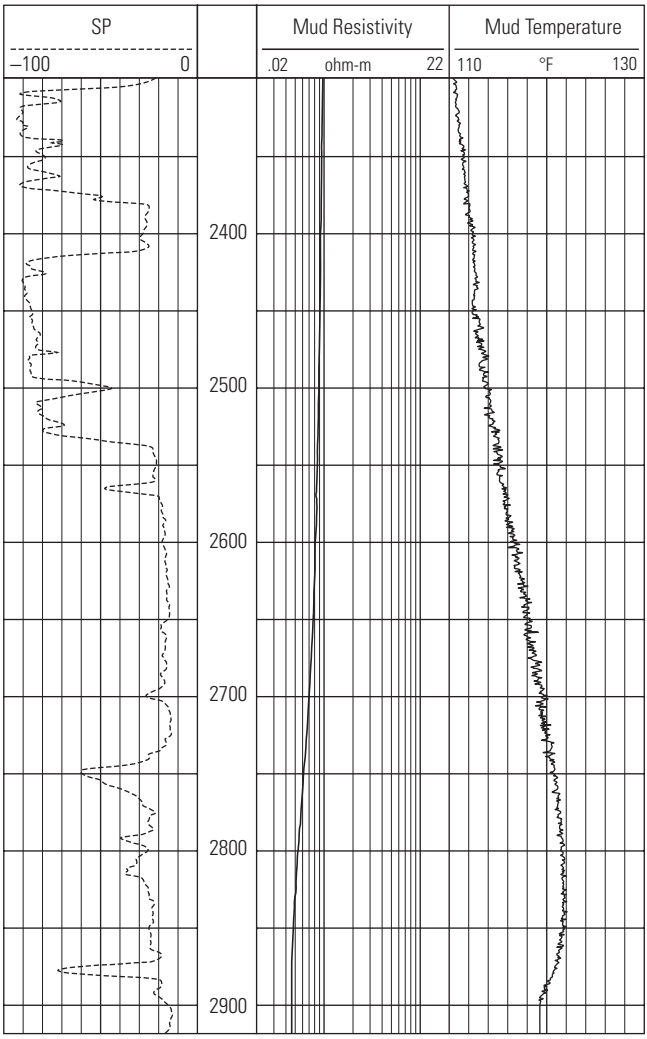


Fig. 3.14 A log of SP, borehole mud resistivity, and temperature.

4

Empiricism: The Cornerstone of Interpretation

4.1 INTRODUCTION

Before considering the details of measuring the resistivity of earth formations, let us look at the usefulness of such a measurement. The desired petrophysical parameter from resistivity measurements is the water saturation S_w. In the previous chapter, the resistivity of various materials, including brines, was discussed. There the focus was on the resistivity of a porous rock sample filled with a conductive brine in order to relate this measurable parameter to formation properties of interest for hydrocarbon evaluation.

In this chapter the empirical basis for the interpretation of resistivity measurements is reviewed. (The word "empirical" should be taken in its best sense here, meaning based on observation and experiment, and without implying that principles or theory have been disregarded.) For many years, at the outset of well logging, it was not possible to address the water saturation question any more precisely than whether the resistivity of a formation was high or low. It was through the work of Leverett [1] and Archie [2] that it became possible to be more quantitative about the interpretation of a formation resistivity measurement and to link resistivity to formation water resistivity, porosity, and water saturation.

After a review of the basis for the famous Archie equations, we introduce a note of caution by considering various situations in which the Archie method is insufficient. It may come as a surprise that these situations are handled by extending the Archie equations rather than replacing them with more theoretical approaches, but the latter (some of which are briefly reviewed) are not yet able to make a substantially better account of the complexity of rocks. This discussion will bring an appreciation of

the importance of measuring some of the perturbing factors, for example clay or anisotropy, when they are encountered in later chapters.

The chapter ends by presenting the principle of the simplest electrical logging measurements. For this application, a review of some basic notions of electrostatics is made to indicate how, in a very idealized situation, the measurement of isotropic formation resistivity might be made. However to remind the reader that rocks are more complicated than the idealized situation, the notion of electrical anisotropy is introduced.

4.2 EARLY ELECTRIC LOG INTERPRETATION

Figure 4.1 shows a log of spontaneous potential and formation resistivity made prior to 1935. The notations on the figure make clear which zones are oil-bearing and which are water-bearing. It seems possible, noting the higher resistivity, that zone a-A contains more oil (has a lower S_w) than zone B-b. But how can this be verified?

The "standard" procedure at the time was to take a core sample, representative of the zones in question, and to make laboratory measurements of its resistivity under different conditions of water saturation. Figure 4.2 is an example of two such core sample measurements. Presumably the core was saturated with water of the same resistivity as the undisturbed formation water for the resistivity determination. In the laboratory, the water was progressively displaced by hydrocarbon, and the measured resistivity of the sample was plotted as a function of the water saturation.

At about the same time, M. C. Leverett [1] was conducting experiments with unconsolidated sands, to determine the relative permeability of oil and water as a

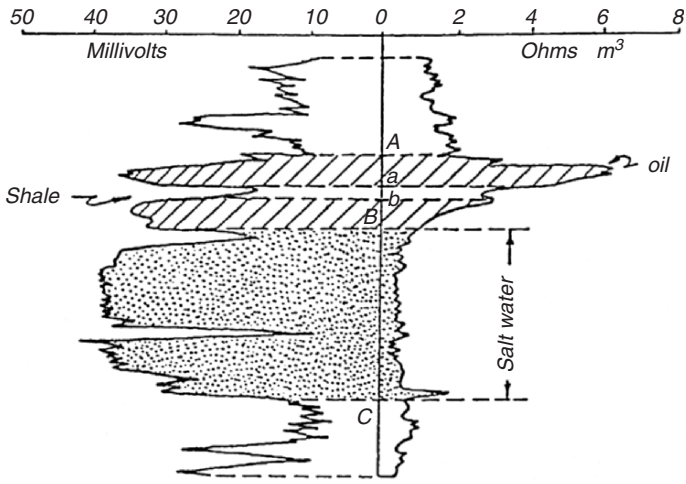


Fig. 4.1 An early resistivity-SP log. The scale "Ohms m^3" presumably refers to ohm-m. From Martin et al. [3].

function of the water saturation. As a by-product of his research, he measured the conductivity of the material in a sample chamber (see Figs. 4.3 and 4.4, and note similarity to the mud cup of Fig. 3.4), after a calibration of the system constant, in order to conveniently determine the fraction of kerosene and water in his permeable samples.

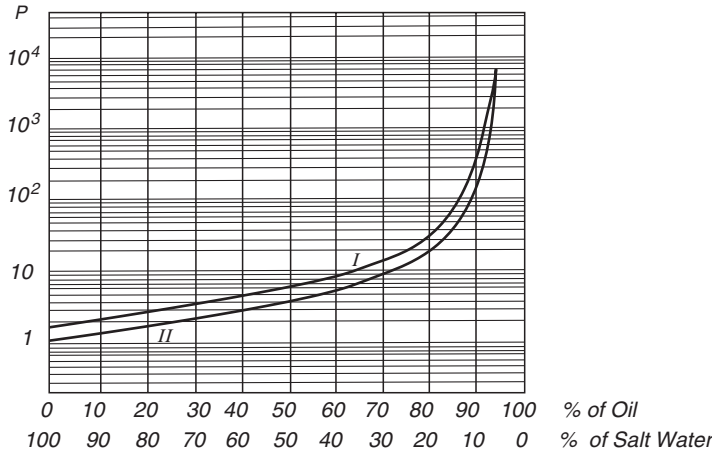


Fig. 4.2 Resistivity measurements of two core samples as a function of water saturation for use in electric log interpretation. From Martin et al. [3].

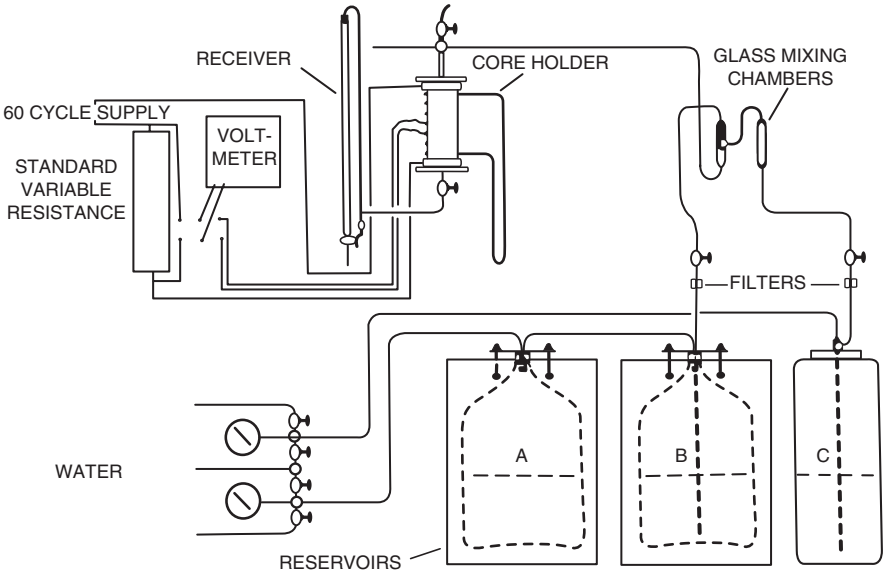


Fig. 4.3 Schematic of Leverett's experimental setup for measuring the relative permeability of sand packs. From Leverett [1].

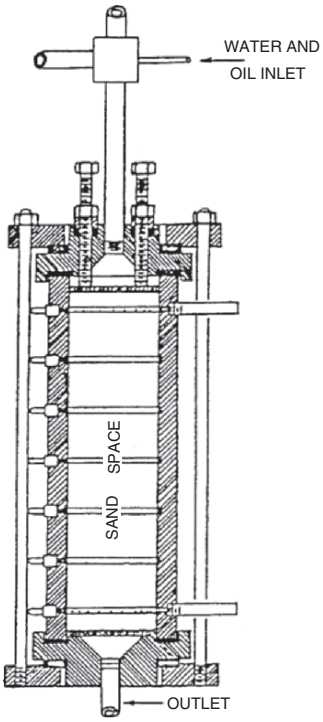


Fig. 4.4 Detail of the core holder from Leverett's experiments. Note the similarity to the mud cup. From Leverett [1].

Figure 4.5 is a summary of his calibration data. The fractional water saturation (S_w) is plotted versus the normalized conductivity. The normalizing point for this latter scale was taken to be the conductivity of the sample in the chamber when it was completely saturated with saltwater. Appropriately normalized points from the core measurements of Fig. 4.2 can be shown to clearly track Leverett's measurements and indicate the possibility of a general method for relating the resistivity of a porous sample to the water saturation (see Problem 4.2).

4.3 EMPIRICAL APPROACHES TO INTERPRETATION

4.3.1 Formation Factor

Shortly after the publication of Leverett's work, G. E. Archie of Shell was making electrical measurements on core samples, with the aim of relating them to permeability [2]. His measurements consisted of completely saturating core samples with saltwater of known resistivity R_w and relating the measured resistivity R_o of the fully saturated core to the resistivity of the water. He found that, regardless of the resistivity

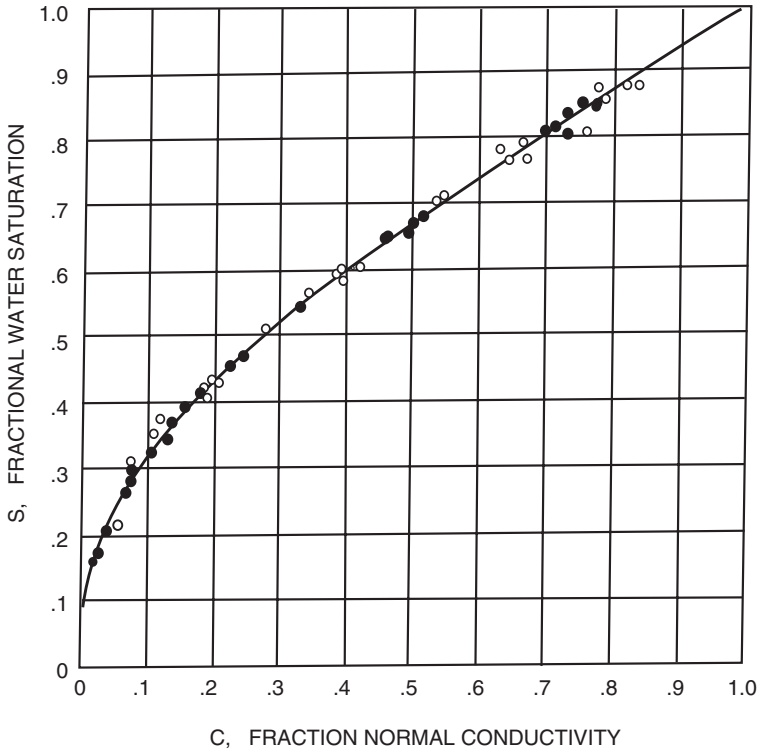


Fig. 4.5 Calibration curve of Leverett's core holder with sand pack, showing variation of relative conductivity as a function of water saturation. From Leverett [1].

of the saturating water, the resultant resistivity of a given core sample was always related to the water resistivity by a constant factor F. He called this the formation factor, and his experiments are summarized by the following relation:

$$R_{sample} \equiv R_o = F\, R_w\,. \tag{4.1}$$

Figure 4.6 is an example of his work on cores from two different locations, where the formation factor F is plotted as a function of permeability and, almost as an afterthought, porosity (on a much compressed scale). Although he was searching for a correlation with permeability, he finally admitted that a generalized relationship between formation factor and permeability did not exist, although one seemed to exist for porosity. His summary graph (Fig. 4.7) shows the hopelessness of a formation factor/permeability correlation. However it indicates that the formation factor is a function of porosity and can be expressed as a power law of the form:

$$F \approx \frac{1}{\phi^m} \tag{4.2}$$

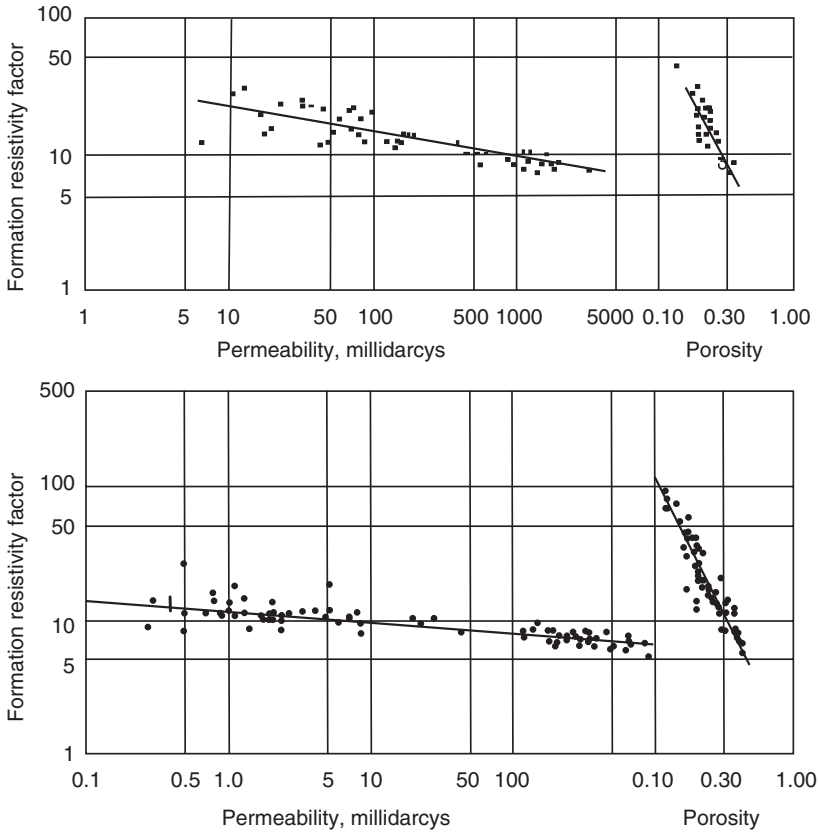


Fig. 4.6 Examples of the attempts to correlate the electrical formation factor with permeability and porosity for water-saturated rock samples from two regions. From Archie [2].

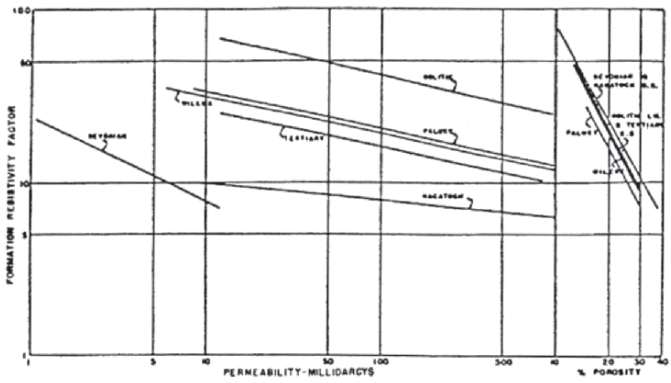
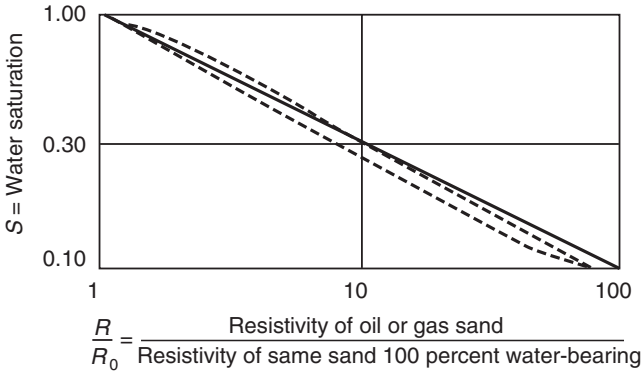


Fig. 4.7 A summary of an exhaustive set of measurements of formation factor, concluding with a strong correlation with porosity and an unpredictable one with permeability. From Archie [2].

where the exponent m is very nearly 2 for the data considered. This empirical observation can be used to describe the variation in formation resistivity for a fixed water resistivity when the porosity changes: the lower the porosity, the higher the resistivity will be. The exponent m was soon named the cementation exponent, as it was observed to increase with the cementation of the grains [4]. In general, it was recognized that m increased with the tortuosity of the electric path through the pore space.

4.3.2 Archie's Synthesis

The practical application of resistivity measurements is for the determination of water saturation. This was made possible by another observation of Archie. He noticed that the data of Leverett and others could be conveniently parameterized after having plotted the data in the form shown in Fig. 4.8. On log–log paper, the data of water



Legend and Data

Curve	Investigator	Type Sand	Salinity of Water. Grams NaCL per Liter	Oil or Gas	Porosity Fraction
———	Wyckoff	Various		CO_2	Various
———	Leverett	Uncons.	8 approx.	Oil	0.40
— — —	Martin	Cores	130	Oil	0.20 and 0.45 (?)
———	Jakosky	Friable	29 approx.	Oil	0.23

Fig. 4.8 A synthesis of various resistivity/saturation experiments, indicating a general power-law relationship. From Archie [2].

saturation versus relative resistivity plotted as a straight line, suggesting a relationship of the form:

$$S_w = \left[\frac{R_t}{R_o}\right]^{-\frac{1}{n}} . \tag{4.3}$$

The exponent n, called the saturation exponent, is very nearly 2 for the data considered.

From this, an approximate expression for the water saturation is:

$$S_w \approx \sqrt{R_o/R_t} . \tag{4.4}$$

However, the fully saturated resistivity R_o (which is not usually accessible in formation evaluation), can be related to the water resistivity using the previously discovered Archie relationship. So the expression becomes:

$$S_w \approx \sqrt{F \frac{R_w}{R_t}} , \tag{4.5}$$

and with the porosity dependence, the final form is:

$$S_w \approx \sqrt{\frac{1}{\phi^2} \frac{R_w}{R_t}} , \tag{4.6}$$

which can be used for purposes of estimation. However, a more general form, is:

$$S_w^n = \frac{a}{\phi^m} \frac{R_w}{R_t} , \tag{4.7}$$

where the constants a, m, and n need to be determined for the particular field or formation being evaluated.

From the above analysis it is clear that, in order to interpret a resistivity measurement in terms of water saturation, two basic parameters need to be known: the porosity ϕ and the resistivity of the water in the undisturbed formation R_w. To illustrate the basic procedures of resistivity interpretation, it is of some interest to turn back to the log example in Chapter 2.6 (Fig. 2.18) to make use of the empirical observations. As a starting point, the value of the water resistivity R_w needs to be estimated. This can be done in either zone D' or zone C', which have tentatively been identified as water zones. In either case, the porosity is about 28 p.u., so the formation factor F is $1/(0.28)^2$, or 12.8. Thus the apparent resistivity of about 0.2 ohm-m in these zones, which is assumed to be the fully water-saturated resistivity R_o, corresponds to a water resistivity of 0.2/12.8, or 0.016 ohm-m.

It is clear that the increase in deep resistivity in zone C to about 4 ohm-m must correspond to a decrease in water saturation compared to zone C'; the porosity seems to be constant at 28 p.u. over both zones. The saturation in zone C can be estimated from:

$$S_w = \sqrt{\frac{R_o}{R_t}} = \sqrt{\frac{.2}{4.0}} = 22\% , \tag{4.8}$$

so the hydrocarbon saturation is about 78%.

Another zone of hydrocarbon (A) indicates the same resistivity value as zone C. However, in the upper zone the porosity is much lower and can be estimated to be about 8 p.u. Thus the formation factor in zone A is $1/(0.08)^2$, or 156. If it were water-filled, the resistivity would be expected to be about 2.5 ohm-m compared to the 4 ohm-m observed. Thus the zone may contain hydrocarbons, but the water saturation can be expected to be higher than in zone C. The water saturation in this zone can be estimated from Eq. 4.6 to be:

$$S_w = \sqrt{156\,\frac{0.016}{4.0}} = 79\%\,, \tag{4.9}$$

so it appears to be only about 21% hydrocarbon-saturated. The limit of confidence in the estimate of saturation can be determined from Eq. 4.6 and is left as an exercise.

4.4 A NOTE OF CAUTION

As Archie was aware, his equations worked well in rocks that have simple, uniform pore systems filled with saline water. Rocks with heterogeneous-pore systems, multiple-conduction mechanisms, or that are oil-wet need a more complete solution [5]. The problems can be considered with reference to Archie's three equations: the relation to porosity (m), the relation to S_w (n), and the definition of formation factor (F). We will consider m and n first, leaving the definition of F, which is mainly an issue of clay conductivity, until the end. Anisotropic reservoirs will be considered in a later section.

4.4.1 The Porosity Exponent, *m*

Although Archie could fit his data with a single parameter, m, in general a fit of F vs. ϕ throughout a reservoir will require two parameters, a and m. In practice the error caused by fitting with one parameter is often small [6]. In either case it would be better if the variations through the reservoir could be related to some physical property, rather than relying on a general average.

Early efforts focused on finding a relation with porosity, the idea being that as porosity decreased it was likely that the tortuosity, and hence m, increased. Many relations were developed but proved to be specific to particular reservoirs or areas, and not generally applicable. Clearer relations can be obtained if the reservoir contains vugs or fractures. Fractures offer a straight path for current, with minimum tortuosity. If, in a fractured reservoir, we can measure the proportion of porosity due to fractures and if we assume that the conductive paths through the fractures and the intergranular porosity are in parallel, with no interaction between them, we can calculate the total effective m. The left-hand side of Fig. 4.9 shows such a calculation assuming $m = 2$ for intergranular porosity and $m = 1$ for the fractures.

Isolated pores have porosity but do not contribute to rock conductivity, so that their $m = \infty$. The right-hand side of Fig. 4.9 shows the effective m for a reservoir

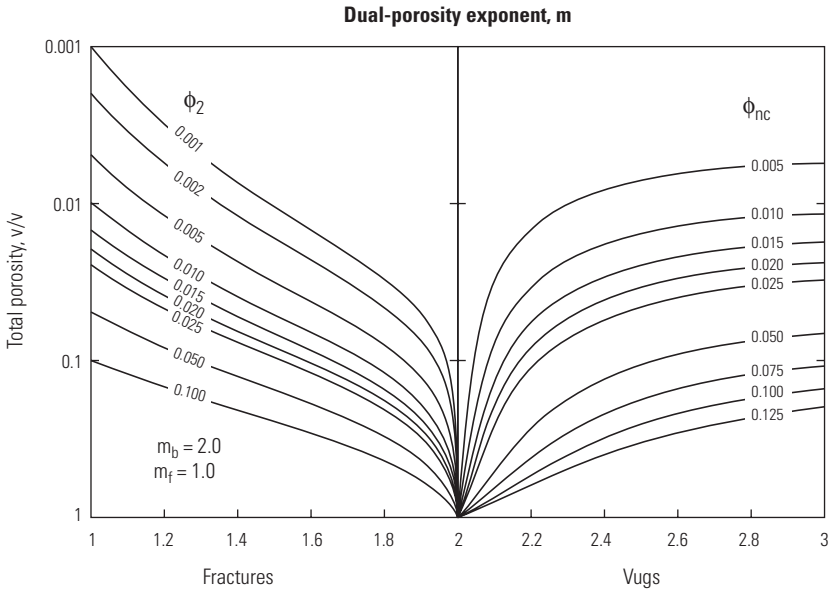


Fig. 4.9 Effect of fractures (left) and non-connected vugs (right) on the total porosity component (m, along the x-axis) of dual-porosity rocks in which m_b of the intergranular fraction is 2. From Aguilera [7]. Used with permission.

with isolated porosity, such as occurs with vugs, oomolds, and microporous grains. The pores do not have to be completely isolated to have almost the same effect. As with fluid flow, conductivity in a rock is controlled primarily by the constrictions to flow, which are the pore throats. A large vug contributes a large porosity but little conductivity. Its m is therefore large. The charts in Fig. 4.9 are useful because the volume of fractures and vugs can be estimated from images of the borehole wall and from acoustic logs.

More generally, whatever the cause of the variations in m, it can be measured directly from resistivity and porosity in a water zone, and then assumed to be the same in the hydrocarbon zone. Alternatively, if the water saturation can be measured by another means in addition to resistivity, then either m or n can be calculated from Archie's equation. One such method uses dielectric measurements in the invaded zone.

4.4.2 The Saturation Exponent, *n*

It takes much longer to complete the type of experiment made by Leverett that leads to the saturation exponent than to measure m. Each core sample must be measured at several saturation states. Displacing water with oil or gas takes time, especially in low permeability samples. Unlike m, it is not possible to derive n from logs in a water zone. As a result there is much less data on n, and values other than 2 are less often used.

However, laboratory experiments have highlighted two main conditions in which n can be significantly different than 2. The first is related to wettability. The traditional view that reservoirs are water-wet was supported by core data, but this was largely because before making any measurements, core samples were thoroughly cleaned of all their natural fluids and left in a highly water-wet state, whatever their state originally. Experiments with native state or restored state samples, or simply rendering the samples oil-wet by injecting suitable fluids, have shown n values much larger than 2 in oil-wet cores. In a water-wet core the water coats the grains and provides a continuous conduction path down to water saturations of 20% or less. In an oil-wet core the oil coats the grains and starts blocking the pore throats when even small volumes are introduced. The result is a sharp increase in resistivity and a high n (Fig. 4.10).

The second condition occurs in rocks in which the pore space is no longer uniform but consists of an irregular mixture of different sized pores. When oil or gas is introduced into such rocks, the water in some pore types may be displaced more easily than in others. For example the oil should easily displace the water in fractures, but may not do so in vugs if they are poorly connected. Carbonates are particularly heterogeneous, and are also more likely to be oil-wet, so that for both reasons the relation between resistivity and S_w is likely to be complicated, with n not equal to 2 and also varying with saturation. These issues will be discussed further in Section 23.4.

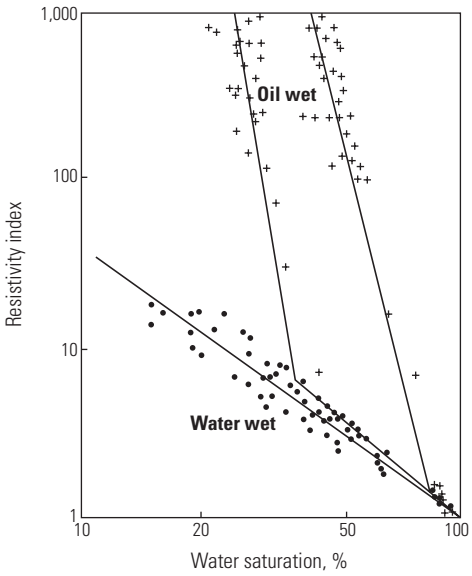


Fig. 4.10 Resistivity-saturation measurements on carbonates that have been flushed to make them water-wet or oil-wet, showing a large increase in n for the latter. The knee in the oil-wet data suggest the other major reason for non-Archie n values – the presence of two or more pore sizes. Adapted from Sweeney and Jennings [8].

4.4.3 Effect of Clay

The electrical effect of clay in core samples was studied by Hill and Milburn [10], Waxman and Smits [11] and others. Figure 4.11 shows the resistivity of a fully saturated rock being compared to the resistivity of the saturating water (Archie's experiment). Two types of behavior can be seen: the linear response, documented earlier by Archie, in the clean sandstone, and the curved response for a shaly sandstone. The presence of clay is seen to decrease the overall resistivity of the sample and to cause $F = R_o/R_w$ to be a function of R_w. This behavior is more clearly seen in Fig. 4.12 where it is expressed in terms of conductivity. A sample containing no clay minerals would be expected to have no conductivity when the value of the saturating water conductivity, C_w, falls to zero. The clay appears to provide an additional conductivity, C_s, which is constant except below a certain low salinity. This allows us to modify the Archie definition of formation factor as follows:

$$C_0 = \frac{C_w}{F} + C_s \tag{4.10}$$

where $1/F$ is the slope in Fig. 4.12 and is independent of salinity but depends on temperature and ion type (although this is generally assumed to be NaCl).

To understand this phenomenon, it is necessary to know that the structure of clay minerals produces a negative surface charge, because of substitution at the surface of the clay crystals of atoms of lower positive valence. The excess negative charge is neutralized by adsorption of hydrated cations which are physically too large to fit inside the crystal lattice. The neutralization occurs at locations referred to as exchange sites. In an ionic solution, these cations can exchange with other ions in solution. A measurement of this property is called the cation exchange capacity, or CEC.

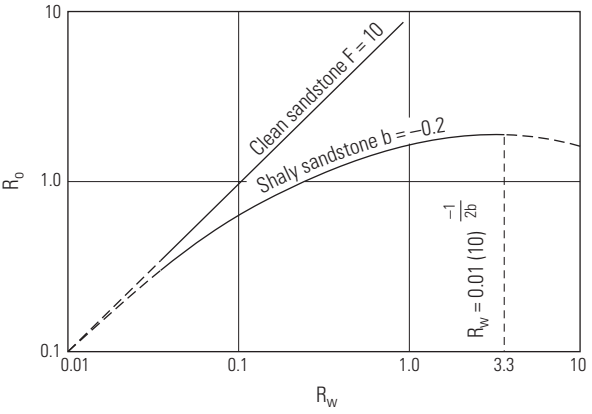


Fig. 4.11 Schematic representation of the observations of Hill and Milburn [10]. The Archie formation factor has been determined on a clay-free rock and one containing shale. From Lynch [12].

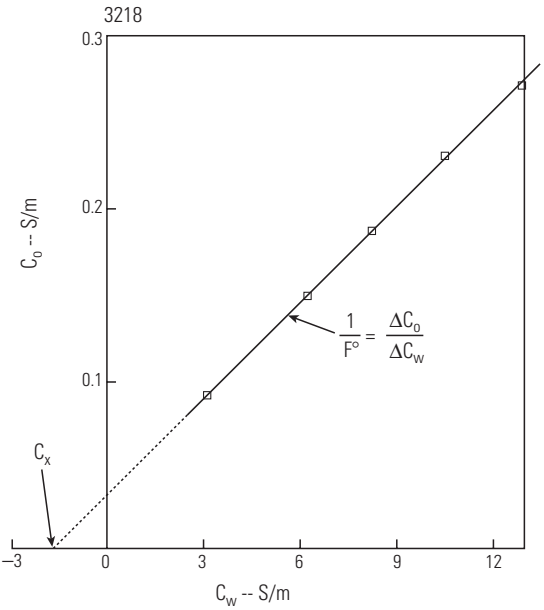


Fig. 4.12 A representation of the measurements of Waxman and Smits on one core-containing clay. The conductivity of the fully saturated rock has been measured for several saturating waters of different conductivities. The units (S/m or Siemens/m) are the inverse of ohm-m. Adapted from Clavier [13].

Many models have been developed to quantify the additional conductivity of clay-bearing rocks. They all have in common the idea of the presence of two conduction paths. The first is the usual charge transport of ions of the electrolyte in the pore space. The second is conduction which occurs because of exchange of cations at negatively charged sites on the clay mineral particles. This secondary path of conduction is viewed differently by several current theories. In one model, it is held to be due to charge transport from the electrolyte to fixed exchange sites on the clay, by transport through the adjacent electrolyte from site to site, and between sites on different clay particles [11]. Regardless of the details, the magnitude of this secondary path of conduction will depend among other factors on the volume of clay, which can be estimated from logs. These estimates, and the conductivity of clay, will be discussed further in Chapter 21.

4.4.4 Alternative Models

It may seem surprising that much log interpretation is based on the relatively simple experimental results of Archie. In fact many attempts have been made to place these equations on a more theoretical basis, and it is worth considering briefly the directions these attempts have taken. One such direction treats the pores as a set of tortuous capillary tubes. In 1950 Wyllie and Rose applied the concept of tortuosity to describe

the electrical current paths in such tubes [14]. Suppose the pore space of a rock sample of length L and cross-sectional area A is replaced by a single sinuous tube of length L_a and constant cross section A_a that has the same water content as the rock and runs from one end of the sample to the other. The end-to-end resistance of the two systems must be equal, i.e.,:

$$R_t \frac{L}{A} = R_w \frac{L_a}{A_a} \tag{4.11}$$

where the resistivity of the sample is R_t and the resistivity of the water is R_w. Since they have the same water content, the volume of the sinuous tube $L_a A_a$ equals the volume of pores ϕLA. Substituting above leads to $F = R_t/R_w = T/\phi$ where T is defined as the tortuosity and equal to L_a^2/L^2. Tortuosity is a useful concept, but it proved to be limited. The tortuosity measured by the time that ions take to pass through a sample was found to be greater than that predicted by F [15]. In reality the electrical path does not have a constant cross section and the concept ignores the branching nature of pore networks.

The next step was therefore to construct network models of pores and pore throats. These have a natural and useful link to the problem of fluid flow. They tend to predict the importance of pore throats [16] or pore-size distribution [17]. An alternative is to model the grains, and in particular to model the geological process of cementation and the reduction in porosity over geological time [18]. The Archie formation-factor relationship can be approximated by allowing the grains to grow in a particular way, while the effect of vugs or fractures can be simulated by other ways. Such models can help establish parameters in complex saturation equations.

Effective medium theories are used in studies of other composite media and have been applied to rocks. These theories are based on treating the rock components (pores and/or grains and/or oil) as inclusions in a host material and calculating the properties of an "effective" homogeneous medium that has the same electrical properties as that given by summing the effect of the individual inclusions. The difficulty is deciding what to use as host. If the grains are taken as the host and pores as the inclusions, the latter will not be connected. With the pore water as host, Hannai and Bruggeman derived an expression for rock conductivity that has been applied by several authors [19, 20]. Alternatively, self-consistent models treat grains and pores on an equal footing by making the effective medium the host. Its properties are adjusted until the total effect of the grains and pores is zero. The pores are then found to be connected but only down to a certain porosity. In actual rocks pores stay connected down to remarkably low values of porosity (they have a low "percolation threshold"). Various schemes have been proposed to simulate the low threshold. One is the self-similar model, in which the solid grains are coated with smaller solid grains that are themselves coated with even smaller grains and so on [21]. With spherical grains, this reduces to an Archie equation with $m = 1.5$; with ellipsoids m is higher. Another introduces a ghost medium that has insignificant volume but has a very low percolation threshold and is conductive [22]. Parameters can be introduced into the model to match experimental data from both shaly and clean sands.

Finally, the form of the Archie formation factor has been called into question. Rock conductivity depends on the volume of water in the sample, i.e., the porosity. Thus, since F $(= C_w/C_t)$ already includes a dependence on porosity, it is not surprising that F correlates well with ϕ. Among others, Herrick and Kennedy [23] pointed out that it might be better to separate the effect of pore volume from the effect of pore distribution and define conductivity as:

$$C_t = C_w S_w \phi E \tag{4.12}$$

where E is a purely geometrical factor which they called the electrical efficiency. They then showed that in many non-shaly rocks E was a linear function of ϕS_w, thereby reducing to Archie's equation in this limit.

In spite of the many attempts to find alternatives, most log interpretation is still based on Archie's equations or extensions to them. The underlying reason is that reservoirs are too complex and varied to be described theoretically. Most alternative models reduce to Archie's equations in some limit. Beyond that limit they either use parameters that prove no more general than m and n, or introduce extra parameters that cannot be measured or easily estimated. The main result of research has been a better understanding rather than practical application. Those extensions to Archie's equations that are most useful are all based on adding formation components or parameters that can be measured on logs or cores, for example clay, vug, or fracture volume.

4.5 A REVIEW OF ELECTROSTATICS

Now that the fundamental ideas of resistivity interpretation have been explored, it is appropriate to consider the question of how resistivity measurements of sedimentary formations are made in situ. First we make a rapid review of some basic notions of electrostatics, which forms the basis for resistivity measurements. This serves as an introduction to the actual resistivity measurement described in the following chapters.

One concept of considerable use is that of the electrostatic potential, which follows directly from Coulomb's law. To arrive at an understanding of the electrostatic potential and to derive a simple expression for it, consider the case (Fig. 4.13) of two charges (q_1 and q_2) at a distance r from one another. Coulomb's law states that the force of repulsion between the two charges is inversely proportional to the square of the separation and varies directly with the product of the magnitudes of the charges. This can be expressed as:

$$F = \frac{1}{4\pi\epsilon_o}\frac{q_1 q_2}{r^2}\,. \tag{4.13}$$

This leads directly to an expression for the electric field vector $\overline{E}$, which is defined as the force per unit charge, from which it follows that,

$$\overline{E} = \frac{1}{4\pi\epsilon_o}\frac{q}{r^2}\hat{r}\,. \tag{4.14}$$

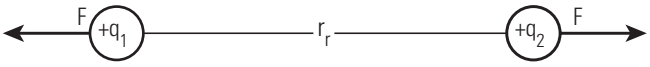


Fig. 4.13 Two charged particles separated by a distance r, exhibiting a repulsive force F.

Here $\hat{r}$ is the unit vector in the direction from the charge producing the field to the point of observation. Equation 4.14 gives the electric field strength at any point r from a charge of magnitude q.

From the definition of work W, which is the integral of the opposing force over the distance travelled, one can write:

$$W = -\int_a^b \bar{F} \cdot d\hat{s} \,, \tag{4.15}$$

which for a unit of charge in an electric field is:

$$\begin{aligned} W = -\int_a^b \bar{E} \cdot d\hat{s} \quad &= \quad -\frac{q}{4\pi\epsilon_o}\int_a^b \frac{dr}{r^2} \\ &= \quad \frac{q}{4\pi\epsilon_o}\left[\frac{1}{r_a} - \frac{1}{r_b}\right] . \end{aligned} \tag{4.16}$$

It is to be noted that the amount of work done in moving from point a to point b is independent of the path taken. It depends only on the value of the two end points. Thus in analogy with the notion of potential energy, the electrostatic potential $\phi(P)$ is defined as:

$$\phi(P) = -\int_{P_o}^{P} \bar{E} \cdot d\hat{s} \,, \tag{4.17}$$

or

$$\overline{E} = -\overline{\nabla}\phi \,. \tag{4.18}$$

The reference point P_o is usually taken to be at a distance infinitely removed from the charge producing the potential, and $\phi(P_o)$ is set to zero. In this case $\phi(P_0)$ is also called the voltage V. For a point charge, this results in:

$$\phi(r) = \frac{q}{4\pi\epsilon_o}\frac{1}{r} = V(r) \,. \tag{4.19}$$

4.6 A THOUGHT EXPERIMENT FOR A LOGGING APPLICATION

Figure 4.14 shows the setup for measuring the resistivity of a homogeneous formation whose conductivity σ (or its inverse, the resistivity) is isotropic. It consists of a current source of intensity I and a voltage-measurement electrode M at some distance r from

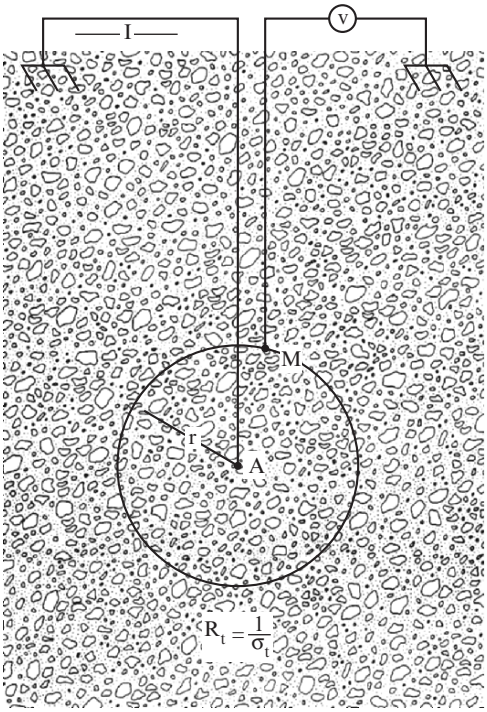


Fig. 4.14 Idealized experiment for determination of the resistivity of an infinite uniform medium of conductivity $\sigma (= 1/R_t)$. It consists of the injection of a current at point A, and measurement of the potential at point M at a distance r from the current electrode.

the current emission at point A. The resistivity of the homogeneous medium is R_t, so its conductivity σ is given by $\sigma = 1/R_t$. (Conductivity is usually written as σ in measurement physics, and as C in log interpretation.)

One way to determine the relationship between the potential at M and the current I is to use some of the relationships from electrostatics. The current I, being a continuous source of charge, can be thought of as producing a potential V, just as would be expected from some equivalent point charge q:

$$V(r) = \frac{1}{4\pi\epsilon_o}\frac{q}{r}\,. \tag{4.20}$$

The problem is to relate the equivalent charge q to the current I.

At any point in the system there will be a current density $\bar{J}$ given by:

$$\bar{J} = \sigma\bar{E} = -\sigma\frac{\partial}{\partial r}V(r) \tag{4.21}$$

$$= \frac{\sigma}{4\pi\epsilon_o}\frac{q}{r^2}\hat{r}\,, \tag{4.22}$$

where $\hat{r}$, the unit vector, is directed radially outward from the current source. In order to put the expression for potential in terms of the total current, I, the current density is integrated over the surface of a sphere enclosing the current source:

$$I = \int \bar{J} \cdot dS = \frac{\sigma q}{4\pi\epsilon_o r^2} 4\pi r^2 = \frac{\sigma q}{\epsilon_o}, \tag{4.23}$$

and q is solved for in terms of I:

$$q = \frac{\epsilon_o I}{\sigma} = \epsilon_o I \; R_t \; . \tag{4.24}$$

This expression for q is now put back into the potential for a single-point charge, Eq. 4.19, to obtain the voltage at a distance r from the current source:

$$V(r) = \frac{\epsilon_o I R_t}{4\pi\epsilon_o r} \; . \tag{4.25}$$

A less tortuous determination of the potential is obtained from Ohm's law in spherical geometry. For the source of current I, the current density on the surface of a sphere of radius r centered on the source is:

$$J = \frac{I}{4\pi r^2} \; . \tag{4.26}$$

The relation between current density and electric field E implies that:

$$E = \frac{R_t I}{4\pi r^2} \; . \tag{4.27}$$

From this expression, the voltage at a distance r from the current source is obtained from:

$$V(r) = \phi(r) = -\int_{\infty}^{r} \frac{R_t I}{4\pi r^2} dr = \frac{R_t I}{4\pi r} \; . \tag{4.28}$$

Thus the value of R_t is found to be:

$$R_t = 4\pi r \frac{V}{I} = k \; \frac{V}{I} \; . \tag{4.29}$$

The setup of Fig. 4.14 can be considered as a rudimentary monoelectrode measurement device for determining formation resistivity. For this device the tool constant k is seen to be $4\pi r$, where r is the spacing between the current electrode and the measurement point. Knowing the injected current and the resultant voltage, the resistivity of the homogeneous medium R_t may then be found.

As an exercise, it is interesting to determine the sensitivity to resistivity variations of such a device following the treatment of Tittman [24]. This question can be examined by considering the current electrode to be at the center of a number of concentric spheres of differing resistivities, as indicated in Fig. 4.15. The object is to find the sensitivity of the measurement to the layers beyond the measurement electrode.

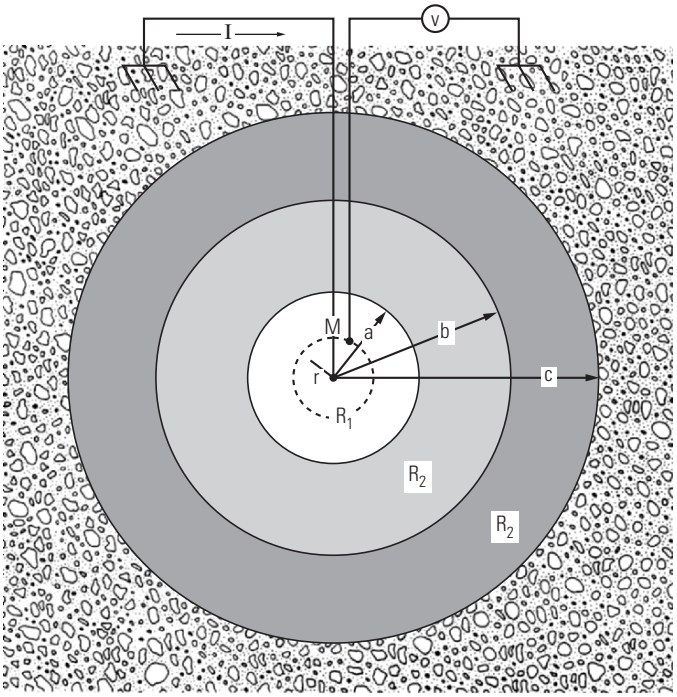


Fig. 4.15 Geometry for determining the sensitivity of the two-electrode device to concentric layers of different resistivities. Adapted from Tittman [24].

This can be found from the differential form of the basic tool response, that is:

$$V(r) = \frac{1}{4\pi r} I R_t \rightarrow dV = -\frac{I R_t}{4\pi r^2} dr \,. \tag{4.30}$$

From this expression of the incremental potential, the voltage at point r can be found by integrating the effect of all the layers, starting at the outermost, up to the point r:

$$V(r) = \int_{\infty}^{r} dV = -\frac{I}{4\pi} \int_{\infty}^{r} \frac{R(r)}{r^2} dr = \frac{I}{4\pi} \int_{r}^{\infty} \,. \tag{4.31}$$

This integration can be broken up into sums over the various regions,

$$V(r) = \frac{I}{4\pi} \left[R_1 \int_{r}^{a} + R_2 \int_{a}^{b} + R_3 \int_{b}^{c} + \cdots \right] . \tag{4.32}$$

This can finally be simplified to

$$V(r) = I R_1 / 4\pi r \left[\left(1 - \frac{r}{a} \right) + \frac{R_2}{R_1} \left(\frac{r}{a} - \frac{r}{b} \right) + \cdots \right] . \tag{4.33}$$

For the case of $r \ll a$ this expression reduces to the result of Eq. 4.29 for a homogeneous medium of resistivity R_1.

4.7 ANISOTROPY

For the student with only a passing exposure to electromagnetics the concept of conductivity (or its inverse, resistivity) being something other than a scalar may come as a surprise. In fact the concept that the current flow is along the line of the applied electric field is deeply ingrained. A material in which this is not the case is said to be electrically anisotropic.

The formal expression of anisotropy starts with a more careful definition of the current vector than was given in Eq. 4.21. Instead we should write:

$$\mathbf{J} = \widehat{\sigma}\mathbf{E} \tag{4.34}$$

$$\begin{bmatrix} J_x \\ J_y \\ J_z \end{bmatrix} = \begin{bmatrix} \sigma_x & 0 & 0 \\ 0 & \sigma_y & 0 \\ 0 & 0 & \sigma_z \end{bmatrix} \mathbf{E}, \tag{4.35}$$

where the conductivity tensor $\widehat{\sigma}$ is written for a coordinate system with three orthogonals aligned along the so-called principal axes of the material whose conductivity is under discussion. In some other rotated coordinate system it would take all nine components of the conductivity matrix to describe the current flow for an arbitrarily imposed electric field. It is easy to show that in general, if the electric field is not aligned along one of the three principal axes and if the three components have distinct values then the direction of the current vector will not lie along the direction of the imposed E vector (Problem 4.10).

One simplification that is frequently applied to sedimentary formations is to treat them as being transversely isotropic, meaning that the horizontal conductivity (σ_h) is independent of orientation in the plane of bedding, but different from the vertical conductivity (σ_v). For a simple example of such a formation imagine a finely layered sand-shale sequence. The sand might be largely hydrocarbon-saturated with a high-resistivity or small-conductivity σ_{sa} and the interlayered shale layers might have a fairly high-conductivity σ_{sh}. Depending upon the relative volume of the shale V_{sh} and the orientation of the electric field (either parallel to the imagined bedding or perpendicular to it for this simple example) the formation resistivity will vary widely. When the electric field creating the current is horizontal and parallel to the bedding the conductivities of the two components add volumetrically, leading to a horizontal conductivity of:

$$\sigma_h = V_{sh}\sigma_{sh} + (1 - V_{sh})\sigma_{sa} \tag{4.36}$$

For the case of a vertical electric field, it is the resistivities that add volumetrically. Until the 1990s most resistivity devices measured the electric field perpendicular to the device, so that in vertical wells they measured R_h and σ_h. This was a pity, since σ_h is sensitive to the higher shale-conductivity (σ_{sh}) and insensitive to the sand conductivity, while it is just the opposite for σ_v. The proof of this is left as an exercise. It was the advent of horizontal wells, and later of triaxial induction devices, that led to the measurement of R_v and σ_v.

Anisotropy is also caused by alternate laminations of fine-grained and coarse-grained sand. The fine-grained sand will normally have high irreducible water

saturation and low resistivity while the coarse-grained sand has high oil saturation and high resistivity. The result is similar to sand-shale laminations with R_h reflecting mainly the low-resistive, water-bearing, fine-grained sand. Laminated sands are one type of low resistivity pay, so-called because the traditionally measured R_h is low even though the sand may produce oil.

Anisotropy can affect the values of m and n in surprising ways. One might think that a layered formation or core sample in which each layer has the same m would have the same total m. Not so, if the layers have different porosity, because the conductivity of each layer, which is proportional to ϕ^m, is different. The total conductivity then depends on the proportion of each type of layer. Kennedy and Herrick showed that the total m of such a rock depended on this proportion and was also very different parallel to and perpendicular to the layers (Fig. 4.16) [25]. Similar results are found for n when, for example, the only difference between the layers is S_w. These results are all due to the logarithmic definition of m and n and the lack of any simple arithmetic

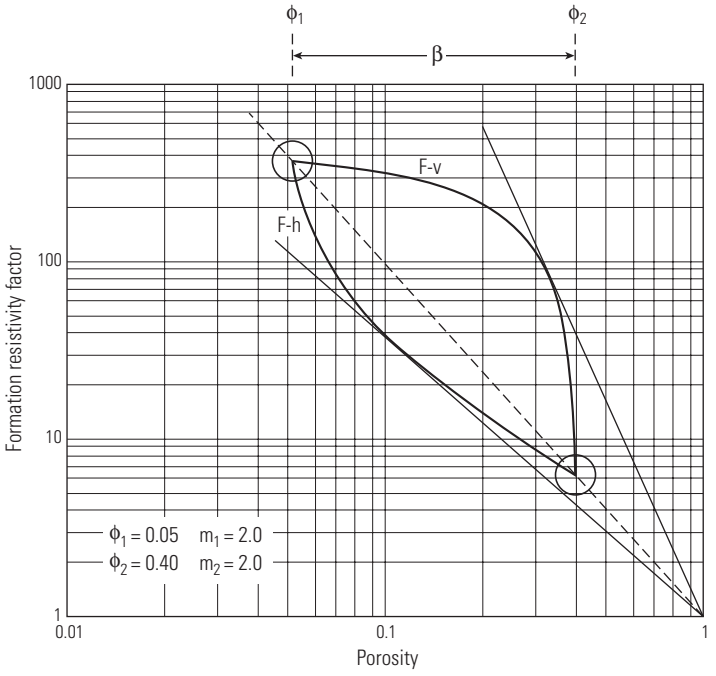


Fig. 4.16 An example of the variations in formation factor and m in an anisotropic, layered medium. In this case there are alternating layers with porosities of 0.4 and 0.05 v/v, but both with the same m. As the proportion β of layer type 1 increases, the total m decreases below 2 if measured horizontally ($F - h$) or increases above 2 if measured vertically ($F - v$). The minimum slope of ($F - h$) is 1.6, and the maximum slope of ($F - v$) is 4.0. From Kennedy and Herrick [25]. Used with permission.

averaging. Laminated sands should be interpreted with specific saturation equations, as will be seen in Section 23.3.4.

The axes of anisotropy are not always horizontal or vertical, nor are boreholes always vertical. So what happens in between? For an induction-logging device, which measures perpendicular to the axis of the tool, the measured conductivity will lie between σ_h, when the relative dip between the device and the horizontal is 0°, and a value of $\sqrt{\sigma_h \sigma_v}$, the geometric mean, when the relative dip is 90°. Other resistivity-measurement devices do not measure exactly perpendicular to the tool and are more influenced by the resistivity parallel to it.

Where does this mysterious factor of $\sqrt{\sigma_h \sigma_v}$ come from? As it appears frequently in the literature of electrical anisotropy it may be of some interest to see how it arises and how it is related to the so-called paradox of anisotropy.

Well, it involves a lot of details (which can be found in any number of venerable texts on electrical methods applied to geophysics [26–28]). To sketch out the origin, we note that, in the case of anisotropy, to find the potential due to a point source a form of Maxwell's equations is used which states that the divergence of the current at any point not containing a source must be zero.

So the equation to be solved for the distribution of a potential in a conductive medium with a current source is:

$$-\nabla \cdot \mathbf{i} \;=\; \nabla \cdot (\widehat{\sigma} \nabla \phi) \;=\; 0. \tag{4.37}$$

Assuming that the conductivity can be specified by three values along the three principal axes we can write:

$$\sigma_x \frac{\partial^2 \phi}{\partial x^2} \;+\; \sigma_y \frac{\partial^2 \phi}{\partial y^2} \;+\; \sigma_z \frac{\partial^2 \phi}{\partial z^2} \;=\; 0. \tag{4.38}$$

For the case of a horizontally isotropic medium which has only two distinct values of conductivity σ_h and σ_v we can rewrite the equation as:

$$\sigma_h \left(\frac{\partial^2 \phi}{\partial x^2} \;+\; \frac{\partial^2 \phi}{\partial y^2} \right) \;+\; \sigma_v \frac{\partial^2 \phi}{\partial z^2} \;=\; 0. \tag{4.39}$$

The usual approach to solving this equation in the homogeneous case (where the σ is the same in all directions and can be factored out) is to recognize the spherical symmetry and define a new variable R given by $R^2 = x^2 + y^2 + z^3$. In this case the Laplace equation (Eq. 4.37) becomes:

$$\frac{\partial}{\partial R} \left(R^2 \frac{\partial \phi}{\partial R} \right) = 0 \tag{4.40}$$

which can be solved on sight as

$$\phi = -\frac{A}{R} + B. \tag{4.41}$$

The boundary conditions determine the two constants. It is conventional to consider the potential, ϕ, to be zero at large values of R, so B is set to zero. The constant A is determined by considering the total current being emitted.

To find a solution of Eq. 4.39 the conductivities must be factored out of the left-hand side in order to use the simple formulation of Eq. 4.41. This is achieved by a coordinate transformation to stretch the anisotropic space into an isotropic one. It is arrived at by multiplying the x- and y-axes by $\sigma_h^{-1/2}$, *and the z-axis by* $\sigma_v^{-1/2}$ *to modify the radial coordinate R as follows:*

$$R = \left(\frac{x^2}{\sigma_h} + \frac{y^2}{\sigma_h} + \frac{z^2}{\sigma_v}\right)^{1/2} \tag{4.42}$$

Using this formulation allows the writing of Eq. 4.39 as the Laplace equation using the transformed coordinate system.

In the solution it is convenient to use the coefficient of anisotropy λ *which is defined as* $\lambda \equiv \sqrt{\frac{\sigma_h}{\sigma_v}}$. *What is found is that the equipotential surfaces are no longer spheres but ellipsoids of revolution and that the ratio of the principal axes is* λ.

Finding the value of the constant A involves computing the current-density components from the potential. One component looks like:

$$j_x = -\sigma_h \frac{\partial \phi}{\partial x} = \frac{A x {\sigma_h}^{3/2}}{(x^2 + y^2 + \lambda^2 z^2)^{3/2}}. \tag{4.43}$$

Then the three components are added quadratically to produce the total-current density magnitude that depends on R and the angle θ *measured from the z-axis. This current density is then integrated over the surface of a sphere centered on the current source (as was done in Eq. 4.23 for the isotropic case) and allows relating the constant A to the current I. The result of the messy integration is that*

$$I = \frac{4\pi A}{{R_h}^{3/2}\lambda}, \tag{4.44}$$

reverting to the use of resistivity rather than conductivity.

This result now determines the constant A so that the potential is then given by:

$$\phi = \frac{I\lambda {R_h}^{3/2}}{4\pi {R_h}^{1/2}\left(x^2 + y^2 + \lambda^2 z^2\right)^{1/2}} = \frac{I\sqrt{R_v R_h}}{4\pi\left(x^2 + y^2 + \lambda^2 z^2\right)^{1/2}}. \tag{4.45}$$

By comparison to the earlier result for the isotropic case (Eq. 4.28) it is seen that the resistivity controlling the anisotropic mixture is given by $\sqrt{R_h R_v}$, *in place of* R_t.

REFERENCES

1. Leverett MC (1939) Flow of oil-water mixtures through unconsolidated sands. Pet Trans, AIME 132:149–171

2. Archie GE (1942) The electrical resistivity log as an aid in determining some reservoir characteristics. Pet Trans, AIME 146:54–62

3. Martin M, Murray GH, Gillingham WJ (1938) Determination of the potential productivity of oil-bearing formations by resistivity measurements. Geophysics 3:258–272

4. Guyod H (1944) Fundamental data for the interpretation of electric logs. Oil Weekly 115(38):21–27

5. Herrick DC, Kennedy WD (1996) Electrical properties of rocks: effects of secondary porosity, laminations and thin beds. Trans SPWLA 37th Annual Logging Symposium, paper C

6. Maute RE, Lyle WD, Sprunt ES (1992) Improved data-analysis method determines Archie parameters from core data. Paper 19399 in: J Pet Tech January: 103–107

7. Aguilera MS, Aguilera R (2003) Improved models for petrophysical analysis of dual porosity reservoirs. Petrophysics 44(1):21–35

8. Sweeney SS, Jennings HY (1960) The electrical resistivity of preferentially water wet and preferentially oil wet carbonate rock. Prod Mont 24(7):29–32

9. Roberts JN, Schwartz LM (1985) Grain consolidation and electrical conductivity in porous media. Phys Rev B 31(9):5990–5997

10. Hill HJ, Milburn JD (1956) Effect of clay and water salinity on electro-chemical behavior of reservoir rocks. Pet Trans, AIME 207:65–72

11. Waxman MH, Smits LJM (1968) Electrical conductivities in oil-bearing shaly sands. Paper 1863-A in: SPE J June:107–122

12. Lynch EJ (1962) Formation evaluation. Harper & Row, New York, p 213

13. Clavier C, Coates G, Dumanoir J (1984) Theoretical and experimental basis for the dual water model for interpretation of shaly sands. Paper 6859 in: SPE J April:153–168

14. Wyllie MRJ, Rose WD (1950) Some theoretical considerations related to the quantitative evaluation of the physical characteristics of reservoir rock from electrical log data. Pet Trans, AIME 189:105–118

15. Winsauer WO, Shearin HM, Masson PH, Williams M (1952) Resistivity of brine-saturated sands in relation to pore geometry. AAPG Bull 36:253–277

16. Owen JE (1952) The resistivity of a fluid-filled porous body. Pet Trans, AIME 195:169–174

17. Wong P-Z, Koplik J, Tomanic JP Conductivity and permeability of rocks. Phys Rev B 30(11):6606–6614

18. Schwartz LM, Kimminau S (1987) Analysis of electrical conduction in the grain consolidation model. Geophysics 52(10):1402–1411

19. Bussian AE (1983) Electrical conductance in a porous medium. Geophysics 48(9):1258–1268

20. Berg CR (1996) Effective-medium resistivity models for calculating water saturation in shaly sands. The Log Analyst 37(3):16–28

21. Sen PN, Scala C, Cohen MH (1981) A self-similar model for sedimentary rocks with application to the dielectric constant of fused glass beads. Geophysics 46(5):781–795

22. de Kuijper A, Sandor RKJ, Hofman JP, Koelman JMVA, Hofstra P, de Waal JA (1995) Electrical conductivities in oil-bearing shaly sand accurately described with the SATORI saturation model. Trans SPWLA 36th Annual Logging Symposium, paper M

23. Herrick DC, Kennedy WD (1993) Electrical efficiency: a pore geometric model for the electrical properties of rocks. Trans SPWLA 34th Annual Logging Symposium, paper HH

24. Tittman J (1986) Geophysical well logging. Academic Press, Orlando, FL

25. Kennedy WD, Herrick DC (2004) Conductivity anisotropy in shale-free sandstone. Petrophysics 45(1):38–38

26. Smythe WR (1950) Static and dynamic electricity. McGraw-Hill, New York, Toronto, London

27. Jakosky JJ, (1940) Exploration geophysics. Times-Mirror Press, Los Angeles, CA

28. Keller GV, Frischknecht FC (1966) Electrical methods in geophysical prospecting. Pergamon Press, Oxford, New York, Toronto, Sydney, Braunschweig

Problems

4.1 Table 4.1 is a copy of some of Archie's original data. For the samples listed, plot the formation factor versus porosity, and graphically determine an expression for a reasonable fit to the data.

What is the maximum percentage error in F if the approximate form $F = 1/\phi^2$ is used?

4.2 Figure 4.2 shows resistivity measurements versus saturation for two core samples. Using information derived from curve I, plot the values of relative conductivity for $S_w = 0.1$, 0.2, 0.4, 0.6, and 0.9 on Fig. 4.5 (which presents equivalent data from Leverett's experiments on sand packs).

4.3 The original text accompanying Fig. 4.2 states that the salinity of the saturating water for the two samples was identical and that the porosity of sample I is 45 p.u.

Table 4.1 Data for Problem 4.1. From Archie [2].

Core analysis data			
Porosity	Formation factor	Porosity	Formation factor
30	9	27	10
32	7	30	9
25	13	28	10
27	11	20	8
34	14	28	8
27	11	27	11
30	9	28	9
31	9	27	10
25	9	25	1
30	9	21	20
20	14	23	15
25	14	24	14
27	11	25	13
26	12		

and that of sample II is 25 p.u. What two inconsistencies are indicated by the data shown in the figure?

4.4 Consider a two-electrode device, such as that shown in Fig. 4.14, where the spacing, A−M, between the current source and voltage monitor is 1 m.

4.4.1 What is the resistance seen by this device in a completely water-saturated 20 p.u. porous limestone formation? The formation water is seawater (20 kppm NaCl), and the temperature is 100°F.

4.4.2 What resistance does it see in a zero porosity limestone (marble)?

4.5 The water resistivity R_w in the log example of Fig. 2.18, was estimated to be 0.016 ohm-m, based on the assumption that a water zone had been identified.

4.5.1 What is the estimate of R_w, if 10% residual oil saturation is present in the "water" zone?

4.5.2 Assuming that the water contains only dissolved NaCl, what is a reasonable value for the concentration at a temperature of 200°F?

4.6 The water saturation in zone A of Fig. 2.18 was estimated to be 79% assuming a cementation exponent of 2.

4.6.1 What value of cementation exponent produces a water saturation of 50%?

4.6.2 What value of porosity would be required to yield a value of S_w of 50% using a cementation exponent of 2?

4.7 Suppose a series of core measurements on reservoir rocks in the range of 20–30 p.u. porosity has established that the cementation exponent is between 1.8 to 1.9, i.e., $F = 1/\phi^{1.8}$ or $F = 1/\phi^{1.9}$.

4.7.1 What percentage error in the logging measurement of R_t can be tolerated so that its influence on the saturation estimate is smaller than that induced by the possible variation in cementation exponent? Assume a saturation exponent of 2.

4.7.2 Show that a 20% error in R_t can be tolerated if the porosity is 10 p.u.

4.8 Work through the derivation of tortuosity given in the text and prove that $T = F\phi$. (Note that the derivation given in Wyllie and Rose [14] is incorrect).

4.8.1 Calculate T at $\phi = 0.1$ and $\phi = 0.2$ assuming $m = 2$. Show that the assumption that $m = 2$ implies that tortuosity increases as porosity decreases.

4.9 Consider a formation consisting of alternating horizontal layers of sand and shale. The resistivity of the sand is 500 ohm-m and the resistivity of the shale is 1 ohm-m. If the shale volume, V_{sh}, is 10%, calculate the horizontal resistivity, R_h and the vertical resistivity R_v of the formation and show that R_v is a closer estimate of the sand resistivity, while R_h is a better estimate of the shale resistivity.

4.10 Consider a transversely isotropic formation, as in the case above. This implies $\sigma_x = \sigma_y = \sigma_h$, and the vertical conductivity is $\sigma_h = \sigma_z$, using the convention that the horizonal formation is in the x–y plane and the vertical is aligned with the z-axis. The anisotropy is such that $\sigma_h/\sigma_v = 10$. If an electric field is established at 45° from the vertical, compute the angle between the current vector **J** and the electric-field vector **E**.

5

Resistivity: Electrode Devices and How They Evolved

5.1 INTRODUCTION

We have seen the utility of knowing formation resistivity and an idealized approach to making the measurement. This chapter focuses on the evolution of one type of electrical logging tool: electrode devices, so named because the measurement elements are simply metallic electrodes. These devices utilize low-frequency current sources, in most cases below 1,000 Hz. The historical progression from the normal device to traditional focused dual laterologs will be traced. An indication of the measurement limitations for each of these types of tools will be given and related to their design. The methods used for the prediction and interpretation of their response will be discussed.

The traditional focused dual laterolog was the main device used for electrode measurements of resistivity for many years, even though it had several known shortcomings. Many of these shortcomings were solved by the introduction of array devices, a development that was made possible partly by the availability of fast inversion software. The chapter concludes with a description of array devices and an example of their application.

5.2 UNFOCUSED DEVICES

5.2.1 The Short Normal

The earliest commercial device, the *short normal*, is illustrated in Fig. 5.1. It bears a strong resemblance to the thought experiment of the preceding chapter. The

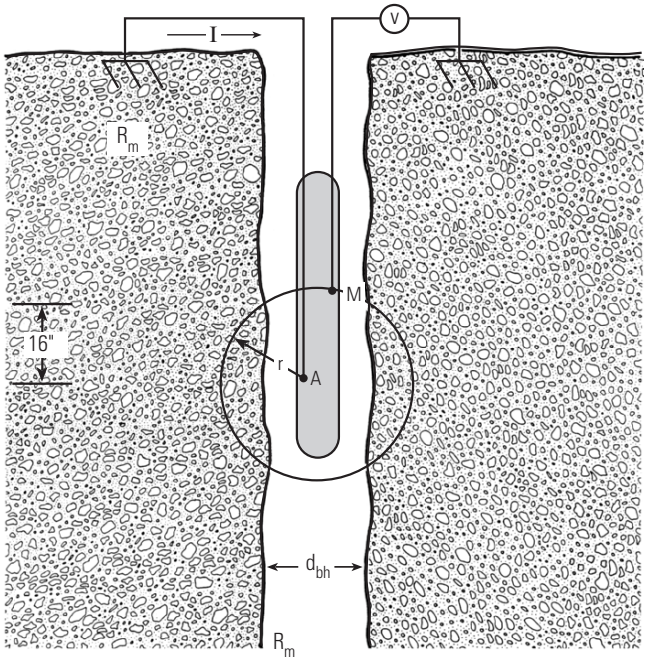


Fig. 5.1 A schematic representation of the short normal. A 16 in. spacing is indicated between current electrode A and measure electrode M.

differences include the presence of a borehole and a sonde (on which the current electrode A and measure electrode M are located). As indicated in the figure, the spacing between the current electrode and voltage electrode was 16 in., and thus the designation "short."

Two basic problems are associated with the short normal, both related to the presence of the borehole, which is normally filled with a conductive fluid. There is a sensitivity of the measurement to the mud resistivity and hole size, as indicated in Fig. 5.2. In a borehole filled with very conductive mud, the current tends to flow in the mud rather than the formation. In this case, the apparent resistivity as deduced from the injected current and resultant voltage will not reflect the formation resistivity very accurately.

The second difficulty with this measuring technique is illustrated in Fig. 5.3. Once again, the conductive borehole fluid provides an easy current path for the measure current into adjacent shoulder beds of much lower resistivity (R_s) than the formation (R_t) directly opposite the current electrode. In this case, the apparent resistivity (from the measurement of the voltage of electrode M and the current I, in combination with the tool constant) will again be representative not of the resistive bed, but, more likely, of the less resistive shoulder bed.

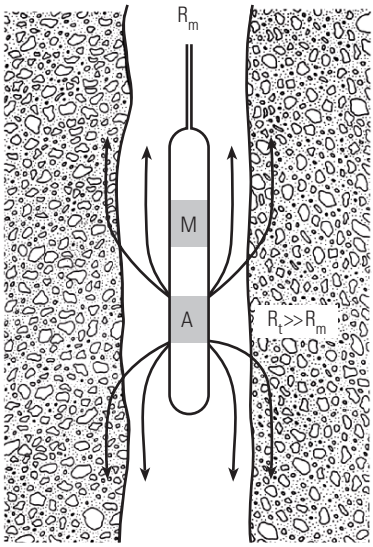


Fig. 5.2 Idealized current paths for the short normal in a very conductive borehole mud.

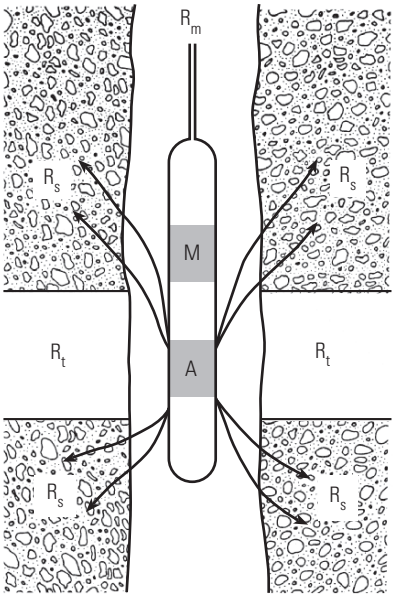


Fig. 5.3 Idealized current paths for the short normal in front of a thin resistive bed ($R_t \gg R_s$).

5.2.2 Estimating the Borehole Size Effect

To get an idea of the effect of the borehole size on the short normal and to gain an appreciation for the need for computational methods to attack such questions, a simple approach is investigated.

For estimating the borehole size effect, first assume that the potential distribution caused by the current source is spherical. This means ignoring the presence of the borehole, on the one hand, and on the other, considering that the borehole represents a small current loss from the injected measure current. In this way, a simple model for the tool and formation can be used as indicated in Fig. 5.4. The measure current is presented with two equivalent resistance paths: Res_t, which represents the resistance presented by the formation of resistivity R_t, and Res_m, the effective resistance of the borehole between the current electrode and the voltage measure electrode.

Taking advantage of the first assumption, that the equipotential surfaces are spherical, Eq. 4.28 can be used to define the formation resistance, out to a distance r, in terms of the formation resistivity R_t:

$$V = \frac{I\ R_t}{4\pi r} . \tag{5.1}$$

This yields the effective resistance of the formation (if the borehole were not present):

$$Res_t = \frac{R_t}{4\pi r} . \tag{5.2}$$

The borehole resistance can be estimated from its geometry, using the analysis developed earlier in conjunction with the mud cup. The radius of the borehole and measurement sonde are given by r_{bh} and r_s, respectively. The mud resistance Res_m, is given, in terms of its resistivity, R_m, by:

$$Res_m = R_m \frac{l}{A} , \tag{5.3}$$

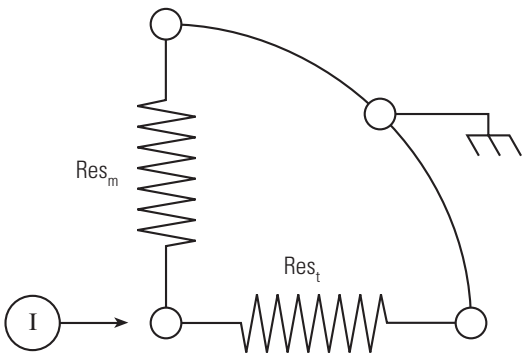


Fig. 5.4 A simple equivalent circuit for estimating the short normal borehole effect. The effective resistance of the mud is Res_m, and the effective resistance of the formation is given by Res_t.

where l, in this case, is the electrode spacing r. So:

$$Res_m = R_m \frac{r}{\pi(r_{bh}^2 - r_s^2)}, \tag{5.4}$$

where no electrical interaction has been assumed between the borehole and the formation.

To evaluate the sensitivity of the model to the borehole mud, an expression will now be derived for the ratio of the apparent resistivity (R_{16}) to the mud resistivity R_m. First, the apparent resistivity is expressed in terms of the formation resistance and the mud resistance of the equivalent circuit of Fig. 5.4:

$$\frac{1}{R_{16}} = \frac{1}{4\pi r}\left[\frac{1}{Res_t} + \frac{1}{Res_m}\right]. \tag{5.5}$$

This can be rewritten as:

$$\begin{aligned}\frac{1}{R_{16}} &= \frac{1}{4\pi r}\left[\frac{4\pi r}{R_t} + \frac{\pi(r_{bh}^2 - r_s^2)}{r\ R_m}\right] \\ &= \frac{1}{R_t} + \frac{1}{R_m}\left[\frac{1}{4}\frac{(r_{bh}^2 - r_s^2)}{r^2}\right] \\ &= \frac{1}{R_t} + \frac{1}{R_m^*}.\end{aligned} \tag{5.6}$$

This expression is then inverted to get the desired form:

$$\frac{R_{16}}{R_m} = \frac{R_t}{R_m}\frac{R_m^*}{R_t + R_m^*}. \tag{5.7}$$

Evaluating the second part of Eq. 5.7 for the case of an 8 in. borehole and a sonde of 4 in. diameter, letting $x = R_t/R_m$, yields

$$\frac{R_{16}}{R_m} \approx x\left[\frac{1}{1 + 0.01x}\right], \tag{5.8}$$

which is plotted in Fig. 5.5, along with the standard presentation of the borehole size effect for the short normal device. It is clear that this simple analysis has indicated a trend but is considerably in error in predicting the actual perturbation that results from hole size and mud resistivity contrast. The figure shows that in front of a formation with a resistivity 100 times that of the mud, the simple model predicts an error of a factor of 2, whereas in fact there will be none. At higher contrasts the difference between this simple model and the actual tool behavior becomes even greater.

A look at the correction chart data shows that for an 8 in. hole size, the short normal does a fairly good job of measuring the correct formation resistivity, except for very large mud/formation resistivity contrasts. However, for the 16 in. borehole size, this is not the case. For a mud/formation contrast of 100, the measurement will

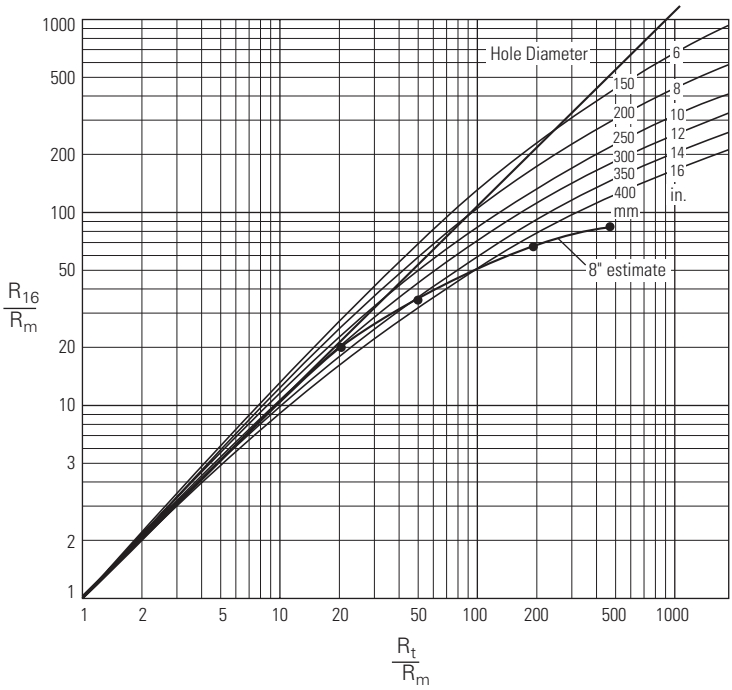


Fig. 5.5 Borehole correction chart for the 16 in. short normal. Indicated is the approximate model correction for an 8 in. borehole, showing the need for a careful evaluation. Courtesy of Schlumberger.

be in error by a factor of 2. Thus the need for such correction charts. But how are they constructed?

Borehole correction charts for electrical logging tools are constructed by obtaining a solution of Laplace's equation:

$$\nabla^2 V = 0, \tag{5.9}$$

subject to the boundary conditions imposed by the borehole and tool configuration. There are three approaches to obtaining solutions to this equation: analog simulation, analytic solutions, and computer modeling. Figure 5.6 is a sketch of the situation to be modeled, indicating the zones of interest, including an invaded zone of resistivity different from the formation resistivity. For the analog simulation, the axially symmetric rings of formation about the borehole axis are replaced by sets of resistors, as indicated in Fig. 5.7. The construction of such analog computers calls for hundreds of thousands of individual resistors to be soldered into place. Such simulators were constructed in the 1950s and were used over a period of about 20 years. Advances in analytical solutions and high-speed digital computers supplanted this technique.

The geometry for the analytical solution of Laplace's equation for the logging problem is shown in Fig. 5.8. The three components of current density are indicated

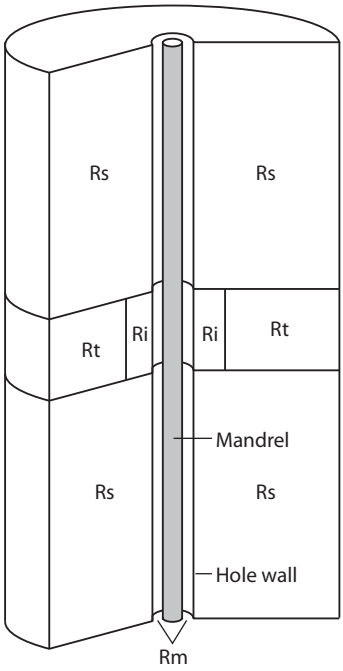


Fig. 5.6 A geometric and electrical model of the borehole and formation used for generating electrical tool response to layered beds with step profile invasion. The centered tool is referred to as a mandrel.

at a point $P(\rho, \phi, z)$ some distance from the current source. For this axially symmetric situation, the equation reduces to:

$$\frac{1}{\rho}\frac{\partial}{\partial\rho}\left[\rho\frac{\partial V}{\partial\rho}\right] + \frac{\partial^2 V}{\partial z^2} = 0\,, \tag{5.10}$$

and the two components of current density are related to the potential by:

$$J_\rho = -\sigma\frac{\partial V}{\partial\rho} \tag{5.11}$$

and

$$J_z = -\sigma\frac{\partial V}{\partial z}. \tag{5.12}$$

The azimuthal component of current is zero. The solution for the potential $V(\rho, z)$ is found by assuming a form that is separable:

$$V(\rho, z) = R(\rho)Z(z). \tag{5.13}$$

The solution is found, after using boundary conditions of potential and normal current continuity across the borehole interface, to be expressed as infinite integrals of Bessel functions [2]. These can be evaluated numerically to give good predictive behavior for various borehole sizes, mud contrasts, and depth of invasion.

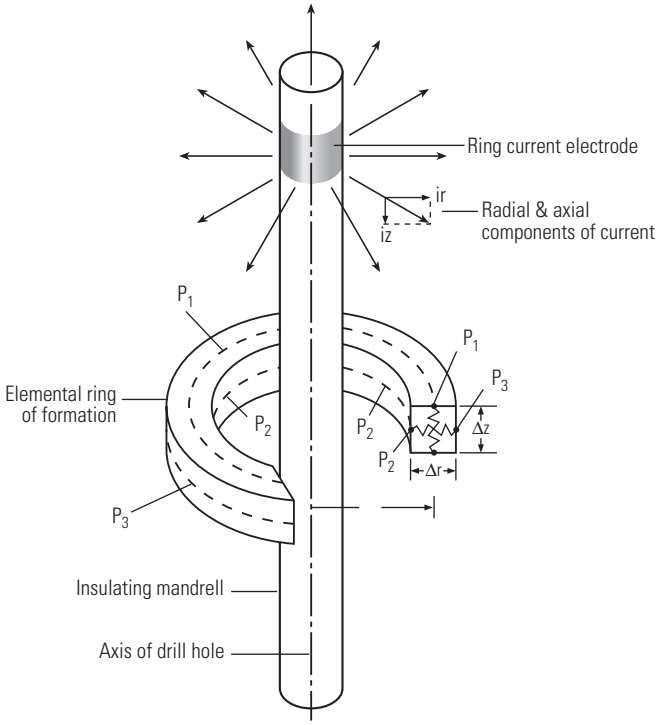


Fig. 5.7 Analog simulation of the borehole/formation replaces axial rings of formation by a network of resistor pairs.

For the more complicated case of tool response to bed boundaries, computer modeling techniques such as the finite elements method can be used [3, 4]. In this technique a grid is set up to represent the borehole and formation. A solution of Laplace's equation is then sought, subject to the boundary conditions, using a trial function for the potential, which is then evaluated at each one of the node points. The final solution is obtained by determining at each point the potential that minimizes the energy of the system.

A continuing examination of the shortcomings of the short normal in Fig. 5.9 reveals the kind of response problems encountered for large contrasts between the shoulder beds and the bed of interest. Note that in the upper part of the figure some idea of the actual tool implementation is given. The electrode B is at the surface, whereas the electrode N, to which the potential measurement is referenced, is actually located down-hole on the measurement sonde. In this particular case, the resistivity contrast between beds is 14, and the borehole diameter is half the spacing between current source and voltage electrode. Even for a bed 3 ft thick, it is seen that the central value of resistivity does not attain the desired value. If the bed is only 6 in. thick, then the behavior becomes nonintuitive, with the apparent resistivity dipping below the value of the shoulder bed.

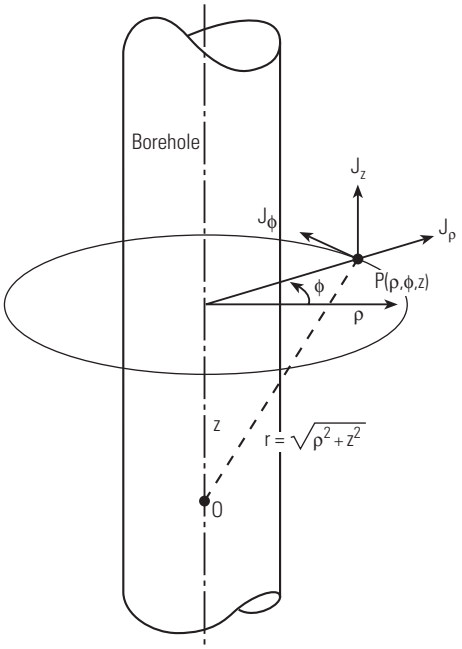


Fig. 5.8 Geometry for the analytic solution of Laplace's equation in the cylindrical symmetry of the borehole.

When attempts were made to improve this bed-boundary resolution, the normal device evolved to the lateral device, illustrated in Fig. 5.10. The lateral sonde is much like the normal sonde except that there are two voltage electrodes, and the potential difference between them is used to indicate the resistivity of the formation layer between them. This will be nearly the case for beds whose thickness exceeds the spacing between the electrodes marked A and N. The bottom of the figure shows the response to two beds, whose thickness is given in terms of the electrode spacing. It is clear that there has been some improvement for bed resolution, but the response is still quite complicated because of current flow through the mud to zones other than the one directly in front of the measuring points. Russian tool developers perfected the art of combining different normal and lateral devices, so that most resistivity tools run in the former Soviet Union are of this type. The most common combination, known as the BKZ log, consists of up to five laterals, one inverted lateral and one normal [6].

5.3 FOCUSED DEVICES

5.3.1 Laterolog Principle

The next step in the evolution of electrical tools was the implementation of current focusing. Figure 5.11 illustrates, on the left half of the diagram, the current paths for

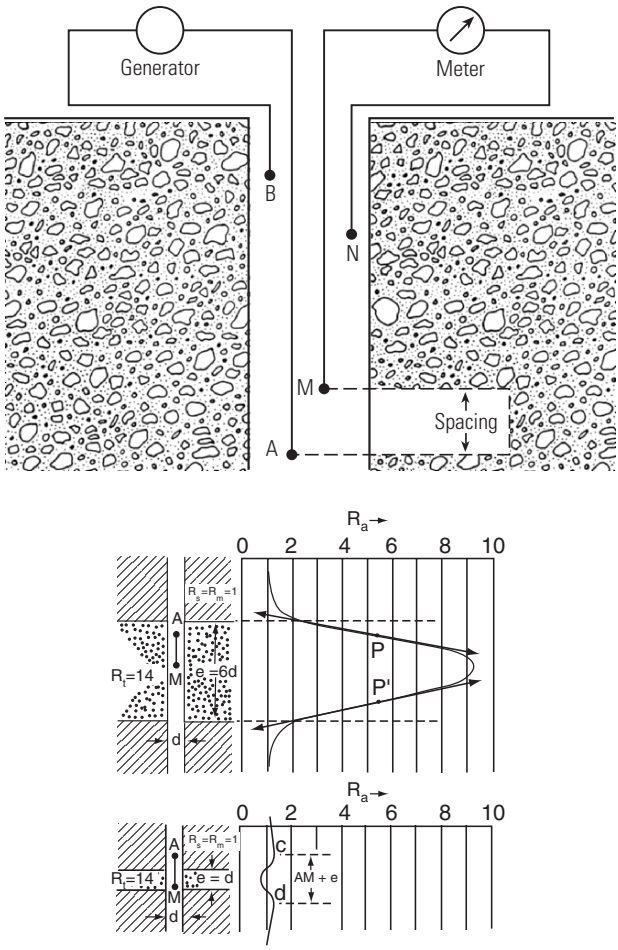


Fig. 5.9 A schematic of the short normal and its response in two common logging situations. The bed thickness is e and d is the borehole diameter. Adapted from Doll et al. [5].

the normal device in the case of a resistive central bed. The current tends to flow around it, through the mud, into the less resistive shoulders. The desired current path is shown on the right half of the figure, where the measure current is somehow forced through the zone of interest.

The principle of focusing is shown in Fig. 5.12, where there are now three current-emitting electrodes, A_0, A_1, and A_1'. This type of array is known as a guard focusing device and is commonly referred to as a Laterolog-3 (LL3), device. The potential of electrodes A_1 and A_1' is held constant and at the same potential as the central electrode A_0. Since current flows only if a potential difference exists, there should, in principle, be no current flow in the vertical direction. The sheath of current therefore emanates

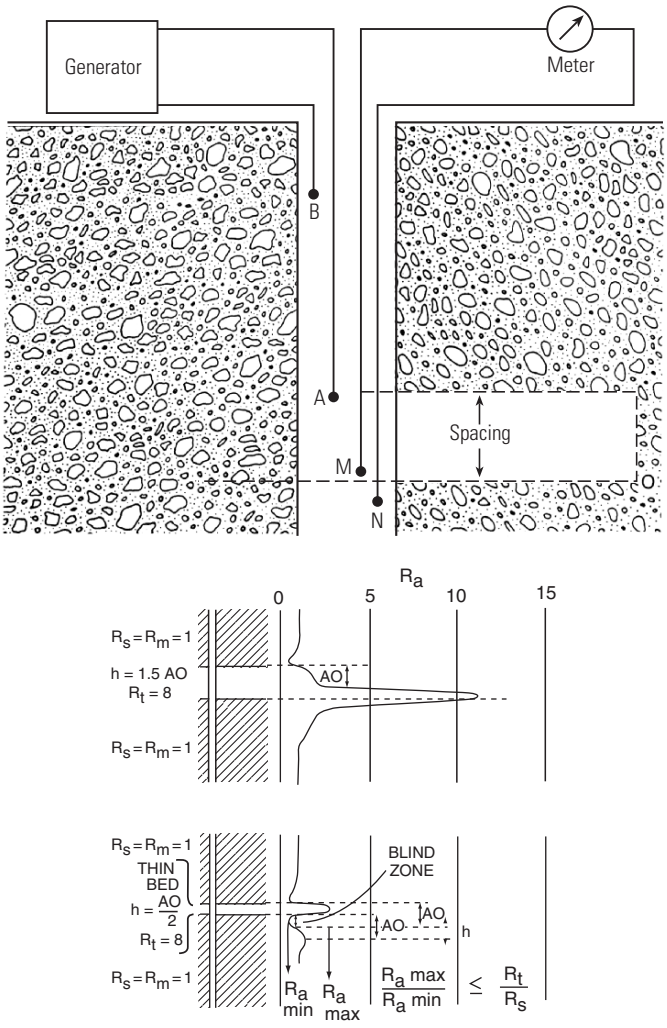


Fig. 5.10 A schematic representation of a lateral device which uses a differential voltage measurement to define its response. Two cases of its response in common logging situations are shown. O is the midpoint of M and N, *h* is the bed thickness. Courtesy of Schlumberger.

horizontally from the central measurement electrode. The current emitted from the focusing, or "guard" electrodes is often referred to as the "bucking" current, as its function is to impede the measure current from flowing in the borehole mud. It is the continuous adjustment of the bucking current which keeps A_1 and A_1' at the same potential as A_0. Since the electrodes A_1 and A_1' are elongated, the current lines at their inner ends are nearly horizontal, which forces the current sheath from A_0 to remain horizontally focused deep into the formation.

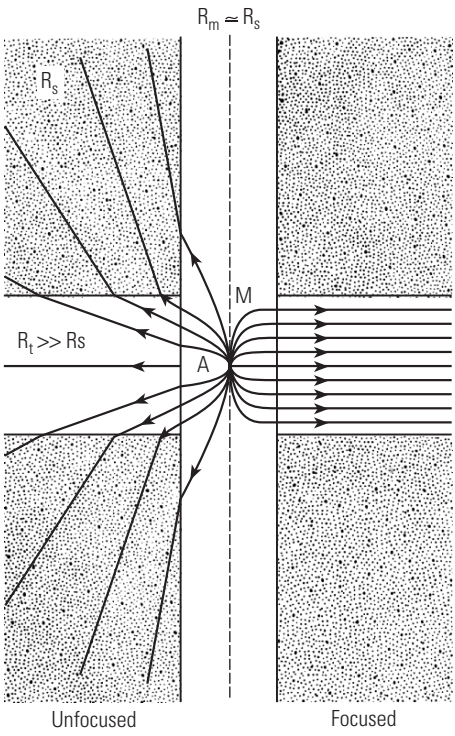


Fig. 5.11 Idealized patterns of current flow in the borehole and formation from a central electrode. On the left the pattern is altered from the expected radial pattern because of the presence of a highly resistive bed. On the right is the desired flow, so that the resistivity of the bed of interest is sampled properly. Courtesy of Schlumberger [7].

Despite these good intentions, the LL3 device still showed some difficulty with bed boundaries. This is illustrated in Fig. 5.13, which shows cases of large contrast between the shoulder bed resistivity and the value of R_t. For the thick resistive bed in the upper portion of the figure, the principal measure current is seen to be escaping through the mud and into the shoulder. In the lower example, for a thin conductive streak, current is seen to seek it out sooner than expected, giving a broader apparent bed thickness than in the previous case.

Another approach to focusing the measure current is the seven electrode device, or LL7. The electrode configuration of one such device is sketched in Fig. 5.14. The guard electrodes A_1 and A_1' are no longer elongated: instead, additional monitoring electrodes have been introduced in order to impede the flow of current parallel to the sonde though the borehole mud. This is achieved by varying the bucking current of the guard electrodes so that the potential drop between the pairs of monitor electrodes (i.e., $M_1 - M_1'$ and $M_2 - M_2'$) is zero. Since the potential drop is zero along this vertical direction, the current will be focused into the formation.

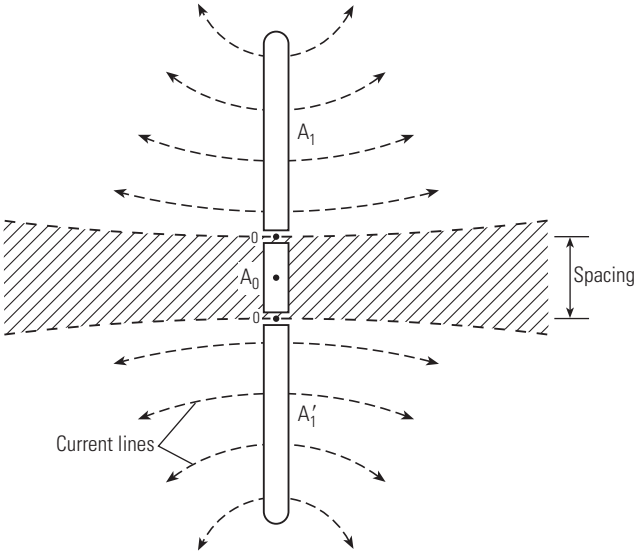


Fig. 5.12 Idealized current distribution from the Laterolog-3 device in a homogeneous formation, with current focused into the formation. From Serra [8].

If the distance between A_0 and the midpoint of the monitors is defined as a and the distance between A_0 and A_1 or A_1' as na, then n is known as the spread of the array. If m is the ratio of currents from A_1 and A_0 required to maintain equal potentials on the monitor electrodes, then it can be shown (Problem 5.5) that the array is focused when:

$$m = \frac{(n^2-1)^2}{4n}. \tag{5.14}$$

This relation ensures focusing near the tool body for any spread but does not determine how the focusing behaves radially into the formation. A small spread would seem desirable (less tool length and less current), but then the focusing becomes rapidly worse radially. As the spread increases – and with it the current from A_1 – the focus is maintained further into the formation (a result which is somewhat counterintuitive). However, if the spread increases too much, the current from A_0 is actually squeezed into a smaller beam. Doll proposed that the optimum spread was near 2.5 [9].

The voltage at the midpoint of the monitors can be determined using Eq. 5.1 to give the voltage due to each of the current electrodes:

$$V_{mon} = R_a\left[\frac{mi_0}{4\pi(na+a)} + \frac{i_0}{4\pi a} + \frac{mi_0}{4\pi(na-a)}\right] \tag{5.15}$$

where R_a is the apparent formation resistivity, and i_0 is the measure current from A_0. V_{mon} is often written as $V_{mon} = R_a i_0/K$ where K is known as the tool constant for the

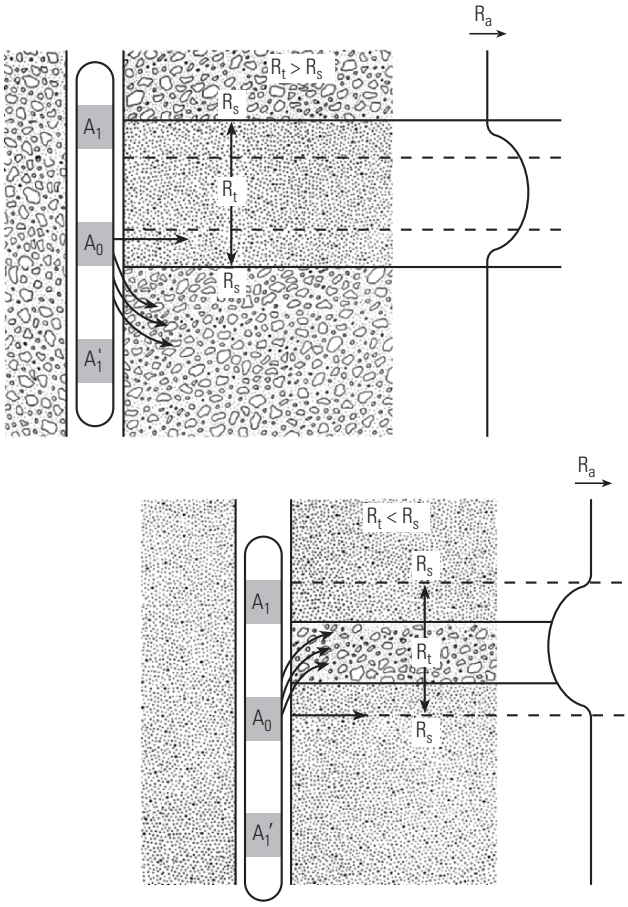


Fig. 5.13 The effects of shoulder bed resistivity on the behavior of an LL3 device. The top sketch indicates current passing through the mud into a highly conductive shoulder. The bottom sketch indicates the effect of a thin conductive bed.

device. For the LL7 with a typical a of 1 ft and a spread of 2.5, K is approximately 1.5 m. However, there is always a borehole signal while logging. It is common practice to take this into account by adjusting K so that the borehole correction is negligible in some standard condition, e.g. an 8 in. borehole with R_t/R_m between 1 and 100. This ensures that the borehole correction is small in all but extreme conditions.

5.3.2 Spherical Focusing

Another approach to compensating for the effect of the borehole is the concept of spherical focusing. In this technique, which has been adopted for medium and shallow

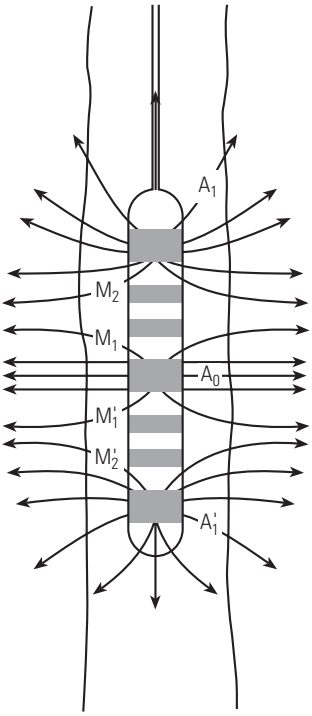


Fig. 5.14 The electrode configuration of the Laterolog-7. Monitor electrodes drive the bucking current in the guard electrode to maintain a differential voltage of zero. The array is symmetric with A_0 in the center. Adapted from Serra [8].

resistivity measurements, bucking currents attempt to establish the spherical equipotential surfaces that would exist if no borehole were present. Figure 5.15 is a rough sketch of the equipotential surfaces which surround the current electrode in a normal device, as a result of the presence of the conductive mud in the borehole. Instead of spherical surfaces, they are of elongated shape. The objective of the spherical focusing is to provide a bucking current to force the equipotential lines to become spherical once again. Then the potential difference at two points along the sonde will be determined by the resistivity of a slice of formation in a spherical shell with radii equal to the two spacings. The depth of investigation can be controlled by the size of the shell. The idea is more clearly presented in Fig. 5.16.

The electrode A_0 furnishes two sources of current; the measure current, which is returned to a distant electrode, and the bucking current. The bucking current returned to the electrodes A_1 and A_1' is varied so that the potential difference between two sets of monitor electrodes (M_1–M_2 and M_1'–M_2') is zero. The measure current is adjusted to maintain a constant potential between M_0 and the two sets of monitor electrodes. The dashed lines then trace out approximately two surfaces of constant potential. These cause the measure current injected by the central electrode to flow

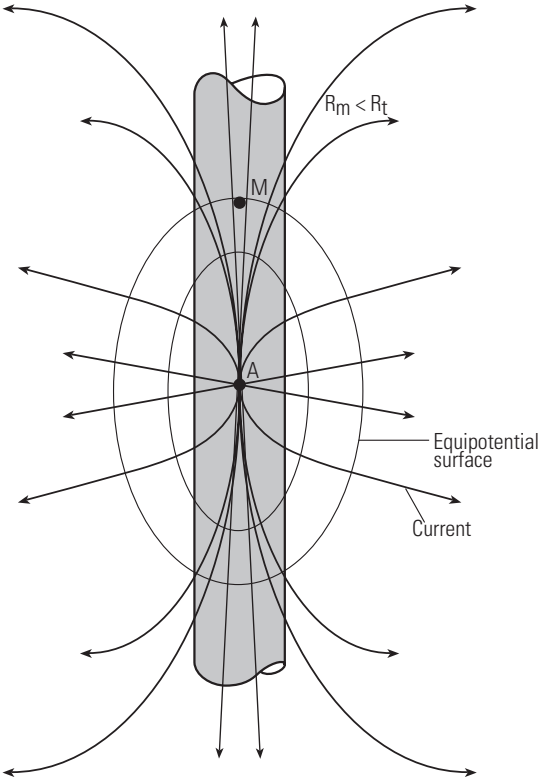


Fig. 5.15 Approximate current lines and equipotential surfaces for the short normal in a borehole.

radially outward, at least until the outer potential surface is reached. The volume of formation investigated will be nearly the space between the two equipotential surfaces, with the exclusion of the region close to the borehole interface, which is "plugged" by the bucking current. The bucking current can be viewed either as setting up the equipotential surface or providing the current through the mud so that the actual measure current is forced into the formation.

By the principle of reciprocity the same spherical focusing could be achieved by replacing all current electrodes by voltage electrodes and vice versa. The main advantage of the device described is that the only external electrode required is the measure current return (B), which can be placed at the surface. The reciprocal device requires an external voltage reference electrode (N), which must be isolated from the device itself. In practice this means placing a long insulated cable (known as a bridle) between the top of the tool and the cable. The spherical device shown in Fig. 5.16 was successful because it did not need a bridle, whereas the LL3, LL7, and other laterologs did.

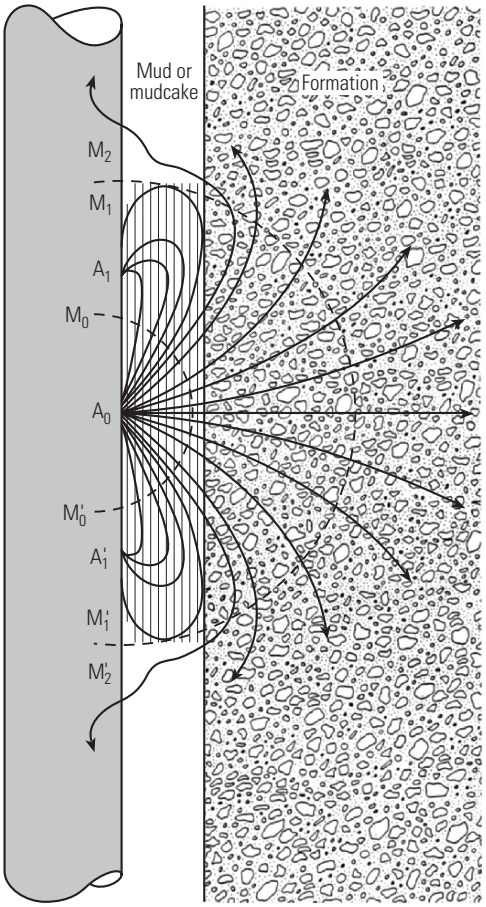


Fig. 5.16 The electrode configuration of the spherically focused array. Courtesy of Schlumberger [7].

5.3.3 The Dual Laterolog

The most common traditional electrode devices use a dual focusing system. Those known as dual laterologs combine the features of the LL3 and LL7 arrays, in an alternating sequence of measurements [2, 10]. By rapidly changing the role of various electrodes, a simultaneous measurement of deep and shallow resistivity is achieved. Figure 5.17 shows the current paths computed for such a device. On the left side of the figure, the electrodes are in the deep configuration. The length of the guard electrodes, which use parts of the sonde, is about 28 ft to achieve deep penetration of a current beam of 2 ft nominal thickness. On the right side, they are in the shallow (or medium) configuration.

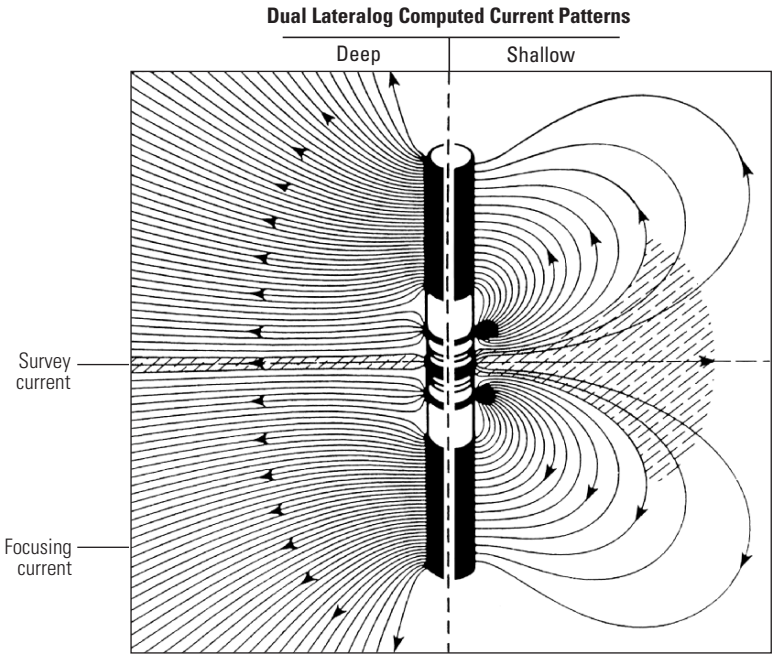


Fig. 5.17 The current distributions computed for the dual laterolog in its two modes of operation. The central electrode is the source of measure current for both shallow and deep modes. In the deep mode, both the two long electrodes and the smaller electrodes next to them are sources of bucking current. In the shallow mode, the bucking current is sent from the small to the long electrodes to provide a type of spherical focusing. From Chemali [2]. Used with permission.

For purposes of comparison of the different electrical measuring devices, it is convenient to think of the signal measured as being the result of the influence of three distinct regions of the measuring environment, as shown earlier in Fig. 2.4: the borehole, the invaded zone, and the undisturbed formation. Each of these zones is attributed its own characteristic resistivity: R_m, R_{xo}, and R_t. Generally the mud resistivity R_m is much less than either R_{xo} or R_t.

In this model, the response of an electrode device can be conveniently thought of as an approximately linear combination of the invaded zone and the true resistivity. This is expressed as:

$$R_a = J(d_i)R_{xo} + (1 - J(d_i))\,R_t, \tag{5.16}$$

where R_a is the apparent resistivity. The pseudogeometric factor J is a normalized weighting factor which gives the relative contributions of the invaded zone (of diameter, d_i) and virgin zone, to the final answer. It is referred to as the pseudogeometric factor (as opposed to a pure geometric factor, as will be seen later with the induction tool) since the weighting function will actually be influenced by the contrast between

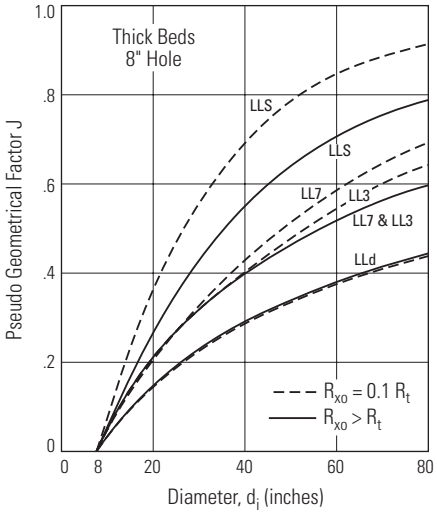


Fig. 5.18 The comparison of calculated pseudogeometric factors for a number of common electrode devices. LLd and LLs refer respectively to the deep and shallow arrays of a dual laterolog device. Courtesy of Schlumberger [7].

R_{xo} and R_t. Figure 5.18 illustrates the pseudogeometric factor for several of the devices discussed, for the case of invaded zone resistivity that is greater than that of the virgin zone as well as the case of an invaded zone that is one tenth the resistivity of the virgin formation.

The pseudogeometric factors can be used to estimate the influence of the invaded zone on the measurement of resistivity when there is a contrast between R_t and R_{xo}. The shallow curve (marked LLs) rises steeply and indicates that in the case of a more conductive invasion zone ($R_{xo} = 0.1R_t$), half of the shallow response comes from the first 8 in. of invasion and 90% comes from within a diameter of about 80 in. The deep measurement (marked LLd) shows less sensitivity to the invaded zone since only about 15% of its response comes from a diameter of 20 in. (or the first 6 in. of invasion in this calculation for an 8 in. borehole). The actual *signal* from the invaded zone depends not only on the responses shown in Fig. 5.18 but also the resistivity. Thus if $R_{xo} = R_t$, 15% of the total signal will come from the invaded zone for d_i = 20 in., whereas if $R_{xo} = 0.1R_t$ only 1.5% will. The laterolog signal, like all electrode devices, is more linear in resistivity, not conductivity, as can be seen in Eq. 5.16. This issue is discussed further in Chapter 7.9.

It is important to note the laterolog's sensitivity to the borehole. Figure 5.19 shows the correction chart for the deep and shallow measurement of a particular dual laterolog device, plotted in a manner similar to Fig. 5.5 for the short normal. This chart is for a centered tool. Other charts are available for an eccentered tool, the eccentricity being characterized by the standoff between tool and borehole wall. It is seen that the deep reading is rarely in error by more than 10%, for a variety of borehole sizes and

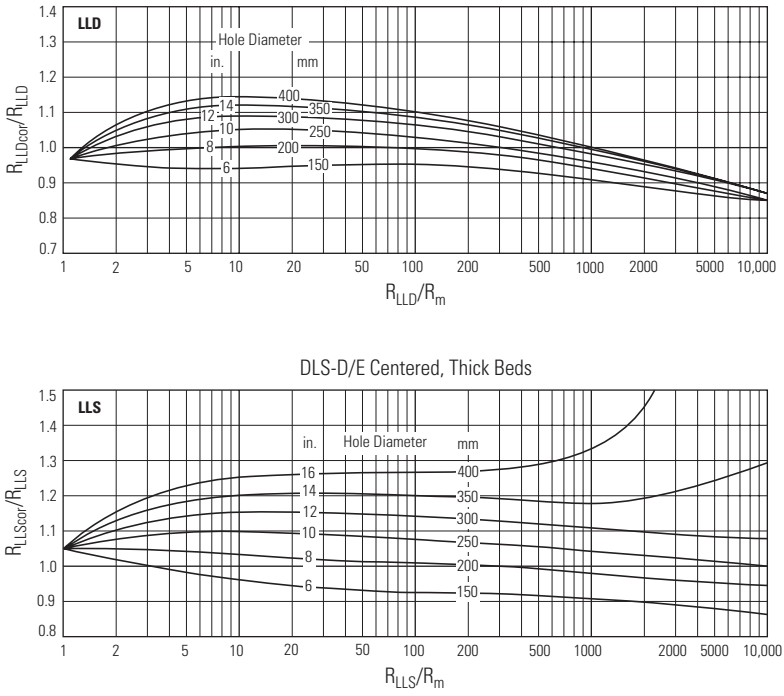


Fig. 5.19 A borehole correction chart for the deep and shallow laterolog measurements. It is to be compared to Fig. 5.5, for the short normal, to appreciate the improved response due to focusing. Adapted from Schlumberger [1].

resistivity contrasts. The shallow measurement, however, may differ by as much as 30% from the value of R_t in large boreholes and for resistivity contrasts in excess of 1,000. In both cases the tool constant, K, has been adjusted to give small borehole corrections in normal conditions, as described above for the LL7.

5.3.4 Dual Laterolog Example

Figure 5.20 shows a typical dual laterolog presentation for a hypothetical reservoir (which is used again in succeeding chapters to demonstrate the response of other logging tools). The reservoir consists of a water zone and a hydrocarbon zone of moderate porosity. Only two of the curves shown on the log are uniquely associated with the dual laterolog, coded LLs and LLd. The additional resistivity curve, denoted by MSFL, is produced by a microresistivity device (indicating shallow depth of investigation, because of small electrode spacings), discussed in Chapter 6. The curve in track 1 is a gamma ray, which can be taken to indicate clean zones, as mentioned in Chapter 2.

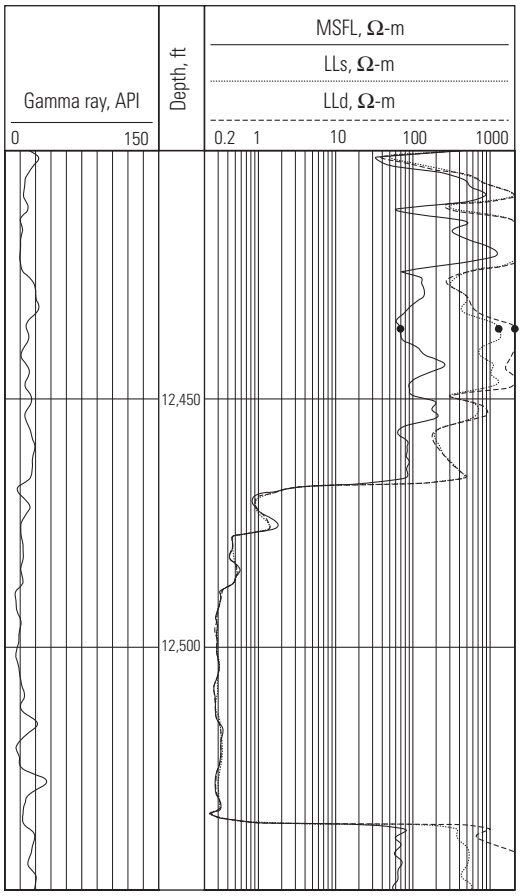


Fig. 5.20 The response of a laterolog in an simulated and idealized reservoir. The marked section shows need of invasion corrections.

The water zone at the bottom is characterized, in this case, by rather low-resistivity readings and the lack of separation between the deep and shallow laterolog readings. The hydrocarbon zone is indicated by the high-resistivity readings above 12,470 ft. For 20 ft below this zone the readings are higher than in the water zone. This could indicate a small amount of hydrocarbons or a change in porosity. Any further quantification of the contents of this formation will depend on further measurements or knowledge. One of the most important pieces of information will be an estimate of the porosity.

If the logs are to be used for a qualitative decision, for example on whether or not to continue drilling, further processing is probably not necessary. For an accurate quantified interpretation, it will be necessary to apply corrections to the resistivity readings. Although the corrections are normally applied by software, they are most easily understood in the form of published correction charts [1, 11]. Asquith et al. detail the steps involved in performing the corrections [12]. Most of the corrections

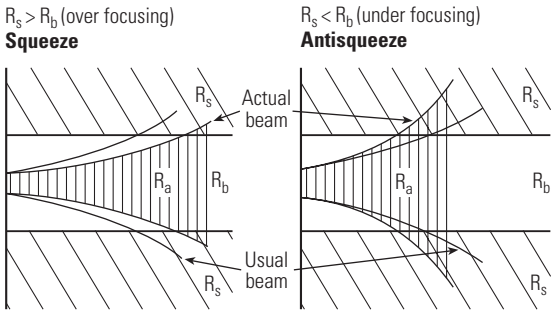


Fig. 5.21 Comparison of the current beams from a laterolog when (left) the shoulder beds are more resistive than the central bed and (right) when they are less resistive. The "usual beam" is the beam found in a homogeneous formation using an optimal spread for the array. From Crary and Smith [13]. Used with permission.

are made in terms of the mud resistivity (R_m) and mud filtrate (R_{mf}) resistivity, which can be obtained from the log heading. The first step is to convert these two resistivity readings to the values they would have at formation temperature. This can be estimated from a recorded bottom hole temperature or from typical geothermal gradients for the region. The next step, for zones of interest, is to correct the resistivity readings for the influence of the borehole, as in Fig. 5.19.

The third step is to correct for the remaining effect of shoulder beds that has not been handled by the focused arrays. The cause of this effect is the alteration of the current lines near high-contrast boundaries (Fig. 5.21). High-resistivity shoulders squeeze the current into the low-resistivity bed, altering the tool constant computed for a homogeneous formation and raising the apparent resistivity. Low-resistivity shoulders cause the opposite. The effect is only significant for the LLs when bed thicknesses are less than 10 ft, but can be seen on the LLd for beds up to 100 ft thick with strong contrasts.

The final step is the correction for invasion. Chartbook-based invasion corrections assume a step profile model with three unknowns (R_{xo}, R_t, and d_i) that can be solved with three measurements (LLs, LLd, and microresistivity). It is assumed that the microresistivity curve reads R_{xo}. The charts are parameterized in terms of resistivity ratios: R_{xo} compared to the deep resistivity, and the medium resistivity to the deep. In Fig. 5.20, at 12,435 ft, the separation between deep and medium resistivity is a factor of 2, while the deep and microresistivity are separated by a factor of 30. This indicates moderate invasion. Deep invasion would be signaled by a larger separation between deep and medium.

The resistivity ratios are entered into the appropriate chart, often referred to as a "tornado" or "butterfly" chart (Fig. 5.22). Despite the clutter of curves, there is a wealth of information. First, the intersection of the two ratios indicates that R_t/R_{LLd} is about 1.28. This means that the deep measurement is about 28% in error from the value of R_t because of invasion effects; R_t is 1.28 times the value of R_{LLd}. Other parameterized sets of curves indicate a diameter of invasion of about 30 in. and that the

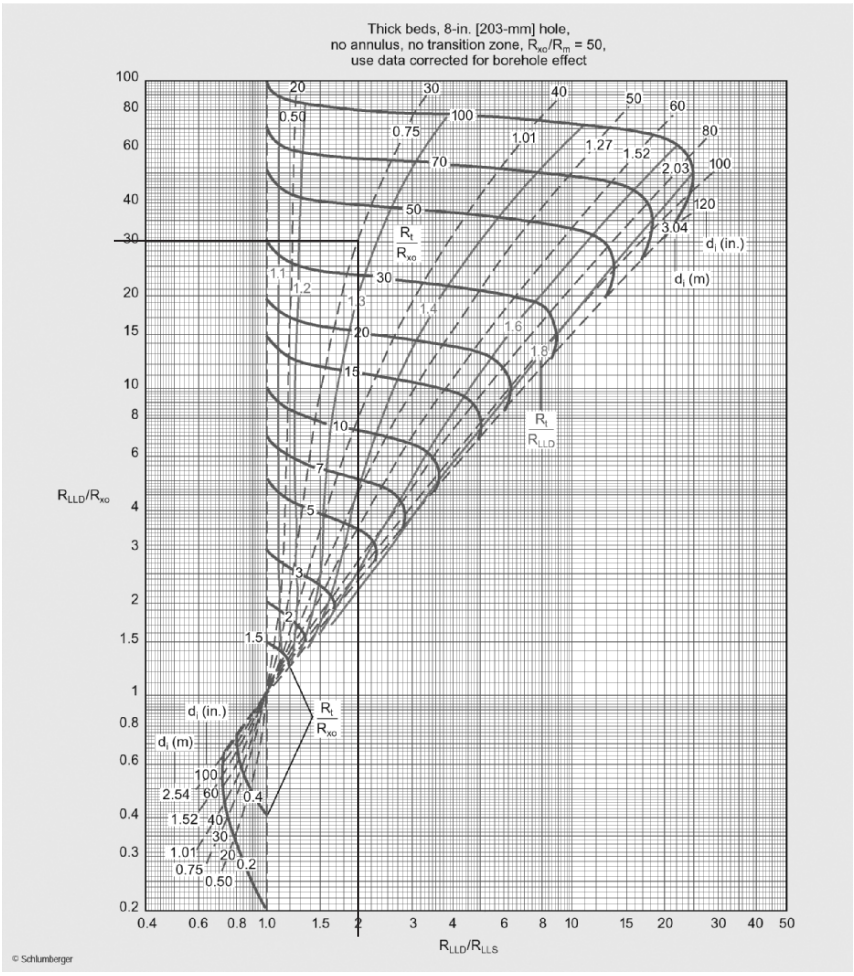


Fig. 5.22 A dual laterolog invasion correction chart. Courtesy of Schlumberger [1].

value of R_t is about 40 times the value of R_{xo}. In the zone below, 12,455–12,466 ft, the shallow and the deep laterolog readings overlay. This indicates, as can be confirmed from the correction chart, that there is little invasion and that the deep resistivity needs no correction.

A further correction may be needed in anisotropic formations. As might be judged from the current lines in Fig. 5.17 the LLd is mainly sensitive to horizontal resistivity in a vertical well. However it can also be seen that there is a small vertical component to some of the current lines. This explains qualitatively why the LLd has some sensitivity

to vertical resistivity R_v even in a vertical well. The LLs has greater sensitivity to R_v than the LLd, as can also be judged from Fig. 5.17. Chemali et al. show the effect of anisotropy for different anisotropy ratios and dip angles [14]. A typical case is shown later in Fig. 20.3.

It is important to note that all charts assume that the effects are independent of one another: shoulder bed charts assume that there is no invasion, invasion charts assume there are no shoulder beds, and borehole correction charts assume a homogeneous formation. The consequence of having significant corrections from different sources at the same time is discussed in Section 5.4.2.

5.4 FURTHER DEVELOPMENTS

For 20 years after the development of the dual laterolog in the late 1960s only minor improvements were made. Then, in the early 1990s, azimuthal laterologs, able to measure resistivity at different azimuths around the borehole, appeared [15]. Azimuthal features will be described in Chapter 6, but the electrode configuration used for these measurements also produced a deep measurement with a high vertical resolution of 8 in., as opposed to 2 ft for the LLd. The depth of investigation with no invasion is slightly less than LLd. Another device aims for the performance of previous laterologs but with a tool that is half the length [16]. One other device was designed to give high vertical resolution by using a 2 in. high A_0 electrode, mounted on a pad, with long guard electrodes in a LL3 configuration [17]. The depth of investigation, with no invasion, is approximately that of the LLs. In some of these tools software focusing was introduced. In software focusing, a unit current is sent sequentially from each electrode and the voltage measured on each other electrode. These apparent resistances are then combined in software according to the monitoring and current conditions of the dual laterolog [6].

In spite of these developments, laterologs continued to suffer from three major disadvantages: the need for a bridle above the tool in order to isolate the measurement reference electrode (N) from the tool; problems with the placement of this electrode; and the poor depth of investigation in thin beds. These disadvantages have been overcome to a large extent by the introduction of array tools. Before describing the new tools let us first review the issues involved.

5.4.1 Reference Electrodes

Reference electrode problems have plagued laterologs from the beginning. The laterolog measurement assumes that the current return, B, is at infinity and that the voltage reference, N, is at zero potential (see Fig. 5.23). However, in early days B and N were placed at the top of and near the top of an 80 ft. bridle, respectively (B1 and N1 in the figure). When B was opposite a highly resistive bed the return current was forced to flow down the borehole causing a negative potential on N. This invalidates the assumption of zero voltage on N and causes a false increase in measured resistivity, since the potential measurement is taken from the difference of V_M and V_N.

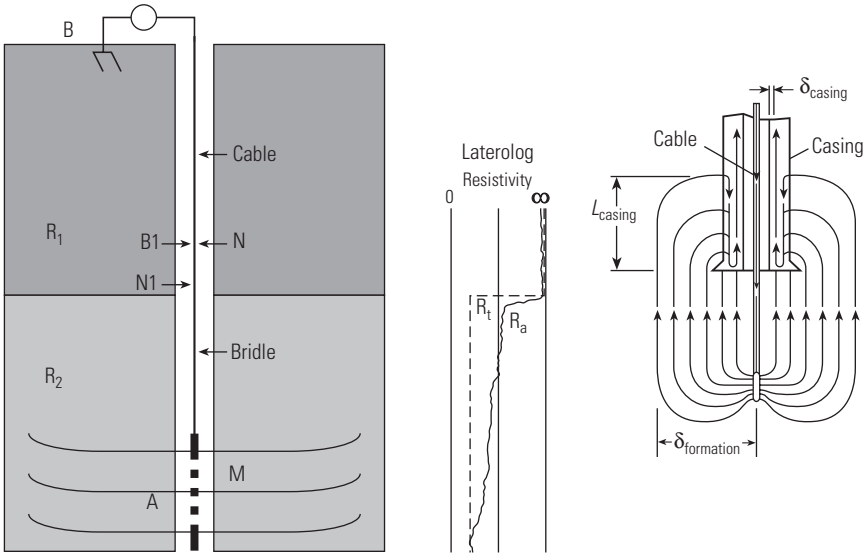


Fig. 5.23 Left, a laterolog device with the original positions of the reference electrodes (N1 and B1) and after changes to correct for the Delaware and anti-Delaware effects (N and B). Center, a characteristic Groningen effect. Right, current paths in a casing with an a.c. source. δ is the skin depth, and L is the characteristic length over which current enters the casing (e.g., 950 ft in a 10 ohm-m formation). Adapted from Anderson [6].

Although the problem was solved long ago, it is useful to understand it as background to the more complicated Groningen effect, discussed below. The effect of B1 on N1 can be understood by considering the paths taken by the current flowing between source A and return B1. For a laterolog in Fig. 5.23, A includes both the measure current and the bucking current, which are both focused away from the borehole. In normal circumstances the formation resistance is much smaller than the borehole resistance because, although the resistivity of the mud is lower, the area of the formation is several orders of magnitude higher. Thus very little current flows past N1 to B1. However, as the resistivity opposite N1 and B1 increases, more current takes the easier path through the borehole. The potential on N1 now becomes significant. It is opposite in sign to the potential on the measure electrode M because the resistance and hence the potential drop between N1 and B1 is less than that between N1 and A. As the tool moves upwards into the resistive bed an increasing amount of current flows past N1, causing it to go increasingly negative.

This effect, known as the Delaware effect after the basin in which it was first observed, was cured by placing B at the surface, as shown in Fig. 5.23. The current could now return to B through a large area of formation with only a small fraction passing by N1. A further problem, known as the anti-Delaware effect, was then observed when the top guard electrode entered a highly resistive bed, causing bucking currents to flow directly up the borehole. The resistance between N1 and A is now less than

between N1 and B, and N1 becomes positive. Moving the measurement reference further away to the bottom of the cable at N solved this problem.

Even after these changes a false increase in resistivity is still observed in low resistivity reservoirs below highly resistivity beds. The increase is of the order of 1 ohm-m except when a casing was set inside the resistive bed in which case it can reach 10 ohm-m [6]. This is known as the Groningen effect after the large Dutch gas field. The explanation lies in the fact that alternating currents are used for laterolog measurements. Direct currents are not used because they cause electrode polarization and affect the SP.

Alternating currents only penetrate a certain distance in conductive media. Even at the low frequencies used for laterologs – 35 Hz for the deep laterolog – the skin depth (in ft), which characterizes the penetration, equals $280 \times \sqrt{R}$ where R is the formation resistivity in ohm-m (see Section 7.6 for more on skin effect). This is small in comparison with the thousands of feet the current has to travel between the A electrode and the B electrode on surface. The current therefore flows in a cylinder around the borehole, thereby substantially reducing the area open to flow and increasing the apparent resistance of the formation. We are now back to the conditions that caused the Delaware effect, and with the same result: too much current in the borehole, a negative potential on N and a false increase in resistivity as N enters a resistive bed.

The situation is exacerbated by the presence of two other conductive elements: the cable and the casing. The cable carries some of the return current thereby increasing the amount of current flowing past N. It can be shown that the potential at N increases as $\sqrt{R_1}$ where R_1 is the resistivity opposite the cable in Fig. 5.23 [18]. If R_2 is also high then the potential on M is high (for the same current) and the effect is negligible. If R_2 is low, the effect of nonzero N is significant.

Casing has an even more dramatic effect because of the very small skin depth in casing (typically 0.1 in.). Modeling shows that the current actually flows to the bottom of the casing before flowing up to the surface (Fig. 5.23, right). This further increases the current passing N and explains why the Groningen effect is stronger in casing. Casing and cable also ensure that the resistance between B and N is less than between N and A, so that the potential on N is negative.

Various solutions have been proposed to detect and correct for the Groningen effect. The most complete rely on the fact that the skin effect also causes a change of phase in the signal, and hence a measurable out-of-phase component. When there is no casing the error is a simple function of the out-of-phase signal, which can be measured and used to make a correction. With casing, the function is no longer simple, and two passes with two different tool guard electrode configurations are needed to solve the problem.

A final problem with the reference electrode is that in highly deviated wells wireline laterolog tools may be conveyed to the bottom of the hole attached to the drill string. The flexible bridle is replaced by a 30 ft section of insulated pipe and N is taken from the drill pipe. The current flow is similar to that in the casing, and a correction is needed. When $R_t/R_m < 100$, this correction is significant [18].

5.4.2 Thin Beds and Invasion

It was noted above that the chartbook corrections for borehole, shoulder bed, and invasion assume that these effects are independent and can be treated sequentially. Unfortunately, although borehole effects are generally small, and can be treated independently without large errors, shoulder beds and invasion are more closely linked, and in some cases cannot be treated sequentially.

The effect of invasion in a thin bed is shown in Fig. 5.24. In this case the chartbook shoulder bed corrections to LLd and LLs are insignificant. A subsequent invasion correction using Fig. 5.22, and assuming R_{xo} is available from another device, gives R_t less than 2 ohm-m, when the true resistivity is 10 ohm-m. This large error is an example of antisqueeze that is greatly exacerbated by the conductive invaded zone. Currents seek the path of least resistance and so tend to flow from the invaded zone up and down into the low-resistivity shoulder bed to a much greater extent than in the case of antisqueeze with no invasion shown in Fig. 5.21. The result is that as invasion increases and the bed becomes thinner the LLd resembles increasingly the LLs: for this reason large separations between LLs and LLd are not observed in thin beds. For the conditions of Fig. 5.24 the bed needs to be more than 10 ft thick before the

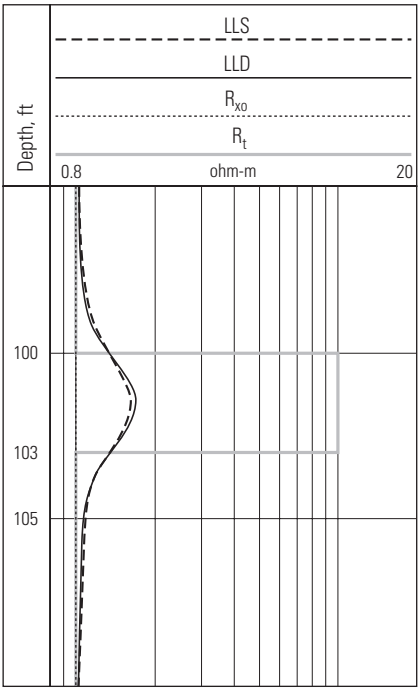


Fig. 5.24 The combined effect of a thin low-resistivity invaded zone (R_{xo} = 1 ohm-m, R_t = 10 ohm-m, d_i = 40 in.) with low-resistivity shoulders (R_{sh} = 1 ohm-m) cause a strong antisqueeze effect on the dual laterolog. As a result the LLd reads nearly the same as the LLs and both are far from R_t [19]. Used with permission.

separation begins to increase: for the invasion corrections to be satisfactory the bed needs to be many tens of feet thick.

Another notable effect in this example is the lack of sharpness at the bed boundaries, compared, for example, to that seen in Fig. 5.20. This is because there is no change in R_{xo} at the bed boundaries in Fig. 5.24. It can be shown that sharp vertical changes in resistivity can only be detected if they are close to the borehole. When the resistivity close to the borehole does not change, the vertical resolution is much poorer.

The results of Fig. 5.24 were obtained by defining the formation R_{xo}, R_t, and D_i and computing the LLs and LLd response using a suitable computer model. This procedure can also be used for the inverse problem – finding the formation parameters when they are not known, as in an actual well log. The bed boundaries are defined from the LLs/LLd inflection points or other measurements and reasonable formation parameters are chosen. Theoretical LLs and LLd curves are computed and compared with the actual curves. If they do not agree, the parameters are adjusted until there is agreement. The final parameters are then taken as the correct formation values. As with any such inversion the results might not be unique, i.e., other formation parameters may lead to the same input logs.

Although this technique of iterative forward modeling can be done manually, to be of general use the comparison of curves and the adjustment of parameters need to be automatic. However, with only the LLs and LLd curves, and even if R_{xo} is known, there is too little information for an automatic procedure to give unambiguous results. The need for more radial information led to the development of array tools.

5.4.3 Array Tools

Two types of array tool have been constructed. The High Definition Lateral tool has a single current electrode and 19 electrodes above and below. The tool records 8 potential, or normal, measurements and 16 electric field, or lateral, measurements from the difference in potential between 2 electrodes [20]. Different measurements are superimposed to form three synthetically focused field measurements. The real power comes from 2D or 3D inversion of the large amount of data with different volumes of investigation to find R_{xo}, R_t, and d_i. Being normal and lateral measurements, there can be strong borehole and long shoulder bed effects, but in principle they can be taken into account by the inversion. However, the fact that each measurement is made at a different depth can introduce errors due to erratic tool motion.

The second array tool, the High Resolution Laterolog Array, makes six LL3-type measurements from one central A_0 electrode and six electrodes above and below (Fig. 5.25) [21]. Six different resistivities, or modes, are recorded by using a different combination of electrodes as bucking and current return electrodes. For example in mode 2 the three innermost electrodes on each side are bucking electrodes, held at the same potential as A_0, with the remaining electrodes acting as returns for both the A_0 and bucking current. This gives a moderate depth of investigation, close to that of LLs. The shallowest mode, mode 0, has no bucking electrode and is used to measure mud resistivity. The other modes use an increasing number of bucking electrodes to give successively greater depths of investigation up to that of LLd (Fig. 5.26).

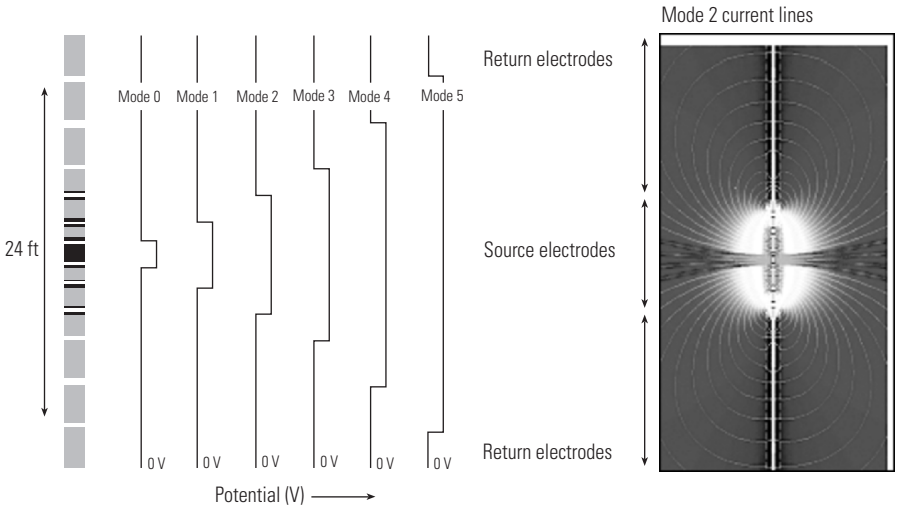


Fig. 5.25 Left, electrode array and potential profiles for the different modes of an Array Laterolog. The central current and measure electrode is black, the monitoring electrodes are also black and the other electrodes are grey. White sections are insulated. Right, current lines for Mode 2. The arrows indicate which are the source and return electrodes for this mode. Courtesy of Schlumberger.

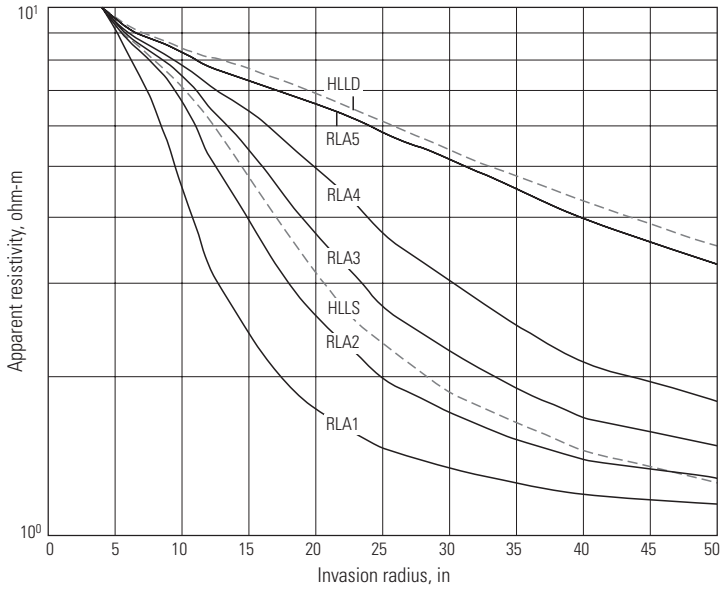


Fig. 5.26 Radial response of modes 1 to 5 of an Array Laterolog compared with HLLd and HLLs from the high-resolution azimuthal tool. The y-axis shows borehole corrected measured resistivities in a thick bed as a function of invasion radius. R_t = 10 ohm-m, R_{xo} = 1 ohm-m, d_h = 8 in. and R_m = 0.1 ohm-m. Courtesy of Schlumberger.

The necessary equipotential conditions are enforced using feedback from the monitor electrodes and through superposition of signals in software. In this way the raw measurements are focused and therefore have minimum borehole and shoulder bed effects.

The six resistivities are computed simultaneously at different frequencies using the A_0 current and the potential between the center of the tool and cable armor. In this way the measurements are intrinsically resolution matched and erratic tool motion problems are minimized. Note that there is no surface B electrode, since all currents return to the tool body. This configuration avoids the Groningen and other reference electrode effects and there is no need for a bridle, thereby resolving two of the main problems with dual laterolog tools. There is a price to pay for this, since with a current return on surface it would be possible to design a deeper reading array than mode 5. Instead, 2D or 3D inversion is relied on to improve the depth of investigation, especially in thin beds.

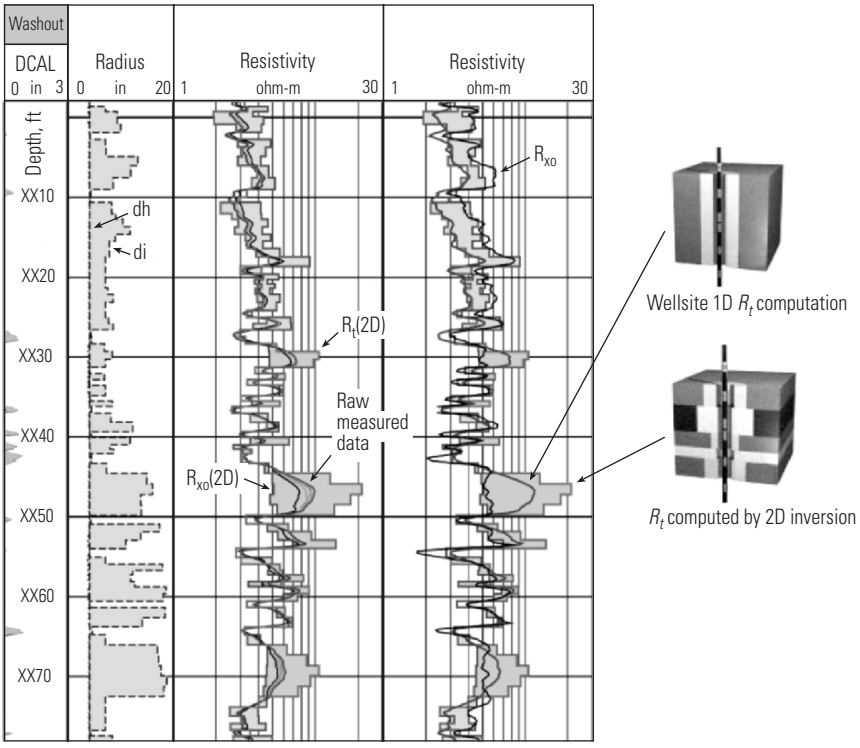


Fig. 5.27 Comparison of the raw Array Laterolog curves with the result of a 1D and a 2D inversion. The MCFL is a measurement of R_{xo}, which will be discussed in Chapter 6. Courtesy of Schlumberger.

After making any small remaining borehole correction, a fast 1D inversion, equivalent to an invasion correction chart for an infinitely thick bed, can be made in real time. The 2D inversion takes longer but is sped up by automatically segmenting the logs into sections of constant properties. The example in Fig. 5.27 compares the results. At XX50 ft, where $R_t > R_{xo}$, the 1D inversion finds R_t only slightly greater than the deepest mode, but the 2D inversion more than doubles the value. The R_{xo} value computed from the arrays agrees well with R_{xo} from an independent measurement. The inversion also works when $R_{xo} > R_t$, as in the shaded section at the top.

How reliable is this? A full analysis depends on knowing the magnitude of different types of noise (e.g., electronic, calibration errors, borehole rugosity) and whether the assumptions of the model have been respected (e.g., azimuthal symmetry, step profile invasion). What is certain is that in normal cases the 2D result is closer to the truth than the 1D result or the raw measurements.

REFERENCES

1. Schlumberger (2005) Log interpretation charts. Schlumberger, Houston, TX
2. Chemali R, Gianzero S, Strickland R, Tijani SM (1983) The shoulder bed effect on the dual laterolog and its variation with the resistivity of the borehole fluid. Trans SPWLA 24th Annual Logging Symposium, paper UU
3. Anderson B, Chang S-K (1983) Synthetic deep propagation tool: response by finite element method. Trans SPWLA 24th Annual Logging Symposium, paper T
4. Zienkiewicz OC (1971) The finite element method in engineering sciences. McGraw-Hill, New York
5. Doll HG, Tixier MP, Martin M, Segesman F (1962) Electrical logging. In: Petroleum production handbook, vol 2, SPE, Dallas, TX
6. Anderson BA (2001) Modeling and inversion methods for the interpretation of resistivity logging tool response. DUP Science, Delft, The Netherlands
7. Schlumberger (1989) Log interpretation principles/applications. Schlumberger, Houston, TX
8. Serra O (1984) Fundamentals of well-log interpretation. Elsevier, Amsterdam, The Netherlands
9. Doll HG (1955) Electrical resistivity well logging method and apparatus. US Patent No 2712627
10. Suau J, Grimaldi P, Poupon A, Souhaite P (1972) The dual laterolog-R_{xo} tool. Presented at the 47th SPE Annual Technical Conference and Exhibition, paper SPE 4018

11. Dresser Atlas (1983) Well logging and interpretation techniques, the course for home study. Dresser Industries, Houston, TX

12. Asquith GB, Gibson CR (1982) Basic well log analysis for geologists. AAPG, Tulsa, OK

13. Crary S, Smith D (1990) The use of electromagnetic modeling to validate environmental corrections for the dual laterolog. Trans SPWLA 31st Annual Logging Symposium, paper C

14. Chemali R, Gianzero S, Su SM (1987) The effect of shale anisotropy on focused resistivity devices. Trans SPWLA Annual Logging Symposium, paper H

15. Davies DH, Faivre O, Gounot M-T, Seeman B, Trouiller J-C, Benimeli D, Ferreira AE, Pttman DJ, Smits J-W, Randrianavony M, Anderson BI, Lovell J (1992) Azimuthal resistivity imaging: a new generation laterolog. Presented at the 67th SPE Annual Technical Conference and Exhibition, paper SPE 24676

16. Smits JW, Benimeli D, Dubourg I, Faivre O, Hoyle D, Tourillon V, Trouiller JC, Anderson BI (1995) High resolution from a new laterolog with azimuthal imaging. Presented at the 70th SPE Annual Technical Conference and Exhibition, paper SPE 30584

17. Khokhar RW, Johnson WM (1989) A deep laterolog for ultrathin formation evaluation. Trans SPWLA 30th Annual Logging Symposium, paper SS

18. Trouiller JC, Dubourg I (1994) A better deep laterolog compensated for Groningen and reference effects. Trans SPWLA 35th Annual Logging Symposium, paper VV

19. Griffiths R, Smits JW, Faivre O, Dubourg I, Legendre E, Doduy J (1999) Better saturation from new array laterolog. Trans SPWLA 40th Annual Logging Symposium, paper DDD

20. Itskovitch GB, Mezzatesta A, Strack KM, Tabarovsky L (1998) High-definition lateral log resistivity device: basic physics and resolution. Trans SPWLA 39th Annual Logging Symposium, paper V

21. Smits JW, Dubourg I, Luling MG, Minerbo GN, Koelman JMVA, Hoffman LJB, Lomas AT, Oosten RKvd, Schiet MJ, Dennis RN (1998) Improved resistivity interpretation utilizing a new array laterolog tool and associated inversion processing. Presented at the 73rd SPE Annual Technical Conference and Exhibition, paper SPE 49328

Problems

5.1 Figure 5.18 shows, among other things, the pseudogeometric factor for the deep and shallow laterolog (LLd and LLs). Using this information, what is the apparent

resistivity that you would expect for the LLd and LLs in a 30 p.u. water-bearing formation which has a diameter of invasion of 30 in.? The borehole is filled with relatively fresh water of 2.0 ohm-m resistivity, and the formation water resistivity is 0.1 ohm-m at the same temperature.

5.2 Using the log values of Fig. 5.20 and assuming the porosity of the water zone at 12,500 ft to be 20%:

5.2.1 What do you estimate the porosity at the bottom of the log to be, assuming that it is also water-filled?

5.2.2 What value of R_w would produce the resistivity observed at 12,460 ft if it were also a 20% porosity water zone rather than a hydrocarbon zone?

5.3 Can you say which of the zones of Fig. 5.20 indicate the presence of invasion?

5.4 For the logs in Fig. 5.24 compute R_t in the center bed from LLs, LLD and the R_{xo} given using chartbooks for borehole correction, shoulder correction, and invasion. Assume an 8 in. diameter borehole with $R_m = 0.1$ ohm-m. If porosity is 20% and $R_w = 0.1$ ohm-m, what is S_w? What is the true S_w?

5.5 Prove the formula in Eq. 5.14. (Write down the potential at the center of the monitor electrodes due to the three current electrodes, and set the gradient of this potential to zero.)

5.6 Given the formula for skin depth from Chapter 7, calculate the skin depth for a LLd in a 1 ohm-m formation. The magnetic permeability is 1.2×10^{-6} H/m.

5.7 Calculate the skin depth for the LLd in a 10 ohm-m formation. Estimate the resistance of such a formation between a deep laterolog current source at 6,000 ft and a return at surface.

6

Other Electrode and Toroid Devices

6.1 INTRODUCTION

Electrode devices have been put to many other uses than those described in Chapter 5, the earliest of these being the measurement of the resistivity of the invaded or flushed zone R_{xo}. Historically, the first use of the invaded-zone resistivity was, in the absence of any other measurement, to make an estimate of the formation porosity. Since then R_{xo} has found many applications. In earlier chapters we saw that R_{xo}, when compared with R_t, gives a visual indication of permeable zones and evidence of moved hydrocarbons. In Chapter 5 we saw the need for R_{xo} in obtaining a better estimate of the deep-resistivity R_t. R_{xo} can be combined with other information to determine the water saturation of the invaded zone, S_{xo}, and thereby estimate the efficiency of hydrocarbon recovery. S_{xo} can also be a useful indicator of hydrocarbons on its own.

Before discussing these applications, we will examine a few of the electrode devices which have been designed to measure R_{xo}. Their development has paralleled the development of laterologs, but with electrodes mounted on pads and applied against the borehole wall. Similar devices have been put to excellent use to measure the size and direction of formation dip and, later, to make detailed images of the resistivity near the borehole wall. These devices will be mentioned in this chapter but their application is primarily geological and beyond the scope of this book.

A further use for electrode devices has been on drill collars to provide logs while drilling. It is now possible to record a resistivity as soon as the bit penetrates a formation. Toroids are used instead of electrodes for current generation and focusing. The final electrode device to be considered measures the resistivity through casing. It might be thought impossible to measure resistivity through a material as conductive

as casing, but this can now be done. Indeed the measurement sees remarkably deep into the formation.

Electrodes have thus been put to a wide range of use for logging with wireline or while drilling. One word of warning: with few exceptions, electrode devices will not work in nonconductive muds, such as oil-based muds. For such muds, induction and propagation measurements are needed, as will be seen in Chapters 7–9.

6.2 MICROELECTRODE DEVICES

Microelectrode devices, as their name implies, are electrical logging tools with electrode spacings on a much-reduced scale compared to the mandrel tools previously considered. A further distinction, a result of the smaller spacings, is that their depth of investigation is also much reduced. The electrodes are mounted on special devices, called pads, which are kept in contact with the borehole wall while ascending the well.

The development of microelectrode devices has undergone the same evolution as electrode tools. The first was the microlog device (Fig. 6.1), which was an unfocused measurement based on the principle of a normal and a lateral. Current is emitted from the button marked A_0, and the potentials of the two electrodes M_1 and M_2 are measured. To ensure a shallow depth of investigation, the spacing between electrodes

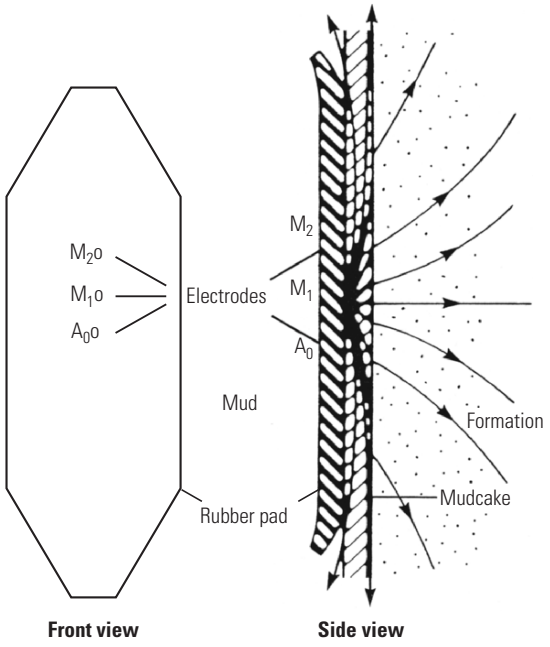


Fig. 6.1 A microlog device: a pad version of the short normal and the lateral. The spacing between the electrodes is 1 in. From Serra [1].

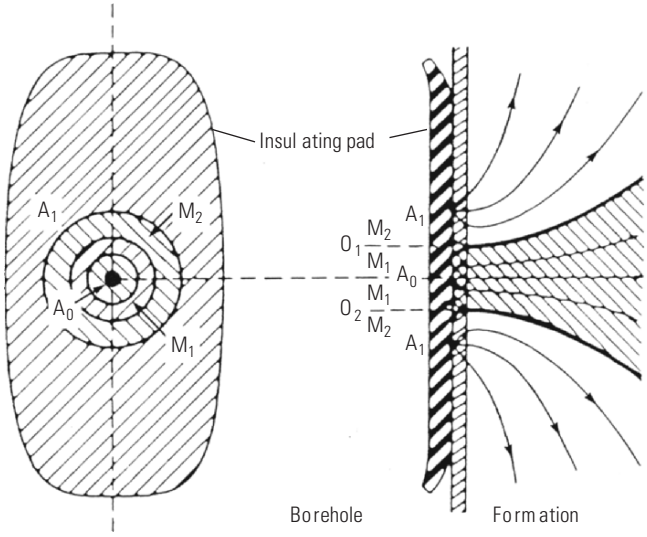


Fig. 6.2 A microlaterolog device: a reduced scale and pad version of the laterolog. From Serra [1].

is 1 in. The difference in potential between electrodes M_1 and M_2 forms a lateral, or inverse, measurement that is mostly influenced by the presence of mudcake. The potential on electrode M_2 forms a normal measurement which, being farther from the current source, is influenced more by the flushed zone.

The influence of mudcake, especially in the case of a resistive formation and a very conductive and thick mudcake, was a major disadvantage for the purpose of determining R_{xo}, but meant that the two curves separated when there was invasion. This separation proved to be a reliable indicator of permeable zones, much beloved by many log analysts, to the extent that modern tools create synthetic microlog curves just for this purpose. Examples of many microelectrode-device logs and their interpretation can be found in Jordan and Campbell [2].

In order to improve the determination of R_{xo}, a focused or microlaterolog device was the next innovation. Figure 6.2 is a schematic of this device, which shares many features of the laterolog, except for dimensions. As indicated in Fig. 6.2, the bucking current from electrode A_1 focuses the measure current to penetrate the mudcake. Depending on the contrast between R_{xo} and R_t, 90% of the measured signal comes from the first 2–4 in. of formation.

Various other microelectrode devices followed the microlaterolog, each trying to minimize the effect of mudcake while not reading too deep into the formation. The two mudcake-correction charts in Fig. 6.3 allow comparison between two types of devices – the microspherical log and the microlaterolog. The microspherical device is based on the same principle as the spherical log described in Section 5.3.2. The spherical focusing, as well as a larger pad, causes it to be much less sensitive to the presence of mudcake.

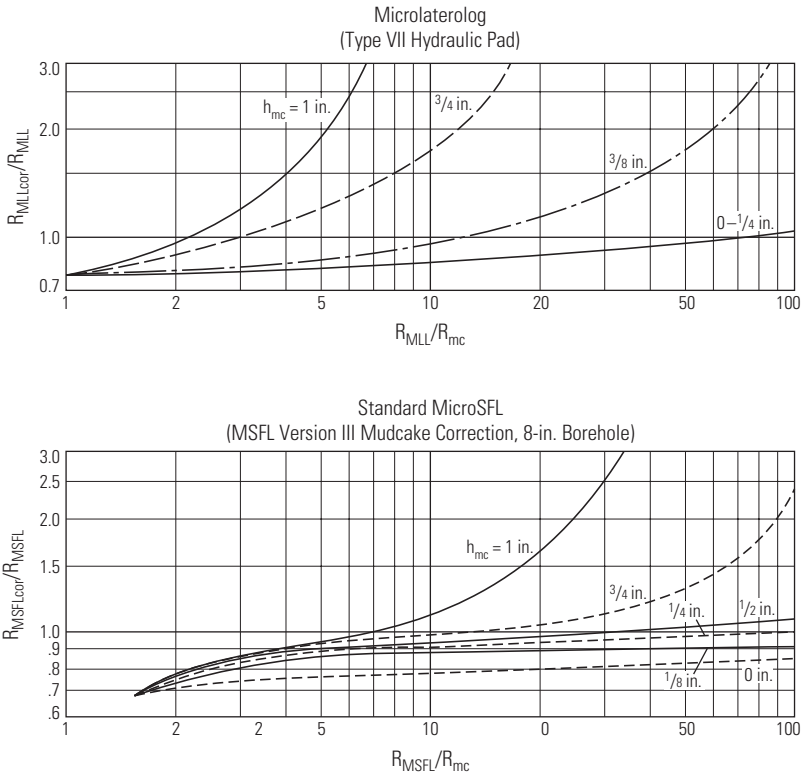


Fig. 6.3 Mudcake corrections for two types of microresistivity device. Courtesy of Schlumberger [3].

The micro-cylindrically focused log developed the measurement further [4]. It uses a rigid metal pad, unlike earlier devices that used flexible rubber pads. The rigid design prevents deformation and makes a more consistent standoff correction. The pad itself forms the guard electrode A_0 within which, and insulated from, are inserted three small measure electrodes (Fig. 6.4). The measure electrode B_0 is focused along the vertical axis by A_0 in a passive LL3-type design, with current being emitted from B_0 so as to maintain it at the same potential as A_0. The electrodes B_1 and B_2 are less focused, and therefore read shallower, because they are closer to the top edge of the pad. Focusing in the horizontal plane is more difficult because the pad's width is necessarily smaller than the pad's length, so that the area available for focusing is smaller. Horizontal focusing is therefore active, with two bucking electrodes on each side of the pad emitting the current needed to maintain the monitor electrodes at the potential of A_0. The combination of vertical and horizontal focusing ensures cylindrical equipotential lines near the center of the pad.

With three measurements of three different radial sensitivities it is possible to solve for three unknowns, R_{xo}, R_{mc}, and t_{mc}, where the latter is the mudcake thickness. The

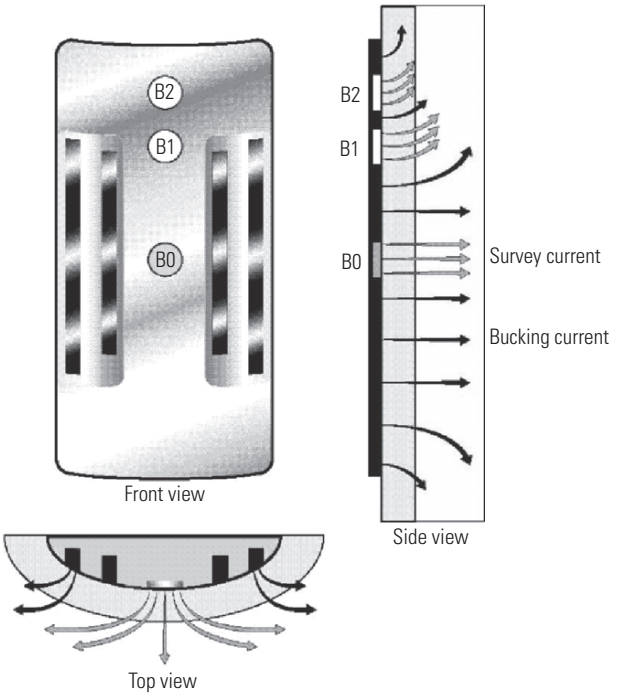


Fig. 6.4 Pad layout for the Micro Cylindrically Focused Tool. The two bars near the outer edges on each side of the pad are bucking electrodes; the inner two bars are monitor electrodes. The pad itself forms the A_0 electrode. Courtesy of Schlumberger.

solution is obtained by iterating through a forward model of the electrode responses, rather than looking up in a table as for previous devices (or in a chart if done manually). This allows more flexibility to handle different conditions and allows constraints to be added, such as that R_{mc} can only vary slowly up the borehole.

6.3 USES FOR R_{XO}

In the early years of resistivity logging, no porosity information was available from other logging devices. For this reason, the first use of R_{xo}, the estimation of porosity, is of historical interest only. This estimation is based on knowledge of the mud-filtrate resistivity R_{mf} (obtained from a mud sample) and a very shallow-resistivity measurement.

Following the definition of the formation factor F, which relates the fully water-saturated formation resistivity to the water resistivity,

$$R_o = F\, R_w\,, \tag{6.1}$$

one can write an analogous expression for the invaded zone:

$$R_{xo} = F\, R_{mf} \,. \tag{6.2}$$

Here, it is supposed that the mud filtrate of known resistivity R_{mf} has displaced the connate water. Also, by analogy, an expression for the mud-filtrate saturation of the invaded zone can be written:

$$S_{xo} = \sqrt{F\,\frac{R_{mf}}{R_{xo}}}\,, \tag{6.3}$$

where the mud-filtrate resistivity has replaced R_w in the usual formula, R_{xo} has replaced R_t, and the exponent n is assumed to be 2.

In order to get an estimate of the porosity, one can further make the assumption that the invaded zone is completely water-saturated and that the porosity dependence of F is $1/\phi^2$. From this, one obtains:

$$\frac{1}{\phi^2} = \frac{R_{xo}}{R_{mf}}\,. \tag{6.4}$$

Since the water saturation may not be complete, this can be used to obtain a lower limit to porosity, which is given by:

$$\phi \geq \sqrt{\frac{R_{mf}}{R_{xo}}}\,. \tag{6.5}$$

With porosity now measured by many other devices, the procedure above is rarely used. However R_{xo} has proved useful in many other ways. We have already seen its use for invasion corrections (Chapter 5) and for the identification of movable oil (Chapter 2). It is worthwhile investigating the latter more thoroughly by quantifying the separation often observed between the microresistivity curves, which correspond to R_{xo}, and the deep-resistivity curves, which are usually close to R_t.

From the generalized saturation equation:

$$S_w^n = \frac{a}{\phi^m}\,\frac{R_w}{R_t}\,, \tag{6.6}$$

it is possible to write an expression to compare the initial value of the water saturation (that in the uninvaded zone, S_w) to the water saturation in the invaded zone (S_{xo}). This is given by:

$$\left(\frac{S_w}{S_{xo}}\right)^n = \frac{\frac{R_w}{R_t}}{\frac{R_{mf}}{R_{xo}}} = \frac{R_w}{R_{mf}}\,\frac{R_{xo}}{R_t}\,. \tag{6.7}$$

which may also be rewritten as:

$$\frac{R_{xo}}{R_t} = \frac{R_{mf}}{R_w}\left(\frac{S_w}{S_{xo}}\right)^n\,, \tag{6.8}$$

It is clear that the ratio R_{xo}/R_t should be equal to the ratio of the mud-filtrate resistivity to the water resistivity in a water zone. The same is true if $S_{xo} = S_w$, as may happen in a zone with residual hydrocarbons that are not displaced by invasion, or in a zone with high-viscosity hydrocarbons such as tar or heavy oil. However, if there are any movable hydrocarbons, S_{xo} will be greater than S_w and the ratio R_{xo}/R_t will decrease. This ratio therefore indicates movable hydrocarbons when it decreases below R_{mf}/R_w. In practice the ratio is often formed by taking the microresistivity log as R_{xo} and the deep-resistivity log as R_t.

An example of this type of behavior can be seen in the laterolog example of Fig. 6.5. Shown is a log of the bottom 800 ft of a hydrocarbon reservoir. In zone 1 it can be assumed, in the absence of other information, that only water is present; the formation is fully water-saturated, with a shallow (MSFL) and deep-resistivity separation of about a factor of 2. Moving up to zones 2 and 3 all three resistivity curves increase. This could be due to a reduction in porosity, but if these zones were water-filled there should be the same separation between the curves as in zone 1. The reduction in ratio to about 1 clearly indicates movable oil. Moving further up the reservoir, the water saturation and hence the resistivity in the invaded zone remains roughly constant while the water saturation in the uninvaded zone becomes progressively smaller and the hydrocarbon saturation progressively greater. The ratio steadily decreases to about 1/50 in the upper part of the reservoir.

In the preceding example, we looked at relative saturations between the invaded and deep zones. However, the saturation of the invaded zone is of interest in its own right. For its determination, additional information is necessary. If the value of porosity is known from an additional measurement, then the residual oil saturation can be calculated from:

$$S_{xo}^n = \frac{a}{\phi^m}\frac{R_{mf}}{R_{xo}} . \tag{6.9}$$

This saturation can be used to determine the efficiency of water-flood production, because it quantifies the residual hydrocarbon saturation after flushing with mud filtrate. In a water flood, or a reservoir in contact with a water zone, hydrocarbons are displaced by water leaving a certain volume of residual hydrocarbon behind. The same mechanism occurs during invasion, but the rate is higher and the time shorter in the latter so that the displacement can be less efficient. The residual hydrocarbon saturation estimated from invasion, $(1 - S_{xo})$, may then be too high.

S_{xo} is also a useful indicator of hydrocarbons when the formation water salinity is variable or unknown. For example if, in Fig. 6.5 we only saw the top section of the log down to 11,900 ft, we might conclude that this was a water zone with $R_w = 50 \times R_{mf}$. But we can now calculate S_{xo} from the known R_{mf} and porosity from another log. If it is less than 1, there are hydrocarbons, although we cannot be sure whether or not they are movable. This application is particularly useful in sedimentary basins where formation waters are fresh, since when they are fresh they also tend to vary rapidly between reservoirs.

The calculations described above are often presented in the form of "quicklook" logs that are used as visual indicators of hydrocarbons. Which logs are used tends to vary with time and place. At one time "F logs" were popular [5]. These

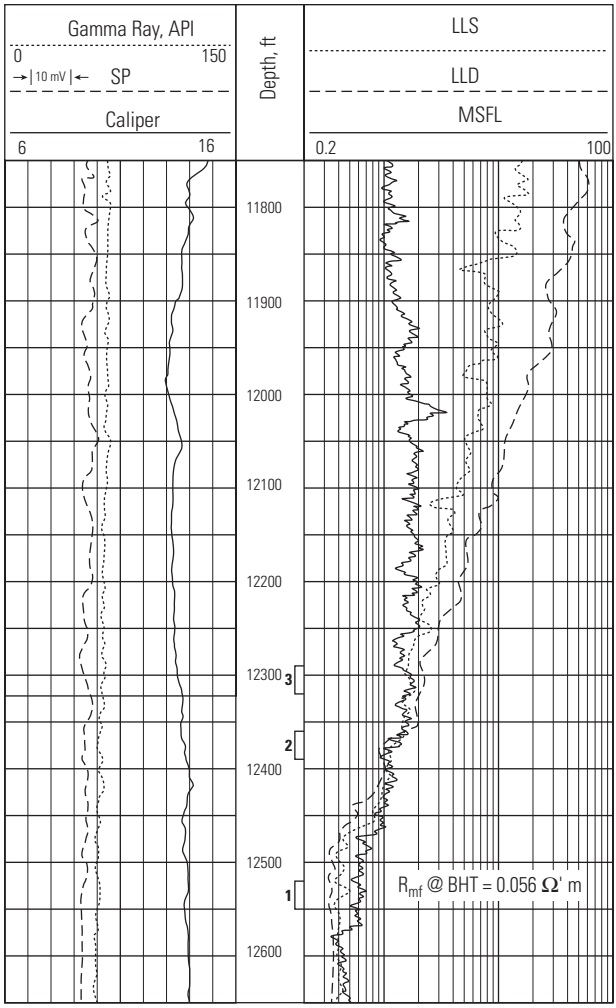


Fig. 6.5 Idealized log to be expected from a dual laterolog with a microresistivity device in a thick reservoir. The bottom zone is a water zone and the uppermost portion is hydrocarbon. A long transition zone is apparent.

were calculations of formation factor from a porosity log (e.g., $F_s = 1/\phi^2$), the microresistivity log ($F_{xo} = R_{micro}/R_{mf}$) and the deep-resistivity log ($F_t = R_{deep}/R_w$). If all three agree there is water. If $F_t = F_{xo}$ and both are higher than F_s there are residual hydrocarbons, since the calculation of F from resistivity is only valid if $S_{xo} = 1$. If $F_t > F_{xo}$ there are movable hydrocarbons.

Two commonly used quicklook logs are R_{wa} and R_{xo}/R_t. R_{wa} is the apparent water resistivity calculated from the deep resistivity and porosity assuming that $S_w = 1$, i.e., $R_{wa} = \phi^m R_{deep}$. If it is higher than the actual R_w there are

hydrocarbons. A common rule of thumb says that when $R_{wa} > 3 \times R_w$ there should be movable hydrocarbons. R_{wa} is really just the deep resistivity with porosity variations removed. In the same way the ratio R_{mfa} is a useful indicator when R_w is not known ($R_{mfa} = \phi^m R_{xo}$). The ratio R_{xo}/R_t is useful because it does not require a knowledge of porosity. As shown above this ratio will be reduced in a zone with movable hydrocarbons. An example of these curves is shown later in Fig. 23.3.

6.4 AZIMUTHAL MEASUREMENTS

The concept of small electrodes mounted on a pad was quickly extended to sondes with three or four arms, known as dipmeters. Each arm held one or more electrodes pressed against the borehole wall and sampled with a fine vertical resolution on the order of 0.1 in. Although the measurements are not necessarily calibrated in terms of resistivity, the vertical sequence of resistivity anomalies is of interest for determining the 3D orientation of strata intersecting the borehole. For a vertical well traversing horizontal layers of formation, the resistivity variations encountered by the measurement pads should correlate at the same depth. Depending on the orientation of the sonde (which is determined by an inertial platform or a magnetometer and pendulum), dipping beds will produce resistivity anomalies at different depths for each arm. The shift required to bring them into alignment will depend on the formation dip angle and borehole size.

The raw-resistivity curves of the dipmeter are rarely used directly but are subjected to various correlation or pattern recognition processing programs. These produce a summary log of the correlated events, which indicates the bedding orientation (dip angle and azimuth). The interpretation of the summary log, or "tadpole plot", in terms of structural geology and depositional environment, is beyond the scope of this book but is thoroughly treated in several references [1, 6–8].

In the 1980s the dipmeter evolved into the electrical microscanner, a device that incorporates a large number of small electrodes, or buttons, on several pads [9]. A typical pad contained 27 electrodes of 0.2 in. diameter arranged in four rows. The tool measures the current emitted by each electrode, while maintaining the potential of each electrode and the surrounding pad constant relative to a return electrode on the tool string above. The arrays of staggered electrodes are sampled at a high rate and processed to provide an electrical image of a portion of the borehole wall. Details on the scale of a few millimeters are resolved, so that the electrical image is nearly indistinguishable from a core photograph. The main drawback of early tools was that the pads did not cover a sufficient fraction of the borehole wall, particularly in large holes. Modern imaging devices contain a few hundred electrodes mounted on six arms, or else on four arms with movable flaps, so that up to 80% of the borehole wall can be covered in an 8 in. hole.

Another drawback was that the devices did not work in nonconductive muds because of the high impedance presented by the mudcake. Initially, dipmeters were fitted with sharp protruding electrodes designed to cut through the mudcake, but this was never very satisfactory. The Oil-Base Dipmeter Tool used micro-induction sensors [10], but results were sensitive to the borehole environment. Acoustic images,

described in Chapter 19, are dominated by surface effects and are poor in heavy muds. Then, beginning in 2001, new pad designs allowed images to be recorded in many nonconductive muds [11, 12]. These designs rely on the fact that both mudcake and formation do have some small conductivity due to their clay content, and that the distance between pad and formation is small. This makes it possible to send current through the formation between electrodes at the top and bottom of a pad and to measure the potential, and hence the resistivity, between buttons in the center.

Figure 6.6 compares a log from such a device with a core photograph over a 5 ft interval. On the right, the core photograph shows a sequence of thin sand and shale beds. The images on the left were obtained from four microelectrode arrays on measurement pads at different azimuths around the borehole wall. Beds as thin as 0.5

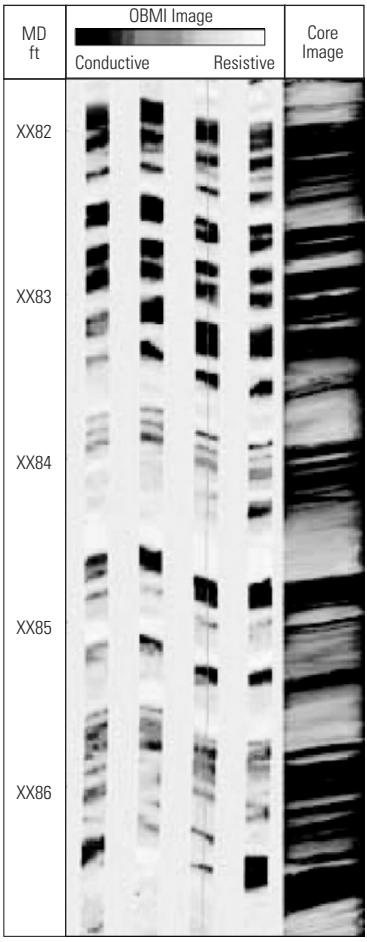


Fig. 6.6 An electrical image of the borehole produced by arrays of microelectrodes on an Oil-Base MicroImager tool laid alongside a core photograph of the same section of hole.

in. can be identified. This high resolution is very useful in the analysis of laminated sands (Section 23.3.4). Additional features such as the nonplanar bed boundary at 83.4 ft can also be seen. These images are a considerable enhancement over the conventional dipmeter measurements, which can be recorded at the same time. Bed boundaries, fractures and other events can now be picked manually from the images, and their dip and strike automatically computed. This gives an experienced geologist close control over the interpretation [13].

Images can also be obtained from azimuthal laterolog devices by sectioning one of the cylindrical current electrodes into separate segments [14]. The current emitted by each segment is adjusted so that the potential on a monitor electrode in its center is the same as that on two-ring electrodes above and below the segments. The remainder of the long-guard electrode lies above and below these electrodes, so that the whole assembly makes a monitored LL3 configuration. The resultant image is poorer than that of the microelectrode imaging tools, but can identify major structural features.

6.5 RESISTIVITY MEASUREMENTS WHILE DRILLING

The first resistivity measurement made while drilling was a short normal with electrodes mounted on an insulated sleeve, itself mounted on a drill collar. This was subsequently improved by the use of two guard electrodes in an LL3 arrangement that was also mounted on an insulated sleeve (the Focused Current Resistivity Tool, 1987 [15]). Insulated sleeves are not popular in the drilling environment as they tend to wear faster than the steel collars. A much better solution was to use toroids, as proposed by Arps in 1967 [16]. Toroids also offered a solution to the problem of measuring resistivity at the very bottom of the drill string, i.e., at the bit. It has always been highly desirable to measure the resistivity of the formation as soon as it is penetrated, or even beforehand. With this information it is possible, for example, to steer a highly deviated well within a reservoir or to stop drilling as soon as the reservoir is penetrated, as shown in the example of Fig. 6.7. These applications will be discussed in Chapter 20. In this chapter we will discuss how the measurements are made.

6.5.1 Resistivity at the Bit

The first device to measure the resistivity at the bit was the Dual Resistivity MWD Tool†, which also makes a type of lateral measurement [17]. The second device was the Resistivity at the Bit Tool (RAB*), which also makes a focused resistivity measurement [18]. A removable sleeve with button electrodes can be added to the tool in order acquire data that varies azimuthally and has different depths of investigation. An improved version of the RAB is known as the GVR*, geoVISION Resistivity sub.

†Mark of Halliburton
*Mark of Schlumberger

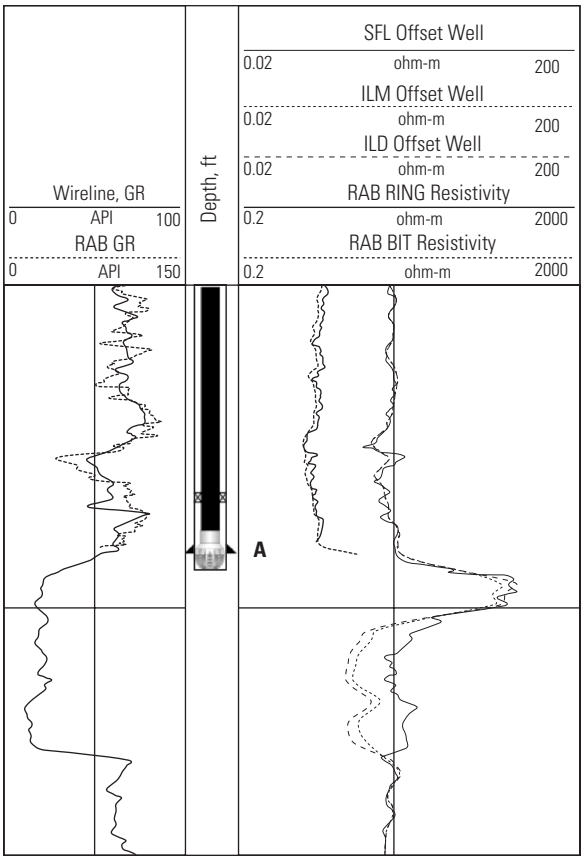


Fig. 6.7 Example of a log recorded by the RAB tool. The increase in bit resistivity at A indicates the top of the reservoir sand. This top can be seen in logs from the offset well (right). Drilling was stopped to set casing. Adapted from Bonner et al. [18]. Used with permission.

In both the Dual Resistivity MWD Tool and the RAB, a current is sent down the drill collar and out through the bit by a toroidal transmitter before returning through the formation (Fig. 6.8). The toroidal transmitter, shown in Fig. 6.9a, is a transformer with its coils acting as the primary, and the drill collar and return path through the formation acting as the secondary. A low (1,500 Hz) alternating voltage is applied to the coil inducing a voltage difference between the collar sections above and below the toroid. This voltage difference, which is almost entirely in the formation due to the low resistance of the collar, is equal to the input voltage divided by the number of turns in the toroid. The axial current is measured by a toroidal monitor (Fig. 6.9b). This is also a transformer with, in this case, the drill collar and formation acting as the primary and the coils as the secondary. The current flowing in the coils is equal to the axial current divided by the number of turns.

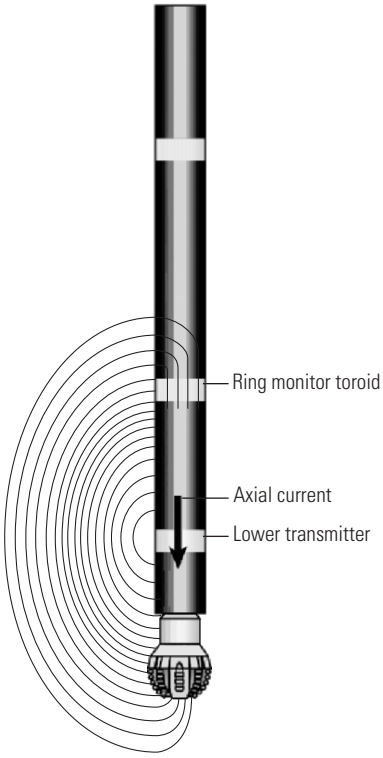


Fig. 6.8 An illustration of how resistivity is measured at the bit. The toroid transmitter sends current down the drill collar and out through the bit. The current lines that travel through the formation return further up the collar where they are measured by a monitor toroid. Courtesy of Schlumberger.

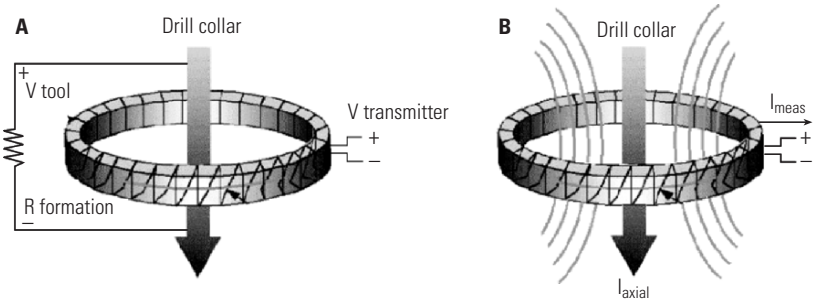


Fig. 6.9 (a) A toroidal transmitter formed by wrapping a coil around a ferromagnetic toroid. The voltage $V_{tool} = V_{transmitter}/N$, where N is the number of turns in the coil. (b) A current monitor formed by connecting a toroidal coil to a low impedance circuit. The current $I_{meas} = I_{axial}/N$. From Bonner et al. [18]. Used with permission.

It is important to maximize the amount of current flowing out through the bit but at the same time to place the transmitter and monitor far enough apart that the measured current flows through the formation and not the borehole. For this reason the transmitter is placed as close to the bit as possible and the monitor is placed further up the string (Fig. 6.8). Resistivity is calculated from:

$$R_{app} = K \frac{V_{tool}}{I_{meas}}, \tag{6.10}$$

where V_{tool} is the formation voltage drop measured by the toroid and I_{meas} is the current at the monitor. K depends on the drill collar geometry.

The result is an unfocused device whose characteristics depend strongly on the distance between transmitter and bit. When the main purpose of the log is to measure the resistivity of the formation as soon as it is penetrated, the RAB should be placed immediately above the bit. This gives a reasonable vertical response of a few feet as well as the earliest response to resistivity changes. If the RAB tool is placed further up the tool string, the response is less well-defined and the measurement is more qualitative than quantitative.

Surprisingly, this measurement works in most oil-based muds, even though they are nonconductive. The reason is that the formation is in contact with the bit as well as with some part of the drill collar, usually through a stabilizer. There is thus a current return path. However in nonconductive mud the current returning through the monitor shown in Fig. 6.8 is unpredictable, so it is measured at another monitor placed just below the transmitter (not shown). There is no concern about current flowing through the borehole in this situation.

6.5.2 Ring and Button Measurements

Horizontal (or radial) formation resistivity, such as is measured by wireline devices, is derived in the RAB from a set of ring electrodes and three button assemblies, all of which are insulated from the body of the collar (Fig. 6.10). The central ring electrode is focused using monitor electrodes in a LL7 configuration, while the button assemblies also use monitor electrodes in an arrangement similar to the microlaterolog. The resistivity seen by each electrode can then be calculated from the measure current sent by the large central ring, the voltage on the monitor electrodes and using an equation similar to Eq. 6.10.

In practice it is not quite as simple as this. First, there is some potential drop in the drill collar because it does not have infinite conductivity and because, in spite of the low-operating frequency, skin effect confines the current to a small cross section of the collar. This correction is handled by a transform for each electrode established by modeling and verified in salt water tanks. Different transforms are needed for different drill collar geometries.

Secondly, as with standard electrode devices, the use of a single transmitter and detector leads to distortion at bed boundaries (Fig. 6.11a). In other words it needs to be focused. This is achieved by adding a second transmitter and two monitor toroids (Fig. 6.11b). The upper and lower transmitter (T_1 and T_2) are driven 180° out of

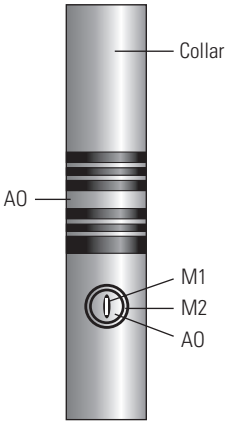


Fig. 6.10 Mounting of the ring assembly (top) and one of the button assemblies on the collar. Black parts are insulation, grey parts are conductive. The rings above and below the A_0 ring are monitor electrodes. Courtesy of Schlumberger.

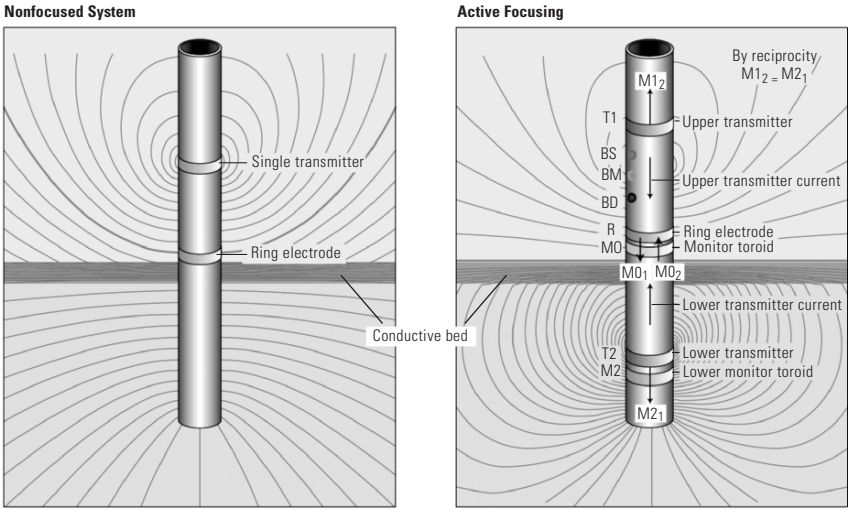


Fig. 6.11 From the simple concept to the practical device with attendant complications. Left panel: the unfocused current map that results from using a single transmitter when a conductive bed prevents the current flowing radially at the ring. Right panel: in the RAB tool, multiple transmitter and monitor toroids are used to maintain radial focusing at the ring electrode. The current lines at the ring are now nearly radial. The notation M_{01} indicates the current at M_0 due to transmitter T_1. Adapted from Bonner et al. [18]. Used with permission.

phase so that in a homogeneous formation the axial current at the ring is zero and the radial current is perpendicular to the collar. *When the formation resistivities above and below the ring are not identical this symmetry must be maintained by adjusting the outputs of T_1 and T_2. They are first adjusted so that the axial current at M_0 is zero. The ring is close enough to M_0 to also have zero axial current. This adjustment could be done in hardware by firing the transmitters simultaneously and measuring the net current at M_0. In practice it is done in software by firing the transmitters sequentially, measuring the currents that each produce at the monitor, labeled M_{01} and M_{02} in the figure, and adjusting the transmitter outputs accordingly.*

The outputs from T_1 and T_2 must be further adjusted since the current losses between T_1 and the ring can be different to those between T_2 and the ring. These losses are measured by the ratio of currents generated by T_1 at M_0 and M_2 (M_{01}/M_{21}) and by a similar ratio for T_2. This can only be done with one transmitter firing. For this reason measurements must be made alternatively from T_1 and from T_2 and both adjustments done in software. One final twist – there is no monitor toroid at the upper transmitter since by the principle of reciprocity the current M_{12} can be assumed equal to M_{21} which is already measured.

The result of focusing is that the equipotential surfaces near the ring are cylinders for a significant distance into the formation. Much effort has been put into focusing the ring, but what about the buttons? These are intended to be less focused than the ring and are therefore placed nearer one of the transmitters. As can be appreciated from the current lines in Fig. 6.11b the nearer the button is to the transmitter the less focused it is, and therefore the shallower the depth of investigation. With three buttons of different depths of investigation it is possible to make invasion corrections in the traditional manner.

6.5.3 RAB Response

The general features of RAB response are determined by the size and position of the electrodes and the fact that it is a resistivity device. Like a laterolog the RAB responds to resistivity and therefore performs best when formation resistivity is high, mud resistivity is low and $R_{xo} < R_t$. The small size of the electrodes and the proximity of the buttons to the transmitter give a vertical resolution of approximately 2 in. and shallow depths of investigation of approximately 1, 3, and 5 in. for the buttons, and 8 in. for the ring. These depths are considered sufficient to probe the shallow invasion expected at the time of logging. However, invasion can be significant when LWD logs are run, as discussed in Chapter 2.

The same types of environmental factors apply as for wireline electrode devices: borehole, shoulder bed, and invasion. RAB tools are designed for particular bit sizes, as are all drill collars and LWD tools. Providing the hole is at bit size, borehole corrections are negligible since the distance between drill collar and borehole wall is less than an inch. There are two exceptions. First, if the hole washes out, the corrections on the shallower and then the deeper measurements rapidly become significant. Second, as the ratio R_t/R_m drops below 10, the corrections also become increasingly significant. Charts for the borehole effect are available [3].

The effect of distant shoulders is small, which is not surprising considering the small electrode size and the long drill collars. There are, however some squeeze and anti-squeeze effects at bed boundaries that cause horns at large-contrast boundaries.

The most important effect by far is invasion. We saw in Fig. 5.18 that the pseudogeometric factors for the laterolog varied with the resistivity contrast R_{xo}/R_t. This is even truer for the RAB. The depths of investigation quoted above are the depths at which the pseudogeometric factor is 0.5 for the 6.75 in. diameter tool used in 8.5 in. boreholes when $R_{xo} = 10$ ohm-m and $R_t = 100$ ohm-m. If the contrast is higher the depths are less.

Although pseudogeometric factors give a convenient picture of depth of investigation, it can often be more instructive to consider the actual log reading in case of invasion. The actual reading depends on R_{xo} and R_t as well as the pseudogeometric factor (Eq. 5.16). The top panel of Fig. 6.12 shows the readings on the ring and button

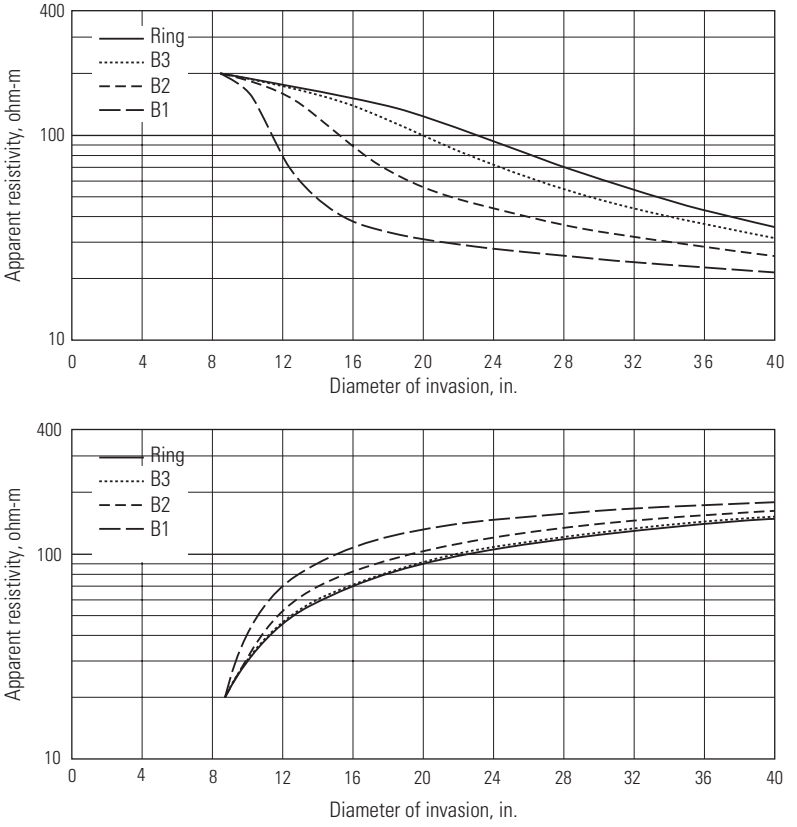


Fig. 6.12 Top panel: the apparent resistivity seen by the ring and button electrodes for a 10:1 conductive invasion and varying invasion diameter. Bottom panel: the apparent resistivity seen by the ring and button electrodes for a 10:1 resistive invasion and varying invasion diameter. Adapted from Bonner et al. [18]. Used with permission.

electrodes as invasion increases for the case where $R_{xo} = 20$ ohm-m and $R_t = 200$ ohm-m, i.e., with conductive invasion. The results are plotted in terms of diameter so that at 8.5 in. (the borehole size) there is no invasion and all measurements read R_t. As invasion diameter increases all measurements tend to R_{xo}. At an invasion diameter of 23 in., which is a depth of invasion of 7.75 in., the ring reads 50% of R_t. The large separation between the curves indicates that it will be easy to invert the logging measurements when R_t, R_{xo}, and D_i are not known. The bottom panel of Fig. 6.12 shows the opposite case of resistive invasion. Here the ring reads 50% above R_t at the very small D_i of 10 in., illustrating again that elecrode devices are not suitable with resistive invasion.

Tornado charts can be formed for a given contrast and other conditions providing there is conductive invasion. For the RAB we have the luxury of four measurements (if the sleeve with the buttons has been run). As one might deduce from Fig. 6.12a the three buttons are used when invasion is very shallow, and the two deeper buttons and the ring when invasion is deeper. More sophisticated techniques that use all four measurements are also available [19]. In Chapter 5 we saw that tornado charts are only valid for thick beds. Given the small size of the buttons and the high vertical resolution, the effect of surrounding beds and other 2D effects are much less severe than with a laterolog.

6.5.4 Azimuthal Measurements

The RAB buttons respond to the resistivity in front of them, so that if the drill string is rotated it is possible to record an image of the formation at different azimuths. This is a powerful feature as it allows images of formation features to be seen while drilling. Magnetometers orient the tool with respect to the earth's magnetic field. RAB images do not have the vertical resolution of electrical microscanners but do reflect bedding and structural features from which formation dip can be determined. This information can be very useful in near real time. For example, in highly deviated wells an image can determine whether a new bed is being entered from above or below, something that cannot be done with non-azimuthal measurements. An example of this is given in Chapter 20.

6.6 CASED-HOLE RESISTIVITY MEASUREMENTS

The ability to measure water saturation through casing is highly desirable, mainly in old wells to monitor changes with depletion and identify zones that still have producible oil. It has been done for many years using pulsed neutron devices (Chapter 15). However these have relatively shallow depths of investigation and do not always give satisfactory answers. At first sight it would seem impossible to measure resistivity through the highly conductive casing, but the method has been recognized for years, with the first patent being filed in the 1930s [20]. The main difficulty is the extremely small electrical potential that must be measured, but this was overcome in two devices

that appeared in the late 1990s: the Through Casing Resistivity Tool and the Cased-Hole Formation Resistivity Tool [21, 22].

Both tools work on the same basic principle (see Fig. 6.13). In the current leakage mode, current is sent between a downhole injection electrode and the surface. This current flows down the casing past three voltage-measuring electrodes A, B, and C, each 2 ft apart. Although most of the current stays within the casing, a small fraction leaks into the formation (ΔI). This leakage is seen as a progressive reduction in current flowing in the casing, which leads to a different potential drop from A to B than from B to C. This difference also depends on the casing resistance from A to B and B to C. If it is the same then $V_2 - V_1$ is a direct measure of ΔI, but since we are dealing with very small voltages any small difference in casing resistance is important. This difference, ΔR_c, is therefore measured in a second "calibrate" mode, in which the current is returned downhole instead of to the surface. In this configuration the leakage current is found to be negligible so that $V_2 - V_1$ is a direct measure of ΔR_c.

The signal to noise ratio is low enough that measurements must be made with the tool stationary. Logging speed is therefore slow, so there have been several efforts to speed it up. By adding a fourth electrode and duplicating circuits it is possible to make measurements at two depths, 2 ft apart, during one station. In a recent tool the two modes are performed at the same time [23]. This is achieved by a voltage generator that feeds back current around the calibrate path during the current leakage mode so as to cancel the voltage V_2. The computation now no longer depends on ΔR_c but on

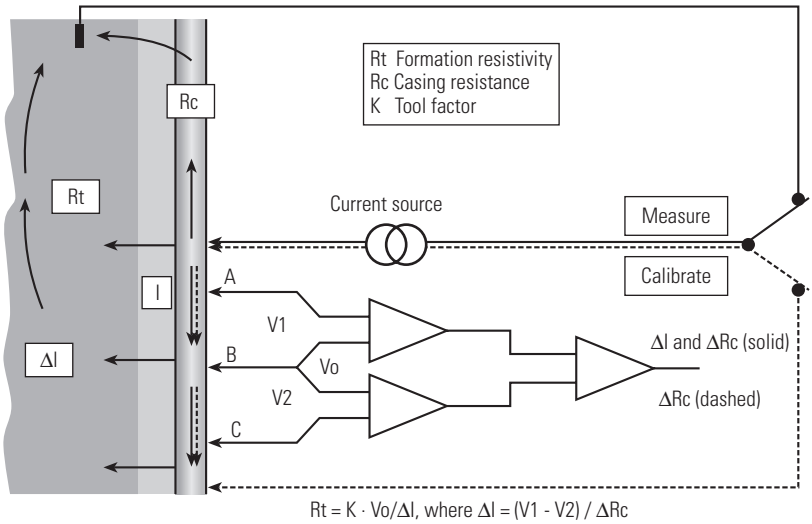


Fig. 6.13 The basic principle of measuring resistivity through casing. The formation current, ΔI, and the variation in casing resistance between AB and BC, ΔR_c, are measured in two steps, labeled Measure and Calibrate. In some later tools more complex circuitry allows this to be done in one step. From Beguin et al. [22]. Used with permission.

V_1 and the R_c between A and B. The latter can be measured at the same time as, but with a different frequency than, the current leakage. The result is a reduced sensitivity to measurement errors and a one-step, faster, recording.

With the formation current ΔI known, R_{app} can be calculated from Eq. 6.10 with the voltage on the casing at the electrodes, V_0, and a K-factor. V_0 is measured by sending current as in the current leakage mode and measuring the voltage between the downhole voltage electrodes and a surface reference (not shown in Fig. 6.13). Although V_0 varies slowly with depth it is not easy to measure accurately because it is small (less than 100 mV) and because of problems with the surface reference electrode: for example, it may not be possible to place the electrode far enough from the casing to be considered at zero potential. In practice cased-hole resistivity logs may need to be shifted to match openhole logs in a shale or other zone where formation resistivity should not have changed with time. Any such shift needs to be adjusted near the bottom of the casing where voltage changes fast with depth.

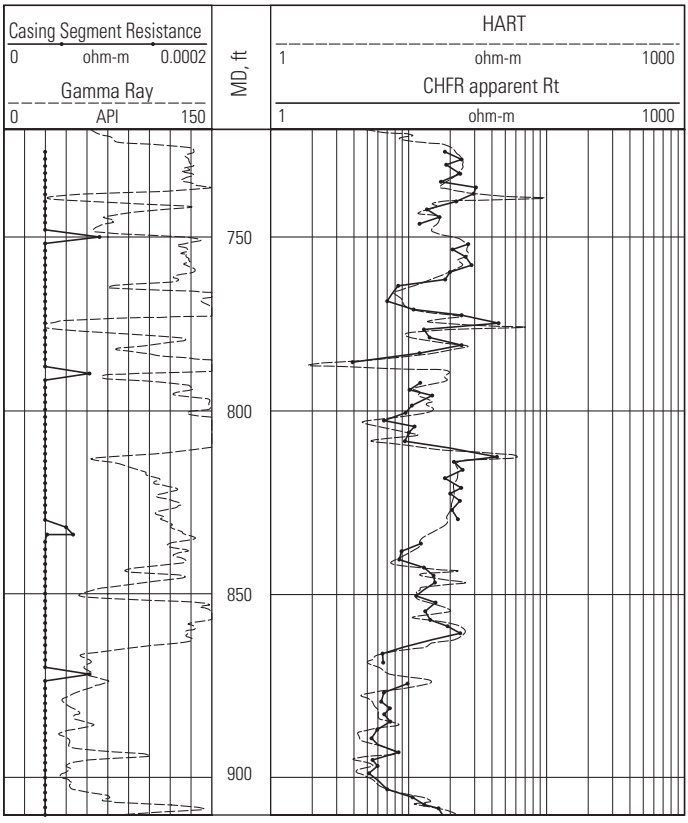


Fig. 6.14 A cased-hole formation resistivity log in a newly cased well versus a laterolog previously recorded in the open hole. From Beguin et al. [22]. Used with permission.

Understandably there are some limitations to the through-casing measurement. First we should appreciate that formation resistivity is typically nine orders of magnitude larger than that of the casing. However the formation presents a much larger area than the casing, so that the ratio of resistances and hence of leakage current to total current is around 10^{-4}. This current is measured through a casing resistance that is a few tens of micro-ohms, leading to a differential voltage $V_2 - V_1$ that is in nanovolts. In order to achieve sufficient signal to noise, this small voltage must be measured over a period of time with the tool stationary. The measurement frequency is no more than a few Hz: at higher frequencies the skin depth in the casing would be reduced, confining even more of the current within the casing and further decreasing the leakage current, while a direct current would polarize and drift.

For the time being the tool works best in the formation resistivity range 1 ohm-m to 100 ohm-m. Below 1 ohm-m the measurement becomes sensitive to the cement resistivity and thickness, neither of which are well known. As resistivity increases, the formation current drops. This can be partially overcome by repeating the measurement for a longer period at each station, but there is a practical limit on how much this can be done. The good agreement that can be obtained within the 1–100 ohm-m range between cased-hole resistivity and an openhole laterolog can be seen in Fig. 6.14.

Once measured, the resistivity through casing has some appealing features. The casing acts as a giant guard electrode so that the leakage current is particularly well focused. In an infinitely thick formation the depth of investigation is of the order of tens of feet, much larger than a laterolog. Like any laterolog, this is reduced in thinner beds. Also like a laterolog, an invaded zone or cement that is more resistive than R_t affects strongly the measurement.

REFERENCES

1. Serra O (1984) Fundamentals of well-log interpretation. Elsevier, Amsterdam, The Netherlands

2. Jordan JR, Campbell FL (1986) Well logging II – electric and acoustic logging. SPE Monograph Series, SPE, Dallas, TX

3. Schlumberger (2005) Log interpretation charts. Schlumberger, Houston, TX

4. Eisenmann P, Gounot M-T, Juchereau B, Trouiller J-C, and Whittaker SJ (1994) Improved R_{xo} measurements through semi-active focusing. Presented at the 69th SPE Annual Technical Conference and Exhibition, paper SPE 28437

5. Schlumberger (1989) Log interpretation principles/applications. Schlumberger, Houston, TX

6. Schlumberger (1970) Fundamentals of dipmeter interpretation. Schlumberger, New York

7. Serra O (1985) Sedimentary environments from wireline logs. Schlumberger, New York

8. Doveton JH (1986) Log analysis of subsurface geology, concepts and computer methods. Wiley, New York

9. Ekstrom MP, Dahan CA, Chen MY, Lloyd PM, Rossi DJ (1986) Formation imaging with microelectrical scanning arrays. Trans SPWLA 27th Annual Logging Symposium, paper BB

10. Adams J et al. (1989) Advances in log interpretation in oil-base mud. Oilfield Rev. 1(2):22–38

11. Cheung P et al. (2002) A clear picture in oil-base muds. Oilfield Rev. winter 2001/2002:2–27

12. Lofts J, Evans M, Pavlovic M, Dymmock S (2003) New microresistivity imaging device for use in non-conductive and oil-based muds. Petrophysics 44(5):317–327

13. Luthi S (2001) Geological well logs: their use in reservoir modeling. Springer, Berlin

14. Smits JW, Benimeli D, Dubourg I, Faivre O, Hoyle D, Tourillon V, Trouiller JC, Anderson BI (1995) High resolution from a new laterolog with azimuthal imaging. Presented at the 70th SPE Annual Technical Conference and Exhibition, paper 30584

15. Evans HB, Brooks AG, Meisner JE, Squire RE (1987) A focused current resistivity logging system for MWD. Presented at the 62nd SPE Annual Conference and Exhibition, Dallas, paper 16757

16. Arps JJ (1967) Inductive resistivity guard logging apparatus including toroidal coils mounted in a conductive stem. US patent No 3,305,771

17. Gianzero S, Chemali R, Lin Y, Su S, Foster M (1985) A new resistivity tool for measurement while drilling. Trans SPWLA 26th Annual Logging Symposium, paper A

18. Bonner S, Bagersh A, Clark B, Dajee G, Dennison M, Hall JS, Jundt J, Lovell J, Rosthal R, Allen D (1994) A new generation of electrode resistivity measurements for formation evaluation while drilling. Trans SPWLA 35th Annual Logging Symposium, paper OO

19. Li Q, Rasmus J, Cannon D (1999) A novel inversion method for the interpretation of a focused multisensor LWD laterolog resistivity tool. Trans SPWLA 40th Annual Logging Symposium, paper AAA

20. Alpin LM (1939) The method of the electric logging in the borehole with casing. U.S.S.R. Patent No 56026

21. Maurer HM, Hunziker J (2000) Early results of through casing resistivity field tests. Trans SPWLA 41st Annual Logging Symposium, paper DD

22. Beguin P, Benimeli D, Boyd A, Dubourg I, Ferreira A, McDougall A, Rouault G, and van der Wal, P (2000) Recent progress on formation resistivity measurement through casing. Trans SPWLA 41st Annual Logging Symposium, paper CC

23. Benimeli D, Levesque C, Rouault G, Dubourg I, Pehlivan H, McKeon D, Faivre O (2002) A new technique for faster resistivity measurements in cased holes. Trans SPWLA 43rd Annual Logging Symposium, paper K

Problems

6.1 Using the SP and resistivity fundamentals, show that the following relation holds for clean formations:

$$SP = -K\left[log_{10}\frac{R_{xo}}{R_t} + 2\,log_{10}\frac{S_{xo}}{S_w}\right]. \tag{6.11}$$

6.2 A section of sandstone reservoir was logged and found to have a porosity of 18%. The water resistivity is estimated to be 0.2 ohm-m, and R_t was measured to be 10 ohm-m.

6.2.1 What is the water saturation?

6.2.2 What error in S_w (in saturation units) is induced by a 10% relative uncertainty for each of the three parameters?

6.3 Given the log of Fig. 6.5 with R_{mf} indicated at formation temperature, answer the following:

6.3.1 Over the zone 11,800–12,200 ft, what is the average value of the lower limit to porosity which can be established?

6.3.2 Evaluate S_w every 50 ft over the above interval and make a linear plot of S_w versus depth.

6.3.3 The actual average porosity over the zone in question is 30 p.u. How does this compare with your estimate? Is this discrepancy reasonable? How does this additional information impact the actual value of S_w along the zone (replot curve)?

6.4 In the bottom section of the well studied in question 6.3, assume that the porosity is constant at 30% over the entire interval and answer the following:

6.4.1 In the zones marked 1, 2, and 3, determine the corrected values of R_{LLd} and the diameter of invasion.

6.4.2 Estimate the value of R_w in this reservoir.

6.5 In the same well (Fig. 6.5) calculate the value of R_{xo}/R_t at 12,550, 12,450, 12,400, 12,200 and 11,800 ft. Use the results to identify intervals of water, residual oil, and movable oil. Calculate S_w using the value derived for R_w in the last question and the often-used empirical relation $S_{xo} = S_w^{0.2}$.

6.6 A common rule of thumb is that when $R_{wa} = 3 \times R_w$ or greater there are movable hydrocarbons. Assuming $m = n = 2$ what S_w does this correspond to?

6.7 At what diameter of invasion does the J-factor equal 0.5 for the ring electrode in the top and bottom panels of Fig. 6.12? In which of these cases would you say that the ring reads deeper?

7

Resistivity: Induction Devices

7.1 INTRODUCTION

The presence of a conductive mud in the borehole is somewhat of a nuisance for electrode devices, as was illustrated in the last chapter. Many improvements have been made in electrode tool design to compensate for the problems. However, conductive borehole mud does provide one advantage: it effectively places the current and voltage measurement electrodes into electrical contact with the formation whose resistivity is to be measured.

What about those cases in which the mud is nonconductive (oil-base mud) or nonexistent (air-filled hole), or in which a plastic liner has been inserted into the borehole? It is for these cases that the induction tool was designed originally, although it has since found widespread use in conductive muds. Induction devices use medium frequency (several 10s of KHz) alternating current to energize transmitter coils in the sonde; they, in turn, induce eddy currents in the formation whose strength is proportional to the formation conductivity. The magnitude of the induced currents is measured by receiver coils in the tool that sense the magnetic field generated by the induced currents.

Before discussing the principles involved in the design and operation of induction tools, this chapter reviews some of the basics of electromagnetic theory. This review will serve as the basis for analyzing the characteristics of a two-coil device in detail. The analysis will develop the notion of the geometric factor, which is used to predict the radial and vertical tool response. The development of traditional multi-coil focused devices follows directly from geometric factor theory. A modification to this simple theory is shown to be necessary to account for attenuation and phase shift

of the magnetic induction field, known as skin effect. The chapter concludes with a discussion of the preferred conditions for choosing induction or electrode devices. Multi-array and triaxial induction devices are discussed in the next chapter.

7.2 REVIEW OF MAGNETOSTATICS AND INDUCTION

Induction devices employ alternating currents in transmitter coils to set up an alternating magnetic field in the surrounding conductive formation. This changing magnetic field induces current loops in the formation that are detectable by a receiver coil in the sonde. The details of the relationships between electric currents and magnetic fields, both steady-state and time-varying, are reviewed in this section to provide the basis for the geometric factor theory that is used to demonstrate the response of induction logging tools.

7.2.1 Magnetic Field from a Current Loop

Ampere's law states that a magnetic field will be associated with the flow of an electric current and directed at right angles to it. The strength of the magnetic field B is related to the current I. In particular the integral of the tangential component of B around any closed path Γ *is proportional to the current piercing the area enclosed by* Γ. *This is expressed as:*

$$\int_{\Gamma} \overline{B} \cdot d\bar{l} = \frac{I}{\epsilon_o c^2} , \tag{7.1}$$

where $d\bar{l}$ *is a unit vector directed along the path* Γ, ϵ_o *is the permittivity of free space and c the speed of light. (Through the use of a vector identity, this is often written as:*

$$\nabla \times \bar{B} = \frac{\bar{j}}{\epsilon_o c^2}, \tag{7.2}$$

where $\bar{j}$ *is the current density, or the normal component of the current I divided by the surface area enclosed by* Γ.*)*

One simple application of this relation is the calculation of the magnetic field associated with the current flowing in a long wire, shown in Fig. 7.1. At a radial distance r from the wire, the path integral is just $B \cdot 2\pi r$, *since the magnetic field B is in the form of closed circles around the current-carrying wire, and since B and I are known to be at right angles to one another. Thus the magnetic field strength relation may be determined from:*

$$B \cdot 2\pi r = \frac{I}{\epsilon_o c^2}, \tag{7.3}$$

or

$$B = \frac{1}{4\pi\epsilon_o c^2} \frac{2I}{r}. \tag{7.4}$$

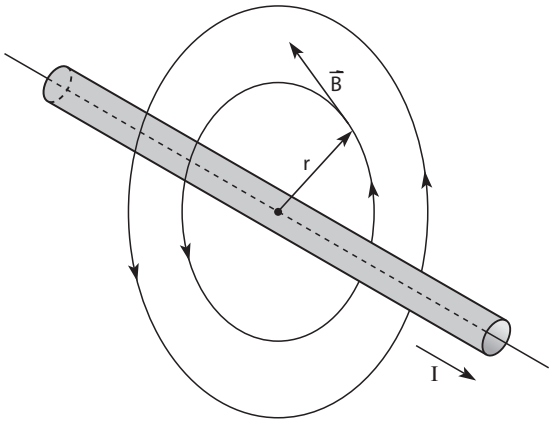


Fig. 7.1 Circular lines of magnetic flux B, surrounding a very long straight wire carrying a current. Adapted from Feynman et al. [1].

The generalized expression for calculating the magnetic field from a current element is called the law of Biot–Savart and resembles the preceding expression:

$$\overline{B} = -\frac{1}{4\pi\epsilon_o c^2}\int \frac{I\, d\hat{r} \times d\hat{l}}{r^2}\,, \tag{7.5}$$

where $d\hat{l}$ is an elemental length along the current path Γ and $d\hat{r}$ is the unit vector in the direction of the observation point from the current element.

A simple application of the law of Biot–Savart which will be useful in the discussion of the induction device is the calculation of the component of the magnetic field perpendicular to the plane of a circular loop of current (such as that observed in the receiver coil). As shown in Fig. 7.2, the application is simple for reasons of symmetry. The vertical component B_z is to be calculated on the axis of the current loop. The sketch shows that the component $d\bar{B}$ is the result of one element of the current loop; it is oriented at right angles to the current element. The magnitude of this contribution to the magnetic field at a distance z above the loop of radius a is given from the law of Biot–Savart by:

$$dB \propto \frac{I_o a\, d\phi}{a^2 + z^2}\,, \tag{7.6}$$

where the element of current is of length $a \times d\phi$.

It is clear that all but the z-component of the B field will be canceled when the whole current loop is considered. The component dB_z is seen to be:

$$dB_z = dB\ \sin\Theta = dB\ \frac{a}{\sqrt{a^2 + z^2}}\,. \tag{7.7}$$

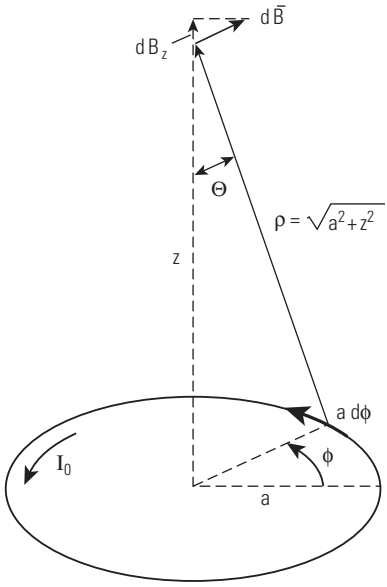


Fig. 7.2 Geometry for the calculation of the vertical component of the magnetic field on the axis of a current-carrying circular loop of radius a.

The total contribution to the z-component is given by the integral of all the elements of current around the loop. Merging the above two equations gives:

$$B_z = \int_0^{2\pi} \frac{I_o a^2}{(a^2 + z^2)^{3/2}} d\phi = \frac{2\pi I_o a^2}{\rho^3} \,. \tag{7.8}$$

7.2.2 Vertical Magnetic Field from a Small Current Loop

Another relation for which there will be a need is that of the vertical component of the magnetic field away from the axis of a small current loop. For this problem, recourse is made to the magnetic vector potential $\overline{A}$, which is defined by:

$$\overline{B} = \nabla \times \overline{A} \tag{7.9}$$

and can be related to a current distribution in a fashion analogous to the relation between the electrostatic potential and a charge distribution:

$$\overline{A} = \frac{1}{4\pi\epsilon_o c^2} \int \frac{\overline{j} dV}{r} \,. \tag{7.10}$$

Here, the current density distribution must be integrated over the volume (dV) which contains it. Once the vector potential is obtained, then the z-component of the magnetic field is simply obtained from:

$$\begin{aligned} B_z &= (\nabla \times \overline{A})_z \\ &= \frac{\partial A_y}{\partial x} - \frac{\partial A_x}{\partial y}. \end{aligned} \tag{7.11}$$

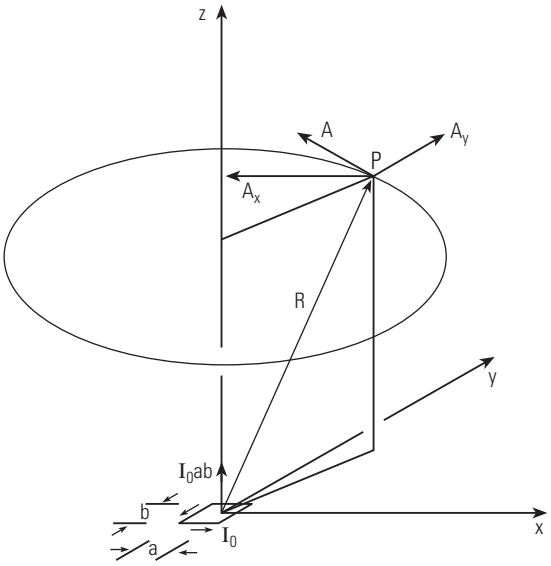


Fig. 7.3 The vector potential $\overline{A}$, from a small current-carrying loop of rectangular cross-section. Adapted from Feynman et al. [1].

The vector potential of a small current loop can be written in analogy with the electrostatic potential at a distance r from a dipole which is given by:

$$\phi(r) = \frac{1}{4\pi\epsilon_o}\frac{p\ \cos\theta}{r^2}, \tag{7.12}$$

where p is the dipole moment (the charge times separation distance) and θ is the angle between the orientation of the dipole and the observation point. For the current loop in the x–y plane shown in Fig. 7.3, we will write an expression for the vector potential at the point P indicated. It will consist of only two components, A_x and A_y, since there is no current distribution in the z-direction. To find the x-component of $\overline{A}$, only the current in the x-direction is considered, as shown in Fig. 7.3. The two parallel current paths are equivalent to the concept of an electric dipole. By analogy with two charged rods, each with charge per unit length λ, the dipole moment would be the total charge times the separation or:

$$p = \lambda ab, \tag{7.13}$$

and the cosine of the angle between the point P and the dipole moment is $-\frac{y}{R}$. Transferring the analogy to current flow in a coil with a flowing charge I_0, and combining the above two equations gives:

$$A_x = -\frac{I_0\, ab}{4\pi\epsilon_o c^2}\frac{y}{R^3}. \tag{7.14}$$

The y-component can be found in the same manner to be:

$$A_y = \frac{I_0\, ab}{4\pi\epsilon_o c^2}\frac{x}{R^3}. \tag{7.15}$$

From the two components of the vector potential the spatial dependence of the vertical component of the magnetic field can be determined:

$$\begin{aligned} B_z &\propto \frac{\partial}{\partial x}\left(\frac{x}{R^3}\right) - \frac{\partial}{\partial y}\left(\frac{-y}{R^3}\right) \\ B_z &\propto \frac{1}{R^3} - \frac{3z^2}{R^5}. \end{aligned} \tag{7.16}$$

7.2.3 Voltage Induced in a Coil by a Magnetic Field

The final review item is that of Faraday's law of induction. From experimental observations, Faraday deduced that a changing magnetic field would set up a current in a loop of conductor present in the field. He also demonstrated that a changing current in one loop of wire could induce a current in another loop of wire, as illustrated in Fig. 7.4. The induced electromotive force associated with the induced current was found to be proportional to the rate of change of magnetic flux linking the circuit. This is most compactly expressed as:

$$\nabla \times \overline{E} = -\frac{\partial \overline{B}}{\partial t}. \tag{7.17}$$

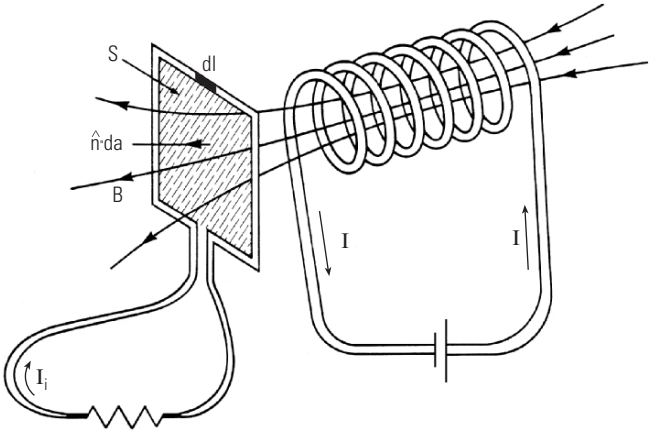


Fig. 7.4 One aspect of Faraday's law of induction. An alternating current in the primary loop (right) produces an induced current in the receiver loop (left).

By Stokes's theorem the integral of $\nabla \times \overline{E}$ *over the surface S of the receiver loop is equal to the line integral of* $\overline{E}$ *around the loop* Γ *so that:*

$$\oint_{\Gamma} \overline{E} \cdot d\bar{l} = \int_{S} (\nabla \times \overline{E}) \cdot \hat{n}\, da = -\int_{S} \frac{\partial \overline{B}}{\partial t} \cdot \hat{n}\, da. \tag{7.18}$$

This last expression is seen to be the time rate of change of the normal component of magnetic flux through a surface S. The integral on the left gives the voltage seen at the terminals of the receiver.

7.3 THE TWO-COIL INDUCTION DEVICE

Figure 7.5 shows the essential features of an induction logging device. It consists of a transmitter coil, excited by an alternating current of medium frequency ($\approx$20 kHz) and a receiver coil. The two coils, contained in a nonconductive housing, are presumed to be surrounded by a formation of conductivity σ. One axially symmetric ring of current-bearing formation is indicated in the figure. Before analyzing the geometric sensitivity of such a device, it is worthwhile to step through the sequence of physical interactions which produce, finally, a signal at the receiver. In this way we will be able to see the dependence of the detected signal on excitation frequency and formation conductivity, as well as the phase relation between received and transmitted signal. The so-called skin effect is ignored for the time being, so that the results in the next three sections are only strictly valid at low conductivity.

The first step to consider is the excitation of the transmitter coil by the transmitter current I_t:

$$I_t = I_o e^{-i\omega t}. \tag{7.19}$$

The transmitter coil, which can be considered as an oscillating magnetic dipole, sets up throughout the formation a magnetic field B_t, whose vertical component is of interest. The vertical component will have a time dependence given by:

$$(B_t)_z \propto I_o e^{-i\omega t}. \tag{7.20}$$

A ring of formation material that is axially symmetric with the tool axis forms the perimeter of a surface through which passes the time-varying magnetic field. From Faraday's law, an electric field E will be set up that is proportional to the time derivative of the vertical component:

$$E \propto -\frac{\partial (B_t)_z}{\partial t} \propto i\omega I_o e^{-i\omega t}. \tag{7.21}$$

This electric field, which curls around the vertical axis, will induce a current density in the loop of formation sketched. It will be proportional to the formation conductivity:

$$J \propto \sigma E \propto i\omega\sigma I_o e^{-i\omega t}. \tag{7.22}$$

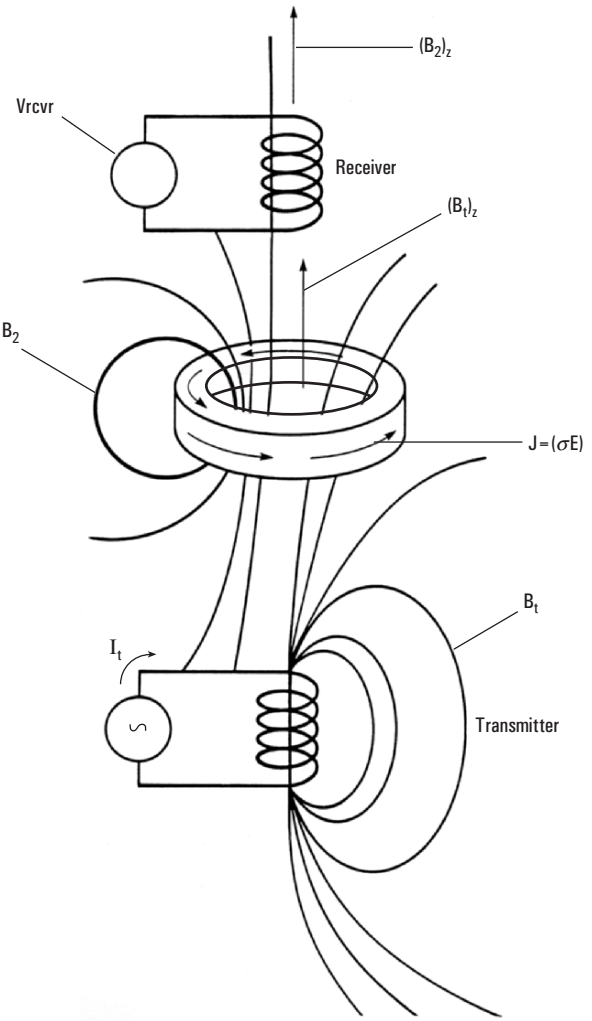


Fig. 7.5 The principle of the induction tool. The vertical component of the magnetic field from the transmitting coil induces ground loop currents. The current loops in the conductive formation produce an alternating magnetic field detected by the receiver coil.

The current in the ground loop considered will behave like the transmitter coil; that is, it will set up its own magnetic field B_2. The vertical component of the secondary magnetic field $(B_2)_z$ has the same time dependence as the current density in the loop:

$$(B_2)_z \propto i\omega\sigma I_o e^{-i\omega t}, \tag{7.23}$$

and its time dependence will induce a voltage V_{rcvr} at the receiver coil:

$$V_{rcvr} \propto -\frac{\partial (B_2)_z}{\partial t} \propto -\omega^2 \sigma I_o e^{-i\omega t}. \tag{7.24}$$

This final result indicates that the voltage detected at the receiver coil will vary directly with the conductivity of the formation and with the square of the excitation frequency. It is also seen to be 180° out of phase with the transmitter current driving signal, whereas the voltage induced by the direct flux linkage from the transmitter will be 90° out of phase, as can be seen from the expression for the direct electric field in Eq. 7.21. These two signals are separated either electronically, by phase sensitive detection, or by adding a third so-called bucking coil. This coil is oppositely wound and designed so as to cancel the direct linkage, or mutual coupling, as is discussed further in Section 7.7.

7.4 GEOMETRIC FACTOR FOR THE TWO-COIL SONDE

In order to determine the geometric sensitivity of the two-coil induction sonde we now make use of the relations derived in the review of magnetostatics. The first expression to be derived is the component of the driving magnetic field, which sets up the ground current indicated in Fig. 7.6. The driving coil is considered to be a magnetic dipole source which produces a vertical component of magnetic field at a distance z above

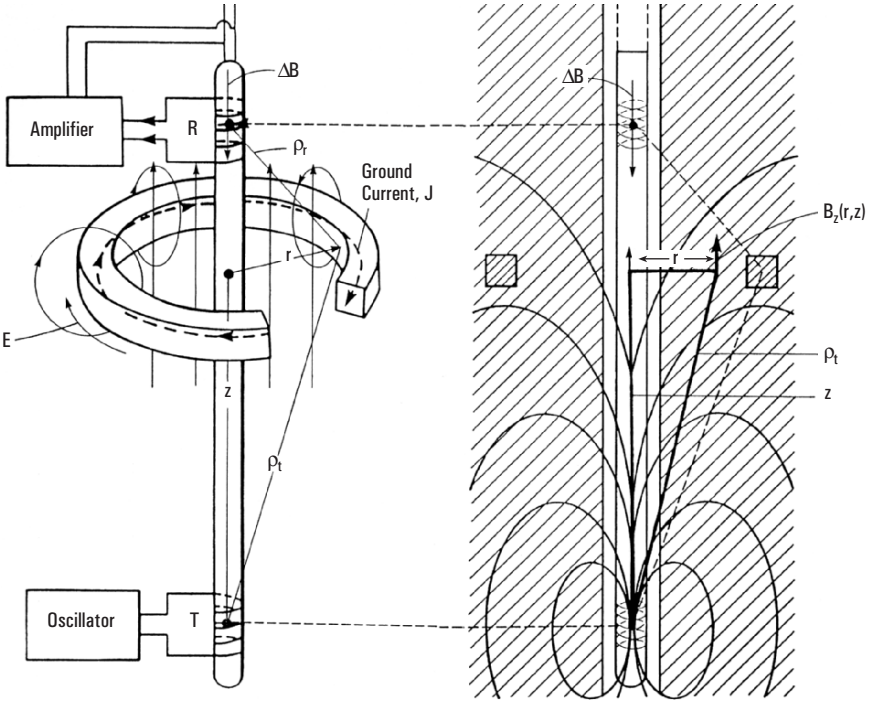


Fig. 7.6 Geometry for the development of the geometric factor for a two-coil induction sonde. Adapted from Doll [2].

the transmitter. In this case, the dipole moment of the transmitter is given by the product of the current I_o, the winding area A_t, and the number of transmitter winding turns n_t, ($I_o n_t A_t$). At any position identified by the coordinates (ρ_t, z), the vertical component, from Eq. 7.16, is given by:

$$(B_t)_z \propto I_o e^{-i\omega t} A_t n_t \left(\frac{1}{\rho_t^3} - \frac{3z^2}{\rho_t^5} \right). \tag{7.25}$$

The left side of Fig. 7.6 shows the geometry to be considered for determining the magnitude of the current density set up in the indicated ground loop. Dropping, for convenience, the time-dependent terms and other constants, the relation for the induced electric field, from Eq. 7.18 is:

$$\oint_\Gamma E \cdot d\bar{l} = -\frac{\partial}{\partial t} \int_S B_n \, dS \,, \tag{7.26}$$

where the line integral is around the loop Γ whose length is $2\pi r$ and where the surface integral is over the element whose area $S = \pi r^2$ so that $dS = 2\pi r dr$. Since the normal component of the magnetic field, B_n, is B_z, the result is:

$$\oint_\Gamma E \cdot d\bar{l} = E \cdot 2\pi r \propto \int_o^r \left(\frac{1}{\rho_t^3} - \frac{3z^2}{\rho_t^5} \right) r dr, \tag{7.27}$$

In the right-hand integral, ρ_t is a function of r so that the integral must be evaluated through a change of variable (see Problem 7.5) to give:

$$E \cdot 2\pi r \propto \frac{r^2}{\rho_t^3} \tag{7.28}$$

or

$$E \propto \frac{r}{\rho_t^3}. \tag{7.29}$$

This electric field then causes a current density J which is given by:

$$J = E \, \sigma \,, \tag{7.30}$$

where σ is the formation conductivity. Thus the geometric dependence of the induced formation current is given by:

$$J \propto \frac{\sigma r}{{\rho_t}^3} \,. \tag{7.31}$$

As in Eq. 7.24, but without the time dependence, the induced voltage in the receiver coil will be proportional to the vertical component of the secondary magnetic field which passes through the receiver coil, indicated by ΔB in Fig. 7.6. From Eq. 7.8, it is seen to be:

$$V_{rcvr} \propto \Delta B \propto J \frac{r^2}{\rho_r^3} \,, \tag{7.32}$$

where J is the current density in the ground loop in question of radius r, and ρ_r is the distance from any point along the current loop to the receiver coil.

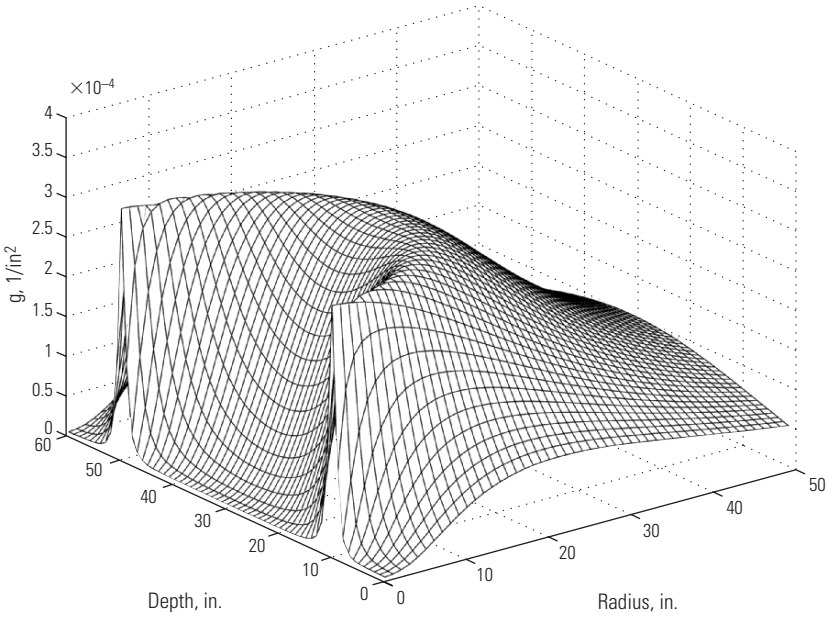


Fig. 7.7 Two-dimensional plot of the geometrical factors of loops around a two-coil sonde (homogeneous formations, no skin effect). The spikes near the z axis occur at the locations of the transmitter and receiver.

Inserting Eq. 7.31 and separating out those factors that depend on the geometrical position of the loop, the measured voltage is given by:

$$V_{rcvr} \propto g(r,z) = \frac{L}{2}\,\frac{r}{\rho_t^3}\,\frac{r^2}{\rho_r^3}\,. \tag{7.33}$$

The above expression for $g(r,z)$ is known as the differential geometric factor (or Doll geometric factor), since it gives the contribution of a single ground loop of unit cross-section at position z and radius r to the final receiver output [2]. The factor $L/2$ is a normalization factor so that when $g(r,z)$ is integrated over all r and z the result is 1. The geometric factors around a single transmitter and receiver are shown in Fig. 7.7.

It is convenient to define two other geometric factors which give information on the tool response after cumulating the response in one dimension. The first is the differential *radial* geometric factor, which is defined to be:

$$g(r) = \int_{-\infty}^{\infty} g(r,z)dz\,. \tag{7.34}$$

It predicts the relative importance of each of the cylindrical shells of radius r to the overall response. This factor and a sketch of its radial dependence are shown in

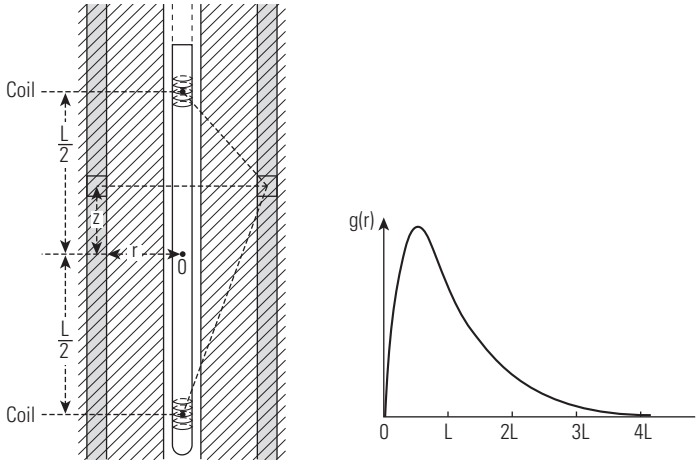


Fig. 7.8 Integration of the geometric factor with respect to z at a constant radial value r produces the differential radial geometric factor (homogeneous formations, no skin effect).

Fig. 7.8. The peak in relative importance occurs at a radius somewhat less than the dimension of the coil separation.

In a similar fashion, the differential *vertical* geometric factor is defined as:

$$g(z) = \int_o^\infty g(r, z)dr \tag{7.35}$$

and gives the response of a unit-thickness slice of formation, located at position z, to the overall tool response. The geometry corresponding to the integration and the response curve are shown in Fig. 7.9. A fairly flat response is obtained from a slice of formation contained between the two coils, but the tapering-off of the response above and below the coils will produce signals at distances that are far above and below the coils. This is known as shoulder effect.

In order to get an idea of the bed boundary response, we can make an integration of the differential vertical geometric factor. Figure 7.10 shows an example of the integrated vertical factor G_v for a two-coil device with a 40 in. coil separation. A sharp transition of formation resistivity is seen by the tool as a gradual change over a distance which is roughly 80 in., or two times the coil spacing. It is obvious that the conductivity readings in thin beds will be considerably affected by this type of coil arrangement.

The integrated radial geometric factor G_r for the two-coil device is shown in Fig. 7.11. Approximately half the contribution comes from within 45 in. of the device. There is therefore some sensitivity to the region nearest the borehole. It would be desirable to eliminate this sensitivity to a presumed invaded zone and to put more weight on the region farther from the borehole, where the true resistivity could be measured.

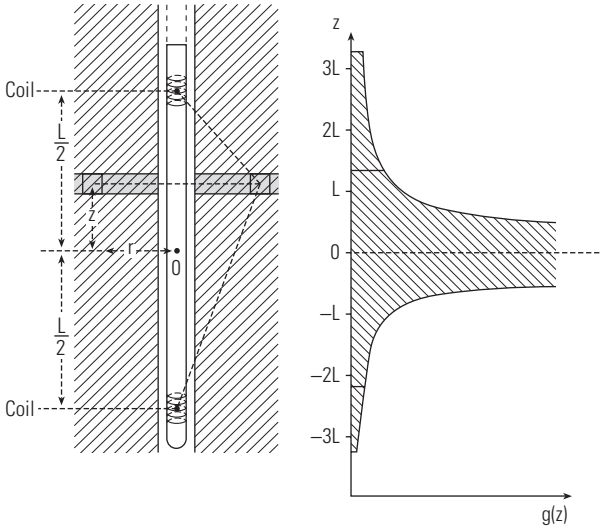


Fig. 7.9 The differential vertical geometric factor produced by integration with respect to r, at fixed z (homogeneous formations, no skin effect).

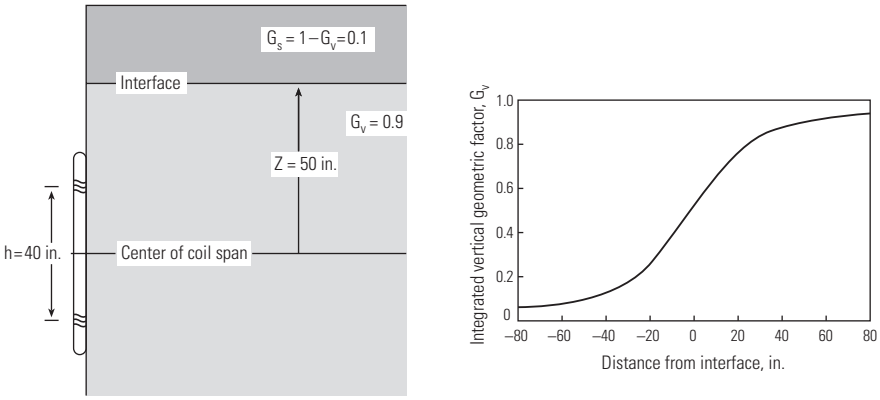


Fig. 7.10 At right, the integrated vertical geometric factor, G_v, for estimating the influence of shoulder beds. At left, G_v and G_s in the shoulder bed with the coil center 50 in. from the interface (homogeneous formations, no skin effect). Adapted from Dresser [3].

7.5 FOCUSING THE TWO-COIL SONDE

The response of the two-coil device examined above can be altered to minimize the "tail" of sensitivity to beds above and below the measurement coils or to decrease the sensitivity to layers closest to the borehole. For an illustration of how the response is altered or focused, we examine the technique for changing the depth of investigation of the two-coil sonde. The idea is simply to add a second receiver coil which is a bit

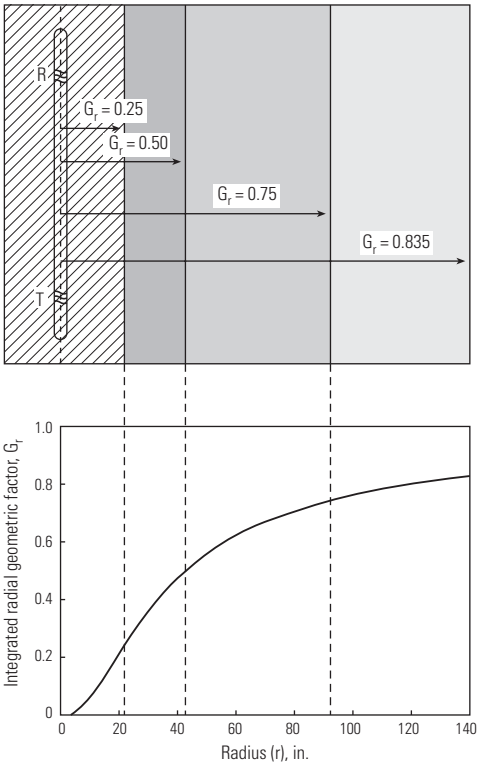


Fig. 7.11 Below, the integrated radial geometric factor, G_r, for estimating the importance of invasion. Above, illustration of different regions (homogeneous formations, no skin effect). Adapted from Dresser [3].

closer to the transmitter and to use its response, which will be somewhat shallower than the original receiver, to subtract from the response of the original. By placing the receivers suitably and selecting the proper number of turns, this subtraction should eliminate much of the signal from regions close to the borehole. This principle is shown schematically in Fig. 7.12. A similar procedure is used to sharpen the vertical resolution of the tool. This will change the sensitivity of the tool measurement to layers of different conductivity above and below the measurement coils.

Traditional induction devices employ focused arrays of coils, usually providing two measurements of conductivity (resistivity) at different depths of investigation. The improvement of the depth of investigation of one such device can be seen by comparing the integrated radial response functions of the two-coil device in Fig. 7.11 with the six-coil device in Fig. 7.13. Most of the response closer than about 30 in. has been eliminated.

Tailoring the response by the addition of coils may sound too good to be true. Of course there are limitations; the addition of focusing coils leaves some residual features in the geometric response that can cause problems in some in logging situations.

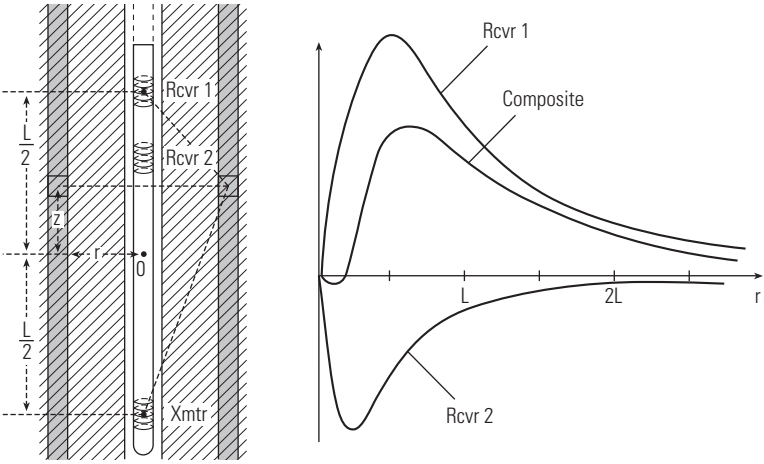


Fig. 7.12 The principle of three-coil focusing. A second coil, wound with reverse polarity, produces a signal which cancels some of the signal from close to the borehole. Adapted from Doll [2].

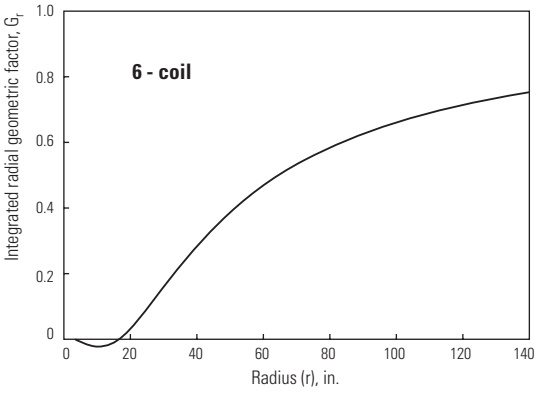


Fig. 7.13 The radial depth of investigation of a six-coil induction device (homogeneous formations, no skin effect). Adapted from Dresser [3].

In the preceding discussion, we have considered only homogeneous formations. In reality, layered formations of differing conductivity will be the rule, not to mention radial conductivity profiles which are far from uniform because of invasion or the presence of dipping beds. How will these affect the response of the induction tool?

An idea can be obtained from a closer examination of the composite radial geometric factor of Fig. 7.13. Note the small undershoot. The impact of this imbalance is that the conductivity of the initial portion of the formation near the borehole will make a negative contribution to the total signal. This is no problem in a homogeneous

formation. However, suppose there is a conductive anomaly near the borehole: Taken to the extreme, this can cause a negative reading.

7.6 SKIN EFFECT

One characteristic of electromagnetic waves has so far been overlooked in the discussion of induction devices. It is referred to as skin effect and is simply the result of the fact that electromagnetic waves suffer an attenuation and phase shift when passing through conductive media. The parameters which govern this effect can be made apparent for the case of a time-varying electric field at the surface of a conductive formation, as shown in Fig. 7.14.

To simplify the situation, the displacement current that is associated with dielectric effects is ignored and the electric field at the surface of this infinite half-space is taken to vary only in the z-axis.

From three of Maxwell's equations:

$$\nabla \cdot \overline{E} = 0 \tag{7.36}$$

$$\nabla \times \overline{B} = \mu \overline{j} \tag{7.37}$$

$$\nabla \times \overline{E} = -\frac{\partial \overline{B}}{\partial t} \tag{7.38}$$

and the current relationship:

$$\overline{j} = \sigma \overline{E}, \tag{7.39}$$

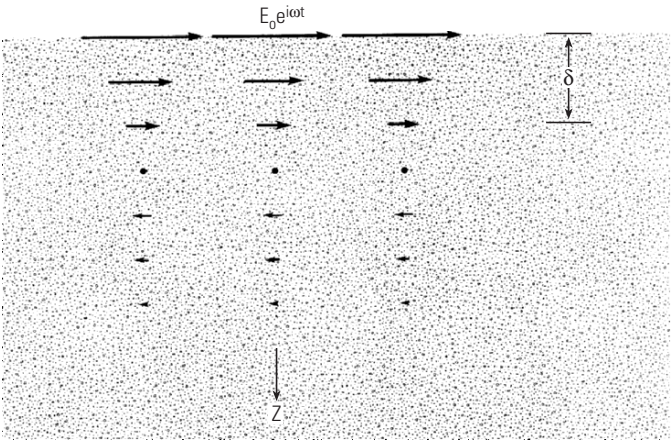


Fig. 7.14 A one-dimensional model of a time-varying electric field at the surface of a conductor. Due to its conductivity, the intensity of the electric field diminishes with depth of penetration into the conductor.

a wave equation can be derived by using a vector identity. First the curl of Eq. 7.38 is taken:

$$\nabla \times \nabla \times E = \nabla(\nabla \cdot \overline{E}) - \nabla^2 \overline{E} = -\frac{\partial}{\partial t} \nabla \times \overline{B}. \tag{7.40}$$

From Eq. 7.36, which implies that no free charges are present in this conductive medium, and from Eqs. 7.37 to 7.39 this reduces to:

$$-\nabla^2 \overline{E} = -\frac{\partial}{\partial t} \mu\sigma \overline{E}, \tag{7.41}$$

where μ is the magnetic permeability, which is generally low and constant in rocks. Some formations have been observed in which either the magnetic permeability or the dielectric effects cannot be ignored, but they are rare and affect almost exclusively the out-of-phase signal [4]. Dielectric properties are discussed in Chapter 9.

If a sinusoidal time dependence $E = E_o e^{i\omega t}$ is assumed for the electric field, this reduces to:

$$\frac{\partial^2 \overline{E}}{\partial^2 z} = i\omega\mu\sigma \overline{E} = k^2 \overline{E}\ . \tag{7.42}$$

The solution to this equation is of the form:

$$E = E_o e^{ikz}, \tag{7.43}$$

where k can be written as:

$$k = \sqrt{i}\sqrt{\omega\mu\sigma}. \tag{7.44}$$

Using the relation that:

$$\sqrt{i} = \frac{1 + i}{\sqrt{2}}, \tag{7.45}$$

and taking the positive square root so that the field vanishes at large distances, k can be written as:

$$k = \frac{1 + i}{\delta}, \tag{7.46}$$

where δ, is given by:

$$\delta = \sqrt{\frac{2}{\omega\mu\sigma}}. \tag{7.47}$$

Thus the form of the electric field in the z-axis (into the conductive half-space) is given by:

$$E(z) = E_o e^{-\frac{z}{\delta}} e^{\frac{i}{\delta} z}, \tag{7.48}$$

where the real exponent indicates an attenuation and the imaginary exponent indicates a phase shift increasing with penetration into the conductive formation. The parameter δ is the skin depth, which is the distance over which the electric field will be reduced by a factor of 1/e. The magnitude of this distance is shown in Fig. 7.15 as a function of formation resistivity. It can be seen that there will be some noticeable effect on induction measurements if the resistivity is less than about 10 ohm-m. At this point the skin depth is on the order of the depth of investigation and can no longer be ignored.

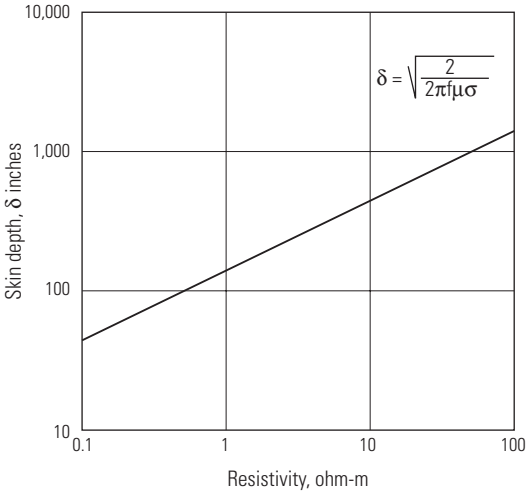


Fig. 7.15 The numerical value of the skin depth in inches as a function of the formation resistivity in ohm-m for operating frequencies around 20 kHz.

7.7 TWO-COIL SONDE WITH SKIN EFFECT

Skin effect complicates the derivations of the total voltage in the receiver coil and the geometrical factors. We will not attempt to go through these derivations here but instead refer the reader to Moran and Kunz [5] for the general formulation of the problem and to Moran [6] for the geometrical factors. A feeling for the results can be obtained by observing that, as shown in the last section, the attenuation and phase shift introduced by skin effect can be accounted for by introducing the factor $e^{ik\rho}$ in the electric field, where ρ is the distance from the transmitter. When skin effect and the direct mutual coupling between transmitter and receiver are taken into account, the voltage at the receiver of a two-coil sonde is a complex quantity, which is given by:

$$V_{rcvr} \propto i\omega\mu(1 - ikL)\frac{e^{ikL}}{L^3}e^{-i\omega t}. \tag{7.49}$$

where L is the transmitter–receiver spacing. Using Eq. 7.46 to relate k to δ and expanding the exponential in terms of L/δ we find, to first order:

$$V_{rcvr} = K(\sigma + \frac{2i}{\omega\mu L^2} - \frac{2L}{3\delta}\sigma(1 + i) + ...) \tag{7.50}$$

where the constant of proportionality is given by $K = (n_t A_t I_0\ n_r A_r\ \omega^2\mu^2/4\pi L)$, where n_t and n_r are the number of turns on the transmitter and receiver, and A_t and A_r are their cross-sectional areas. The first term, which is real, is simply the formation conductivity and is equivalent to Eq. 7.24 above. Although the real (or R) signals are

180° out of phase with the transmitter, log results are presented as a positive number. Thus in the derivation of Eq. 7.50 the sign of the real component has been changed.

The second term is the direct transmitter–receiver coupling, which is independent of formation conductivity and, being imaginary, is 90° out of phase with the transmitter. It can be many times the R signal and overwhelm it. In a practical version of the three-coil sonde shown in Fig. 7.12 the second receiver would be placed so as to minimize this direct signal, as well as to focus the response. As can be seen from Eq. 7.50 and the definition of K, the direct signal drops off as n_r/L^3 whereas the formation signal drops off as n_r/L. It is therefore possible to position the second receiver, known as the "bucking" coil, with the correct number of turns so as to cancel the direct signal without overly reducing the formation signal.

The third term is the first term of the skin effect signal. As expected it reduces the magnitude of the R signal and introduces phase shift through the imaginary (or X) component. Note that in this first-order skin effect term the X component is equal in magnitude to the R component.

Several authors have derived the differential geometric factor with skin effect. In Moran's method the formation is considered to be homogeneous with a finite conductivity σ into which is introduced a current loop of conductivity $\sigma + \delta\sigma$. Since this is similar to the Born approximation in quantum mechanics it is often known as the Born response function:

$$g_B(r, z, \sigma) = g_D(r, z)\ (1 - ik\rho_T)e^{ik\rho_T}\ (1 - ik\rho_R)e^{ik\rho_R} \tag{7.51}$$

where $g_D(r, z)$ is the differential Doll geometric factor given in Eq. 7.33. When $\sigma = 0$, k is zero and this equation reduces to the Doll factor. Underlying this solution (as well as the Doll solution) is the assumption that the interactions between ground loops are negligible. In the limit of small ground loops and small conductivity contrasts this is reasonable. The total measured conductivity can then be found by integrating the formation conductivity weighted by its Born response at each r and z over the entire formation:

$$\sigma_R + i\sigma_X = \int_{-\infty}^{\infty}\int_{0}^{\infty} g_B(r, z, \sigma)\ \sigma(r, z)\ dr dz \tag{7.52}$$

The Born response function is used to examine the response of multi-array induction and propagation tools in Chapters 8 and 9.

7.8 MULTICOIL INDUCTION DEVICES

The principle of focusing using multiple coil arrays was known early on and exploited in a variety of configurations in the 1950s. The industry eventually settled on a standard deep reading array known as the 6FF40 because it had six coils (three transmitter and three receiver) with so-called fixed radial and vertical focusing (FF) and 40 in. between the main transmitter and receiver. This remained the standard, with only minor modification, until the introduction of multi-array devices in the 1990s. The

relatively large volume of formation surveyed means that both shoulder and skin effect can be significant, and therefore corrections are applied before displaying the log. It was realized early on that shoulder effect could be removed by applying a suitable filter, in other words deconvolving the response. The problem was to find simple filters that suited a wide range of conditions, since complex functions could not be handled at the wellsite at that time. Originally, different options were offered for different conditions, but for consistency these were soon reduced to one – a three-station average that was considered suitable for a shoulder bed resistivity of 1 ohm-m:

$$\sigma_d(z) = -0.05\sigma_a(z-78) + 1.1\sigma_a(z) - 0.05\sigma_a(z+78) \tag{7.53}$$

where σ_d is the deconvolved reading at depth z, and the σ_a are the measured readings at z and 78 in. above and below [7]. This result was then corrected for skin effect using an exponential function chosen to give the correct response in a homogeneous medium of conductivity 0.5 S/m. This is an approximation that was easy to implement in early analog logging units.

The resulting log is known as the deep induction log (ILd or ID). Although it has various deficiencies (as will be discussed below), it has stood the test of time and is generally considered to be a good compromise. The radial response is shown in Fig. 7.16. Note the influence of skin effect at $R_t = 1$ ohm-m. Although the total signal has been corrected for skin effect losses, there is less signal from deep in the formation, thereby reducing the depth of investigation.* Also, if the diameter

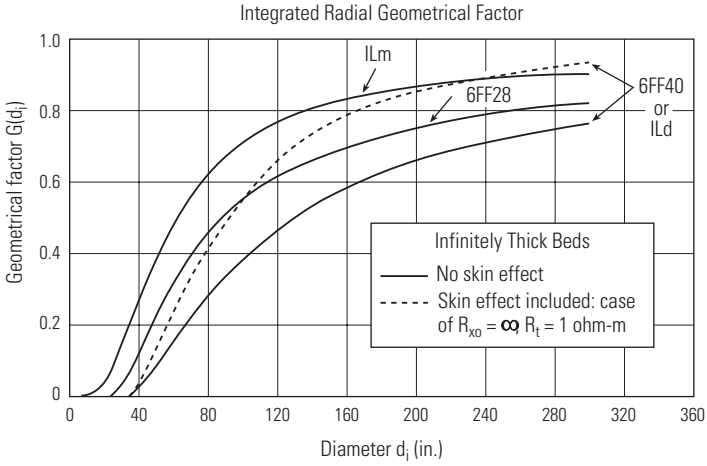


Fig. 7.16 The integrated radial geometric factor of several commercial induction arrays at zero conductivity, and the influence of skin effect on the 6FF40 array (negative factors below 40 in. have been cut). Courtesy of Schlumberger [8].

*The depth of investigation is generally defined as the radius within which 50% of the response occurs. Thus for the ILd it is 65 in. without skin effect.

of invasion is more than about 40 in., an invasion correction is needed. As with laterologs, we assume a step profile model of invasion to solve for R_t, for which we need three logs with different radial response. Since shallow induction devices may have very large borehole signals, the shallow log is provided by a microresistivity device or a shallow laterolog such as a spherically focussed log (see Section 5.3.2). The medium log is provided by a modified 5FF40 induction array (two transmitters and three receivers), to which several small coils have been added. Skin effect and shoulder effect are both less, so that no automatic shoulder correction is needed but a skin effect correction is made on the same principle as the ILd. The result is known as the ILm, or IM. Tornado charts are available to solve for R_t, R_{xo}, and d_i from ILd, ILm, and SFL [9].

Although both ILm and ILd have radial focusing that minimizes any contribution from the borehole, there are situations where the borehole signal can be significant – for example salty, highly conductive muds with low conductivity formations. Borehole correction charts are available to make the appropriate corrections in smooth boreholes [9]. Charts also exist to correct the remaining shoulder bed effect for both ILm and ILd. All these charts and their corresponding software, as well as the automatic shoulder bed and skin effect corrections, are 1D corrections: they assume that apart from the effect being considered the formation is homogeneous. As with laterologs, it is important to consider what happens when there is, for example, both invasion and a shoulder bed.

An idea of this more complicated response can be gained from Fig. 7.17, which shows the 2D geometric factors for the 6FF40 array and the ILm. These 3D displays show the contribution of all the significant rings of formation material; the portions below the plane correspond to negative contributions to the total signal. Both arrays exhibit negative lobes near the borehole axis and the center of the array. It is these lobes that can cause the appearance of "horns" at bed boundaries of sufficient conductivity contrast, and spikes to high resistivity in conductive boreholes with caves. If the cave occurs opposite one of the lobes and nowhere else, the total borehole signal is a strong negative conductivity. However, if the borehole is smooth and the induction tool is parallel to the borehole wall, the positive and negative lobes sum up over depth to a small positive number, which is the borehole signal shown in charts and integrated radial geometrical factors.

Some examples of this behavior can be seen from the formations modeled in Fig. 7.18. In the high-resistivity bed at 100 ft the remaining shoulder effect causes ILd and even ILm to read lower than they should in the resistive beds. The separation is such that the beds appear to be invaded even though they are not. A chartbook invasion correction would further accentuate the difference between the predicted and actual R_t. In the thin 3 ft bed near 80 ft, ILd and even ILm do not reach the true resistivity because the bed thickness is less than the vertical resolution of either curve. The vertical resolution of ILd is about 8 ft and ILm 6 ft depending on conditions. (For induction devices the most common definition of vertical response is the distance over which 90% of the main lobe of the response occurs.) In the lower resistivity beds between 40 and 70 ft, the shoulder effect disappears but there are horns at the bed boundaries. Finally an anomalously low resistivity reading is found in the bed at

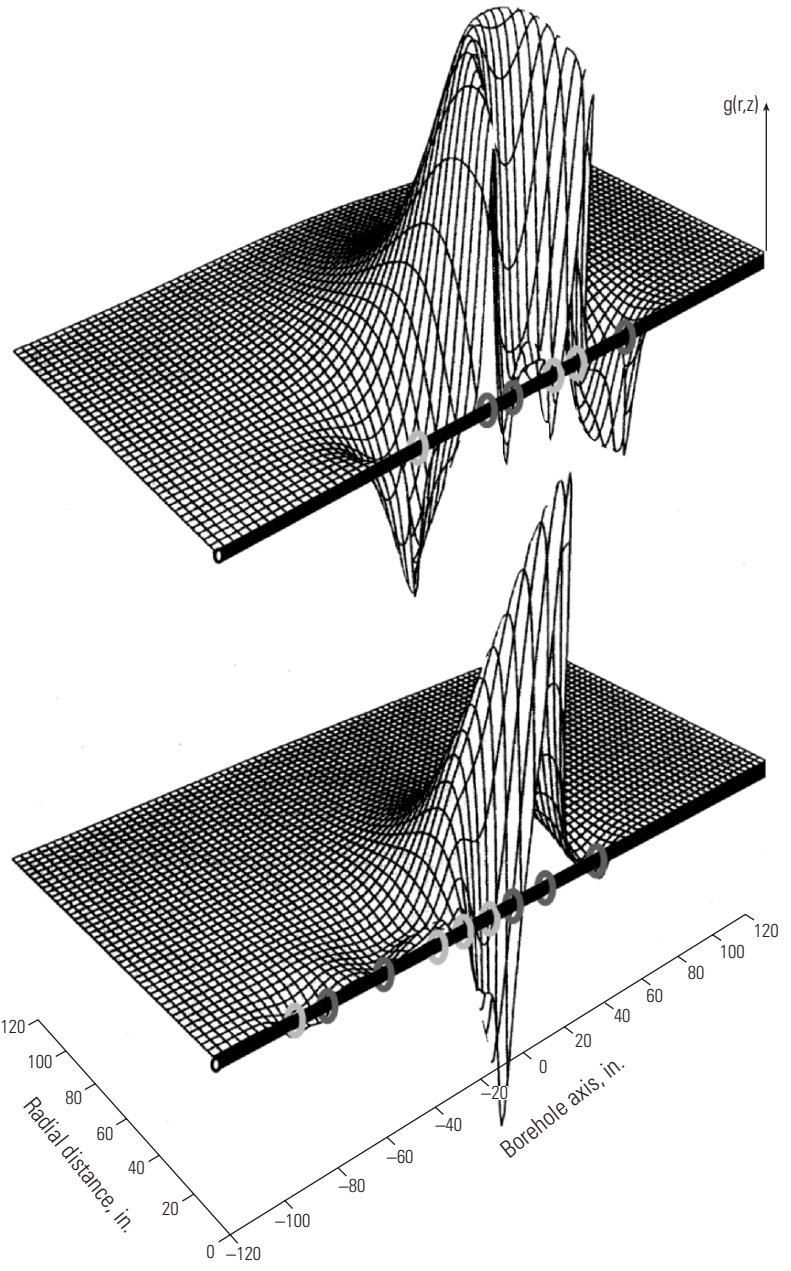


Fig. 7.17 2D geometrical factor maps for deep (top) and medium (bottom) induction arrays. The rings on the borehole axes show the position of the coils (homogeneous formations, no skin effect). From Anderson and Barber [7]. Courtesy of Schlumberger.

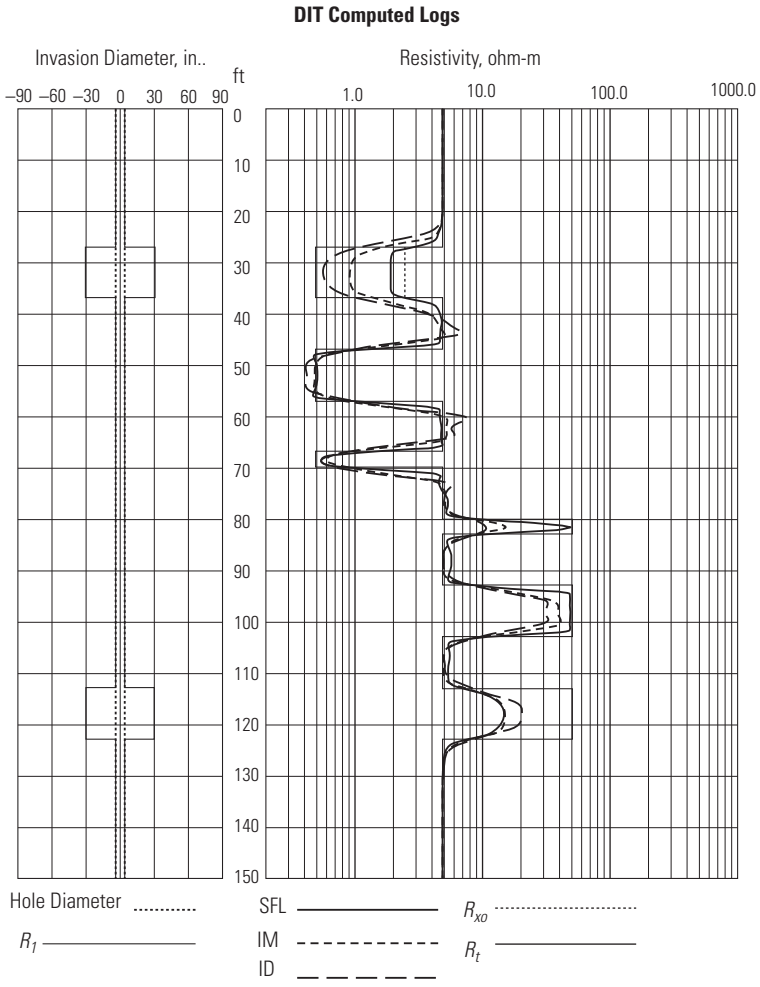


Fig. 7.18 A dual induction log modeled through a series of invaded and uninvaded formations, illustrating various features of the response. Adapted from Anderson [10].

50 ft due to an overcorrection for skin effect. Many studies have been made of ILd and ILm response to specific situations such as caves, bed boundaries, anisotropy, dipping beds, and thin beds [11–14]. These studies led to the development of the improved induction devices to be discussed in Chapter 8.

7.9 INDUCTION OR ELECTRODE?

When is an induction device used in preference to an electrode tool? We have seen that an induction signal is proportional to conductivity whereas the signal from an

electrode tool is proportional to resistivity. This means that for measuring R_t the induction is preferred when the conductivities near the borehole are low, i.e., mud resistivity R_m is high and $R_t < R_{xo}$. On the other hand when R_t is high the induction signal is low and the measurement is less accurate. For laterologs the conditions are the reverse.

To be quantitative we need to consider the size of the borehole signal, the resistivity level, the ratio R_t/R_{xo}, and the diameter of invasion, d_i. Two types of chart are commonly presented. The first shows the resistivity range within which each measurement is accurate: an example of such a chart is shown for the array induction and array laterolog in Chapter 8, Fig. 8.13. As expected, the induction goes out of range above a certain resistivity and above a certain ratio of borehole to formation signal (or, equivalently, R_t/R_m). The second type of chart attempts to advise when a laterolog or an induction gives the most accurate results. Figures 7.19 and 7.20, which appeared in the 1970s, are examples of such charts for a deep induction (ILd) and deep laterolog (LLd) [15].

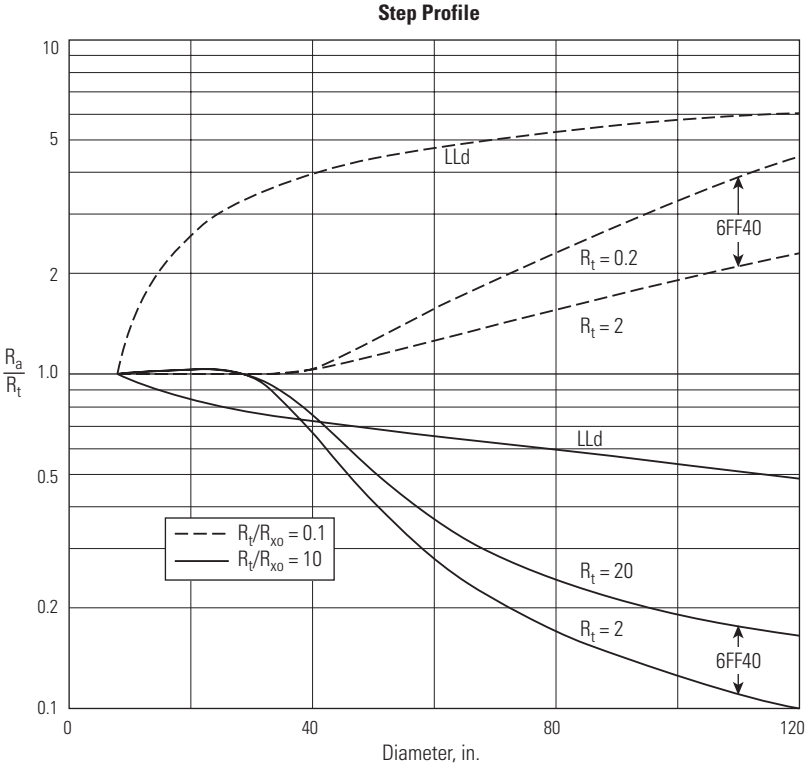


Fig. 7.19 Comparison of R_a/R_t for different conditions of R_t/R_{xo} and d_i, where R_a is the apparent resistivity measured by LLd and ILd (6FF40) devices. From Souhaite et al. [15]. Used with permission.

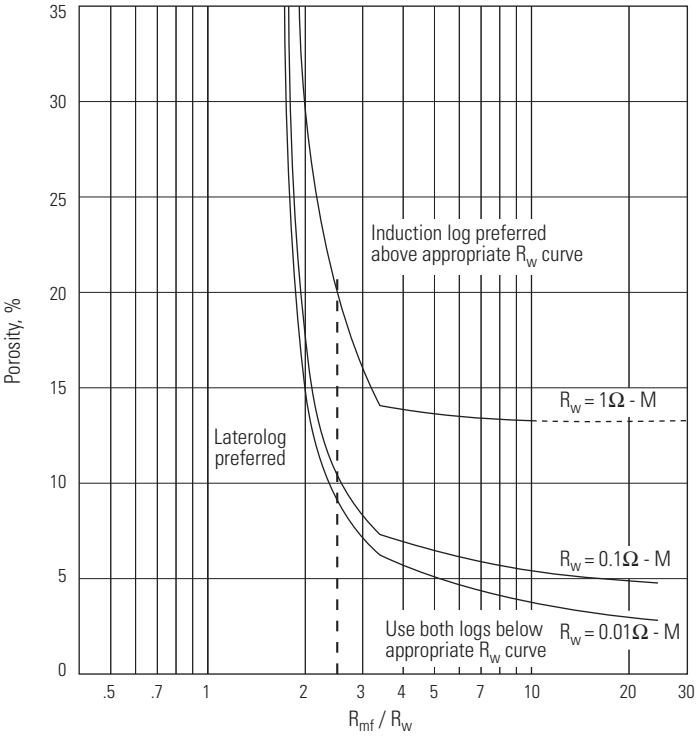


Fig. 7.20 Range of application of induction and laterolog in order to observe the largest contrast between oil and water zones. Courtesy of Schlumberger [8].

The first question is what criterion to use. For Fig. 7.19 the authors wanted to show which device gave a more accurate R_t for different ratios R_t/R_{xo} and d_i. Ideally they would both read R_t, so that the y-axis R_a/R_t would read 1 in all conditions. In practice when there is resistive invasion ($R_t/R_{xo} = 0.1$) the laterolog reads further from R_t as soon as there is any invasion, and therefore the induction is preferred. For conductive invasion ($R_t/R_{xo} = 10$) the induction reads closer to R_t until invasion reaches 40 in., due to the blind zone in its radial response. For deeper invasion the laterolog is preferred. This remains true for all higher ratios of R_t/R_{xo} and for lower ratios down to 2. Below this the deeper geometric response of the induction gives a more accurate R_t.

Figure 7.20 uses a different criterion: which device gives a larger contrast in reading when going from a water to an oil zone, i.e., which is greater of ILd(oil)/ILd(water) and LLd(oil)/LLd(water)? It is assumed that in the oil zone $S_w = 0.25$ and therefore, using the common relation $S_{xo} = S_w^{1/5}$ [9], that $S_{xo} = 0.76$. Then given R_{mf}, R_w and ϕ, R_{xo} and R_t can be calculated in both oil and water zone. With these values ILd and LLd are calculated for d_i between 0 and 60 in. Allowance is made for the loss of accuracy of the ILD at very high resistivity, for some uncertainty in the borehole

correction, and for the possibility of a conductive annulus. Putting all this together, the chart indicates the device with the larger contrast between oil and water in different conditions. As expected the induction is preferred when R_{mf}/R_w, and hence R_{xo}/R_t is high. The need for both logs below a certain value of R_w even when $R_{mf} \gg R_w$ is due to inaccuracies in the induction at high resistivity.

The astute reader might object that he would never use ILd or LLd as R_t, but would correct for invasion. This is true, and if the corrections are valid both devices will give R_t. However the charts still indicate which is the preferred device. It is always preferable to start with the log reading that is closest to R_t because the step profile model assumed by the charts may not be correct, and because there can be errors in the other inputs. If a device is operating outside its range, the invasion corrected value will still carry any error.

Finally these last two charts assume infinitely thick beds and ignore issues of vertical resolution. The loss of depth of investigation in thin beds has not been allowed for, and may also influence the decision on which device to use. This 2D effect cannot be illustrated conveniently in a single chart: each case must be modeled with appropriate modeling codes.

7.10 INDUCTION LOG EXAMPLE

For the sample induction log, another simulated reservoir is used. Two thick clean zones are indicated as A and B. Two much thinner clean streaks are shown as C and D. These four zones can be easily identified on the sample log presentation of Fig. 7.21. For the identification of the clean zones, the SP is shown in track 1 along with a gamma ray. The ILd, ILm, and SFLU logs are displayed in tracks 2 and 3. These three resistivity curves come from a typical dual induction – shallow resistivity tool of the 1970s and 1980s. The SFLU curve is an unaveraged spherically focussed log (see Section 5.3.2). In typical induction conditions ($R_{xo} > R_t$) the SFL provides reasonable information on R_{xo} and, not being pad-based, does not have the sensitivity to rugosity of microdevices.

As in the case of the laterolog curves, the induction curves must be checked for any necessary corrections before attempting quantitative interpretation. In addition to the same general types of borehole corrections, the induction may also require correction for bed thickness and shoulder effect. The magnitude of this correction will depend on an estimate of the bed thickness and the resistivity of the shoulder beds [9]. This type of correction will certainly be necessary for the two thin streaks of zones C and D. Jorden and Campbell [11] give a step-by-step example of correcting induction log reading for borehole effects, invasion, and bed thickness.

A final word should be added about the calibration of induction devices. Two calibrations are made at surface: one in air and one from a single copper loop with a resistor in series. The loop is placed around the device at a specified position and with a resistor chosen to give a signal equivalent to a formation of, for example, 0.5 S/m. In air there should ideally be no R signal, only a small remaining X signal from the direct mutual coupling. In practice, even though traditional sondes are made of

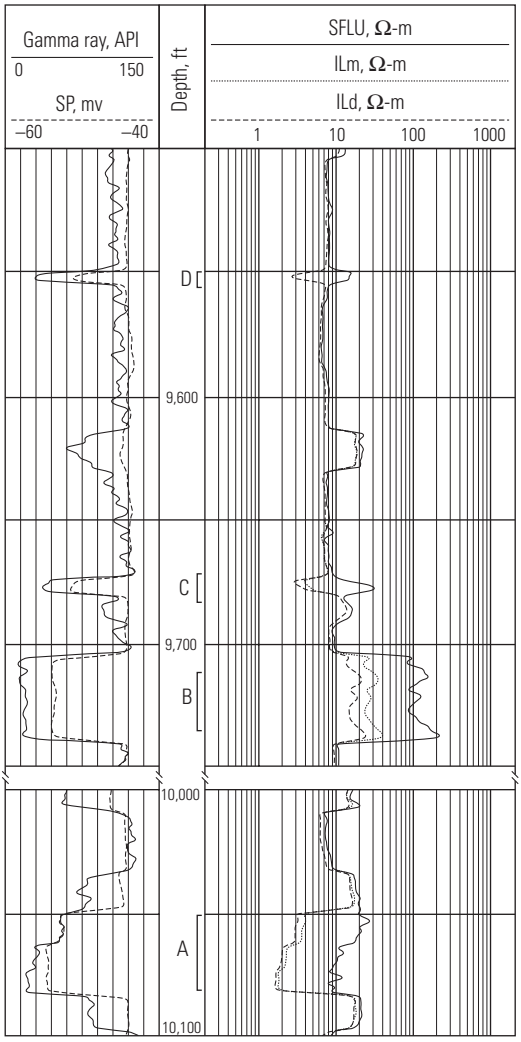


Fig. 7.21 A sample induction log.

nonmetallic materials there are always some metallic parts, for example from pressure bulkheads and cable shields, that give an R signal. This is known as the sonde error. It is measured by the calibration in air and canceled during logging. Adjustments may be made to allow for change in the sonde error under temperature and pressure.

An early method of correcting for sonde error was to null the measurement in a thick nonconductive formation such as an anhydrite. This is risky without taking into account the borehole and shoulder effects. (To avoid the latter the formation needs to be at least 100 ft thick.) The best sonde error measurement is therefore made in air far from any buildings, and at two or more heights above the ground so that the ground conductivity can be measured and allowed for [16].

REFERENCES

1. Feynman RP, Leighton RB, Sands ML (1965) Feynman lectures on physics, vol 2. Addison-Wesley, Reading, MA
2. Doll HG (1949) Introduction to induction logging and application to wells drilled with oil base mud. Pet Trans AIME 1(6):148–162
3. Dresser Atlas (1983) Well logging and interpretation techniques: the course for home study. Dresser Atlas, Dresser Industries, Houston, TX
4. Barber T, Anderson B, Mowatt G (1995) Using inductions to identify magnetic formations and to determine relative magnetic susceptibility and dielectric constant. The Log Analyst 36(4):16–26
5. Moran JH, Kunz KS (1962) Basic theory of induction logging and application to study of two-coil sondes. Geophysics 27(6):829–858
6. Moran JH (1982) Induction logging – geometrical factors with skin effect. The Log Analyst 23(6):4–10
7. Anderson B, Barber TD (1997) Induction logging. Schlumberger, Houston, TX
8. Schlumberger (1989) Log interpretation principles/applications. Schlumberger, New York
9. Schlumberger (2005) Schlumberger interpretation charts. Schlumberger, New York
10. Anderson B (2001) Modeling and inversion methods for the interpretation of resistivity logging tool response. DUP Science, Delft, The Netherlands
11. Jorden JR, Campbell FL (1984) Well logging II – electrical and acoustic logging. SPE Monograph, SPE, Dallas, TX
12. Gianzero S, Anderson B (1982) A new look at skin effect. The Log Analyst 23(1):20–34
13. Anderson B, Chang SK (1982) Synthetic induction logs by the finite element method. The Log Analyst 23(6):17–26
14. Anderson B (1986) The analysis of some unsolved induction interpretation problems using computer modeling. The Log Analyst 27(5):60–73
15. Souhaite P, Misk A, Poupon A (1975) R_t determination in the eastern hemisphere. Trans SPWLA 16th Annual Logging Symposium, paper LL
16. Barber T, Vandermeer W, Flanagan W (1989) Method for determining induction sonde error. US Patent No 4,800,496

Problems

7.1 You are logging with a rudimentary two-coil induction device through a 40 in. thick water-bearing sandstone with very thick shale beds above and below. You know that $R_o = 5$ ohm-m and that the shale resistivity is 10 ohm-m. Using the integrated vertical geometric factor for the induction device given in the text (remembering that the geometric factors for induction devices apply to conductivity and neglecting skin effect).

7.1.1 Sketch the log response as the tool approaches and passes through the zone of sandstone.

7.1.2 Calculate the minimum resistivity you would measure in the sandstone.

7.1.3 Calculate the maximum resistivity that you would measure if the sandstone resistivity was $R_o = 10$ ohm-m and the shale resistivity 5 ohm-m. Is the result more accurate in this case or the preceding one, and why?

7.1.4 Assuming that you can read the resistivity to 10% accuracy, what is the minimum bed thickness you could detect for the resistivity contrasts in the two situations?

7.2 In the log of Fig. 2.12, estimate the hydrocarbon saturation in the zone of interest, before and after correcting the deep induction reading for bed thickness but without correcting for invasion. The correction can be made by use of appropriate charts [9]. The bed thickness appears to be 4 ft.

7.2.1 Correct the medium induction for bed thickness. What can you say about the invasion profile? Is there a reason to doubt the result?

7.3 A formation is known to have a water saturation of 60% and water resistivity of 2 ohm-m. A well drilled through this formation was logged with the deep induction and microlaterolog. The values observed were $R_{ILd} = 145$ ohm-m and $R_{Mll} = 180$ ohm-m. The mud filtrate had a resistivity of 3.8 ohm-m. The estimated diameter of invasion, d_i, was 60 in. What would you expect the residual oil saturation of this reservoir to be after water flooding?

7.4 In the log of Fig. 7.21, apply invasion corrections from the appropriate charts [9] to obtain a corrected R_t and R_{xo} at A, B, and C. Why does the chart depend on the value of R_{xo}/R_m? What do the results tell you about the accuracy of the SFL as a measurement of R_{xo} ?

7.5 From the log of Fig. 7.18 deduce whether LLd or ILd should read closer to R_t at 30 and at 120 ft.

7.6 Show that for large values of z the differential vertical geometric factor $g(z)$ varies as $\frac{1}{z^2}$. This is in contrast with an electrode tool which varies as $\frac{1}{z}$ and is the reason why induction tools are less influenced by shoulder beds.

7.7 Verify the derivation of Eq. 7.27. In particular show that the following is true:

$$\int_o^r \left(\frac{1}{\rho_t^3} - \frac{3z^2}{\rho_t^5} \right) r dr \propto \frac{r^2}{\rho_t^3} . \tag{7.54}$$

Hint: change the variable of integration using the expression for ρ_t in terms of z and r.

8

Multi-Array and Triaxial Induction Devices

8.1 INTRODUCTION

The traditional deep-induction measurement (6FF40, or ILd) discussed in Chapter 7 was developed in 1960 and remained the standard for over 30 years. Indeed it is still being run today, and in the right conditions can still give accurate answers. However, as it has been applied to ever more stringent conditions its deficiencies have become apparent. These were recognized early on but it was not until computer modeling was applied to the problem in the 1980s that the limitations were fully explained and documented. Even then there was a reluctance to change the standard, so that the first new developments kept the same array but used processing to improve the response. Changes in measurements take time to be accepted. From a reservoir manager's point of view it is often better to live with a measurement that has some shortcomings but is the same in all wells, rather than to have to compare different responses in different wells.

Nevertheless a major change did come in 1990 with the introduction of so-called multi-array induction tools–devices with multiple simple arrays whose outputs are combined in processing to form the desired vertical and radial response. The principle was known in the 1950s but had not been implemented because of the amount of data that must be sent to a processor on the surface. By the early 1990s this was no longer an issue. Although some of the deficiencies of the 6FF40 array could be corrected in processing, further advances required the extra data available from multi-array tools.

Another major change came in the late 1990s with the introduction of triaxial induction measurements. With these the vertical formation resistivity could be measured in addition to the horizontal formation resistivity that is measured by all previous

devices. Such information is essential for the evaluation of anisotropic formations, as was discussed in Chapter 4. Note that, unless otherwise mentioned, the text assumes a vertical borehole with the induction device aligned within it. Thus "vertical" means aligned with the borehole and "horizontal" or radial means perpendicular to it.

This chapter traces the development of induction devices from the ILd through multi-array inductions to triaxial devices. Some space is devoted to the immediate successors of the ILd – the phasor and the high resolution induction – since they form a good introduction to many of the later devices.

8.2 PHASOR INDUCTION

The major deficiencies in the ILd and ILm response were discussed in Chapter 7, and can be summarized as follows: in resistive formations distant beds of higher conductivity cause too low readings and separations that could be mistaken for invasion (this is known as shoulder effect); poor vertical resolution (8 ft for ILd, 6 ft for ILm); horns or overshoots at the boundaries of low-resistivity beds; anomalously low ILd readings in some very conductive beds.

These deficiencies are all problems of vertical response and skin effect. There are also problems with the radial response, but they are generally less severe. Also, it is easier to do something about the vertical problems because the tool acquires much information vertically as it moves to different positions up and down the borehole; in the radial direction, only one measurement position is possible. The vertical response, g_{vB}, is given by integrating the differential geometrical factor with skin effect (Eq. 7.51) over all radii (as was done for the Doll geometrical factor in Eq. 7.34). The apparent conductivity measured at a depth z in the well is then a convolution between this vertical-response function and the vertical variation in conductivity:

$$\sigma_a(z) \;=\; \sum_{z'=z_{min}}^{z_{max}} g_{vB}(z - z', \sigma)\, \sigma_f(z') \tag{8.1}$$

where z' is the distance with respect to the measure point, and $\sigma_f(z')$ the formation conductivity. (The convolution is shown as a sum rather than an integral because the data is sampled at discrete intervals.) The effect of the vertical-response function is to blur sharp changes in conductivity and cause layers quite far from the center of the tool to have an effect. This can be seen in Fig. 8.1, which shows the convolution producing a single point on the log. Note that the response function extends as far as 50 ft each side of the measure point: in other words a layer 50 ft above the tool can affect its reading. When the tool moves up to the next sampling point, the response function is convolved with a slightly different section of the profile to produce the next point on the log, and so on until the whole log is obtained. The result is a smoothed-out version of the formation profile that, in the left half of Fig. 8.1, does not respond well in the thin beds near 60 ft and has a large shoulder effect in the low-conductivity bed near 80 ft. In the right half of Fig. 8.1 the conductivity is 100 times higher, and therefore the response function shown in the center is different due to skin effect. The overall

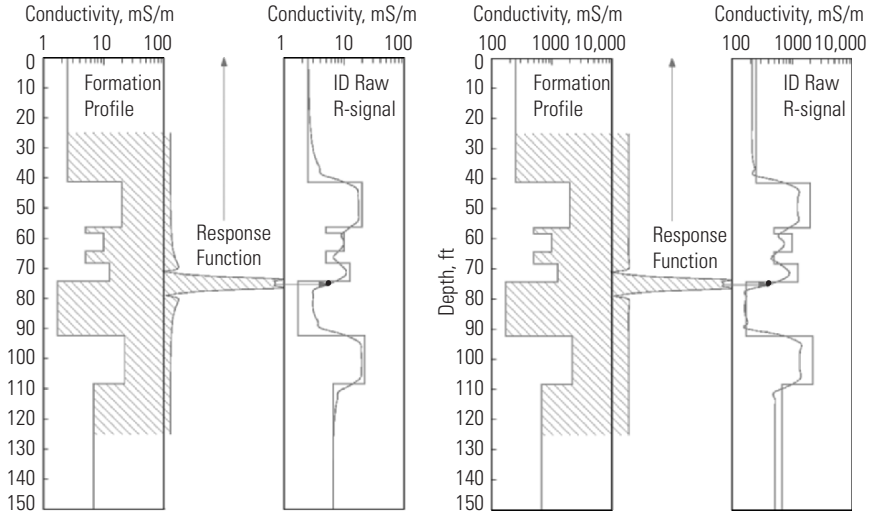


Fig. 8.1 The effect of blurring at (two left panels) low conductivity and (two right panels) high conductivity. The appropriate ILd response function, convolved with the formation profile forms the single black point on the log. Moving the response up level by level forms the R-signal logs. Note that these are raw logs not corrected for skin effect. From Anderson and Barber [1]. Courtesy of Schlumberger.

log reads less than formation conductivity because there has been no correction for skin effect, but the shoulder effect at 80 ft has disappeared.

Reversing such blurring functions is a well-known problem in signal processing that would be straightforward except for two factors: the variation of g_{vB} with conductivity caused by skin effect, and the minimum bed thickness required to obtain full information from the array. Ignoring these factors for the time being and taking advantage of the nearly noise-free induction measurements, it is relatively easy to design an inverse filter for the low-conductivity case that turns the measured signal back into the original formation profile. This is illustrated on the left of Fig. 8.2. The resulting deconvolved log matches well the actual profile except at bed boundaries and in the thinnest bed. Like the response function, the inverse filter extends 50 ft each side of the measure point. Mathematically, the filter is a set of weights h that, when applied to the measured conductivity, gives the true profile:

$$\sigma_f(z) = \sum_{z'=z_{min}}^{z_{max}} h(z - z')\, \sigma_a(z') dz'. \tag{8.2}$$

If this same filter is applied to the high-conductivity profile the result is poor, as might be expected since the filter was designed for low conductivity (see Fig. 8.2). We can certainly design another filter for these conditions – but how to decide which to use?

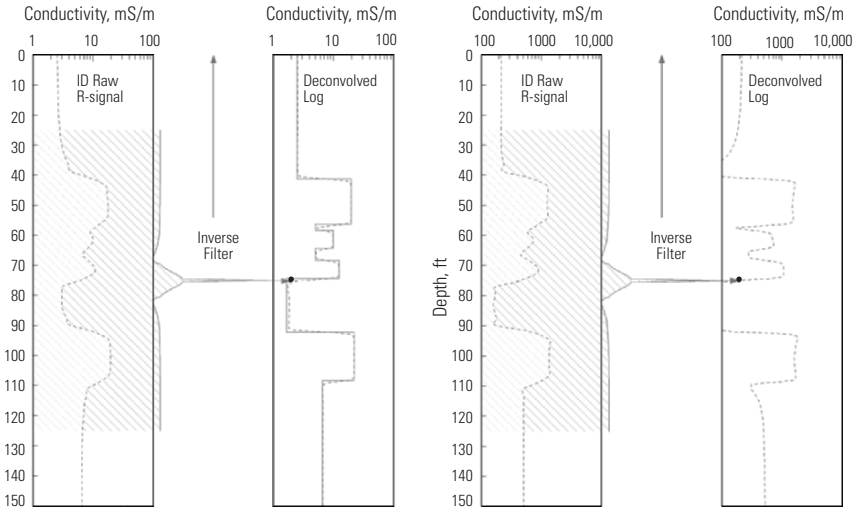


Fig. 8.2 Two left panels: inverting the low conductivity R-signal log from Fig. 8.1 with an inverse filter gives a good match to the original formation profile. Two right panels: applying the same filter to the high-conductivity R-signal from Fig. 8.1 gives a poorly deconvolved log. From Anderson and Barber [1]. Courtesy of Schlumberger.

In the phasor* tool the solution is based on the concept of skin effect signal, introduced by Moran and Kunz [2]. This fictitious signal is the difference between an actual log at high conductivity and what would have been obtained if the zero-conductivity Doll geometrical factor had been applied to the same formation profile. In a homogeneous formation at conductivities below about 2S/m it is simply the second real term in Eq. 7.50, $(2\sigma L/3\delta)$, which is exactly equal to the imaginary term – the formation X-signal. At higher conductivities, higher-order terms become important and there is no longer an exact correspondence. However, the correspondence is good enough that the phasor became the first tool to measure and use the X-signal.

The big advantage of the skin-effect signal is that it takes into account the spatial *distribution of skin effect. In the ILd, skin effect was removed by boosting the signal according to its value at each level. In a homogeneous medium this is correct, but in layered media it matters where the signal comes from. A high-conductivity layer above the tool affects the skin-effect correction just as it affects the geometrical response. Moran showed that the vertical distribution of the skin-effect signal strongly resembled the vertical distribution of the X-signal [2]. It does not match exactly so it needs to be filtered and also boosted to allow for the lack of correspondence at high conductivities. The resulting skin-effect log is then added to the log that was deconvolved with the zero-conductivity inverse filter to give a result that is valid over all normal ranges of conductivity.*

*Mark of Schlumberger

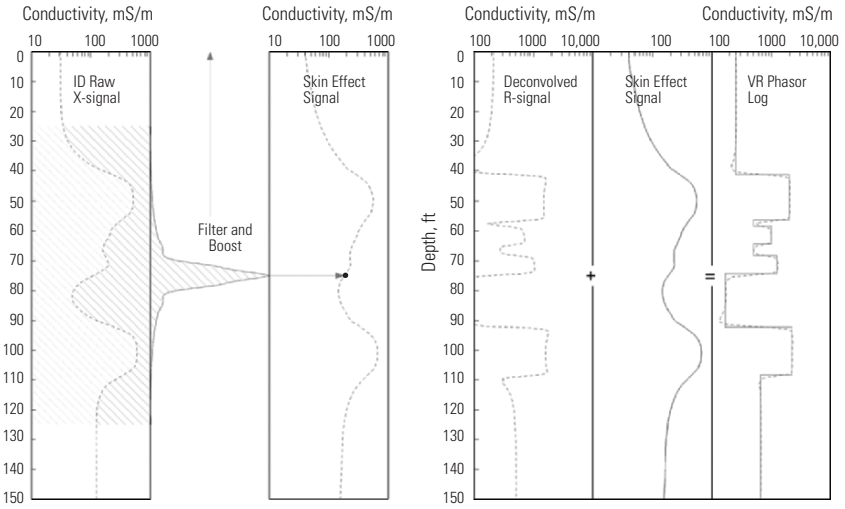


Fig. 8.3 The X-signal (left) is filtered and boosted to form the skin-effect signal which, when added to the high-conductivity deconvolved log R-signal (identical to that in Fig. 8.2) matches well the original formation profile. From Anderson and Barber [1]. Courtesy of Schlumberger.

Figure 8.3 illustrates this process for the high-conductivity formation shown in Fig. 8.2. The X-signal is first filtered and boosted to give the skin-effect signal. The similarity between the two is evident. When the skin-effect signal is added to the log deconvolved with a zero-conductivity filter, the result is a good match to the original formation.

Combining the inverse filter and the skin-effect correction, the phasor-processing algorithm [3] is therefore:

$$\sigma_P(z) = \sum_{z'=z_{min}}^{z_{max}} h(z-z')\sigma_R(z') + \alpha(\sigma_X(z)) \sum_{z'=z_{min}}^{z_{max}} b(z-z')\sigma_X(z') \qquad (8.3)$$

where σ_P is the phasor-corrected apparent conductivity, σ_R is the measured R-signal, σ_X is the measured X-signal, $b_{z-z'}$ is the function that filters the X-signal and α is the nonlinear function that boosts it.

8.2.1 Inverse Filtering

In the last section we saw how an induction measurement was the convolution of a long vertical response function with formation conductivity. We also saw how a combination of filters and the X-signal could deconvolve the logs and get back to the true conductivity. In the final results, artifacts such as shoulder effect were removed and the vertical response was sharpened. This section examines more closely the methods involved and their limitations.

The Doll three-point filter, Eq. 7.53, is an early example of a simple inverse filter that works only in specific conditions. The inverse filter $h(z-z')$ above is ideally the inverse of the response function g_{vB} in Eq. 8.1. It can be conveniently designed and understood in the frequency domain by applying a Fourier transform to convert the response g_{vB}, which is a function of depth, into the response as a function of spatial frequency k in cycles per foot, $G_{vB}(k)$. A high spatial frequency means high sensitivity to vertical changes and therefore good vertical resolution. $G_{vB}(k)$ is shown for ILd and ILm in Fig. 8.4. The spatial response of the measurement is imperfect in that it does not respond equally to all frequencies, doing much better in very thick beds (low k) than in thin beds (high k). The job of the filter is thus to boost or cut frequencies in $G_{vB}(k)$ to produce the desired response.

Unfortunately a simple inverse does not work in practice. First the dual induction logs are only sampled every 6 in. Thus it is not possible to measure spatial frequencies higher than 1/(2×6 in.) = 1 cycle (the Nyquist limit). The second, more serious limit can be seen in Fig. 8.4. The ILd log has zero response at 0.2 cpf, corresponding to a bed thickness of 2.5 ft. This is a blind frequency at which the measurement has no information: if the ILd passes through a series of thin beds 2.5 ft thick it records a straight line [5]. In terms of the filter this means that the weight at k = 0.2 cpf would need to equal infinity. Moreover, for thinner beds the response is negative and the log is inverted.

As a result of all these issues, a practical filter is designed not to make a perfect inversion but to satisfy a target-function $T(k)$ such that:

$$H(k) = \frac{T(k)}{G_v(k)}. \tag{8.4}$$

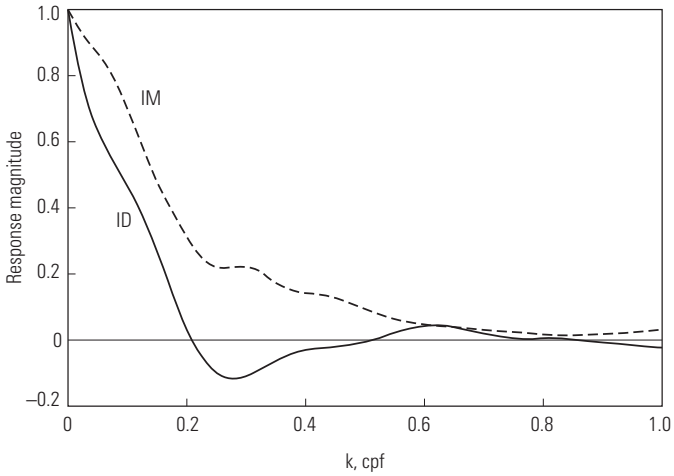


Fig. 8.4 Spatial frequency response of the Ilm and Ild arrays in cycles/ft. The inverse of frequency represents twice the bed thickness (one bed being only half a cycle). From Barber [4]. Used with permission.

In the phasor algorithm the target ignores all spatial frequencies above 0.2 cpf and includes techniques to avoid ripples caused by overly boosting high frequencies [3]. In the depth domain the Fourier transform of $T(k)$ is a single symmetric peak of a certain width with no side lobes. The final step is to transform $H(k)$ back into the depth domain to give the actual filter that will be applied to a log, $h(z - z')$.

Such inversion techniques work well with induction logs because the logs are almost noise free and are only mildly nonlinear. (Nuclear and acoustic logs have much lower signal to noise ratios, while laterolog response is more nonlinear.) Induction response is nonlinear in the sense that, because we need to know the skin-effect spatial distribution, we need to know part of the answer to find a solution. Many processing schemes for post-ILd induction tools are aimed at getting around this problem.

An aggressive inverse filter could sharpen the ILd response but is not possible due to the blind frequency described above. One solution is to add information from the ILm array [4] on the basis that all high spatial frequency comes from near the borehole anyway, as can be seen qualitatively from the 2D ILd response in Fig. 7.17. With this information ILd inverse filters (the $h(z - z')$ in Eq. 8.2) and ILm filters can be designed to give medium and deep logs with matched vertical resolutions of 2 or 3 ft.

The result is shown in Fig. 8.5, which should be compared with Fig. 7.18 for the traditional, unfocussed ILD. Why not always use enhanced resolution filters? Mainly because the high spatial frequencies that are enhanced occur near the borehole, and may actually come from the borehole when it is rugose or caved. Also, the invaded zone may have a different contrast to the surrounding beds than the uninvaded zone. These and other effects will be discussed later in conjunction with the multi-array induction tools.

8.3 HIGH RESOLUTION INDUCTION

Another approach to the problem of vertical resolution was taken in the high resolution induction (HRI) tool that appeared in 1987 [6]. This tool broke away from the traditional 6FF40 array and used a central receiver coil flanked by two bucking coils equally spaced on each side and two transmitter coils also equally spaced at a further distance each side. A medium induction was formed using the same central main receiver but with a different spacing to the transmitter coils. The deep and medium measurements can be described as 5FF75 and 5FF35 arrays respectively.

The idea behind these arrays is that the vertical response is sharp and controlled by the distance from main receiver to the bucking coils while the radial response is deep and controlled by the distance from receiver to transmitter. In the 6FF40 array the different spacings control both responses. The HRI also has no blind frequencies so it is possible to boost the higher spatial frequencies of both arrays directly to produce matching high vertical resolutions between 2 and 3 ft. However, as with the phasor tool, the high vertical resolution information only comes from near the borehole. Similar limitations as to borehole rugosity and invasion therefore apply.

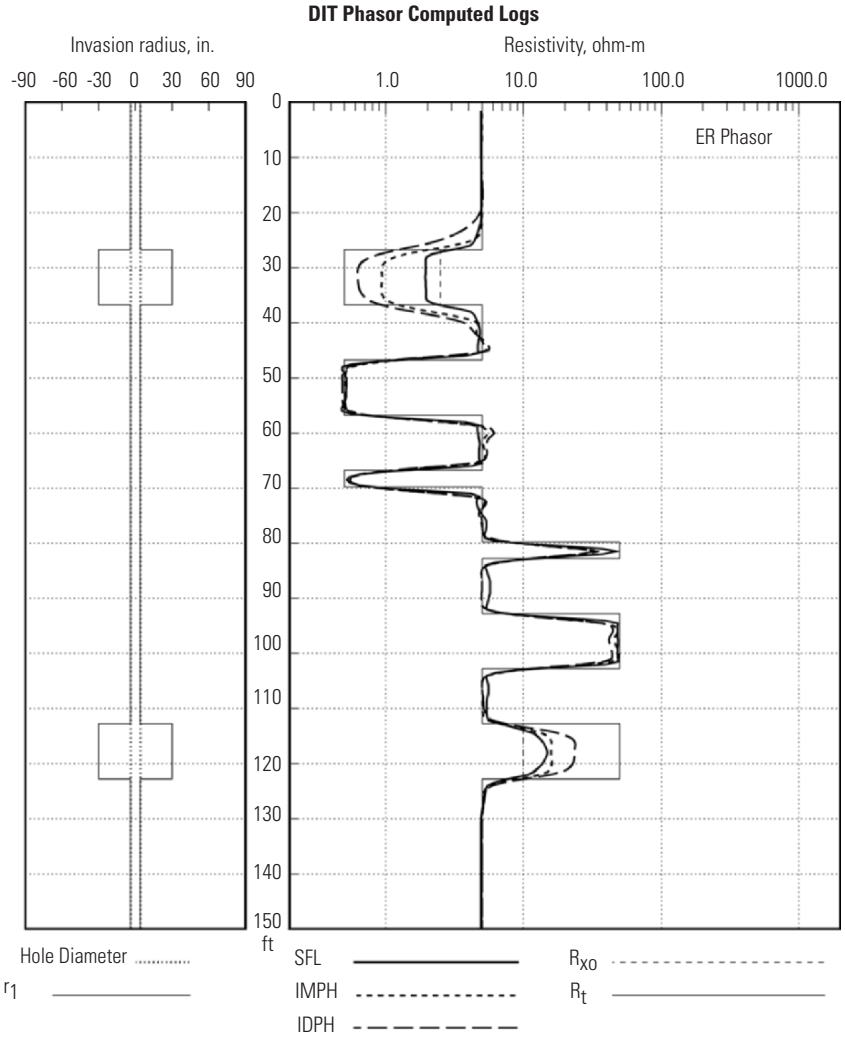


Fig. 8.5 A phasor induction log with the vertical resolution of ILd and ILm enhanced and matched at 3 ft, and modeled through a series of invaded and uninvaded formations. Compare with the results from the traditional ILd and ILm in the same formations shown in Fig. 7.18. Adapted from Anderson [31].

8.4 MULTI-ARRAY INDUCTIONS

A multi-array induction device is a set of simple coil arrays whose measurements are combined in software to form outputs that have certain desired vertical and radial responses. By the early 1990s technical advances made the construction of such devices feasible. These advances included the ability to transmit large volumes of

data to surface; accurate computer modeling with which to design the processing; and more stable sondes that reduced downhole signal drift for short-spaced as well as long-spaced arrays. Also, once the major defects of the 6FF40 array had been corrected, other deficiencies became more apparent. Most of these were linked with the radial response, as will now be reviewed.

The phasor and HRI tools made medium and deep induction measurements but relied on an electrode device such as the SFL or MSFL for shallow information. This has some disdvantages. First, with three curves it was only possible to invert for a step profile invasion: annuli and more complex invasion profiles could not be handled. Second, the combination of electrode and induction measurements made formations with conductive invasion ($R_{xo} < R_t$) difficult to interpret. A laterolog is usually preferred with conductive invasion, but there are inevitably wells and reservoirs where both conductive and resistive invasion are present (e.g., an oil zone with conductive invasion and a water zone below with resistive invasion). Finally in oil-based mud the shallow electrode device gave no data.

Multi-array inductions offered a means to solve these problems by providing more radial information. The increased amount of data would also allow further improvements in vertical response, mainly improving shoulder bed correction at very high contrast boundaries and enhancing resolution even with moderate rugosity. Furthermore, this information would help solve for the effect of dipping beds. The basic principle is shown in Fig. 8.6. On the left are the 2D responses of a set of simple 3-coil arrays (transmitter, main and bucking coil) of different lengths. On the right are four examples of desired log responses, formed by weighting and summing individual array responses in different ways inside a multichannel filter. The responses labeled

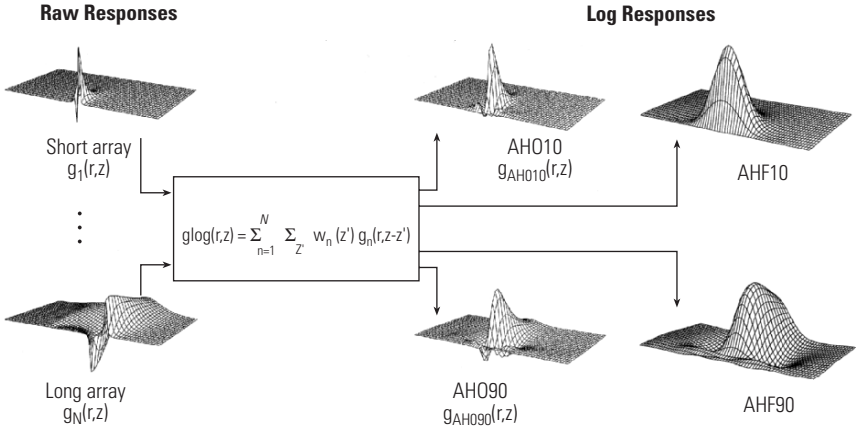


Fig. 8.6 Schematic representation of the log forming process in multi-array induction tools. The individual array responses at left, $g_N(r, z)$, are combined in a multichannel filter in the center to form the output logs at right. AH = from AITH tool, O and F = 1ft and 4ft vertical resolution, 10 and 90 = 10 in. and 90 in. median radial response. The weights $w_n(z')$ are different for each output log response. Adapted from Anderson and Barber [1].

AHF10 and AHF90 are designed to be smooth with no negative lobes. (Compare them with the ILd and ILm responses in Fig. 7.17). The responses labeled AHO10 and AHO90 have much sharper vertical responses in the z-axis but have negative overshoots. The processing methods are discussed below. In the meantime, note how the same array data can be formed to give a range of different responses.

8.4.1 Multi-Array Devices

The first multi-array induction tool was designed to emulate the ILd [7]. The first device to exploit the potential of multiple arrays was the Array Induction Tool (AIT*), one version of which has eight 3-coil arrays with a common transmitter for all arrays (Fig. 8.7) [8]. It can be shown that in order to sample the radial information uniformly, the spacings should increase exponentially [10]. Each array has a bucking coil in

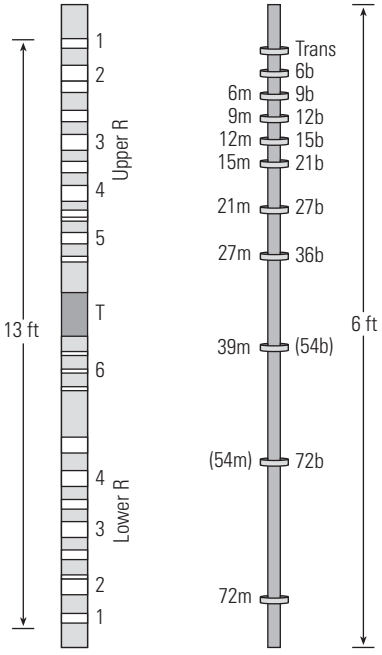


Fig. 8.7 (Left) Coil layout for the high-resolution array induction tool. Coils 1 are two identical 3-coil arrays equidistant either side of T. Coils 2–6 are 4-coil arrays. Not all bucking coils are shown. From Beste et al. [13]. Used with permission. (Right) Coil layout for the AIT-H tool. *m* are the main coils and *b* the bucking coils. In most cases the bucking coils are co-wound with the main coils of the next smallest array. The spacings of the main receivers increase approximately exponentially from 6 in. Coil spacings are given in inches. Adapted from Barber and Minerbo [9].

*Mark of Schlumberger

order to provide some natural radial focusing, as discussed in Section 7.5, and to cancel the direct mutual coupling (Section 7.7). A 2-coil array would be simpler but the cancellation would have to be done electronically. Also the 3-coil arrays have naturally higher spatial frequencies and have no blind frequency, unlike the 6FF40 discussed above. The formation X-signals are measured on the longer arrays, but not on the short arrays because magnetic materials in the mud can affect them strongly. In earlier AIT tools the number of channels was increased by acquiring data at multiple frequencies.

An important impetus for the development of the AIT was the discovery that coils could be mounted on a hollow metal mandrel [11]. It was always believed that any conductive material near the receiver would create spurious signals. In fact a nonmagnetic but perfectly conducting mandrel forces the electric field on its surface to zero, thereby generating no in-phase signal at the receiver. With the materials and dimensions used for actual mandrels, the in-phase signal, or sonde error (see Section 7.10) is small, but above all changes little and predictably with temperature. In addition, a hollow rigid mandrel minimizes downhole changes in coil spacing and allows the connecting wires to be placed inside the mandrel, where they are effectively shielded from the coils. With the fiberglass construction of earlier devices small changes in the coil spacing or the position of electrical connections could lead to significant changes in sonde error downhole. Shallow arrays are particularly sensitive to such changes.

The high-definition induction log [12] also uses 3-coil arrays with similar quantity but different spacings than the AIT. It does not measure the formation X-signal but instead records data at 8 frequencies from 10 to 150 kHz. This data is used for skin-effect correction and for quality control.

The High-Resolution Array Induction Tool develops the ideas of the HRI tool but inverted, with a central transmitter and eight 4-coil receiver arrays as well as two deep 3-coil arrays (Fig. 8.7) [13]. The transmitter is operated at 8 kHz and at 32 kHz. The principle of achieving independent vertical and radial focusing is the same as for the HRI. The focusing is dynamically adjusted to achieve the optimum vertical resolution considered appropriate for the measured R_t and R_m.

8.4.2 Multi-Array Processing

The borehole signals for the shallow arrays are much larger than those of the ILd or ILm, and can be several times higher than those for the longer arrays and the signal from the formation. The first task is therefore to remove the borehole contribution from the arrays before combining them in the multichannel filter. Since this contribution can be so large, the corrections need to very accurate. In addition, skin effect causes the corrections to depend on the contrast in conductivity between borehole and formation, a dependence that was often ignored with traditional arrays. On the other hand we can model the borehole signal accurately. Also, there are four parameters controlling this signal (borehole size and conductivity, standoff, formation conductivity) but we have four or more shallow arrays with spacings less than 24 in. It is therefore possible to invert the array data to find the parameters that best fit the modeled response. In

practice it is common to invert for the two parameters that are least well known (formation conductivity and stand-off) and use external measurements for the others [14].

The result is a set of borehole-corrected array data that are accurate to within 1 mS/m providing the external data is accurate, and providing the borehole is smooth and circular and the tool is parallel to the borehole wall. The process is automatic, but the large number of charts required to represent each array in different conditions means that none are published. For the log analyst this avoids the tedium of looking up charts but makes it hard to judge the accuracy of results in difficult conditions.

With the borehole signal removed, the array data are boosted to remove the skin effect for a homogeneous medium, and then combined to form the desired log responses. An ideal response has three components: a good vertical resolution with no side lobes; controlled radial characteristics, so that deep-reading logs have little response to shallow invasion and shallow-reading logs have no response from deep in the formation; and a well-behaved 2D response with no undesirable spikes along the borehole that would induce sensitivity to borehole irregularities (caves).

Actual designs are a compromise, mainly between vertical resolution and 2D response. The information on high vertical resolution comes from near the borehole, as seen from the spikes on the 2D raw array responses in Fig. 8.6. Since it is not possible to use this information without keeping some sensitivity to borehole irregularities, the commonly accepted standard is to compute three sets of logs with vertical resolutions of 1, 2, and 4 ft. The 4ft log has a smooth 2D response with minimum sensitivity to cave effect. The 1 ft log has much better vertical resolution but the 2D response is not smooth. The vertical responses are shown in Fig. 8.8; the 2D responses were already illustrated in Fig. 8.6. Each of the three sets consists of five logs with different radial response which are known by their midpoint values, i.e., 10, 20, 30, 60, 90 in. (Fig. 8.9).

The design of the multichannel filters is significantly more complicated than for the single channel filter described in Section 8.2.1. While there is plenty of information on vertical changes in the formation from measurements at different depth levels, there is much less information on radial changes, since measurements can only be made from within the borehole. The radial response can therefore only be formed by adding and subtracting the total contribution from a subset of arrays. The problem is then to find the filters for each array in this subset that give the desired vertical response. The filter weights are designed for the zero-conductivity Born response, after which the spatial distribution of skin effect is handled by one of the methods given below. These filters must also satisfy the 2D constraints, for example that the response near the borehole has no undesirable spikes. Ideally the filter weights are calculated simultaneously, taking into account all these considerations. One method of solving this problem is to treat it as a problem in matrix inversion [15].

In theory, data from all arrays can be used to form all logs. In practice the shallow arrays are more susceptible to errors in borehole correction, which it is undesirable to transfer to the deep logs. It is possible to use only the deeper arrays to form the deeper logs. High vertical resolution is achieved by boosting the higher spatial frequencies in the deep arrays. Unlike the 6FF40, 3-coil arrays have no blind frequencies to worry about.

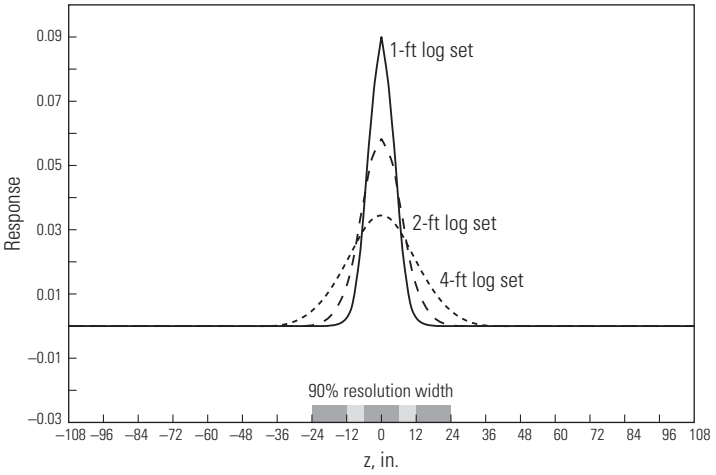


Fig. 8.8 Vertical responses of the three sets of AIT logs. Vertical resolution is defined as the distance over which 90% of the response occurs. From Anderson and Barber [1]. Courtesy of Schlumberger.

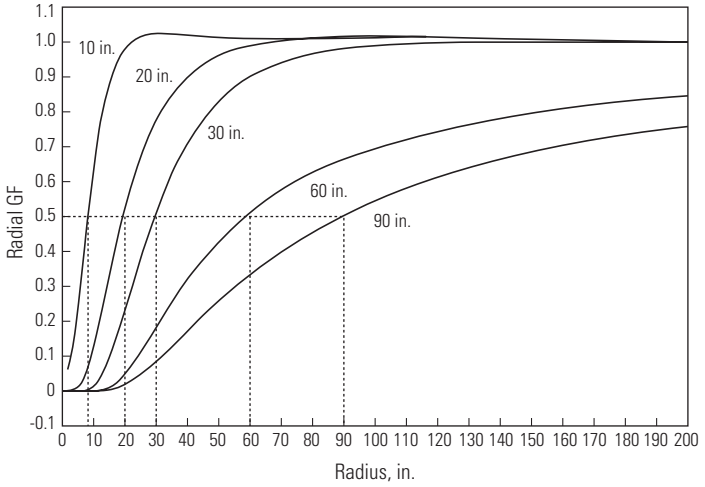


Fig. 8.9 Integrated radial response of the AIT family of logs at zero conductivity. Depending on the processing, the depth of investigation of the deeper logs may be reduced as conductivity increases. From Anderson and Barber [1]. Courtesy of Schlumberger.

The remaining skin effect due to spatial distribution can be handled in several ways: by using the X-signal, as in the phasor tool; by measuring at multiple frequencies and using the variation of skin effect with frequency; or by forming different filters at different conductivity levels and interpolating between them according to a

slowly varying background conductivity, calculated from the deep arrays. One final method, called inhomogeneous background-based focusing [16], is based on a more exact handling of the Born response function (Eq. 7.51) in which the background conductivity is separated out and the Born response function appropriate for that conductivity is only applied to the residual difference between the actual signal and the background.

8.4.3 Limitations of Resolution Enhancement

It has been stated several times that all high vertical resolution information comes from near the borehole, and that all resolution-enhancement techniques assume that the changes seen near the borehole are also present deeper in the formation. These assumptions are clearly not valid when there is invasion, or when the formation layers are not perpendicular to the borehole, both very common situations. Before examining the effect of these assumptions let us see what happens without resolution enhancement. Figure 8.10 shows the vertical response of six logs with different depths of investigation, in which each log has the vertical resolution that is found naturally at the midpoint of its radial response. Although these responses are the most faithful to the physics of the measurement, unfortunately they give an apparent indication of invasion when there is none. Thus in spite of the erroneous assumptions, wellsite logs from multi-array tools are commonly presented with the same, matched resolution for all curves.

How significant is the error caused by invasion? In principle there are six cases of invaded thin beds, each of which has a different relationship between R_{xo}, R_t, and

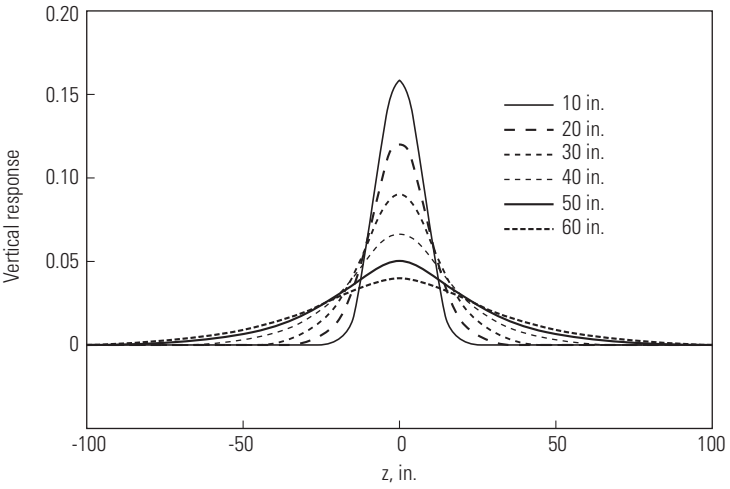


Fig. 8.10 Vertical response functions in which the vertical resolution is that found at the midpoint of the radial response. These are known as true resolution logs in the HDIL tool. From Beard et al. [12]. Used with permission.

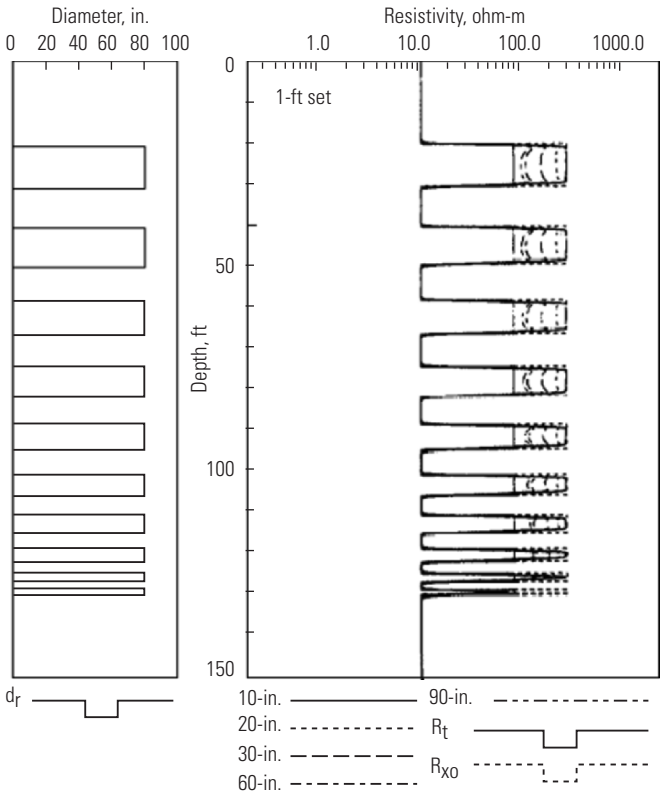


Fig. 8.11 AIT 1 ft logs computed for a series of invaded thin beds with $R_{xo} > R_t > R_{sh}$, $d_i = 80$ in. R_{sh} is the shale, or shoulder bed resistivity. Adapted from Barber and Rosthal [17].

R_{sh}. Here we will examine two cases, the first of which is with $R_{xo} > R_t > R_{sh}$ (Fig. 8.11). This is an easy case since the vertical changes at the bed boundaries are in the same direction near and far from the borehole. Even with a moderately high d_i of 80 in. the readings of the 5 logs are the same in the thick beds at the top as in thin beds down to 1 ft at the bottom. The sharp changes at the boundaries on these 1 ft resolution logs are also preserved.

The second case, with $R_{xo} > R_{sh} > R_t$ is not so easy because the changes from shale to invaded zone are in the opposite direction to those with the uninvaded zone (Fig. 8.12). This causes problems because the near-borehole data that provide the high vertical resolution do not reflect the changes far from the borehole. The result is a clear loss of sharpness at bed boundaries in comparison to the previous case. By the time the bed thickness has been reduced to 3 ft these 1 ft logs no longer read R_t in the middle of the bed. However, there are no horns or undesirable artifacts.

Of the other cases the worst artifacts occur when R_{xo} is the lowest resistivity and therefore acts somewhat like a large cave. The less enhanced 2 or 4 ft logs

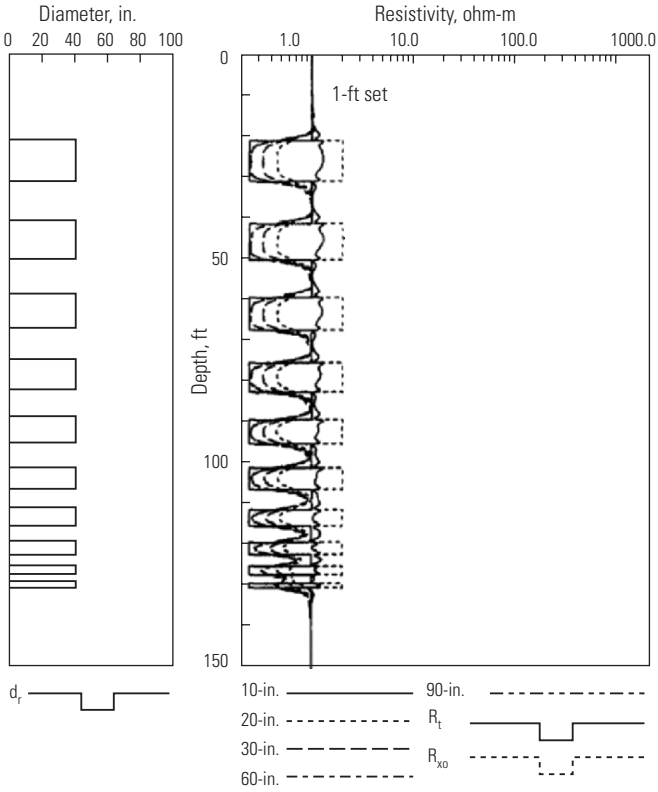


Fig. 8.12 AIT 1 ft logs computed for a series of invaded thin beds with $R_{xo} > R_{sh} > R_t$, $d_i = 40$ in. R_{sh} is the shale, or shoulder bed resistivity. Adapted from Barber and Rosthal [17].

generally give acceptable results. In other cases the main result is a loss of vertical resolution rather than the introduction of artifacts. Thus, although invasion contradicts the assumption on which vertical resolution enhancement is made, the results are not as damaging as might be feared.

The absence of correction charts for multi-array induction logs makes it hard to get a feel for when these corrections are large and likely to introduce errors. Most devices output diagnostic flags or curves that indicate when there are large borehole corrections, magnetic mud or rugose holes. The chart shown in Fig. 8.13 recommends the limit of use for different resolution curves based on resistivity level and formation/borehole resistivity contrast.

8.4.4 Radial and 2D Inversion

In the last few sections we saw the improvements and limitations of multi-array induction logs from the point of view of vertical response. In this section we turn to

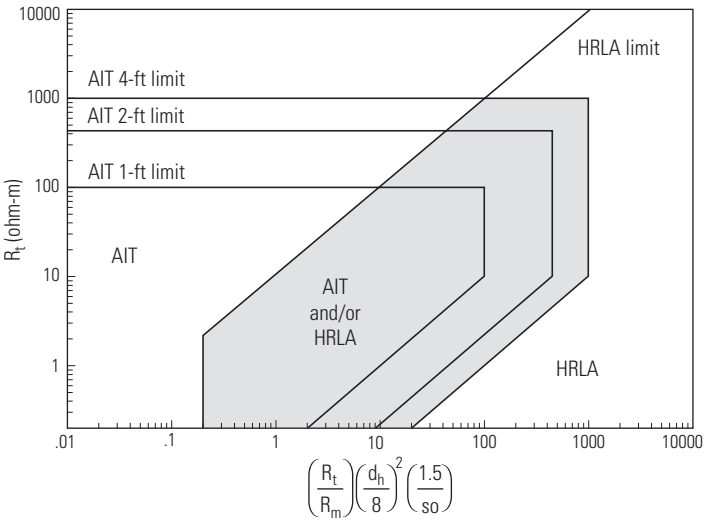


Fig. 8.13 Chart indicating the recommended limits of use of the vertical resolution logs for the AIT tool, and the limit of use for the array laterolog HRLA tool. so = stand-off, d_h = borehole diameter. Courtesy of Schlumberger.

the radial direction and see how to obtain the main goal of induction logging, R_t. A quick visual check of the 60 and 90 in. logs is often enough. If they read the same, then that value is a good estimate of R_t. This simplicity is a great advantage of multi-array devices, but R_{xo} is rarely so easily obtained (see Problem 8.3). If needed, the next step is to make a 1D inversion of the logs at each level, like the invasion charts for earlier tools except that with five radial logs it is possible to solve for more than the traditional 3-parameter step profile[†]. The AIT routinely solves for a 4-parameter profile, R_{xo}, R_t, the midpoint and slope of the transition from R_{xo} to R_t [18]. Annuli can be readily recognized by an out-of-order curve (see Fig. 8.14, and Problem 8.4). When recognized, the inversion is rerun, this time solving for R_{xo}, R_{ann}, R_t, and the inner and outer radii of the annulus.

A more complete solution to the whole problem of finding R_t is to make a 2-D inversion of either the original array data or the computed logs. This can take into account the vertical and radial responses of the arrays simultaneously. By avoiding the assumptions made at each step of a sequential processing, this can in principle find the best R_t, even at bed boundaries. Initial estimates of R_{xo}, R_t, and d_i throughout an interval are made from the logs and given to a 2D forward model, which calculates what the array data should read over that interval. If there are differences, the estimates

[†]A typical array induction tool could generate a much larger number of radial logs if required. However these do not necessarily contain extra information because of the large overlap in radial response of the arrays. It can be shown by eigen analysis that there are only five or six logs that are independent in the sense that they cannot be derived from a linear combination of the other logs [17].

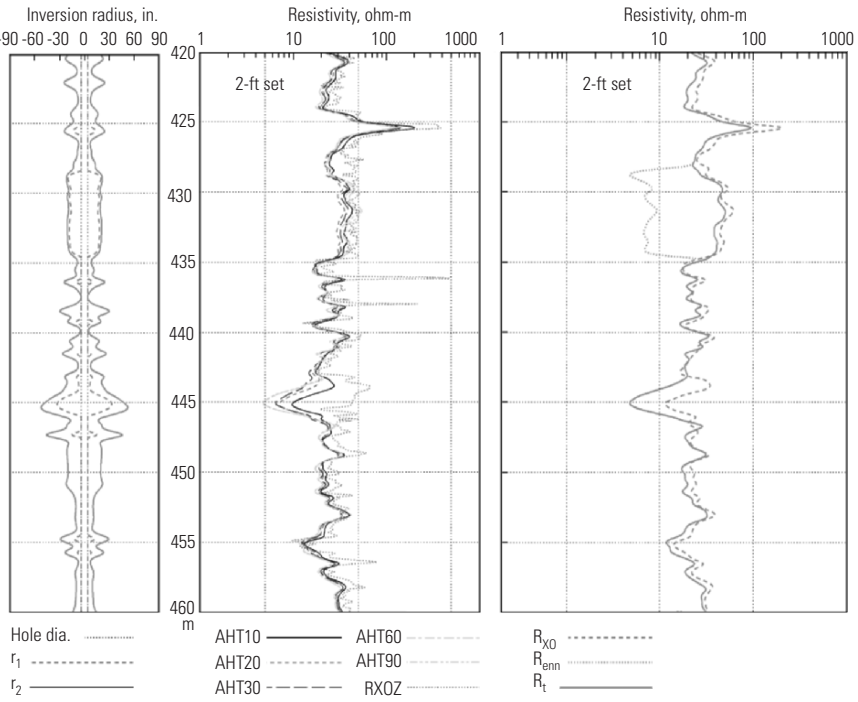


Fig. 8.14 An example of annulus. The 20 and 30 in. logs in the center panel read lower than the others indicating an annulus. The logs have been inverted to give the resistivities (right) and radii (left) of the different regions. Courtesy of Schlumberger.

are adjusted and the procedure repeated until the best fit is found. The final estimates of R_{xo}, R_t, and d_i are the answers that are output for that interval.

Several such techniques have been developed and are customarily applied post-logging. There are several reasons for this. A full 2D model is slow because the nonlinearity of the problem leads to several iterations through the model for each interval. It can be speeded up by dividing the problem into a sequence of simpler problems, such as first determining vertical layers and then invasion depth, but then it is no longer a truly simultaneous solution [19].

Also, the best fit between modeled and actual data is usually found by looking for the minimum least-squares difference. With induction logs the large conductivity contrasts between layers means that other terms are needed to avoid unstable results. These terms may minimize the roughness [20] or maximize the entropy.‡ The weight given to these terms may need to be adjusted for different conditions, a choice that

‡The mathematical expression used in the smoothing term has the form of an entropy term in thermodynamics. Maximum entropy, as applied to log data, is a measure of the departure of the computed log from its average value [21, 22].

is more appropriately made post-logging. 2D inversions are therefore normally done post-logging and under guidance from a log analyst so that other information and other logs can be added to improve results [23]. In these conditions, 2D inversions have proved better than filters in cases of extreme conductivity contrast and unfavorable invasion. For wellsite logs, the repeatability of the sequential methods is preferred.

8.4.5 Dipping Beds

Until the mid-1980s the effect of dip on induction logs was ignored. This assumption was not unreasonable since the dip angle of most reservoirs is less than 30° in which case the effect on induction response in vertical wells is small. Moreover this effect was masked for many years by the stronger shoulder effect. Once shoulder effect was removed, the importance of dip became evident. At the same time it became increasingly common to drill highly deviated wells through reservoirs. Clearly what affects the induction is the *relative* dip between tool and formation. Since relative dip can reach high values, the effect on induction response can be serious. Note that from now on "dip" is taken to mean relative dip.

The three direct effects of dip can be seen in Fig. 8.15. First the apparent thickness of a resistive layer is lengthened as the tool takes a longer distance through it. This can be easily corrected, if desired, by changing the depth index to one that is perpendicular to the bedding planes. This depth index is known as the true bed or stratigraphic

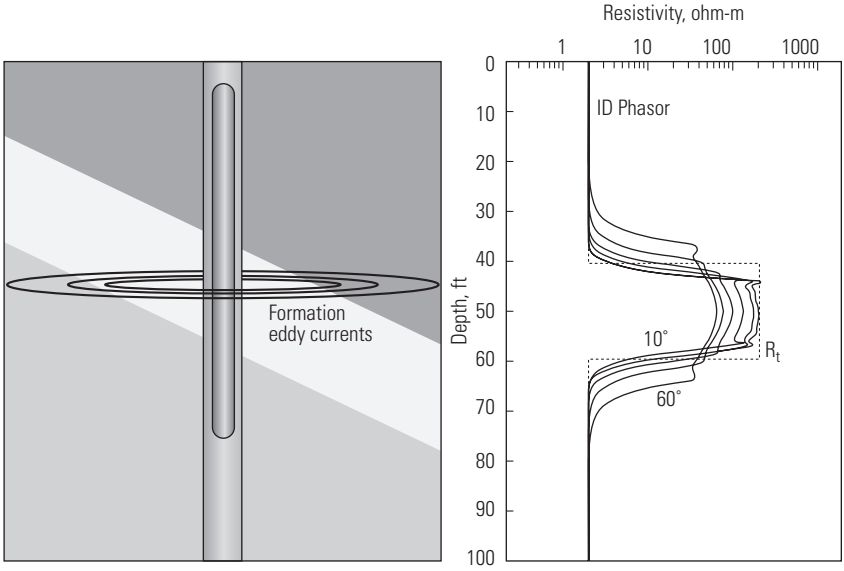


Fig. 8.15 (Left) Illustration of formation eddy currents from an induction logging device crossing a dipping bed. (Right) Response at different dip angles. The spikes at the edges of the bed on the 60 in. curve are due to the polarization effect. Adapted from Barber [24].

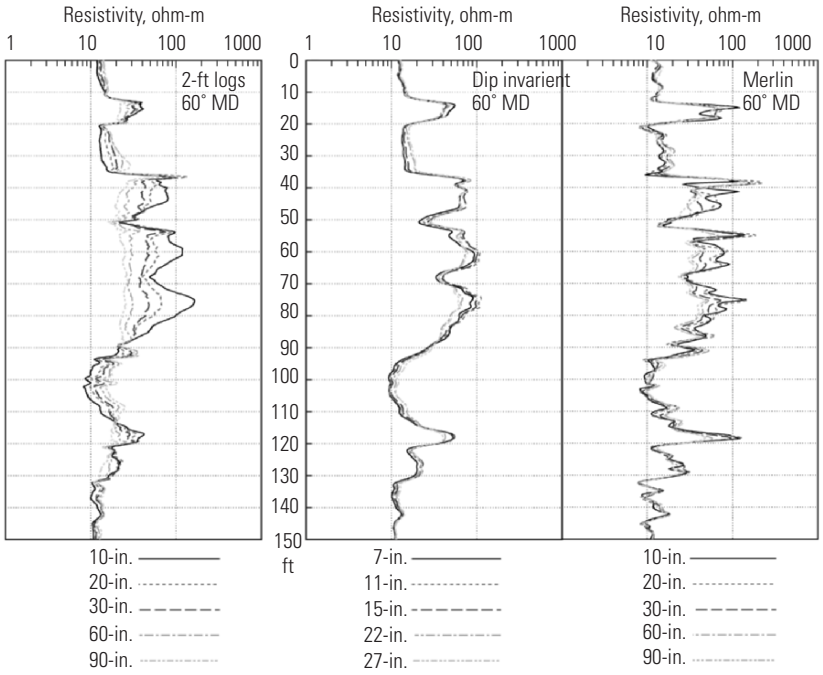


Fig. 8.16 Example of multi-array logs in a well with relative dip of 60°, plotted on measured depth. The uncorrected logs (left) show apparent invasion in all beds with an unlikely difference in curve order between conductive and resistive beds. The dip-corrected Grimaldi logs (center) remove this and show a small invasion effect in the central beds. The inversion-corrected logs (right) show more invasion in these beds since the curves are deeper-reading. The shoulder beds show no invasion, as expected. Courtesy of Schlumberger.

thickness, and is calculated by multiplying the original depth index by the cosine of the dip angle. Second, the eddy current lines, which circulate in a loop that is concentric with the tool, now cross regions of two different conductivities. This is a type of shoulder effect, reducing the resistivity near the boundary. On a multi-array induction log, the deep logs are much more affected than the shallow logs, giving the impression that there is invasion (see the example in Fig. 8.16, left). Thirdly, a polarization horn is observed, caused by electrical charge build up at the boundary. Finally, an indirect effect of dip is that, like invasion, it breaks the assumption on which vertical resolution enhancement is achieved so that standard filters can introduce artifacts.

The polarization horns can just been seen in Fig. 8.15 for the case with 60° dip. The reason for the artifact, discussed by Barber and Howard [24], is related to the induced eddy currents, coaxial with the tool, which are required to cross a bed boundary separating regions of differing conductivity. To insure the continuity of the eddy current (because it isn't going to disappear at the boundary) Ohm's law requires that there is a jump in the electric field in that vicinity. Such a jump in the electric field can only be caused by a charge buildup (or separation) that develops at the boundary.

The charge build-up will oscillate with the driving frequency of the transmitter and thus becomes a secondary transmitter. Only when the receiving coils pass close to this boundary does the signal from this oscillating charge interfere with the normal induced signal from the eddy currents and produce the artifact. The magnitude of the perturbation increases with contrast between bed resistivities and as the dip angle increases, with a maximum for a boundary that is parallel to the sonde axis. It is not surprising that this effect is commonly seen in high deviation or horizontal wells.

As in the case without dip, there are two methods of correction: filtering and iterative inversion. Both require the dip angle to be input, and since dip angle is not always well known and since it can vary along the well the dip correction tends to be made post-logging. Filters are designed to correct for both the shoulder and charge effects, and to handle each array at different dip angles and different conductivities [25]. At high dip the contrast between beds also becomes important. One 1D inversion method corrects the array data using maximum entropy and other terms to smooth the calculation [22]. It has proved reliable up to 80° when dip angle is known within ±5° and borehole conditions are favorable. If the dip angle is incorrectly chosen, the corrected logs show characteristic oscillations and spikes: this helps establish the correct dip angle but may require several trials. Once corrected, the normal radial processing procedures are applied to obtain R_t.

In 2003 a new method of dip correction appeared, this time without having to know the dip angle and fast enough to be run at the wellsite [9]. It relies on the observation that for a 2-coil array the shoulder contributions from above and below the coils drop off in proportion to $1/z^2$ *where* z *is the distance from the center of the array (see Fig. 7.9). This drop off is the same for a second array that is centered at the same point but is slightly shorter. Now if the two array signals are subtracted, and with appropriate normalization, all shoulder signals are cancelled out beyond the outermost coil positions (see Problem 8.5). This observation is sufficiently exact even in the presence of dip, thereby allowing formation conductivity to be determined without having to correct for shoulder effect and without knowing the dip angle. Since signals beyond the arrays have been removed, the shoulder and charge effects have effectively been cancelled out.*

This feature was discovered by P. Grimaldi in the 1960s but never published or implemented, because there was no obvious means of implementing it until one was found with the AIT. The AIT uses 3-coil arrays but a 2-coil array can be simulated by subtracting the voltage on the bucking coil, which is conveniently located at the same position as the main coil of the next smallest array (Fig. 8.7). The bucking coil voltage can be estimated from the measurement of this array in an iterative procedure [9]. The set of 2-coil measurements can then be depth shifted to the same center point and subtracted to remove the shoulder effect.

The Grimaldi method gives dip-corrected logs that are practically independent of dip angle and can be calculated at the wellsite. The main disadvantage is that the logs have less depth of investigation than normal multi-array induction logs and may therefore be affected by invasion. Figure 8.16 shows a set of multi-array logs without dip correction, with the Grimaldi method and with the maximum entropy inversion method.

8.5 MULTICOMPONENT INDUCTION TOOLS AND ANISOTROPY

One environmental effect not handled by the multi-array inductions so far discussed is anisotropy. In Chapter 4 we saw that thinly laminated reservoirs could cause significant macroscopic anisotropy with the average horizontal resistivity, R_h, being dominated by the least resistive laminae. Since the latter are usually shale or water-saturated silt, R_h is insensitive to the higher resistivity laminae which may be oil-bearing. On the other hand the vertical resistivity, R_v, *is* sensitive to these laminae and can be used to evaluate their water saturation.

Unfortunately, in vertical wells with horizontal laminations, normal induction tools measure R_h, as might be guessed from the picture of horizontally circulating eddy currents (see, e.g., Fig. 8.15). However, as the relative dip increases the tool measures an apparent resistivity, R_{app}, that contains a fraction of R_v which increases with angle. When the tool is parallel to the laminations it reads $\sqrt{R_v R_h}$ (see Section 4.7). In between, R_{app} depends on the relative dip angle θ and the anisotropy coefficient $\lambda = \sqrt{R_v/R_h}$ [26]:

$$R_{app} = \frac{\lambda R_h}{\sqrt{\lambda^2 \cos^2\theta + \sin^2\theta}} . \tag{8.5}$$

If we can find two measurements that have a different response to anisotropy we can solve for both R_v and R_h, as is done by combining laterolog and induction, or combining different LWD propagation measurements (Chapter 9). With multi-array induction measurements alone it is not practical: although the skin effect is altered as a function of anisotropy, the effect on the logs is small except at high dip angle and high anisotropy [27]. What is needed is a device specifically designed to measure R_v, for example by orienting the induction coils in a different direction. Such a device was considered by Moran and Gianzero in 1979, but not implemented because at that time the response was considered too complex [26].

8.5.1 Response of Coplanar Coils

The basic multicomponent tool has a triaxial transmitter and triaxial bucking and main receivers all with orthogonal coils in the X,Y, and Z axes (Fig. 8.17). Such an array produces voltages V_{ab} at the receiver triad from nine couplings, where the subscripts denote the relevant transmitter and receiver coils. We will ignore the cross-coupled components, V_{xy}, V_{xz}, etc. for the time being, and only consider the three direct couplings V_{xx}, V_{yy}, and V_{zz}. The latter, in which the coils point along the same axis, is the standard induction device considered so far. V_{xx} and V_{yy} are not only oriented differently to V_{zz} but are also parallel to each other rather than aligned on the same axis, i.e., coplanar rather than coaxial. This leads to different and often surprising responses, particularly in heterogeneous formations.

One basic difference is that the current lines of the coplanar coils cross the axis between the coils, rather than circle round the axis as with coaxial coils (Fig. 8.18). In a homogeneous medium without borehole the coplanar R- and X-signals still increase

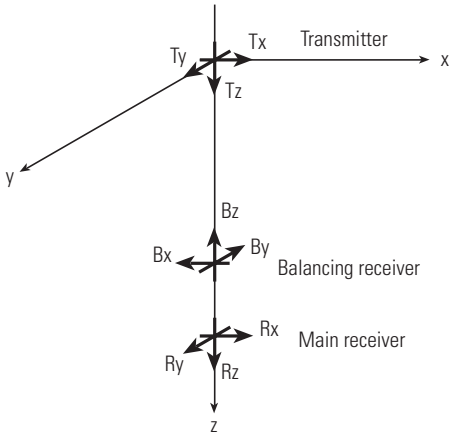


Fig. 8.17 Coordinate system and layout of a 3-coil triaxial array. Adapted from Barber et al. [28].

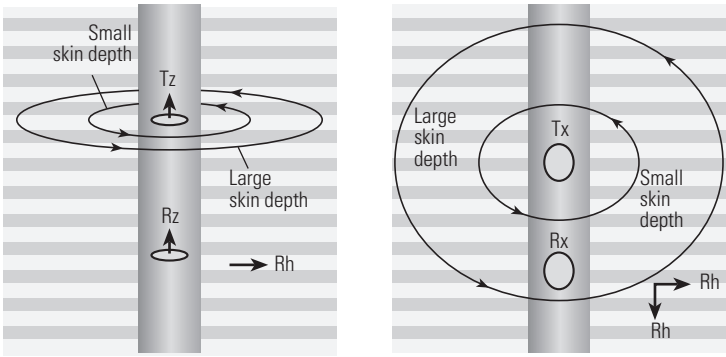


Fig. 8.18 Induced currents in an anisotropic formation. (Left) Conventional coaxial coils. The current flow is circular and only affected by R_h. (Right) Coplanar coils with the dipole axis facing into the page. The current lines are elliptical and are affected by both R_v and R_h. Adapted from Yu et al. [29]. Used with permission.

with conductivity at low values, but the skin effect turns out to be much stronger so that the R-signal peaks at a much lower value than with coaxial coils. As the conductivity increases, the skin depth decreases and the current lines close around the transmitter so that at the receiver, which is now outside the skin depth, the signal becomes increasingly weaker and shifted in phase. The R-signal soon reaches a peak and then decreases, eventually going negative when the phase angle is more than 90°.

This effect is accentuated in an anisotropic formation. Since the horizontal conductivity σ_h is usually larger than σ_v the current lines are elliptical not circular, causing the receiver to be even further outside one skin depth for the same average conductivity. The plot of X versus R signals in Fig. 8.19 shows a typical result. Starting at $\sigma_R = 0$

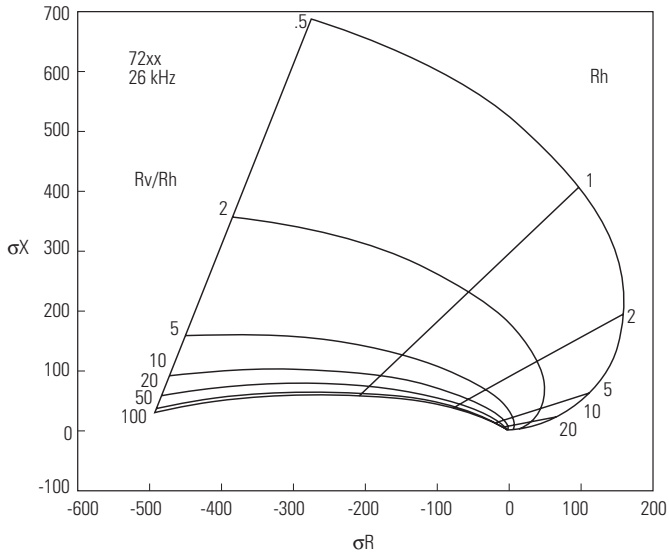


Fig. 8.19 Response (in S/m) of the R- and X-signals from a 72 in. xx array in an anisotropic medium, with a relative dip angle of 0°, for several values of R_h (indicated in ohm-m) and R_v/R_h. Adapted from Barber et al. [28].

and following the outermost curve for $R_v/R_h = \sigma_h/\sigma_v = 0.5$, σ_R increases as R_h decreases until it reaches a maximum near 2 ohm-m after which it starts decreasing, becoming zero at about 0.8 ohm-m. For higher R_v/R_h the R-signal zero crossing occurs at increasingly high R_h. σ_X also reaches some maximum as R_h decreases. These results show the sensitivity to skin effect and above all the good sensitivity of coplanar coils to anisotropy. Mathematically it can be shown [26] that V_{xx} is given by an expression similar to the one for coaxial coils in Eq. 7.49, but with an extra term in k^2:

$$V_{xx} \propto i\omega\mu \left(1 - ikL - \left(\frac{k_h^2 + k_v^2}{2}\right) L^2\right) \frac{e^{ikL}}{L^3} e^{-i\omega t} \tag{8.6}$$

where $k_h^2 = i\omega\mu\sigma_h$ and $k_v^2 = i\omega\mu\sigma_v$. On expansion, the higher terms in L/δ, ($\delta^2 = 2i/k^2$ from Eq. 7.46), are stronger than for the coaxial coils. In other words the skin effect is stronger, enough to shift the phase of the formation signal beyond 90° and cause negative R signals.

Before considering actual devices we will examine the response of coplanar coils to common heterogeneities. It can be appreciated that the current lines shown in Fig. 8.18 cross the borehole and can lead to a large borehole signal, with the borehole acting as a waveguide and accentuating its contribution. This was one of the reasons that earlier researchers considered a multicomponent tool undesirable. The signal is particularly sensitive to eccentering perpendicular to the direction of the coils, with a much larger effect than for the standard V_{zz} array, as shown in the example of Fig. 8.20. Since

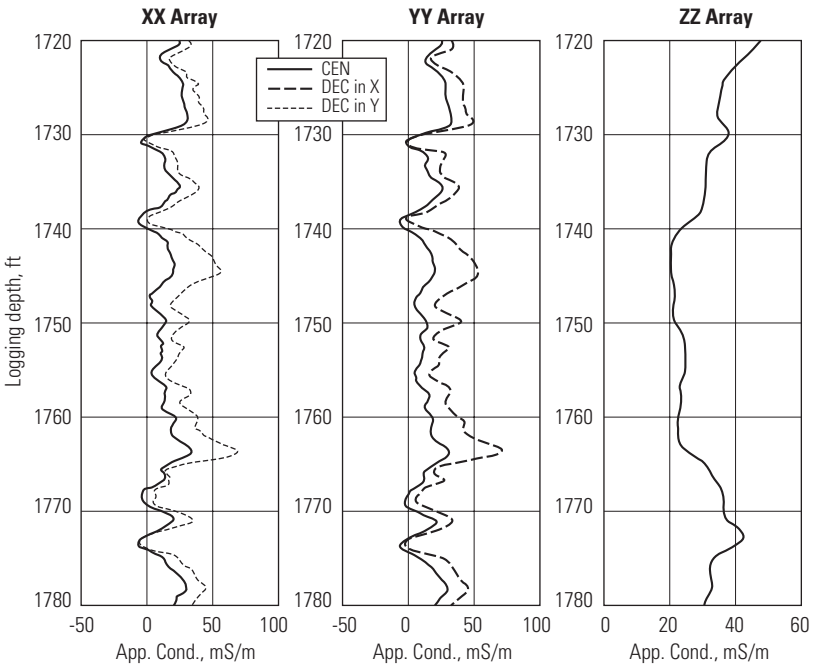


Fig. 8.20 Field data showing the response of the xx, yy, and zz arrays with the tool centered and de-centered in the borehole. De-centering causes no visible effect on the traditional zz array but is large in the others. From Wang T et al. [30]. Used with permission.

the amount of eccentering is not well controlled, particularly in rugose hole, borehole corrections are difficult. Furthermore the current loops extend some way above and below the coils so that the borehole signal depends not only on the formation between the coils but also that above or below them. Even in oil-based muds the borehole effect on coplanar arrays is significant due to the fact that the current lines are obliged to flow around the nonconductive borehole.

The radial depth of investigation of a coplanar array is deeper than a coaxial array of the same spacing at low or moderate conductivity (Fig. 8.21). This is a positive result and means that even if the invaded zone is isotropic there is sensitivity to anisotropy beyond the invaded zone. However at shallow invasion the coplanar array reads higher than either σ_{xo} or σ_t because the invaded zone acts as a waveguide.

Horizontal bed boundaries cause large horns on logs from coplanar coils (Fig. 8.22). This is equivalent to the polarization horn seen on a coaxial array when it crosses a steeply dipping bed. As might be expected these horns are attenuated when the bed boundary is dipping (Fig. 8.23). Although these figures only show the R-signal response of the three direct couplings, there are six cross-coupled responses and X-signals to consider. When there is azimuthal symmetry, as in Fig. 8.22, each xx and yy are identical and the cross-coupling terms sum to zero. If there is dip with the tool oriented so that one axis is parallel to the layering, as in Fig. 8.23, xx and yy

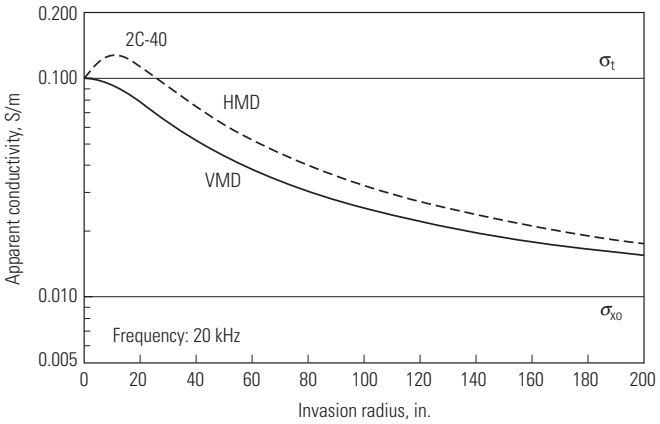


Fig. 8.21 Response of HMD and VMD arrays to increasing invasion. Both are 2-coil arrays spaced 40 in. apart. HMD and VMD stand for horizontal (xx or coplanar) and vertical (zz or coaxial) magnetic dipoles respectively. Adapted from Anderson [31].

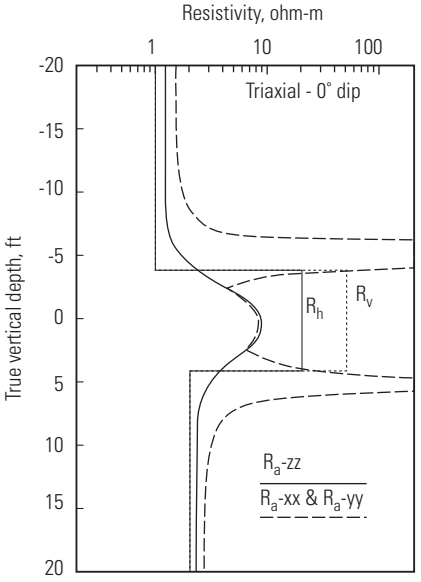


Fig. 8.22 Response of the R-signals from the xx, yy and zz arrays to a thin bed perpendicular to the tool. The X-signals (not shown) show similar features. Adapted from Anderson [31].

are different and some of the cross-terms are active. If the orientation is arbitrary, all the cross-terms are active. This is useful since, by minimizing the magnitude of the cross-coupling terms, it is possible to estimate the dip angle and azimuth from the induction data alone.

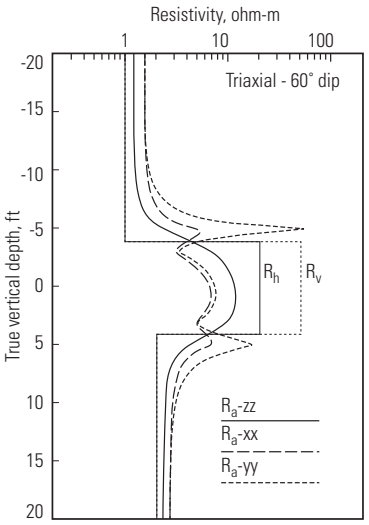


Fig. 8.23 Response of the R-signals from the xx, yy, and zz arrays to a thin bed at 60° dip. The X-signals (not shown) show similar features. Adapted from Anderson [31].

These examples give some feeling for both the wealth of information and the difficulties faced when interpreting triaxial array data. On the positive side there is good sensitivity to anisotropy and to dip. Boundaries are well indicated by the sharp response of the coplanar arrays. On the negative side the borehole signals are large, and features such as fractures or cross-bedding can break the azimuthal symmetry and be mistakenly interpreted as dip. Above all, there is no easy intuitive interpretation of the very large volume of data. Instead interpretation of all but the standard zz component must rely on complex processing and inversion.

8.5.2 Multicomponent Devices

The first multicomponent device (the 3D Explorer) appeared in 2000 [32]. It has three orthogonal transmitters and a corresponding set of receivers and bucking coils, as illustrated in Fig. 8.17 except that the orthogonal components are not at exactly the same location on the tool axis. The tool operates at ten frequencies between 20 and 200 kHz. As well as V_{xx}, V_{yy}, and V_{zz} it measures two cross-coupled components, V_{xy} and V_{xz}, which are used to determine the relative dip and orientation. The real-time processing removes the borehole and near-borehole signals by identifying and separating out that part of the signal affected by skin effect, since this occurs deeper in the formation [33]. These deeper signals also have much simpler responses than those illustrated above, and can be inverted to give R_v and R_h using a 1-D model that includes dip.

The processing is based on multiple-frequency measurements, since higher frequencies have larger skin effect. By combining data at different frequencies it

is possible to remove the contribution near the borehole, as is done by combining data at different spacings in traditional-focused array tools. In this case it is found that the second term in the expansion of the V_{xx} response (Eq. 8.6), which is a function of $(frequency)^{3/2}$, does not depend on near-borehole properties. The coefficient of the second term is extracted by fitting the expansion to data recorded at two or more frequencies, the more the better. The value of this coefficient is then compared with that expected in an isotropic medium for the measured R_h, which may be determined from the V_{zz} array or a standard multi-array tool. The difference is related to R_v/R_h. Since the technique relies on the presence of skin effect there is an upper limit of resistivity above which it becomes insensitive. In practice many anisotropic reservoirs are low-resistivity shaly sands where skin effect is large.

Another device, the Multi-Array Triaxial Tool is an adaptation of the AIT in which the transmitter consists of three orthogonal coils all located at the same position on the tool axis [28]. The six longest arrays also consist of triaxial main and bucking coils while the three shortest arrays remain as single component axial arrays (Fig. 8.7). The multiple triaxial arrays give different amounts of radial investigation, while the nine couplings between transmitter and each triaxial receiver provide a full tensor of measurements that can be transformed into the desired coordinate system, at the same time giving dip angle and azimuth.

The tool's conductive mandrel has the effect of shorting out the current loops in the borehole from the coplanar arrays. This reduces their borehole signal by two orders of magnitude and makes them more easily correctable. Nevertheless borehole corrections are still needed. These are handled in the same way as the AIT but this time with two extra variables, an effective σ_v in addition to σ_h and the direction of tool eccentricity.

A variety of processing techniques are used to extract R_v and R_h from the data. The Grimaldi technique can be applied so that, as with standard multi-array data, the resulting logs are free of shoulder effect at any dip angle. The result may need further correction for invasion. Otherwise various 1D and 2D inversion methods can be chosen according to the appropriate conditions of dip and invasion. There is also sufficient data to obtain a 3D image by inversion and to calculate the distance to boundaries in a horizontal well. As with all inversions the accuracy of the results depends on the sensitivity to inputs. Some of these sensitivities have been documented [34].

Figure 8.24 is an example of the logs recorded by a Multi-Array Triaxial Tool and the results of their interpretation. The resistivity image recorded at the same time shows thin laminations, indicating that the formation is probably anisotropic. The multi-array data were processed to obtain the relative dip angle, which was found to be near 25° and agreed with that interpreted from the resistivity image. The data were inverted to obtain R_h and R_v using a model of parallel layers, each of which is transversely isotropic but may have different vertical and horizontal properties [35]. The results show that the calculated R_h agrees with the standard AIT resistivity but that, as expected, R_v is significantly higher. Note that it is the relative dip between tool and bed boundaries that is estimated from the measurements and used for dip correction. Thus R_h and R_v are actually the resistivities parallel and perpendicular to bedding, not horizontal or vertical in the absolute sense.

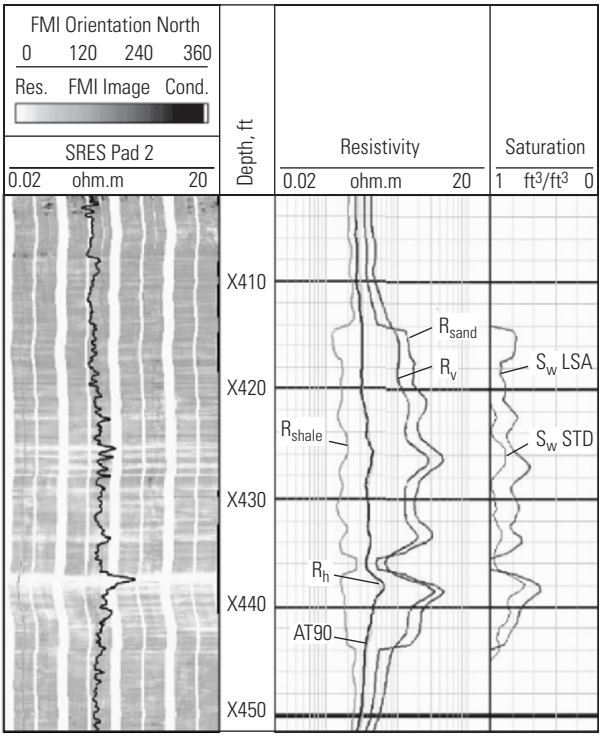


Fig. 8.24 Track 1: a resistivity image of a thinly bedded sand-shale sequence. Track 2: R_v and R_h from a multicomponent induction tool, from which R_{sand} and R_{shale} are derived using the model described in the text. R_h agrees well with the AIT 90 in. curve (AT90). Track 3: the water saturation calculated from AT90 ($S_w std$) is less representative than that calculated from R_{sand} ($S_w lsa$). Adapted from Wang H et al. [35].

Now that we have R_h and R_v what should we do with them? R_h should be used for correlation between wells and comparison with older logs, since it is the closest to the traditional "R_t." (But because the multicomponent R_h measures parallel to bedding it may disagree with R_t from a single component induction log when there are steeply dipping beds in a vertical well). Otherwise, the two resistivities in combination allow for a much improved analysis of laminated sands. Recall from Eq. 4.36 that R_h can be expressed as the parallel sum of the sand and shale laminations:

$$\frac{1}{R_h} = \frac{V_{sh}}{R_{sh}} + \frac{(1 - V_{sh})}{R_{sd}} \tag{8.7}$$

where V_{sh} is the fraction of shale and R_{sh} and R_{sd} are the shale and sand resistivities. Likewise R_v can be expressed as the series sum of the laminations:

$$R_v = V_{sh} R_{sh} + (1 - V_{sh}) R_{sd}. \tag{8.8}$$

These equations can be combined to solve for R_{sd} and one other unknown, for example V_{sh}:

$$R_{sd} = R_h \left(\frac{R_v - R_{sh}}{R_h - R_{sh}}\right) \tag{8.9}$$

$$V_{sh} = \frac{R_{sd} - R_v}{R_{sd} - R_{sh}}. \tag{8.10}$$

Alternatively, if V_{sh} is well defined then the equations can be solved for R_{sd} and R_{sh}. The resulting equations are not so neat and are left as an exercise. Both solutions can be extended to handle laminae that are themselves anisotropic, providing information is available on their anisotropy.

In the example of Fig. 8.24, V_{sh} was estimated from the image and from nuclear spectroscopy logs, leading to the calculation of sand and shale resistivities shown in the middle track. As expected these resistivities are respectively higher and lower than R_v and R_h. In the right-hand track the water saturation calculated from R_{sd} is compared with that calculated from R_h. Not surprisingly the calculation based on R_{sd} shows less water, and therefore more oil. This step will be explained in Chapter 23.

REFERENCES

1. Anderson B, Barber TD (1997) Induction logging. Schlumberger, Houston, TX

2. Moran JH, Kunz KS (1962) Basic theory of induction logging and application to study of two-coil sondes. Geophysics 27(6):829–858

3. Schaefer RT, Barber TD, Dutcher C (1984) Phasor processing of induction logs including shoulder and skin effect correction. US Patent No 4471436

4. Barber TD (1988) Induction vertical resolution enhancement – physics and limitations. Trans SPWLA 29th Annual Logging Symposium, paper O

5. Anderson B (1986) The analysis of some unsolved induction interpretation problems using computer modeling. The Log Analyst 27(5):60–73

6. Sinclair PL, Strickland RW (1991) Coil array for a high resolution induction logging tool and method of logging in earth formations. US Patent No 5065099

7. Martin DW, Spencer MC, Patel H (1984) The digital induction – a new approach to improving the response of the induction measurement. Trans SPWLA 25th Annual Logging Symposium, paper M

8. Hunka J et al. (1990) A new resistivity measurement system for deep formation imaging and high-resolution formation evaluation. Presented at the 65th SPE Annual Technical Conference and Exhibition, paper SPE 20559

9. Barber TD, Minerbo GN (2003) An analytic method for producing multi-array induction logs that are free of dip effect. Paper SPE 86914 in: SPE Reservoir Evaluation and Engineering 6(5):342–350

10. Zhou Q, Beard DR, Hillker DJ (1994) Induction tool resolution. Trans SEG 64th Annual Technical Meeting:761–764

11. Barber TD, Chandler RN, Hunka JF (1989) Induction logging sonde with metallic support having a coaxial insulating sleeve member. US Patent No 4873488

12. Beard DR, Zhou Q, Bigelow EL (1996) A new fully digital, full-spectrum induction device for determining accurate resistivity with enhanced diagnostics and data integrity verification. Trans SPWLA 37th Annual Logging Symposium, paper B

13. Beste R, Hagiwara T, King G, Strickland R, Merchant GA (2000) A new high resolution array induction tool. Trans SPWLA 41st Annual Logging Symposium, paper C

14. Grove GP, Minerbo GN (1991) An adaptive borehole correction scheme for array induction tools. Trans SPWLA 32nd Annual Logging Symposium, paper P

15. Chandler RN, Rosthal RA (1992) Induction logging method and apparatus including means for combining in-phase and quadrature components of signals received at varying frequencies and including use of multiple receiver means associated with a single transmitter. US Patent No 5157605

16. Xiao J, Geldmacher IM (1999) Interpreting multi-array induction logs in high R_t/R_s contrast environments with an inhomogeneous background-based software focusing method. Trans SPWLA 40th Annual Logging Symposium, paper FFF

17. Barber TD, Rosthal RA (1991) Using a multi-array induction tool to achieve high resolution logs with minimum environmental effects. Presented at the 66th SPE Annual Technical Conference and Exhibition, paper SPE 22725

18. Howard AQ (1992) A new invasion model for resistivity log interpretation. The Log Analyst 33(2):96–110

19. Tabarovsky L, Rabinovitch M (1996) High-speed 2-D inversion of induction log data. Trans SPWLA 37th Annual Logging Symposium, paper P

20. de Groot-Hedlin CD (2000) Smooth inversion of induction logs for conductivity models with mud filtrate invasion. Geophysics 65(5):1468–1475

21. Dyos CJ (1987) Inversion of the induction log by the method of maximum entropy. Trans SPWLA 28th Annual Logging Symposium, paper T

22. Barber TD, Broussard T, Minerbo GN, Sijercic Z, Murgatroyd D (1999) Interpretation of multi-array induction logs in invaded formations at high relative dip angles. The Log Analyst 40(3):202–217

23. Fishburn T, Geldmacher I, Rabinovitch M, Tabarovsky L (1998) Practical inversion of high-definition induction logs using a priori information. Trans SPWLA 39th Annual Logging Symposium, paper WW

24. Barber TD, Howard AQ (1989) Correcting the induction log for dip effect. Presented at the 64th SPE Annual Technical Conference and Exhibition, paper SPE 19607

25. Xiao J, Geldmacher I, Rabinovitch M (2000) Deviated-well software focusing of multi-array induction measurements. Trans SPWLA 41st Annual Logging Symposium, paper DDD

26. Moran JH, Gianzero S (1979) Effects of formation anisotropy on resistivity logging measurements. Geophysics 44(7):1266–1286

27. Anderson B (1995) The response of induction tools to dipping, anisotropic formations. Trans SPWLA 36th Annual Logging Symposium, paper D

28. Barber T et al. (2004) Determining formation resistivity anisotropy in the presence of invasion. Presented at the 79th SPE Annual Technical Conference and Exhibition, paper SPE 90526

29. Yu L, Fanini ON, Krieghauser BF, Koelman JMV, van Popta J (2001) Enhanced evaluation of low-resistivity reservoirs using multicomponent induction log data. Petrophysics 42(6):611–623

30. Wang T, Yu L, Krieghauser B, Merchant G (2001) Understanding multicomponent induction logs in a 3D borehole environment. Trans SPWLA 42nd Annual Logging Symposium, paper GG

31. Anderson B (2001) Modeling and inversion methods for the interpretation of resistivity logging tool response. DUP Science, Delft, The Netherlands

32. Krieghauser B, Fanini O, Forgang S, Itskovitch G, Rabinovitch M, Tabarovsky L, Yu L, Epov M (2000) A new multicomponent induction logging tool to resolve anisotropic formations. Trans SPWLA 41st Annual Logging Symposium, paper D

33. Rabinovitch M, Tabarovsky L (2001) Enhanced anisotropy from joint processing of multicomponent and multi-array induction tools. Trans SPWLA 42nd Annual Logging Symposium, paper HH

34. Anderson B, Barber T, Habashy T (2002) The interpretation and inversion of fully triaxial induction data: a sensitivity study. Trans SPWLA 43rd Annual Logging Symposium, paper O

35. Wang H, Barber T, Morriss C, Rosthal R, Hayden R, Markley M (2006)] Determining anisotropic formation resistivity at any relative dip using a multi-array triaxial induction tool. Presented at the 2006 SPE Annual Technical Conference and Exhibition, paper SPE 103113

Problems

8.1 The ILd reads anomalously low in highly conductive beds, e.g., in the bed at 50 ft in Fig. 7.18. If this was a water zone what would be the percentage error in calculating R_w in this zone? If R_w was calculated from the ILd log and used to calculate S_w in the reservoir above what would be the error in S_w?

8.2 The differential vertical geometric factor of a 2-coil array with spacing L at low conductivity (the Doll factor) is $g_z = 1/2L$ between the arrays and $g_z = L/8z^2$ outside the arrays, i.e., for $z = \pm L/2$. Suppose a 40 in. array is sitting in the middle of a bed 80 in. thick, calculate the integrated vertical factor for the shoulder beds.

8.2.1 Suppose the central bed has a conductivity of 100 ohm-m and the shoulder beds have a conductivity of 1 ohm-m, what will the array read in the middle of the bed?

8.3 Why does the 10 in. curve in Fig 8.12 not read R_{xo} even in the thickest bed? Explain the reading using the radial response shown in Fig 8.9.

8.3.1 In which conditions of R_{xo} and R_t would you expect the shallow curves to give a good estimate of R_{xo}?

8.4 Draw the radial profile of conductivity and water saturation from a flushed zone through an annulus to the uninvaded zone. Assume that $\phi = 0.2$, $R_{mf} = 1$ ohm-m, $S_{xo} = 0.8$, $R_w = 0.1$ ohm-m, $S_w = 0.2$, and that the annulus has the same water saturation as the flushed zone but that the water is all formation water.

8.4.1 If the inner diameter of the annulus is 48 in., and the borehole diameter is 8 in., calculate the volume of formation water displaced from the flushed zone and hence the maximum possible thickness of the annulus.

8.4.2 Suppose that there is no annulus in the transition zone, but that within the transition zone the water saturation changes linearly from S_{xo} to S_w, and the water conductivity changes linearly from C_{mf} to C_w. What is the conductivity in the center of the transition zone? (The result shows that it is possible to have an apparent annulus effect on a induction log without there being a physical annulus.)

8.5 To show how the Grimaldi method works draw the differential vertical responses of two 2-coil arrays, centered at the same point, one with 40 in. spacing and the other with 36 in. spacing. Then draw the differential vertical response of the difference

between the two arrays. What normalization factor is needed so that there is no shoulder bed signal?

8.6 In the response of a coplanar array (Eq. 8.6) expand the exponential in ikL to k^4L^4 and express the R- and X-signals in terms of L/δ (as was done for the coaxial array in Eq. 7.50).

8.6.1 For a 40 in. array operating at 20 kHz at what conductivity does the R-signal read zero?

8.7 Use the data in Fig. 8.24 to calculate V_{sh} every 10 feet between X414 ft and X444 ft assuming that R_{sh} is constant at 0.15 ohm-m.

8.7.1 Derive R_{sd} and R_{sh} in terms of R_v, R_h, and V_{sh} from Eqs. 8.7 and 8.8.

9

Propagation Measurements

9.1 INTRODUCTION

The electromagnetic measurements that we have considered in the last four chapters have all operated at relatively low frequencies, 100 kHz or less. At these frequencies the dielectric properties of rocks can safely be ignored in all but extreme cases, thereby simplifying the interpretation. Above these frequencies, dielectric properties play an increasingly important part, so that it is possible to measure not only the conductivity but also the dielectric permittivity of the formation. This is potentially of great interest since one common component of rocks – water – has a far higher permittivity than other components. A device that measures dielectric permittivity is therefore sensitive to the amount of water and can distinguish it from oil or gas.

Several devices that operate from tens of MHz to GHz were built for this purpose in the 1970s and 1980s but unfortunately none became widely accepted. In practice their interpretation was complicated by the borehole environment and the effects of rock texture. A new device measures permittivity and conductivity at several frequencies in order to determine aspects of the rock texture in addition to fluid content.

As frequency increases the signals induced in the receiver are increasingly phase shifted and attenuated. At induction frequencies this was referred to as skin effect and treated as a small correction. At higher frequencies the correction is no longer small; in fact the skin effect is high enough that we can easily measure the phase shift and attenuation directly, and derive conductivity and dielectric permittivity from them. This technique has been put to wide use in LWD devices operating up to 2 MHz.

All high-frequency devices rely on measuring the propagation characteristics of electromagnetic waves, in other words phase shift and attenuation rather than absolute

signal level. For this reason they are known as propagation tools. This chapter reviews the characteristics of dielectrics and the dielectric properties of rocks, and then discusses the devices that measure them.

9.2 CHARACTERIZING DIELECTRICS

One electrical property of material that is of interest for logging applications is usually associated with insulators: the dielectric constant or dielectric permittivity. The implication of the dielectric constant of a material can be best understood from a familiar application. It consists of the use of a dielectric material to increase the capacitance of a condenser such as that shown in Fig. 9.1. Without the dielectric material between the parallel plates, the capacitance C is given by:

$$C = \frac{\epsilon_o A}{d} , \tag{9.1}$$

where A is the area of the plates, ϵ_o is the dielectric permittivity of free space, and d the separation. The charge Q, stored on the plates, and the voltage V are related by:

$$Q = CV . \tag{9.2}$$

It is observed that when a dielectric material is placed between the plates of a parallel capacitor, and the charge is held constant, the voltage drops. Since the voltage is the integral of the electric field across the plates, it is apparent that the electric field somehow decreases.

The explanation for this lies in the polarizability of the atoms which make up the insulating dielectric. Under the influence of an applied electric field, positive charges are displaced with respect to the negative. In the presence of the applied electric field, the charge q can be imagined to physically separate a distance δ, thereby creating a number of dipoles, each of dipole moment $q\delta$. If N is the total number of atoms per cubic meter, then the dipole moment per unit volume P is:

$$P = Nq\delta . \tag{9.3}$$

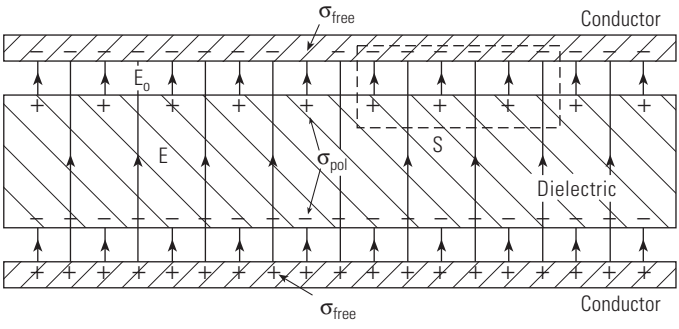


Fig. 9.1 A parallel plate capacitor containing a dielectric material. From Feynman et al. [1].

Despite the charge separation at each atom, there will be charge neutrality throughout the volume of the material, except for the outer layer of thickness δ, where a surface charge is present. The surface charge density can be found from the total number of excess charges in the layer of thickness δ, which is given by $N\delta A$, where A is the surface area. Since the charge associated with each dipole is q, the surface charge density (charge per unit area) is just $N\delta q$. This is numerically equivalent to the dipole moment/unit volume. The reduction in electric field inside the dielectric can be seen with reference to the surface sketched by a dotted line in Fig. 9.1. From Gauss' law, the electric field outside of this enclosed volume is given by the contained net charge divided by ϵ_o. In this case, the volume contains two surface charges: a negative one of free charge, which has been stored on the capacitor plates, and a positive one on the surface of the dielectric, which has been induced. As the two are opposite in sign, the field is found to be:

$$E = \frac{\sigma_{free} - \sigma_{pol}}{\epsilon_o}, \tag{9.4}$$

from which it is apparent why the electric field decreases when a dielectric is placed between the plates.

In all substances except a few such as ferroelectrics, the polarization density (number of induced dipoles/unit volume) is proportional to the applied electric field, providing it is not excessive:

$$P = \chi \epsilon_o \overline{E}, \tag{9.5}$$

where the constant of proportionality χ is known as the electric susceptibility. This equation holds in the frequency domain. In the time domain, the polarization at a given time depends on the field at previous times, and a convolution over time is necessary.

The susceptibility is usually quoted in terms of permittivity. The two are related through Maxwell's equations. Before the existence of the polarization charge was appreciated, these equations were defined in terms of the total electric flux per unit area, or electric displacement $\overline{D}$, which is a linear combination of the electric field vector and the polarization density:

$$\overline{D} = \epsilon_o \overline{E} + \overline{P}, \tag{9.6}$$

leading to the following relationship between $\overline{D}$ and $\overline{E}$:

$$\overline{D} = \epsilon_o(1 + \chi)\overline{E} = \epsilon' \epsilon_o \overline{E}, \tag{9.7}$$

in which ϵ' is defined as the relative dielectric permittivity, but often referred to as the dielectric constant. The (total) dielectric permittivity is then given by:

$$\epsilon = \epsilon' \epsilon_o = (1 + \chi)\epsilon_o. \tag{9.8}$$

Table 9.1 gives ϵ' for a number of substances. Of all those listed it can be seen that water has the highest value. There is a large difference between the relative permittivities of oil and water, which is one of the motivations for making a dielectric logging measurement. To understand why water is so different we need to examine dielectric properties at the microscopic level.

Table 9.1 Relative dielectric permittivity ϵ' and propagation time t_{pl} for various materials. t_{pl} is an output of the EPT* tool (see Section 9.5).

Material	ϵ'	$t_{pl}(ns/m)$
Sandstone	4.65	7.2
Dolomite	6.8	8.7
Limestone	7.5–9.2	9.1–10.2
Anhydrite	6.35	8.4
Dry colloids	5.76	8.0
Halite	5.6–6.35	7.9–8.4
Gypsum	4.16	6.8
Petroleum	2.0–2.4	4.7–5.2
Shale	5–25	7.45–16.6
Fresh water at 25°C and below 10^{10} Hz	78.3	29.5

*Mark of Schlumberger

9.2.1 Microscopic Properties

So far we have discussed dielectric properties in terms of macroscopic quantities such as χ and ϵ, but these are in fact the sum of several microscopic properties. There are four main phenomena that contribute to the permittivity (Fig. 9.2): the displacement of the electron cloud that surrounds atoms, the relaxation of ions bound in a lattice, the coherent orientation of preexisting microscopic dipoles, and the effect of polarization at interfaces. As shown in Fig. 9.3 each type of polarization disappears above a certain frequency, which is determined by the inertial moment of the particle in question, frictions and electrostatic forces. In normal oilfield rocks, ionic relaxation (which is important in crystals) can be ignored. In general, the relation between macroscopic and microscopic properties is not trivial. For our purposes it is important to have a qualitative understanding of the microscopic properties, but for quantitative interpretation of logging measurements, the macroscopic quantities are sufficient.

Electronic polarization is caused by the displacement of the electron cloud surrounding an atom under an oscillating electric field. Due to the small mass of the electron the cloud is able to follow the oscillations of the field and contribute to polarization up to very high frequencies.

Molecular orientation occurs in molecules that have a permanent dipole moment. In nonpolar molecules such as oxygen, the centroid of positive charges, from the nuclei, and the negative charges, from the electrons, perfectly overlap (Fig. 9.4). An external electric field will cause electronic polarization but that is all. Water, however, is a polar molecule. There is a naturally occurring geometric separation between the centroids of the positive and negative charges due to the nonsymmetric shape of the molecule. Each molecule, then, is a tiny dipole. Due to thermal agitation, the orientation of these dipoles is at random in the absence of an applied field. However, upon application

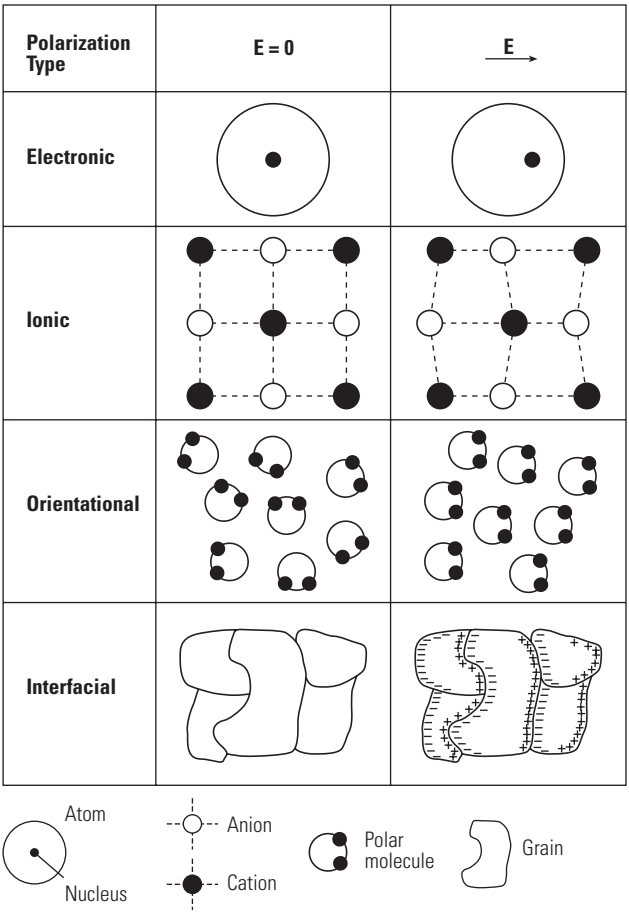


Fig. 9.2 Four types of microscopic polarization, showing the position of the particles before (left) and after (right) the application of an electric field. Ionic relaxation is not of concern in oilfield rocks, but the others are. Adapted from Orlowska [2].

of an external electric field, the dipoles will tend to align and produce a rather large dipole moment per unit volume.

Frequency, temperature, and salinity all have important effects on the dielectric permittivity of water. As the frequency of the external field increases, the water molecules have an increasingly hard time to follow the field and their contribution to the polarization decreases and eventually disappears. As the temperature increases, thermal agitation reduces the interaction between the dipoles and the electric field, and therefore reduces the permittivity. At the same time the molecules can reorient themselves faster, so that they contribute to the polarization at higher frequencies.

These two effects can be seen in Fig. 9.5 for pure water. This figure also shows that molecular orientation (like other microscopic polarizations) is a relaxation

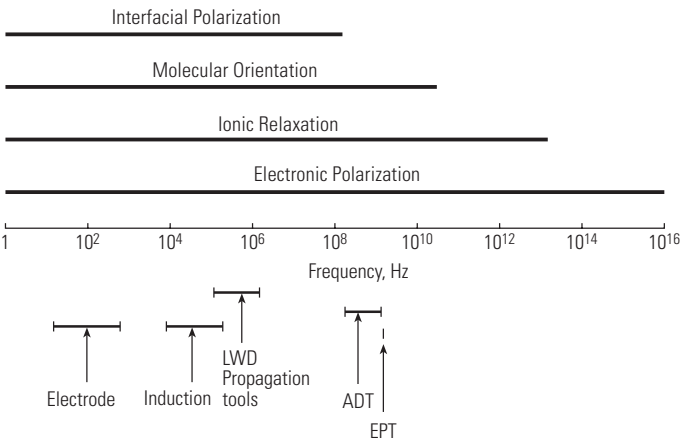


Fig. 9.3 The frequency range over which different types of polarization are effective. Also indicated are the ranges over which various logging devices operate. ADT indicates an array dielectric tool. From Hizem [3]. Courtesy of Schlumberger.

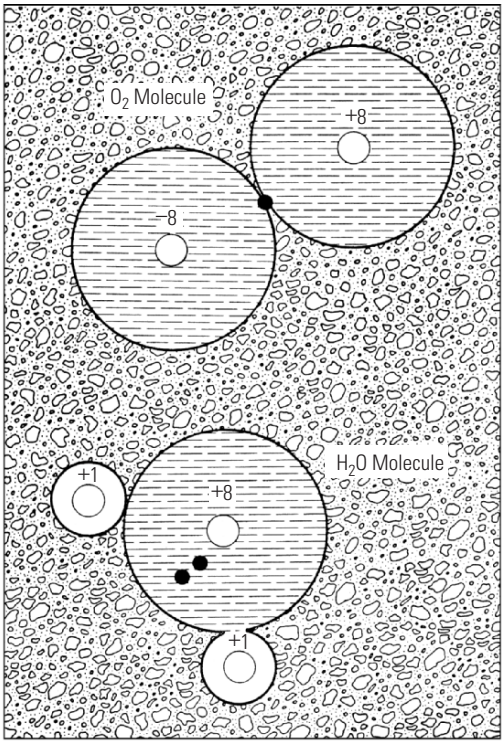


Fig. 9.4 A schematic representation of the charge distribution of the O_2 and H_2O molecules. Because of the position of the hydrogen, water shows a large polarizability.

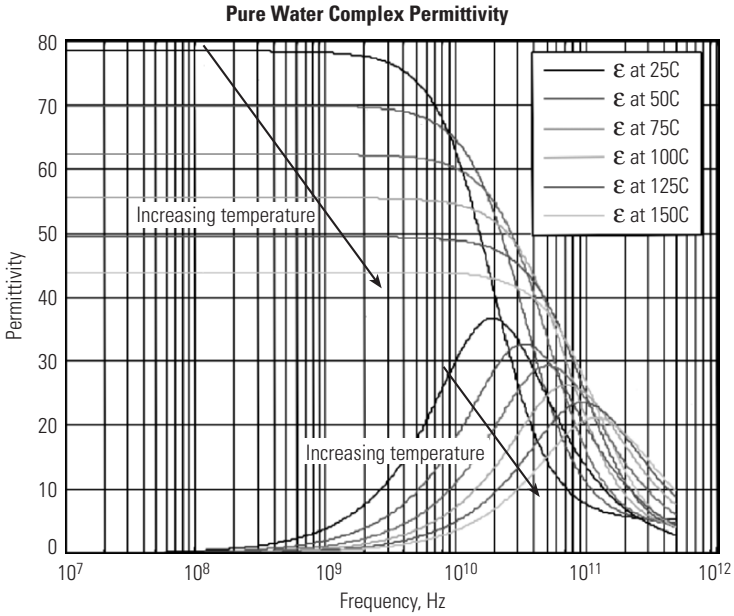


Fig. 9.5 The real (top) and imaginary (bottom) part of the relative dielectric permittivity of pure water as a function of frequency for different temperatures. From Hizem [3]. Courtesy of Schlumberger.

phenomenon. This means that for frequencies at which the water molecules are having a hard time to follow the electric field they absorb energy from the field. This loss of energy is conveniently expressed as the imaginary component of a complex permittivity.

The addition of a salt to water has a number of different effects. First, the concentration of water is reduced. Second, since each salt ion is hydrated (i.e., has a number of water molecules loosely attached to it), the polarization of those water molecules is reduced. Third, the salt ions displace and reorient water molecules when moved by the electric field. The overall result is that the permittivity is reduced, as shown in Fig. 9.6. In theory the permittivity of water can be predicted from a relaxation model, but in practice the model needs to be adjusted with empirical parameters, as was done for the data in Figs. 9.5 and 9.6 [3].

9.2.2 Interfacial Polarization and the Dielectric Properties of Rocks

The third type of microscopic polarization that concerns us is interfacial polarization, also known as the Maxwell–Wagner effect. When a d.c. electric field is applied to a system that contains insulating and conducting components, there is a build-up of charge at the interface between the two materials in the same way as for a capacitor. When the field is removed the ions move around the grains to neutralize the polarization with a characteristic relaxation time (see Fig. 9.7). At low frequencies

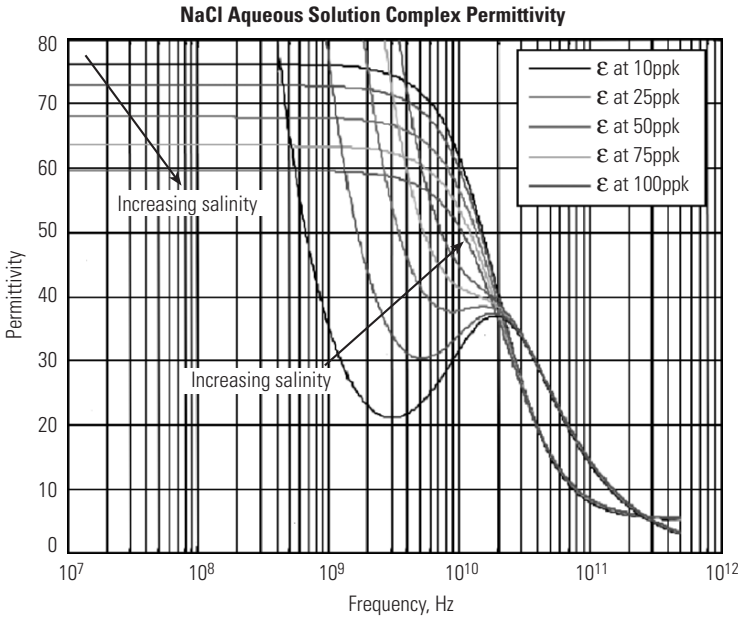


Fig. 9.6 The real (top) and imaginary (bottom) part of the relative dielectric permittivity of water as a function of frequency for different salinities at 25°C. From Hizem [3]. Courtesy of Schlumberger.

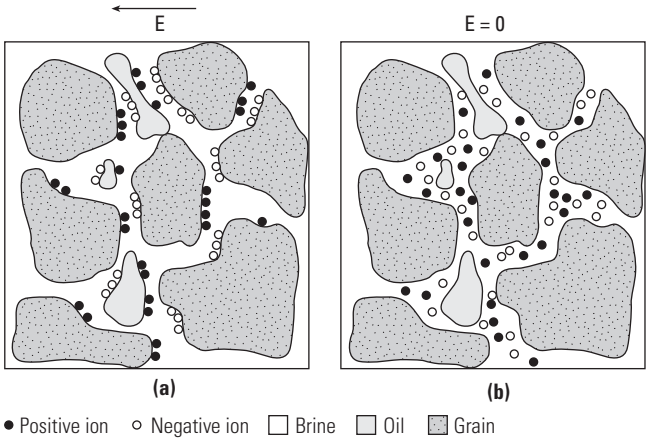


Fig. 9.7 A schematic representation of Maxwell–Wagner polarization with oil and brine in a water-wet rock. Adapted from Bona et al. [4].

the field changes slowly enough that the ions can follow the variations and develop the maximum polarization. At high frequencies there is not enough time for the charge to build up and the effect is reduced. There is also a loss of energy during the charge

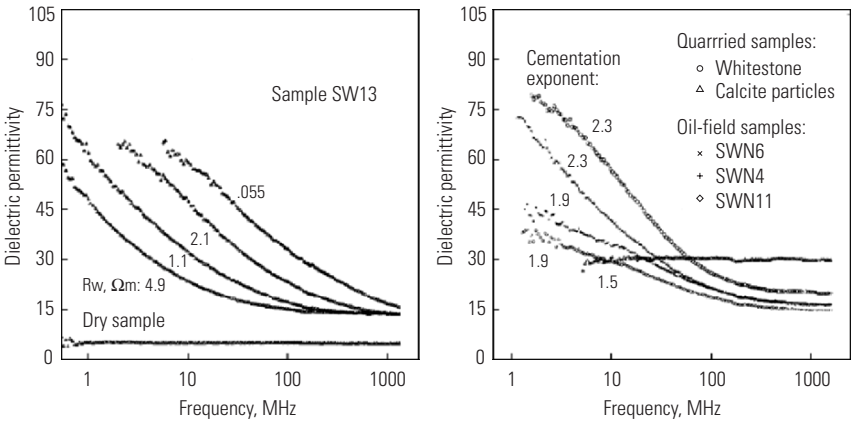


Fig. 9.8 Conductivity and grain shape effects on relative dielectric permittivity. Left panel: relative dielectric permittivity versus frequency for a single oilfield carbonate sample, both dry and saturated with water of different resistivities. Right panel: relative dielectric permittivity vs frequency for 5 carbonate samples at R_w = 1.07 ohm-m. The more plate-like the grains, the higher both the cementation exponent and the permittivity. Adapted from Kenyon and Baker [5].

build-up and dissipation due to frictional and viscous forces, so that the permittivity is a complex number.

Interfacial polarization is affected not only by frequency, but also by water salinity and, in rocks, by the grain shape and pore shape. At high salinity the free charges in the water follow the field variations more easily than the water molecules on their own, so that the polarization is higher at a given frequency. This is illustrated in the results from a sample of carbonate rock shown in the left-hand panel of Fig. 9.8. The difference between the dry sample and the high-frequency limit of the wet samples shows the effect of molecular polarization from the water. The remaining increase is caused by interfacial polarization. It can be seen that the increase due to salinity is approximately the same as the decrease due to frequency.

Thin, platy grains also increase the polarization. The thinner the grain the larger the electrostatic attraction across the grain and therefore the larger the charge build-up. At the same time it is more difficult for the charge to move and neutralize the polarization on the opposite side of the grain when the latter is disk-like rather than spherical. These effects are shown in the right-hand panel of Fig. 9.8 for different samples filled with the same salinity water. The polarization is greatest when the cementation exponent m is greatest, since in both cases the more platy the grains the more tortuous the electrical path. Other mechanisms than the Maxwell–Wagner effect have been suggested to explain large values of ϵ in rocks [6]. For example, clays can have high permittivities, not only because they contain platy gains but also because of their surface charge and the ions in the surrounding electrical double layer.

The permittivity of water-filled rocks below 10^{12} Hz can therefore be summed up as follows: matrix permittivity is controlled by electronic polarization and is constant

within the frequency range of well logging; water permittivity is dominated by molecular orientation up to about 10^{10} Hz after which there is only electronic polarization; and the total rock permittivity is controlled by interfacial polarization up to about 10^8 Hz above which it becomes negligible.

So far no mention has been made of the effect of hydrocarbons. Oil has dielectric properties that are similar to the grains and has a similar effect (as was already illustrated in Fig. 9.7). It is therefore the shape of oil droplets and their distribution, particularly as expressed in the wettability, that have the most effect on the overall rock properties.

9.3 PROPAGATION IN CONDUCTIVE DIELECTRIC MATERIALS

Having reviewed the dielectric properties of rocks we now turn to the propagation of electromagnetic waves and the parameters that define it. We begin with a succinct summary of the principal results. An e-m wave propagating in the x-direction changes amplitude and phase according to:

$$E(x,t) \;=\; E_o\, e^{-\beta x} e^{i(\alpha x \,-\, \omega t)} \;=\; E_o\, e^{ikx}\, e^{-i\omega t} \tag{9.9}$$

where β is the attenuation per meter, α is the phase shift per meter, $k \;=\; \alpha + i\beta$ is the complex propagation coefficient or wavenumber, and ω is the angular frequency. Note that this is the same expression as for the skin effect loss δ of the induction tool considered in Chapter 7, except that when dielectric permittivity is ignored $\alpha = \beta = 1/\delta$.

Dielectric logging tools measure α and β but these are related to the relative dielectric permittivity ϵ' and conductivity σ through the propagation coefficient:

$$k^2 \;=\; \omega^2 \mu \epsilon_o (\epsilon' \;+\; i \frac{\sigma}{\omega \epsilon_o}) \tag{9.10}$$

where μ is the magnetic permeability. Dielectric measurements can therefore be converted into ϵ' and σ. This equation can also be written as:

$$k^2 \;=\; \omega^2 \mu \epsilon_o (\epsilon' \;+\; i\epsilon'') \,. \tag{9.11}$$

Values of ϵ' were shown in Table 9.1. The imaginary part, $\epsilon'' = \sigma/\omega\epsilon_o$, includes both the losses from different polarization mechanisms and the charge transport that gives rise to d.c. conductivity. The dependence of the imaginary part on σ explains the strong dependence on salinity of the experimental data in the bottom portion of Fig. 9.6. In a similar way charge transport in rocks is not purely conductive and contributes to ϵ'. In sum, the real component ϵ' represents the electrical storage capacity of the rock while the imaginary component ϵ'' represents its energy dissipation. The symbol ϵ^* is used for the complex permittivity $(\epsilon' \;+\; i\epsilon'')$, so that for a plane wave:

$$k \;=\; \omega\sqrt{\mu\epsilon_o}\,\sqrt{\epsilon' \;+\; i\epsilon''} \;=\; \omega\sqrt{\mu\epsilon_o}\,\sqrt{\epsilon^*} \tag{9.12}$$

The remainder of this section explains the relationship between these quantities and the derivation of the equations above.

We will proceed much as for the derivation of skin effect in Chapter 7. In that earlier example, we were only concerned with a material that was a pure conductor. For our more general case, Maxwell's equations are somewhat modified, to account for the displacement current associated with the polarization of the material. The Maxwell equation linking the magnetic field to the currents is now written as:

$$\nabla \times \overline{H} = \overline{J} - i\omega\overline{D}\,, \tag{9.13}$$

where the time dependence of all vector quantities is represented by $e^{i\omega t}$*. The constitutive equations which link the material properties* σ, μ, *and* ϵ *to the basic vector quantities are simply:*

$$\overline{J} = \sigma\overline{E}\,, \tag{9.14}$$

$$\overline{B} = \mu\overline{H}\,, \tag{9.15}$$

and

$$\overline{D} = \epsilon\overline{E}\,. \tag{9.16}$$

Using these relationships, Eq. 9.13 can be written as:

$$\nabla \times \overline{H} = \frac{1}{\mu}\nabla \times \overline{B} = \sigma\overline{E} - i\omega\epsilon\overline{E}\,, \tag{9.17}$$

or

$$\nabla \times \overline{B} = (\mu\sigma - i\omega\mu\epsilon)\overline{E}\,. \tag{9.18}$$

From another of Maxwell's equations (Eq. 7.38) we have:

$$\nabla \times \overline{E} = -\frac{\partial\overline{B}}{\partial t} = i\omega\overline{B}\,. \tag{9.19}$$

As before, for the skin depth example, we take the curl of both sides of the equation:

$$\begin{aligned}\nabla \times \nabla \times \overline{E} &= i\omega\,\nabla \times \overline{B} = i\omega(\mu\sigma - i\omega\mu\epsilon)\overline{E} \\ &= (\omega^2\mu\epsilon + i\omega\mu\sigma)\overline{E}\,,\end{aligned} \tag{9.20}$$

from the result obtained in Eq. 9.18. The left side of Eq. 9.20 can be simplified by using the vector identity:

$$\nabla \times \nabla \times \overline{E} = \nabla(\nabla \cdot \overline{E}) - \nabla^2\overline{E} = -\nabla^2\overline{E}\,, \tag{9.21}$$

since there are no free charges so that $\nabla \cdot \overline{E} = 0$.

Thus the final result is:

$$\nabla^2\overline{E} + (\omega^2\mu\epsilon + i\omega\sigma\mu)\overline{E} = 0\,, \tag{9.22}$$

or for the much simpler one-dimensional case:

$$\frac{\partial^2 E}{\partial x^2} + (\omega^2\mu\epsilon + i\omega\sigma\mu)E = 0\,. \tag{9.23}$$

This is the wave equation for an $E-M$ wave traveling in the x-direction in a medium characterized by a magnetic permeability μ, conductivity σ, and dielectric constant ϵ. A solution to this equation is the expression for a traveling wave:

$$E(x,t) = E_o e^{i(kx - \omega t)}, \tag{9.24}$$

as can be verified by substitution. The wave number or propagation constant k must then satisfy the requirement that:

$$\begin{aligned} k^2 &= \omega^2\mu\epsilon + i\omega\sigma\mu \\ &= \omega^2\mu(\epsilon + i\frac{\sigma}{\omega}) . \end{aligned} \tag{9.25}$$

This relationship implies that the wave number k will be a complex number which can be represented as:

$$k = \alpha + i\beta . \tag{9.26}$$

The relationship between k and the attenuation and phase shift of the transmitted plane wave can be seen by substituting this expression into the traveling wave solution, which yields the result quoted at the beginning of the section:

$$E(x,t) = E_o\, e^{-\beta x} e^{i(\alpha x - \omega t)} . \tag{9.27}$$

Thus an e-m wave travelling over a distance x will be attenuated by a factor $e^{-\beta x}$ and suffer a phase shift of αx radians or α radians per meter. For the case of a plane wave, it is possible to extract σ and the dielectric constant ϵ from the measured values of β and α. This is done by referring to the definition of α and β:

$$k^2 = (\alpha + i\beta)^2 = \omega^2\epsilon\mu + i\omega\mu\sigma , \tag{9.28}$$

which is equivalent to Eq. 9.10. By separating the real and imaginary parts (Problem 9.1) it can be shown that:

$$\epsilon = \frac{\alpha^2 - \beta^2}{\omega^2\mu} \tag{9.29}$$

and

$$\sigma = \frac{2\alpha\beta}{\omega\mu} . \tag{9.30}$$

Thus from a measurement of the attenuation and phase shift of an e-m plane wave, we can in principle obtain the original desired quantities, ϵ and σ.

9.4 DIELECTRIC MIXING LAWS

Much effort has gone into finding out how to express dielectric properties in terms of the volumes of different formation components – the so-called mixing laws. One advantage with dielectric measurements is that the largest volume, the matrix, plays

only a small role (unless it contains clay, in which case its role is significant). Otherwise, the mixing laws are complicated, especially when they try to predict dielectric properties over a range of frequencies. There are two main approaches, one based on effective medium theories and one that uses a power law. Power law equations have the following form:

$$\epsilon_{eff}^{1/m} = \sum_{n=1}^{N} \phi_n \epsilon_n^{1/m} \tag{9.31}$$

for a medium with N components and exponent m. For linear volumetric mixing, $m = 1$. Various values have been used for m, but a value of two has proved particularly useful. When written out in terms of normal rock volumes this equation becomes:

$$\sqrt{\epsilon_{eff}^*} = \phi S_w \sqrt{\epsilon_w^*} + \phi(1 - Sw)\sqrt{\epsilon_h} + (1 - \phi)\sqrt{\epsilon_{ma}}\,, \tag{9.32}$$

where the subscripts eff, w, h, and ma refer to the total rock, water, hydrocarbons, and matrix, respectively. This method is known as the complex refractive index method (CRIM) since from Eq. 9.12, $\sqrt{e^*} \propto k$, and so the equation is linear in k, which is also known as the refractive index.

Of the many mixing laws that have been proposed, CRIM has often proved to be the most successful for frequencies around 1 GHz. In this region, where interfacial polarization can be ignored, the permittivity responds to the total water volume, whether it is connected or not. (The conductivity may therefore be responding to a different water volume than that of an induction or laterolog.) After measuring the dielectric properties of carbonate samples at 1 GHz and comparing the results with those predicted by different mixing laws, Seleznev et al. concluded that CRIM gave the most satisfactory agreement in clay-free carbonates [7]. Figure 9.9 shows one of their results.

The CRIM equation can be separated into real and imaginary parts and solved for two unknowns, normally water saturation and water salinity, using the known relations of ϵ^* with salinity and temperature. The matrix is assumed to nonconductive and known from other logs. Porosity is taken from another source. Conductive minerals like clays are normally treated by including a term for their bound water. It is interesting to note that at low frequency, where conductivity dominates, Eq. 9.32 reduces to $\sigma = \phi^2 S_w^2 \sigma_w$, which is Archie's law with an exponent of 2 (Problem 9.2). It may not be coincidence that at the two extremes of frequency the same exponents are found.

CRIM does not do so well below 1 GHz, which is not surprising since it is unlikely that interfacial polarization can be explained simply by the volume of components. Parameters related to the texture of the rock will be needed to explain these effects. There is no obvious way to add such parameters to power law equations, but there is with effective medium theories. These theories calculate the dielectric response of a material consisting of a background into which inclusions are placed, for example pores inserted in a matrix. Different assumptions can be made as to whether the background should be the matrix, the pore network or some other composite.

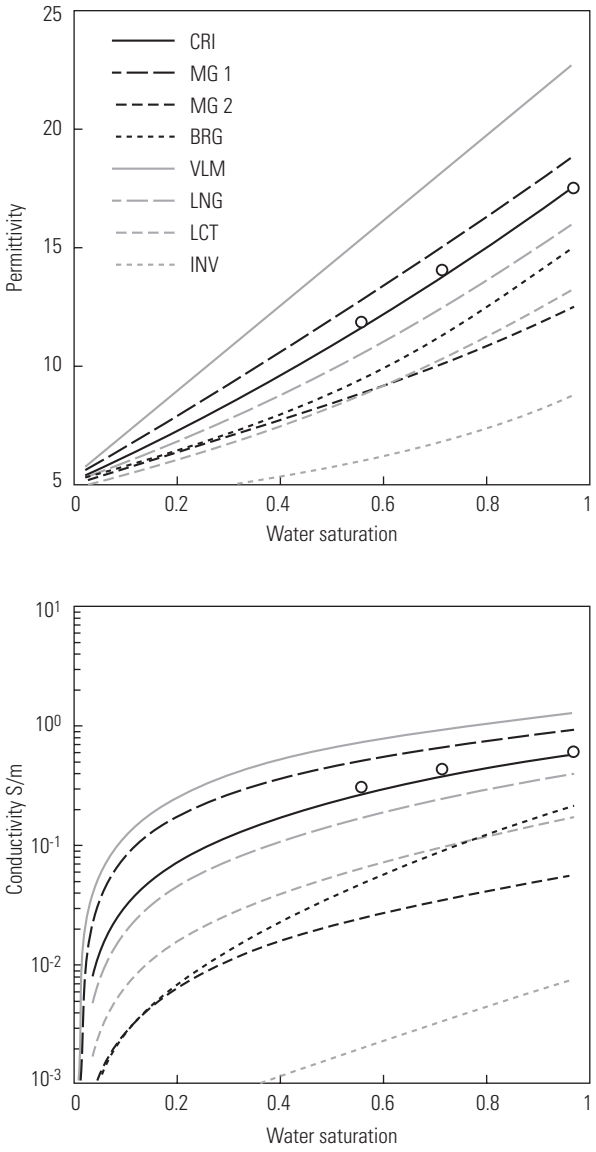


Fig. 9.9 The relative permittivity and conductivity of a carbonate sample at partial saturations compared with various mixing models: the circles are the measured data; "CRI" is the complex refractive index model; "MG1" is the Maxwell–Garnett model with the water phase as background; "MG2" is the Maxwell–Garnett model with the solid phase as background; "BRG" is the Bruggeman model; "VLM" is the volumetric model; "LNG" is the Looyenga model; "LCT" is the Lichtenecker model; "INV" is the inverse model, with an exponent of -1. See Seleznev et al. for details [7]. From [9]. Used with permission.

In the simplest case the effective medium consists of spherical inclusions of only one type. However, the equations can be readily expanded to handle ellipsoidal inclusions that may be of different types, for example oil- and water-filled pores.

For all but the simplest situation, the equations are complicated and we will not attempt to derive them here. They can be generalized into one equation for the case of spherical inclusions [7]:

$$\frac{\epsilon_{eff} - \epsilon_b}{3\epsilon_a + (\epsilon_{eff} - \epsilon_b)} = \sum_{n=1}^{N} \phi_n \frac{\epsilon_n - \epsilon_b}{3\epsilon_a + (\epsilon_n - \epsilon_b)} \tag{9.33}$$

where $\epsilon_a = \epsilon_b + \eta(\epsilon_{eff} - \epsilon_b)$ and the subscript b refers to the permittivity of the background. The different assumptions about the background are handled by setting different values for η. For example, $\eta = 0$ leads to the Maxwell–Garnett equation [8], in which one phase, e.g., the solid matrix, is the background and the pores are discontinuous inclusions. Implicit in the above equation is an expression for the polarizability of a sphere. For ellipsoids the polarizability must be described in terms of three depolarization factors, one for each axis. The ellipsoids are normally simplified as oblate spheroids (which have two equal large semi-axes) or prolate spheroids (which have two equal small semi-axes). In both cases the ellipsoid can be described in terms of a single aspect ratio (the ratio of the major to minor axis). The three depolarization factors then modify the expression $(\epsilon_n - \epsilon_b)$ in the above equation. The overall result is that the effective permittivity depends on the aspect ratios of the different types of inclusion.

The effective medium approach can be applied in different ways. Seleznev et al. assumed that the background obeyed the CRIM mixing law to which was added ellipsoid inclusions of grains, water, and hydrocarbons as illustrated in the cartoon of Fig. 9.10 [9]. With measurements at multiple frequencies in the range from

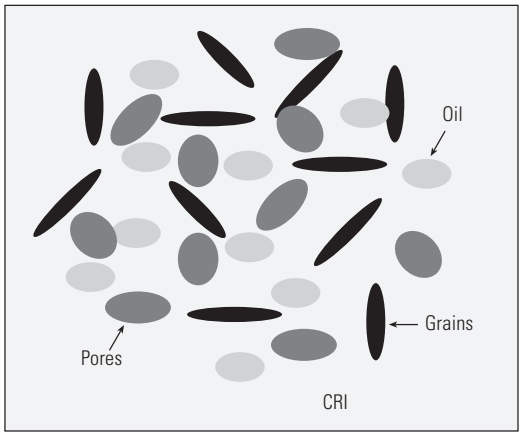


Fig. 9.10 Graphical representation of an effective medium mixing law. The oblate grains, water-filled and oil-filled pores are randomly distributed in a background medium described by the CRI model. From [9]. Used with permission.

1 to 1,000 MHz there is enough independent data to invert the equation and solve for the aspect ratio of one or more component, and other quantities such as water salinity and water saturation. With these parameters, the equation can be used to compute the low frequency rock conductivity from which the cementation exponent, m, can be calculated using Archie's equations.

To sum up, there is reasonable confidence in the CRIM method at 1 Ghz. From there down to 1 MHz there is some hope that effective medium theories can provide a reliable basis of interpretation. If they prove satisfactory, dielectric measurements can add valuable information on rock texture. The effect of clay, however, has not yet been implemented in a mixing law. Also, although there is an abundance of laboratory data, it is only recently that the results have been applied to downhole log data.

9.5 THE MEASUREMENT OF FORMATION DIELECTRIC PROPERTIES

Table 9.1 showed why there is interest in the measurement of the dielectric permittivity: nearly an order of magnitude separates the values of water from other formation constituents. This feature provides an alternative means of evaluating water saturation, which is of particular interest in cases where the formation water is relatively fresh or variable. In such cases resistivity-based methods are difficult because of the small and uncertain contrast between hydrocarbons and water. Permittivity is also of interest in evaluating zones where the water salinity is unknown, as might be the case in secondary recovery projects where water injection has altered the formation water.

Up to this point, we have not considered how the dielectric permittivity might actually be measured for porous rocks saturated with conductive fluids. At low frequencies conduction masks the dielectric effect. However, at very high frequencies, the dielectric properties will dominate. This is not immediately obvious from plots such as Fig. 9.8 since the permittivity is always seen to decrease with frequency. The reason is that ϵ' must be compared with $\frac{\sigma}{\omega\epsilon_o}$ and not σ (Eq. 9.10). At laterolog and induction frequencies the second term dominates, but at higher frequencies its importance diminishes (Problem 9.3). Devices designed to measure dielectric properties therefore operate at frequencies between 10 MHz and 2 GHz. Above this frequency range the depth of investigation becomes too small to be useful.

The electromagnetic propagation tool (EPT) appeared in the later 1970s, and was one of the earliest devices to measure dielectric properties. It operates at a frequency of 1.1 GHz and, because of the close spacing of the two receiver antenna (4 cm), has very good vertical resolution [10]. The antennas are mounted on a mandrel that is pressed against the borehole wall. The depth of investigation depends on the skin depth of the microwaves as well as the antenna spacing, and ranges from about 5 cm in low resistivity formations to 30 cm in high resistivity, lossless formations [11]. The EPT tool therefore evaluates the invaded zone. EPT logs are recorded in terms of propagation time (which is directly related to the phase shift) and attenuation, rather than permittivity and conductivity. The logs were interpreted using the CRIM equation and other methods [12].

The EPT tool is thought of as a device for evaluating formations with fresh water, because in freshwater conditions a dielectric measurement makes a clearer distinction than resistivity between oil and water zones. However, it is responding to the lower oil saturation in the invaded zone. Naturally this works best in heavy oil reservoirs where very little oil is displaced by invasion. In more saline conditions the S_{xo} from the EPT measurements can be combined with R_{xo} to give an estimate of cementation exponent m, by working backwards through Archie's equation and assuming the saturation exponent n. More generally with three measurements (attenuation and phase shift at EPT frequency, R_{xo} at low frequency) it is possible to solve for three unknowns, for example S_{xo}, water salinity and a texture parameter such as m. The water salinity measurement can be interesting in heterogeneous rocks in which not all the formation water has been flushed from the invaded zone. The EPT sees the total water volume, connected or not, whereas the R_{xo} measurement sees the connected water.

Although much research has been done on the dielectric properties of rocks, the enthusiasm of the oil industry to run dielectric logs has so far been tempered by the limitations of the measurement. By the end of the 1990s EPT logs had become a rare speciality, partly because of environmental effects, partly because the dielectric response of rocks had often proved to be more complicated than expected, and possibly because R_{xo} measurements were found to give a sufficiently accurate S_{xo} in most conditions. Several dielectric devices have been designed to investigate beyond the invaded zone [13, 14]. For this they need to operate in the 10–50 MHz range. Unfortunately none of these devices gained acceptance due partly to the difficulty of interpretation and partly to environmental effects, which can be especially difficult to handle as the invaded zone acts as a waveguide in this frequency range.

The most recent device is a pad-mounted tool consisting of two transmitters and eight receivers placed symmetrically above and below (Fig. 9.11). Each transducer consists of two colocated magnetic dipoles that are highly isolated and mounted perpendicular to each other. In one direction the dipoles are aligned coaxially to give the so-called endfire mode, and in the other direction they are coplanar to give the broadside mode. Also present is a pair of electric dipoles which are used in propagation mode to give a very shallow depth of investigation, or in reflection mode to measure the mudcake or other material directly in front of the pad.

The symmetric design allows full borehole correction and compensation for pad tilt. By processing the array data, the effect of the invaded zone can be distinguished from that of the mudcake. Figure 9.12 shows a log run with this device at three frequencies between 100 MHz and 1 GHz. The two central tracks show the

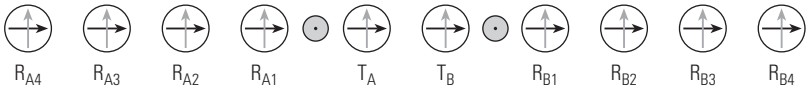


Fig. 9.11 Layout of an array dielectric device. The transducers are laid along the long axis of a pad that is pressed against the borehole wall. Each transducer has two crossed magnetic dipoles. T = transmitter, R = receiver. The two circles between the transmitters and receivers are electric dipoles. Courtesy of Schlumberger.

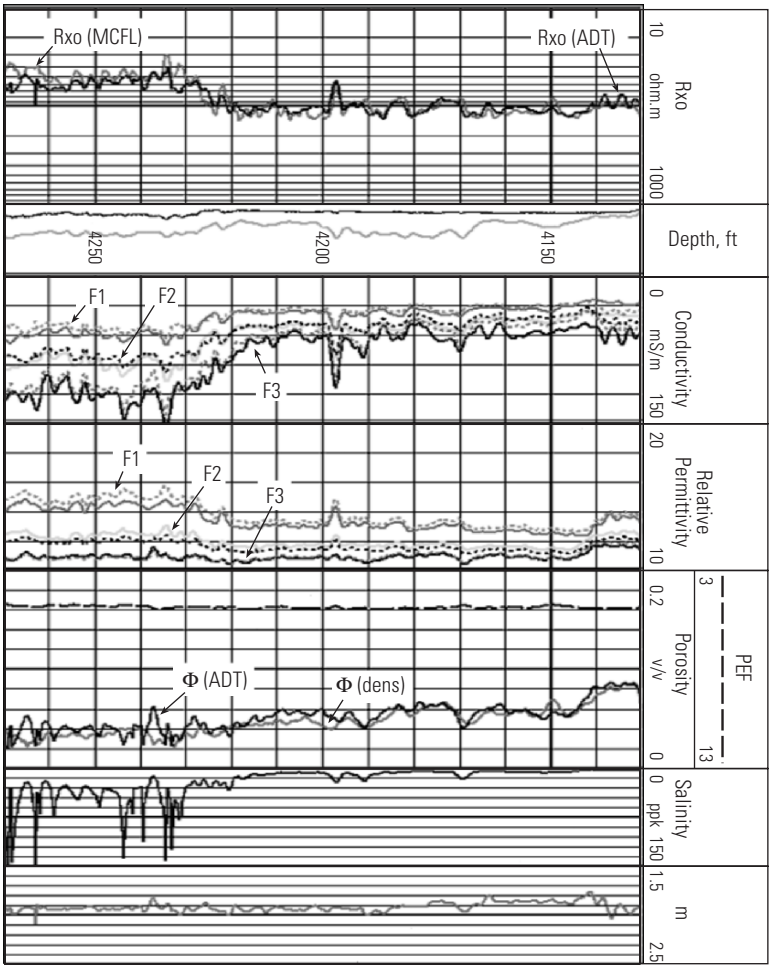


Fig. 9.12 A log recorded by an array dielectric device through a water-filled carbonate formation. The conductivity and permittivity are measured at three frequencies and passed through an interpretation model to determine water-filled porosity, salinity, m and R_{xo}. The solid lines in tracks 2 and 3 are the mudcake corrected measurements; the dotted lines are the logs reconstructed from the model results. From Hizem [3]. Courtesy of Schlumberger.

conductivity and relative permittivity at the three frequencies after mudcake correction. Using these six measurements and a suitable model such as the one described at the end of Section 9.4, the data was inverted to give matrix permittivity, water-filled porosity, water salinity and cementation exponent (see the bottom tracks in Fig. 9.12). In this case the formation was known to be water filled, but the salinity of the water near the borehole was not known. The computed porosity agrees well with that calculated from a density log, and the cementation exponent m looks reasonable. R_{xo} was computed from the porosity, salinity, and cementation factor and agrees well with that

measured by an MCFL log. Such examples give hope that the potential of dielectric measurements will be fulfilled.

9.6 2 MHZ MEASUREMENTS

Early electrical measurements on drill strings used the configuration of a short normal or similar device. By the 1980s, it was evident that this was insufficient and that an induction-type device was desirable. However a standard induction measurement was considered impractical in the drilling environment. Induction measurements require an accurate knowledge of the sonde error (the signal generated within the tool, Section 7.10). The steel drill collar is insufficiently conductive to act like the perfectly conducting mandrel of the array induction tool (see Section 8.4.1), with the result that it contributes a significant signal at the receiver that may vary unpredictably in downhole conditions. Furthermore the tight mechanical tolerances required to maintain a stable sonde error were considered too difficult to engineer in the drilling environment.

An induction device was eventually implemented on a drillpipe in 2004 [15]. The "TRIM" tool sits in a side pocket of the drill collar which is lined by a highly conductive metal layer. This shields the tool from the drill collar and effectively removes its influence. This, plus improvements in mechanical design, have led to a viable drillpipe induction measurement. In the meantime, after the large effort put into their development over the last 20 years, propagation devices have become the standard resistivity measurement for the LWD environment.

The first LWD propagation device measured the phase shift between two receivers [16]. A high frequency was desirable in order to increase the skin effect and hence the phase shift, but the higher the frequency the smaller the depth of investigation. The frequency chosen, 2 MHz, was the lowest frequency at which a sufficiently accurate phase shift could be measured. This has since become the standard, although more recent tools also measure at 400 kHz and even 100 kHz. Subsequent devices, such as the CDR* tool, added a measurement of the attenuation between the receivers and a second transmitter, as shown in Fig. 9.13 [17]. The two transmitters are fired sequentially to give up and down measurements that are averaged to compensate for borehole rugosity, as in the borehole compensated sonic log. The design has other advantages. By measuring the difference in signal between two receivers, any transmitter gain variations are canceled out, while the borehole compensation corrects for any receiver gain variations and gives a symmetrical vertical response.

9.6.1 Derivation of the Field Logs

Based on the earlier discussion of dielectric measurements, we might expect the phase shift and attenuation to be combined and converted into dielectric permittivity and conductivity. Using the relationships between Eq. 9.29 and 9.30 we can construct the appropriate chart and find ϵ' and R_t, as shown in Fig. 9.14. This is sometimes done,

*Mark of Schlumberger.

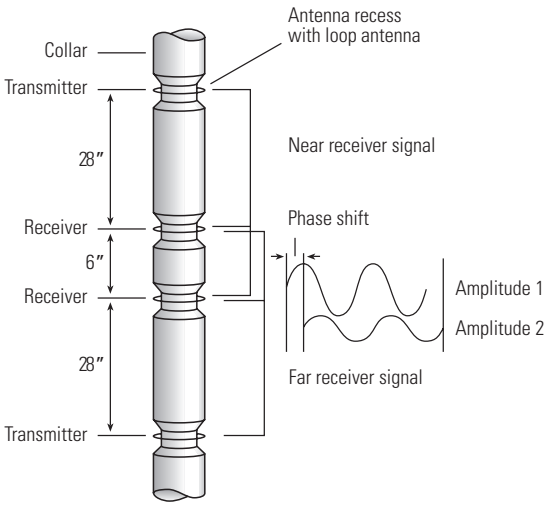


Fig. 9.13 Antenna configuration for the 2 MHz Compensated Dual Resistivity Tool (CDR). The transmitters are fired alternatively, and the phase shift and attenuation measured between the receivers. From Clark et al. [18]. Used with permission.

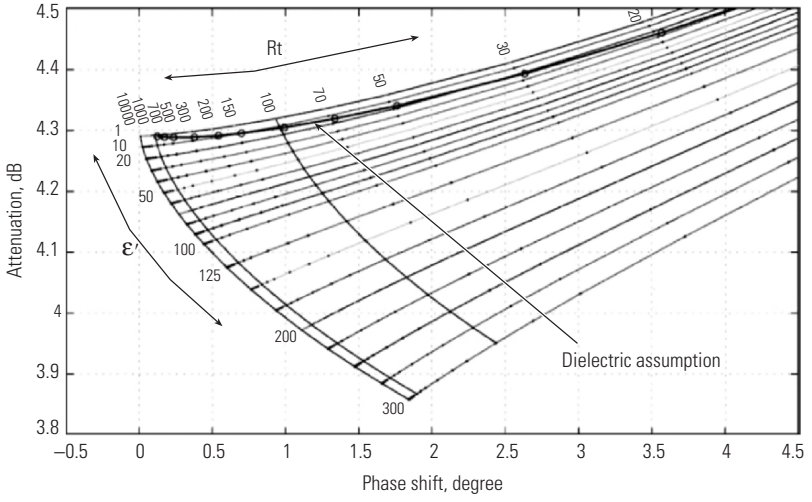


Fig. 9.14 The relationship of dielectric permittivity, ϵ', and resistivity R_t to the phase shift and attenuation measured with a transmitter at 34 in. from the midpoint of the receivers in the "ARC5" tool. The dark line indicates a typical "dielectric assumption" used to relate ϵ' and R. (Note that the assumption drawn is based on a different equation to that shown in Fig. 9.15). Adapted from Wu et al. [19].

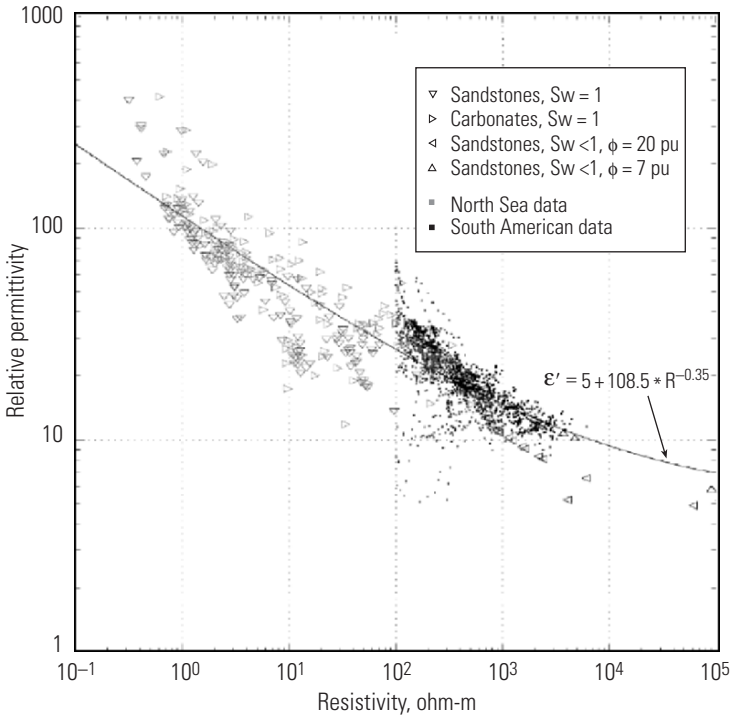


Fig. 9.15 Dielectric permittivity versus resistivity measured at 2 MHz on a wide range of core samples (triangles) and log data (squares). The formula relating ϵ' and R takes into the account the typical value for $\epsilon' = 5$ in zero porosity rock. Adapted from Wu et al. [19].

but more often each signal is transformed into a resistivity: R_{ps} from the phase shift and R_{ad} from the attenuation.

How is this possible? The reason is that at 2 MHz the permittivity term, ϵ', is small in comparison to the conductivity term, $\epsilon'' = \frac{\sigma}{\omega\epsilon_o}$, and can be treated as a correction. Since the amount of water in the formation affects both permittivity and conductivity, there is a rough correlation between the two, as shown in the data from a large number of cores and logs in Fig. 9.15. This correlation leads to a "dielectric assumption," and allows us to convert both phase shift and attenuation into a resistivity. For example, referring to Fig. 9.14, if the phase shift is 3.5° the dielectric assumption gives R_t = 20.5 ohm-m and $\epsilon' = 25$. If ϵ' were actually 50, R_t would be 21 ohm-m, not a large error. The phase shift remains relatively insensitive to ϵ' until the resistivity exceeds a few hundred ohm-m. In this same range, the attenuation becomes independent of resistivity, but remains sensitive to permittivity. Thus at high resistivity it is better not to use the dielectric assumption and to calculate ϵ' and a single R_t.

The chart in Fig. 9.14 could be derived theoretically using the equations for plane waves given in Section 9.3, except that the signals at the receivers are not plane waves, and are influenced by the presence of the drill collar. The signals also include the direct

mutual coupling. This coupling is less than for an induction device, partly because we are only concerned with the difference between the receivers, and partly because the ratio of formation signal to mutual coupling decreases with frequency (refer to Eq. 7.50). In practice the response of the measurements is modeled using an accurate description of the collar and the coils, and is verified in water tanks of different salinity [17]. Small differences between individual tools are handled by calibrating them in air. The result of modeling and calibration is a nonlinear transform of each measurement to resistivity that is then combined with the dielectric assumption to give the chart shown in Fig. 9.14 for one particular type of tool.

The calibration in air is effectively a sonde error measurement. One of the reasons for not using an induction tool was the sonde error, so what is the advantage? Basically, the sonde error is smaller and more stable with the 2 MHz device, because it is a differential measurement so that the transmitter and anything between transmitter and receiver is irrelevant, and because the skin depth inside the collar is less at 2 MHz so that the collar is closer to acting as a perfectly conducting shield. Overall measurement accuracy after calibration is estimated to be 0.03° and 0.005 dB [19]. These can be entered in Fig. 9.14 to gauge the accuracy in terms of resistivity.

Finally, our knowledge of the dielectric properties of rocks would lead us to suspect that the conductivity at 2 MHz is higher than at induction frequency. Several authors have looked for such dispersion but it has rarely been observed [20]. The different environmental effects and the difference in invasion between LWD and wireline time make it difficult to identify with certainty. After a careful analysis of all factors, dispersion has been identified in a few shales [21].

9.6.2 General Environmental Factors

The 2 MHz measurements are affected by the same factors that affect other electromagnetic tools: borehole, invasion, shoulder beds, dip, and anisotropy. Borehole corrections are generally small, especially when the log is recorded while drilling, since the borehole should be close to gauge. (There are exceptions at high or low R_t/R_m, in particular when the tool is eccentered.) Before considering other environmental factors it is useful to examine the variation of tool response with resistivity level.

Figure 9.16 shows where the phase shift and attenuation signals come from in two homogeneous formations of different resistivity. Note that in both cases the phase shift is more focused vertically and reads shallower than the attenuation. But both attenuation and phase shift are measured on the same signals so why do they have a different geometrical response? Figure 9.17 helps understand why. The contours of constant phase are spherical because the wave travels with the same speed in all directions in a homogeneous formation. The contours of constant amplitude are toroids because the transmitter is a vertical magnetic dipole that is characteristically stronger in the radial than the vertical direction. If a shaded arc is followed from one of the receivers near the bottom of the drawings, it can be seen that the toroids penetrate further than the spheres into the formation both vertically and radially. Thus R_{ad} always reads deeper and is less vertically focused than R_{ps}.

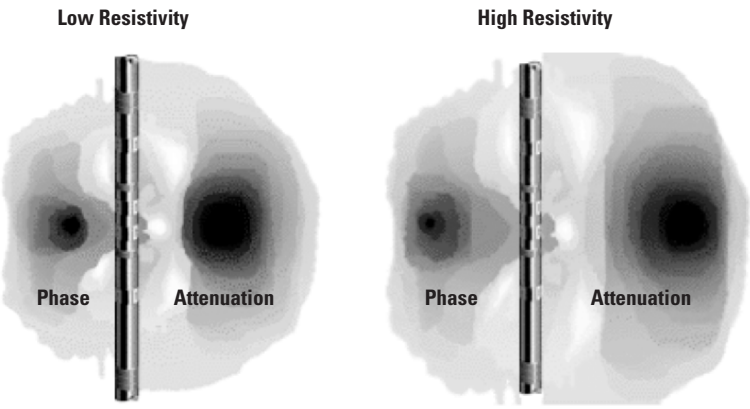


Fig. 9.16 Response of the phase shift and attenuation at $R_t = 2$ ohm-m (left) and 10 ohm-m (right) shown in a different presentation than the usual 3D geometric factor plots. Here the darker the shade the larger the positive response, and the light regions represent negative responses. Calculations are made using the Born approximation. The responses are actually the same at all azimuths around the tool but are shown separately for clarity. Courtesy of Schlumberger.

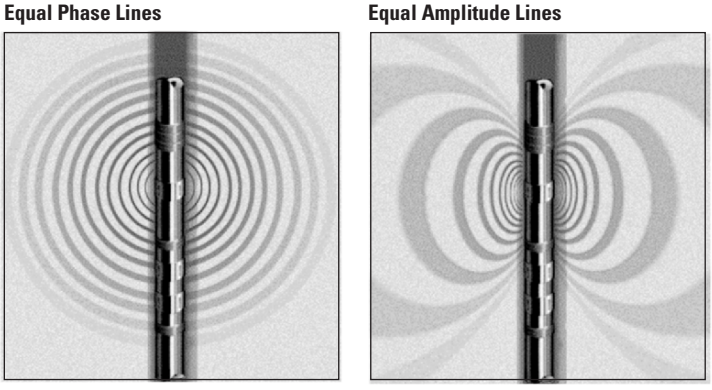


Fig. 9.17 Contour lines showing signals of equal phase (left) and equal amplitude (right) around a 2 MHz transmitter in a 1 ohm-m formation. Adapted from Clark et al. [18]. Used with permission.

9.6.3 Vertical and Radial Response

Returning to Fig. 9.16, we see that the higher skin effect at 2 ohm-m causes the signal to originate closer to the tool, so that both vertical resolution and depth of investigation are less than at 10 ohm-m. In induction tools, skin effect was treated as a correction that must be removed to give the same response in all conditions. The 2 MHz tools depend on skin effect for the measurement and as a result their response is much more sensitive to resistivity level and formation contrasts. Readers

of Chapter 8 will spot an opportunity to deconvolve the data in order to restore the same vertical resolution at all levels. This can be done for deviation angles below about 50° [22, 23], and for resistivities below 100 ohm-m, but requires regular depth sampling. LWD measurements are sampled in time, which must be resampled in depth, a process that can introduce significant errors. For this reason LWD logs are rarely deconvolved. Also, for the highly deviated wells in which LWD logs are often run, vertical resolution is not the issue.

In highly deviated wells the problem is not to improve vertical resolution but to remove the effect of layers lying above or below the well (the surrounding or shoulder beds). It is possible to do this for one such layer, by ignoring the effect of invasion and solving for the resistivity in the reservoir and the distance to, and resistivity of, the surrounding bed [24]. For this purpose it is helpful to have deeper-reading, lower frequency measurements at 400 kHz or less. The correction can be improved if the resistivity of the bed above the well is known because the well has already passed through it or because it is, for example, a regional cap rock.

Figure 9.16 showed that the geometrical factors of 2 MHz tools are more dependent on resistivity level than induction tools and comparable to the pseudogeometrical factors of laterologs. Single numbers for vertical resolution and depth of investigation can be misleading. For example the depth of investigation (as defined by the radius within which 50% of the response occurs) changes from about 10 in. at 0.1 ohm-m to 30 in. at 100 ohm-m for R_{ps}; and from 15 in. to 60 in. for R_{ad}. It is therefore better to look at modeled results for the conditions under study rather than use geometrical factors. Figure 9.18 shows the radial response for two cases of resistive and conductive invasion, both with high contrasts. Note how R_{ad} always reads deeper than R_{ps}, usually by about 20 in. radius, and how with conductive invasion the higher skin effect in the invaded zone cause both to read shallower.

The vertical responses are illustrated in Fig. 9.19. Although R_{ps} and R_{ad} can respond to beds as thin as 0.5 ft, shoulder effect prevents them reaching the true bed reading until the beds are considerably thicker. As expected for a device that responds to conductivity, conductive shoulders have a much larger effect than resistive shoulders: for example, R_{ps} only just reaches the true reading in the 10 ft uninvaded bed at 100 ft. One other interesting feature is that the point of crossover between R_{ps} and R_{ad} is a good indicator of the bed boundary when it is perpendicular to the tool.

Although invasion is normally less at LWD time, the depths of investigation are significantly shallower than those of wireline devices so that some correction might be needed to obtain R_t. With two measurements there is not enough information to invert the data or to establish a proper invasion profile. The solution is an array of measurements but, before we consider such devices the remaining environmental effects – namely dipping beds, polarization horns, and anisotropy – need to be discussed.

9.6.4 Dip and Anisotropy

In general the shallower depth of investigation and the sharper vertical response of the 2 MHz device makes it less susceptible to dipping beds than an induction device. The deeper a measurement the more it is affected by dip, so that R_{ad} is more affected than

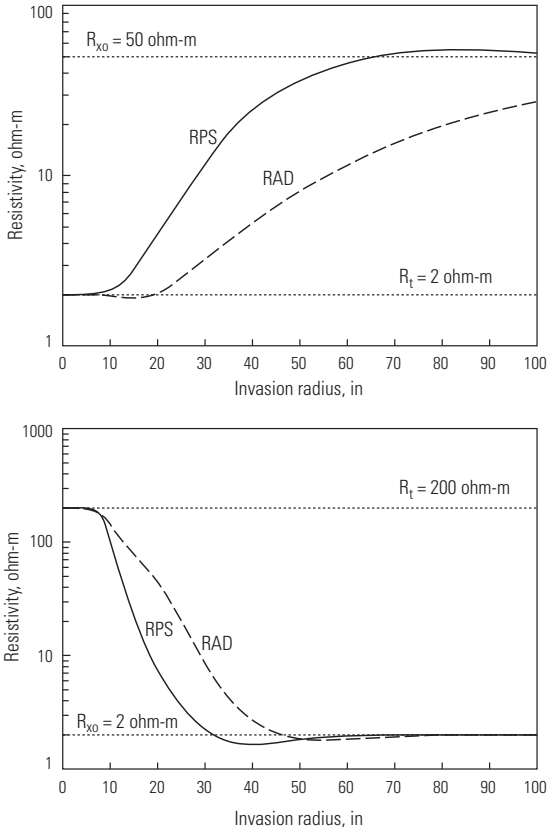


Fig. 9.18 Radial response of the phase shift and attenuation resistivity from a CDR tool for a case of resistive invasion (top) and conductive invasion (bottom). From Anderson [25]. Courtesy of Schlumberger.

R_{ps} and both are sensitive at high resistivity. Modeling shows that at 1 ohm-m and for moderate contrasts, neither are significantly affected even at 70° [26]. However at 10 ohm-m R_{ps} starts to be affected at this dip angle and R_{ad} even more so.

The 2 MHz devices show the same sharp increase in resistivity as an induction device when the tool crosses a dipping bed boundary. This effect, called the polarization horn, is significant when the relative dip is above about 50° and increases with increasing resistivity contrast. Its origin was discussed in Section 8.4.5. It is much stronger on R_{ps} than R_{ad} and can be used as a reliable indicator of a bed boundary in highly deviated wells. The response to dipping beds can be modeled, but it is impractical to use this response to correct the logs, because of the difficulty discussed above in applying any deconvolution to irregularly sampled data.

Finally, anisotropy has an important effect on 2 Mhz measurements for deviations above 60° (Fig. 9.20). In fact, it was the observation of these effects in horizontal wells that caused the industry to examine anisotropic formations more closely. While

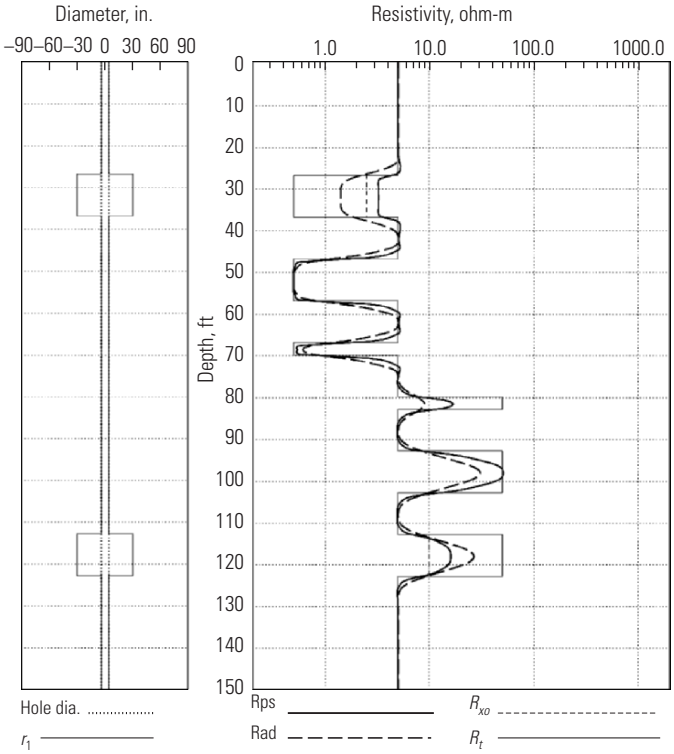


Fig. 9.19 The vertical response of the CDR tool in a series of invaded and uninvaded formations, the same as were used for ILd (Fig. 7.18) and phasor induction (Fig. 8.5) logs. From Anderson [25]. Courtesy of Schlumberger.

the effect of dipping anisotropic beds on the attenuation is similar to an induction, there is a much stronger effect on the phase shift. Figure 9.17 suggests the reason. In a horizontal well the lines of equal phase pass equally in the vertical as in the horizontal direction, while those of equal amplitude are more often horizontal. Figure 9.20 also shows that the effect increases with transmitter–receiver spacing. This makes for an ambiguity in the response, since a separation at different spacings can also be caused by an isotropic, but invaded, formation. Array propagation devices generate data at different spacings, so it is now appropriate to consider their features and interpretation.

9.6.5 Array Propagation Measurements and their Interpretation

The advantages of multiply spaced devices, which were already seen for laterolog and induction devices, were soon extended to 2 MHz propagation measurements. The Electromagnetic Wave Resistivity tool was introduced in 1991 with three arrays,

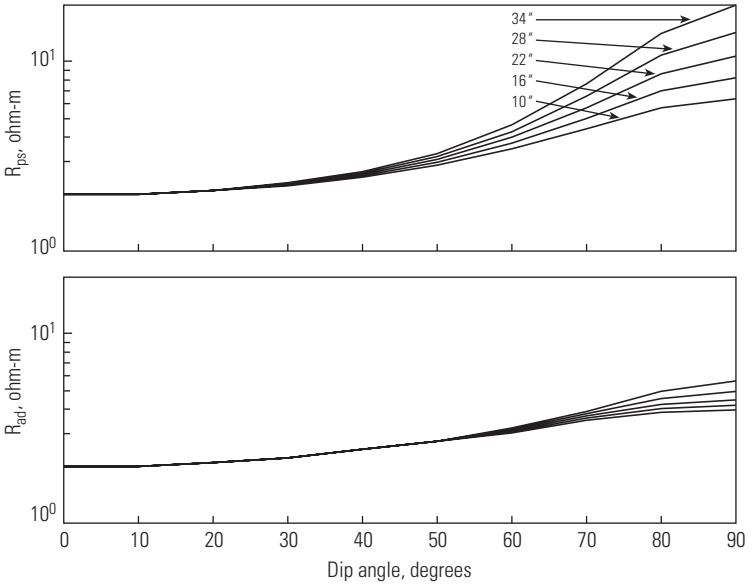


Fig. 9.20 The response of 5 phase shift and attenuation resistivities to a formation with R_v = 13 ohm-m and R_h = 2 ohm-m. The curves are for different spacings from transmitter to receiver midpoint, as indicated for R_{ps}. The curves are in the same order for R_{ad}. Adapted from Bonner et al. [27].

which were later extended to four in the device shown in Fig. 9.21 [28]. Each array has one transmitter and two receivers. The outermost array is driven at 1 MHz and the others at 2 MHz. Also illustrated is the Multiple Propagation Resistivity tool, with two borehole compensated arrays (two transmitters and two receivers) [29], and the Array Resistivity Compensated tool with five borehole compensated arrays [27]. In the two latter devices each transmitter is driven sequentially and at either 2 MHz or 400 kHz. Most tools measure both phase shift and attenuation, so that the number of channels produced is the number of arrays times four (two measurements and two frequencies).

This large number of measurements should allow environmental effects to be detected and removed easily. In low angle wells this is nearly true. Providing the data can be deconvolved to remove shoulder effect, the remaining effects are invasion and errors in the dielectric assumption. Dielectric effects can be removed, if necessary, by combining phase shift and attenuation, while invasion can be handled by the multiple spacings. However, high angle wells are much more difficult, since deconvolution is no longer feasible and anisotropy must be considered. For example in Fig. 9.22, is the separation between the curves due to invasion, anisotropy, or the presence of a nearby resistive bed? Are the differences between R_{ps} and R_{ad} due to the same factors or an incorrect dielectric assumption?

There are too many ambiguities in the response to provide a unique answer. However, in practice we have some external knowledge that can reduce the

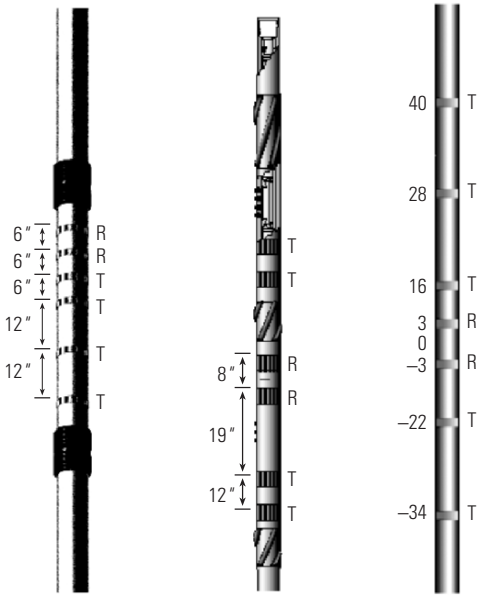


Fig. 9.21 Examples of three array propagation devices. (Left) An Electromagnetic Wave Resistivity tool. From Oberkircher et al. [28]. Used with permission. (Center) A Multiple Propagation Resistivity tool. From Meyer et al. [29]. Used with permission. (Right) An Array Propagation ("ARC5") tool with spacings in inches. Borehole compensation in the "ARC5" is achieved by averaging data from two adjacent transmitters to form a pseudotransmitter at the same distance as a transmitter on the opposite side of the receivers. Adapted from Bonner et al. [27].

possibilities. In development wells we have a good idea of whether $R_{xo} >$ or $<$ R_t (or at least whether $R_m >$ or $< R_w$). Dielectric errors only have a significant effect at high R_t, so that if we ignore them we can construct a logic such as in Table 9.2. This gives a means of recognizing which are the main effects, but is also nonunique, since one effect can cancel another, and also does not provide quantitative answers for R_v and R_h.

Ignoring nonuniqueness, quantitative answers can be obtained by inverting the data. Since a horizontal well in a layered formation is a 3D problem, we should ideally invert the data with a full 3D model that takes into all account all effects simultaneously. This can be done, but is too time-consuming and manually intensive to be used for all but special problems such as fractured rocks or eccentric invasion [31]. Simpler, more automatic approaches are preferred even if they involve some inconsistencies. One method first looks for and removes the effect of a surrounding bed, and then simultaneously inverts the data to find the best fit solution for invasion, anisotropy, and dielectric constant (at each frequency) [32]. The results are presented as the anisotropy ratio λ, ϵ', and R_h at different depths of investigation. The latter can then be inverted by traditional means to give R_{xo}, R_t, and d_i.

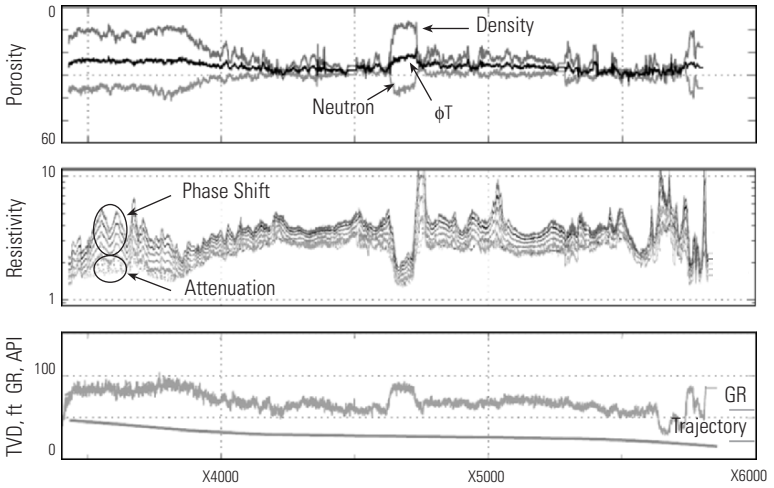


Fig. 9.22 A set of LWD logs with (top) density and neutron logs and a calculated ϕ_T; (bottom) gamma ray and borehole trajectory; (center) five phase shift (solid) and five attenuation logs (dotted) from an "ARC5" propagation tool. The five logs come from five different transmitter-receiver spacings (10, 16, 22, 28, and 34 in.). For both phase shift and attenuation the measured resistivity increases with increasing spacing. From Tabanou et al. [30]. Used with permission.

Table 9.2 Possible causes of longer spaced propagation logs reading higher than shorter spaced logs, assuming borehole corrections have been correctly applied.

R_{xo} vs. R_t	R_{ad} vs. R_{ps}	Reason
$R_{xo} > R_t$	$R_{ad} > R_{ps}$	Tool in conductive bed close to boundary
$R_{xo} > R_t$	$R_{ad} < R_{ps}$	Anisotropy
$R_{xo} < R_t$	$R_{ad} > R_{ps}$	Conductive invasion, or Tool in conductive bed close to boundary
$R_{xo} < R_t$	$R_{ad} < R_{ps}$	Anisotropy

By correcting simultaneously for the three main effects the inversion can provide the most accurate answers but, as with all inversions, there is a tendency to find some amount of each effect even when none is justified, for example finding invasion in shales. An alternative approach is to invert for each effect independently and then use logic to decide which is most appropriate [33]. External inputs such as a gamma ray log can be used to identify shale, for example, and therefore rule out invasion. Otherwise the model that gives the best fit is selected. If none fit sufficiently well, the zone is flagged as needing further analysis, for example by 3-D modeling.

It can be seen that to obtain R_t, or R_h and R_v, from 2 MHZ tools in horizontal wells requires interpretation skills as much as processing. However, in many cases accurate values of these parameters are less important than the information needed to steer the well while drilling. This aspect is covered in Chapter 20.

REFERENCES

1. Feynman RP, Leighton RB, Sands ML (1965) Feynman lectures on physics, vol 2. Addison-Wesley, Reading, MA

2. Orlowska S (2003) Conception et prediction des characteristiques dielectriques des materiaux composites a deux et trois phases par la modelisation et la validation experimentale. PhD thesis, Ecole Centrale de Lyon

3. Hizem M (2006) Personal communication.

4. Bona N, Rossi E, Capaccioli S (2001) Electrical measurements in the 100 Hz to 10 GHz frequency range for efficient wettability determination. Paper SPE 69741 in: SPE J March:80–88

5. Kenyon WE, Baker PL (1984) EPT interpretation in carbonates drilled with salt muds. Presented at the 59th SPE Annual Technical Conference and Exhibition, paper 13192

6. Sen P (1980) The dielectric and conductivity response of sedimentary rocks. Presented at the 55th SPE Annual Technical Conference and Exhibition, paper 9379

7. Seleznev NV, Boyd A, Habashy T, Luthi S (2004) Dielectric mixing laws for fully and partially saturated carbonate rocks. Trans SPWLA 45th Annual Logging Symposium, paper CCC

8. Maxwell-Garnett JC (1904) Colors in metal glasses and in metal films. Trans Royal Society, vol CCIII, pp 420–429

9. Seleznev N, Habashy T, Boyd A, Hizem M (2006) Formation properties derived from a multi-frequency dielectric measurement. Trans SPWLA 47th Annual Logging Symposium, paper VVV

10. Wharton R, Hazen G, Rau R, Best D (1980) Electromagnetic propagation logging: advances in technique and interpretation. Presented at the 55th SPE Annual Technical Conference and Exhibition, paper 9267

11. Anderson B, Liu Q-H, Taherian R, Singer J, Chew WC, Freedman R, Habashy T (1994) Interpreting the response of the electromagnetic propagation tool in heterogeneous environments. The Log Analyst 35(2):65–83

12. Cheruvier E, Suau J (1986) Applications of microwave dielectric measurements in various logging environments. Trans SPWLA 27th Annual Logging Symposium, paper MMM

13. Huchital GS, Hutin R, Thoroval Y, Clark B (1981) The deep propagation tool (a new electromagnetic logging tool). Presented at the 56th SPE Annual Technical Conference and Exhibition, paper 10988

14. Janes TA, Hilliker DJ, Carville CL (1984) 200 MHz dielectric logging system. Trans SAID 9th International Formation Evaluation Symposium, paper 28

15. Allen V, Sinclair P, Prain S, Page S (2004) Design, development and field introduction of a unique low-frequency (20 kHz) induction resistivity logging-while-drilling tool. Trans SPWLA 45th Annual Logging Symposium, paper XX

16. Rodney PF, Wisler MM (1986) Electromagnetic wave resistivity MWD tool. Paper 12167 in: SPE Drilling Eng October:337–346

17. Clark B, Allen DF, Best D, Bonner SD, Jundt J, Luling MG, Ross MO (1988) Electromagnetic propagation logging while drilling: theory and experiment. Presented at the 63rd SPE Annual Technical Conference and Exhibition, paper 18117

18. Clark B, Luling MG, Jundt J, Ross M, Best D (1988) A dual depth resistivity measurement for formation evaluation while drilling. Trans SPWLA 29th Annual Logging Symposium, paper A

19. Wu PT, Lovell JR, Clark B, Bonner SD, Tabanou JR (1999) Dielectric-independent 2 MHz propagation resistivities. Presented at the 74th SPE Annual Technical Conference and Exhibition, paper 56448

20. Meyer WH (1999) In-situ measurement of resistivity dispersion (or lack of it) using MWD propagation resistivity tools. Trans SPWLA 40th Annual Logging Symposium, paper J

21. Rasmus JC, Tabanou J, Li Q, Liu C, Pagan R, Pacavira N, Higgins T (2003) Resistivity dispersion – fact or fiction. Trans SPWLA 44th Annual Logging Symposium, paper RR

22. Rosthal R, Allen D, Bonner S (1993) Vertical deconvolution of 2 MHz propagation tools. Trans SPWLA 34th Annual Logging Symposium, paper W

23. Meyer WH (1993) Inversion of the 2 MHz propagation resistivity logs in dipping thin beds. Trans SPWLA 34th Annual Logging Symposium, paper BB

24. Meyer WH (1998) Interpretation of propagation resistivity logs in high angle wells. Trans SPWLA 39th Annual Logging Symposium, paper BB

25. Anderson B (2001) Modeling and inversion methods for the interpretation of resistivity logging tool response. DUP Science, Delft, The Netherlands

26. Anderson B, Bonner S, Luling M, Rosthal R (1992) Response of 2 MHz LWD resistivity and wireline induction tools in dipping beds and laminated formations. Petrophysics 33(5):461–475

27. Bonner SD, Tabanou JR, Wu PT, Seydoux JP, Moriarty KA, Seal BK, Kwok EY, Kuchenbecker MW (1995) New 2 MHz multiarray borehole-compensated resistivity tool developed for MWD in slim holes. Presented at the 70th SPE Annual Technical Conference and Exhibition, paper 30547

28. Oberkircher J, Steinberger G, Robbins B (1993) Applications for a multiple depth of investigation MWD resistivity measurement device. Trans SPWLA 34th Annual Logging Symposium, paper OO

29. Meyer WH, Thompson LW, Wisler MM, Wu JQ (1994) A new slimhole multiple propagation resistivity tool. Trans SPWLA 35th Annual Logging Symposium, paper NN

30. Tabanou JR, Anderson B, Bruce S, Bonner S, Bornenamnn T, Hodenfield K, Wu P (1999) Which resistivity should be used to evaluate thinly bedded reservoirs in high angle wells? Trans SPWLA 40th Annual Logging Symposium, paper E

31. Anderson B, Druskin V, Lee P, Luling MG, Schoen E, Tabanou J, Wu P, Davydycheva S, Knizherman L (1997) Modeling 3-D effects on 2 MHz LWD resistivity logs. Trans SPWLA 38th Annual Logging Symposium, paper N

32. Meyer WH (1997) Multi-parameter propagation resistivity interpretation. Trans SPWLA 38th Annual Logging Symposium, paper GG

33. Li Q, Liu C, Maeso C, Wu P, Smits J, Prabawa P, Bradfield J (2004) Automated interpretation for LWD propagation resistivity tools through integrated model selection. Petrophysics 45(1):14–26

Problems

9.1 Prove the relationships between ϵ', σ and the propagation parameters α and β given in Eqs. 9.29 and 9.30.

9.2 Show that the CRIM model (Eq. 9.32) reduces to Archie's equation in the limit of low frequency.

9.3 Show that at induction and laterolog frequencies the effect of the real component of ϵ^* is small in comparison with the imaginary component.

9.4 Suppose the phase shift and attenuation measured by the device whose response is shown in Fig. 9.14 are 2.2° and 4.34 dB. What are R_t and ϵ'?

9.4.1 Using the dielectric assumption shown in this figure, what are R_{ps} and R_{ad}?

9.4.2 Using the dielectric assumption shown in Fig. 9.15, what are R_{ps} and R_{ad}?

9.5 Construct a table similar to Table 9.2 but for the case where the short-spaced propagation measurements read higher than the long-spaced measurements.

9.5.1 Modify Table 9.2 for the case in which no borehole corrections have been applied, and in which the mud is conductive. Do the same for the case in which oil-base mud is used.

9.5.2 Modify the table you have just constructed in the same way as the last problem.

9.6 What do you think is the most likely reason for the separation in response of the resistivity logs in Fig. 9.22?

10

Basic Nuclear Physics for Logging Applications: Gamma Rays

10.1 INTRODUCTION

In the preceding chapters, electrical devices are seen to respond primarily to the fluid content of earth formations. They are not used, therefore, to obtain information about the predominant constituent of formations, the rock matrix. Nuclear measurements used in logging respond to properties of both the formation and the contained fluids. These measurements employ gamma rays and neutrons. These two types of penetrating radiation are the only ones which are able to traverse the pressure housings of the logging tools and the formation of interest and still return a measurable signal.

One input to a more complete description of an earth formation is an analysis of its chemical composition. Knowledge of its major elemental constituents would be indicative of the dominant mineralogy. Instead of the obvious but time-consuming and expensive laboratory chemical analysis of formation samples, in situ gamma ray spectroscopy can be used. This is based on the fact that the nucleus of any atom, after having been put into an excited state by a previous nuclear reaction, can emit gamma rays of characteristic energies which uniquely identify the atom in question. Gamma ray spectroscopy refers to the detection and identification of these characteristic gamma rays.

Another important property of an earth formation is bulk density. Its use in seismic interpretation is well known, but more important bulk density is linearly dependent on formation porosity, a key ingredient for the interpretation of electrical measurements. Gamma rays are typically used to measure bulk density since their scattering and transmission are strongly affected by this material property. At very low energies the transmission of gamma rays is influenced additionally by the formation chemical composition. This additional absorption is related to the atomic number, Z, of the absorber and thus provides a third application of gamma rays.

Neutrons are used in well logging because of several different properties of their interaction with matter. First, the transmission and moderation of neutrons are influenced by the bulk properties of the medium, in particular, by the amount of hydrogen present. The scattering of neutrons by hydrogen is very efficient in reducing the neutron energy. Second, the interaction of high-energy neutrons can excite nuclei to emit characteristic gamma rays. The elemental identification can be achieved by gamma ray spectroscopy. At very low energies, neutrons can be absorbed, causing the emission of another set of characteristic gamma rays. Some of these so-called (thermal neutron) capture gamma rays are emitted after considerable delay and are referred to as activation gamma rays. In summary, there are two types of measurements which can be based on the use of neutrons: the scattering or slowing-down properties of formations, and neutron production of gamma rays (either by absorption or inelastic high-energy reactions with elements) of characteristic energies for use in spectroscopic identification. These are discussed in Chapters 11 through 13.

In this chapter, a basic vocabulary for the description of nuclear* radiation is developed which can be applied to the discussion of gamma rays or neutrons. This includes the quantification of intensity and energy, and the notions of cross sections, reactions, and counting statistics. The principal interactions of gamma rays with matter are described in relation to the physical parameters of the formation and methods for their detection. Unlike most of the resistivity devices considered, which consist of complicated arrays of very simple sensors, logging tools which use gamma rays have somewhat more sophisticated sensors. Understanding the detectors allows a better understanding of the limitations of the measurements.

10.2 NUCLEAR RADIATION

In the earliest investigation of radioactive materials, three types of radiation were identified and named, quite unimaginatively, α, β, and γ radiation. It was subsequently discovered that α radiation consisted of fast-moving He atoms stripped of their electrons, and that β radiation consisted of energetic electrons. The gamma rays were found to be packets of electromagnetic radiation also referred to as photons.

The discovery of this radiation was followed by its quantification, namely the measurement of the amount of energy transported. The unit chosen is known as the electron-volt (eV), which is equal to the kinetic energy acquired by an electron accelerated through an electric potential of 1 volt. For the types of radiation discussed in the following sections, the range of energies is between fractions of an eV and millions of electron volts (MeV). Another convenient multiple for discussing gamma ray energies is the kilo-electron-volt (keV).

Since α and β radiation consist of energetic charged particles, their interaction with matter is primarily Coulombic in nature. This leads to atomic excitation or ionization; that is, the interactions are with the electrons of the medium. The α and β particles

*Much of this chapter appears in slightly different form in the *SPE Petroleum Production Handbook* [1].

rapidly lose energy as they transfer it to electrons in their passage through the medium. Their ranges of penetration are rather limited and in most materials are a function of the material properties (Z, the number of electrons per atom, and density) and the energy of the particle. Consequently they have not been of any practical importance for well logging applications. Gamma rays, on the other hand, are extremely penetrating, which makes them of great importance for well logging applications.

10.3 RADIOACTIVE DECAY AND STATISTICS

Radioactive decay is a property of nuclei, in which a transition from one nuclear energy state to another lower one is made spontaneously. The excess energy is shed by the nucleus, by means of one or more of the types of radiation previously mentioned. The basic experimental fact associated with radioactivity is that the probability of any one nucleus decaying, within an interval of time Δt, is proportional to Δt; i.e., it is independent of external influences, including the decay of another nucleus. So for a *single* radioactive atom, the probability $P(dt)$ of decaying in the interval of time dt is expressed as:

$$P(dt) = \lambda dt \,, \tag{10.1}$$

where λ is the decay constant. For a *collection* of N_p identical radioactive particles, the number decaying dN is just:

$$dN = N_p P(dt) = -\lambda dt N_p, \tag{10.2}$$

resulting in the expression for radioactive decay:

$$N_p = N_i e^{-\lambda t} \,, \tag{10.3}$$

where N_p is now the number of particles remaining in the collection at time t, out of the initial number of particles N_i present at time zero. The constant of proportionality λ is related to the better-known parameter, the half-life $t_{\frac{1}{2}}$, by:

$$t_{\frac{1}{2}} = \frac{0.693}{\lambda} \,. \tag{10.4}$$

One can never measure any physical quantity exactly, but in the case of nuclear processes, where the number of events observed is small, randomness is important. The practical complication of the statistical nuclear decay process is that only the bulk or average properties can be predicted with any certainty. We can only talk about the measurement of a group of particles together and the distribution of the measured value about some mean.

In order to understand an important property of nuclear radiation, it is necessary to digress a moment for a short review of the binomial distribution which was discovered in the eighteenth century by Bernoulli. It describes the probability, P_x, that a discrete event, which has a probability P of occurring (and a probability q of not occurring) in a single observation, will occur x times when the observation is repeated z times.

The probability thus specified was identified with the binomial expansion of $(P+q)^z$ for which the general term of the expansion is:

$$P_x = \frac{z!}{x!(z-x)!} P^x (1-P)^{z-x}. \tag{10.5}$$

This equation gives the probability of x occurrences in z trials after using the substitution of $1 - P$ for q.

This expression can be applied to radioactive decay, in which P_x represents the probability of having x nuclei decay in time dt when there are z atoms present. For this case, the probability P of observing the decay of a single nucleus in a unit time is very small, but the number of particles observed (z) is very large. This condition allows simplification of Eq. 10.5: to

$$P_x = \underline{\mu}^x \frac{e^{-\underline{\mu}}}{x!}, \tag{10.6}$$

which is known as the Poisson distribution. It gives the probability of observing x decays in a given time in which an average of $\underline{\mu}$ decays is to be expected. Figure 10.1 shows the general form of the Poisson distribution with the maximum probability at the mean value $\underline{\mu}$, which was chosen as 100 for this example. For this case, with $\underline{\mu} \gg 1$, the distribution is nearly symmetric about the mean value. It resembles

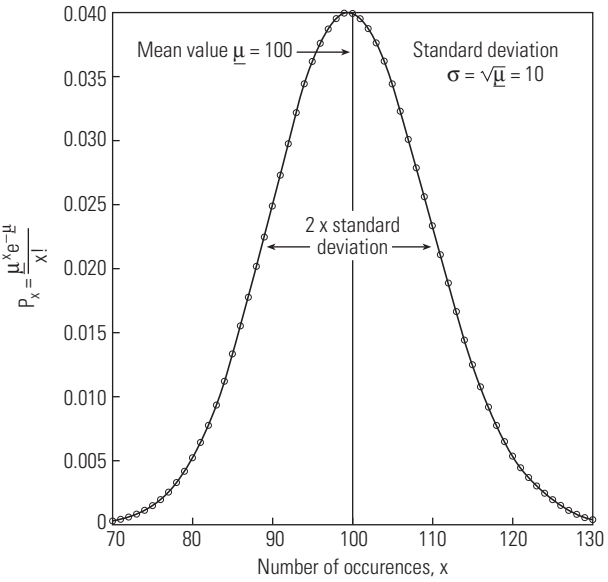


Fig. 10.1 The Poisson distribution evaluated for an expected number of counts (100) in a given interval. The standard deviation is 10; 68% of all observations will deviate from the mean by a value less than this. Adapted from SPE Petroleum Production Handbook [1].

the usual bell-shaped distribution curve whose width is specified by an independent parameter σ, the standard deviation.

An important property of the Poisson distribution is that the appropriate standard deviation (σ) for the Poisson distribution which characterizes the statistics of counting random nuclear events is not an independent parameter (as is the case for most measurements) but is related to the mean value $\underline{\mu}$ by:

$$\sigma = \sqrt{\underline{\mu}}\,. \tag{10.7}$$

Hence, if N_r counts from a radiation detector are expected per time interval, then in repeated observations about 32% of the measurements will exhibit deviations beyond values of $N_r \pm \sqrt{N_r}$. The only sure approach to reduce this type of statistical fluctuation is to increase the absolute number measured, either by using higher output sources, more efficient counters, or longer counting times per sample.

This important implication of Poisson statistics is a consequence of the fact that the value of the mean determines the distribution of measurements about the mean; $\underline{\mu}$ specifies the distribution completely. The error reduction noted above can be seen by considering the fractional uncertainty on a single measurement. The fractional uncertainty f can be expressed as:

$$f = \frac{\sigma}{N}, \tag{10.8}$$

where N is the average number expected in the time interval considered. Since σ is given by the square root of the mean, f can be written as:

$$f = \frac{\sqrt{N}}{N} = \frac{1}{\sqrt{N}}\,. \tag{10.9}$$

Since N increases linearly with both t, the time of observation, and the source strength Q:

$$f \propto \frac{1}{\sqrt{Q\,t}}\,. \tag{10.10}$$

Thus if the source strength or observation time is increased by a factor of four, then the fractional uncertainty decreases by a factor of two.

10.4 RADIATION INTERACTIONS

There are certain interactions between radiation and materials that are of special interest in well logging. Before discussing these, a few mathematical definitions are presented to help describe the mechanisms of the interactions.

Using Fig. 10.2, consider the question of how readily these reactions will take place. A beam of radiation (e.g., gamma rays or neutrons) of intensity Ψ_i is seen to enter the slab of material and exit with an intensity Ψ_o. The intensity of the radiation Ψ is referred to as the flux and has dimensions of numbers of particles per unit surface area per unit time.

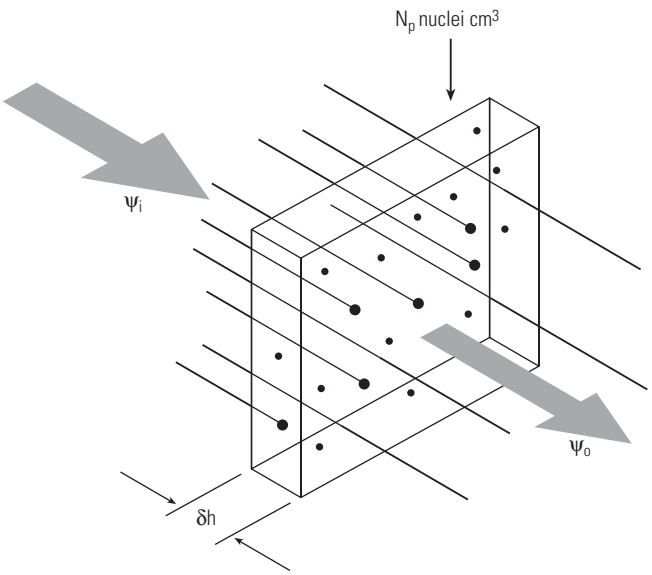


Fig. 10.2 A flux of gamma rays of intensity Ψ_i impinging on a thin slab of material characterized by N_p interacting particles per cubic centimeter. The flux reduction in traversing the material is found to be proportional to the thickness of the slab δh and the number density of interacting particles N_p. Adapted from SPE Petroleum Production Handbook [1].

The slab of material is characterized by N_p, the number of particles per unit volume with which the flux of radiation may interact. The experimental observation is that after passing through a slab of material of thickness δh, a certain fraction of the incident particles have undergone interactions, and that number is proportional to the thickness and the number of target nuclei, and the incident flux. This is expressed mathematically as:

$$\delta\Psi \;=\; \Psi_i \;-\; \Psi_o \;=\; \sigma\Psi N_p\,\delta h\;, \tag{10.11}$$

where the constant of proportionality σ is called the total cross section for the interaction. The units of this microscopic cross section σ are area/interacting target nucleus. Cross section is used, because in a classical sense it is the apparent area each target nucleus presents to the incoming beam. In effect, it collects all the nuclear interaction details into one useful number. The practical unit of cross section is called the "barn" and is defined as 10^{-24}cm^2. The so-called macroscopic cross section, Σ, is the product of σ and N_p, and has the dimensions of inverse length and is the reciprocal of the interaction mean free path. From σ, Σ can be calculated easily because N_p is related to Avogadro's number, N_{Av}, and the material density, ρ_b, by:

$$N_p \;=\; \frac{N_{Av}}{M} \;\times\; \rho_b, \tag{10.12}$$

where M is the molecular weight of the target material for a single particle per molecule.

In general, the cross sections for most reactions have to be determined experimentally. They depend on the incoming radiation, the type of interaction and the material. The cross section also typically depends on the energy of the radiation and the angle between the incoming radiation direction and the resultant radiation. For this reason the data are often available in graphical or tabular form.

The quantity $\sigma \Psi N_p$ in Eq. 10.11 has dimensions of $(\text{cm}^3\text{-sec})^{-1}$ and represents the reaction rate per unit volume between the incident flux and the target material.

10.5 FUNDAMENTALS OF GAMMA RAY INTERACTIONS

For our purpose, there are three types of gamma ray interactions in earth formations that are of interest: the photoelectric effect, Compton scattering, and pair production. The probability of a specific gamma ray interaction occurring will depend on the atomic number of the material and the energy of the gamma ray. The ordering of these three interactions in the following discussion reflects the change of the dominant process as the gamma ray energy increases.

The photoelectric effect results from interaction of a gamma ray with an atom in the material. In this process the incident gamma ray disappears and transfers its energy to a bound electron. If the incident gamma ray energy is large enough, the electron is ejected from the atom and begins interacting with the adjacent material. Normally the ejected electron is replaced by another less tightly bound electron with the accompanying emission of a characteristic fluorescence x-ray with an energy (generally below 100 keV) which is dependent on the atomic number of the material.

The cross section for the photoelectric effect σ_{pe} varies strongly with energy, falling off as nearly the cube of the gamma ray energy (E_γ). It is also highly dependent on the atomic number (Z) of the absorbing medium. In the energy range of 40 to 80 keV, the cross section per atom of atomic number Z is given by:

$$\sigma_{pe} \propto \frac{Z^{4.6}}{E_\gamma^{3.15}} \quad . \tag{10.13}$$

For most earth formations, the photoelectric effect becomes the dominant process for gamma ray energies below about 100 keV.

The photoelectric effect is an important process in the operation of conventional gamma ray detection devices. Also it is the mechanism by which one type of well logging tool is made sensitive to the lithology of the formation. This tool measures the so-called photoelectric absorption factor, P_e, which is proportional to the photoelectric cross section per electron (i.e., $\frac{\sigma_{pe}}{Z}$). Since P_e is very sensitive to the average atomic number of the medium (Z), it can be used to obtain a direct measurement of lithology or rock type. This is due to the facts that the principal rock matrices (sandstone, limestone, and dolomite) have different average atomic numbers and thus, considerably different photoelectric absorption characteristics, and that the pore fluids play only a minor role because of their low average atomic numbers.

Moving up the gamma ray energy scale, the next dominant process is Compton scattering, which involves interactions of gamma rays and individual electrons. It is

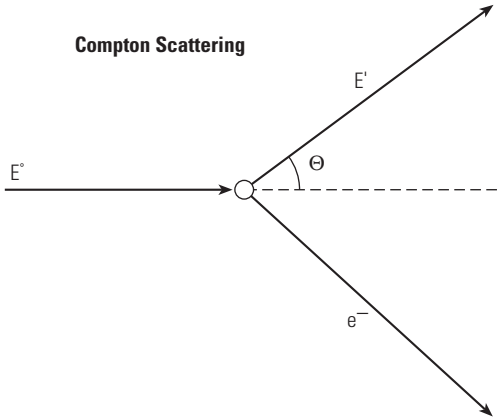


Fig. 10.3 Schematic representation of the Compton interaction. A gamma ray of energy E^o transfers a portion of its energy to an electron, and a gamma ray of reduced energy E' leaves the site of the collision at an angle Θ with respect to the direction of the incident gamma ray.

a process in which only part of the gamma ray energy is imparted to the electron; the remaining gamma ray is of reduced energy. Unlike the photoelectric effect, the cross section for Compton scattering changes relatively slowly with energy.

Compton scattering is of great importance both as a measurement technique and as an interaction mechanism for gamma rays in detector materials. Therefore we will consider it in more detail. Figure 10.3 illustrates the process: A gamma ray of incident energy E^o interacts with an electron of the material, scatters at an angle Θ, and leaves with an energy E'. The difference between the incident gamma ray energy and the scattered gamma ray energy is imparted to the electron.

Figure 10.4 illustrates the Compton energy-angle relationship for an incident gamma ray energy of 660 keV. This relationship gives the gamma ray energy as a function of the initial energy and scattering angle:

$$E' = \frac{E^o}{1 + \frac{E^o}{m_o c^2}(1 - \cos\Theta)}, \tag{10.14}$$

where m_o is the rest mass of the electron, and c the velocity of light. The quantity $m_o c^2$ is numerically equivalent to 511 keV.

Since in all gamma ray detectors it is the energetic secondary electron which is used to produce a measurable signal, it is of some interest to look at the distribution of electron energies which result from Compton scattered gamma rays. Because the initial gamma ray energy is shared between the outgoing gamma ray and the scattered electron, it is relatively simple to derive a curve for the energy of the resultant electron energy as a function of the gamma ray scattering angle. This is is shown in Fig. 10.5 where it is seen that minimum electron energy is zero and that the maximum is around 450 keV (in this example, for 660 keV incident gamma rays) when the gamma ray is back-scattered at 180°.

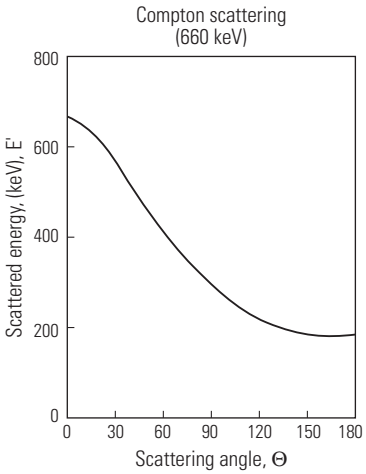


Fig. 10.4 The energy-scattering angle relationship for Compton-scattered gamma rays of initial energy 660 keV.

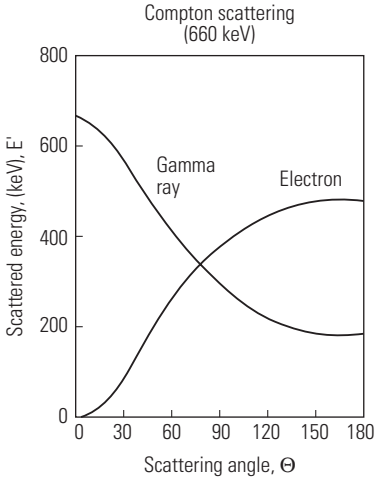


Fig. 10.5 The energy-scattering angle relationship for the Compton electron. The curve for the electron energy is derived from energy conservation and the gamma ray scattering-angle relationship from the previous figure. Note the relative insensitivity of the electron energy to the gamma ray scattering angle above about 120° scattering.

The results of Fig. 10.5 show the energy of the electron as a function of all possible scattering angles. To determine the distribution of electron energies, something must be known about the distribution of scattering angles. In general, scattering is not isotropic; there is a probability distribution associated with the scattering angle Θ. For Compton scattering, the preferred scattering angle at very high energy is close

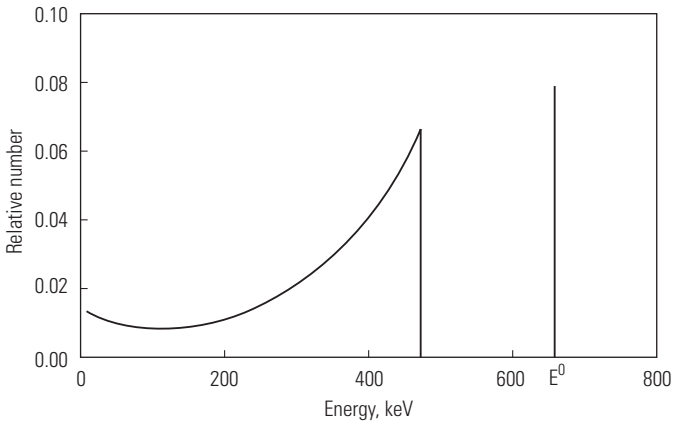


Fig. 10.6 The distribution of Compton electron energy based on the assumption of isotropic scattering of the gamma rays.

to zero. At low energies, however, Compton scattering is not too far from being isotropic, so that the curve of electron energies in Fig. 10.5 can be transformed into the electron distribution curve of Fig. 10.6 by considering the solid angle available for the gamma ray scattering, which varies as $\sin\Theta$. The resulting electron distribution seen in Fig. 10.6 has a close connection with observed gamma ray spectra. In the figure, the full energy of the gamma ray is indicated. This is the energy which would be registered by a detector if all of the incident gamma ray energy were absorbed in the detector material. However, if the gamma ray incident on the detector interact by a single Compton scattering, then they will register a distribution of energies as indicated. In gamma ray spectroscopy this degradation, or induced feature, is referred to as the Compton tail. The uppermost portion of this distribution is called the Compton edge (see Fig. 10.12).

To appreciate the bulk effect of Compton scattering in a material consisting of atoms of mass A, and atomic number Z, one can examine the so-called linear absorption coefficient. This macroscopic cross section is just the Compton cross section σ_{Co}, multiplied by the number of electrons per cubic centimeter:

$$\Sigma_{Co} = \sigma_{Co} \frac{N_{Av}}{A} \rho_b Z. \tag{10.15}$$

The final factor, Z, in the equation above takes into account that there are Z electrons per atom. Consequently the attenuation of gamma rays due to Compton scattering will be a function of the bulk density ρ_b and the ratio Z/A. The fact that Z/A is constant ($\simeq \frac{1}{2}$) for most elements of interest is the basis for the determination of bulk density from gamma ray scattering devices.

The third and final gamma ray interaction is pair production. Like the photoelectric process, pair production is one of absorption rather than scattering. In this case the gamma ray interacts with the electric field of a nucleus, and if the gamma ray energy

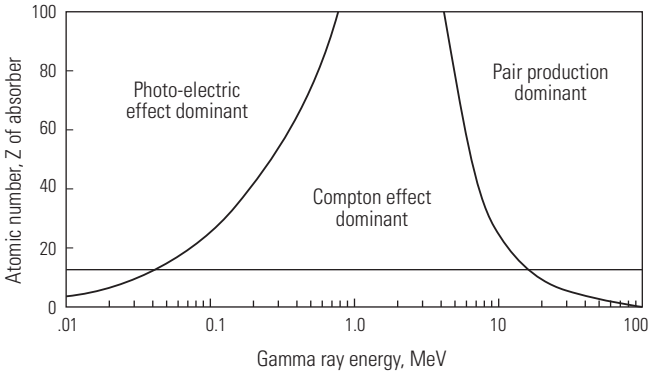


Fig. 10.7 Regions of dominance of the three principal gamma ray scattering mechanisms as a function of energy and the atomic number, Z, of the scattering material. Adapted from Evans [2].

is above the threshold value of 1.022 MeV, it disappears and an electron-positron pair is formed. The onset of this interaction corresponds to the rest mass energy of the electron and positron. The subsequent annihilation of the positron (positively charged electron) results in the emission of two gamma rays of 511 keV each. The nuclear cross section of this process is zero below the threshold energy of 1.022 MeV and rises quite rapidly with increasing energy. It is also dependent on the charge of the nucleus, varying approximately as Z^2.

In order to observe the regions of dominance of the three types of interactions, refer to Fig. 10.7. It shows, as a function of gamma ray energy and atomic number of the absorber, the boundaries at which the linear absorption coefficients for the adjacent processes are equal. The horizontal line, corresponding to an atomic number of 16, indicates the upper limit of Z for common minerals encountered in logging.

10.6 ATTENUATION OF GAMMA RAYS

From the earlier definition of cross section, the fundamental law of gamma ray attenuation can be stated as:

$$\Psi = \Psi_i \, e^{-n\sigma h}, \tag{10.16}$$

where Ψ_i is the flux incident on a scatterer of thickness h, n is the number of scatterers per unit volume, σ is the cross section for scattering per scatterer, and Ψ is the flux leaving the scatterer.

For gamma rays in the energy range of hundreds of keV, the primary interaction is Compton scattering. In this case, the scatterers are electrons and σ_{Co}, the Compton cross section/electron is the appropriate cross section. This results in the following expression for the attenuation of the source energy gamma rays:

$$\Psi = \Psi_i \, e^{-\rho_b \frac{Z}{A} N_{Av} \sigma_{Co} h}. \tag{10.17}$$

The attenuation of the gamma rays is seen to be proportional to the thickness of material h, the bulk density, and a property of the scattering material, Z/A. For most sedimentary rocks the ratio of Z/A is nearly $\frac{1}{2}$, as has been noted earlier.

Another unit for measuring the gamma ray attenuation properties of a material is the mass absorption coefficient μ, which regroups the constants in Eq. 10.17, i.e.,:

$$\mu = \frac{Z}{A} N_{Av} \sigma, \tag{10.18}$$

so that the gamma ray attenuation equation can be written as:

$$\Psi = \Psi_i e^{-\mu \rho_b h} . \tag{10.19}$$

The mass absorption coefficient has units of $cm^2\ g^{-1}$. The convenience of using the mass absorption coefficient for Compton scattering stems from the fact that it is the same for all materials to within the approximation that $Z/A = \frac{1}{2}$. Figure 10.8 shows the mass absorption coefficients (in cm^2/g) for aluminum.

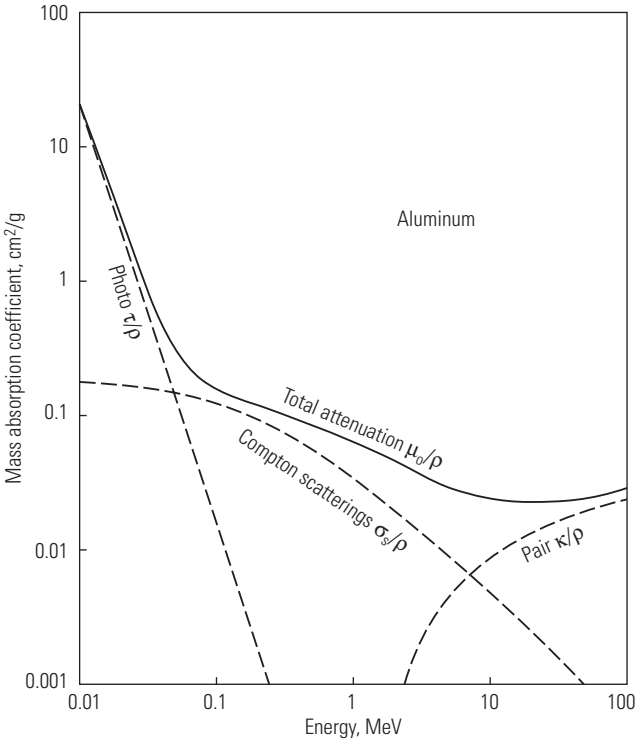


Fig. 10.8 The gamma ray mass absorption coefficient for aluminum as a function of gamma ray energy. Adapted from Evans [2].

10.7 GAMMA RAY DETECTORS

The detection of gamma rays is a two-step process. First, the gamma rays interact with the detector material. In doing so they convert some or all of their energy into ionizing radiation, for our consideration this will consist of energetic electrons. In the second phase, the electrons are converted to an observable electrical signal. In the first phase, all common gamma ray detectors exploit one or more of the three modes of gamma ray interactions with matter described earlier. Three general types of gamma ray detectors in current use will be described next. The first variety, the gas ionization counter, is a direct descendant of one of the earliest efforts at nuclear radiation detection. The second and most common present-day gamma ray detector used in well logging is the scintillation detector. The third type of device, the solid state detector, has found only limited use in logging applications.

10.7.1 Gas-Discharge Counters

The common form of the ionized gas or gas-discharge counter consists of a metal cylinder with an axial wire passing through it (Fig. 10.9) and insulated from it. The cylinder is filled with a gas which is normally nonconductive, and a moderate (several hundreds of volts) electrical potential is maintained between the central wire and the cylinder. For gamma rays to be detected with such a device, the gas must somehow be initially ionized. As the gas density, even at the rather high pressure available in commercial tubes, is moderate and the atomic number of useful gases is relatively low, there is little possibility of the gamma rays interacting directly with the gas. The main detection mechanism is photoelectric absorption or recoil electron ejection from Compton scattering in the metal shield. For the gamma rays absorbed near the inner radius of the cylinder, there is some probability of the ejected electron escaping into the gas and providing the initial ionization of detector gas molecules. The electrons freed in this process are accelerated by the radial electric field and, in collisions with gas molecules, produce additional free electrons. A fraction of the electrons are collected at the central wire, producing a voltage pulse.

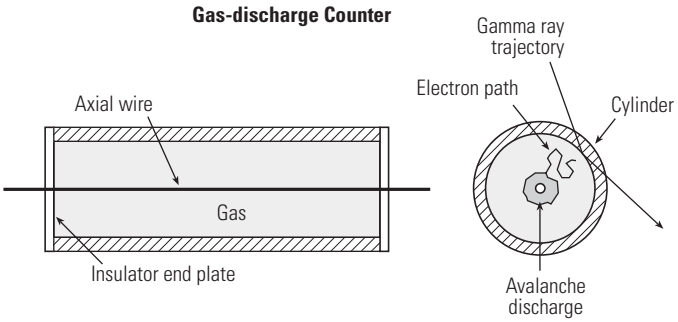


Fig. 10.9 Schematic diagram of a gas-discharge counter, a simple but inefficient GR detector.

The detection efficiency of such detectors is not high. It can be improved somewhat by the incorporation of conductive high atomic number gamma ray absorbers, such as silver, as an inner lining of the cylinder. Although they can be operated in a proportional mode,† the energy resolution of these detectors is not exploited in logging due to the poor efficiency. The most positive aspects of gas-discharge counters are their simplicity, ruggedness, and reliability for functioning in the hostile environment of well logging. For this reason, gas-discharge counters have had a recent renaissance because they are suitable for LWD applications [3].

10.7.2 Scintillation Detectors

A more common type of gamma ray detector employs a scintillation crystal. Here too the active detector element is sensitive to ionizing radiation such as energetic electrons. When these particles travel within the crystal lattice, they impart their energy to a cascade of secondary electrons which are finally trapped by impurity atoms. As the electrons are trapped, visible or near-visible light is emitted. The light flashes are then detected by a photomultiplier tube optically coupled to the crystal and transformed into an electrical pulse. This is indicated schematically in Fig. 10.10. The output pulse height can be related to the total energy deposited in the crystal by the initial energetic electron. The great advantage of such a detection scheme is the possibility of doing gamma ray spectroscopy, that is, deducing the actual energy of the incident gamma ray. This, in some cases, permits identification of the source of the emitted gamma ray, as in the case of induced gamma ray logging.

A scintillation detector is a detector of gamma rays only to the extent that an electron is produced in the crystal through one or more of the three basic gamma ray interaction mechanisms. Thus the gamma ray detection efficiency of a scintillator depends upon its size, density, and average atomic number (for photoelectric

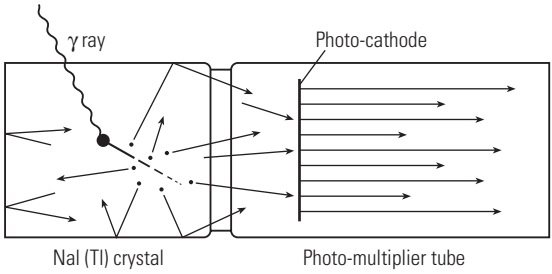


Fig. 10.10 A scintillation detector with its associated photomultiplier. The photo cathode responds to a flash of light in the crystal by releasing electrons. The release of electrons is amplified by the rest of the photomultiplier structure into a detectable electrical pulse.

†This mode can be attained by a reduction of the voltage between the outer cylinder and the central wire. In this case, the size of the output pulse will be proportional to the initial ionization produced by the ejected electron and thus to the absorbed gamma ray energy.

absorption). The most commonly used scintillator is sodium iodide doped with a thallium impurity, NaI(Tl). It has good gamma ray absorption properties and a fairly rapid scintillation decay time ($\approx$0.23 μs). The latter permits spectroscopy at high counting rates.

Recently, two new scintillators have been developed and have found some application in well logging. The first is the high-density bismuth germinate (BGO) detector [4] which offers the possibility of high-detection efficiency with physically small crystals. Its density of 7.13 g/cm^3 is nearly double that of NaI and the characteristic decay time of the scintillation luminosity is only slightly longer at 0.3 μs. Its disadvantage is its relatively poor light output, at room temperature, which is about 10% that of NaI, and then degrades very rapidly with increasing temperature to that point that it is often used in a dewar flask in logging operations to keep it from becoming too warm [5, 6]. A second scintillator, gadolinium orthosilicate, or GSO has been found useful in very high counting-rate applications [7]. Its chief advantage is that the decay time is on the order of 50 ns. Additionally, it has a very large effective atomic number and its density of 6.7 g/cm^3 is nearly double that of NaI [8]. One of its disadvantages is its somewhat smaller (compared to NaI) light output, which however, grows at the temperature increases. Fabrication difficulties and expense of production have resulted in detectors of relatively small volume that are conveniently used in logging applications that require small diameter instruments [9].

10.7.2.1 Gamma Ray Spectroscopy The use of a scintillator device for gamma ray spectroscopy implies that the output light pulse is related uniquely to the incident gamma ray energy. However this is only possible for the case of total absorption of the gamma ray. Some of the difficulties that can complicate the detected spectrum are shown in Fig. 10.11. This schematically depicts a tool designed to look for the unique gamma rays emitted by excited states of carbon and oxygen. The figure illustrates what might happen to a 4.44 MeV gamma ray from carbon which is produced at the site marked (IS). It first makes a Compton scattering in the borehole fluid (CS) and loses 390 keV of energy before traversing the tool housing and entering the NaI detector with an energy of 4.05 MeV. At the point marked (PP) it suffers a pair production interaction, producing one electron and one positron with kinetic energies of 2.00 and 1.03 MeV, the missing 1.02 MeV having gone into the creation of the electron-positron pair. Both particles impart their energy to the scintillation process. When the positron has given up all its kinetic energy, it annihilates with an electron to produce two gamma rays, each of 0.51 MeV energy. One of the gamma rays undergoes Compton scattering at (CS) and the reduced-energy gamma ray (0.41 MeV) is finally absorbed photoelectrically within the crystal at point (Ph.A). The other 0.51 MeV gamma ray is shown escaping the crystal, to the right, and being absorbed in the tool housing (at another point marked Ph.A) without contributing to the total energy transferred to the crystal. The light flash produced in the crystal for the sequence of events depicted corresponds to 3.54 MeV (4.05 MeV – 1.02 MeV pair-production +0.511 MeV annihilation) instead of the 4.44 MeV which we would like to be measuring.

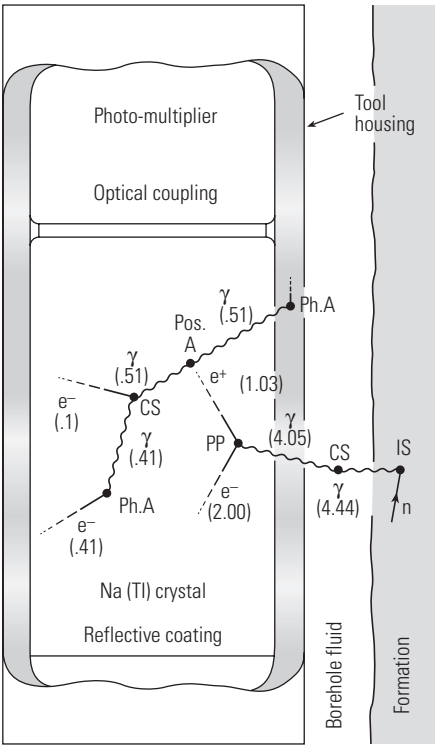


Fig. 10.11 The life of a single gamma ray of 4.44 MeV which is emitted in the formation and ultimately detected by an NaI detector in the borehole.

Thus the structure of the measured gamma ray spectrum is seen to be complicated by the physics of the many processes involved in the detection. Only if the energy of the gamma ray is totally absorbed by the detector is the light output of the scintillator proportional to the incident gamma ray energy. This would be the case for photoelectric absorption, for example. Figure 10.12 shows the energy deposited in this case as the single line to the right marked E_γ. If a Compton interaction occurs, and the gamma ray then leaves the crystal, only a fraction of the energy will be registered. The possible range of energy deposition in this case follows the distribution shown earlier in Figure 10.6. It extends from zero to the Compton edge, which corresponds to maximum energy being transferred from the gamma ray to the electron. Additionally, if the gamma ray is of sufficiently high energy, there may be a pair production reaction. In this case, if one or more of the 511 keV photons escapes the detector without interaction there will be produced in the detected spectrum the so-called first and second escape peaks. Figure 10.13 indicates the additional complication introduced by this process; instead of a single line, three are present, and they are far from looking like "lines."

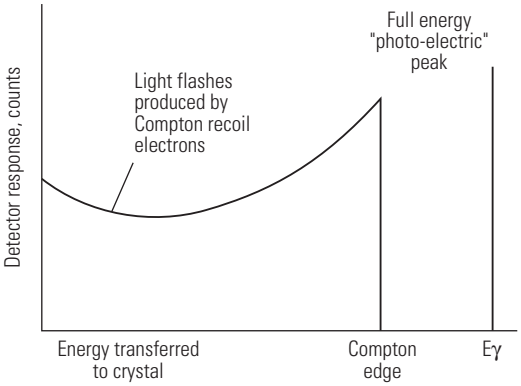


Fig. 10.12 A representation of the detection of a monoenergetic gamma ray by an NaI detector. It shows the full energy peak, where gamma rays have been absorbed by the photoelectric process, and a broad Compton tail for gamma rays which have undergone Compton collisions in the crystal, transferring only part of their energy to electrons which provide the detection.

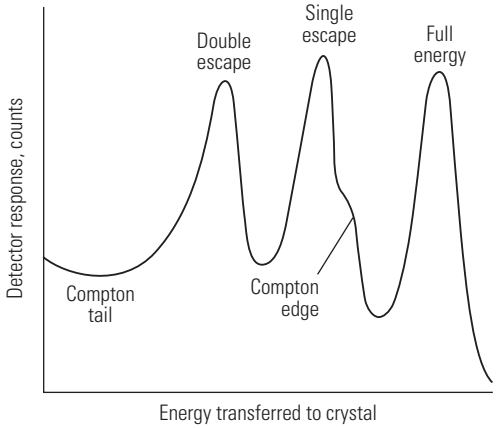


Fig. 10.13 An example of further complication which takes place in the detector. Shown are the two escape peaks and the full-energy peak. The two escape peaks, present only for gamma rays above the pair production threshold, correspond to the escape of one or both of the 511 keV annihilation gamma rays. The resolution of the detector is seen to have broadened each of the otherwise sharp peaks.

The broadening of the line spectra, represented in Fig. 10.13, is a distortion produced by the detector. A measure of this broadening is referred to as the detector resolution. The width of the observed gamma ray lines is, in the case of an NaI detector, primarily a function of the gamma ray energy, the size of the crystal, and the optical coupling between the crystal and photomultiplier, as well as the characteristics of the photomultiplier.

10.7.3 Semiconductor Detectors

One of the major drawbacks of scintillation detectors is their poor energy resolution.‡ In this type of device, detection requires a number of inefficient steps. The result is that the energy required to produce one information "carrier" (a photoelectron in the photomultiplier) is about 1,000 eV. Thus the number of carriers for a typical radiation detection is rather small. The statistical fluctuations on such a small number place an inherent limitation on the energy resolution.

The use of semiconductor materials as radiation detectors can produce many more information carriers per detected event and thus achieve a very high-energy resolution. In a solid state device such as the germanium detector, the semiconductor properties are used to transfer the charged particle energy into a usable electrical pulse in a much more direct manner. The energetic charged particles transfer energy to electrons bound (by only 0.7 eV for Ge) in the crystal lattice, enabling many of them to become free. Each free electron leaves a positive hole in the electron structure of the crystal. Under a strong electrical field applied to the detector crystal, the free electrons and holes migrate quickly to electrodes and create an electrical impulse.

The excellent resolution arises because the band gap is so small. About 3.5×10^5 electrons are freed by the detection of a 1 MeV gamma ray. These contribute to the resulting pulse with no intervening inefficient steps. The result is sharp-energy resolution. Another requirement, however, is that the detector must be operated at extremely low temperatures. This is because at room temperature (not to mention borehole temperatures) some electrons have sufficient thermal energy to cross the 0.7 eV band gap and camouflage those freed by gamma ray interactions. Although the gamma ray spectra obtained with Ge detectors are superb, their overall efficiency is poorer than that obtained by NaI detectors. This latter disadvantage is due to the small detector volumes available for this type of device. Applications of solid-state detectors are limited to devices concerned with precise spectroscopic elemental definition or in situ chemical analysis.

REFERENCES

1. Ellis DV (1987) Nuclear logging techniques. In: Bradley H (ed) Petroleum production handbook. SPE, Dallas, TX

2. Evans RD (1967) The atomic nucleus. McGraw-Hill, New York

3. Mickael M, Phelps D, Jones MD (2002) Design, calibration, characterization and field experience of new high-temperature, azimuthal, and spectral gamma

‡The resolution is usually quoted in percentage. It compares the observed width (ΔE) to the energy (E) of the gamma ray line at which it is measured. The width is determined at half the maximum of the peak. For a NaI detector at 600 keV, a typical value is about 10%.

ray logging-while-drilling tools. Presented at the 77th SPE Annual Technical Conference and Exhibition, paper SPE 77481

4. Rozsa C, Dayton R, Raby P, Kusner M, Schreiner R (1990) Characteristics of scintillators for well logging to 225°C. IEEE Trans Nucl Sci 37(2):996–971

5. Flanagan WD, Bramblett RL, Galford JE, Hertzog RC, Plasek RE, Olesen JR (1991) A new generation nuclear logging system. Trans SPWLA 32nd Annual Logging Symposium, paper Y

6. Truax JA, Jacobson LA, Simpson GA, Durbin DP, Vasquez Q (2001) Field experience and results obtained with an improved carbon/oxygen logging system for reservoir optimization. Trans SPWLA 42nd Annual Logging Symposium, paper V

7. Melcher CL, Schweitzer JS, Manente RS, Peterson CA (1991) Applicability of GSO scintillators for well logging. IEEE Trans Nucl Sci 38(2):506–509

8. Melcher CL, Schweitzer JS, Utsu T, Akiyama S (1990) Scintillation properties of GSO. IEEE Trans Nucl Sci 37(2):161–164

9. Scott HD, Stoller C, Roscoe BA, Plasck RE, Adolph RA (1991) A new compensated through-tubing carbon/oxygen tool for use in flowing wells. Trans SPWLA 32nd Annual Logging Symposium, paper MM

Problems

10.1 Show that the maximum of the Poisson distribution occurs for $x = \underline{\mu}$ when $\underline{\mu} \gg 1$.

10.2 As will be seen in Chapter 12, one method of measuring the density of a formation is to use the attenuation of gamma rays. The gamma–gamma density tool is basically measuring the attenuation of 662 keV gamma rays over a path length of about 40 cm.

10.2.1 Using the simple exponential flux attenuation law ($N = N_o e^{-\mu\rho x}$), derive an expression which relates the uncertainty in density ρ to the uncertainty in the measured counting rate dN.

10.2.2 Using the results from the preceding part, what fractional uncertainty in the counting rate would permit the determination of porosity to within 1 p.u. (i.e., 1% porosity) in a sandstone of porosity 10 p.u.?

10.2.3 What counting rate does this imply for a 1 s measurement?

10.3 The ^{137}Cs gamma ray source which is used in the density logging sonde emits 10^{10} gammas/s and has a half-life of approximately 30 years. The actual form of the source material is microspheres of CsCl, which has a density of 4 g/cm^3. Assuming cubic packing for the microspheres, what volume in cm^3 does the source occupy?

10.4 Show that the efficiency of a γ-ray detector should vary as $(1 - e^{-\mu\rho x})$, where x is the thickness of the detector.

10.5 Using the data of Fig. 10.8, sketch the efficiency curves of a detector of density 3 g/cm^3 and $Z = 13$ for thickness of 1 in. and 2 in. between 10 keV and 100 keV.

10.6 Radioactive decay is responsible for a portion of the thermal gradient observed in the earth. Show that the heat generation of the ^{137}Cs density logging source is on the order of a milliwatt ($1eV = 1.6 \times 10^{-19}$ Joule).

11

Gamma Ray Devices

11.1 INTRODUCTION

Previous log examples demonstrate that two logging measurements are reputed to respond to the difference between clean and shaly formations. One of the measurements, the SP (see Chapter 3), has been analyzed in some detail, and it is known to have a marked response to clean permeable zones. This is evident in the right track of Fig. 11.1 where the more negative potential of the zone between 8,510 and 8,540 ft is due to the simultaneous absence of clay and free communication between the borehole fluid and the formation waters. For the same well, on the left side of the figure, the gamma ray log (or GR) has a structure similar to the SP trace: a low reading in the clean zone and a high reading in an apparently shaly zone. Figure 2.18 shows another example, in track 1, where the GR log and SP correlate to a high degree.

As is evident from its name, the gamma ray responds to the natural gamma radiation in the formation. We shall first address the question of the origin of this natural radiation. The few isotopes which are responsible for it can be attributed to a small list of common minerals. The association of measurable quantities of radioactive isotopes in shales is primarily due to the presence of clay minerals, some of which are naturally radioactive or have radioactive ions associated with them.

Gamma ray logging was introduced in the late 1930s as the first nonelectrical logging measurement. It was immediately useful for distinguishing shaly from clean formations, among other applications to be discussed. Two types of devices are routinely used for determining formation radioactivity. The *GR tool*, in a form nearly indistinguishable from its 1930s predecessor, uses a simple gamma ray detector to measure the total radioactivity of the formation. *Spectral gamma tools* additionally

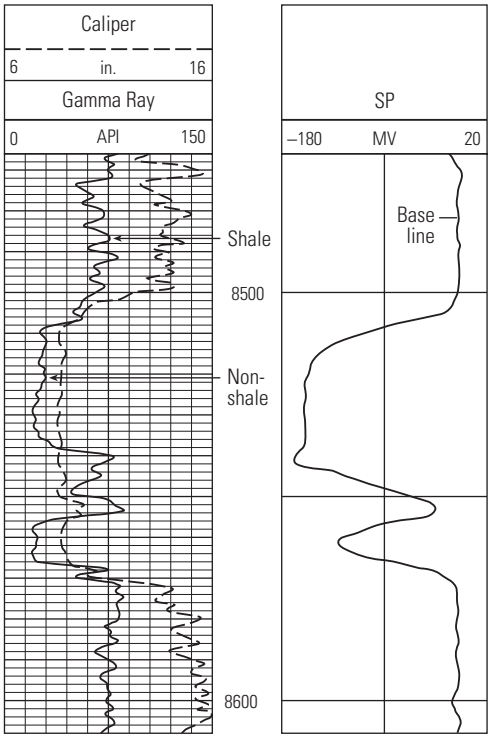


Fig. 11.1 Comparison of the gamma ray curve with the SP and caliper over clean and shale zones.

quantify the concentrations of the radioisotopes present. The two types of devices have similar depths of investigation and suffer from minor environmental effects. The calibration of both types of devices is made with respect to artificial "shale" formations in the laboratory.

Although the GR log is an important component of the traditional analysis of shaly formations, the interpretation of this measurement is somewhat imprecise. A few examples are shown to illustrate the usefulness of spectral gamma ray measurements. Numerous interpretation schemes utilizing the additional spectral information have been proposed and enjoy varying degrees of success.

11.2 SOURCES OF NATURAL RADIOACTIVITY

In order to suggest which naturally occurring isotopes might be responsible for the GR activity of formations, it is instructive to compare half-lives with the estimated age of the earth, which is about 4×10^9 years. There are only three isotopes of the elements potassium, thorium, and uranium with half-lives of that magnitude or greater: ^{40}K: 1.3×10^9 years,^{232}Th: 1.4×10^{10} years, and^{238}U: 4.4×10^9 years. The decay of ^{40}K

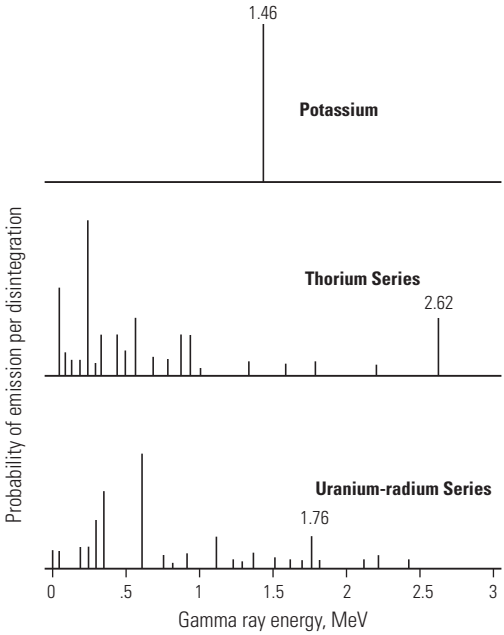


Fig. 11.2 The distribution of gamma rays from the three naturally occurring radioactive isotopes.

is accompanied by the emission of a single characteristic gamma ray at an energy of 1.46 MeV. Thorium and uranium both decay through two different series of a dozen or more intermediate isotopes to a stable isotope of lead. This gives rise to complicated gamma ray spectra with emissions at many different energies, as shown in Fig. 11.2. The prominent gamma ray emission from the uranium series is due to an isotope of bismuth, while that of the thorium series is from thallium. In addition to potassium, the source of all significant gamma ray activity in sedimentary rocks is attributed to isotopes of the thorium or uranium series.

The largest source of formation radioactivity is potassium, a fairly common element in the earth's crust. Figure 11.3 shows the crustal abundances of the common elements, not in volume fraction, but in weight percent. Only eight elements are found at concentrations of 1% or greater. Potassium and magnesium both occur at the 1% level. The minerals containing potassium in sedimentary formations are numerous. Table 11.1 lists a number of evaporites which are potassium-rich, the most commonly known being sylvite. Feldspars, which, after quartz, are the most abundant minerals found in sandstones, have a family of potassium-rich members. One of the five groups of clay minerals prevalent in sedimentary formations (mica) contains potassium as part of the lattice structures. It should be noted that for purposes of log interpretation, the term "mica" generally refers to minerals that do not contribute to "clay" volume (V_{cl}). The reason is related to the low cation exchange capacity of this family of clay

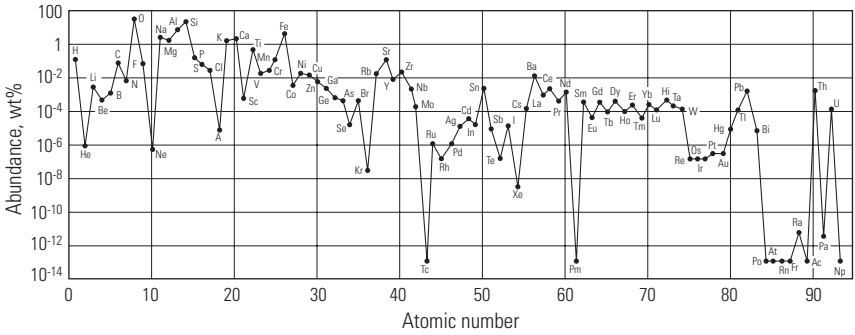


Fig. 11.3 Concentration of the elements in the earth's crust in weight percent. Adapted from Garrels and MacKenzie [1].

Table 11.1 Potassium-bearing evaporitic minerals. Adapted from Serra [2].

Name	Composition	K (% weight)
Sylvite	KCl	52.44
Langbenite	K_2SO_4 $(MgSO_4)_2$	18.84
Kainite	$MgSO_4KCl(H_2O)_3$	15.7
Carnallite	$MgClKCl(H_2O)_6$	14.07
Polyhalite	$K_2SO_4MgSO_4(CaSO_4)_2(H_2O)_2$	13.4
Glaserite	$(KNa)_2SO_4$	24.7

minerals and thus their minimal influence on electrical measurements. However, two members of the group, illite and glauconite, do have a significant cation exchange capacity and contribute to V_{cl}. Further discussion of this subject can be found in Chapter 21.

By contrast, thorium- and uranium-bearing minerals are rare. In logging applications, the uranium may be due to the odd rare mineral, but frequently it is from the precipitation of uranium salts. The solubility of uranium compounds accounts for its transport and its frequent occurrence in organic shales. In the latter case, the presence of uranium results from the absorption of uranium by plant or animal substances which later make up the shale. Thorium is frequently associated with heavy minerals, such as monazite or zircon, which are also known as resistates. Unlike potassium, which we can expect to find at mass concentration at the level of a few percent, thorium and uranium may be expected, at most, at the level of tens of parts per million. The largest concentrations are seen to be associated with shales, which are considered next.

For this discussion, shale is considered to be a fine-grained rock composed of silt and clay minerals. The silt is predominantly quartz but may contain feldspars and organic matter. The clay minerals are primarily responsible for two sources of

radioactivity, potassium, and thorium, associated with most shales. We have already seen that the illite group contains potassium. It shows up in association with other clay minerals as well, such as montmorillonite, and micas such as biotite and muscovite [2]. Clay minerals, which are formed during the decomposition of igneous rocks, in general have a high cation exchange capacity. As a result of this property, they are able to retain trace amounts of radioactive minerals which may have originally been components of the feldspars and micas which go into their production. This property may be responsible for the retention of trace amounts of thorium, which occurs in relatively insoluble minerals. Uranium, because of its solubility, is easily transported from the site of clay mineral formation. It is associated with the organic matter in the shales rather than the clay minerals.

A statistical study of the geochemistry of more than 500 core samples, conducted by Hassan et al. [3], supports the view presented above. The correlation between clay minerals and elemental concentrations was found to be largest for thorium and potassium, while that for uranium was negligible. The correlation between clay minerals and thorium was largest, because potassium is also associated with other components of the shale, such as feldspars. The only significant correlation for uranium was found to be the organic carbon content of the samples.

11.3 GAMMA RAY DEVICES

One of the principal uses of the gamma ray log is to distinguish between the shales and the nonshales. The first gamma ray devices measured only the total gamma ray flux emanating from the formation. These older gamma ray devices use Geiger counters or NaI scintillation detectors, measuring the gamma rays above some practical lower limit (on the order of 100 keV). This total counting rate is a function of the distribution and quantity of radioactive material in the formation. It will be influenced by the size and efficiency of the detector used. For this reason, some calibration standards have been established by the API, and all total intensity GR logs are now recorded in API units.

The definition of the API unit of radioactivity comes from an artificially radioactive formation, constructed at the University of Houston facility to simulate about twice the radioactivity of a typical shale. This formation, containing approximately 4% K, 24 ppm Th and 12 ppm U, was defined to be 200 API units. The details of this calibration facility can be found in another work [4].

The response of a gamma ray device GR_{API} is given by:

$$GR_{API} = \alpha\, {}^{238}U_{ppm} + \beta\, {}^{232}Th_{ppm} + \gamma\, {}^{39}K_{\%}, \tag{11.1}$$

where the subscripts refer to the mass concentration units of the isotope. Note that although ${}^{40}K$ is the radioactive isotope, the reference concentration is for the much more commonly occurring ${}^{39}K$. The relative natural abundance of ${}^{40}K$ is only 0.012%. The coefficients α, β, and γ depend on the actual detector used and the sonde design details. It was for this type of variability that the API calibration standard was proposed.

However, different types of shale have different total gamma ray activity, depending on the Th, U, and K concentrations associated with them. Figure 11.2 shows the various gamma ray lines associated with each radioactive isotope. This indicates that, by determining the intensities of particular gamma rays, it is possible to identify the quantity of each radioactive emitter in the formation. With the development of improved spectroscopic-quality gamma ray detectors, it was natural to refine the gamma ray tool into a device capable of determining the actual concentrations of the three components.

Spectral gamma ray devices employ the same basic type of detection system as the total gamma ray devices, but instead of using one broad energy region for detection, the gamma rays are analyzed into a number of different energy bins. Calibration in standard formations, where the concentrations of K, U, and Th are known, then permits determination of the mass concentrations present in a measured formation as well as the total activity.

To first order, the gamma ray intensity from a uniformly distributed source of constant mass concentration, is independent of the formation density, even though the attenuation is a direct function of the formation density. This can be seen from the following argument.

Consider an infinite homogeneous medium containing n gamma ray emitters per unit volume, each with an emission rate of one gamma ray per second. To calculate the total gamma ray flux which would be detected at any given point in this medium, refer to Fig. 11.4. The contribution to the total counting rate from a spherical shell of thickness dr, at a distance r from the detector, is proportional to the flux $d\Psi$ from

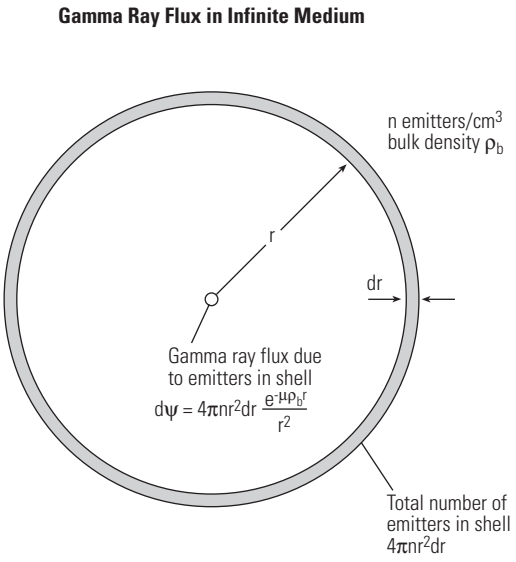


Fig. 11.4 Geometry for calculating the total gamma ray intensity at a point detector due to a uniform distribution of gamma ray emitters.

this volume. The flux itself is given by the number of emitters contained in this shell multiplied by the attenuation over the path length r to the detector:

$$d\Psi = n\, 4\pi r^2 dr \; \frac{e^{-\mu\rho_b r}}{4\pi r^2}\,, \tag{11.2}$$

and the total flux is the integral:

$$\Psi = n \int_0^\infty e^{-\mu\rho_b r} dr = n \frac{1}{\mu\rho_b}\,. \tag{11.3}$$

Since μ , the mass absorption coefficient, is independent of the bulk density, ρ_b, the total counting rate is a direct measure of n/ρ_b, which can be expressed as the weight percent of the isotope which is radioactive. Consequently, the GR log responds directly to the mass concentration of radioactive elements.

Gamma ray measurements suffer to some degree from the borehole environment. Because of mud in the borehole and varying hole diameters, the gamma rays emitted from the formation have to pass through different amounts of gamma ray absorber in order to reach the detector. Correction charts [5] exist to compensate measurements made in conditions that deviate from the standard conditions: tool eccentered in a water-filled 8 in. diameter borehole. The correction depends on an absorption parameter which is the product of the difference between borehole and sonde diameter and the normalized mud density. These corrections were initially determined painstakingly by laboratory measurements but virtually all now are generated from Monte Carlo simulations similar to the procedure described in reference [6].

Additional complications can arise from mud additives such as barite or KCl. Barium in the mud is a very efficient absorber of low-energy gamma rays emanating from the formation. Correction charts for specific instruments can be derived similar to the ones mentioned above. The potassium in KCl makes the mud an unwanted source of radioactivity. Ellis [7] discusses a method for correcting spectral gamma ray measurements for these effects. In more modern spectral tools [8] it is possible to implement a correction for K in the mud by recognizing the difference in the shape of the potassium gamma ray spectrum coming from the mud caused by fewer scatterings than that from deeper into the formation.

11.4 USES OF THE GAMMA RAY MEASUREMENT

The GR log has traditionally been used for correlating zones from well to well, for crude identification of lithology, and for rough estimation of the volume of shale (sometimes denoted as V_{cl}) present in the formation. Continuous shale beds can be readily identified in wells separated by large distances from their characteristic gamma ray "signature." Due to the simplicity of the GR tool, it is present as an auxiliary sensor on most other logging services to provide routine depth control. With the current state of knowledge of clay composition and with other more refined lithology determinations available, it seems likely that the GR log will be used in the future only for correlation, depth control, and in low-cost development wells for an estimate of V_{cl}.

The use of the GR measurement to estimate the shaliness of a formation has been the subject of some confusion, which arises from two sources. First, log analysts have used the terms *clay* and *shale* interchangeably. Second, the GR log responds to neither clay nor shale, but rather to associated radioactive isotope concentrations. For estimating the volume fraction of shale in a formation V_{sh}, the traditional approach is to scan the log for minimum and maximum GR readings, γ_{min} and γ_{max}. The minimum reading is then assumed to be the *clean point* (0% shale), and the maximum reading is taken as the *shale point* (100% shale). Then the GR reading in API units at any other point in the well (γ_{log}) may be converted to the GR index I_{GR} by linear scaling:

$$I_{GR} = \frac{\gamma_{log} - \gamma_{min}}{\gamma_{max} - \gamma_{min}} . \tag{11.4}$$

This index can be scaled into percent of shaliness according to charts (see Fig. 11.5) depending on rock type. The linear transformation of I_{GR} to shale fraction is frequently used. The two nonlinear conversions of Fig. 11.5, which result in small shale volume estimates for a given GR index, attempt to compensate for the clay mineral proportions of different shales. At best, this is seen to be a somewhat fuzzy approach to determining the nature of a shaly sand. Depending upon the application, sometimes the shale fraction is desired, and sometimes the clay mineral volume would be more appropriate. The linear interpolation for shale volume is appropriate for shaly zones which contain the same proportions of clay minerals as those zones used for the determination of the GR end points. Of course, one of the largest sources of error

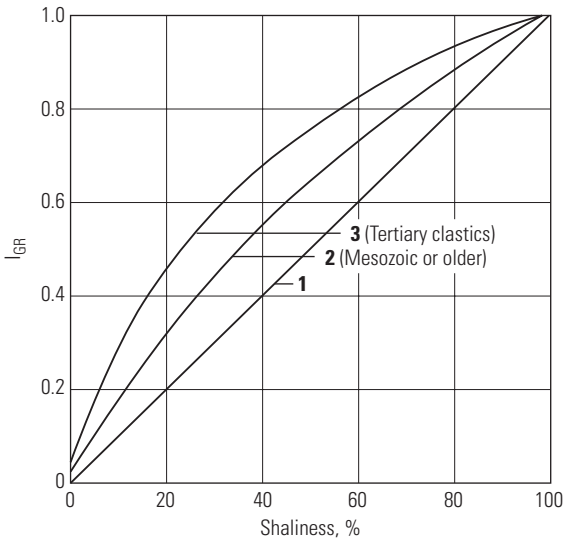


Fig. 11.5 Conversion of the GR index to shaliness depending on rock types, based on work of Larinov. Heslop proposed a modification based on a distinction between "shale" and "clay" [10]. Adapted from Dresser Atlas [9].

occurs when the zone picked for the minimum GR signal is not clay free. Further discussion of this technique, which attempts to determine too much from too little information, may be found in Heslop [10].

11.5 SPECTRAL GAMMA RAY LOGGING

One of the difficulties in the interpretation of the gamma ray measurements is a lack of uniqueness. There are nonradioactive clays, and there are "hot" dolomites. The use of spectral gamma ray devices can point out anomalies such as a "hot" dolomite or other formations with some unusual excess of U, K, or Th. They permit recording the individual mass concentrations of the three radioactive components of the total gamma ray signal. A clear example of the utility of this decomposition can be seen in Fig. 11.6. In track 2 the three components, Th, U and K, are shown in a carbonate section. In track 1 two curves are to be found. The one marked GR is the total gamma ray signal calibrated in API units as in an ordinary tool that does not employ spectroscopy. The second curve is the so-called computed GR (CGR) curve. It consists of the sum of counting rates from Th and K converted to API units. In this way it is uninfluenced by uranium which has little association with clay minerals. It can be seen that the activity in the GR signal was due to uranium fluctuations. Interpreting the total GR signal for clay would have given misleading results in a zone that is essentially clay-free.

For one type of tool, the relationship between the concentration of the three radioactive components and the total gamma ray signal in API units (γ_{API}) is given approximately by:

$$\gamma_{API} = 4\,Th + 8\,U + 16\,K, \tag{11.5}$$

when thorium (Th) and uranium (U) are measured in ppm and potassium (K) in percent by weight. This expansion shows, for example, that a shaly sand containing a mineral rich in potassium, such as mica, could be interpreted erroneously. A false indication of the percentage of shale would be reported as a result of the additional radioactivity produced by the mica (by which is meant those mica minerals that have no influence on resistivity logs). Another use of this decomposition is to provide a total GR signal minus the uranium contribution. This can provide a uranium-free GR index which is more representative of the clay minerals in the shale, by eliminating effects of organic shales or the deposit of uranium salts in fractures [12]. Examples of the use of the spectral gamma ray device to detect such anomalies are presented next.

Figure 11.7 shows a log example in a micaceous sand. At 10,612–10,620 ft, a shale is indicated having a total GR signal of about 90 API units. If only the total gamma ray is used as an indicator, it appears that the zone between, 10,522 and 10,568 ft contains about half the amount of shale estimated for the lower zone. However, the decomposition of the GR signal shows quite clearly that the amounts of U, Th, and K in these two zones are quite different. In fact, the upper zone is a mixture of sand and mica, whereas the lower zone is indeed shale.

In the next example, Fig. 11.8, the GR log alone would indicate that below the lower boundary of the shale bed, at 12,836 ft, there is a relatively clean sand. It can be seen,

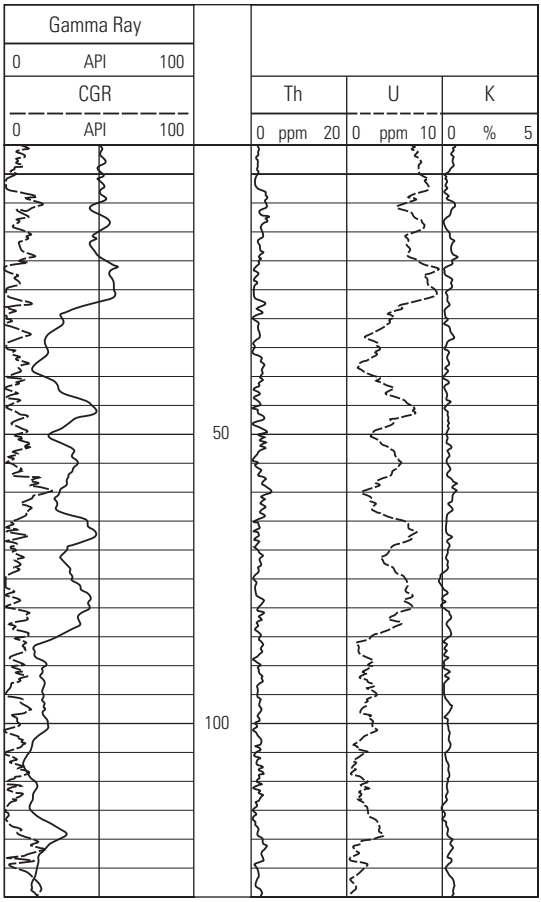


Fig. 11.6 Decomposition of the natural gamma ray activity of a carbonate section into concentrations of Th, U and K. The total gamma ray (GR) signal has considerable activity, seen to correlate with fluctuations in U content. The CGR trace is computed from the GR trace by subtracting the contribution of uranium. The CGR curve is more consistent with the knowledge that this is a largely clay-free zone. Adapted from Luthi [11].

however, from the K trace that the high level of potassium in the shale zone persists below 12,836 ft. This excess potassium was found from subsequent core analysis to result from the presence of feldspar. This is an important piece of knowledge because feldspar affects the choice of grain density to be used in the interpretation of density logs.

The third example, Fig. 11.9, shows how a uranium-rich formation would be misinterpreted (in a simple gamma ray analysis) as being shale. The sudden increase in uranium content, at the indicated depth, suggests that this is not a simple shale like those at nearby depths. Core analysis showed this zone to be rich in organic material. This is consistent with the notion that U is often trapped in organic complexes.

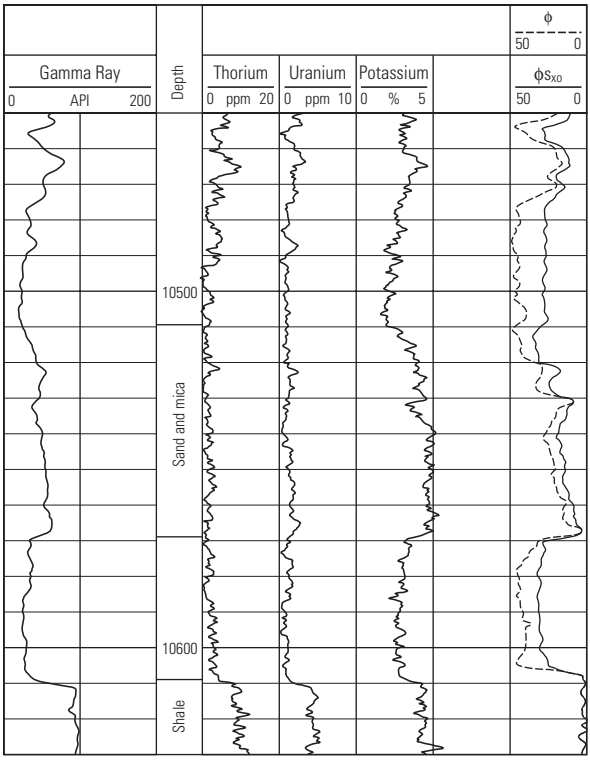


Fig. 11.7 A spectral gamma ray log indicating the concentration of Th, U, and K. The zone indicated as containing mica shows an abnormally high K content. In the zone, the GR curve would incorrectly imply the presence of a nonnegligible amount of clay. Adapted from Ellis [13].

There are two important reasons for using a spectral gamma ray measurement rather than the standard gamma ray, which is reliable only for correlation. The first is for the resolution of radioactive anomalies like those described above. The second is to help identify the clay types by classifying them in terms of the relative contributions of the three radioactive components. It will become apparent in Chapter 21 that clay mineral identification is a task much too complicated to be attempted solely from a knowledge of the associated radioactive elements. However, several schemes for extracting some additional information from spectral GR logs, discussed below, enjoy a certain amount of success.

As indicated earlier, the distinguishing of mica from shale has been an important application for the spectral gamma ray tools. Resistivity logs need to be corrected for the presence of conductive clay minerals, but mica is an insulator. Hodsen et al. [14], in the tradition of well log data analysis, used a cross plot of measured thorium and potassium values to distinguish shaly sands from those containing mica, as shown in Fig. 11.10. The end members in this plot correspond to clean sand, shale (appropriate

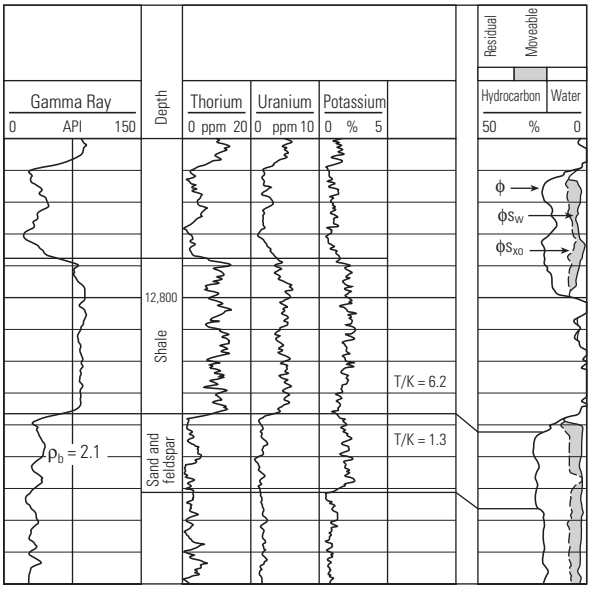


Fig. 11.8 A log showing the effect of feldspar on the spectral and total gamma ray logs. Adapted from Ellis [13].

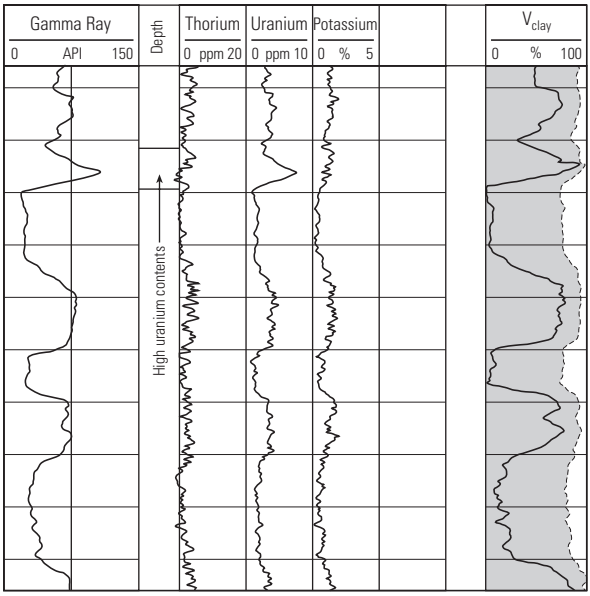


Fig. 11.9 A log showing the result of an anomaly of U. If undetected, the volume of clay in the entire zone is compromised. Adapted from Ellis [13].

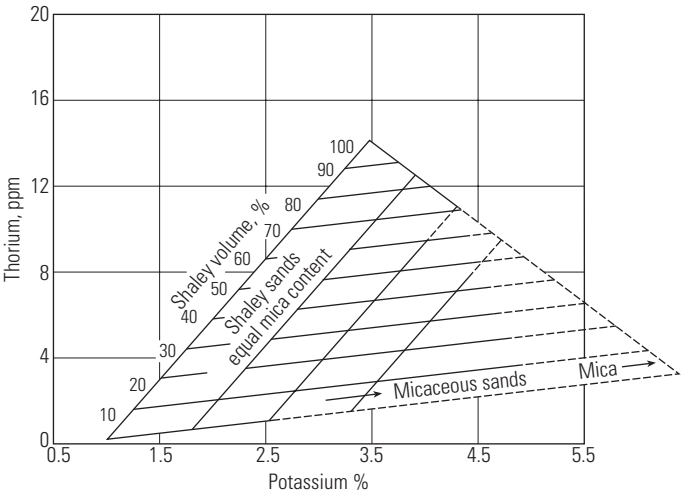


Fig. 11.10 A cross plot of Th and K for determining shale volume and distinguishing micaceous sands from shaly sands. From Hodsen et al. [14].

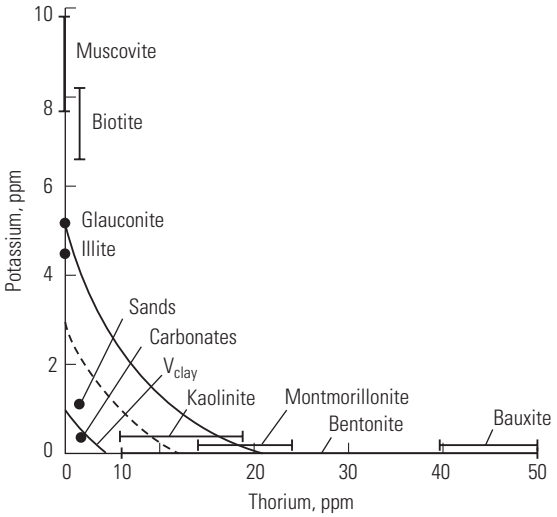


Fig. 11.11 Determination of V_{cl} for thorium and potassium distributions. After Ruhovets and Fertl [15].

to certain zones of a particular well), and mica. The plot can be scaled to give the fractional volumes of the three components. An improved clay indicator was proposed by Ruhovets and Fertl [15]. It is based on an approximate knowledge of potassium and thorium contents of some common clay minerals, as shown in Fig. 11.11. Lines of constant clay volume should follow a parabolic shape, as indicated in the figure. The

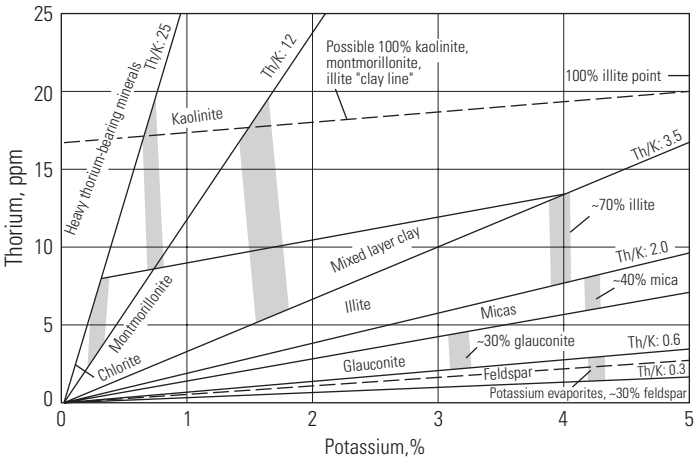


Fig. 11.12 Identification of clay minerals from thorium and potassium. From Schlumberger [5].

scaling is adopted to the clay minerals present in the zones under investigation and determined from the cross plot. Quirein et al. have suggested a means to determine the presence of major clay minerals, such as illite and kaolinite, and to separate them from feldspars [16]. The method is summarized in Fig. 11.12 and consists of an ambitious reinterpretation of the potassium–thorium cross plot.

Two special applications for spectroscopic gamma analysis have been developed. One is for environmental logging – specifically to detect the presence of ^{137}Cs and ^{60}Co in the near subsurface. The second is for improved vertical resolution for correlating logs with core measurements. These two will be detailed in Section 11.6 after a discussion of spectral stripping.

11.5.1 Spectral Stripping

The subject of spectral stripping has evolved over the years, although the basic technique of least-squares fitting remains the same. We begin the discussion with the crude spectral estimation available in the early 1970s from a few analog window counting rates.

To measure the concentration of the three radioactive isotopes responsible for the total GR signal, a spectral analysis of the detected gamma radiation is performed. Figure 11.13 shows how the line emission spectrum of the three isotopes are distorted in an NaI detector. Of the roughly 20 lines, only 3 are seen clearly.

One data-reduction technique divides the observed spectrum into a number of windows [17]. In the illustration of Fig. 11.13, the number of windows is five. By a series of measurements in specially constructed formations containing known concentrations of the three radioactive isotopes, it is possible to construct a *response matrix*. This matrix relates the counting rates ($W_1, \ldots, W_5$) in the five windows to

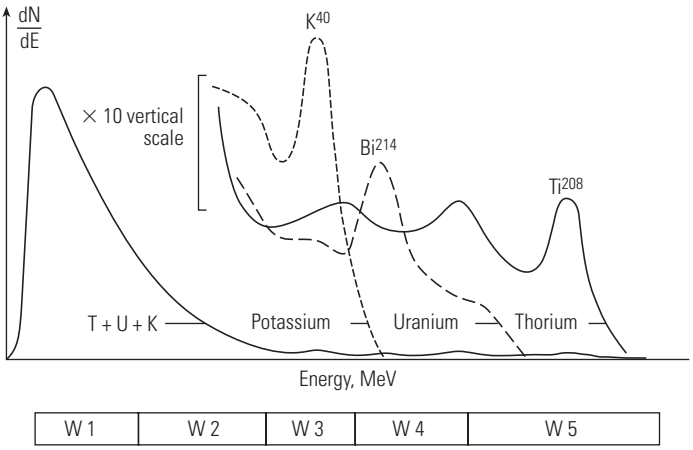


Fig. 11.13 A schematic representation of the distortion of the spectrum of natural radiation as registered by an NaI detector.

the concentrations of U, Th, and K. This is shown symbolically as:

$$\begin{bmatrix} W_1 \\ W_2 \\ W_3 \\ W_4 \\ W_5 \end{bmatrix} = \overline{A} \times \begin{bmatrix} Th \\ U \\ K \end{bmatrix}, \tag{11.6}$$

where the response matrix $\overline{A}$ is a 5×3 matrix. The entries of $\overline{\mathbf{A}}$ correspond to the counting rate contributed by each radioactive material to each window. Normally, if the number of equations were equal to the number of unknowns, the solution of Eq. 11.6 for the concentrations would be simple. In this overdetermined system, the method of least squares can be used to determine the coefficients of the inverse matrix. The procedure begins by considering that there is statistical noise present in the five window counting rates. Consequently, in a formation with precisely known Th, U, and K concentrations, there will be a residual counting rate r_i for each window measurement, when compared to the noise-free standard response of Eq. 11.6. The residual can be expressed by:

$$\sum_{i=1}^{5} W_i - A_i Th - B_i U - C_i K = \sum_i r_i , \tag{11.7}$$

where A_i, B_i, C_i are the appropriate elements of $\overline{\mathbf{A}}$. The least-square procedure is to minimize the square of the residuals:

$$\sum_{i=1}^{5} (W_i - A_i Th - B_i U - C_i K)^2 = \sum_i r_i^2 . \tag{11.8}$$

This can be done by taking the derivative of Eq. 11.8 with respect to Th, U, and K. This results in three equations in three unknowns. The solution is of the form:

$$\begin{bmatrix} Th \\ U \\ K \end{bmatrix} = \overline{\mathbf{m}} \begin{bmatrix} W_1 \\ W_2 \\ W_3 \\ W_4 \\ W_5 \end{bmatrix}, \tag{11.9}$$

where the elements of $\overline{\mathbf{m}}$ are a combination of the elements of the original response matrix. *The optimized solution takes into account the variance of the counting rates of each window (the square root of the counting rate times the observation time), and the set of equations to be solved are determined from differentiating the following expression:*

$$\sum_{i=1}^{5} \frac{1}{W_i}(W_i - A_i Th - B_i U - C_i K)^2 = \sum_i r_i^2 . \tag{11.10}$$

The set of coefficients $\frac{1}{W_i}$*, or weights, may represent the inverse of average counts in each channel expected in shales, for example, or can be determined, on a measurement-by-measurement basis, using the actual accumulated counts. Bevington treats this data-reduction problem in terms of matrix operations and provides programs for their implementation [18].*

For more modern spectroscopic tools with digitization of the detector output signal, a large number of windows (~256) are used to record the natural gamma emissions with large, more efficient detectors with good spectroscopic energy resolution. The response matrix $\overline{\mathbf{A}}$*, above then becomes a set of so-called standards. These standards represent the response of the spectrometer to single sources of Th, U, K and sometimes other isotopes. Before the analysis can proceed, the measured spectra must be carefully gain adjusted to match the window/energy correspondence of the standards. Due to temperature effects on the detectors, often mitigated by using thermally insulating dewars, and deteriorating crystals or crystal/photomultiplier connections, the energy resolution of the measured spectrum may be worse than the "standard" tool with which the standards were recorded. Before processing, the energy resolution of the standards are "degraded" by software to match the measurement resolution.*

The procedure for extracting the concentrations of the three elements is called weighted least squares analysis and is a commonly used technique. For its usefulness, it is worth laying out the matrix representation since a number of higher level programming languages allow one-line solution of this intricate set of linear equations. As mentioned above, the matrix $\overline{\mathbf{A}}$ *represents the "standards," which might just be those for Th U, and K, or some others might be included, such as Cs and Co, or K from the borehole. Each standard will correspond to a column of the matrix which will have as many rows as the number of channels in the output of the detector.* $\overline{\mathbf{W}}$ *is a diagonal weighting matrix (related to but not identical to the weights of Eq. 11.10), whose elements correspond to the inverse square root of the number of counts in each*

channel of the spectrum to be analyzed or of the spectrum of a "typical shale." Then the estimate, $\overline{\mathbf{x}}$, of the vector of concentrations of T, U, and K (and any other items included in the standard matrix $\overline{\mathbf{A}}$) can be obtained from the measured spectrum $\overline{\mathbf{p}}$ by the following matrix operation:

$$\overline{\mathbf{x}} = (A'WA)^{-1}A'W\overline{\mathbf{p}}, \tag{11.11}$$

where $(A'WA)^{-1}$ represents the inverse of the matrix product and A' represents the transpose.

11.6 DEVELOPMENTS IN SPECTRAL GAMMA RAY LOGGING

Developments of natural gamma ray spectrometry have been slow and incremental. There have been improvements in instrumentation and signal processing; development of new geophysical applications from exploiting improved hardware and signal processing; and finally the appearance of a new family of instruments developed for operation in high deviation or horizontal wells, while drilling.

Improvements have been made in moving from analog acquisition of the detector signal to multichannel digital acquisition of spectra, and in detector spectroscopic quality. Because of the generally low natural activity, obtaining statistically significant measurements at reasonable logging speed is an unavoidable problem. To improve this situation, tools have been developed that make use of either more efficient and/or longer detectors than the conventional 12 in. NaI crystals. In one early tool [19] a 2 in. by 12 in. CsI detector was used. An early digital acquisition system, employing a conventional NaI detector, has the additional feature of a low atomic number (Z) housing around the detector section for extending the usable energy range to lower energies [20]. Another tool designed for digital acquisition of an efficient spectroscopic detector and high temperature operation, employs a pair of large BGO detectors in a dewar flask [8].

Two non-oilfield applications merit mention. The first is a tool developed for the Ocean Drilling Program to improve the matching of gamma ray log data with other high vertical resolution measurements made on cores. For this application a multisensor tool was developed [21] employing four small 2 in. by 4 in. NaI detectors spaced 2 ft apart. Each of the detectors provides spectroscopic data that are stacked in depth to reduce statistics and to obtain improved spatial resolution. Using this tool and processing technique provides a noticeable improvement in resolving thin radioactive markers compared to the data acquired by a commercial log with a single 12 in. long detector.

A second application is the use of a spectral gamma ray tool in environmental logging for the detection and mapping of ^{137}Cs and ^{60}Co, commonly occurring subsurface contaminants associated with nuclear weapon production. In one example, an upgraded spectral logging sonde equipped with BGO detectors was provided with two additional standards that represented ^{137}Cs and ^{60}Co for the spectral analysis. This enabled making logs of subsurface contamination of ^{137}Cs and ^{60}Co at the Hanford Site [22]. Another approach used a modified instrument with a 12 in. long NaI crystal

with a detector section that was made of a low Z material (graphite) in order to be sensitive to low energy gamma rays. After logging a contaminated site at Hanford, analysis of the low energy data from this tool indicated that the ^{60}Co, detected previously, was actually adsorbed on the inside of the corroded casing rather than in the formation [23].

In the latest chapter in the slow evolution of natural gamma tools, the 1980s saw the development of natural gamma ray measurements for LWD applications in horizontal wells. Despite the development of families of tools by a number of major service companies, the literature is largely absent of description. The LWD environment is difficult for delicate spectroscopic devices – there are excessive vibrations and the detectors must be accommodated in the drill collar, often a substantial thickness of gamma ray absorbing steel. Generally the LWD measurements provide a total GR signal, although spectral versions exist. An early version [24] attempted to contribute to sensing the proximity of radioactive bed boundaries by "focusing" the detector. This consisted of placing some additional shielding behind the centrally located axial detector providing about a 30% increased detection sensitivity in the forward direction. In principle, as the tool rotates, the detected GR signal should become sinusoidal with an amplitude determined by the distance to a nearby bed of contrasting activity. The utility of such an approach for geo-steering is dubious and has certainly been supplanted by electrical measurements to be discussed in Chapter 20.

A new family of gamma ray tools [25] for LWD applications employs, in two different instruments, an axially centered detector with mud flow in the annulus between detector and inner drill collar; or groups of detector embedded in the circumference of the drill collar. Calibration of these devices, whose diameter ranges from 4.75 to 8 in., is complicated by the construction of the API calibration pit at the University of Houston which accepts only the smallest diameter device. Using this calibrated tool, a secondary standard for the calibration of the larger diameter devices was constructed. Computer modeling was also used for determining the response characteristics for a variety of collar thickness and environmental conditions.

A frequently asked, but poorly documented question concerns the difference between wireline and LWD gamma ray readings in the same well. The response sensitivity of a variety of logging instruments – wireline and LWD – was evaluated with Monte Carlo simulation [26] and resulted in two important conclusions. The first was that, although there was variation due to borehole size and mud composition, the sensitivity (i.e., the coefficients in Eq. 11.5) to formation radioactivity is very similar between wireline and several varieties of LWD tools. This relative invariance of sensitivity results in very small differences in the total gamma ray signal (in API units) attributable to the structural differences of the various tools. The largest source of variation, however, was found to be linked to environmental corrections. Especially in the case of heavily weighted barite muds, the failure to implement the environmental corrections of one of the tools under comparison could lead to noticeable discrepancies.

11.7 A NOTE ON DEPTH OF INVESTIGATION

How deeply does the GR tool see into the formation? The depth of investigation of such a device is difficult to measure experimentally; however, it can be determined from Monte Carlo simulations. For simplicity, the depth of investigation for a single component of the GR signal is considered. Figure 11.14 shows the depth of investigation of detected radiation from the decay of ^{40}K computed in this manner [27]. For this simulation, the tool was taken to be eccentered in an 8 in. diameter borehole. The figure shows the normalized integrated signal J(r) produced by coaxial cylinders of K-bearing formation around the borehole. What is seen from this figure, computed for a density of 2.5 g/cm^3, is that 90% of the signal of unscattered gamma rays comes from an annulus which is about 15 cm thick. For multiply scattered gamma rays, the depth of investigation increases by only a few centimeters. This is to be contrasted, for example, with the integrated radial geometric factor of the deep induction, which shows a total insensitivity for such a shallow zone.

The result of the sophisticated calculation can be approximated rather easily by considering the mean free path of gamma rays. The general gamma ray attenuation relationship (Eq. 10.19) can be written as:

$$N = N_o e^{-\mu \rho_b x}, \tag{11.12}$$

where μ is the mass absorption coefficient, ρ_b is the material bulk density, and x is the distance over which the attenuation is taking place. From this expression, the mean free path λ is taken to be:

$$\lambda = \frac{1}{\mu \rho_b}. \tag{11.13}$$

It is the distance over which the flux is reduced by a factor of 1/e. The mass absorption coefficient of a 1.46 MeV gamma ray in nearly any substance is found to be 0.05 cm^2/g

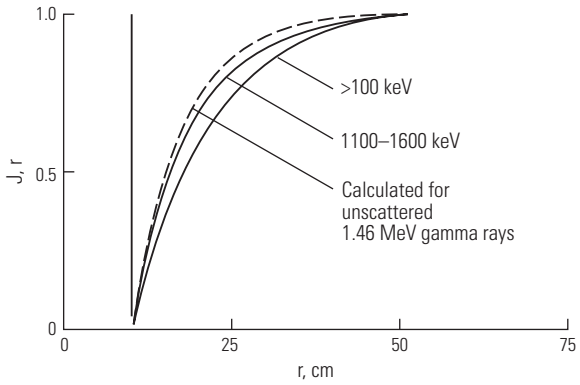


Fig. 11.14 The computed radial geometric factor for the detection of K gamma rays by a borehole sonde in an 8 in. borehole. Adapted from Wahl [27].

(see Fig. 10.8) so the mean free path, in centimeters, is given by:

$$\lambda = 20/\rho_b \,, \tag{11.14}$$

where ρ_b is in gram per cubic meter. This means that the mean free path for 1.46 MeV gamma rays varies between 7 and 10 cm for formations with densities between 2.0 and 3.0 g/cm^3. With reference to Eq. 11.3, but only carrying out the integration to a distance r, an expression for the integrated radial geometric factor $J(r)$ can be developed. It shows the signal to grow as:

$$J(r) \propto \left(1 - e^{-\frac{r}{\lambda}}\right) . \tag{11.15}$$

To compare this prediction with the Monte Carlo calculation, λ is taken to be 8 cm, corresponding to a density of 2.5 g/cm^3. The 90% point will be attained for a shell (in this spherical approximation) of total thickness of about 18 cm, which is in close agreement with the Monte Carlo calculation.

REFERENCES

1. Garrels RM, MacKenzie FT (1971) Evolution of sedimentary rocks. W. W. Norton, New York
2. Serra O (1984) Fundamentals of well-log interpretation. Elsevier, Amsterdam, The Netherlands
3. Hassan M, Hossin A, Combaz A (1976) Fundamentals of the differential gamma ray log-interpretation technique. Trans SPWLA 17th Annual Logging Symposium, paper H
4. Belknap, WB, Dewan JT, Kirkpatrick CV, Mott WE, Pearson AJ, Rabson WR (1978) API calibration facility for nuclear logs. Gamma ray, neutron and density logging, SPWLA Reprint, paper E
5. Schlumberger (1985) Interpretation charts. Schlumberger, New York
6. Koizumi CJ (1985) Computer determination of calibration and environmental corrections for a natural spectral gamma ray logging system. Presented at the 60th SPE Annual Technical Conference and Exhibition, paper SPE 14186
7. Ellis DV (1982) Correction of NGT logs for the presence of KCl and barite muds. Trans SPWLA 23rd Annual Logging Symposium, paper O
8. Flanagan WD, Bramblett RL, Galford JE, Hertzog RC, Plasek RE, Olesen JR (1991) A new generation nuclear logging system. Trans SPWLA 32nd Annual Logging Symposium, paper Y
9. Dresser Atlas (1983) Well logging and interpretation techniques: the course for home study. Dresser Atlas, Dresser Industries, Houston, TX

10. Heslop A (1974) Gamma-ray log response of shaly sandstones. Trans SPWLA 15th Annual Logging Symposium, paper M

11. Luthi SM (2000) Geological well logs: their use in reservoir modelling. Springer, Berlin Heidelberg, New York

12. Serra O, Baldwin J, Quirein J (1980) Theory, interpretation and practical applications of natural gamma ray spectroscopy. Trans SPWLA 21st Annual Logging Symposium, paper Q

13. Ellis DV (1987) Nuclear logging techniques. In: Bradley H (ed) Petroleum production handbook. SPE, Dallas, TX

14. Hodsen GW, Fertl WH, Hammack GW (1976) Formation evaluation in Jurassic sandstones in the Northern North Sea area. The Log Analyst 17(1):22–32

15. Ruhovets N, Fertl WH (1982) Digital shaly sand analysis based on Waxman-Smits model and log-derived clay typing. The Log Analyst 23(3):7–26

16. Quirein JA, Gardner JS, Watson JT (1982) Combined natural gamma spectral/litho-density measurement applied to complex lithologies. Presented at the 57th SPE Annual Technical Conference and Exhibition, paper SPE 11143

17. Marett G, Chevalier P, Souhaite P, Suau J (1976) Shaly sand evaluation using gamma ray spectrometry applied to the North Sea Jurassic. Trans SPWLA 17th Annual Logging Symposium, paper DD

18. Bevington PR (1969) Data reduction and error analysis for the physical sciences. McGraw-Hill, New York

19. Mathis GL, Tittle CW, Rutledge DR, Mayer R Jr, Ferguson WE (1984) A spectral gamma ray (SGR) tool. Trans SPWLA 25th Annual Logging Symposium, paper W

20. Smith HD Jr, Robbins A, Arnold DM, Gadeken LL, Deaton JG (1983) A multifunction compensated spectral natural gamma ray logging system. Presented at the 58th Annual Technical Conference and Exhibition, paper SPE 12050

21. Goldberg D, Meltser A, ODP Leg 191 Scientific Party (2001) High vertical resolution spectral gamma ray logging: a new tool development and field test results. Trans SPWLA 42nd Annual Logging Symposium, paper JJ

22. Ellis DV, Perchonok RA, Scott HD, Stoller C (1995) Adapting wireline logging tools for environmental logging. Trans SPWLA 36th Annual Logging Symposium, paper C

23. Gadeken LL, Madigan WP, Smith HD Jr (1995) Radial distribution of ^{60}Co contaminants surrounding wellbores at the Hanford site. IEEE Nuclear Sci Symp Med Imaging Conf Rec 1:214–218

24. Jan Y-M, Harrell JW (1987) MWD directional-focused gamma ray – a new tool for formation evaluation and drilling control in horizontal wells. Trans SPWLA 28th Annual Logging Symposium, paper A

25. Mickael M, Phelps D, Jones MD (2002) Design, calibration, characterization and field experience of new high-temperature, azimuthal, and spectral gamma ray logging-while-drilling tools. Presented at the 43rd SPE Annual Technical Conference and Exhibition, paper SPE 77481

26. Mendoza A, Ellis D, Rasmus, JC (2006) Why the LWD and wireline gamma ray measurement may read different values in the same well. Presented at the 1st International Oil Conference and Exhibition in Mexico, paper SPE 101718

27. Wahl JS (1983) Gamma-ray logging. Geophysics 48(11):1536–1550

Problems

11.1 It was stated in the derivation of the counting rate from a uniformly distributed gamma ray emitter (with n emitters per cubic centimeter) that $\frac{n}{\rho}$ is proportional to the percent by weight of the isotope. What is the constant of proportionality?

11.2 Estimate the counting rate (in counts per second) for a perfectly efficient gamma ray detector with surface area of 1 cm^2 which is placed in the 200 API gamma ray standard formation. Recall that the material in this standard consists of 12 ppm U, 24 ppm Th, and 4% ^{39}K. For this calculation assume a reasonable average value of the mass absorption coefficient μ for the energy range of emissions, and further assume that only 1 gamma ray is emitted per decay of the radioactive material.

11.3 On the log of Fig. 11.1, estimate the amount of clay, V_{cl}, at the following depths: 8,540, 8,549, and 8,560 ft. Do the same using the SP curve and compare. Why does the SP yield higher values for V_{cl} in the bottom zone?

11.4 Using the total GR curve of Fig. 11.7, compute the value of V_{cl} at the top and bottom of the zone indicated as "sand + mica."

11.5 Using the response matrix of Eq. 11.6, derive an expression for an appropriate two-window estimate of Th and U. Write it in terms of elements of the response matrix; for example, a_{13} corresponds to the contribution in window 1, due to the concentration of K, and a_{24} corresponds to the counting rate in window 4 from U.

11.6 For the spectral gamma device described in Fig. 11.13 where the gamma rays from Th and U are predominantly in windows 4 and 5, and where the K gamma ray is contained only in window 3 and below, determine the response equations for U and Th. This can be done from a single measurement where the window counting rates are known, as well as the Th and U concentrations. Suppose window 5 and window 4 have 40 and 100 counts, respectively, in a formation containing 5 ppm Th and 20 ppm U.

12

Gamma Ray Scattering and Absorption Measurements

12.1 INTRODUCTION

As noted in Chapter 10, the transmission of gamma rays through matter can be related to the electron density if the predominant interaction is Compton scattering. In the borehole environment, a transmission measurement is not possible. However, a gamma ray transport measurement through a formation can be used to determine its density. With some information on the material composition (lithology and pore fluids), the porosity can be determined.

The motivation for the measurement of formation bulk density comes from its direct relationship with the formation porosity and from geophysical applications. As seen earlier, porosity is an essential petrophysical descriptor and an important ingredient in the interpretation of resistivity measurements in terms of water saturation, S_w. Bulk density is used to compute the acoustic impedances of adjacent layers for seismic interpretation and for estimating overburden pressure.

The basic equation which relates the bulk density of the formation, ρ_b, to the porosity ϕ is:

$$\rho_b = \phi \rho_f + (1 - \phi)\rho_{ma} , \tag{12.1}$$

where ρ_f is the density of the fluid filling the pores and ρ_{ma} is the density of the rock matrix. Although this equation is exact, it presents several problems for the determination of porosity. What value is to be used for the matrix density? For normally encountered formations, it is generally between 2.65 and 2.87 g/cm^3, depending on the lithology. For values of fluid density, it is necessary to know the type of fluid in the pores. The fluid density for hydrocarbon ranges from 0.2 to 0.8 g/cm^3. Salt-saturated water (NaCl) density may be as high as 1.2 g/cm^3, and with the presence of $CaCl_2$,

values even as great as 1.4 g/cm^3 may occur. It is fortunate that the uncertainty that can be tolerated in ρ_f is much greater than that for ρ_{ma}.

For the moment, this problem of interpretation is overlooked while we discuss, instead, the measurement technique for density determination and how it naturally leads to an auxiliary measurement of the photoelectric factor P_e, which is closely related to the formation lithology.

12.2 DENSITY AND GAMMA RAY ATTENUATION

In Chapter 10 it is shown that the interaction of gamma rays by Compton scattering is dependent only upon the number density of the scattering electrons. This in turn is directly proportional to the bulk density of the formation. The reduction of the flux Φ_o in traversing a thickness of material x is given by:

$$\Phi = \Phi_o e^{-\rho_b \frac{Z}{A} N_o \sigma x} , \tag{12.2}$$

where the term $\rho_b \frac{Z}{A} N_o$is the number density of electrons in a material of mass density ρ_b, and σ is the cross section for Compton scattering.

It is natural, therefore, to exploit the attenuation of gamma rays for the determination of bulk density. An idealized device would consist of a detector and a source of gamma rays whose primary mode of interaction is Compton scattering. Finding such a source would be difficult for any arbitrary group of materials. However, for the types of earth formation generally encountered in hydrocarbon logging, the average atomic number rarely exceeds 13 or 14. It was seen from Fig. 10.7 that, for logging applications, there is a large range of gamma ray energies which will be predominantly governed by Compton interaction.

It is worth noting that the basic gamma ray flux attenuation law, Eq. 12.2, indicates that there is a slight difficulty in the interpretation of a flux attenuation measurement. The attenuation will be strictly related to the bulk density ρ_b only if the ratio of Z/A remains constant. For most elements the value of Z/A is about $\frac{1}{2}$, but there are several significant departures; hydrogen, for example, has a Z/A ratio of nearly 1. For this reason, it is convenient to define a new quantity, ρ_e, the *electron density index*, to be:

$$\rho_e \equiv 2\frac{Z}{A}\,\rho_b . \tag{12.3}$$

In this manner the tool response (or measured flux, Φ) can be specified as:

$$\Phi \propto e^{-\rho_e x} , \tag{12.4}$$

where x corresponds to the source-detector spacing.

Table 12.1 lists the density and photoelectric parameters of a number of common elements, minerals and liquids. Of interest for this discussion are the two columns labeled ρ_b and ρ_e. It can be seen by comparison that the bulk density and electron density index for the three major minerals (calcite, dolomite, and quartz) are practically identical in these three cases. However, for the case of water there is an 11%

Table 12.1 Density and photoelectric parameters for various materials. From Bertozzi, Ellis and Wahl [6].

Name	Formula	Mol. wt.	Z	$\mathbf{P_e}$	$\rho_\mathbf{b}$	$\rho_e(3)$	U(4)
A. Elements							
	H	1.008	1	0.00025			
	C	12.011	6	0.15898			
	O	16.000	8	0.44784			
	Na	22.991	11	1.4093			
	Mg	24.32	12	1.9277			
	Al	26.98	13	2.5715	2.700	2.602	
	Si	28.09	14	3.3579			
	S	32.066	16	5.4304	2.070	2.066	
	Cl	35.457	17	6.7549			
	K	39.100	19	10.081			
	Ca	40.08	20	12.126			
	Ti	47.90	22	17.089			
	Fe	55.85	26	31.181			
	Sr	87.63	38	122.24			
	Zr	91.22	40	147.03			
	Ba	137.36	56	493.72			
B. Minerals							
Anhydrite	$CaSO_3$	136.146		5.055	2.960	2.957	14.95
Barite	$BaSO_4$	233.366		266.8	4.500	4.011	1070.
Calcite	$CaCO_3$	100.09		5.084	2.710	2.708	13.77
Carnallite	$KCl\cdot MgCl_2\cdot 6H_2O$	277.88		4.089	1.61	1.645	6.73
Celestite	$SrSO_4$	183.696		55.13	3.960	3.708	204.
Corundum	Al_2O_3	101.90		1.552	3.970	3.894	6.04
Dolomite	$CaCO_3\cdot MgCO_3$	184.42		3.142	2.870	2.864	9.00
Gypsum	$CaSO_4\cdot 2H_2O$	172.18		3.420	2.320	2.372	8.11
Halite	NaCl	58.45		4.65	2.165	2.074	9.65
Hematite	Fe_2O_3	159.70		21.48	5.210	4.987	107.

Continued overleaf.

Table 12.1 *Continued.*

Name	Formula	Mol. wt.	Z	$\mathbf{P_e}$	ρ_b	ρ_e(3)	U(4)
Ilmenite	$FeO \cdot TiO_2$	151.75		16.63	4.70	4.46	74.2
Magnesite	$MgCO_3$	84.33		0.829	3.037	3.025	2.51
Magnetite	Fe_3O_4	231.55		22.08	5.180	4.922	109.
Marcasite	FeS_2	119.98		16.97	4.870	4.708	79.9
Pyrite	FeS_2	119.98		16.97	5.000	4.834	82.0
Quartz	SiO_2	60.09		1.806	2.654	2.650	4.79
Rutile	TiO_2	79.90		10.08	4.260	4.052	40.8
Sylvite	KC1	74.557		8.510	1.984	1.916	16.3
Zircon	$ZrSiO_4$	183.31		69.10	4.560	4.279	296.
C. Liquids							
Water	H_2O	18.016		0.358	1.000	1.110	0.40
Salt water	(120,000 ppm)			0.807	1.086	1.185	0.96
Oil	$CH_{1.6}$			0.119	0.850(1)	0.948(1)	0.11
	CH_2			0.125	0.850(1)	0.970(1)	0.12
D. Miscellaneous							
"Clean" sandstone	(1)			1.745	2.308	2.330	4.07
"Dirty" sandstone	(1)			2.70	2.394	2.414	6.52
Average shale	(2)			3.42	2.650(1)	2.645(1)	9.05
Anthracite Coal	C:H:O = 93:3:4			0.161	1.700(1)	1.749(1)	0.28
Bituminous Coal	C:H:O = 82:5:13			0.180	1.400(1)	1.468(1)	0.26

(1)Variable; values shown are illustrative.
(2)Pettijohn [14].
(3) ρ_e is electron density = $\rho_b \times 2Z/A$.
(4)U = $P_e \rho_e$.

discrepancy between the two (due to the anomalous Z/A value for H). Thus there will be an increasing discrepancy between ρ_b and the density tool response parameter ρ_e, for increasing porosity.

For this reason, the density reading on logs has been adjusted slightly to give precisely the bulk density of water-filled limestone. The relationship between the log reading ρ_{log} and the electron density index ρ_e is:

$$\rho_{log} = 1.0704\rho_e - 0.188 . \tag{12.5}$$

This relationship is illustrated in Fig. 12.1 which shows the log density as a function of $\rho_e$for calcite and for water. The straight line joining the two points is described by the equation above and provides the exact bulk density for water-filled limestone.

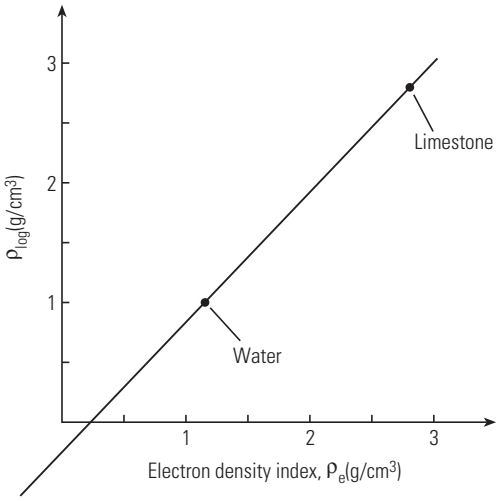


Fig. 12.1 The transform between the measured parameter, electron density (ρ_e), and the density value presented on logs.

Further reference to the data of Table 12.1 will indicate that Eq. 12.5 is nearly true (to within a few 1/1000s g/cm^3) for many other matrices.

12.2.1 Density Measurement Technique

Figure 12.2 shows schematically the evolution of the density device from the notion of the simple transmission of monoenergetic gamma ray through a thin sample, to a borehole device consisting of a source, shield, and gamma ray detector. In the upper panel, the gamma rays are transmitted without much scattering, as indicated by the line spectrum detected. As the sample thickness is increased, the gamma ray line intensity decreases, due to exponential attenuation. At the same time, it is accompanied by a buildup of low energy Compton-scattered gamma rays. In the final example, the detector is well shielded from the source. No source-energy gamma rays reach it. However, the level of multiply scattered gamma rays will still vary exponentially with the scattering material density.

One explanation for this behavior considers the multiply scattered gamma rays, detected far from the source, to have undergone most of their scattering in the formation close to the detector. These multiply scattered gamma rays are fed by a virtual source consisting primarily of unscattered source-energy gamma rays which travel, nearly parallel to the borehole wall, to reach the site of their last few collisions before detection. Their intensity will depend on the probability of source gamma rays arriving at this site unscattered, and thus varies exponentially with formation density. Tittman prefers to treat this as a diffusion problem and also concludes that the amplitude of the multiply scattered spectrum will vary exponentially with the formation density [1, 2].

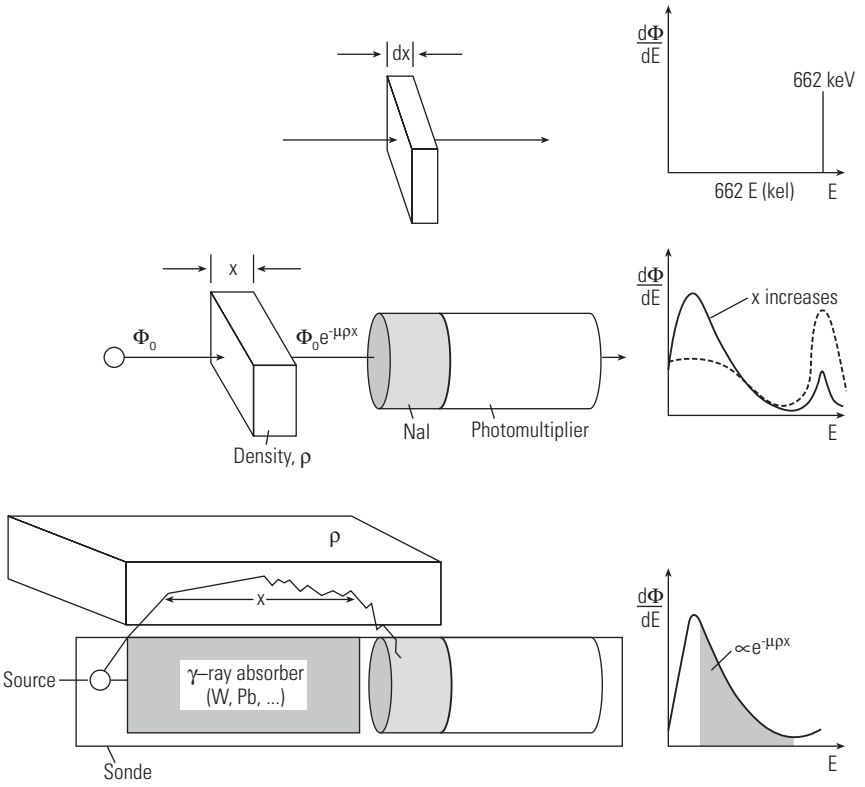


Fig. 12.2 A schematic view of the effect of geometry on the determination of density by the use of the attenuation and scattering of gamma rays. In the top panel, the idealized experiment is shown for a very thin piece of material. In the second panel, the thickness has increased so that there is considerable scattering of gamma rays. In the third panel, an approximation to the logging situation is shown.

The gamma ray source usually used in density logging is ^{137}Cs, which emits gamma rays at 662 keV, well below the threshold for pair production. This isotope has a half-life of about 30 years, thus providing a stable intensity during a reasonable period of time. Some devices use ^{60}Co, which emits two gamma rays at 1,332 and 1,173 keV.

The earliest devices consisted of the gamma ray source and a single detector, as indicated in Fig. 12.2 [2]. However, to compensate for the frequent occurrence of intervening mudcake, modern devices (Fig. 12.3) incorporate two or more detectors (generally NaI) in a housing that shields them from direct radiation from the source [3, 4]. Although not indicated in the figure, the tool is pressed up against one side of the borehole by a back-up arm that also serves to measure a diameter (along one axis) of the borehole. This measurement is usually listed on the log as a caliper (an example of which can be found in track 1 of Fig. 12.23).

Shown in Fig. 12.3 are two detectors at fixed spacings from the source. These are analogous to having two samples of two different thicknesses in the transmission

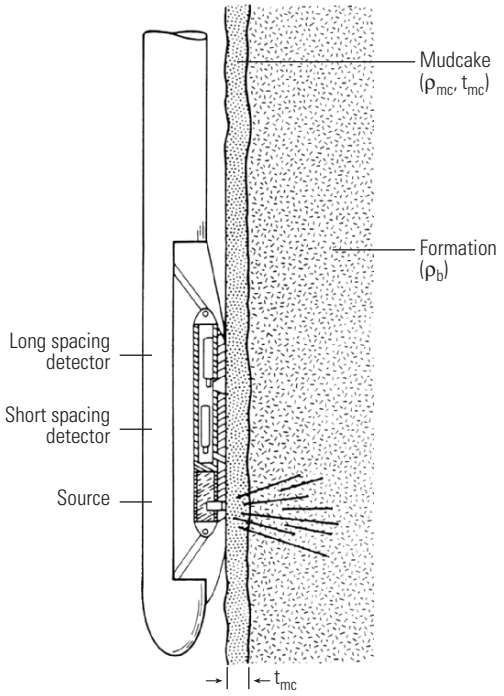


Fig. 12.3 A formation density device in the borehole situation applied to the borehole wall and separated from it by the thickness of the mudcake, t_{mc}. Adapted from Ellis et al. [3].

experiment. Unlike the transmission experiment, the source is well shielded from the two detectors and only scattered gamma radiation is detected. Of course, the intensity of the scattered radiation will in large measure be dominated by the density variations along the path from source to detector. The typical situation shown in the figure is that the density of the formation must be determined through an unknown amount of standoff of material with an unknown density. Traditionally this has been addressed by including a second detector, or more recently, multiple detectors that attempt to make a compensation of the standoff to greater or lesser degrees of success. First we examine the operation in the simplest situation with no intervening mudcake.

The measurement principle derives from the fact that the counting rate of a detector varies exponentially with the density of the formation, as expected from the general attenuation relation:

$$N = N_o e^{-\mu\rho x}, \tag{12.6}$$

where N is the counting rate of a detector at a distance x from the source. This is illustrated in Fig. 12.4 which shows an exponential relationship between the counting rate and the bulk density. Note that the shorter spacing detector has less density resolution or sensitivity than the farther detector. For a given density variation, its counting rate exhibits a smaller fractional change than that of the far detector.

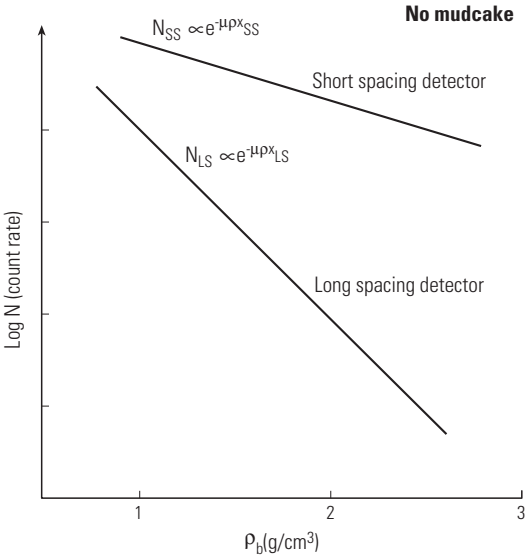


Fig. 12.4 Idealized counting rate response of two detectors for variation of formation density in the presence of no mudcake.

This can be seen from the preceding equation, where the product μx corresponds to the slope of the logarithm of the counting rate as a function of density. The spacing x of the nearer detector produces a slope in its response curve that is less than that of the long-spacing detector. The formation density could be determined simply from an observed counting rate from either detector. Generally the longer-spaced detector, with its larger depth of investigation is taken as the formation density estimate.

12.2.2 Density Compensation

Figure 12.3 shows the usual logging condition with the intervening mud or mudcake. When material of unknown density and/or thickness is placed between the instrument face and the rock whose density is to be determined, there will be a perturbation of each counting rate. However, each counting rate can be translated into an apparent density using Eq. 12.6 or Fig. 12.4. Because of the different density sensitivities of the two detectors, the apparent densities for the two detectors will differ and the apparent long-spacing density will no longer be equal to the formation density; it requires compensation or correction. This correction is traditionally referred to as $\Delta\rho$ and is the quantity which is added to the long-spacing density (ρ_{LS}) to get the formation bulk density (ρ_b):

$$\rho_b = \rho_{LS} + \Delta\rho \,. \tag{12.7}$$

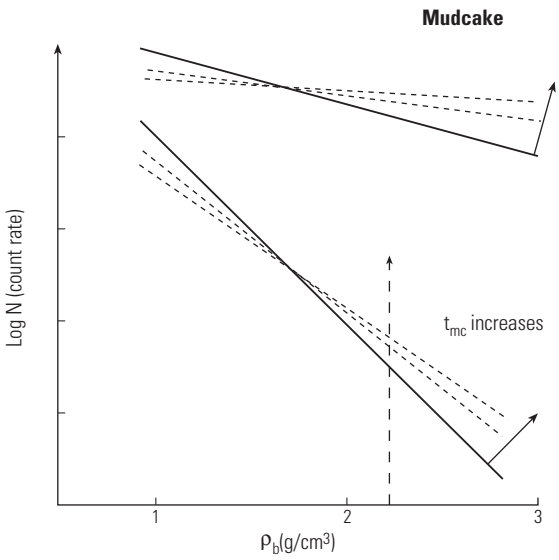


Fig. 12.5 Idealized response of the two detectors for two different thicknesses of mudcake. Its density is approximately 1.8 g/cm^3. For a given thickness of mudcake and formation density/mudcake density contrast, both detectors experience approximately the same percentage of change in counting rate.

Figure 12.5 indicates the counting-rate behavior for the two detectors in this situation. At a fixed formation bulk density, if the mudcake density is less than the value of ρ_b, then the counting rates of the two detectors increase by approximately the same percentage. This behavior is sketched in Fig. 12.5, where the mudcake density shown is about 1.8 g/cm^3 (this is the point about which the counting rate/mudcake thickness curves pivot). For a given mudcake density, it is seen from the figure that, depending on the formation density, the counting rates either increase or decrease in comparison to the counting rate expected for a clean borehole wall. If the mudcake is more dense than the formation, then the counting rates decrease, and if the mudcake density is less than the formation density, then the counting rates increase.

This behavior is further elaborated in Fig. 12.6 which shows the behavior of the normalized counting rates. Each detector's counting rate is normalized to its counting rate with no mudcake present. The parameter that controls the counting rate is the density contrast $\rho_b - \rho_{mc}$ between formation and mudcake, multiplied by the mudcake thickness. This is equivalent to considering the last layer of formation, through which the gamma rays have to pass in order to reach the detector, as a filter of variable density. Note that as the mudcake thickness (t_{mc}) increases, the normalized counting rates appear to saturate. The saturation of the short spacing detector occurs earlier and thus is said to have a shallower depth of investigation.

Figure 12.7 is the traditional way of presenting the instrument response to standoff or mudcake. Although this "spine and ribs" plot is illustrative, it is not as convenient

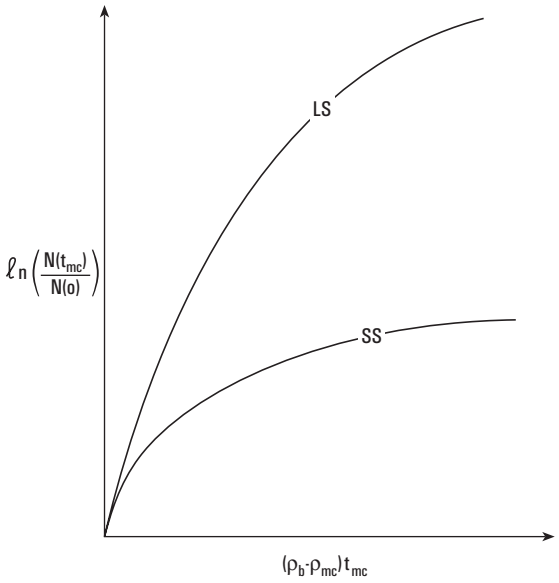


Fig. 12.6 Effect of mudcake on the normalized counting rate of near and far detectors. The controlling parameter is the contrast in mudcake and formation density multiplied by the mudcake thickness.

as some other representations for making a correction for the presence of mudcake. The "spine" is the locus of the two counting rates without mudcake. The "ribs" trace out the counting rates, at a fixed formation density, for the presence of intervening mudcake.

As an operational procedure for correcting the intervening mudcake, one can use apparent densities of the long- (ρ_{LS}) and short-spacing (ρ_{SS}) detectors (from the counting-rate calibration determined with no mudcake present) from a series of laboratory measurements to define the algorithm for determining the correction, $\Delta\rho$. Data of this type are shown in Fig. 12.8 as a function of the apparent-density differences between the long- and short-spacing detectors. A common misconception is that $\Delta\rho$ is a measure of the mudcake thickness t_{mc}. It is, in fact, proportional to the product of mudcake thickness and the density contrast between the mudcake, ρ_{mc}, and the formation density, i.e.,:

$$\Delta\rho \;\propto\; t_{mc}\,(\rho_b - \rho_{mc})\;. \tag{12.8}$$

The correction scheme for density has some limitations. Beyond some thickness ($\approx$1 in.), depending on the tool design details that control, in part, the depth of investigation, the compensation scheme breaks down and the estimate of ρ_b will be in doubt. However, this point cannot be identified by use of a simple, single cutoff value of $\Delta\rho$. A very small gap of water ($\rho_{mc} = 1$ g/cm^3) in front of a low-porosity formation (high density) would yield a large value of $\Delta\rho$ and yet be perfectly compensated for,

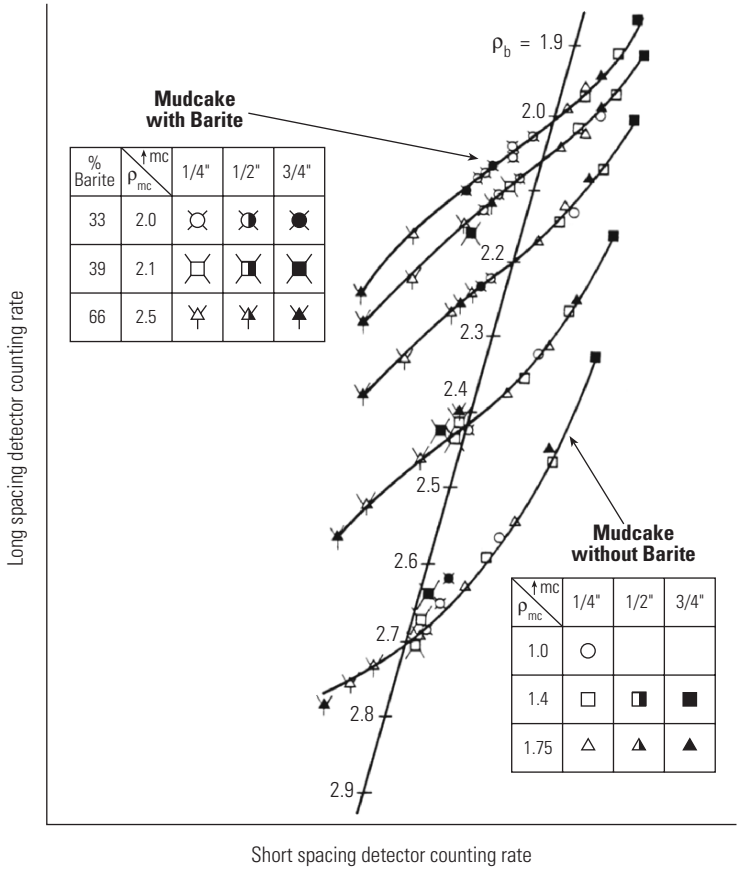


Fig. 12.7 A "spine and ribs" representation of the response of a two-detector density device to formation density and mudcakes. Because of its characteristic outline, it is known as the "spine and ribs" chart. From Tittman et al. [2].

whereas a 1 in. thick mudcake of medium density in front of a high-porosity zone may yield a small $\Delta\rho$ with some residual error in the compensation.

An example of the use of the $\Delta\rho$ curve as a quality control is shown in the log of Fig. 12.9 taken from the shaly sand portion of the simulated reservoir model. Portions of the $\Delta\rho$ curve are highlighted, as well as the corresponding smooth portions of the caliper. In these cases the $\Delta\rho$ curve shows negligible correction, which is probably indicative of little or no mudcake. In the very rough sections of the borehole, the value of $\Delta\rho$ is seen to be quite large, because of poor pad contact with the borehole wall.

A correction curve (labeled Delta Rho) can be also seen in the left-hand track of the log of Fig. 12.23. In section **A** there is a long stretch where $\Delta\rho$ is nearly zero, indicating good contact between tool face and formation. However, above and immediately below this smooth section there are a couple of positive $\Delta\rho$ spikes,

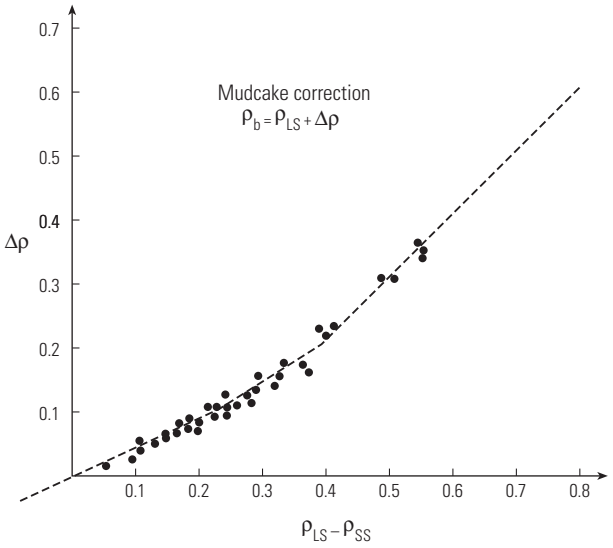


Fig. 12.8 A normalized "spine and ribs" chart showing the correction necessary for the case of light mudcakes. Adapted from Ellis et al. [3].

indicating some standoff between the tool face and the formation, and that the material in this gap is of lower density than the formation.

In the case of weighted muds or mudcakes whose densities exceed the formation density the opposite will be true. The short-spacing density will be larger than the long spacing and their difference will be negative. A corresponding negative $\Delta\rho$ correction value will be generated to reduce the long-spacing estimate to the appropriate formation value.

12.3 LITHOLOGY LOGGING

As alluded to in the introduction, knowledge of the matrix density of the rock formation is an important factor in converting the measured density to porosity. The ability to distinguish sandstone from limestone or dolomite would be very useful in assigning a matrix density. Figure 12.10 indicates how this might be achieved. The matrix densities of the major sedimentary minerals are plotted versus the corresponding average atomic number. Consequently, measurement of the average atomic number, or a related parameter P_e, would be valuable. The next section describes how that is achieved in one type of logging device.

12.3.1 Photoelectric Absorption and Lithology

The Eq. 12.2 that describes the attenuation of gamma rays contains the cross section, σ, which until now has been treated as just the Compton cross section. In fact, it is the



Fig. 12.9 A sample density log showing the qualitative nature of the $\Delta\rho$ curve for identifying smooth sections of borehole.

sum of two principal contributions, Compton scattering and photoelectric absorption. The probability of photoelectric absorption depends on the gamma ray energy and on the atomic number, Z, of the scattering material. This means that σ is not a constant but a function of the gamma ray's energy, E. Furthermore, as the energy of the gamma ray decreases (as it does as it scatters) or if the scattering medium has a high atomic number, the photoelectric absorption could easily dominate the attenuation law.

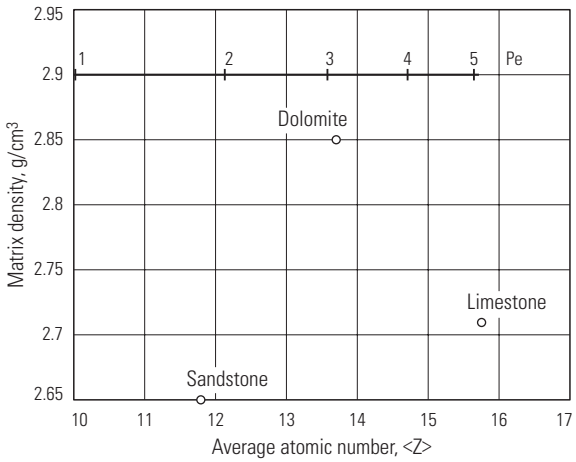


Fig. 12.10 Three types of sedimentary rock matrices characterized by matrix density and average atomic number. The scale of the nonlinear transform to the photoelectric factor P_e is shown near the top of the figure.

In order to appreciate the relationship between average atomic number (determined essentially by lithology) and the photoelectric effect, recall that the cross section for photoelectric absorption τ, is given by:

$$\tau = 12.1E^{-3.15}Z^{4.6}, \tag{12.9}$$

where τ is in barns (10^{-24} cm^2) per atom, E is the energy of the gamma ray in keV, and Z is the atomic number of the absorber. The attenuation of a flux Φ_o, of gamma rays by photoelectric absorption alone can be written as:

$$\Phi = \Phi_o e^{-n\tau x}, \tag{12.10}$$

where n is the number of *atoms* per cm^3 and x is the attenuation depth. In Fig. 12.11, the behavior of τ is shown as a function of Z for several energies.

It is convenient to define a new parameter P_e, the photoelectric index, as:

$$P_e \equiv \left(\frac{Z}{10}\right)^{3.6}, \tag{12.11}$$

where we see from Eq. 12.9 that P_e is proportional to the photoelectric cross section per *electron* with the energy dependence suppressed. Then the attenuation equation for photoelectric absorption can be rewritten as:

$$\Phi \propto \Phi_o e^{-n_e P_e x}, \tag{12.12}$$

where n_e is the number density of *electrons*, as in the case of Compton scattering.

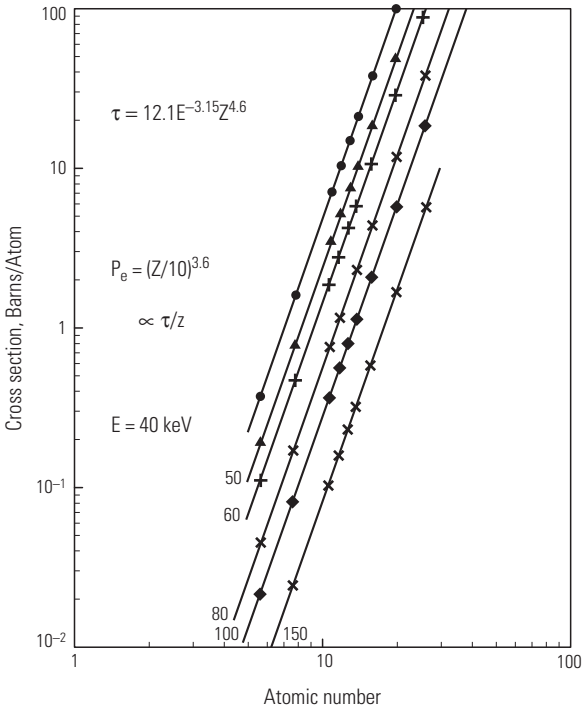


Fig. 12.11 The variation of the photoelectric cross section with atomic number. From Bertozzi et al. [6].

The implication of a two component cross section is that for a hypothetical gamma ray transmission experiment such as shown in the top panel of Fig. 12.2, a change in transmitted flux (or in detected counting rate in a practical realization) associated with a change in sample of material (assuming that the thickness is kept constant) could be caused by either a change in sample density or change in atomic number, or both. The attenuation of gamma rays can be rewritten as:

$$\Phi = \Phi_o e^{-N_o \rho_b (a(E) P_e + b(E)) x}, \tag{12.13}$$

where now the cross section, σ, has been replaced by $a(E)Pe + b(E)$ indicating that the coefficients a and b are energy-dependent. However the coefficient a, associated with P_e varies as approximately $1/E^3$ whereas the coefficient b, associated with the Compton scattering is practically constant. If the object of the experiment is to measure the density then the effects of variable Z can be minimized by using a high-energy gamma ray source and detecting high-energy gamma rays, as is done in the logging devices explained in Section 12.2.1.

In borehole density logging, far from the simple transmission experiment, the detected gamma rays may have scattered many times on their path from source to detector, producing gamma rays with a wide distribution of energies. The variations in

Z in the formation or in absorbing mud will affect the energy distribution of gamma rays arriving at the detector – the highest energy gamma rays will carry density information while the lowest will be affected by density and the Z of the scattering medium.

12.3.2 P_e Measurement Technique

In modern density tools, the shape of the low-energy portion of the scattered-GR spectrum is measured [3, 5]. The technique of comparing the propagation of gamma rays at higher and lower energies can be used to determine the amount of absorption due to the photoelectric effect and thus to deduce the P_e of the scattering material (rock). Now let us examine how the measurement is actually made.

Qualitatively, the gamma ray spectra observed with a logging device equipped with a window nearly transparent to low-energy gamma rays (such as Be) is shown in Fig. 12.12. As the average atomic number, Z, of the formation increases, the lower energy portion of the spectrum is progressively reduced. Thus a measurement of this spectral shape at low GR energies should yield the photoelectric absorption properties, and thereby the Z of the formation.

But first one may ask why the spectrum of gamma rays looks the way it does in Fig. 12.12. In fact, the first question is: "How would the spectrum of gamma rays, emitted in an infinite homogeneous medium containing uniformly distributed Cs sources, look without the presence of any photoelectric absorption?" The answer

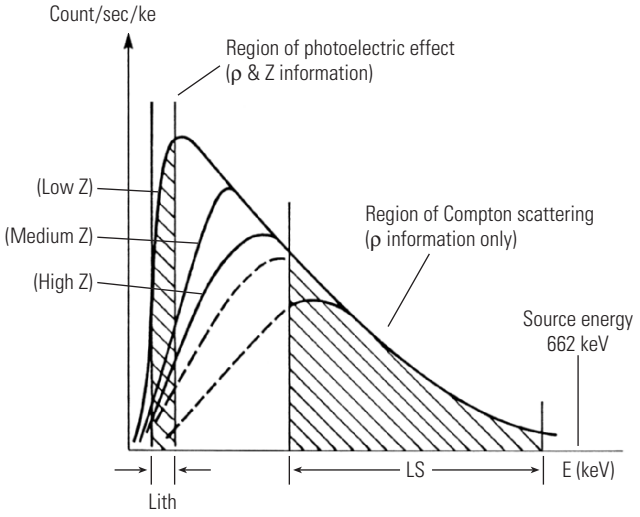


Fig. 12.12 A schematic representation of the detected spectral variation of gamma rays in three formations of increasing average atomic number. Two dash-line curves indicate the trend of additional low-energy attenuation expected for the presence of two thicknesses of absorbing barite mudcake. Adapted from Ellis et al. [3].

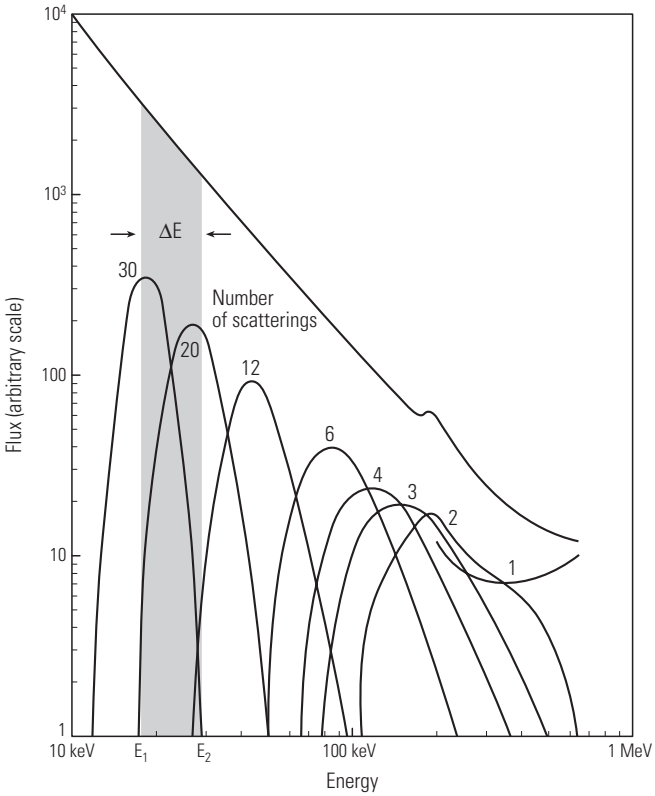


Fig. 12.13 The theoretical behavior of the multiply scattered gamma ray spectrum produced by an infinite homogeneous formation containing uniformly distributed sources. It is for the special case of no photoelectric absorption. The spectrum is composed of the contribution of individual spectra of scattering order K. The total spectrum between E_1 and E_2 can be computed from the contributions of the individual spectra for gamma rays that have scattered between 20 and 30 times. From Bertozzi et al. [6].

is contained in Fig. 12.13, which shows the results of a Monte Carlo calculation for this situation. It indicates that the steady-state multiply scattered spectrum falls off with energy as 1/E. The components of this spectrum (grouped by multiplicity of scattering) are shown individually. The spectra formed by gamma rays which have scattered, once, twice, three times, etc., are shown beneath the nearly straight line that results. Each one of these spectra can be imagined to be a snapshot view of the energy distribution of gamma rays that have experienced the same number of scatterings. As shown in the figure, the value of the total flux in an interval ΔE can be computed by summing the individual fluxes over the scattering order K.

When photoelectric absorption is included in the calculation, it is necessary to take into account the fact that at each collision there is a probability that the gamma ray will

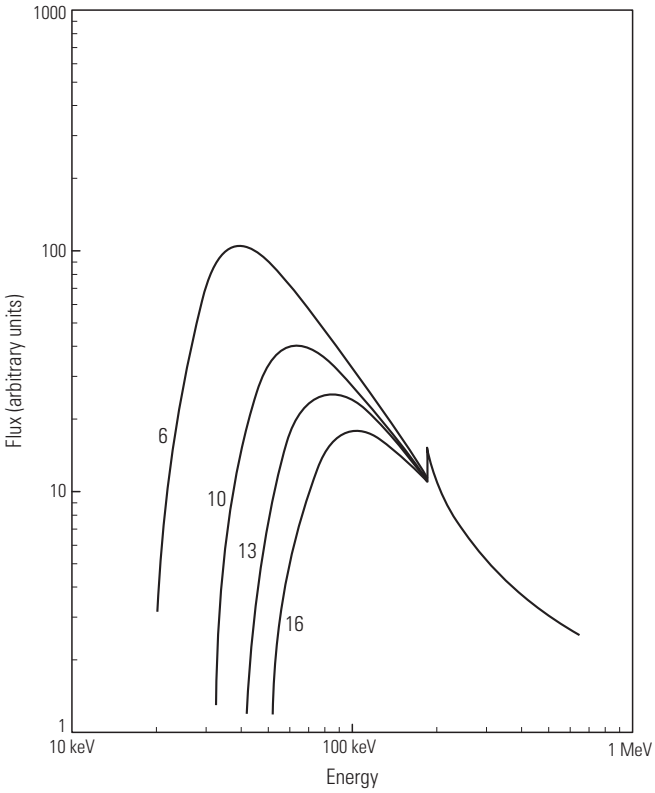


Fig. 12.14 A Monte Carlo calculation of the spectrum due to uniformly distributed sources, including the effect of photoelectric absorption. The evolution of the spectra is seen for materials of four different atomic numbers. As the atomic number increases, the low-energy portion of the spectrum is attenuated. From Bertozzi et al. [6].

be absorbed rather than scattered. The lower the gamma ray energy and the higher the Z of the scattering material, the greater is this probability. The spectra which result are shown in Fig. 12.14, for the range of Z values of interest to us, assuming all the formations have the same density.

Experimental curves over a much narrower range of Z values are shown in Fig. 12.15. Although the curves are not exactly the same shape as Fig. 12.14, there is considerable similarity in the behavior of the low-energy region as the Z of the scattering material changes. Furthermore the curves of Fig. 12.14 are calculations of the actual gamma ray flux and do not include the effects of the NaI detector, which considerably modify the spectra.

As indicated in Fig. 12.15, two bands of gamma ray energy can be used to determine the density and the lithology effects in a simple manner. The higher-energy window contains density information, and the lower window, a combination of density and

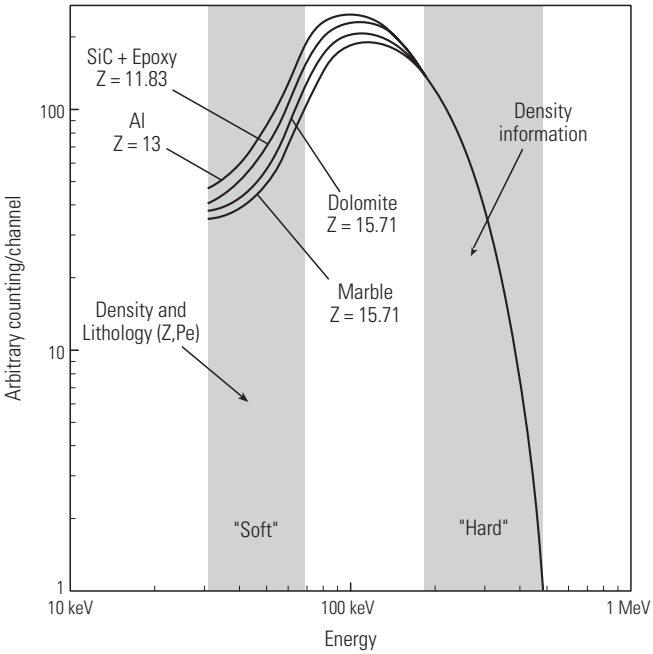


Fig. 12.15 Experimental GR spectrum taken with a density device which also measures photoelectric absorption properties of the formation. The spectra have been normalized in the high-energy region to emphasize the variations due to atomic number and to eliminate overall amplitude levels due to differences in formation density. A measure of the formation atomic number can be obtained from the ratio of counting rates in the two windows indicated. From Bertozzi et al. [6].

lithology information. The ratio of the two is primarily dependent on Z. The experimental data of Fig. 12.16 illustrate this. Modern tools may employ a different scheme when multiple energy windows are available from a number of detectors – it involves the inversion of a forward model and is discussed in a later section.

The calibration data for the photoelectric portion of one type of tool is shown in Fig. 12.17. Once this calibration curve has been established for a given tool, the counting-rate ratio can be used to provide a value of P_e at any depth. The soft/hard ratio dependence seen in Fig. 12.17 agrees with the results of theoretical analysis [6].

12.3.3 Interpretation of P_e

In the simplest of circumstances, in distinguishing sand from limestone or dolomite, the measurement of P_e would be very useful. In binary mixtures it can also be useful when combined with the density measurement or with some other logging measurement. However, often the use of such techniques is highly compromised by the

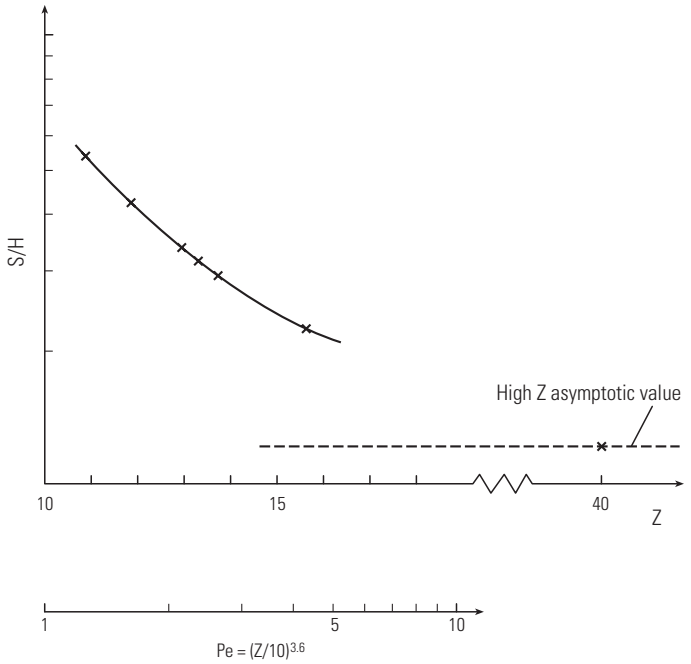


Fig. 12.16 The ratio of the "soft" to "hard" windows of Fig. 12.15, as a function of the formation average atomic number, Z. Also shown is a scale corresponding to the photoelectric factor P_e, which is normally presented on logs. From Bertozzi et al. [6].

presence of barite weighting agents in the drilling mud. The large Z of Ba (56) makes it a very efficient low-energy gamma ray absorber, so any amount of it in mudcake or in the invasion fluids can seriously alter the apparent P_e of the formation to the point of rendering it useless for interpretation. On the other hand there are many examples where the borehole rugosity is smooth enough or where there is no mudcake or invasion, that the P_e values can still be used in much of the logged section.

In normal logging circumstances, the P_e log readings should range between 1 and 6. This can be seen from Table 12.1, which also lists the value of P_e for the three principal matrices: 1.83 for quartz, 3.1 for dolomite, and 5.1 for calcite. Figure 12.18 contains logs in a shaly sand portion of the simulated reservoir; the value 1.8 has been indicated in the track corresponding to P_e. It can be seen that only a few portions of the log correspond to this value. However, where the value of P_e indicates sandstone, the gamma ray reading is also at a minimum, indicating that higher P_e readings, in this case, may be associated with the shaliness.

Figure 12.19 shows a cross plot of P_e versus ρ_b, with lines indicating expected P_e values for porosity variation from 0 to 50 p.u. for the three principal matrices. Data from a 400 ft interval have also been plotted. It is relatively straightforward to separate the sands from the shaly sands and from the shales on this presentation. One

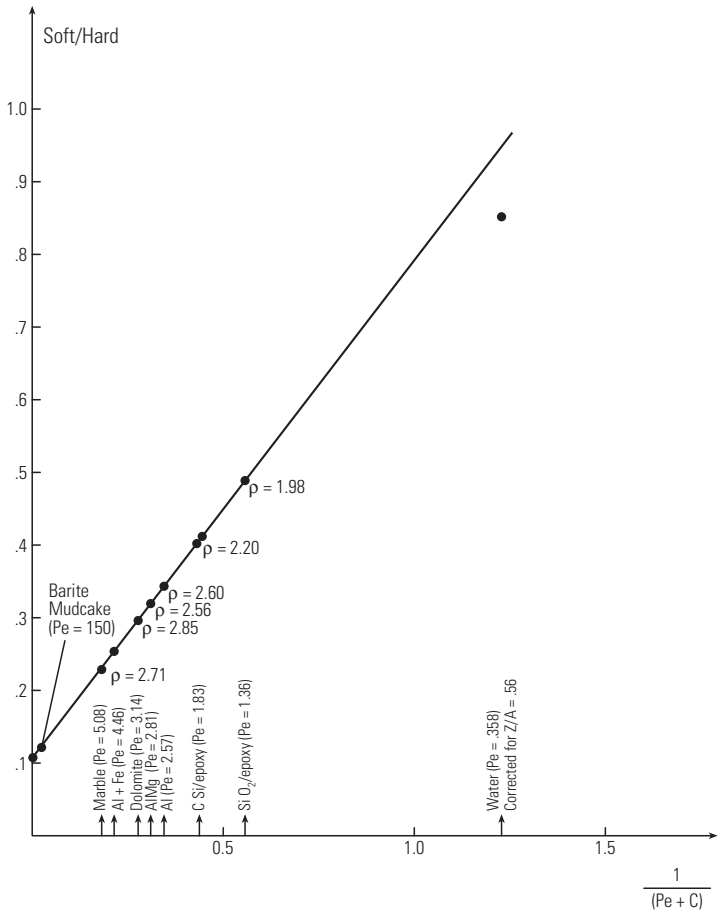


Fig. 12.17 The response of an experimental lithology-sensitive device to the photoelectric factor of various laboratory formations. A fitting constant, C, is introduced to linearize the experimental results at low values of photoelectic absorption.

anomaly, appearing at a P_e value of about 4.25, corresponds to the presence of an unidentified heavy (high Z) mineral.

After having seen an example of the variation of P_e with lithology, it is natural to wonder how to scale intermediate values of P_e in the case of a mixture. For example, what value of P_e would be expected for a sandstone with a large amount of calcite cement?

Since P_e is proportional to the photoelectric cross section per electron, the mixing law must be formulated in terms of the electron density. Equation 12.12 makes clear that the calculation of P_e for a mixture will involve weighting the electron density of each atomic species by the Z for that species. It is the mass fraction that enters, rather than the usually desired volume fraction.

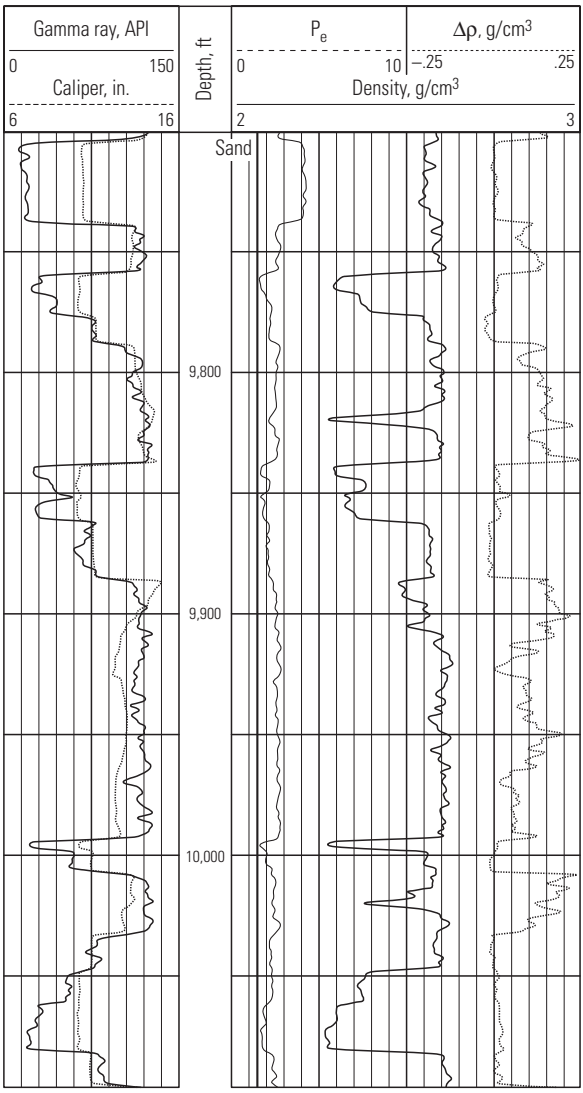


Fig. 12.18 The P_e and density response of a logging tool in the shaly sand section of the simulated reservoir.

Since the P_e of mixtures does not combine volumetrically, for interpretation purposes a new parameter, U, was developed which has the property of combining volumetrically for mixtures. This parameter is suggested by Eq. 12.12. Since the electron density n_e is proportional to the electron density index ρ_e, the attenuation is proportional to $e^{-P_e \rho_e x}$. From this we can see that the product of P_e and electron-density index, or U, appears to be a macroscopic linear cross section and

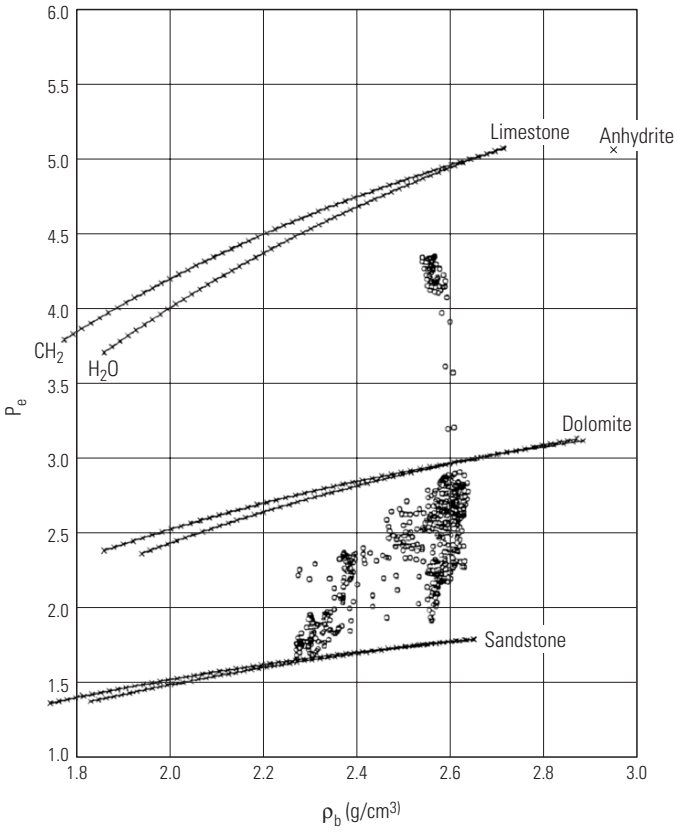


Fig. 12.19 A P_e – density cross plot of the data of Fig. 12.18. The three groups of lines correspond to the three major lithologies: sand, dolomite, and limestone. Porosity increases to the left on each of the mineral lines and is marked in 1 porosity unit intervals. The two sets of lines for each mineral correspond to water-filled and hydrocarbon-filled porosity.

specifies the absorption of a given thickness of material. The dimensions of U are cross section/cm^3, which indicates that it combines volumetrically.

From this definition of U, the recipe for obtaining the P_e of any mixture first involves computing the U value:

$$\begin{aligned} U_{total} &= U_1V_1 + U_2V_2 + \cdots \\ &= P_{e,1}\rho_{e,1}V_1 + P_{e,2}\rho_{e,2}V_2 + \cdots , \end{aligned} \tag{12.14}$$

where $\rho_{e,i}$ is the electron density of material i, $P_{e,i}$ is the photoelectric factor of material i, and V_i is the volume fraction of that material. The final value of the average, $\overline{P_e}$, is obtained from:

$$\overline{P_e} = \frac{U_{total}}{\overline{\rho_e}} , \tag{12.15}$$

where the average electron-density index, $\overline{\rho_e}$, is given by:

$$\overline{\rho_e} = \rho_{e,1}V_1 + \rho_{e,2}V_2 + \cdots \quad (12.16)$$

Table 12.1 lists some useful values of U and ρ_e for a number of commonly encountered minerals. The use of U in quantitative evaluation of mineral content of a formation will be covered in Chapters 21 and 22.

Table 12.1 shows the enormous sensitivity of the parameter U or P_e to elements with large atomic number. In particular, note the values of P_e for the several iron compounds and for barium. In the case of iron, this sensitivity can be exploited to make a determination of the shale content of the formation if there is iron associated with the clay mineral. This application is also discussed in Chapter 21. However, the sensitivity to barite makes the P_e measurement difficult in heavily weighted barite muds.

12.4 INVERSION OF FORWARD MODELS WITH MULTIDETECTOR TOOLS

Most modern two-detector density devices use multiple-energy windows to derive the density, the photoelectric factor, and the correction curve as described above. In one three-detector wireline version [7], the combination of multiple detectors and multiple-energy windows produce on the order of a dozen counting rate measurements at each depth. Each counting rate can be described by a forward model relating the rate to the five important parameters of density logging (and as indicated in Fig. 12.3): formation density, ρ_b, formation photoelectric factor, P_e, mudcake density, ρ_{mc}, mudcake photoelectric factor, P_e^{mc}, and the thickness of the mudcake, t_{mc}. The window counting rate for the ith window of the jth detector might have a form similar to:

$$W_{i,j} = c^1_{i,j}\, e^{(-c^2_{i,j}\rho_b + c^3_{i,j}P_e)}\, e^{-c^4_{i,j}\,(\rho_b-\rho_{mc})t_{mc}}\, e^{-c^5_{i,j}(P_e^{mc}-P_e)t_{mc}} + c^6_{i,j} + \cdots \quad (12.17)$$

The coefficients, $c^k_{i,j}$ of the forward model are determined from data recorded (the window counting rates) during placement of the tool in a large number of formations with, and without, interposed thickness of artificial mudcakes of different compositions. Then an inversion scheme determines the five parameters by updating estimates for each of the five until the forward model-predicted counting rates agree, in a least-squares sense, with the measured counting rates. Measurement quality estimates abound with this approach. The estimated value of t_{mc} , the goodness of the counting rate reconstruction and a computed value of $\Delta\rho$ can be used to establish confidence in the measured value.

12.5 LWD DENSITY DEVICES

Since LWD density devices are derived from their earlier cousins, the wireline devices, their similarities are many. LWD devices also have a source and a long-spaced and a short-spaced detector. The only difference is that the LWD density devices are built

into the drilling collars and are generally close to the bit. As part of the drilling string they also rotate. Consequently the data is generally acquired as a function of time along with orientation information so that the data can be binned with respect to hole orientation. In Fig. 12.20 the data is collected in four geometric sectors (for imaging purposes many more bins may be used). In the figure on the left, the horizontal borehole is at the boundary of two formations with different densities, foreshadowing a difference in the measured density between the upper and lower quadrants. In the figure on the right, where the tool is run without a stabilizer, the density most representative of the formation corresponds to the bottom quadrant, and a significant correction should be apparent when the tool is pointed towards the top of the hole.

Figure 12.21 shows one version of the multiple-density traces that might be available from an LWD density measurement. In this example there is a fairly obvious discrepancy between the upper and bottom quadrant density estimates. This discrepancy can be caused by the wellbore lying at the intersection of beds of two different densities as indicated in the left-hand sketch in Fig. 12.20. Due to the action of gravity, in a highly deviated well, the bottom quadrant is frequently the curve with the least perturbation. Inspection of the correction curves in the log of Fig. 12.21 confirms that the $\Delta\rho$ curve in the bottom quadrant is the least active of the four presented and is the one that is closest to zero over most of the section displayed. In an over-sized or washed-out hole, the measurements around the circumference may contain significant error if the compensation range is exceeded. Another benefit of the rotational measurement, in appropriate sized boreholes, is the possibility of deriving density- or P_e-based images as an alternative method of sensing and quantifying dipping beds [8].

Although the density measurements around the circumference may contain significant errors this information can be turned to good advantage to derive a "caliper" measurement [9]. The basis for this measurement is the relationship in Eq. 12.8 between the $\Delta\rho$ and standoff distance. For this application the material in front of the pad is mainly mud, not mudcake. The mud density must be known to provide a good value of the stand-off distance. Using a good value of the formation density and the

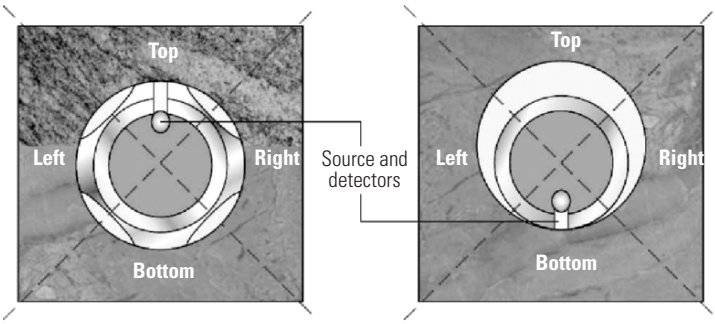


Fig. 12.20 An example of an LWD density tool is seen built into one side of the drill collar. As the pipe rotates the density is collected continuously and binned, in this example into four quadrants.

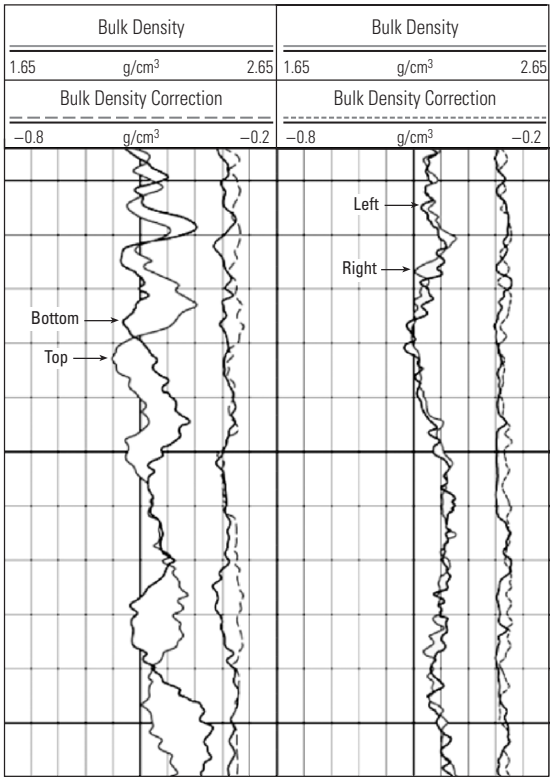


Fig. 12.21 An example of a LWD density log where the data has been collected in oriented quadrants. From Bourgois et al. 1998.

long-spacing detector apparent density, the standoff, unlike the compensation, can be estimated reliably up to approximately three inches.

One of the advantages of the LWD density, with its proximity to the drilling bit, is the relatively short time between drilling and measurement. From this fact come two advantages. The first is the condition of the borehole wall that usually deteriorates with time. Thus rugosity is at a minimum. The second is the short time available for invasion to proceed. This means that the value of ρ_f must not be assumed to be mud filtrate but rather the virgin formation fluid. Hansen and Shray [10] have documented the consequences of using an incorrect fluid density for interpreting an LWD density log in an oil reservoir containing light hydrocarbons.

12.6 ENVIRONMENTAL EFFECTS

Since the object of the density measurement is to obtain a reasonable estimate of porosity, a good sense of when a density measurement can be trusted is required. The most important shortcoming of the density measurement is related to the relatively

short range of penetration of the gamma rays. A parameter for helping to quantify this is the so-called mean-free-path. It is defined as the distance over which 1/e of the gamma rays will have been scattered. For the medium range gamma rays used in well logging, the approximate mean free path is between 4 and 6 cm for the density range of 2–3 g/cm^3. Of course, the spacing between the gamma ray detector and the source, usually several multiples of the mean-free-path, will also have an influence on depth of investigation. Because of the relatively short mean-free-path and the spacings of the compensating detector(s) there is some practical range of parallel stand-off (caused for instance by a layer of mudcake) for which the compensation can be made. This distance is likely to be on the order of 1–2 in. for most logging tools but can vary with equipment design.

To illustrate the depth of investigation of a hypothetical density logging tool refer to Fig. 12.22. It shows the density response map for a long-spaced and below, for a short-spaced detector. The positions of the source and detector are indicated by the symbols "S" and "D" in the figure. These maps are analogous to the geometric factor maps of the various arrays of an induction tool (see Figs. 7.7 and 7.17, for example). Note the exaggeration of the radial scales. The radially integrated depths of investigation are projected onto the back plane of both figures. The 90% response point for the shorter spacing detector is on the order of 1.5 in. whereas that same point for the farther spaced detector is somewhat greater than 4 in.

Unlike neutrons, gamma rays can be collimated with reasonable amounts of not-so-exotic materials. By using dense shielding materials, such as Pb or W, borehole gamma–gamma density devices can be highly collimated so that source gamma rays are favored to enter into the formation at the face of the device in contact with the formation, and the detectors are back-shielded to make them nearly immune to gamma rays coming from the borehole and to detect only those gammas that arrive from the formation. Consequently a gamma–gamma device can be made nearly insensitive to the borehole environment.

The list of environmental effects of the density tool, then, is quite short. There is some hole-size effect because the radius of curvature of the pad of the measuring device cannot conform to all borehole sizes. A region of mud, with a crescent-shaped cross section, may be present along the sides of the skid. If the density contrast between the mud in this crescent and the formation is large it is possible that some correction needs to be made. Charts [11] are provided for such corrections, but generally they are of very small magnitude.

However, the number one problem for obtaining a good density estimate comes from the rugosity of the borehole wall. Although the compensation schemes described earlier are relatively successful, they are strictly applicable only for parallel stand-off. In the case of rugosity (which we will define as some irregularity in the borehole wall with a length scale less than the source-detector spacings and with an amplitude in excess of a few mm), the effect on the measurement can be deleterious. In Fig. 12.23, zone **B** shows a region of obvious rugosity; the borehole irregularity is seen on the caliper curve and also manifests itself in a high degree of correlation between the $\Delta\rho$ curve and the caliper. The anti-correlation between the density curve (or DPHI here)

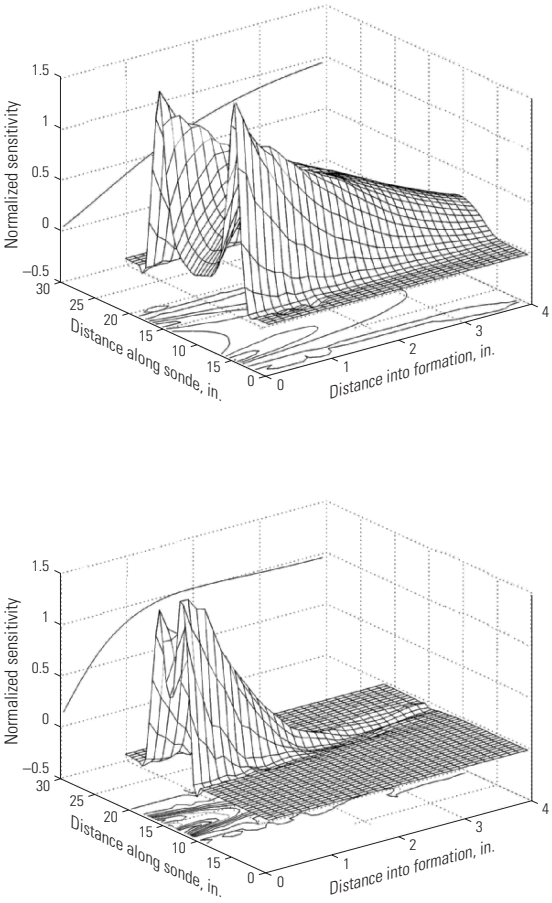


Fig. 12.22 Density-response maps for a hypothetical two-detector density device. The top figure corresponds to a far-spaced detector and the bottom figure to a short-spaced detector.

also suggests an incomplete compensation of a highly perturbed long-spaced detector. Thus, the density curve is probably not representative of the formation in this zone.

Of course it is imagined that because the measurements are not made just at a point, but while moving along the formation and averaging the counting rates (and thus the density), any rugosity will just average out to some equivalent stand-off. This may often be the case. However, there are certainly times when this is not the case. The example of zone **B**, above, is one of those cases. It is quite evident from the response maps in Fig. 12.22, that most of the signal comes from the formation closest to the tool face; an unavoidable consequence of the small mean-free-path of the gamma rays. Since rugosity simply represents patches of low-density formation, the response peaks in front of the source and detectors will exaggerate the influence of the rugosity on the counting rate.

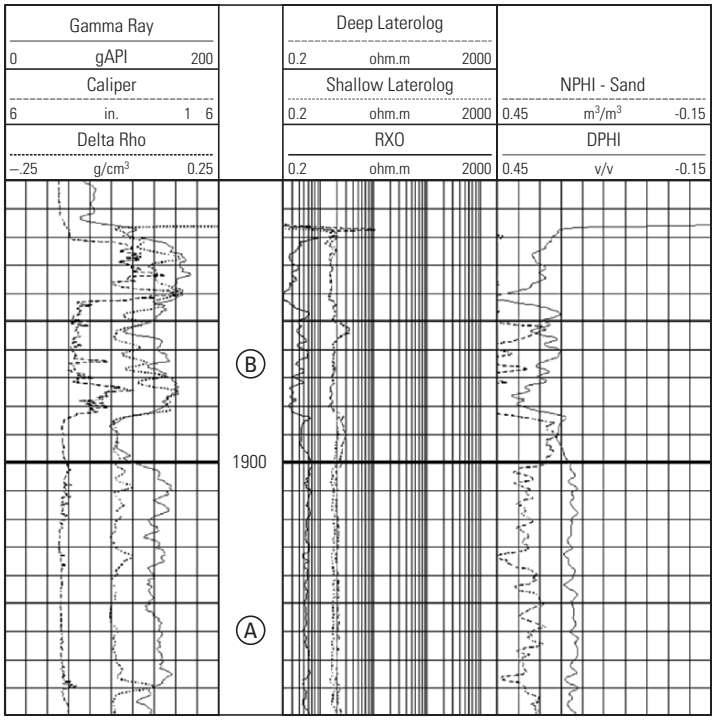


Fig. 12.23 Density log example. Track 1 contains the caliper, gamma ray and the correction curve $\Delta\rho$. Track 3 displays neutron porosity (NPHI) and density porosity (DPHI). Track 2 contains the usual three resistivity curves of differing depths of investigation. In zone B nearly all the traces show evidence of borehole rugosity or wash-outs.

The auxiliary measurement that is most helpful to indicate suspicious density readings is the caliper (for LWD, use the next best, $\Delta\rho$). If there is a high degree of correlation between the compensated density and the caliper on length scales shorter than source-detector spacings, then one should be wary. Generally speaking, if the amplitude of small-scale irregularities can be seen on a normal caliper logging scale, then it will have a density that is most probably perturbed by the borehole roughness.

12.7 ESTIMATING POROSITY FROM DENSITY MEASUREMENTS

To estimate the porosity[†] of a piece of rock, the measurement of its density is the most straightforward approach since there is a well-known and very appealing linear relation between density and porosity. In Eq. 12.1, ρ_b is the bulk density of the formation and ϕ, the porosity, or volume fraction that is not rock, or "matrix." It

[†]Much of this material appears in a slightly different form in Ellis [12].

is assumed to be saturated with a fluid of known density. Defined in this manner, the porosity corresponds to what petrophysicists call "total" porosity, ϕ_t. Note that porosity is dimensionless (v/v) so it is often reported as a decimal between zero and unity. It is sometimes convenient to use porosity units (p.u. or percent) which is simply 100 times the volume fraction associated with porosity.

It is an easy matter to see that a density measurement can easily be translated into porosity; it's just a matter of scaling. Solving Eq. 12.1 for porosity yields:

$$\phi = \frac{\rho_b - \rho_{ma}}{\rho_f - \rho_{ma}} = a\rho_b + b, \tag{12.18}$$

where the scaling constants a and b are not constants but depend on the formation parameters specific to the zone being investigated:

$$a = \frac{1}{\rho_f - \rho_{ma}}, \quad b = \frac{-\rho_{ma}}{\rho_f - \rho_{ma}}. \tag{12.19}$$

Thus, to estimate porosity properly, two important parameters must be known: the rock matrix (or grain) density ρ_{ma} and the density of the saturating fluid ρ_f since they determine the slope and intercept of this wonderfully simple relationship.

12.7.1 Interpretation Parameters

The first thing to remember when you see a curve on a log labeled "density porosity," such as in Fig. 12.23 (where it is actually called DPHI), is that someone else has done an interpretation for you. They have chosen values for ρ_{ma}, and for the density of the saturating fluid ρ_f. These may be appropriate for your particular situation or not.

First of all, how important is it to choose the appropriate values of the matrix and fluid values? For typical sedimentary rock, theoretical values of matrix density range from 2.65 g/cm^3 for quartz to 2.96 g/cm^3 for anhydrite. The fluid density may range from 1.00 to 1.4 g/cm^3 for water, mud filtrate or brine, depending on the salinity. In the case of light hydrocarbons the value could be as low as 0.6 g/cm^3 or much lower, as in the case of low-pressure gas. Table 12.2 summarizes the density ranges.

To illustrate the effect of errors in fluid and matrix density on the accuracy of the porosity estimate, imagine a water-saturated rock (ρ_f = 1 g/cm^3) whose density has been determined to be 2.5 g/cm^3. If you are uncertain as to whether it is sandstone (quartz) or limestone(calcite) then its porosity is either 12% or 9% – an uncertainty that would be intolerable for making economic or engineering decisions.

Now, assuming a calcite matrix, let's look at the impact of the uncertainty in fluid density. If the saturating fluid is a very dense brine (1.4g/cm^3) then the porosity corresponding to the measured density of 2.5 g/cm^3 is 16%. On the other hand if the saturating fluid is a low-density hydrocarbon of density 0.6 g/cm^3 then the corresponding porosity would be about 10%. Table 12.3 lists all possible values of porosity estimates, in porosity units, for a formation of density 2.5 g/cm^3 for some extremes of fluid and matrix densities.

The plots in Fig. 12.24 summarize, at three values of formation density (2, 2.25, 2.5 g/cm^3), the approximate error in porosity when the matrix density and fluid density

Table 12.2 Typical ranges of matrix and fluid densities.

	Density ranges (g/cm^3)
Fluids	ρ_f
Water	1.00
Salt water	<1.2–1.4
Oil/condensates	0.6–1.0
Gas	0.4 or lower
Matrices	ρ_{ma}
Limestone	2.71
Dolomite	2.87
Sandstone	2.65
Anhydrite	2.96

Table 12.3 Range of porosity estimates (p.u.) for a formation of density 2.5 g/cm^3.

	ρ_f	0.6	1.0	1.4
ρ_{ma}				
2.71		10	12.2	16
2.65		7.3	9.1	12

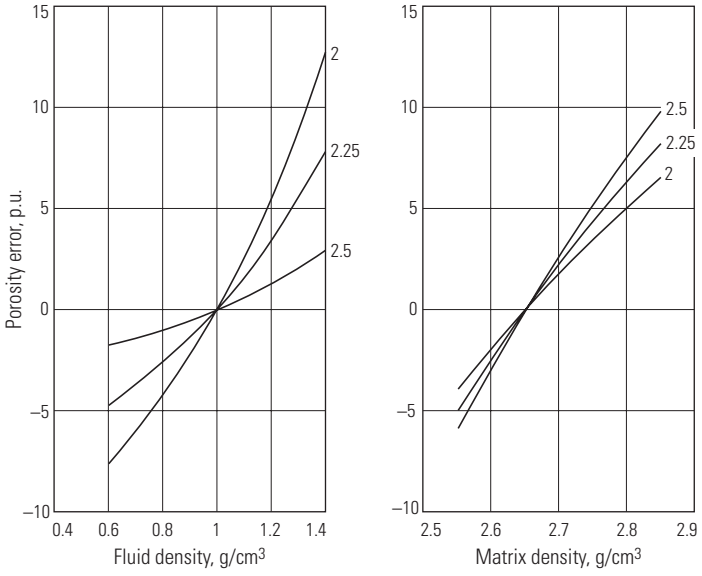


Fig. 12.24 A summary of errors in estimated porosity for errors in fluid density and grain density, evaluated for three values of formation density between 2.00–2.50 g/cm^3.

deviate from the nominal values used for the initial estimation of porosity (ρ_f =1.0 and ρ_{ma} = 2.65 g/cm^3 in this case). The error shown is in porosity units. At low porosity the influence of the fluid density error, shown in the left-hand plot, is relatively small but grows with increasing porosity. The converse is true for errors in the grain density, seen in the right-hand plot.

How accurate does the density measurement have to be? The answer of course depends on how well the porosity needs to be known. Since porosity is often translated into barrels and then into dollars, it perhaps makes more sense to assign an absolute value rather than a fractional value to the accuracy of porosity. For sake of discussion, a tolerable uncertainty on porosity is often taken to be 1% of volume fraction or 1 p.u. Using this standard, the results in Fig. 12.24 can be used to determine how well the interpretation parameters need to be estimated.

Since the density is not measured with absolute precision, what are the tolerable limits? Let us use the same standard and require that the precision on the porosity must also be 1 p.u. By using nominal values for fluid and matrix density (to be precise 1.00 and 2.65 respectively) in Eq. 12.1 we can find the sensitivity of porosity to density by differentiating the expression which results in:

$$\partial\rho \;=\; 1.0 \times \partial\phi \;+\; 2.65 \times (-\partial\phi) \;=\; -\,1.65\partial\phi. \qquad (12.20)$$

This leads to the rule of thumb that a precision on the porosity of 1 p.u. requires a precision on the density measurement of 0.0165 g/cm^3.

So how are reasonable values of matrix density and fluid density arrived at? In the case of matrix density, many petrophysicists feel that only core analysis can provide the correct value. Although the matrix density of a quartz sandstone is known, this type of idealized reservoir will rarely be encountered. Other minerals, including clay minerals, may be present causing the matrix or grain density to deviate, perhaps significantly, from the textbook value of 2.65 g/cm^3. In the case of carbonates it is common to have mixtures of limestones and dolomites/anhydrites in addition to the ubiquitous presence of clay minerals. In both cases the grain density needs to be determined from core, cross-plotting other logging measurements, the use of the photoelectric factor or perhaps from using a relatively recently developed interpretation (Herron and Herron [13]) of the analysis of formation elements from GR spectroscopy.

The fluid density can often be taken as 1 g/cm^3 if the formation water salinity is not too elevated and if the mud system is fresh, since the fluid density in the invaded zone will correspond to the mud filtrate. However, in the case of logging while drilling, at a time relatively soon after the drilling when invasion has not proceeded to any great extent, the density of the formation fluid could be much different from the mud filtrate density since the undisturbed formation fluids would saturate the formation. Interpretation difficulties would arise, for example, in a light-hydrocarbon zone if the fluid density is routinely assigned to 1.0 g/cm^3.

Regardless of the complexity of the rock and fluid system (imagine a porous shaly sand saturated with residual gas and water) the simple linear density interpretation treats the system as binary. Some appropriate matrix density will characterize the partial volumes of the various minerals that make up the shaly sand and some intermediate

fluid density will provide the best porosity estimate. The use of fall-back values for the two parameters may produce a useable first estimate, but combining the density with other measurements is the best way to determine the porosity. Grain or matrix densities for shales are a considerably more complex issue and will not be covered here. The obvious remaining problem is assigning a matrix density, which clearly requires some knowledge of the lithology. In essence, all of density interpretation aimed at porosity determination revolves on this. Various approaches to this problem are presented in Chapter 22.

REFERENCES

1. Tittman J (1986) Geophysical well logging. Academic Press, Orlando, FL
2. Tittman J, Wahl JS (1965) The physical foundations of formation density logging (gamma-gamma). Geophysics 30(2):284–293
3. Ellis D, Flaum C, Roulet C, Marienbach E, Seeman, B (1983) The litho-density tool calibration. Presented at the 58th SPE Annual Technical Conference and Exhibition, paper SPE 12048
4. Wahl JS, Tittman J, Johnstone CW, Alger RP (1964) The dual spacing formation density log. Presented at the 39th SPE Annual Technical Conference and Exhibition, paper 989
5. Minette DC, Hubner BG, Koudelka JC, Schmidt M (1986) The application of full spectrum gamma-gamma techniques to density/photoelectric cross section logging. Trans SPWLA 27th Annual Logging Symposium, paper DDD
6. Bertozzi W, Ellis DV, Wahl JS (1981) The physical foundation of formation lithology logging with gamma rays. Geophysics 46(10):1439–1455
7. Eyl KA, Chapellat H, Chevalier P, Flaum C, Whittaker SJ, Jammes L, Becker AJ, Groves J (1994) High-resolution density logging using a three detector device. Presented at the 69th SPE Annual Technical Conference and Exhibition, paper SPE 28407
8. Bornemann E, Hodenfield K, Maggs D, Bourgeois T, Bramblett R (1998) The application and accuracy of geological information from a logging-while-drilling density tool. Trans SPWLA 39th Annual Logging Symposium, paper L
9. Labat C, Brady S, Everett M, Ellis D, Doghmi M, Tomllinson J, Shehab G, (2002) 3D azimuthal LWD caliper. Presented at the 43rd SPE Annual Technical Conference and Exhibition, paper SPE 77526
10. Hansen P, Shray F (1996) Unraveling the differences between LWD and wireline measurements. Trans SPWLA 37th Annual Logging Symposium

11. Schlumberger (1979) Log interpretation charts. Schlumberger, Houston, TX

12. Ellis D (2003) Formation porosity estimation from density logs. Petrophysics 44(5):16–22

13. Herron SL, Herron MM (2000) Application of nuclear spectroscopy logs to the derivation of formation matrix density. Trans SPWLA 41st Annual Logging Symposium, paper JJ

14. Pettijohn FJ (1957) Sedimentary rocks, 2nd edn. Harper & Row, New York, Evanston, London

Problems

12.1 In the lowest portion (which is water-bearing) of a clean sandstone reservoir known to be of constant porosity, the density tool reads 2.21 g/cm^3. Further up in the same reservoir, above the oil-water contact (where the formation is fully hydrocarbon-saturated), the density tool reads 2.04 g/cm^3. What is the density of the hydrocarbon?

12.1.1 The equation:

$$\rho_{log} = 1.0704\,\rho_e - 0.188 \tag{12.21}$$

relates the electron density ρ_e to the tool reading ρ_{log}, which is closely related to the bulk density ρ_b. This equation has been defined so that the tool reading corresponds to ρ_b in water-limestone mixtures. What transform would be used for the log reading to coincide with the bulk density of mixtures of 120 kppm saltwater and sand (SiO_2)?

12.2 Figure 12.25 is a short section of the LDT log in the carbonate section of the simulated reservoir model.

12.2.1 From a knowledge of the density curve alone, what ranges of porosity would you ascribe to the seemingly uniform layer from about 12,490–12,540 ft?

12.2.2 By including the P_e measurement, could you refine your porosity estimate? What new average value would you estimate it to be?

12.2.3 What proportion of dolomite and limestone does the matrix seem to be? If not constant, what is the range of mixtures?

12.3 Figure 12.19 shows the overlay of P_e versus ρ_b for three different matrices as a function of porosity for lithology determination.

12.3.1 Frequently salt plugging occurs in dolomite formations which contain very saline formation waters. In this case the preexisting porosity of the dolomite can be replaced with depositions of NaCl. Plot the trend line on this cross plot for the case of a 20 p.u. water-filled dolomite in which the porosity progressively becomes salt-filled. Make use of the mixing law for U.

12.3.2 From this cross plot alone, with what might you confuse the fully plugged case?

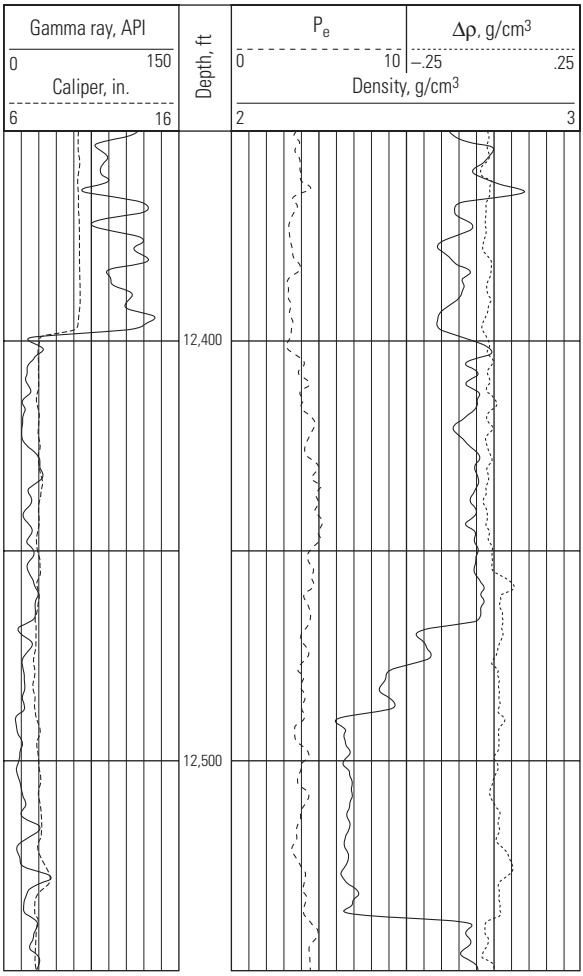


Fig. 12.25 Log example for Problem 12.2.

12.4 The sensitivity of porosity to matrix density can be determined from:

$$\partial\phi = \left[\frac{\rho_b - \rho_{ma}}{(\rho_f - \rho_{ma})^2} - \frac{1}{\rho_f - \rho_{ma}}\right] \partial\rho_{ma}. \tag{12.22}$$

For the case of a sand of about 30% porosity, show that for the uncertainty in ϕ to be less than 0.02 g/cm^3, the uncertainty in ρ_{ma} must be less than 0.05 g/cm^3.

12.5 A density log has been run in a sandstone reservoir where core analysis has determined porosity to be 23%. In this zone the density reading is 2.40 g/cm^3.

12.5.1 What do you estimate the grain density of the sandstone to be?

12.5.2 What is the error in porosity if you assume the matrix to be pure sandstone (SiO_2)?

12.5.3 From the core analysis the formation is known to consist of SiO_2 and pyrite (FeS_2). What volume fraction of the matrix does the apparent grain density correspond to?

12.5.4 The actual grain density from core analysis gives a value of 2.76 g/cm^3. What does this imply as a value for ρ_{fl}?

13

Basic Neutron Physics for Logging Applications

13.1 INTRODUCTION

The use of neutrons to probe formations has had a long history in well logging. The first neutron device appeared shortly after World War II. The initial application was to determine formation porosity. Currently, in addition to logging tools that detect neutrons in order to determine formation hydrogen content, there are tools which use pulsed neutrons to analyze the absorption rate of the emitted neutrons, and gamma ray spectroscopy tools which detect neutron-induced gamma rays to produce a limited chemical analysis of the formation. The key to understanding the responses of these tools is the interactions that are exploited. The purpose of this chapter is to describe these interactions in order to provide a basis for succeeding chapters.

As in the case of gamma rays, neutrons can interact with materials in a number of different ways, each with an appropriate cross section to describe its probability of occurrence. The interactions of neutrons with matter are much more varied and complex than those of the gamma rays. For simplicity, we will confine ourselves to two groups of those interactions: scattering and absorption. Four types of cross sections to describe these interactions will be taken up, after a review of some useful terminology and the kinematics of neutron elastic scattering.

Unlike gamma ray sources, which come from naturally occurring or easily produced isotopes, neutron sources used in logging are the result of deliberate nuclear reactions. Several of these reactions will be discussed, along with the techniques for the detection of neutrons.

13.2 FUNDAMENTAL NEUTRON INTERACTIONS

The reaction rate of neutrons with matter depends on four parameters. The first two are the density (number/volume) of neutrons, n, and their velocity, v. The product of these two quantities is called the flux (identical with Ψ, used earlier to describe gamma ray intensities), and the unit is the number of neutrons per centimeter square per second. The reaction rate also depends on the nuclear density, N_i, of the particles with which they will interact, and finally upon the cross section σ_i for the particular reaction. Thus an expression for R, the reaction rate (number of neutron reactions of type i per cm^3), is given by:

$$R = n\, v\, \sigma_i\, N_i\ . \tag{13.1}$$

The density of particles of type i in a material of molecular weight M and bulk density ρ is:

$$N_i = \frac{6.02 \times 10^{23}}{M}\,\rho, \tag{13.2}$$

if there is a single nucleus of type i per molecule.

Figure 13.1 defines, in broad terms, the energy range of interest for neutrons. For logging applications, this range is over about nine decades: from source neutrons 5–15 MeV, in the broad fast neutron range above 10 eV, to epithermal neutrons in the

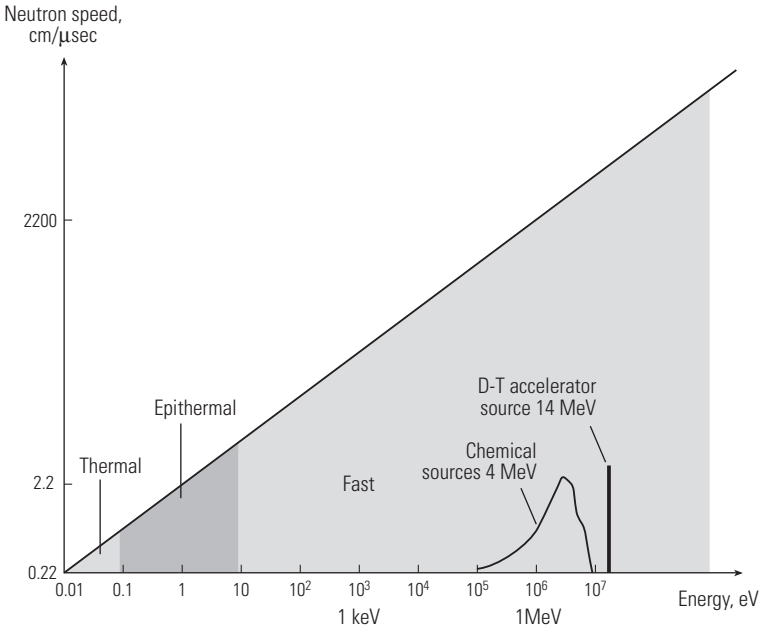


Fig. 13.1 The classification of neutrons according to broad energy ranges and their corresponding velocities. Adapted from Ellis [1].

range of 0.2–10 eV, and thermal neutrons which are distributed around 0.025 eV at room temperature.

For later discussions of the timescale associated with the slowing-down process, it is useful to note the relationship between neutron energy and its associated velocity. To evaluate the velocity of a neutron, we can use, at low energies, the classical relationship between kinetic energy E, velocity v, and mass m:

$$E = \frac{1}{2}mv^2, \tag{13.3}$$

so that the velocity v is given by:

$$v = \sqrt{\frac{2E}{m}} \cdot \tag{13.4}$$

If this expression for velocity is evaluated for thermal energies (0.025 eV), the result is 2,200 m/s or 0.22 cm/μs. Thus the velocity at any energy E (in eV) is given by:

$$v = 0.22\sqrt{\frac{E}{0.025}}\ , \tag{13.5}$$

where v is in cm/μs. Therefore the speed of an epithermal neutron of 2.5 eV is 2.2 cm/μs, and for a near-source-energy neutron of 2.5 MeV, its velocity is 2,200 cm/μs. These velocities are also noted on Fig. 13.1.

Of the four principal types of interaction, the first two are generally referred to as moderating interactions, or interactions in which the energy (or speed) of the neutron is reduced. One of these is known as elastic scattering, and the other as inelastic scattering. Let us consider elastic scattering first. Classical mechanics (in analogy to billiard ball collisions) can be used to describe the moderating power of the struck nucleus. The energy of the neutron is reduced more efficiently in collisions with nuclei of mass not too different from the mass of the neutron. Thus hydrogen and other low atomic mass elements are quite effective in reducing fast neutron energy.

The physical variables for describing elastic scattering can be obtained by a consideration of the concept of center of mass. Figure 13.2 shows the laboratory view of a collision between a stationary nucleus and a neutron moving with velocity v. After collision, the neutron has deviated from its initial direction by an angle Θ and has some reduced velocity, v'.

Another approach is to define the center of mass as shown in Fig. 13.3. This new coordinate system is defined by:

$$Mx_o = m(x - x_o), \tag{13.6}$$

where M is the mass of the target, and m is the mass of the neutron. The coordinate x_o is given by:

$$x_o = \frac{mx}{m + M} = \frac{x}{1 + A}\ , \tag{13.7}$$

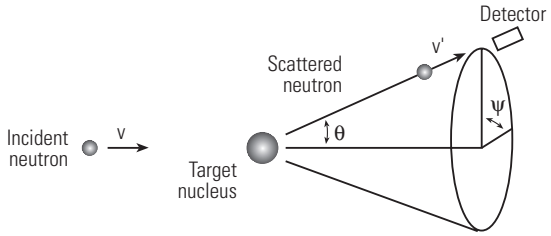


Fig. 13.2 The idealized scattering of a neutron with a target nucleus. Adapted from Weidner and Sells [2].

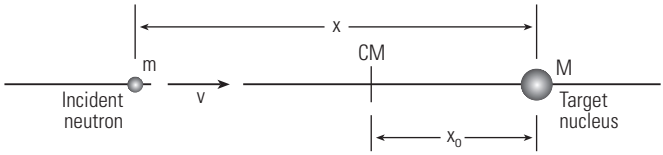


Fig. 13.3 The scattering reaction drawn to suggest the center of mass (CM) system. Adapted from Weidner and Sells [2].

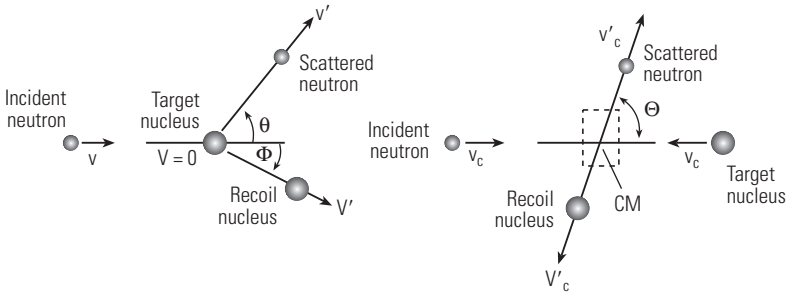


Fig. 13.4 The scattering reaction drawn from the perspective of the laboratory (left) and center of mass (right) systems. Adapted from Weidner and Sells [2].

after substituting unity for the mass of the neutron and A for the mass of the nucleus. The velocity of the center of mass v_{cm}*, as seen in the laboratory system, can be found from:*

$$v_{cm} = \frac{dx_o}{dt} = \frac{1}{1+A}\frac{dx}{dt} = \frac{1}{1+A}\,v\,. \tag{13.8}$$

Two views of the reaction are shown in Fig. 13.4: the laboratory view on the left and the center of mass system on the right. In the center of mass system, the two particles are seen to be approaching each other with velocities v_c *and* V_c*. These two velocities are given by:*

$$v_c = v - v_{cm} = \left(1 - \frac{1}{1+A}\right) v = \frac{A}{1+A}\, v\,, \tag{13.9}$$

and

$$V_c = -v_{cm} = -\frac{1}{1+A}\, v\,. \tag{13.10}$$

The total momentum in the center of mass system is given by:

$$m v_c + M V_c = \frac{A}{A+1}\, 1 \cdot v - \frac{1}{1+A} A \cdot v\,, \tag{13.11}$$

which is seen to be zero. This unique result, for an elastic collision viewed in the center of mass system, means that the neutron and nucleus enter and leave the reaction with the same velocities and are oppositely directed.

An analysis of conservation of energy [3] shows that the neutron energy E', after scattering through an angle Θ in the center of mass system, can be related to the energy E_o before the collision by the following:

$$\frac{E'}{E_o} = \frac{A^2 + 2A\cos\Theta + 1}{(A+1)^2}\,. \tag{13.12}$$

From this expression, it is seen that the minimum energy after collision occurs when $\Theta = 180°$, at which point the energy is a fraction α of the initial energy, where α is related to the mass A of the scattering nucleus by:

$$\alpha = \left(\frac{A-1}{A+1}\right)^2\,. \tag{13.13}$$

Under the assumption of isotropic elastic scattering (not too far from reality) this also implies that the probability for a neutron to scatter into any energy E in the allowed energy range of E_o to αE_o is equal. The inset to Fig. 13.5 indicates this explicitly for a couple of common elements.

Figure 13.5 illustrates, for most of the elements of interest, the possible ranges of reduction in neutron energy on a single collision. It is seen that for the most common earth formation elements the maximum energy reduction per collision for the heavy elements is about 10–25%. However, for the case of hydrogen, the entire neutron energy can be lost in a single collision. This sensitivity of elastic scattering energy loss to hydrogen is exploited in neutron porosity devices.

In the case of inelastic scattering, a portion of the energy of the incident neutron goes into exciting the target nucleus. This reduces the energy of the incident neutron. The target nucleus will usually produce one or more characteristic gamma rays upon de-excitation. This type of reaction always has a threshold energy (below which it will not happen). The de-excitation gamma ray is exploited in the measurement of the carbon-to-oxygen ratio in earth formations.

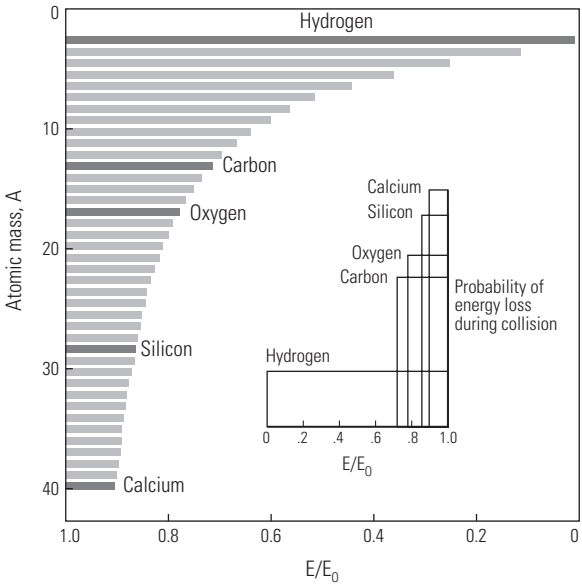


Fig. 13.5 The allowed distribution of neutron energy after a single elastic scattering with nuclei ranging in mass from H to Ca. The energy scale is normalized to the incident neutron energy and increases to the left. The inset shows, for a couple of important elements, the relative probability of scattering into the allowed range. Since the probability of scattering into any available energy is equal, the probability amplitude is smaller for larger possible scattering energy intervals. Adapted from Ellis [1].

Another general category of neutron interaction is known as *absorption.* It also is divided into two types: radiative capture and reactions which produce nuclear particles. In radiative capture, unlike the moderating elastic interactions considered above, the neutron (usually near thermal energies) is absorbed by the target nucleus, producing a compound nucleus. This nucleus de-excites instantly with the emission of characteristic gamma rays. This type of reaction is exploited in pulsed neutron logging tools or in gamma ray spectroscopy of the induced gamma rays for chemical analysis.

The cross section for radiative capture, more generally known as thermal absorption, varies with neutron energy, E, as $1/\sqrt{E}$. Its maximum value is therefore at the lowest possible energies, i.e., thermal energies. The magnitude of this cross section varies wildly, unlike the cross section for elastic scattering, among the various isotopes. There are isotopes with enormous absorption cross sections such as Gd, B, and Cl, but for the common rock minerals, the values are much smaller and, on a per atom basis, decrease in the following order: Ca, H, Si, Mg, C, and O.

Thermal capture terminates the life of a neutron released into a formation, and consequently the probability of absorption controls the distance that the neutron diffuses during its thermal lifetime. In the borehole/formation environment, this

absorption is provided by the H or Ca content of the formation. However, the presence of other strong absorbers can also perturb the thermal neutron flux levels expected at a given porosity. Since the presence of large amounts of absorbers will depress the thermal neutron flux and reduce the thermal diffusion length, the thermal neutron counting rates from borehole devices sometimes need correction. The Cl in salt water is one such absorber, and boron and gadolinium associated with clay minerals are two other efficient thermal neutron absorbers.

The category of particle reactions is quite broad; it is sufficient to say that the interaction of neutrons with some nuclei can provoke the emission of particles such as αs, protons, βs, or even additional neutrons. These reactions, although common, have a very small probability for occurring relative to the other interactions of interest in logging described above. Usually they are possible only above a relatively high neutron energy.

The complexity of the cross sections for neutron interactions is illustrated in Fig. 13.6, which schematically indicates the variations with energy. The top figure refers to the total cross section as a function of neutron energy E, and the four following figures indicate how this can be decomposed. The first, (n, n), refers to elastic scattering, which is shown to be rather constant with energy except for some resonances at low energies. The next sketch shows inelastic interactions, (n, n'), showing some characteristic threshold below which this reaction is not possible; the third sketch is one of the many particle reactions possible, (n, α); and the final (although there could be others) is the radiative capture, (n, γ), which is seen to increase in probability at low energies.

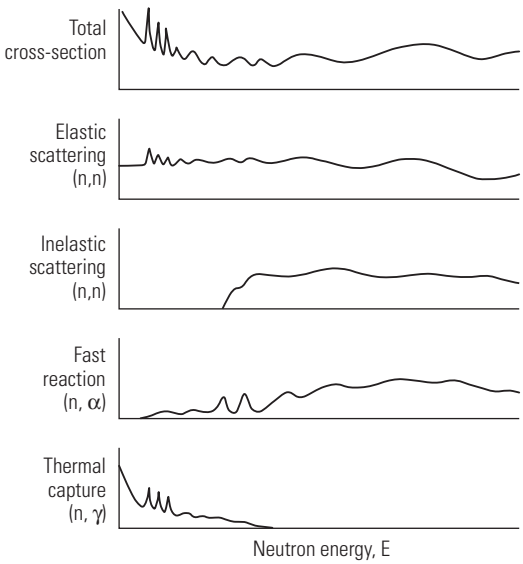


Fig. 13.6 A schematic illustration of the energy variation of the total neutron cross section and four of its components. Adapted from Ellis [1].

13.3 NUCLEAR REACTIONS AND NEUTRON SOURCES

Since neutron sources are almost never found in nature, it is appropriate to briefly discuss the techniques for creating them. There are two types in use in logging: so-called chemical, or encapsulated, sources, and accelerator sources.

The classic reaction, which resulted in the discovery of the neutron, was the bombardment of beryllium by α particles. It can be written as:

$$^4Be + {}^2He \rightarrow {}^6C + n + 5.76\,\text{MeV}\,. \tag{13.14}$$

This forms the basis for the cheapest, easiest, and most reliable method for neutron production. The physical explanation of this reaction is beyond the scope of interest of the present work and may be found in References [2] and [4]. The practical construction of this kind of chemical neutron source consists of mixing a naturally occurring α-emitter with an appropriate light element having a large $(\alpha, n)^*$ cross section. Some α-emitters which have been used for this purpose are Pu, Ra, Am, and Po. Three common target elements are Be, B, and Li. The actual spectrum (energy distribution) of emitted neutrons is quite complicated. It depends somewhat on the geometric details of the α-emitter and target, but the peak of the neutron distribution for AmBe is around 4.2 MeV.

Another method of exploiting particle-induced reactions in the production of neutrons is by the use of charged particle accelerators [5]. In one realization, currently in use in well logging, deuterium and tritium ions are accelerated toward a target impregnated with the hydrogen isotopes deuterium (D) and tritium (T). The reaction is written as:

$$^2D + {}^3T \rightarrow {}^4He + n + 17.6\,\text{MeV}\,. \tag{13.15}$$

The cross section for this reaction has a maximum at about 100 keV of ^2D projectile energy. This dictates the required accelerating voltages in such a device.

Despite the engineering difficulties of constructing such a device, the advantages for logging are many. One is the relatively high energy of the produced neutrons. They are emitted at 14.1 MeV (not 17.6 MeV, because some of the energy of this reaction is given up to the alpha particle, see Problem 13.1). These high-energy neutrons are useful for producing various interesting nuclear reactions in the formation, as is discussed later. Another advantage is that a source of this type can be controlled, i.e., switched off and on at will. This provides a degree of safety unparalleled for radioactive sources as well as permitting measurements involving timing as a means of determining some interesting nuclear properties of the formation, a topic covered in Chapter 15.

*This shorthand, (α, n), indicates a reaction of an α particle with an unspecified nucleus, resulting in the production of a neutron and another unspecified nucleus.

13.4 USEFUL BULK PARAMETERS*

13.4.1 Macroscopic Cross Sections

Despite the complexities of the cross sections shown in Fig. 13.6, which govern the details of the interactions, some gross properties can be specified for neutron interactions with materials. The first is the macroscopic cross section, which is defined as the product of the cross section (σ_i) in question times the number of atoms per cubic centimeter, N, i.e.:

$$\Sigma_i = N\,\sigma_i = \frac{N_{Av}\rho_b}{A}\,\sigma_i\,, \tag{13.16}$$

where N_{Av} is Avogadro's number, ρ_b, is the bulk density, and A is the atomic weight. The dimensions of the macroscopic cross section Σ_i, are inverse centimeters. Its reciprocal is the mean free path length between interactions of type i. Figure 13.7 shows the total mean free path in limestones of 0, 20, 40, and 100 p.u. (porosity units) as a function of energy for fast neutrons. At the energy of chemical source emission (2–4 MeV), it is seen that there is very little porosity dependence. It is only as the neutrons are slowed down that the mean free path becomes strongly dependent on the hydrogen concentration of the formation.

Frequently, in logging, special use is made of the macroscopic absorption cross section evaluated at thermal energies. Table 23.3 shows the thermal neutron absorption

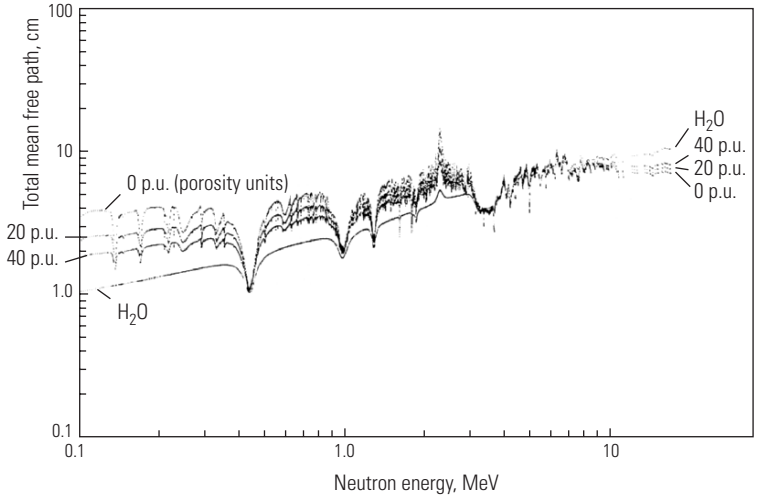


Fig. 13.7 The mean free path of neutrons in limestones of various porosity and water. They are given as a function of the neutron energy. Adapted from Ellis [1].

*Much of the material in this section appeared earlier in slightly different form in Ellis et al. [6].

Table 13.1 Thermal neutron absorption parameters for selected elements. Adapted from Ellis [1].

Element		A Average atomic weight (Atomic mass units)	σ Average atomic absorption Cross section (barns)	σ_m Mass-normalized absorption cross section (cm^2/g)	A_m Mass-normalized chlorine absorption equivalents
Gd	Gadolinium	157	49, 000	188	333
B	Boron	10.8	759	42.3	75.0
Sm	Samarium	150	5, 800	23.3	41.2
Eu	Europium	152	4, 600	18.2	32.3
Cd	Cadmium	112	2, 450	13.1	23.3
Li	Lithium	6.94	70.7	6.14	10.9
Dy	Dysprosium	163	930	3.45	6.11
Ir	Iridium	192	426	1.34	2.37
Cl	Chlorine	35.45	33.2	0.564	1.00
Ag	Silver	108	63.6	0.355	0.630
H	Hydrogen	1.008	0.332	0.198	0.352
Cs	Cesium	133	29.0	0.131	0.233
K	Potassium	39.1	2.10	0.0323	0.0573
Fe	Iron	55.9	2.55	0.0275	0.0488
Na	Sodium	23.0	0.530	0.0139	0.0246
S	Sulfur	32.1	0.520	0.00977	0.0173
Ca	Calcium	40.1	0.43	0.00646	0.0115
Al	Aluminium	27.0	0.230	0.00513	0.0091
Si	Silicon	28.1	0.16	0.0034	0.0061
Mg	Magnesium	24.3	0.063	0.00156	0.00459
C	Carbon	12.0	0.0034	0.00017	0.00030
O	Oxygen	16.0	0.00027	0.0000102	0.000018

parameters of a few selected elements. As noted earlier, the cross section per nucleus measured in barns ($10^{-24}cm^2$) varies wildly. However, a more useful quantity is the macroscopic absorption cross section contributed by each particular element (or isotope). The macroscopic absorption coefficient, Σ_a, is computed from Eq. 13.16 where σ_i is replaced by σ_a where the subscript "a," refers to absorption. In this case, σ_a refers to the thermal absorption cross section which dominates at thermal energies for most elements.

A more useful unit for computing the effect of a given concentration of thermal absorbers on neutron measurements is the mass-normalized macroscopic cross section, σ_m, indicated in column 4. It is simply the expression in Eq. 13.16 with density divided out, Σ_a/ρ. It is common in petrophysics to use a derivative of the mass-normalized cross section called the capture unit (cu). (The common but confusing symbol for this quantity, nearly universally used, is Σ.) It is convenient to define special units for it. These so-called capture units are 1,000 times the Σ_a values defined above. So the mass-normalized cross section is a handy unit since 1,000 times the value of σ_m is the

number of cu contributed by 1 gm of the absorber in question per cubic centimeter. In this manner it is easy to estimate (from hydrogen alone) that the capture cross section Σ for fresh water is about 22 cu ($0.198 \times 1{,}000 \times 1/9$ g of hydrogen per cubic centimeter).

Although not a cross section, there is another very useful parameter called the hydrogen index (HI). It is the ratio of the hydrogen content (expressed in terms of grams per cubic centimeter) of any material or mixture compared to the hydrogen content of water at s.t.p., or 1/9 g/cm^3. Obviously, in porous freshwater saturated rocks the hydrogen index and the porosity are identical, as long as there is no hydrogen associated with the rock fabric.

13.4.2 Lethargy and Average Energy Loss

As mentioned earlier in the discussion of elastic scattering, low mass nuclei are very effective in reducing the energy of the scattered neutron. As can be inferred from Fig. 13.5, the result of a collision can be considered, on average, as a percentage decrease of the neutron energy. This is usually expressed as the average logarithmic energy decrement ξ, which is defined by:

$$\xi \equiv \langle \ln(E_i) - \ln(E) \rangle = \langle -\ln(E/E_i) \rangle , \tag{13.17}$$

where E_i is the initial energy and E is the energy of the neutron after collision. To compute the average log energy decrement we need only note from the inset of Fig. 13.5 that the probability for scattering into any of the possible energy values below the initial energy is equal. This can be expressed as:

$$P(E)dE = \frac{dE}{(1-\alpha)E_i} , \tag{13.18}$$

where α, the mass ratio that controls the maximum energy loss in elastic scattering, was defined in Eq. 13.13. Then the average log decrement follows from:

$$\langle \ln(E_i/E) \rangle = \int_{\alpha E_i}^{E_i} \ln\left(\frac{E_i}{E}\right) \frac{dE}{E_i(1-\alpha)} \tag{13.19}$$

$$= \frac{1}{(1-\alpha)} \int_{E_i}^{\alpha E_i} \ln\left(\frac{E}{E_i}\right) \frac{dE}{E_i} \tag{13.20}$$

$$= 1 + \frac{\alpha}{1-\alpha} \ln(\alpha). \tag{13.21}$$

Since α is zero for hydrogen, it can be seen that for neutron interactions with hydrogen, the average log energy decrement, ξ, is unity. For much more massive nuclei it can be shown [3] that the average log energy decrement is simply related to the atomic mass, A, of the struck nucleus by:

$$\xi \approx \frac{2}{A + 2/3} , \tag{13.22}$$

for large values of atomic mass A.

13.4.3 Number of Collisions to Slow Down

It is interesting to estimate the number of scatterings that it takes for a neutron's energy to be reduced from source energy (4.2 MeV average energy for an AmBe source neutron) to epithermal energies of 0.4 eV. In pure hydrogen where the average energy reduction is a factor of 2 for each collision, the number of collisions might be found by solving the following expression for n:

$$\left(\frac{1}{2}\right)^n \times 4.2 \times 10^6 \;=\; 0.4, \tag{13.23}$$

that yields about 23 collisions. This naive calculation, of course, is in error because we need to use the average log energy decrement.

The average log energy decrement allows an estimation of the average number of collisions, n, to reduce the neutron from an initial energy E_i to some lower energy E, from the following reasoning. If the sequence $E_1, E_2, ..., E_n$ represents the average energy after each collision, then we can write:

$$\left\langle \ln\left(\frac{E_i}{E_n}\right)\right\rangle \;=\; \left\langle \ln\left(\frac{E_i}{E_1}\frac{E_1}{E_2}\cdots\frac{E_{n-1}}{E_n}\right)\right\rangle \tag{13.24}$$

$$\;=\; \left\langle \ln\left(\frac{E_i}{E_1}\right)\right\rangle^n \;=\; n\left\langle \ln\left(\frac{E_i}{E_1}\right)\right\rangle \tag{13.25}$$

$$\;=\; n\xi\ . \tag{13.26}$$

Thus the average number of collisions is given by:

$$n \;=\; \frac{1}{\xi}\left\langle \ln\left(\frac{E_i}{E_n}\right)\right\rangle\ . \tag{13.27}$$

Returning to the problem of hydrogen, using the fact (from Eq. 13.21) that ξ for hydrogen is unity, coupled with the preceding result (Eq. 13.27), we see that the average number of collision is simply $\ln(10^7)$, or just over 16.

The constant ξ can be computed for a mixture of elements by weighting the value of each ξ_i for element i with the appropriate total scattering cross section $N_i\sigma_i$. Table 13.2 shows some typical values for the average logarithmic energy decrement and the number of collisions necessary to reduce source energy neutrons (4.2 MeV) to 0.4 eV.

Of course, actual scattering between neutrons and hydrogen will result in a distribution of the number of collisions about this mean value. For some slightly more realistic cases we can compute the distribution of collisions assuming equal scattering cross sections for the elements involved in water and limestone (not far from the actual case). The number of collisions required to slow down neutrons in four cases is shown in Fig. 13.8. The average number of collisions to slow a neutron down in water is about 20 and it is an impressive 150 collisions in 0 p.u. limestone where no hydrogen is present. The two intermediate cases are the water-saturated 20 p.u. limestone with about 65 collisions, and the gas-saturated case, which rises to about 90 collisions because of the reduced density of hydrogen in the pore space.

Table 13.2 Average logarithmic energy decrement and average number of collisions for reducing neutron energy from 4 MeV to 0.4 eV for selected moderators.

Neutron slowing-down parameters		
Moderator	ξ	n
H	1.0	16
C	0.158	110
O	0.12	131
Ca	0.05	330
H_2O	0.7	22.5
20 p.u. limestone	0.23	70
0 p.u. limestone	0.115	138

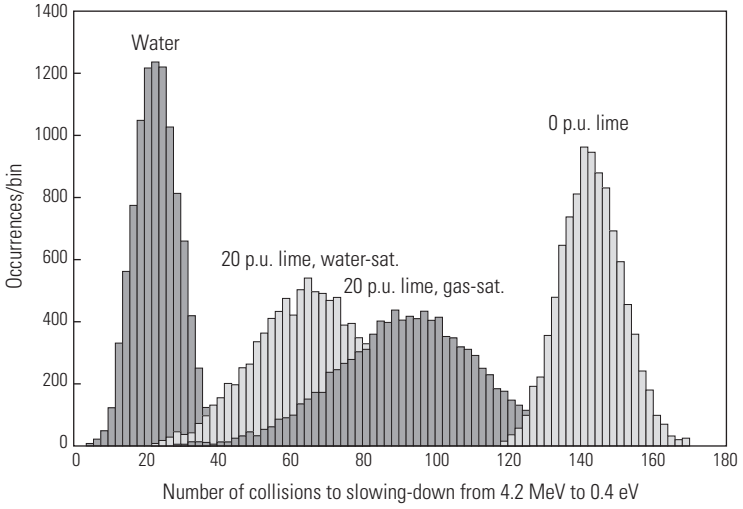


Fig. 13.8 Distribution of the number of collisions required to slow down source energy neutrons in four different materials with a range of hydrogen content computed from 10,000 source neutrons. From Ellis et al. [6]. Used with permission.

13.4.4 Characteristic Lengths

There are two more parameters which help to characterize neutron interactions with bulk material. One parameter is known as the slowing-down length, L_s and the other as the thermal neutron diffusion length, L_d. The slowing-down length is proportional to the root-mean-square distance that a neutron covers between the time it is emitted from the source at high energy to the time it reaches a much lower energy, usually the lower edge of the epithermal energy region. The diffusion length, L_d, can be thought of as the rectified distance a thermal energy neutron travels between the point at which it became thermal until its final capture.

13.4.4.1 Slowing-down Length Moderate energy neutrons emitted into earth formations "slow down" or lose energy primarily through the elastic scattering interaction previously discussed. The reason why we are interested in the population and distribution of low-energy neutrons is that the detectors in logging instruments are most sensitive to low-energy neutrons. The ratio of counting rates from detectors at different spacings from the source, used to estimate formation porosity or hydrogen index, will be seen to be closely related to measuring the L_s of the formation.

In the simple scenario of a source of high-energy neutrons in an infinite homogeneous medium, we know that once the neutrons are emitted, they travel from collision site to collision site, losing energy, and changing direction at each interaction until they ultimately are captured by some isotope. During this time they travel some finite distance from the source. The slowing-down length is used to characterize the spatial distribution of the low-energy scattered neutrons resulting from a point source in an infinite medium.

Although the problem of a point source of neutrons at the center of an infinite homogenous medium has been studied mathematically [7], we have chosen a simulation to illustrate the details here. Figure 13.9 summarizes the results of a number of Monte Carlo calculations in this simple geometry. The medium was water-saturated limestone of porosity ranging from 0 to 30 p.u. The calculations show the total neutron flux (neutrons/cm^2-s) estimated in concentric shells 2 cm thick. The semilog plot shows a nearly exponential fall off in the total flux 10 cm beyond the immediate region of the source. The slope of each of the flux distributions was calculated over the interval of 30–70 cm from the source. As indicated by the solid lines in the

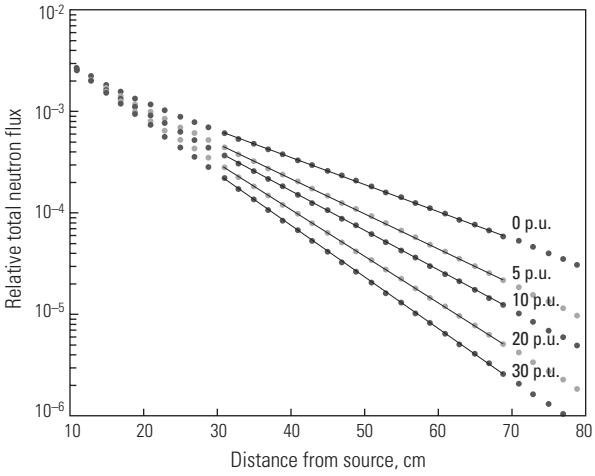


Fig. 13.9 The results of Monte Carlo calculations of the radial dependence of the total neutron flux in infinite limestone formations with water-saturated porosity ranging from 0 to 30 p.u. From Ellis et al. [6]. Used with permission.

five distributions, the slope is seen to increase as the porosity (or hydrogen content) increases. So how is this related to the slowing-down length?

Any one of curves in Fig. 13.9 is, in fact, the spatial distribution of the neutron flux, $\phi(r)$, for neutrons of energy above thermal in an infinite medium of a given porosity. To obtain some typical distance, r, that the "average" neutron travels from the source in this process of slowing-down from a curve of this type, one can use the mean square distance (or the second-moment of the distribution), given by:

$$\overline{r^2} = \frac{\int_0^\infty 4\pi r^2 \phi(r) r^2 dr}{\int_0^\infty 4\pi r^2 \phi(r) dr}. \tag{13.28}$$

The definition of L_s is that it is a fraction ($1/\sqrt{6}$) of the root-mean-square distance:

$$L_s = \frac{1}{\sqrt{6}} \sqrt{\overline{r^2}}. \tag{13.29}$$

One practical method of computing L_s [8, 9] considers the slowing-down process as proceeding through a series of discrete steps and computes the diffusion length from the scattering and removal cross sections in each of the many descending energy bins, and then sums up the quadratic combination. It has been implemented in a useful code called Schlumberger NUclear PARameter code (SNUPAR) [10]. The slowing-down length, according to this prescription, can be computed for any source and detection energy and material whose elemental constituents and density are specified.

Figure 13.10 shows the slowing-down lengths for three common sedimentary lithologies as a function of water-filled porosity. As can be seen, when little or no hydrogen is present, the slowing down length, L_s, is quite large – on the order of 20–30 cm. As the amount of hydrogen increases (in the form of water in this instance), the values quickly converge. Note that the slight differences in slowing-down lengths for the three different lithologies are mainly apparent at low porosity.

In Fig. 13.11, the L_s (and a related quantity to be discussed below, L_m) values for the same water-filled limestone formations are plotted versus the inverse of the computed slope (which has dimensions of length). Although the exponential fall-off of the total flux is not given exactly by L_s it is easily seen to be related to the empirically derived slope.

The conclusion to be drawn from this numerical demonstration is that the characteristic length for the decline of the total neutron flux with distance from the source in an infinite homogenous medium, can be characterized by L_s for the case of water-filled limestone (and by extension, any other water-filled formation).

In order to understand the variations of the slowing-down length seen in Fig. 13.10, it is interesting to compare it with a random walk. The random walk in one dimension is shown in Fig. 13.12, which plots for three trials (three different neutrons) the distance from the starting point as a function of the number of equal-length steps taken. At each step the probabilities for a forward or backward displacement are equal. It is obvious that the average displacement from the starting point for a large number of trials, N, is zero. However, there is a distribution of terminal points around the origin. A measure of the width, or spread, of the distribution is the root-mean-square

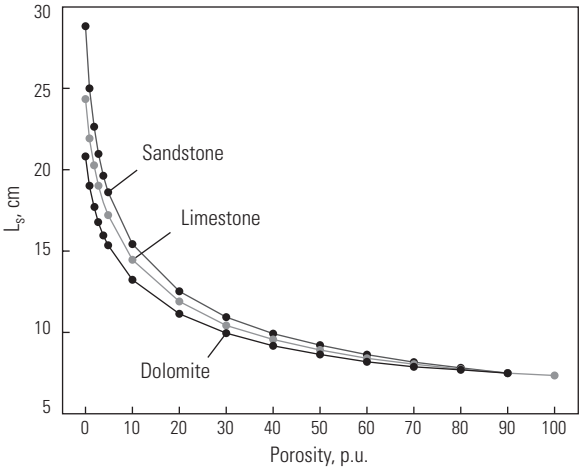


Fig. 13.10 Computations of the slowing-down lengths for AmBe source neutrons to reach 0.4 eV. Results are shown for water-saturated limestone, sandstone, and dolomite formations. From Ellis et al. [6]. Used with permission.

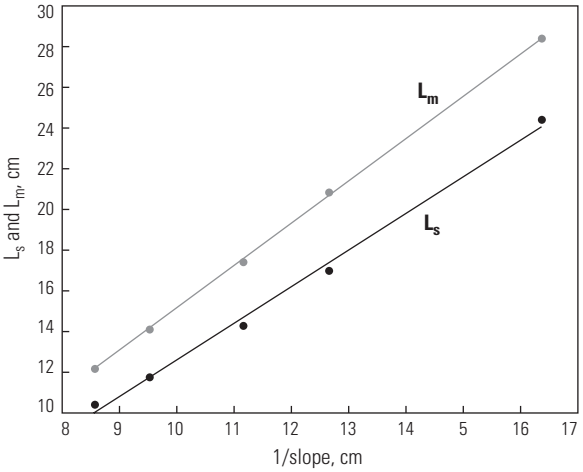


Fig. 13.11 The SNUPAR-calculated values of L_s and L_m for infinite limestone formations as a function of the characteristic decay lengths from the Monte Carlo flux fall-off shown in Fig. 13.9. From Ellis et al. [6]. Used with permission.

displacement, which can be shown to be equal to $\sqrt{N}$ times the length of the step. Figure 13.13 shows the probability distribution for three series of random walks, each containing a different number of steps. They all center about zero (no displacement from the origin), but the width increases as the number of steps taken increases.

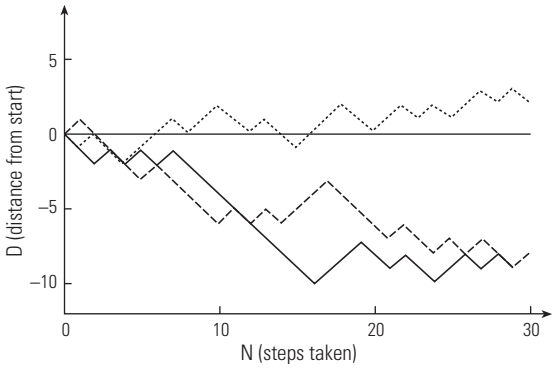


Fig. 13.12 Three trials of a random walk. Adapted from Feynman [11].

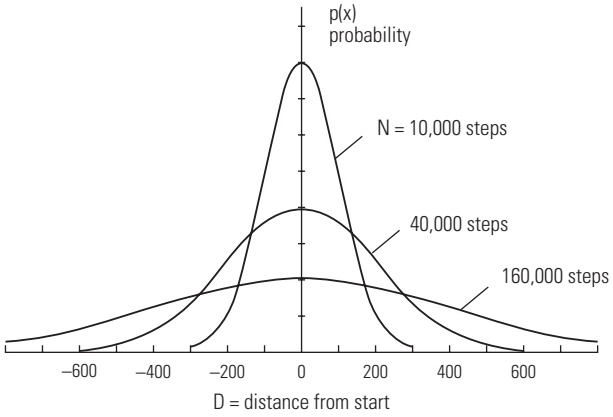


Fig. 13.13 The probability distribution of terminal points for random walks with three large step numbers. Adapted from Feynman [11].

Although the slowing-down of neutrons is a three-dimensional process, and the free path between collisions varies somewhat, it can still be thought of as a random walk. One important feature which distinguishes the random walk in a zero porosity limestone from one in water is the number of collisions (the number of steps taken in the random walk). Figure 13.14 illustrates this idea, along with a few useful parameters. The sketch shows the path of two "typical" neutrons: one slowing down in water in about 22–23 collisions and the other slowing down in 0 p.u. limestone in about 138 collisions. Consequently if we associate the slowing-down length with the root-mean-square displacement for a random walk, we expect the "average" distance each travels to be proportional to the square root of the number of collisions. Thus, the neutron in 0 p.u. limestone should travel about 2.5 times farther than the one in water since it takes about 6 times more collisions, if the mean free path in the two formations were equal. Also indicated in the figure are the approximate slowing-down

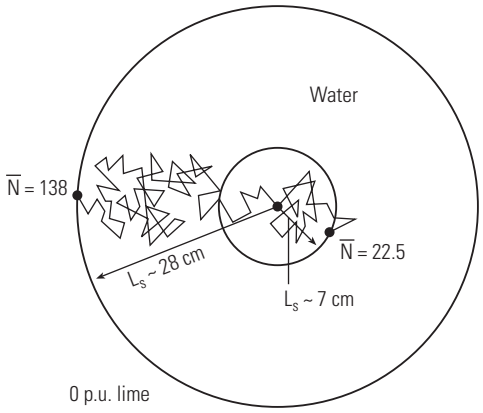


Fig. 13.14 An illustration of the relationship between the number of collisions for slowing down neutrons and the neutron slowing-down length in water and 0 p.u. limestone. Adapted from Ellis [1].

lengths for the two formations: approximately 7 cm in water and 24 cm (or about 3.5 times longer) in 0 p.u. limestone, indicating that the mean free path in the limestone is $\approx$35% larger than in water.

This larger mean free path in limestone should have been anticipated from the data in Fig. 13.7 that show the mean-free-path in 0 p.u. limestone becoming gradually larger than that in water for neutron energies below about 4 MeV.

13.4.4.2 Diffusion Length and Migration Length The diffusion length L_d can be thought of as the root-mean-square distance a thermal energy neutron travels between the point at which it became thermal until its final capture after a series of many collisions. This phase can also be considered a random walk and the characteristic length should depend on the square root of the number of collisions before capture.

How many collisions will a thermal neutron undergo before it is absorbed? Consider a simple case of water. Since the scattering cross section for hydrogen is so much larger than that of oxygen and there are two hydrogen for each oxygen, we neglect the presence of oxygen. Thus, we can arrive at an estimate from hydrogen data alone. Since, at thermal energies, the absorption cross section is only $\sim$0.33 barns and the scattering cross section is about 38 barns, then for each collision with hydrogen the probability of absorption is $\frac{33}{38}$ or 1/115. If we were to follow the histories of a large number of neutrons and keep track of how many collisions each underwent before absorption, the distribution of collisions would not be peaked as in the slowing-down distribution of Fig. 13.8, but rather an exponential with a slope of $-1/115$.

A Monte Carlo calculation was performed in an "infinite" sphere of water for 10,000 source neutrons and the results are presented in Fig. 13.15 to see how well it agrees with the approximate method just mentioned. It is interesting to compare the rough estimate with the Monte Carlo calculation which uses all the energy-dependent

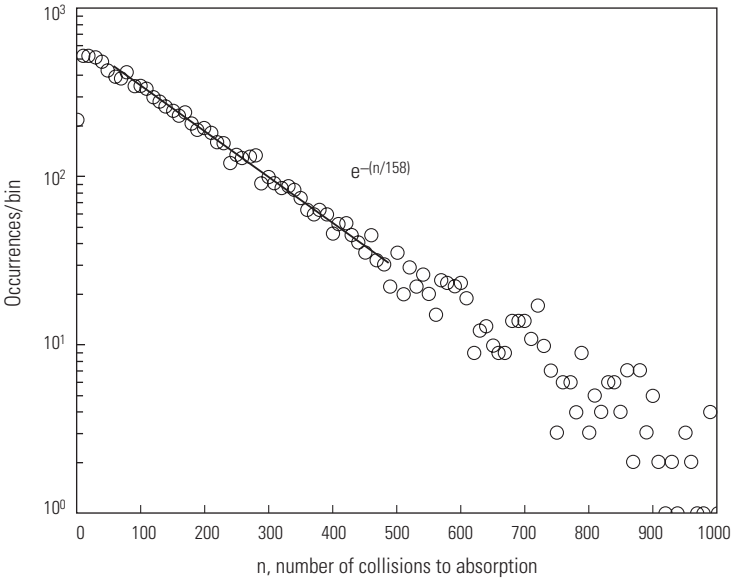


Fig. 13.15 The histogram of the number of collisions required for a population of 10,000 thermal neutrons to be absorbed in water. From Ellis et al. [6]. Used with permission.

cross sections for both elastic scattering and absorption (as well as other processes) for both hydrogen and oxygen. Results from the complete Monte Carlo simulation shows an exponential fall off with a slope that gives the characteristic number of collisions as 158. This somewhat slower fall off is a result of including the elastic scattering with oxygen and taking into account the thermal up-scattering (an increase in neutron energy after a scattering rather than a decrease) that occurs at equilibrium. This up-scattering extends the life of the neutrons, i.e., the higher the neutron energy, the lower the probability that they will be absorbed.

What we have described above is a diffusion process. For this diffusion process there is a characteristic length associated with the steady-state spatial distribution formed by neutrons in their many collision before being absorbed. This characteristic length is determined in large part by the absorption cross section Σ and is given by:

$$L_d = \sqrt{(D/\Sigma)}\,, \tag{13.30}$$

where D is the thermal diffusion coefficient (discussed in Section 14.4) and Σ is the macroscopic thermal absorption cross section of the material. The diffusion coefficient D can also be calculated using SNUPAR from knowledge of the cross sections of the material. It is shown in Fig. 13.16 as a function of porosity for the three principal matrices.

Since thermal neutrons are strongly affected by the presence of thermal absorbers, it is interesting to look at an abbreviated list of elements frequently found in formations which have large macroscopic thermal absorption cross sections. This is found in

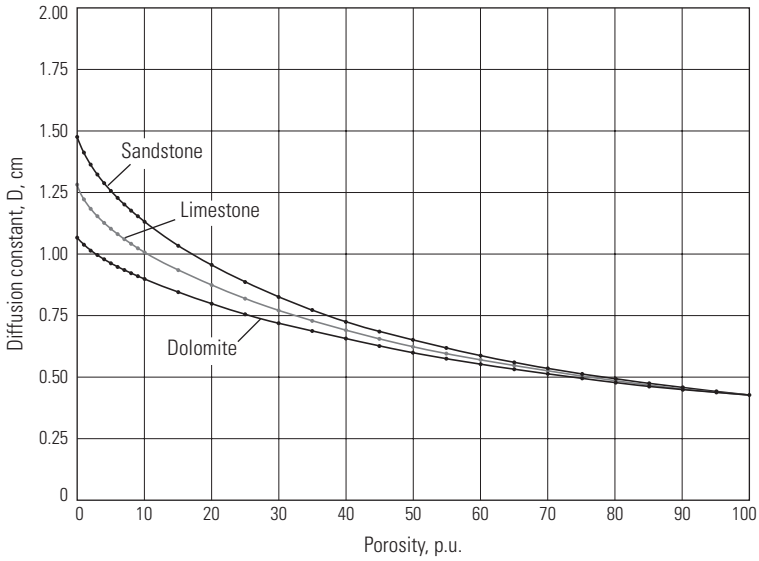


Fig. 13.16 The diffusion coefficient of thermal neutrons as a function of porosity for the three principal rock types.

Table 23.3 where the units in the penultimate column are capture cross section (cu) per milligram of material per cubic centimeter. As already stated, chlorine is of particular interest since saltwater will have a measurable effect on the thermal neutron population. Iron and boron, which are frequently associated with clays, may dominate the capture cross section of the formation if present in sufficient concentration.

Another sometimes useful parameter, the migration length (L_m), has been defined as:

$$L_m^2 = L_s^2 + L_d^2 . \tag{13.31}$$

It can be viewed as a distance which represents the combination of the path traveled during the slowing-down phase (L_s) and the distance traveled in the thermal phase before being captured (L_d). Note also, in Fig. 13.11, that the empirically derived slopes of the calculated neutron flux of Fig. 13.9 are also related to L_m. This parameter provides a convenient way of predicting the response of a thermal neutron porosity device, which is discussed in more detail in the next chapter.

13.4.5 Characteristic Times

For the two principal characteristic length scales of neutron interactions there are also two characteristic time ranges associated with each.

The time it takes for a neutron to have its energy reduced from source energy to the the bottom of the epithermal energy range (~0.4 eV) is known as the slowing-down time. As might be expected from the earlier discussion it is quite dependent on the

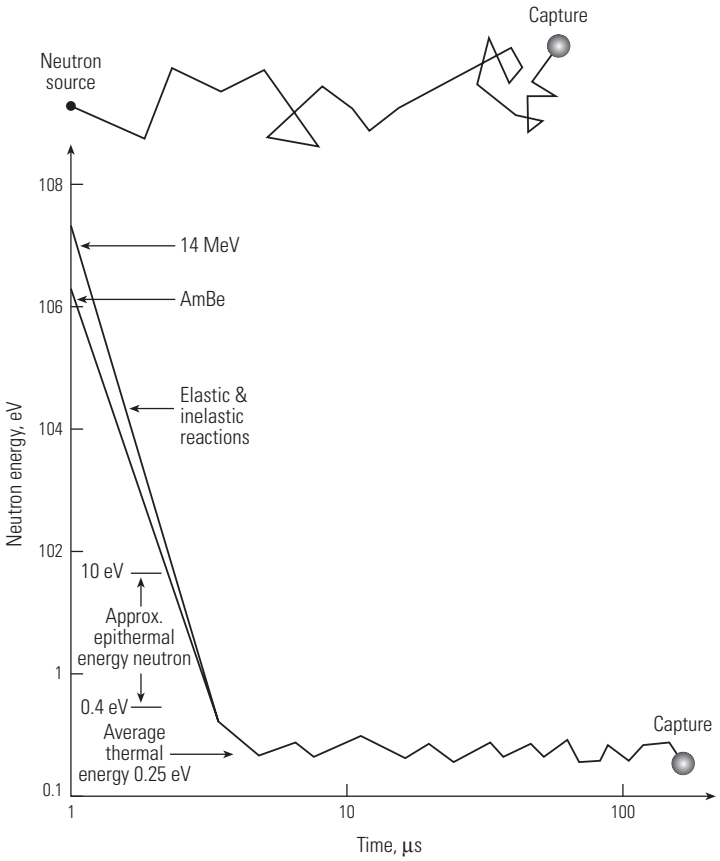


Fig. 13.17 A representation of the timescales associated with neutron slowing-down and with the capture of thermal neutrons.

amount of hydrogen present for neutron interaction. In the cartoon of Fig. 13.17 this timescale is indicated to be on the order of 10 μs. We shall see later that it is about 2 μs in water and about 12 μs in zero porosity formations.

The time it takes for a thermalized neutron to be captured is indicated by the figure to be on the order of 100 μs. This of course will vary widely depending upon the macroscopic thermal absorption cross section, Σ, in the medium. When the Σ value is large the capture time is quite short. In pure water it is about 200 μs.

13.5 NEUTRON DETECTORS

Neutrons are detected in a two-step process. First, the neutrons react with a material in which energetic charged particles are produced. Then the charged particles are detected through their ionizing ability. Thus, most neutron detectors consist of a

target material for this conversion, coupled with a conventional detector, such as a proportional counter or scintillator (see Section 10.7), to achieve the measurement. Since the cross section for neutron interactions in most materials is a strong function of neutron energy, different techniques have been developed for different energy regions. For well logging applications, at present, it is the detection of thermal and epithermal neutrons which is of interest. The detection schemes considered in this section are appropriate for these low-energy neutrons.

Nuclear targets useful for neutron detectors must satisfy several criteria: the cross section for interaction must be very large, the target nuclide should be of high isotopic abundance, and the energy liberated in the reaction following the neutron absorption should be high enough for ease of detection by conventional means. Three target nuclei have been found to generally satisfy these conditions: ^{10}B, ^{6}Li, and ^{3}He. In the case of the first two targets, the (n, α) reaction is utilized, and for ^{3}He, it is the (n, p) reaction.

The boron reaction is widely exploited in the form of BF_3 in a proportional counter. In this case the boron trifluoride serves as both the target and the ionization medium. For this application the gas is enriched in ^{10}B to attain a high detection efficiency. Another approach is to use a boron coating on the inner wall of a proportional counter, which may use some other proportional gas more suitable than BF_3 for applications involving fast timing, for example.

Since a suitable lithium compound gas does not exist, the lithium reaction is not exploited in proportional counters. However LiI scintillators, similar to sodium iodide for gamma ray detection, are available. Due to the large energy released by the (n, α) reaction, neutrons are registered at an energy of about 4.1 MeV, which provides a means of discriminating against the gamma rays, which are also readily detected by the LiI crystal.

The most common neutron detector in well logging, however, is based on the ^{3}He (n, p) reaction. In this case, ^{3}He is used as the target and proportional gas in a counter. It is preferred since it has a higher cross section than the boron reaction and the gas pressure can be made much higher than for BF_3 without degradation of its proportional operation. The simplicity of a proportional counter is also preferred to the complications associated with a scintillator.

For the three reactions discussed above, the cross sections vary inversely with the square root of the neutron energy, so that the detection efficiency for neutrons will vary in the same manner. The detectors employing these reactions respond primarily to thermal neutrons. For some logging applications it is desirable to measure the epithermal neutron flux, while being insensitive to thermal neutrons. This can be achieved by making a minor modification to any of the three types of detectors previously mentioned. It consists of using a shield of thermal-neutron absorbing material with a large cross section, such as cadmium, around the detector. In Fig. 13.18 the process is schematically described starting with a ^{3}He detector of cross-section dimension l. The graph to the right is a sketch of its detection efficiency, given by $1 - e^{-\Sigma_{He} l}$. It is shown to be nearly unity at very low energies and falling off at higher energies. The term Σ_{He} is energy dependent and depends on the gas pressure of the neutron detector. The epithermal detector shown below in Fig. 13.18 is the same "thermal"

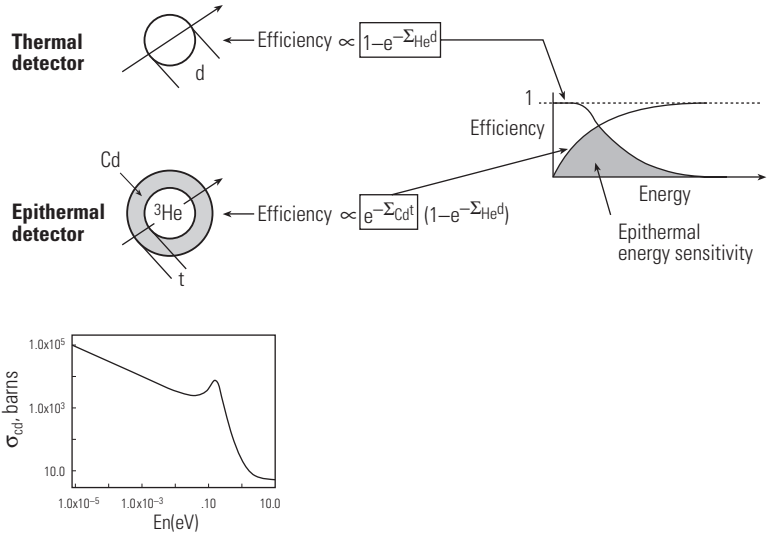


Fig. 13.18 An epithermal neutron detector is shown schematically to consist of a thermal neutron detector (^{3}He, in this case) surrounded by a foil of thickness t of an efficient absorber such as Cd. The Cd cross section, shown in the panel, is seen to increase dramatically below ~0.4 eV. A shift of the energy sensitivity of the detector is seen as the result of the large Cd absorption at low energies combined with the normal thermal efficiency of the ^{3}He detector.

detector, but now wrapped in a foil of neutron absorbing Cd of thickness t. The low-energy cross section behavior of Cd, $\sigma_{cd}(E)$, is shown in the panel and is seen to rise from a couple of barns to many orders of magnitude more at about 0.4 eV, giving rise to the casual use of 0.4 eV as being the epithermal cut-off energy.

Thermal neutrons will be absorbed in the shield (through the (n, α) reaction), but the α particles, whose range is small (on the order of tenths of mm), will not reach the counter. Neutrons of energy E that attempt to pass through the shield are attenuated exponentially as $e^{-\Sigma_{cd}(E)d}$. The lowest energy neutrons are completely attenuated owing to the large Cd cross section. The higher energy epithermal neutrons which manage to penetrate the shield are detected with somewhat reduced efficiency. The Cd attenuation function is sketched in the graph of Fig. 13.18 and the resultant detector efficiency is shown as the shaded area.

REFERENCES

1. Ellis DV (1987) Nuclear logging techniques. In: Bradley H (ed) Petroleum production handbook. SPE, Dallas, TX

2. Weidner RT, Sells RL (1960) Elementary modern physics. Allyn and Bacon, Boston, MA

3. Glasstone S, Sesonske A (1967) Nuclear reactor engineering. D. Van Nostrand, Princeton, NJ

4. Evans RD (1967) The atomic nucleus. McGraw-Hill, New York

5. Smith RC, Bush CH, Reichardt JW (1988) Small accelerators as neutron generators for the borehole environment. IEEE Trans Nuclear Sci 35(1):859–862

6. Ellis DV, Case CR, Chiaramonte JM (2003) Porosity from neutron logs I: measurement. Petrophysics 44(6):383–395

7. Tittle CW (1961) Theory of neutron logging I. Geophysics 26(1):27–39

8. Kreft A (1972) A generalization of the multigroup approach for calculating the neutron slowing down length. Report No. 32/I, Institute of Nuclear Physics and Techniques, Cracow

9. Kreft A (1974) Calculation of the neutron slowing down length in rocks and soils. Nukleonika 19:145–156

10. McKeon DC, Scott HD (1988) SNUPAR-a nuclear parameter code for nuclear geophysics applications. Nuclear Geophysics 2(4):215–230

11. Feynman RP, Leighton RB, Sands ML (1965) Feynman lectures on physics vol 1. Addison-Wesley, Reading, MA

Problems

13.1 A neutron generator used in logging applications employs the D–T reaction illustrated in Fig. 13.19. The result of the reaction is two particles (a neutron and a ^{4}He) which share 17.6 MeV of energy.



Fig. 13.19 The D–T reaction used for producing 14 MeV neutrons.

13.1.1 Applying conservation of energy and momentum to the reaction products, calculate the neutron energy.

13.1.2 If the reaction products were instead a neutron and a ^{3}He, sharing the same 17.6 MeV, what would the resultant neutron energy be?

13.2 Using the data of Table 23.3 and Fig. 13.16.

13.2.1 Compute the diffusion length in water.

13.2.2 Compute the diffusion length in 0 and 20 p.u. limestone.

13.3 From the data in Table 23.3, estimate the macroscopic thermal absorption cross section of salt water with 100 kppm NaCl. Assume that the oxygen and sodium can be neglected. Express the answer in capture units.

13.3.1 What is the mean free path of a thermal neutron in water? What is the mean free path of a 4 MeV neutron in water?

13.3.2 Analysis of a shale core sample whose density is 2.60 g/cm^3 indicates that the concentration of boron is 400 ppm. What is its contribution, in cu, to the total Σ of the sample?

14

Neutron Porosity Devices

14.1 INTRODUCTION

Historically, the neutron logging tool was the first nuclear device to be used to obtain an estimate of formation porosity. The measurement principle is based on the fact that hydrogen, with its relatively large scattering cross section and small mass, is very efficient in the slowing-down of fast neutrons. A measurement of the spatial distribution of epithermal neutrons resulting from the interaction of high-energy source neutrons with a formation can be related to its hydrogen content. Since hydrogen in the formation is sometimes in the form of hydrocarbons or water and tends to occur in the pore spaces, the correlation with formation porosity is easily made. Development of methods to quantify the extraction of porosity from the neutron measurement began seriously in the 1950s and continues today. Unfortunately, it is only under extremely rare and controlled circumstances that the neutron tool actually measures "porosity." Later sections in this chapter describe what the neutron porosity tool actually responds to and how to better understand its readings (the log) and corrections.

A simple version of the device, illustrated in Fig. 14.1, consists of a source of fast neutrons, such as Pu–Be or Am–Be, with average energy of several MeV; some well-placed radiation shielding; and a detector (or two), sensitive to much lower-energy neutrons, at some distance from the source. Two general categories of neutron porosity tools will be considered in the following discussion. These are distinguished by the energy range of neutrons detected, epithermal or thermal. Because this particular type of tool consists of a neutron source and neutron detectors, we refer to it as a neutron-neutron (n-n) device, as opposed to a nuclear density tool that uses a gamma ray source and gamma ray detectors, a (γ-γ) device, which measures formation density.

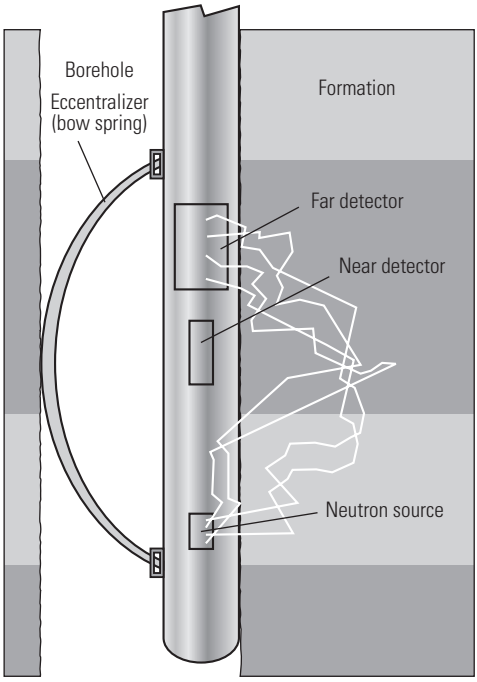


Fig. 14.1 Schematic of a generic neutron logging tool. From Ellis et al. [1]. Used with permission.

(There are other types of "neutron" tools that, for example, detect gamma rays produced when neutrons interact with individual elements in the formation, an (n-γ) device, but that is covered in another chapter.)

Although neutron interactions are complicated, a simple theory useful for predicting the response trends of neutron porosity devices will be reviewed. The results of this theory will be compared to laboratory measurements with logging devices. The general design of neutron porosity logging tools will be shown to be a consequence of severe environmental perturbations to the measurement. One goal of this design is to minimize the influence of the hydrogen-rich borehole on the estimation of formation hydrogen content. To illustrate the response characteristics of neutron tools, a generic device is modeled using Monte Carlo simulation to avoid complications associated with one particular type of commercial device or another.

Several important effects that complicate the porosity interpretation of neutron logs will be considered. They are related to the response of the neutron porosity devices to rock type, shale, and the presence of gas in the invaded zone. For this latter effect, the sensitivity of neutron porosity tools is largely dependent on the depth of investigation of the measurement; gas displaced by mud filtrate beyond this depth of investigation will not be sensed. To give an idea of the limits of gas detection, the experimental determination of the depth of investigation of neutron porosity tools is compared to modeling results for a wireline and an LWD device.

14.2 USE OF NEUTRON POROSITY DEVICES

If neutron logs are plagued by so many peripheral sensitivities and since they rarely measure porosity, then what are neutron porosity logs used for?

In common practice, the neutron log is almost exclusively used, in open-hole conditions, in conjunction with a density log. By comparing the neutron log response to the density log response, using the separation of the curves visually or plotting the two values on a special graph, it is possible to determine the lithology of the formation. This will be seen to arise from the fact that different elements have different effects on neutron transport and absorption.

A second use is for identifying gas-bearing formations from a potentially dramatic graphical crossover of the neutron and density curves. In part this arises because the neutron log, largely related to the formation hydrogen content, senses a lower hydrogen content associated with the gas (compared to water or more dense hydrocarbons) and meanwhile the density log has a reading that is less than expected in a water-saturated formation.

As noted, the density log can be perturbed by the presence of gas, depending on the depth of filtrate invasion. The neutron log can provide a gas-correction to the density log. A better estimate of the total porosity in gas-filled formations is obtained by taking weighted averages of the two readings to match with core data or with logs in adjacent wells, for example.

The neutron/density separation can also be used to assist in clay typing and to provide an additional constraint on an inversion solution based on a number of porosity-sensitive log measurements. The interpretation aspects of neutron logs are discussed in detail in later sections.

14.3 TYPES OF NEUTRON TOOLS

In the nomenclature of nuclear logging there are both thermal and epithermal neutron porosity (n–n) tools. Thermal and epithermal refer to the energy level of neutrons detected in the device.

Thermal neutron devices have a large sensitivity to the presence of thermal absorbers in the formation; some prominent formation absorbers are boron and gadolinium, often associated with shales, and chlorine, contained in nearly all formation brines. Another factor that can affect the count rate of thermal detectors is the formation/borehole environment temperature. As the formation temperature increases, the average neutron energy increases, and because the efficiency of the detector decreases with increasing neutron energy, the count rate diminishes.

Most neutron porosity tools use neutron sources that are a mixture of two elements – one an alpha-emitter and the other a neutron-producing target element such as Beryllium (Be). One common source in use in neutron logging is Americium–Beryllium (commonly referred to as Am–Be.) Environmental concerns along with growing concerns for the use of such sources as “dirty bomb” material in a terrorist action may soon prohibit the use of AmBe and encourage alternates. One example is a

neutron porosity tool that replaces the so-called chemical source with an accelerator-based neutron source and uses epithermal detection. However, in this chapter, only the chemical based neutron porosity tools will be discussed.

Before discussing neutron porosity devices in any detail, we begin with a short introduction to the basic equation of neutron transport pertinent to logging applications. The solution of this equation in an idealized geometry involves the slowing-down length, L_s and the thermal neutron capture cross section Σ, introduced in the last chapter. Practical solutions involve the use of Monte Carlo simulation, also briefly described.

14.4 BASIS OF MEASUREMENT

How can the detection rate of neutrons in the device illustrated in Fig. 14.1 be related to the properties of the formation? Formally this is a problem of neutron transport: neutrons are emitted at one point and transported, through a material, to another point (where they are detected, in our case). The properties of the material affect the transport process. They influence the spatial and energy distribution of the neutron population and, consequently, the counting rate at any detector location.

A formal description of the transport of neutrons is given by the Boltzmann transport equation (BTE). In its time-independent form, appropriate for neutron porosity logging, it may be written as [2–4]:

$$\overline{\Omega} \cdot \overline{\nabla \Phi} + \Sigma_t \overline{\Phi} = \int dE' \int d\overline{\Omega}' \; \Sigma_s(E' \rightarrow E, \Omega' \rightarrow \Omega)\overline{\Phi} + S. \tag{14.1}$$

This formidable-looking equation is nothing more than an expression of the conservation of the total number of neutrons in an elemental cylindrical volume, shown in Fig. 14.2. *It is written in terms of the angular flux $\overline{\Phi}$, a vector quantity which specifies the number of neutrons crossing a unit surface area per unit time, in a given direction ($\overline{\Omega}$) and energy interval at any point in space. The BTE relates the loss rate of neutrons in the volume by absorption and scattering to the rate of increase of neutrons through source production and scattering from other regions of space and from neutrons of higher energies (which may even be contained within the volume considered). The first term, $\overline{\Omega} \cdot \overline{\nabla \Phi}$, represents the net leakage rate of neutrons out of the volume in the direction $\overline{\Omega}$ due to streaming of the neutrons into and out of the volume. The loss rate of neutrons from the volume, energy region, and direction of interest is given by the reaction rate $\Sigma_t \overline{\Phi}$, where Σ_t represents the total interaction cross section.*

The two preceding loss rate terms are balanced by the rate at which neutrons from within the volume scatter into the energy and direction of interest, and by any sources (S) contained within the region. The scattering term is written as:

$$\int dE' \int d\overline{\Omega}' \; \Sigma_s(E' \rightarrow E, \overline{\Omega}' \rightarrow \overline{\Omega})\overline{\Phi}, \tag{14.2}$$

where the integration is performed over neutrons of energy E' (greater than E), and over all other directions, $\overline{\Omega}'$. The scattering cross section $\Sigma_s(E' \rightarrow E, \overline{\Omega}' \rightarrow \overline{\Omega})$

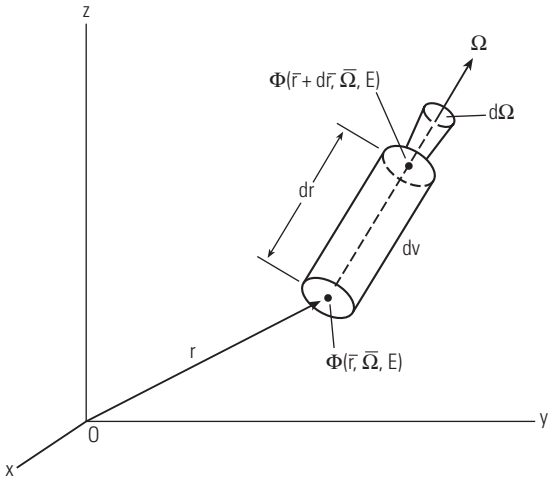


Fig. 14.2 The geometry for deriving the neutron flux balance in a typical cell of material leading to the Boltzmann transport equation.

must take into account the angular dependence of scattering as well as the fact that there may be a limited energy range (E') over which neutrons can scatter to the specified energy E.

As it stands, the BTE is difficult if not impossible to solve analytically. However, a number of numerical approaches have been developed. The discrete ordinates method reduces the BTE to a set (usually large) of coupled equations by allowing the variables in the equation to take on only a limited set of discrete values. Cross sections corresponding to discretized energies and angles must be computed from continuous data (when it exists) for the sampling intervals chosen. The Monte Carlo method, in its simplest form, performs a numerical simulation of the neutron transport by using cross-section data to compute probabilities of interactions, path lengths between interactions, and angles of scattering. Appropriately transformed random numbers, in conjunction with the calculated probabilities, are used to trace the events in a neutron's life from birth to capture. By sampling large numbers of these "typical" histories, we can predict the behavior of a specified system containing neutron sources. For any serious computation of tool response, the Monte Carlo method is used. However, a look at analytical solutions for simple cases gives some idea of the important parameters to use to characterize tool response.

Analytical solutions of the BTE all depend in one way or another on reducing the complexity of the problem by integrating or averaging over one or more of the variables. One of the more useful approaches is the diffusion approximation. The basic simplification employed is that the angular flux is only weakly dependent on direction. A further simplification which considers only a single-energy group of neutrons allows the BTE to be written in terms of the scalar flux, $\Phi(r)$, which has only a spatial variable. *Consideration of the weak angular dependence or direct*

application of Fick's law (the current of neutrons is proportional to the gradient of the flux) allows the net leakage portion of the BTE to be expressed as a term containing a diffusion coefficient. In this case the BTE reduces to [2–4]:

$$D\nabla^2\Phi(r) - \Sigma_a\Phi(r) + S = 0, \tag{14.3}$$

where the diffusion coefficient D is given by:

$$D = \frac{1}{3(\Sigma_t - \overline{\mu}\Sigma_s)}. \tag{14.4}$$

It depends on the difference in the total cross section (Σ_t) and the scattering cross section (Σ_s) times the average cosine ($\overline{\mu}$) of the scattering angle. The absorption cross section Σ_a in Eq. 14.3 is related to the previous cross sections by:

$$\Sigma_t = \Sigma_a + \Sigma_s. \tag{14.5}$$

A slight refinement of the preceding approach, which reduces the nine decades or so of neutron energy variation into a single average quantity, is to admit two broad energy regions of interest: epithermal and thermal. In this case, two coupled diffusion equations can be written, one for each of the energy bands [2–4]:

$$D_1\nabla^2\Phi_1 - \Sigma_{r1}\Phi_1 + Q = 0 \tag{14.6}$$

and

$$D_2\nabla^2\Phi_2 - \Sigma_{r2}\Phi_2 + \Sigma_{r1}\Phi_1 = 0. \tag{14.7}$$

The first of these is for the broad epithermal (subscript 1) energy region, which contains the source of strength Q, and the second is for the thermal (subscript 2) region, in which scattering from the epithermal region ($\Sigma_{r1}\Phi_1$) plays the role of the source. The cross section Σ_{r1} is called the removal cross section. It accounts for the portion of scattering which may reduce the neutron energy sufficiently for it to be counted in the lower-energy group. The cross section Σ_{r2} is the familiar thermal absorption cross section.

In simple geometries, these coupled equations can be solved for the spatial distribution of the flux. For the case of a point source in an infinite medium, the epithermal flux is given by:

$$\Phi_1(r) = \frac{Q}{4\pi D_1}\frac{e^{-r/L_1}}{r}, \tag{14.8}$$

where L_1, also known as the slowing-down length (L_s), is given by $\sqrt{D_1/\Sigma_{r1}}$, where D_1 is the diffusion coefficient associated with the high-energy neutrons. Chapter 13 provides a less formal definition of this same quantity.

The thermal flux is given by the slightly more complicated expression:

$$\Phi_2(r) = \frac{QL_2^2}{4\pi D_2(L_1^2 - L_2^2)} \times \left(\frac{e^{-\frac{r}{L_1}}}{r} - \frac{e^{-\frac{r}{L_2}}}{r}\right). \tag{14.9}$$

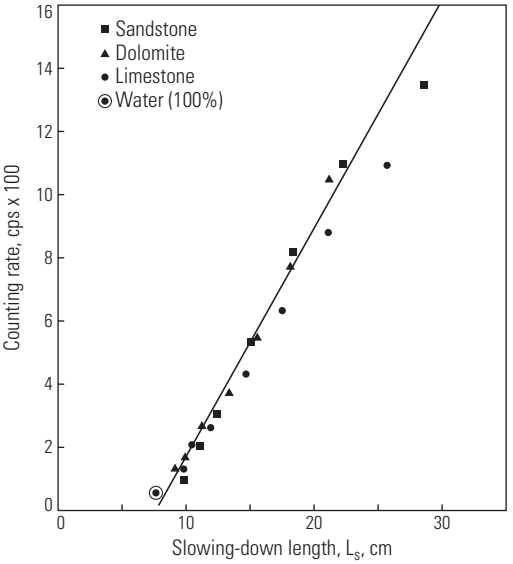


Fig. 14.3 The counting rate of a single-detector epithermal device as a function of slowing-down length of calibration formations. Adapted from Edmundson and Raymer [5].

In this expression $L_2 = \sqrt{D_2/\Sigma_{r2}}$, where D_2 is the thermal diffusion coefficient. L_2 is also known as the thermal diffusion length and is usually written as L_d.

In order to anticipate the response of an epithermal neutron porosity device we can use the result of Eq. 14.8. It shows that the flux of epithermal neutrons, in an infinite homogeneous medium containing a point source of fast neutrons, falls off exponentially with distance from the source r, with a characteristic length L_s, determined by the constituents of the medium. The implication for a borehole device such as that shown in Fig. 14.1 is that the epithermal neutron counting rates should vary nearly exponentially with the slowing-down length of the formation. An indication of this type of behavior can be seen in Fig. 14.3 which shows the counting rate of one of the early epithermal neutron devices as a function of slowing-down length in three types of formations. In Fig. 14.4 the same data is shown as a function of porosity. The separation of response trends according to formation lithology, seen in Fig. 14.4, is referred to as the matrix or lithology effect, discussed later in Section 14.9.1. The matrix effect is much reduced in the first presentation but not entirely eliminated. However, slowing-down length is the more representative parameter for describing counting rate variations, as expected from Eq. 14.8.

Figure 14.3 also shows how the counting rate of this particular instrument in any other material can be estimated, once its slowing-down length has been calculated. Conversely, the slowing-down length of the formation can be determined from a measurement of the epithermal flux. Since the slowing-down length of a formation is strongly dependent on the amount of hydrogen present, the porosity can be determined

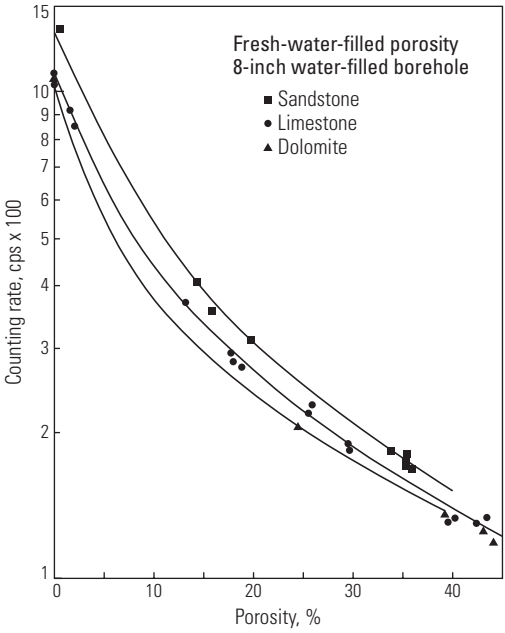


Fig. 14.4 The same data as Fig. 14.3, but plotted as a function of porosity in formations of sandstone, limestone, and dolomite. Adapted from Edmundson and Raymer [5].

using the data of Fig. 13.10. Referring back to this figure, we see that if the rock matrix type is known, the formation porosity can be determined from the formation slowing-down length.

14.5 HISTORICAL MEASUREMENT TECHNIQUE

One of the first quantitative neutron porosity devices employed a single epithermal detector in a skid applied mechanically against the borehole wall [6]. This sidewall epithermal neutron device had the advantage of reducing borehole size effects, but it could be disturbed by the presence of mudcake between the pad surface and the borehole wall.

To first order, compensation for these two environmental effects was achieved by the addition of a second detector. The compensated device (see Fig. 14.1) uses a pair of thermal neutron detectors, which increases the counting rate and therefore decreases the statistical uncertainty of the derived porosity values at large formation porosity. The detector closest to the source is used to provide compensation for borehole effects on the farthest detector by a simple division of counting rates. Although thermal neutron detection is used, it can be seen from an examination of Eq. 14.9 that if the source-detector spacings are chosen to be large enough, the second exponential

term can be neglected (since the diffusion length is generally much smaller than the slowing-down length), so the ratio of the two counting rates should vary exponentially as the inverse of the slowing-down length, just as in the case of the single epithermal detector.

In order to characterize the laboratory data of the thermal neutron tool, which are at some variance with the predictions of Eq. 14.9, use is made of another characteristic length, L_m. It is called the migration length and corresponds to the quadratic sum of the slowing-down length and the diffusion length:

$$L_m{}^2 \equiv L_s{}^2 + L_d{}^2. \tag{14.10}$$

Use of the migration length (rather than L_s) accounts explicitly for the additional perturbation due to absorption in the formation on the measurement of porosity by the thermal neutron tool. The thermal absorption of the formation is characterized by the macroscopic thermal absorption cross section, or Σ_a. Logging devices for the measurement of this important parameter are discussed in the next chapter.

The migration length, as defined above, provided a convenient way to characterize the response of one thermal neutron device. Figure 14.5 shows, in the upper panel, the

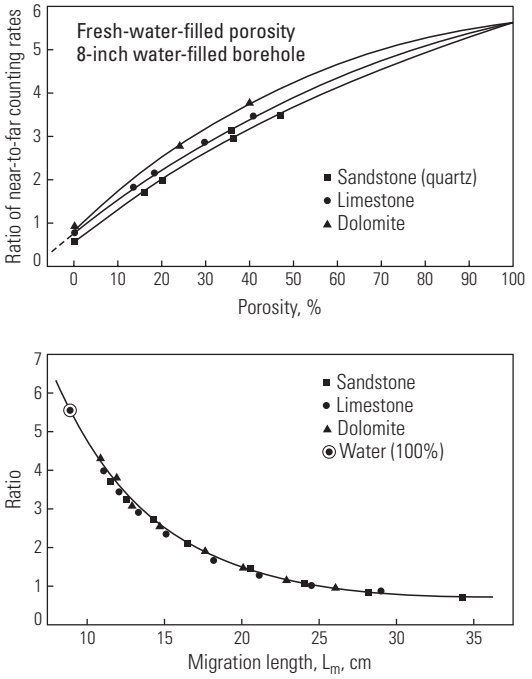


Fig. 14.5 The measured response of a thermal neutron porosity device in formations of three different lithologies. In the upper figure, the data are plotted as a function of porosity. In the lower, they are plotted as a function of the appropriate migration length for the formation conditions used. Adapted from Edmundson and Raymer [5].

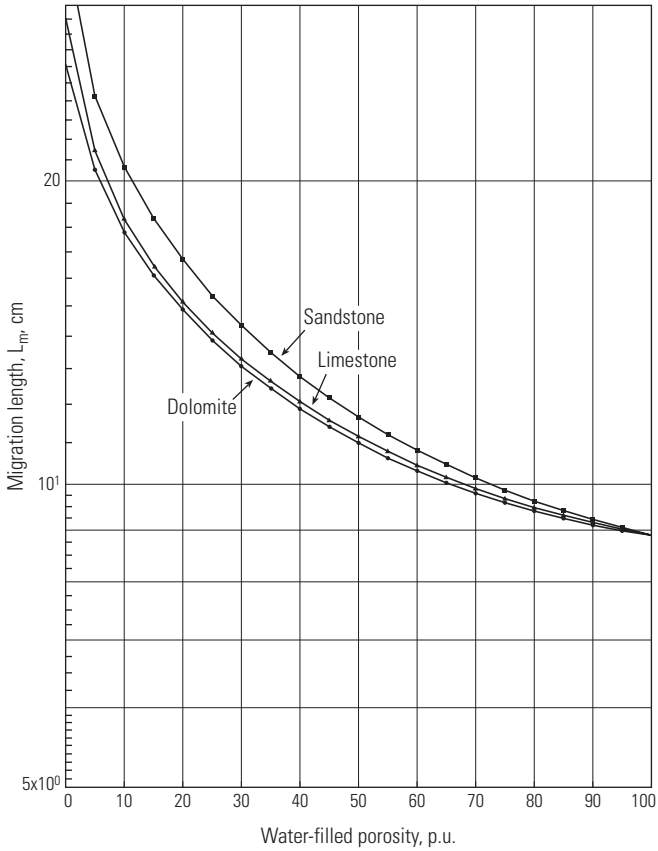


Fig. 14.6 The calculated migration length as a function of formation porosity for the three principal lithologies. Adapted from Ellis [7].

ratio of the near to far counting rate of such a device, for three types of lithologies, as a function of porosity. Notice the three trend lines, corresponding to the three lithologies present among the calibration formations. If the porosity values corresponding to the measurement points of this plot are converted through the use of Fig. 14.6, which shows the migration length L_m as a function of porosity, then the counting rates for the three lithologies are found to lie on a single line, as seen in the lower part of Fig. 14.5. This demonstrates that the response characteristics of the thermal neutron porosity tools can be described, for this limited set of data, by a function of the slowing-down length and diffusion length, rather than by porosity. For data ranging over a larger variation of Σ, induced by formation and borehole salinity, modification to the migration length [8] is necessary to provide a good estimator.

From the preceding discussion, conversion from the measured ratio, or migration length, to formation porosity would seem to be straightforward. Because of the dependence on the diffusion length, thermal absorbers in the formation and borehole

can cause some deviation from the response derived from the limited set of calibration data shown in Fig. 14.5. In practice, it is found that some additional corrections have to be made to the inferred porosity if the thermal capture properties of the borehole and formation are significantly different from one another. These are generally provided by the service companies in the forms of charts or nomographs [9–11], or as a part of computerized interpretation.

Although the API committee that set up the GR calibration standards also took some steps to standardize neutron log responses*, their recommendations for API units have not been implemented [12]. The conventional approach has been to calibrate the tool in limestone formations and to report all tool readings in apparent "limestone porosity." Conversion charts are then necessary to correct the apparent limestone porosity for the matrix in which the measurement was actually made. Based on the preceding discussion, some consideration should be given to using the slowing-down length and migration length as the quantities for reporting the log measurements. The conversion to porosity by use of charts similar to Fig. 14.6 would then lie entirely in the realm of interpretation.

14.6 A GENERIC THERMAL NEUTRON TOOL

Monte Carlo modeling is useful for interpolating between limited data points, for determining correction charts, and for understanding the detailed response of a neutron porosity instrument. Since neutron porosity logging has been practiced commercially for nearly 60 years, a plethora of tools has evolved [13–17]. Rather than examine details of a tool of a particular service company, a generic thermal neutron tool that is similar to a number of commercial tools on the market was constructed mathematically [1, 18]. A few results from this model are discussed below to illustrate the magnitude of the borehole size effect, a better delineation of the lithology effect, and how the slowing-down length as well as the migration length can be used for the basic characterization.

The computed ratio of near to far counting rates for the generic thermal tool was determined in an 8 in. water-filled borehole in limestone formations over the entire range of porosity. The computed ratio is shown in Fig. 14.7 as a function of the inverse slowing-down length and the inverse migration length of each of the limestone formations. The statistical nature of the Monte Carlo calculations is evident in the scatter, but it is clear that the ratio predicts either the migration length or the slowing-down length of the formation in this lithology and fluid type.

To get an idea of the effect of the borehole size, an idealized ratio response was calculated for a point source in an infinite medium of water-filled porous limestone.

*At the time of the introduction of neutron porosity logging, the usual scale was neutron counting rate. This, of course, could vary significantly not only with porosity, but also from service company to service company, depending upon the source-to-detector spacings (usually marked on the log heading), the neutron source activity, and types of detection. Interpretation of porosity required comparison with core or cutting analysis, and makes today's interpretation problems look minimal.

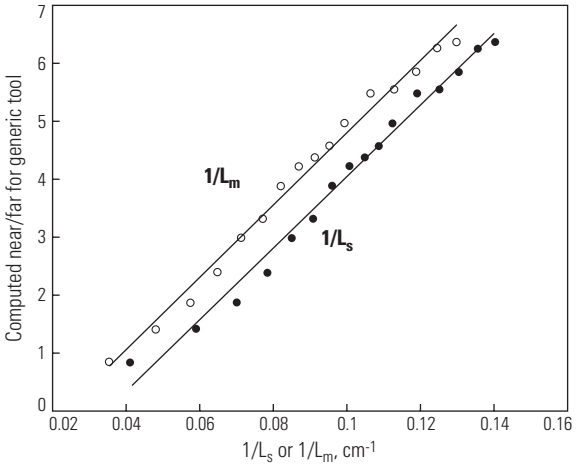


Fig. 14.7 The near/far ratio of the generic thermal tool for a range of formation porosities, plotted as a function of the formation L_s and L_m values. From Ellis et al. [1]. Used with permission.

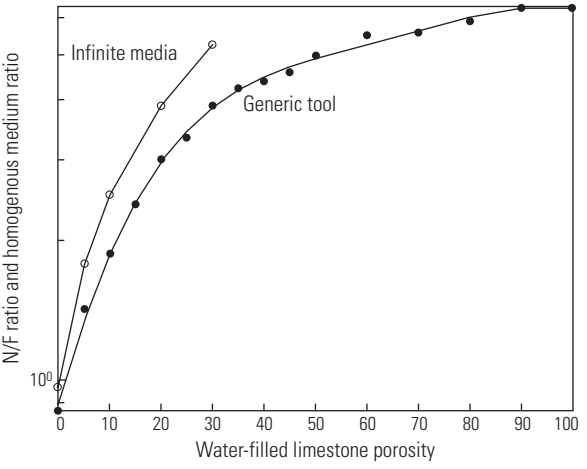


Fig. 14.8 Comparison of the near/far ratio for the generic thermal tool in an 8 in. water-filled borehole with the results for an infinite homogeneous formation. The water-filled porosity sensitivity of the tool is less than the idealized calculations suggest. From Ellis et al. [1]. Used with permission.

In Fig. 14.8 the results of the idealized ratio computation (in infinite media) are compared to the values obtained for the generic thermal tool. Both sets of these ratios are plotted as a function of the water-filled porosity. It is clear that the ratio in the idealized situation has a much greater dynamic range. The discrepancy between the

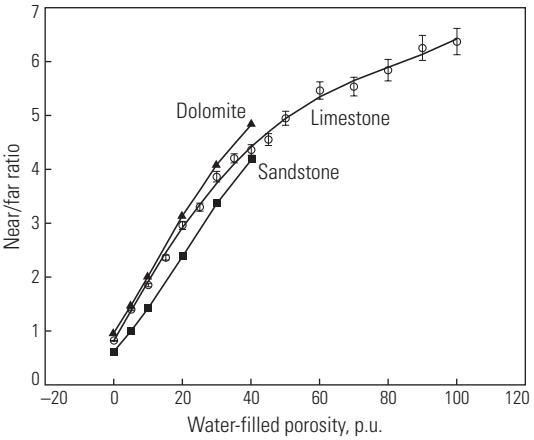


Fig. 14.9 The matrix effect for the generic thermal tool. The calculated ratios versus porosity are shown for three water-saturated lithologies. From Ellis et al. [1]. Used with permission.

two ratio behaviors can be ascribed to the presence of the instrument and the high-hydrogen content in the borehole. The dynamic range of the ratio versus porosity curve would be seen to diminish with increasing borehole size. In fact, the size of the borehole will be a very important parameter to know for the correction of the neutron measurement back to standard 8 in. conditions.

The lower curve in Fig. 14.8 is the so-called limestone transform for the generic tool. The polynomial fit through the computed values of ratio versus water-filled porosity for the generic model constitutes a transform for converting any measured ratio from this device into an equivalent "limestone porosity."

Calibration curves can be constructed in a similar manner for water-filled sandstone and dolomite formations. The data generated from the Monte Carlo model are shown in Fig. 14.9. Three separate trend lines are apparent. It is clear from this figure that the ratio in 20 p.u. sandstone lies below the limestone line and thus will have an "apparent limestone porosity" a few p.u. less than the true porosity. The opposite is true for dolomite.

As mentioned in the previous section, it has been traditional to describe the performance of the thermal tool in terms of the migration length, L_m. However, it is also possible to use the slowing-down length as we have seen from Fig. 14.7. If the ratio data from Fig.14.9 are replotted as a function of their corresponding computed L_s values, the curve in Fig. 14.10 is obtained. The water-filled limestone points are indicated by circles (with error bars), the sandstone points from 0 to 40 p.u. by squares, and the dolomite points by diamonds. All three lithologies lie along basically the same response line, allowing us to conclude that the major portion of the response is dominated by the formation slowing-down length.

We conclude that L_s can be used to predict the ratio in water-filled formations. We accept for the moment that the introduction of salt-water or other thermal neutron

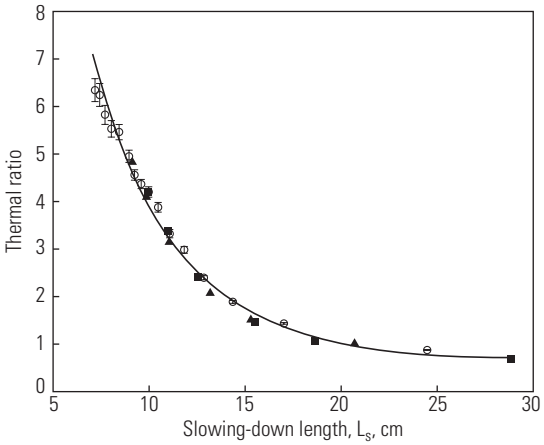


Fig. 14.10 The response of the generic tool for three lithologies, plotted as a function of the slowing-down length of each porous formation. The symbols have the same association with lithology as in Fig. 14.9. From Ellis et al. [1]. Used with permission.

absorbers will make a perturbation that might be better described by L_m, but we continue with this simplified explanation, because even L_m has to be modified to make it a better predictor [8].

14.7 TYPICAL LOG PRESENTATION

Figure 14.11 displays the "standard presentation." Perhaps it should be called a traditional presentation: with the computing and graphics capabilities within reach of most logging engineers and petrophysicists, there may no longer be a "standard." Why is the porosity curve, NPHI, labeled "sand" and why does the scale for NPHI seem to be presented backwards?

In Fig. 14.11, the neutron and density traces are found in track 3 in a compatible scale overlay. The particular scheme shown assumes that the lithology is expected to be predominantly sandstone. The idea behind the overlay is to adjust the gain and offset of the two traces so that they agree, or overlay, when the formation is water-filled sandstone. For this reason, the neutron curve is denoted "sand." It will be seen that there are two other common lithology outputs, "lime" and "dolomite". Presumably, when the tool measurement is presented in the selected units, the readings will agree with the porosity of the water-filled rock of the type selected.

Returning to the gain and offset, it has been traditional to present a dynamic range of 1 g/cm^3 on the density trace across the full track (or sometimes two tracks). It is easy to show that a change in bulk density of 1 g/cm^3 in a water-filled formation corresponds to a porosity change of about 60 units (p.u.). Consequently, the neutron trace is usually shown with a dynamic range of 60 p.u. across the density track.

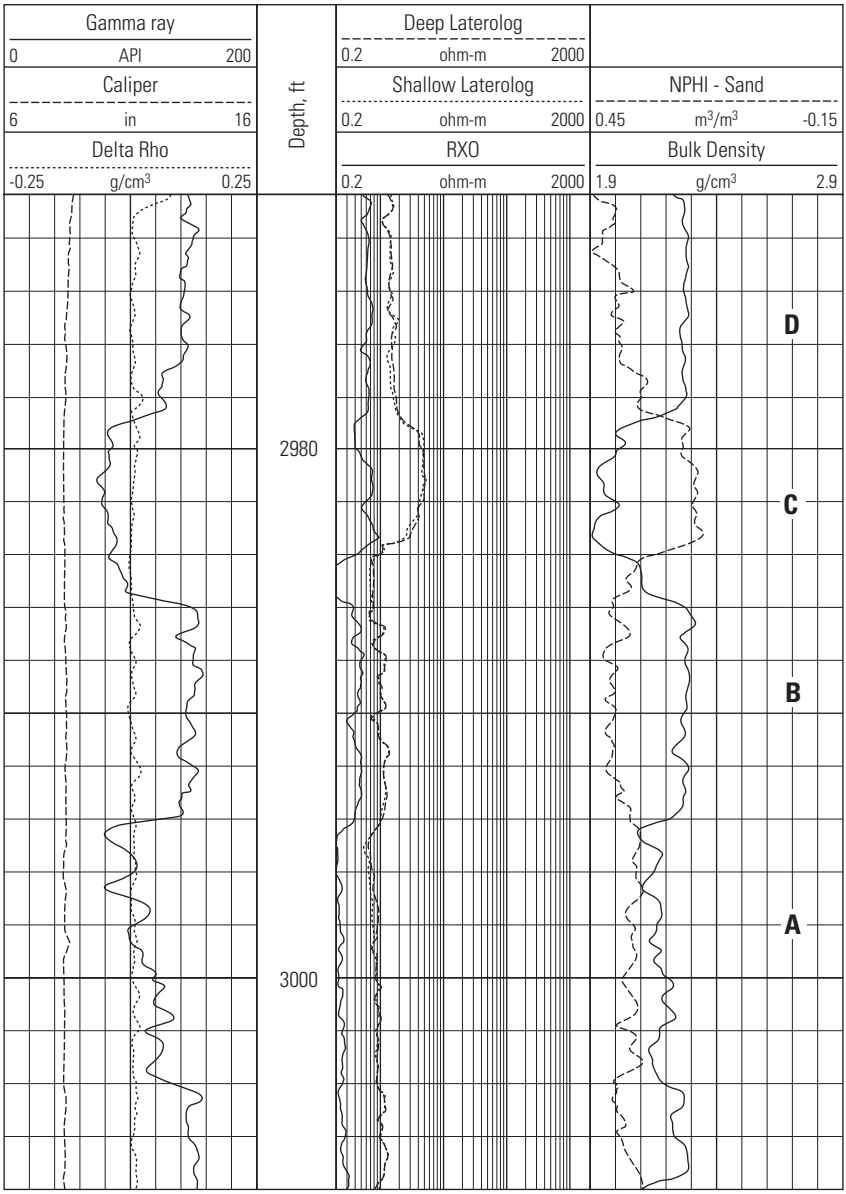


Fig. 14.11 A "typical" neutron-density presentation is shown in track 3. The neutron porosity, indicated to be in "sand" units, is scaled from 0.45 to −0.15 v/v, increasing to the left. The density scale is from 1.9 to 2.9 g/cm^3, increasing to the right. From Ellis et al. [1]. Used with permission.

The offset simply shifts the zero point on the neutron track to the density of the matrix; in this case of quartz sandstone, 2.65 g/cm^3. The density is also shifted so that the scale runs from 1.9 to 2.9 g/cm^3. In this scheme, the 0 p.u. point is two and a half divisions from the right hand of the track. The consequence of accommodating the 60 p.u. swing of the neutron makes it range from −15 p.u. on the right edge to 45 p.u on the left hand of the track.

The limestone compatible scale (which may be a standard, or may depend on locale) will be seen in another example. For that case, the density scale generally runs from 1.95 to 2.95 g/cm^3. The matrix density of limestone is 2.71 g/cm^3 so the neutron scale (but it is in limestone units – more about that later) remains at 45 to −15 p.u. for an approximate match at 0 p.u. Another scale, common in the Gulf of Mexico, where the apparent neutron porosity generally is high, has the neutron running from 60 to 0 p.u. and the density from 1.65 to 2.65 g/cm^3.

14.8 ENVIRONMENTAL EFFECTS

We have seen from laboratory measurements and Monte Carlo simulations that the generic thermal neutron porosity tool (in an 8 in. water-filled borehole) responds to the presence of hydrogen in the formation, and that a useful parameter to predict the neutron tool response is the slowing-down length (L_s) of the formation. However, there are effects that alter the value of the measured ratio other than formation porosity. One of the most obvious is the size of the borehole. The more hydrogen there is in the vicinity of the source and detectors, the less sensitive the tool is to hydrogen changes in the formation. So the first correction that must be made is for the borehole size – a correction that is routinely applied to neutron logs from knowledge of the tool characteristics and the simultaneous measurement of the borehole size from the caliper.

In Table 14.1 is a list of many of the factors that affect the apparent porosity reading of a thermal (or epithermal to some extent) neutron logging tool. In general they all concern the local hydrogen density. The parameters with the largest effect are the borehole size and standoff, whether in borehole mud or resulting from mudcake. The magnitude of the effects of the borehole size and standoff are of course related to the properties of the borehole fluid. Both temperature and pressure will also affect the density and therefore the hydrogen density in the formation and borehole.

Another fairly important factor for the thermal tool response is the salinity of the formation water and borehole fluid. Water salinity has two competing effects that can alter the thermal neutron flux in the vicinity of the detectors. First, the addition of salt to the water displaces hydrogen by dissolution, reducing the hydrogen index (HI). (A convenient empirical relation, $\mathrm{HI} = 1 - 2.93 \times 10^{-3} S - 5.34 \times 10^{-5} S^2$, relates the HI to the salinity, S, expressed in weight percent.) At the maximum concentration of NaCl (26% by weight) the HI is reduced to about 0.89 [19]. This effect by itself would tend to decrease the apparent porosity because of the decrease in hydrogen. On the other hand, the addition of NaCl increases the thermal neutron absorption cross section and depresses the thermal flux as approximately $1/\Sigma_a$. However, the

Table 14.1 Some of the formation and borehole properties that affect the reading of a thermal neutron porosity device.

Formation	Borehole
Matrix type	Borehole fluid
Porosity	Mud solids
Pore fluid type	Fluid type
Hydrogen index (H.I.)	Salinity
Density	Temperature
Salinity	Pressure
Temperature	Mudcake H.I.
Pressure	Geometry
	Diameter
	Ovality
	Tool standoff

magnitude of the effect varies as a function of distance from the detector, and the overall observed effect is an increase in the ratio so that it tends to cancel the lack of hydrogen. However such cancellation is not perfect, and therefore correction charts must be established for each particular tool geometry.

The temperature is of particular interest for the thermal tool because the ^{3}He thermal detector is most efficient at low neutron energy. If the ambient temperature is much higher than room temperature, for example, the detection efficiency of these "hotter" thermalized neutrons will be reduced compared to the case when they are lower in energy.

14.8.1 Introduction to Correction Charts

The original name for correction charts was "departure" curves. This makes it clearer that the neutron tool is calibrated in a standard condition, usually an 8 in. water-filled borehole in fresh-water-filled limestone formations at room temperature. Any change from this standard condition will cause a tool reading that represents a "departure" from the normal calibration curve that does not relate to "porosity." Consequently, for conventional neutron logging devices, measurements were made, and later supplemented by Monte Carlo calculations, to predict the apparent porosity seen by the tool in any number of situations that departed from the standard conditions. Initially these were incorporated into nomograms, examples of which are presented below in Fig. 14.12. Recently these correction charts reside in software that can be applied at the discretion of the client or user.

An inspection of Fig. 14.12, the set of correction charts for one particular thermal neutron porosity device, will reveal a correlation with Table 14.1. Each panel of the correction chart on the left deals with a property of the borehole or formation that

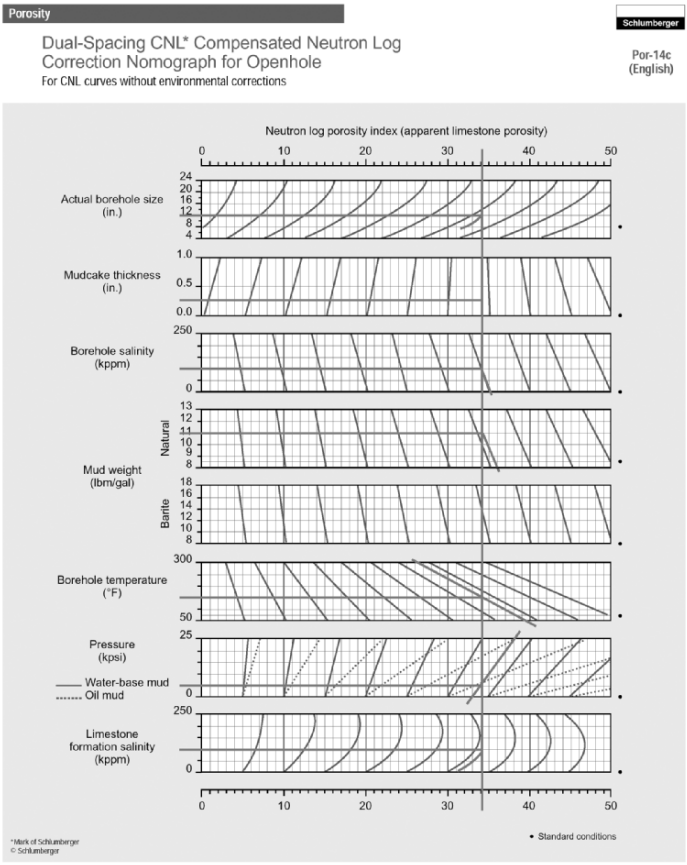


Fig. 14.12 The correction charts for one particular thermal neutron porosity device from Schlumberger [10]. Courtesy of Schlumberger. (*Continued on next page*)

can affect the apparent porosity read by the device. The entire right side of Fig. 14.12 is devoted to the standoff correction that is seen, additionally, to be a function of the borehole size.

Generally, field logs are corrected only for the borehole size, either using the caliper reading or using the constant value of the bit size. The multitude of other corrections is often left to the discretion of the user. However, there is one that should not be overlooked when logging hot wells – the temperature effect. Simply stated, the apparent thermal neutron porosity decreases as the formation and borehole temperature increase. Although the effect of temperature is smaller at low porosities, the magnitude of the effect in the mid-porosity range of ≈30 p.u. can be estimated from Fig. 14.12 – roughly 2.4 p.u./50°F.

In addition to borehole size and temperature one very important effect is that of standoff – arising from poor contact between the tool and the borehole wall.

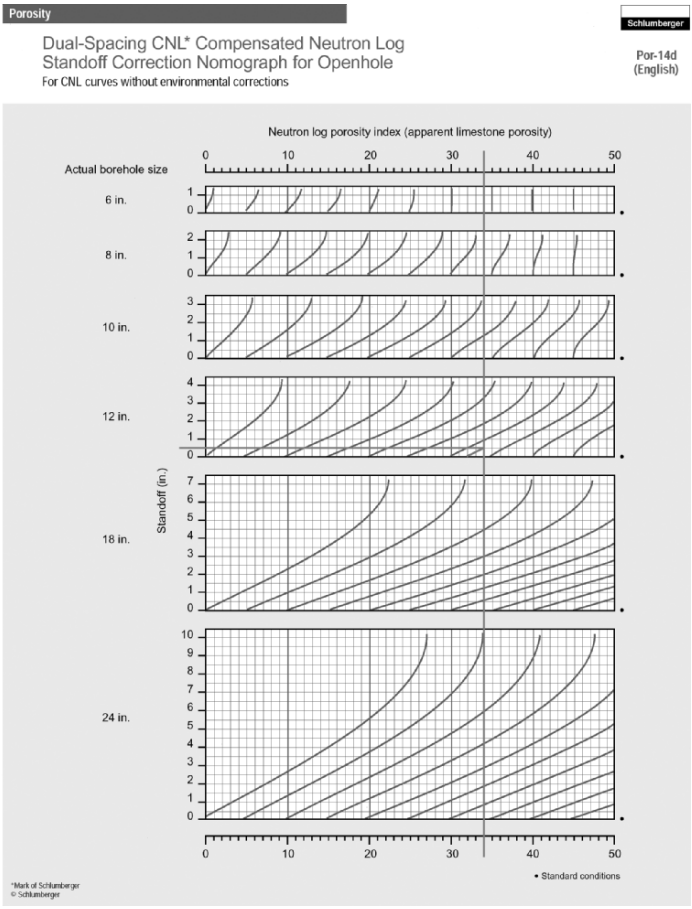


Fig. 14.12 *Continued.*

A glance at the correction chart of Fig. 14.12 will give an appreciation of the magnitude of the standoff effect. The fact that standoff is such an important perturbation to the measurement is not surprising since the borehole fluid in which the tool makes its measurements is generally very hydrogen-rich compared to the formation being analyzed. For a conventional thermal tool, the amount of standoff, perhaps caused by the combination of hole irregularity and a long tool string, is not known. It is usually assumed to be some small, constant value. Sometimes the standoff is used to shift the log reading to the desired value. However, there is no reason to assume that standoff would be a constant value. In the next chapter (see Section 15.4) we will discuss a relatively new type of neutron tool [20] that uses a pulsed 14 MeV neutron source. One of its auxiliary measurements is the tool standoff, used to monitor and correct for this potentially large environmental perturbation.

14.9 MAJOR PERTURBATIONS OF NEUTRON POROSITY

There are three formation properties that can significantly perturb the neutron porosity reading: the lithology or mineral composition of the rock fabric, the presence of shale minerals in the matrix, and the presence of gas or low-density hydrocarbons in the pore space.

14.9.1 Lithology Effect

The so-called lithology effect refers to the fact that the neutron tool, if calibrated in water-filled limestone tanks, will produce an output in limestone units that is numerically equal to the water-filled porosity, but for no other rock type. Using this calibration in a sandstone formation of the same water-filled porosity, the tool would read somewhat lower than the true porosity. For the case of a dolomitic formation the limestone-calibrated tool would read a slightly larger porosity. Thus the neutron log, which is traditionally labeled in "limestone" units, will tend to read correctly only in fresh water-filled limestone. If labeled in "sandstone" units it will read correctly only in sandstone formations.

The effect of using an inappropriate lithology transform is illustrated in the simulated logs shown in Fig. 14.13. Both the density and neutron logs are presented in limestone porosity units. (This means that for the density, the grain density was assumed to be 2.71 g/cm^3 with fresh water in the pores.) In zone 5 of Fig. 14.13, the two curves overlay in 20 p.u. water-filled limestone as they should. Just below, in zone 4, a 20 p.u. water-filled dolomite, the density reads a lower apparent porosity because the dolomite grain density (2.87 g/cm^3) is greater than that of limestone and so the curve moves to the right. The neutron porosity, on the other hand, overestimates the porosity by about 2.3 p.u. in zone 4. In zone 3, a 20 p.u. water-filled sandstone, the density reads a slightly higher apparent porosity since the sandstone grain density (2.65 g/cm^3) is lower than that of limestone. In this case, the neutron porosity underestimates the true porosity by about 4.5 p.u. when the limestone transform is used.

To give a better understanding of the process that produces curves on logs labeled "limestone", "sandstone" or "dolomite" porosity, consider Fig. 14.14. The tool is in standard conditions of 8 in. borehole, with no standoff, and normal conditions of temperature and pressure. The upper panel is a representation of the universal 8 in. water-filled borehole calibration curve that allows the conversion of the measured ratio into a slowing-down length. (Although the data shown is a particular tool model, it could just as well be replaced by the calculated response of the generic tool discussed in the preceding reference). A particular value of ratio is measured by the tool, in this case 4.4. From the curve, this ratio corresponds to an L_s of about 11 cm.

The lower panel in Fig. 14.14 is a representation of the variation of slowing-down length as a function of water-filled porosity for sandstone, limestone, and dolomite. The inferred slowing-down length of the formation is converted to a "porosity" value using the lower panel, depending on the choice of assumed lithology. Of course, an

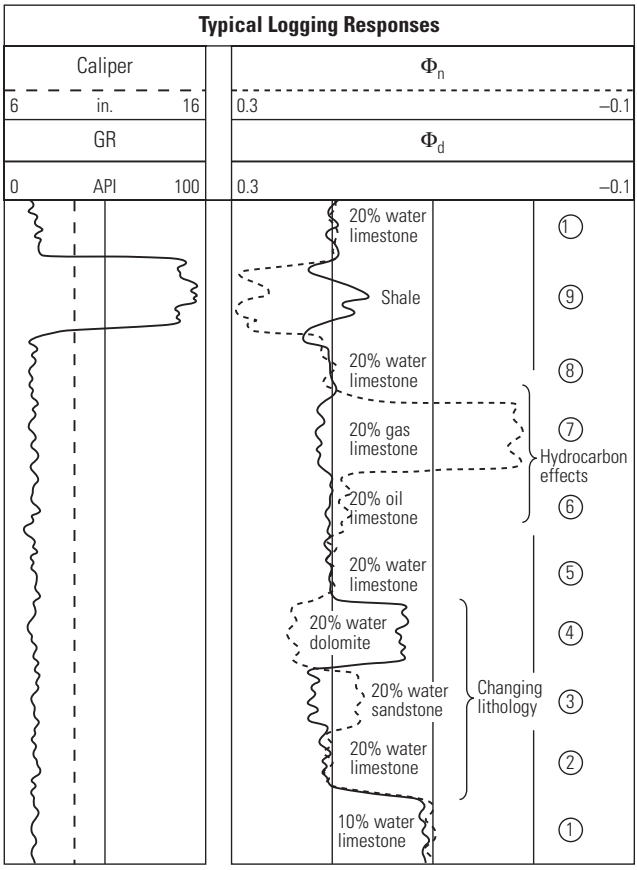


Fig. 14.13 Hypothetical neutron and density log responses in 20 p.u. formations of various lithologies, fluid content and borehole conditions. From Ellis et al. [1]. Used with permission.

infinite number of slowing-down length versus water-filled porosity curves could be drawn using a code such as SNUPAR [21] which can compute slowing-down length based upon the details of the formation composition. In this case, the three classical formations are represented. The upper curve represents the variation of L_s with porosity in sandstone, the middle curve for limestone, and the lower curve corresponds to dolomite.

The value for "limestone" porosity is deduced from the middle curve as indicated in the lower panel at about 25 p.u. The "sandstone" porosity value would be obtained by using the upper curve. Following the L_s value, corresponding to the ratio, over to the upper curve will result in an intercept at a somewhat larger porosity value. This is the lithology or matrix effect and its practical consequence is to underestimate the porosity of a clean, water-filled sandstone formation if the ratio is converted into limestone units.

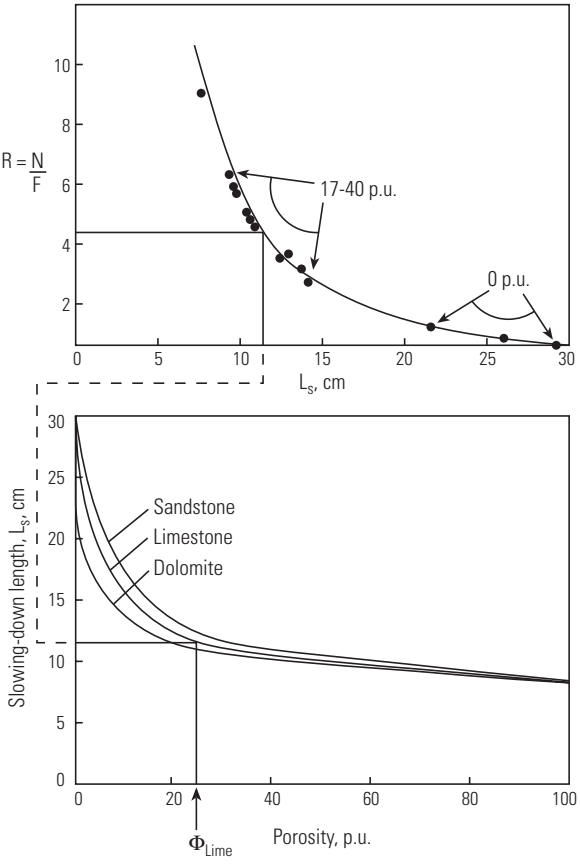


Fig. 14.14 An illustration of the conversion of the measured ratio, via slowing-down length, to an apparent porosity in "limestone" units. Adapted from Ellis [22].

In a similar manner, the value for "dolomite" porosity is obtained by finding the intercept of the corresponding L_s value on the lower of the three curves. It is seen that this ratio will produce a lower apparent porosity. When considering the case of fixed formation porosity, the slowing-down length in dolomite is less than the corresponding limestone formation so that the apparent limestone porosity exceeds the expected value. Conceptually, this is how the three curves of apparent porosities are produced.

14.9.2 Shale Effect

One of the characteristics of neutron porosity logs is that it indicates rather large values of apparent porosity in shale zones (and elevated values in porous shale-bearing zones). A common misconception is that the error in the thermal porosity readings in

shales is caused by associated trace elements with large thermal capture cross sections. However, even without the additional effect of thermal absorbers, clays and shales present a problem for all neutron porosity interpretation because of the hydroxyls associated with the clay mineral structure [22]. The large apparent porosity values are due primarily to the hydrogen concentration associated with the shale matrix.

A cartoon example of the shale effect is shown in zone 9 of Fig. 14.13. More realistic examples can be seen in zones "B" and "D" of Fig. 14.11. In both of these cases the apparent neutron porosity on a "sandstone" matrix exceeds the density porosity (using 2.65 as the grain density, i.e., sandstone) in the two zones where the increased gamma ray reading would normally indicate the presence of shale. Further elaboration of this effect can be found in Section 21.3.2.

14.9.3 Gas Effect

Neutron porosity devices are calibrated in formations containing liquid-filled porosity. In a gas-filled formation, with lower-than-expected hydrogen density, an error will result in the apparent porosity. This is because the replacement of the liquid in the pores by gas has considerable impact on the slowing-down length of the formation and thus on the apparent porosity. Partial replacement of the water component of the formation by a much less dense gas increases the neutron slowing-down length, and thus the apparent porosity decreases. The decrease in apparent porosity is a function primarily of the true porosity, the water saturation, the gas density, and to some extent the lithology. Replacement of fluid in the pores by a less dense gas also decreases the bulk density of the formation. These two effects have been exploited in well logging by making the density and neutron porosity measurements in a single measurement pass. On the log presentation, the density and neutron traces separate in a direction which makes the presence of gas easily visible.

A cartoon example of the so-called gas effect can be seen in zone 7 of Fig. 14.13 labeled "hydrocarbon effects." The apparent neutron porosity is seen to become very small while the apparent density porosity increases due to the replacement, presumably, of the normally expected water by lower density gas. An actual log example can be seen in zone "C" of Fig. 14.11. In this more realistic case the apparent neutron porosity descends to only about 20 p.u. from an anticipated value of something around 33 p.u. Before examining the reasons for this response, let us look first at the idealized gas response, sometimes called the gas or excavation effect.

The gas effect results from the fact that under most in situ conditions found in hydrocarbon wells, the hydrogen density, as well as the bulk density of the gas is less than that of water. Thus a gas-saturated formation will have less ability to slow down neutrons and the mean free path between collisions will be larger due to the decreased density. To demonstrate the effect of gas-filled formations on the generic tool, the Monte Carlo model was used to compute the response in 5, 10, 20, and 30 p.u. limestones. These formations were saturated with a CH_4 gas of density 0.176 g/cm^3.

The calculated near/far ratios are indicated in Fig. 14.15 and are seen to lie along the previously determined response line (Fig. 14.10) connecting ratio and slowing-down

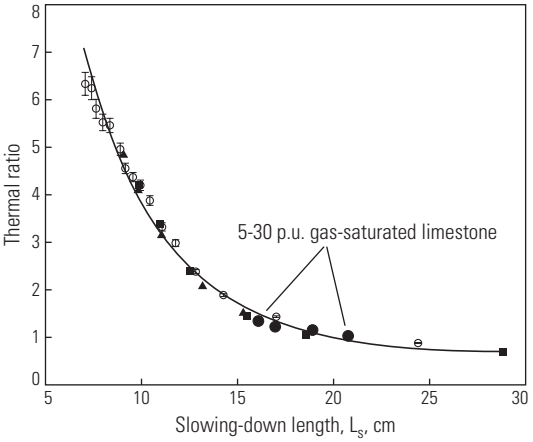


Fig. 14.15 The response to gas-saturated limestone formations is indicated on top of the previously established liquid-filled response line. From Ellis et al. [1].

length. It can be seen that all four gas points lie near the extreme right-hand portion of the response curve at very long slowing-down lengths and thus will have apparent porosities that are small.

So once again, this response characteristic of neutron logs can be explained and understood by simple recourse to slowing-down length. At any given porosity, if the water is replaced by a gas of lower density, the calculated slowing-down length will be found to be longer than in the water-filled case. The actual magnitude of the decrease of the apparent porosity will depend on the pore volume, the gas composition and its density. If the gas-filled slowing-down length is longer than the equivalent 0 p.u. slowing-down length (because the excavated density of the formation is less than the matrix density), then the implied apparent porosity might be thought to be negative, but by tradition is forced to zero or some small value by the tool software.

14.10 DEPTH OF INVESTIGATION

The depth of investigation for neutron devices is of interest when we are trying to evaluate gas saturation. However, unlike the depth of investigation of induction devices, it is a quantity which is rather illusive. The depth of investigation for a thermal neutron porosity device can be determined experimentally [23] or computationally [26]. First we consider the experimental approach.

For the determination of depth of investigation for a single formation porosity, the experimental setup is shown in Fig. 14.16. The test formation consisted of a number of coaxial cylinders of loose dry sand. The porosity of this formation was approximately 35 p.u. With the tool in place, the cylindrical layers of sand nearest the borehole were saturated with water, one at a time. The observed change in apparent

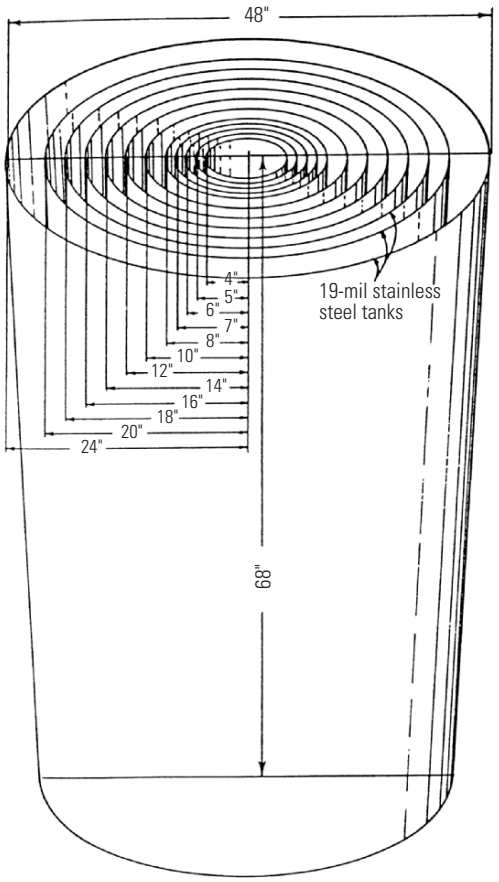


Fig. 14.16 The laboratory setup for the determination of the depth of investigation or pseudo-geometric factor of neutron porosity tools. Adapted from Sherman and Locke [23].

porosity as a function of this water-invasion depth is shown in Fig. 14.17. Data from an experimental epithermal neutron porosity device are shown. The three curves correspond to the values of porosity derived for the individual detectors and from the ratio of the two counting rates.

As we expect intuitively, the depth of investigation of the far detector is somewhat greater than that for the near detector. In practice neither of these detectors is used alone for the determination of porosity; rather their ratio is used. We see that the ratio has a depth of investigation larger than either of the two individual curves. This is somewhat analogous to the case of the induction tool described earlier. In that case, a second receiver coil was introduced to remove some of the signal originating close to the borehole from the farther receiver, thus weighting the signal contributions from deep in the formation more strongly than those from nearby. In the case of the neutron

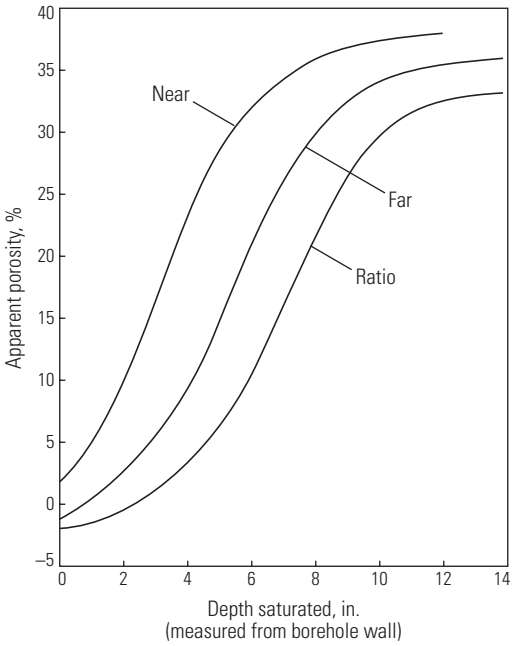


Fig. 14.17 The results of the determination of the depth of investigation of a dual-detector epithermal neutron porosity device. Note that the combined measurement has a greater depth of investigation than either of the single detectors. Adapted from Sherman and Locke [23].

tool, taking the ratio of the near and far detector counting rates partially eliminates the common response of the two detectors to the shallow zone. This has the effect of increasing the relative sensitivity to hydrogen in the region beyond the near detector depth of investigation.

The curves of Fig. 14.17 are similar in nature to the pseudogeometric factors for the resistivity electrode devices. The exact shapes of the response curves are dependent upon the actual experimental conditions. However, it is clear that the gas-sensitivity in a 35 p.u. formation comes from roughly the first 8 in. of formation.

Now we turn to the use of Monte Carlo to compute the depth of investigation. One type of depth of investigation can be computed by the simulation of mud filtrate invasion into a gas-filled formation. This is in close analogy to logging situations where the neutron response in a gas-saturated formation will be altered by the presence of any invading mud filtrate and the depth to which it invades. At each position of the invasion front, the Monte Carlo code is used to calculate the response of the two detectors, from which an apparent porosity can be determined.

To illustrate the depth of investigation, the series of Monte Carlo runs are summarized with a relative integrated radial geometric factor, or so-called J-factor, that varies between 0 and unity as a function of invasion radial extent. Figure 14.18 shows the J-factor computed for the apparent porosity of the generic tool. There is very little

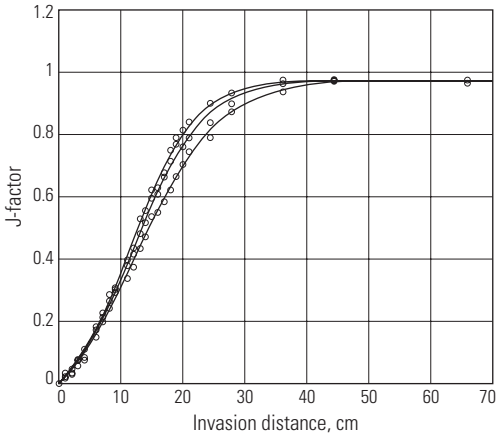


Fig. 14.18 Using Monte Carlo simulation for filtrate invading gas-filled formations, the collection of invasion J-factors was computed for a variety of porosities from 5 to 30 p.u. From Ellis et al. [18]. Used with permission.

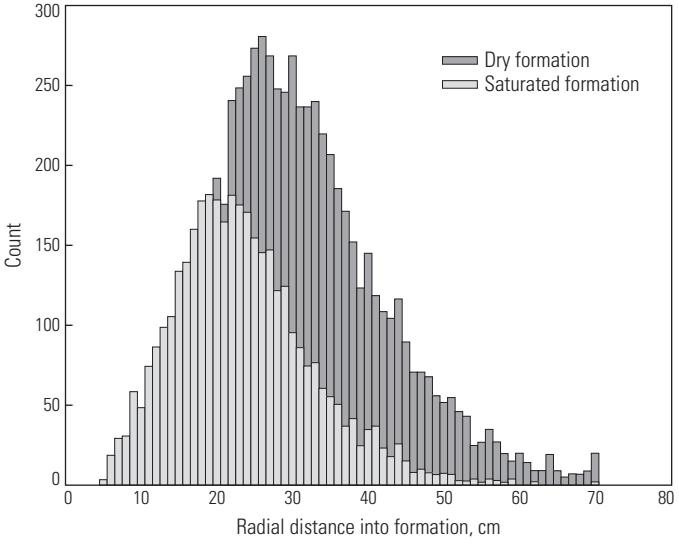


Fig. 14.19 Maximum radial penetration into formation by successful neutrons detected at the Far detector. From Ellis et al. [1]. Used with permission.

variation observed in the shape of the J-factor with formation porosity. The depth of investigation that can be defined as the 50% or 90% point, as one wishes, is about 15 or 25 cm, respectively.

To highlight the dependence of the depth of investigation on saturating fluid, Fig. 14.19 shows distributions of the maximum penetration that particles detected

in the Far detector attained on their tortuous path in a 20 p.u. formation, traveling from source to detector. The peaks in the distributions show a shift of approximately 10 cm, with the greater depth of penetration for the case of the gas-filled formation, in line with expectation from the much longer slowing-down length of the gas-filled formation.

14.11 LWD NEUTRON POROSITY DEVICES

After the exhaustive treatment of wireline devices there is little to be said about LWD neutron devices. They are basically the familiar wireline devices fitted into drill collars at the bottom of the drill string but with a few differences. In one realization [24, 25], the near and far detectors are banks of detectors at two spacings. Their measurements may be summed or binned into azimuthally-oriented responses. Sometimes four traces are shown corresponding to top, bottom, left, and right quadrants.

These devices, like their wireline cousins, have correction or departure charts of a similar nature. The largest correction happens, not surprisingly, to be for the borehole size (or bit size). To accommodate the needs of drilling, LWD tools are constructed inside drill collars of several sizes. When the collar diameter is close to the drill bit size the borehole corrections are minimized.

The LWD neutron devices are also sensitive to standoff, a quantity that could be significant depending on the difference between the tool size and the drill bit size with which it is being operated. Although correction charts exist for this effect, the more mismatched the tool and bit size are the poorer the measurement because of the reduction in sensitivity to formation hydrogen.

The depth of investigation of an LWD neutron porosity tool is very similar to the wireline devices we have already studied. It has been detailed in one particular formation – a 22 p.u. sand – and is shown in the left panel in Fig. 14.20. This was computed for the case in which mud filtrate invades a gas-saturated formation. The complementary case in which gas invades a water-filled formation is shown on the right. The contrast in depth of investigation is seen to be enormous between the two situations and is responsible for the gas sensitivity of neutron instruments. The answer to the discrepancy lies in the fact that the neutrons can travel relatively unimpeded (called streaming) in the portion of the formation with the longest slowing-down length. When the gas saturation is close to the borehole wall the neutrons stream through that shallow path with greater ease than the deeper, water-saturated zone – resulting in the shallow depth of investigation as indicated by the curve on the right in Fig. 14.20. When the gas saturation is behind an invaded zone, the few neutrons that manage to reach the gas-saturated zone can easily stream to the region of the detector where there is some probability of being detected. This results in the much deeper depth of investigation as shown in the left-hand panel of Fig 14.20. This effect will be seen (in Chapter 20) to be responsible for an interesting artifact observed on neutron logs in highly deviated wells.

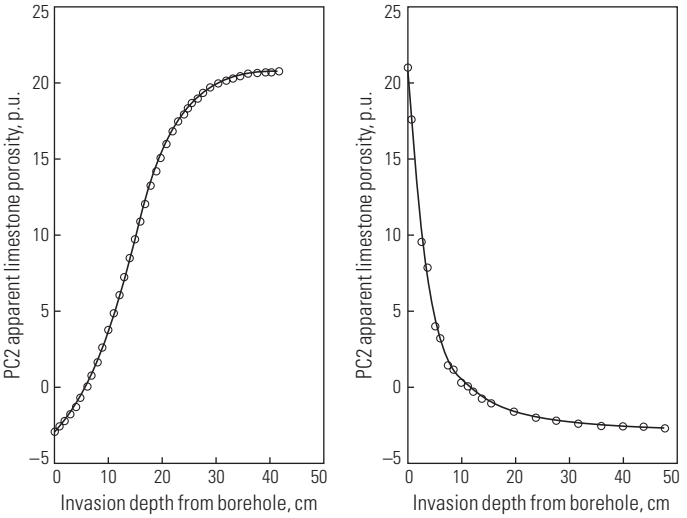


Fig. 14.20 Two versions of depth of investigation for an LWD neutron tool. From Ellis and Chiaramonte [26]. Used with permission.

14.12 SUMMARY

For the reader who has arrived here, following the tortuous path laid out to convey the complexities of neutron porosity logging, it will not be necessary to reiterate that the neutron porosity tool does not measure porosity – except in the most restricted of circumstances. If the tool is well calibrated and operated in an environment similar to the standard calibration, or if the appropriate corrections have been performed, the measurement might be more usefully linked to the HI of the formation. This is a better concept because the apparent porosity read by neutron porosity tools is sensitive to all sources of hydrogen. Any hydrogen that is part of the clay minerals that may be present will affect the tool reading.

We have also shown that the widely used commercial thermal neutron porosity tools mainly respond to the slowing-down length of the formation plus a perturbation for any strong thermal neutron absorbers that might be present. The slowing-down length of the formation provides a framework for understanding the perturbing effects of varying lithology, the presence of shale, and of gas-bearing formations. Further use and cautions for the use of neutron logs can be found in references [1, 18].

REFERENCES

1. Ellis DV, Case CR, Chiaramonte JM (2003) Porosity from neutron logs I: measurement. Petrophysics 44(6):383–395

2. Duderstadt JJ, Hamilton LJ (1976) Nuclear reactor analysis. Wiley, New York

3. Henry AF (1975) Nuclear-reactor analysis. MIT Press, Cambridge, MA

4. Glasstone S, Sesonske A (1967) Nuclear reactor engineering. Van Nostrand, Princeton, NJ

5. Edmundson H, Raymer LL (1979) Radioactive logging parameters for common minerals. Trans SPWLA 20th Annual Logging Symposium, paper O

6. Tittman J, Sherman H, Nagel WA, Alger RP (1966) The sidewall epithermal neutron porosity log. J Pet Tech 18:1351–1362

7. Ellis DV (1987) Nuclear logging techniques. In: Bradley H (ed) Petroleum production handbook. SPE, Dallas, TX

8. Ellis DV, Flaum C, Galford JE, Scott HD (1987) The effect of formation absorption on the thermal neutron porosity measurement. Presented at the SPE 62nd Annual Technical Conference and Exhibition, paper SPE 16814

9. Dresser Atlas (1983) Well logging and interpretation techniques: the course for home study. Dresser Atlas, Dresser Industries, Houston, TX

10. Schlumberger (1997) Log interpretation charts. Schlumberger, Houston, TX

11. Gilchrist WA, Galford JE, Flaum C, Soran PD, Gardner JS (1986) Improved environmental corrections for compensated neutron logs. Presented at SPE 61st Annual Technical Conference and Exhibition, paper SPE 15540

12. Belknap, WB, Dewan JT, Kirkpatrick CV, Mott WE, Pearson AJ, Rabson WR (1978) API calibration facility for nuclear logs. Gamma ray, neutron and density logging, SPWLA Reprint, paper E

13. Alger RP, Locke S, Nagel WA, Sherman H (1971) The dual-spacing neutron log-CNL*. Presented at the 46th SPE Annual Technical Conference and Exhibition, paper SPE 3565

14. Allen LS, Tittle CW, Mills WR, Caldwell RL (1967) Dual-spaced neutron logging for porosity. Geophysics 32(1):60–68

15. Arnold DM, Smith HD Jr (1981) Experimental determination of environmental corrections for a dual-spaced neutron porosity log. Trans SPWLA 22nd Annual Logging Symposium, paper W

16. Davis RR, Hall JE, Boutemy YL (1981) A dual porosity CNL logging system. Presented at SPE 56th Annual Technical Conference and Exhibition, paper SPE 10296

*Mark of Schlumberger

17. Scott HD, Flaum C, Sherman H (1982) Dual porosity CNL count rate processing. Presented at SPE 57th Annual Technical Conference and Exhibition, paper SPE 11146

18. Ellis DV, Case CR, Chiaramonte JM (2004) Porosity from neutron logs II: interpretation. Petrophysics 45(1):73–86

19. Kleinberg RL, Vinegar HJ (1996) NMR properties of reservoir fluids. The Log Analyst 37(6):20–32

20. Scott HD, Wraight PD, Thornton JL, Olesen J-R, Hertzog RC, McKeon DC, DasGupta T, Albertin IJ (1994) Response of a multidetector pulsed neutron porosity tool. Trans SPWLA 35th Annual Logging Symposium, paper J

21. McKeon DC, Scott HD (1988) SNUPAR – a nuclear parameter code for nuclear geophysics applications. Nucl Geophys 2(4):215–230

22. Ellis DV (1986) Neutron porosity devices-what do they measure? First Break 4(3):11–17

23. Sherman H, Locke S (1975) Depth of investigation of neutron and density sondes for 35-percent-porosity sand. Trans SPWLA 16th Annual Logging Symposium, paper Q

24. Holenka J, Best D, Evans M, Sloan B (1995) Azimuthal porosity while drilling. Trans SPWLA 36th Annual Logging Symposium, paper BB

25. Evans, M, Best D, Holenka J, Kurkoski P, Sloan W (1995) Improved formation evaluation using azimuthal porosity data while drilling. Presented at the SPE 70th Annual Technical Conference and Exhibition, paper SPE 30546

26. Ellis DV, Chiaramonte JM (2000) Interpreting neutron logs in horizontal wells: a forward modeling tutorial. Petrophysics 41(1):23–32

Problems

14.1 You are faced with interpreting a set of old epithermal logs which were inadvertently run with a matrix setting of "LIME." The section of interest is quite certainly a sandstone.

14.1.1 Based on your understanding of the response of epithermal neutron porosity devices, construct a correction chart for use in converting the log porosity values to "true" sandstone porosity. This correction should be of the form: $\phi_{true} = \phi_{log} + \Delta\phi$. Plot $\Delta\phi$ vs. ϕ_{log} for values of ϕ_{log} between 0 and 30 p.u. in 5 p.u. steps.

14.1.2 If the log readings are running between 15 and 30 p.u., can you simply shift the values to obtain a good porosity value?

14.2 The thermal porosity device response can be characterized rather well by the use of the migration length, L_m. As you recall, ${L_m}^2 = {L_s}^2 + {L_d}^2$, where ${L_d}^2 = \frac{D}{\Sigma}$.

(D is the thermal diffusion coefficient, and Σ is the macroscopic thermal neutron absorption cross section.)

14.2.1 What apparent "limestone" porosity would you expect the tool to read in a freshwater-saturated 40 p.u. sandstone?

14.2.2 Neglecting, for the moment, the effects of hydrogen displacement, what porosity would you expect it to read if the freshwater were replaced by salt-saturated water (260 kppm NaCl)?

14.2.3 However, you cannot neglect the effect of hydrogen displacement in this case, since the density of the salt solution is 1.18 g/cm^3. When you take this into account, in addition to the salinity, what is the apparent "limestone" porosity? (Hint: First calculate an equivalent porosity due to the lower hydrogen concentration in the saltwater.)

14.3 An epithermal neutron porosity device basically measures the slowing-down length, as described in the text. Suppose the counting rate ratio from which the slowing-down length is derived is 10% in error for one reason or another. How much error does this translate to, in porosity units, for a 5% porosity sandstone? A 30% porosity limestone?

14.4 Using the example of the clean sand zone just below 2,994 ft associated with zone "A" of Fig. 14.11, what is its porosity?

14.4.1 If the thermal neutron porosity log had been run in a borehole with a temperature of 300°F instead of at 50°F, what apparent porosity value would it read? Sketch the resulting neutron/density gas crossover.

14.5 What is the neutron-density separation to be expected in a 10% porous sandstone with a 50% gas saturation? The density of the gas can be taken as 0.25 g/cm^3. Compute ϕ_n in limestone units and ϕ_d in limestone units.

14.6 Refer to the gas zone ("C") example of Fig. 14.11. Why does the apparent neutron porosity descend so little. Can you think of three possible reasons?

14.7 What is the epithermal porosity reading (sandstone units) expected to be in a 20% porous shaly sandstone, when the rock matrix is composed of 50% (by volume) illite?

15

Pulsed Neutron Devices and Spectroscopy

15.1 INTRODUCTION

The availability of pulsed neutron sources allowed the development of several valuable formation evaluation techniques: thermal die-away logging and spectroscopy of neutron-induced gamma rays. At the heart of these techniques is the neutron generator discussed in Chapter 13. In thermal die-away logging, the pulsing capability of this generator is fundamental to the determination of the formation thermal neutron absorption properties – a method of distinguishing saline formations waters from hydrocarbons. Chlorine, which is nearly always present in formation waters, has a large absorption cross section. Measurement of the macroscopic absorption cross section (Σ) can provide the means for identifying salt water and for estimating the water saturation.

A limited chemical analysis of the formation can be obtained from a combination of the controlled injection of high-energy neutrons into the formation and spectroscopy of the neutron-induced gamma rays. By exploiting the high-energy neutron reactions, we can determine the ratio of carbon to oxygen in the formation. If the lithology and porosity are known, this ratio can also yield water saturation.

Spectroscopy of gamma rays produced by subsequent thermal neutron capture reactions allows the detection of a dozen or so important elements present in the formation. Not limited to pulsed neutron sources, instruments have been developed for capture GR spectroscopy that use chemical neutron sources. The extraction of elemental concentrations from the measurements will be discussed in this chapter but the methods for producing a quantitative lithology is described in a later chapter.

Pulsed neutron techniques are also employed to monitor and quantify oil and water flow in producing wells by producing and detecting oxygen activation, or measuring the passage of injected tracers of radioactive particles or efficient absorbers. Other applications suggest the possibility of measuring formation density.

The pulsed neutron generator can also be used to replace the traditional AmBe source in a device to measure neutron porosity in addition to another parameter of interest – the slowing-down time.

15.2 THERMAL NEUTRON DIE-AWAY LOGGING

Pulsed neutron devices found their first logging application in the determination of water saturation in cased producing wells. The traditional method for obtaining S_w, of course, relies on electrical measurements. However, for many years the metallic casings of producing wells rendered electrical measurements useless and spurred the development of alternative methods. It was natural to think of using neutrons which penetrate the casing without much difficulty and consequently are applied to the problem of probing the formation in such situations. In recent years some instruments have appeared that allow measurement of resistivity through casing as described in Section 6.6. However, the use of pulsed neutron techniques to monitor reservoir saturation seems to be well established.

Thermal neutron die-away devices respond to the macroscopic thermal capture cross section (Σ), which depends on the chemical constituents of the matrix and pore fluids. To motivate the measurement of Σ, we will first look at the relationship between the concentration of thermal absorbers and the value of the macroscopic cross section. This will give an indication of the dynamic range of Σ expected in logging applications. The technique for determining the value of Σ from borehole measurements is examined, illustrating some of its limitations. An introduction to interpretation of the Σ measurement and some applications are given.

15.2.1 Thermal Neutron Capture

As discussed in Chapter 13, neutron capture is one of many reactions which can take place during neutron interactions with matter. The cross section for capture varies as $1/v$ at low energies, where v is the neutron velocity. Thus, it is the predominant interaction mechanism at thermal energies and the only way neutrons are removed from the system. In the capture of neutrons, the target nucleus with atomic mass A transmutes into another isotope of the element with mass $A + 1$. This "compound nucleus" is formed in an excited state that, in many cases, decays nearly immediately, with the emission of one or more gamma rays. The GR energy can range up to a maximum of about 8 MeV.

To appreciate the magnitude of the thermal absorption cross section of a selected few common (and not so common) elements, refer back to Table 23.3, which orders the elements by mass-normalized absorption cross section. This is a useful unit since

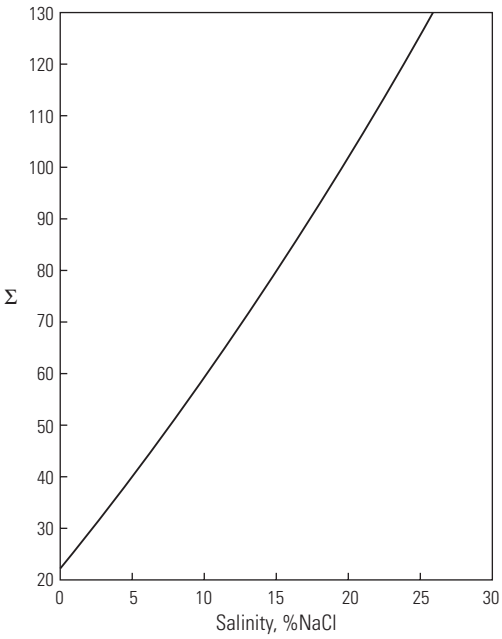


Fig. 15.1 The macroscopic thermal neutron absorption cross section of water (in capture units) as a function of salinity. The salinity is given in weight percent of dissolved NaCl.

a thousand times the mass-normalized cross section is numerically equivalent to the number of capture units (cu) contributed per gram of element per cubic centimeter of bulk material.

It is seen that, in terms of the mass normalized absorption cross section, chlorine is quite prominent on this list of elements generally associated with petrophysical applications. Exceptions are boron and gadolinium, which are often associated with clays, and cadmium, which is used in the construction of epithermal neutron detectors. The next most important and frequently encountered element is hydrogen, which has an atomic cross section two orders of magnitude less than chlorine. However, because of its concentration in water, it plays a greater role than most other elements.

Figure 15.1 shows how the macroscopic cross section (in capture units) of saltwater varies as a function of the NaCl concentration. The relatively large capture cross section for fresh water (22 cu) is due primarily to the hydrogen, but the addition of NaCl, which has, in its crystalline form, a capture cross section of about 750 cu, increases the capture cross section of the liquid dramatically. Due to the lack of effective absorbers in most rock matrices, their capture cross sections are generally less than 10 cu. Thus, the capture cross section of a formation will depend primarily on the salinity of the interstitial water, porosity, and water saturation. Water saturation is an important ingredient in the Σ of a formation, since the capture cross section of hydrocarbons is about the same as that of fresh water. Neutron die-away or pulsed-neutron capture (PNC) logs are generally presented on a scale 0–60 cu, which

reflects the anticipated range of variation of this formation parameter. A 30% porous formation containing only saturated saltwater (26% NaCl by weight), will have a Σ in excess of 40 cu, depending on the absorbers associated with the rock matrix. The presence of a significant oil saturation will consequently reduce the observed value of Σ.

15.2.2 Measurement Technique

In order to determine the macroscopic thermal cross section of a formation, the quantity that is measured is the lifetime, the inverse of the decay rate, of thermal neutrons in an absorptive medium. The practical realization of a device for this measurement is contingent on the availability of a pulsed source of high-energy neutrons. This allows the periodic production of a population of rapidly thermalized neutrons whose absorption is then monitored.

The basic mode of operation consists of pulsing the source of 14 MeV neutrons for a brief period. This forms a cloud of high-energy neutrons in the borehole and formation, which becomes thermalized through repeated collisions. The neutrons then disappear at a rate which depends upon the thermal absorption properties of the formation and borehole. As each neutron is captured (by most typical isotopes in the formation), gamma rays are emitted. The local rate of capture of neutrons is proportional to the density of neutrons, which decreases with time. Thus the rate of production of capture gamma rays decreases in time. Measurement of the decay of the gamma ray counting rate reflects the decay of the neutron population. For this reason the logging tool generally consists of a detector of gamma rays in addition to the source of 14 MeV neutrons.

The operation of such a device is summarized in Fig. 15.2. Neutrons emitted at high energy are shown, shortly prior to thermalization, forming a cloud of neutrons in the first panel at a time t_1. As time passes, the neutrons make numerous collisions, spreading further from the point of emission, which is shown in a panel representing the situation at a later time t_2. The characteristic dimension of the cloud of neutrons, just prior to thermalization, is the slowing-down length. When the neutrons reach thermal energies and the cloud has attained a size which is related to the migration length, they begin to be absorbed through the thermal capture process. As time passes, the density of neutrons in the ever-expanding cloud decreases, depending upon the rate of absorption, as indicated in the sketch of the neutron density as a function of time in Fig. 15.2.

In a manner analogous to radioactive decay, the time-dependent behavior of the capture of thermal neutrons can be predicted. The reaction rate for thermal neutron absorption is given by the product of the macroscopic absorption cross section Σ_a and the velocity of the neutron v. So, for a system of N_t neutrons, the number absorbed in a time dt is:

$$dN_t = -N_t \, \Sigma_a \, v \, dt \, . \tag{15.1}$$

When integrated, this yields:

$$N_t = N_i \, e^{-\Sigma_a v t} \, , \tag{15.2}$$

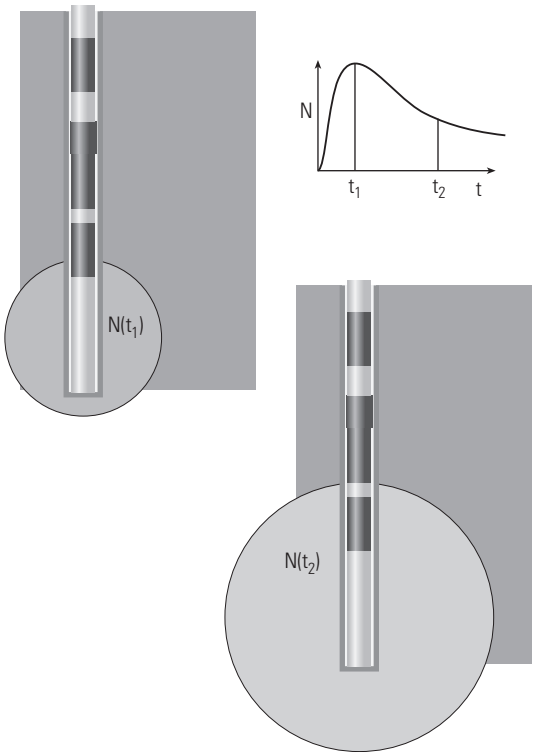


Fig. 15.2 Evolution of the thermal neutron population produced by a pulsed neutron device.

Table 15.1 Capture cross sections and decay time constants for various materials at a temperature of 300°K.

Material	Σ (cu)	τ_d (μs)
Quartz	4.26	1,086
Dolomite	4.7	968
Lime	7.07	643
20 pu lime	10.06	452
Water	22	206
Salt water (26% NaCl)	125	36

which relates the number present at time t to the initial number N_i at time zero. The decay time constant is equal to $1/v\Sigma_a$.

The value of the capture cross section Σ_a, at a temperature of 300°K, is listed in Table 15.1 for a number of materials of interest. Included in the table is the decay time constant associated with each value of Σ_a. It has been computed, using the thermal

capture cross section in cu, from the relationship:

$$\tau_d = \frac{1}{v\Sigma_a} = \frac{4550}{\Sigma_a} \ [\mu s] \ . \tag{15.3}$$

The derivation of the decay-time relationship was based on a simple model which starts with a cloud of thermal neutrons at time zero. It is of interest to know how much time elapses, after the burst of 14 MeV neutrons, before the cloud of thermalized neutrons is present. Estimates based on the average number of collisions required to reduce the energy of the neutrons to the thermal region and the variation of the mean free path between collisions indicate that the thermalizing timescale is on the order of 1–10 μs, much shorter than typical decay times shown in Table 15.1.

The simple derivation of the capture GR time-dependence misses an important aspect encountered in actual measurement: the thermal neutron diffusion effect. The diffusion of neutrons in a *homogeneous* medium arises from spatial variation in the neutron density (or flux). Intuitively, we feel that the thermalized neutron cloud will have such a spatial variation; initially, the flux of thermal neutrons will be highest near the source and will decrease with increasing distance from it. Physically, the diffusion of neutrons is to be expected since in regions of high flux the collision rate will be high, with the result that neutrons will be scattered more frequently toward regions of lower collision density. This results in a net current of neutrons from regions of higher flux to those of lower flux. The rate at which the diffusion occurs depends on the diffusion coefficient and the gradient of the neutron flux (see Chapter 14). The implicit assumption in the derivation of Eq. 15.2 was that somehow the global behavior of the neutron density could be monitored at all times. In this case, diffusion is of no consequence. However, in the actual logging application, decay of the neutron population is monitored only in the vicinity of the detector, and thus it is a local measurement.

At any observation point, the local thermal neutron density decreases because the neutrons are diffusing and being captured. To quantify the effect of the diffusion component on the local decay time constant, it is necessary to use the time-dependent diffusion equation. *The time-dependent diffusion equation for the density of thermal neutrons, n, is given by:*

$$\frac{\partial n}{\partial t} = S \ - \ nv\Sigma \ + \ Dv\nabla^2 n, \tag{15.4}$$

where v is the thermal speed and D is the thermal diffusion coefficient. (Compare it to Eq. 14.3 which was for the steady-state case; the time derivative was zero. In this equation the flux (Φ) has been replaced by the product of neutron velocity (v) and thermal neutron density (n).) After the burst, the source term, S, becomes zero, and the governing equation is:

$$\frac{\partial n}{\partial t} = -nv\Sigma \ + \ Dv\nabla^2 n \ , \tag{15.5}$$

or

$$\frac{1}{n}\frac{\partial n}{\partial t} = -v\Sigma \ + \ Dv\frac{\nabla^2 n}{n} \ . \tag{15.6}$$

It is the term $Dv\frac{\nabla^2 n}{n}$ *which is absent from the global analysis performed earlier. By comparing Eq. 15.6 with the result from the global model, an apparent decay time of the neutron population,* τ_a*, can be anticipated. The global behavior of the neutron population decayed exponentially* ($e^{-t/\tau}$) *with time,* t*, and the inverse of the decay constant was identified as the product* $v\Sigma$.

In this manner, the apparent decay time constant of the neutron population, τ_a*, can be seen from Eq. 15.6 to be the sum of two terms: an intrinsic time constant and a diffusion time constant. The intrinsic time constant is given by:*

$$\frac{1}{\tau_{int}} = v\Sigma \ , \tag{15.7}$$

and the diffusion time is defined as:

$$\frac{1}{\tau_{diff}} = -Dv\frac{\nabla^2 n}{n}, \tag{15.8}$$

so that the local apparent time relationship is given by:

$$\frac{1}{\tau_a} = \frac{1}{\tau_{int}} + \frac{1}{\tau_{diff}} \ . \tag{15.9}$$

The result is that the apparent decay time of the local neutron population contains two components: τ_{int} is the intrinsic decay time of the formation (i.e., that expected from global monitoring of absorption alone), and τ_{diff} is the diffusion time, which corresponds to the density reduction of neutrons as a function of time due to the diffusion of neutrons away from the center of the cloud. In a homogeneous medium, the value of τ_{diff} depends on the distance from the source emission point and the diffusion coefficient. The practical result of the diffusion effect is that, without correction, the measured Σ of a formation will appear greater than the intrinsic value due to the diffusion rate of the thermal neutron population in the vicinity of the detector. The effect will also be larger at low porosity, since the diffusion coefficient D decreases with increasing porosity (see Fig. 13.16).

If this seems complicated, it is, but it pales by comparison to the real-world case that generally involves an instrument that is an efficient thermal neutron absorber in a borehole that may, or may not, be filled with absorbing brine. If the borehole is filled with brine then a few tens of microseconds after the burst of high-energy neutrons the borehole region will begin to be depleted; at any point in the formation the diffusion becomes complicated by the competing effect of diffusion of the cloud of neutrons and the diffusion inward to the borehole which has now become a sink for neutrons.

At the other extreme is a borehole full of fresh water and a formation saturated with brine. In this case the Σ of the formation is much larger than the Σ of the borehole so that the borehole becomes an additional source of neutrons at later times. As the neutrons in the formation are captured and diffuse, additional uncaptured neutrons from the borehole (where the initial density was the highest) begin to diffuse into the formation making the apparent decay rate at any point slower than expected. The addition of a steel casing and sheath of cement, which might have been made with

salt water, further complicate the situation. These scenarios have been investigated by Preeg and Scott [1] using Monte Carlo modeling to elucidate the contribution of the borehole and the formation to the measured signal at detectors at various spacing from the source.

15.2.3 Instrumentation

Since the PNC measurement is designed for saturation measurements in cased producing wells they are generally very slender, typically 1 $\frac{11}{16}$ in. diameter. This allows insertion of the tool into producing wells that may contain tubing. Of course, the small diameter complicates the engineering of such tools. Numerous schemes are used for controlling the period during which the 14 MeV neutrons are produced and the period during which the gamma rays are measured. Some devices use dual-detector systems in an attempt to correct for the disturbance that can be introduced by the borehole, as well as to provide an estimate of the porosity. Techniques for extracting the intrinsic formation capture cross section have proliferated along with the number of experimental measurements in formations of different porosity and salinity and varied casing and borehole conditions.

One of the challenges in making the thermal decay measurement is the separation of the borehole and formation signals. Although one would like to monitor the neutron population of the formation only, capture gamma rays from the borehole are in fact detected also. This component is of little interest for the determination of the formation properties. Figure 15.3 shows the approach used in one device [2]. A short time after

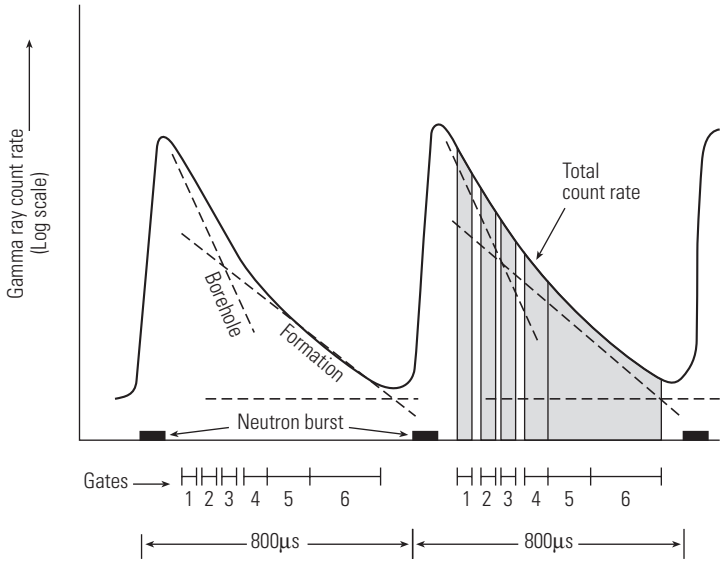


Fig. 15.3 The gamma ray time distribution illustrates the decay of the borehole portion of the signal and the portion due to the formation. Adapted from Schultz et al. [2].

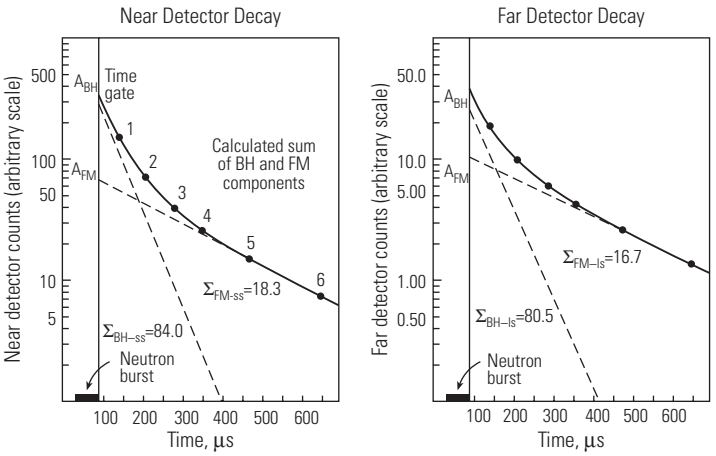


Fig. 15.4 Laboratory data from a dual-detector device illustrating the two-component time decay. Comparison of the observed formation Σ with the intrinsic value of 15.7 cu shows that the diffusion effect is smaller for the far detector. Adapted from Schultz et al. [2].

the neutron burst, a series of timed gates accumulates the gamma ray counting rate as it decays. This cycle is repeated every 800 μs. After 1,250 of these cycles, a background signal is determined, which is then appropriately subtracted from the preceding sequence of pulsed measurements.

An example of the two-component behavior is shown in the data of Fig. 15.4. The decay rate of gamma rays is shown for two detectors at two spacings from the source. In this experimental set up the borehole absorption (Σ_{bh}) exceeds the formation absorption (Σ_{for}), giving rise to the rapid decay of the borehole component. Two exponentials have been fitted to the data. The curve with the longer decay time constant is related to Σ_{for} and could also have been determined from the composite decay curve by waiting a sufficient period of time (400 μsec in this case) before determining the rate of decay. In another situation in which the borehole fluid is fresh and the formation fluid saline, so that $\Sigma_{for} > \Sigma_{bh}$, the fastest-decaying component will be associated with the formation. In this case, waiting a sufficiently long time before determining the decay constant will result in obtaining only the Σ_{bh} value. In such a case, the decomposition of the decay curve into its components is seen to be an advantage.

Getting rid of the borehole component in the measured decay curve is just one part of the problem. The diffusion effect can also be seen in the data of Fig. 15.4. The 42 p.u. sandstone formation in which the measurements were made had a matrix Σ independently determined to be 11.1 cu. The borehole is filled with salt water, and the actual Σ of the formation filled with fresh water is 15.7 cu. On the left, the nearer of the two detectors sees the formation component decay with an apparent Σ of 18.3 cu while, on the right, the detector farthest from the source yields an apparent Σ of 16.7. As expected, this latter value is quite close to the intrinsic value, but the effect of diffusion is still seen. Table 15.2 compares, for some pure materials, values of intrinsic Σ with those observed with one early measurement system. Note, in particular, the

Table 15.2 Comparison of intrinsic and observed values of Σ, for pure materials, from an obsolete early measurement system. Adapted from Clavier et al. [6].

Material	Σ (cu)	Σ_{meas} (cu)
Sandstone	4.32	8–13
Limestone	7.1	8–10
Dolomite	4.7	8–12
Anhydrite	4.7	8–12
Gypsum	18	18
Water (fresh)	22	22
Oil	22	16–22
Shale		20–60

large discrepancies in the matrix materials; part are due to absorptive impurities in the samples and part to the diffusion effect, uncorrected in this early device.

Another approach to eliminating the borehole effect and determining the diffusion effects from the measured data is based on an instrument that uses a double pulsing of the neutron source [3]. This instrument first uses a short pulse whose decay is mainly dominated by the borehole environment to determine an approximation of Σ_{bh}, followed by a much longer pulse that combines borehole and formation sigma effects together, along with diffusion effects.

Despite the improvements in these measuring systems, to obtain closer agreement between measurement and intrinsic formation capture cross sections it has been necessary to combine a number of measured parameters from the instruments in conjunction with an extensive data base [4]. In one case [5], a data base of 2,500 different combinations of borehole and formation salinities was used to validate the processing algorithm.

15.2.4 Interpretation

Regardless of the engineering details and variations in the pulsing modes, the devices described above are used for the determination of water saturation, particularly in cased wells. The most common important thermal neutron absorber is chlorine, which is present in most formation waters. Hence a measurement of the parameter Σ resembles the usual open-hole resistivity measurements. It can distinguish between oil and salt water contained in the pores. If the porosity is known, gas/oil interfaces can be localized. When salinity, porosity, and lithology are known, the water saturation S_w can be computed. This type of analysis is simplified if porosity is known from another, presumably open-hole, log. However, in many applications such a log is not available and the presence of tubing in the cased well prohibits the use of another larger compensated porosity device. For these occasions, an *estimate* of the porosity can be provided from the ratio of integrated counting rates from a dual detector device. The estimate must take into account borehole size, casing size and lithology [7], and presumably the size of the cement annulus.

Despite the complexity of the physics of the measurement and its engineering implementation, Σ has a particularly simple mixing law. In the simplest case of a single mineral, the measured value Σ consists of two components, one from the matrix and the other from the formation fluid:

$$\Sigma = (1 - \phi)\Sigma_{ma} + \phi\Sigma_f \, . \tag{15.10}$$

This simple equation can be written because we are dealing with macroscopic cross sections; by definition, they combine volumetrically. To determine water saturation, the fluid component is broken further into water and hydrocarbon components:

$$\Sigma = (1 - \phi)\Sigma_{ma} + \phi S_w \Sigma_w + \phi(1 - S_w)\Sigma_h \, . \tag{15.11}$$

In a clean (shale-free) formation the graphical solution of this particularly simple equation for $S_w$is shown in Fig. 15.5. In order to use this approach, the values of Σ_w, Σ_h, and Σ_{ma} must be known or determined from logs. The presence of a water zone in the logged interval simplifies this task.

For saturation determination, the interpretation of the measurement is questionable if the water salinity is less than 100,000 ppm and if the porosity is below 15%. This is particularly true in shaly zones, due to the limited range of Σ-variation with saturation. The presence of shale, which may contain thermal absorbers such as boron, seriously disturbs this simple interpretation scheme, but a number of references indicate methods for dealing with the problem [8]. The response of Σ to clay minerals is discussed in Chapter 21.

Perhaps the most successful application of this type of measurement is in the time-lapse technique. In this procedure, the change in saturation between two runs in a

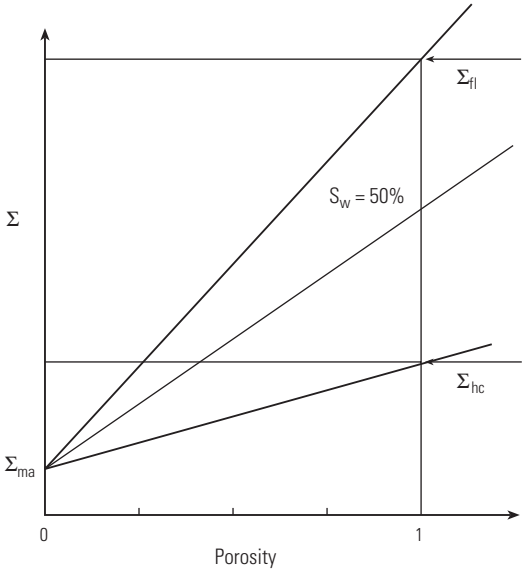


Fig. 15.5 A graphical solution of water saturation from the measurement of Σ, when porosity is known in a clean formation.

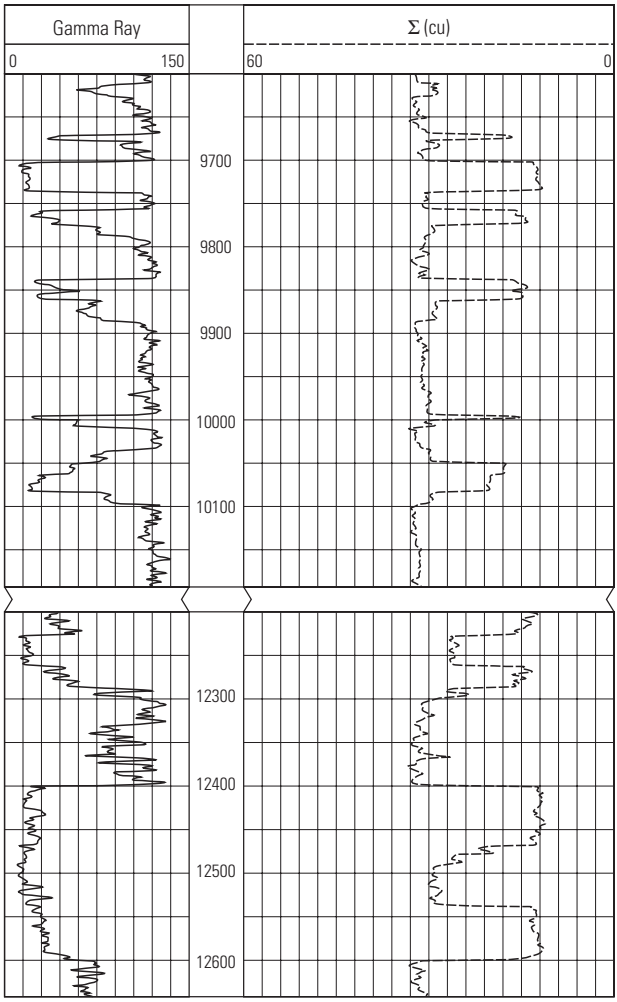


Fig. 15.6 A typical presentation of a Σ log in the simulated reservoir.

producing reservoir can be determined directly from the difference between the two measured Σ values, the difference in $\Sigma_w$and Σ_h, and the porosity value, i.e.:

$$S_{w1} - S_{w2} = \frac{\Sigma_1 - \Sigma_2}{\phi(\Sigma_w - \Sigma_h)}. \tag{15.12}$$

Uncertainties in the quantities such as Σ_{ma}, Σ_{cl}, and clay volume disappear in this differential measurement technique. Practical considerations for designing a reservoir-monitoring program are summarized elsewhere [9].

To illustrate the behavior of a pulsed neutron log, refer to Fig. 15.6, which shows carbonate and shaly sand sections of the simulated reservoir. Notice that in this

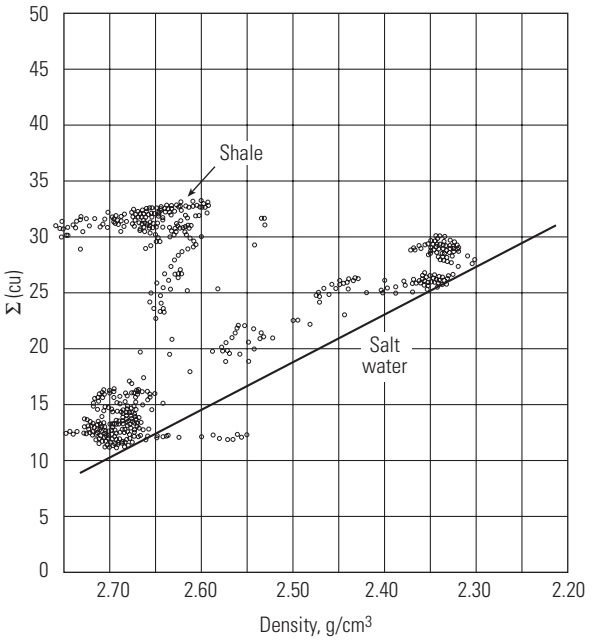


Fig. 15.7 A cross plot of Σ and ρ_b from a zone of the simulated reservoir. Since the interval used contains no hydrocarbon, the determination of Σ_w is possible.

presentation format the Σ and GR anticorrelate. Thus, high-capture cross sections correlate with high gamma rays and thus, presumably, clay. Also the presentation of the Σ curve is in the same manner as other porosity tools (increasing to the left, or to the bottom, depending on how you hold the log). Also it indicates higher water saturation in a manner similar to the resistivity logs. The zone below 12,200 ft, in Fig. 15.6, has been plotted as a function of the corresponding density values and shown in Fig. 15.7. A trend line of probable 100% water saturation is shown. The cluster of very low porosity points is easy to identify, as is the cluster of "shale" points.

15.3 PULSED NEUTRON SPECTROSCOPY

The evolution to a different type of pulsed neutron device – the induced gamma ray spectroscopy tool – was primarily motivated by the desire to make oil saturation measurements in the presence of unknown or changing water salinity. This, in principle**,** can be done by measuring the ratio of carbon to oxygen atoms in the formation. The devices that were designed to perform this measurement are often referred to as C/O tools, but as we shall see they have spawned a number of other uses.

Induced gamma ray spectroscopy tools are a somewhat more complex family of pulsed neutron tools. They exploit the identification of gamma rays resulting from

neutron interactions with the formation nuclei rather than simply the time behavior of the detected gamma ray flux. These reactions are of the three general types discussed previously: capture, inelastic, and particle reactions. In all three cases, the resultant nucleus is left in an excited state which decays, yielding gamma rays with energies which are characteristic of the particular nucleus which has undergone de-excitation. The standard technique, pioneered in first generation tools [10, 11] and continued in succeeding generations [12–14], for separating the inelastic gamma rays from the capture is to perform the measurement during a succession of short (on the order of tens of microseconds) neutron bursts. The inelastic interactions, which occur only above an energy threshold that varies from nucleus to nucleus, are produced by relatively high-energy neutrons. Thus, gamma rays detected during the average neutron burst and immediately thereafter, before the neutron energy has fallen too far, are most likely to be inelastic. At sufficient time after the neutron generator is turned off, capture gamma rays will begin to appear as the neutrons thermalize. Various capture spectroscopy tools have varied the burst width and repetition rate to enhance measurement of the C/O ratio, the capture cross sections (Σ) or capture spectroscopy for elemental analysis (discussed later).

Figure 15.8 schematically indicates the important reactions which are observed during the inelastic phase of operation of a pulsed neutron spectroscopy device. In one case, carbon is excited by the fast neutron and emits a gamma ray of 4.43 MeV. Two other kinds of reactions with oxygen are shown. In one, the oxygen is transmuted to nitrogen. It subsequently decays and emits a gamma ray of 6.13 MeV. The third case is more complicated, in that the oxygen is transmuted to ^{13}C, which then emits a gamma ray of 3.68 MeV.

Two actual gamma ray spectra taken with a second generation instrument in the inelastic mode, in an oil-filled tank and in a water-filled tank, for greatest contrast, are shown in Fig. 15.9. It is easy to identify the peaks of oxygen and carbon despite the distortion induced by the detector. The second generation measurement devices [13, 15] no longer rely on NaI but use detectors with better operating characteristics and spectroscopic properties, such as GSO and BGO (see Chapter 10), to enhance the detection of the gamma rays associated with C and O. Regardless of the detector type distortion exists and for this reason standard spectra are carefully determined [16] in the laboratory for elements with significant gamma ray emission spectra. The set of inelastic standards used in the analysis of a measured spectrum from one instrument is shown in Fig. 15.10. A technique referred to as weighted-least-squares (WLS) [11] is used in order to quantify the relative amounts of carbon and oxygen (and other elements). The spectrum measured in the borehole is compared to a linear sum of weighted standard spectra. The weights applied to each of the standards is varied until the sum is, in a least-squares sense, the best fit to the observed spectrum. The weights then represent the relative concentration of the elements in the standard set. The normalized weights are generally referred to as the spectral yields. Another measurement system takes a more direct approach and uses the counting rates in windows at appropriate locations in the spectrum to determine the C/O ratio [17] while yet another uses a combination of the windows method and WLS [18].

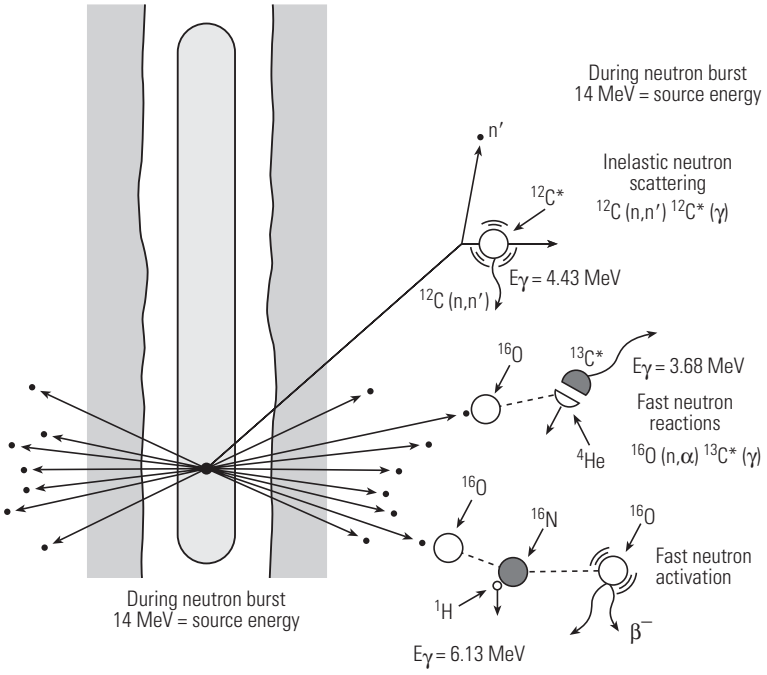


Fig. 15.8 Inelastic neutron reactions of interest in borehole logging applications. Adapted from Hertzog [11].

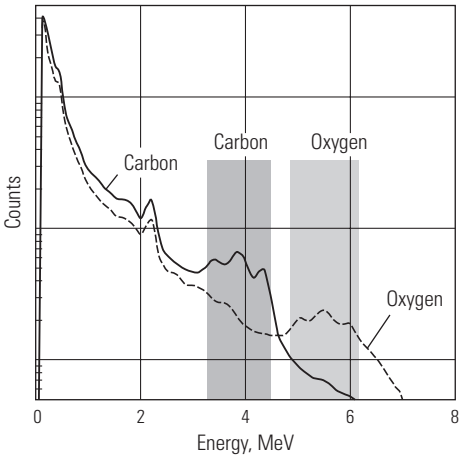


Fig. 15.9 Inelastic spectra recorded with a second generation C/O instrument in an oil and a water tank. Windows used to extract a statistically improved value of C/O are indicated.

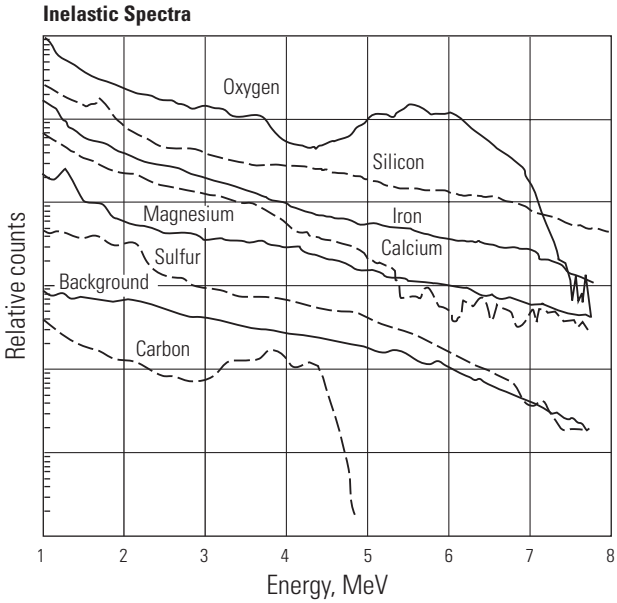


Fig. 15.10 A set of inelastic elemental spectra used to extract the relative signals of carbon and oxygen from spectra like the ones shown in Fig. 15.9.

The interest in making the inelastic measurements (which is the only way to produce gamma rays from carbon and oxygen) can be understood from a glance at Table 15.3. There is a great contrast between the atomic carbon and oxygen densities in water and in oil. The upper portion of Fig. 15.11 shows the effect of oil saturation on the elemental C/O ratio as a function of porosity for limestone, dolomite, and sandstone. The lower portion illustrates an actual tool response; the ratio of relative spectral weights of carbon and oxygen are shown as a function of porosity and oil saturation. The impact of making the measurements in the real world is evident in the great loss of dynamic range. The interpolated curves are based on just a handful of measurements (the six points with error bars) in a 10 in. borehole with a 7 in. casing and a 1.5 in. annulus of cement. In this case there are certainly extra sources of C and O in the borehole and cement that form a "background" that tends to reduce the dynamic range of the measurements compared to the theoretical expectation. From this figure of fan charts, it is clear that for clean formations of a given lithology and completion geometry, the interpretation is relatively straightforward when porosity is known; estimates of the porosity can be obtained from a dual detector system. However, it can be complicated: for example, in a sandstone, calcite cement could be confused with the presence of hydrocarbon. Also, an inherent difficulty in the measurement is immediately obvious. At low porosities the dynamic range of the C/O ratio, as a function of water saturation, shrinks to zero. Examples of interpretation of this ratio in more complex situations can be found in References [10] and [17].

Table 15.3 Comparison of atomic densities of carbon and oxygen (in units of Avogadro's number) in formations and fluids of interest. Adapted from Westaway et al. [10].

	Bulk density	Atomic Densities (6.023×10^{23})	
Formation	Density (g/cm^3)	Oxygen ($/cm^3$)	Carbon ($/cm^3$)
Limestone	2.71	0.081	0.027
Dolomite	2.87	0.094	0.031
Quartz	2.65	0.088	–
Anhydrite	2.96	0.087	–
Oil	0.85	–	0.061
Water	1.0	0.056	–

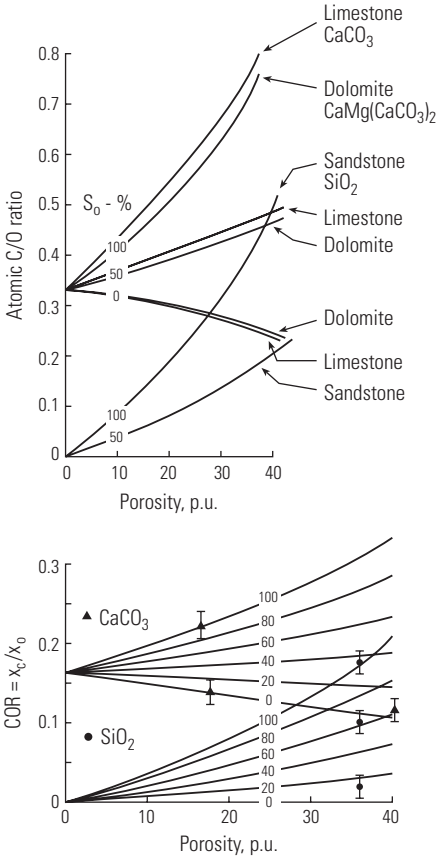


Fig. 15.11 Fan charts showing the ratio of elemental carbon to oxygen, as a function of porosity and oil saturation, in the upper panel. The fan chart for a particular tool response COR is shown in the lower panel. Adapted from Hertzog [11].

15.3.1 Evolution of Measurement Technique

The group of instruments loosely called C/O tools were initially introduced to measure the carbon to oxygen ratio. However their spectroscopic ability can be employed in a number of additional ways. Analysis of the capture GR spectrum can reveal the lithology of the formation, useful for correction of the C/O measurement and in its own right; the possibility of altering the pulsing duration and intervals can also provide a measurement of oxygen activation for water flow; the time analysis of the capture gamma spectrum can be used for, as was the case of the PNG tools, a measurement of the Σ of the formation.

15.3.1.1 C/O For tools with an emphasis on the C/O measurement there have been two issues. First, is that of detectors. In trying to separate the carbon and oxygen inelastic gamma rays it is necessary to have a detector with two distinct qualities. It needs to be of high spectroscopic quality and of good photoelectric efficiency. It must also be able to register pulses arriving in close proximity to one another, implying a characteristic light-decay curve that is very short to permit the extremely high instantaneous counting rates which are typical during the neutron burst. This has led to the use of GSO and BGO detectors in different realizations.

Regardless of the type of detection system or spectral processing technique there is a fundamental difficulty in processing the C/O ratios in the varied environments in which they are employed. Variables that affect the simple interpretation of the fan charts of Fig. 15.11 are the specific lithology, the porosity and the borehole size, casing size, cement thickness, and borehole fluid.

One of the biggest concerns in the interpretation of C/O measurements is the contribution from oil in the borehole, in a producing well for instance. For this reason, one variety of tool, made in a slightly larger diameter than the usual $1\frac{11}{16}$ in. diameter, includes a second detector shielded from the formation to enhance its measurement of C/O in the borehole. By combining the apparent C/O from this shorter borehole-focused detector with a longer spaced detector which sees the combination of the two it is possible to get information on the borehole oil holdup (the relative volume fraction of oil) and the formation water saturation. A typical cross plot of the two measured C/O ratios is shown in Fig. 15.12. This plot, which eliminates the explicit input for formation porosity, shows the four points of a quadrilateral (for the extremes of oil saturation and borehole oil holdup) for a particular environment consisting of casing size, formation lithology, and hydrocarbon density. An extensive data base is required to implement this approach [14, 15]. Other approaches to this problem parameterize the fundamental minimum and maximum C/O lines of the fan charts as a function of porosity with a set of 90 coefficients that have been determined from a calculated data base of 2,500 different cases [19].

An example of a C/O log in a borehole with oil in it is shown in Fig. 15.13. In the second track the C/O ratios for the two detectors are shown along with the oil holdup interpretation generated from a plot like Fig. 15.12. Using the porosity information from the open hole logging shown in track 1, the interpreted oil saturation is displayed

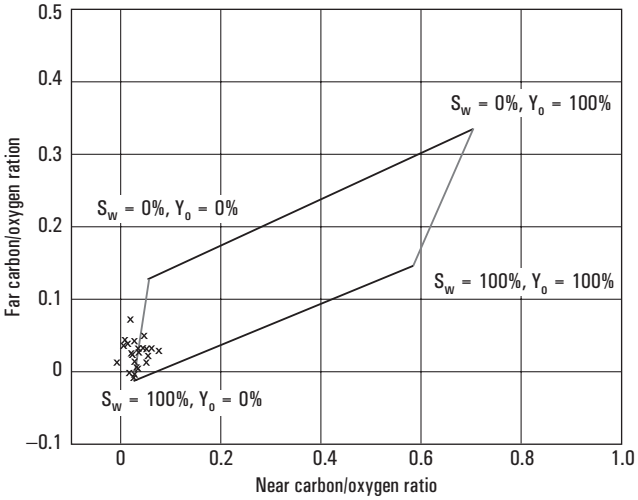


Fig. 15.12 The result of combining the fan chart response for the C/O ratio from a two-detector device is an interpretation diagram that eliminates the explicit need for porosity. The parallelogram allows an estimate of formation S_w and the borehole oil hold up Y_o from a pair of C/O ratios. The end-points of the parallelogram depend on the lithology, casing size, and hydrocarbon carbon density.

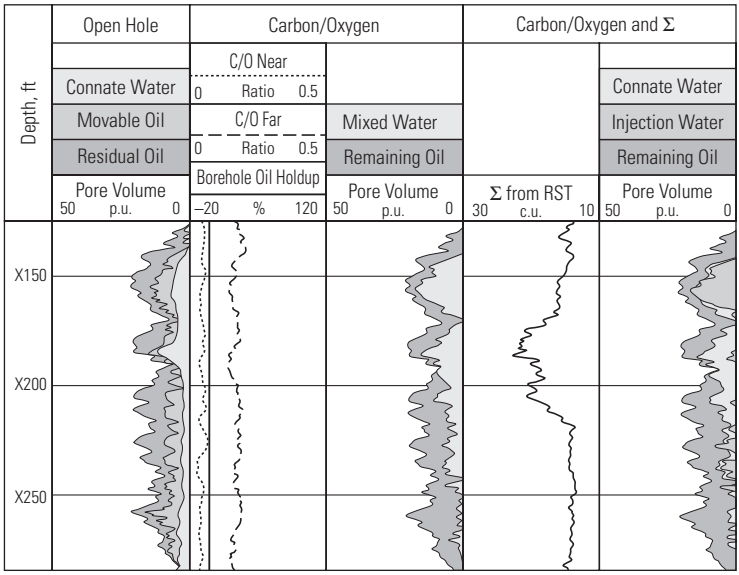


Fig. 15.13 Example of the use of a dual detector PNG tool for interpreting the oil saturation (from C/O) and progress of water flooding by including Σ and open hole porosity.

as oil and water volume in track 3. Using the measured Σ, shown in track 4, allows a further segregation of the "mixed water" volume of track 3 into connate water and injection water.

15.3.1.2 Capture Cross Section, Σ When the formation salinity is high enough, and constant, it is preferable to use Σ logging rather than using C/O for the determination of saturation for reservoir monitoring. One reason for this is that Σ logging can usually be done with greater speed due to its inherent better statistical precision compared to C/O logging. Thus the versatile C/O tools have pulsing schemes, similar to the PNC tools mentioned earlier, for separating borehole Σ from formation Σ. One improved tool design and processing scheme [20] for determining intrinsic formation Σ uses an interpolation scheme in a multidimensional data base. Rather than a parameterized interpretation solution the approach is to construct a multidimensional data base consisting of multicomponent measurements from several detectors in approximately 1,000 borehole and formation conditions. These so-called components, C_i, might be, for example, the apparent Σ_{bh} and Σ_{for} from the near and far detectors, the ratio of inelastic counting rates (during the neutron burst) from the two detectors etc. Using each point in the data base, where the desired value of intrinsic capture cross section is known, it is possible to make a linear predictor for Σ_{int} of the following form:

$$\Sigma_{int} = a_o + \sum_i a_i C_i . \tag{15.13}$$

To improve the estimate at a particular point (for a particular set of conditions and Σ_{int}), only the nearest neighbors in the data base would be used to compute the weighting coefficients a_i. To estimate the intrinsic capture cross section of a formation from a single measurement of the C_i components, in practice all of the data base is used for the estimator, but the contribution to the least-squares solution for a_i is moderated by the "distance" from each point in the data base to the "position" of the unknown formation's measured components. This process of obtaining an interpolated answer is referred to as weighted multiple linear regression.

15.3.1.3 Capture Gamma Ray Spectroscopy Another mode of operation requires waiting sufficiently long after the burst to avoid the detection of the inelastic events. In this time regime, the gamma rays result from the capture of thermal neutrons. The spectra measured in this mode are much like those shown in Fig. 15.10. The identification and quantification of elements from the capture reactions is carried out by the use of standards in the same manner as described for the inelastic spectra.

In one type of logging equipment, the timing procedure for making inelastic and capture measurements is shown in Fig. 15.14. Its features include inelastic data acquisition during the neutron burst, a background measurement period immediately following, and then, after the neutrons are thermalized, a phase that records the capture gamma rays. A portion of the background is subtracted from the early acquisition in time gate A to obtain the inelastic spectrum from which the C/O ratio is extracted.

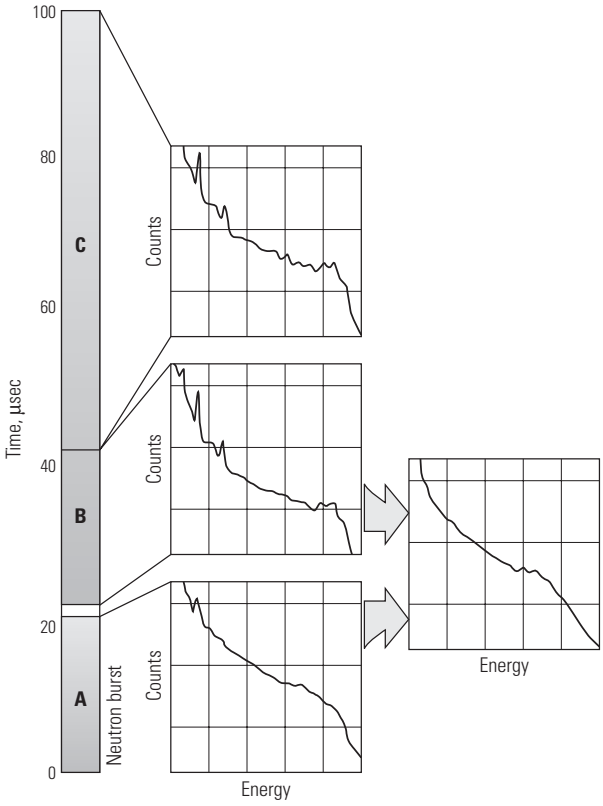


Fig. 15.14 Timing for a particular PNG device. The vertical column to the left is the time of one cycle of operation, divided into to three windows. Window A, during the neutron burst, is used to acquire data containing inelastic gamma rays and background counts from early capture events. Just after the neutron burst, in window B, the background is estimated and subtracted from the spectrum accumulated in A to get the inelastic spectra. The data accumulated in the window C contain the capture gamma rays, which are analyzed for formation elemental concentration.

From induced capture gamma rays detected in the later window *C*, a large number of elements can be identified: hydrogen, silicon, calcium, iron, sulfur, chlorine, and others. Lithology identification can be made by comparing the yields of particular elements. For example, anhydrite is easily identified by the strong GR yield from the sulfur and calcium comprising this mineral. Limestone can be distinguished from sandstone by comparing the silicon and calcium yields. Numerous references show examples of this type of procedure, as well as interpretation schemes proposed by some service companies [21, 22]. Chapter 21 further discusses the application of this measurement to the determination of formation mineralogy.

Although the foregoing description of the capabilities of inelastic and capture spectroscopy sounds very promising, there are a few problems inherent to making

this type of measurement in the borehole. One of the most important is that introduced by statistics. In the inelastic mode, the production of gamma rays characteristic of carbon and oxygen is governed by the cross sections, which are extremely small. Thus for realizable neutron generator outputs, the detected GR flux is much smaller than desired for reliable continuous logging. Another problem is associated with the distortion in the gamma ray spectrum produced by the traditional NaI detector. This type of detector does not have adequate resolution to do more than a crude analysis of the wealth of gamma rays emanating from a typical formation.

High-resolution spectroscopic devices, using solid state gamma ray detectors having energy-resolving power, orders of magnitude better than NaI were applied to the problem of mineralogical identification. However no commercial logging tool evolved beyond the novelty stage. The progress in gamma ray spectroscopy has resulted from the development of alternative, but less exotic detectors, such as BGO and GSO. The use of the former in an instrument solely dedicated to the determination of formation elemental concentrations is described in a later section.

15.3.1.4 Water Flow An early application of PNC devices was for the detection and monitoring of water flowing behind casing, as might occur in the case of a poor cementing job. The idea for this, explored by many authors, involves the irradiation of an imagined slug of water near the neutron source. There is a small cross section for an n, p reaction with ^{16}O to produce ^{16}N. This latter isotope decays, producing a gamma ray (6.13 MeV, 70% of the time) with a half-life of 7.13 s. Measurement of the delayed gamma rays at the detector, some time after the neutron burst, indicates the presence of flowing water and allows an estimate of its velocity. The considerations for making this measurement with a PNC instrument are described by Ostermeir [23] and the successful validation and operation of such a device is described by McKeon et al. [24].

The water flow measurements pioneered with early PNC devices appear to be a standard feature of the second generation pulsed neutron spectroscopy tools. One tool incorporates a third detector to facilitate the detection of oxygen activation to monitor water flow or the injection of short lived radioactive tracers [12]. In another system the measurement is made using the two C/O detectors and an additional GR tool. Figure 15.15 illustrates the process. After a burst of 14 MeV neutrons to activate the oxygen in the flowing water in the borehole, the signal arrival at the three detectors is monitored with the intent of measuring the time delay, easily converted to velocity. The width of the neutron pulse and the delay time for making the measurements can be varied to accommodate a variety of flow rates.

15.3.1.5 Oil Flow To measure oil flow, one type of tool can be run with a mechanical fluid injector [25]. The fluid to be injected consists of a gadolinium compound, chosen for its very large thermal neutron capture cross section and its ability to preferentially dissolve in hydrocarbons. The operation is initiated by injecting this special fluid, creating a plume of oil-miscible marker. The signal to be detected is the borehole capture cross section, Σ_{bh} which will show a strong variation when the highly absorbing Gd passes near the detector. The time delay between the injection of the miscible fluid and the arrival of the large Σ signal can provide the oil phase velocity.

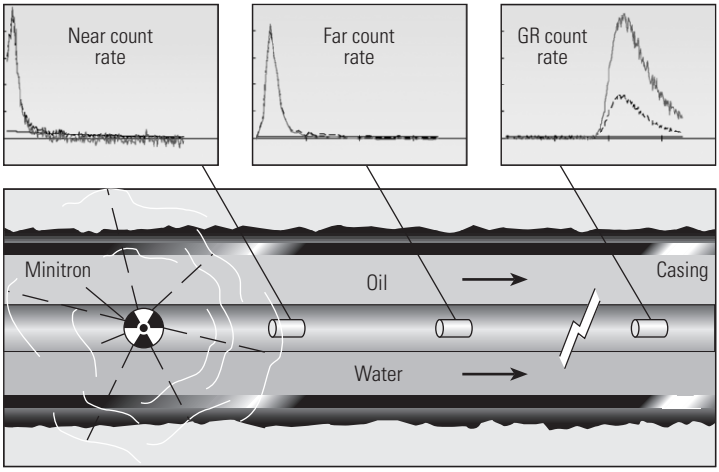


Fig. 15.15 Schematic operation of a PNG tool used to measure water flow. The burst of 14 MeV neutrons from the Minitron activates oxygen near the source. The decaying gamma rays from oxygen in the water are successively detected by the near, far, and a more distant GR detector. The delay of detection among the various detectors is used to deduce the water velocity.

15.3.1.6 Pseudo Density One intriguing possibility that exploits a pulsed source of high-energy neutrons is to perform a pseudo-density measurement. This approach might be attractive where safety reasons rule out chemical sources for the traditional gamma–gamma approach, or perhaps for the estimation of density through casing, which is quite difficult when using only the gamma–gamma approach. The idea is to exploit the inelastic gamma rays produced in the formation during the burst of high-energy neutrons [26]. The simplistic view is that nuclei (primarily oxygen) in the vicinity of the neutron source (and presumably in the formation) will act as a sort of diffuse source of gamma rays. If they are detected at two different spacings, the relative attenuation between the two gamma ray detectors could be scaled as density, since the attenuation might be largely governed by Compton scattering. One version of the versatile pulsed neutron measurement device claims to make a density measurement by including a far-spaced gamma ray detector [27]. This so-called pulsed-neutron density measurement is being pursued in LWD measurements mentioned below.

15.4 PULSED NEUTRON POROSITY

Now we consider a device that uses a pulsed neutron source with multiple neutron detectors but does not employ gamma ray spectroscopy. A device of this type [28] has been commercially available for a number of years and is employed as an alternative to the conventional neutron porosity devices discussed in Chapter 14. The

environmental and security advantages of using a pulsed neutron source rather than the conventional AmBe have already been mentioned. To perform the porosity measurement, epithermal detectors are used so that the response is more nearly proportional to the hydrogen index of the formation and lacks sensitivity to absorption variations that could otherwise affect the estimate.

To take advantage of the pulsed nature of the source, an additional interesting physical quantity – the slowing down time – is also measured. This characteristic time is strongly related to the local hydrogen content which can be translated into water-filled porosity or, in one application [28], the instrument standoff or distance from the borehole wall. The physical behavior of the epithermal neutron time distribution that allows these two applications is shown in Fig. 15.16. In the top panel the time distributions are shown for formations of hydrogen index that vary from zero to unity. The initial slope of the decay can easily be correlated with the hydrogen index of the formation. In the lower panel the time distributions are shown for a variety of standoff distances between the tool and a 0 p.u. formation. The initial slope, or other attribute of the time decay spectrum, can easily be converted to standoff distance.

The porosity estimate has a rather shallow depth of investigation but a good vertical resolution [29]. The measure of the actual tool stand off from the formation wall (a quantity that cannot be determined from the measurements of a conventional two-detector neutron porosity device) is routinely used to provide an automatic correction for one of the largest environmental factors for neutron logging. It is the additional slowing-down measurement that also allows, within limits of cement thickness, to measure the formation hydrogen index in cased wells [30].

The second benefit from the pulsed source is the measurement of capture cross section. In this tool, unlike the previous variants discussed, the measurement is made by a thermal neutron detector rather than a gamma ray detector. Thus the thermal neutron population is monitored directly, rather than indirectly by the gamma rays emitted as neutrons are captured. Compared to the gamma ray based measurement of Σ, the thermal neutron measure is somewhat shallower because the characteristic length for the process, the diffusion length, is generally much smaller than the mean free path of capture gamma rays in earth formations.

This same technology was exploited in an experimental LWD application. It was developed in a joint research project between Schlumberger and JNOC [31] and provided a measurement of neutron porosity, capture cross section, pulsed-neutron density, and the relative abundance of elements for computing mineralogy. Additionally a pair of far-spaced gamma detectors, time-gated to detect inelastic GRs provided a pseudo-density measurement that compares favorably with a companion open-hole density log as seen in Fig. 15.17. A commercial LWD service that is essentially a more mature version or this device has been recently announced [32]. It uses a ^{137}Cs source and a pair of gamma ray detectors for a traditional gamma–gamma density measurement during a phase of evaluation of the pulsed-neutron density measurement.

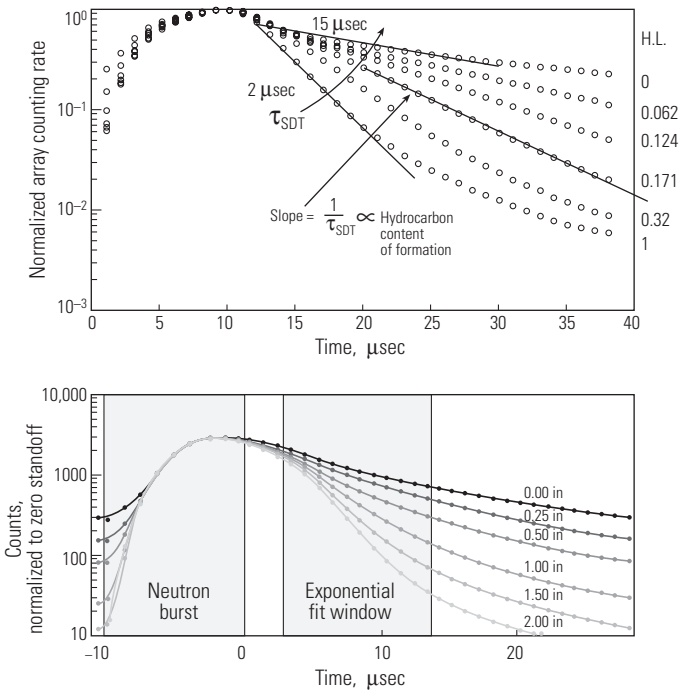


Fig. 15.16 Experimentally measured slowing-down time curves showing the epithermal neutron detector counting rate versus time. The neutron burst is on for approximately 10 μs. In the upper panel the tool is in an 8 in. borehole and in contact with formations of various porosity (or HI) The characteristic decay time (τ) is seen to vary inversely with the hydrogen index. In the bottom panel the epithermal counting rate curves are shown for various amounts of standoff (up to 2 in.) in a formation of constant porosity. In this case the characteristic decay constant can be connected to standoff.

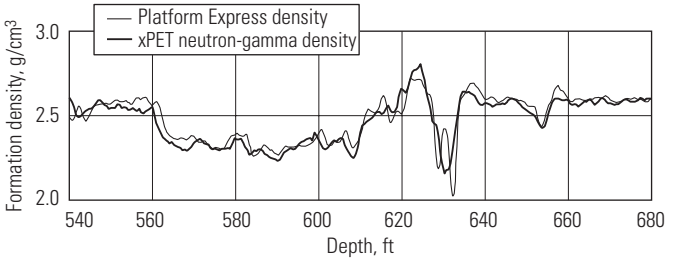


Fig. 15.17 Comparison of a wireline density measurement with a pulsed neutron density measurement in an LWD device.

15.5 SPECTROSCOPY

Finally we come to a subject that does not necessarily require a pulsed-neutron source, although it has been touched upon during the discussion of several such devices in previous discussions. The development of gamma ray spectroscopy for use in determining formation mineralogy has had a long history involving the use of chemical neutron sources. It began in the late 1970s with a spectroscopy device [33] that was capable of simultaneously measuring naturally occurring K, Th, and U; prompt capture gamma rays from Si, Ca, Fe, S, Tl, and Gd; and the activation gamma ray from Al. Although this was an interesting test bed for the idea of using elemental information to compute mineralogy, the device, a combination of 6 sondes including an early PNC device, was a cumbersome 70 ft in length and required a special low-energy ^{252}Cf neutron source – the operational difficulties exceeded the research interest. Some 10 years later a redesigned version, known as the elemental capture spectroscopy (ECS*) sonde, using a single conventional neutron source and a large spectroscopic quality BGO detector was produced along with an interpretation scheme to derive mineralogy from its measurements [34].

Here we briefly review [33] the extraction of elemental concentration (weight fractions) in the formation from the capture spectrum of a device similar to the ECS. First we begin with the spectrum detected in a sandstone formation such as that illustrated in Fig 15.18. The top trace is the total spectrum; the result of applying the weighted least-squares fitting approach with standards allows the separation of the contributions from the various elements such as Fe, Gd, Si, Cl, H, and one last portion due to the excitation of inelastic gamma rays which needs to be discarded.

In order to concentrate on elements associated with the formation, the hydrogen and chlorine portions of the spectrum are also discarded and what remains can be converted into the spectral yields – the fraction of the GR spectrum contributed by each element. The next step is to adjust the yields by the sensitivity factor for each of the detected elements. The sensitivity factor, an experimentally determined quantity, is related to the relative likelihood of thermal neutron absorption for the particular elements, the gamma ray production caused by thermal neutron absorption for the particular element, the range of gamma rays produced and their relative detectability by the spectrometer in use in the borehole environment.

To convert the relative yields to the elemental concentrations requires using a closure model. If all the elements in the formation were measured then the relative yields corresponding to each would sum to unity – the so-called closure. The closure model (where each detected element is associated with an appropriate oxide or carbonate [35]) is used to account for unmeasured elements; the largest concentration is generally associated with oxygen. The weight fraction of oxygen in most sedimentary formations is close to 50%. Thus an approximate way to think about the implementation of the oxide closure model is to simply normalize the sum of

*Mark of Schlumberger.

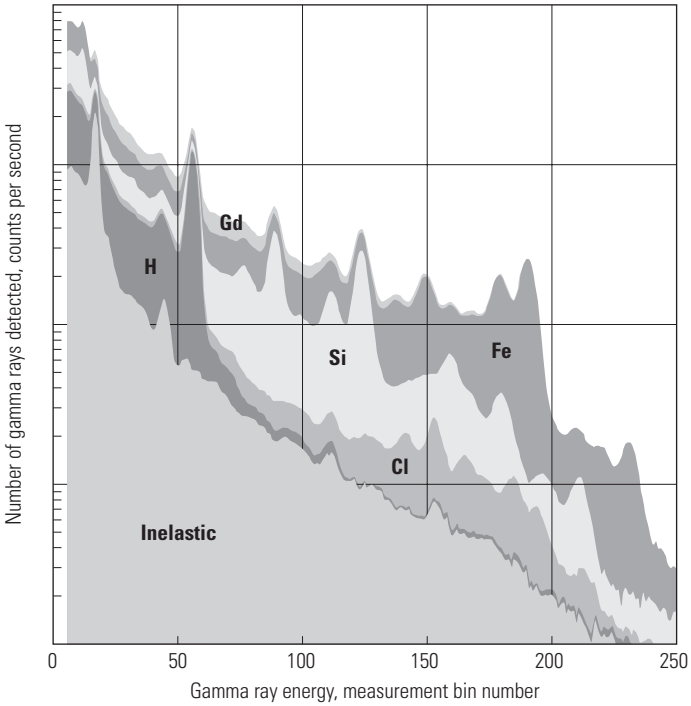


Fig. 15.18 A measured capture gamma ray spectrum from an ECS in a sandstone formation. The composite spectrum corresponds to the top trace. The partial spectra contributed by a number of elements are indicated.

the normalized yields to 50%. Obviously formations can be imagined where the oxide closure model is not going to work; for example a halite bed. Two common elements, K and Al, are not detected by capture spectroscopy, but since they occur most often in clays, they have a strong correlation with Fe and can be associated with it. However, for the most part, the derived elemental concentrations agree quite closely with core-derived values. An example of such a good comparison between log- and core-measured concentrations of Si, Ca, S, Ti, and Gd is seen in Fig. 15.19. The third track indicates that the iron spectrum is contaminated by some contribution from Al, which is no longer measured using the activation technique in the ECS tool.

The conversion of these elemental weight fractions to mineralogy is discussed in Section 21.5.

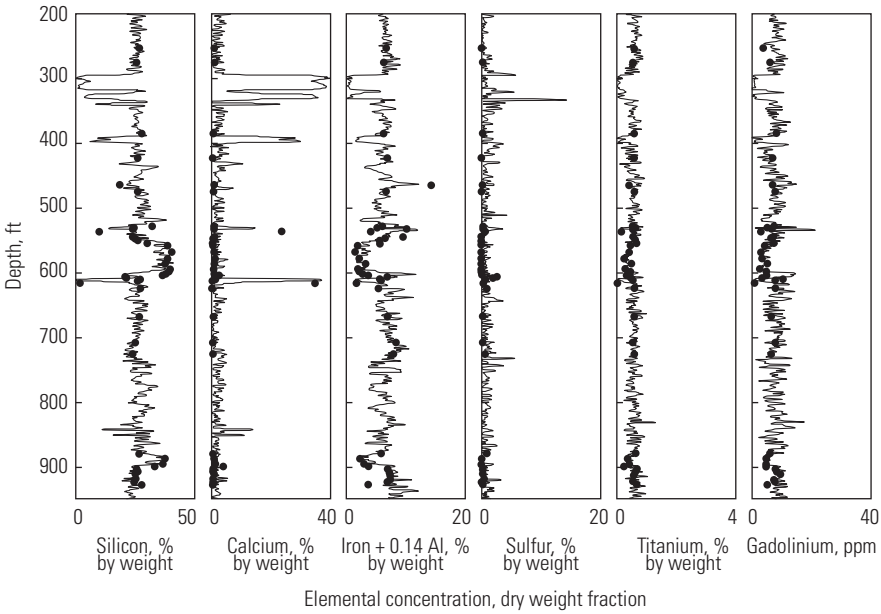


Fig. 15.19 A comparison between six elemental concentrations obtained from the decomposition of ECS capture spectra and from core analysis of a well. Note that the Fe signal is contaminated with some contribution from Al which is otherwise not measured with the instrument. Adapted from Herron and Herron [34].

REFERENCES

1. Preeg WE, Scott HD (1981) Computing thermal neutron decay time environmental effects using Monte Carlo techniques. Presented at the 56th SPE Annual Technical Conference and Exhibition, paper SPE10293

2. Schultz WE, Smith HD Jr, Verbout JL, Bridges JR, Garcia GH (1983) Experimental basis for a new borehole corrected pulsed neutron capture logging system. Trans SPWLA/CWLA 24th Annual Logging Symposium, paper CC

3. Steinman DK, Adolph RA, Mahdavi M, Preeg WE (1986) Dual-burst thermal decay time logging principles. Presented at the 61st SPE Annual Technical Conference and Exhibition, paper SPE15437

4. Smith HD, Wyatt DF Jr, Arnold DM (1988) Obtaining intrinsic formation capture cross sections with pulsed neutron capture logging tools. Trans SPWLA 29th Annual Logging Symposium, paper SS

5. Olesen J-R, Mahdavi M, Steinman DK (1987) Dual-burst thermal decay time logging overview and examples. Presented at the 5th SPE Middle East Oil Show, paper SPE15716

6. Clavier CL, Hoyle WR, Meunier D (1971) Quantitative interpretation of thermal neutron decay time logs. J Pet Tech 23(June):756–763

7. Jeckovich GT, Olesen J-R (1989) Enhancing through-tubing formation evaluation capabilities with the dual-burst thermal decay tool. Presented at the 64th SPE Annual Technical Conference and Exhibition, paper SPE 19580

8. Hoyer WA (ed) (1979) Pulsed neutron logging. SPWLA, Houston, TX

9. Kimminau SJ, Plasek RE (1990) The design of pulsed-neutron reservoir-monitoring programs. Presented at the 65th SPE Annual Technical Conference and Exhibition, paper SPE20589

10. Westaway P, Hertzog R, Plasek RE (1980) The gamma spectrometer tool, inelastic and capture gamma-ray spectroscopy for reservoir analysis. Presented at the 55th SPE Annual Technical Conference and Exhibition, paper SPE 9461

11. Hertzog RC (1978) Laboratory and field evaluation of an inelastic-neutron scattering and capture-gamma ray spectroscopy tool. Presented at the 53rd SPE Annual Technical Conference and Exhibition, paper SPE 7430

12. Gilchrist WA Jr, Prate E, Pemper R, Mickael MW, Trcka D (1999) Introduction of a new through-tubing multifunction pulsed neutron instrument. Presented at the 74th SPE Annual Technical Conference and Exhibition, paper SPE56803

13. Truax JA, Jacobson LA, Simpson GA, Durbin DP, Vasquez Q (2001) Field experience and results obstined with an improved carbon/oxygen logging system for reservoir optimization. Trans SPWLA 42nd Annual Logging Symposium, paper W

14. Hemingway J, Plasek R, Grau J, Das Gupta T, Morris F (1999) Introduction of enhanced carbon-oxygen logging for multi-well reservoir evaluation. Trans SPWLA 48th Annual Logging Symposium, paper O

15. Scott HD, Stoller C, Roscoe BA, Plasek RE, Adolph RA (1991) A new compensated through-tubing carbon/oxygen tool for use in flowing wells. Trans SPWLA 32nd Annual Logging Symposium, paper MM

16. Grau, JA, Schweitzer JS (1987) Prompt γ-ray spectral analysis of well data obtained with NaI(Tl) and 14 MeV neutrons. Nuclear Geophys 1(2):157–165

17. Oliver DW, Frost E, Fertl WH (1981) Continuous carbon/oxygen logging: instrumentation, interpretive concepts and field applications. Trans SPWLA 22nd Annual Logging Symposium, paper TT

18. Stoller C, Scott HD, Plasek RE, Lucas AJ, Adolph RA (1993) Field tests of a slim carbon/oxygen tool for reservoir saturation monitoring. Presented at the SPE Asia Pacific Oil and Gas Conference and Exhibition, paper SPE25375

19. Mickael M, Trcka D, Pemper R (1999) Dynamic multi-parameter interpretation of dual-detector carbon/oxygen measurements. Presented at the 74th SPE Annual Technical Conference and Exhibition, paper SPE56649

20. Plasek RE, Adolph RA, Stoller C, Willis DJ, Bordon EE, Portal MG (1995) Improved pulsed neutron capture logging with slim carbon-oxygen tools: methodology. Presented at the 70th SPE Annual Technical Conference and Exhibition, paper SPE30598

21. Gilchrist WA Jr, Quirein JA, Boutemy YL, Tabanou, JR (1982) Application of gamma ray spectroscopy to formation evaluation. Trans SPWLA 23rd Annual Logging Symposium, paper B

22. Flaum C, Pirie G (1981) Determination of lithology from induced gamma ray spectroscopy. Trans SPWLA 22nd Annual Logging Symposium, paper H .

23. Ostermeier RM (1991) Pulsed oxygen-activation technique for measuring water flow behind pipe. The Log Analyst 32(3):309–317

24. McKeon DC, Scott HD, Olesen J-R, Patton GL, Mitchell RJ (1991) Improved oxygen-activation method for determining water flow behind casing. Presented at the 66th SPE Annual Technical Conference and Exhibition, paper SPE20586

25. Roscoe BA, Lenn C, Jones TGJ, Whittaker C (1996) Measurement of the oil and water flow rates in a horizontal well using chemical markers and a pulsed-neutron tool. Presented at the 71st SPE Annual Technical Conference and Exhibition, paper SPE 36563

26. Wilson RD (1995) Bulk density logging with high-energy gammas produced by fast neutron reactions with formation oxygen atoms. IEEE Nuclear Sci Symp Med Imaging Conf Rec 1:209–213

27. Odom RC, Hogan GP III, Crosby BW, Archer MP (1987) Applications and derivation of a new cased-hold density porosity in shaly sands. Presented at the 62nd SPE Annual Technical Conference and Exhibition, paper SPE 38699

28. Scott HD, Wraight PD, Thornton JL, Olesen J-R, Hertzog RC, McKeon DC, Das-Gupta T, Albertin IJ (1994) Response of a multidetector pulsed neutron porosity tool, Trans SPWLA 35th Annual Logging Symposium, paper J

29. Ellis DV, Perchonok RA, Scott HD, Stoller C (1995) Adapting wireline logging tools for environmental logging applications. Trans SPWLA 36th Annual Logging Symposium, paper C

30. Scott HD, Darling HL, Toufaily AK, Wijeyesekera NI (1997) Hydrogen index and sigma measurements in air-filled boreholes and cased boreholes using an array neutron tool. Proceedings of The 3rd Well Logging Symposium of Japan, paper B

31. Evans M, Adolph R, Vilde L, Corriss C, Fisseler P, Sloan W, Grau J, Liberman A, Ziegler W, Loomis WA, Yonaza T, Sugimura Y, Seki H, Misawa RM, Holenka J, Borkowski N, Dasgupta T, Borkowski D (2000) A sourceless alternative to conventional LWD nuclear logging. Presented at the 75th SPE Annual Technical Conference and Exhibition, paper SPE 62982

32. Adolph A, Stoller C, Archer M, Codazzi D, el-Halawani T, Perciot P, Weller G, Evans M, Grant J, Griffiths R, Hartman D, Sirkin G, Ichikawa M, Scott G, Tribe I, White D (2005) No more waiting: formation evaluation while drilling. Oilfield Rev 17(3):4–13

33. Colson L, Ellis DV, Grau J, Herron M, Hertrzog R, O'Brien M, Seeman B, Schweitzer J, Wraight P (1987) Geochemical logging with spectrometry tools. Presented at the 67th SPE Annual Technical Conference and Exhibition, paper SPE 16972

34. Herron SL, Herron MM (1996) Quantitative lithology: an application for open and cased hole spectroscopy. Trans SPWLA 37th Annual Logging Symposium, paper E

35. Grau JA, Schweitzer JS, Ellis DV, Hertzog RC (1989) A geological model for gamma-ray spectroscopy logging measurements. Nuclear Geophys 4(4):351–359

Problems

15.1 Figure 15.1 shows Σ as a function of salinity. Since Σ has a linear volumetric mixing law, how do you explain the nonlinearity shown in the figure?

15.2 Show that the constant of proportionality between τ and $\frac{1}{\Sigma}$ is 4330 μs, by considering the speed of thermal neutrons and the dimensions of capture units.

15.3 Using the data of Table 23.3, compute Σ for NaCl whose density is 2.17 g/cm^3. Express the answer in capture units.

15.4 You are using a pulsed neutron device to log a well of a limestone section in a secondary recovery project. Freshwater injection wells are located in the vicinity. The original formation water was known to contain 120 kppm NaCl.

15.4.1 Construct an interpretation chart to convert Σ to water saturation as a function of density in the limestone section.

15.4.2 In the lowest section of the limestone, the porosity is 20 p.u. and the temperature is 100°C. The LLD reading is 2.75 ohm-m, and Σ is 12 cu. Calculate S_w from the laterolog and Σ. What is a reasonable explanation for the discrepancy?

15.4.3 Quantify the cause of the discrepancy.

15.5 Figure 15.20 shows a cross plot of Σ and density in a sandstone reservoir containing a water zone, a hydrocarbon zone, and a gas zone. The points associated with the gas zone have been identified. Construct on the figure an interpretation chart similar to Fig. 15.5.

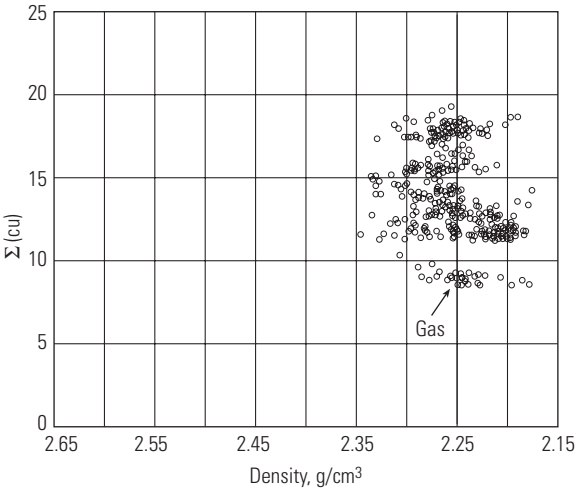


Fig. 15.20 A cross plot of Σ and ρ_b for Problem 15.5.

15.5.1 What is the estimated value of Σ_{ma}?

15.5.2 What do you estimate Σ_w to be?

15.6 In the well of Problem 5, the water resistivity is known to be 0.18 ohm-m in a zone at 115°F. Assuming that the water contains NaCl only, what value of Σ_w does this imply?

15.6.1 What is the value of S_w in the water zone, using this new input?

15.6.2 The induction log clearly sees this zone as 100% water: however, the drilling fluid is oil-based mud. What does this say about the relative depth of investigation of the Σ measurement?

15.7 From the data of Table 23.3, estimate the capture cross section of water in capture units.

15.7.1 Estimate the capture cross section in capture units, of salt water with 100 kppm NaCl dissolved. How well does it agree with Fig. 15.1?

15.8 Using the data from the logs in Fig. 15.13, and assuming that the injection water was fresh, compute the salinity of the connate water at the depth X150.

16

Nuclear Magnetic Logging

16.1 INTRODUCTION

It is remarkable that measurement of esoteric quantum properties (spin and magnetic moment) of nuclei led to a household word – nuclear magnetic resonance (NMR). Begun before World War II, the attempt to measure magnetic resonance was finally successful in 1946. Although this phenomenon was initially exploited by physicists and chemists to study matter at the molecular scale, it was not long after that the first well logging application was developed by Chevron in 1960. NMR, with its multitude of medical applications and visual diagnostic tools, enabled by ubiquitous high-powered computers and graphics algorithms, made its way into every day conversation – in a politically-correct version – as magnetic resonance imaging.

The interest of magnetic resonance for logging was initially based on this newly discovered method for detecting protons (that is hydrogen in common pore fluids) and consequently a measure of porosity. The first logging tools used in the 1960s were designed to measure just that – the free fluid index. As they relied on the earth's magnetic field, their sensitivity to hydrogen in the borehole required expensive and time-consuming mud treatment, which rather limited their utility. Thus they remained a speciality, requested by devotees of the method and not producing sufficient revenues to inspire more development. However, in the mid-1990s there was a resurgence of interest in borehole NMR sparked by an invention 10 years earlier, the "inside-out NMR" by Jasper Jackson of Los Alamos [1], as well as a great deal of NMR laboratory measurements in porous media. With new logging tool designs there came the possibility of measuring not just the porosity, but characteristics of the fluid (distinguishing between oil and water, for example) and delimiting the nature of the microstructure of

the pore structure to enable permeability estimates. In fact some enthusiasts claimed that NMR was the measurement to end all petrophysical measurements. Although we will not examine that claim in this chapter we will provide an overview of the physics of the earlier free induction decay device, as well as the modern devices with external magnetic fields that are responsible for the renaissance in application of NMR measurements to petrophysics.

To introduce the subject of nuclear magnetic logging, rather than get involved with the powerful analytical technique of NMR used by physicists and chemists, we will be concerned first with the description of the proton magnetometer. This commonly used geophysical exploration tool is directly related to one type of nuclear magnetic logging tool. A description of the magnetometer's physical principles will suffice to put the logging measurements into perspective.

16.1.1 Nuclear Resonance Magnetometers

Most nuclei have a magnetic moment. From the classical point of view each nucleus is equivalent to a tiny magnetic dipole. It is to be expected, then, that in the presence of an externally imposed magnetic field, the dipoles would tend to line up in the direction of the field lines. As we continue further with this classical description we must note that each nucleus has, in addition to a magnetic moment, an angular momentum. The angular momentum can be described by a vector which is oriented along the axis of rotation. The magnetic moment and the angular momentum are coaxial.

Two important implications exploited in NMR measurements follow from these two properties of nuclei. The first is that the existence of the magnetic moment allows electromagnetic energy (at a resonant frequency) to be absorbed by the magnetic dipole, by changing the orientation of the magnetic dipole moment with respect to the external magnetic field. The second is that the existence of the angular momentum, or spin, along the same axis as the dipole moment will tend to resist any change in the orientation of the angular momentum vector.

The interaction between the magnetic moment and an external applied magnetic field produces a torque, which in turn produces a precession of the angular momentum vector about the axis of the applied field. This precession is analogous to the precession of a gyroscope whose vector of angular momentum is off-axis from the force of gravity. In the case of the nucleus, the precession frequency is governed by the intrinsic magnetic moment and the applied external magnetic field. It is known as the Larmor frequency.

Hydrogen, since it corresponds to a single proton, is the simplest example of a nucleus of a chemical element which possesses both spin and a magnetic moment. Oxygen, on the other hand, has no magnetic moment. Water is a substance which readily exhibits nuclear magnetic polarization when a field is applied to it, and it can be used as the sensitive element of a magnetometer.

The operating principle of a magnetometer consists of using a coil to apply a magnetic field, roughly 100 times the magnitude of the earth's field, to the water sample, which may be simply a bottle of water. After a period of a few seconds, some of the magnetic moments of the protons are aligned with the external field, which

is oriented nearly perpendicular to the earth's field. This alignment of proton spins and magnetic moments in the direction of the applied magnetic field produces a net magnetic moment in the water bottle.

When the applied magnetic field is removed, the induced magnetic moment will begin to precess about the remaining field, i.e., the earth's magnetic field. The frequency of precession is proportional to the local magnetic field strength. The precession of the induced bulk magnetic moment of the sample will induce a sinusoidal voltage in the same coil as was used previously to establish the magnetic field. This effect is referred to as nuclear free induction. The measurement of the local geomagnetic field consists, then, of determining the frequency of the voltage induced in the coil.

At this stage some questions may come to mind. For example, what has this to do with a logging tool? Perhaps you are more curious about the operation of the magnetometer. Why does the polarizing field have to be applied for several seconds, rather than, say, an hour? Once the field is removed, does the Larmor precession continue indefinitely? How can this effect be exploited in logging, and what has it to do with obtaining an evaluation of a formation for the production of hydrocarbons?

16.1.2 Why Nuclear Magnetic Logging?

As we have seen from the description of the proton magnetometer, there exists a very powerful technique for identifying the free precession of protons. Of what interest is this for well logging? The answer is more apparent if one knows that hydrogen is the only nuclear species encountered in earth formations that can be easily detected by the nuclear induction technique.

The details of detectability will be discussed in a later section, but the first requirement is that a nucleus have a nuclear angular momentum and magnetic moment. Many of the common elements do not have sufficient numbers of isotopes which possess these attributes, notably carbon, oxygen, magnesium, sulfur, and calcium. The few common elements that possess the attributes will be seen to be much less detectable than hydrogen. For this reason, proton free-precession measurements in earth formations will reflect, nearly exclusively, hydrogen. Because of the technique used to measure this free precession, the only hydrogen detectable will be that associated with fluids in the formation pores, either water or hydrocarbons. The measurement will not be sensitive to the hydrogen associated with hydroxyls in clay minerals contained in shale. Thus one of the important deductions from a nuclear magnetic measurement in a wellbore is related to the porosity of the formation.

First, to understand the basis of laboratory NMR measurements of hydrogen content we begin with a review of gyroscopic behavior and the interaction of magnetic moments with magnetic fields. This is followed by some details of nuclear induction which introduces the polarization of nuclear spins of a sample, their manipulation with pulsed RF fields and the two characteristic relaxation rates and their sources.

To motivate the use of pulsed NMR in petrophysics, a discussion of the NMR properties of bulk fluids follows. They include, the HI, T_1 and T_2 relaxation times, and the diffusion coefficient. The possibility of fluid typing is linked to the determination

of diffusion coefficients by exploiting magnetic field gradients, coupled with the existence of empirical relationships between diffusion coefficients and viscosity.

To lead into petrophysical interpretation of measured relaxation rates the various sources of relaxation of protons in porous media are discussed. The measurement possibilities that have been developed include inference of pore size distributions, porosity, free-fluid volume, and permeability estimation.

Finally, turning to borehole devices, a quick description of the conventional free-induction decay tool is made followed by a description of the "inside-out" device that sparked a renaissance in NMR logging by making possible, in the borehole, many of the pulsed NMR measurements developed in the laboratory over the last 50 years. With commercial competition, several types of instruments, both wireline and LWD, have been developed, each with advantages and drawbacks that will be outlined. Sample log outputs will illustrate the various petrophysical uses to which programmable downhole NMR measurements have been put to use.

16.2 A LOOK AT MAGNETIC GYROSCOPES

The free precession of hydrogen nuclei in a magnetic field, exploited in nuclear magnetic logging, results from the fact that the nuclei possess both a magnetic moment and angular momentum, both vector quantities. Before considering the case of the nuclei, let us start with the connection between angular momentum $\overline{J}$, and the magnetic moment $\overline{\mu}$, for the case of a circulating electron with charge q_e at some distance r from the center of its orbit, shown in Fig. 16.1. In this circular path, its instantaneous velocity is v, and the angular momentum of this system is perpendicular to the plane of the orbit. Its magnitude is given by:

$$J = m_e v r, \tag{16.1}$$

where m_e is the mass of the electron.

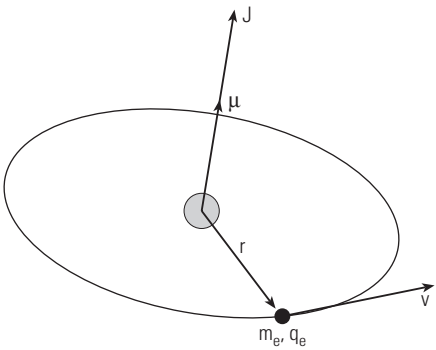


Fig. 16.1 The angular momentum and magnetic moment of a charged particle in circular orbit. From Feynman [2].

To compute the magnetic moment of this simple system, we use the expression for a circular current-carrying loop: it is equal to the current times the area of the loop. The current, which is represented by the circulating charge, is just the amount of charge per unit time passing any given point:

$$I = q_e \frac{v}{2\pi r} . \tag{16.2}$$

Since the area of the loop is πr^2, the magnitude of the magnetic moment is:

$$\mu = \pi r^2 I = \frac{q_e v r}{2} , \tag{16.3}$$

and is directed in the same direction as the angular momentum. Thus we can write:

$$\overline{\mu} = -\frac{q_e}{2m_e} \overline{J} , \tag{16.4}$$

where q_e is the charge of the electron (taken to be negative). When the quantum mechanical description of the electron is used, the relation becomes:

$$\mu = -g \left(\frac{q_e}{2m_e} \right) J , \tag{16.5}$$

where g is a factor characteristic of the atom.

Although the above calculation was for an orbital electron, it also holds for the case of a spinning charge distribution. For the pure spin of an electron, the g factor is 2. In the case of the proton, we could expect the magnetic moment to be given by:

$$\mu = g \left(\frac{q_e}{2m_p} \right) J . \tag{16.6}$$

However, for the proton the g factor is not 2 but rather 2.79 times greater. Frequently the constant $g \left(\frac{q_e}{2m_p} \right)$ is replaced by the symbol γ and is referred to as the gyromagnetic ratio.

16.2.1 The Precession of Atomic Magnets

The consequence of having a magnetic moment coaxial with angular momentum is that such an atomic particle will precess in an applied magnetic field. A magnetic field of strength $\overline{B}$ will exert a torque, $\overline{\tau}$, on the magnetic moment $\overline{\mu}$ given by:

$$\overline{\tau} = \overline{\mu} \times \overline{B} . \tag{16.7}$$

However, the torque will be resisted by the angular momentum, and instead a precession of the angular momentum vector will take place around the direction of the magnetic field vector, $\overline{B}$, such that the rate of change of the angular momentum is equal to the torque applied. The position of the angular momentum vector is shown

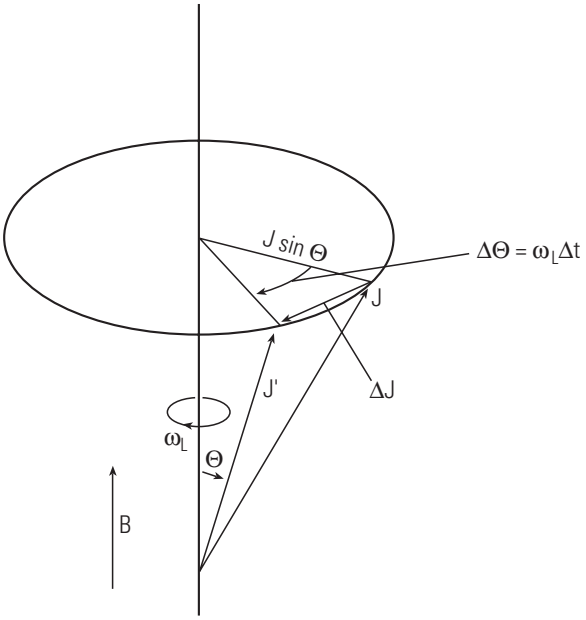


Fig. 16.2 Precession of the angular momentum of an object with a magnetic moment subjected to a torque from an external magnetic field of strength B. From Feynman [2].

at two instants in time in Fig. 16.2 to illustrate the variables necessary to define the precessional angular velocity ω_L.

In a time Δt, the angle of precession is shown to be $\omega_L \Delta t$. From the geometry, the vector change of angular momentum $\overline{J}$ is given by:

$$\Delta \overline{J} \; = \; (J \; \sin \Theta) \; (\omega_L \Delta t) \; . \tag{16.8}$$

The rate of change of the angular momentum is:

$$\frac{dJ}{dt} \; = \; \omega_L J \; \sin \Theta \; . \tag{16.9}$$

This must equal the torque ($\mu B \sin\Theta$) so that:

$$\omega_L \; = \; \frac{\mu}{J} B \; . \tag{16.10}$$

Since the ratio of μ to J is the gyromagnetic ratio, γ, the angular precession (or Larmor) rate is:

$$\omega_L \; = \; \gamma B \; . \tag{16.11}$$

When this is evaluated for the general case of any nucleus, the Larmor frequency is given by:

$$f_L \; = \; \frac{\omega_L}{2\pi} = .76 \; g \; B \; \left[\frac{kHz}{Gauss} \right] \; . \tag{16.12}$$

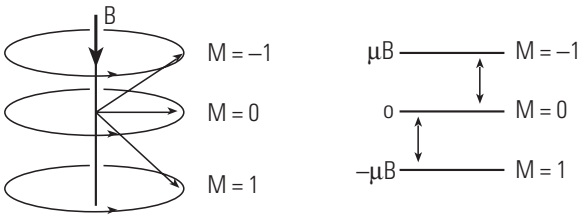


Fig. 16.3 Possible orientations of a particle of spin 1 in an external magnetic field.

For the case of the proton, g is about five (2×2.79), and the strength of the earth's magnetic field is about 0.5 Gauss, which means that the Larmor frequency is somewhere around 2,000 Hz. In modern NMR devices that use internal magnets, the fields present in the sensitive regions are much higher ($\approx \times 1,000$) than the earth's magnetic field. Consequently the operating frequency of these devices is on the order of 1–2 MHz.

16.2.2 Paramagnetism of Bulk Materials

Consider a sample of some substance that has particles with magnetic moments, such as the hydrogen atoms in water. What happens, on a gross scale, when a magnetic field is applied? Before it is applied, presumably the orientation of the magnetic moments is at random. After the magnetic field is applied, there will be more of the moments aligned in the direction of the field than away from it, and the object as a whole will be magnetized to some degree.

The magnetization $\overline{M}$, a vector quantity, is defined as the net magnetic moment per unit volume. So if each particle has an average magnetic moment $\overline{\mu}$, the magnetization will be:

$$\overline{M} = N < \overline{\mu} >, \tag{16.13}$$

if there are N particles per unit volume. The net magnetization is proportional (the constant of proportionality is known as the magnetic susceptibility) to the vector sum of the magnetic moments which will align in response to the applied field. For an evaluation of the detectability of the induced magnetic moment, the derivation of the factors involved in the magnetic susceptibility is given below.

The quantum mechanical picture of spin assigns spin values to nuclear particles in multiples of one half. The second observation is that in an external magnetic field, orientation of particles with spin and magnetic moment is limited to a number of discrete values equal to $2(J + \frac{1}{2})$*, where the spin of the particle is J. Thus for a particle of spin 1, there are three possible orientations, as illustrated in Fig. 16.3. These multiple orientations will have an impact on the total magnetization, which can be induced by an external magnetic field.*

If we consider the quantum mechanical picture of the case of particles (like hydrogen) with spin $\frac{1}{2}$ *and a magnetic moment* μ_o *(from the evaluation of Eq. 16.6 with* $J = \hbar/2$*), then there are only two possible energy states: those with spins*

aligned, and those with spin and magnetic moment opposed to the imposed magnetic field. The energy associated with the alignment, E is either $+\mu_o B$ or $-\mu_o B$. According to the Boltzmann equation, the probability that a nucleus is in one state or the other is proportional to $e^{-(E)/kT}$.

In the applied magnetic field, the number of atoms with spin up is:

$$N_{Up} = ae^{+\mu_o B/kT} , \tag{16.14}$$

and the number with spin down is:

$$N_{Down} = ae^{-\mu_o B/kT} . \tag{16.15}$$

The constant a is determined from the condition:

$$N_{Up} + N_{Down} = N , \tag{16.16}$$

where N is the total number of atoms per unit volume. From this we obtain:

$$a = \frac{N}{e^{+\mu_o B/kT} + e^{-\mu_o B/kT}} . \tag{16.17}$$

The average magnetic moment $< \mu >$ is given by the difference between the atoms aligned up and down:

$$< \mu >= \mu_o \frac{N_{Up} - N_{Down}}{N} . \tag{16.18}$$

This can be evaluated and related to the magnetization, M, by:

$$M = N\mu_o \frac{e^{+\mu_o B/kT} - e^{-\mu_o B/kT}}{e^{+\mu_o B/kKT} + e^{-\mu_o B/kT}} . \tag{16.19}$$

Figure16.4 illustrates this behavior, which is seen to be linear for values of the interaction energy small compared to kT. Under this condition, the above expression can be reduced to:

$$M = \frac{N{\mu_o}^2 B}{kT} , \tag{16.20}$$

which demonstrates the assertion that the magnetization is proportional to the applied field B. The constant $N{\mu_o}^2/kT$, or χ, is known as the magnetic susceptibility of the sample.

Now we have obtained the formalism for estimating the induced magnetism for a substance placed in a magnetic field. In order to get an appreciation of the delicate nature of the nuclear induction technique, let us first look at the question of how many nuclei are actually participating in the production of the induced magnetic moment.

Consider the case of protons in a sample of water. Because of the presence of the applied field, a certain number of protons will be in the up state and a certain number in the down state. The ratio of these two numbers can be found from the Boltzmann distribution to be:

$$\frac{N_{Up}}{N_{Down}} = \frac{e^{\mu_o B/kT}}{e^{-\mu_o B/kT}} . \tag{16.21}$$

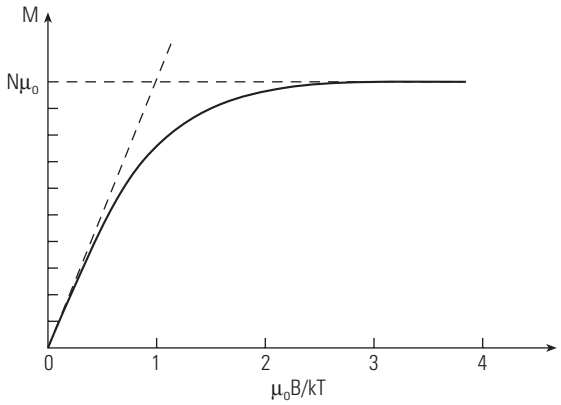


Fig. 16.4 The variation of induced magnetic moment as a function of the magnetic field strength. From Feynman [2].

In the case of a small magnetic interaction energy, compared to the thermal energy kT (which is always the case except at very low temperatures), this reduces to:

$$\frac{N_{Up}}{N_{Down}} \approx 1 + 2\frac{\mu_o B}{kT}. \tag{16.22}$$

If this is evaluated for a relatively large magnetic field (10,000 Gauss) at room temperature, we find that about 10 out of 10^6 nuclei are contributing to the internal polarization of the sample. A rough calculation for water indicates that the induced field is about 10^{-6} Gauss. Thus it can be seen that the direct detection of the magnetic moment will be somewhat difficult. It is for this reason that resonance electrical methods are used.

The next section examines the sensitivity of detection in the case of nuclear induction. It will give a better idea of why the only nuclei of practical detectability in borehole experiments are the protons of hydrogen.

16.3 SOME DETAILS OF NUCLEAR INDUCTION

The process of NMR involves some basic steps that are common for laboratory measurements or similar implementations adapted for borehole measurements. The first step is the alignment of protons in an external magnetic field. In one early logging application the earth's magnetic field provided the polarization, albeit weak. However, laboratory measurements and all modern NMR logging instruments impose an external magnetic field on the sample to produce the initial proton magnetic moment alignment. The time constant associated with the polarization is called the longitudinal time constant, or T_1.

In a second step, to produce a measurable signal, the polarized protons are then rotated by 90° to the "transverse plane" by applying a magnetic field at the appropriate

Larmor frequency, "in resonance" with the precessing protons aligned with the external field. Once rotated, the polarized protons continue their precession, but now in a plane perpendicular to the polarizing field, creating an easily detectable fluctuating magnetic field. The protons begin to dephase rapidly and this so-called transverse magnetic field disappears rapidly.

Depending on the instrument, much of the dephasing of the proton precession in the transverse plane might be caused by imperfections in the polarizing magnetic field at the location of the proton. These dephasings are reversible and do not really belong to the interesting physical sources of irreversible dephasing. These latter sources of dephasing are described by a characteristic time constant, T_2. Many so-called pulse echo schemes, consisting of polarizing pulse sequences, have been devised to overcome the reversible dephasing and will be discussed later.

16.3.1 Longitudinal Relaxation, T_1

We saw earlier that the application of a magnetic field produces an induced magnetic moment in the sample which is proportional to the applied field strength B. The mechanism behind this induced magnetic moment is the redistribution of the protons between higher- and lower-energy states. But how quickly is this redistribution of states achieved?

To examine this process qualitatively, let us define n as the difference between the number of spins per unit volume in the upper state and those in the lower-energy state:

$$n = N_{Up} - N_{Down} . \tag{16.23}$$

We now assume some probabilities, P_+ and P_-, which give the probability per unit time that a nucleus will make an upward or downward transition. These two probabilities, yet undefined, can be shown to be unequal. *This can be seen by considering the condition of equilibrium which will be attained at some later time. From the definition of equilibrium, the number of transitions between upper and lower levels must be equal. This can be expressed as:*

$$P_- N_{Up} = P_+ N_{Down} , \tag{16.24}$$

or by taking the ratio:

$$\frac{P_+}{P_-} = \frac{N_{Up}}{N_{Down}} \tag{16.25}$$

$$\approx 1 + 2\frac{\mu_o B}{kT} . \tag{16.26}$$

Consider now the approach to equilibrium: An upward transition increases n by 2, and a downward transition decreases it by 2. Thus on a unit time basis we can write:

$$\frac{dn}{dt} = 2N_{Down} P_+ - 2N_{Up} P_- . \tag{16.27}$$

Returning to the previous practical example of a water sample in a relatively large field of 10,000 Gauss, the two probabilities differ from one another by very little. They can be replaced with a suitable average P (the absolute difference between the up and down probability), so that we can write:

$$\frac{dn}{dt} = -2P(N_{Up} - N_{Down}) = -2Pn\,. \tag{16.28}$$

The solution to this is simply:

$$n = n_o e^{-t\times 2P} + c = n_o e^{-t/T_1} + c, \tag{16.29}$$

where the time constant T_1 is referred to as the spin-lattice or longitudinal relaxation time. To determine the value of the two constants in the solution, consider that as $t \to \infty$ the difference between the up and down states becomes a maximum, n_{max}, so the value of the constant c is n_{max}. At time $t = 0$, when no magnetic field is applied, the difference between the numbers in the two states is zero and consequently $n_o = -n_{max}$. Note also that the induced magnetization M is proportional to the difference in the up and down states, n, so that we can write:

$$M \propto n = n_{max}(1 - e^{-\frac{t}{T_1}}) \tag{16.30}$$

Figure 16.5 shows this behavior, in the central graph, computed for a small collection of protons with an arbitrary 5% chance of making the upwards transition and a 0.5% chance of making a downward transition, per unit time. At the top and around the edge of the central graph are a series of five panels that represent the spin orientation of the protons. The evolution of the spin orientations is shown as time increases. In the top panel, at the onset of the numerical experiment, there is no net magnetization in the direction of the applied field, because of the random orientation of the magnetic moments. As soon as the polarizing magnetic field, B_o is applied, at time = 0, the projections of the spins line up either in the direction of the applied field or opposed to it, still with no net magnetization. For clarity, the angle between the spin and the direction of the magnetic field has been greatly reduced from the 54° that it should be for a particle of spin $\frac{1}{2}$ (see Problem 16.3). At each time step, the number of spin transitions, from up to down and from down to up, are computed and the excess is plotted in the central figure along with the prediction of net magnetization from Eq. 16.30. Two of the panels show the condition of the polarization after 10 and 20 units of time. In the final panel, after 100 units of time, the polarization is well into equilibrium at 110 particles (see Problem 16.6.2).

In the simulation described above, T_1 can be computed from the imposed transition probabilities. However, in general, the parameter T_1 quantitatively describes the observed rate of change of magnetization in a sample, which can only occur as the nuclei give up or absorb quanta* of energy from the surroundings. This might result

*This is where the "R" in NMR comes from. The quanta that cause the spin flipping have an energy $E = h\nu_o$ where $\omega_o = 2\pi\nu_o$ is the Larmor angular frequency of the protons in the polarizing magnetic field B_o. Only quanta of this energy can flip the spins and hence it is referred to as a resonance.

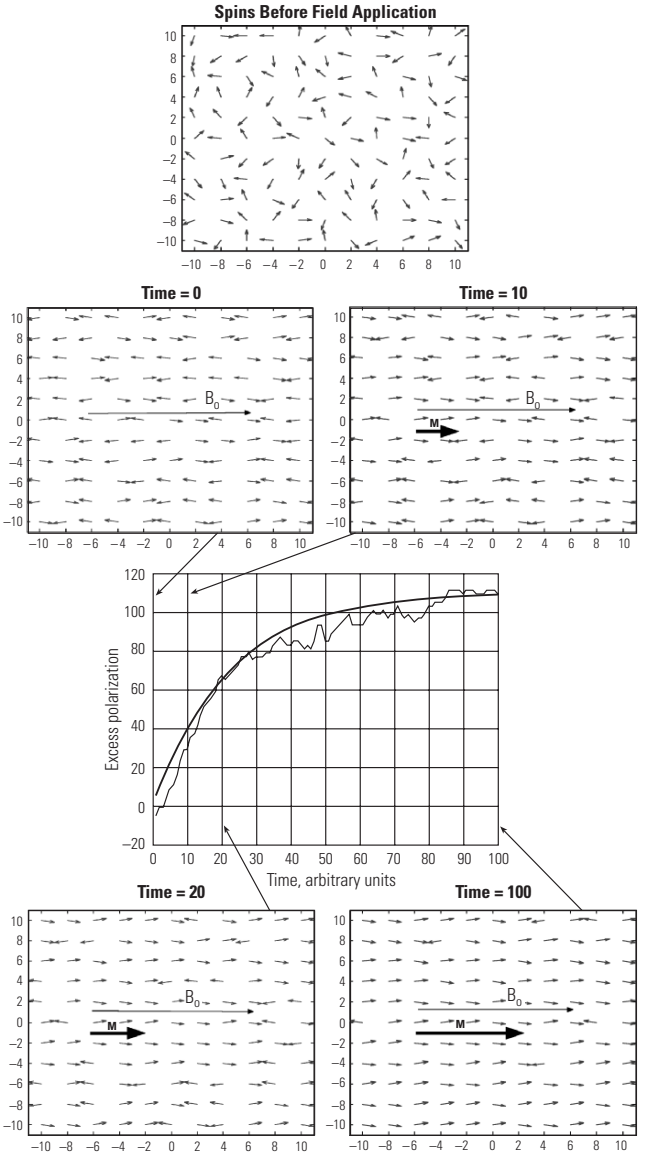


Fig. 16.5 The evolution of induced magnetization in a sample of 121 protons where the probability, per time step, of alignment is 5% and that of opposition is one tenth that value. The central figure shows the computed and predicted growth of induced magnetization, defined as the difference between aligned and anti-aligned protons. The panels around the periphery allow visualization of the state of the spin alignment at various times. At the top, before the field is applied, spins are randomly oriented; at $T = 0$, the spin projections are aligned with, or opposed, to the field B_o with equal probability. The next two panels show the state of polarization at 10 and 20 time steps. The final panel shows an equilibrium state calculated at 100 time steps.

from fluctuating magnetic fields arising from protons in other molecules in thermal agitation. The surrounding molecules which can absorb or transmit this energy via a fluctuating magnetic field are collectively called the lattice, since the earliest workers in this field were solid state physicists. The value of the spin-lattice or longitudinal relaxation time, T_1, varies considerably with the type of nucleus and environment.

To understand the measurement of T_1 it is useful to introduce the concept known as the rotating frame, and a technique of magnetic field pulsing for manipulating the polarized spins. The discussion will lead naturally to another important relaxation time constant known as T_2.

16.3.2 Rotating Frame

To understand the measurement of relaxation times, we abandon the quantum view and look first at a particular experimental procedure of the nuclear induction measurement. As indicated in Fig. 16.6, a spherical sample is placed in a large uniform steady-state magnetic field. After a time longer than T_1, the magnetic moment M of the sample

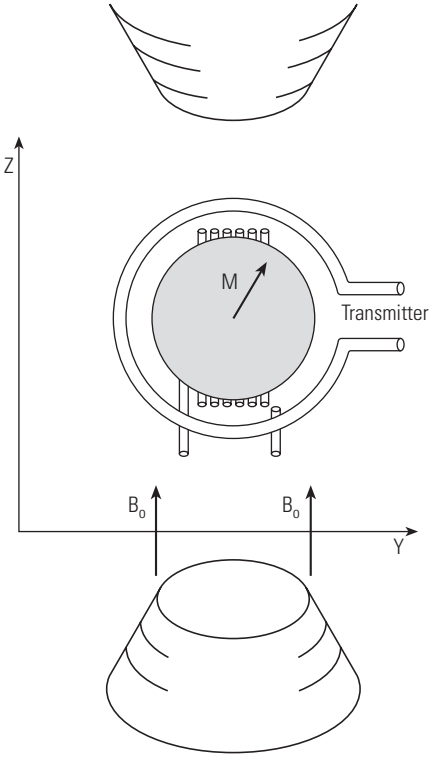


Fig. 16.6 Experimental setup for observing the decay of nuclear induction. Adapted from Bloch [3].

will line up with this constant field. We have already seen that the magnitude of this induced magnetic field is rather small and that to observe it another technique will be needed.

One of the common laboratory techniques for observing the induced magnetic moment is to produce a much weaker alternating magnetic field at right angles to the principal field by pulsing another coil oriented for this purpose. The frequency of this alternating field (produced by a coil, encircling the sample, as indicated in the figure) is chosen to be exactly the Larmor frequency of the magnetic moments in the principal field B_o.

To see the effect of this second, alternating field (B_1), it is convenient to make use of a rotating coordinate system (x', y', z') which has an angular frequency equal to the Larmor frequency. In this system, initially, the sample magnetization is aligned with the z-axis as shown, on the left, in Fig. 16.7. The alternating magnetic field produced by the additional coil will appear stationary in the new frame of reference, illustrated on the right.

Viewed in this frame, the magnetic vector $\overline{M}$ will begin to rotate about the new applied field and to deviate from its initial direction. Of course, the deviation from its initial z-axis direction will induce Larmor precession at a frequency of γB_o, but in the rotating frame of reference it will appear stationary and will just begin to tilt. The tilting, in fact, is due to the magnetic vector trying to precess (although at a much lower frequency due to the weak oscillating field strength) around the new field, B_1. The rotation of $\overline{M}$ away from the z-axis can be controlled by pulse parameters – the strength and length of time during which the oscillating field is left on.

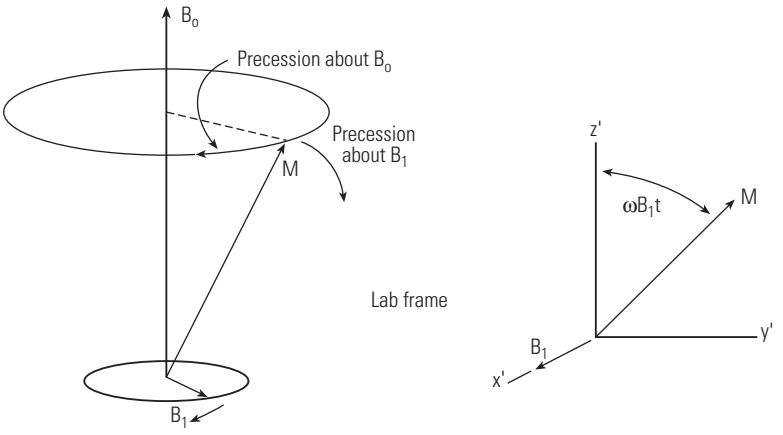


Fig. 16.7 Two views of the motion of the magnetization vector M produced by the stationary polarizing field H_o and perturbed by the rotating field H_1. In the rotating frame, M is seen to rotate away from the z'-axis linearly with time.

16.3.3 Pulsing

In order to maximize the signal from the precessing bulk magnetic moment, $\overline{M}$, the rotation angle is made 90°, as shown in the upper portion of Fig. 16.8. This is referred to as a 90° pulse. After the pulse is applied, the magnetization vector, seen in the laboratory frame, right, begins to rotate in the $x - y$ plane as indicated. If this magnetization vector is contained within a coil, below, it will induce, because of the changing flux linkage, an alternating signal. Now the induced signal in the coil should ideally pick up a sinusoidal signal as $\overline{M}$ rotates in the $x - y$ plane, which gradually decays with a time constant T_1 as $\overline{M}$ begins to align, because of thermal relaxation, with the z-axis. However, it is observed to decay with another, faster, time constant T_2^*. To separate T_1, the relaxation that depends on the physics, from the relaxation that depends on the experimental setup, a more complicated procedure is required.

One method of measuring T_1 is called saturation recovery. It is a double pulsing method, in which the first pulse prepares the spins and the second allows them to be measured. As stated earlier, to improve detectability (since for most materials the induced magnetic field is extremely small) the magnetization vector is rotated first with a 90° pulse so that a measure of the initial polarization amplitude can be made from the envelope of the free induction decay. Part of that decay is caused by the loss of spins that have flipped back to the direction of the polarizing magnetic field. It is these spins that we wish to measure. After some short (compared to the anticipated value of T_1) time interval τ, another 90° rotation is made. The detectable vector then precessing in the transverse plane will consist solely of the spins that had flipped back to the initial field direction during the time τ. If this sequence – polarization,

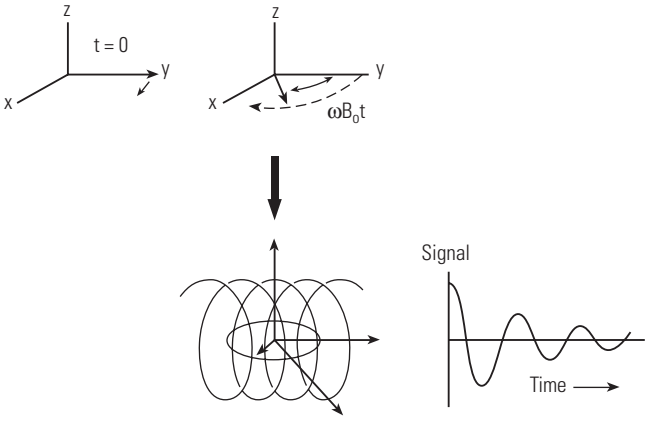


Fig. 16.8 The condition for obtaining maximum signal from the nuclear induction experiment. The magnetization vector has been rotated by 90° away from the z-axis. The coil which contains the rotating system will have a decaying sinusoidal voltage induced as sketched. Adapted from Fukishima and Roeder [4].

followed by a 90° flip, an increased delay time τ, and the second 90° flip – is repeated a number of times, the saturation curve evolution over a time t (i.e., $1 - e^{-t/T_1}$) can be deduced from the series of amplitude measurements made after the second flips.

16.3.4 Transverse Relaxation, T_2, and Spin Dephasing

Now we come to another relaxation time of interest, T_2. It is related to the dephasing of the nuclear spins that are the result of local field inhomogeneities, among other things. The sources of this widely quoted relaxation mechanism are best examined by returning to the situation after the magnetic vector $\overline{M}$ has been rotated by 90°. Figure 16.8 shows a schematic representation of the signal induced in the receiver coil by the free precession of the magnetization vector and referred to as the free induction decay. The envelope will often appear as an exponential decay with a characteristic time constant T_2^*. The signal decays with a relaxation rate faster than that expected from the value of T_1.

One source of this apparent decay comes from the behavior of the individual spins that contribute to the rotated vector $\overline{M}$ – they should all be rotating together at the Larmor frequency. However, for one reason or another, they do not rotate at exactly the same frequency. Thus in time they begin to noticeably get out of phase. In doing so, the magnitude of the vector $\overline{M}$ will decrease with time. Alteration of the spin-precession frequency can come from the mutual interaction (spin–spin) of the proton spins, or local field inhomogeneities. The apparent decay time will be composed, in part, of the spin–spin interactions (T_2), as well as a component due to local field inhomogeneities.

Another cause of the signal decay will be, not the dephasing, but the reorienting of the rotated spins to the direction of the primary field that has remained on. Since the primary magnetic field has remained on, the z-component of the source magnetization will increase from its initial value of zero to a final value of M, with a characteristic time constant T_1 which is generally much longer than T_2 except in bulk liquids. Another source of dephasing, of interest for protons in fluids contained in pores, concerns interaction of the proton spins with spins in the pore walls and will be discussed later. All of the sources of relaxation (or signal decay) that are not reversible are lumped into the quantity referred to as T_2.

The source of the decaying field, resulting from magnetic field inhomogeneity, can be understood by considering the state of the magnetized vector $\overline{M}$ in the rotating system after application of the 90° pulse. The time evolution is suggested in Fig. 16.9. After the $\overline{M}$ vector has been rotated by 90° it is seen at its maximum along the y′-axis. If there are slight field inhomogeneities at various parts of the sample, then each of the protons may have a slightly different precessional frequency. In regions where the field is slightly larger by an amount δB the protons will precess at a slightly faster rate, $\gamma(B_o + \delta B)$. After a time t these protons will have advanced by an amount $(\gamma\, \delta B)t$ radians over the ones precessing in the nominal field B_o. The converse is true for the protons that find themselves precessing in a slightly smaller field. In time, the spins from these various regions will tend to separate. As time progresses the spins dephase, decreasing the size of the y′-axis projection.

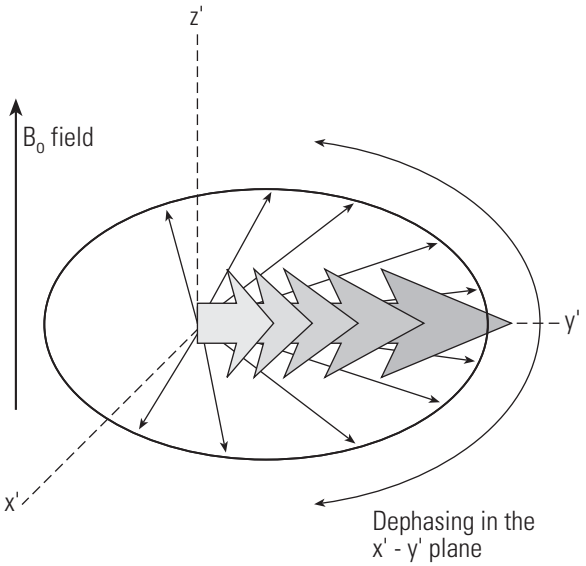


Fig. 16.9 Behavior of the transverse component of the magnetization vector M during free induction decay. The initial synchronization of the protons is lost, over time, by inhomogeneities in the B_o field and molecular interactions. The decrease of the transverse component also reflects the reorientation of the induced magnetic field M to the direction of B_o with time constant, T_1.

16.3.5 Spin Echoes

Once the proton spins have been tipped into the transverse plane (perpendicular to the polarizing field B_o) they precess at the Larmor frequency, but they are seen to dephase with time. This is the situation depicted in panels (a) and (b) of Fig. 16.10. To make a measurement of T_2 that reflects the spin relaxation rate caused by the spin–spin interactions of the protons arising from other fluid molecules or molecules at the pore surfaces, it is necessary to remove from the measurement any reversible dephasing. The type of reversible dephasing described earlier was directed to spatial inhomogeneities in the polarizing field B_o. For this purpose, a number of pulsing sequences have been developed.

By applying another pulse of about twice the duration of the 90° flipping pulse the entire arrangement of proton spins can be flipped around their position on the transverse plane so that now the slower-precessing protons will lead, and the faster ones will follow. This concept is illustrated in panels (c) and (d) of Fig. 16.10. In time the spins, in their precession around the polarizing field B_o, will coincide (before smearing apart again) to create a local maximum of coherent magnetic field called a "spin echo." After the smearing out has occurred, at a time T_e after the last pulse, another flipping pulse can be applied starting the process over again. The procedure can be repeated many times if the echo spacing, T_e, is small compared to the T_2 of

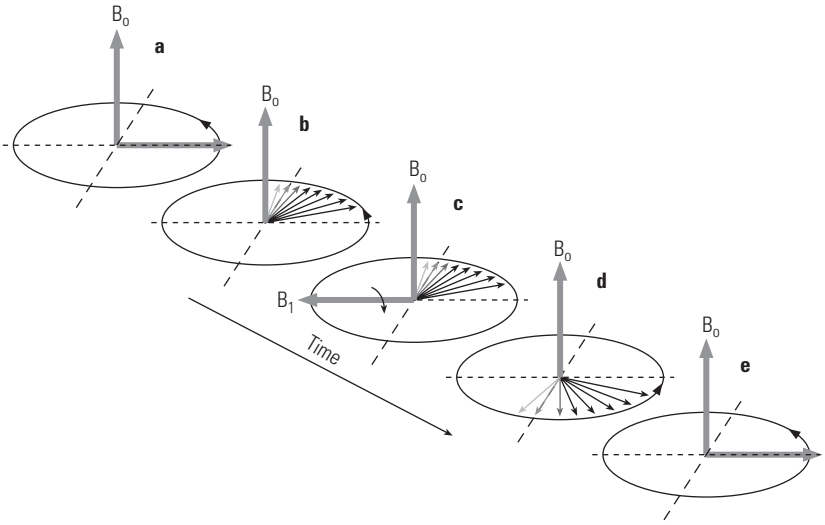


Fig. 16.10 A visualization of the Carr–Purcell pulsing scheme to defeat reversible dephasing of the protons in a slightly inhomogeneous field. In panels (a) and (b), the spins begin to dephase. In panel (c), a field is applied of sufficient magnitude and duration to rotate (precess) the fanned-out spins by 180° so that they appear in reverse order in the longitudinal plane. In frame (e) the spins have rotated to produce a local maximum, since the fastest have caught up with the slowest. It is this configuration of spins that produces the "pulse-echo." Courtesy of Schlumberger.

the sample. The appearance of the detected wave train is shown in Fig. 16.11. This pulse sequence is referred to as the CPMG pulse train after its inventors Carr and Purcell [6], and Meiboom and Gill [7].

As can be seen from the figure the echo amplitudes decrease with time because there are sources of relaxation that are not reversible, like the random interactions with the spins of other molecules in the fluid or nearby surfaces. The spin-echo technique just takes care of small magnetic field inhomogeneities. It is the time constants associated with the decreasing echo amplitudes that will reveal a wealth of information regarding the pore geometry and its contents.

16.3.6 Relaxation and Diffusion in Magnetic Gradients

Now we take a moment to explore the ramifications of, not the random inhomogeneities of the polarizing field but the presence, deliberate or otherwise, of a strong spatial gradient in the polarizing field. To facilitate discussion the sample is considered to be a bulk liquid. If there is a magnetic field gradient in the sample volume, then after the 90° flip of the CPMG pulse sequence, some of the protons will migrate to some new position where a slightly different magnetic field is present and their frequency will shift slightly, in proportion to their displacement. To keep the random field effects in check, the CPMG sequence was developed to flip the magnetization

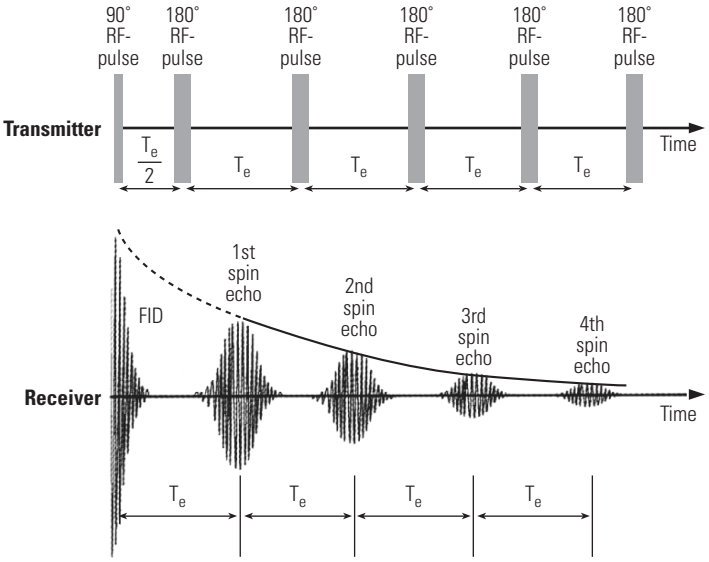


Fig. 16.11 A representation of the sequence of operation of a logging tool utilizing the CPMG sequence. The first pulse, in the top frame, rotates the spins to the transverse plane, where they are seen to decrease in magnitude in the free induction decay mode. Then, in the upper panel, a pulse is emitted to flip the spins by 180°, that is shortly followed by a build-up and decay, in the lower panel, of the spins in the "echo." The application of the 180° pulse is then repeated at regular intervals for up to thousands of times. The maxima of the spin-echo amplitudes decays with the time constant T_2. Adapted from Appel [5].

vector and produce the spin "echoes." However, for particles that have been displaced by diffusion to a new field value, their Larmor frequency will change and as time progresses, the smearing, despite the 180° flips, will continue to grow, reducing the number of available spins for a coherent signal. This is an instance of a nonreversible relaxation and it will add to the so-called T_2 decay rate, decreasing the amplitude of the magnetization in the transverse plane:

$$\frac{1}{T_2} = \frac{1}{T_{2B}} + \frac{1}{T_{2D}}, \tag{16.31}$$

where $\frac{1}{T_{2B}}$ is the decay rate associated with the bulk fluid and $\frac{1}{T_{2D}}$ is the decay rate associated with the magnetic field gradient. As shown in the appendix this additional decay rate is proportional to the square of the gyromagnetic ratio (γ) and the gradient (G) and the product of the diffusion coefficient (D) and the square of the time T_e (known as the echo spacing) between the 180° CPMG pulses:

$$\frac{1}{T_{2D}} = \frac{(\gamma G T_e)^2 D}{12}. \tag{16.32}$$

We will see later how this effect can be exploited to measure the coefficient of diffusion, which might be related to the viscosity of the fluid, and how its time evolution can be used to learn more about the geometric shape of the pore structure.

16.3.7 Measurement Sensitivity

It is of interest to calculate the detection sensitivity of a nuclear induction measurement. For simplicity, we take the case of a coil enclosing a sample in a uniform magnetic field of strength B_o, where a magnetic moment M has been produced in the sample at right angles to the field B_o. The flux F, which will be intercepted by the coil as the magnetic moment M rotates at the Larmor frequency, will depend on the coil details: its area, A, and number of turns, N_t. The flux may be written as:

$$F \propto N_t \; A \; M \; \sin(\omega t) \; . \tag{16.33}$$

From the law of induction, the voltage, V, induced in the coil, will be proportional to the time rate of change of this flux:

$$V \propto \frac{dF}{dt} \propto N_t \; A \; M \; \omega \; \cos(\omega t) \; . \tag{16.34}$$

The magnitude of M is proportional (where the constant of proportionality is the magnetic susceptibility, χ, see Eq. 16.20) to the initial polarizing field B_o. Thus the signal induced can be written as:

$$V \propto N_t \; A \; \chi \; B_o \; \omega \; \cos(\omega t). \tag{16.35}$$

The quantum mechanical version of susceptibility depends on the nuclear spin, J, and the gyromagnetic factor γ (accounting for the multiple orientations of the magnetic moment and consequent decrease of magnetization). It is given by:

$$\chi \; = \; N \frac{J(J+1)}{3kT} (\gamma \hbar)^2 \; . \tag{16.36}$$

Substituting the frequency relation for B_o (i.e., $\omega = \gamma B_o$ from Eq. 16.11) gives the final result for the voltage:

$$V \propto N_t \; A \; N \frac{J(J+1)}{3kT} \hbar^2 \gamma \omega^2 \; \cos(\omega t) \; . \tag{16.37}$$

An evaluation of Eq. 16.37, along with a few more details, indicates that a sample of 2 cm^3, completely enclosed by the detection coil, will generate a signal of a few millivolts for a strong field of 1,800 Gauss.

It is the relationship in Eq. 16.37, the product of $J(J+1)\gamma\omega^2$, which is used to establish the relative sensitivity of detection of various isotopes as shown in Table 16.1. For a logging application, the fear of interference for the proton signal would come from spins associated with fluids that would be capable of having relatively long relaxation times. For borehole logging, the only species of any consequence (in solution)

Table 16.1 Properties of nuclear species. $\nu_o = \omega_o/2\pi$. μ_N is the magnetic moment of the neutron. Adapted from Davis [9].

Isotope	ν_o for 10,000-Gauss field (MHz)	Relative sensitivity for equal numbers of nuclei			μ (in units of μ_N)	J (in units of $\hbar$)
		Natural abundance (%)	At constant field	At constant frequency		
n_1	29.167	—	322	0.685	−1.91315	1/2
H^1	42.576	99.9844	1.000	1.000	2.79268	1/2
H^2	6.357	1.56×10^{-2}	9.64×10^{-2}	0.409	0.85738	1
B^{11}	13.660	81.17	0.165	1.60	2.6880	3/2
C^{13}	10.705	1.108	1.58×10^{-2}	0.251	0.70220	1/2
N^{14}	3.076	99.635	1.01×10^{-3}	0.193	0.40358	1
N^{15}	4.315	0.365	1.04×10^{-3}	0.101	−0.28304	1/2
O^{17}	5.772	3.7×10^{-2}	2.91×10^{-2}	1.58	−1.8930	5/2
F^{19}	40.055	100	0.834	0.941	2.6273	1/2
Na^{23}	11.262	100	9.27×10^{-2}	1.32	2.2161	3/2
Al^{27}	11.094	100	0.207	3.04	3.6385	5/2
P^{31}	17.236	100	6.64×10^{-2}	0.405	1.1305	1/2
Cl^{35}	4.172	75.4	4.71×10^{-3}	0.490	0.82091	3/2
Mn^{53}	11.00	—	0.361	5.41	5.050	7/2
Co^{59}	10.103	100	0.281	4.83	4.6388	7/2
Sn^{119}	15.87	8.68	5.18×10^{-2}	0.373	−1.0409	1/2
Tl^{205}	24.57	70.48	0.192	0.577	1.6115	1/2
Pb^{207}	8.899	21.11	9.13×10^{-3}	0.209	0.5837	1/2
Free Electron	27.994	—	2.85×10^{-8}	658	−1836	1/2

is that of Na associated with saltwater. From the table it can be seen to be about 30% more detectable than hydrogen at a constant frequency. Since the concentration of Na, even in highly salt-saturated solutions, is rather small compared to hydrogen, it would be of marginal detectability in the type of experimental setup described above. The sensitivity to Na of the first generation logging tool, described in a later section, is even poorer because of its mode of operation.

However, in some versions of modern NMR logging tools that use dipole magnets, whose fields decrease as the inverse square of the distance from the tool/magnet center-line, the situation is a bit different. In such a tool the operating frequency is chosen so that protons resonate in a volume, far enough from the tool to be in the formation. It is easy to show that the radius of resonance for Na will be at about half that distance. If that distance happens to be in the borehole, filled with very salty mud, there will be a considerable effect. For one tool [8] the effect is the equivalent

of several porosity units per 100 kppm of NaCl in the mud. Specially devised charts allow for the correction of this effect or it can be eliminated by using an attachable device, called a fluid excluder, around the tool.

16.4 NMR PROPERTIES OF BULK FLUIDS

Since the protons examined in petrophysical applications with laboratory and borehole instruments are associated with fluids saturating porous rocks, it is appropriate to look at some of the properties of fluids to note their relation to NMR-measured properties. For fluids there are four quantities of interest for NMR measurements: the hydrogen index, the longitudinal relaxation time T_1, the transverse relaxation time constant T_2, and the diffusion coefficient which can be related to viscosity. We begin with the most obvious important quantity, the hydrogen index (HI) mentioned earlier in Chapter 13.

16.4.1 Hydrogen Index

Since the magnitude of the NMR signal will depend on the proton density associated with the fluids, it is the hydrogen concentration that needs to be computed to estimate variations among fluids. The convenient scale is the HI which compares the hydrogen concentration of the fluid in question to that of water at STP. Although this concept is simple, the details arising from practical applications can become complicated.

As a simple first example, in brines routinely encountered in geological formations, the HI is reduced as the concentration of NaCl increases in the brine (see Section 14.8). Also, pure hydrocarbons may have different hydrogen densities than water depending upon their molecular structure and their bulk density. Regardless of the details of the computation of the hydrogen density of the hydrocarbon, it needs only to be compared to 1/9, the hydrogen density in water. Appel [5] presents a convenient summary of the computation of HI for brines, gas, and hydrocarbon mixtures. In the latter case the mass density and H:C ratios for the various components must be known.

Another approach for some indication of the HI of crude oils, with no gas in solution (unlike measurements made at downhole conditions), comes from empirical correlations with the API gravity of the hydrocarbon. Kleinberg and Vinegar [10] indicate departures of the apparent HI (as measured by NMR) from unity only below API gravity of 20 with the value reaching as low as 0.7 for API of 10. This reduction is attributed to decay components that are shorter than 1 ms and inaccessible to the measurement. Consequently in heavy oils, where a large portion of the decay occurs at short times, the apparent HI will be dependent on the echo spacing (T_e of Eq. 16.32) of the device used in the measurement. Supplemental data showing similar trends measured on a different suite of oils, as well as the dependence of apparent HI on echo spacing, can be found in Dunn et al. [11].

16.4.2 Bulk Relaxation in Water and Hydrocarbons

Longitudinal (T_1) and transverse (T_2) relaxations are caused by fluctuating magnetic interactions between the oriented protons and other sources of magnetic moments (intermolecular protons, neighboring protons, and up-paired orbital electrons are on the list). In liquids the T_1 and T_2 relaxation rates are usually very close to being equal. In the case of bulk water, the relaxation times are very long, both T_1 and T_2 decay rates are nearly 3 s, but could be somewhat reduced to around a second, depending on the presence of dissolved oxygen (paramagnetic, thus providing ample opportunity to dephase protons) in the sample. Magnetic relaxation is possible whenever a polarized proton encounters a fluctuating magnetic field with a time component close to the Larmor frequency. In this case the proton can be dephased (affecting T_2) or transfer enough energy to change its orientation with respect to the polarizing field B_o (affecting T_1). The decay rate is due to the random interactions of the polarized spins with the magnetic moments of other molecules. These decays can be substantially characterized by a single exponential.

The behavior of T_1 depends on proton mobility and the sources of local magnetic fields. For this relaxation to proceed there must be interactions between the spin and the lattice-molecular motion on a time scale compatible with the inverse Larmor angular frequency. The correlation time, τ_c, is a measure of the interaction time. The decay rate $1/T_1$ will be at a maximum when the correlation time is equal to the inverse Larmor frequency as sketched in Fig. 16.12. For correlation times either larger or smaller, the probability of the fluctuations in the magnetic field having a sufficient component to flip the spin state decreases. From this it can be concluded that relaxation *time* is long both for very low molecular mobility (i.e., a very viscous fluid) or when the molecular mobility is very high (i.e., gas). This latter case is the result of an interaction time that is too short to affect the energy transfer.

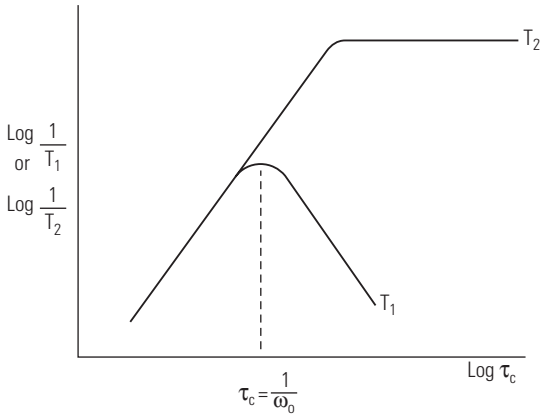


Fig. 16.12 A sketch of the T_1 and T_2 decay rates as a function of the molecular correlation time.

The trend of the T_2 decay rate follows that of T_1 until the correlation time exceeds the critical value. For larger correlation times there is more and more opportunity to dephase the 90° flipped spins, up to some point of saturation. This is also depicted in Fig. 16.12, where it can be seen that T_2 is always less than or equal to T_1. In this plot, gas would be found to the extreme left, followed by low-viscosity fluids, and then high-viscosity fluids and solids to the right.

Because the random interactions of the protons with other magnetic moments are controlled by temperature and self-diffusion coefficients of the molecules associated with the protons, the decay rates of the fluids will be controlled by physical properties like viscosity. A classic intriguing example of the correlation of T_1 with crude oil viscosity comes from the work of Brown [12], a pioneer in the field, and shown in Fig. 16.13. A simple theory developed nearly 60 years ago [13, 14] predicts that $1/T_1$ depends on the correlation time between protons. Using the Stokes–Einstein relation, it can be shown to vary as the ratio of the viscosity to the temperature $(\frac{\eta}{T})$ (see Problem 16.8.). For simple alkanes Winkler et al. [15] show a convincing experimental confirmation of this as seen in Fig. 16.14. Unlike liquids, the case of gas is unusual in that its relaxation time is directly proportional to its density.

In Fig. 16.15 the relaxation times for bulk water are displayed as a function of temperature. The upper curve is for the T_1 relaxation and shows that the relaxation time increases monotonically with increasing temperature. This is a result of the decrease of the correlation time as the thermal agitation of the molecules increases. The second set of curves for T_2 are a result of diffusion in magnetic fields with a spatial gradient; if the measurements had been made in a uniform magnetic field, then T_2 would be equal to T_1. However, if a gradient is present, the diffusion of the polarized water molecules into regions of the magnetic field that change the Larmor

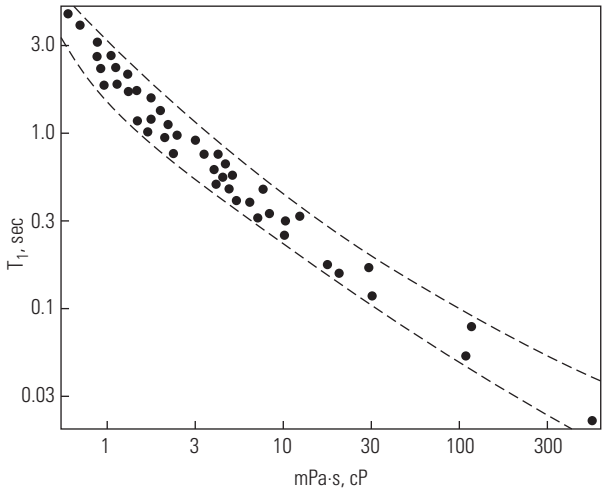


Fig. 16.13 The measured relaxation times for crude oil samples as a function of their viscosity. Adapted from Brown [12].

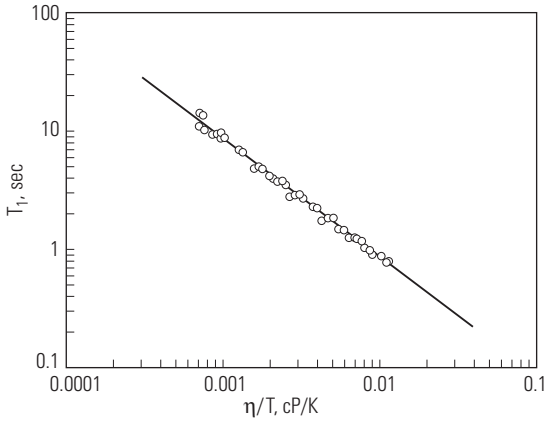


Fig. 16.14 Measured T_1 relaxation time for higher alkanes as a function of the viscosity (η) divided by the temperature. From Winkler et al. [15]. Used with permission.

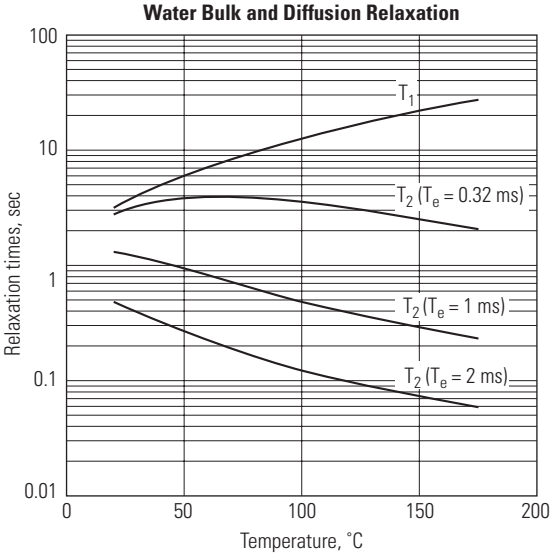


Fig. 16.15 The bulk relaxation time (T_1) for water as a function of temperature. Also the effect of echo spacing (T_e) on the apparent values of T_2 as a function of temperature for a fixed magnetic tool gradient. From Kleinberg and Vinegar [10]. Used with permission.

frequency, provide another mechanism for relaxation since some of the spins will be irrevocably dephased as mentioned earlier in Section 16.3.6. Thus, in a gradient, the diffusion of molecules will cause the T_2 to speed up. From Eq. 16.32 the relaxation rate will vary as the product of the square of the echo spacing, T_e, and the diffusion coefficient, which is known to be temperature-dependent; it increases a factor of

three between 70°C and 150°C [10]. The curves have been computed for a particular magnetic field gradient in the sensitive volume of the instrument and for a series of echo spacings, demonstrating that the instrumental design has a large influence on the absolute values obtained, but it is the temperature-dependence of the diffusion coefficient that is responsible for the T_2 variation with temperature (see Problem 16.5 with accompanying sketch of the variation of the diffusion coefficient for water as a function of temperature).

Up to this point in the discussion, the fluctuating magnetic fields that the protons experience are caused by variations in the intermolecular distances. The fields are provided by the other protons. But paramagnetic ions can be a more important source. In solution, paramagnetic ions can considerably shorten T_1 and T_2.

16.4.3 Viscosity Correlations for Crude Oils

We saw above that the behavior of simple alkanes for the T_1 relaxation rate is quite consistent with the simple correlation time theory. Early work by Brown [12] showed a fair correlation between measured T_1 and viscosity. However the situation is a bit more complicated for the case of T_2 measurements on actual crude oils, which have broad distributions of relaxation times even when measured in a uniform magnetic field (eliminating any diffusion contribution to the decay rate). Figure 16.16, presented in the style pioneered by Jackson [17], now adopted by the industry for analyzing and displaying the nonexponential T_2 decay curves into constituent decay times, indicates the complexity. The relative magnetization is shown as a function of T_2 on a logarithmic scale. The distributions span several decades in T_2 because of the mixture of hydrocarbon types present. They are characterized by a peak at long relaxation time corresponding to the most mobile chains and tail off to very short decay times for the least mobile types (longer chains with greater viscosity).

A convenient way to capture the viscosity-dependence is to summarize the T_2 distribution curves, using the i discrete values of the magnetization m_i for each of the T_{2i} values to compute the log mean T_2, or T_{2LM}. Its definition is simply:

$$T_{2LM} = exp\left[\frac{\sum m_i log_e(T_{2i})}{\sum m_i}\right]. \tag{16.38}$$

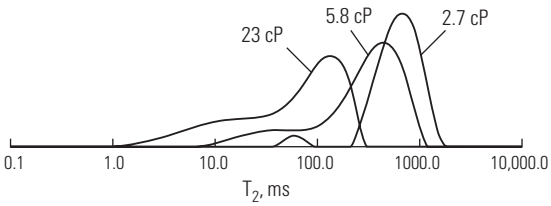


Fig. 16.16 T_2 distributions measured on bulk oil samples of three different viscosities. Adapted from Morriss et al. [16].

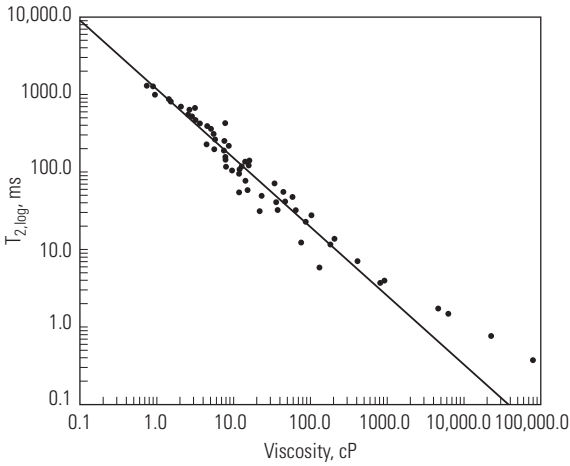


Fig. 16.17 The logarithmic mean of T_2 distributions of bulk oil samples plotted as a function of the viscosity. From Morriss et al. [16]. Used with permission.

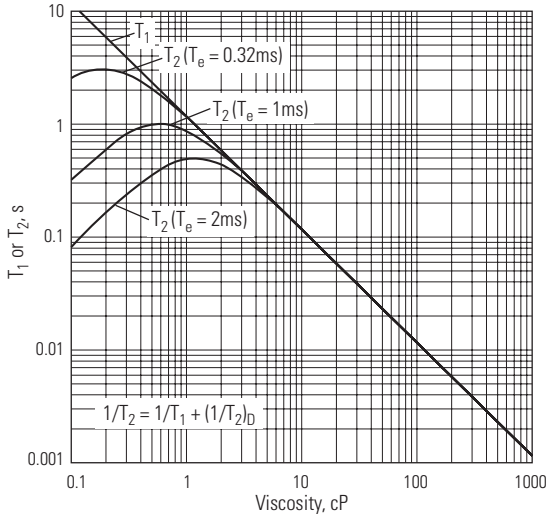


Fig. 16.18 Variation of relaxation times of crude oil as a function of viscosity and echo spacing for a tool gradient of 20 Gauss/cm. From Kleinberg and Vinegar [10]. Used with permission.

Figure 16.17 shows that T_{2LM} captures the viscosity-linked variation quite well and thus provides a method of predicting the log mean T_2 value if the oil viscosity is known. A graph for making this type of estimate and extending it to the case of an NMR measurement with a particular magnetic field gradient, for a variety of echo spacings, is shown in Fig. 16.18.

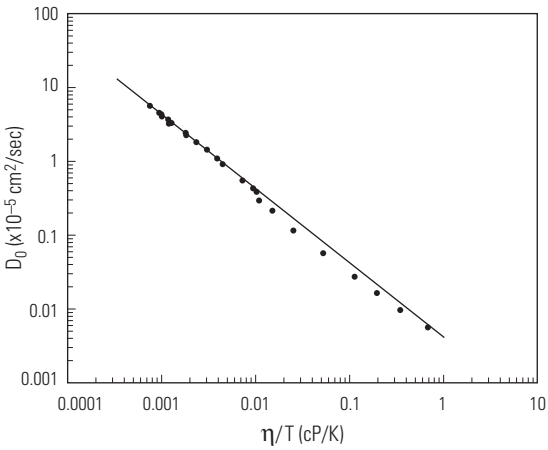


Fig. 16.19 The diffusion coefficient of oils as a function of the ratio of their viscosity to temperature. From Vinegar cited in Winkler et al. [15]. Used with permission.

In order to make predictions of the T_2 distribution when using a device with a magnetic field gradient, the diffusion constant is required. To this end, one of the consequences of the Bloembergen et al. theory [13] is that the diffusion coefficient is also related to the ratio of the temperature to the viscosity [15]. One example of this behavior, attributed to Vinegar [15] is shown in Fig. 16.19. Additional work has been done by Lo et al. [18] for mixtures of alkanes and gas in which the measured diffusion coefficient is a distribution. Using the log mean of the diffusion coefficient, similar correlations are made to the temperature normalized viscosity.

16.5 NMR RELAXATION IN POROUS MEDIA

Local magnetic fields at the surfaces of the rock grains are another major factor in the determination of the effective T_1 and T_2 for fluids in porous formations. If a proton is near a surface, there is a large probability that it will interact with paramagnetic sites on the surface and thus have its precessing phase disturbed. For this to happen, the proton need not be bound to the surface. The quantity governing the interaction is the fluid diffusion length ($\sqrt{DT_1}$) and its relation to the pore size.

Early experiments by Brown [19] showed that the relaxation times (T_1) in confined fluids were much shorter than those associated with the bulk fluid. The T_1 and T_2 differences between bulk fluids and those observed in porous media are a result of molecular diffusion and the nearby presence of grain surfaces. The liquid molecules, some containing polarized protons, diffuse and approach the pore-grain interface. There the protons have some finite probability of being relaxed. In this section we discuss the sources of the relaxation, the differences between fast diffusion limit and slow diffusion limit and give the petrophysical justification for linking the distribution of relaxation time with the pore size distribution (at least in clastics).

Although both T_1 and T_2 are important measurements for logging, in modern devices the convenience of the more rapid T_2 logging has taken precedence. Unfortunately much of the early laboratory measurements in petrophysical applications were done on T_1 since it avoided the difficulties of having a gradient-free magnetic field. Pore wall or surface relaxation effects, discussed below, are usually dominant in water-saturated rocks. In these cases the relaxation effects are similar for both T_1 and T_2. Some efforts have been made to correlate the two in water-saturated rocks [20] finding that T_1 exceeds T_2 by 50%–60%, after carefully excluding the diffusion component which could otherwise be a large source of difference. In this section, the discussion of T_1 and T_2 will be freely alternated for historical reasons.

16.5.1 Surface Interactions

It has been observed that the thermal relaxation time of water in porous media is decreased from the value expected in a bulk sample of water. A recent demonstration of this is cited by Kenyon [21] and shown in Fig. 16.20. It is a measurement of T_1, using the inversion recovery pulse sequence (which employs a 180° flip of the magnetization vector, followed by a 90° pulse after a wait time that is varied through successive repetitions similar to the saturation recovery scheme discussed earlier) for a water sample and a water-saturated sample of Berea sandstone. In the sandstone, the approximate T_1 derived from the relaxation curve is 214 ms while the original water, before and after extraction from the rock, has a much slower relaxation of about 3.8 s. The conclusion is that the faster relaxation of the water protons must be related to the enhanced relaxation at the pore walls since the water was not altered.

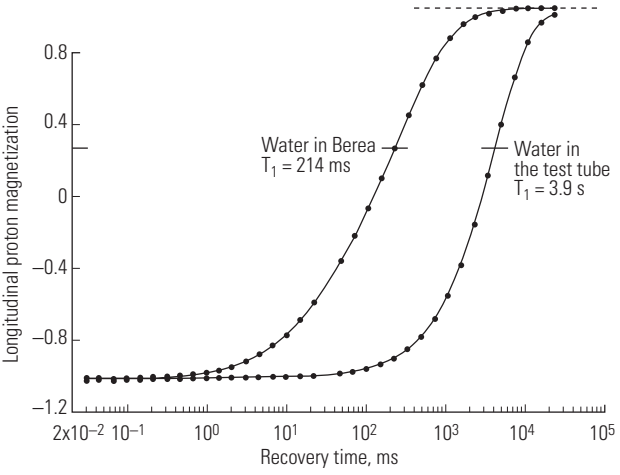


Fig. 16.20 T_1 relaxation curves for water and a water-saturated sandstone. The experimental procedure used an inversion-recovery scheme in which the polarized protons are flipped by 180°. It is clear from the curves that the water in the sandstone relaxes much faster than the bulk water. Adapted from Kenyon et al. [21].

Brownian motion allows liquid molecules to diffuse relatively large distances during the course of NMR logging measurements which are on the order of a second. The distance can be estimated from one definition of diffusion, which states that the mean square distance travelled in time t, is proportional to the product of the diffusion coefficient (D) and time:

$$< x^2 >= 6Dt. \tag{16.39}$$

Since the molecular diffusion coefficient of water at room temperature is 2×10^{-5} cm^2/s, a molecule can diffuse on the order of 100 microns in a second. For many porous rocks this is much larger than the dimensions of a pore. This means that the molecule can have many opportunities for approaching or striking the pore wall during a measurement period. There is some probability each time this close approach is made that the spin will be relaxed. Either the spin will realign with the imposed field (a T_1 process) or the spin will be irreversibly dephased (a T_2 process). However there may be several collisions before a relaxation occurs. The relaxation is thought to be due to paramagnetic ions such as iron at the surface of the grains; for sandstone the iron content is on the order of a percent. In carbonates lower rates of relaxation are found and will be discussed later.

The ability of a surface to relax the spin is called the *relaxivity* or surface relaxivity coefficient, ρ, with a subscript 1 or 2 to indicate the ability to influence either the transverse or longitudinal relaxation. This coefficient is a convenient way to account for all the messy details of the atomic interactions between the fluid molecules with magnetically polarized protons and the atoms, with significant magnetic moments, located in the walls of pores. The magnitude is material-dependent, but for many cases can be assumed constant for certain rock types (read sandstones).

Reasoning on the basis of a single pore, a model (KST) [22] treats the decay rate as a volume average of the bulk decay rate $\frac{1}{T_{1B}}$ in the center of the pore (see Fig. 16.21)

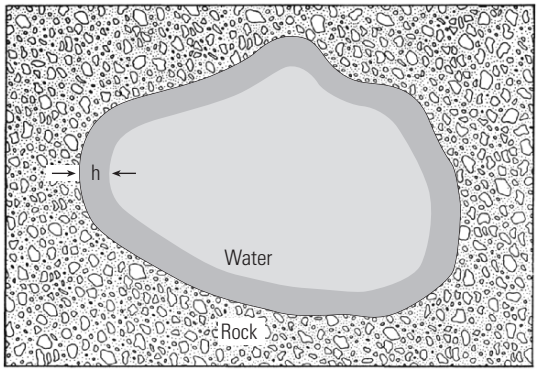


Fig. 16.21 The KST model for the NMR behavior of liquid contained in a pore space. hA is the volume fraction contained in the layer of thickness h next to the pore surface of area A, and V is the total pore volume.

and a different rate $\frac{1}{T_{1S}}$ in the layer of thickness h around the pore. The decay rate $1/T_1$ can be written as:

$$\frac{1}{T_1} = \frac{1}{T_{1B}}\left(1 - \frac{hS}{V}\right) + \frac{1}{T_{1S}}\frac{hS}{V}, \tag{16.40}$$

where V is the volume of the pore and S is interior surface area. From this we identify the ratio h/T_{1S} as the surface relaxivity ρ_1. Noting that $hS/V \ll 1$ for typical measurement setups and measuring times,the expression becomes:

$$\frac{1}{T_1} = \frac{1}{T_{1B}} + \rho_1\frac{S}{V}. \tag{16.41}$$

Following similar arguments an equation can be written for T_2:

$$\frac{1}{T_2} = \frac{1}{T_{2B}} + \rho_2\frac{S}{V}. \tag{16.42}$$

Using this approach, a plausible relationship is established between the observed T_1 or T_2 and the surface-to-volume ratio of laboratory samples. This is of interest in making an estimate of the permeability of the formation.

To understand the possible distribution of relaxation times from a sample with multiple-pore sizes there is a clarification to be made about the diffusion regime. If the molecules diffuse sufficiently in the characteristic time T_{1B} (or T_{2B}) so that the distance travelled is larger than the dimension of a pore volume then there are multiple chances that a proton in a diffusing molecule can approach the surface and be dephased. For a single pore there will be a single decay rate that depends on the pore size, a and and surface relaxivity, ρ, as indicated in the previous two equations. An estimate of the pore size, a, can simply be obtained from the ratio of volume and the surface area, V/S.

The formal definition of the fast diffusion regime is arrived at by requiring the time to diffuse a distance of the order of the pore size to be less than the decay time:

$$\frac{a^2}{D} \ll T_{1,2} = \frac{1}{\rho_{1,2}}\frac{V}{S} = \frac{1}{\rho_{1,2}}a \tag{16.43}$$

or

$$\frac{\rho a}{D} \ll 1. \tag{16.44}$$

What about the situation for slow diffusion? Reasoning on the level of a single pore, the slow-diffusion regime would imply a range of decay rates or, in the extreme, a pair of decay rates. From the fluid in the center of the pore the decay rate should correspond to the bulk-fluid rate. In the thin layer adjacent to the pore surface there will be an enhanced rate attributable to the wall.

It is interesting to know which regime is dominant in rocks. It has been found, by comparing T_1 distributions made at a series of temperatures, that for clastics and some carbonates the fast diffusion regime is operating [23]. This means that from each pore size there will be a corresponding enhanced decay rate. We can then expect from a

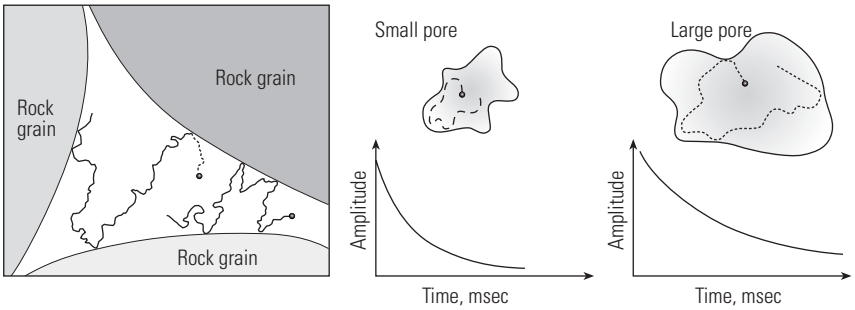


Fig. 16.22 The notion of grain relaxation and the role of small and large pores in the decay time of the relaxation curve.

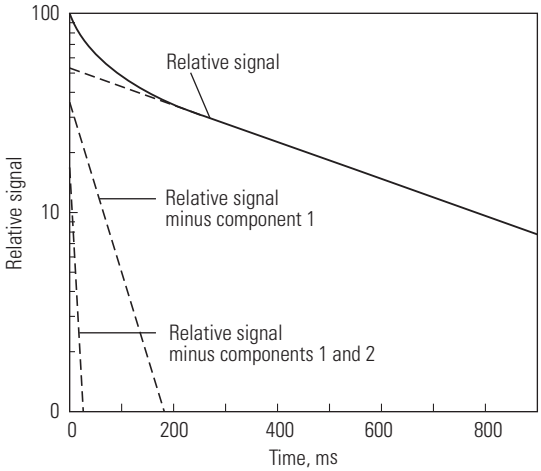


Fig. 16.23 The measured relaxation time for a sandstone core sample. Adapted from Timur [24].

rock with a distribution of pore sizes that the measured decay rates will be composed of a spectrum of decay rates. A cartoon of this notion is shown in Fig. 16.22. In the next section we examine the experimental evidence for this important inference and observation of such great utility for petrophysical evaluation.

16.5.2 Pore Size Distribution

In the fast diffusion limit the decay of magnetization (either T_1 or T_2), from a single pore, should exhibit a single exponential. As expected, real rocks show a slightly more complicated behavior. Figure 16.23 shows the results for a determination of T_1 for a sandstone. The quite apparent nonexponential decay has been decomposed, in this early analysis [25] into the sum of three different decays. The distribution of the

values of the three components is related to the granular nature of the sample, perhaps to the pore size distribution [26]. The supposition is that there are many pore sizes, or a distribution of pore sizes, in a rock sample.

To exploit this interpretation there are two steps. The first is the non-trivial problem of how to analyze the (often noisy) decay curves into a distribution of characteristic times. This has been solved by a variety of means, one of which, in wide use, is described in Kenyon et al. [28]. The process essentially makes a modified least-squares determination of the amplitude of a set of pre-determined and logarithmically spaced decay curves. An example of a noisy T_2 decay curve and its decomposition into a distribution of T_2 values is shown in Fig. 16.24.

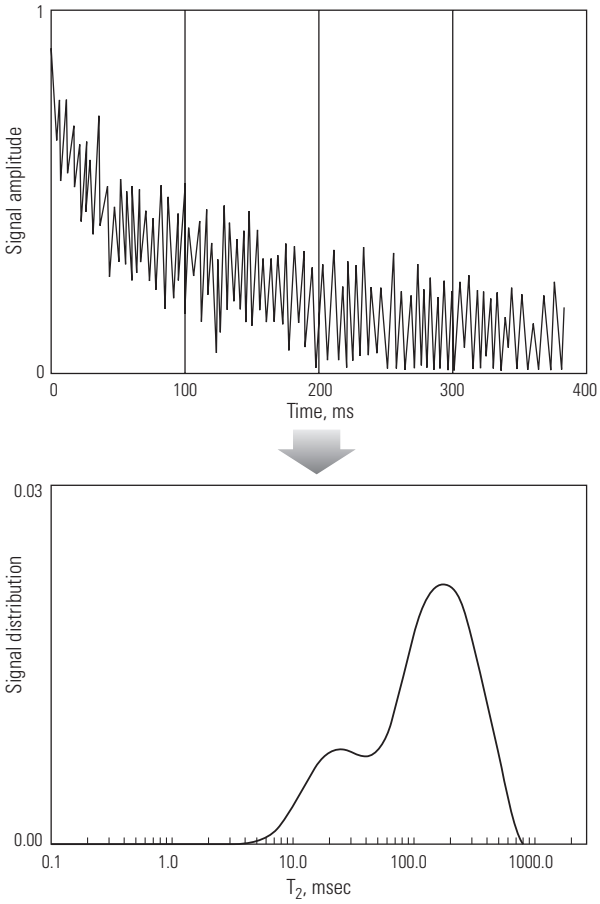


Fig. 16.24 A noisy T_2 relaxation measurement curve and its decomposition into a distribution of decay times. The resultant distribution is strongly bimodal. Presumably the very fast decaying components are associated with smaller pore sizes. The total integral under the properly normalized curve is the porosity.

For the distribution of decay times to be viewed as a distribution of pore sizes, there is an important set of assumptions: each pore is in the fast diffusion limit so that the protons in the volume all sample the relaxing properties of the wall, the relaxing properties of the walls of all the pores are the same, and there is no diffusion between pores. Later we will see some examples of behavior of systems that do not obey this last assumption.

What is the experimental verification of this correspondence? This has been studied by numerous researchers, only a couple of whom will be referenced here. One notable work was by Straley et al. [27] who measured the T_1 of water-saturated rocks that were centrifuged at successively higher rotor speeds between measurements. The expelled water came from successively smaller pores as the centrifugal pressure exceeded the capillary pressure. The relaxation measurements show that the longest T_1 components disappeared earliest while the shortest components progressively disappeared as the rotor speed was increased. This showed an association between the longer decay times with pores that are easier to drain.

Mercury porosimetry was also used to study the connection between pore size and relaxation rate by Kenyon [28] and Morriss et al. [29]. The results suggest that there is a correspondence between the relaxation time distribution and microgeometric features of the sandstones studied. The correspondence between results obtained in earlier work performed using T_1 measurements, and results when using T_2 measurements was shown by Straley et al. [30].

All of these studies show a correlation between pore size, or rather the surface-to-volume ratio, and the T_1 or T_2 distributions. To get an actual pore size distribution, a surface relaxivity needs to be assigned and some model of the geometry needs to be employed. It may be more prudent to take the position that the distribution of relaxation times is simply a reflection of the distribution of the S/V ratio. The utility and power and limitation of such a concept will be examined later in Section 16.8.2.

This powerful interpretation of the NMR relaxation spectra rests on an implicit assumption. If a certain geometry for the pore structure is assumed and if the surface relaxivity is constant (usual assumption), then there will be a relation between the pore size distribution and the T_1 and T_2 distributions, since the latter depend on the surface to volume ratio. Assuming a certain geometry also is equivalent to establishing a connection between a measure of the pore size and the S/V ratio. Further NMR petrophysical applications depend on a correlation between pore body size and pore throat dimension which is frequently the case for sandstones. (One of the difficulties in applying the technique to limestones may be the looser relationship between pore bodies and pore throats.) In these cases the relaxation distributions can be used to estimate capillary pressure curves.

16.5.3 Diffusion Restriction

The enhancement of the T_2 decay rate that we saw in Section 16.3.6 referred to the additional dephasing of spins due to their diffusional displacement in a magnetic field with a gradient. The actual analytical form given in Eq. 16.32 predicts a magnitude that depends on the diffusion coefficient, D. This predicted decay rate was derived for

unhindered motion of the polarized molecules. For the case of, say, water molecules confined to a small pore in a porous rock, the diffusion well might not be unhindered. Depending on the size of the pore and the magnitude of the self-diffusion coefficient, the molecule may be prevented from reaching its predicted mean squared displacement. In fact, for a saturated rock sample in the fast diffusion limit, it is expected that the molecules will encounter the grain surfaces a number of times during an echo spacing.

This discrepancy can be exploited experimentally using a pulsed gradient spectrometer, where a gradient is actually applied to the magnetic field to enhance the effect, which can appear as a time-dependence of the self-diffusion coefficient. At very early time D has the value expected for the unconfined fluid; its apparent value will be seen to decline as time increases and can be construed as a measure of the pore size and tortuosity [31,32]. With the development of gradient tools coupled with sophisticated pulsing and signal-processing tools, D and T_2 can be measured simultaneously. These measurements add a second dimension to the traditional measurements and will be very useful for determining fluid properties and perhaps wettability. The interpretation of these cross-plots may require consideration of pore system diffusion restriction.

16.5.4 Internal Magnetic Gradients

The increases to the T_2 dephasing rate have, up to this point, been attributed to gradients that exist in the polarizing magnetic field or imposed on them precisely for inducing the sensitivity to diffusion. There are other reasons that could account for magnetic field gradients besides inhomogeneities in the construction of the magnet. These internal gradients arise, in the presence of strong magnetic fields, from the magnetic susceptibility contrast between the saturating fluids and the rock grain material.

Computing the distribution of spatial gradients is a difficult problem and depends on many factors not well determined for real materials. The impact for logging measurements, if present, is to contribute to an increase in the dephasing of the spins. This will act contrary to the effects of diffusion restriction and may complicate interpretation of some logging data presented as maps of diffusion coefficient versus T_2, to be discussed later.

16.6 OPERATION OF A FIRST GENERATION NUCLEAR MAGNETIC LOGGING TOOL

Nuclear magnetic logging (NML) tools owe their conception and birth to the oil industry and Chevron in particular. Researchers from Chevron were the first to push for logging tools to measure NMR properties of saturated formations. One of the earliest published references to borehole logging was in 1960 [33]. As early as 1952 Chevron scientists along with the participation of Varian started a joint project to study

the feasibility of earth field NMR. With the goal of obtaining free precession signals from oil and water in formations beyond the borehole, and to be able to distinguish between oil and water on the basis of relaxation times, an experimental tool was finally produced in 1956. Tentative commercial services were provided by a predecessor of Dresser Atlas in the early 1960 followed by Schlumberger in 1965.

In 1962 Chevron halted their theoretical and experimental NMR program, but not their interest in this powerful technique. They lobbied Schlumberger, with the help of Shell, to produce an improved version of the NML* logging tool in 1971. In 1984 the final version of an earth's field NMR logging instrument was produced by Schlumberger and is described next.

The basic element of a conventional logging tool configuration [34], which was used up until the mid-1980s, consisted of a coil through which a large amount of current was passed. Due to the nature of its winding, it produced a magnetic field roughly perpendicular to the earth's magnetic field. This served to align a certain fraction of the protons in water, oil, and gas, within the depth of investigation, if the polarizing field were left on for a long enough time (≈2 s).

After a sufficient period (depending on the mode of tool operation), the current was turned off in the polarizing coil. The same coil was then used to receive the induced signal from the previously aligned protons as they precessed at the Larmor frequency around the earth's magnetic field. The signal received had a frequency of about 2 kHz and was found to be damped with a time constant of roughly 50 μs in rocks, as opposed to the 2 or 3 s damping observed in large volumes of pure water. Figure 16.25 schematically illustrates, at several moments of elapsed time, the behavior of

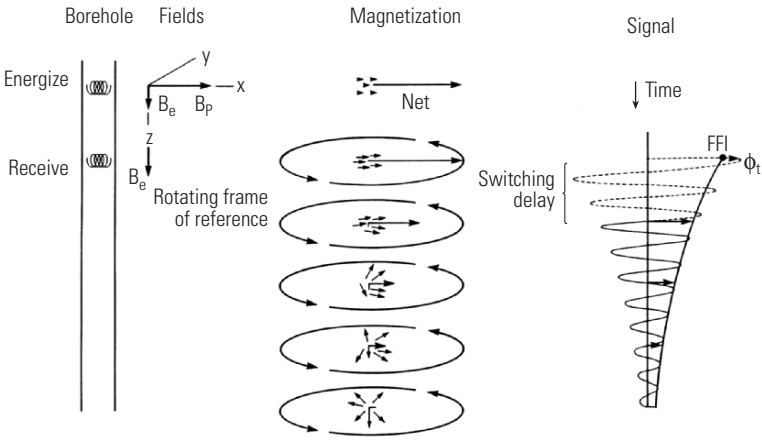


Fig. 16.25 Schematic representation of the generation of the observed nuclear magnetic logging tool signal and its extrapolation to the start of the free induction decay.

*Mark of Schlumberger

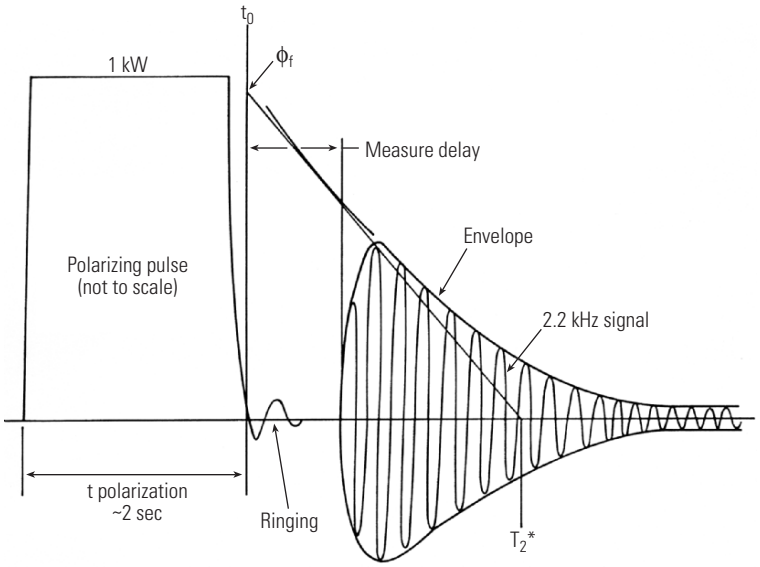


Fig. 16.26 Extraction of the free fluid index, ϕ_f, from the free induction decay curve.

the magnetic moment induced by the polarization field B_p. It is seen to start out with the individual moments in phase. As time elapses, the phase begins to get out of step and the oscillating signal decreases monotonically since there is no Carr–Purcell pulsing to realign the spins. The dephased spins ultimately reorient themselves along the earth's field, B_e in the so-called free induction decay.

The signal that is observed is indicated schematically in Fig. 16.26. Note that there is a delay of some 20 μs between the end of the polarizing pulse and the beginning of the observation. This is both an annoyance and a benefit. During this period, signals with very short T_2 components decay, and do not affect the later measurements. These may be the result of the signal from the mud, which must be doped with magnetite (to keep the borehole hydrogen from overwhelming the measurement), or from the hydrogen in the shale or silt, or from very high-viscosity fluid.

The annoyance comes from the uncertainty in obtaining the primary objective of the measurement, which is to extrapolate the envelope which is decaying with a time constant T_2^*, back to the end of the polarizing pulse. This is also shown in Fig. 16.26. The value of the envelope at this point is called the free fluid index, or FFI. After tool calibration and environmental corrections, it corresponds to the volume fraction of movable fluids in the formation.

Following from the earlier analysis (see Eq. 16.34), the major factors concerning the signal strength from this logging tool can be described. The basic relation for the induced voltage is the same:

$$V \propto N_t A M \omega, \tag{16.45}$$

where $\omega = \gamma B_e$. However, M is obtained by the polarizing pulse and will thus depend on the field B_p produced by the logging tool. Thus the final dependence for the signal strength (see Eq. 16.37) is:

$$V \propto \frac{J(J+1)}{kT}\gamma^2 \omega B_p = \frac{J(J+1)}{kT}\gamma^3 B_e B_p. \tag{16.46}$$

The field strength B_e is fixed by the earth's field, and B_p is limited by down-hole power considerations. This indicates that the sensitivity to other isotopes will depend on $I(I+1)\gamma^3$. The data of Table 16.1 show that the sensitivity of this measurement to Na is about 1/10 that of hydrogen, under the condition of equal numbers of nuclei. The concentration differences actually encountered in borehole applications made it of little practical concern.

In Eq. 16.46 corrections had to be made to the signal amplitude before the FFI could be extracted. The first correction dealt with the magnetic inclination and is necessary when the tool's magnetic field and the earth's field are not at right angles. The signal amplitude is a function of the cosine of the magnetic declination. Another correction was for temperature – it has an impact on the magnetic susceptibility of the formation material. The borehole size also influenced the signal strength, since a relatively constant volume of material is "seen" by the receiver coil. The formation signal was at a maximum when the borehole size and tool diameter were of equal size, and it decreased (since "doping" allowed no signal to come from the mud) as the borehole size increased.

16.7 THE NMR RENAISSANCE OF "INSIDE-OUT" DEVICES

One of the unintended consequences of the first oil embargo in the 1970s was a revolutionary idea that was to change NML. Following the embargo, the Carter administration called upon the US National Laboratories to become involved in fossil fuels research to avoid another energy crisis. Jasper Jackson of the Los Alamos National Laboratories was one of those assigned to a new geophysics group for that purpose. His introduction to the subject of NMR logging was through contact with scientists at Chevron and attending a Schlumberger NML logging run for Chevron. Witnessing the time and effort spent mixing the magnetite to kill the borehole signal made a big impression on him [36].

As noted earlier, for the conventional logging tool to be able to see a signal from the formation, steps must be taken to "kill" the borehole signal. This is done by adding paramagnetic ions to the mud system and circulating it to produce a uniform mixture. Detractors of this method point out the expense and time involved in such a procedure. For Jackson it was a point of inspiration.

16.7.1 A New Approach

A new tool concept that avoids these problems, in principle, was proposed by Jackson [1]. His design is called the inside-out NMR. Instead of using the earth's magnetic

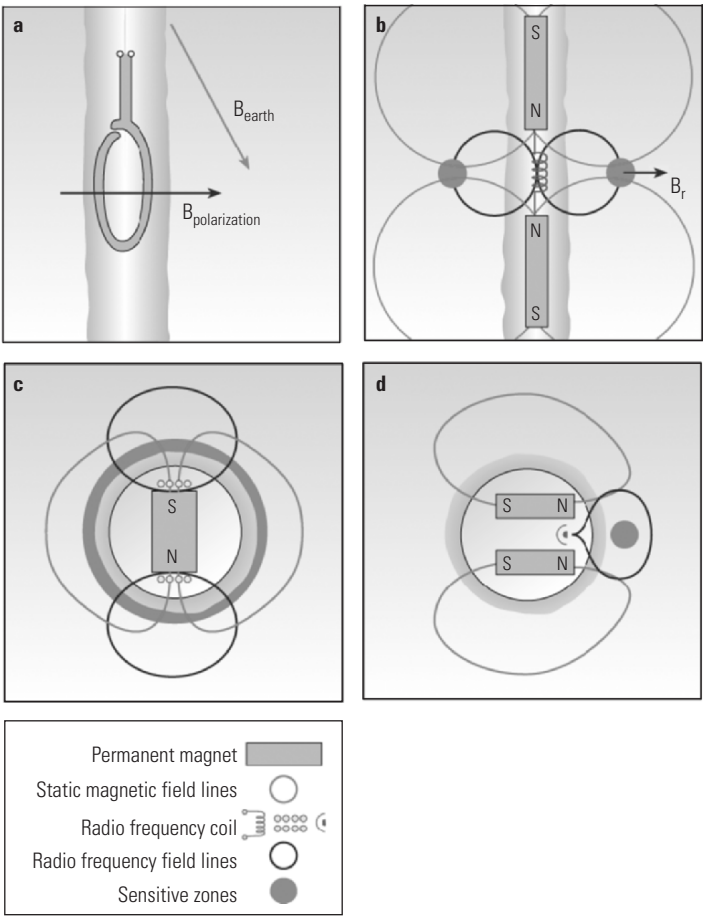


Fig. 16.27 The evolution of NMR logging tool design. a. The first generation device that used the earth's magnetic field for polarization. b. The configuration of an NMR logging tool proposed by Jasper Jackson. Shown are the two opposing dipoles and the toroidal zone of nearly constant radial magnetic field. The coil used to rotate the polarized protons and then monitor the subsequent T_2 decay is shown to be coaxial with the polarizing magnets. c. The basic design of the NUMAR tool utilizing a single elongated dipole with strong spatial gradient. d. The design of the CMR with two side-by-side elongated dipoles producing a relatively flat magnetic field inside the formation.

field for producing the precession of the protons, two opposed permanent magnets are located in the tool for this purpose, see Fig. 16.27. The opposition of these two dipole magnets produces a radial magnetic field in the plane halfway between the two magnets. The variation of the radial magnetic field with distance is unusual; first it increases to a broad maximum, controlled by the magnet length, and then decreases with increasing distance. This creates a region of roughly toroidal form, around the

sonde, in which the field is relatively constant, producing a net magnetization M pointing radially outward along B_r. With this type of configuration, the more classical pulsed NMR experiments may be performed, and the signal was not expected to be influenced by the borehole.

To make the measurement, an oscillating current in the coil, with a frequency of the Larmor frequency of the toroidal region, is used for the appropriate length of time to flip the net magnetization vector M by 90°. Once the flipping pulse is turned off (which can be done in 0.5 μs, as opposed to 20 μs in the first generation tool, since large-polarizing signals are not needed), the coil functions as the receiver to record the signal from protons precessing about B_r.

The primary advantage of such a system is the avoidance of mud doping. An additional aspect is the availability of the signal with minimum delay. This enables a more precise determination of the volume of movable fluids, or FFI, since the uncertainties of extrapolating to the end of the polarizing pulse are avoided. The behavior of the T_1 curve can be examined at early times and deconvolved to give a pore size distribution. Jackson is the first to be given credit for this procedure [17] that is now a standard fare in data analysis and presentation.

The defects of the prototype tool center on the small signal strength, which requires lengthy data accumulation times to take advantage of signal averaging. Also the depth of investigation is rather small, and is linked to the size and strength of the permanent magnets which are already too large in diameter for practical applications. However, because of the promise that it held, the technique was worthy of further instrumentation refinements.

Before refining the prototype, there was a significant change in national politics. In 1983, a directive was issued from the Reagan administration that the federal government should not be doing petroleum research and the project was cancelled. However, the ideas that the Los Alamos project sparked soon grew into competing commercial devices.

16.7.2 Numar/Halliburton MRIL

The NUMAR Corporation acquired exclusive rights to the Jackson patent in 1985. They set about to improve the signal-to-noise problems of the prototype and to tackle the problem that the resonant volume of the Jackson magnet extended into the borehole and provided a large fraction of the measured signal from borehole hydrogen.

In the process of adding magnets to the Jackson design a novel departure was pursued instead. This consisted of designing a long magnet polarized transversely to its axis. Unlike the Jackson design which sought to have a reasonable formation volume at a constant magnetic field this new design, a 2-D dipole (or slab magnet), provided for a magnetic field falling off as the inverse square of distance into the formation. Coils (see Figs. 16.27 and 16.28) wrapped along the long axis of the magnet, oriented at right angles to the magnetic polarization provided an electromagnetic field perpendicular, nearly everywhere, to the static field.

The obvious advantage of this design is that at any reasonable frequency a resonant volume could be found and the volumes are represented by concentric cylinders

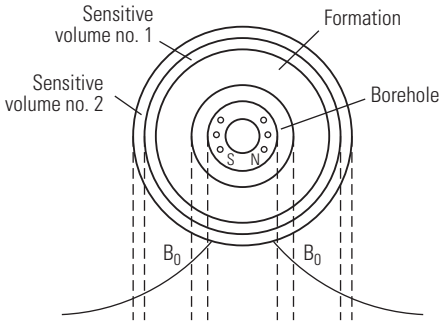


Fig. 16.28 The radial field dependence of the first NUMAR device that consisted of an elongated dipole with a moment perpendicular to the logging tool axis. Adapted from Prammer [35].

around the tool axis (see Fig. 16.28). During 1989 two versions of prototypes were field tested extensively and showed the technical feasibility. However the three major service companies felt that the market for such a device was unproven and NUMAR felt compelled to launch its own service company. In 1991, NUMAR began commercial logging with a version of the MRIL with a single-sensitive volume. The pulse-echo train was analyzed into a fast and a slow component only. Improvements on the basic concept consisted of adding a second frequency of operation so that a second sensitive volume could be simultaneously investigated [37].

16.7.3 Schlumberger CMR and Subsequent Developments

During the same time period that NUMAR was acquiring the Jackson patent and attempting to improve the prototype, Schlumberger researchers [38] were pursuing a different approach to adapt the interesting "inside-out" approach of Jackson. To improve the signal-to-noise problem they decided on using a skid-type tool, eventually called the CMR* tool. Figure 16.27 shows the evolution of the magnet design from the original opposed cylindrical long magnets, to a slab magnet, and finally to a pair of slab magnets that give a saddle point in the external magnetic field inside the formation located at about an inch from the tool face.

The two slab magnets generate a field about 1,000 times the earth's field so the operation (Larmor frequency) is on the order of 2 MHz. The field produces a zone of relatively constant flux at a position about 1 in. inside the formation (see Fig.16.29). A typical polarization time, in optimum conditions, is on the order of 1.3 s to allow for full polarization. This is followed by about 600 pulses to produce the pulse echoes, each separated by 320 μs, according to the CPMG technique for measuring T_2 [29].

This skid-mounted device can be combined with other logging instruments, unlike its earlier predecessor. The sidewall design has the advantage of avoiding

*Mark of Schlumberger

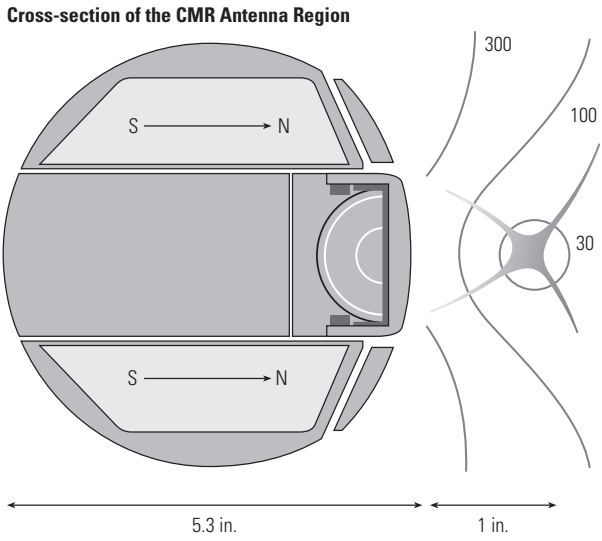


Fig. 16.29 A cross section of the CMR attenna region showing the saddle point of constant magnetic field about an inch from the face of the device. Courtesy of Schlumberger.

the interference of conductive muds on the operation of the antenna and permits a convenient calibration of the device by placing a bottle of water against the skid to simulate 100% porosity.

The early tools suffered from slow logging speeds and shallow depths of investigation. Some improvements to improve logging speed and good resolution were achieved by using long pre-polarization magnets. In the intervening decade much research was done by service companies, academia, and oil companies regarding the use of NMR measurements for fluid identification in ways that we have already discussed. To take advantage of the possibility of fluid characterization and invasion profiling, and improvements made in signal processing and acquisition, the next generation tools (MRIL Prime for Halliburton and MRX* for Schlumberger) exploited the gradient of the tool-produced magnetic field. The Larmor frequency for resonance can be met over a large range of frequencies, each corresponding to measuring polarized protons at different distances from the magnet. (The NMR technique enables the definition of a very well-defined volume of investigation unlike most other logging measurements.) By operating the tool at a number of frequencies, multiple depths of investigation can be obtained. These are determined by the dimension of the RF antenna, the magnet size and design. They open up the possibility of making a radial profile of the formation fluid. Figure 16.30 shows, for the MRIL-prime tool, the arrangement of concentric rings of resonance and the frequency associated with each. The regions of resonance for the skid-mounted MRX instrument, which provides a more focused measurement, are shown in Fig. 16.31.

Using a polarizing magnet with a spatial gradient opens up the possibility of new diffusion-based techniques. The gradient, coupled with appropriate spin manipulation

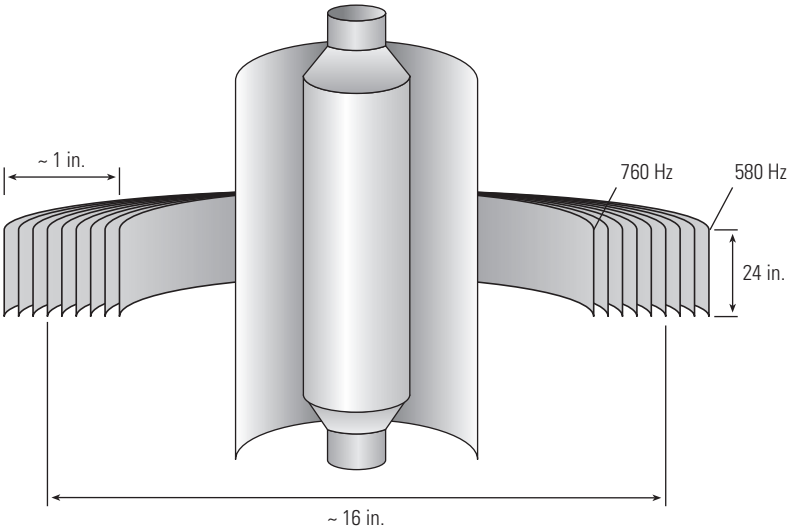


Fig. 16.30 A sketch of the radial rings of resonance for the MRIL-Prime along with the range of resonance frequencies. Adapted from Coates et al. [44].

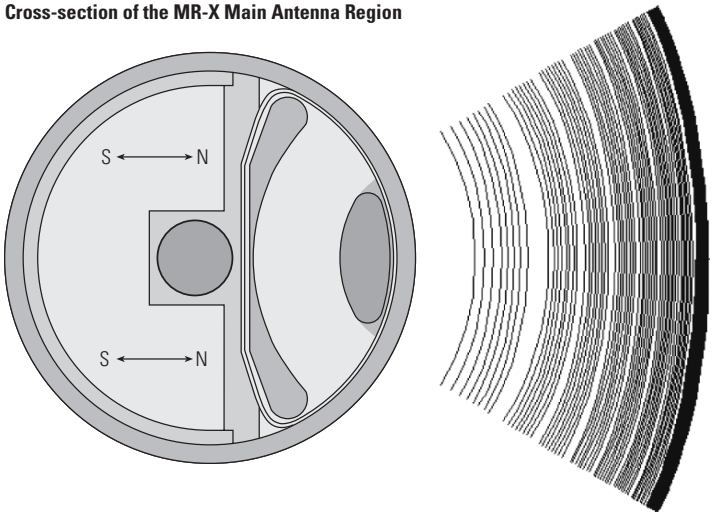


Fig. 16.31 A cross section of the MRX showing the region of resonance zones. Courtesy of Schlumberger.

cycles, allows fluid analysis – the estimate of viscosity, fluid saturations, the determination of the fluid diffusion coefficient, D, and the production of diagnostic $D - T_2$ maps. The new generation of tools are versatile with a programable pulsing sequence so that the measurements can be tailored for the application of interest.

Some guidelines on the programing of these devices as well as some logging examples will be discussed later.

16.7.4 LWD Devices

Making NMR measurements while drilling presents additional challenges related to the motion of the drill string during this not so gentle procedure. Although development of LWD versions of the tool began in the early 1990s it was nearly a decade before commercial services were offered [39, 40].

The design of one of these instruments (see Fig. 16.32) shows the symmetric device containing opposing dipole magnets. These long magnets produce a resonant zone that resembles a shell about 6 in. long with a diameter of 14 in. which means that it extends nearly 3 in. away from the tool surface. One of the tools can measure both T_1 and T_2, simultaneously or separately, but as usual, the statistical repeatability of the T_2 is greatest. Its generally faster decay allows many replicate measurements to be made in the time interval necessary to make a single determination of the decay time of the lengthier T_1 distribution.

For the real-time application, the data must be transmitted by the mud-pulse telemetry so the raw measurements must be processed down-hole by appropriate algorithms. Only a few important petrophysical measurements such as the total porosity, and bound fluid porosity, and the logarithmic mean of the T_2 distribution are sent to surface.

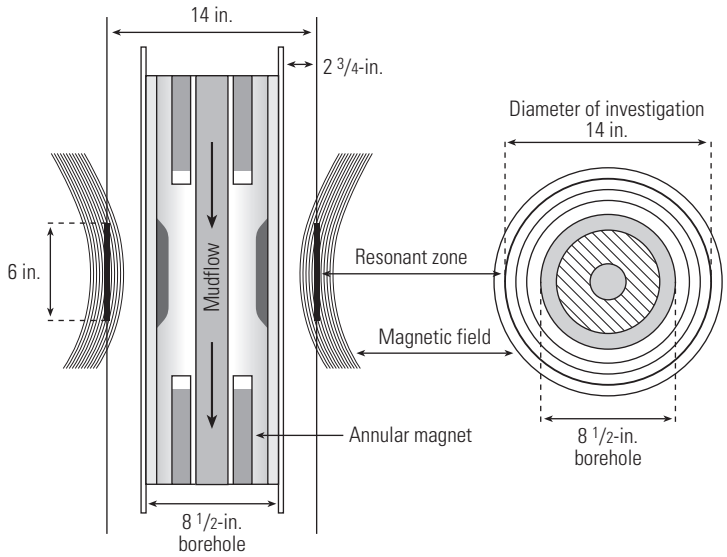


Fig. 16.32 Cross section of an LWD NMR device. This centered tool utilizes a pair of annular magnets to establish a gradient field with a nominal measurement diameter of 14 in.

16.8 APPLICATIONS AND LOG EXAMPLES

Despite the multitude of NMR logging tools available, either wireline or LWD, coupled with their large variety of operational modes, the raw measurements are common to them all. All the tools employ an arrangement of magnets to polarize the protons in a sensitive volume, and then the spins are manipulated by the oscillating magnetic field from an antenna so that their relaxation can be observed. The most fundamental measurement is the strength of the induced magnetism, i.e., the initial amplitude of the magnetization relaxation curve. Decomposing the relaxation curve into its components is the next step. The relaxation can consist of contributions from a number of distinct sources; bulk relaxation from the liquids themselves when the polarized protons only interact with each other, the relaxation caused by interaction with the wall of the pores, and increased relaxation caused by molecular diffusion in a magnetic field with a gradient.

From the (detailed) observation of the magnetization relaxation curve a vast number of petrophysical applications can be extracted. A partial list includes the total porosity, the pore size distribution, the volume of irreducible water, estimates of permeability, wettability and the analysis of the pore volume fluids. Before looking at some example logs that illustrate these varied petrophysical characteristics, it is worthwhile to discuss measurement strategy. Exploiting these complicated and versatile new NMR logging instruments requires optimizing the measurement procedure for the properties of greatest concern.

16.8.1 Tool Planners

An early attempt at a tool planner was made by Kenyon [21]. In the early version of a pulsed NMR tool (prior to the adjustment of pulsing sequences used to enhance diffusion in a gradient field) there were only three parameters that could be altered for the data acquisition. These are the polarizing time or wait time, the echo spacing, and the total number of echoes acquired. Increasing the wait time may ensure total polarization to obtain the full porosity response. Shortening it will discriminate against components like gas with long relaxation times. If the echo spacing is shortened then the effect of diffusion is reduced and more emphasis is placed on the rapidly relaxing signal that may be associated with clay. Changing the number of echoes acquired or the time spent on the echoes impacts the logging speed and the signal to noise ratio. Numerous references exist to assist the detailed planning of NMR logging jobs [41–43] and others will doubtless appear as logging instruments evolve. However some of the fundamental considerations are discussed below.

Prior to an NMR logging job it is advisable to determine the NMR fluid properties expected to be encountered. This would include computing the bulk T_1 and T_2 relaxation times, the diffusion coefficient and the HI. Table 16.2 gives some rules of thumb for computing the bulk relaxation rates and diffusion coefficients as functions of the ratio of temperature over viscosity. The longest value of the expected T_1 will give an estimate for the wait time. Ideally it should be on the order of three to five

Table 16.2 Estimating NMR fluid properties. T is in ^{o}K, η is viscosity in cP, and ρ is density in g/cm^3. Adapted from Coates et al. [44].

	Bulk relaxation time (s)	Diffusion coefficient 10^{-5}cm^2/s	Hydrogen index
Water	$\approx 3\frac{T}{298\eta}$	$\approx 1.3\frac{T}{298\eta}$	≈ 1
Oil	$\approx 2.1\frac{T}{298\eta}$	$\approx 1.3\frac{T}{298\eta}$	≈ 1
Gas	$\approx 2.5 \times 10^4 \frac{\rho}{T^{1.17}}$	$\approx 8.5 \times 10^{-2}\frac{T^{0.9}}{\rho}$	2.25ρ

times the mean T_1 value of the fluids. There are means to correct the measurement for incomplete polarization [43].

A second item to assess is the expected decay spectrum of the fluids in a formation, a slightly more speculative matter. If the fluid is a mixture of water, gas, and oil then the decay spectrum will depend on the tool design and whether it uses a magnetic field gradient or not. The gradient will contribute an additional decay rate (see Eq. 16.32) and will obviously depend on the magnitude of the gradient and the echo spacing chosen. This quantity increases the relaxation rate for both gas and for oil, assuming that the rock is water-wet. The decay rate of the water will be dominated by surface effects, in this case. It will be complicated by not only the free-diffusion component, but also the interaction with the pore wall that will depend on the surface to volume ratio (S/V) (most likely a distribution) and the relaxation rate of the pore-wall material ρ which may be difficult to know with any certainty.

16.8.2 Porosity and Free-Fluid Porosity

One of the claims for using NMR is to obtain a lithology-independent porosity. However, this minimizes the complications from having to know, accurately, the HI of the pore fluids and underemphasizes the ability of NMR to determine the irreducible water saturation. The irreducible water saturation, intimately related to the so-called water-cut, helps to establish the production potential of a zone: whether it will flow hydrocarbons, or a mixture of hydrocarbons and water, or just water.

This most valued petrophysical parameter is the result of a rather remarkable finding made by Straley [30] that the T_2 distributions can be used to determine an estimate of producible porosity in the manner done earlier for T_1 [27] (see Section 16.5.2). The technique is based on the principle that producible fluids reside in larger pores with longer T_2 times, and the capillary and clay bound fluids are associated with the smaller pores and thus shorter T_2 values. Integrating a properly normalized or calibrated T_2 distribution gives total porosity. To obtain the bound fluid volume, a cutoff value of T_2 was determined by finding the lower limit of the integration

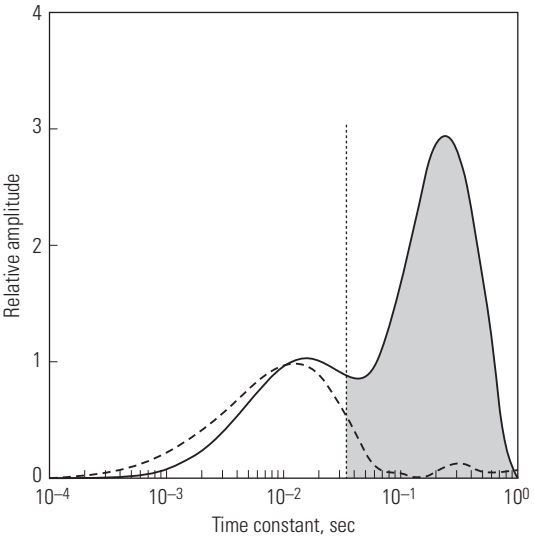


Fig. 16.33 The T_2 distribution of a water-saturated core, before and after centrifuging to remove the free-fluid. The usual practice of using a 33 μs cutoff is based on plots like this. From Straley et al. [30]. Used with permission.

of the normalized distribution to match the fractional volume of fluid obtained by centrifuging the sample at a 100 psi air-brine equivalent capillary pressure. Figure 16.33 shows the measured T_2 distribution fully saturated and again after desaturation by centrifuging. From this graph a cutoff of 33 μs was established. It is remarkable how well this value seems to work for clastic reservoirs around the world. In a similar set of measurements it was established that clay-bound water corresponded to T_2 values less than about 3 μs. A summary of the situation for the interpretation of water-wet clastics is shown in Fig. 16.34. These considerations then provided the basis for the most typical NMR logging presentation, an example of which can be seen in Fig. 16.35.

Additional measurements [30] made on a small sample of carbonates indicate that a cutoff value of 93 μs produces the best agreement between NMR porosity and the centrifuged volume. This latter value has not been as universally applicable in carbonates because of variability of the density of paramagnetic sites in carbonate rocks, and because the pore geometry tends to be much more complex than what is typically found in clastic environments.

The log of Fig. 16.36 compares the NMR porosity estimates with the conventional neutron and density estimates in a sand and shale sequence. In the third track is a representation of the T_2 distributions on a semi-logarithmic grid. The shale zone is clearly identified by:(1) the elevated gamma ray in track 1 above $\times$540 ft and (2) by the clustering of the T_2 distribution around 3 μs. These low values, below the bound fluid cutoff, signal fluid that is intimately in contact with the rock matrix or

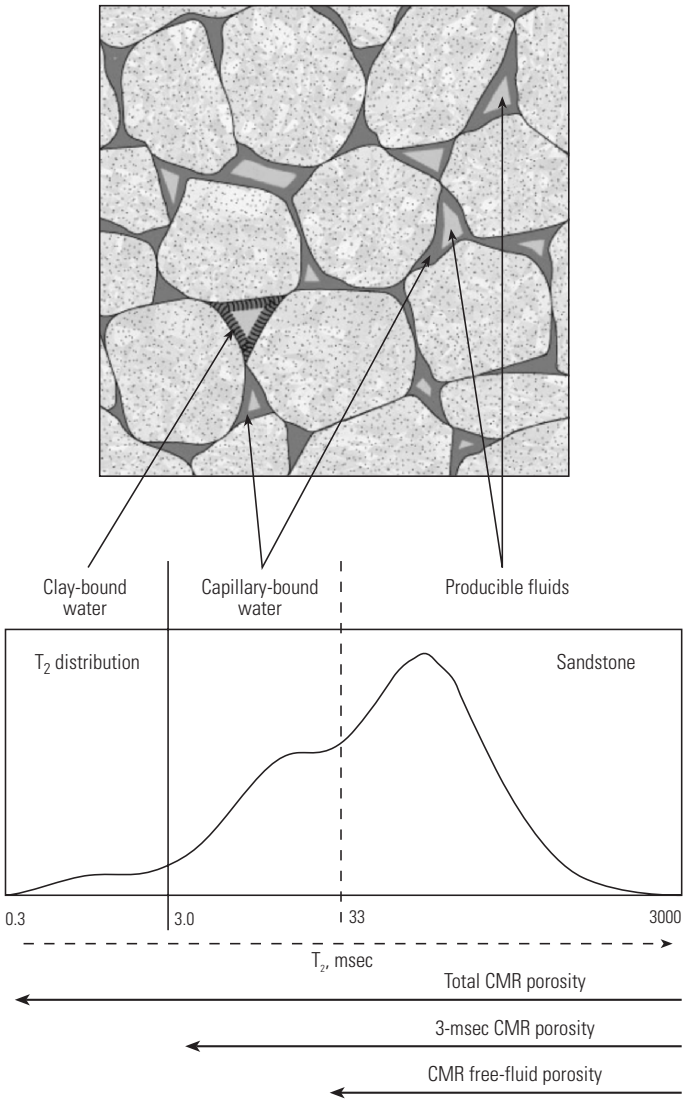


Fig. 16.34 A summary of the idealized interpretation of T_2 distributions for water-wet clastics. The producible fluids are found in the distribution with T_2 values greater than 33 μs, while the capillary bound water is found between 3 and 33 μs. The components that decay with a time constant faster than 3 μs are attributed to clay-bound water. The magnitude of the signal above 33 μs is called the free-fluid porosity.

other surface with paramagnetic sites or with very tiny pore sizes. An estimate of the volume is made, by comparing the portion of the signal below 12 μs to the total NMR porosity. With this special choice of cutoff, it is seen to follow the GR curve as an alternative indication of shale.

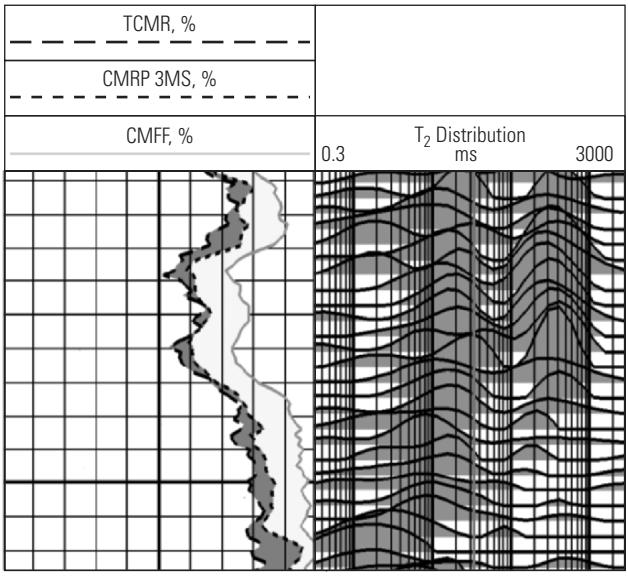


Fig. 16.35 Two tracks of a CMR display. The track on the right displays a representation of the T_2 distributions as a function of depth. The track on the left shows three version of porosity on a scale of 0% to 30%. The lowermost curve corresponds to the sum of amplitudes greater than the 33 μs cutoff – the free-fluid porosity. Between this lower limit and the dotted line, shaded in grey is the additional contribution between 3 and 33 μs that corresponds to capillary bound (irreducible) water and the dark shaded region beyond that corresponds to the fastest component with T_2 less than 3 μs.

Note also that the three estimates of porosity all agree in the water-filled section below ×540 ft. However above ×540 ft the total CMR porosity (indicated as TCMR) agrees with the density porosity estimate. The neutron porosity is reading much higher because it is sensitive to the hydroxyls associated with the clay minerals in the shale.

16.8.3 Pore Size Distribution and Permeability Estimation

The messiness of carbonate rocks or their inherent heterogeneity, compared to clastics, is one source of interpretation difficulties for NMR measurements in these rocks. Traditional interpretation of T_2 distributions in clastics is based upon a reasonably strong correlation between pore size and the observed T_2 values. This is a result of a fairly constant surface-relaxivity value in sandstones, and a lack of interaction between pores in a system of somewhat regular definition. In contrast, carbonates can contain pores on three major length scales; from extremely small micropores in the grain-like material that supports some sort of intermediate sized porosity, to the very large and often hydraulically isolated vugs. Despite the existence of pores on these large scale difference, T_2 distributions rather than being bimodal are often only uni-modal. Several studies of this phenomena [51, 52] indicate that this type of

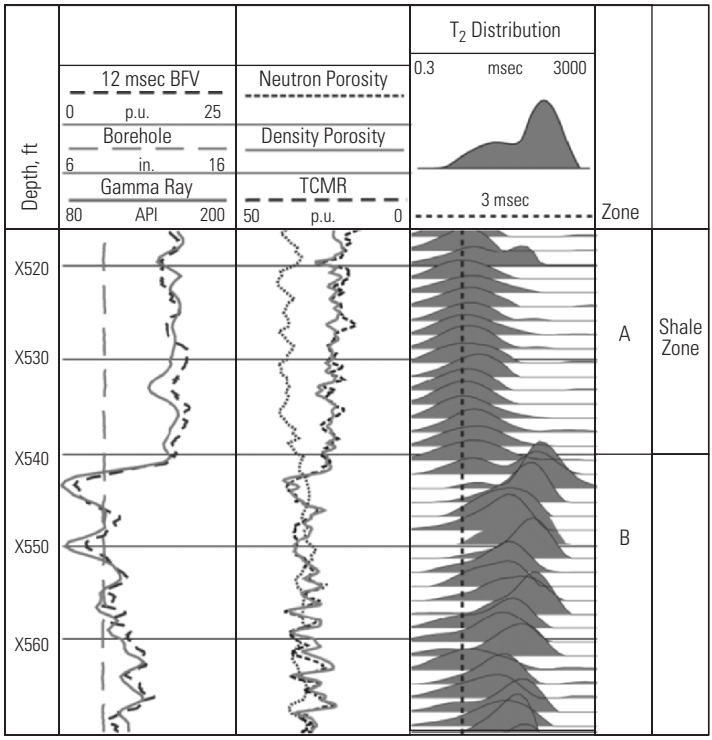


Fig. 16.36 The NMR total porosity compared to neutron and density estimates. In the sand zone B, the three estimates agree. In the shale zone A, the neutron porosity overestimates because it is sensitive to the hydroxyls in the clay minerals. In the first track an estimate of the bound water fraction is made by comparing the fraction of the NMR signal below 12 μs to the total NMR porosity. It tracks the GR signal as an alternative indication of shale.

behavior is caused by an interplay between surface relaxivity and communication by diffusion between the small and larger-pore systems. The upshot is that in carbonates it is often difficult to establish good T_2 cutoff values to use for free versus bound-water determination or to make permeability estimates. By contrast, the situation with clastics is much more rosy.

Estimating permeability of porous rocks from NMR measurements has had a long history extending from the early works of Seevers [45] and Timur [46] to much more recent contributions from Kenyon et al. [47]. All of the relationships that have been developed are based on a combination of theoretical relationships and experimental measurements.

The physical basis comes from the notion that permeability, the coefficient that links the flow rate through a porous sample to the pressure drop, depends most strongly on the size of the pore throats of the medium. The casual link to NMR is that some measure of the T_2 distribution (such as the log mean value) is related to a typical pore dimension. The next seemingly weak link is that the pore size dimension is

also related to the throat size. This latter link is more reliable among sandstones than carbonates.

At present there are two general transforms in widespread use to estimate the permeability. The first, referred to as the Coates–Timur relationship is given by:

$$k = a\phi^4 \left[\frac{\text{FFI}}{\text{BVI}}\right]^2 \tag{16.47}$$

where FFI is the volume of free fluid, estimated by the NMR amplitude above some threshold (say 33 μs) and BVI corresponds to the bound volume fraction.

The second is the so-called SDR relationship:

$$k = a\phi^4 {T_{2,LM}}^2 \tag{16.48}$$

where $T_{2,LM}$ is the logarithmic mean value of the measured T_2 distribution. For both approaches the constant a may need to be adjusted to local conditions or perhaps the exponents on porosity (4) or on the NMR parameter (2) might be adjusted to give a better fit to known values of permeability determined on core samples or by other means.

Figure 16.37 shows an example of a continuous NMR estimation of the permeability compared to core measurements.

16.8.4 Fluid Typing

Although porosity is one of the parameters of primary concern, it is desirable to distinguish between water and hydrocarbon in the pore space. Many methods involving electrical and nuclear methods have been devised to do this. However, the power of NMR can be harnessed to do some of these old analyses in addition to some new ones, such as making a continuous log of viscosity.

First we look at some simple methods for detecting the presence of gas or bitumen, in conjunction with another porosity log.

16.8.4.1 Gas and Tar Determination An early method to recognize the presence of gas with an NMR measurement was proposed by Akkurt [48] for a borehole NMR instrument that incorporated a magnetic field gradient. The diffusion of the gas molecules in the gradient contributes to the T_2 decay rate. The technique relies on this and on the much longer T_1 of gas. Consequently the data is acquired in pairs; a first acquisition of echoes after a short polarization time (or wait time) followed by acquisition of echoes after a much longer polarization time. Performing the data inversion on the difference between the two spectra will cause a separation of oil signal and gas signal to give a qualitative stand-alone indication of the presence of gas.

A conceptually simpler way to detect the presence of gas is to compare a log of the total NMR porosity with that of a neutron/density cross-plot porosity. To first order, the neutron/density cross-plot porosity compensates for the low HI effect on the neutron log, and for the low fluid density effect on the density log. This results, in clean formation, in a surprisingly good estimate of porosity. Comparing the NMR porosity

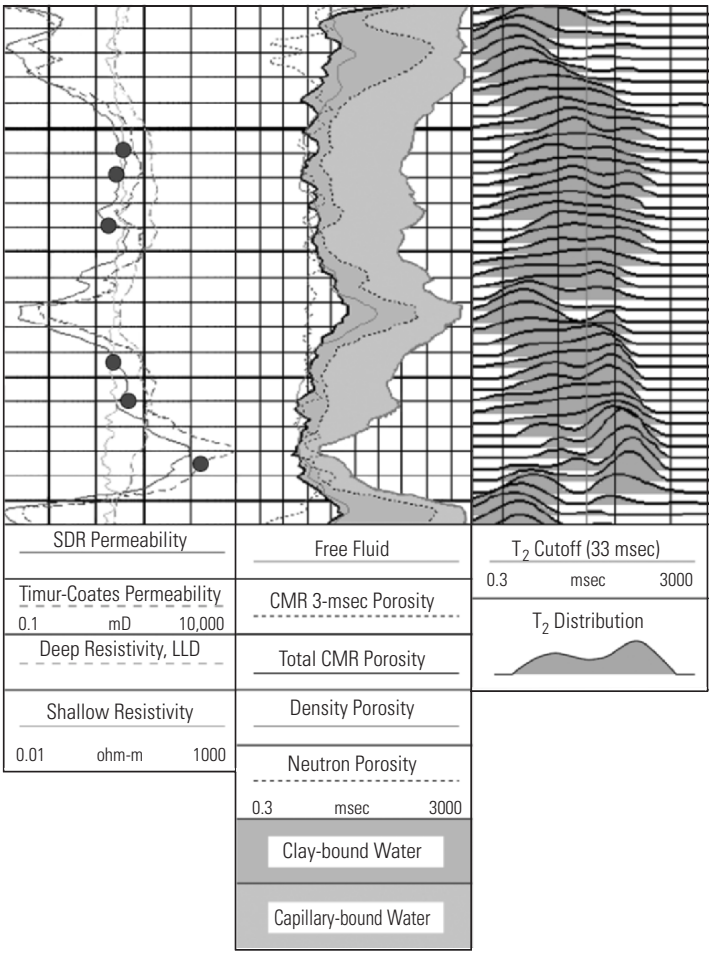


Fig. 16.37 The comparison of two estimates of permeability from the NMR measurements with that derived from a down-hole sampling device is shown in the first track. The partition of porosity from the NMR measurement is shown in the middle track for the T_2 distributions displayed in track 3.

in a gas zone with the neutron/density porosity will show the NMR to be deficient. It will be deficient for two reasons. The first is the low HI of the gas phase, and the second is the possible long polarization time of gas (a function of its density) which can result in incomplete polarization. The two effects will lead to an underreporting of the NMR porosity compared to the neutron/density estimate. A full development of this idea can be found in Freedman et al. [49].

For the case of bitumen, unlike gas, the HI is similar to that of water. However, its viscosity is extremely large and leads to a very small value of T_2 – on the order of a millisecond. For current-day borehole NMR instruments this decay time is too

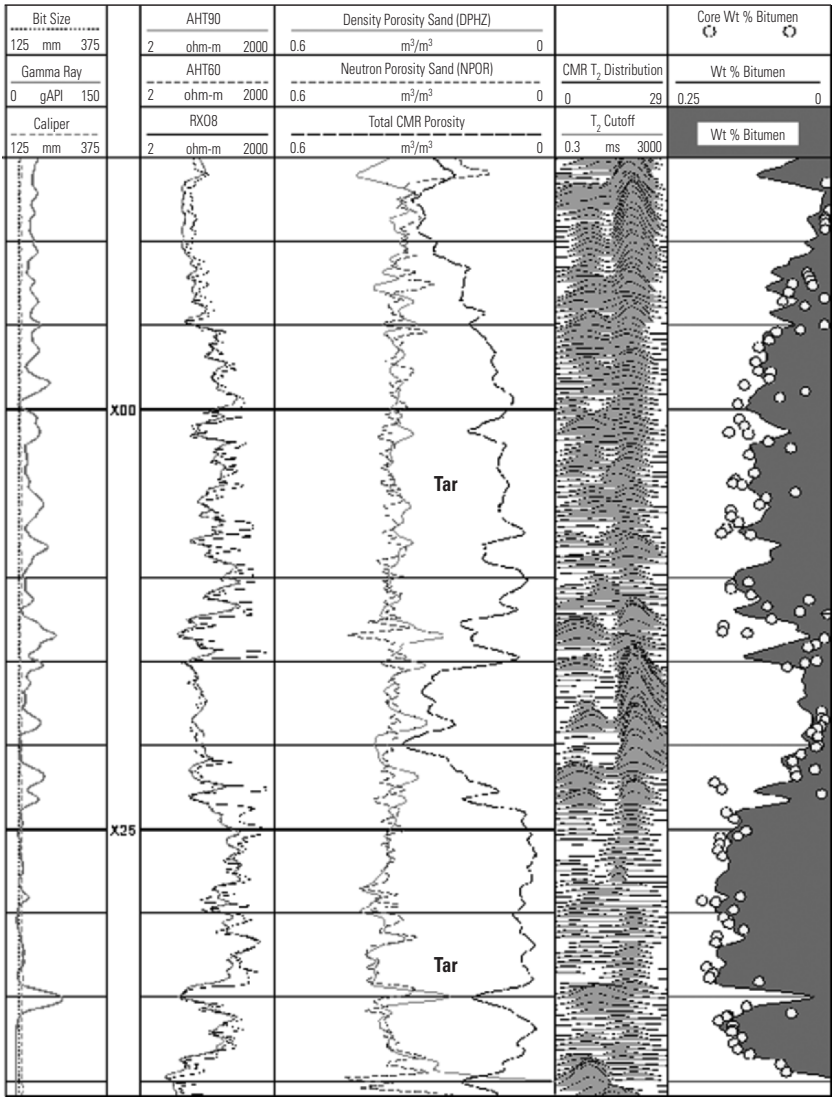


Fig. 16.38 Two zones of tar are identified by the large preponderance of T_2 contribution at very short time and a large difference between the TCMR (total porosity) curve and the neutron/density estimates of porosity. The proof of the method is contained in the last track which compares the bitumen core analysis with that derived from the porosity deficit. Adapted from Mirotchnik et al. [50].

short to be observed. So the bitumen is simply not seen – its signal is as unmeasurable as the hydroxyls found in clay minerals. Consequently, the simplest method to find bitumen is to compare the NMR porosity with either the neutron or density porosity. An example is shown in Fig. 16.38, where the fraction of formation bitumen is seen

to be directly related to the porosity deficit between the nuclear log estimates and the NMR estimate.

The next question is how to separate oil from water.

16.8.4.2 Viscosity In an earlier section (16.4.3) we saw how the the viscosity of crude oils is correlated with T_2. Thus, one method of separating the oil signal from the water signal in the T_2 spectrum would be, assuming that something was known about the oil properties, to look for the contribution at the expected value of T_2 that corresponds to the assumed viscosity (usually greater than water or at least with a shorter T_2) at the formation temperature. The difficulty with this approach can be seen in any measurement that shows a bimodal T_2 distribution. The bimodal distribution might be a result of regions of water where a relatively long T_2 is observed, as well as portions where the surface relaxation dominates. If oil is actually present, depending on its viscosity, its contribution to the T_2 spectrum might be easily obscured. A much better solution exists: it relies on an instrument with a magnetic field gradient so that diffusion of polarized protons can be readily exploited.

In Fig. 16.39 the upper curve in the upper panel shows a bimodal T_2 distribution. This one is actually composed of a combination of oil and water, as has been indicated by the two component curves below it. The ability to make this separation comes

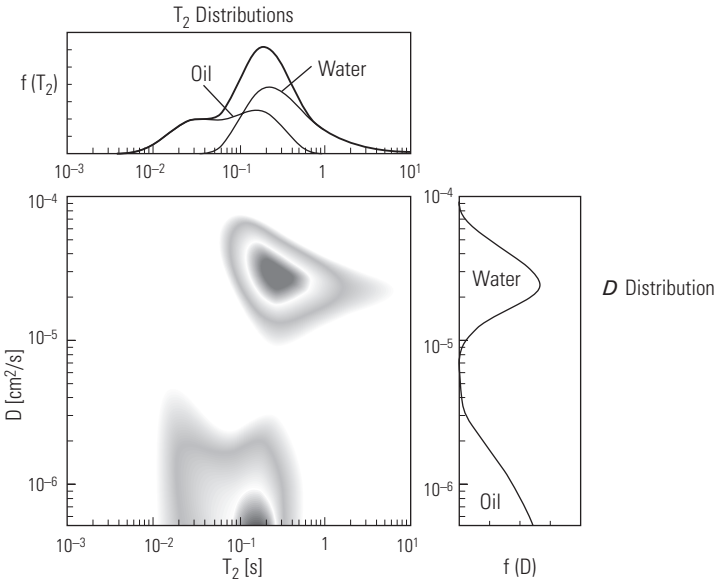


Fig. 16.39 An example of the decomposition of an observed bimodal T_2 distribution into contributions from oil and water. The partition of the T_2 distribution is shown in the top panel. Below it is the $D - T_2$ cross plot of the data with the amplitudes indicated by shading. Two regions are clearly distinct. In the right-hand panel, the distribution of diffusion coefficients is shown which allows easy identification of the water and oil components.

from the simultaneous inclusion of a measurement of the distribution of diffusion coefficients that have contributed to the enhanced T_2 decay rate. The cross plot of $D - T_2$ shows two concentrations of amplitudes, also seen in the right-hand panel where the separation of water from oil, on the basis of diffusion coefficient, is easily made in this case.

In Section 16.4.3 the diffusion coefficients and viscosities of various fluids were discussed. For water, oil, and gas the diffusion coefficients are a function of temperature. At a fixed temperature, water has a single value of diffusion constant. However, this is not the case for oils – at a given temperature, depending on the oil composition, there may be a range of T_2 values and values of D. Experimentally it has been observed for oil that there is a correlation between the T_2 value and the diffusion coefficient and it is dependent on the value of viscosity. These empirical correlations for oils can be expressed as :

$$\frac{1}{T_{2bulk}} = \frac{\eta\, f(GOR)}{aT} \tag{16.49}$$

and,

$$D = \frac{bT}{\eta}, \tag{16.50}$$

where $f(GOR)$ is a dimensionless function of the gas/oil ratio [53].

Thus, on a plot of D vs. T_2 the locus of oil points (where $f(GOR) = 1$) should be located along a line with slope b/a. Furthermore the location of the measured points $(D_i - T_{2i})$ along the line should give an indication of the oil viscosity. Figure 16.39, without any helpful overlays, showed how this cross plot can easily help to distinguish oil from water in this example. Using the cross-plot analysis, the spectrum of T_2 values can be partitioned into the portion that is associated with water and that with oil.

A number of methods has been proposed to extract the parameters for these two-dimension maps from NMR relaxation data. The fundamental physical property exploited is that the decay rate of magnetization attributable to diffusion is proportional to the product of the diffusion coefficient and the square of the echo spacing $(1/T_{2D} \propto DT_e^2)$, as shown in Section 16.3.6 and the appendix). The basis of all the methods is a repetition of a measurement with differing amounts of echo spacing so that the diffusion portion of the T_2 decay can be unraveled from the other sources of decay rate. One particularly elegant method has been described by Hürlimann et al. [54].

Figure 16.40 shows the data from a water zone on a $D-T_2$ map with superimposed sketches of the loci of oil, water, and gas. The uppermost horizontal line is the trend line for gas, with the diffusion coefficient plotted for a given temperature. The second trend line below it is for water (where the data is concentrated), again with the diffusion coefficient appropriate for the bulk fluid at a given temperature. The sloped line, as noted above, corresponds to oil. Oils with large viscosity would plot to the lower left of the diagram while lighter oils would plot towards the upper right. In fact, one difficulty of this interpretation is that some light oils may be indistinguishable from water when the data fall close to where the two lines cross.

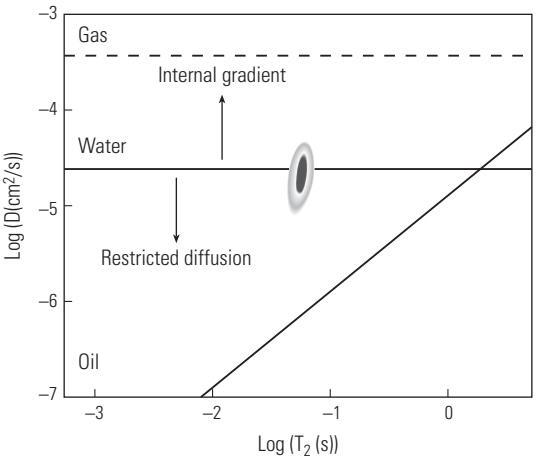


Fig. 16.40 A diffusion-T_2 map of a water zone with "exceptions" to the classical interpretation noted. Adapted from Cao Minh et al. [42].

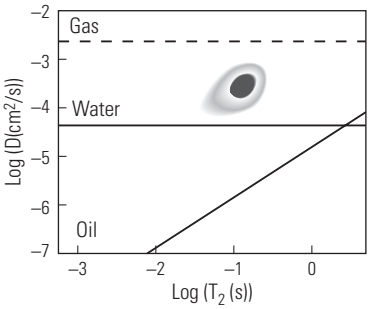


Fig. 16.41 The effect of internal gradients on the appearance of data in a water zone of a clay-rich sandstone. Adapted from Cao Minh et al. [42].

In addition to that scenario a number of "exceptions" to the neat interpretation scheme are indicated on the diagram. Internal gradients, caused perhaps by iron associated with clay particles, will increase the apparent diffusion constant to account for the increased T_2 decay rate. In Fig. 16.41 the concentration of amplitudes, measured in a water-bearing zone of a clay-rich sandstone, is seen to fall well above the water line. The interpretation is that this is the result of an internal gradient effect.

As a final note, water points may plot below the diffusion value of bulk water for a number of reasons, one of which may be restricted diffusion [31]. This might occur if the pores and throats are small enough so that diffusion of the protons associated with the water are impeded from their full ability to diffuse because of collisions with the pore and throat structure.

On a historical note, this elegant $D - T_2$ processing technique, coupled with judicious T_2 cutoffs, is a very efficient way to replace one of the features of the first-generation NMR tool. That tool also was capable of making a measurement of residual oil saturation. It consisted of making two passes in the well, the second after a doping of the mud with paramagnetic ions (manganese EDTA) and waiting for them to invade the formation. In this manner, the water signal in the formation was also "killed" and the remaining NMR signal was due to the residual oil saturation.

16.9 SUMMARY

It has been a long path from magnetometers to the viscosity of oils. To understand the basis of NMR logging we have had to learn how hydrogen acts as a magnetic gyroscope, and then enter into the details of nuclear induction and the relaxations that accompany it. These details are complicated, but it is because there are several different types of relaxation that the NMR signal contains so much information. One type of relaxation, spin dephasing, depends on variations in the magnetic field and not the formation, but can be removed by using a clever pulse sequence. The other types of relaxation – longitudinal and transverse, and the effects of fast, slow or restricted diffusion – lead naturally to the NMR properties of fluids and porous media. We have seen how these properties could not be fully exploited by the earliest logging devices, but that the concept of inside-out magnets allowed resonance methods to be applied downhole and caused a renaissance in nuclear magnetic logging. The basic data acquired by an NMR measurement is a plot of relaxation times at each depth level. More information can be acquired by separating out the effects of diffusion, which can be done by recording with different polarization times and echo spacing.

If there was to be only one nuclear particle in the earth that could be easily detected by nuclear induction, nature was kind to make it hydrogen. There is no other particle that can give us so much information about the microscopic properties of rocks, and in particular about the fluids in them. And we have seen the extent to which this has been exploited. NMR logs give us information on the total amount of fluids, their distribution among different pore sizes, and the fraction that is likely to be producible. Furthermore we are now able to distinguish between different fluids and to say something about their properties. Nature was not so kind in making rocks such complex bodies, so that unraveling the conflicting effects is not easy. In carbonates, for example, it remains difficult to extract useful information because of their relatively weak relaxation. However, one big advantage of NMR is that the downhole measurement is almost identical to that made on core samples in the laboratory. While other measurements have to be made on inconveniently large blocks of formation, or else studied with computer models, NMR laboratory results can be applied directly to the logging measurement. There is therefore good reason to hope that as new discoveries are made in the laboratory, NMR signals will reveal more information useful for unraveling the properties of reservoirs.

16.10 APPENDIX A: DIFFUSION

This short section is written to provide the student with a physically-based derivation of one of the important effects that can be measured with NMR techniques – diffusion. In the literature of the Carr–Purcell technique there is a time T_e associated with flipping the transverse spins by 180° so as to defeat the decay of magnetization caused by the inevitable magnetic field gradient $\frac{\partial B}{\partial x}$, assumed here to be only in the x-direction in this 1-D example. What follows next is a derivation of how the diffusion of magnetized protons in the molecules produces an additional decay rate to the spectrum of decays that is given by $DT_e{}^2$, where T_e, the so-called pulse-echo time, is any arbitrary time between 180° flips.

First we return to the topic of diffusion first introduced in Chapter 3 where Fick's law was used to relate a current of particles J to a change in gradient of particle density dN/dx. Sticking to a 1-D example, the current is just the time rate of change of the density of particles. So the total current at any point can be obtained by finding the difference between the current in the left and right directions:

$$\frac{dN}{dt} = J_+ - J_- = D\frac{dN}{dx}\bigg|_+ - D\frac{dN}{dx}\bigg|_- \tag{16.51}$$

or

$$\frac{dN}{dt} = -D\frac{\partial^2 N}{\partial x^2} \tag{16.52}$$

A solution of this equation, as can be verified by substitution is:

$$N(x,t) = \frac{1}{4\pi\sqrt{Dt}} e^{-\frac{x^2}{Dt}} \tag{16.53}$$

This equation describes how the density of particles, initially all at $x = 0$, will spread out as a function of time and distance from the source. The interesting and useful result from this is that the mean-square displacement after time t, is given by the product Dt, where D is the molecular self-diffusion coefficient.

Consider the magnetization vector M. It consists of many small contributors, m_i that have been polarized by the static field. Confining ourselves to a 1-D argument and imagine that all the contributors m_i are to be found at the position $x = 0$. Then the 90° tipping pulse is applied and the magnetization vector M begins to rotate in the x–y plane with the Larmor frequency. Now let us look at what happens to the magnetization vector M when viewed in the rotating system of coordinates. At some time t, the position of individual contributors m_i will spread out with a distribution in x given by the equation above.

If the polarizing field B_o is not homogenous, but contains some gradient $\partial B/\partial x$, then each will precess at a slightly different rate inducing a phase shift with respect to the main magnetization vector. The phase angle induced, at the end of each pulse echo period, T_e, will depend on the position, x, of each contributor and is given by

$$\Delta = \gamma \frac{\partial B}{\partial x}\, x\, T_e \tag{16.54}$$

This will cause a smearing of the magnetization vector as shown in the sketch of Fig.16.11. To compute the magnitude of the magnetization vector of the pulse echo we need to sum up the contribution (cosine of the phase angle) of all of the m_i at each position of x that they have drifted to by the end of an echo spacing time T_e. The magnetization vector of the nth pulse echo at time t is then given by:

$$M(t) = \int N(x,t)cos(\Delta)dx = \int \frac{1}{4\pi\sqrt{Dt}} e^{-\frac{x^2}{Dt}} cos\left(\gamma \frac{\partial B}{\partial x} x T_e\right) dx \qquad (16.55)$$

Rather than go through the pain of actually doing the integral we will approximate the first portion as a product of the amplitude and width of the function, which can be taken as $2\sqrt{Dt}$. Also we will expand the cosine to 1st order resulting in the following approximate expression for $M(t)$:

$$M(t) \approx \frac{1}{4\pi\sqrt{Dt}} 2\sqrt{Dt}\left(1 - \left(\gamma \frac{\partial B}{\partial x} x T_e\right)^2\right). \qquad (16.56)$$

Since we are looking for an equation with a decay rate we then approximate this first term expansion to the exponential function and substitute the value of $\sqrt{Dt}$ for the distance x at which to evaluate the magnetic field gradient:

$$M(t) \propto e^{-(\gamma \frac{\partial B}{\partial x})^2 Dt {T_e}^2}. \qquad (16.57)$$

This expression clearly gives a decay rate that is proportional to $D{T_e}^2$, the desired result.

REFERENCES

1. Jackson JA (1984) Nuclear magnetic well logging. The Log Analyst 25(5):16–30
2. Feynman RP, Leighton RB, Sands ML (1965) Feynman lectures on physics v2. Addison-Wesley, Reading, MA
3. Bloch F (1946) Nuclear induction. Phys Rev 70(7–8):460–474
4. Fukishima E, Roeder S (1981) Experimental pulse NMR: a nuts and bolts approach. Addison-Wesley, Reading, MA
5. Appel M (2004) Nuclear magnetic resonance and formation porosity. Petrophysics 45(3):296–307
6. Carr HY, Purcell EM (1954) Effects of diffusion on free precession in nuclear magnetic resonance experiments. Phys Rev 94(3):630–638
7. Meiboom S, Gill D (1958) Modified spin-echo method for measuring nuclear relaxation times. Rev Sci Instrum 29:688–691

8. Mardon D, Prammer MG, Taicher Z, Chandler RN, Coates GR (1995) Improved environmental corrections for MRIL pulsed NMR logs run in high-salinity boreholes. Trans SPWLA 35th Annual Logging Symposium, paper DD

9. Davis JC Jr (1965) Advanced physical chemistry, molecules, structure, and spectra. Ronald Press, New York

10. Kleinberg RL, Vinegar HJ (1996) NMR properties of reservoir fluids. The Log Analyst 37(6):20–32

11. Dunn K-J, Bergman DJ, Latorraca GA (2002) Nuclear magnetic resonance: Petrophysical and logging applications. Pergamon, New York

12. Brown RJS (1961) Proton relaxation in crude oils. Nature 189:387–388

13. Bloembergen N, Purcell EM, Pound RV (1948) Relaxation effects in nuclear magnetic resonance absorption. Phys Rev 73(7):679–703

14. Pople JA, Schneider WG, Bernstein HJ (1959) High-resolution nuclear magnetic resonance. McGraw-Hill, New York

15. Winkler M, Freeman JJ, Appel M (2005) The limits of fluid property correlations used in NMR well logging: an experimental study of reservoir fluids at reservoir conditions. Petrophysics 46(2):104–112

16. Morriss CE, Freedman R, Straley C, Johnston M, Vinegar HJ, Tutunjian PN (1997) Hydrocarbon saturation and viscosity estimation from NMR logging in the belridge diatomite. The Log Analyst 38(2):44–59

17. Brown JA, Brown LF, Jackson JA, Milewski JV, Travis BJ (1982) NMR logging tool development: laboratory studies of tight gas sands and artificial porous material. Presented at the SPE Unconventional Gas Recovery Symposium, paper SPE 10813

18. Lo S-W, Hirasaki GJ, House WV, and Kobayashi R (2000) Correlations of NMR relaxation time with viscosity, diffusivity and gas/oil ratio of methane/hydrocarbon mixtures. Presented at the SPE 75th Annual Technical Conference and Exhibition, paper SPE 63217

19. Brown RJS, Fatt I (1956) Measurements of fractional wettability of oil fields' rocks by the nuclear magnetic relaxation method. Pet Trans AIME 207:262–270

20. Kleinberg RL, Straley C, Kenyon WE, Akkurt R, Farooqui S (1993) Nuclear magnetic resonance of rocks: T_1 vs. T_2. Presented at SPE 68th Annual Technical Conference and Exhibition, paper SPE 26470

21. Kenyon WE (1997) Petrophysical principles of applications of NMR logging. The Log Analyst 38(2):21–43

22. Korringa J, Seevers DO, Torrey HC (1962) Theory of spin pumping and relaxation in systems with a low concentration of electron spin resonance centers. Phys Rev 127(4):1143–1150

23. Latour LL, Kleinberg RL, Sezginer A (1992) Nuclear magnetic resonance properties of rocks at elevated temperatures. J Colloid Interface Sci 150(2):535–548

24. Timur A (1969) Pulsed nuclear magnetic resonance studies of porosity, movable fluid, and permeability of sandstones. JPT 21:775–779

25. Timur A (1968) An investigation of permeability, porosity and residual water saturation relationships for sandstone reservoirs. The Log Analyst 9(4):8–17

26. Loren JD, Robinson JD (1969) Relations between pore size fluid and matrix properties, and NML measurements. Presented at the SPE 44th Annual Technical Conference, paper SPE 2529

27. Straley C, Morriss CE, Kenyon WE, Howard JJ (1991) NMR in partially saturated rocks: laboratory insights on free fluid index and comparison with borehole logs. Trans SPWLA 32nd Annual Logging Symposium, paper CC

28. Kenyon WE, Howard JJ, Sezginer A, Strayley C, Matteson A, Horkowitz K, Ehrlich R (1989) Pore-size distribution and NMR in microporous cherty sandstones. Trans SPWLA 30th Annual Logging Symposium, paper LL

29. Morriss CE, Macinnis J, Freedman R, Smaardyk J, Straley C, Kenyon WE, Vinegar HJ, Tutunjian PN (1993) Field test of an experimental pulsed nuclear magnetism tool. Trans SPWLA 34th Annual Logging Symposium, paper GGG

30. Straley C, Rossini D, Vinegar HJ, Tutunjian PN, Morriss CE (1997) Core analysis by low-field NMR. The Log Analyst 38(2):84–94

31. Sen PN (2004) Time-dependent diffusion coefficient as a probe of geometry. Concepts Magn Reson Part A 23A(1):1–21

32. Kleinberg RL (1999) Nuclear magnetic resonance. In: Wong P-Z (ed) Experimental methods in the physical sciences v35. Academic Press, San Diego, CA

33. Brown RJS, Gamson BW (1960) Nuclear magnetism logging. Pet Trans AIME 219:201–209, paper SPE 1305

34. Herrick RC, Couturie SH, Best DL (1979) An improved nuclear magnetism logging system and its application to formation evaluation. Presented at the SPE 54th Annual Technical Conference, paper SPE 8361

35. Prammer MG (2001) NUMAR (1991–2000). Concepts Magn Reson 13(6): 389–395

36. Jackson JA (2001) Los Alamos NMR well logging project. Concepts Magn Reson 13(6):368–378

37. Prammer MG (1994) NMR pore size distributions and permeability at the well site. Presented at the SPE 69th Annual Technical Conference and Exhibition, paper SPE 28368

38. Kleinberg RL (2001) NMR well logging at Schlumberger. Concepts Magn Reson 13(6):396–403

39. Prammer MG, Drack E, Goodman G, Masak P, Menger S, Morys M, Zannoni S, Suddarth B, Dudley J (2000) The magnetic resonance while-drilling tool: theory and operation. Presented at the SPE 75th Annual Technical Conference and Exhibition, paper SPE 62981

40. Morley J, Heidler R, Horkowitz J, Luong B, Woodburn C, Poitsch M, Borbas T, Wendt B (2002) Field testing of a new nuclear magnetic resonance logging-while drilling tool. Presented at the SPE 77th Annual Technical Conference and Exhibition, paper SPE 77477

41. Akkurt R, Prammer MG, Moore MA (1996) Selection of optimal acquisition parameters for MRIL logs. The Log Analyst 37(6):43–52

42. Cao Minh C, Heaton N, Ramamoorthy R, Decoster E, White J, Junk E, Eyvazzedeh R, Al-Yousef O, Fiorini R, McLendon D (2003) Planning and interpreting NMR fluid-characterization logs. Presented at the SPE 78th Annual Technical Conference and Exhibition, paper SPE 84478

43. Morriss CE, Deutch P, Freedman R, McKeon D, Kleinberg RL (1996) Operating guide for the combinable magnetic resonance tool. The Log Analyst 37(6):53–60

44. Coates GR, Xiao L, Prammer MG (1999) NMR logging principles and applications. Halliburton Energy Services, Houston, TX

45. Seevers DO (1967) A nuclear magnetic method for determining the permeability of sandstone. Trans SPWLA Annual Logging Symposium, paper L

46. Timur AT (1972) Nuclear magnetism studies of carbonate rocks. Trans SPWLA 13th Annual Logging Symposium, paper N

47. Kenyon WE, Straley C, Sen PN, Herron M, Matteson A, Takezaki H, Petricola MH (1995) A laboratory study of nuclear magnetic resonance relaxation and its relation to depositional texture and petrophysical properties – carbonate Thamama group, Mubarraz field, Abu Dhabi. SPE Middle East Oil Show, Bahrain, paper SPE 29886

48. Akkurt R, Vinegar RJ, Tutunjian PN, Buillory AJ (1996) NMR logging of natural gas reservoirs. The Log Analyst 37(6):33–42

49. Freedman R, Cao Minh C, Gubelin G, McGinness T, Terry B, Freeman J, Rawlence D (1998) Combining NMR and density logs for petrophysical analysis

in gas-bearing formations. Trans SPWLA 39th Annual Logging Symposium, paper II

50. Mirotchnik KD, Allsopp K, Kantzas A, Curwen D, Badry R (1999) Low field NMR-tool for bitumen sands characterization: a new approach. Presented at the SPE 74th Annual Technical Conference and Exhibition, paper SPE56764

51. Anand V, Hirasaki G (2005) Diffusional coupling between mico and macroporosity for NMR relaxation in sandstone and grainstones. Trans SPWLA 46th Annual Logging Symposium, paper KKK

52. Ramakrishnan TS, Schwartz LM, Fordham EJ, Kenyon WE, Wilkinson DJ (1999) Forward models for nuclear magnetic resonance in carbonate rocks. The Log Analyst 40(4):260–270

53. Freedman R, Lo S, Flaum M, Hirasaki GH, Matteston A, Sezginer A (2001) A new NMR method of fluid characterization in reservoir rocks: experimental confirmation and simulation results. SPEJ 6(4):452–464

54. Hürlimann M, Venkataramanan L, Flaum C, Speier P, Karmonk C, Freedman R, Heaton N (2002) Diffusion-editing: new NMR measurements of saturation and pore geometry. Trans SPWLA 43rd Annual Logging Symposium, paper FFF

Problems

16.1 What is the magnetic field required to produce a Larmor frequency of 2 Mhz for protons?

16.2 Suppose the field strength in one portion of the measurement volume is 1% larger than the nominal field to produce the 2 Mhz Larmor frequency. How many cycles of precession will it take for those spins to lead the pack by 45°?

16.3 From the rules of quantum mechanics a particle of spin J can have $2(J+1/2)$ projections of spins of multiples of $\hbar/2$ and the magnitude of the spin vector is given by $\sqrt{J(J+1/2)\hbar^2}$. For the proton with spin 1/2, show that the angle between the spin vector I and an applied magnetic field is 54°.

16.4 In Fig. 16.15, why is the slope of T_1 as a function of temperature the way it is? Can it be explained by the viscosity/temperature relation even though viscosity is a function of temperature?

16.5 Using the data on the diffusion coefficient as a function of temperature for water, Fig. 16.42, compute the T_2 value of water for an instrument with a field gradient of 20 Gauss/cm and an echo spacing of 2 ms at 150°C. (Should agree with Fig.16.15)

16.6 Using the information in the text and caption concerning the numerical simulation of induced magnetization of Fig. 16.5:

16.6.1 Compute the value of T_1.

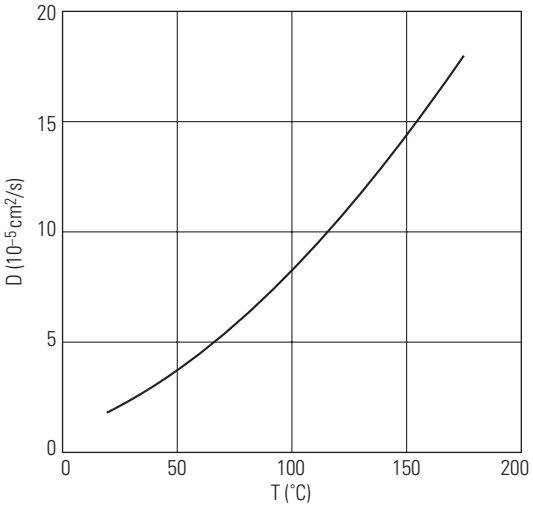


Fig. 16.42 The diffusion coefficient of water as a function of temperature. From Kleinberg and Vinegar [10]. Used with permission.

16.6.2 Prove that the equilibrium value of magnetization of this example of 121 particles results in exactly 110 particles aligned with the field.

16.7 For a centered borehole logging tool with a coaxial dipole magnet, the polarizing field varies with the distance from the center of the borehole, r, as: $B(r) = \frac{B_o}{r^2}$. Show that the radius at which Na ions will resonate, r_{Na} is given by:

$$r_{Na} = \sqrt{\frac{\gamma_{Na}}{\gamma_H}} r_H, \tag{16.58}$$

where r_H is the radius for the resonance of protons. Evaluate the fraction from the values given in Table 16.1.

16.8 Derive the relationship between the T_1 relaxation rate and the correlation time τ_c in terms of the the liquid viscosity, η and temperature T. Suggestion: First relate the diffusion coefficient to the fluid viscosity of a particle of radius a, from relations developed in Chapter 3. Then using the definition of the diffusion coefficient from the statistical point of view (Eq. 16.39) identify the the correlation time as being close to the time required to diffuse a distance a.

17

Introduction to Acoustic Logging

17.1 INTRODUCTION TO ACOUSTIC LOGGING

Although the acoustic properties of rocks are of interest for their own sake, academic interest was not responsible for the development of acoustic borehole logging. The requirements of hydrocarbon exploration and evaluation were the stimuli for the introduction of this third category of physical measurements into well logging. Unlike resistivity measurements, which could be used directly for hydrocarbon detection, and nuclear measurements, which were initially directed at the determination of porosity, acoustic logging started out as a companion to seismic exploration. The first part of this chapter relates the history of how acoustic measurements finally came to be an integral part of wireline logging, after a shaky start as a seismic adjunct.

As a basis for understanding some of the applications of acoustic measurements, both realized and promised, a review of elastic properties of materials is presented. The relationship between the various types of elastic parameters used to describe materials is summarized and related to the velocity of propagation of shear and compressional waves in elastic media. A rudimentary logging device for the simplest and most common logging measurement, the interval transit time of an acoustic compressional wave, is presented, along with the basic empirical data relating transit time to porosity, which changed the entire application of acoustic logging. These data indicate the need for acoustic models of rocks to explain observations in detail.

17.2 SHORT HISTORY OF ACOUSTIC MEASUREMENTS IN BOREHOLES

The use of acoustic energy to produce an image of the subsurface has had a long history. Reflection seismic prospecting consists of using a low-frequency acoustic source at the surface to create down-going pulses of energy which are partially reflected by layers more or less directly below the source. A surface array of detectors, usually close to the source, detects the reflected waves. This technique was the outgrowth of a number of years of refraction seismic work, in which the source and receivers were separated by large distances compared to the depth of reflectors. Some of the earliest refraction work was done in Germany during World War I. It was used for the location of enemy artillery positions by a type of triangulation. This approach was extended to the search for petroleum and had its first application in the detection of a salt dome around 1920.

The reflection seismic technique was immediately put to use in the petroleum exploration business and had its first successful demonstration in mapping a previously discovered salt dome. Its first solo success came in 1925 with the mapping of a petroleum deposit in Oklahoma. From then on it became a much-used tool, and in some cases a standard exploration technique.

The biggest interpretation problem for the early seismic pioneers was the correlation between time and depth. Even with knowledge of the speed of sound in a variety of rock types, it was impossible to be certain of the depth of a given reflector. To deal with this problem, velocity surveys began to be conducted in 1927. These consisted of the setting off of explosions at the surface and the recording of the arrival times at known depths in a well. The business of velocity surveys increased rapidly.

Seeing the opportunity for additional revenue, Schlumberger Well Surveying Corporation entered the business of velocity surveys in the mid-1930s, by making available, for rent, the trucks and cables for these operations. At about the same time, Conrad Schlumberger patented a device for measuring the velocity of sound over a short interval of rock traversed by the borehole [1]. The cover page of the patent is shown in Fig. 17.1. What is not apparent from the drawing is that the source of downhole acoustic energy was the horn of a Model A Ford. The initial version of this device was tested but failed to work. It was an idea ahead of its time. The achievement of a workable device required the improved technology that was to become available at the end of World War II.

The desire to know local formation velocities prompted the development, nearly simultaneously, of borehole logging devices by three oil companies: Humble, Magnolia, and Shell. Two of the companies produced a two-receiver device, while the third used only a single receiver. At that time, Schlumberger had one enterprising individual who invented and implemented a sort of inverted velocity survey [2, 3]. Instead of drilling many shot holes at the surface, he proposed putting the explosive in the well and recording arrivals at the surface. The first source was the side-wall sample taker (an explosive device which drove a steel cup into the formation to extract a sample of the rock), but it did not create enough acoustic energy to be detectable very easily

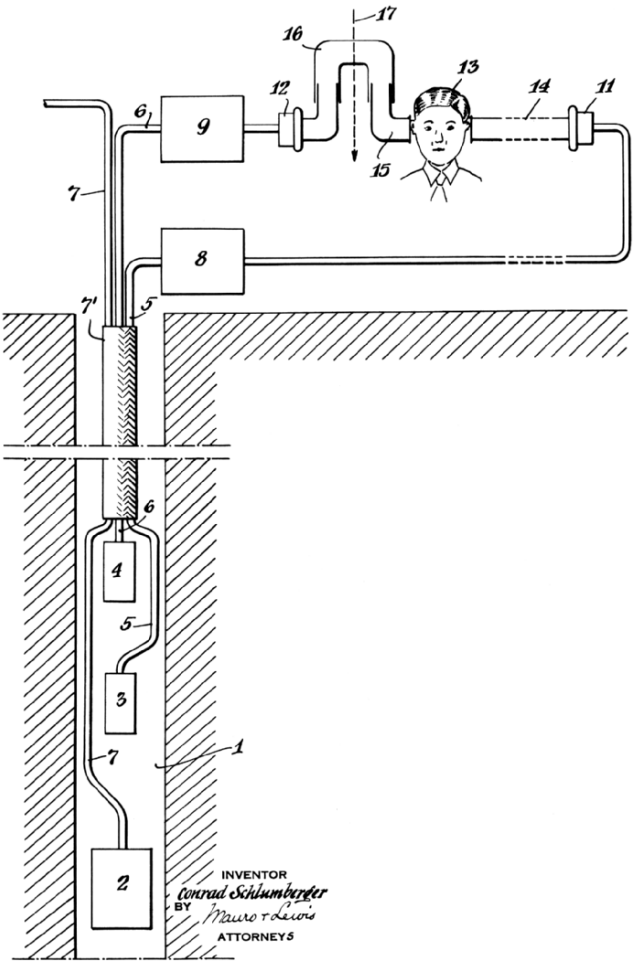


Fig. 17.1 Front cover of a 1935 patent for obtaining the interval transit time [1].

at the surface. He later tried the conventional perforating gun, using dummy Bakelite bullets, which worked for depths shallower than about 3,500 ft.

The inverted velocity survey then evolved into the precursor of the sonic log when the perforating gun was suspended from 400 ft of special low velocity cable. At the top of this special cable hung a geophone, and 400 ft higher a second geophone. This device allowed the determination of the velocity continuously, up and down the well, with a check on each 400 ft section. However, the idea was abandoned due to the unwieldly nature of the apparatus.

In 1955, Schlumberger entered the velocity logging business in earnest by acquiring the Humble velocity logging patent. The design was modified to produce a practical logging tool without any notion of sonic log interpretation. Fortunately, during the same years researchers at Gulf were measuring the relation between velocity and

porosity on real and synthetic rock samples. The publication of this data led to the well-known Wyllie time-average relation, which provided the needed breakthrough to make velocity logging an important tool in well logging and formation evaluation.

As experience in the acquisition of sonic logs (initially used for the velocity surveys) progressed, a correlation between bad logs and washed-out boreholes was made. This led to a new tool design (borehole compensated, (BHC) incorporating a pair of transmitters and receivers to compensate for the borehole enlargements. Initially unexplained loss of signal in cased wells was attributed to a lack of cement to casing bonding and spurred an entire parallel development of ultrasonic devices to measuring casing and cement properties.

Later, the alteration of the mechanical properties of the the formation closest to the borehole was seen to have undue influence on the measurements, so deeper-looking devices were constructed. These long-spaced sonic devices, with increased source-detector spacing, allowed the measurement of undisturbed compressional velocity used for the velocity survey.

The recognition of the importance of the measure of shear velocity spurred the recording of the downhole wavetrains, a task greatly aided by developments in waveform digitization. Many technical improvements ensued in both electronics, transducer design and signal-processing that have culminated in devices that use multiple monopole and dipole transmitters and multiple-oriented receiver arrays that allow, at a minimum, shear wave logging in addition to the usual compressional wave logging, and measurement of acoustic anisotropy among other interesting parameters.

17.3 APPLICATIONS OF BOREHOLE ACOUSTIC LOGGING

The conventional approach to acoustic logging uses the transmission method. It consists of a transmitter of acoustic energy and a receiver at some distance from it. The acoustic energy is in the frequency range of about 20 kHz and is transmitted in short bursts rather than continuously. The detected acoustic signal has been transmitted through a portion of the rock formation surrounding the borehole. This method commonly measures the velocity of compressional and (more recently) shear acoustic waves. The most common use of the velocity measurements is to relate them to formation porosity and lithology. However, as discussed in Chapter 19, it is also possible to infer and estimate abnormally high pore pressures and to estimate mechanical rock properties from the acoustic measurements.

An additional parameter that can be measured in the transmission mode, besides the velocities, is the attenuation. Although not as common as the simple interval transit time measurement, it is exploited with variable success in the detection of fractures. On the other hand, the attenuation method has been used routinely to evaluate the quality of the cement bond to the steel casing.

The second method of borehole acoustic measurement is the reflection mode. In this case the source of acoustic energy is at much higher frequencies, on the order of 500 kHz. Usually the transmitter and receiver are a single element. Depending upon the application, the transit time between emission and reception, or attenuation,

of the signal is measured. One of the applications of the reflection technique is to obtain an acoustic image of the borehole wall. This method has achieved considerable success in the detection and evaluation of fractures. Another application, described in Chapter 19, is also for the evaluation of cement bonding.

A new class of measurements has sprung up since the introduction of dipole transmitters and arrays of receivers; the incorporation of sophisticated signal processing; and detailed acoustic modeling. Developments in these areas has allowed the measurement and exploitation of dispersive borehole acoustic waves. The application of dispersion analysis to geomechanics is introduced in Chapter 19.

17.4 REVIEW OF ELASTIC PROPERTIES

Two important types of energy transport mechanisms are supported by elastic media: compressional waves and shear waves. Figure 17.2 illustrates the notion of the compressional wave for a system of masses suspended or linked to one another by springs. This might represent the atoms in a crystalline structure with the electrostatic repulsion replacing the springs. If the far end of this mass-spring assembly is moved rapidly to the right, causing a compression, and then is suddenly stopped, the compression will propagate to the right with a velocity v_p. The traveling of this compressional disturbance will cause local stresses (forces) and local displacements, as noted in the bottom portion of the figure. For this type of wave, the particle displacement and disturbance propagation are in the same direction.

To illustrate the notion of a shear wave in which the particle displacement is at right angles to the motion of the disturbance, refer to Fig. 17.3. In this case the 1D mass-spring assembly of Fig. 17.2 is replaced by a 2D structure with spring

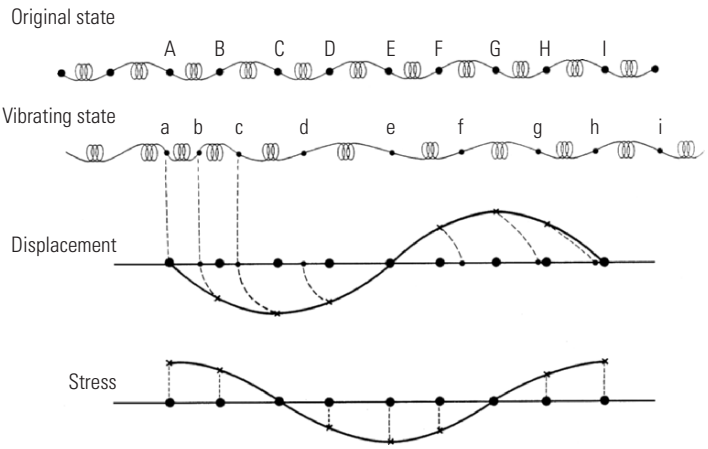


Fig. 17.2 Representation of an elastic medium by coupled springs and masses. A vibration induced in the material is seen to induce variable displacements and stresses on individual sites.

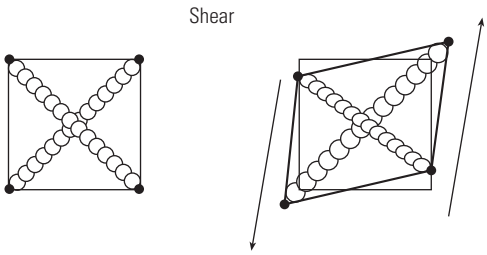


Fig. 17.3 Representation of shear forces in an elastic material which involves consideration of the cross-coupling of mass elements.

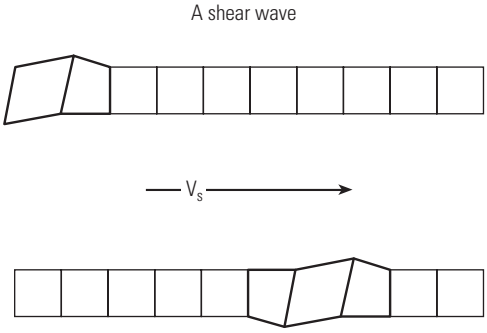


Fig. 17.4 The propagation of a wave of induced shear forces.

cross-members. The element of material composed of two linked masses is shown, on the right, to undergo a shearing action. The result of this motion is that one of the diagonal springs is elongated and the other is compressed. Once the shearing force is removed, the small system will realign itself to relieve the compression of one spring and the tension of the other.

In Fig. 17.4 a series of these elements is shown linked together. A shearing distortion is seen to be applied at the left end. If the left edge is held fixed while the shearing force is released, then the shear distortion will propagate to the right with a velocity v_s.

In order to quantify these two elementary types of wave propagation, it is necessary to review the parameters used to characterize elastic media. The first is Young's modulus, Y (sometimes E). In Fig. 17.5, the effects of stretching a bar under uniform tension are illustrated. From Hooke's law the elongation Δl will be proportional to the force F applied to the stretching. The stress σ, under which the bar is placed, is defined as the force F, divided by the cross-sectional area A, and Young's modulus is the constant which links this stress to strain, or fractional change in length in the direction of the stress:

$$\frac{F}{A} = Y \frac{\Delta l}{l} . \tag{17.1}$$

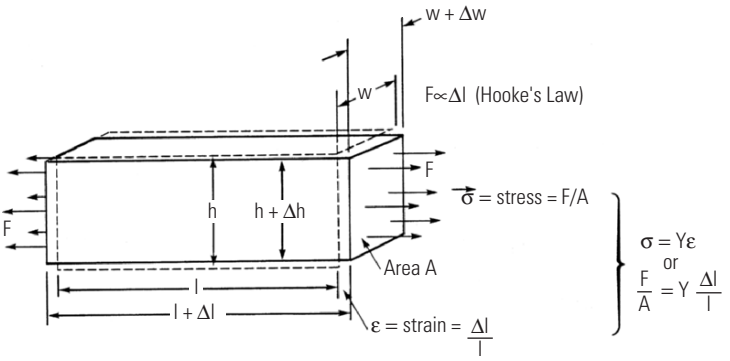


Fig. 17.5 Deformation of a bar under uniform horizontal tension. Adapted from Feynman et al. [4].

The stress on the illustrated bar will also produce contractions in the width $\frac{\Delta W}{W}$, and contractions in height $\frac{\Delta h}{h}$. Both of these contractions will be proportional to the elongation and will be reductions, if the elongation is taken to be positive. This can be written as:

$$\frac{\Delta W}{W} = \frac{\Delta h}{h} = -\nu \frac{\Delta l}{l}, \tag{17.2}$$

where ν (sometimes written as σ) is Poisson's ratio. Thus the elongation in one axis multiplied by Poisson's ratio will yield the contraction in the other two axes when a uniform stress is applied. These two constants, Young's modulus and the Poisson ratio, are the only two parameters necessary to completely specify the elastic properties of a homogeneous, isotropic material. However, there are a variety of other commonly used elastic constants that also describe the same medium. They arose from either the experimental methods used to study materials or from theoretical considerations.

One of the other common constants used is the bulk modulus B (sometimes K). It is the measure of the compressibility of a material put under a uniform confining pressure. The defining relation for the bulk modulus is:

$$p = -B\frac{\Delta V}{V}, \tag{17.3}$$

where the bulk modulus B is seen to relate the pressure p, necessary to change the volume by the fractional amount $\frac{\Delta V}{V}$. Figure 17.6, and the discussion below, indicate how this parameter, an obvious one for measurement in the laboratory, can be related to Young's modulus and Poisson's ratio.

The forces on the bar, which is under uniform pressure, are considered in only one direction at a time. The analysis first examines the change in the length of the bar from the three components. The confining force F_1 will produce a change in length given by:

$$\frac{\Delta l}{l} = -\frac{p}{Y}. \tag{17.4}$$

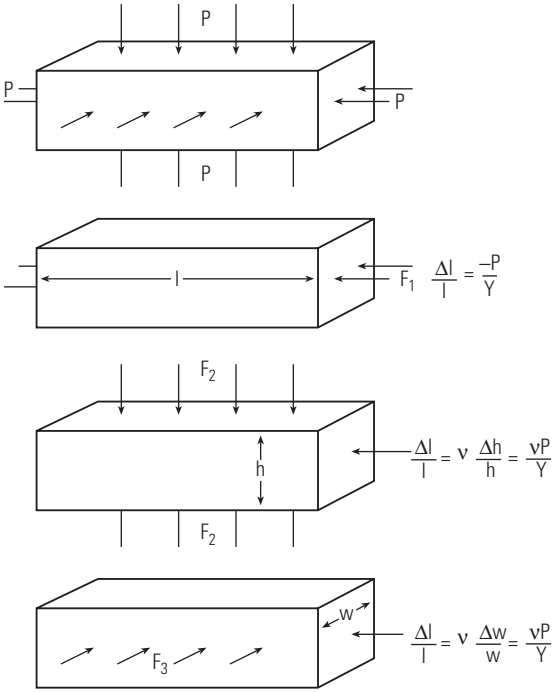


Fig. 17.6 Deformation of a bar under uniform pressure. Adapted from Feynman et al. [4].

It is negative because the length will decrease. The result of the decrease in length will, as the second sketch in the sequence shows, produce an increase in the height of the bar.

In a second step, consider the change in length of the bar due to the pressure applied to the top and bottom of the bar. The fractional change in height of the bar will produce a lengthening of the bar:

$$\frac{\Delta l}{l} = \nu \frac{\Delta h}{h} . \tag{17.5}$$

The fractional change in height due to the force F_2 is just as in the last equation, $\frac{p}{Y}$, thus:

$$\frac{\Delta l}{l} = \nu \frac{\Delta h}{h} = \frac{\nu p}{Y} . \tag{17.6}$$

In the third sequence, the effects of the pressure on the sides, which produces a change in width and a subsequent change in fractional length, can be seen to be, by analogy:

$$\frac{\Delta l}{l} = \nu \frac{\Delta w}{w} = \frac{\nu p}{Y} . \tag{17.7}$$

Thus the total fractional change in length due to these three components of the pressure is:

$$\frac{\Delta l}{l} = -\frac{p}{Y}(1 - 2\nu) . \tag{17.8}$$

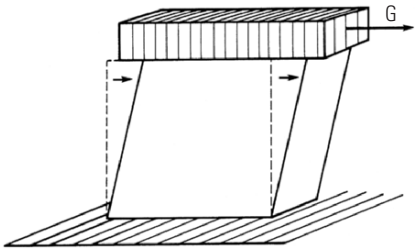


Fig. 17.7 Deformation of a cube under uniform shear. Adapted from Feynman et al. [4].

From this, the total volume strain $\frac{\Delta V}{V}$ can be found; it is three times the length change just established:

$$\frac{\Delta V}{V} = 3\frac{\Delta l}{l} = -3\frac{p}{Y}(1 - 2\nu) . \tag{17.9}$$

From this expression, it is seen that a constraint on Poisson's ratio is that it must be less than $\frac{1}{2}$.

The relation of the shear modulus to the two initial constants is considered next. In Fig. 17.7, an example of pure shear is shown. A tangential force G is applied to a surface area A, to produce a uniform shear. Figure 17.8 shows that two pairs of shear forces can be considered equivalent to a pair of compressional and stretching forces, shown in the lower portion of the figure. The shear modulus μ relates the shear strain Θ to the shear stress $\frac{G}{A}$, which is the tangential force per unit area. Figure 17.9 shows the definition of the shearing angle Θ, which is the ratio of the maximum displacement δ, divided by the length of the cube under shear. With reference to these definitions, the relations are:

$$\Theta = \frac{\delta}{l} = \frac{1}{\mu}\frac{G}{A} . \tag{17.10}$$

To relate the shear modulus to the previous elastic constants, consider Fig. 17.8, which shows the equivalent diagram for shear stress. The change in the diagonal lengths needs to be evaluated. Along the diagonal indicated, the elongation that results from the stretching force is given by the Hooke relation:

$$\frac{\Delta D}{D} = \frac{1}{Y}\frac{G}{A} . \tag{17.11}$$

The compressional force will produce a similar elongation. It is given by:

$$\frac{\Delta D}{D} = \nu\frac{1}{Y}\frac{G}{A} . \tag{17.12}$$

Thus the total change in the one diagonal length is given by:

$$\frac{\Delta D}{D} = \frac{1}{Y}(1 + \nu)\frac{G}{A} . \tag{17.13}$$

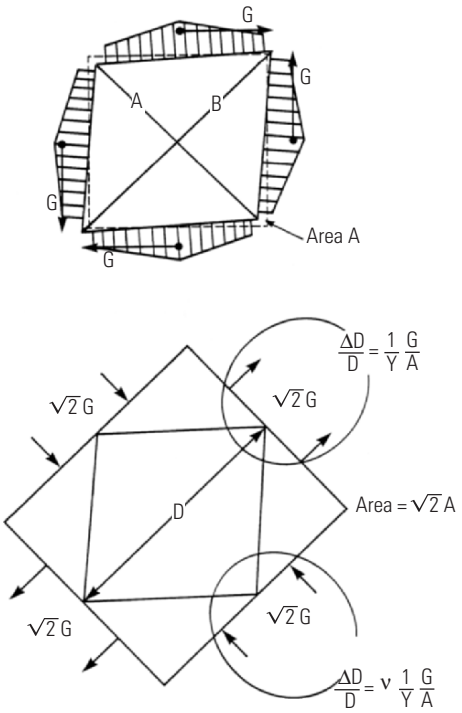


Fig. 17.8 Resolution of forces on cube into equivalent stretching and compressive forces. Adapted from Feynman et al. [4].

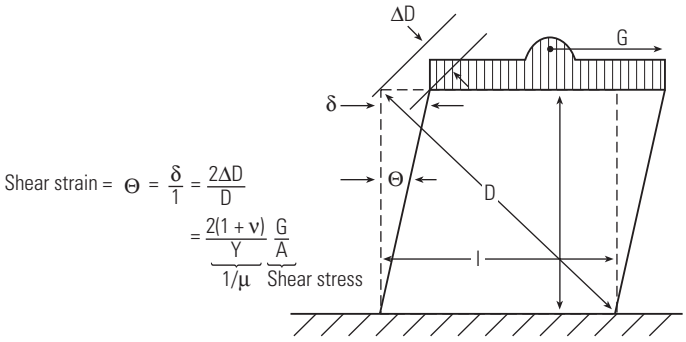


Fig. 17.9 Definition of shear strain. Adapted from Feynman et al. [4].

The total shear strain will be twice this quantity, since the same relations will be found for the other diagonal.

Thus the shear strain relation can be written as:

$$\Theta = \frac{\delta}{l} = \frac{2\Delta D}{D} = \frac{2(1 + \nu)}{Y} \frac{G}{A} . \tag{17.14}$$

From the relation given above, the identification of the shear modulus μ can be made:

$$\mu = \frac{Y}{2(1 + \nu)} . \tag{17.15}$$

The third constant used to describe elastic media is the so-called Lamé constant, λ. In conjunction with the shear modulus μ, it is used to relate the stress and strain tensors in a compact representation [5, 6]. An additional advantage is that the compressional and shear velocities have rather simple mathematical expressions when this formulation is used [7].

17.5 WAVE PROPAGATION

Figure 17.10 shows an idealized representation of a compressional wave. The periodic pressure variation of period T (s) has a frequency f of $\frac{1}{T}$. It is shown by increased

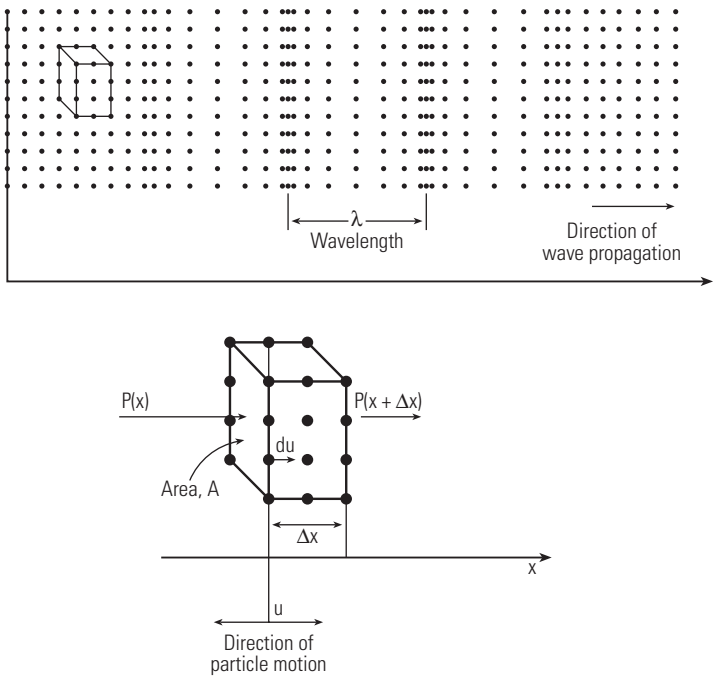


Fig. 17.10 One-dimensional wave propagation in a very stiff material.

particle density, which is seen to be separated by the wavelength λ. The separation λ between pressure disturbances is related to the frequency of the disturbance by the velocity of propagation v_c of compressional waves, by the well-known relation:

$$\lambda f = v_c . \tag{17.16}$$

Assuming that the material represented in the figure can be described by an appropriate Young's modulus Y and density ρ, we will derive, for a special case of 1D propagation, the velocity of the compressional wave, v_c.

The approach is to consider a small element of volume with thickness Δx and area A, and write the equation of motion for it. First note the frame of reference which is indicated in Fig. 17.10. The x-axis position will denote the location of the element of volume, and a superimposed axis u will denote the movement of the particles about their rest position x. The equation of motion ($F = M\,a$) can be expressed as:

$$F = \rho\, A\, \Delta x\, \frac{d^2u}{dt^2} , \tag{17.17}$$

where the force F is the difference in force experienced by the two faces of the volume:

$$F(x) - F(x + \Delta x) . \tag{17.18}$$

This in turn can be related to the pressure difference by dividing both sides of the equation by the cross-sectional area A:

$$P(x) - P(x + \Delta x) = \rho\, \Delta x\, \frac{d^2u}{dt^2} . \tag{17.19}$$

To put this equation in terms of Young's modulus, we now relate the pressure on the two faces to the change in the length of the unit volume:

$$P(x) = Y\, \frac{\Delta l}{l} = Y\, \left.\frac{du}{\Delta x}\right|_x , \tag{17.20}$$

$$P(x + \Delta x) = Y\, \left.\frac{du}{\Delta x}\right|_{x\,+\,\Delta x} . \tag{17.21}$$

From the preceding two equations, and the definition of the derivative, the pressure gradient is given by:

$$\frac{dp}{dx} = Y\, \frac{d^2u}{dx^2} . \tag{17.22}$$

Using this relationship, the equation of motion can now be written as:

$$Y\, \frac{d^2u}{dx^2}\Delta x = \rho \Delta x \frac{d^2u}{dt^2} , \tag{17.23}$$

or

$$\frac{d^2u}{dt^2} = \frac{Y}{\rho}\, \frac{d^2u}{dx^2} , \tag{17.24}$$

which is recognized as a wave equation. The velocity of wave propagation is given by the square root of the ratio of elastic constants:

$$v_c = \sqrt{\frac{Y}{\rho}}\,. \tag{17.25}$$

This velocity of propagation, however, is a special case, because for the general case it is:

$${v_c}^2 = \frac{Y}{\rho}\frac{1-\nu}{(1+\nu)(1-2\nu)}\,, \tag{17.26}$$

which involves Poisson's ratio (ν here). Thus the special case of wave propagation which we considered is appropriate for a very stiff material ($\nu = 0$), so that no bulging occurs perpendicular to an applied compression.

The velocity of a shear wave is given by a much simpler expression: $\sqrt{\mu/\rho}$. The derivation of this fact is much like the preceding but a bit more complicated. However, if we use the approach with the Lamé constant, it can be found almost by inspection [8].

Table 17.1 gives a number of useful relations between the elastic constants and the two types of wave velocities. From this table some constraints on the elastic constants can be deduced, as well as relations between shear and compressional velocity.

From the definition of the bulk modulus:

$$B = -\frac{p}{\frac{\Delta V}{V}}, \tag{17.27}$$

Table 17.1 Relationships among elastic constants and wave velocities. Adapted from White [8].

	Y, ν	B, μ	λ, μ	ρ, v_c, v_s
Lamé, λ	$\frac{Y\nu}{(1+\nu)(1-2\nu)}$	$\frac{(3B-2\mu)}{3}$	λ	$\rho({v_c}^2 - 2{v_s}^2)$
Shear, μ	$\frac{Y}{2(1+\nu)}$	μ	μ	$\rho {v_s}^2$
Young's, Y	Y	$\frac{9B\mu}{(\mu+3B)}$	$\frac{\mu(3\lambda+2\mu)}{(\lambda+\mu)}$	$\frac{\rho {v_s}^2(3v_c^2-4v_s^2)}{v_c^2-v_s^2}$
Bulk, B	$\frac{Y}{3(1-2\nu)}$	B	$\lambda + \frac{2}{3}\mu$	$\rho(v_c^2 - \frac{4}{3}v_s^2)$
Poisson, ν	ν	$\frac{3B-2\mu}{2(3B+\mu)}$	$\frac{\lambda}{2(\lambda+\mu)}$	$\frac{v_c^2-2v_s^2}{2(v_c^2-v_s^2)}$
${v_c}^2$	$\frac{Y(1-\nu)}{\rho(1+\nu)(1-2\nu)}$	$\frac{(B+\frac{4}{3}\mu)}{\rho}$	$\frac{(\lambda+2\mu)}{\rho}$	${v_c}^2$
${v_s}^2$	$\frac{Y}{\rho\ 2(1+\nu)}$	$\frac{\mu}{\rho}$	$\frac{\mu}{\rho}$	${v_s}^2$

we can immediately say that $B > 0$. With reference to the table, one implication is that:

$$v_c{}^2 - \frac{4}{3} v_s{}^2 > 0. \tag{17.28}$$

Thus we should expect v_c to exceed v_s by at least 15%. However, another estimate of this contrast of velocities can be obtained by examination of the constraints on the Poisson ratio, ν.

The upper limit on ν can be obtained from an inspection of the bulk modulus as a function of Young's modulus and Poisson's ratio. This expression:

$$B = \frac{Y}{3(1 - 2\nu)} \tag{17.29}$$

shows that $\nu < \frac{1}{2}$. The lower limit can be obtained from the expression for Poisson's ratio as a function of the bulk modulus and the shear modulus:

$$\nu = \frac{3B - 2\mu}{2(3B + \mu)} . \tag{17.30}$$

If B is set to zero, the minimum value of ν is -1. However, this implies an expansion of the perpendicular dimensions of a sample material for a stretching in the other. A real material, like a rock, will not exhibit this bizarre behavior. A reasonable limiting behavior would be no change in dimension in the direction perpendicular to the stretching. Thus a practical limit for ν is zero. The expression for velocities in terms of ν shows that for the minimum value of Poisson's ratio, the compressional velocity will exceed the shear velocity by 40%.

The reflection and refraction of acoustic waves can be visualized by use of Huygen's principle, familiar to students of optics. Figure 17.11 shows the interface of two media which are characterized by two different densities, ρ_1 and ρ_2, and compressional and shear velocities denoted by v_p and v_s, which are different in the two regions. The parallel rungs of the ladder correspond to maxima in the incident periodic pressure disturbance. At point A, the pressure disturbance will create an outgoing wave in medium 2. This will be characterized by a speed v_{p2}, which in this case is taken to be greater than that of the speed in region 1. (For this example, we consider only the P wave (compressional) propagation, but the same applies for the shear (or S) wave, which is generated at this interface.) As the wave front at point C, in the first medium, travels the distance x to the interface marked at point B, the compressional disturbance in medium 2 will have expanded to a radius larger than x by the factor $\frac{v_{p2}}{v_{p1}}$. Thus the point marked D will be in phase with the new wave commencing at B. The net result is that the incident wave, which made an angle i, with respect to normal incidence, will be seen to leave the interface with a new angle r. The relation between the two is controlled by the velocity contrast in the two media:

$$\frac{\sin i}{\sin r} = \frac{v_{p1}}{v_{p2}} , \tag{17.31}$$

which is known as Snell's law. One interesting aspect of this relationship is that if the angle of incidence i becomes large enough, then the refracted wave will travel parallel to the interface surface. This critical incidence angle, i_{crit}, is given by:

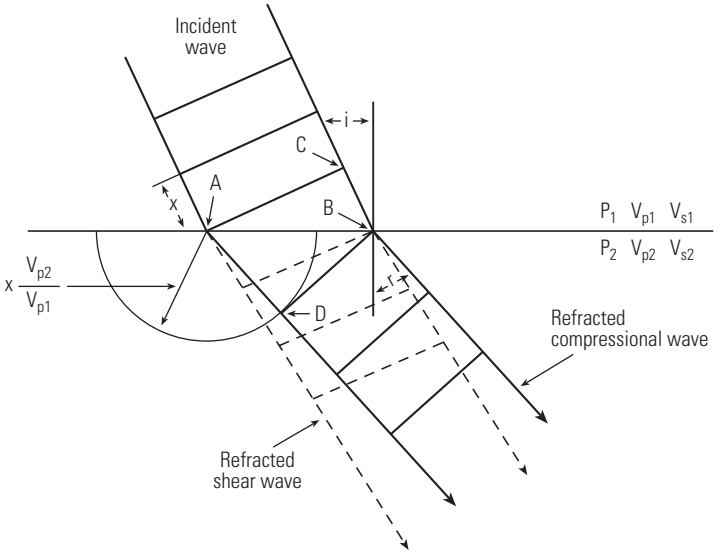


Fig. 17.11 The ray representation of transmitted acoustic energy. Refraction is shown at the boundary between two materials of different acoustic properties.

$$\sin i_{crit} = \frac{v_{p1}}{v_{p2}} . \tag{17.32}$$

Waves which are critically refracted and travel along the boundary are referred to as head waves. As they travel along the interface, they radiate energy back into the initial medium. It is this phenomenon which allows the detection, by an acoustic device centered in the borehole, of acoustic energy which has propagated primarily in the formation.

17.6 RUDIMENTARY ACOUSTIC LOGGING

Figure 17.12 illustrates the necessary elements of a device for the measurement of the compressional velocity of a formation. It consists of a transmitter of acoustic energy and a receiver. This device is centered in a borehole filled with fluid which has a compressional velocity of approximately 5,000 ft/s. The ray diagram, sketched at the side, indicates two paths for the acoustic energy, one in the mud and the other refracted in the formation at the critical angle. The compressional velocity in the formation is somewhere between 10,000 and 20,000 ft/s. The measurement consists of recording the time from the transmitter firing until the first detectable signal arrives.

Even for such a rudimentary device, some design precautions must be taken. The spacing between transmitter and receiver must be large enough so that the acoustic energy traveling in the borehole mud does not arrive before the signal from the formation. The ray diagram of Fig. 17.12 shows the parameters of interest for obtaining the

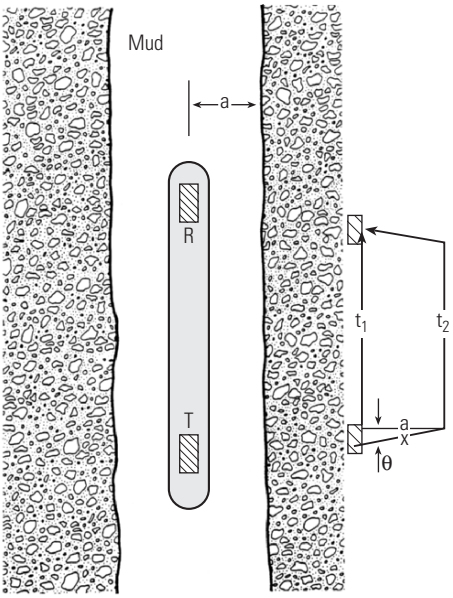


Fig. 17.12 A rudimentary borehole device for measuring the interval transit time Δt. Shown, to the side, are the ray paths of the acoustic energy refracted from the borehole into the formation and back to the receiver.

minimum spacing d between transmitter and receiver to obtain this condition. The mud travel time must be greater than the travel time in the formation plus the two-way travel time in the mud. The mud travel time $t_1$is the separation distance d divided by the mud velocity v_1. The travel time in the formation t_2 is approximately $\frac{d}{v_2}$. The two-way travel time in the mud to the formation can be found from the length x. Using the definition of the critical angle, the distance x is given by:

$$x = \frac{a}{\sqrt{\frac{v_2{}^2 - v_1{}^2}{v_2{}^2}}}. \tag{17.33}$$

The final result for the separation distance d is that:

$$d > \frac{2a\sqrt{v_2{}^2 - v_1^2}}{v_2 - v_1}. \tag{17.34}$$

17.7 RUDIMENTARY ACOUSTIC INTERPRETATION

The work of Wyllie and others was the breakthrough necessary to put acoustic logging into a central role in log interpretation [9, 10]. It occurred at a time when porosity logs were almost unknown; only a rudimentary neutron device was available. Their measurements of acoustic velocities of materials, including core samples, gave log

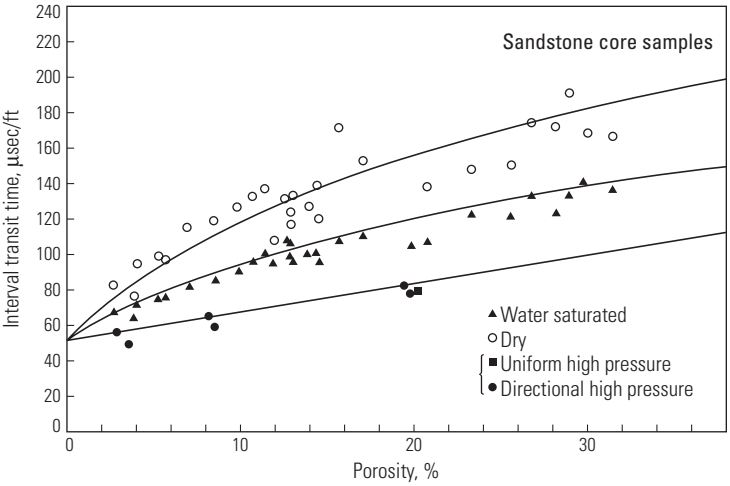


Fig. 17.13 Laboratory data showing the relationship between interval transit time and porosity of core samples. Adapted from Wyllie et al. [9].

interpreters a way to convert the measured travel time into something other than integrated travel time for seismic corrections. It gave them a way to relate it to porosity of the rock.

The data that launched this revolution are shown in Fig. 17.13. The measurements consist of velocity (presented as the reciprocal and referred to as the interval transit time, or Δt) of sandstone core samples of different porosities. These were carried out under several different conditions. The upper two trends show that the dry, unconfined samples had the slowest velocity, which increased when saturated with water. However, it is the bottom trend which is of interest. This corresponds to a few water-saturated samples which were confined by pressure during the measurement. The reciprocal velocities for these points follow the expression:

$$\frac{1}{v} = \frac{1}{v_{solid}}(1 - \phi) + \frac{1}{v_{fluid}}\phi, \tag{17.35}$$

or

$$\Delta t = \Delta t_{solid}(1 - \phi) + \Delta t_{fluid}\phi\,, \tag{17.36}$$

which has come to be known as the Wyllie time-average equation. It is a linear relationship between the interval transit time and the porosity.

What is remarkable about Eq. 17.35 is that it was devised by Wyllie for artificial samples of alternating parallel layers of aluminum and Lucite. It is reasonable for such a laminated model that the total time delay is given by a sum of the delays in the various lengths of formation and fluid which scale as the porosity. Why this should be so for pressure-confined sandstone core samples is not so clear.

In the course of their investigations, Wyllie and others, discovered that travel time depended on other parameters. Some of these were the matrix material, cementation,

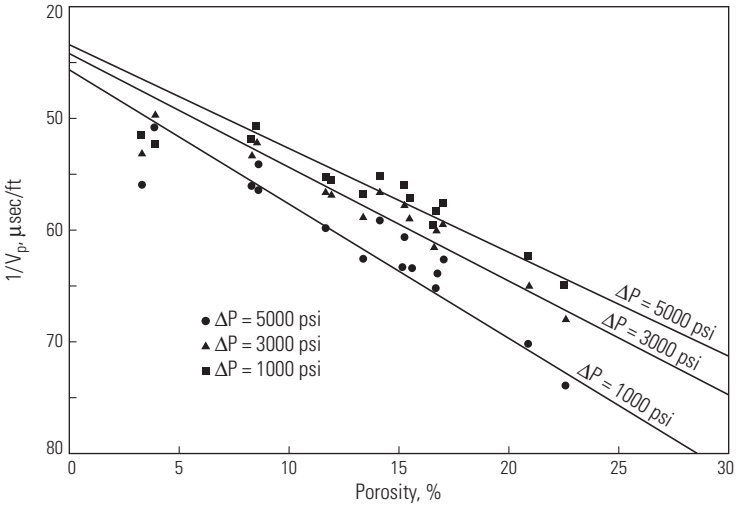


Fig. 17.14 Laboratory data showing the dependence of interval transit time on the differential pressure applied to rock samples. Adapted from Pickett [11].

type of fluid in the pores, and pressure. As an example, Fig. 17.14 shows the interval travel time in dolomites as a function of porosity for various effective pressures. It is clear that the slope is dependent not only on the fluid velocity but also the difference between the pore pressure and the external pressure. To cope with these realities, we will have to look next at some models of rocks which have been developed to explain these velocity variations.

REFERENCES

1. Schlumberger C (1935) Procede et appareillage pour la reconnaisance de terrains traverses par un sondage. Republique Francaise Brevet d'Invention, numero 786, 863

2. Kokesh FP (1952) The development of a new method of seismic velocity determination. Geophysics 17(3):560–574

3. Kokesh FP (1956) The long interval method of measuring seismic velocity. Geophysics 21(3):724–738

4. Feynman RP, Leighton RB, Sands ML (1965) Feynman lectures on physics, vol 2. Addison-Wesley, Reading, MA

5. Turcotte DL, Schubert G (1982) Geodynamics. Wiley, New York

6. Hearst JR, Nelson PH (1985) Well logging for physical properties. McGraw-Hill, New York

7. Tittman J (1986) Geophysical well logging. Academic Press, Orlando, OK

8. White JE (1983) Underground sound: application of seismic waves. Elsevier, Amsterdam, The Netherlands

9. Wyllie MRJ, Gregory AR, Gardner LW (1956) Elastic wave velocities in heterogeneous and porous media. Geophysics 21(1):41–70

10. Wyllie MRJ, Gregory AR, Gardner LW, Gardner GHF (1958) An experimental investigation of factors affecting elastic wave velocities in porous media. Geophysics 23(3):459–493

11. Pickett GR (1974) Formation evaluation. Unpublished lecture notes, Colorado School of Mines, 1974

Problems

17.1 Formation compressional velocities generally range between 10,000 and 20,000 ft/s, while the compressional velocity of the mud is about 6,000 ft/s.

17.1.1 What is the variation in the critical angle, in degrees, for these extremes?

17.1.2 For a transmitter–receiver pair with a nominal 3 ft separation, centered in a 10 in. diameter borehole, what is the actual distance of formation traversed by the first arrival compressional wave in the case of the largest critical angle determined above?

17.2 To understand the timing constraints on the Δt measurement and the difficulties of performing this measurement successfully, consider the connection between the frequency of acoustic emission and the space between transmitter and receiver for obtaining the compressional transit time to a given degree of accuracy.

17.2.1 Using the original data of Wyllie (see Fig 17.13) determine a representative figure for the precision of the Δt measurement required for determining porosity to within 1 porosity unit.

17.2.2 For a source-to-receiver distance of 3 ft, what is the lower limit of the frequency of emission that can be established to meet the 1 p.u. resolution, assuming that the detection system is capable of determining the first arrival somewhere in the first quarter of a cycle of the sinusoidal emission wavetrain?

17.2.3 What is the frequency required if the first arrival is detected somewhere between 0.1 and 0.5 times the maximum amplitude of the detected wavetrain?

17.3 With reference to Fig. 17.12, determine the minimum spacing required for the first arrival to be a compressional formation signal rather than the direct mud arrival. The bore hole diameter is 16 in., with a 189 μs/ft mud and a 120 μs/ft formation. In some shales the transit time may be as great as 150 μs/ft. What is the minimum spacing required?

17.4 What is the conversion factor between the conventional units of transit time Δt, in μs/ft and velocity in km/s?

Note that it is numerically equal to the constant c, which relates the expected Δt (in μs/ft) of a fluid to $\sqrt{\frac{\rho}{B}}$ where B is the bulk modulus in (Gigapascals GPa = 10 kB = 10 kbar) and the density ρ is in g/cm^3, i.e.:

$$\Delta t \; = \; c \sqrt{\frac{\rho}{B}} \, . \tag{17.37}$$

18

Acoustic Waves in Porous Rocks and Boreholes

18.1 INTRODUCTION

The previous chapter reviewed the parameters necessary to describe perfect elastic media. The relationship between the elastic moduli and the velocity of propagation of compressional and shear waves was also derived. At the conclusion of the chapter, a possible logging application noted the use of the measured compressional slowness for the determination of porosity using the Wylie time-average, an empirical relationship.

In addition to porosity, other rock properties such as lithology and environmental effects such as pressure might be important factors determining the acoustic velocity of compressional and shear waves. What are the important factors which affect the acoustic velocity of rocks? How can these factors be related to elastic constants which are representative of the rock? How can a measurement of the shear and compressional velocities be used to derive some useful petrophysical, geophysical, or mechanical properties? These are some of the questions to be addressed in this chapter.

As background, we begin with a description of the experimental procedure used in investigating acoustic rock properties. This is followed by a review of some of the laboratory and field data accumulated by a wide variety of researchers who have studied the acoustic properties of rocks. This work shows that the velocity of acoustic propagation is a rather more complex phenomenon than would be implied by the simple Wyllie time-average equation. As a consequence of the laboratory observations, some models of rocks which attempt to describe actual rock acoustic properties have been developed. The approach used in several models is described. Returning to logging applications, the final portion of the chapter is an introduction to some

aspects of acoustic waves in boreholes and to the propagation of acoustic energy at the interface between materials with different properties.

18.2 A REVIEW OF LABORATORY MEASUREMENTS*

An examination of the literature shows that compressional acoustic velocity in rocks depends primarily on six factors: porosity, composition, or lithology, the state of stress, temperature, fluid composition for a saturated porous rock, and the rock texture [1, 2]. Of all these items temperature is the least important and is not considered here. Before we examine some of the experimental data, it is worth examining how acoustic properties of rocks are measured.

Figure 18.1 shows a schematic of a typical laboratory apparatus for the measurement of acoustic velocities of rock samples. It consists of a P-wave or S-wave transducer (usually piezoelectric) which is energized by an electrical pulse. At the other end of the sample is a similar transducer, which produces an output voltage that is the result of strains induced in the transducer. The time delay between the firing pulse and the received pulse is converted to the appropriate acoustic velocity.

One of the important influences on acoustic velocity is the effective state of stress of the rock. Although this condition is rarely known with any precision for an actual formation, it is a laboratory expedient to approximate it with a differential pressure which is the difference between the confining pressure and the pore pressure. To study the effect of stress on velocities, the sample can be placed in a special cell similar to the one illustrated in Fig. 18.2. It can be seen that the sample is completely enclosed by a rubber jacket, which is then surrounded by a fluid whose pressure can be varied to produce the equivalent of an overburden pressure. There is an additional connection, seen at the lower right of the figure, which allows communication with

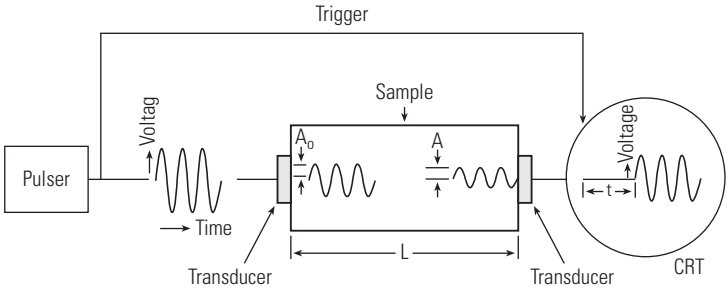


Fig. 18.1 The laboratory setup for the measurement of acoustic properties of rock samples. Adapted from Timur [1].

*For much of the original chapter, inspiration (and figures) were drawn from "Acoustic Logging," by A. Timur, in *SPE Petroleum Production Handbook* [1], and *Well Logging II: Resistivity and Acoustic Logging*, by J. R. Jordan and F. Campbell [2].

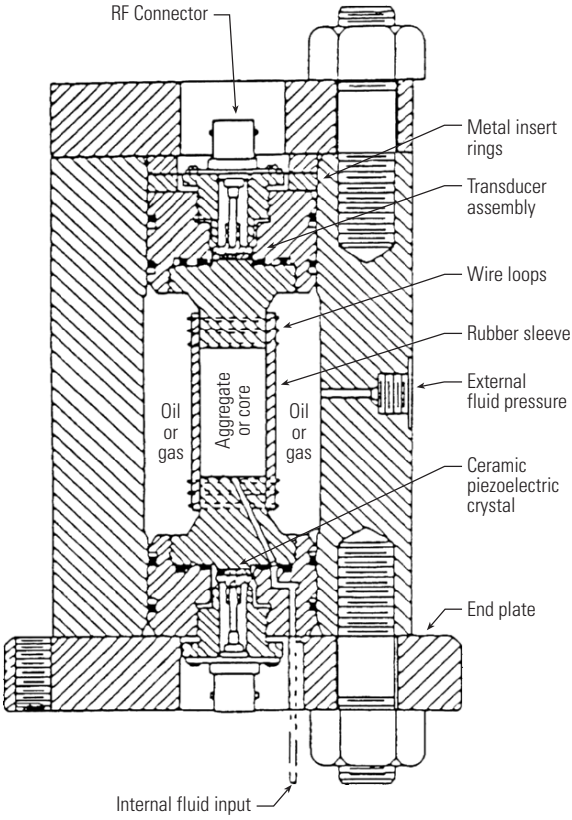


Fig. 18.2 Details of a differential pressure cell for the simulation of overburden and pore pressure. Adapted from Wyllie et al. [3].

the fluid saturating the porous sample. Thus the pressure of the pore fluid may also be changed, and the velocity can be determined as a function of the difference of the two pressures.

The effect of porosity on the compressional velocity of a number of sandstone samples can be seen in Fig. 18.3. The porosity is plotted as a function of the measured travel time and the straight line is the time-average fit to the data. The matrix and fluid travel times used in the fit are given in the figure. These measurements were made with no confining pressure, and the scatter may represent other factors which are important, such as texture. The effect of matrix is clearly seen in Fig. 18.4, in which porosity is plotted versus travel time for quartz and calcite core samples. The matrix velocity of calcite is somewhat greater than that of quartz, as indicated in the figure. A summary of some of the fluid and matrix velocities for both shear and compressional waves is shown in Table 18.1.

To study the effect of total confining pressure on velocities, measurements are made with the pore fluid at atmospheric pressure, and the confining pressure (the

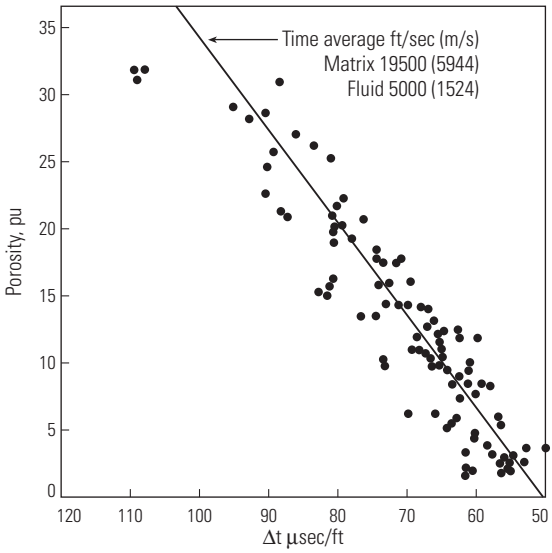


Fig. 18.3 Measurements of the effect of porosity on compressional transit time for sandstone samples. Adapted from Wyllie et al. [4].

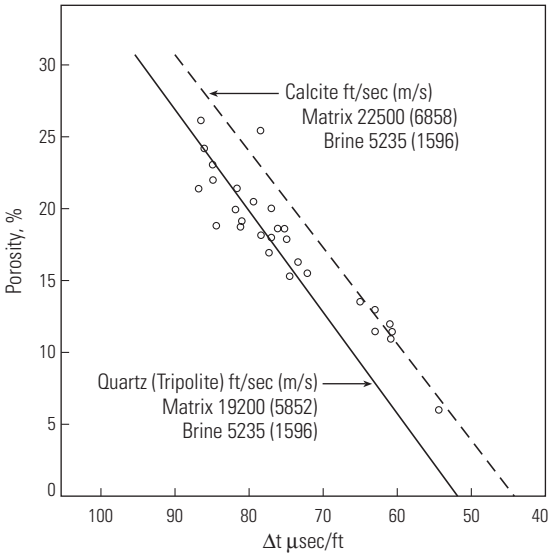


Fig. 18.4 Effect of rock composition on the relationship between porosity and transit time. Adapted from Timur [1].

Table 18.1 Acoustic velocities for various materials. Adapted from Timur [1].

Nonporous solids		V_c (ft/s)	V_s (ft/s)
Anhydrite		20,000	11,400
Calcite		20,100*	
Cement (cured)		12,000	
Dolomite		23,000	12,700
Granite		19,700	11,200
Gypsum		19,000	
Limestone		21,000	11,100
Quartz		18,900*	12,000
Salt		15,000*	8,000
Steel		20,000	9,500
Water-saturated porous rocks in situ			
	Porosity		
Dolomites	5−20%	20,000−15,000	11,000−7,500
Limestones	5−20%	18,500−13,000	9,500−7,000
Sandstones	5−20%	16,500−11,500	9,500−6,000
Sands (unconsolidated)	20−25%	11,500−9,000	4,000 – 1,700
Shales		7,000−17,000	
Liquids**			
Water (pure)		4,800	
Water (100,00 mg/1 of NaCl)		5,200	
Water (200,00 mg/1 of NaCl)		5,500	
Drilling mud		5,700 – 3,600	
Petroleum		4,200	
Gases**			
Air (dry or moist)		1,100	
Hydrogen		4,250	
Methane		1,500	

*Arithmetic Average of Values Along Axes (Wyllie et al. [3])
**At Normal Temperature and Pressure

pressure in the fluid surrounding the rubber jacket of Fig. 18.2) is varied. The result of this type of measurement in samples of the three major types of lithology is shown in Fig. 18.5. Substantial changes in velocity are noted: nearly 20% in the case of the sandstone samples, but less than 10% for the limestone.

The separate effects of confining pressure and pore pressure are investigated by making velocity measurements for differences of pore and overburden pressure. An example of this type of data is shown in Fig. 18.6. The upper trace shows the velocity variation as a function of overburden pressure with the pore fluid at atmospheric

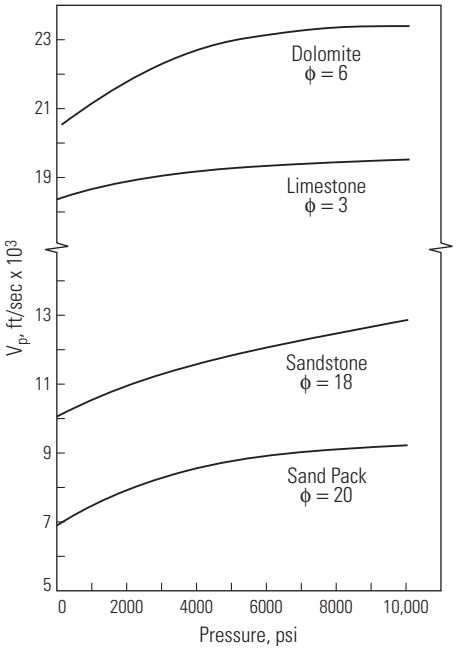


Fig. 18.5 Compressional velocity for several rock samples as a function of confining pressure. Adapted from Timur [1].

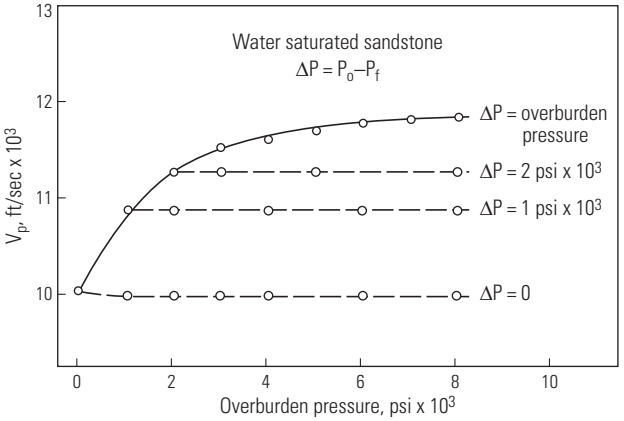


Fig. 18.6 The effect of simulated differential pressure on compressional velocity. Adapted from Wyllie et al. [3].

pressure, as was the case for the data in Fig. 18.5. The other three traces, however, are for cases where the pore fluid pressure tracked or was slightly less than the overburden pressure. The nearly horizontal line for $\Delta P = 0$ indicates that, to first order, if the

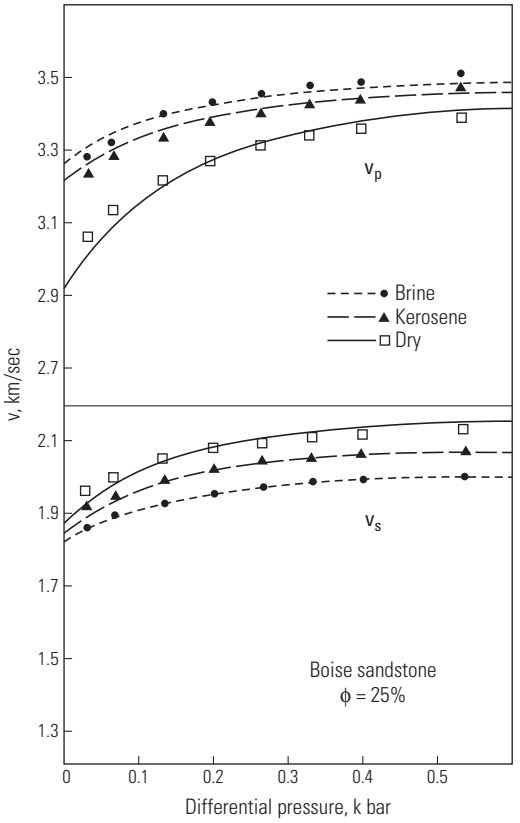


Fig. 18.7 Effect of the saturation fluid on the compressional and shear velocity of 25% porous sandstone. Adapted from Timur [1].

confining pressure and pore pressure are equal, then the average elastic properties of the sample have not changed compared to the unstressed state. The observations can be generalized by noting that the compressional velocity increases for increasing overburden pressure and decreases for increasing pore pressure.

Since we have already seen that the pore fluid has an influence on the acoustic velocities, through the time-average representation of the data, it is no surprise to see the velocity differences in Fig. 18.7 for the three different types of pore fluids: water, kerosene, and air. However, the magnitude of the velocity change as a function of the differential pressure on the sample depends upon the fluid. What is even more striking, in Fig. 18.7, is the reversed behavior of the compressional and shear velocities.

The effect of saturating fluid type on the compressional and shear velocities of porous rocks under confining pressures has also been studied. Representative data is shown in Fig. 18.8. The first conclusion that can be drawn from this data summary is that the effect of water saturation will be largest for the compressional (or P) waves. Note that the shear wave behavior hardly changes under the two extreme conditions

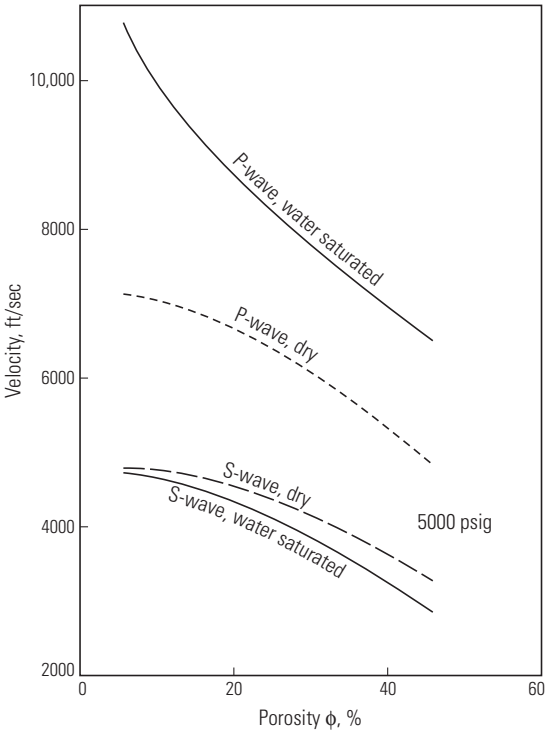


Fig. 18.8 A summary graph of the effect of the extremes of water saturation on compressional and shear wave velocities as a function of porosity. The shear wave velocity increases slightly with the density decrease that results from replacing water with gas. The compressional velocity decreases when gas replaces water because of the change in the rock bulk modulus. Adapted from Timur [1].

considered. This is because liquids do not support a shear wave. However, especially at low porosities, the compressional velocity is quite sensitive to water saturation. The difference in behavior for shear and compressional waves leads naturally to a technique for distinguishing gas-bearing formations. The ratio of the two velocities can be used as a gas indication.

A qualitative explanation of this effect can be obtained from the basic parameters which govern velocity. The shear velocity is governed by the ratio of the shear modulus, μ, to the density, ρ:

$$V_s = \sqrt{\frac{\mu}{\rho}}. \tag{18.1}$$

At a fixed porosity, if water is exchanged for low-density gas, the shear modulus will not change, but the density will decrease, thus producing the inversion seen in the figure. In the case of the compressional wave there is an additional dependence on the formation bulk modulus, K. One expression (see Table 17.1) for compressional velocity is:

$$V_p = \sqrt{\frac{K + (4/3)\mu}{\rho}}. \tag{18.2}$$

As argued above, μ does not change. However, the decrease in density must be overcompensated by a change in the bulk modulus. At a fixed porosity, the replacement of liquid, which has a very large bulk modulus, by gas, which is very compressible, will certainly reduce the contribution of the pore fluid to the overall bulk modulus of the formation. According to the data, this reduction will dominate the velocity, regardless of the porosity. Just how the compressibility of the fluid influences the overall rock compressibility is the kind of question which is answered by rock models, to be discussed in the next section.

The data just considered treat the two extremes of either full water or gas saturation. What about those cases in between? What is the effect of partial saturation? Beyond a dramatic decrease in V_p with the introduction of a small amount of gas there is little sensitivity of the velocity ratio to saturation, as has been confirmed by both laboratory and model calculations, which are shown in Fig. 18.9. These curves indicate a large change in the compressional velocity as soon as the gas saturation attains 10%, and little afterwards. As expected, there is no sensitivity indicated for the shear velocity.

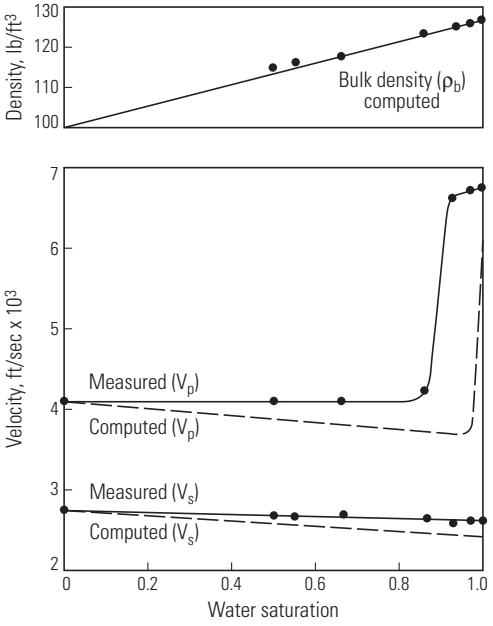


Fig. 18.9 The effect of partial water saturation on the compressional and shear velocity. The change in bulk modulus occurs dramatically with a slight introduction of gas. Adapted from Timur [1].

In an effort to more realistically address the state of rocks, which typically have horizontal stresses that differ from vertical stresses, modern laboratory testing on rocks use triaxial cells. These devices are able to measure stress/strain curves, useful for determining rock failure, along with shear and compressional velocities. The simplest form of a triaxial cell allows the addition of a confining pressure independent from the conventional uniaxial stress. One method of operation is to maintain the confining pressure while changing the simulated overburden stress.

An instructive set of laboratory measurements made on a sandstone at a constant confining pressure of 30 MPa is shown in Fig. 18.10. There are three sets of data plotted together, the upper two curves correspond to shear and compressional velocity. The bottommost is the stress/strain curve that shows the typical elastic behavior in the initial application of stress up to about 120 MPa. As the stress is increased beyond that point, up to about 200 MPa, the strain increases faster than the earlier linear trend in what is known as plastic yielding or ductile deformation. This is also known as formation damage. Beyond this point, a small increase in stress causes the rock to fail by the production of cracks, faults, or fractures.

Now we turn to the interesting behavior of V_p and V_s leading up to (and beyond) this failure. In the elastic region of stress both V_p and V_s, the uppermost two curves, plotted normalized to their initial velocities, are seen to increase, although the fractional change in the shear velocity is somewhat smaller than that for the compressional. In the region of the rock deformation, or damage, both velocities level off and begin to decrease as numerous microfissures begin to form. The shear velocity declines by about 15% of the unstressed velocity before failure of the sample, after which there is

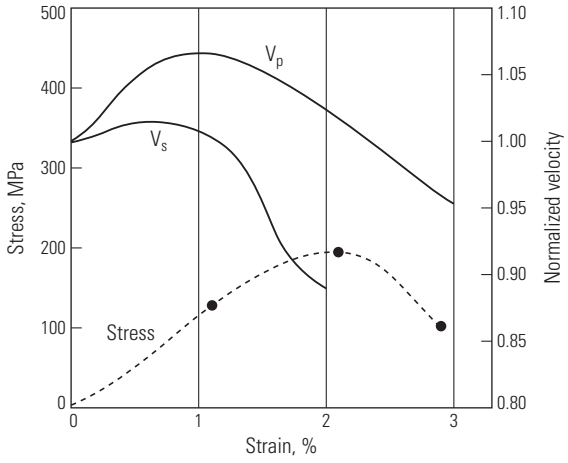


Fig. 18.10 Data obtained on a sandstone sample with a triaxial stress-strain measuring device. The confining stress was held constant at 30 MPa. The axial stress was raised until the sample failed at slightly under 200 MPa. The bottom curve shows the measured strain as a function of the stress; the upper two curves are the normalized S- and P-wave velocities. Adapted from Sammonds et al. [5].

no further shear propagation. The compressional velocity also decreases as the stress increases, even beyond the failure point.

18.3 POROLELASTIC MODELS OF ROCKS

Classical wave theory predicts none of the effects discussed above. The velocities of the compressional and shear waves are given by simple combinations of the material moduli and bulk density. Realistic rock models will have to provide a means of extracting appropriate elastic constants for fluid-saturated rocks – a method of predicting the average elastic properties from a knowledge of the elastic properties of the constituents and some details of the rock fabric.

The goal for rock models is, from some set of reasonable parameters, to predict the behavior of acoustic velocities under a variety of conditions, such as confining pressure, differential pressure, and pore fluid properties. For the case of the effect of fluid properties on the acoustic velocity of saturated porous rock, one notable and frequently cited attempt at such a model was made by Gassmann [6]. His model for porous rocks consisted of a rock skeleton filled with fluid and was based on the assumption that the properties of the fluid and skeleton materials are known. The major simplification incorporated is that the relative motion between the fluid and skeleton during acoustic wave propagation is negligible.

The basic definitions used in the model are shown in Fig. 18.11. Following the convention of Gassmann, the symbol for bulk modulus used here is k. We start with a knowledge of the material properties of the skeleton material, in particular its density ρ_s and bulk modulus k_s. The known properties of the evacuated skeleton are its porosity ϕ, its density $\overline{\rho}$, its bulk modulus $\overline{k}$, its shear modulus $\overline{\mu}$. The fluid properties are denoted by its density ρ_f and bulk modulus k_f. The object of the model is to obtain the average properties of the saturated rock – its density ρ, bulk modulus k, shear modulus μ – so that the low-frequency acoustic velocities can be determined.

The bulk density is given simply by:

$$\rho = \phi\rho_f + (1-\phi)\rho_s, \tag{18.3}$$

and the shear modulus will be the same as for the skeleton $\overline{\mu}$. However, the average bulk modulus is not obvious but can be determined from the following analysis. In the case of saturated rock, the bulk modulus now is to be found as a function of porosity and the moduli of the formation and of the saturating fluid. Thus, the Gassmann model is another example of a petrophysical mixing law.

In order to determine the bulk modulus, we need first to refer to the defining equation:

$$k = -\frac{\Delta P}{\frac{\Delta V}{V}}. \tag{18.4}$$

Consider what the change in volume of our saturated skeleton is when a pressure ΔP is applied, as shown in Fig. 18.11. First, the applied pressure can be separated into two components:

$$\Delta P = \overline{\Delta P} + \Delta P_f, \tag{18.5}$$

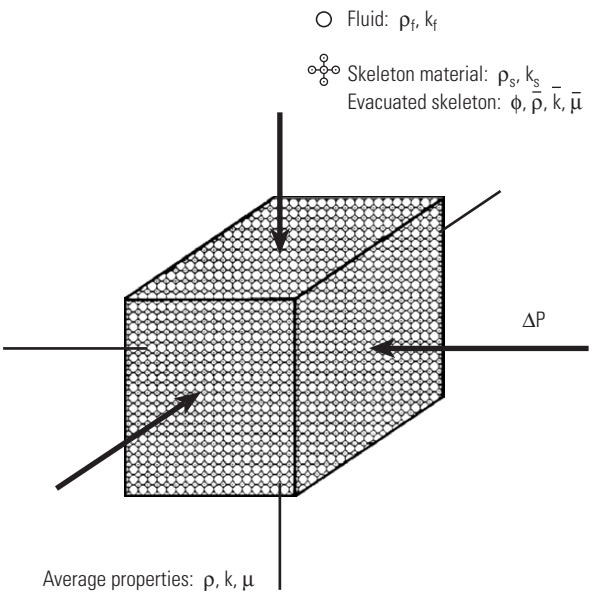


Fig. 18.11 Model of a porous rock according to Gassman. It is considered to consist of a stiff frame and a saturating fluid. The elastic constants of the frame material and fluid are known. The model predicts the elastic constants of the ensemble.

where $\overline{\Delta P}$ is the portion of the overburden pressure which is actually supported by the skeleton, and ΔP_f is the portion of the applied pressure which is supported by the fluid. This applied pressure will induce a change in the volume ΔV, which is given by the sum of two contributions:

$$\Delta V = \Delta V_f + \Delta V_s , \tag{18.6}$$

which are the fluid compression and the actual skeleton compression.

The first of these two is given quite simply by:

$$\Delta V_f = -\phi V \frac{\Delta P_f}{k_f}, \tag{18.7}$$

which follows directly from the definition of the bulk modulus. The skeleton change has two components: one the result of the pressure portion actually borne by the skeleton and the other the result of the pressure of the fluid. This is given by:

$$\Delta V_s = -(1-\phi)V \frac{\Delta P_f}{k_s} - \frac{V\overline{\Delta P}}{k_s} . \tag{18.8}$$

The first term is the shrinkage of the skeleton constituents, and the second term is the shrinkage of the entire skeleton framework. Thus the total volume change is given by the sum of these two:

$$\frac{\Delta V}{V} = \left[-\frac{\phi}{k_f} - \frac{1-\phi}{k_s}\right]\Delta P_f - \frac{1}{k_s}\overline{\Delta P}\,. \tag{18.9}$$

The other relation that is available is:

$$\frac{\Delta V}{V} = -\frac{1}{k_f}\Delta P_f - \frac{1}{\overline{k}}\Delta\overline{P}, \tag{18.10}$$

which follows from the pressure breakdown specified initially (Eq. 18.5) and the definition of the bulk modulus. After algebraic manipulation [7, 8], it can be shown that the bulk modulus for the fluid-saturated rock, k, is given by that expected for the dry skeleton plus an additional term that involves the porosity and the moduli of the fluid, rock matrix, and dry frame:

$$k = \overline{k} + \frac{(1-r)^2}{\frac{\phi}{k_f} + \frac{1-\phi}{k_s} - \frac{\overline{k}}{k_s{}^2}}\,, \tag{18.11}$$

where $r = \frac{\overline{k}}{k_s}$. An equivalent form of the Gassmann equation that looks more like a conventional mixing law is given by [9]:

$$\frac{k}{k_s - k} = \frac{\overline{k}}{k_s - \overline{k}} + \frac{k_s}{\phi(k_s - k_{fl})}. \tag{18.12}$$

In order for this model to be of any use, some relationship between the bulk modulus of the dry frame $\overline{k}$, and the rock matrix k_s must be established. Initially, Gassman was able to do this for a very special case in which he approximated a loose sand by a set of cubic-packed spheres [10]. By considering the grain contact area as a function of applied stress, he could relate the compressibility to the particle size and grain properties. For practical applications, the unknown skeleton bulk modulus can be deduced from the acoustic velocities and density of the water-saturated formation in conjunction with other empirical relations. An example of such an approach using log data is shown in a later section.

Despite the usefulness of Gassmann's relation to predict the velocities expected for saturating fluids of different properties (as a function of porosity), Eq. 18.11 is still somewhat unsatisfying. One of the observational facts which it must predict is the dependence of the compressional velocity V_p on the differential pressure. This dependence, however, is hidden in the term $\frac{\overline{k}}{k_s}$. Reformulations of the Gassman theory for cubic packed spheres by White and Pickett show this dependence explicitly [11, 12]. This formulation contains five parameters in addition to effective stress for the prediction of porosity from inverse velocity, or slowness, Δt.

A more complete model was developed by Biot [13]. The additional approach to reality was to allow relative motion between fluid and the rock skeleton. The fluid motion is assumed to obey Darcy's law (which relates fluid flow to differential pressure, viscosity, and permeability) so that additional terms of permeability and fluid viscosity appear in the analysis. The Biot theory predicts a frequency-dependence for

compressional wave velocity. However, in the low frequency limit, the theory reduces to that of Gassmann. Further models which deal specifically with the rock texture have been developed by Kuster and Toksoz, for example [14]. They derive average elastic parameters for a matrix containing spheroidal cavities of differing aspect ratios. This model has been quite successful in fitting the data, similar to that in Fig. 18.9. A much more complete summary of the various rock models that have been developed in recent years can be conveniently found in handbook form [9].

Although porosity derived from acoustic logs has largely been replaced, in practice, by porosity determination from nuclear or NMR logs, it is still used in some cases. Despite the existence of detailed but unwieldy acoustic rock models, in practical logging interpretation the Wyllie time-average equation has been widely used to estimate porosity from measurements of Δt. The justification, if anything beyond simplicity is required, is due to Geertsma [7]. He showed that in the limit of low porosity, the Biot theory predicts a simple porosity-dependence for the inverse compressional velocity in dry rock:

$$\frac{1}{V_p} \propto a + b\phi \,. \tag{18.13}$$

where the value of b depends on the compressibility of the pores and thus on the fluid. However, in a further paper [8] he points out that the time-average approach ignores the important role of the pressure-dependent bulk deformation properties of the formation.

Besides the Wylie time-average there are other empirical methods for estimating porosity from compressional slowness. One transform [15] developed from field data attempts to correct some of the low-porosity deficiencies of the Wylie transform and implicitly takes into account the transition from a solid rock to a liquid suspension at very high porosities. Another set of transforms [16] was developed from laboratory data of shaley sands at various confining pressure and clay volume fractions. It is useful if there is an auxiliary estimate of the amount of clay present. A number of other models can be found in summary form in Mavko et al. [9].

Figure 18.12 is an example from a chartbook [17] which shows the solution to the time-average expression for the three common matrices. However, note the cluttered appearance of the chart. The three principal lines correspond to a solution of:

$$\phi = \frac{\Delta t - \Delta t_{ma}}{\Delta t_f - \Delta t_{ma}}, \tag{18.14}$$

where the fluid velocity has been fixed to 5,300 ft/s. In addition to the three linear relations expected for three matrices of differing matrix travel times, there are three slightly curved lines for the same three matrices. Raymer et al. [15], established these additional transforms, which correspond to their judgments based on the observation of much field data. They basically take into account that the sonic travel time seems to consistently underestimate the porosity in mid-range. The additional lines to the right, carrying the notation B_{cp}, or compaction factor, correspond to an empirical method for correcting the transit time measurements for formations which are not sufficiently compacted or which do not have sufficient effective stress.

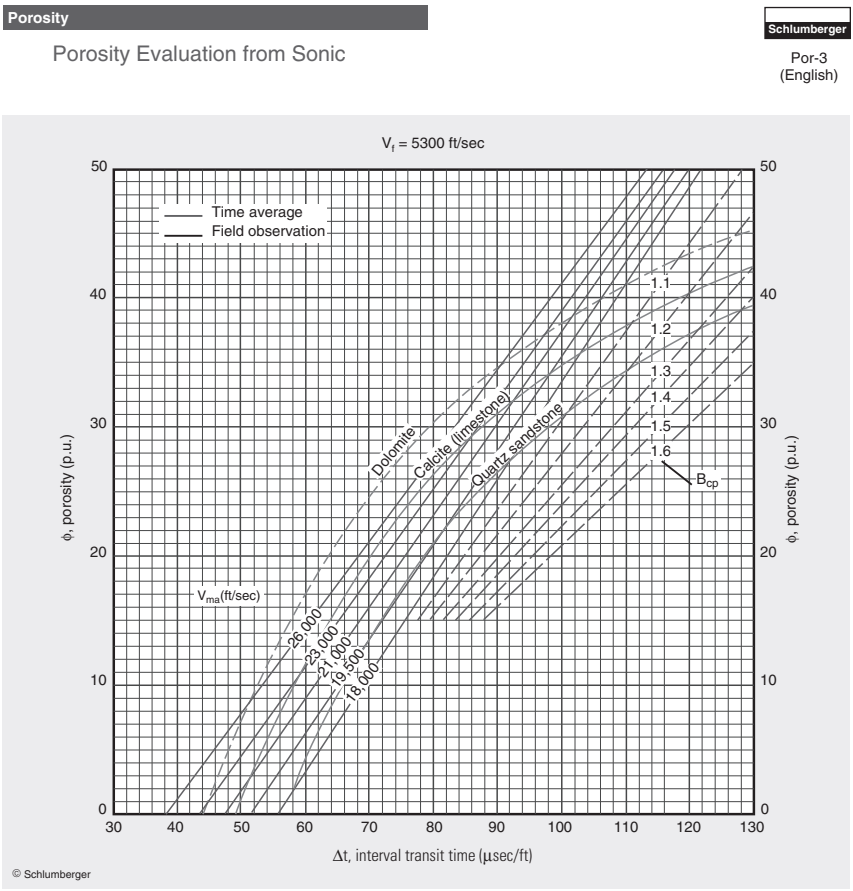


Fig. 18.12 Chart for estimating porosity from compressional interval transit time. In addition to the Wyllie time-average solution and compaction corrections, another empirical solution by Raymer et al. [15] is shown. Courtesy of Schlumberger [17].

18.4 THE PROMISE OF V_P/V_S

Before investigating the challenge of obtaining continuous measurements of V_p and V_s in the borehole environment, one that has stimulated a great deal of physical insight and engineering ingenuity, we examine the promise of having the simultaneous measurement of these two fundamental quantities available.

18.4.1 Lithology

For petrophysical applications the interpretation of the compressional transit time into porosity depends, in part, upon knowledge of the rock type. This is because the linear

equation that links porosity to observed travel time contains a term that is determined by the compressional velocity in the pure rock matrix. Thus it is of interest to know the rock type.

The determination of lithology from borehole acoustic measurements is based on the variations of elastic parameters between rock types. These variations are reflected in both the shear and compressional velocities. One convenient method of classifying lithologies is to compare the compressional velocity to the shear velocity, as suggested by Pickett [18]. His laboratory and field data for many different formations showed that measurements corresponding to limestone and dolomites were found along lines of constant but different ratios: $V_p/V_s \approx 1.9$ for limestone and ≈ 1.8 for dolomite. Sandstones showed a variation of velocity ratio from about 1.6 to 1.75, with the upper limit corresponding to high-porosity sands under low effective stress.

Pickett's compilation of field points was made from painstaking manual analysis of recorded wavetrains. With the availability of routine shear and compressional velocities this technique becomes useful for lithology determination and the identification of gas. Working with Pickett's original data Domenico [19] determined Poisson's ratio for all of the samples. The data, shown in Fig. 18.13, plots the value of Poisson's ratio (ν) as a function of the ratio of V_p/V_s. It shows a clear separation between sandstone and limestones despite the wide range of values associated with these two rock types.

Turning from laboratory data to field data, Fig. 18.14 is a cross plot of the interval transit time for shear and compressional waves in the format of Pickett's original work. It is a composite of logging data from four different wells which contained, dolomite, limestone, halite, and sand formations. Some of the latter were gas-bearing.

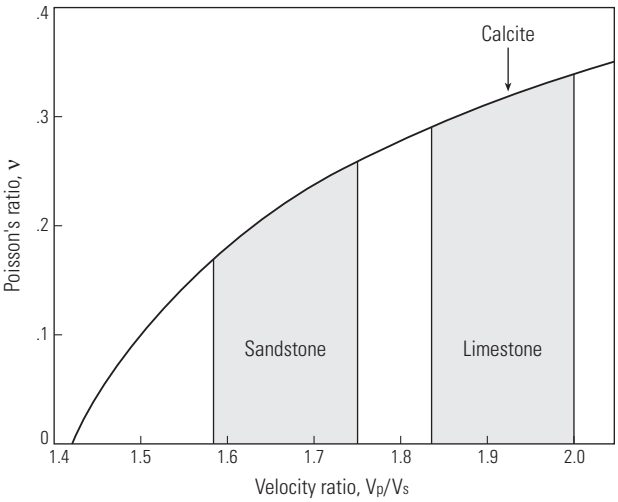


Fig. 18.13 A summary of Pickett's data on rock samples of Poisson's ratio (ν) as a function of the velocity ratio, V_p/V_s. It forms the basis for distinguishing among the three major rock types. From Domenico [19].

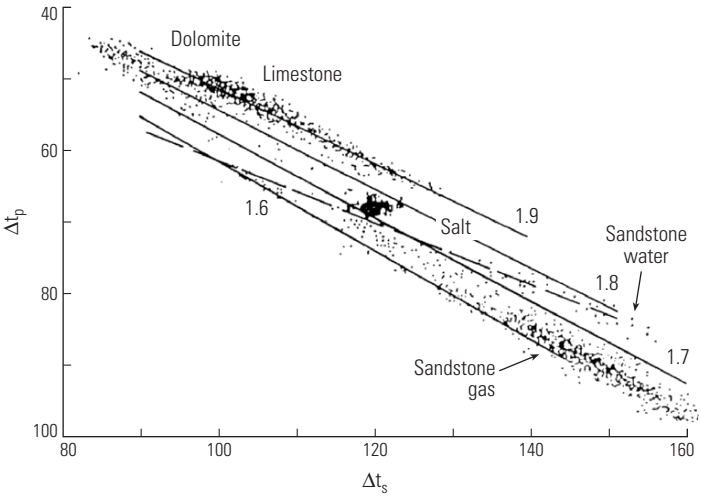


Fig. 18.14 Composite log data of shear and compressional interval transit time in the presentation proposed by Pickett for lithology identification [18]. Identification of dolomite, limestone, and salt is indicated. The trends observed for water- and gas-saturated sandstones are predicted by Biot theory. From Leslie and Mons [20]. Used with permission.

As found earlier, the limestones and dolomites fall on lines of constant ratios. The water-filled sandstone ratios vary from 1.6 to 1.8. However, the gas-filled points lie along a constant ratio of 1.6. This behavior has been shown to be consistent with predictions of the Biot theory [13]. In order to exploit this possibility, the logging tool must have the capability of separating the shear from the compressional arrivals.

18.4.2 Gas Detection and Quantification

The fundamental link between acoustic velocities and rock properties was already already given in Eqs. 18.2 and 18.1. The change of compressional or shear velocity with the replacement of water by gas in a porous formation has been discussed. By taking the ratio of the two velocities, say V_p/V_s, the density is eliminated. Thus, the ratio of velocities depends on the ratio of bulk modulus to shear modulus of the rock. From all the previous studies it is known that the bulk modulus depends strongly on the fluid-bulk modulus, whereas the shear modulus doesn't depend on it. If a compressible gas replaces relatively incompressible fluids in a porous rock, the ratio $\frac{V_p}{V_s}$ will reflect the bulk modulus change and can be used as an indicator for the presence of gas. However, in acoustic borehole logging there was some hope of being more quantitative about the actual gas saturation rather than just indicating its presence.

One promising technique to extract a more quantitative analysis of the gas saturation was based on a cross-plot of the velocity ratio V_p/V_s versus the compressional velocity V_p – a porosity proxy in sandstones. To elaborate on earlier observations that

the ratio V_p/V_s tends to increase with porosity in water-bearing sands, an estimation of this trend was made by Brie et al. [21]. The steps involve first taking the ratio of the two previous equations to get the results:

$$\left(\frac{V_p}{V_s}\right)^2 = \frac{k}{\mu} + \frac{4}{3}, \tag{18.15}$$

which represents the ratio for the water-filled rock. Now how to determine its evolution as a function of porosity, ϕ? The Biot–Gassmann equation (Eq. 18.11) relates the bulk modulus of the water-filled rock, k to dry-rock frame modulus, $\overline{k}$, and the fluid properties. In analogy with Eq. 18.15 the dry-rock velocity ratio can be written as:

$$\left(\frac{V_p}{V_s}\right)^2_{dry} = \frac{\overline{k}}{\overline{\mu}} + \frac{4}{3}, \tag{18.16}$$

where $\overline{\mu}$ is the dry frame shear modulus. Since the value of V_p/V_s in dry sandstones is generally taken to be 1.58 it is deduced that $\overline{k}/\overline{\mu} = 1.163$.

Unfortunately the Gassmann equation does not include explicit dependence of the dry-frame moduli on porosity so it is necessary to appeal to empirical relations derived from data to get the desired results. In this case, Brie took the variation of $\overline{\mu}$, the dry-frame shear modulus, to be related to the mineral shear modulus by:

$$\overline{\mu} = \mu_m(1-\phi)^c \tag{18.17}$$

where the value of c was taken to be 7.1. With this empirical link it is now possible, for any value of porosity ϕ, to compute the value of $\overline{\mu}$, and from the relationship that $\overline{k}/\overline{\mu} = 1.163$, to find the value of $\overline{k}$. This result is now plugged into Eq. 18.11 to get the value of k. Armed with the value of k and taking μ to be the same as the dry-frame value, $\overline{\mu}$, Eq. 18.15 can be used to get the value of V_p/V_s, a function of porosity which is then plotted against the corresponding value of the compressional slowness according to the Wyllie time average for sandstone. This trend can be seen on Fig. 18.15. Just above it is another trend drawn as an estimate for shales where V_p/V_s was taken to be 1.8 for the clay minerals; the compressional slowness, 60 μs/ft; and the porosity exponent for computing the shear modulus was taken to be 8.

The plotted points show trends of the logging measurements, in gas bearing zones, that lie between the water-filled trend and the dry gas sandstone line. It is possible to scale the gap in terms of the gas saturation. Using a traditional mixing law, useful at seismic frequencies (known erroneously as Wood's law but is actually the Reuss lower bound [9]), the effective modulus of a water-gas mixture is given by:

$$\frac{1}{k_f} = \frac{S_{xo}}{k_w} + \frac{1-S_{xo}}{k_g}, \tag{18.18}$$

which produces a large effect as soon as a small amount of gas saturation is present, which is not consistent with log observations. Thus a special empirical pore fluid mixing law was developed. The approach taken was to derive the effective pore fluid bulk modulus from the shear and compressional velocities [22] and to correlate these

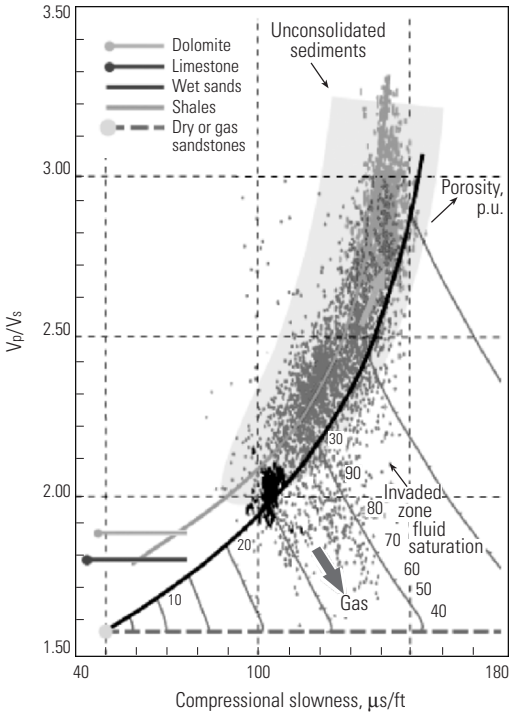


Fig. 18.15 A crossplot method to determine gas saturation from a simultaneous measurement of V_p and V_s.

results, on log data, against determinations of gas saturation made from other logs. Details can be found in [21].

Despite the appeal and the cleverness of the solution this technique has not found universal usefulness or acceptance.

18.4.3 Mechanical Properties

An entire domain of expertise, mechanical properties, uses the inputs from acoustic logging (and density) to predict three different and rather important types of formation behavior. The first concerns the prediction of formation collapse under producing conditions, also known as sanding analysis. The second is well bore stability – a prediction of the likelihood that the borehole might collapse during drilling. The third is the prediction of formation behavior under the introduction of excess pressure – to produce fractures. Glibly, predictions in these three general areas, all related to failure mechanics, can be made from a combination of knowledge of the elastic moduli of the formation coupled with theoretical and some empirical models. Some applications of modern acoustic measurements to obtaining formation mechanical properties will be treated in the next chapter.

18.4.4 Seismic Applications (AVO)

A recent development in seismic processing, known as AVO (amplitude versus offset) has changed, not only how seismic data is acquired and processed, but the type of information that can be extracted. Routinely, now it is possible to make direct prediction of the presence of hydrocarbons from properly processed seismic traces.

Nearly a hundred years ago the physics of the reflection and transmission of seismic waves at plane boundaries was understood. A set of equations, known by the name of one of the workers in this field, Zoepritz, predicts the amplitude of reflected P-waves from a plane interface as a function of the angle of incidence. The complicated function depends on the contrast in density, P-wave, and S-wave velocity of the two adjacent layers.

The stereotypical seismic section is a "wiggle" plot representing the reflections of acoustic energy that generally shows the position of subsurface layers that have contrasting density and velocity – it is processed to resemble a cross-sectional map of the geological layers. In AVO the variation of reflection (depending upon its illumination angle, or offset from the seismic source) from the various layers is examined in detail. This process is indicated schematically in Fig. 18.16. By fundamentally changing the

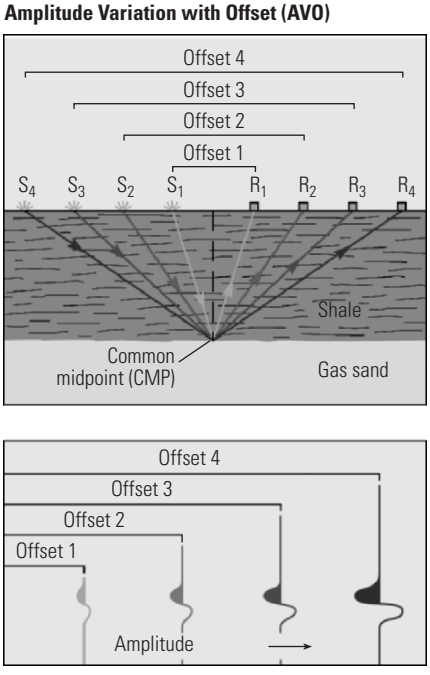


Fig. 18.16 A schematic illustration of AVO. In the top panel, the locations of sources and receivers associated with a common midpoint (CMP) are shown. In the lower panel the stylized trace from AVO processing shows a growing amplitude with increasing offset, in this example.

method of processing seismic data, the variation of reflected amplitude as a function of incidence angle is enhanced as indicated in the top portion of the figure. To interpret the measurements, a good model of the subsurface is needed, in particular, knowledge of the compressional and shear velocity and density. Using the Gassmann equation, the effects of fluid substitution can also be predicted so that observed variation of reflected amplitude vs angle can be used to distinguish between lithology changes and differing formation fluids.

The requirements for good input data to the AVO models has brought acoustic logging back to its origins. Once again, borehole acoustic logging, which started out as an adjunct to seismic analysis, has returned because of the need for continuous knowledge of both V_p and V_s. This need will justify the great efforts made to provide continuous borehole measurements of V_s – a topic to follow.

18.5 ACOUSTIC WAVES IN BOREHOLES

The picture of borehole acoustic logging presented earlier (see Fig. 17.12) is very simplified and it corresponds to the use of a monopole, one of two commonly used types of sources, although a third (quadrupole) source has been proposed for LWD applications [23]. The monopole emits acoustic energy isotropically whereas a dipole source emits in a preferential direction. What is implied in the figure is that the received signal is something approximating the transmitted pulse. However, that this is not the case can be seen clearly in Fig. 18.17 which shows an actual acoustic waveform recorded with a logging device in a borehole. In this particular example, three distinct packets of energy are seen. The first is indicated to be the result of the compressional wave moving through the formation. The second, with a much larger amplitude, is the result of a slower shear wave moving through the formation. Finally, arriving some 1,500 μs later is a wave of large amplitude, known as the Stoneley wave, which is due to the presence of the borehole, as we shall see later. Although the transmitter pulse is brief and fairly uncomplicated, the received signal is quite complex, because of the various reflections and interferences which can be produced as a result of waves travelling in the borehole.

In order to understand the two basic arrivals of Fig. 18.17 the wavefronts produced in a 2D medium of mud and formation have been computed for different times after emission and are shown in Fig. 18.18. The case taken here is for a fast, or "hard," formation in which the shear velocity in the solid is greater than the compressional velocity in the mud, i.e., $V_s > V_{mud}$. The first frame, at 40 μs after emission, shows a spherical wavefront traveling out from the source toward the formation. At 70 μs, the pressure wave has hit the borehole and three things have happened: There is a wave reflected back into the mud, a shear and a compressional wave have been created in the formation, and all of these have begun expanding.

If we follow the compressional wave through the rest of the frames, we see that it goes on expanding in time. At somewhere around 90 μs, the angle it makes with respect to the interface is 90°, and from that point on it travels down the interface with a speed of V_p. This is the so-called head wave. It can be thought to create a series of

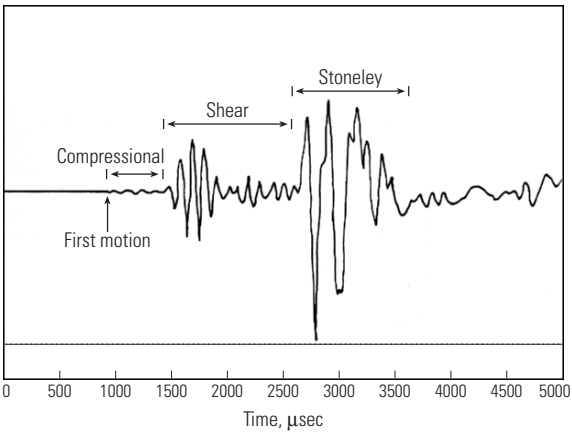


Fig. 18.17 A typical acoustic waveform recorded in a borehole. Three distinct arrivals are indicated. Courtesy of Schlumberger.

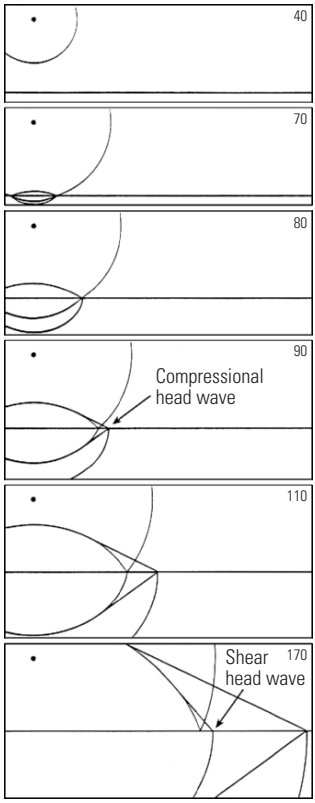


Fig. 18.18 Simulation of the wavefronts in a two-dimensional medium consisting of mud and a fast formation. Courtesy of Schlumberger.

disturbances along the borehole wall which reradiate into the mud as a plane wave, resembling the wake created by a boat. The angle of this "wake" will be related to the ratio of the formation compressional and mud velocities. Turning our attention to the shear wave, whose expansion is much slower because of its reduced velocity, we see that it does not make a right angle with respect to the interface until somewhere between 110 and 170 μs, at which point it travels to the right with the shear velocity creating a wave in the borehole mud, just as in the compressional case.

Figure 18.19 shows the situation after nearly 10 times as much time has elapsed (at 1,300 μs). The distance scale has been much enlarged and shows the location of 8 receivers. In this view, the compressional disturbance has already passed through all 8 receivers, and the next one to arrive will be the result of the shear wave. It will then be followed by the direct mud arrival, which will be followed shortly by the reflected mud pulse.

In practice direct mud arrivals are rarely seen and there is no single identifiable reflected mud pulse. This is where the 2D simulation with infinitely large borehole shown in Figs. 18.18 and 18.19 breaks down. If the mathematics of the 3D description of wave propagation are followed in detail, an additional propagating wave is found – an evanescent surface wave. It propagates along the interface without loss but decays exponentially away from the surface on either side of the interface. When the presence of the cylindrical borehole is included in the mathematical description, the decay of the evanescent wave in the borehole fluid is minor since the size of the borehole and the wavelength are of the same order of magnitude. The energy of this wave goes into a variety of modes that are associated with the P- and S-waves and most importantly, the Stoneley wave, to be discussed later.

In fast formations the shear signal detection is often improved at large distances from the transmitter. Returning to data recorded in a borehole, Fig. 18.20 shows waveforms at five different receivers at increasing distances from the transmitter. The shear arrivals are well-separated from the very low amplitude compressional arrivals, and the separation improves with increased transmitter-to-receiver distance. However,

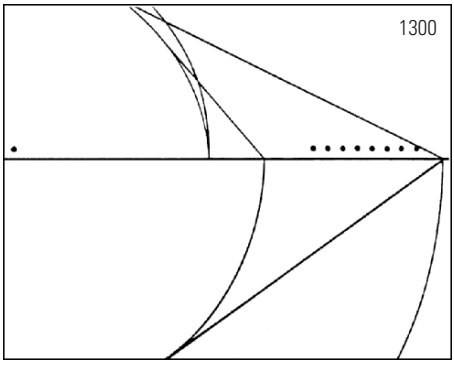


Fig. 18.19 Much later in the simulation, when the wavefronts have passed the detector array. Courtesy of Schlumberger.

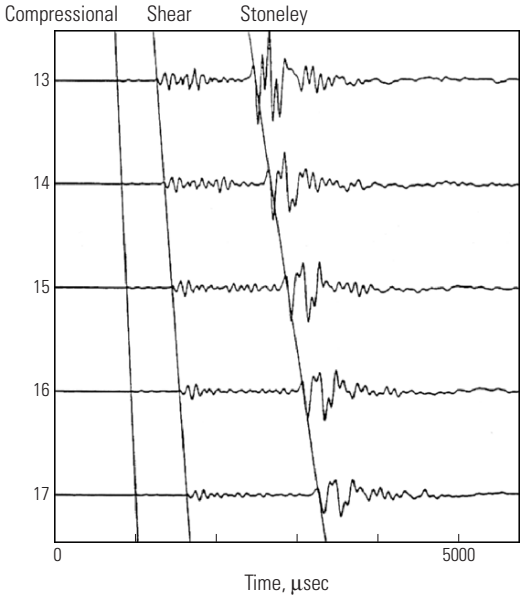


Fig. 18.20 Acoustic wavetrains recorded between 13 to 17 ft from the transmitter in a fast formation. The compressional, shear, and Stoneley arrivals are clearly separated. The slopes of the lines indicating each of the three types of first arrivals is proportional to their velocity. Courtesy of Schlumberger.

as shown in Fig. 18.21 for a soft formation, it is clear that there is no shear arrival present. In this example, the mud velocity is greater than the formation shear velocity.

To understand the lack of shear development, refer to Fig. 18.22, which shows the wavefronts in the 2D simulation of a soft formation at some time after emission. It is clear that there will be a compressional arrival. The compressional wavefront is perpendicular to the interface and travels along it at a speed of V_p, which is larger than V_{mud} in this case. However, the shear wave does not make a right angle since $V_s < V_{mud}$. The head wave does not appear, because the condition for constructive interference between the disturbance along the borehole wall and its transmission in the mud does not occur. Thus the "wake" will not develop.

Referring to the ray tracing discussion of Section 17.5 it can be seen that if the formation shear velocity equals the mud velocity there is no refraction (deflection) of the shear wave with respect to the incident wave ray direction. If $V_s < V_{mud}$ then the deflection will be increasingly towards the normal as the formation shear velocity decreases, and regardless of the incident angle it will always be directed into the formation with no possibility of head wave generation.

It must be noted that these conclusions about lack of shear wave development in slow formations is based on a very simple ray tracing model – a model that admits only planar boundaries and plane waves. The actual logging situation in a nearly cylindrical borehole with nonplanar acoustic waves is far from the conceptual model. Thus it is

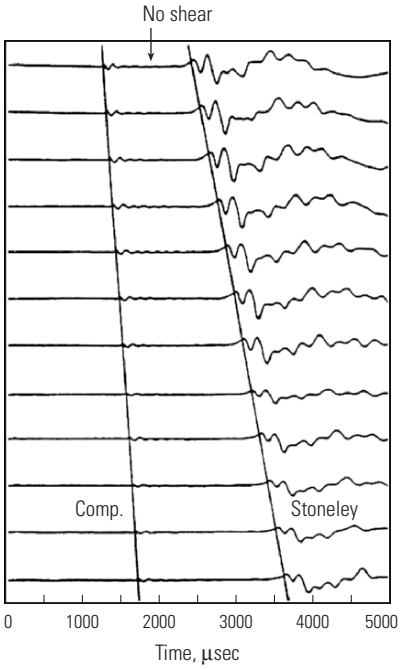


Fig. 18.21 Acoustic wave trains recorded at 1 ft intervals in a slow formation where the shear arrival is seen to be absent. Courtesy of Schlumberger.

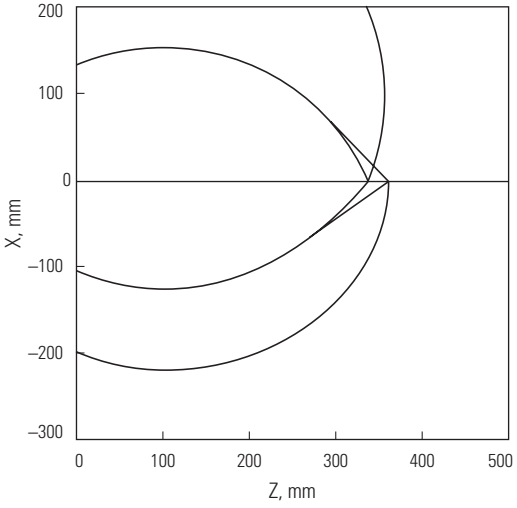


Fig. 18.22 Results of the two-dimensional wavefront simulation for a slow formation. The shear velocity is such that a head wave never develops and thus is not observed in the borehole. Courtesy of Schlumberger.

not surprising that detailed modeling [24] of a more realistic logging situation shows that even with a monopole transmitter, shear head waves can be developed in slow formations. However, they are apt to be swamped by the accompanying Stoneley wave. While a shear headwave in slow formations is theoretically possible in cylindrical geometries with particular formation/mud parameters, the practical excitation by a real tool is unlikely and does not lead itself to a reliable measurement of shear velocity.

18.5.1 Borehole Flexural Waves

The measurement of V_s in all logging cases, even for slow formations, awaited the development of dipole sources – devices capable of the generation of a pressure pulse in a preferential direction [25]. To generate information about the formation shear velocity, the orientation of the dipole is such that the pressure wave generated by the source is perpendicular to the acoustic tool sonde body. The pressure wave generated by the source impinges on one side of the borehole, and then the opposite, as the driving signal polarity changes, shaking the borehole side-to-side. Through the borehole fluid some of the acoustic energy is coupled into the formation and produces an undulation of the borehole wall known as the flexural wave. The flexural wave propagates along the borehole wall with particle displacement perpendicular to the wave travel as shown in Fig. 18.23.

As the flexural wave progresses along the borehole wall its displacement produces a measurable pressure wave in the mud just as does the more familiar head wave. Although, the flexural wave is similar to the shear wave it is not quite the same. It is a dispersive wave, which means that its velocity is a function of frequency. One manifestation of this is seen in Fig. 18.24 which shows the changing appearance of the flexural waveform as the distance from the source increases. Only at zero frequency is its velocity equal to the shear velocity. Thus, more complex signal processing is required to extract the shear velocity, but it is done routinely [27–29] on modern devices.

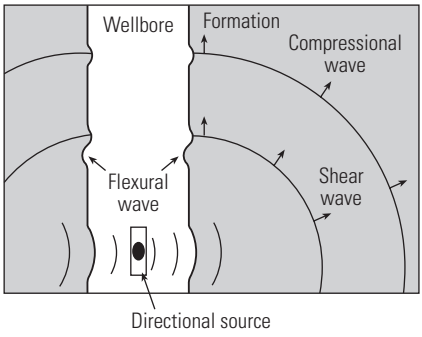


Fig. 18.23 Elastic wave propagation in a slow formation excited by a dipole source. Shown is the development of the borehole flexural wave. Adapted from Sinha and Zeroug [26].

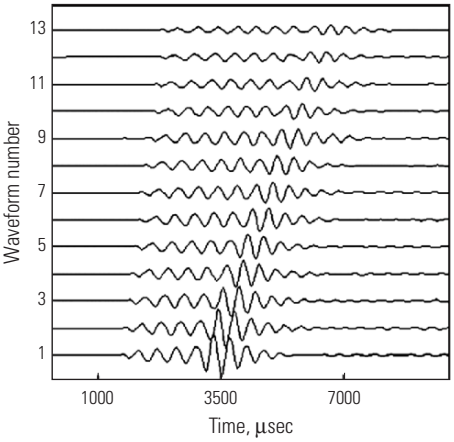


Fig. 18.24 A stationary measurement from a multi-receiver instrument that shows the evolution of the dipole flexural waveform as a function of distance from the source. Receiver distance increases with waveform number.

18.5.2 Stoneley Waves

The last aspect of the borehole sonic waveforms to be considered is the Stoneley wave. A good example of this is shown in Fig. 18.25. The full sonic waveform is shown from a tool in a borehole over a 200 ft section. The variations, due to lithology or porosity changes, are clearly seen in the shear and compressional arrivals. The Stoneley wave is also seen to have some variation in its arrival time, even though it is a pulse of energy which is traveling mainly in the borehole. What causes the variations in the Stoneley wave velocity?

Figure 18.26 illustrates the basic notions of the Stoneley, or tube wave. In a liquid-filled tube which has very rigid walls, a low-frequency pressure wave will travel as a nearly plane wave at the compressional velocity of the fluid. This type of phenomenon is responsible for the so-called water hammer. In that case, however, the sound is produced by the small distortion of the walls of the pipe carrying the water, which has been suddenly stopped. For a borehole, with semirigid confining walls, the speed of the pressure disturbance is related to the elastic constants of the wall as well as the fluid.

White [11] has shown in the low-frequency limit that the speed of this tube wave, in a non-permeable elastic formation, is given by:

$$V_{tube} = V_m \left(\frac{1}{1 + \frac{\rho_m {V_m}^2}{\rho {V_s}^2}} \right)^{\frac{1}{2}}, \tag{18.19}$$

where V_m is the compressional velocity in the mud, V_s is the shear velocity in the formation, ρ is the density of the formation and ρ_m the mud density [11]. Thus the shear velocity of the formation V_s can be obtained in the absence of a shear arrival

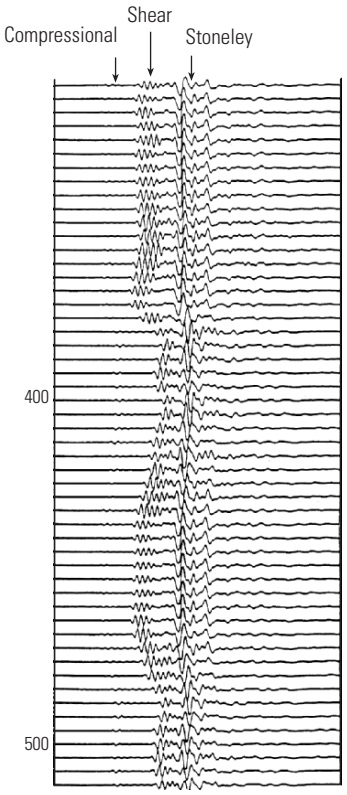


Fig. 18.25 A sequence of acoustic waveforms recorded at discrete depths in the borehole, at a single receiver, is shown in log-like format; shear and Stoneley arrivals are clearly seen. In addition to variations in the shear velocity, which reflect formation properties, the Stoneley wave is also seen to have velocity variations. Courtesy of Schlumberger.

from the speed of the tube wave if the density of the formation is known. This was a technique used sometimes to extract the shear wave in slow formations before the development of acoustic devices with dipole sources, which provide a much more straightforward means to get the shear velocity.

Using the elastic constant relationships developed in Chapter 17, the tube wave velocity dependence on the mud bulk modulus K_m and the formation shear modulus μ can be found from the preceding expression to be:

$$V_{tube} = \left[\frac{1}{\rho_m \left(\frac{1}{K_m} + \frac{1}{\mu} \right)} \right]^{\frac{1}{2}}. \tag{18.20}$$

This illustrates the role of the borehole wall rigidity in modulating the mud velocity.

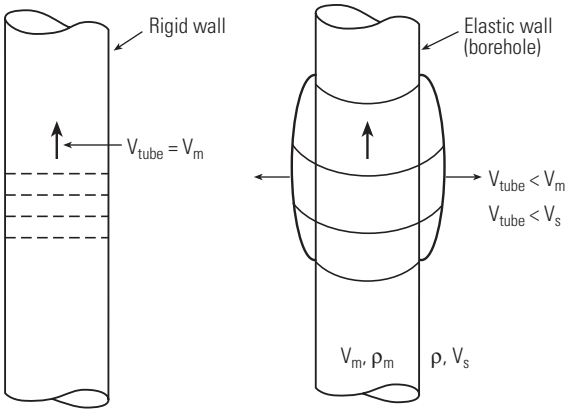


Fig. 18.26 A simplified representation of the low frequency Stoneley, or tube wave.

Propagation of the Stoneley wave in a borehole through porous sections of rock is a much more complicated phenomenon. In this case there is some fluid movement between formation and borehole. The result of this movement is that the wave is attenuated and its velocity changes. The magnitude of these effects is frequency-dependent. Models based on the Biot poroelastic theory have been developed to elucidate the the frequency dependence of the attenuation and slowness, and the interesting relationship between these two attributes and the fluid mobility (ratio of formation permeability to fluid viscosity) [30]. Experiments on laboratory rocks confirmed the frequency dependence of velocity and attenuation, especially at low frequencies. At low frequencies it was also confirmed that by increasing the fluid mobility the Stoneley velocity is decreased and the attenuation increased [31].

REFERENCES

1. Timur A (1987) Acoustic logging. In: Bradley H (ed) Petroleum production handbook. SPE, Dallas, TX
2. Jordan JR, Campbell F (1986) Well logging II: resistivity and acoustic logging. Monograph Series, SPE, Dallas, TX
3. Wyllie MRJ, Gregory AR, Gardner LW, Gardner GHF (1958) An experimental investigation of factors affecting elastic wave velocities in porous media. Geophysics 23(3):459–493
4. Wyllie MRJ, Gardner GHF, Gregory AR (1961) Some phenomena pertinent to velocity logging. JPT 13:629–636
5. Sammonds PR, Ayling MR, Meredith PG, Murrell SAF, Jones C (1989) A laboratory investigation of acoustic emission and elastic wave velocity changes during

rock failure under triaxial stresses. In: Maury V, Fourmaintraux D (eds) Rocks at great depth. Balkema, Rotterdam, The Netherlands

6. Gassman F (1951) Elasticity of porous media. Vierteljahrschr Naturforsch Ges in Zurich, 96(1):1–23

7. Geertsma J (1961) Velocity-log interpretation: the effect of rock bulk compressibility. SPE J 1:235–248

8. Geertsma J, Smit DC (1961) Some aspects of elastic wave propagation in fluid-saturated porous solids. Geophysics 26(2):169–181

9. Mavko G, Mukerji T, Dvorkin J (1998) The rock physics handbook. Cambridge University Press, New York

10. Gassman F (1951) Elastic waves through a packing of spheres. Geophysics 16(18):673–685

11. White JE (1983) Underground sound. Elsevier, Amsterdam, The Netherlands

12. Pickett GR (1960) The use of acoustic logs in the evaluation of sandstone reservoirs. Geophysics 25:250–274

13. Biot MA (1956) Theory of propagation of elastic waves in fluid-saturated porous solids. J Acoust Soc Am 28(2):179–191

14. Kuster G, Toksoz MN (1974) Velocity and attenuation of seismic waves in two-phase media. Geophysics 39(5):587–606

15. Raymer LL, Hunt ER, Gardner JS (1980) An improved sonic transit time-to-porosity transform. Trans 21st SPWLA Annual Logging Symposium, paper P

16. Han D-H, Nur A, Morgan D (1986) Effect of porosity and clay content on wave velocity in sandstones. Geophysics 51:2093–2107

17. Schlumberger (1997) Schlumberger log interpretation charts. Schlumberger, Houston TX

18. Pickett GR,(1963)Acoustic character logs and their applications in formation evaluation. JPT 15:650–667

19. Domenico SN (1984) Rock lithology and porosity determination from shear and compressional wave velocity. Geophysics 49(8):1188–1195

20. Leslie HD, Mons F (1982) Sonic waveform analysis: applications. Trans SPWLA 23rd Annual Logging Symposium, paper GG

21. Brie A, Pampuri F, Marsala AF, Meazza O (1995) Shear sonic interpretation in gas-bearing sands. Presented at the 70th SPE Annual Technical Conference and Exhibition, paper SPE 30595

22. Murphy W, Reischer A, Hsu K (1993) Modulus decomposition of compressional and shear velocities in sand bodies. Geophysics 58(2):227–239

23. Tang XM, Dubinsky V, Wang T, Bolshakov A, Paterson D (2003) Shear-velocity measurement in the logging-while-drilling environment: modeling and field evaluations. Petrophysics 44(2):79–90

24. Wang K (2006) Numerical simulation and field examples of critically refracted shear arrivals in a borehole in soft formations. Presented at 76th SEG Annual Meeting, extended abstracts:344–348

25. Zemanek J, Williams DM, Schmitt DP (1991) Shear-wave logging using multipole sources. The Log Analyst 32(3):233–241

26. Sinha B, Zeroug S (1999) Geophysical prospecting using sonics and ultrasonics. In: Webster JG (ed) Wiley encyclopedia of electrical and electronics engineering. Wiley, New York

27. Harrison AR, Randall CJ, Aron JB, Morris, CF, Wignal AH, Dworak RA, Rutledge LL, Perkins JL (1990) Acquisition and analysis of sonic waveforms for a borehole monopole and dipole source for the determination of compressional and shear speeds and their relation to rock mechanical properties and surface seismic data. Presented at 65th SPE Annual Technical Exhibition and Conference, paper SPE 20557

28. Kimball CV (1998) Shear slowness measurement by dispersive processing of the borehole flexural mode. Geophysics 63(2):337–344

29. Pistre V, Kinoshita T, Endo T, Schilling K, Pabon J, Sinha B, Plona T, Ikegami T, Johnson D (2005) A modular wireline sonic tool for measurements of the 3d (azimuthal, radial, and axial) formation acoustic properties. Trans SPWLA 46th Annual Logging Symposium, paper P

30. Chang SK, Liu HL, Johnson DL (1988) Low-frequency tube waves in permeable rocks. Geophysics 44(4):519–527

31. Winkler KW, Liu HL, Johnson DL (1989) Permeability and borehole Stoneley waves: comparison between experiment and theory. Geophysics 54(1):66–75

Problems

18.1 Using Table 17.1, find an expression for compressional velocity V_c as a function of the bulk modulus and the shear modulus. The quantity $B + \frac{4}{3}\mu$ is known as the plane wave modulus.

Show that the plane wave modulus can be expressed as $\lambda + 2\mu$, where λ is the Lamé constant.

18.2 Consider two immiscible liquids of bulk modulus k_1 and k_2 which are mixed together with volume fractions V_1 and V_2. What is the mixing law for the bulk modulus of the mixture of two liquids? Write it in terms of the volume fractions of the two components.

18.3 It was seen that the Gassman equation predicts the bulk modulus k of a liquid-filled rock of porosity ϕ to be:

$$k = k_{df} + \frac{(1 - \frac{k_{df}}{k_{ma}})^2}{\frac{\phi}{k_f} + \frac{1-\phi}{k_{ma}} - \frac{k_{df}}{k_{ma}^2}}, \tag{18.21}$$

where the subscripts of the bulk moduli are as follows: df refers to the dry frame, ma to the matrix, and f to the fluid.

18.3.1 Using the mixing law of Problem 18.2, write the above expression for bulk modulus in terms of the state of water saturation.

18.3.2 Describe how you would obtain a value of k_{df} if your laboratory measurements limited you to a judicious choice of compressional velocity measurements. An explicit equation for the value of k_{df} may be more than you want to do, but please indicate the procedure.

18.4 Given the bulk modulus of a rock sample to be 141.7 GPa and a compressional velocity of 7.8 km/s, what is an upper limit to be expected for the shear velocity? What is the actual shear velocity if the density of the rock is 5.00 g/cm^3?

18.5 Figure 18.7 shows some data for a 25% porosity sandstone that indicate the effect of the saturating fluid on compressional and shear velocities. The implied change in apparent formation Δt for the compressional arrivals is at a maximum for the case of no differential pressure.

18.5.1 Using the Wyllie time-average approach, what value of Δt (in μs/ft) would you ascribe to air? The velocities of typical materials in Table 18.1 may be of some use in this calculation.

18.5.2 If, while logging a sandstone formation, you encountered a formation Δt corresponding to this minimum velocity and did not recognize the presence of gas, what porosity would you estimate it to be?

18.5.3 The curves for shear waves are inverted on this figure compared to the compressional. Show, however, that they are in the anticipated order and that the magnitude of the separation is as expected for no differential pressure.

19

Acoustic Logging Methods

19.1 INTRODUCTION

The measurement of the simple interval transit time, or slowness, of downhole formations has been accomplished by a variety of logging devices. Despite the seeming simplicity of this measurement, which extracts only a part of the information contained in the complex acoustic waveform, a number of innovations were necessary to make valid measurements under a variety of borehole conditions. This chapter starts by examining the techniques prevalent in borehole acoustic logging tools up to the mid-1980s.

After reviewing the typical log presentation format, the performance of sonic logging tools is contrasted with other porosity-sensitive devices, most of which are more sensitive to borehole conditions. One of the limitations of conventional acoustic tools is a shallow depth of investigation. An early enhancement of tool design increased the transmitter–receiver distance. These long spacing sonic tools were developed to overcome the perturbations caused by alteration of the formation near the borehole.

Newer acoustic devices employ arrays of receivers, both monopole and dipole, some at extremely long spacing. Wavetrain recording and signal processing help avoid some of the defects which mar conventional sonic logging under certain conditions. To provide reliable V_s measurements, even in slow formations, dipole sources have been designed to produce a borehole flexural wave from which the formation shear velocity can be extracted from multidetector waveform data. In addition to shear measurements, newer devices also provide a measurement of the tube wave or Stoneley wave. All these measurements allow applications beyond the conventional estimation of porosity, that are primarily related to rock properties. They have to do with the

detection and delineation of fractures, prediction of rock failure, or sanding – useful information for perforation or for drilling mechanics. Ultrasonic devices operating in the range of 1 MHz have opened the door to acoustic borehole imaging. These can be used in the detection of naturally occurring fractures and, in another application, the evaluation of the cementing of cased wells.

19.2 TRANSDUCERS – TRANSMITTERS AND RECEIVERS

Acoustic measurements rely on the production of a pulse of pressure which is applied, through the borehole mud, to the formation. Two types of transducers have been in use both as acoustic source generators and receivers. One type is based on the magnetostrictive behavior of certain materials. For these, application of a magnetic field causes a volume reduction in the material. Consequently the sudden application of a magnetic field initiates a pressure pulse which is completed upon the removal of the magnetic field. This is accompanied by a subsequent volume relaxation.

The general form of the magnetostrictive transducer used in logging is a torus. The magnetic field is produced by supplying current to a coil which completely wraps the toroidal core material. Since the magnetostrictive material is also magnetized, it can operate as a receiver. Any impinging compressional acoustic energy will cause volume distortions in the core and thus vary the magnetic field which threads the coil windings. This changing magnetic field will produce a voltage at the terminals of the coil which is representative of the acoustic signal.

The second type of device in common use is based on ceramic materials, such as $BaTiO_2$, which have piezoelectric properties. This dielectric material responds to an applied electric field by changing its volume. A typical monopole source is a cylindrical shell of ceramic. Applying a voltage pulse between the inner and outer surfaces of the ceramic shell produces a subsequent fluctuation in its volume that can generate a pressure disturbance. As a receiver, the incoming compressional wave distorts the ceramic, setting up a polarization charge, which appears as a voltage across the two surfaces of the cylindrical shell.

The output power and operating frequency of both types of devices are limited by surface area and material properties. The dimensions dictated by logging sondes result in frequencies from 1 to 25 kHz. As a transmitter, the application of a voltage pulse results in a "ringing" at the central frequency which lasts for several periods.

As mentioned in the previous chapter, the reliable borehole measurement of shear velocity awaited the development of the dipole source. An early identification of this problem and solution was made by Kitsunezaki [1] who sketched out a few ideas for transducers, including an electromagnetically actuated double-ended piston, similar to a speaker, that is currently used today. Such a device, seen in Fig. 19.1, when activated, produces a positive pressure pulse on one side of the tool and a negative pressure on the other; and then the cycle reverses.

Although a dipole source can also be constructed of two oppositely phased ceramic monopole transducers (see Fig. 19.2) they generally are not capable of coupling enough energy into the formation wall at low frequencies to be of practical use.

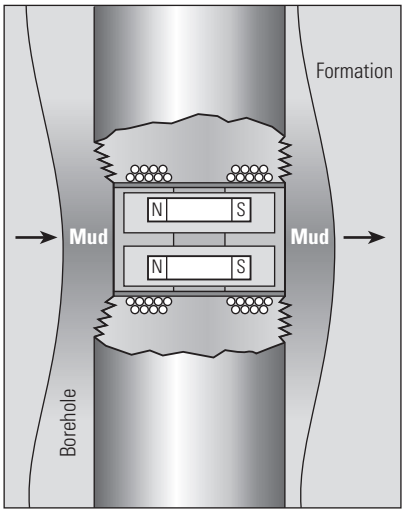


Fig. 19.1 A schematic of an electromagnetic piston dipole source, which induces a flexural wave in the surface of the borehole wall.

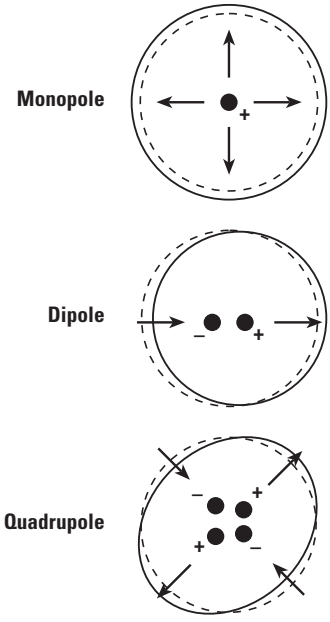


Fig. 19.2 A schematic shows how dipole and quadrupole transmitters can be formed by appropriately phased monopole acoustic transmitters. The convention is that a positive pressure pulse is produced radially by the monopole indicated by a "+" sign.

For LWD sonic applications, quadrupole sources are of interest for coupling energy into the formation rather than into the drill collar. In principle these can be made of an assemblage of four properly phased monopole sources. Figure 19.2 shows schematically the arrangement of four monopole sources that constitute a quadrapole.

19.3 TRADITIONAL SONIC LOGGING

Traditional sonic logging, for this discussion, is taken to mean the determination of the transit time of compressional waves in the material surrounding the borehole by a device with two receivers. These are typically located at 3 and 5 ft from the transmitter. This type of device is illustrated in Fig. 19.3. The technique consists of measuring the difference in the arrival times of the acoustic energy at the two transducers. This difference divided by the span between the two detectors yields a transit time Δt, or slowness (usually expressed in μs/ft) for the formation. The depth of investigation of this measurement is somewhat difficult to define in the case of a uniform formation. Since only the transit time of the first detectable signal is being measured, the measurement will be sensitive only to the acoustic path which has the

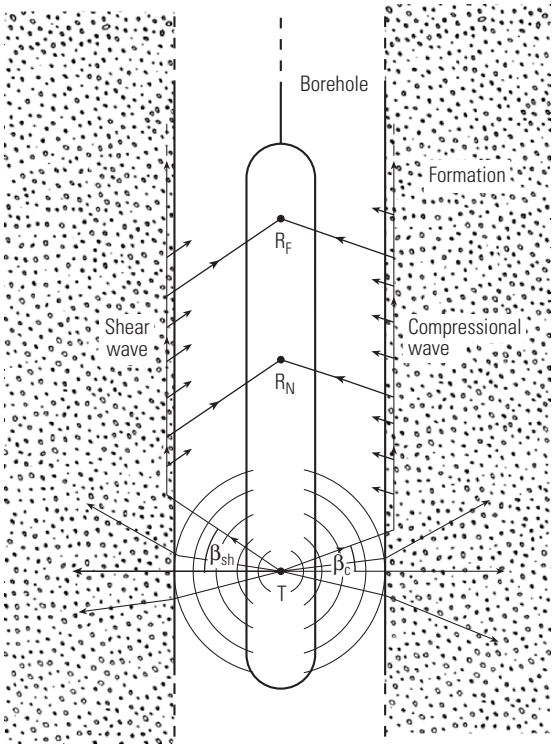


Fig. 19.3 A standard sonic tool in the centered logging configuration. From Tittman [2].

shortest time. This is generally the one parallel to the borehole wall and very close to its surface. The notion of depth of investigation will become meaningful only when we consider the problems of alteration, and damage (both imply a reduction in the formation velocity in the vicinity of the borehole) to the borehole wall.

The first arrival transit time may characterize the undisturbed formation, depending on the source-to-detector spacings, the velocity contrast between the invaded (or altered) and undisturbed zone, and the thickness of this altered zone. Some authors have attempted to define a pseudogeometric factor for the first arrival time [3]. Their results, shown in Fig. 19.4, can be interpreted as giving the maximum thickness of an altered zone for which the measured Δt is still representative of the virgin formation. This depth of investigation increases with source-to-detector spacing and for increased velocity contrasts between the two zones. For the conventional sonic tool a typical value may be on the order of 6 in.

The typical presentation format for a standard sonic log is shown in Fig. 19.5. The formation transit time is presented in tracks 2 and 3. Increasing transit times (or slowness, as it is more chic to say in acoustic logging circles) are shown to the left, which is also the trend for increasing porosity. An additional trace consists of a series of little pips every so often. These are seen at the beginning of track 2 in the figure. Each pip represents 1 msec of integrated travel time and serves as a reminder of the origin of the sonic log: It was developed to correlate time with depth in seismic sections.

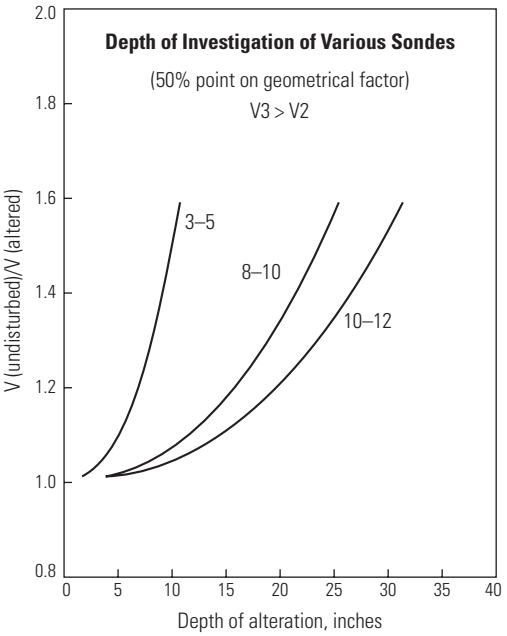


Fig. 19.4 Estimates of the depth of investigation for three types of conventional sonic arrays. Adapted from Chemali et al. [3].

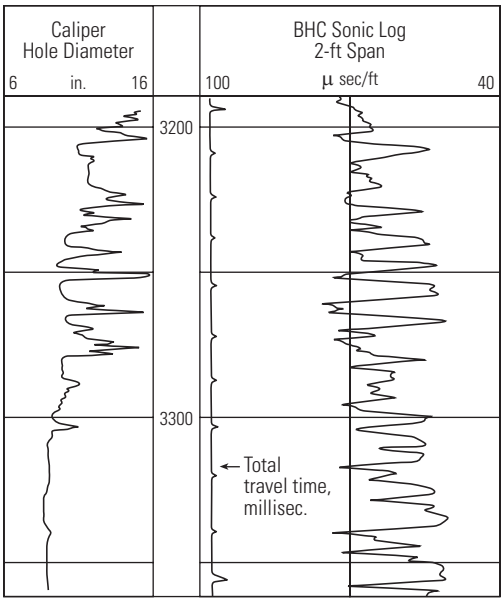


Fig. 19.5 A standard acoustic log presentation format with the integrated travel time pips. From Timur [4].

The conventional sonic log presentations for portions of the simulated reservoir are shown in Fig. 19.6. The bottom zone is from the carbonate section, and the upper from the shaly sand section. To emphasize the porosity sensitivity of the sonic log, comparison with the neutron and density logs over the same intervals is provided.

The use of two-detector devices, with normal spacing of 3 and 5 ft from transmitter to receiver, introduces some problems with the resolution of thin beds whose compressional velocity is different from the surrounding medium. This problem is considered in Fig. 19.7, which shows a fast limestone bed surrounded by slower shales. As indicated in part a, if the span between the two receivers exceeds the bed thickness, then the measured Δt will never attain the true value but some weighted average over a length which is equal to the difference between the span and the bed thickness. In part b of the figure, the span is shorter than the thickness of the bed, and for a short stretch, the value of Δt attains the true value of the fast formation – a problem shared by most logging tools.

One of the real advantages of sonic logging is its relative insensitivity to borehole size variations. Figure 19.8 qualitatively compares borehole size effects for the density device, the neutron porosity device, and an acoustic tool. In the section of log shown, there is an enormous borehole irregularity over a 20 ft interval that is seen on the caliper trace. Although the $\Delta\rho$ curve for the density log is not shown, an experienced interpreter might question the value of ρ_b indicated in this region.

In the middle log, the neutron porosity can be seen to be nearly flat just below the shale section. However, at the point of largest caliper activity there is also a peak in the

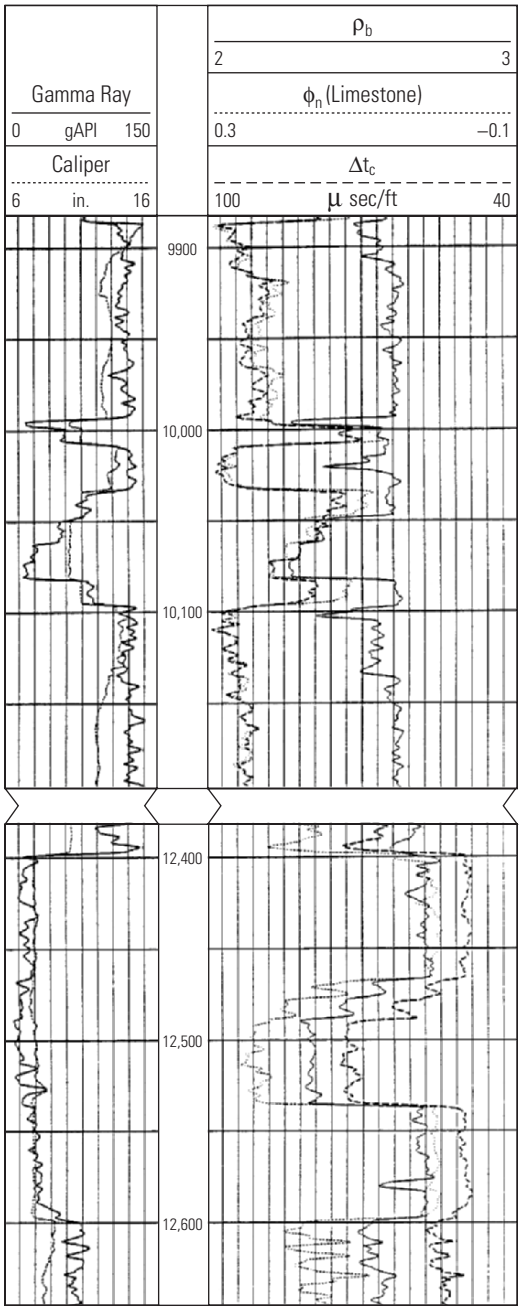


Fig. 19.6 A sample interval transit time log from the simulated reservoir model.

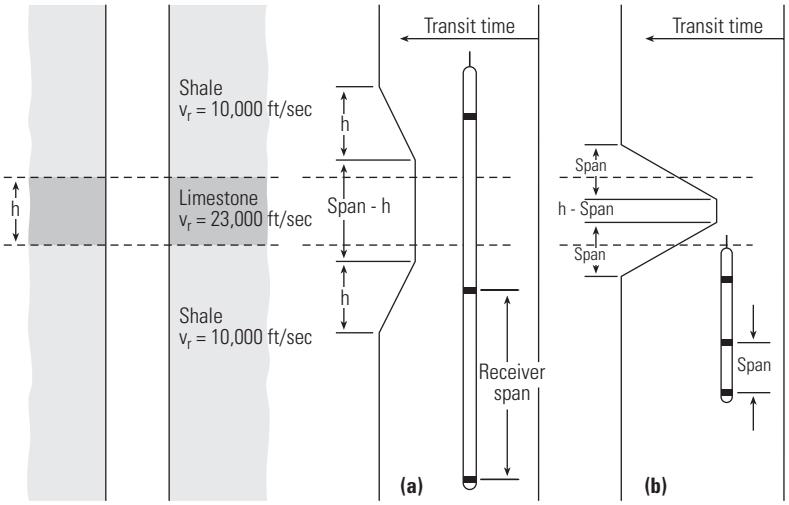


Fig. 19.7 The effect of the spacing between two receivers on the measured acoustic travel time of a thin high velocity bed. From Timur [4].

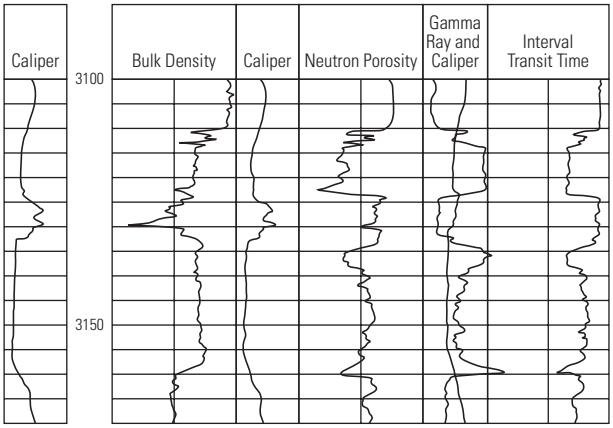


Fig. 19.8 Illustration of the insensitivity of the acoustic measurement to extremely poor borehole conditions. Compared are the responses of a density and a neutron porosity tool; both show incorrect responses in the caved section of the borehole. From Timur [4].

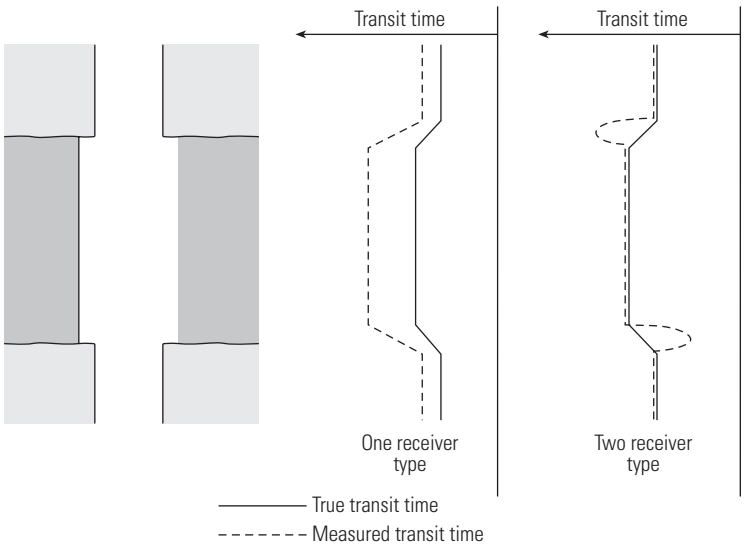


Fig. 19.9 The effects on the integrated travel time at the boundaries of hole diameter changes. From Timur [4].

neutron porosity, which no doubt is the result of an inadequacy in its compensation scheme. The dramatic data, however, are in the third log, which shows the measured Δt in this zone. It is very steady despite the large caliper excursions. No doubt the porosity of this zone is quite constant, a fact that could not be deduced from either of the other two porosity devices. The question remains: How is the sonic borehole compensation achieved?

As Fig. 19.9 indicates, in a region of changing borehole size, a single source-detector sonic device will measure abnormally long transit times when the hole becomes enlarged. This is a result of the increased transit time from the transmitter across the mud to the formation and back to the receiver. A partial solution to this problem is obtained by use of one transmitter and two receivers. By determining the travel time to the two detectors and using the difference to determine the travel time, as indicated in the figure, the effect of the borehole diameter is eliminated except at the boundaries, where "horns" can appear on the log response.

The more general logging situation is shown in Fig. 19.10. Not only can there be changes in borehole diameter, but the tool is not necessarily centered in the borehole, because of deviation of the borehole and differential sticking of the tool string. As indicated, this more general case can be solved by the use of two transmitters and two pairs of closely spaced receivers. Two sets of differential travel time measurements are made: an up-going one and a down-going one. In the case sketched in Fig. 19.10, the up-going transit time will exceed the down-going case. By averaging the two results, the effect of existing unequal mud travel paths is eliminated, and the measurement reflects the travel time of the formation. Tools of this type are said to be borehole compensated (BHC).

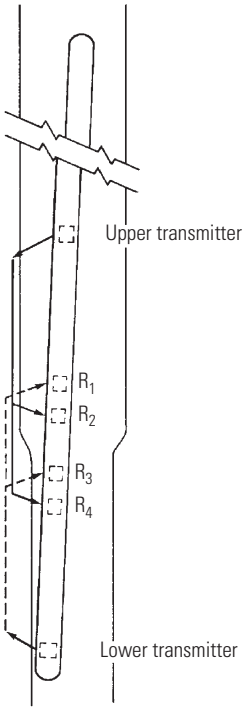


Fig. 19.10 The use of four detectors to compensate for borehole size and tool tilt.

19.3.1 Some Typical Problems

Despite the good performance of the compensated sonic tool, as noted above, there are a few situations which can cause problems. One of them results from the possibility that, in slow formations, with very large borehole sizes, the direct mud arrival will precede the formation arrival. In the conventional sonic tool, an amplitude rise in the detected pulse is sensed to determine the first arrival. However, it is not necessarily the result of a signal from the formation. Because of the generally large contrast between formation compressional velocities and mud velocities (generally the formation velocity can exceed the mud velocity by a factor of 2), the formation arrival and mud arrival separation can be increased by simply increasing the distance between transmitter and receiver. However, for a given spacing it is possible for the two signals to overlap, if the mud transit time to and from the formation is large (because of a very large borehole size). This notion is quantified, for a centralized tool, in Fig. 19.11. The area of reliable Δt measurements is indicated for receivers at three different distances: The slower the formation, the smaller the borehole size must be in order to see the formation arrival before the direct mud arrival. The situation improves dramatically for increased spacing. Also eccentering can pick up formations signals in larger holes.

One serious environmental effect for the sonic device is that of damage or alteration of the material near the borehole wall. Generally this occurs in some clays, commonly

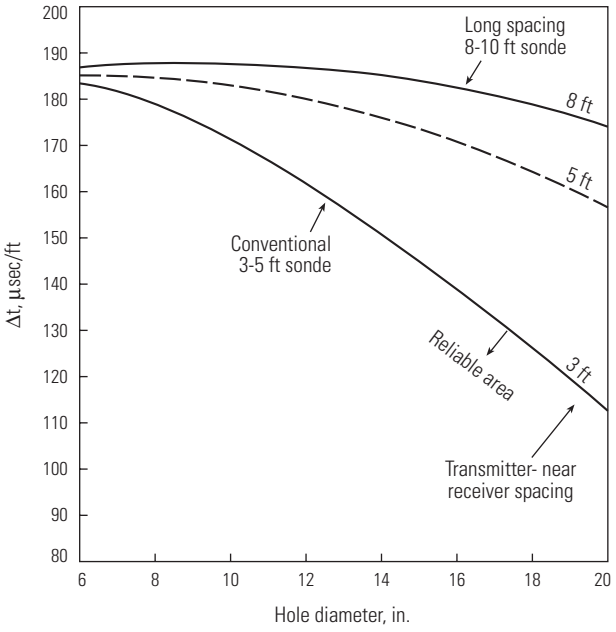


Fig. 19.11 Areas of confidence for conventional two-receiver tools as a function of borehole diameter. From Goetz [5].

known as swelling clays, which take on water, expand, and suffer changes in density as well as velocity. Another source of alteration can be induced stress-relief fracturing around the wellbore, which can largely alter the acoustic properties of the material. A striking example of the former type of shale alteration is shown in Fig. 19.12, which shows the transit time measured in the same well 2 months apart. In general the transit times have increased by about 20 μs/ft due to the shale alteration. In a case such as this, the first arrival travels through the slower altered medium. This is due to the thickness or depth of alteration; the two-way travel time through it to reach the faster undamaged formation exceeds the time difference between them, and thus the first signal to arrive travels only through the altered zone.

An annoying feature which sometimes appears on acoustic logs is cycle-skipping, which is shown in Fig. 19.13. This condition is immediately recognized by the spiky nature of the Δt trace; apparent travel time changes on the order of 40 μs/ft are visible. Figure 19.14 indicates the origin of these problems: Either the timing circuitry is triggered by random noise, or the anticipated signal strength falls below that expected and the arrival is not detected until a full cycle ($\approx$40 μs at 25 kHz) later.

19.3.2 Long Spacing Sonic

The measurement of compressional velocity was natural. Since this wave has a larger velocity, it always arrives at the detector first. The shear arrival can be masked if it

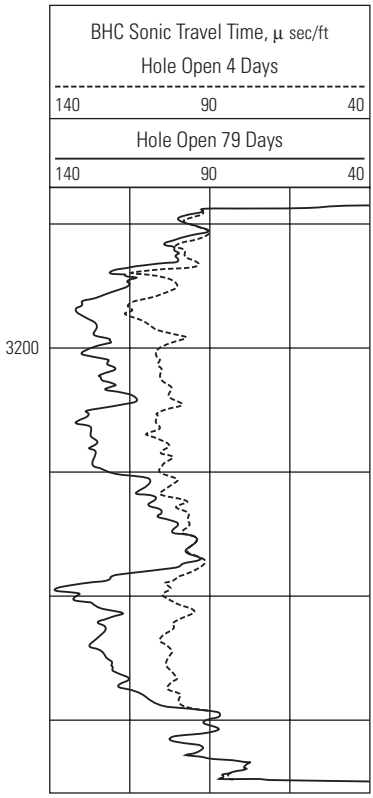


Fig. 19.12 Log example of the effect of formation alteration observed between two logging runs with 75 days of elapsed time. From Timur [4].

arrives in the midst of the ringing portion of the transmitter signal, or it can be lost in some of the other modes produced by acoustic waves in boreholes. In the best cases, the problem of detecting the shear arrival is one of just looking for it after the compressional arrival. Such a case is illustrated in Fig. 19.15. In the waveform shown, the shear arrival is clearly distinguishable.

The stacked waveforms from six receivers placed from 3 to 16 ft from the transmitter, as shown in Fig. 19.15, indicate that the separation of shear from compressional arrivals is greatly aided by spacing. This was one of the motivations for the development of long spacing sonic sondes. A second reason for their development was to combat the problem of the altered zone. As might have been guessed from the results of Fig. 19.11 and the discussion on depth of investigation, the longer the spacing, the more reliably one can measure the transit time of the faster, undamaged formation. A common detector configuration is at 8 and 10 ft from the transmitter.

The quantification of this improvement for early acoustic tools operating in the 20 kHz range can be found in Fig. 19.16. It indicates the reliable zone of measurement

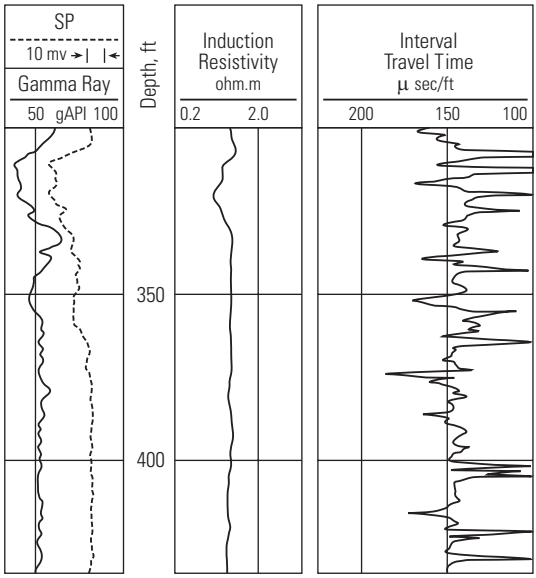


Fig. 19.13 An example of cycle-skipping on the interval transit time log. From Timur [4].

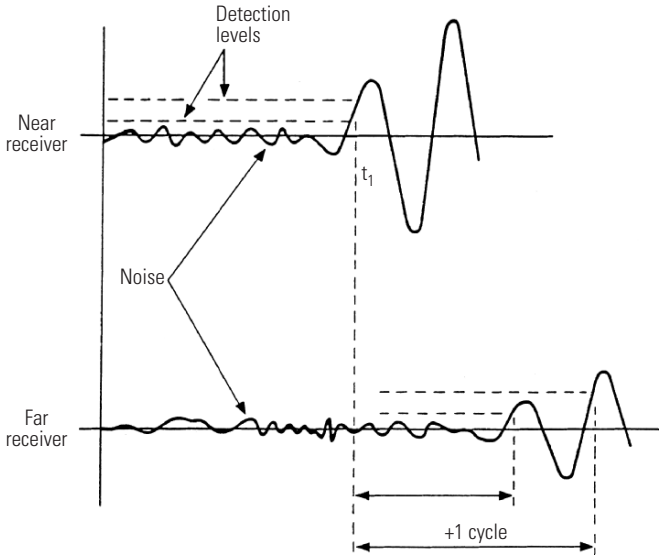


Fig. 19.14 The origin of cycle-skipping. From Timur [4].

(to the left of the indicated curves) for the conventional and long spacing sonde. The change in velocity of the damaged zone which can be tolerated as a function of its thickness is indicated as a function of the formation travel time. In a formation characterized by a Δt of 100 μs/ft, a 20 μs/ft alteration can be tolerated up to 5

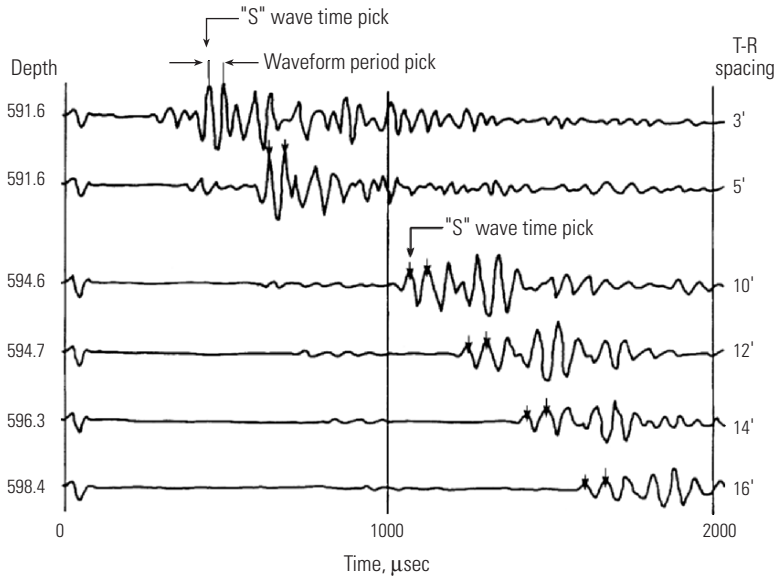


Fig. 19.15 The effect of spacing on the separation of shear and compressional arrivals. From Timur [4].

in. thick for the conventional sonde, but it can be up to 14 in. thick with the long spacing device. This tolerance to alteration also eliminates problems with direct mud arrival in very large borehole sizes.

Another variation of the borehole compensation technique, used for long spacing devices, is shown in Fig. 19.17. In this case, two transmitters and two receivers are used to produce the same result as the six-transducer tool of Fig. 19.10. For the long spacing device, there are two receivers at the top of the tool and two transmitters at the bottom (a saving of two transducers). The measurement is made in two phases. At one position in the well, the bottom transmitter fires and the transit time between the two top receivers is measured. Shortly after, when the tool has moved so that the two transmitters are nearly in the position previously occupied by the two receivers, the two transmitters are fired in succession, and the two transit times (from the different transmitters) are measured to the lower detector. As the figure indicates, this is equivalent to the use of two transmitters and four receivers, and the technique is referred to as depth-derived borehole compensation.

19.4 EVOLUTION OF ACOUSTIC DEVICES

The preceding discussion was the state of affairs in the mid-1980s – using monopole sources to get V_p and using the refracted shear wave to get V_s in fast formations. Since then many new devices, of varying sophistication, have become available to provide

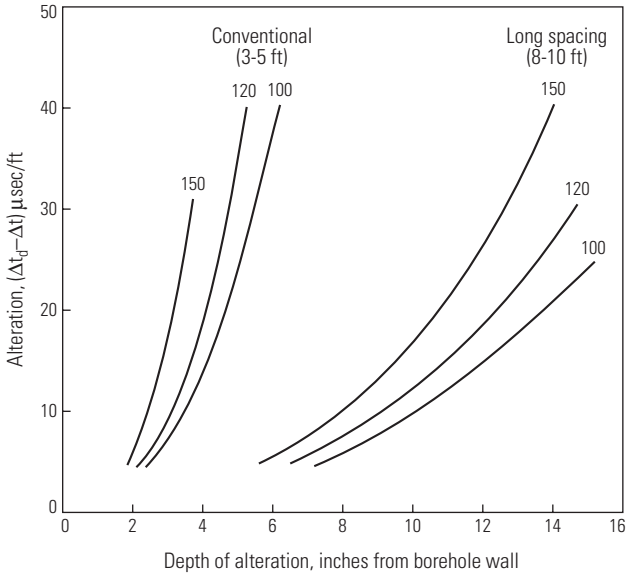


Fig. 19.16 The effect of alteration as measured by the difference between the observed interval transit time and the formation transit time as a function of alteration depth into the formation. As expected, the long spaced tool is able to tolerate deeper alteration before noticeable effects appear. From Goetz [5].

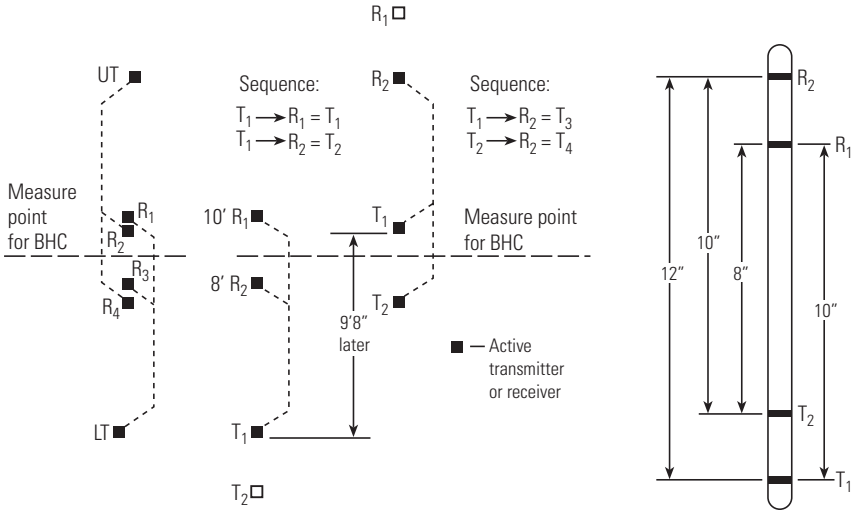


Fig. 19.17 The principle of the depth-derived borehole compensation. Courtesy of Schlumberger.

improvement of these basic measurements or additional measurements of interest for geomechanical applications. Some of the important developments, some of which have been discussed in the previous chapter, listed here in more or less historical order, are:

- arrays of monopole detectors plus advanced signal processing, used to get a better estimate of compressional and shear slowness;
- development of dipole transmitters for measurement of shear velocity in slow formations;
- beginning of the use of dispersion analysis to extract the formation shear slowness from the borehole flexural wave;
- development of a family of tools referred to as cross-dipole sonic tools with pairs of orthogonal transmitters and arrays of dipole receivers, to enable detection and orientation of formation anisotropy as well as continuous measurements of shear slowness;
- development of LWD sonic tools;
- latest evolution in tool design takes modeling into account for ease of later removal of tool perturbation from formation signal.

Details of a few of these developments are now considered.

19.4.1 Arrays of Detectors

Acoustic array tools containing a battery of receivers, variable detector spans, and waveform digitization were used to make progress in extracting reliable shear measurements. An example of one of these devices with eight receivers is shown in Fig. 19.18. In an array tool such as this, waveform processing and signal extraction is aided by the possibility of stacking signals recorded at the same depth from different receivers, for noise elimination as well as discrimination against other acoustic signals produced within the borehole. Typical waveforms from a more modern device with 13 receivers is shown in the upper left-hand portion of Fig. 19.19; clearly seen are the compressional, shear, and Stoneley arrivals. To deal with cases less clear than this example, an elaborate signal processing scheme known as slowness-time coherence (STC) has been successful in extracting the various arrivals [7]. Basically, it measures the similarity of the 13 waveforms by comparing a portion of wavetrain 1 to shifted portions of the other 12 waveforms. Using this processing, a plot such as that shown in the lower left of Fig. 19.19 can be developed. The ordinate is the time (in μs) along the wavetrain of receiver 1. The abscissa is Δt or slowness, determined from the conversion of the delays applied to the other receiver waveforms measured at a single depth. The contours, which clearly delineate the three arrivals, indicate regions of largest similarity between the shifted waveforms and the signal from receiver 1. A sample log section from this type of processing is shown in Fig. 19.19. In

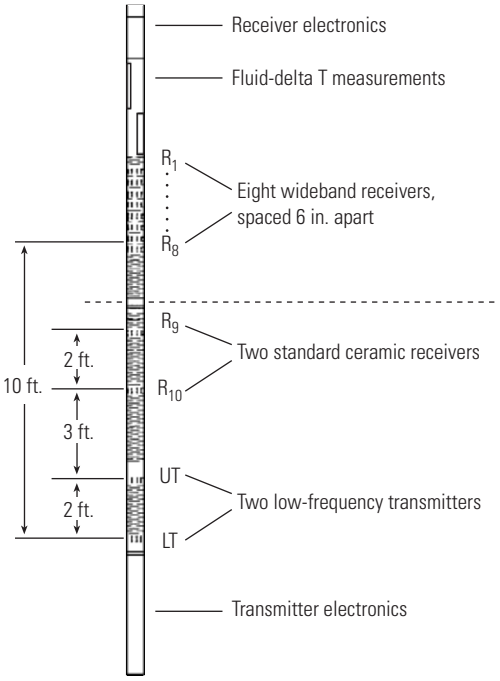


Fig. 19.18 An eight-receiver sonic array tool. From Morris et al. [6].

addition to the simple interval transit time of the compressional, shear, and Stoneley waves, regions of confidence, generated from successions of STC plots are placed, in a continuous fashion around each computed slowness curve [8].

19.4.2 Dipole Tools

The development of dipole transducers led to an evolution of tool design that used dipole receivers as well as dipole sources. The dipole receivers are formed from pairs of monopole receivers properly phased, or differenced – generally done by software. The combined use of dipole sources and coupled monopole receivers allows the detection of the induced borehole flexural wave.

The first task of such an instrument is to measure the shear velocity of the formation. However, it is not as straightforward as one would think. The flexural wave is similar to, but not exactly the same as a shear wave. Its velocity of propagation is only equal to the formation shear velocity at zero frequency. This presents some difficulty since the measurement is not made at zero frequency, but in some window of much higher frequencies. Due to the dispersion of the flexural wave, which means that each frequency component propagates at a different velocity, the simplest approach, initially, was to introduce a bias correction for an increased slowness when deriving

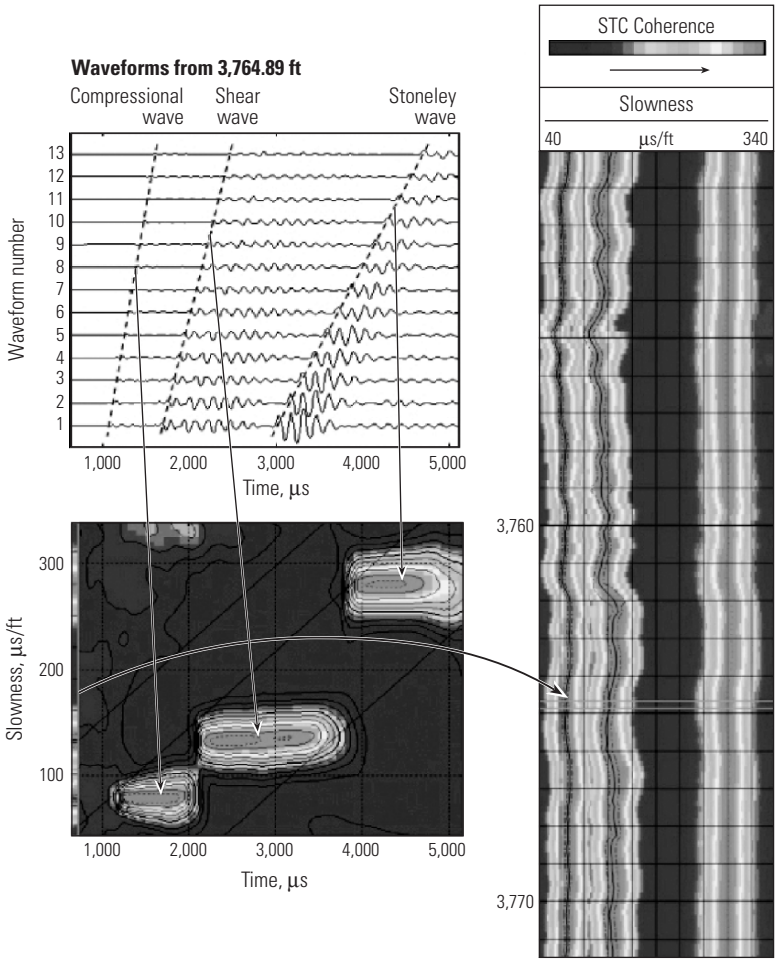


Fig. 19.19 Waveforms from a 13-receiver array tool clearly show the compressional, shear, and Stoneley arrivals (top left). The STC plot (lower left), for a particular depth, contains a thin strip, on the left-hand side of the plot, of the projected coherence values that appear on the generated slowness log (right) as regions of confidence.

slowness from a STC plot using signals of some finite frequency. A more sophisticated approach uses modeled dispersion curves for the flexural waves to "undo" the effects prior to the STC processing [9].

Figure 19.20, shows the computed dispersion of the waveforms, resulting from two types of sources, detected by an array of detectors in a borehole. In this example, associated with the firing of a monopole transmitter, there is a very strong Stoneley arrival which is nondispersive as well as a refracted shear wave that also is not dispersive. The middle data points correspond to the dispersion observed in the induced borehole

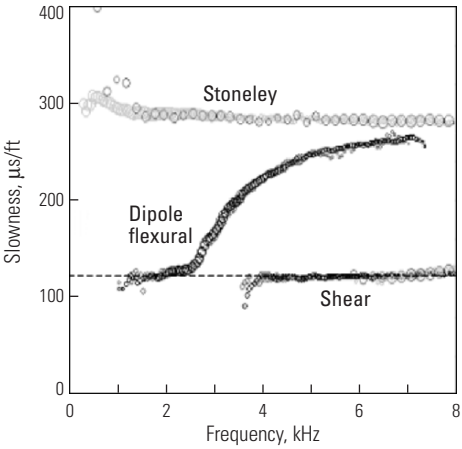


Fig. 19.20 The computed dispersion curves from a two-source array sonic device in an isotropic formation. In this fast formation, the firing of the monopole source has produced refracted shear waves as well as Stoneley wave propagation in the borehole. The flexural wave, produced by the dipole source, is seen to be highly dispersive.

flexural wave, produced by the firing of a dipole transmitter. Its typical behavior is to have a larger slowness at high frequencies; only at very low frequencies does the slowness actually match the formation slowness, as mentioned above. To produce a figure such as this requires an array of detectors at different spacing from the receivers and some complex signal processing [8]. But once this dispersion curve is displayed it would seem a simple matter to extract the shear velocity as long as there is enough low-frequency power in the transmitter pulse.

19.4.3 Shear Wave Anisotropy and Crossed Dipole Tools

The development of sonic devices with arrays of detectors, the development of sophisticated processing of the array of receivers for extracting slowness without having to rely on the crucial measurement of "first motion," and the development of dipole transducers lead to a natural evolution into a type of tool referred to as crossed-dipole array devices. A number of service companies have had such devices since the early 1990s. These arrays of detectors are generally arrays of dipole receivers, both aligned and perpendicular to a pair of dipole transmitters which are also crossed. This allows for four sets of detector/transmitter orientations at each array spacing. The use of crossed dipoles allows collection of the data necessary for characterizing anisotropic formations, at least in vertical wells.

The crossed dipole sonic tools served as a stimulation for a great deal of theoretical and laboratory work as well as realistic computational modeling of acoustic wave propagation in the borehole/tool environment. Numerous studies elucidated the role of borehole size and tool characteristics in determining the nature of the P- and

S-wave dispersion curves. Advances in signal processing allowed the determination of the dispersion curves from arrays of detectors. One of the results from the routine display of dispersion curves was the discovery of a method to identify the presence of stress-induced anisotropy.

One of the interesting and useful things that cross-dipole sonic logging tools can measure is shear anisotropy. Although we like to think of rocks as isotropic, sedimentary rocks are far from that in terms of their acoustic or mechanical properties. One type of anisotropy can result from an inherent structural attribute such as layering or aligned fractures as seen in the bottom two panels of Fig. 19.21. When a formation with intrinsic anisotropy propagates shear waves, they split or are polarized into two directions corresponding to the "slow" axis and the "fast" axis. In the case of aligned fractures (assumed fluid-filled) the "slow" axis would be perpendicular to the fracture and the "fast" axis would be parallel to the fractures.

These signals might be difficult to discern in a crossed-dipole device with an arbitrary azimuthal orientation. However thanks to an ingenious discovery called Alford rotation after its discoverer, it is possible to mathematically reprocess the wave forms into the natural orthogonal axes and to determine the orientation with respect to the measurement tool azimuth. This information, coupled with a tool-borne orientation device, is useful in determining the direction of the principal source of anisotropy.

From the four sets of dipole receiver orientations from the crossed-dipole tool, after Alford rotation, it is possible to extract dispersion curves corresponding to the two polarizations. The dispersion curves are displaced from one another as schematically illustrated in Fig. 19.22(b), which is to be compared with the isotropic formation in (a). Another point to note is that the two dispersion curves do not cross.

We have already seen in Section 18.2 that acoustic velocities depend on the imposed stress. Anisotropy can also be caused by differences in horizontal stress, such as that generated by tectonic forces. The differential stress of a formation will cause shear waves to separate into two directions: along the maximum horizontal stress direction, and along the minimum horizontal stress direction.

A borehole drilled in such a stressed material will exhibit an unusual stress distribution around it. An example is shown in Fig. 19.23 with the uniaxial strain imposed from the top of the figure at an azimuth of 0°. Compressive stress concentration appears at 90° and 270° whereas tensile stress is concentrated along 0° and 180°. The former are associated with the commonly encountered breakout features and the latter correspond to drilling induced fractures. The borehole breakouts have long been known [11] to be associated with tectonic stress and their orientation was an early means of determining the direction of local minimum stress.

This induced stress deformation decays within a short distance of the borehole so its influence on acoustic wave propagation will depend on the depth of penetration. At low frequency the shear waves propagate deeply in the formation (up to several borehole diameters) and thus the two polarizations will propagate with different slowness as seen in the third panel of Fig. 19.22. However at higher frequencies, the shear waves are confined to propagation near the surface of the borehole and the two polarization directions will sample the altered stress around the borehole. The shear waves

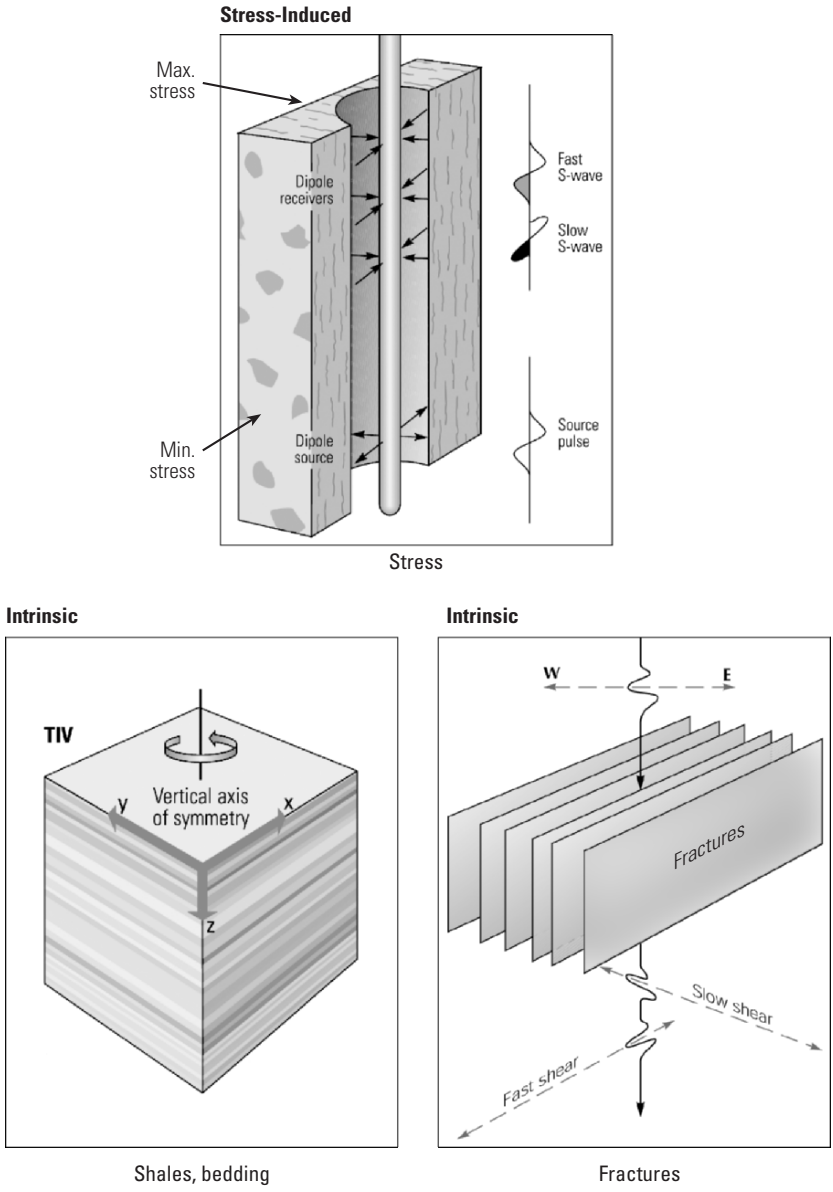


Fig. 19.21 Two versions of intrinsic formation S-wave anisotropy and one stress-induced example.

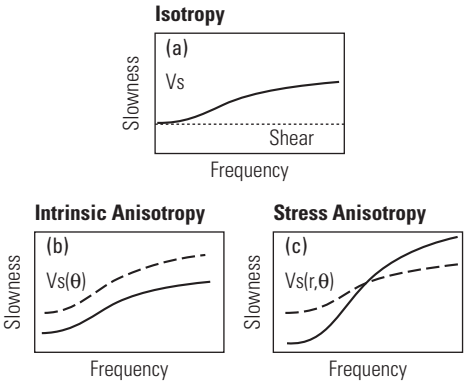


Fig. 19.22 Idealized borehole flexural wave dispersion curves. In an isotropic formation with no stress, only one curve results (a). For intrinsic anisotropy, such as parallel fracturing or bedding planes, two displaced dispersion curves result corresponding to the fast and slow polarizations (b). The presence of uniaxial stress produces a characteristic cross over of the fast and slow dispersion curves (c). From Plona et al. [22]

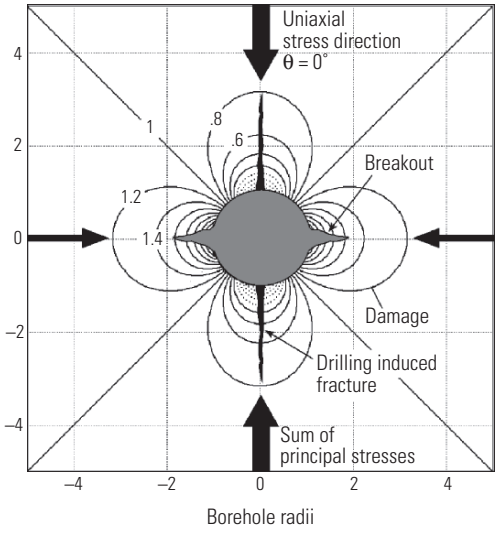


Fig. 19.23 The stresses around a borehole in a medium with an imposed unilateral stress. Indicated along the direction of maximum differential compressive stress is the formation of breakouts. Drilling induced fractures are indicated along the direction of maximum differential tensile stress. Adapted from Winkler [10].

propagating in the direction of the far field will now be influenced by material that is understressed and travel with a slower velocity while the contrary is true of the other polarization. The upshot is that the dispersion curves for the two polarizations will exhibit a characteristic crossover at some intermediate frequencies. It is this signature

that can indicate the presence of large differential stress and from the orientation of the polarizations the direction can be determined.

19.4.4 LWD

The drilling environment hardly seems the best place to attempt to do acoustic logging, regardless of the anticipated benefits. It is a very acoustically noisy environment and the drill collar, which must house the instrument components, is a stiff cylindrical pipe capable of producing high amplitude arrivals to obscure the measurement. Despite these obstacles, by designing a periodic grooved structure to isolate the transmitter from the receivers in certain frequency bands and placing the receivers far from the bit, the first LWD acoustic tools capable of measuring compressional and fast shear velocities appeared in the mid-1990s [12, 13].

Next, it was logical to attempt to make a direct shear velocity measurement using a dipole source as is done in wireline acoustic tools. Although some devices with dipole sources were constructed, it soon became apparent that there were additional problems associated with the LWD environment. First of all, the drill collar is stiff and cannot be made as flexible as a wireline tool can, so the dipole source excites flexural waves in the drill collar that cannot be easily separated from the formation signal [14]. Some tools have been designed with attenuators in the drill collar to reduce the energy transmitted through the tool but the dispersion of the borehole flexural signal makes it difficult to get an accurate formation shear slowness.

Theoretical studies and modeling [15, 16] indicate that the use of a quadrupole source would provide a good possibility to couple energy to the formation while avoiding exciting the drill collar. Quadrupole wave propagation in the drill collar has a cutoff frequency so that for a given collar thickness it is possible to find a frequency below which energy is only coupled to the formation. Unfortunately the most easily detected quadrupole-excited borehole wave has a quite different dispersion relation compared to the wireline dipole flexural wave dispersion. Rather than having an asymptote at low frequencies that gives the formation shear slowness, the quadrupole dispersion ends abruptly at some low-frequency cutoff (like the collar behavior) making it difficult to determine the precise value of the shear slowness. Solutions to these issues are currently under development and new tools are on the horizon to exploit this type of source (and detection) for the shear velocity information.

19.4.5 Modeling-driven Tool Design

In acoustic logging, the measurement device containing transmitters and receivers represents an enormous perturbation to the pressure wave-field that might be expected from an analysis of a theoretical device with point sources and detectors with no massive supporting structure. After decades of designing borehole acoustic tools to be acoustically "transparent" through the use of complicated but mechanically weak structures, with slotted sleeves, a new type of tool design has appeared [17]. Based on the experience gained from decades of modeling and processing crossed-dipole

tool array data, with its heavy reliance on dispersion analysis for the extraction of the shear velocity from the flexural wave, a simple tool architecture, amenable to precise modeling, was designed. The simple design was chosen such that the effect of the tool on the formation and borehole wave propagation could be calculated and thus removed prior to any dispersion processing.

To furnish measurements for the different applications ranging from radial profiling to anisotropy extraction, and Stoneley permeability to imaging, this new device is fitted with a variety of transmitters and receivers. Among the multiple monopole transmitters, a low-frequency device is used to excite the Stoneley wave; two crossed dipole transmitters can be excited with a "chirp" driving signal to provide a nearly constant energy output over a frequency range of a few tenths of a kHz to about ten kHz for efficient flexural wave production. The detectors are arranged in a 6 ft array with 6 in. spacing; near and far transmitters above and below are used to mimic the performance of the classical long spacing sonic devices; the axial orientation of the detectors (at 45°, every 6 in.), constitutes an array of about a hundred detectors processed as oriented dipole receivers. Signal processing of the vast amount of acquired data plays a very large role in extracting numerous formation physical parameters from this new generation device.

19.5 ACOUSTIC LOGGING APPLICATIONS

One of the first extensive uses of borehole sonic logs was for geological correlation. Wyllie and others observed that there was a strong correlation between sonic travel time and the porosity of consolidated formations. This resulted in the so-called Wyllie time-average equation discussed earlier. The laboratory data seemed to indicate that a volumetric mixing law held for the case of transit time. Knowing the matrix transit time and the fluid transit time, one could obtain the appropriate porosity from a measurement of any intermediate travel time.

Despite the very empirical approach to the common interpretation of sonic logs, they do yield useful porosity estimates under many circumstances. For the technique to work well, the type of rock and its appropriate matrix travel time must be known, or a local transform between travel time and porosity must be established. Often, in cases of extreme hole rugosity or washout, when porosity readings from the density or neutron devices are useless, the sonic measurement will still be reliable.

Determination of other interesting formation properties can be made by using the sonic measurement in conjunction with other logging tools. One example of the sonic measurement in conjunction with two other porosity measurements is shown in Fig. 19.24. In the middle of the log, both the neutron and density readings indicate an increase in porosity, to a maximum of about 3 p.u. The rest of the zone appears to be a zero porosity dolomite. However, in this same zone, where the dolomite appears to have 3% porosity, notice that the Δt curve has not shifted. It still indicates zero porosity.

The explanation for this type of occurrence, especially in carbonate rocks, is the presence of so-called secondary porosity (from the geological term for any porosity

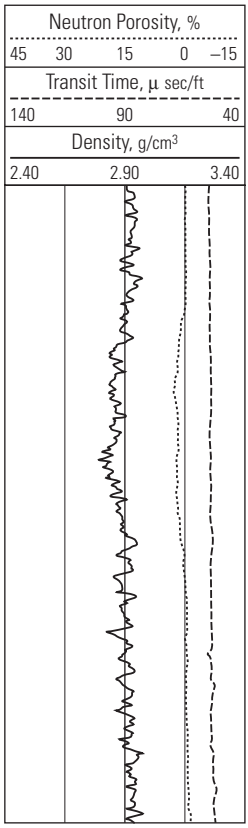


Fig. 19.24 A log example of a carbonate section, showing indications of the presence of "secondary" porosity. This is inferred from the increase of density porosity and neutron porosity with no corresponding change in the Δt. From Timur [4].

created by the alteration of rock after deposition). Much of this porosity is unevenly distributed throughout the rock in vugs and fractures. The acoustic wave energy finds a faster path around these inclusions, for example from another side of the borehole. In the extreme case there is no alteration of the travel time from that of the zero porosity matrix. In this sense, the sonic measurement does not "see" the secondary porosity. Vugs and oomolds also exist as evenly distributed spherical pores. For the same porosity, such pores have less influence on the acoustic wave than more normal elongated pores, resulting in a shorter travel time and the same secondary porosity effect.

19.5.1 Formation Fluid Pressure

One of the most practical applications of sonic compressional data is in the detection or prediction of overpressured shale zones. The procedure is schematically illustrated

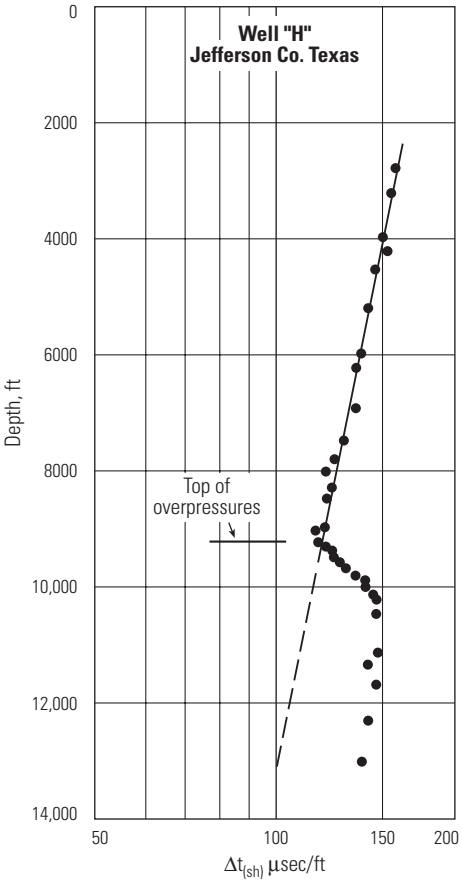


Fig. 19.25 Determination of overpressured shale zones from a departure from the Δt-depth trend. From Hottman and Johnson [18].

in Fig. 19.25. Normally the Δt measured in shales increases in a regular, if not logarithmic, fashion with depth or compaction. This may be related to changes in density as well as confining pressure as a function of depth. However in overcompacted shales, where the pore pressure is greater than hydrostatic pressure, a deviation from the normal trend is observed. According to Hottman and Johnson [18], the overpressure can be estimated from the difference in the observed transit time Δt_{ob} and the normal transit time Δt_n expected for that depth. Further quantification of pore pressure from this deviation was made by Eaton [19].

LWD acoustic measurements have provided the possibility of detection of overpressured zones in real time [20]. Wireline measurements can only "detect" overpressured zones from the deviations from a trend after the fact. It is of much greater utility, during the drilling process, to be able to detect the onset of an overpressured zone so that a reaction to it can be made before it gets too large.

19.5.2 Mechanical Properties and Fractures

From the relationships reviewed in Chapter 17 and summarized in Table 17.1, it is relatively easy to show that the elastic parameters of a rock formation can be obtained from a knowledge of its compressional and shear wave velocity, and its density. For example, the bulk modulus is given by:

$$B = \rho(v_c^2 - \frac{4}{3}v_s^2) , \tag{19.1}$$

and the shear modulus by:

$$\mu = \rho v_s^2 . \tag{19.2}$$

Until the development in the late 1970s of full waveform acoustic logging, the determination of shear velocities was a tedious exercise, and it was not routine to apply it in determining the mechanical properties of wellbore rocks. However, one potential application received considerable attention: the prediction of fracture initiation.

Like any material, rock will fail either in tension, compression, or shear when the applied stresses exceed a critical threshold. This threshold is commonly termed the "failure criterion." In general, this threshold depends on the cohesion and the internal friction angle. The former is often correlated empirically with the shear modulus. The latter governs the increase in compressive strength with applied pressure. In porous rocks, the compressive strength is reduced by pore pressure. The difference between overburden pressure and pore pressure, or the effective confining pressure, plays an important role in the mechanical properties of rocks. The tensile strength of rocks, on the other hand, is only a fraction of the compressive strength. This is especially the case in poorly cemented sandstones. Fractures can be induced by producing a pressure in the wellbore which will cause rock failure to occur. At any point on the borehole wall three forces are acting: the overburden pressure, the effective tangential stress which is a result of the overburden and pore pressure, and the pressure which is the result of the mud column. If the mud column pressure, P_{wf}, increases, it can effectively cancel the compressive tangential stress and place the rock forming the borehole wall in tension. Once the tensile strength is exceeded, the fracture is initiated. Hubbert [21] gives an estimate of the fracture pressure P_{wf} to be:

$$P_{wf} = 2(P_o - P_f) \frac{\nu}{1-\nu} - P_f , \tag{19.3}$$

where P_o and P_f are the overburden and pore pressures. This expression involves a number of simplifications. The first is that the rock can be considered as an elastic material, so that the ratio of horizontal to vertical stresses is simply given by $\frac{\nu}{1-\nu}$, and the tensile strength of the rock is negligible.

Although not the complete story, a continuous measurement of the Poisson ratio is useful in predicting the relative ease of fracturing a formation. Knowledge of the elastic parameters, computed from the density, V_p and V_s, allows prediction of zones suitable for hydrofracturing. This technique consists of hydraulically isolating a zone which is pressurized by surface pumps and increasing the borehole pressure until

fracturing of the rock occurs. This method is often used to stimulate production of low-porosity and low-permeability hydrocarbon reservoirs.

Although inducing fractures is sometime desirable, the spontaneous occurrence is not – it is one form of borehole stability problem that should be avoided. This instability results when the hydrostatic pressure in the wellbore is so high that the fracturing occurs spontaneously while drilling. On the other hand, it is possible for the hydrostatic pressure of the mud in the wellbore to be too low to support the stress distributions around the borehole that are caused by tectonic stress and pore pressure. In that case, breakouts will occur causing caving of the borehole walls – a second form of borehole instability than can impact drilling or cause drilling pipe or logging tools to become stuck [22]. Considerable effort is now spent making models of the formation to be encountered (mechanical earth models) that use not only acoustic inputs for elastic parameters but measurements of formation pore pressure and models for its evolution with depth [23]. One output of this type of study is a plot indicating the upper and lower limits of the mud weight as a function of depth to avoid borehole instability – a mud-weight window. These graphs indicate how the mud weight should be changed with drilling depth, and when casing needs to be set to avoid either of the two instability problems.

Identification of naturally occurring fracture zones from acoustic logs has received much attention in the past and is extensively reviewed by Timur [4] and by Jordan and Campbell [24]. Most of these methods, which use some portion of the acoustic wavetrain displayed in an analog form, are qualitative. One approach to the determination of the presence of fractures is to analyze the amplitude of the shear arrivals; the presence of fractures should decrease the ability of shear waves to be transmitted. Another method is a crude type of acoustic imaging. The presence of fractures intersecting the borehole wall is inferred from a characteristic chevron pattern in the displayed analog representation of the acoustic signal. The development of these chevron patterns arises from the conversion of shear and compressional energies at the boundary of the fracture.

The presence of fractures can also be deduced from the Stoneley wave amplitude and chevrons. In zones containing fractures, the Stoneley wave amplitude has been seen to change considerably, producing a noticeable effect on the a variable density log (VDL) or microseismogram presentation [25]. Figure 19.26 illustrates the notion that, in passing a fracture (in this case depicted as horizontal and open), the low-frequency tube wave actually forces fluid into the fracture, thereby reducing its amplitude. Note also that a given fracture will be apparent in the measurement over a distance equivalent to the transmitter–receiver spacing.

A more recent update on fracture detection [26] indicates that the Stoneley wave, extracted from low-frequency monopole transmitters and receivers is still a standard diagnostic tool, and that the rotated dipole flexure dispersion curves can also be of use in fracture identification.

19.5.3 Permeability

One of the most important rock parameters for the evaluation of hydrocarbon reservoirs is permeability. This parameter is obtained routinely through core analysis, well testing, or by correlation to other more easily measured rock properties such as porosity. These correlation methods are reviewed in Chapter 23. The importance of the Stoneley wave is that it measures permeability in a way that is unique for a logging method because it is dynamic, i.e., fluid is actually moved through the rock.

As the Stoneley wave passes a permeable formation there is some fluid movement between formation and borehole (Fig. 19.26). The result of this movement is that the wave is attenuated and its velocity changes. The magnitude of these effects is frequency dependent. Models based on the Biot poroelastic theory have been developed to elucidate the frequency dependence of the attenuation and slowness, and the interesting relationship between these two attributes and the fluid mobility (ratio of formation permeability to fluid viscosity) [27, 28]. Experiments on laboratory rocks confirmed the frequency dependence of velocity and attenuation, especially at low frequencies. At low frequencies it was also confirmed that by increasing the fluid mobility the Stoneley velocity is decreased and the attenuation increased [29].

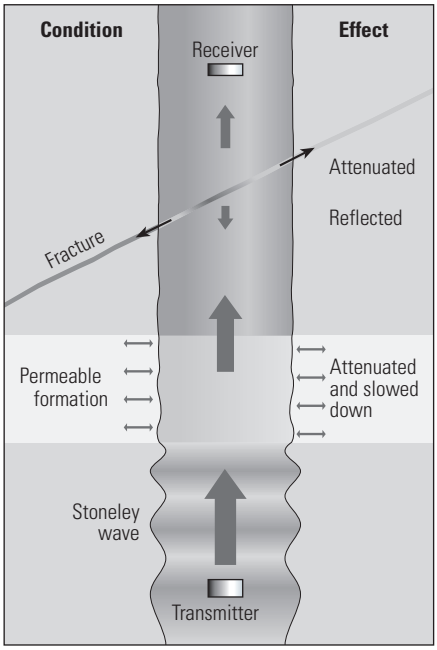


Fig. 19.26 Schematic illustration of the Stoneley wave guided in a borehole intersected by an open fracture. The wave is both attenuated and reflected at the boundary of the fracture, and is attenuated and slowed down by the permeable formation.

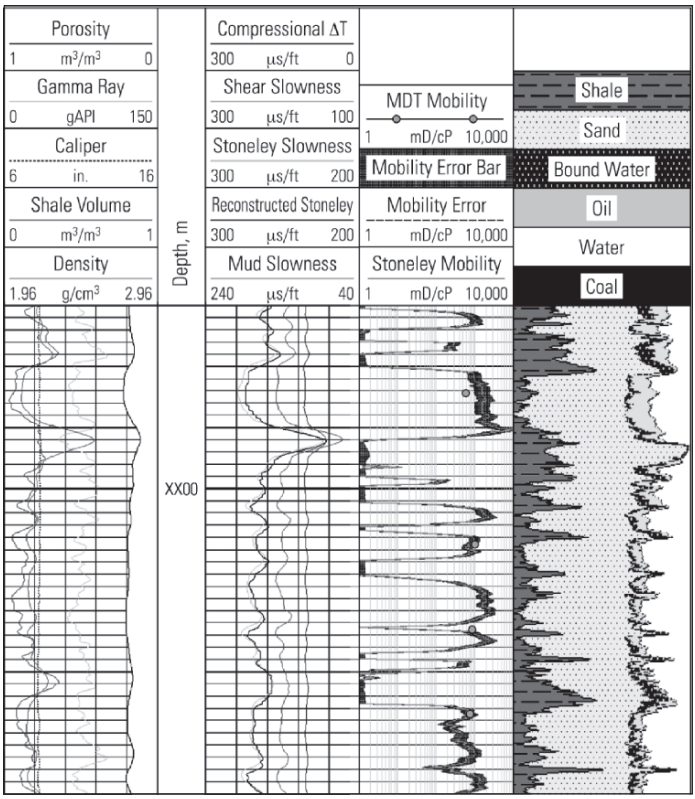


Fig. 19.27 A log example of Stoneley derived mobilities compared to a few formation tester results.

When the effect of permeability on Stoneley waves was first observed, the Stoneley slowness or attenuation was correlated to core permeability. The sensitivity of slowness to permeability is only a few percent, but it can be measured accurately. The effect on attenuation is larger, but the measurement is less precise. Using both measurements, it is now possible to invert the Biot models to derive fluid mobility [30]. The models require knowledge of the elastic properties of the borehole, the formation and its contents. Although all these parameters can be estimated from acoustic and density logs, the cumulative error can be large. In practice, therefore, the method is restricted to mobilities well above 10 mD/cP. A typical result is shown in Fig. 19.27.

The mudcake is another concern. Mudcake is formed with the express purpose of preventing fluid movement between borehole and formation. How then can the Stoneley method work? The answer is that mudcake is flexible and therefore bends into the pore spaces, allowing pressure but not fluid to be transmitted. The effect of the mudcake has been analyzed in terms of its stiffness [31] – the stiffer the mudcake the less pressure is transmitted. Unfortunately there is no method of independently mea-

suring mudcake stiffness. In practice it is considered constant and adjusted to match core permeability at some depth. However the addition of extra information from another source may resolve the problem. The relative movement of pore fluid and rock matrix creates an electrokinetic signal that travels with the Stoneley wave [32]. There is evidence that this signal can help separate the effects of mudcake and mobility. The addition of electrokinetic information also extends the range of practical application to well below 10 mD/cP.

19.5.4 Cement Bond Log

The cement bond log (CBL) has been around since the early 1960s [33] and was an attempt to use the sonic tool for applications other than porosity determination. The primary objective of the measurement is to determine zones in a cased well where the cement may be imperfect. The simple idea, that could be carried out with a rudimentary tool with a single transmitter and one or two receivers, was that the first arrival was related to the so-called plate (or Lamb) wave traveling in the casing. This wave, which is close to but not exactly equal to the compressional wave because its wavelength is larger than the casing thickness, loses energy through coupling with the cement. Its amplitude is related to the adherence of the cement to the casing. If this amplitude is very large then the casing is unencumbered by cement and easily resonates. A simple model of the geometry of a poor cement job – the point of using such a monitoring measurement – considers the annulus of cement around the casing to only cover a part of the circumference. It was shown that the aperture not covered by cement is logarithmically related to the ratio of the amplitude of the first positive detected casing arrival (called E_1 in the logging literature) compared to the measured amplitude of the first arrival from a free pipe. In the conventional sonic tool, with transmitters at 3 and 5 ft, this amplitude measurement (converted to a bond index ranging from 0 to 1) is made at the 3 ft receiver. The 5 ft detector is used to make a microseismogram display (called a variable density log or VDL) of the detected wave train to give a visual indication of the pipe signal and formation signal. A typical display is seen in Fig 19.28.

Of course there are many reasons why the amplitude of the first arrival might be large, indicating "free pipe." One of the famous bete noires of this measurement technique is the so-called microannulus. Apparently poor adhesion of the cement – a separation of a few microns between cement sheath and pipe – can cause this erroneous signal. Sometimes this can be obviated by shutting in the well and letting the pressure rise so that the microannulus would be closed by the slight expansion of the casing. Another reason for anomalous first arrival amplitudes can occur in a very fast formation with good cement bonding – the formation signal may travel so fast as to interfere with the amplitude of the first arrival from the pipe. Normally the measurement is to be performed with the tool centered in the casing. Eccentering also produces erroneous amplitude readings of the first arrival.

One of the large drawbacks of the sonic method is the lack of azimuthal resolution – the casing signal is an azimuthal average. This makes it difficult to distinguish a bad cement job from a vertical channel or void in the cement which

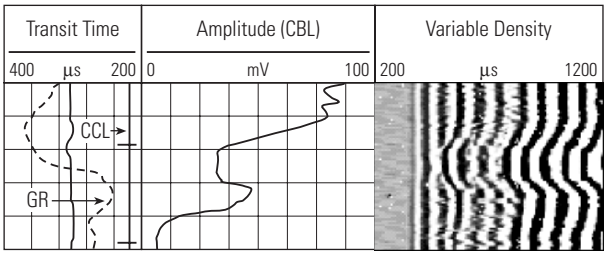


Fig. 19.28 Schematic presentation of the CBL log. In track 3 is the so-called variable density log (VDL), a type of microseismogram display of the recorded wavetrain as a function of time to the right. The ringing of the the casing is clearly seen at the beginning of the traces while the formation signal shows up later. In track 2 the amplitude of the first arrival, E_1, used for the estimation of the cement bond, is shown.

might be responsible for interzonal formation communication. The use of segmented detectors was a first evolution of this device. Despite the drawbacks and uncertainties of this type of measurement it has been a standard for many years and may have become so despite other ultrasonic devices designed to overcome these deficiencies (discussed in the next section). Evidence for this is seen by the inclusion of CBL capabilities in recent third generation sonic tools [17].

19.6 ULTRASONIC DEVICES

Unlike the conventional sonic tools which operate at frequencies below 25 kHz, ultrasonic devices employ transducers capable of operating from several hundred kHz to the MHz region. At these frequencies the wavelength can be as small as a millimeter. This opens the possibility of performing a number of different types of measurements. One of the most widely used is that of acoustic imaging.

One imaging device which has been used extensively for fracture identification is a imaging tool known as a televiewer. In this type of device, the centralized source and receiver rotates rapidly (see Fig. 19.29) to obtain a finely wound spiral image of the reflected signal from the borehole wall. Images can be made from either the amplitude of the reflected signal or its transit time. The presentation represents the unwrapping of the cylindrical borehole wall image. An example of the amplitude-derived image from the UBI* ultrasonic imager is shown in Fig. 19.30, which indicates the presence of dipping fractures. The dipping fracture appears as a sinusoid in this unwrapped display. Other examples clearly show the presence of borehole "breakout" and the transit time data can be used to visualize the borehole cross section.

*Mark of Schlumberger

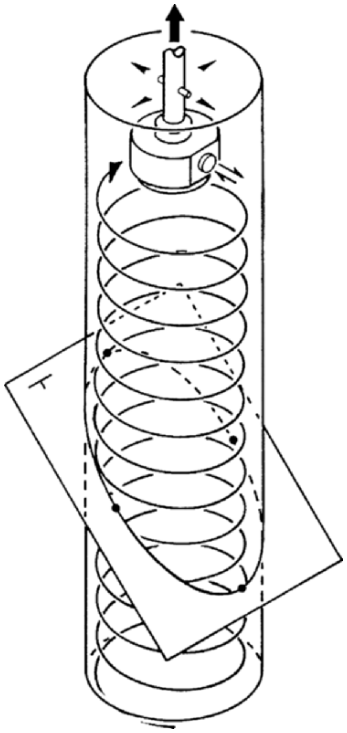


Fig. 19.29 The principle of BHTV operation. A rapidly rotating high-frequency transducer transmits and receives pulses of acoustic energy as it moves in the borehole. Bedding features which intersect the well will produce a characteristic sinusoidal pattern on the unfolded borehole wall image. Courtesy of Schlumberger.

19.6.1 Pulse-Echo Imaging

Ultrasonic (~MHz) pulses, in a pulse-echo mode, have been applied to evaluate the condition of cemented casing. High-frequency pulses allow for the possibility of good annular resolution and the reflection mode uses a completely different physics from attenuation of a wave propagating along the casing. The operation of an early device is illustrated in Fig. 19.31. The measurement is initiated with a pulse of ultrasonic energy close to the casing resonance frequency (related to twice the thickness divided by the compressional speed in the casing). Using the same transducer, now in receiving mode, the reverberations in the casing are recorded and analyzed. The casing resonance will be quickly damped in the presence of a good cement bond. In front of a casing, bonded to cement, the received signal contains several pieces of information. The internal reflections of acoustic energy in the casing can be used to determine its thickness and thus monitor its wear. The decay rate of the signal following the casing arrival is determined by the coupling between the casing and cement. An early logging tool used an array of transducers to provide circumferential coverage.

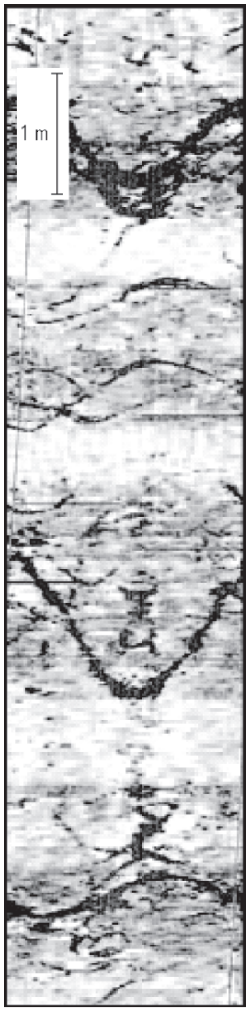


Fig. 19.30 An image obtained from the UBI ultrasonic scanner, showing dipping fractures. Courtesy of Schlumberger.

A more modern device [35] uses a rotating transmitter to provide a full 360° coverage. The various measurements made with such a device can also be used to determine the condition of the casing. From the transit time of the echo the internal radius is measured, and the thickness is computed from the resonant frequency. Using a model, which requires knowledge of the mud impedance, the cement impedance (density times compressional velocity) can be computed from the measured damping. The required mud impedance is computed in a calibration phase of the logging, in which a steel plate reflector in the tool is positioned in front of the transducer so that waves only travel a fixed distance in the mud.

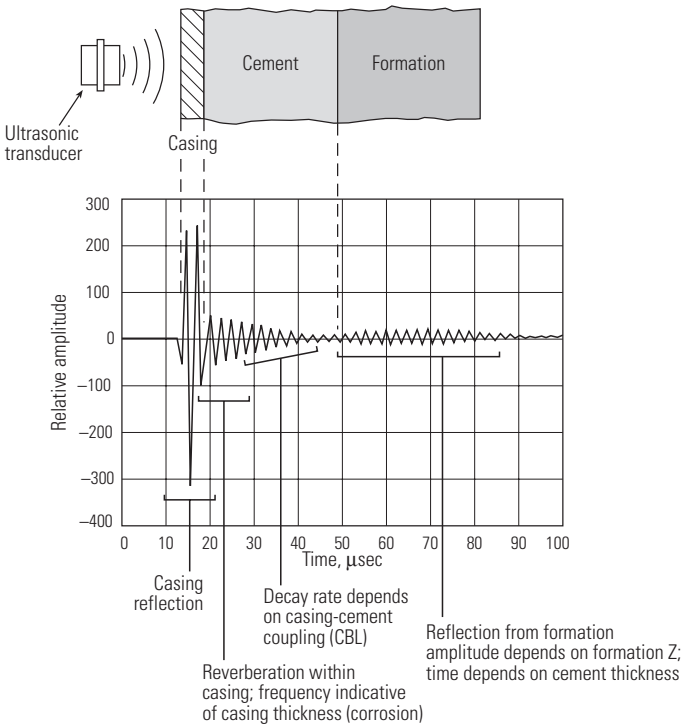


Fig. 19.31 Use of an ultrasonic device for the inspection of cement behind a steel casing. From Havira [34].

The full azimuthal coverage provides a map of the cement impedance which, in many cases, allows easy visualization of channels in the cement as well as a map that indicates the presence of casing corrosion. Microannulus is less of a problem for this device and laboratory measurements [35] have shown that with microannulus of up to 100 μm it is still possible to distinguish between water and cement behind the casing.

19.6.2 Cement Evaluation

A common drawback of sonic and ultrasonic measurements is the shallow depth of investigation. Investigation beyond the cement region by the pulse-echo technique is difficult mainly resulting from the high acoustic impedance contrast presented by the steel casing – not much of the transmitter energy is transmitted through the casing to the cement. To combat this, an evolutionary design [36] uses an additional rotating nonnormal transmitter to excite a flexural wave at a somewhat lower frequency (≈200 kHz) in the casing. This allows the coupling of energy into the material surrounding the casing and in optimum circumstances provokes a third interface reflection from the formation boundary. Several closely spaced ≈15–25 cm nonnormal receivers detect the attenuated flexural wave and the third reflection. This reflection carries

information about the wall geometry (roughness) and the acoustic contrast with the material (cement?) in the annulus.

Combined with the simultaneous pulse-echo information, the casing fluid properties can be estimated without resort to the reflection calibration used on the pulse-echo device. The data is processed to provide a map of impedance of the casing sheath material, simplified into three major types – gas, liquid, and solid – through an algorithm that uses derived impedance and flexural wave attenuation. A second output can be an image of the cement sheath indicating the position of the casing and the frequently nonconcentric borehole.

REFERENCES

1. Kitsunezaki C (1980) A new method for shear-wave logging. Geophysics 45(10):1489–1506

2. Tittman J (1986) Geophysical well logging. Academic Press, Orlando, FL

3. Chemali R, Gianzero S, Su SM (1984) The depth of investigation of compressional wave logging for the standard and the long spacing sonde. In: Ninth SAID Colloquium, Paper 13

4. Timur A (1987) Acoustic logging. In: Bradley H (ed) Petroleum production handbook. SPE, Dallas, TX

5. Goetz JF, Dupal L, Bowler J (1979) An investigation into discrepancies between sonic log and seismic check shot velocities. APEA J 19:131–141

6. Morris CF, Little TM, Letton W (1984) A new sonic array tool for full waveform logging. Presented at the 59th SPE Annual Technical Exhibition and Conference, Paper SPE 13285

7. Kimball CV, Marzetta TM (1984) Semblance processing of borehole acoustic array data. Geophysics 49(3):274–281

8. Plona T, Kane M, Alford J, Endo T, Walsh J, Murray D (2005) Slowness-frequency projection logs: a new QC method for accurate sonic slowness evaluation. Trans SPWLA 46th Annual Logging Symposium, paper T

9. Brie A, Kimball CV, Pabon J, Saiki Y (1997) Shear slowness determination from dipole measurements. Trans SPWLA 38th Annual Logging Symposium, paper F

10. Winkler KW (1997) Acoustic evidence of mechanical damage surrounding stressed boreholes. Geophysics 62(1):16–22

11. Prensky S (1992) Borehole breakouts and in-situ rock stress – a review. The Log Analyst 33(3):304–312

12. Minear J, Birchak R, Robbins C, Linyaev E, Mackie B, Young D, Malloy R (1995) Compressonal slowness measurements while drilling. Trans SPWLA 36th Annual Logging Symposium, paper VV

13. Aron J, Chang SK, Dworak R, Hsu K, Lau T, Masson JP, Mayes J, McDaniel J, Randall C, Kostek S, Plona TJ (1994) Sonic compressional measurements while drilling. Trans SPWLA 35th Annual Logging Symposium, paper SS

14. Hsu C-J, Sinha BK, (1998) Mandrel effects on the dipole flexural mode in a Borehole. J Acoustic Soc Am 104(44):2025–2039

15. Sinha BK, Asvadurov S (2004) Dispersion and radial depth of investigation of borehole modes. Geophys Prospect 52(44):271–286

16. Tang XM, Dubinsky V, Wang T, Bolshakov A, Patterson D (2003) Shear-velocity measurement in the logging-while-drilling environment: modeling and field evaluations. Petrophysics 44(2):79–90

17. Pistre V, Kinoshita T, Endo T, Schilling K, Pabon J, Sinha B, Plona T, Ikegami T, Johnson D (2005) A modular wireline sonic tool for measurements of the 3D (azimuthal, radial, and axial) formation acoustic properties. Trans SPWLA 46th Annual Logging Symposium, paper P

18. Hottman CE, Johnson RK (1965) Estimation of formation pressures from log-derived shale properties. J Pet Tech 9:717–722

19. Eaton BA (1975) The equation for geopressure prediction from well logs. Presented at Fall Meeting of the Society of Petroleum Engineers of AIME, Paper SPE 5544

20. Hsu K, Hashem M, Bean CL, Plumb R, Minerbo GN (1997) Interpretation and analysis of sonic-while-drilling data in overpressured formations. Trans SPWLA 38th Annual Logging Symposium, paper FF

21. Hubbert MK, Willis DG (1957) Mechanics of hydraulic fracturing. Trans AIME 210:153–166

22. Plona T, Sinha B, Kane M, Shenoy R, Bose S, Walsh J, Endo T, Ikegami T, Skelton O (2002) Mechanical damage detection and anisotropy evaluation using dipole sonic dispersion analysis. Trans SPWLA 43rd Annual Logging Symposium, paper F

23. Plumb R, Edwards S, Pidcock G, Lee D, Stacey B (2000) The mechanical earth model concept and its application to high-risk well construction projects. Presented at the 2000 IADC/SPE Drilling Conference, paper SPE 59128

24. Jordan JR, Campbell F (1986) Well logging II: electric and acoustic logging. Monograph Series, SPE, Dallas, TX

25. Paillet FL (1980) Acoustic propagation in the vicinity of fractures which intersect a fluid-filled borehole. Trans SPWLA, 21st Annual Logging Symposium, paper DD

26. Donald A, Bratton T (2006) Advancements in acoustic techniques for evaluating open natural fractures. Trans SPWLA 47th Annual Logging Symposium, paper QQ

27. Chang SK, Liu HL, Johnson DL (1988) Low-frequency tube waves in permeable rocks. Geophysics 44(4):519–527

28. Tang XM, Cheng CH, Toksoz MN (1991) Dynamic permeability and borehole Stoneley waves: a simplified Biot-Rosenbaum model. J Acoustic Soc Am 90(3):1632–1646.

29. Winkler KW, Liu HL, Johnson DL (1989) Permeability and borehole Stoneley waves: comparison between experiment and theory. Geophysics 54(1):66–75

30. Brie A, Endo T, Johnson DL, Pampuri F (2000) Quantitative formation permeability evaluation from Stoneley waves. Paper SPE 60905 in: SPE Reservoir Eval Eng 3(2):109-117

31. Liu HL, Johnson DL (1996) Effects of an elastic membrane on tube waves in permeable formations. J Acoustic Soc Am 101(6):3322–3329

32. Singer J, Saunders J, Holloway L, Stoll JB, Pain C, Stuart-Bruges W, Mason G (2006) Electrokinetic logging has the potential to measure permeability. Petrophysics 47(5):427–441

33. Pardue GH, Morris RL, Gollwitzer LH, Moran, JH (1963) Cement bond log interpretation of casing and cement variables. J Pet Tech May:545–555

34. Havira RM (1982) Ultrasonic cement bond evaluation. Trans SPWLA 23rd Annual Logging Symposium, paper N

35. Hayman AJ, Hutin R, Wright PV (1991) High-resolution cementation and corrosion imaging by ultrasound. Trans SPWLA 32nd Annual Logging Symposium, paper KK

36. van Kuijk R, Zeroug S, Froelich B, Allouche M, Bose S, Miller D, le Calvez J-L, Schoeph V, Pagnin A (2005) A novel ultrasonic cased-hole imager for enhanced cement evaluation. Presented at the International Petroleum Technology Conference Paper SPE 10546-PP

Problems

19.1 From the log of Fig. 19.6, determine the two sets of constants, a and b, which best relate Δt to porosity, i.e., $\Delta t = a + b\phi$.

19.2 If the full waveform is acquired with an appropriate sonic logging tool, it is possible to extract the formation compressional velocity v_p and shear velocity v_s. With an additional knowledge of the formation bulk density ρ_b, the elastic properties of the formation can be specified.

Suppose you do not have a measurement of the formation density but know instead the mud properties (ρ_{mud}, v_{mud}, and its bulk modulus). How would you go about obtaining, for example, Young's modulus and Poisson's ratio of the formation? Write explicit expressions for the two moduli.

19.3 The log of Fig. 19.32 shows the results of an induction-sonic run in a shaly sand. Using the sonic log and the interpretation charts, answer the following questions.

19.3.1 Estimate the average porosity in the reservoir zone. What is the range of porosity in this zone?

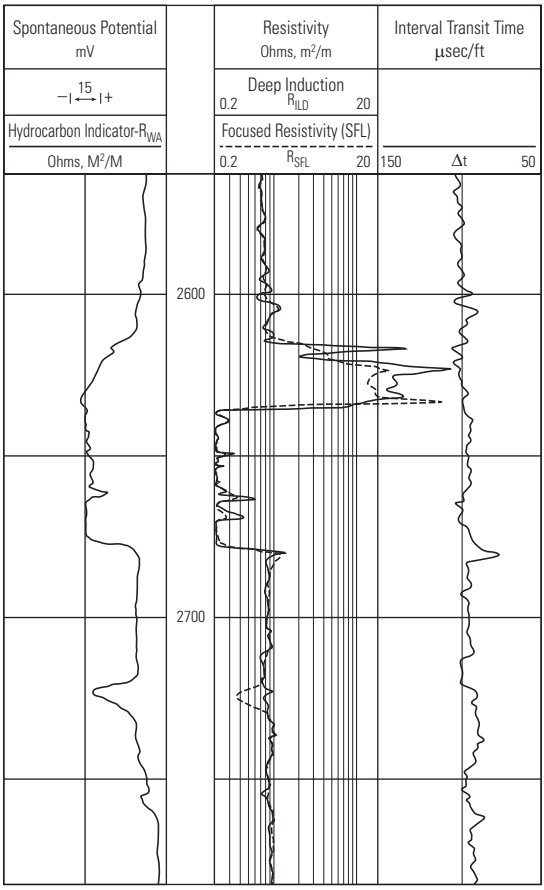


Fig. 19.32 A typical low budget logging suite, the induction-sonic.

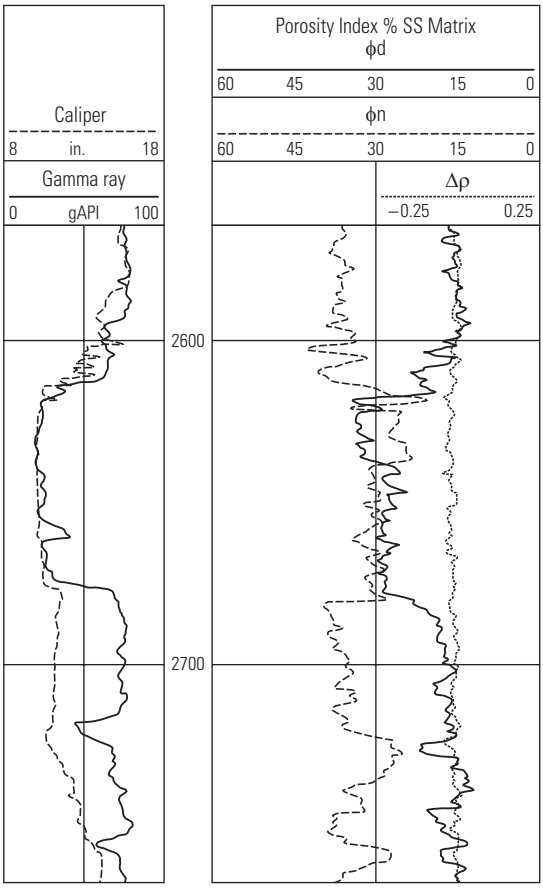


Fig. 19.33 A companion density, neutron, gamma ray, and caliper for the log of Fig. 19.32.

19.3.2 How can the sonic trace, in conjunction with the resistivities, immediately indicate the presence of hydrocarbons?

19.3.3 By comparing the neutron and density curves of the same zone, shown on Fig. 19.33, you can identify the gas zone. Why does the sonic trace not indicate the presence of gas?

19.3.4 To what is the sudden decrease in the sonic transit time at 2,678 ft due? Is it a real feature? Explain by comparison to the other logs.

19.3.5 What is the composition of the zones above and below the reservoir? Why does the density increase while the sonic transit time remains constant?

19.3.6 In the zone from 2,660 to 2,680 ft, determine the values of Δt_{ma} and Δt_{fl} which best match the porosity estimated from the density.

19.4 Data obtained from three consecutive reservoir zones is given in Table 19.1 below, where the average Δt is compared with core porosity measurements. Your job

Table 19.1 Data for Problem 19.4.

	Δt	ϕ_{core}
Upper	95	21
zone	97	25
	93	23
Middle	75	15
zone	87	23
	85	21
Lower	75	15
zone	65	10

is to identify the appropriate parameters to be used in the time-average equation for future use in determining porosity from sonic log measurements. Using the interpretation chart of Fig. 18.12, do you obtain a consistent result for the three zones? What conclusion can you reach about the nature of the three zones?

19.5 The depth of investigation of an acoustic tool was estimated to be on the order of 6 in. How does this compare to the wavelength of the transmitted pulse in the case of a 20% porous, water-saturated sandstone?

20

High Angle and Horizontal Wells

20.1 INTRODUCTION

In previous chapters it was assumed, unless otherwise mentioned, that the borehole was vertical and the formation layers horizontal. Most discussions of the physics of borehole measurements do the same. The assumptions are natural and mainly historical, since it was not until the 1980s that highly deviated wells became common, and not until the 1990s that horizontal wells were drilled in numbers. On the other hand, highly dipping formations are rare, and only affect the deeper reading resistivity devices significantly.

Why should it matter whether the borehole is vertical or horizontal? Logging devices are necessarily designed to measure away from the body of the tool and to focus beyond the mud, mudcake and if possible the invaded zone that surrounds it. These factors are present in all wells, and in a homogeneous formation the borehole inclination should not matter. Formations, though, are never homogeneous, and they have boundaries. Inhomogeneities and anisotropy affect horizontal well measurements differently than vertical well measurements, while the boundaries between formations also play a different role. Thus, even though the basic principles of logging measurements are the same whatever the borehole inclination, the interpretation can be very different. The significance of this difference depends on whether the logs are used qualitatively or quantitatively.

Early horizontal wells were development wells drilled in well-known reservoirs. They were drilled geometrically, that is to say they were positioned using knowledge of the geometry of the reservoir from seismic data and vertical wells. It was soon found that the geological variations along the path of the well were much greater

than expected. They were mainly logged by wireline tools, so that it was only after the well had been drilled that it was known whether it had actually stayed in the reservoir. This led to a new application for logging measurements – geosteering, in which the measurements from LWD devices were used to alter the course of the well while drilling. The success of this technique has been a major cause of the increased number of horizontal wells.

Among other factors, this success has led to horizontal wells being drilled not only for development but also for appraisal and exploration [1]. This requires a more thorough understanding of logging tool response. Whereas a qualitative interpretation may be sufficient in a development well to choose completion intervals and for geosteering, in exploration or appraisal wells an accurate quantitative evaluation is necessary.

This chapter reviews the particular effects of high angle and horizontal wells on logging measurements, and the application to geosteering. Once the particular effects of these wells have been understood, the conversion of logging data to petrophysical quantities such as porosity and saturation is the same as for vertical wells.

20.2 WHY ARE HA/HZ WELLS DIFFERENT?

It is wise to start with a definition of a high angle (HA) or horizontal (HZ) well. Following Passey et al. [1] we will define a vertical well as one in which the apparent deviation angle with respect to bedding is less than 30°; a moderately deviated well as one where the apparent deviation angle is between 30° and 60°; a HA well as one where the angle is between 60° and 80°; and a HZ well as one where the angle is greater than 80°. These four groups roughly define wells in which logs need few corrections (<30°); those in which resistivity and acoustic logs need correction, but this can be done with routine procedures (30°–60°); those in which most logs are affected and where the angle must be well known (60°–80°); and HZ wells in which all logs are affected and where the angle must be known accurately for quantitative interpretation.

These definitions refer to the relative angle between the borehole and the formation bedding. This relative angle has two main effects on log measurements: that due to surrounding beds and that due to anisotropy. Both are illustrated in Fig. 20.1, which shows an outcrop of interbedded sands and shales with a resistivity device overlaid. The current loop drawn around the device is such as would be induced by a conventional induction or propagation tool. When the tool is vertical, the measurement responds mainly to the horizontal resistivity R_h. In this position, it is unlikely that the current encounters large changes in resistivity since these are uncommon in the horizontal plane. When the tool is horizontal, the current in the loop flows horizontally at the top and bottom of the loop but vertically on the sides. Resistivity measurements are therefore affected by both R_h and R_v. There can also be strong changes in formation above or below the well. Other measurements are also affected by such changes, although generally the contrasts are less.

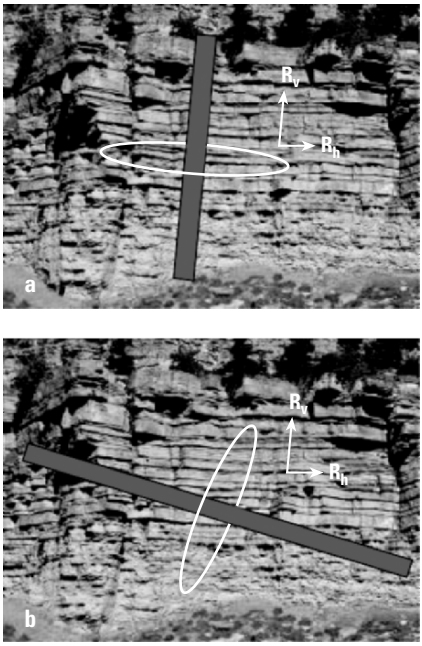


Fig. 20.1 A sequence of interbedded sands and shales shown penetrated by (a) a vertical well and (b) a HA well. Note the different relation between the bedding and the current loops from a conventional resistivity device, and the different effect of the vertical fractures and the formation change at the bottom of the picture. From Passey et al. [1]. Used with permission.

Another effect of relative angle is that as it increases, faults and fractures, which are commonly sub-vertical, are more often encountered. For example, in Fig. 20.1 the large fractures seen to the left and right of the picture would certainly be encountered by a high-angle borehole through the outcrop, but much less certainly by a vertical one.

The borehole/formation geometry is the major cause of difference between vertical and HA/HZ well logs, but it is not the only one. The angle of the well itself also has an effect, due to invasion and other changes in borehole environment when the well is near horizontal. In a vertical well it is assumed that invasion is azimuthally symmetric around the well. This is reasonable since the effect of gravity on the mud filtrate will be the same at all azimuths, and the formation permeability is often transversely isotropic. In HZ wells these same two factors can cause asymmetric invasion. Gravity may lead the filtrate to slump below the well in the presence of light hydrocarbons while, since vertical permeability is often less than horizontal permeability, the invasion profile may be elliptical.

Asymmetric invasion can cause difficulties with all measurements, but mostly with shallow-reading focused pad devices such as the density. Pad tools are also affected by the tendency of cuttings to accumulate on the bottom of the well. A thin layer of cuttings, which often build up in a dune-like fashion along the well, appears like a

high-porosity layer with significant effect on the measurement [1]. Finally, a practical difference between logs in vertical and HA/HZ wells is the means of conveyance used: a mixture of wireline and LWD in vertical wells, almost exclusively LWD in HZ wells. If there are differences between the logs from vertical and HA/HZ wells in one area, the effect of using LWD or wireline should be examined first, before looking for other causes.

20.3 MEASUREMENT RESPONSE

One might expect the logs from a well drilled horizontally through a reservoir to be straight lines. In the middle of a thick, uniform reservoir this is true but in many cases they look more like the logs of Fig. 20.2, which were recorded on wireline in an early HZ well and illustrate some typical features of logs in HA/HZ wells. They are far from straight lines as the well moves in and out of thin layers of sand and shale. It takes a small variation in well deviation or formation dip to cause such changes.

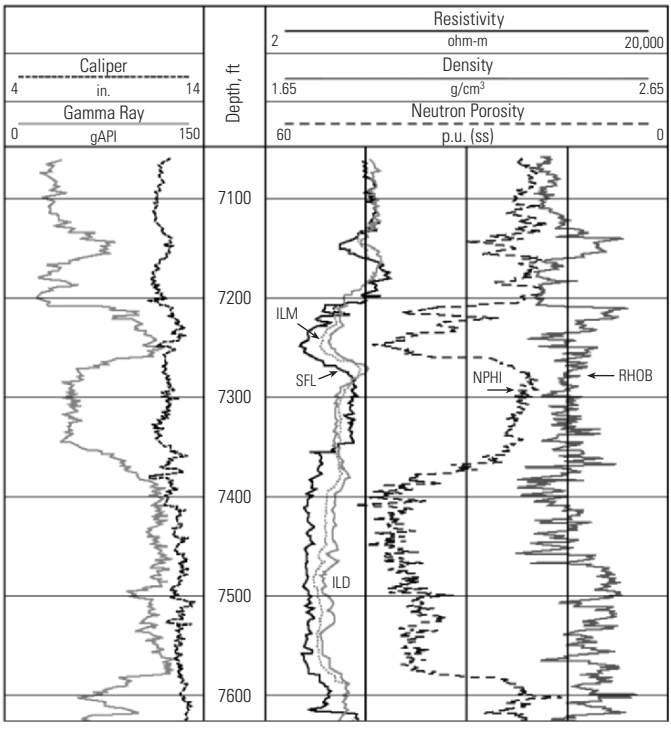


Fig. 20.2 A set of logs acquired with wireline tools in an early HZ well. The deviation of the well (not shown) builds up from 80° to reach 90° at 7,360 ft, after which it remains near horizontal. From Singer [2]. Used with permission.

The resistivity logs separate in the shales at 7,250 ft and below 7,400 ft, not due to invasion, but due to the effect of the reservoir above or below on the deeper-reading logs. The gamma ray and neutron logs show a long transition from sand to shale near 7,350 ft, as the well slowly moves out of the reservoir. The effect of the nearby shale bed must be removed before using these logs to calculate the shaliness of the reservoir. On the other hand there is a sharp transition near 7,200 ft – too sharp to be caused by a normally dipping bed boundary and most likely caused by the well crossing a fault.

It is useful to consider the true thicknesses of the formations logged in this example. The well deviation (not shown) averages 84° through the shale between 7,205 ft and 7,265 ft. If the structural dip is flat, the true vertical thickness of the shale can be calculated as 6 ft. The calculation is easy, but any small error in the deviation or the assumption of zero dip has a large impact on the calculated thickness. For this reason a resistivity or density image is invaluable for obtaining an accurate relative angle between borehole and formation. The calculation of reservoir thicknesses is particularly difficult in HA/HZ wells, but further discussion is beyond the scope of this book.

At this point it is worth defining the terms used for the depths presented on logs in HA/HZ wells. Measured depth (MD) is the depth measured by logs along the borehole. True vertical depth (TVD) is the vertical distance from any one point in the well to the surface vertically above it. This depth is calculated taking into account the direction and deviation along the well from the surface. The true vertical thickness (TVT) of a formation is the distance that would be travelled by a vertical well drilled through it. The true stratigraphic thickness (TST, sometimes called the true bed thickness, TBT) is the distance perpendicular to the dip of the formation. The true vertical depth thickness (TVDT) is the difference between the TVDs at the points where the well enters and leaves the formation. A drawing of these distances is left as an exercise.

The change from vertical to horizontal affects different measurements in different ways, depending mainly on their depth of investigation and whether or not the measurement is azimuthally focused. These factors are reviewed in the following sections. It is assumed that the reader is familiar with the physics of measurement from earlier chapters.

20.3.1 Resistivity

The general effect of anisotropy and surrounding beds on induction and propagation devices was described above and in Fig. 20.1. This description is valid for conventional induction and propagation devices with axially-mounted coils, and for electrode tools. Multi-component devices induce current loops at other orientations but will not be discussed in this section.

In vertical wells, anisotropy can be ignored since conventional induction and propagation devices are only sensitive to R_h, while electrode devices are only slightly dependent on R_v. The theoretical effect of anisotropy on resistivity measurements was discussed in Chapter 4, where it was shown that the conductivity measured perpendicular to a logging device varies from σ_h in a vertical well to $\sqrt{\sigma_h \sigma_h}$ in a horizontal well. The response of actual devices depends on several factors of tool design and must be

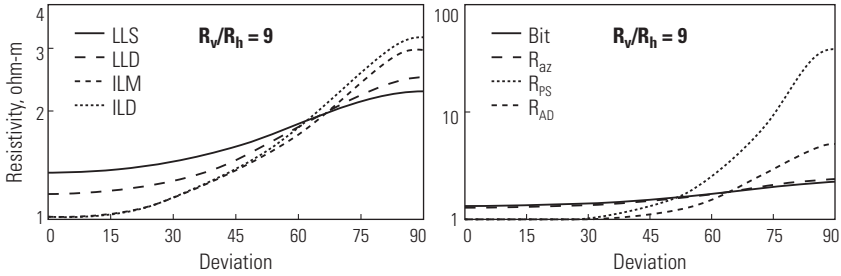


Fig. 20.3 The effect of relative deviation on log response in a formation with moderately strong anisotropy. (Left) Wireline devices: LLD and LLS (laterolog deep and shallow); ILD and ILM (traditional deep and medium induction). (Right) LWD devices: Bit and Raz (resistivity at bit and ring resistivity from the RAB tool); Rps and Rad (phase shift and attenuation from a propagation tool). Note the different y-axis scales for the two figures. Courtesy of Schlumberger.

modelled. Results for several different tools are shown in Fig. 20.3. Anisotropy has by far the strongest effect on the propagation device, but this is also an advantage since by combining the phase shift and attenuation data it is possible to derive both R_v and R_h (Section 9.6.5).

When comparing vertical and horizontal wells, which resistivity should be used? For correlation purposes it is normal to use R_h since this is what is most available in the vertical wells. For evaluation purposes, it is best to use both R_v and R_h, and link the anisotropy to a petrophysical cause such as laminated sands. With a suitable model, water saturation in the productive layers can be determined (Chapter 23). Note that depending on the relative angle and method used for processing, R_v and R_h may actually mean parallel and perpendicular to bedding rather than truly horizontal and vertical resistivity.

The effect of shoulder beds in a vertical well can be removed in processing: their position and resistivity are known because the well passes through them. In HZ wells, the resistivity of beds above the well can be estimated from logs further up the well, but the resistivity of beds below the well must be estimated from offset wells. Even then, their distance from the well is not known accurately and varies continually.

In general the effects of shoulder beds and anisotropy should not be considered in isolation from other environmental effects such as borehole and invasion. A proper description of all these effects involves a full 3D model, which is then inverted to find the different parameters. Anderson et al. [3] show examples of applying a 3D model to understand the response of array induction logs in HA wells. However such studies are generally limited to particular cases of anomalous logs. It is not yet practical to apply such inversions routinely because of the slowness of computation and because too many different solutions are possible. The situation is easier for LWD logs since in many cases the invasion at the time of logging is small enough to be ignored and borehole and dielectric effects are insignificant. It is then possible to invert for resistivity and distance to boundary [4]. In the example shown in Fig. 20.4 the HZ well passes from a shale into a reservoir sand. The logs show characteristic polarization

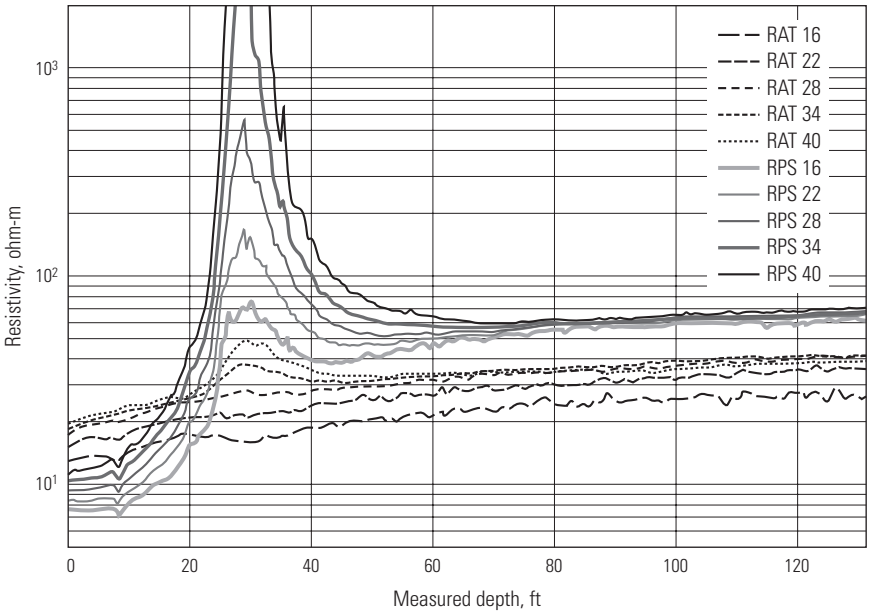


Fig. 20.4 Attenuation (RAT) and phase shift (RPS) logs at different spacings from an LWD propagation device run in a 8.5 in. borehole drilled with OBM. Relative deviation is 80°. From Yang et al. [4]. Used with permission.

spikes at the boundary and have significant separations before and after the transition due to shoulder bed effect. The data was inverted every few inches using a 2D model with five components: the resistivities of the bed in which the borehole lies and of the shoulder beds above and below the well, and the distances from the borehole to the boundaries above and below.

The results are shown in Fig. 20.5 in terms of the resistivity of the central bed and the nearest bed, and the distance to the nearest boundary. There are some oscillations near the boundary at 40 ft, and near 90 ft. Otherwise the results appear reasonable, and agree with those from a deeper-reading directional device to be discussed in Section 20.4.1 [4]. This process may appear simple, but is not. With no a priori information on the beds it is necessary to assume several different starting points for the inversion, and decide from the goodness of fit which is the most suitable. One typical assumption is that the bed resistivity is more than the top shoulder resistivity but less than the bottom shoulder resistivity. Some further constraints are needed, particularly close to the boundary within the polarization horn. Nevertheless reasonably robust results can be achieved. They do not, however, allow for anisotropy in any of the beds. It is not yet possible to solve for both shoulder bed and anisotropy effects from conventional propagation logs without other measurements or a priori information. Even with such information the solution is difficult, since the two effects are similar.

For LWD electrode measurements (ring and button resistivities) the effect of shoulder beds on the response is generally less than with propagation devices. This is

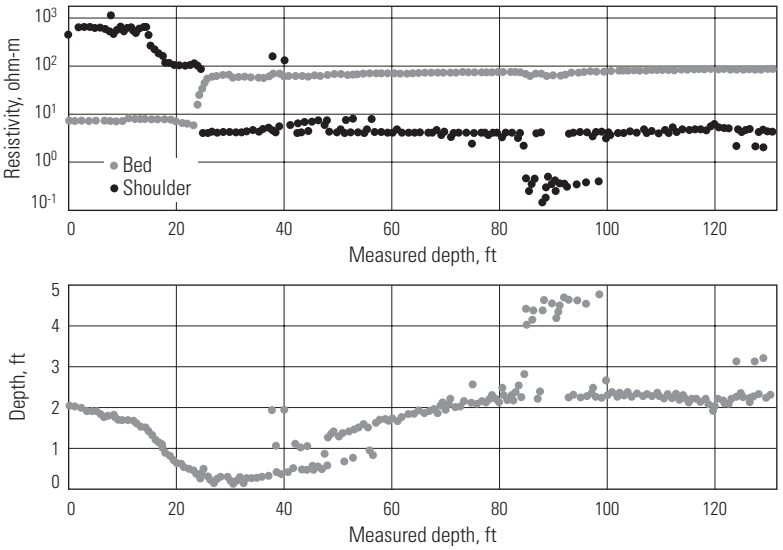


Fig. 20.5 Bed and shoulder bed resistivities (top) and distance to boundary (bottom) derived from inversion of the logs in Fig. 20.4. From Yang et al. [4]. Used with permission.

partly because the depths of investigation are only a few inches, and partly because shoulder beds tend to be less resistive than the reservoir in which the well is drilled (thereby affecting the conductivity-sensitive propagation device more than the resistivity-sensitive electrode device). The bit resistivity reads a few tens of inches into the formation but inversions are not attempted because the response is qualitative in many environments. The button resistivities, being azimuthally focused, are particularly useful for geosteering and for mapping the geometry of the formations cut by a high angle well, as will be discussed in Section 20.4.

20.3.2 Density

The great advantage of LWD density devices in HA/HZ wells is their ability to measure at different azimuths (Chapter 12). In HA/HZ wells the best reading is often in the bottom quadrant since it is there that the measurement is most likely to be in contact with the formation. However, several factors can complicate the interpretation: the presence of a bed of cuttings, which can cause the bottom density to read too low if it is thick; the tendency during rotation for the drill collar to ride up one side of the hole, causing some standoff on the bottom density; and the effect of invasion and of bed boundaries.

An example of the latter is shown in Fig. 20.6. In zone A, the neutron–density separation indicates gas while the bottom density reads higher than the others. Since the DRHO curves indicate no standoff in any quadrant, the likely interpretation is that gravity has caused gas to displace the filtrate above and at the sides, with only

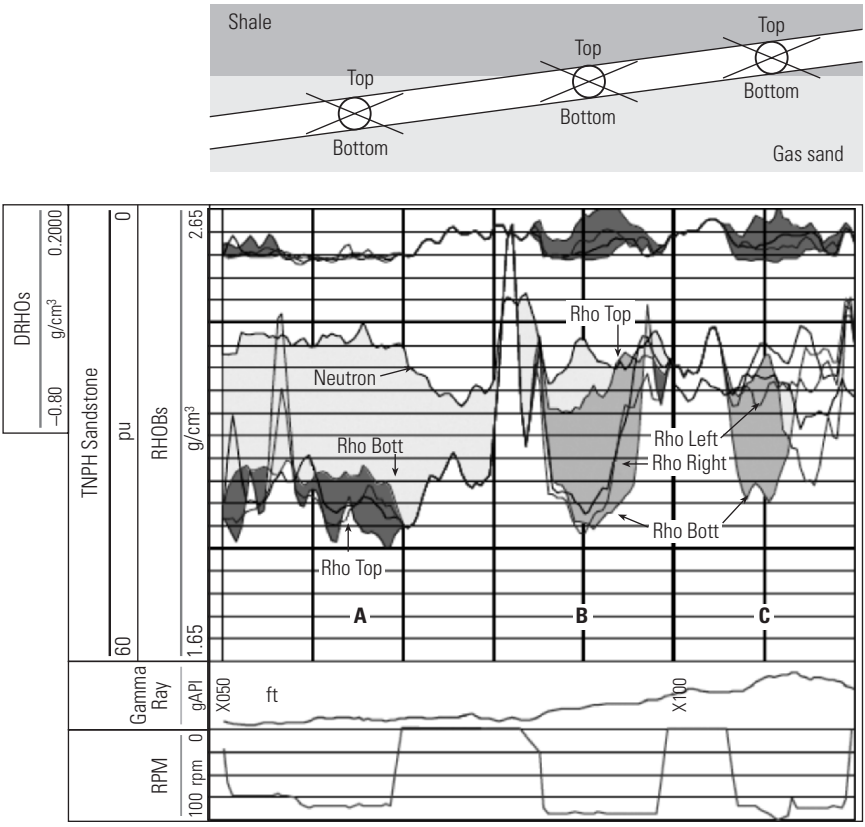


Fig. 20.6 Density and neutron logs from a HZ well with (above) an interpretation of the borehole moving up from a gas sand into a shale. RPM = revolutions per minute of drillstring. From Holenka et al. [5]. Used with permission.

the bottom quadrant seeing filtrate. Between A and B, the RPM log in track 1 shows a section with no rotation. The detectors are normally oriented towards the bottom when sliding, as here, and therefore see filtrate. At B the top density reads higher than the others, which is best explained by the drill collar entering a shale. By C the left and right quadrants have entered the shale, soon followed by the bottom quadrant. In this example the neutron–density separation clearly indicates the presence of gas. If there had been oil instead, the effect on the density readings would have been less, but much harder to interpret. This example illustrates the variety of factors – invasion, standoff and bed boundaries – that must be kept in mind when studying HA/HZ logs.

Given these factors it is perhaps not surprising that several studies have shown systematically lower density readings from HA/HZ wells than from vertical wells in the same reservoir [1, 6, 7]. The causes of the differences could not always be uniquely identified, and therefore could not be easily corrected. Nonetheless, in one particular case of a formation which consisted of alternating thin sand-shale sequences

a satisfactory explanation for the density difference seen between logging vertical and highly deviated wells was achieved by the use of detailed tool modelling [8]. In the case of vertical logging, the resolution of the measurement is determined by the tool vertical resolution which is on the order of the source-detector spacing. For beds of thickness much smaller than this dimension (30–40 cm) the device simply returns the average density of the beds contained within that spacing. When the tool is nearly parallel to the laminated beds, it is the depth of investigation (generally much smaller than the source-detector spacing) that controls the measurement. The tool will read the correct density of a bed of only a few inches thickness if it lies next to the HZ well bore. Thus, it can be anticipated that when the bed thickness is much less than 30–40 cm, the porosity of the sand beds estimated from the horizontal measurement will be more representative of the reservoir property than one derived from a vertical density measurement.

A further use for the LWD density measurement is for identifying layers and determining relative dip. Figure 20.7 shows an image of the density measurements through a sequence of denser fine-grained silt and lighter coarse-grained reservoir sand. The image was formed from density measurements taken in 16 azimuthal sectors. The image not only allows an estimate of the proportion of sand in the well, but also of the relative dip of the laminae.

20.3.3 Neutron

The traditional compensated neutron device is itself relatively unfocussed. However the borehole and formation environment can cause the measurement to respond primarily in one direction. For example a wireline device pressed against one side of the borehole responds primarily to the formation in front of it because the mud on the opposite side prevents neutrons reaching the detectors. With LWD tools this effect is much less because the annulus between drill collar and formation is small. If there is little contrast around the well, the LWD neutron measurement is an approximate average of the azimuthal properties. This is not true if there are large contrasts in the vicinity of the well – for example a gas-bearing formation even at a considerable distance ($\approx$20 cm) below the bottom of a HZ well. An interesting counter-effect occurs when the borehole lies in a gas zone – the tool response is nearly immune to the presence of a formation with a high hydrogen content below the wellbore.

The answer to the discrepancy lies in the fact that the neutrons can travel relatively unimpeded (called streaming) in the portion of the formation with the longest slowing-down length. When the tool is in a gas zone in a HZ well, the neutrons do not easily penetrate and travel in a nearby zone with high hydrogen content. On the other hand, when the tool is in a borehole contained within a formation with high hydrogen content, a nearby (within tens of cm) gas formation will provide an easy streaming path for the few rare neutrons that manage to reach it.

To visualize these two situations refer to Fig. 20.8 where, on the left, a concrete example is shown – the presence of a gas sand below a 25 p.u. water-saturated sand. Although this is a geologically improbable situation, the point is to examine the response of the tool as it traverses a zone of high HI, and enters one of a low hydrogen

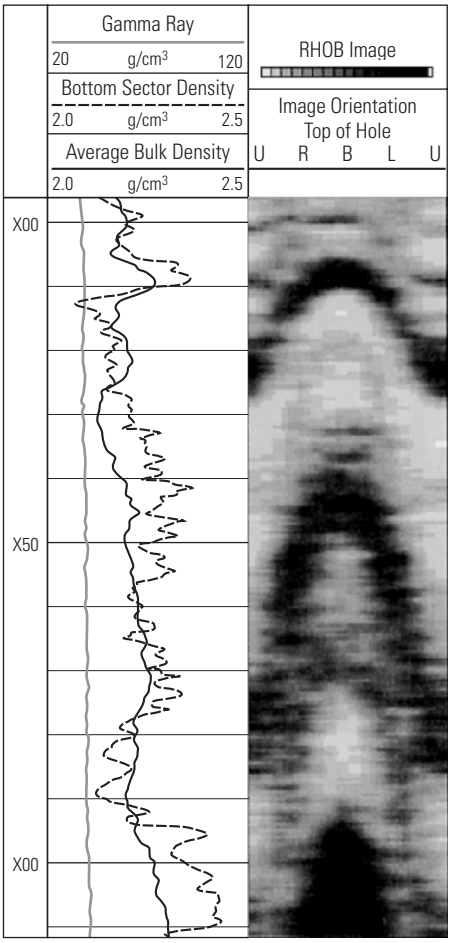


Fig. 20.7 Density log and image formed from the segments of an LWD density device from the same HZ well as Fig. 9.22. The dark bands are silt and the light bands are sand. Depths are in feet. From Tabanou et al. [9]. Used with permission.

index below the first zone. In the sketch above the left graph, imagine the tool descending in a highly deviated borehole from right to left. At first, the borehole is completely contained within the 25 p.u. water-saturated formation, and the top and bottom portions of the tool read an apparent (limestone) porosity of 21 p.u. As the tool approaches the gas bed, the bottom detector begins to sense it first when it is within $\approx$20 cm of the bottom of the hole. Shielding by the mud in the drill pipe causes the upper detectors to sense the approach a bit later, perhaps when the bed is only 10 cm away from the bottom of the borehole. As the tool progresses into the thick gas sand, both detectors (top and bottom) finally read the true gas sand value when the borehole is completely immersed in the sand formation by 5–10 cm.

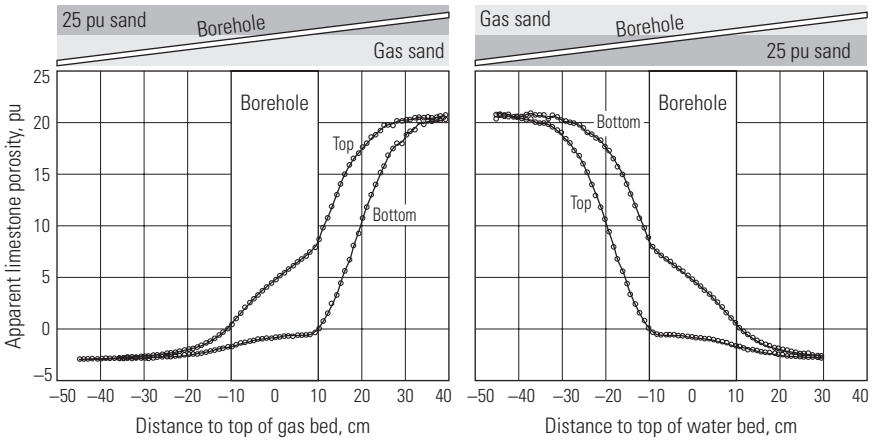


Fig. 20.8 On the left, the response of top and bottom LWD neutron detectors approaching a gas sand from right to left. The gas sand becomes apparent to the bottom detectors when the bed is ≈20 cm below the borehole. On the right, the response of top and bottom LWD detectors approaching a water-filled sand which is nearly invisible to the tool. From Ellis and Chiaramonte [10]. Used with permission.

In the complementary case, on the far right, the neutron response to a high-porosity layer below a gas sand is shown. As the tool descends, again from right to left, note that even the bottom detector only starts to sense the presence of this high-porosity layer a few centimeters away. The upper detectors sense the bed only when the borehole is completely contained within the high-porosity layer. The bottom detectors have to be at least 10 cm into the high-porosity layer to be completely free from the influence of the gas bed above. This means that the neutron device is nearly blind to the approach of the high-porosity layer below. On the other hand, it would be quite sensitive to the drift of the borehole from the gas zone into the high-porosity zone with a resolution on the order of centimeters!

20.3.4 Other Measurements

Standard acoustic devices measure compressional and shear head waves or borehole-related modes such as Stoneley or flexural waves. These all travel close to the borehole wall and are not azimuthally focused. They will therefore measure some average of the formation around the borehole and will not often be affected by surrounding beds. However, acoustic measurements are known to be sensitive to anisotropy. Thomsen has characterized the dependence of compressional and shear wave velocities on anisotropy and relative angle by three parameters [11]. Determining these factors is challenging [1].

Acoustic devices with large transmitter – receiver separations and multiple receivers have been developed to make reflection measurements from the borehole, in the manner of a surface seismic survey. In HA wells this can be used to track the path

of a reflector away from the well and tie the well into the seismic section [12]. The reflector normally needs to be strong, for example a coal bed or a gas zone.

The rather shallow depth of investigation of NMR tools preclude most of the weird geometric effects that plague electrical tools, for example. The biggest problems concern the condition of the borehole at the bottom of the hole. Efforts are made to keep the measurement off the bottom.

Most GR devices are insensitive to azimuth (although some are constructed specifically to be focused in one direction [13]), and give similar responses whether run on wireline or drill collar (see Section 11.6). GR logs therefore reflect an average of the formation around the well, within the depth of investigation of the order of 18 cm.

20.4 GEOSTEERING

The term "geosteering" means deciding the direction in which to drill from knowledge of the geology and from measurements taken while drilling. Instead of drilling to reach a preset target the course of the well is altered according to the formations encountered during drilling. At first sight this may seem simple: detecting from an LWD gamma ray device when the well has exited a sand into a shale should not be difficult. However it is necessary to know in which direction the well has exited the sand. The basic problem is illustrated in Fig. 20.9. Has the well exited from the top or the base of the sand, or has it hit a fault? A second, practical, problem is that to do this successfully the measurements must be as close to the bit as possible, otherwise the bit will have gone too far before any change can be detected and made.

To examine this further we can consider the four possibilities: either the well enters a shale or a sand, and either from the top or from the bottom, as shown in Fig. 20.10. If the well has entered a shale, as in the left half of the figure, the well must be turned to reenter the sand. With two non-azimuthal measurements, such as a gamma ray and a propagation resistivity, it is not possible to know whether the sand is now above or below the well. With two directional measurement, either from resistivity buttons or density segments, it is possible to tell by observing whether the up measurement changes before or after the down measurement. With only one azimuthal measurement, it is still possible to separate the cases by observing whether it changes at the beginning or end of the slope on a non-azimuthal measurement.

In the other two cases, of a well entering a sand, the current course can be held, but it may be better to turn and run parallel to the sand-shale boundary. In the case of a fault, the two non-azimuthal measurements should respond at the same depth. Clearly a measurement at a single azimuth might respond to other formation features than a boundary, for example a nodule or a fracture. Complete images from multiple azimuthal measurements will provide a much clearer picture as to whether the well is passing through a boundary or some other feature (see the bottom of Fig. 20.10).

Unfortunately not all situations are as simple as those of Fig. 20.10. There are often multiple sand-shale layers, so that it is difficult to know which one is being penetrated. Furthermore the resistivity buttons and density detectors that make these azimuthal measurements are all shallow-reading devices, responding to changes a

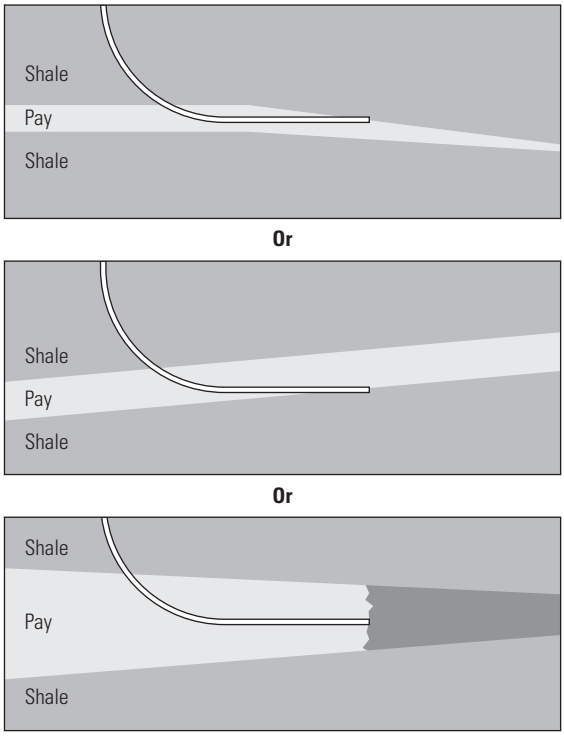


Fig. 20.9 The three possibilities when a HA well goes out of a pay zone into a shale. Courtesy of Schlumberger.

few inches above or below the drill collar. Propagation resistivity devices see a few tens of inches away from the drill collar but are not azimuthally focused.

To make use of the nondirectional measurements other procedures based on modeling are needed, as illustrated in Fig. 20.11 [15]. On the left, and before the well is drilled, information is gathered from the reservoir descriptions, offset wells and maps of the area surrounding the planned horizontal section. Then the resistivity logs in the offset wells are squared up so that a resistivity can be assigned to each of the layers. The result is a layer column with petrophysical properties. The next step is to use these properties and knowledge of tool responses to create a database of tool readings at different relative angles of the well to the layers, and at different positions within the layers. Due to polarization horns and the effects of surrounding beds on the measurements, these responses are not always intuitive. Modeling every relative angle and every position would be very time consuming so it is normal to calculate a selected number of angles and positions and interpolate between them.

Then, by looking up in this database, simulated logs can be generated for the planned trajectory of the well through the layer column. Other reasonable scenarios can also be modeled, for example the possibility that the depth or dip of the target reservoir is different than planned; that the well cuts through a fault; or that the

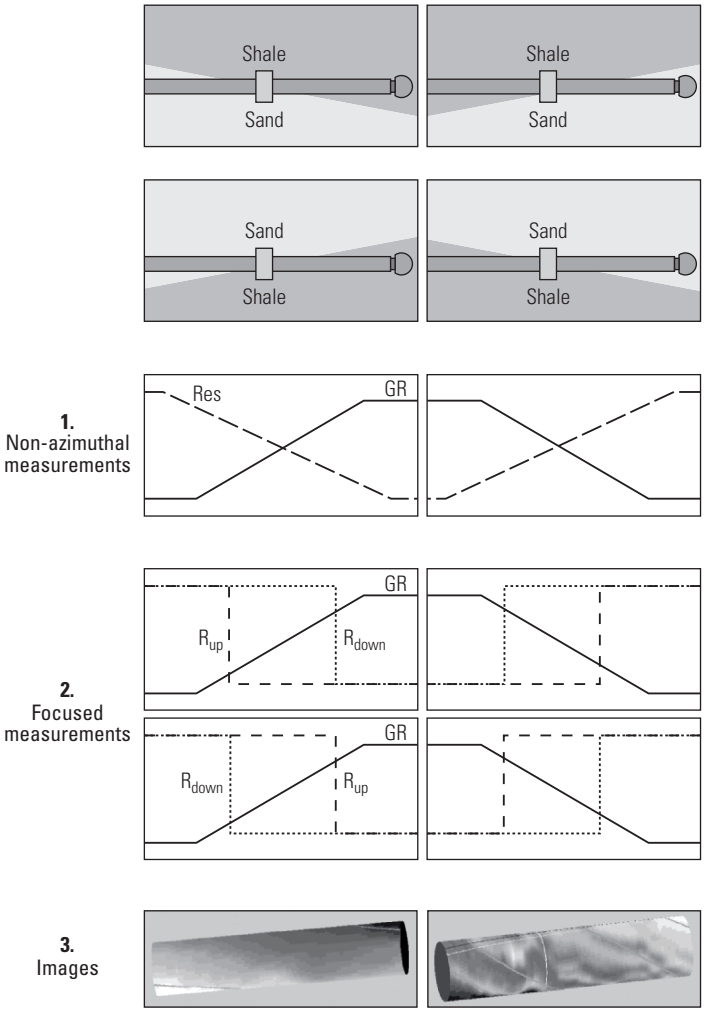


Fig. 20.10 The four possibilities when a well moves up or down from sand to shale or vice versa, showing the response of non-azimuthal measurements, focused measurements (up or down), and resistivity images (light color is high resistivity). Images adapted from Rasmus et al. [14].

boundaries are not planar. Other logs can be modeled, for example the gamma ray, but here the tool responses are simpler and more intuitive.

During the drilling of the well the actual recorded logs are compared with the simulated logs. Since the actual trajectory and geology may be different than planned, the simulations may need updating as drilling proceeds. If the recorded logs match the simulated logs, it is a reasonable assumption that the well is on target (although as with any modeling exercise there are no unique solutions). If a difference starts to develop, the recorded logs can be compared with the data bank of alternative scenarios

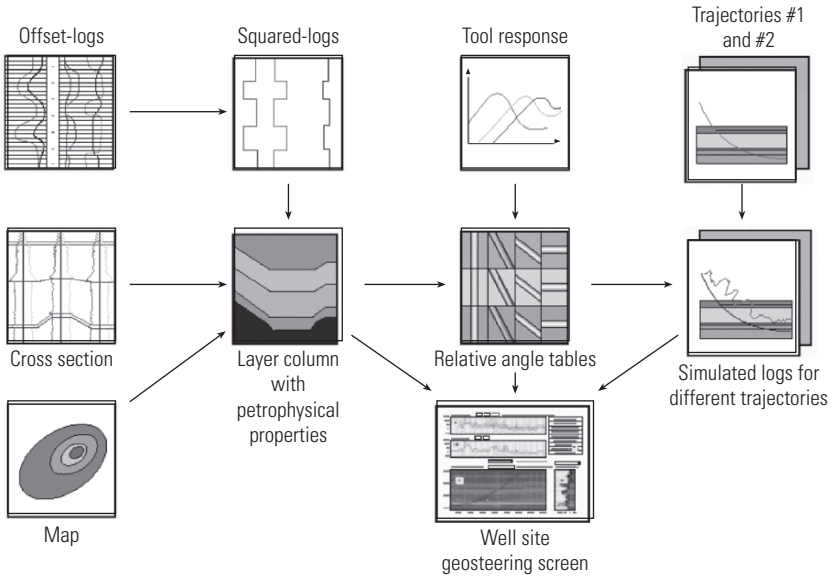


Fig. 20.11 Diagram of the process for modeling the expected response of logs in a high angle well. See text for explanation. From Well Evaluation Conference – Venezuela 1997 [16]. Courtesy of Schlumberger.

to try and understand what might have happened; for example has the well exited the target into the shale above, or is it just crossing a thin stringer in the middle of the reservoir?

The result of a successful geosteering is that the well is kept within the reservoir. It is normally impossible to prove that the result is the best that could have been achieved, but an example from the Grane reservoir in Norway gives some confirmation [17]. Figure 20.12, left, shows the typical resistivity profile of the reservoir as seen in a vertical well. For optimum exploitation, studies showed that the HZ wells must be drilled 9 m above the oil water contact: lower and the water is likely to cone up from the water zone; higher and the injected gas is likely to break through from the top. The wells have up to 3,000 m of horizontal section, but at the time of drilling in the early 2000s the position of the well could not be measured with an accuracy of better than ± 6 m at the heel of the well, and ± 12 m at the toe. Better accuracy can be achieved from geosteering. Figure 20.12, right, shows the result of modeling six resistivity measurements at many positions from below the oil–water contacts (OWC) to above the cap rock. Other models were constructed for the effect of shale below the well, which in some parts of the reservoir rises above the OWC.

The different measurements have different sensitivities to the distance above the OWC or the bottom shale. When measured while drilling, they can be inverted to provide this distance. A typical example is shown in Fig. 20.13. For the first 300 m the survey measurements show the well dropping. After adding the computed distance to OWC, the OWC is found to be consistent and flat, as it should be. Beyond 2,400 m

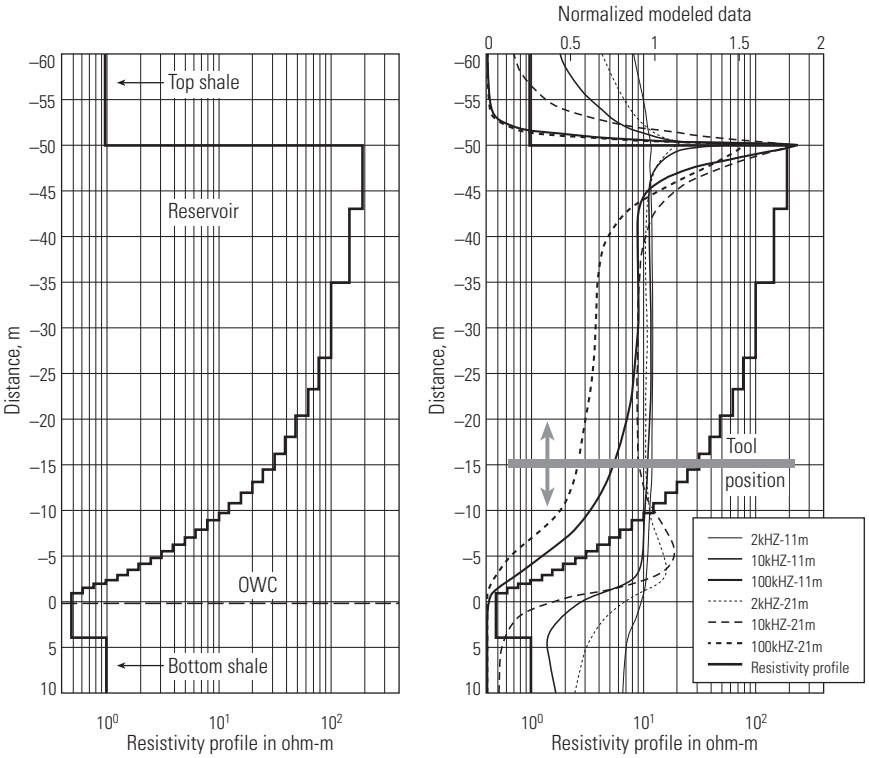


Fig. 20.12 (Left) Resistivity profile for the Grane reservoir, as derived from vertical well logs. (Right) Modeled response of six resistivity measurements calculated at many horizontal positions through the reservoir. From Iversen et al. [17]. Used with permission.

the inversion shows the lower boundary rising. This cannot be a rising OWC, but is consistent with the bottom shale rising towards the well. Applying this model the shale can be seen to rise until the well breaks into it at 2,560 m, as confirmed by the gamma ray log. When this well was logged the results were not computed soon enough after drilling to steer the well above this shale. In later wells the results were available as soon as logged (21 m after the bit), and the well would have been steered upwards as soon as the rise was confirmed. Most reservoirs are more complex than Grane, but this example serves to confirm the validity of geosteering inversion techniques.

20.4.1 Deep Reading Devices for Geosteering

Wells can be geosteered with conventional LWD devices, but it is clearly an advantage to use devices that read as deep as possible, and are preferably directional. Several devices have been specially developed for geosteering.

The logs discussed above and in Fig. 20.13 were recorded by one such device, which makes a conventional induction log from a receiver 14 m behind the bit and two

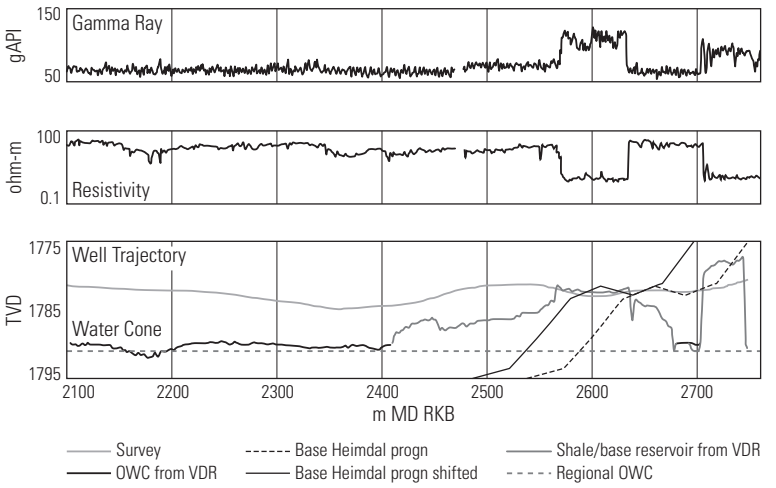


Fig. 20.13 Logs from a Grane HZ well, showing the OWC/shale base calculated from resistivity modeling compared with the regional OWC and the seismic predictions (before and after adjustment). The calculated OWC is the active dark curve from the 2,100 m to 2,400 m; the shale base is the active lighter line from 2,400 m to the bottom. VDR stands for Very Deep Resistivity Tool. From Iversen et al. [17]. Used with permission.

transmitters at 25 m and 35 m, driven at 2, 10, and 100 kHz [18]. At such separations, an order of magnitude larger than for wireline induction devices, the response is very deep, but the signals are small. However at normal drilling speeds the measurement is repeated sufficiently often to give a reasonable signal to noise ratio. The problems that plague wireline induction devices – large mutual coupling, borehole signals and signals from the steel drill collar – are all reduced at these large transmitter-receiver separations. No attempt is made to focus the measurements. The different response to the boundary is provided by the different transmitter-receiver separation and the different skin effect at the three frequencies.

The Grane example is ideal for such a device, with its high-resistivity shale-free reservoir above a water table or shale whose resistivity is 100 times less. Another device for such conditions uses a transmitter and two receivers at similar long distances, but measures the attenuation and phase shift between receivers at 20 and 50 kHz [19]. Both devices claim depths of investigation up to 12 m, an order of magnitude improvement over normal LWD propagation measurements. This large depth of investigation is achievable in ideal contrasts such as Grane and where the top and bottom boundaries are well separated. However, they have the disadvantage of being nondirectional. In thinner or more complex reservoirs it would therefore not be possible to differentiate the approach of shale from the top or bottom.

One device that does is shown in Fig. 20.14. In addition to a set of transmitters and receivers that are arranged as axial magnetic dipoles as in a conventional propagation resistivity device (T1 to T5, R1, and R2), it has two receivers oriented at 45° to the tool axis and one transmitter oriented perpendicular to the tool axis [20]. The device

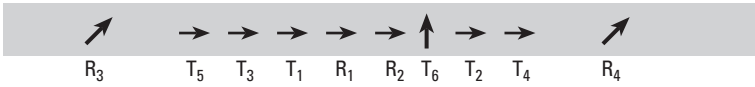


Fig. 20.14 Layout of a LWD propagation device with directional transmitters (T) and receivers (R). From Li et al. [20]. Used with permission.

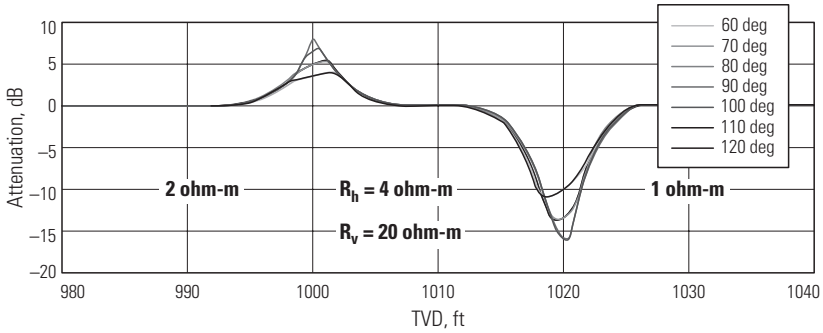


Fig. 20.15 Response of the directional attenuation from the LWD device of Fig. 20.14 to an anisotropic reservoir with lower resistivity boundaries above and below. The response is modeled with the device at various TVD depths and at various apparent dip angles. From Li et al. [20]. Used with permission.

runs at 100 kHz in addition to the conventional 400 kHz and 2 MHz. Phase shift and attenuation measurements can be derived from many combinations of transmitters and receivers. The longest spacing, of 96 in., is obtained by comparing the signals from the outermost transmitters to the receivers at the opposite end, i.e., T5 to R4 and T4 to R3. In the middle of the formation these signals cancel out, but as the device approaches a bed boundary in a HA well the characteristic polarization horn develops (Fig. 20.15). The interesting feature of this response is that the polarity is different depending on whether the boundary is approached from above or below. This is a result of the 45° orientation of the receivers, and provides the required azimuthal sensitivity.

As can be seen in Fig. 20.15 the size of the horn depends only slightly on the angle in a HA/HZ well. It is also independent of anisotropy in the middle bed. This has been shown to be the results of using a symmetrical pair (T5 to R4 and T4 to R3) and is not true if only one transmitter is used. The sensitivity to the bed boundary is a function of resistivity contrast and TR spacing. For a 10:1 contrast and 84 in. spacing the horn starts to be measurable when it is 14 ft from the borehole. Below 14 ft, the distance and direction to the boundary is easily determined from the magnitude and polarity of the signal.

The reason that it is possible to determine distance to boundary independent of anisotropy or dip can best be understood by referring back to the triaxial antennas discussed in Section 8.5. In that discussion the cross-dipole interactions, e.g., V_{xz}, V_{zx},

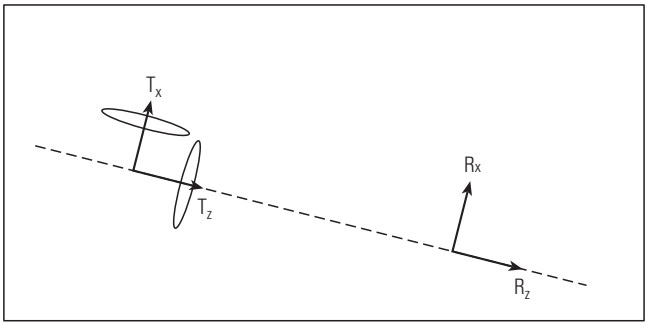


Fig. 20.16 Two orthogonal transmitters and receivers. Cross-dipole voltages are obtained by measuring at Rx using transmitter Tz (V_{zx}) and measuring at Rz using Tx (V_{xz}).

were ignored. Here, however, they are the key to the measurement. If we place two pairs of orthogonal coils in an anisotropic bed at any angle, as in Fig. 20.16, then the signal at R_x from transmitter T_z (V_{zx}) is equal to the other cross-dipole signal, V_{xz}, as would be expected from a symmetry argument. But, if a boundary is introduced there will be a difference in the signals due to the different orientations of the induced currents. This difference increases as the boundary is approached. Furthermore the polarity of ($V_{zx} - V_{xz}$) is different for boundaries above and below the well. This illustrates the principle that the distance to a boundary can be determined independent of anisotropy and dip by combining two T-R pairs, one the mirror image of the other. For further explanation refer to Minerbo et al. [21].

In the LWD environment, propagation measurements (phase shift and attenuation) are used instead of the induction-type voltage measurement just discussed. These are normally formed by taking the difference in signal between two receivers. In the case of nonaligned coils we can use the fact that in all but homogeneous formations the signal varies as the tool rotates. Thus from a single T-R pair, such as T5 and R4 or T4 and R3 in Fig. 20.14, it is possible to define a "directional" phase shift and attenuation that is a function of the azimuthal position of the tool, the angles of the coils to the tool axis and the different components of the voltage at the receiver (V_{zz}, V_{xz}, V_{zx},...) [20]. The magnitude of these components appear as coefficients in a Fourier series and can be determined by analysis of the rotating signals. The directional phase shift and attenuation are therefore functions of the cross-dipole couplings V_{xz} and V_{zx} that are needed to identify the bed boundary. Note also that these measurements compare signals at different azimuths as the tool rotates, so that electronic and other drifts are normalized out, as with the conventional phase shift and attenuation.

The final step is to note that the directional phase shift and attenuation measurements do not distinguish the direction of the boundary when the coils are orthogonal. Instead at least one of the antennas must be tilted at an angle to the tool axis. Then, using the mirror image principle discussed above, it is possible to know the direction of the boundary at the same time as being insensitive to anisotropy and dip. In the tool shown in Fig. 20.14 the receivers are oriented at 45° *to the tool axis.*

The distance to boundary computations discussed in this section are not only useful for geosteering. In combination with conventional propagation-resistivity measurements it is possible to construct charts to remove the effect of the boundary and determine formation resistivity for evaluation purposes. The charts will vary with shoulder bed resistivity, but if the latter is much less than formation resistivity its value is unimportant.

Armed with the correct formation resistivity and with density, neutron, gamma ray and other readings suitably chosen and corrected for the effect of surrounding beds, the formation can be evaluated using the standard techniques to be discussed in the following chapters.

REFERENCES

1. Passey QR, Yin H, Rendeiro CM, Fitz DE (2005) Overview of high-angle and horizontal well formation evaluation: issues, learnings, and future directions. Trans SPWLA 46th Annual Logging Symposium, paper A
2. Singer JM (1992) An example of log interpretation in horizontal wells. The Log Analyst 33(2):85–95
3. Anderson B, Barber T, Druskin V, Lee P, Dussan E, Knizhnerman L, Davydycheva S (1999) The response of multiarray induction tools in highly dipping formations with invasion and arbitrary 3D geometries. The Log Analyst 40(5):327–344
4. Yang J, Omeragic D, Liu C, Li Q, Smits J, Wilson,M (2005) Bed-boundary effect removal to aid formation resistivity interpretation from LWD propagation measurements at all dip angles. Trans SPWLA 46th Annual Logging Symposium, paper F
5. Holenka J, Best D, Evans M, Kurkoski P, Sloan W (1995) Azimuthal porosity while drilling. Trans SPWLA 36th Annual Logging Symposium, paper BB
6. Bedford J, Cuddy S, White J (1997) The empirical investigation of density anisotropy in horizontal gas wells. Trans SPWLA 38th Annual Logging Symposium, paper I
7. Rendeiro C, Passey Q, Yin H (2005) The conundrum of formation evaluation in high angle/horizontal wells: observations and recommendations. Presented at the 80th SPE Annual Technical Conference and Exhibition, paper SPE 96898
8. Radke RJ, Evans M, Rasmus JC, Ellis DV, Chiaramonte JM, Case CR, Stockhausen E (2006) LWD density response to bed laminations in horizontal and vertical wells. Trans SPWLA 47th Annual Logging Symposium, paper ZZ
9. Tabanou JR, Bruce S, Bonner S, Wu P (1999) Which resistivity should be used to evaluate thinly bedded reservoirs in high angle wells? Trans SPWLA 40th Annual Logging Symposium, paper E

10. Ellis DV, Chiaramonte JM (2000)Interpreting neutron logs in horizontal wells: a forward modeling tutorial. Petrophysics 41(1):23–32

11. Thomsen L (1986) Weak elastic anisotropy. Geophysics 51(10):1954–1966

12. Arroyo Franco JL, Mercado Ortiz MA, De GS, Renlie L, Williams S (2006) Sonic investigations in and around the borehole. Oilfield Rev 18(1):14–33

13. Jan Y-M, Harrell JW (1987) MWD directional-focused gamma ray – a new tool for formation evaluation and drilling control in horizontal wells. Trans SPWLA 28th Annual Logging Symposium, paper A

14. Rasmus J, Farruggio G, Low S (1999) Optimizing horizontal laterals in a heavy oil reservoir using LWD azimuthal measurements. Presented at the 74th SPE Annual Technical Conference and Exhibition, paper SPE 56697

15. Allen D et al. (1995) Modeling logs for horizontal well planning and evaluation. Oilfield Rev 7(4):47–63

16. Well evaluation conference – Venezuela 1997. Schlumberger Surenco, Caracas

17. Iversen M, Fejerskov M, Skjerdingstad A-L, Clark AJ, Denichou JM, Ortenzi L, Seydoux J, Tabanou JR (2004) Geosteering using ultradeep resistivity on the Grane field, Norwegian North Sea. Petrophysics 45(3):232–240

18. Seydoux J, Tabanou J, Ortenzi L, Denichou JM, De Laet Y, Omeragic D, Iversen M, Fejerskov M (2003) A deep resistivity logging-while-drilling device for proactive geosteering. Presented at the Offshore Technology Conference, Houston, paper OTC 15126

19. Helgesen TB, Meyer WH, Thorsen AK, Baule A, Fulda C, Ronning KJ, Iversen M (2005) Accurate wellbore placement using a novel extra deep resistivity service. Presented at the SPE Europec/EAGE Annual Conference, Madrid, paper SPE 94378

20. Li Q, Omeragic D, Chou L, Yang L, Duong K, Smits J, Yang J, Lau T, Liu C, Dworak R, Dreuillault V, Ye H (2005) New directional electromagnetic tool for proactive geosteering and accurate formation evaluation while drilling. Trans SPWLA 46th Annual Logging Symposium, paper UU

21. Minerbo G, Omeragic D, Rosthal R (2003) Directional electromagnetic measurements insensitive to dip and anisotropy. US Patent Application No 2003/0085707A1

Problems

20.1 Assuming the deviation of the borehole near 7,365 ft in Fig. 20.2 is 90°, use your knowledge of the depth of investigation of the gamma ray log to calculate the formation dip for the bed boundary at this depth.

20.1.1 Calculate the dip of the boundary at 7,205 ft.

20.1.2 Given that the neutron log was eccentralized in the borehole, is the shale most likely to be approaching the well from above or below near 7,365 ft ?

20.2 Draw a HA well crossing a dipping formation which has parallel top and bottom boundaries. Mark the measured depth through the formation, and the TVD, TVT, TST, and TVDT.

20.3 Using your calculation of formation dip in Problem 20.1, compute the TVT and TST of the sand above 7,365 ft.

20.3.1 This estimate of dip is approximate, and the deviation of the borehole is only known to a certain accuracy. What would the TVT and TST be if the borehole deviation were 91° and if the actual dip were 2° greater than assumed in the direction of the borehole?

20.4 For the vertical and horizontal resistivities used in Fig. 20.3 what resistivity should be recorded at a relative deviation of 90° by a logging device that measures perpendicular to itself? Which of the logging measurements shown in the figure is closest to this resistivity?

20.5 From the response of the density logs, estimate the angle of the borehole illustrated in Fig. 20.6, assuming its diameter is 8.5 in.

20.6 If the borehole diameter for the data shown in Fig. 20.7 is 8.5 in., what is the average relative deviation of the borehole? If the well had been drilled perpendicular to the formation, approximately what density would have been measured?

21

Clay Quantification

21.1 INTRODUCTION

The presence of shale in hydrocarbon reservoirs has a large impact on estimates of reserves and producibility. The clay minerals present in the shale complicate the determination of saturation and porosity. Permeability is often controlled by very low levels of clay minerals in the pore space. Without specific knowledge of the clay minerals present, there is a risk of impairing the permeability of a reservoir by introducing improper fluids.

Log examples in earlier chapters show that clay in rocks affects all of the log readings that have been considered. How is clay different from any other mineral? The distinction lies, perhaps, in the magnitude of the effects which are observed. For example, the presence of hydrogen associated with the clay can increase the apparent neutron log porosity by up to 40 p.u. Unlike other minerals, clays alter the conductivity of the formation so that a straightforward application of the Archie relation yields water saturations which are too large.

In traditional well log analysis, a large body of successful techniques for dealing with the effects of clay is based on crossplotting log measurements over large depth intervals that include massive shales and so-called clean (clay-free) zones. Clay volumes are determined by scaling some function of the log reading between the minimum and maximum values, which are taken to represent 0% and 100% shale, respectively. Such techniques are subjective and produce an estimate of the volume fraction present with little regard for the details of its composition or distribution. They also assume that the clay composition in the reservoir is the same as that in the shales. However, in many circumstances, this is the best that can be done.

This chapter starts by reviewing the characteristics of clays and shales, and the effect of their physical properties and distribution on porosity and log response. It continues with a resumé of techniques for determining clay volumes from a single measurement, and explores the effect of clay on three nuclear measurements in more detail. The use of the neutron–density plot is examined, in particular how results can be improved by basing the controlling parameters on knowledge of the clay composition in the reservoir. Further improvements have come from the introduction of elemental analysis from capture gamma ray spectroscopy. Logs are now able to provide a partial geochemical analysis of the formation.

21.2 WHAT IS CLAY/SHALE?

In common with many log interpreters and petrophysicists we have used the terms shale and clay interchangeably throughout the text. More correctly, shale is a fine-grained rock containing a sizable fraction of clay minerals and silt. From the point of view of log measurements, the average properties of silt are often similar to those of sand while those of clay are distinctly different. It is difficult to determine the silt fraction from logs, so that a shaly sand may be treated either as a mixture of sand and clay (with the silt being part of the sand) or as a mixture of sand and shale (with the silt being part of the shale). The details are beyond the scope of this book. Rather than attempt to completely answer the question posed in the title, this section will concentrate on the properties of clay minerals which are important for well logging.

The hundreds of clay minerals that have been studied by crystallographers, chemists, soil scientists, and clay mineralogists can be lumped, on the basis of structure and composition, into five groups: kaolinite, mica, montmorillonite, chlorite, and vermiculite. They are all aluminosilicates, which gives a clue as to the dominant elements present. The clay mineral structures are sheetlike as a result of the geometric nature of the fundamental structural units which contain the aluminum and silicon.* One sheet type consists of octahedral units of oxygen or hydroxyl around a central atom (usually aluminum but sometimes magnesium or iron). The other is a tetrahedral unit consisting of a central silicon atom surrounded by oxygen. The five groups listed above are formed from different stacking combinations of these two types of sheet structure. Figure 21.1 indicates the layer structure and composition of members of the five groups, each of which has characteristic lattice dimensions or spacings.

The simplest structure belongs to kaolinite and its 1:1 stacking of single octahedral and tetrahedral sheets to form one layer, or platelet. The other clay minerals consist of a 2:1 stacking of two tetrahedral sheets sharing oxygen atoms with an octahedral sheet between them. The difference between groups is related to the amount of charge

*See Grim, for example, for detailed discussion of clay crystal structure [1]. The terminology of clays is confusing, with different authors using different terms for the same clay minerals and groups. For example, smectite may refer to a clay in the montmorillonite group or vice versa.

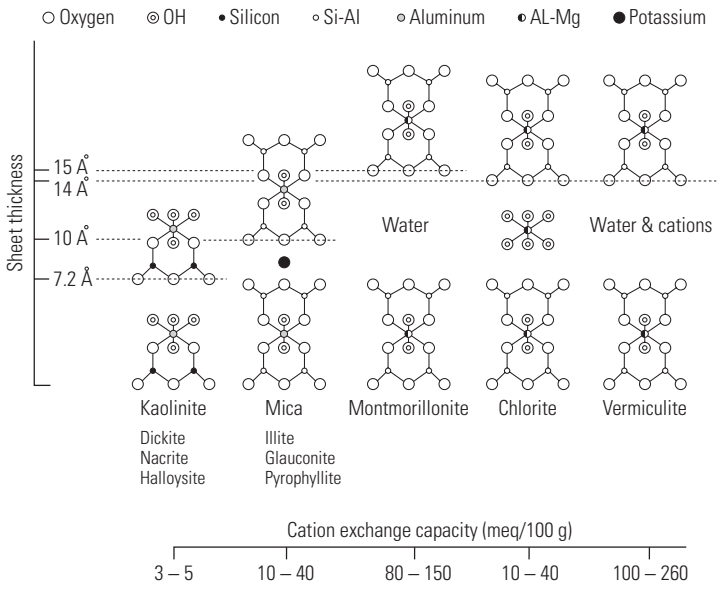


Fig. 21.1 Schematic representation of the structure and composition of members of the five clay mineral groups. In this plane view only three of the atoms in the tetrahedral sheets appear connected to a central atom, and only six in the the octahedral sheets. Adapted from Brindley [2].

in the lattice, created by isomorphous substitution (i.e., retaining the same geometric form, as with Mg^{+2} for Al^{+3} or Al^{+3} for Si^{+4}), and the type of interlayer complex present to balance the charge deficiency. Micas have the greatest substitution in the lattice, but the charge is balanced by dehydrated cations, usually K^{+}, in the interlayer space. The K^{+} ion fits particularly well in this space leading to a compact structure. Montmorillonite has less substitution, and it is mainly by Mg^{+2} in the octahedral sheet. Because the charge is lower than Al^{+3} and because the octahedral sheet is further from the interlayer space, there is a weaker bonding between the layers. This allows water and hydrated cations to enter the space, often causing montmorillonite to swell. Vermiculites and chlorites both have intermediate charge deficiencies created by substitutions. Chlorites balance their charge by interlayer complexes of Al and Mg hydroxide sheets, much like the octahedral sheet in the lattice. In vermiculites the negative lattice charge is also balanced by hydrated cations, though unlike with montmorillonite there is little swelling because of the increased attractive forces between lattice and cation. Finally there are mixed-layer clays, not shown in Fig. 21.1, in which two-sheet and three-sheet layers are mixed together.

21.2.1 Physical Properties of Clays

Since the structure of clay minerals, normally determined by x-ray diffraction, is not available while logging, the immediate interest of the information presented in

Fig. 21.1 is to highlight the elements that are susceptible to identification by logging techniques. Unfortunately this task is complicated by the lack of standard chemical formulas for most of the members of each family. This lack is the result of the previously mentioned substitution in the lattice and interlayer sites.

Hydrogen is a prominent member of all the clay minerals listed. It has a large impact on the neutron porosity response. Identification of some of the other elements can be made using gamma ray spectroscopy, since this has proven to be a practical, although indirect, means of formation chemical analysis in the borehole. We have already seen in Chapter 11 an example of the identification of clays by determining the range of U, Th, and K concentrations. From the abbreviated set of clay minerals presented in Fig. 21.1, we can see that K is principally associated with one group (the mica group).

One abundant and characteristic element in clays is Al. By itself, the Al content of a formation will not thoroughly quantify the presence of clay minerals, since feldspars contain Al and the concentration of Al in clay minerals is variable. In a number of clay mineral families, there is substitution of Al for Si and Fe for Al; this latter substitution is frequently observed in chlorite and some micas, and to a much lesser degree in kaolinite. Iron is easily detectable either through capture gamma ray spectroscopy or the attenuation of low-energy gamma rays in the determination of P_e.

There are features of clay minerals other than elemental composition that affect log response. The first is associated with their platy nature, which results from their structure. Water trapped between the plates contributes to conductivity and to porosity measurements, although it not considered a part of "effective" porosity. Layers of water can be trapped in the inner layers during sedimentation. Some of this water is released during compaction or as a result of mineralogical reactions. If the permeability of the surrounding material is not sufficiently high, the water cannot escape and overpressured shales can result.

An important property of clay minerals is their ability to adsorb ions on their exposed surfaces, primarily cations. This is a result of a negative surface charge caused by their platy nature and by the isomorphous substitution within the lattice discussed above. In some instances these ions are radioactive and account for the gamma ray activity frequently associated with clay minerals. In the presence of an electrolyte this surface charge is also responsible for creating a thin layer of altered composition in the surrounding fluid. Polar water molecules, and sodium or potassium ions are adsorbed whereas chlorine ions are repelled. This double layer, often referred to as bound water, was introduced in Chapter 3 and is considered in more detail in Section 21.2.2. It has large implications for resistivity measurements.

The ability of a clay mineral to form the electrical double layer is measured by its CEC. It corresponds to the excess of cations over anions on the surface of a solid. One method of measuring this property is to first saturate the clay-bearing sample with salt water and then to pass a barium solution through it. The barium will replace the Na, and the quantity that does so can be measured. The units for CEC often are *milli-equivalents* (meq) per 100 g of material. An *equivalent* corresponds to the number of cations required to neutralize the charge of 6.023×10^{23} electrons. Typical ranges of CEC values of the five groups of clays are shown along the bottom of Fig. 21.1

Table 21.1 Typical values for specific surface areas and other properties of clay minerals. Adapted from Almon and Davies [6] and Yariv and Cross [4]. The larger the CEC the more bound water and the larger the porosity of the wet clay.

Mineral	Specific surface area (m^2/g)	CEC (meq/100g)	Wet clay porosity (p.u.)
Smectite	700–800	80–150	40
Illite	113	10–40	15
Chlorite	42	10–40	15
Kaolinite	15–40	3–5	5

and in Table 21.1. As expected, kaolinite with its tight 1:1 packing and low isomorphic substitution has low CEC. The large interlayer surfaces cause montmorillonites and vermiculites to have large CEC. Micas, with their balanced charge and compact structure, ideally have zero CEC but with two important exceptions – glauconite and illite. Although of mica structure, they have a significant CEC caused by imperfect substitution and other factors. Illite happens to be one of the commonest clays in hydrocarbon reservoirs.

Although Berner attributes the trends of cation exchange capacity to the substitution (or lack of it) of Al for Si in the clay mineral structure there are other sources [3]. One important source of the negative surface charge is the presence of broken bonds in the sheet structure. Yariv and Cross suggest that the cation exchange capacity should depend on the surface area; they cite a study of kaolinites which demonstrated a linear relationship between CEC and particle size [4]. Patchett has taken this a step further, suggesting that there is a direct link between specific surface area and CEC [5]. A portion of this data is shown in Fig. 21.2.

This brings us to the final aspect of clay: its physical size. These thin, sheetlike particles can have very large ratios of surface area to volume, based on simple calculations from lattice dimensions. Particle size is typically less than 5 μm. The actual specific surface area depends on the clay mineral. Table 21.1 lists the specific surface areas and other properties for a number of clay minerals.

21.2.2 Total Porosity and Effective Porosity

The term "effective porosity" was introduced above but requires further explanation, in particular to distinguish it from total porosity. Total porosity is the total nonsolid space, as measured by disaggregating a core sample. Effective porosity is less clearly defined. For core analysts, effective porosity means the porosity measured after drying but before disaggregation [7]. The difference is due to unconnected pores, which are rare in sandstones but more common in carbonates. In standard core analysis the samples are dried at 100°C or more, in which case it is considered that all the clay bound water is removed. (In special humidity-dried cores most of the bound water remains.) However for log analysts, effective porosity is the total porosity *less* clay

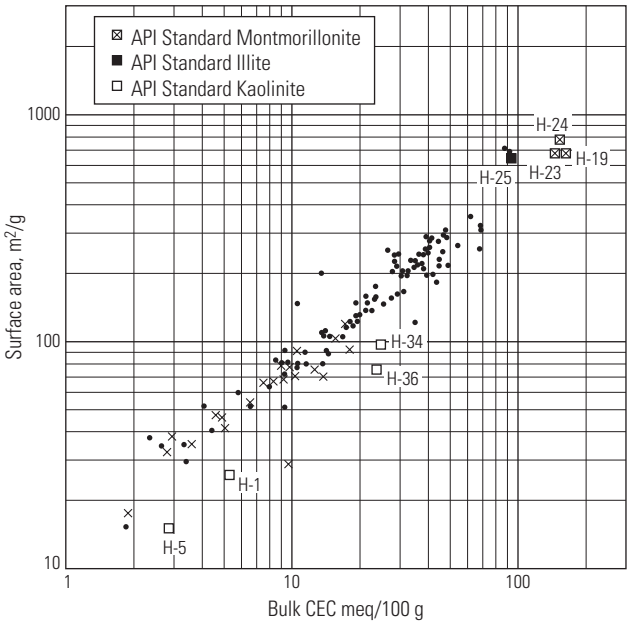


Fig. 21.2 Correlation between specific surface area and bulk cation exchange capacity. For the API standard clays the slope is 450 m^2/meq. Courtesy of Schlumberger [22] with data from Patchett [5].

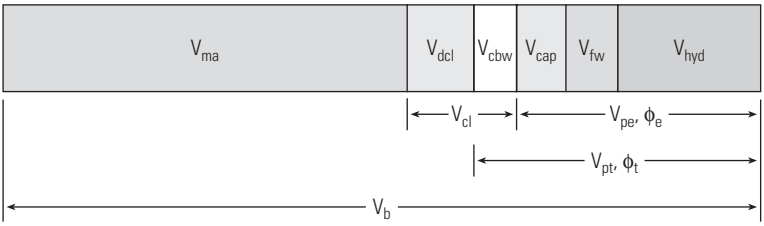


Fig. 21.3 Definition of formation volumes V, as used by log analysts. The subscripts ma = matrix, dcl = dry clay, cl = wet clay, cbw = clay bound water, cap = capillary bound (irreducible) water, fw = free water, hyd = hydrocarbon, b = bulk, p = porosity, e = effective and t = total. From Hook [8]. Used with permission.

bound water, which is assumed not to move on production. On the other hand for many production engineers, effective porosity means the pore space that contributes to production. This pore space excludes capillary-bound (irreducible) water as well as isolated and clay bound water.

The relationship between these different volumes is shown in Fig. 21.3. Which porosity is measured by logs? Most logs respond to all the porosity, but in calculating a porosity value, the answer depends on whether the clay fraction is taken as wet or dry. For example if, in the response of a density log, the clay volume and density refer

to wet clay, then the porosity calculated will be effective porosity; if the clay volume and density refer to dry clay (without the water in the electrical double layer), then the result is total porosity. In either case it is useful to calculate the volume of clay bound water, V_{cbw}, so as to convert from one to another. V_{cbw} reflects the size of the electrical double layer, which, as discussed above, is directly related to the CEC of the formation and affects its resistivity.

In a pure clay the volume of bound water is known as the wet clay porosity, ϕ_{tcl}. It can be estimated from apparent porosity readings in massive shales or using one of the typical values given in Table 21.1. Then in other zones V_{cbw} can be estimated from (V_{cl} ϕ_{tcl}) where V_{cl} is the volume of wet clay. Another useful term is S_{wb}, the fraction of bound water in the total porosity, which is related to the other terms by:

$$S_{wb} = \frac{V_{cbw}}{\phi_t} = \frac{V_{cl}\phi_{tcl}}{\phi_t}, \tag{21.1}$$

where ϕ_t is the total porosity. Both V_{cl} and S_{wb} vary between 0 in a clean zone and 1 in a pure clay, and are determined by the methods described later in this chapter.

There are two more general methods of relating V_{cbw} to CEC and V_{cl}. In both, CEC is first converted from its unit of meq per gram into meq per unit pore volume, Q_v, because from the electrical point of view it is this quantity that is more proportional to the effect of the clay. From its definition, Q_v can be written as:

$$Q_v = \frac{\rho_{dcl}\ V_{dcl}\ CEC_{cl}}{\phi_t}. \tag{21.2}$$

where ρ_{dcl} is the dry clay density, $V_{dcl} = (1 - \phi_{tcl})V_{cl}$ is the dry clay volume and CEC_{cl} is the CEC of the pure clay. Hill, Shirley, and Klein found an empirical relationship between V_{cbw} and Q_v for saline or moderately saline water [9]:

$$V_{cbw} = Q_v\phi_t\left(\frac{0.084}{\sqrt{n}} + 0.22\right) \tag{21.3}$$

where n is the salt concentration in moles per liter. Alternately, in the Dual Water model, V_{cbw} is calculated from the surface area of the layer and its thickness [10]. The surface area per meq, v, is 450 m^2/meq from Fig. 21.2. In sufficiently saline solutions the thickness of the double layer, x_s, is determined by the thickness of the Stern layer, which is approximately 6.2Å at room temperature (see Fig. 3.9). The volume of bound water, $v_Q^s = vx_s$, can then be calculated as 0.28 mL/meq at room temperature. Multiplying by Q_v gives the volume of bound water per unit pore volume, and then by ϕ_t to obtain bound water as a fraction of rock volume:

$$V_{cbw} = \alpha v_Q^s\ Q_v\ \phi_t. \tag{21.4}$$

The parameter α accounts for the fact that as the salinity drops the diffuse layer in Fig. 3.9 becomes increasingly important and contributes to the bound water. The value of α is unity if salinity is above approximately 20 ppk but increases above 1 for lower salinities. The variation of α and v_Q^s with temperature is calculated theoretically and experimentally in the Dual Water model [10].

Thus, using either the Dual Water or the Hill, Shirley, and Klein equations, V_{cbw} can be calculated from Q_v and ϕ_t, while Q_v can be related to V_{dcl} using Eq. 21.2 assuming values for the density and CEC of the clay present.

21.2.3 Shale Distribution

The manner in which clay is distributed in formations has an impact on some log measurements. For this reason, log analysts have identified three types of distribution: laminated, structural, and dispersed. These are illustrated in Fig. 21.4, which is best understood by considering how the porosity is affected when shale is introduced into an initially clean sand. Dispersed shale is present throughout the pore space, and reduces the original porosity without affecting the grain space. Structural shale is part of the framework structure, so that the original porosity is not altered. Laminated shale appears as discrete interspersed layers of shale in an otherwise clean sandstone, with the shale reducing the volume of both matrix and porosity.

Thus, as shale volume increases, a plot of porosity versus shale volume will show different trends depending on the distribution. Figure 21.5 shows an example of adding shale with 15% bound water to a sand of 33% porosity. The results are plotted in terms of total porosity and the sand fraction that might be derived from a GR log. As shale laminations are added to the sand, the sand fraction and the porosity drop until the laminations fill the whole volume, leading to a total porosity equal to the wet clay porosity and a sand response of zero. When dispersed shale is added, its volume increases until it fills the original pore volume, while the structural shale increases until it has replaced all the sand. The end points for the dispersed and structural cases are not so obvious as for the laminated case, and are left as an exercise (Problem 21.4). The plot illustrates how the trend of porosity with sand volume in a formation

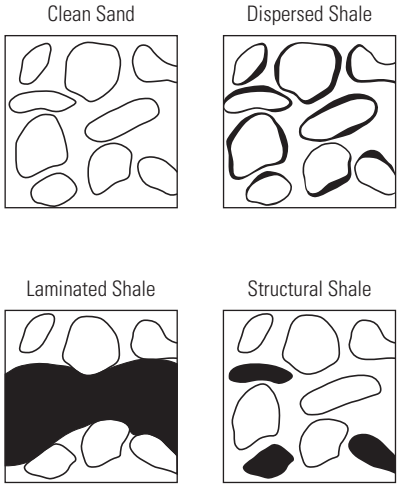


Fig. 21.4 Classification of shale by distribution. From Poupon et al. [11].

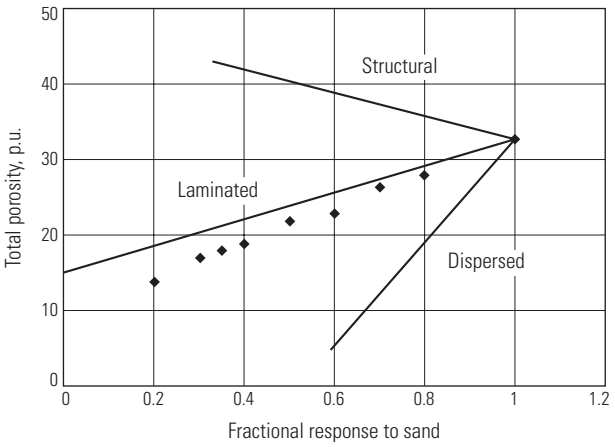


Fig. 21.5 Effect of shale distribution when adding a shale with 15% bound water to a sand with 33% porosity. For the hypothetical data points shown, the plot suggests that the shale was mainly laminated. Adapted from Thomas and Stieber [12]. Used with permission.

can be used to determine the type of shale distribution [12]. However, some caution is needed since in practice the bound water associated with the three types of shale may not be the same. The method also assumes that no other factors are affecting the porosity or its determination from logs.

Dispersed shale is of great interest for hydrocarbon reservoir evaluation even if it occurs at small volume concentrations. (In practice this type of shale is essentially clay.) As a result of the use of the scanning electron microscope, several types of distributions have been identified: pore filling, pore lining, and pore bridging. Dramatic photomicrographs of these three types are shown in Fig. 21.6.

Almon and Davies have studied the impact of some dispersed clay minerals on hydrocarbon production [6]. The problem resulting from the occurrence of kaolinite is related to its structure. Stacks of kaolinite, seen in the upper photograph of Fig. 21.6, are characterized by a booklike shape. These stacks are loosely attached to sand grains and can be detached by high flow rates. Because of the large size of these stacks, they can block large pore throats, resulting in a permanent, irreversible damage to the permeability.

The members of the montmorillonite family pose problems because of their large specific surface area and their swelling capability. Due to the affinity of the clay particles for water, the production of water-free oil in the presence of high water saturation has been attributed to montmorillonite. Unless its presence is recognized, productive zones may be abandoned because of derived S_w values which appear too high. The swelling of the clays (produced by fresh water) also can cause the particles to dislodge and plug pore throats. In this case, oil-based mud or KCl additives must be used to prevent formation damage. Under temperature and with depth, montmorillonite is gradually changed into illite, so that in a given region there is a certain depth below which montmorillonite is unlikely.

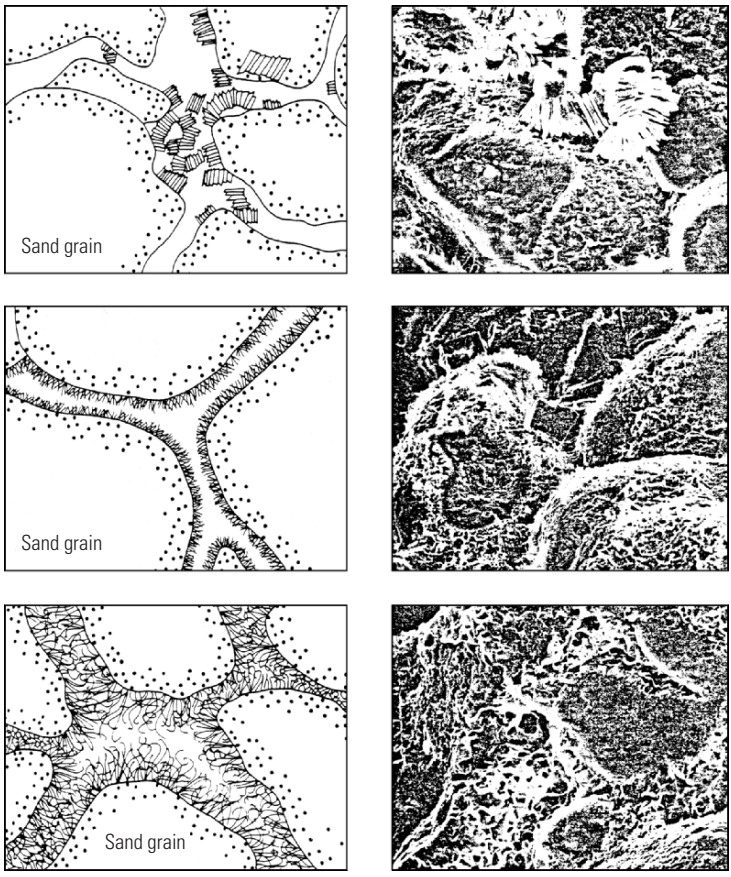


Fig. 21.6 Photomicrographs of dispersed clay in sandstone reservoir rocks, described as (from top) pore filling, pore lining, and pore bridging. Adapted from Almon [13]. Used with permission.

The large specific surface area of illite can create large volumes of microporosity that result in high values of S_w. In the lower photo of Fig. 21.6, long filaments of illite are shown to have completely bridged the pore volumes. In this case, the porosity reduction may not be very great, but certainly the impact on permeability will be significant. Members of the chlorite family, particularly the iron-rich types, are sensitive to acid, which is sometimes injected to stimulate production by dissolving carbonate cements. Exposing chlorite to acid precipitates a gelatinous iron compound, which may permanently halt production.

21.2.4 Influence on Logging Measurements

For a summary of the influence of clay on a few of the log measurements considered thus far, refer to Table 21.2. Implicit in this table is the idea that all measurements

Table 21.2 Influence of different clay properties on logging responses.

Log parameter	Chemistry/ structure	Surface area	Clay distribution
R_t		CEC	Yes
ρ_b	Yes		Yes
P_e	Fe		
ϕ_n	$(OH)_x$	B?	
Σ	K,Fe	B,Gd?	
Δt			Yes
GR	K	Th, U?	
NMR	Fe	surface/vol	
Images			Yes

are affected by the quantity or volume fraction of clay present in the formation. In addition, there are perturbations due to any of three clay descriptors: the chemistry, surface area, or distribution of clay in the formation.

The chemical composition has a large impact on P_e, primarily through the presence of iron. The concentration of hydroxyls will strongly influence the neutron porosity response. As can be seen in Fig. 21.1 the clay groups fall into two types: those with four OH^- ions such as mica, montmorillonite, and vermiculite, and those with eight OH^- such as kaolinite and chlorite. The higher hydrogen content of the latter will have a much large effect on the neutron porosity measurement. Highly absorptive constituents such as iron and potassium will also affect the capture cross section Σ, and the presence of potassium in the clay mineral will influence the gamma ray. Iron increases the NMR surface relaxation, shortening T_1 and T_2.

The surface area of the clay will have a large impact on the resistivity distortion, because of the associated cation exchange capacity, which determines, in part, the inherent resistivity of the clay. The surface area may contribute to the adsorption of other ions, of which some are radioactive and others have a large capture cross section. Consequently it will play a role in the value of Σ and gamma ray measured in a clay. For the same reason, silts, which have a grain size intermediate between clay and sand, are often radioactive. (Silts are also radioactive due to the frequent presence of feldspars, which contain potassium.) In NMR measurements, a large surface area reduces T_1 and T_2 by increasing the chance that protons will relax quickly.

The clay distribution will largely affect the resistivity measurement: a laminated shale will produce quite different results from the same volume of a dispersed clay, because of anisotropy or accessible surface. The effect of distribution on porosity, and hence on porosity measurements, was seen in Fig. 21.5 above. The appropriate grain density and travel time for a laminated shale may also be different from that of a dispersed clay.

A slightly more quantitative list of logging tool responses to a variety of minerals can be found in Table 21.3. The portion concerning clay minerals will be useful in later discussions. It will become apparent that deriving the volume of clay from logs is a rather indirect process in which no one measurement can be relied on to give

Table 21.3 Logging parameters for sedimentary minerals. Note that the clay responses are for wet clays. From Schlumberger [15].

Name	Formula	ρ_{log} g/cm^3	ϕ_{cnl} p.u.	ϕ_{aps} p.u.	Δt_c μs/ft	Δt_s μs/ft	P_e	ϵ fd/m	GR	Σ c.u.
Silicates										
Quartz	SiO_2	2.64	-2	-1	56	88	1.8	4.65	low	4.3
Zircon	$ZrSiO_4$	4.5	-3				69		low	6.9
Carbonates										
Calcite	$CaCO_3$	2.71	0	0	49	88	5.1	7.5	low	7.1
Dolomite	$CaMgCO_3$	2.85	1	1	44	72	3.1	6.8	low	4.7
Siderite	$FeCO_3$	3.89	12	3	47		15	$\tilde{7}$	low	52
Oxidates										
Hematite	Fe_2O_3	5.18	11		43	79	21		low	101
Magnetite	Fe_3O_4	5.08	9		73		22		low	103
Phosphates										
Hydroxy-apatite	$Ca_5(PO_4)_3$ OH	3.17	8		42		5.8		low	9.6
Feldspars										
Orthoclase	$KAlSi_3O_8$	2.52	-3		69		2.9	5	high	16
Albite	$NaAlSi_3O_8$	2.59	-2	-2	49	85	1.7	5	low	7.5
Anorthite	$CaAl_2Si_2O_8$	2.74	-2		45		3.1	5	low	7.2
Clays										
Kaolinite	$Al_4Si_4O_{10}$ $(OH)_8$	2.41	37	34			1.8	5.8	med	14
Muscovite	$KAl_2(Si_3Al$ $O_{10})(OH)_2$	2.82	20	13	49	149	2.4	7	high	17
Glauconite	$K_{0.7}(MgFe_2$ $Al)(Si_4Al_{10})$ $O_2(OH)$	2.86	38	15			4.8		high	21
Chlorite	$(Mg,Fe,Al)_6$ $(Si,Al)_4$ O_{10} $(OH)_8$	2.76	52	35			6.3	5.8	high	25
Illite	$(K_{1,1.5}Al_4$ $(Si_{6.5,7}Al_{1,1.5}$ O_{20} $(OH)_4$	2.52	30	17			3.5	5.8	high	18
Montmor-illonite	$(Ca,Na)_7$ $(Al,Mg,Fe)_4$ $(Si,Al)_8O_{20}$ $(OH)_4(H_2O)_n$	2.12	60	60			2.0	5.8	high	14
Evaporites										
Halite	NaCl	2.04	-3	21	67	120	4.7	6	low	754
Anhydrite	$CaSO_4$	2.98	-2	2	50		5.1	6.3	low	12
Gypsum	$CaSO_4$ $(H_2O)_2$	2.35	60+	60	52		4.0	4.1	low	19
Sylvite	KCl	1.86	-3				8.5	4.7	high	565
Barite	$BaSO_4$	4.09	-2				267		low	6.8
Sulfides										
Pyrite	FeS_2	4.99	-3		39	62	17		low	90
Coals										
Anthracite	$CH_{.36}N_{.01}O_{.02}$	1.47	38		105		0.16		low	8.7
Bituminous	$CH_{.79}N_{.02}O_{.08}$	1.24	60+		120		0.17		low	14
Lignite	$CH_{.85}N_{.02}O_{.21}$	1.19	52		160		0.2		low	13

the right answer in all conditions. How then do we know that we have the "right" answer? Qualitatively the result of the total log interpretation must be consistent with other data, such as production results. Quantitatively the results can be compared with those measured on core samples by x-ray diffraction, x-ray fluorescence or Fourier Transform Infrared (FT-IR) spectroscopy [14]. Such measurements have their own limitations, but these are beyond the scope of this book.

21.3 SHALE DETERMINATION FROM SINGLE MEASUREMENTS

The major effects of shale or clay on individual measurements have been discussed in the relevant chapters. The reduction in the SP was shown in Fig. 3.11. The position of clay bound water in the NMR distribution was shown in Fig. 16.34. Transforms between gamma ray and shale volume were given in Fig. 11.5. Although such an estimate of V_{shale} from gamma ray can be misleading, it is the mainstay of traditional log interpretation and warrants further examination. Some of the pitfalls are illustrated by the log in Fig. 21.7. Taking the minimum reading as 20 gAPI (from the bottom at 18,90 ft) and the maximum at 80 gAPI leads to the GR clay volume shown in Fig. 21.8, where it is compared to the clay volume from cores. Although the GR curve reads correctly around 1,870 ft, it is clearly too high at 1,730 and 1,780 ft. There are also large spikes on the GR curve that are not caused by clay.

The GR clay volume was calculated assuming a linear transform (line 1 in Fig. 11.5). Results could be improved by selecting another minimum reading or by using one of the other GR transforms. In fact it would be possible to develop a local transform between GR index and core data that could be used in other wells of the area. Such local transforms are a feature of many log interpretation procedures, and can give reasonable results. In this case both the SP and the neutron–density give better estimates of clay volume, as discussed below.

This example is typical in that when the gamma ray errs it does so by overestimating the clay volume, as might be expected since minerals other than clay can be radioactive. Other single curve clay indicators such as SP, resistivity and neutron also err by over-estimation. For example, the SP deflection opposite a permeable bed is reduced by clay but is also reduced by shallow invasion or in thin beds. On this basis, early computer programs estimated the clay volume from as many indicators as possible and then took the minimum value calculated at each depth as the correct value [11].

A more direct approach can be taken in laminated formations by using image logs. In an example such as that of Fig. 6.6, a suitable cutoff can be chosen to divide the image into sand or shale. The shale percentage is calculated directly by counting the amount of shale within an interval. This is a convenient and direct method of estimating shale volume in laminated formations.

Otherwise it seems clear that a better estimate ought to be provided by combining two measurements or by a more direct measurement of the elements in clays. Before considering such methods, we will examine in more detail how clay volumes can be

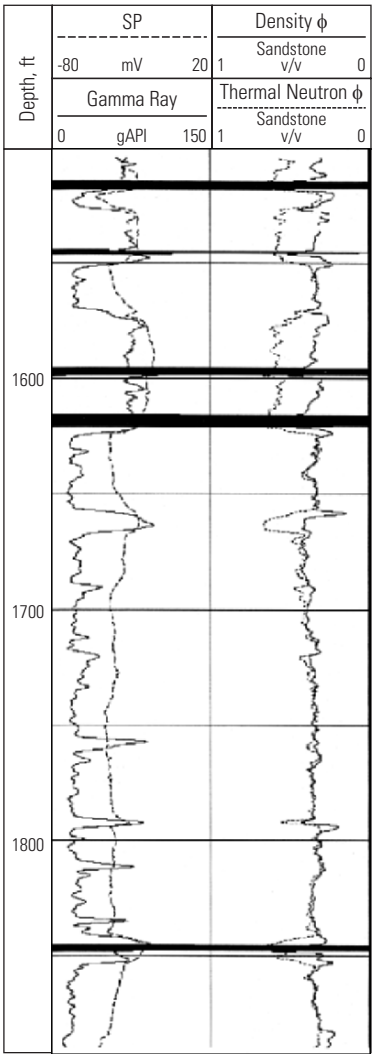


Fig. 21.7 A set of logs from a sand-shale sequence. The black bands are coals. From LaVigne et al. [16]. Used with permission.

obtained from three nuclear measurements – photoelectric effect, neutron porosity, and capture cross section.

21.3.1 Interpretation of P_e in Shaly Sands

An interesting quantitative clay indicator for use in shaly sands can be constructed from the P_e measurement. It is based on the fact that P_e values measured in shales are primarily related to the iron content of the clay minerals. Without the presence of iron,

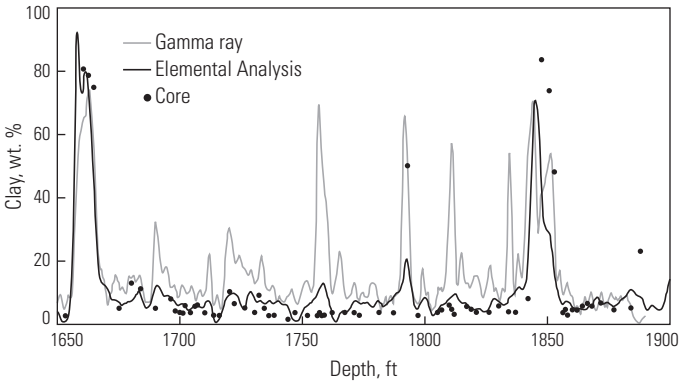


Fig. 21.8 Clay weight % for the well shown in Fig. 21.7 derived from gamma ray, elemental analysis and by FTIR spectroscopy on cores. Adapted from Herron [17].

the P_e of the aluminosilicates would reflect the silicon content and be indistinguishable from sand. A clay indicator can be formed by calculating an artificial P_e curve based on the measured values of formation density, assuming that the matrix is sand, and comparing it to the measured value of P_e. Figure 21.9 shows such an artificial P_e log with shading between the value expected for clean sand and the measured value. The shaded portion of excess P_e is primarily the result of the iron in the clay minerals, although there is an exception near 2750 ft (see Problem 21.8.1).

The quantitative interpretation of the excess P_e can best be understood in terms of another method of calculating the P_e of mixtures. But first we use the parameter U to determine the base P_e curve which reflects the density variations. The tacit assumption here is that in a shaly sand, the matrix density of the sand and the shale are not all that different. Shale can be considered as quartz, silt plus clay minerals which might have grain densities between 2.6 and 2.8 g/cm^3. Thus a rough estimate of porosity, which is sufficient to determine the small variation induced on P_e, can be obtained from ρ_b by assuming a grain density close to 2.65 g/cm^3. The expected sand value $P_{e,exp}$ can then be computed from the volumetric relation for U:

$$U_{exp} = U_{fl}\,\phi + U_{ma}(1-\phi)\,, \tag{21.5}$$

and

$$P_{e,exp} = \frac{U_{exp}}{\rho_{e,log}}\,. \tag{21.6}$$

Consider a log reading of 2.34 g/cm^3. First we estimate the porosity from:

$$2.34 = 1.00\,\phi + 2.65\,(1-\phi), \tag{21.7}$$

from which we find that the porosity, ϕ, is about 20%. From Table 12.1 and Eq. 21.5 the expected value of U is found to be:

$$U_{exp} = (0.4)\,(0.2) + (4.79)\,(0.8) = 3.91\,. \tag{21.8}$$

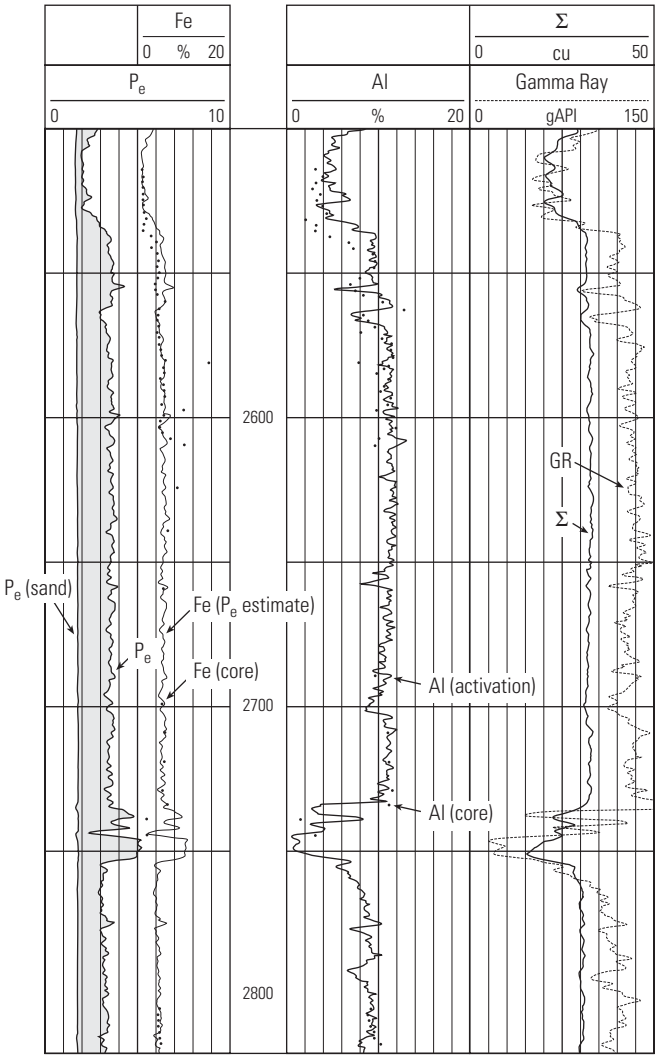


Fig. 21.9 Log example for the determination of iron content from P_e. In track 1, the observed P_e is compared to the value of P_e expected in a sandstone of a porosity determined from a density log. The shading corresponds to the excess P_e. The Fe estimate is compared to core analysis. Track 2 shows a comparison between Al concentration data from an activation log and core measurements. Track 3 displays Σ and gamma ray as indicators of shale.

From Eq. 21.6 the value of $P_{e,exp}$ is found to be 1.67, after converting ρ_b to ρ_e. However, this step can usually be omitted.

It should be obvious that elements with large atomic numbers can have a large effect on the global value of P_e, even when they occur as very small weight concentrations.

Equally obvious is the interpretation of the excess P_e: it is the value expected for the dominant host matrix plus a quantity due to the trace heavy mineral. In the case of iron it can be written as:

$$P_e \approx \sum_i \left(\frac{Z_i}{10}\right)^{3.6} Wt_i + \left(\frac{26}{10}\right)^{3.6} Wt_{Fe} . \tag{21.9}$$

The weight fraction of iron in the formation is simply the excess P_e ($= P_{e,log} - P_{e,exp}$) divided by 31.2. For any other suspected high Z material, the factor of division is $(Z/10)^{3.6}$.

The approximation in Eq. 21.9 results from the fact that presumably the concentrations of the host elements sum to unity, but an additional element, which was unaccounted for, has been added. If 10% of the formation mass is due to iron, then the weight of H, O, and Si must be adjusted downward. However, if we perform the calculation we see that little difference will occur in the expected P_e. This approximation is obviously better for trace amounts of high Z materials.

To demonstrate the validity of this procedure, refer to the first track of Fig. 21.9, which shows the excess P_e and its conversion to the iron weight fraction using Eq. 21.9. The log-derived curve is compared to the analysis of the iron content of core samples, which are shown as small stars. There is very close agreement.

21.3.2 Neutron Response to Shale*

There are three factors that control the response of a neutron device to shale: the hydroxyl content, the presence of thermal absorbers such as Boron or Gd, and the density of the assemblage. The first two effects are clearly seen in Fig. 21.10 where three versions of porosity are shown in a sandstone section bounded above and below by shaly formations. The density porosity is calculated using the appropriate matrix density for sandstone. The two neutron traces correspond to a thermal and an epithermal device recorded simultaneously. All three curves are coincident in the clean sand in the middle of the figure. In the shale section above and below, the curves separate. The largest portion of the separation is due to the quantity of hydroxyls in the clay minerals. The small excess of the thermal measurement over the epithermal measurement is attributed to the additional thermal neutron absorption by elements associated with the clay minerals. Experimental measurements for one particular thermal neutron tool [19] have shown that the excess porosity due to the presence of large amounts of neutron absorbers alone is no more than 6–8 p.u. It is reasonable then to attribute the largest part of the thermal neutron and density separation in shales to the hydroxyls; the thermal absorbers are just a minor perturbation.

Regarding the role of hydrogen, we need to realize that in porous, water-filled, clay-free calibration formations, there is a built-in correlation between the formation hydrogen content and its density. Density does have a role in the response of a neutron

*This section is largely extracted from Ellis et al. [20]

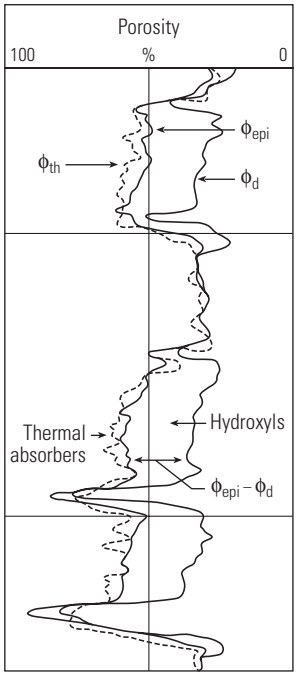


Fig. 21.10 Three versions of apparent porosity: one from density and the others from epithermal and thermal neutron porosity devices. The separations from density porosity are a result of the OH^- content of clay minerals. Additional separation is caused by thermal absorbers. From Ellis [18].

tool and it is certainly an inherent factor in the slowing-down length, since that quantity varies inversely with formation density. In shale, however, depending on the quantity of clay minerals in the mix and whether the 4- or 8-hydroxyl clay mineral is present, there is no reason to expect that the density and hydrogen content will follow the water-filled, clay-free calibration formation correlation. However, this situation is easily accommodated using slowing-down length as the predictor of the neutron response.

A demonstration of this is seen in Fig. 21.11 where the response of a generic tool to porous shaly sands has been indicated. The Monte Carlo model was used to compute the counting rate for a formation consisting of a "rock" that is half sandstone (SiO2) and half kaolinite [21], for water-filled porosities ranging from 0 to 40 p.u. The computed ratios versus the SNUPAR-calculated values of slowing-down length, L_s, are indicated in the figure by black dots. It is seen that the "shaly sand" points lie on a response line relating ratio to formation slowing-down length determined for the generic tool in water-filled formations of the three major lithologies.

To demonstrate the effect of the volume of shale and the type of shale, three numerical examples were run using SNUPAR and described elsewhere [18]. One was a shaly sand containing 50% by volume of illite (an $(OH)_4$ clay mineral) and another

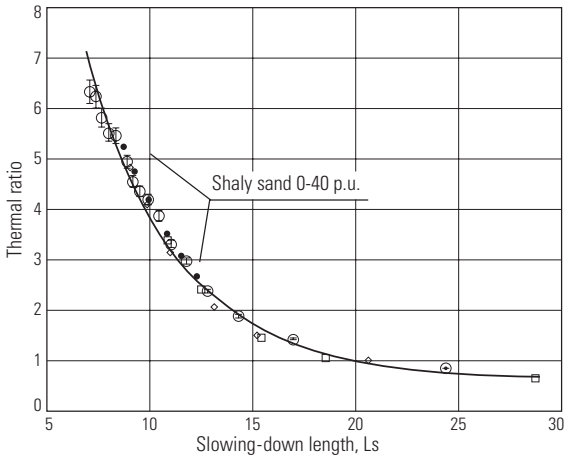


Fig. 21.11 The thermal neutron ratio of shaly sand formations, indicated by the black dots, has the same relation to slowing down length as that of the three major lithologies, indicated by squares (sandstone), diamonds (dolomite), and circles with error bars (limestone). From Ellis et al. [20]. Used with permission.

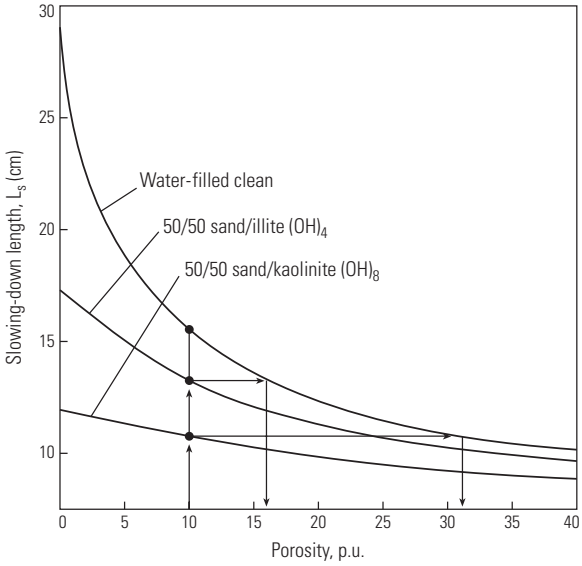


Fig. 21.12 Using L_s to predict the effect of artificial shale-sand compositions on neutron tool response. From Ellis [18].

containing 50% by volume of kaolinite (an $(OH)_8$ clay mineral); the third formation corresponded to a clean water-filled sandstone. In Fig. 21.12, the top curve is the variation of water-filled sandstone and constitutes the "sandstone" transform between

the ratio (or its equivalent slowing-down length) and porosity. Now consider that all three formations are at a porosity of 10 p.u. In the 50/50 sand/illite, the L_s value is less than expected in sand and consequently its apparent porosity is about 16 p.u. The slowing-down length in the 50/50 sand/kaolinite mixture is even lower than expected. Its L_s value corresponds to about 31 p.u., which is similar to the effects we see on logs.

This exercise also points out the danger of converting neutron/density separations into shale volumes since the shift will depend not only upon the shale volume but also upon the shale type or mixture. For example the separation between the epithermal and density porosity, $\phi_{epi} - \phi_d$ in a pure four-hydroxyl clay is 12 p.u. whereas it is 35 p.u. in a pure eight-hydroxyl clay.

21.3.3 Response of Σ to Clay Minerals

Although the conventional use of the formation thermal capture cross section (Σ) is for the determination of water saturation in cased-hole applications, it can also be used as a shale indicator. This is clearly seen in the log of Fig. 21.9 where Σ and gamma ray are presented in the third track. In the shale zones, Σ is in the range of slightly more than 30 cu and decreases significantly in the two clean zones. The observed correlation with shale content is due to the fact that some of the clay groups contain elements with relatively large thermal absorption cross sections. Two examples are potassium and iron (see Table 21.3). Thus if the composition of a clay mineral is well-known, its corresponding Σ can be determined. Table 21.3 indicates some typical Σ values, which range from 14 to 25 cu. The largest values are associated with clay minerals containing K and Fe.

An interesting application of the Σ measurement is in combination with the separation between ϕ_d and ϕ_{epi} (or ϕ_{th} if ϕ_{epi} is not available). This conveniently distinguishes the four main clay types encountered in hydrocarbon reservoirs (Fig. 21.13).

One difficulty in exploiting Σ for quantitative clay volume estimates is that frequently trace elements with extremely large thermal absorption cross sections are associated with some clay minerals. These might include B, Gd, and Sm. Depending on the concentration of these and other rare earth elements, the observed Σ may be much larger than that expected from Table 21.3, which was computed for average chemical compositions of the dominant elements. In the well of Fig. 21.10 (which had extensive core analysis of trace elements), boron, in concentrations of up to 400 ppm, was found to be associated with the illite but not with kaolinite. This may reflect the large difference in specific surface areas between the two clay minerals.

Another difficulty with the use of Σ is that it responds to elements present in both the rock matrix and formation fluid. Chlorine is high on the list of common elements with a significant absorption cross section, and it is present in substantial quantities in formation fluids. Consequently there is some difficulty in extracting the Σ value for the rock matrix if there are uncertainties in porosity or the nature of the formation fluids. A more appealing measurement would be sensitive only to the rock matrix. One such measurement is elemental analysis and is discussed below, after first considering one of the most important methods of clay analysis – the neutron–density cross plot.

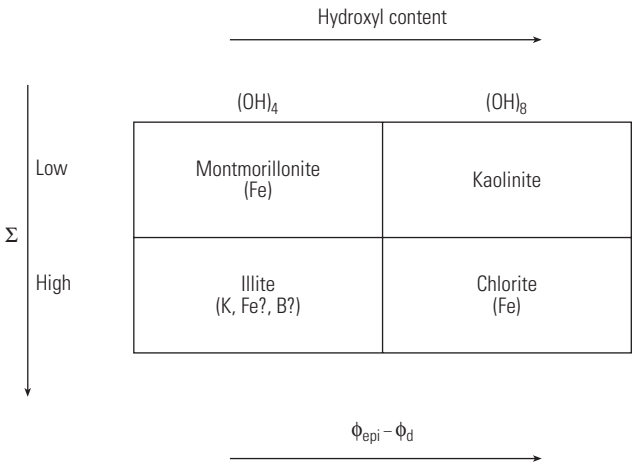


Fig. 21.13 Measurements of capture cross section (Σ) and hydroxyl content (through $\phi_{epi} - \phi_d$) distinguish the four main clay minerals.

21.4 NEUTRON–DENSITY PLOTS

The neutron–density cross plot is of fundamental importance for many log interpretation procedures. Both measurements are affected by porosity, hydrocarbon density, and lithology, which includes both clay and nonclay minerals. If we know two of these factors we can solve for the other two. For example, in an oil- or water- filled shaly sand we can solve for clay volume and porosity. For gas detection in a sand, we can use an estimate of clay volume from another source and calculate porosity and hydrocarbon density.

To understand the traditional approach to these calculations, refer to Fig. 21.14 which shows a cross plot of the neutron and density porosity values for the logs of Fig. 21.7. Clean water-bearing sandstones will fall on the straight line of equal density and neutron porosity estimates. Gas-bearing sandstones would plot to the left of this line. Because of the additional hydrogen in the form of hydroxyls, the apparent neutron porosity in shales is higher than the porosity estimate from the density tool. From the cross plot in a very shaly zone (determined usually by reference to the gamma ray), one can establish a 100% shale point. If we connect this point to the 0 p.u. and 100 p.u. points, we can then establish a linear grid which can (if we believe this model) give the shale fraction and porosity corresponding to any pair of density and porosity readings, as indicated in Fig. 21.15.

This leads to a graphical method for obtaining formation porosity, as well as an estimate of shale volume. Consider the points near the region marked A in Fig. 21.14. According to the scaling procedure for Fig. 21.15, in a water-filled formation they would be interpreted as containing about 25% shale. The porosity would be obtained by projecting a line parallel to the shale trend until its intersection with the sand line. These points appear to be associated with a formation of about 32% porosity. Clearly

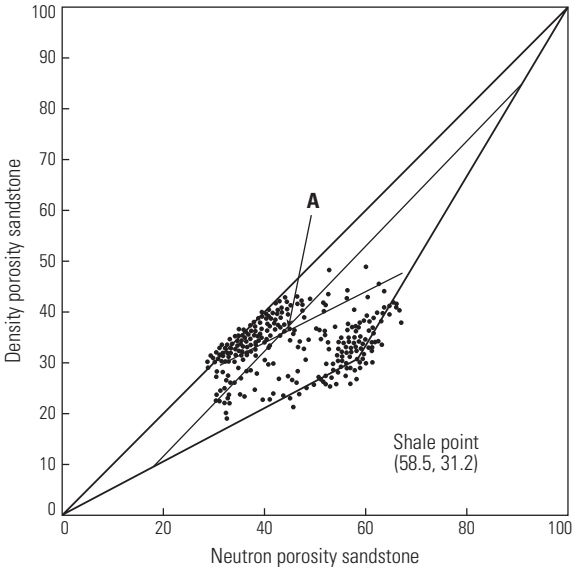


Fig. 21.14 A neutron–density cross plot showing data from the log of Fig. 21.7. The shale point has been picked from the most south-easterly data points. From LaVigne et al. [16]. Used with permission.

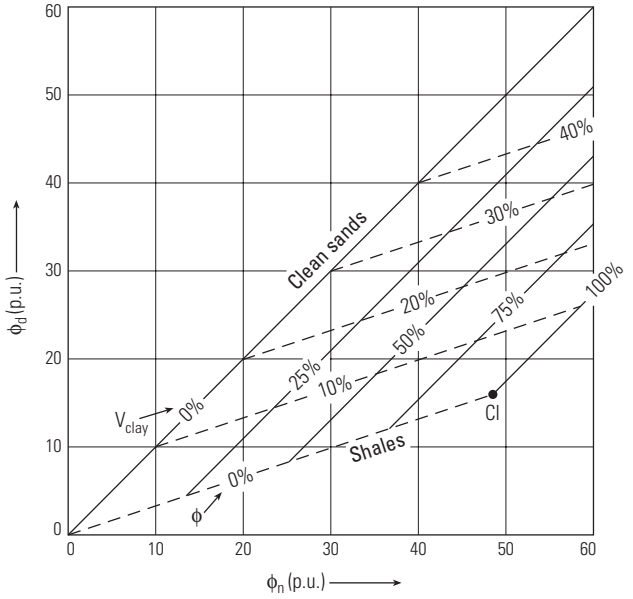


Fig. 21.15 Chart for the determination of clay volume from the neutron–density cross plot or, in the presence of another independent indicator of V_{cl}, the correction of the neutron–density reading for clay. Courtesy of Schlumberger [22].

several conditions need to be satisfied for this method to work. The matrix needs to be sandstone, or be otherwise well-defined; the effect of hydrocarbon, especially gas, needs to be allowed for. Alternatively, if the clay volume is determined from another measurement, the same graphical technique can be used to remove its effect. The crossplot is then employed for gas or lithology analysis.

This method has been the backbone of interpretation in siliciclastic reservoirs since the late 1960s [11]. It does, however, have some limitations. The porosity calculated is an effective porosity, but is not well defined since the massive shales from which the shale points are picked contain both wet clay and isolated pores. The method also assumes that the shale in the reservoir has the same composition as the massive shale. Without other information this is the best that can be done. But for the logs in Fig. 21.7 it is known that the clays in the reservoir are kaolinite. Taking an average chemical composition and structure it is possible to calculate the density and neutron porosity of dry kaolinite (the latter will depend on the neutron device used) [16]. This computation excludes any clay bound water but includes the hydroxyl ions. The result is known as the dry clay point and is plotted along with log data in Fig. 21.16.

The traditional graphical technique can be applied, but using the kaolinite point instead of the empirical shale point. The calculated porosity is then the total porosity, which can be corrected to effective porosity as described in section 21.2.2. The shale lies between the kaolinite point and water, showing that it contains, as expected, some water. How much is not so clear since the shale is known to contain some illite as

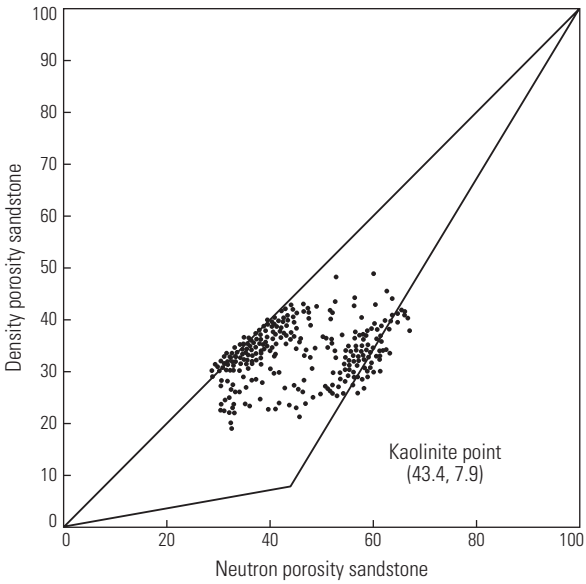


Fig. 21.16 The same neutron–density cross-plot as in Fig. 21.13 but with the kaolinite point calculated from knowledge of chemical composition and measurement response. From LaVigne et al. [16]. Used with permission.

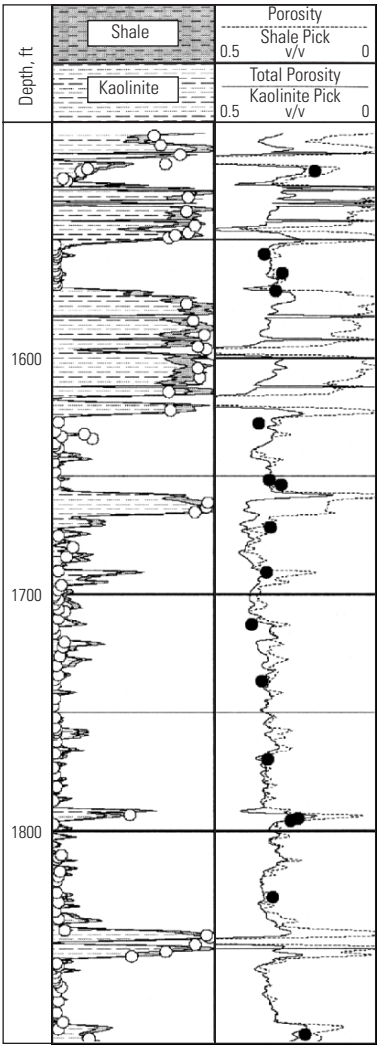


Fig. 21.17 In track 2, porosity as calculated using an empirical shale point, and using a theoretically calculated kaolinite point, and porosity from core. In track 1, kaolinite and remaining dry shale volumes calculated using the kaolinite point, and clay volume from core. From Lavigne et al. [16]. Used with permission.

well as kaolinite, so that a different dry clay point ought to be used to evaluate the shales. Multiple clays can be handled by more sophisticated numerical techniques to be discussed in Chapter 22. The result of applying one such technique is shown in Fig. 21.17 where it is compared to the core porosity and clay volume. Since there are unlikely to be any isolated pores in such a high-porosity sandstone, the core

measurement gives total porosity, and therefore agrees better with results from the kaolinite pick.

Employed in this way, and subject to knowing the nonclay lithology and the hydrocarbon density, the neutron–density cross plot can give one of the most accurate estimates of clay volume. Other cross plots, for example sonic and neutron, or sonic and density, are generally less useful because the response of the sonic measurement to clay is less well understood and depends as much on distribution as on volume. These and other cross plot methods are discussed in Chapter 22 at the same time as their application to lithology determination.

21.5 ELEMENTAL ANALYSIS

We have seen that almost any well-logging device can be used to detect clays under specific circumstances. However, no single method discussed so far can be counted upon to provide an estimate of the clay content at all times. One hope of a more independent method is provided by elemental analysis. Figure 21.18 shows the correlation between total clay content and the weight percent of nine elements that can be measured by natural or induced spectroscopy.

In most wells, aluminum gives the best correlation, which is not surprising because aluminum is an integral part of clay chemical composition. Potassium sometimes correlates strongly when the dominant clay is illite (as in this example), but the correlation is perturbed by potassium in feldspars, micas, and other minerals. Th, U, titanium (Ti), and gadolinium (Gd) are trace elements that are often enriched in shales, but these elements do not generally reveal a sufficiently reliable correlation for quantitative use. Silicon shows a strong anti-correlation, decreasing from 46.8% by weight in pure quartz to about 21% by weight in clays. Iron is associated with heavy minerals, such as siderite and pyrite, and the clay minerals illite, chlorite, and glauconite. Calcium occurs primarily in calcite and dolomite.

Aluminum is the best single elemental indicator of clay but, although reasonable results could be achieved (see Fig. 21.9), it is difficult to measure in the borehole, as discussed in Section 15.5. A more practical method is based on the anti-correlation with silicon [24]. As can be seen from the plot of clay volume versus ($100 - SiO_2$) in Fig. 21.19 the anti-correlation is good, but is disturbed by the presence of carbonate minerals, siderite, and pyrite. These minerals act like clay to reduce the amount of silicon, but can be accounted for by measuring calcium, iron, and magnesium (Mg). Thus, by combining four elements – Si, Ca, Fe, and Mg – it is possible to find a strong correlation with total clay, W_{cl}, that is given by:

$$W_{cl} = 1.67(100 - SiO_2 - CaCO_3 - MgCO_3 - 1.99Fe) \qquad (21.10)$$

where each term is expressed in its percentage weight, and the elements are expressed in terms of their oxides [24].

Figure 21.20 shows the results of applying this method to 12 wells. In each well there is a small degree of scatter and a near-zero intercept. When examining these plots, it is important to focus on the clay-poor region where reservoirs occur – the

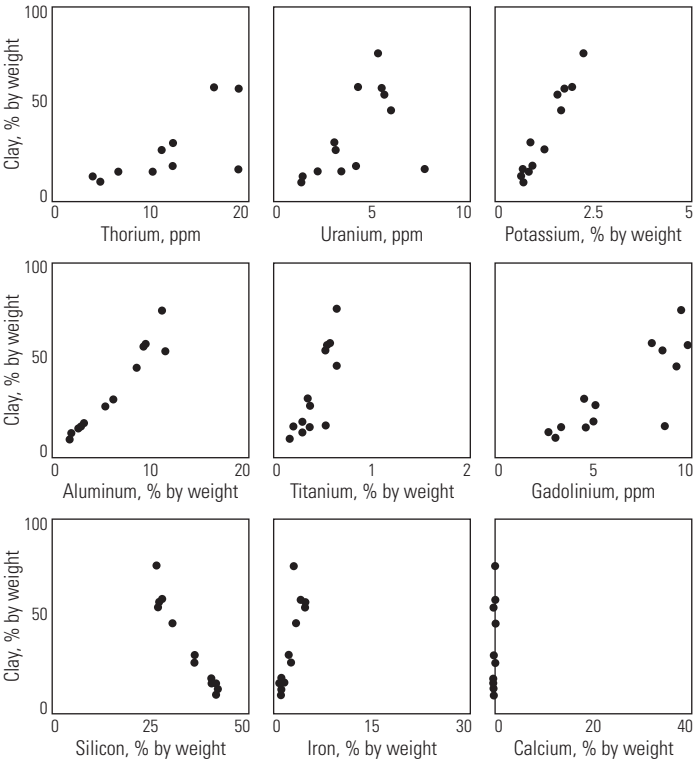


Fig. 21.18 Comparison of the concentrations of various elements measurable by logs with clay concentration in one well. The top row shows elements measured by natural GR spectroscopy. All other elements except Al are measured by capture GR spectroscopy. From Herron and Herron [24]. Used with permission.

correlation in the shales is less important. The slopes are nearly the same except for wells 11 and 12 which contain feldspar-rich sands. Feldspars are aluminosilicates like clays and therefore affect the silicon content. One solution is to use different transforms for arenites (feldspar content < 10%), subarkoses (between 10% and 15%) and arkoses (>25%) .

One problem in applying this method to log data is that magnesium is not measured by either natural or induced gamma ray spectroscopy. However, the amount of magnesium in clays is small so that its absence has little effect on the correlation. Magnesium occurs mainly in dolomite, but in practice the measurement of the total amount of carbonate (calcite + dolomite) from calcium gives a sufficiently accurate correlation in shaly sands. In carbonates, further interpretation may be needed.

Otherwise, as shown in Chapter 15, pulsed-neutron spectroscopy tools measure the weight percent of Si, Ca, Fe, S, Gd, and Ti. Si, Ca, and Fe can be combined to

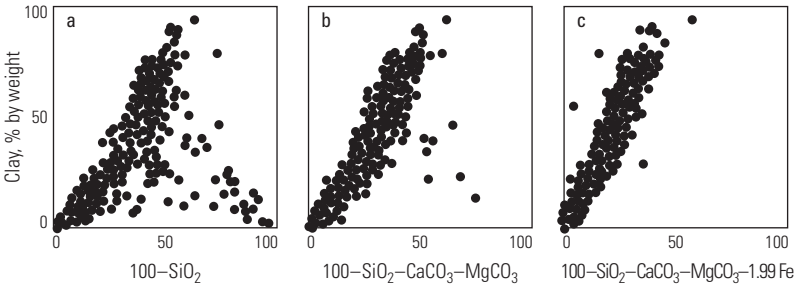


Fig. 21.19 Clay concentration from 12 wells showing (a) the correlation of clay content with (100 – SiO_2); (b) the improvement in correlation once the carbonate minerals have been subtracted; (c) the further improvement once iron-rich minerals such as pyrite and siderite have been subtracted. Adapted from Herron and Herron [24]. Used with permission.

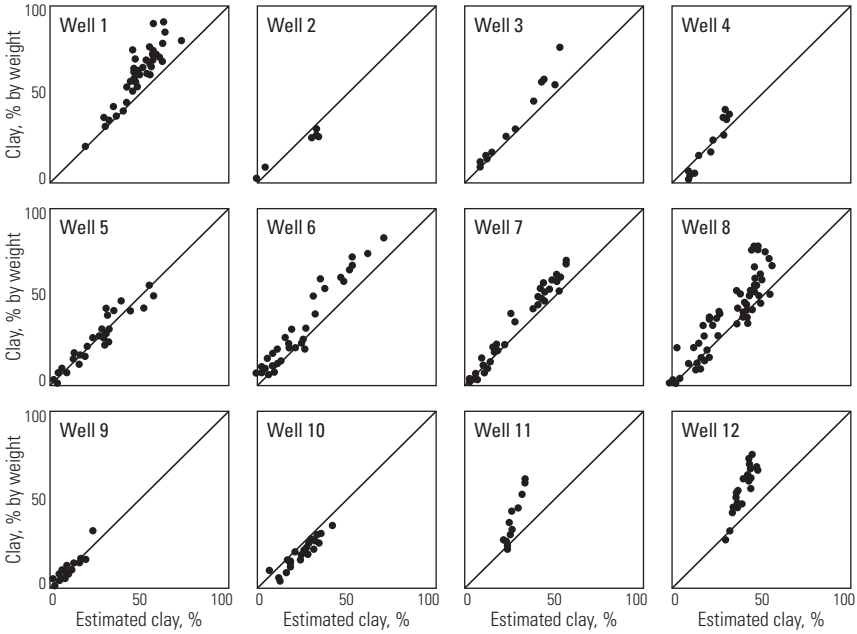


Fig. 21.20 Comparison of measured clay concentration with the concentrations estimated by Si, Ca, Fe, and Mg in the same 12 wells as Fig. 21.19. From Herron and Herron [24]. Used with permission.

give the weight percent of clay from Eq. 21.10 above, which is converted to a volume percent V_{cl} by the equation:

$$V_{cl} = W_{cl}\frac{\rho_{ma}}{\rho_{cl}}(1-\phi) \tag{21.11}$$

where ρ_{ma} is the composite density of all solids, ρ_{cl} is the density of the clay, and ϕ is the porosity.

An example of the results in one well was shown in Fig. 21.8, where they were clearly superior to the clay volume from gamma ray. The advantages of this method are that it is fast, nearly automatic and not subjective. It is well suited to a wellsite or first estimate of total clay volume. However, it is inherently based on correlations that are not always applicable. It also makes no attempt to distinguish between different types of clay, even though these can have important differences on the interpretation of other logs and on producibility. The chapter ends with a brief summary of methods for clay typing.

21.6 CLAY TYPING

For many log interpretations it is sufficient to know the total clay volume. However, as can be judged from Table 21.3 and the preceding discussions, the effect of each clay mineral on a particular measurement can be quite different. Neutron–density separation, P_e and conductivity are especially sensitive to clay type. Thus for the most accurate calculations it is important to know the type and volume of each clay mineral present.

Clay typing is at the heart of geochemical analysis, in which the volumes of each mineral in the formation is determined. When the aluminum measurement was being developed in the 1980s, it was hoped that spectroscopy and other measurements would lead to accurate geochemical analysis from logs [26]. Without Al this is not possible and in the absence of further developments proper geochemical analysis from logs is unlikely.

Some methods of clay typing have already been discussed. The Th vs K cross-plot was discussed in Chapter 11 and the Σ vs $(\phi_n - \phi_d)$ crossplot in Section 21.5 above. The Fe that is present in some clays can be distinguished by either P_e or elemental analysis. Other methods based on multiple measurements are similar to those used to determine non-clay minerals, and will be discussed in Chapter 22. These include further cross plots, and numerical techniques that combine all available measurements to find the solution. Additional information on clay typing will therefore be found in the next chapter.

REFERENCES

1. Grim RE (1968) Clay mineralogy. McGraw-Hill, New York

2. Brindley GW (1981) Structure and chemical composition of clay minerals. In: Longstaffe FJ (ed) Clays and the resource geologist. Mineralogical Association of Canada, Toronto

3. Berner RA (1971) Principles of chemical sedimentology. McGraw-Hill, New York

4. Yariv S, Cross H (1979) Geochemistry of colloid systems for earth scientists. Springer, Berlin

5. Patchett JG (1975) An investigation of shale conductivity. Trans SPWLA 16th Annual Logging Symposium, paper U

6. Almon WR, Davies DK (1981) Formation damage and the crystal chemistry of clays. In: Longstaffe FJ (ed) Clays and the resource geologist. Mineralogical Association of Canada, Toronto

7. American Petroleum Institute (1988) Recommended practices for core analysis (RP40), 2nd ed. API Publishing, Washington, DC

8. Hook JR (2003) An introduction to porosity. Petrophysics 44(3):205-212

9. Hill HJ, Shirley OJ, Klein GE, edited by Waxman MH, Thomas EC (1979) Bound water in shaly sands – its relation to Qv and other formation properties. The Log Analyst 20(3):3–19

10. Clavier C, Coates G, Dumanoir J (1984) Theoretical and experimental bases for the dual-water model for interpretation of shaly sands. Paper 6859 in: SPE J April:153–168

11. Poupon A, Clavier C, Dumanoir J, Gaymard R, Misk A (1970) Log analysis of sand-shale sequences: a systematic approach. J Pet Tech 22(7):867–881

12. Thomas EC, Stieber SJ (1975) The distribution of shale in sandstones and its effect upon porosity. Trans SPWLA 16th Annual Logging Symposium, paper T

13. Almon WR (1979) A geologic appreciation of shaly sands. Trans SPWLA 20th Annual Logging Symposium, paper WW

14. Matteson A, Herron MM (1993) Quantitative mineral analysis by Fourier transform infrared spectroscopy. Society of Core Analysts Technical Conference, paper SCA 9308

15. Schlumberger (2005) Log interpretation charts. Schlumberger, Houston, TX

16. LaVigne J, Herron M, Hertzog R (1994) Density-neutron interpretation of shaly sands. Trans SPWLA 35th Annual Logging Symposium, paper EEE

17. Herron M (1986) Subsurface geochemistry 1. Future applications of geochemical data. Presented at Nuclear Data for Applied Nuclear Geophysics, IAEA Consultants Meeting, April, Vienna

18. Ellis DV (1986) Neutron porosity logs: what do they measure? First Break 4(3):11–17

19. Ellis DV, Flaum C, Galford JE, Scott HD (1987) The effect of formation absorption on the thermal neutron porosity measurement. Presented at the 62nd SPE Annual Technical Conference and Exhibition, paper SPE 16814

20. Ellis DV, Case CR, Chiaramonte JM (2003) Porosity from neutron logs I: measurement. Petrophysics 44(6):383–395
Ellis DV, Case CR, Chiaramonte JM (2004) Porosity from neutron logs II: Interpretation. Petrophysics 45(1):73–86

21. Herron M, Matteson A (1993) Elemental composition and nuclear parameters of some common sedimentary minerals. Nuclear Geophys 7(3):383–406

22. Schlumberger (1989) Log interpretation principles/applications. Schlumberger, Houston, TX

23. Scott H, Smith MP (1973) The aluminum activation log. Trans SPWLA 14th Annual Logging Symposium, paper F

24. Herron SL, Herron MM (1996) Quantitative lithology: an application for open and cased hole spectroscopy. Trans SPWLA 37th Annual Logging Symposium, paper E

25. Grau JA, Schweitzer JS, Ellis DV, Hertzog RC (1989) A geologic model for gamma-ray spectroscopy logging measurements. Nuclear Geophysics 3(4):351–359

26. Colson L, Ellis DV, Grau J, Herron M, Hertzog R, O'Brien M, Seeman B, Schweitzer J, Wraight P (1987) Geochemical logging with spectrometry tools. Presented at the 62nd SPE Annual Technical Conference and Exhibition, paper SPE 16792

Problems

21.1 Compute the specific surface area (m^2/g) for a dry 35% porous sandstone composed of spherical grains with negligible contact area. The diameter of the grains is 250 μm. What is the surface area/cm^3?

21.2 Suppose 1/4 of the available porosity of the sandstone of Problem 21.1 is occupied by kaolinite. What is the surface area/cm^3?

21.3 Verify the relation for Q_v given in Eq. 21.2. Calculate the density of dry kaolinite from the dry clay point shown in Fig 21.16.

21.3.1 From the log in Fig 21.17 calculate Q_v and V_{cbw} in the reservoir at 1,700 ft (ignore the non-kaolinite clays and assume $v_Q = 0.28$ cm^2/meq).

21.4 In Fig 21.5 the fractional response to sand is given by $(R_b - R)/(R_b - R_a)$ where R_b is the response of a measurement such as the GR log in shale, R_a the response in sand, and R the response of a mixture. Assuming $R_b = 5\ R_a$, verify the

end point values of total porosity and fractional response for structural and laminated shale. Use the definition of the end points given in the text, and assume that the initial porosity has no radioactivity.

21.4.1 Plot the relationships between effective porosity and sand volume for dispersed, structural, and laminated shale (analogous to Fig. 21.5 which is for total porosity).

21.4.2 In the sand between 1,670 and 1,790 ft in Fig. 21.17 what do you think is the most likely type of shale distribution?

21.5 In the log of Fig. 21.7 calculate V_{shale} from GR at 1,700 ft taking the minimum gamma ray at 1,870 ft. Compare the result with that shown in Fig. 21.8 where the minimum gamma ray was taken at 1,890 ft.

21.6 From the volumetric mixing law for U:

$$U \approx P_e \rho_b = U_1 V_1 + U_2 V_2 + \cdots + U_n V_n , \tag{21.12}$$

show that the mixing law for any material can be written in terms of the atomic numbers of its constituents as:

$$P_e = (\frac{Z}{10})^{3.6} Wt_1 + \cdots + (\frac{Z_i}{10})^{3.6} Wt_i . \tag{21.13}$$

Wt_i is the weight fraction of element i in the mixture.

21.7 What is the percent by weight of Al contained in the form of kaolinite, as shown in Fig. 21.1? What is the weight percent of potassium in illite?

21.8 In the log of Fig. 21.9 the zone between 2,550 ft and 2,740 ft is known to be predominantly illite. The standard chemical formula for illite can be found in Table 21.3 which shows no iron, although it is known that Fe can substitute for Al. In view of the Al and Fe traces on the log, what is a more reasonable formula for illite in this well?

21.8.1 Taking into account all the log responses what is the most likely explanation for the high Pe values observed near 2,750 ft?

21.9 What is the apparent Fe concentration, as derived from P_e, of a sandstone formation that contains 5% calcite cement?

22

Lithology and Porosity Estimation

22.1 INTRODUCTION

Porosity determination using most of the logging devices presented in earlier chapters relies on a knowledge of the parameters related to the type of rock being investigated. In the case of the density tool, the density of the rock matrix must be known. The matrix travel time is used in interpreting the compressional wave interval transit time. In order to reflect porosity accurately, the matrix setting for the neutron tool must correspond to the rock type for the value of ϕ_n. Determining these parameters is not much of a problem if one has good geological knowledge of the formation and if the lithologies encountered are simple, such as a clean sandstone or limestone reservoir. However, what do you do when you are uncertain of the lithology, or if it is known to vary considerably in its composition, as in the case of limestone formations with variable inclusions of dolomite and anhydrite, or a sandstone with substantial calcite cementing?

To address this uncertainty, a variety of techniques has been developed that combine those logs that primarily respond to porosity yet retain some sensitivity to the rock matrix. The early techniques, developed in the 1960s, combined two or three logs in simple graphical analyses. Generally it was assumed that the clay volume had been estimated and corrected for as described in the previous chapter. These techniques are still useful today for quick evaluations and to develop an understanding of the problem. For this reason the first half of this chapter is devoted to explaining them. The emphasis throughout is on lithology determination since once the lithology is known the calculation of porosity is straightforward. These sections may, at some points, resemble a ramble through the chartbook.

In more complex lithologies there can be mixtures of many different minerals. For these cases one would like to have the use of a large number of logging measurements, each with a slightly different sensitivity to the various minerals, in order to make a complete mineralogical analysis. Graphical techniques for this type of analysis are inadequate. However, the problem can be solved numerically, and several approaches will be discussed.

Although a quantitative evaluation of lithology is essential to determine porosity, a qualitative evaluation is also useful, since it allows the interval logged to be segmented into different lithology types, or facies. Note that the term *lithology*, as used here and by log interpreters, refers mainly to the mineral content of rocks, with little consideration of other aspects such as grain size and texture. Nevertheless it is a useful application of logs for which several techniques are available. The chapter concludes with a discussion of general evaluation methods.

22.2 GRAPHICAL APPROACH FOR BINARY MIXTURES

If we consider, for a moment, the response of the density, neutron, and sonic measurements we can idealize them as follows:

$$\rho_b = f\,(\phi,\ lithology,\ \cdot\ \cdot\ \cdot) \tag{22.1}$$

$$\phi_n = f\,(\phi,\ lithology,\ \cdot\ \cdot\ \cdot) \tag{22.2}$$

$$\Delta t = f\,(\phi,\ lithology,\ \cdot\ \cdot\ \cdot)\,. \tag{22.3}$$

All three contain a dependence on porosity and a perturbation due to lithology. It seems natural to use these three measurements, two at a time, to eliminate porosity and thereby to obtain the lithology. This is precisely what is done in a number of well-known cross plotting techniques which are presented next, in order of their increasing usefulness. The lithology may include clay and other minerals, but in presenting these techniques we will often assume that we are only dealing with the three principal rock types: sandstone, limestone, and dolomite. The term *matrix* is commonly used when referring to them.

The first cross plot is the density-sonic cross plot shown in Fig. 22.1. Because of the differing matrix densities and travel times for the three principal matrices, they trace out three different loci as water-filled porosity increases. As can be seen from the figure, there is not a great deal of contrast between the matrix endpoints, so that a bit of uncertainty in the measured pair (ρ_b, Δt) could cause considerable confusion in the ascribed lithology. In addition there is a large difference depending which sonic transform is used.

The confusion is partially overcome in the next combination considered, neutron-sonic, which is shown in Fig. 22.2. In this case, the travel times are plotted as a function of the apparent limestone porosity for a thermal neutron porosity device. Due to the matrix effect of the neutron device, there is considerably more separation between the three principal matrices which are shown.

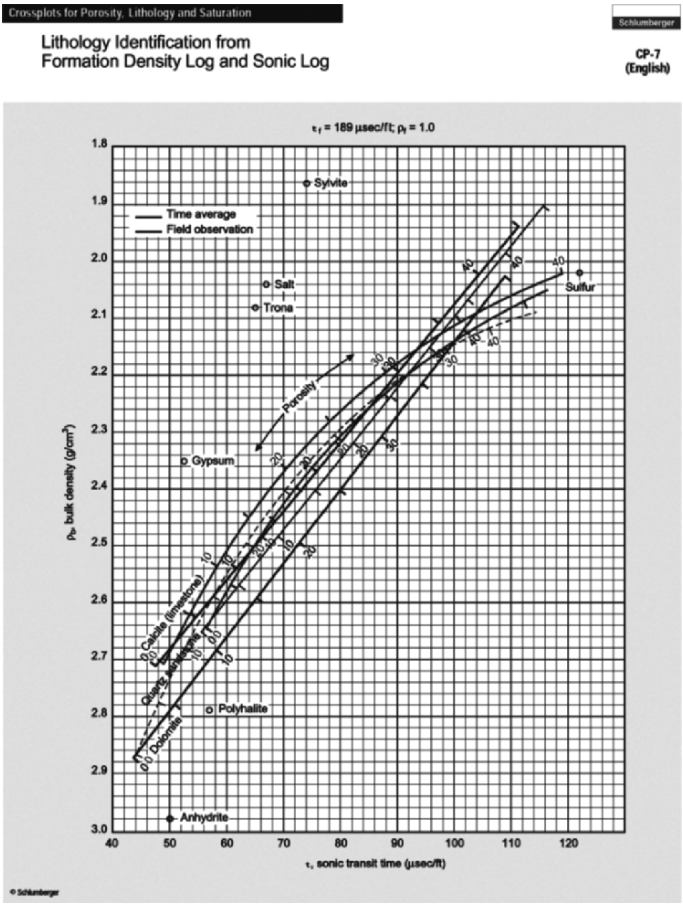


Fig. 22.1 A density-sonic cross plot based on two common sonic porosity transforms. Porosity variations of three major minerals produce trends of compressional interval transit time (indicated as t on the chart and as Δt in the text) and bulk density. Location of measured pairs of values can help to identify the matrix mineral. Deviations from the trends can sometimes be attributed to significant portions of other minerals, some of which are also shown on the plot. Courtesy of Schlumberger [2].

The neutron–density cross plot is one of the oldest quantitative interpretation tools (see for example, Alger et al. [1]), one which we already met for clay evaluation in Chapter 21. Before the development of the photoelectric effect measurement, it was the principal method for determining the formation lithology. It is still much used for matrix identification and estimating the formation porosity in gas-bearing formations, using the option of correcting for clay before entering the plot rather than solving for clay with it. The basic plot capitalizes on the matrix density differences between the three standard rock types and the neutron lithology effect that we saw earlier. When

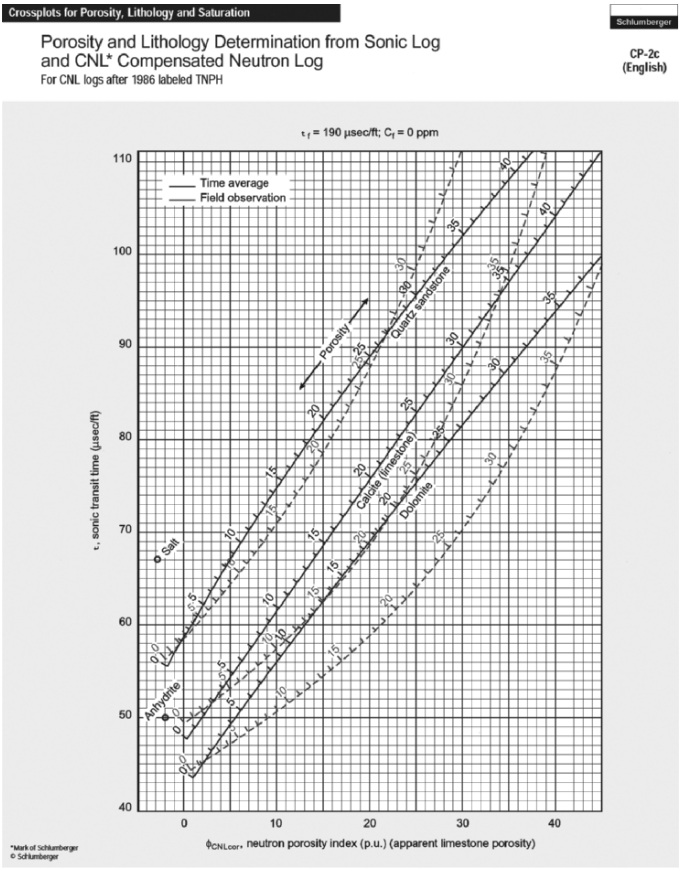


Fig. 22.2 A neutron-sonic porosity cross plot showing an apparently larger resolving power for lithology discrimination. Courtesy of Schlumberger [2].

the density and apparent neutron porosities are plotted, one as a function of the other, three unique lines emerge for the three standard rock types.

One current standard presentation is shown in Fig. 22.3*. In this case the bulk density is plotted as a function of the apparent limestone porosity. When plotting points taken from a neutron log that are reported in units other than "limestone," the porosity markings along the corresponding lithology lines must be used to guide their horizontal positioning. In this manner it can be easily ascertained that a reading on a log of 20 p.u. "sandstone" units must be entered at 15 p.u. on the x-axis of this

*An early version of the cross plot showed a dolomite line with a pronounced bowing at low porosities. This was found by Ellis and Case [4] to have resulted from "field data" points, used to define the response line, which had an unappreciated large salinity effect and some mixture of anhydrite and dolomite at low porosities.

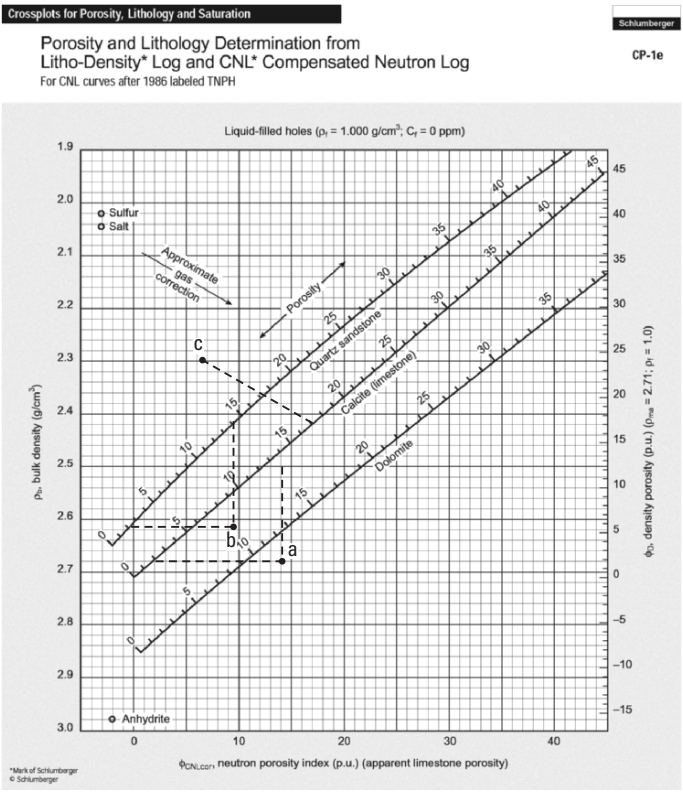


Fig. 22.3 A neutron-density cross plot which is routinely used for lithology and porosity determination in simple lithologies. Courtesy of Schlumberger [2].

particular neutron-density cross plot. The scale on the right is the conversion of the density to the equivalent limestone porosity for freshwater pore fluid. To adjust this chart for other fluid densities, the density values are usually rescaled in accordance with the relation:

$$\rho_b = \phi\rho_{fl} + (1-\phi)\rho_{ma}\ , \tag{22.4}$$

where ρ_{fl} is the density of the fluid filling the pores.

As an example of the use of the neutron–density cross plot for lithology, refer to the log of Fig. 22.4. It shows two apparent-porosity traces from the density and neutron devices, scaled in limestone units. At the depth 15,335 ft, the density porosity reads about 2 p.u., and the neutron 14 p.u. To determine the lithology, we need only to find the intersection of these two points on Fig. 22.3. The surest way is to use the porosity scaling on the matrix curve for which the log was run. In this case it is limestone. By locating the 2 p.u. point on the limestone curve, we see that the corresponding density value is about 2.68 g/cm^3. Dropping a vertical line from the 14 p.u. point for

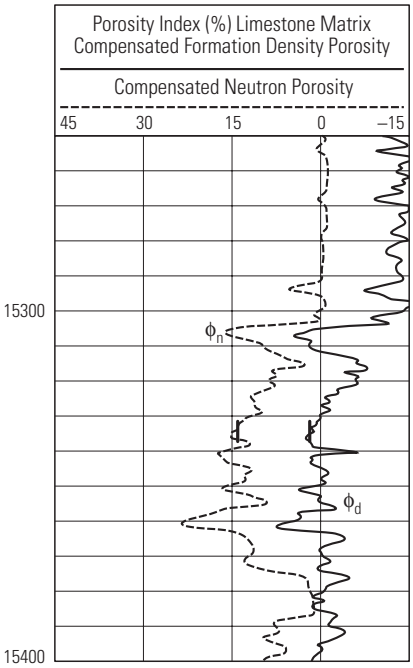


Fig. 22.4 Log of apparent limestone porosity from a neutron and density device. The logged interval includes anhydrite, dolomite, and a streak of limestone. Adapted from Dewan [3].

the neutron value (to the intersection with the horizontal density value), we see that the pair of points corresponds to a dolomite of about 11 p.u., which is marked as point *a* in Fig. 22.3.

If the logs of Fig. 22.4 had been run on a sandstone matrix and yielded the same apparent porosity values, the interpretation would be quite different. This can be seen by finding the 2 p.u. point on the sandstone curve in Fig. 22.3 which corresponds to a bulk density of about 2.62 g/cm^3. The 14 p.u. sandstone porosity for the neutron is equivalent to the reading expected in a 9.5 p.u. limestone. The intersection of these two points is marked at *b*. This corresponds to a formation which seems to be a mixture of limestone and dolomite but could be a mixture of dolomite and sandstone – a less likely possibility.

We have already seen the effect of gas on the neutron and density log presentation. Figure 22.5 is another example which shows the evident separation in a 25 ft zone centered at about 1,900 ft. The neutron reading is about 6 p.u., and the density 24 p.u. Both are recorded on an apparent limestone porosity scale. The location of this zone is shown as point *c* on the cross plot of Fig. 22.3. It is seen to be well to the left of the sandstone line. The trend of the gas effect is shown in the figure. Following this trend, the estimated porosity is found to be about 17 p.u. if the matrix is assumed to be limestone.

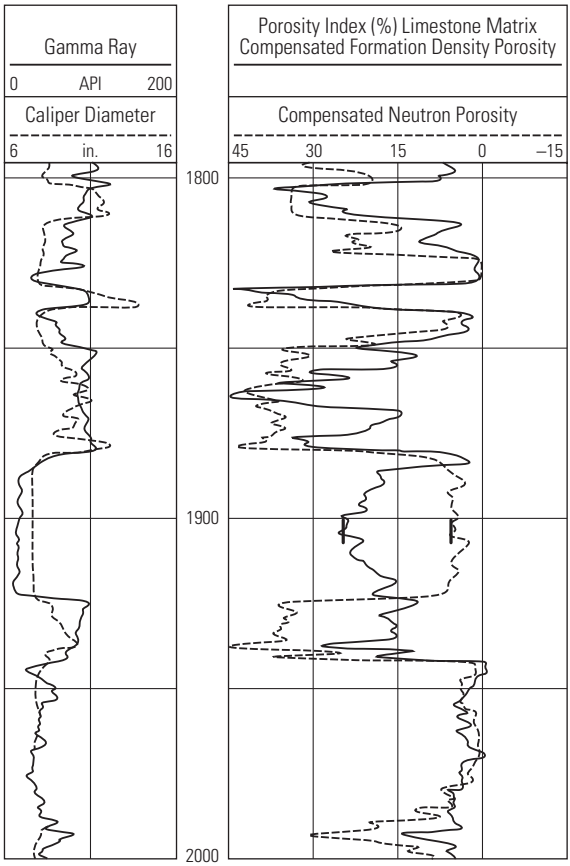


Fig. 22.5 Gas separation between the neutron and density complicates the lithological analysis. Adapted from Dewan [3].

The popularity of the neutron–density log combination for gas detection must be tempered with the need for knowing the matrix and allowing for the effect of clay. Figure 22.6 is a good example of a false gas indication running over nearly the entire section. What we have here is a tight sandstone formation (with some gas, perhaps) which has been presented in limestone units. The crossover is purely an artifact of the presentation in limestone units. Plotting a few of the points from the log onto Fig. 22.3 will be convincing.

It should be apparent from the previous few examples that in the case of gas and clay, at least, additional information concerning the lithology is necessary. It could come from the addition of the sonic measurement, for example. Another possibility is use of the P_e, which can be obtained simultaneously with the density measurement. Figure 22.7 shows an example of its use in a sequence of alternating limestones and dolomites. The first track contains the P_e with sections of dolomite and limestone

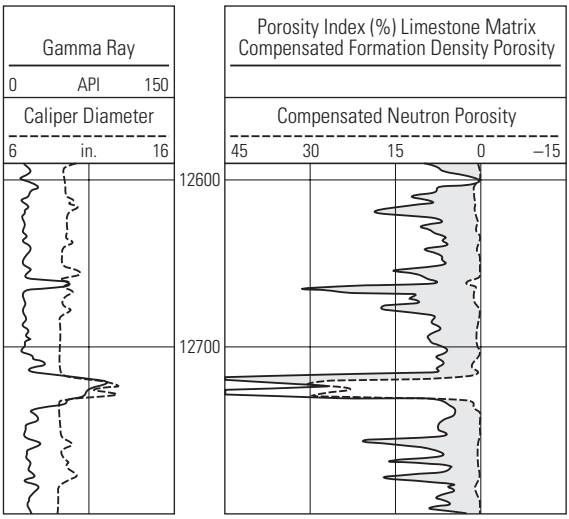


Fig. 22.6 A neutron and density log in a sandstone. An inappropriate matrix setting has been used which falsely suggests the presence of gas through most of the logged interval. Adapted from Dewan [3].

clearly indicated. The density and neutron values which are presented in tracks 1 and 2 are on a scale for which water-filled limestone will show nearly perfect tracking. In the limestone zone, there is a clear separation indicating gas. However, in a short interval just below 10,000 ft, the density and neutron readings are nearly indistinguishable. Without additional information, this would be taken as a water-filled limestone. This can be verified by plotting the peak value of 21 p.u. for the neutron and 2.48 g/cm^3 for the density on the cross plot of Fig. 22.3. However, with the additional knowledge of the P_e, it can be seen to be a gas-bearing dolomite.

22.3 COMBINING THREE POROSITY LOGS

Before the availability of the P_e measurement, several methods were devised to combine the lithology information from the three porosity tools. The first approach was called the M-N cross plot. It attempts to remove the gross effect of porosity from the three measurements before combining them to deduce the matrix parameters.

The parameter M is nothing more than the slope of the Δt-ρ_b time average curve in Fig. 22.1, which varies slightly between the three major lithologies due to the matrix endpoints.

$$M = 0.01 \frac{\Delta t_f - \Delta t_{ma}}{\rho_{ma} - \rho_f} \tag{22.5}$$

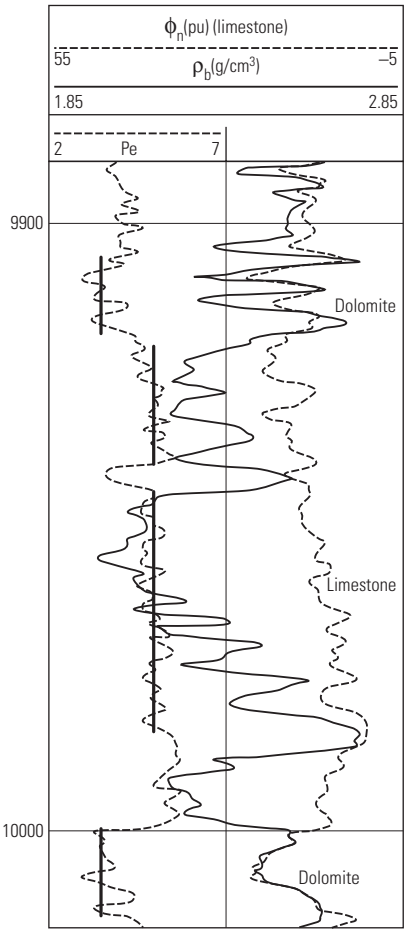


Fig. 22.7 The companion P_e curve simplifies lithology determination in this sequence of alternating limestone and dolomites. The neutron and density information alone would not indicate gas in the lower interval. Adapted from Dewan [3].

The neutron-density cross plot yields a similar slope, designated as N:

$$N = \frac{\phi_{Nf} - \phi_{Nma}}{\rho_{ma} - \rho_f} \tag{22.6}$$

Once again the three matrix types produce slightly different values of N. The end product is indicated in Fig. 22.8 where the two slopes are plotted against one another. The figure shows some spread in the matrix coordinates depending on the fluid density, the sonic value used for sandstone, and the porosity range. Part of the latter is due to the nonlinearity of the neutron response, which in this chart is based on the earlier erroneous curved dolomite line.

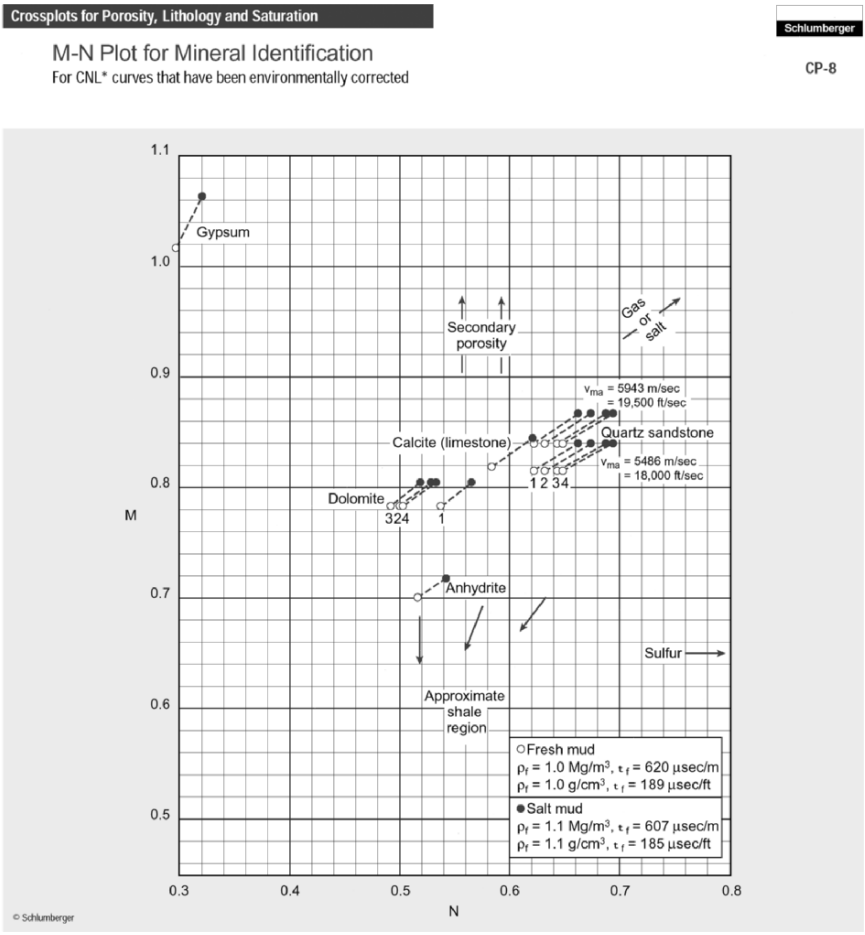


Fig. 22.8 The M-N plot used for mineral identification. Porosity variation has nearly been eliminated, but there remains some sensitivity to the fluid density. This type of plot is also used to identify secondary porosity. Courtesy of Schlumberger [2].

One of the best uses made of this type of presentation is to highlight the presence of secondary porosity, which causes an increase in M without any effect on N. This is because Δt is relatively insensitive to the inclusion of secondary porosity (Section 19.5) while, in the numerator of M, the density decreases. N remains constant as both the density and neutron will change by about the same amount.

The M-N plot was a first order attempt to get rid of the effects of porosity. Its successor, the MID (matrix identification) plot, goes one step further and tries, in a simplified way, to obtain the values of the matrix parameters actually sought. The procedure is to use the neutron-density cross plot to get a cross-plot porosity (often approximated by the average of the two) and then, in the lower half of Fig. 22.9 to enter the measured value of ρ_b, following horizontally to the appropriate cross-

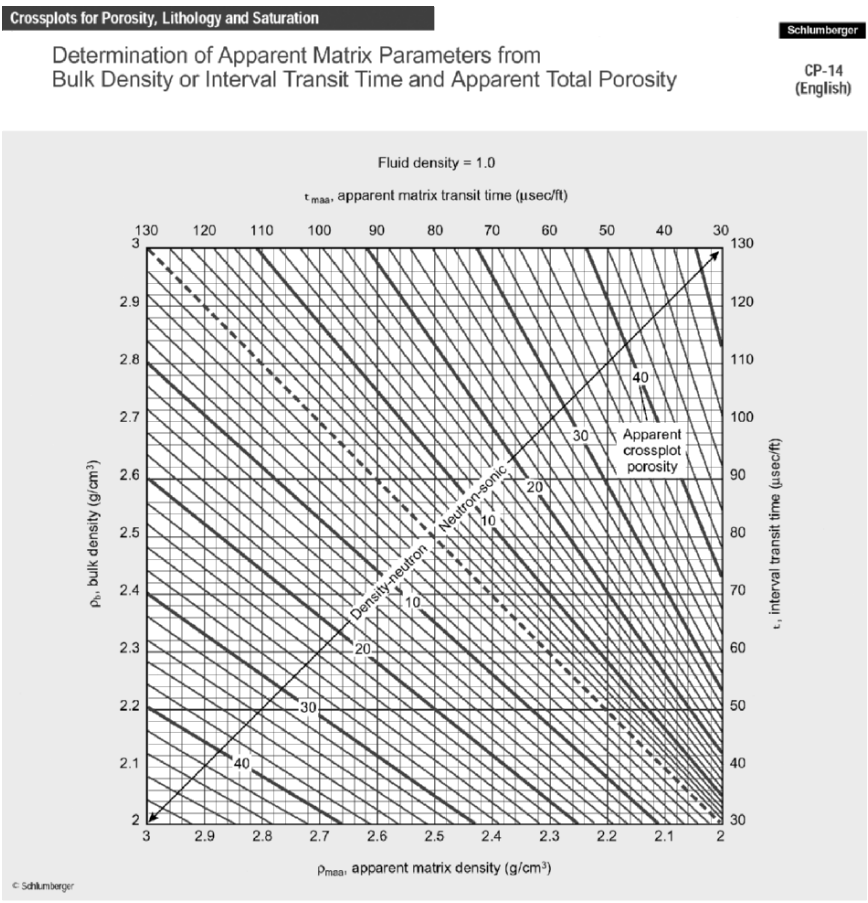


Fig. 22.9 An alternative to the use of M-N variables is the use of apparent matrix values for Δt and ρ_b. These are obtained from using crossplot porosity values from density-neutron and neutron-sonic logs with: (a) the density value to get ρ_{maa} in the lower half, and b) the compressional transit time (indicated as t) to get t_{maa} in the upper half of the graph. Courtesy of Schlumberger [2].

plot porosity line. The x-value of this intersection is the value of ρ_{maa} sought. The apparent matrix travel time is found in a similar manner using the neutron-sonic cross plot porosity and the upper half of Fig. 22.9 to find the appropriate value of t_{maa}.

Armed with these apparent matrix values, we can enter the MID plot of Fig. 22.10. This diagram shows a considerably smaller spread of points than in the M-N plot, and the coordinates have some relationship to known physical parameters, rather than being abstract values.

One can debate the legitimacy of the linear interpolation of the matrix values used in the preceding figures; however, this approach does represent a large improvement

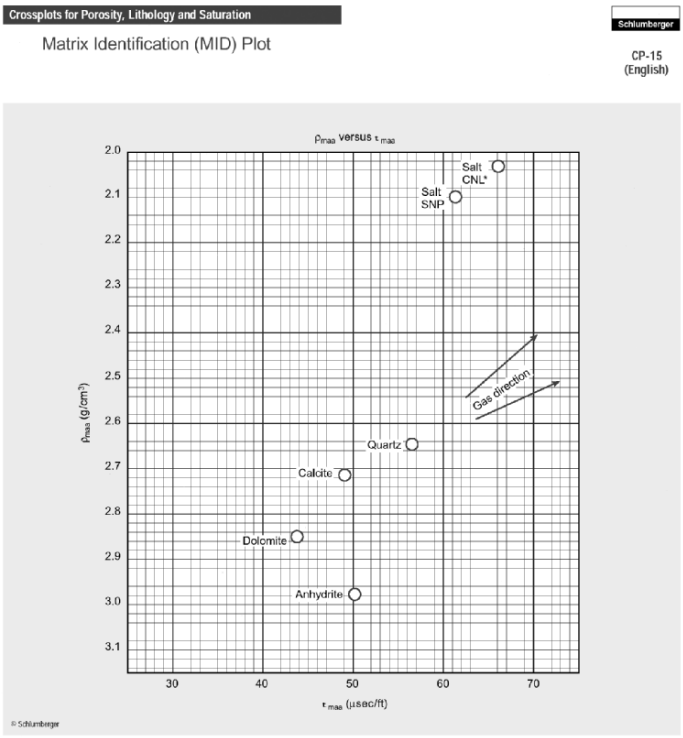


Fig. 22.10 The matrix identification chart obtained using the defined values of apparent matrix density and Δt. Courtesy of Schlumberger [2].

over the M-N plot, for two reasons. First, it gets rid of a conversion to some rather meaningless parameters and attempts instead to find the more familiar values of matrix density and travel time. Secondly, the most appropriate tool response can be used to determine the apparent matrix values, since these are not part of the MID calculation itself, but inputs. One weakness, however, is that this is still a method for presenting only three pieces of information simultaneously. It cannot be used if you want to consider four or more simultaneous measurements.

22.3.1 Lithology Logging: Incorporating P_e

Before leaving the realm of 2D graphical interpretation, let us consider a final example. In the previous techniques, measurements primarily sensitive to porosity were combined to eliminate their mutual porosity dependence and to emphasize their residual lithology sensitivity. However, one common measurement, the photoelectric factor, or P_e, is primarily sensitive to lithology and only mildly affected by porosity. An interesting aspect of the P_e measurement is illustrated by the lithology guide lines in Fig. 22.11. On the left side is the conventional neutron–density cross plot. The

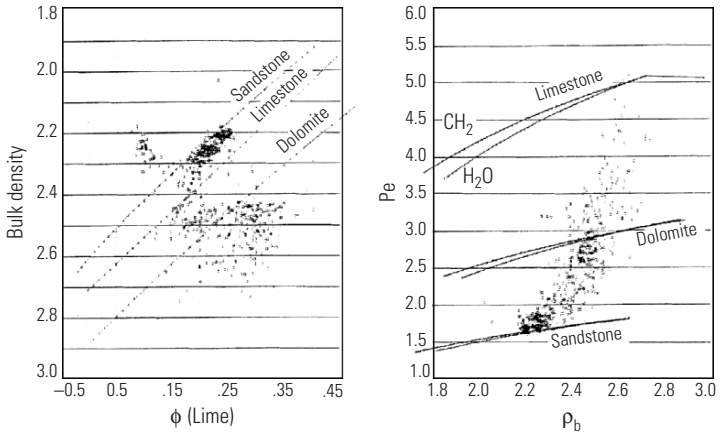


Fig. 22.11 Comparison of log data on a neutron-density cross plot and a cross plot of P_e and density. Trend lines of three matrices from 0% to 50% porosity are shown in the plot of P_e. The upper lines correspond to hydrocarbon in the pores and the lower lines to water-filled porosity. The data points are from a shaly sand.

ordering of the three major lithologies, from top to bottom, is sandstone, limestone, and dolomite, as is the case for the other possible combinations with the sonic measurement. The adjacent figure of P_e vs ρ_b shows a startling difference. In this figure, the upper line is for limestone, while the dolomite matrix line is between the sand and limestone lines. Because of the reordering of the lithological groups, P_e adds a new dimension to the neutron–density cross plot. For this reason, use of the P_e easily resolves questions of binary lithology mixtures.

On the neutron–density cross plot, a data point falling near the limestone line might, in some extreme case, correspond to a dolomitic sand. If the P_e is available, this can be immediately confirmed or disproved. If, in fact, it is a lime/dolomite mixture, then it will lie above the dolomite line on the P_e plot and not below.

Recall that to obtain the P_e of a mixture involves computing the U value:

$$U_{total} = P_{e,1}\rho_{e,1}V_1 + P_{e,2}\rho_{e,2}V_2 + \cdots, \tag{22.7}$$

where $\rho_{e,i}$ is the electron density of material i, $P_{e,i}$ is the photoelectric factor of material i, and V_i is the volume fraction of that material. The final value of the average P_e is obtained from:

$$\overline{P_e} = U_{total}\overline{\rho_e}, \tag{22.8}$$

where the average electron density index $\overline{\rho_e}$ is given by:

$$\overline{\rho_e} = \rho_{e,1}V_1 + \rho_{e,2}V_2 + \cdots. \tag{22.9}$$

An interesting application of this calculation can be seen by referring to Fig. 22.11 and noting that two sets of lines have been drawn for the three matrices: one for

oil-filled and the other water-filled porosity. The P_e value of water is 0.36 and that of oil, 0.12. One might suspect that the upper curve of the three sets would be associated with water. However, the details of the calculation (see Problem 22.3) show that this is not the case.

The most obvious use of the volumetric cross section U is in combination with the grain density to clearly delineate lithologies. The approach is to eliminate porosity from the density measurement and from the P_e measurement to obtain the apparent grain density and the apparent value of U_{ma}. This latter parameter is conveniently found by use of the chart in Fig. 22.12. The measured bulk density and P_e values are entered into the left of the figure, and U_{ma} is finally extracted on the right, based on knowledge of a cross-plot porosity (from a neutron-density cross plot or other source). This type of data is then plotted on Fig. 22.13, which shows a clear triangular separation between the three principal matrices. On this plot, the volumetric analysis of complex mixtures can be done very simply, since everything scales linearly.

This powerful plot also produces a distinct separation between different clays, and can therefore be used for clay typing although, as discussed in Chapter 21, clay composition varies considerably so the clay points shown are only indicative. Unfortunately, the plot is not always unambiguous. For example, a point that plots near

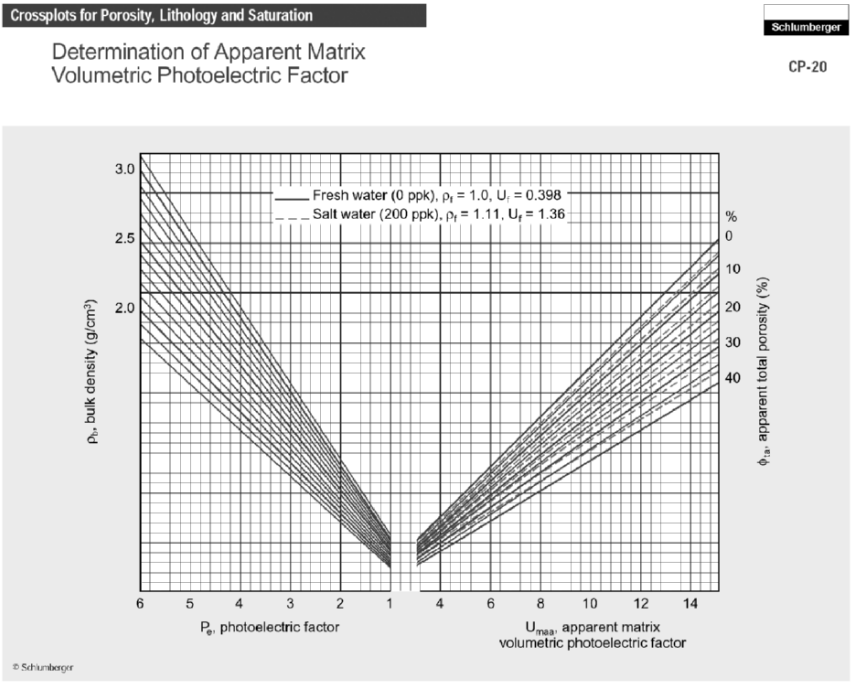


Fig. 22.12 Chart for determining the apparent matrix cross section U_{maa} from a knowledge of P_e, density, and cross-plot porosity. Courtesy of Schlumberger [2].

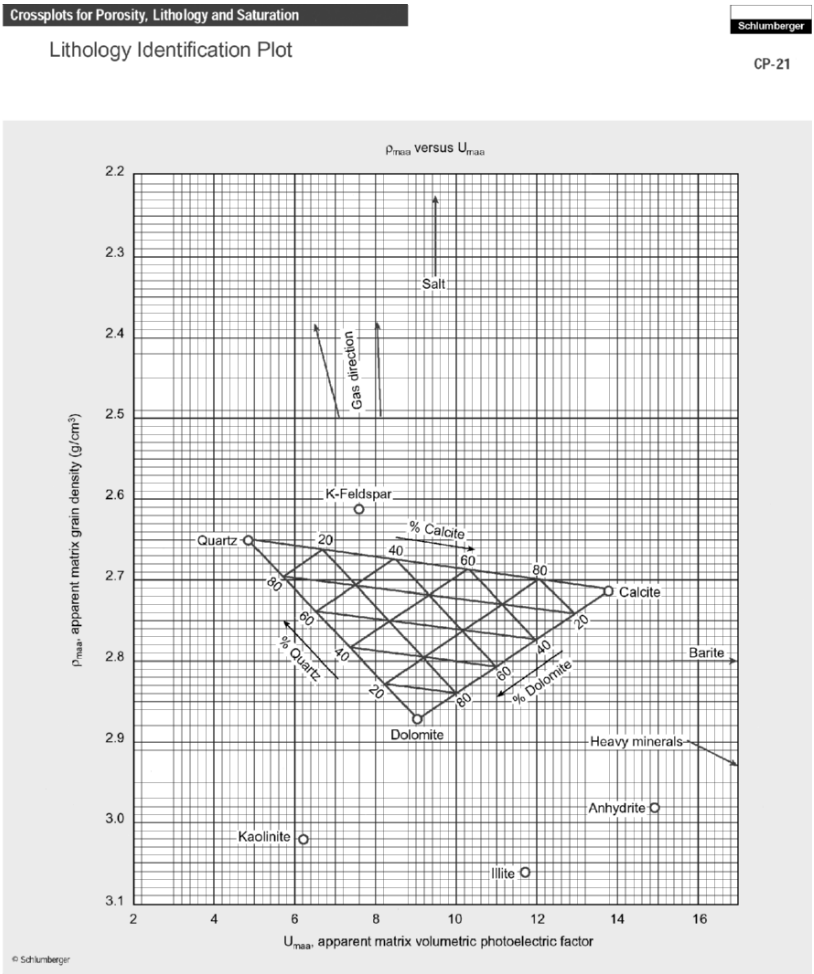


Fig. 22.13 A matrix identification chart which uses the combination of P_e, density, and another porosity device. Both density and U scale volumetrically so that mixture proportions can be easily determined. Courtesy of Schlumberger [2].

dolomite could also be a mixture of quartz and illite. This case can be resolved by the Δt measurement. Δt can be predicted using the porosity already calculated and assuming a quartz matrix. With dolomite the measured Δt will be less than that predicted while with illite it will be higher.

22.3.2 Other Methods

Some other techniques for lithology evaluation have been mentioned in earlier chapters. The use of shear versus compressional Δt was shown in Fig. 18.14. Clay

evaluation was discussed in the last chapter. One other technique discussed in that chapter – elemental analysis – can also be used for general lithology evaluation. Recall that the weight percent of Si, Ca, Fe, S, Gd, Ti, H, and Cl can be obtained from elemental analysis. H and Cl are affected by the fluids present, but can also detect coal and salt beds. Sulfur occurs in pyrite (FeS2) and anhydrite (CaSO4). Since these minerals are unlikely to occur in the same geological environment, it is possible to select which to solve for. The measured weight percent of Ca or Fe can then be deduced accordingly before solving for other minerals, such as siderite (FeCO3), carbonates or clay, as described in Chapter 21. Alternatively, these measurements can be combined with others in the more complete numerical approaches to lithology determination. Having completed the review of two- and three-mineral cross plots, it is time to discuss these methods.

22.4 NUMERICAL APPROACHES TO LITHOLOGY DETERMINATION

2D cross plots have proved very useful for interpretation and will continue to provide a simple method for obtaining quick estimates of the volumes of major minerals. They are also helpful in understanding the basic relationships between measurements. However, other methods must be considered for more complicated lithologies and for the inclusion of multiple logging information at each depth. These methods can be divided into qualitative identification and quantitative evaluation.

The goal of qualitative methods is to identify the lithology over a depth interval within which it is reasonably consistent. The result is a lithologic column, which is a sequence of lithofacies (Fig. 22.14). This result is of great interest to the geologist, and is also a useful guide for the petrophysicist before starting a quantitative analysis. Logs do not contain enough information to define all the characteristics of a lithofacies, since these can include biological and other features not identified by logs. Logs can determine a subset called an *electrofacies*, which is defined as a set of log responses which characterizes a bed and permits it to be distinguished from other beds [5]. Many mathematical techniques have been applied to this problem–see Doveton [6] for a summary. One way to group the different methods is based on whether or not they use a knowledge of log response.

Classification, or discriminant analysis, uses knowledge of log response to identify regions in multidimensional space within which different facies can be expected [7]. Figure 22.15 shows examples of different electrofacies as they would be seen on cross plots. The log data at each level is classified accordingly, using an appropriate function to decide the most likely class when points fall within overlapping regions or outside any region (see, for example, the use of fuzzy logic by Cuddy [8]). Classification is simple and automatic but depends on the accuracy of the database that defines the regions. This database can be adapted to a field or a well using local information.

Electrofacies can also be identified by classifying the results of a log analysis, for example the porosity and mineral volumes. This has the advantage that the properties

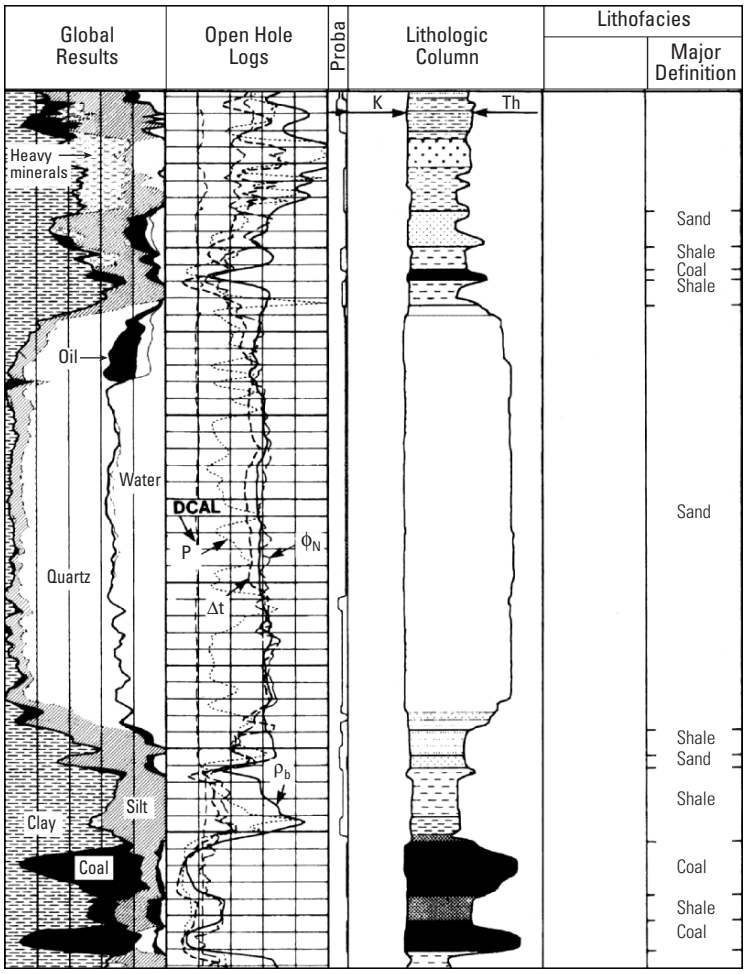


Fig. 22.14 Track 1: output of a program that computes mineral and fluid volumes using simultaneous inversion. Track 2: input porosity logs. Tracks 3 and 4: output of a program for automatically determining lithology from a number of predefined geological models. Adapted from Delfiner et al. [7].

being classified are more closely related to the geology than logs. It is also simpler, since several logs may be giving essentially the same information, for example porosity. (It is possible to study how many independent pieces of information there are in a set of logs, and what they are, using principal component analysis.) However the process of log analysis involves the use of response equations and interpretation parameters, which may be subjective and therefore preferable to avoid.

Clustering is an alternative to classification. It is a technique that ignores any knowledge of log response and simply looks within the interval logged for clusters of

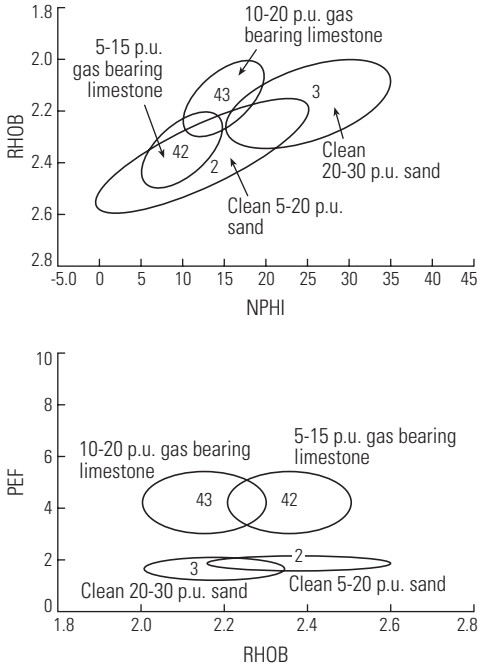


Fig. 22.15 An approach to the N-dimensional space of multiple logging measurements, considering them two at a time. Adapted from Delfiner et al. [7].

data that lie close together in multidimensional space. This clustering can in itself be a useful method of summarizing the log data. For lithology identification, the clusters usually need to be sufficiently large or else aggregated with their nearest neighbors into 10 or 20 larger groups that can be identified using external knowledge, for example from cores [9]. This identification can then be applied to data from other wells in the same area. The method is a purer representation of the data than classification since it does not use prior knowledge, but it necessarily requires an effort of identification. It is particularly useful for logs that are not quantitative measurements, such as the activity on a borehole image that indicates thin beds. There are many statistical techniques for defining and aggregating the clusters [10].

Neural networks can be used to simulate both the classification and clustering processes. In classification, the network is trained to identify the facies in different intervals of a training data set. These facies have been previously defined from external information. In clustering, the network is asked to identify a number of bins, or modes. These are subsequently labeled by the user from external information. In either case, once trained, the network can be applied automatically to new data sets. Different neural networks have different parameters and features to control the process and evaluate results [11].

22.4.1 Quantitative Evaluation

When computer programs were first applied to log interpretation in the late 1960s, they tended to emulate the manual procedures used by interpreters and consist of a series of cross plot evaluations [12]. An alternative method is to express the log response of various tools as equations which relate the response to the volume of each of the minerals present.

Consider the simple example of two logging measurements, density and P_e. First we begin with a model of the formation. We suppose the formation consists of a mixture of two minerals of relative volumes V_1 and V_2 and with densities of ρ_1 and ρ_2. The photoelectric absorption properties of the two minerals are given by U_1 and U_2. The porosity is given by ϕ, and it is assumed to be filled with a fluid characterized by U_{fl} and ρ_{fl}.

The tool response equations, or mixing laws, relate the measured parameters to the formation model. The complete set for this measurement is given by:

$$\rho_b = \rho_{fl}\phi + \rho_1 V_1 + \rho_2 V_2 \tag{22.10}$$

and

$$U = U_{fl}\phi + U_1 V_1 + U_2 V_2 \,. \tag{22.11}$$

The final relation necessary to solve for the three unknowns is the closure relation of the partial volumes:

$$1 = \phi + V_1 + V_2 \,. \tag{22.12}$$

The solution can most easily be seen in terms of the matrix representation of the set of simultaneous equations:

$$\begin{bmatrix} \rho_b \\ U \\ 1 \end{bmatrix} = \begin{bmatrix} \rho_{fl} & \rho_1 & \rho_2 \\ U_{fl} & U_1 & U_2 \\ 1 & 1 & 1 \end{bmatrix} \begin{bmatrix} \phi \\ V_1 \\ V_2 \end{bmatrix}, \tag{22.13}$$

$$or \quad M = R\,V \,, \tag{22.14}$$

where M is the vector of measurements, R is the matrix of response coefficients, and V is the vector of unknown volumes. For the balanced case of N unknowns and N-1 logging values, the solution is the inverse of the response matrix, R^{-1} (and providing for each unknown there is at least one measurement that can distinguish it from other unknowns). A simple inversion of actual measurements might calculate a physically impossible negative volume. To avoid this the volumes must be constrained at zero or greater. Doveton shows a computer program for obtaining the inverse simply [6].

Obviously this approach can be extended to as many measurements as are available. Three practical problems arise. The first is relatively straightforward and concerns the problem of overdetermination, which occurs when the number of logging measurements exceeds the number of minerals in the model. One solution to this problem is to find a least-squares solution to the set of equations. In this case, a weighting matrix is added to express the confidence level (or uncertainty) associated with each measurement and its response equation. The programs necessary for implementing such

an approach are described by Bevington [13]. A number of higher level programing languages allow solution of such sets of equation in a single line of code.

The second problem is that not all response equations are linear with respect to volume. For lithology determination, this problem is rare, the empirical sonic porosity transform being the most common exception. Nonlinear inversions are discussed further below.

The third, most serious problem concerns the more probable occurrence that the number of minerals in the formation will vastly outnumber the set of logging measurements. For quantitative evaluation, the only solution is to reduce the number of minerals until the problem is balanced or overdetermined. Minor minerals might be grouped with major ones: for example, in a feldspathic sand feldspar might be grouped with quartz and the matrix parameters given the properties of the average mixture in that formation. Otherwise, it is good practice to restrict the model to those minerals that are geologically significant (for example, a shaly- sand model would not normally include anhydrite or other evaporites). In complex formations one method provides the facility to run several models in parallel, and then to apply a suitable criterion to decide which model is correct at each depth (for example, an electrofacies log, or an SP log to differentiate sand from shale) [14].

Lithology is normally evaluated as one step in the process of determining porosity and water saturation. As has been seen, this evaluation depends on knowing the effect of the fluid in the invaded zone on the density, neutron, sonic, and other measurements. This effect depends on the water saturation, so that the different steps in the interpretation process are not independent. Although the particular problems of saturation estimation will be considered in the next chapter, it is convenient to conclude this chapter with a discussion of general evaluation methods.

22.5 GENERAL EVALUATION METHODS

Log evaluation software handles the interdependence of different effects by two principal methods. One method works sequentially, for example first estimating lithology, then porosity and finally water saturation, but then iterating back to refine the answer. Such programs are fast and can be made easy to use, but tend to be tailored to particular types of formation, for example shaly sands, or to particular logging measurements and response equations. The complexity of the logic makes it difficult to add a new measurement or response equation. Such programs have been available since the late 1960s [15].

The other method treats the whole problem as one of inversion and solves simultaneously for all the required outputs. The first such commercial program appeared in 1980 [16]. The matrices of Eq. 22.14 are expanded to include fluids as well as minerals, and to handle all logging measurements. The response equations of some measurements (in particular conductivity) are nonlinear so that a simple matrix

inversion is no longer possible. Instead, the optimal solution is found by iterating until the logs computed from the outputs give the best least squares fit to the actual measurements. With nonlinear equations there is a increased risk of instability because two or more solutions may have similar goodness of fits.

Simultaneous methods can handle almost any combination of measurements, minerals and fluids providing the problem is balanced or overdetermined. As already discussed, it is good practice to define models that are geologically reasonable and to compare results from different models. Simultaneous methods give the most coherent agreement between results and measurements within the uncertainty given to them. It is also simpler to add or change a response equation, or to add an unknown. On the other hand the technique is often harder to manipulate and slower to run. Some software combines the two methods, for example using inversion to determine lithology and porosity, then solving for saturation and looping back to improve the inversion.

For both methods there is the practical issue of determining the appropriate model parameters. Many common mineral parameters can be found from tables (see for example Table 21.3). Fluid parameters are more variable and are either measured, as in the case of the mud filtrate, or determined from cross plots and quicklook logs such as R_{wa}. Alternatively, both mineral and fluid parameters may be available in local databases that are specific to a particular reservoir or formation. For unusual minerals one solution is to invert to find the parameters that give the best fit to the data – effectively solving for R in Eq. 22.14, using volumes determined by cores or other logs and the fact that parameters should be constant over an interval [14].

If parameter selection is somewhat subjective, the quality control of results is even more so. Reconstructed logs – logs computed from the solution – show whether the solution respects the input logs but do not indicate whether the parameters or model are correct. In practice, the quality of the result depends on the interpreter's judgment and comparison with non-log data, such as cores and tests. Experienced interpreters do not use software to find the solution for them, but rather to implement and refine the ideas they have gleaned from studying the raw logs. This experience can be obtained quickly in specific reservoirs or areas.

Parameter selection can be minimized by the use of artificial neural networks. These networks are trained to convert logs into results on wells where the latter are known – effectively finding internally the necessary transforms and parameters for the specific model and wells concerned. Once trained, the networks can be applied nearly automatically to other wells where this model applies. Neural networks are mostly used for lithology classification and for cases such as permeability estimation and reduced logging sets where explicit transforms are poor or unavailable. However, they are also applied to volumetric analysis [17].

REFERENCES

1. Alger RP, Hoyle WR, Tixier M P (1963) Formation density log applications in liquid-filled holes. J Pet Tech 15(3):321–332
2. Schlumberger (2005) Log interpretation charts. Schlumberger, Houston, TX
3. Dewan JT (1983) Essentials of modern open-hole log interpretation. PennWell Publishing, Tulsa, OK
4. Ellis DV, Case CR (1983) CNT – A dolomite response. Trans SPWLA 24th Annual Logging Symposium, paper S
5. Serra O, Abbott H (1980) The contribution of logging data to sedimentology and stratigraphy. Presented at the 55th SPE Annual Technical Conference and Exhibition, paper SPE 9270
6. Doveton JH (1994) Geologic log analysis using computing methods. AAPG Computer Applications in Geology, No 2: Tulsa, OK
7. Delfiner PC, Peyrat O, Serra O (1984) Automatic determination of lithology from well logs. Presented at the 59th SPE Annual Technical Conference and Exhibition, paper SPE 13290
8. Cuddy S (1997) The application of the mathematics of fuzzy logic to petrophysics. Trans SPWLA 38th Annual Logging Symposium, paper S
9. Wolff M, Pelissier-Combescure J (1982) Faciolog – automatic electrofacies determination. Trans SPWLA 23rd Annual Logging Symposium, paper FF
10. Ye S-J, Rabiller P (2000) A new tool for electro-facies analysis: multi-resolution graph-based clustering. Trans SPWLA 41st Annual Logging Symposium, paper PP
11. Goncalves CA, Harvey PK, Lovell MA (1995) Application of a multilayer neural network and statistical techniques in formation characterisation. Trans SPWLA 36th Annual Logging Symposium, paper FF
12. Poupon A, Clavier C, Dumanoir J, Gaymard R, Misk A (1970) Log analysis of sand-shale sequences – a systematic approach. J Pet Tech 22(7):867–881
13. Bevington PR (1969) Data reduction and error analysis for the physical sciences. McGraw-Hill, New York
14. Quirein J, Kimminau J, Lavigne J, Singer J, Wendel F (1986) A coherent framework for developing and applying multiple formation evaluation models. Trans SPWLA 27th Annual Logging Symposium, paper DD
15. Poupon A, Hoyle WR, Schmidt AW (1971) Log analysis in formations with complex lithologies. J Pet Tech 23(8):995–1005

16. Mayer C, Sibbit A (1980) Global: a new approach to computer-processsed log interpretation. Trans SPE 55th Annual Technical Conference and Exhibition, paper SPE 9341

17. Quirein JA, Chen D, Grable J, Wiener J, Smith H, Perkins T, Truax JA (2003) An assessment of neural networks applied to pulsed neutron data for predicting open hole triple combo data. Trans SPWLA 44th Annual Logging Symposium, paper R

Problems

22.1 Figure 22.4 is a log of a tight (low porosity) carbonate section. Using the neutron-density cross plot (Fig. 22.3), identify zones of the different matrix types present in this section of the well.

22.2 To gain some practice with the manual determination of lithology and matrix values, consider the following set of data taken from sections of a clean sandstone reservoir. Although the sandstone is free of clay, it does contain some pyrite. The question to answer is: how close does the manual cross-plot technique get you to the true porosity?

Table 22.1, which lists the values painstakingly read off the logs, is in a format which will help you to complete the task. Note the column of matrix density values, which have been determined from core analysis. Make a plot of porosity obtained from the density tool alone under two different conditions: using the core-measured grain density, and using the cross plot grain density $(\rho_{ma})_{n-d}$. For both calculations, assume that the formation fluid has a density of 1.20 g/cm^3.

22.3 To verify the identification of the sets of matrix lines in the P_e plot of Fig. 22.11, compute the ρ_b and P_e values for 50% porosity limestone, dolomite, and sandstone. Consider two cases of pore fluid, water and CH_2. The appropriate values for the computations may be found in Table 12.1

22.4 From the log of Fig. 22.7 calculate the apparent matrix values ρ_{maa} and U_{maa} and hence the percentages of quartz, calcite and dolomite (assuming no clay).

Table 22.1

Δt	ρ_b	ϕ_n	ϕ_{n-d}	$(\rho_{ma})_{(n-d)}$	ϕ_{n-s}	$(\Delta t_{ma})_{(n-s)}$	ρ_{ma}
95	2.35	21					2.74
90	2.40	19					2.74
94	2.41	18					2.84
87	2.52	26					2.70
97	2.36	24					2.84
95	2.38	20					2.70
90	2.38	19					2.76

22.5 With reference to Fig. 22.1 through 22.3, which tool combination would you prefer to use for lithology definition in a carbonate reservoir containing limestone and dolomite? Specifically, what are the maximum errors tolerable in a 5% porous limestone so that it is not misidentified as a dolomite? For each pair of cross plots, you can evaluate the maximum tolerable error by either of the measurements or assume a simultaneous error of the two.

22.6 Consider a barite-loaded mud with a density of 14 lb/gal which is known to be 46% $BaSO_4$ by weight. What is the P_e of the mud? If the mud infiltrates a 20% porous sandstone what P_e do you expect to see?

23

Saturation and Permeability Estimation

23.1 INTRODUCTION

This final chapter discusses the determination of two of the most prized, but also the most difficult, outputs of log interpretation: water saturation and permeability. We will only be concerned with the determination of water saturation from resistivity. Other logs can give water saturation, for example the combination of density logs with the hydrogen index from NMR or neutron logs, but these are only sensitive to gas and measure near the borehole. Pulsed neutron logs can give saturation through casing, as explained in Chapter 15. In most cases log-derived saturation is based on resistivity.

The cornerstone of saturation interpretation from resistivity measurements is the evaluation of the Archie relationship, which was presented in Chapter 4. Because of its simplicity, it has many shortcomings, some of which were presented in that chapter. It is not, for example, directly applicable to shaly or heterogeneous formations. And, despite its simplicity, its application to practical interpretation problems is not always straightforward; constants appropriate to the formation must be determined. In clean formations, this is relatively easy to do, using graphical solutions or their equivalent quick-look logs, as will be shown.

There is no such consensus for determining saturation in shaly formations. Dozens of different prescriptions exist, some of which are based on localized empirical observations and are of limited validity. The majority of the more scientifically based dispersed clay models rely on the concept of cation exchange capacity at the surface of clay minerals. Another group relates to laminated sands. With the ability to measure vertical as well as horizontal resistivity, the evaluation of such sands has improved significantly.

Carbonates and other rocks with heterogeneous pore types present a different challenge. There are even fewer clear-cut methods for determining saturation in these conditions. Even if the correct method could be determined, it is more difficult to measure the fractions of the different pore types than to measure the clay volume for the shaly sand equations. A few models will be considered along with their effect on the cementation and saturation exponents.

Unlike porosity and saturation, which are simple volume fractions, permeability is a tensor and cannot be scaled up easily. It is therefore difficult to define a ground truth permeability against which log-derived estimates can be judged. Permeability is also a dynamic measurement while most logs are static. However, it is known to be strongly correlated with porosity, and to depend on some factor related to texture or surface-to-volume ratio. This chapter examines a few of the ways these factors can be estimated from logs.

23.2 CLEAN FORMATIONS

The basic interpretation problem, given the corrected resistivity of the uninvaded formation R_t and the porosity ϕ, is the evaluation of the Archie relation. In its simplest form, it can be written as:

$$S_w^n = \frac{R_w}{R_t} \frac{1}{\phi^m} . \tag{23.1}$$

The first question, in a practical application, concerns the value to use for R_w, in the case where this is not available from production tests. In the early days of log interpretation this was derived from the SP, but this may present a problem if there is no proper SP development, as is often the case. In addition, if the matrix values for the formation are not known, there may even be some considerable doubt about the porosity values to be associated with the resistivity values measured. Finally, there can be uncertainty about the cementation and saturation exponents, m and n, to be used.

There are two graphical methods available for interpreting the water saturation of a zone when R_w is assumed to be constant but unknown. The basic measurements necessary are R_t, corrected for environmental effects, and a porosity log (usually density or sonic). A further requirement is the presence of a few water-bearing zones of different porosity in the logged interval, and, of course, the formations of interest must be clean (shale-free).

The first cross plot technique to be considered is the Hingle plot [1]. In this case, assuming that a porosity measurement is available, even if the matrix values are unknown, a plot can be constructed which will give porosity and water saturation directly. To see the logic behind the Hingle plot, note that the simplified saturation expression of Eq. 23.1, with $m = n = 2$, indicates that ϕ will vary as $1/\sqrt{R_t}$ at a fixed value of water saturation, assuming, of course, that the water resistivity is constant. This leads to the construction of a plot, shown in Fig. 23.1, of inverse square root of

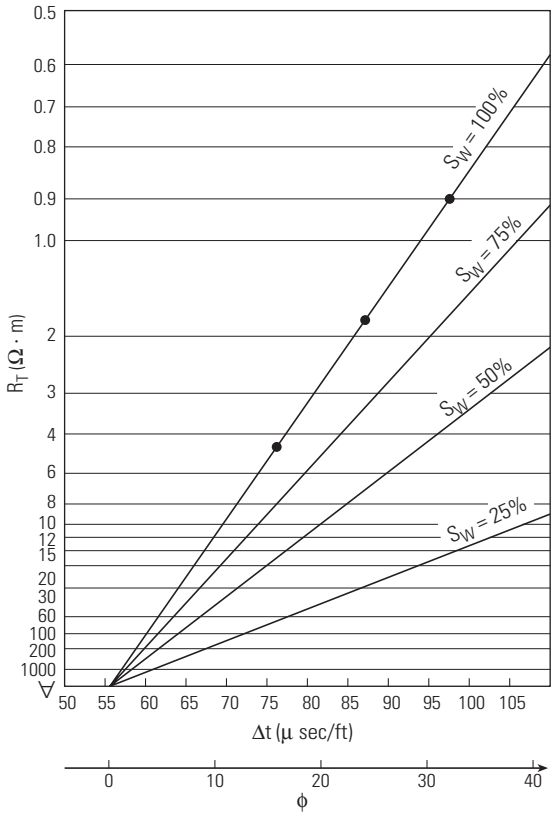


Fig. 23.1 The Hingle plot, which combines resistivity and porosity (in this case the Δt measurement) to estimate water saturation. In constructing the chart, implicit use is made of the square-root saturation relation and in this case of the relation $F = 1/\phi^2$ [1].

resistivity versus porosity. Since we can rewrite Eq. 23.1 as:

$$\frac{1}{\sqrt{R_t}} = S_w \frac{1}{\sqrt{R_w}} \phi \,, \tag{23.2}$$

it is clear that the 100% water-saturated points will fall on a straight line of maximum slope. Less-saturated points, at any fixed porosity, must have a larger resistivity and thus fall below this line. Once these points have been identified and ignored, the line corresponding to $S_w = 100\%$ can be drawn, as shown in Fig. 23.1. It is relatively easy to construct lines of the appropriate slopes corresponding to partial water saturations.

The value of R_w can be determined immediately from inspection of the graph. In the construction of Fig. 23.1, the uppermost line corresponds to R_o, since it is fully water-saturated and satisfies the relationship:

$$F = \frac{R_o}{R_w} = \frac{1}{\phi^2} \,. \tag{23.3}$$

The implication is that at a porosity of 10 p.u. the indicated value of R_o will be 100 times the value of R_w. For the example given, the value of R_o at 10 p.u. is 12 ohm-m, which indicates that the water resistivity is 0.12 ohm-m.

In the case of unknown porosity values, the horizontal axis may be scaled in the raw log reading, e.g., Δt or ρ_b. The intersection of the R_o line with the horizontal axis (corresponding to an infinite resistivity) will give the matrix value for constructing a porosity scale. Other versions of this plot use different F versus ϕ relationships. A common alternative is the Humble relationship, $F = 0.62/R_o^{2.15}$.

The second useful graphical technique is the result of work by Pickett [2]. A knowledge of porosity is required, but the values of m, R_w, and S_w can be obtained. In this method, the power law expression for saturation is exploited by plotting on log–log scales. Starting with the general saturation expression:

$$S_w^n = \frac{a}{\phi^m}\frac{R_w}{R_t} \tag{23.4}$$

and taking the log of both sides of the equation and rearranging results in:

$$log(\phi) = -\frac{1}{m}log(R_t) + \frac{1}{m}(log(a) + log(R_w) - n\,log(S_w)) \; . \tag{23.5}$$

Thus at a constant water saturation, a log–log plot of porosity versus R_t should result in a straight line (see Fig. 23.2) of negative slope whose value is the cementation exponent, and should be in the neighborhood of 2.

If we consider the value of a to be unity, then we can write:

$$log(\phi) = -\frac{1}{m}log(R_o) + \frac{1}{m}log(R_w)\,, \tag{23.6}$$

which represents the line of 100% water saturation. In this case the intercept at the 100% porosity point gives the value of R_w directly. For values of S_w less than 100%,

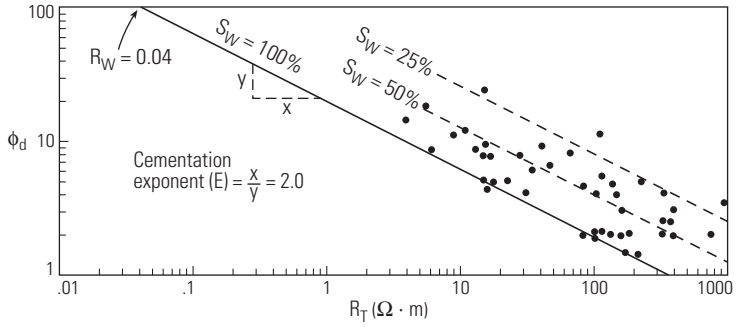


Fig. 23.2 A log–log representation of resistivity and porosity attributed to Pickett [2]. It is useful for determining the cementation exponent that best describes a given formation.

the relationship between ϕ and R_t will be represented by lines parallel to the 100% saturation case but displaced to the right. With a saturation exponent of 2, these lines can be placed in relation to the $S_w = 1$ line by recognizing that at a fixed porosity a saturation decrease by a factor of 2 (i.e., from 1 to 0.5) corresponds to a resistivity increase by a factor of four. Thus one obtains the 50% saturation line by shifting a line parallel to the $S_w = 1$ line by a factor of four in resistivity, and the 25% saturation case by shifting another factor of 2, and so forth. An example of the result of this procedure is shown in Fig. 23.2.

Cross plots are most useful for determining parameters that are constant over an interval, such as R_w or ρ_{ma}, and when neither parameter is known. However, the same information can be obtained by calculating the appropriate quick-look logs. For example R_w can be found from either the R_{wa} or R_{xo}/R_t curves. Recalling that $R_{wa} = \phi^2 R_t$, the water zone (if there is one) has the lowest values of R_{wa} in the reservoir, at which point $R_{wa} = R_w$. If porosity cannot be determined with confidence then it is best to use R_{xo}/R_t, which is at its highest and equal to R_{mf}/R_w in the water zone. R_w can be calculated knowing R_{mf}.

These logs make the same assumptions as the Hingle and Pickett plots and, unlike cross plots, maintain information on trends with depth (although the z-axis of cross plots can give some indication of depth). The visual aspect of cross plots makes them useful when learning to interpret logs. However, neither logs nor cross plots can help much with n. It is generally taken as 2, but may be determined on core samples or from experience in a reservoir.

As an exercise in applying different techniques, let us compare them in a simple interpretation. The logs to be used are shown in Fig. 23.3. Here the total porosity has been estimated from the average of the neutron and density porosities, both on sandstone scales. The gamma ray indicates two sands (2,979–2,986 m and 2,994–3,004 m), while the R_{wa} curve is flat except in the top half of the top sand. This suggests that there are hydrocarbons overlying water. The R_{xo}/R_t curve supports this interpretation.

The water resistivity can be read from the R_{wa} curve in the water zone. Alternatively a Hingle plot can be formed using the data samples taken every 6 in., and R_w deduced from a line drawn through the uppermost points, as has been done in Fig. 23.4. The result is approximately 0.065 ohm-m in both cases. The lowermost points on the Hingle plot are from the hydrocarbon zone and give a water saturation near 40%. This can also be deduced from the R_{wa} curve using the relation $S_w = \sqrt{R_w/R_{wa}}$. A similar analysis can be made with the Pickett technique, but is left as an exercise.

The Hingle plot has many points in between the lines of 100% and 50% saturation. Most of these can be traced to the shale intervals and could have been excluded from the plot (as they are by eye when reading the R_{wa} curve). Does this mean that the shales are partially saturated? The answer is no, and that they only appear so because of the limitations of the Archie equation. It is now time to consider the effect of shale on the saturation equation.

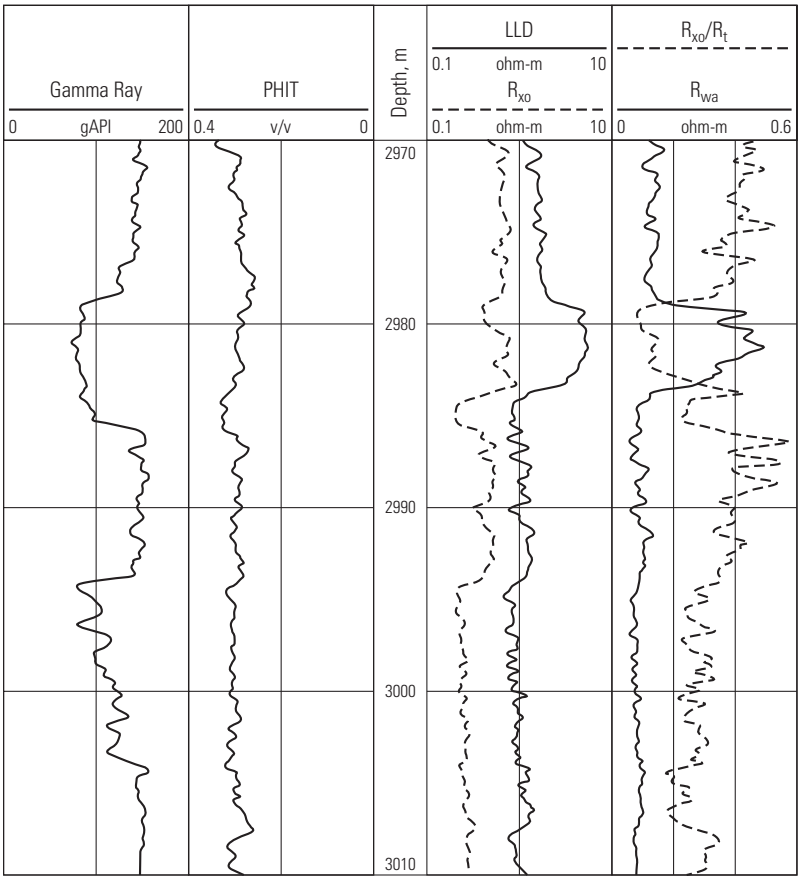


Fig. 23.3 A set of logs from a sandstone/shale sequence with quick-look curves R_{wa} and R_{xo}/R_t. The full set of logs was shown in Fig. 14.11.

23.3 SHALY FORMATIONS

Before reviewing the variety of saturation equations used in the analysis of shaly formations, let us recall why they are necessary, starting for simplicity with rocks that are fully water-saturated. The experimental data which confirm that there is an additional conductivity in rocks with dispersed clay is summarized in Fig. 23.5 (see also Section 4.4.3). The clean sand response, shown as a dashed line, represents the Archie relation; its slope is the reciprocal of the formation factor F. At large values of water conductivity, the response of the shaly formation is seen to be simply displaced with respect to the Archie-type behavior. This additional conductivity associated with the clay can be added to the Archie relation as:

$$C_o = \frac{C_w}{F} + C_s \,, \tag{23.7}$$

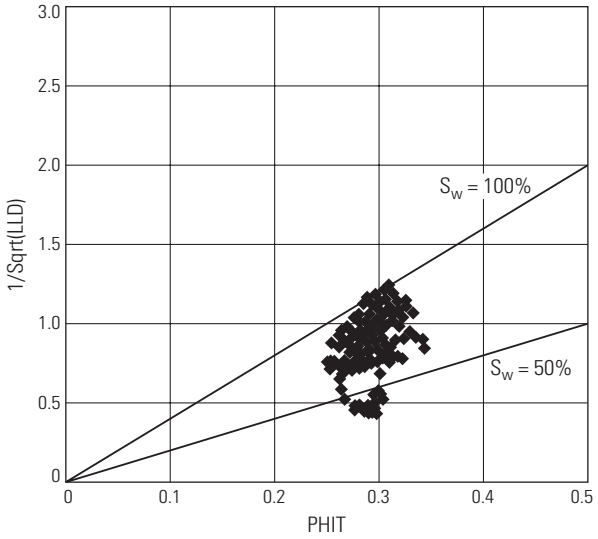


Fig. 23.4 A Hingle plot of the logs shown in Fig. 23.3.

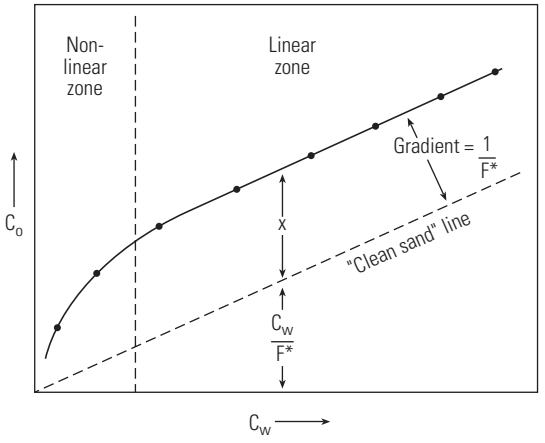


Fig. 23.5 Schematic behavior of the conductivity of water-saturated shaly rocks showing the nonlinear behavior at low values of water conductivity and offset at higher values. Adapted from Worthington [3]. Used with permission.

where C_s, the additional term that results from shale, must decrease to zero as the clay content vanishes. (The terms clay and shale are used interchangeably here.) Above some value of water conductivity, it simply appears as a linear shift. The slope of the line yields the same formation factor F as would be obtained for the rock without the

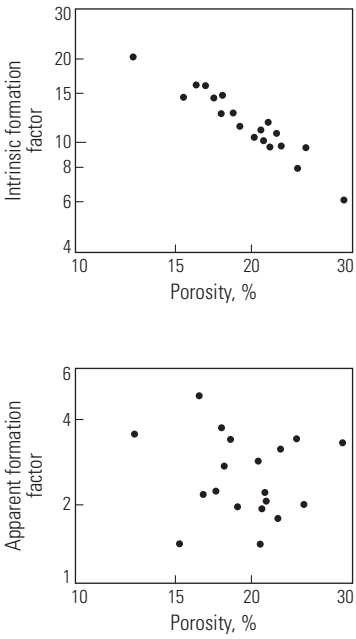


Fig. 23.6 Data from Worthington that demonstrate the influence of clay content at low values of water conductivity [3]. The formation factors of the cores in the upper figure were determined with highly conductive saturating water, the lower set with very fresh water. The spread in the lower set is a reflection of the clay content and cation exchange capacity of the rock.

presence of clay. However, it is seen that at very low values of water salinity there is a nonlinear region in which the additional clay conductivity appears to be a function of C_w.

To further illustrate this problem, Fig. 23.6 shows some measurements of the formation factor as a function of porosity from sandstone core samples. In the top figure, the samples have been saturated with very saline water (C_w is large). The behavior for these shaly samples is as expected for clean cores, since the effect of the clay conductivity is small. There is therefore a definite relationship between formation factor and porosity. Shown in the lower portion of the figure are results of measurements on the same cores, this time with quite low-salinity water. In this instance, the intrinsic conductivity of the shale dominates the conductivity and the apparent formation factors are seemingly random.

From this we can conclude that the abnormal electrical behavior of shaly sands is of less importance when the resistivity of the formation water is low. However, it is much more important when the sand is saturated with a dilute brine or when the saturated sample contains a large fraction of nonconductive hydrocarbon. Because of this, numerous techniques to cope with the clay-affected resistivity measurements have been developed over the years.

23.3.1 Early Models

Equation 23.7 was proposed by Patnode and Wyllie in 1950 [4]. They attributed the additional conductivity to conductive solids and found experimentally that C_s was proportional to the percentage of clay, or shale. C_s could therefore be written as $V_{sh}C_{sh}$. However, Winsauer and McCardell pointed out that shales do not conduct when dry, and showed experimentally that the excess conductivity came from the electrical double layer [5]. They argued that the double layer had the same tortuosity as the electrolyte so that C_o could be written as:

$$C_o = \frac{1}{F}(C_w + C_z) \tag{23.8}$$

where C_z is the conductivity of the ions in the double layer, which they also showed to vary with C_w. This variation explains well the nonlinear zone in Fig. 23.5 but not the linear zone, whereas the conductive solids approach does the opposite. Wyllie and Southwick extended the conductive solids approach by introducing a third term representing an interaction between the solids and the electrolyte that is dependent on a geometrical factor [6]. This successfully models the nonlinear zone but at the expense of an extra parameter.

In parallel with this work many empirical equations were being developed based on cores and logs, or logs alone. They are often known as V_{sh} models since they treat the shale as a conductive volume without attempting any physical explanation. Worthington has classified more than 30 shaly sand models according to how the V_{sh} term enters the saturation equation. Table 23.1 shows the classification in water-filled rocks [3].

The first group is based on a picture of dispersed clay gradually replacing electrolyte in the pore space. When it has replaced all the electrolyte it will have a volume equal to the porosity and by analogy with Archie's equation a conductivity of $V_{sh}^2 C_{sh}$. In the second group the shale causes an excess conductivity, as in Eq. 23.7. In the

Table 23.1 Four types of empirical conductivity relationships for fully water-saturated rock. The shale content of the rock is described by a single bulk parameter V_{sh}. From Worthington [3].

$$C_o = \frac{C_w}{F} + V_{sh}^2\, C_{sh}$$

$$C_o = \frac{C_w}{F} + V_{sh}\, C_{sh}$$

$$\sqrt{C_o} = \sqrt{\frac{C_w}{F}} + V_{sh}\sqrt{C_{sh}}$$

$$\sqrt{C_o} = \sqrt{\frac{C_w}{F}} + V_{sh}^{1-\frac{V_{sh}}{2}}\sqrt{C_{sh}}$$

third group there is a cross term between shale and electrolyte, as can be shown by squaring both sides of the equation. The Wyllie and Southwick model would fall in this group.

Classifying models in this way helps distinguish them but gives limited insight into the underlying assumptions. One has to wonder how much the differences between purely log-based equations were caused by limitations in the measurements of either porosity or V_{sh}. Indeed it is not always clear what porosity is referred to (with or without bound water, i.e., effective or total), or whether V_{sh} should really be the volume of bound water.

Another more fundamental classification depends on the shale distribution, that is whether it is in laminations, structural, or dispersed. In laminated sands the sand and the shale are electrically in parallel. This gives rise to a particular group of models to be discussed in Section 23.3.4. Structural shale acts mainly in series with the intergranular network. There are no specific models for structural shale. In practice it is treated like dispersed clay or like nodules of microporosity. The majority of shaly sand models consider the clays to be dispersed and in direct contact with the electrolyte. In this situation the key is to understand the contribution of the excess cations in the electrical double layer. We will therefore examine the development of double layer models in water-saturated rock before considering the effect of hydrocarbons.

23.3.2 Double Layer Models

The first equation that was based on excess cations in the double layer and which gained wide acceptance was that developed by Waxman and Smits in 1967 [7]. Using measurements made by themselves and others on nearly 200 samples, they found that in the linear portion of Fig. 23.5 the excess conductivity was proportional to Q_v, the cation exchange capacity per unit pore volume. They also assumed, like Winsauer and McCardell, that the current from the counterions in the double layer traveled along the same tortuous paths as through the electolyte. This leads to a conductivity of:

$$C_o = \frac{1}{F^*}(C_w + BQ_v) \tag{23.9}$$

where F^* was defined by the slope of the C_0 versus C_w plot to distinguish it from the Archie F, measured from the origin. B, the counterion equivalent conductance in S/m per meq/cc, was found to be a function of temperature but otherwise a constant in the linear zone. The nonlinear zone was explained by a decrease in the counterion conductance with decreasing salinity. By fitting the core data, B can be expressed as a function of both temperature T and C_w at 25°C over the whole range. Several expressions for B have been proposed, for example Gravestock [8]:

$$B = 1.58144o\ T\ [1 - 0.83\ e^{-C_{w25}/20}], \tag{23.10}$$

with T in °C.

Providing Q_v could be correlated with a log measurement, here was a simple way to handle shaly sands that was firmly based on experimental core data. The same core

data can be used to find an average relationship for m^* (from $F^* = 1/\phi_t^{m^*}$) as a function of Q_v and porosity.

However, the nonlinear zone remained a puzzle, with no good explanation for the curvature and a considerable scatter in the data that defined the variation of B with salinity. Clavier et al. [9] introduced the idea that the pore space could be divided into two volumes each with different conductivities – clay bound water with the conductivity of the counterions, and free water with electrolyte. The volume of clay bound water was determined by Gouy's diffuse layer model, which predicts that the thickness of the double layer decreases as the salinity of the electrolyte increases up to a certain limit beyond which it is fixed and defined by the Helmholz plane (see Fig. 3.9). Conceptually the difference between the fixed and the salinity-dependent thickness provided a clear way of distinguishing the linear from the nonlinear zone. The total conductivity, C_o, is then derived from a volume weighted water conductivity, C_{we}:

$$C_{we} = (1 - \alpha v_Q Q_v)C_w + \alpha v_Q Q_v C_{bw} \tag{23.11}$$

$$C_o = \frac{C_{we}}{F_o} \tag{23.12}$$

where C_{bw} is the conductivity of the bound water and $\alpha v_Q Q_v$, also known as S_{wb}, is the proportion of bound water as explained in Section 21.2.2. The values of α and the temperature dependence of C_{bw} and v_q could be established from theory, but the actual values of C_{bw} and v_q were determined by fitting to the same core data as Waxman and Smits. The dependence of the cementation exponent m_o on Q_v and porosity (from $F_o = 1/\phi_t^{m_o}$) was also determined with this data.

The dual-water model gives a more satisfactory explanation for the nonlinear zone, and explains the curvature at low salinity, but only down to a water conductivity of about 1 S/m, below which it fails. Inspection of the dual water and Waxman–Smits equation shows that the formation factors, F_o and F^* are different, and different from the Archie F. It turns out that the m_o is less sensitive than m^* to the amount of clay. When m is not well known, this is a practical advantage, since there is less error in using a constant value throughout the reservoir.

The basic assumption of both Waxman–Smits and dual-water models is that the two conductivity paths experience the same tortuosity. Given the convoluted surface of clays it is not surprising that Pape and Worthington found evidence that the tortuosity of surface conductivity was considerably greater than that of free water [10]. The idea of different formation factors for the two conductivities was a key element in the equation developed by Sen, Goode, and Sibbit (SGS) [11]. As illustrated in Fig. 23.7, at high salinity the current flows mainly in the center of the pores and is governed by the pore geometry, while at low salinity the current flows close to the pore walls and is governed by their geometry. The exact form of their equation (SGS) was based on theoretical calculations of the conductivity of periodic arrays of spheres with surface conductivity and can be expressed as:

$$C_o = \frac{1}{F}\left[C_w + \frac{AQ_v}{(1 + \frac{CQ_v}{C_w})}\right] + EQ_v. \tag{23.13}$$

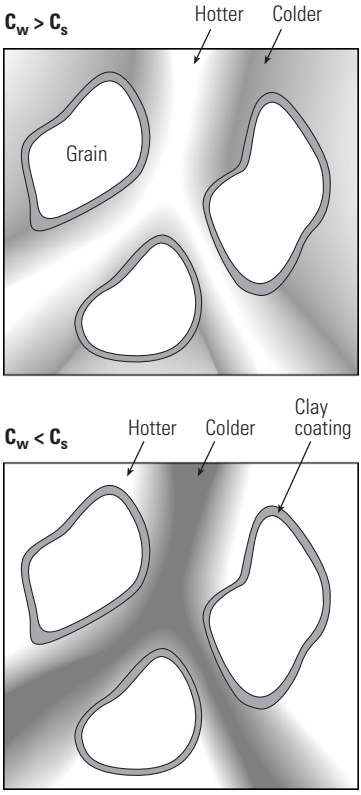


Fig. 23.7 The path taken by the current as the salinity changes, with hotter representing more current flow. When the surface conductivity, C_s, is large compared to water conductivity, C_w, the current prefers the more tortuous surface region, while in the opposite case the current prefers the pore tortuosity. The change in tortuosity explains the curvature of the C_o versus C_w plot. From Sen and Goode [11]. Used with permission.

where A, B, and E are constants to be determined from theory and experiment. Ignoring the term in E for the time being, it can be seen that if $CQ_v << C_w$ the term in brackets reduces to the Waxman–Smits equation with $A = B$, and a slope of $1/F$. However if $CQ_v >> C_w$ the slope becomes $1/[F(1 + A/C)]$ which is necessarily higher than $1/F$ and explains properly the curvature in Fig. 23.5. (Note that the second term is that of two conductivities, C_w and Q_v, in parallel, and as such has some similarity to the interaction term in the Wyllie and Southwick model.)

The theoretical models showed that A depended on tortuosity and could be related to m. E reflects the fact that some shaly cores showed a clear trend to a finite surface conductivity at zero C_w. Values for A, C, and E were found by fitting to the Waxman–Smits data base, with $A = 1.93m$, $CQ_v = 0.7$ and $E = 1.84\phi^m$ (later modified to $1.3\ \phi^m$).

All three double-layer models have parameters that have been found to give the best fit to a certain set of core data filled with a certain range of NaCl solutions. Some reservoirs may not fall within this range and although in principle the parameters can be adjusted to fit the core data from specific reservoirs, in practice this is rarely done. Note also that in all three models the porosity that should be used to calculate the formation factor is the total porosity.

23.3.3 Saturation Equations

So far the discussion of shaly sands has been centered on the electrical behavior of fully water-saturated rock. What will be the effect of introducing nonconductive hydrocarbon in the pore space? Again, it is possible to classify shaly sand models into different types according to how S_w affects the shale terms (Table 23.2). In models that assume that the shale and the sand conduct independently (group 1, such as the laminated sands discussed below), the shale term is unaffected by the hydrocarbons. However, with dispersed clay it is likely that the presence of hydrocarbons affects the contribution from the clay. The other three groups are then distinguished by whether there is an interactive term and which terms affect S_w. For example a classic, and still used, example from the fourth group is the Indonesia equation, which has an interactive term and a factor of S_w^2 in each term:

$$C_t = \frac{C_w S_w^2}{F} + 2\sqrt{\frac{C_w V_{sh}^{(2-V_{sh})} C_{sh}}{F}} S_w^2 + V_{sh}^{(2-V_{sh})} C_{sh} S_w^2 . \qquad (23.14)$$

The equation was developed empirically by Poupon and Leveaux for the fresh formation waters and high shaliness of many Indonesian reservoirs in which oil was produced from zones of low resistivity [12]. As such, the interactive term provides the nonlinear relation of C_o to C_w that will occur in these conditions. The authors specified that effective porosity should be used and the S_w calculated was the fraction

Table 23.2 Four types of saturation equation written in terms of the excess conductivity X due to the contained shale. From Worthington [3].

$C_t = \frac{C_w}{F} S_w^n + X$
$C_t = \frac{C_w}{F} S_w^n + X S_w^s$
$\sqrt{C_t} = \sqrt{\frac{C_w}{F}} S_w^{n/2} + \sqrt{X}$
$\sqrt{C_t} = \sqrt{\frac{C_w}{F}} S_w^{n/2} + \sqrt{X}\, S_w^{s/2}$

of water in the effective porosity. However there is some evidence that the results are closer to the fraction of total porosity [15]. This is typical of the ambiguity that can be associated with such equations.

In the double-layer models, which fall in group 2, the exchange cations become increasingly concentrated in the pore water as S_w decreases. Waxman and Thomas argued that Q_v should be taken as the CEC per volume of water-filled pore space, Q_v/S_w, and supported this with a range of experiments that covered only moderately fresh and shaly formations [13]. Then, using the same relation as Archie for the general geometrical effect of hydrocarbons, Eq. 23.9 is written as:

$$C_t = \frac{S_w^n}{F^*}\left(C_w + \frac{BQ_v}{S_w}\right). \tag{23.15}$$

The same argument was made for the dual-water equation. For the SGS model the idea of different formation factors for surface and bulk conductivity was extended to include hydrocarbons. Sen and Schwartz argued that the tortuosity experienced by surface conductivity is very little affected by the addition of hydrocarbons, but that the bulk conductivity path becomes increasingly tortuous and approaches that of the surface conductivity as S_w decreases [14]. Using a grain consolidation model and for particular cases of water-wet pores, Sen and Schwartz found that the factor C in Eq. 23.13 should be modified to CS_w^{-n} while, as with the other models, $1/F$ should be modified to S_w^n/F.

All three models explain the change in resistivity with S_w when the contribution of clay to conductivity is low or moderate, but in fresh water, shaly formations the SGS model does better than the others. The last term ($1.3\phi^m Q_v$) has a strong influence at low S_w and predicts better the curve in the ratio R_t/R_o as S_w decreases (Fig. 23.8).

Compared with the Archie equation, the application of these models requires one extra measurement, namely Q_v (or equivalently S_{wb}). The simplest method of obtaining Q_v is to find a relationship with gamma ray counts on core data, and apply that to the gamma ray log. Otherwise it can be determined from the log-derived clay volume as described in Section 21.2.2. Of the parameters, n is usually fixed near 2 and m is either fixed near 2 or calculated from the appropriate function of ϕ_t and Q_v found on local data or the Waxman–Smits data base. The calculation of R_w in a water zone is not as simple as with Archie, but can be derived from R_t, ϕ_t, Q_v and by setting $S_w = 1$ in the desired model. This same calculation will give the apparent bound water conductivity, C_{wb}, for the dual-water equation (in the Waxman–Smits and SGS equations the clay conductivity is built into the parameters B, A, and C).

An example of shalysand interpretation is shown in Figs. 23.9 and 23.10. The logs were recorded through a sequence that had been drilled with oil-based mud and from which cores had been cut and well preserved [15]. The volume of water in the cores is therefore expected to represent well the water saturation in the reservoir. ϕ_t is calculated from the density log after adjusting the matrix and fluid density to best fit the core data. V_{sh} is taken from the GR log, and converted to S_{wb} for the

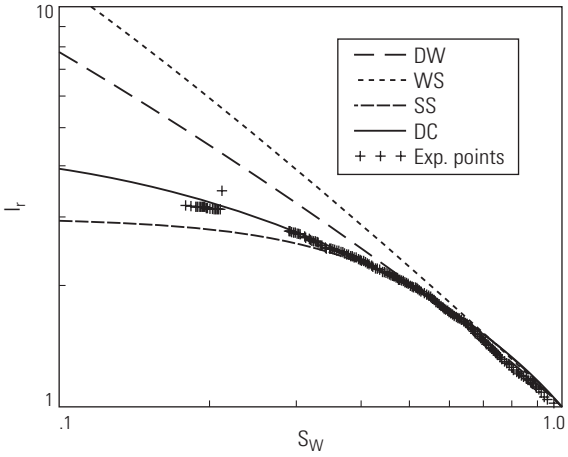


Fig. 23.8 Resistivity index versus saturation measured on a shaly core sample with water of conductivity 0.354 S/m, and as predicted by the dual-water, Waxman–Smits, Sen–Goode–Sibbit and dual conductor models. The saturation index, n, was derived separately for each model from fits to high-salinity data; Q_v was measured chemically; m for the SGS model was determined with the sample water-saturated. The DC model is explained in Section 23.4. Adapted from Argaud et al. [16].

dual-water equation by Eq. 21.1 assuming $V_{sh} = V_{cl}$. Water salinity is moderately low with $R_w = 0.13$ ohm-m taken from samples in nearby wells. $m = n = 1.8$. The water-filled resistivity from the dual water and Indonesia equations (R0DW and R0IND) match the measured R_t at the shaliest points so there is a good chance that the shale parameters, C_{wb} and C_{sh}, have been correctly chosen (although there is no guarantee that the clays in shale are the same as those in the sands).

Figure 23.10 shows the total porosity calculation agreeing well with core porosity, as expected. For the sake of comparison, S_w has been calculated with the Archie, Indonesian, and dual-water equations. Two results are shown for the latter: with $n = 1.8$ (DW), and with $n = 1.42$ after adjustment to give the best fit to core saturation (DWFF). The Archie and dual-water equations use total porosity and water saturation, while the Indonesian equation uses effective volumes. (As pointed out by Woodhouse and Warner, the hydrocarbon volume should be the same in both cases - see Problem 23.5.)

In the clean zone at 6,560 ft the adjusted DWFF S_w gives the best fit to core results (naturally), while the others overlie since they all reduce to the same Archie equation. All are slightly pessimistic. In the shalier zones below, the Archie solution is pessimistic while the Indonesian and dual-water equations are similar. These results illustrate the need for a shale correction, but also the difficulty in obtaining close matches to core data. Part of this may be due to limitations in the equations, but part may be due to limitations in the measurements.

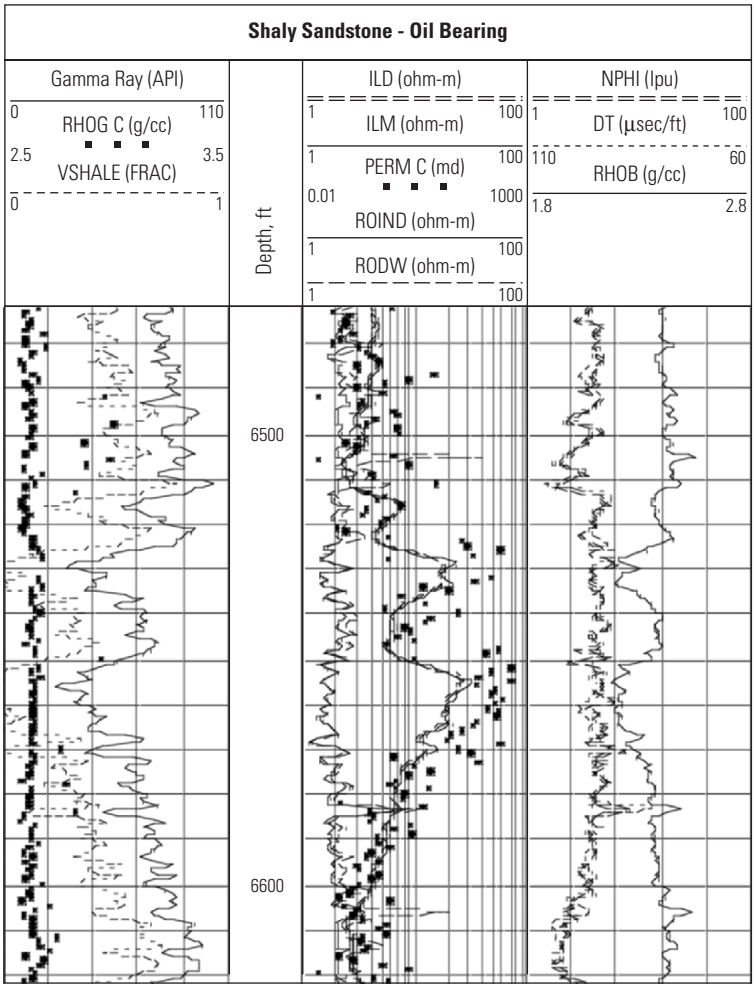


Fig. 23.9 Logs over a shaly sandstone section. R0IND and R0DW are the formation resistivities calculated using the Indonesia and dual-water equations assuming the formation is water-filled. Oil is expected when these curves read less than the measured resistivity. From Woodhouse and Warner [15]. Used with permission.

23.3.4 Laminated Sands

The earliest solution to the problem of laminated sands was proposed by Poupon et al. [17]. Assuming the laminations are smaller than the resolution of the logging measurements and perpendicular to the borehole, then the sand and the shale are electrically in parallel:

$$C_h = (1 - V_{sh})\, C_{sd} + V_{sh} C_{sh} \tag{23.16}$$

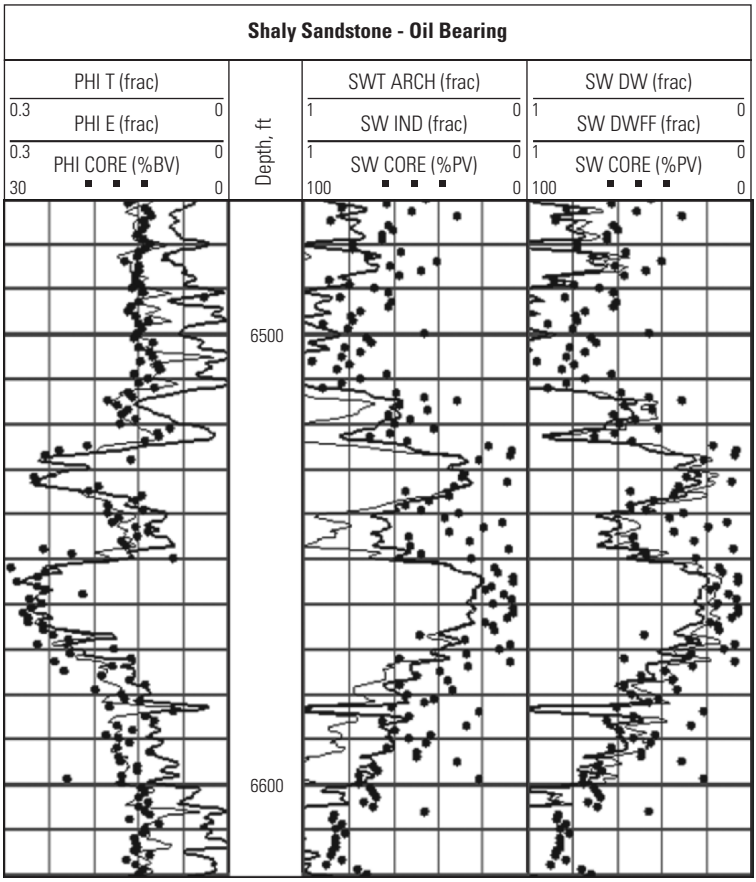


Fig. 23.10 Computed ϕ_t from the neutron-density logs and water saturation from the Archie, Indonesia and dual-water equations. The core measurements were made on well-preserved cores drilled with OBM and are expected give accurate total ϕ_t and hydrocarbon volumes. From Woodhouse and Warner [15]. Used with permission.

where C_h is determined from C_t as measured by conventional resistivity devices in vertical wells. This equation is used to solve for C_{sd}, which can then be interpreted using Archie'e equation, i.e., $C_{sd} = \phi_{sd}^m S_w^n C_w$. The porosity in the sand, ϕ_{sd}, is not measured directly but can be derived as illustrated in Fig. 23.11 from the measured ϕ_t and from ϕ_{sh} in a nearby massive shale. Some caution is needed when applying this procedure. First, S_w is the saturation in the sand streaks and not that of the total formation (sand + shale). Second, ϕ_{sd} and S_w are assumed to be the same in each lamination within the resolution of the measurements. Finally, the sands are assumed to be clean.

Some improvements to laminated sand analysis came with the application of high resolution dipmeter, resistivity, and image logs in the late 1970s. Laminations of

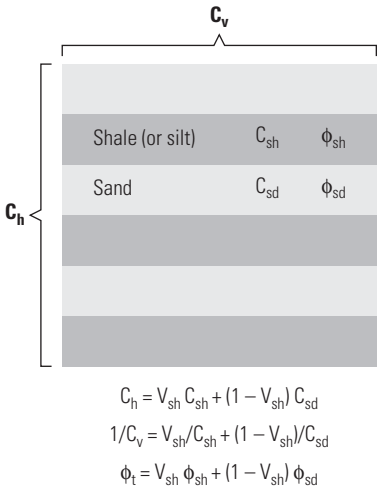


Fig. 23.11 Schematic drawing of a laminated sand, showing the conductivity and porosity of the laminae. The laminations are significantly thinner than the vertical resolution of the porosity or resistivity measurements (ϕ_t, $R_h = 1/C_h$, $R_v = 1/R_v$), but can be related to these measurements by the formulae shown.

a few centimeters could be seen on these logs, allowing more laminated sands to be recognized and also providing an accurate V_{sh} by counting the laminations. The resistivity information from these high-resolution logs was more qualitative than quantitative, but it could be summed over a few feet to match the resolution of the deep-resistivity logs and then calibrated to match these logs. The result was better information on the sands and an improved determination of C_{sd}.

Equation 23.16 can be refined by adding clay to the sands and using one of the dispersed clay models to define their conductivity instead of Archie [18]. The problem then is to define the volume of this clay. This was possible with the EPT log, due to its high vertical resolution and sensitivity to water salinity. A procedure was developed to take advantage of this [19]. However it was still necessary to assume that porosity and water saturation were constant within the resolution of the logging measurements.

In spite of these improvements, the major weakness remains, which is that the traditional horizontal measurement of R_t is dominated by the higher conductivity shale term and insensitive to the sand. For example, a small error in V_{sh} or C_{sh} can lead to a negative C_{sd}. The breakthrough came with the ability to measure vertical resistivity, R_v, from triaxial induction logs or LWD propagation logs in horizontal wells, since R_v is more sensitive to the higher resistivity sand term. Using both R_v and R_h, C_{sd} and C_{sh} can be computed using the method described in Section 8.5.2. The accuracy of the resultant C_{sd} is much improved because it is largely determined by R_v, and because there is no need to rely on picking C_{sh} from a massive shale.

The difference between water saturation from the Archie equation using the traditional R_t, and water saturation from a laminated sand analysis was already illustrated

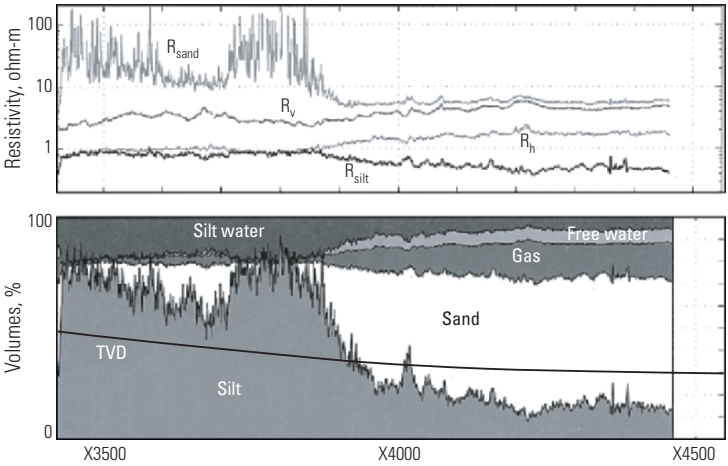


Fig. 23.12 (Top) R_v and R_h are derived from the LWD propagation logs of Fig. 9.22. R_{sand} and R_{silt} are derived from R_v and R_h using the equations in Section 8.5.2 (Eqs. 8.7 and 8.8). (Bottom) Water saturation is then calculated from R_{sand} using the Archie equation with $R_w = 0.035$ ohm-m. The silt is assumed to contain only water. From Tabanou et al. [20]. Used with permission.

in Fig. 8.24. Another example is based on the anisotropy observed on the LWD logs in Fig. 9.22. R_v and R_h were calculated from these logs using knowledge of the tool response. In this case it is known that the anisotropy is not caused by shale laminations but by fine-grained silt streaks, which can be observed on the density image from the same well (Fig. 20.7) and counted to give V_{silt}. Replacing V_{sh} and R_{sh} by V_{silt} and R_{silt} in Eqs. 8.7 and 8.8 gives the result shown in Fig. 23.12 [20]. When there is enough sand to determine R_{sd}, S_w can be calculated from Archie's equation.

This is a classic example of low resistivity pay, since the traditional measurement of R_h would have given a very pessimistic S_w. The measurements of R_h and R_v ensure a much better value for R_{sd}, while the ability to measure the porosity of the sand laminations directly from the density log also improves the S_w estimate.

23.4 CARBONATES AND HETEROGENEOUS ROCKS

The vast literature on shaly sands interpretation might lead one to think that such formations were the most difficult to interpret. In fact carbonates can be at least as challenging because of the wide range and irregular distribution of the pore sizes that can be encountered, from micropores of less than 1μm to vugs of 1 cm, and from spherical pores to fractures. Carbonates may also contain clay, in which case they are treated by one of the shaly sand equations. Some sandstones can also be heterogeneous, with fractures and microporosity.

The effect of fractures, vugs, and oomolds on m was already discussed in Chapter 4. There we saw that m increases in the presence of vugs and oomolds and decreases with fractures. The effect of microporosity depends on its distribution. It can occur in discontinuous nodules, which act like partially filled vugs, adding porosity without altering the resistivity [21]. It can also occur on the surface of grains and be continuous throughout the formation, in which case it adds a surface conductance in the same way as clays [22].

The effect of de-saturation on these different pore types, and hence on the exponent n, is more difficult to predict. When oil or gas is introduced into such a rock, the water in one pore type may be displaced more easily than in another. In addition the wettability may vary with pore type, leading to different n's for different pore types. (Carbonates anyway have a larger tendency to be oil-wet.) For example in virgin reservoirs the fractures should be filled with oil, but providing there is a significant amount of intergranular porosity the effect on resistivity is small. However if the fractures are full of water, as is likely in the invaded zone, they will act as a short circuit and strongly reduce n. If the two systems are assumed to act in parallel, the results are as shown in Fig. 23.13. Fractures tend to reduce n, particularly if they are water filled.

Vugs can be unconnected to the intergranular pore system, in which case they do not contribute to conductivity, or they can be connected, in which case they make a small contribution in relation to their volume. One method of modeling the latter is to treat the vugs as scattered spherical inclusions in a host that has intergranular porosity. This type of problem can be solved by the Maxwell–Garnett equations to give a low-frequency conductivity response of [23]:

$$C_t = C_{host}\left[\frac{1 + 2V_{si}\left(\frac{C_{si} - C_{host}}{C_{si} + 2C_{host}}\right)}{1 - V_{si}\left(\frac{C_{si} - C_{host}}{C_{si} + 2C_{host}}\right)}\right] \tag{23.17}$$

where C_{si} and C_{host} are the conductivities of the inclusions and the host and V_{si} is the volume fraction of the inclusions. C_{si} is then given by the water conductivity and saturation in the vugs ($C_w S_{wsi}$), and C_{host} by an Archie relation for the intergranular volumes. As can be seen in Fig. 23.14, the resulting n depends strongly on whether the vugs are water-filled or not. Equation 23.17 is a simple type of effective medium equation. In principle such equations can be formulated to handle multiple pore types and conductivity systems in a general way [25, 26].

Microporosity tends to be water-wet and water-filled since a large capillary pressure is needed to displace the water. It therefore acts like the clay in Fig. 23.8 and causes a decrease in n with de-saturation. In fact the fourth curve in this figure is based on a dual conductor model in which the pore space is divided into normal intergranular macroporosity and microporosity, which is continuous through the formation and associated with rough surfaces, clays, and other small pores. The two pore systems are assumed to be electrically in parallel. Initially, both pore types are affected equally by the removal of water. However, below some critical saturation (57% in the example) the micropores are unaffected by further removal of water, which only takes place in the macropores. The result is a line of two segments.

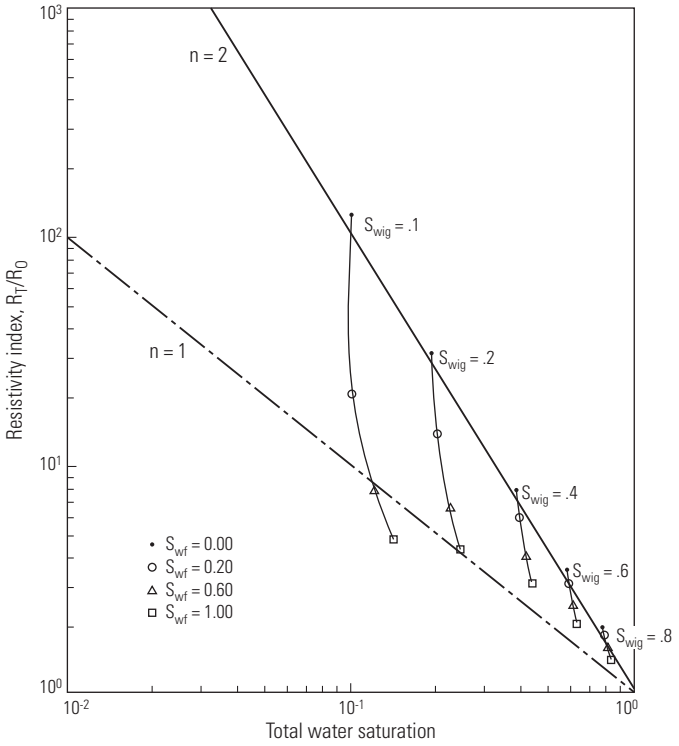


Fig. 23.13 The effect of fractures on resistivity index at different intergranular S_w for an intergranular porosity of 0.2 v/v and a fracture porosity of 0.01 v/v. The results are strongly dependent on the water saturation in the fractures. From Rasmus [24]. Used with permission.

This is one of several models that have been proposed to account for microporous rocks. In another, by Swanson, the microporous nodules are isolated and in series with the larger pores [27]. In this model the micropores do not start to de-saturate until *below* a certain saturation. This leads to a similar decrease in n but by a different mechanism.

These cases illustrate the problem of interpreting heterogeneous reservoirs. Although it is recognized that different pore types may need different m and n it is not clear how they should be combined. Should they be in parallel or in series? Should there be an interaction term? In many ways this is the same problem that was faced in the early days of shaly sand interpretation. The difficulty is that carbonates are much more irregular and so meaningful extrapolations from core data are much more difficult to make. Also while there are many techniques to measure the volume of shale, the same is not so for the different pore types. NMR logs offer some solution for measuring pore size while image logs can help quantify vugs and fractures. Even when these volumes can be estimated m and n still need to be defined for each pore type. The interpretation of many carbonates and heterogeneous rocks remains a challenge.

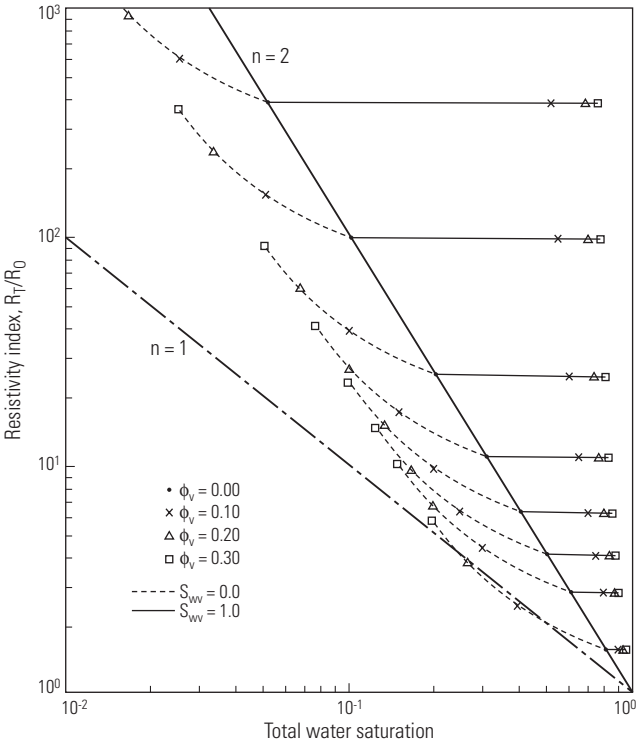


Fig. 23.14 The effect of vugs on resistivity index at different total S_w for an intergranular porosity of 0.1 v/v and various vug porosities. The results depend strongly on whether there is water or oil in the vugs. From Rasmus [24]. Used with permission.

23.5 PERMEABILITY FROM LOGS

When Archie started making resistivity measurements on core samples, one of his main goals was to find a correlation between formation factor and permeability. He did not succeed and, although this work led to the well-known Archie equations instead, his experience has been a common one. The goal of deriving permeability from logs is elusive, which is perhaps not surprising since logs make static measurements whereas permeability is a measure of dynamic properties. The only exception is the Stoneley wave, since the Stoneley actually moves pore fluid in the rock. All other log-based methods rely on a correlation with dynamic permeability measurements made with cores or tests. This section reviews some general log-based methods and shows how they are related. Most of the discussion is not applicable to very heterogeneous pore systems, so that many carbonates are excluded. Specific acoustic and NMR techniques are not discussed here because they were already covered in the appropriate chapters.

Before proceeding it is important to define permeability more closely. Unlike porosity and saturation, permeability is a tensor and often strongly dependent on

direction. For example, the process of sedimentation usually causes vertical permeability to be less than horizontal. Secondly, it is not obvious how permeability should be scaled up to larger volumes – whether it should be averaged arithmetically, harmonically, geometrically, or in some other way. This makes it difficult to compare permeability measured made at different scales. Finally, permeability depends on the fluids within the measured volume. If there are two or more fluids, they can seriously impede each other's flow, so that the effective permeability of each fluid is less than the absolute permeability. In addition the salinity of the water flowing through a shaly sand can affect the clays and alter the permeability of core samples unless care is taken.

Thus permeability measured by different techniques can be very different. Most measurements made on core data are of the horizontal permeability to air, while those made with well tests are of the effective horizontal permeability to oil. The well test samples a volume two to three orders of magnitude larger than that of a core sample. Logging measurements sample an intermediate volume and reflect the core or test data to which they have been correlated. In this section we will only consider how permeability can be derived from logs, and will not consider core or well test based methods, nor the techniques needed to relate the three and apply them to reservoir description. Unless otherwise mentioned the term permeability refers to the absolute permeability, measured with a single fluid in the pore space.

23.5.1 Resistivity and Porosity

The two principal log measurements – resistivity and porosity – can both be used to estimate permeability. Resistivity logs can be used to make some broad and semi-quantitative estimates because they depend to some extent on the result of fluid movement. One method is based on the length of the transition zone between water at the bottom of the reservoir and oil or gas at irreducible saturation above. Reservoir engineering textbooks show that the longer this zone the higher the capillary forces and the lower the permeability. Thus the change in resistivity with depth within the transition zone can be related empirically to permeability [28]. Another type of estimate is based on invasion. The depth of invasion depends mainly on the history of drilling and the permeability of the mudcake, but in very low permeability formations there is some sensitivity to the formation [29]. In high-permeability reservoirs, gravity causes the filtrate to move up or down depending on whether the formation fluid is heavier, e.g., saline water, or lighter, e.g., oil or gas. The vertical invasion profile therefore holds information on vertical permeability. In general the shape of the invasion front radially away from the borehole can be related to the relative permeability of the different fluids [30].

Porosity is used much more frequently than resistivity to estimate permeability. Correlations such as shown in Fig. 23.15 between the logarithm of permeability and porosity are often observed, particularly when the correlation is limited to data from one particular reservoir or formation. The strength of such correlations is surprising, given that many other factors would be expected to contribute, as will be discussed further below. Nelson has summarized the effect of various textural and mineralog-

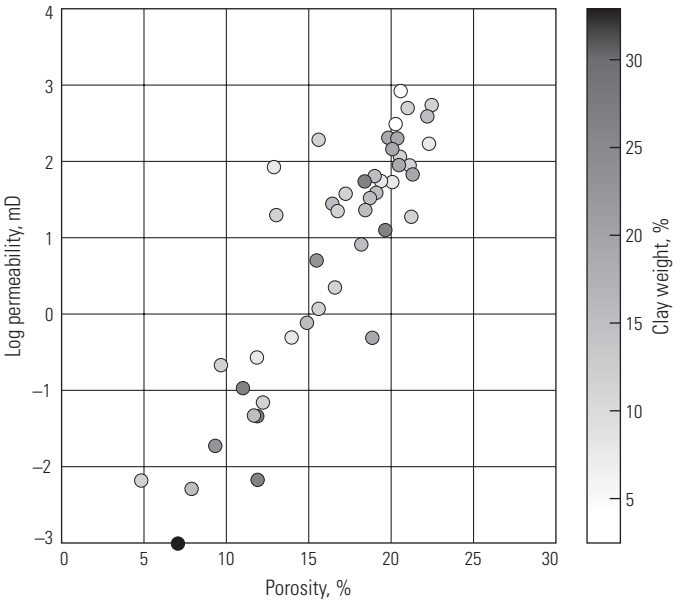


Fig. 23.15 Measured porosity and permeability values for shaly sand samples from Utah, showing the correlation between $log(k)$ and ϕ often observed in shaly sands . Adapted from Herron et al. [39].

ical factors on these plots (Fig. 23.16) [31]. A significant advantage over resistivity methods is that the correlation can be established in the laboratory on core data, and then applied to log-derived porosity.

When a large set of core data is available it is possible, and often necessary, to look for a correlation not only with porosity but also with other parameters that can be derived from logs, such as V_{cl}. It is rare that more than two or three parameters improve the prediction: indeed, if too many are added the prediction can deteriorate. The correlation can also be established directly on log data. Nicolaysen and Svendsen found a correlation for the Troll field between core permeability and a combination of the logs of gamma ray, density and neutron–density separation [32]. Finally, purely statistical techniques such as neural networks or clustering can be used to find a correlation between permeability and log values, ignoring any physical relationships.

23.5.2 Petrophysical Models

Many efforts have been made to improve on the purely empirical correlation methods by applying a suitable petrophysical model. Models can be classified by whether they are based on grain size, pore dimensions, mineralogy, surface area, or water saturation [31]. Grain size and pore dimensions are measured on core samples but only very indirectly on logs, and so will be mentioned only briefly here.

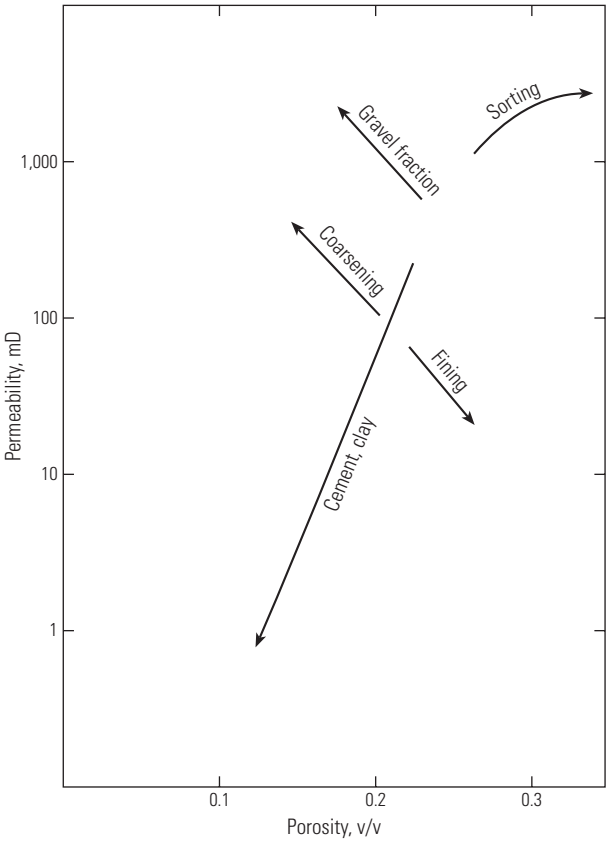


Fig. 23.16 Summary of the impact of grain size, sorting, clay, and interstitial cements upon permeability-porosity trends. From Nelson [31]. Used with permission.

The models are best understood by starting from the Kozeny–Carman relationship [33]. This represents the pore space as a bundle of independent, tortuous tubes of different radii. If the flow rate is low enough that it is laminar and not turbulent, the permeability can be calculated as:

$$k = A\frac{\phi}{\tau S_p^2}\,, \tag{23.18}$$

where A is a shape factor for the tubes, τ is the tortuosity, and S_p is the ratio of pore surface area to pore volume. Since $\tau = F\phi$, from Section 4.4.4, and $F = 1/\phi^m$, permeability can also be written as:

$$k = A\frac{\phi^m}{S_p^2} = A\phi^m r_h^2\,, \tag{23.19}$$

where r_h, the inverse of S_p, is known as the hydraulic radius. In a sample with several contrasting parallel paths, r_h is controlled by the most conductive path; however in any one path, or in a more homogeneous sample, it is controlled by the least conductive elements, which are usually the pore throats. The different petrophysical models are then distinguished by the different ways in which they find S_p or r_h. The pore dimension models are the most direct since they are based on the most direct estimates of r_h. These are obtained from various interpretations of capillary pressure curves, and are considered to reflect the size of pore throats. In grain size models, r_h is related to the grain size and some factor of grain sorting as well as an extra dependence on porosity.

Models based on water saturation assume that a large pore surface to volume ratio means a large irreducible water saturation: S_p is therefore well correlated with S_{wirr}. The relationship was first proposed by Wyllie and Rose [34] and developed by Timur [35]. The models take the form:

$$k = a\frac{\phi^b}{S_{wirr}^c}, \tag{23.20}$$

where a, b, and c are determined from measurements on core samples. In Timur's relation, and with ϕ and S_{wirr} in units of v/v and k in mD, $a = 10^4$, $b = 4.4$ and $c = 2$. Other, similar relationships exist. However, the determination of S_{wirr} from logs is not straightforward. S_w can be used if it is known that the zone being interpreted is at irreducible water saturation, and is not a transition zone. Furthermore, the correlations were established at a given capillary pressure, whereas in a reservoir this pressure varies with height above the oil–water contact. Charts are available to correct for this effect [36]. Nevertheless the method provides a convenient way of estimating permeability from basic log data.

The Timur relation does not specify whether the porosity is effective or total, but since it is generally applied to clean sandstones the difference is not important. In shaly sandstones it is not so clear whether effective or total porosity should be used. Coates proposed an equation that allows for the effect of both irreducible water and clay bound water [37]:

$$k = 10^4(\phi_t - V_{cbw})^4\left[\frac{\phi_t - V_{wirr}}{V_{wirr}}\right]^2, \tag{23.21}$$

where $V_{wirr} = \phi_t S_{wirr}$ is the bulk volume of irreducible water. Volume is used instead of saturation because it has been found that V_{wirr} is generally more consistent and easier to predict in a given reservoir than S_{wirr}.

Another group of petrophysical models is based on estimating S_p from other measures of surface area. One of the most common is the use of T_1 or T_2 from NMR data, as described in Chapter 16. Other relationships have been found between S_p and Q_v [38]. S_p can also be expressed in terms of the surface area per unit mass, S_0 (Problem 23.8). Herron et al. have shown that a particular value of S_0 can be defined for each mineral. The total S_0 can then be calculated from the mass average, using the weight percent of each mineral found by elemental analysis or other logs

[39]. Using core data, a value of A in Eq. 23.19 was found that gave a good fit to the data for permeability above 100 mD. Below 100 mD, A and the coefficients of ϕ and S_p had to be adjusted to another set of values ($0.37A^{1.7}$, $1.7m$, and 3.4, respectively). It is probable that below 100 mD some of the pores become blocked, so that although they contribute to the mineralogical estimate of hydraulic radius they do not contribute to flow: in other words the estimated S_p is too low and r_h too high. With this modification a good fit could be obtained to core samples from the clay-free Fontainbleau sandstones (see Fig. 23.17). This dataset is interesting in that it does not conform at all to the normal $log(k)$ versus ϕ relation. Figure 23.18 shows the results of applying the same method to a more normal dataset, which comes from the well shown in Fig. 23.15. The continuous permeability log was calculated using the clay, carbonate, and quartz concentrations from elemental analysis logs. Results compare well with core permeability.

Having reviewed the different models it is interesting to examine why the linear relation between $log(k)$ and ϕ is so common. Figure 23.19 shows the Kozeny–Carman equation (Eq. 23.19) plotted for different values of r_h, from which it is apparent that the direct dependence on porosity is weak. (The factor $A = 0.018$ is taken from Katz and Thompson's work with capillary pressure curves [40].) The ellipse represents typical data points from one sandstone reservoir. Although the direct dependence of $log(k)$ on ϕ is small, it seems that as ϕ decreases there is an accompanying drop in r_h. It is likely that in a particular reservoir the pore space is reduced by compaction and diagenesis in a way that maintains a consistent relationship between ϕ and r_h. In the atypical Fontainbleau sandstone, the drop in r_h is much smaller.

It is also interesting to note that different models have different exponents for porosity. Nelson suggests that those models that use the most appropriate physical measures of r_h or S_p have the lowest exponent, near 2 [31]. Those that rely on less

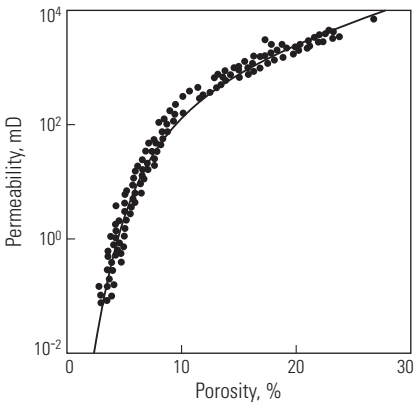


Fig. 23.17 Measured porosity and permeability values and the estimate from the $K - \Lambda$ model for the clay-free Fontainbleau formation quartz arenites, assuming $S_0 = 0.22$ m^2/g. Adapted from Herron et al. [39].

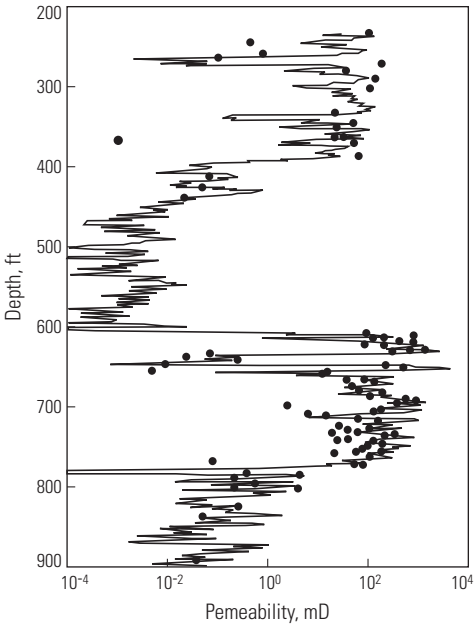


Fig. 23.18 Measured core permeability and the estimate from the $K - \Lambda$ model using the clay, carbonate, and quartz fractions from elemental analysis and S_0 = 60, 2 and 0.2 m^2/g respectively. The core data is the same as that shown in Fig. 23.15. Adapted from Herron et al. [39].

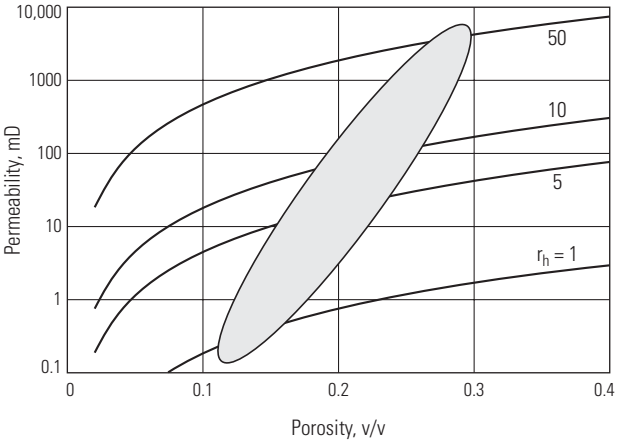


Fig. 23.19 Permeability versus porosity at different hydraulic radii, r_h, in μm, according to the Kozeny–Carman relationship with a factor A of 0.018. The ellipse indicates typical data points from a sandstone reservoir.

related measures, such as water saturation, compensate for their lack of information through a higher exponent, near 4. In these models the estimator reflects the total surface area, which is heavily weighted by the smallest pores. However, the smallest pores may be bypassed and do not contribute as much as larger pores to permeability. The extra porosity term serves to compensate for this bias.

Finally, the estimation of permeability in carbonates is complicated by the heterogeneity of the rock, as it was for water saturation. Heterogeneity means that core samples may be too small to adequately represent the rock, making it difficult to establish a ground truth for log-based estimates. Measurements on whole core sections are more suitable but less often performed. The correlation between permeability and porosity is often poor in carbonates, but can sometimes be improved by developing correlations for specific facies that can be identified on logs. In other cases, identifying the pore type can help. For example, vugs contribute heavily to porosity but not much to permeability. If the volume of vugs can be measured, their contribution to porosity can be removed and the permeability correlation improved. In general, it is difficult to achieve a permeability prediction that is within the factor of ± 3 often considered satisfactory in sandstones. Deriving permeability from logs will always be difficult, but necessity will no doubt continue to motivate work in this area.

REFERENCES

1. Hingle AT (1959) The use of logs in exploration problems. Presented at the 29th SEG Annual International Meeting of SEG, Los Angeles

2. Pickett GR (1963) Acoustic character logs and their application. J Pet Tech June:659–667

3. Worthington PF (1985) The evolution of shaly-sand concepts in reservoir evaluation. The Log Analyst 26(1):23–40

4. Patnode HW, Wyllie MRJ (1950) The presence of conductive solids in reservoir rock as a factor in electric log interpretation. Pet Trans AIME 189:47–52

5. Winsauer WO, McCardell WM (1953) Ionic double-layer conductivity in reservoir rock. Pet Trans AIME 198:129–134

6. Wyllie MRJ, Southwick PF (1954) An experimental investigation of the S.P. and resistivity phenomena in dirty sands. Pet Trans AIME 201:43–56

7. Waxman MH, Smits LJM (1968) Electrical conductivities in oil-bearing shaly sands. Paper 1863-A in: SPE J June:107–122

8. Gravestock DI (1991) Behavior of Waxman-Smits parameter B in high R_w, high temperature reservoirs. The Log Analyst 32(5):596–602

9. Clavier C, Coates G, Dumanoir J (1984) Theoretical and experimental basis for the dual water model for interpretation of shaly sands. Paper 6859 in: SPE J April:153–168

10. Pape H, Worthington PF (1983) A surface-structure model for the electrical conductivity of reservoir rocks. Trans SPWLA 8th European Formation Evaluation Symposium, paper Z

11. Sen PN, Goode, PA (1988) Shaly sand conductivity at low and high salinities. Trans SPWLA 29th Annual Logging Symposium, paper F

12. Poupon A, Leveaux J (1971) Evaluation of water saturations in shaly formations. Trans SPWLA 12th Annual Logging Symposium, paper O

13. Waxman MH, Thomas EC (1972) Electrical conductivity in shaly sands, I. The relation between hydrocarbon saturation and resistivity index, II. The temperature coefficient of electrical conductivity. J Pet Tech February:213–225, paper SPE 4094

14. Schwartz LM, Sen PN (1988) Electrolytic conduction in partially saturated shaly formations. Presented at the 63rd SPE Annual Technical Conference and Exhibition, paper SPE 18131

15. Woodhouse R, Warner HR (2004) Improved log analysis in shaly sandstones – based on S_w and hydrocarbon pore volume routine measurements of preserved cores cut in oil-based mud. Petrophysics 45(3):281–295

16. Argaud M, Giouse H, Straley C, Tomanic J, Winkler K (1989) Salinity and saturation effects on shaly sandstone conductivity. Presented at the 64th SPE Annual Technical Conference and Exhibition, paper SPE 19577

17. Poupon A, Loy ME, Tixier MP (1954) A contribution to electric log interpretation in shaly sands. Paper 311 in: J Pet Tech 6(6):27–34

18. Patchett JG, Herrick DC (1982) A review of saturation models. Shaly Sand Reprint Volume, SPWLA, Houston, TX, pp III:1–7

19. Allen DF (1984) Laminated sand analysis. Trans SPWLA 25th Annual Logging Symposium, paper XX

20. Tabanou JR, Anderson B, Bruce S, Bonner S, Bornemann T, Hodenfield K, Wu P (1999) Which resistivity should be used to evaluate thinly bedded reservoirs in high angle wells? Trans SPWLA 40th Annual Logging Symposium, Paper E

21. Herrick DC (1988) Conductivity models, pore geometry and conduction mechanisms. Trans SPWLA 29th Annual Logging Symposium, paper D

22. Givens WW (1987) A conductive rock matrix model (CRMM) for the analysis of low-contrast resistivity formations. The Log Analyst 28(2):138–151

23. Rasmus JC, Kenyon WE (1985) An improved petrophysical evaluation of oomoldic Lansing-Kansas City formations utilizing conductivity and dielectric log measurements. Trans SPWLA 26th Annual Logging Symposium, paper V

24. Rasmus JC (1986) A summary of the effects of various pore geometries and their wettabilities on measured and in-situ values of cementation and saturation exponents. Trans SPWLA 27th Annual Logging Symposium, paper PP

25. de Kuijper A, Sandor RKJ, Hofman JP, Koelman JMVA, Hofstra P, de Waal JA (1995) Electrical conductivities in oil-bearing shaly sand accurately described with the SATORI saturation model. Trans SPWLA 36th Annual Logging Symposium, paper M

26. Berg CR (1996) Effective-medium resistivity models for calculating water saturation in shaly sands. The Log Analyst 37(3):16–28

27. Swanson BF (1985) Microporosity in reservoir rocks: its measurement and influence on electrical resistivity. Trans SPWLA 25th Annual Logging Symposium, paper H

28. Schlumberger (1989) Log interpretation principles/applications. Schlumberger, Houston, TX

29. Salazar JM, Torres-Verdin C, Sigal R (2005) Assessment of permeability from well logs based on core calibration and simulation of mud-filtrate invasion. Petrophysics 46(6):434–451

30. Ramakrishnan TS, Wilkinson DJ (1999) Water-cut and fractional-flow logs from array induction measurements. Paper 54673 in: SPE Reservoir Eng Eval 2(1):85–94

31. Nelson PH (1994) Permeability-porosity relationships in sedimentary rocks. The Log Analyst 35(3):38–62

32. Nicolaysen R, Svendsen T (1991) Estimating the permeability for the Troll field using statistical methods querying a fieldwide database. Trans SPWLA 32nd Annual Logging Symposium, paper QQ

33. Carman PC (1956) Flow of gases through porous media. Academic Press, New York

34. Wyllie MRJ, Rose W (1950) Some theoretical considerations related to the quantitative evaluation of the physical characteristics of reservoir rock for electrical log data. Paper 950105 in: Petroleum Transactions AIME 189:105–118

35. Timur A (1968) An investigation of permeability, porosity and residual water saturation relationships for sandstone reservoirs. The Log Analyst 9(4):8–17

36. Schlumberger (2005) Log interpretation charts. Schlumberger, Houston, TX

37. Ahmed U, Crary SF, Coates GR (1989) Permeability estimation: the various sources and their interrelationship. Presented at the 64th SPE Annual Technical Conference and Exhibition, paper SPE 19604

38. Sen PN, Straley C, Kenyon WE, Whittingham MS (1990) Surface-to-volume ratio, charge density, nuclear magnetic relaxation and permeability in clay-bearing sandstones. Geophysics 55(1):61–69

39. Herron MM, Johnson DL, Schwartz LM (1998) A robust permeability estimator for siliciclastics. Presented at the 73rd SPE Annual Technical Conference and Exhibition, SPE 49301

40. Katz AJ, Thompson AH (1986) Quantitative prediction of permeability in porous rock. Phys Rev B 34(11):8179–8181

Problems

23.1 Table 23.3 lists the values of R_t and Δt observed in a number of clean zones in a well with zones of hydrocarbons, as well as some water zones of different porosities.

a. Using the Hingle plot technique on the graph paper of Fig. 23.1, determine the value of R_w to be used in the analysis of the suspected hydrocarbon zones.

b. From the Hingle plot, what value should be used for the matrix travel time Δt_{ma}, in order to convert Δt to porosity?

c. Which zones have an oil saturation greater than 50%?

d. What is the porosity of level 16?

23.2 Using your knowledge of porosity from the preceding analysis, use the Pickett plot technique of analyzing the resistivity data. Graphically determine the following:

a. water resistivity

b. cementation exponent

c. water saturation at levels 3, 14, 17, and 19.

23.3 In Fig. 23.5, assume that the scale on the x-axis is 0–10 S/m and the scale on the y-axis is 0–0.5 S/m.

a. Calculate F^*.

b. At $C_w = 5$ S/m, calculate F as it would be used in the Archie equations. Note the difference between F and F^*.

Table 23.3

Zone	Δt	R_t		Zone	Δt	R_t
1	107	0.95				
2	87	1.9		11	75	5.8
3	107	4.1		12	89	5.9
4	76	5.0		13	92	1.9
5	102	6.1		14	71	12
6	96	12		15	97	1.9
7	97	0.88		16	95	6
8	96	1.2		17	82	10
9	65	23		18	102	1.8
10	85	3.2		19	89	15

23.4 Calculate R_{xo}/R_t and R_{wa} for the zones marked A, B, C, C′, D, D′ for the log in Fig. 2.18. What is R_w? Which zones should produce clean oil?

23.5 Write the expression for hydrocarbon volume in terms of total porosity and total water saturation (the latter is defined as the fraction of all water in the total porosity). Write the expression for hydrocarbon volume in terms of effective porosity and water saturation. Show that the hydrocarbon volume is the same in both cases.

23.6 From the fluid volumes shown in Fig. 23.12 find the average S_w between X4,250 and X4,500 ft. Compare this with the S_w that would have been calculated using the Archie equation with $R_t = R_h$.

23.6.1 Calculate S_w using the laminated sand equation (Eq. 23.16) but assuming that only the conventional R_h measurement was available. Note that in that case R_{silt} would have been taken from the resistivity in a sand-free interval such as at X3,750 ft.

23.7 Using the data from Figs. 23.9 and 23.10, plot the core values of porosity and permeability at various levels and establish a correlation to find permeability from porosity.

23.7.1 Use the Timur relation to estimate permeability from the logs at several levels and compare with the results from the permeability/porosity correlation.

23.8 Derive the relation between S_p and S_0 in terms of matrix density and porosity.

Index

2 MHz device, 231–238, 421, 455

Absorption coefficient, linear, 256–258, 273, 285
Absorption cross section, 334, 359, 366, 385, 616
Acoustic logging, 479–496, 519, 553, 557
Anisotropy, 82–85, 114, 200–208, 236–238, 241, 546, 549–556, 577–579
Annulus, 23, 195, 196, 284
Anti-squeeze, 112, 117
API unit, 27, 271, 275, 361
Apparent matrix, 639
Archie equations, 66–71, 74–77, 654, 658, 667–671
Array tool, 118, 179, 546
Attenuation, acoustic, 483, 527, 560, 563
Attenuation, electrical, 164–166, 213, 231, 234, 578
Attenuation, gamma ray, 257, 273, 285, 290, 303, 600

Biot poroelastic theory, 511, 527
Boltzmann transport equation (BTE), 354
Borehole compensated (BHC), 231, 482
Born approximation, 167, 192
Breakout, 550, 558, 562
Bucking coil, 157, 167, 185, 205
Bulk modulus, 485, 492, 506, 509–511, 515

C/O, 395–401, 404
Capture cross section see Cross section, thermal neutron absorption
Capture units, 385
Carbonates, 73, 275, 320, 461, 463, 554, 602, 608, 622, 671–673, 681
Cased-hole resistivity, 142–145
Cation exchange capacity (CEC), 74, 270, 600, 601, 607, 666
Cave, 169, 190
Cementation exponent, 69, 222, 229, 656
Chlorite, 598, 606, 608, 617
Clay bound water, 461, 601–603, 663
Clay minerals, 46, 74, 269–271, 598–601, 616
Clay, pore bridging, 605
Clay, pore filling, 605
Clay, pore lining, 605
Clustering analysis, 645, 646
Coaxial coil, 200–205, 229
Compatible log scale, 28, 366
Compressional velocity, 491–494, 501–519
Compton scattering, 254–256, 290, 405
Conduction, electrolytic, 46
Conductive invasion, 142, 187, 236, 241
Conductivity, 10, 44, 46, 79, 149, 167, 222, 658
Conductivity, electrical, 10
Conductivity, horizontal, 82, 202
Conductivity, vertical, 82
Coplanar coil, 200–206
CPMG, 432, 433
CRIM, 225, 228
Cross plot, density-sonic, 630
Cross plot, neutron-density, 617–621, 631
Cross plot, neutron-sonic, 630
Cross section, Compton, 254
Cross section, macroscopic, 252, 256, 333–336
Cross section, microscopic, 252

Cross section, neutron scattering, 336, 342, 354, 356
Cross section, photoelectric, 253, 303
Cross section, thermal neutron absorption, 330, 335, 343–345, 359, 383–388, 390, 392, 402, 617
Cross section, total, 252, 326, 331
Cuttings, 5, 575

Delaware effect, 116
Delta rho ($\Delta\rho$), 299
Density porosity, 32, 318–321, 373, 468, 617
Density, bulk, 20, 257, 289–292
Density, compensation, 296–300
Density, log, 292
Density, matrix, 289, 319
Density, mudcake, 297
Density, quadrant, 313
Depth of investigation, acoustic, 534, 535, 566
Depth of investigation, electrical, 114, 141, 162, 168, 191, 203, 229, 231, 236
Depth of investigation, nuclear, 285, 315, 352, 374–378, 406, 582, 585
Dielectric properties, 214–222, 228–232
Diffusion length (L_d), 331, 338, 342, 357, 359, 406
Diffusion, ionic, 49–55
Diffusion, NMR, 432–434, 438–440, 442, 444–460, 469, 472
Diffusion, thermal neutron, 343, 355–357, 388, 392
Dip, relative, 84, 197, 200, 205, 206
Dipmeter, 4, 133
Dipole moment, 158, 519, 524, 533, 547
Dipole source, 157, 519, 524, 533, 547
Dipping Beds, effects of, 133, 163, 171, 187, 197–199, 207, 236–238
Discriminant analysis, 644
Distance to boundary, 578, 580, 593
Double layer, 53, 600, 603, 661–665
Dry frame modulus, 511, 516
Dual laterolog, 107–112, 120
Dual-water, 663, 666, 667

Echo spacing, 431, 433, 459, 469
Effective medium, 76, 225–228, 672
Elastic scattering, 327–331, 335, 343
Electrical microscanner, 133, 142
Electrode device, 91, 109, 125, 171, 577
Electrofacies, 644, 648
Electron density, 290, 292, 310, 641
Electron volt, 248
Elemental analysis, 621–623, 644, 679
Energy resolution, 264
Epithermal neutron porosity, 357, 375
EPT, 228, 229

Fast formation, 519, 522, 545, 562
Feldspar, 269, 277, 608, 622
Fick's law, 72, 472
Flexural wave, 524, 533, 547, 549, 553, 565
F log, 131
Flushed zone, 19, 20, 23, 24, 125
Focusing, 101–108, 127, 128, 140, 161–163, 168
Formation damage, 508, 606
Formation evaluation, 1, 9, 17, 383, 482
Formation factor, 67–71, 77, 130, 659, 663, 666
Fractures, 8, 71, 135, 275, 483, 550, 557, 562, 575, 672
Free-fluid porosity, 460–463

Gamma ray spectroscopy, 261–263, 330, 395, 402

Gamma-gamma, 315, 405
Gas detection, 515, 617, 635
Gas-discharge counter, 259
Gassmann theory, 509, 512, 516
Geochemical analysis, 624
Geometric factor, 157–163, 167, 285, 315
GR log, 267, 271, 273, 585
Grimaldi method, 199
Groningen effect, 116, 120
Gyromagnetic ratio, 419, 420, 433

Head waves, 493, 524
High angle well, 239, 574
Hingle plot, 655–657
Horizontal well, 21, 574, 578
Hydrogen index, 335, 366, 406, 436, 460
Hydroxyl, 613, 617

Illite, 280, 601–608, 621, 643
Indonesia equation, 665, 667
Induction device (tool), 150, 156, 163, 172, 231
Induction device, multi-coil, 167–171
Induction device, two-coil, 155–160, 166
Inelastic scattering, 329
Invaded zone, 23, 108, 109, 117, 130, 320, 352, 648
Irreducible water saturation, 18, 82, 460, 678
Isomorphous substitution, 599

J-factor, 376, 377

Kaolinite, 280, 598, 605–608, 619
Kozeny-Carmen, 677, 679

Lamé constants, 489
Laminated sand, 83, 135, 207, 668–671
Larmor frequency, 416–423, 428, 437
Laterolog, 99, 114, 116, 145, 172, 195, 578
Lethargy, 335
Limestone porosity, 361, 363, 370
Liquid junction potential, 49–52, 56
Lithology, 301–312, 370, 403, 513, 630
LL3, 100–102, 118, 129, 135
LL7, 102–104, 138
Log interpretation, 17, 64, 77, 609
Logging, 1–6, 8–11
Longitudinal relaxation, T1, 423–427, 429, 437–442, 445
Low resistivity pay, 83, 671
LWD, 5–7

Macroscopic cross section, 252, 256, 333–335, 385
Magnetic moment, 416, 417
Magnetometer, 133, 142, 416, 417
Matrix, 11
Matrix effect, 357, 370–371
Membrane potential, 49, 52–58
Mica, 269, 275–277, 598
Microannulus, 561
Microlaterolog, 127
Microlog, 126, 127
Microspherical, 127
MID cross plot, 638–639, 640
Migration length (L_m), 342–344, 359–361
M-N cross plot, 636–640
Mobility, 42, 51, 54, 56, 437, 527, 559–560
Monopole source, 532, 534
Monte Carlo, 355, 361, 376
Montmorillonite, 598, 599, 605, 607
Mudcake, 22, 58, 127, 294–300, 560, 561
Multi-array induction, 188–199
Multicomponent induction, 205–208
MWD, 5

Neural network, 646, 649
Neutron detectors, 345–347
Neutron porosity, epithermal, 353
Neutron porosity, gas effect, 373

Neutron porosity, thermal, 353
Neutron sources, 345–347
Neutron, depth of investigation, 374–378
Neutron-neutron device, 351
Nuclear magnetic resonance, 10, 20, 415–473

Oil-wet, 73
Overpressured shale, 8, 555, 556, 600

Pair production, 256, 261–263
P_e, photoelectric absorption factor, 253, 300–313, 610–613, 640–643
Permeability, 7, 66–69, 464–466, 559–561, 674–681
Permeability, magnetic, 165, 222
Permittivity, dielectric, 214–233
Phase shift, 164–167, 224, 228–235, 578, 579, 592
Photoelectric effect, 253, 302
Pickett plot, 656
Poisson distribution, 250, 251
Poisson's ratio, 485, 487, 491, 492, 514
Polarization horn, 198, 203, 237, 579, 591
Polarization (wait) time, 455, 459, 465
Polarization, dielectric, 215–222
Polarization, nuclear magnetic, 416–417, 423, 425, 455, 456, 465, 466
Pore size distribution, 13, 76, 446–448, 463–465
Pore throat, 72, 76, 448, 464, 605, 678
Porosity, 7, 18
Porosity exponent, 71
Porosity unit (p.u.), 28
Porosity, effective, 601–604, 619
Porosity, total, 318, 601–604, 619
Potassium, 268–271, 275–280, 621, 622
Propagation device, 214, 228, 231, 238, 577–580
Pseudogeometric factor, 108, 109, 141, 376, 535
Pulsed neutron capture, 385
Pulsed neutron density, 405, 406
Pulsed neutron porosity, 405
Pulsed neutron spectroscopy, 395–397

Quicklook log, 131, 132

Radial geometric factor, 159, 160, 163, 285, 376
Radioactivity, 267–271
Relaxivity, 444, 445, 448, 464
Residual hydrocarbons, 131
Residual oil saturation, 18, 131, 471
Resistance, 42–46, 94, 95, 143–145
Resistive invasion, 142, 173, 187
Resistivity, 18, 19, 41–58, 78–81
Resistivity, horizontal (R_h), 89, 200, 574
Resistivity, vertical (R_v), 89, 114, 200–208, 670
R_{mf}, 19, 52, 129–132
R_{mfa}, 133
R_t, 19–23
Rugosity, 231, 315, 316, 554
R_w, 19, 52, 56, 654–657
R_{wa}, 132, 657
R_{xo}/R_t, 131–133, 657
R_{xo}, 19–23, 125–135, 657

Saturation equations, 130, 661
Saturation exponent (n), 70, 72
Scintillation detector, 260
Semiconductor detector, 264
Shale, dispersed, 604–606
Shale, laminated, 604–606
Shale, structural, 604, 662
Shear modulus, 487, 489, 506, 526
Shear velocity, 491, 492, 506, 515, 524–526, 547–549
Shear wave, 483, 484, 506, 524, 549–552

Short normal, 91–98
Shoulder beds, 22
Shoulder effect, 102–104, 117–120, 169, 180, 579
Sigma (Σ) see Cross section, thermal neutron absorption
Silt, 270, 582, 598
Skin effect, 167, 169–171
Skin effect signal, 182, 183
Slow formation, 522, 523
Slowing-down length (L_s), 337–342, 356–364, 370–374, 614–616
Slowness, 20, 511, 534
Slowness-time coherence (STC), 546–548
Snell's law, 492
SNUPAR, 339
Solvation number, 51
Sonde error, 175, 189, 231, 234
SP, 20, 27–33, 49–58, 609
Spatial frequency, 184–185
Spectral gamma ray, 273, 275–277, 283, 284
Spectral stripping, 280–283
Spherical focusing, 14–107, 127
Spin echo, 431–433
Spine and ribs, 297–300
Spontaneous potential see SP
Spurt loss, 22
Squeeze effect, 103, 112, 141
SSP, 55
Stabilizer, 6, 138, 313
Standoff, 108, 295, 300, 368, 369, 406, 580
Step profile, 24, 112, 169, 174, 187, 195
Stoneley wave, 519, 525–527, 558–561
Stratigraphic thickness (TST), 197, 577
Streaming potential, 58
Streaming, neutron, 378, 582
Surrounding bed, 574
Susceptibility, electric, 215
Susceptibility, magnetic, 421, 422, 434, 449, 452

Thermal absorber, 334, 343, 384, 385, 393, 613
Thermal diffusion coefficient, 343, 357, 388
Thermal diffusion length see Diffusion length (L_d)
Thermal neutron decay time, 387–391
Thernal neutron capture, 384–386
Thorium, 268–271, 275, 279, 280
Tool constant, 80, 92, 103, 110, 112
Tornado chart, 112, 142, 169
Toroid devices, 135–138
Tortuosity, 69, 71, 75, 76, 449, 663–667
Transit time, interval, 20
Transverse relaxation, T2, 430–433, 437–449, 461–463, 469
Triaxial cell, 508
Triaxial induction, 200–208
True bed thickness (TBT), 577
True vertical depth (TVD), 577
True vertical depth thickness, 577
True vertical thickness, 577
Tube wave, 525–527, 558

U, macroscopic linear cross section, 310–312, 611, 628, 641, 642
Uranium, 268–271, 275, 276

V_{cl}, 269, 273, 603, 623
Velocity survey, 480–482
Velocity, compressional (V_p) see Compressional velocity
Velocity, matrix, 501–503
Velocity, shear (V_s) see Shear velocity
Vermiculite, 598, 599
Vertical geometric factor, 160, 161

Vertical resolution, 114, 140, 162, 180, 185, 190–195, 228, 236, 406, 582, 670
Viscosity, 9, 47–49, 438–443, 465–471, 527
Vug, 72

Wash out, 22, 30, 554
Water-cut, 460
Water flow log, 400, 404, 405
Water saturation (S_w), 8, 18, 63–72, 384, 385, 392–395, 505, 506, 654–674
Water-wet, 73, 460–462
Waxman-Smits, 663–667
Wettability, 73, 672
Wireline, 2–6
Wyllie time average, 495, 512–516

Young's modulus, 484, 485, 490

SOLUTIONS TO END-OF-CHAPTER PROBLEMS

for

Well Logging for Earth Scientists

by

Darwin V. Ellis and Julian M. Singer

Published by Springer, P.O. Box 17,
3300 AA Dordrecht, The Netherlands

2007

Solution to Problems

Chapter 2: Introduction to Well Log Interpretation

2.1 47.6%
2.1.1 85.8%
2.1.2 grain size variations, overburden compaction, cementation, clay-plugging
2.2 80.3%
2.3 39%
2.4 –
2.5 2.8 ft or 1.15 ft into formation.
2.6 114.6 ft

Chapter 3: Basic Resistivity and Spontaneous Potential

3.1 –
3.1.1 less saline
3.1.2 greater
3.1.3 Both GR and SP indicate shale, so $\varphi_n > \varphi_d$
3.1.4 1) 9320 – 9362 ft where $R_{xo} \approx R_t$, and 2) 9363 – 9394ft where $R_{xo} > R_t$. Both probably have hydrocarbons because R_t has increased above that of lower zone. Possible reasons include, decrease in porosity, presence of hydrocarbons or a change in water resistivity.
3.1.5 Lower, since R_{xo}/R_t suggests invasion.
3.2 An exercise in using Chart SP-4. Interpolate between results obtained for charts with $R_{xo} = R_t$ and $R_{xo} = 5\ R_t$ in row for $R_t/R_m = 5$ to obtain $E_{SP}/E_{SPcorr} = 0.675$. So $E_{SPcorr} = -33.33$ mV.
3.3 $R_w = 0.172$ ohm-m. Using the uncorrected value, $R_w = 0.245$ ohm-m.
3.4.1 Using relation between resistance and resistivity; 46.5 k-ohm.
3.4.2 24.2 k-ohm. See chart Gen-6 for handy approximation.
3.4.3 1.26 k-ohm
3.5 –
3.5.3 The resistivity changes by nearly a factor of two but the temperature only by 10°F, so the salinity must change.
3.6 Deviation below 200°F negligible, but ~50% at 350°F.

Chapter 4: Empiricism: The Cornerstone of Interpretation

4.1 –
4.2 –
4.3 1) For any value of Sw the core with the greater porosity should be less resistive

2) Curve separation can be predicted using Archie's relation at any Sw, but separation is not as predicted.

4.4

4.41 R_w for sea water = 0.23 ohm-m (chart Gen-9). Use formation factor $(1/(0.2)^2)$ to find $R_o = 5.75$ ohm-m, so resistance = 0.46 ohm.

4.4.2 Using lower limit of marble resistivity from Table 3.1; resistance = 4 x 10^6 ohm.

4.5

4.5.1 From log find $R_t = 0.2$ ohm-m, so F = 12.5. If $S_w = 0.9$, then $R_w = 0.013$ ohm-m

4.5.2 ~300 kppm.

4.6

4.6.1 Obtain R_t~4 ohm-m from the log; implies $\phi = 8\%$. For $S_w = 50\%$, $m = 1.63$.

4.6.2 $\phi = 12.6\%$

4.7

4.7.1 13–16% depending on porosity.

4.7.2 –

4.8 –

4.8.1 At $\phi = 0.1$, T = 10. At $\phi = 0.2$, T = 5.

4.9 $R_h = 9.8$ ohm-m. $R_v = 450$ ohm-m. R_h is closer to R_{sh} while R_v is closer to R_{sd}

4.10 39.3°or only 5.7° above horizontal.

Chapter 5: Resistivity: Electrode Devices

5.1.1 From givens deduce $R_t = 1.11$ ohm-m and $R_{xo} = 22.22$ ohm-m. Then, from geometric factors: $R_{LLd} = 5.966$m ohm-m and $R_{LLd} = 10.19$ ohm-m

5.2

5.2.1 ~1%

5.2.2 $R_w = 8$ ohm-m.

5.3 The separation between the curves indicates invasion below 12540 ft and above 12470 ft. Elsewhere it is indeterminate.

5.4 $R_t = 1.6$ ohm-m. (All corrections are small). S_w from logs is >100%. S_w with correct R_t is 50%.

5.5 Hint given with problem.

5.6 85 m.

5.7 269 m and 0.08 ohm.

Chapter 6: Other Electrode and Toroid Devices

6.1 –

6.2

6.2.1 78.6%

6.2.2 10% uncertainty in porosity $->$ 10% uncertainty in S_w; 10% uncertainty in R_w or in $R_t -> 5\%$ uncertainty in S_w.

6.3
6.3.1 Taking R_{xo} to be 1 ohm-m yields $\phi = 23\%$.
6.3.2 –
6.3.3 If $\phi = 30\%$, then $S_{xo} \neq 1$, but 78%.
6.4
6.4.1

Interval	R_t, ohm-m	D_i, in.
1	0.21	100
2	Av 1.2	Indeterminate
3	2.55	20

6.4.2 $R_w = 0.019$ ohm-m.
6.5

Depth, ft	R_{xo}/R_t	Fluid	S_w	Comment
12550	2.86	Water	100%	
12450	5	Water	>100%	Uncertain invasion effect
12400	1	Mainly residual oil	51%	
12200	0.34	Movable oil	26%	
11800	0.02	Movable oil	44%	

6.6 $S_w = 58\%$
6.7 In top panel of Fig. 6.12, $D_i = 21$ in. In bottom panel $D_i = 25$ in. In the top panel at J = 0.5, the apparent resistivity from the ring $R_t = 0.55 * R_t$ while in the bottom panel $R_t = 5.5 * R_t$. Therefore the ring reads closer to R_t in the top panel (conductive invasion).

Chapter 7: Resistivity: Induction Devices

7.1
7.1.1 Note minimum at mid-bed.
7.1.2 Using Fig. 7.10 find that 25% of response from below bed and 25% above bed of 40 in. thickness. $R_a = 9.09$ ohm-m.
7.1.3 9.09 ohm-m as above, but closer to correct value for sand bed.
7.1.4 For case of $R_{shale} = 5$ ohm-m, max. reading for detection is 5.5 ohm-m. Find that central bed must contribute 18% of response which corresponds to ~10 in. thick bed
7.2 Use Eq. 6.7 and log data from water zone at 5306 ft to get $S_w \sim 52\%$.
7.2.1 Use chart Rcor-5 which is very sensitive to bed thickness. Charts are presented for values of shoulder bed resistivity, 1.7 ohm-m in this case, so interpolate. Find $R_t \sim 6.4$ ohm-m instead of 5.5 ohm-m. Then $S_w \sim 65\%$.

7.3 Assuming that the residual oil saturation (ROS) is the same after invasion as after water flooding, ROS would be 27%.

7.4

Interval	R_t, ohm-m	R_{xo}, ohm-m	Comment
A	1.8	10.8	In bottom half
B	11.7	129	
C	2.9	46	

The chart depends on R_{xo}/R_m because the radial response of ILd and ILm depends on resistivity level and is less at lower R_{xo}. The SFL reads less than R_{xo} by up to 35% because it sees beyond the invaded zone.

7.5 ILd should read closer at 30 ft, LLd at 120 ft. (Calculate R_{xo}/R_t and refer to Fig. 7–19.)

7.6 Using definition from Eq. 7.35 and noting that for $z>>0$ Eq. 7.33 can be written as $g(r,z) = (r^3)/(\rho^6)$, where $\rho^2 = z^2 + r^2$. Change variable of integration to $u = rmz^2 + r^2$ and integrate over appropriate limits.

Chapter 8: Multi-Array and Triaxial Induction Devices

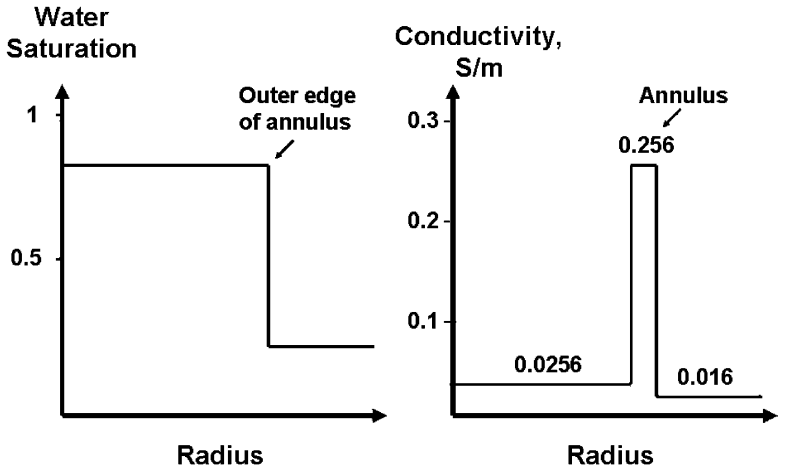
8.1 The error is 20% since R_t reads 0.4 ohm-m instead of 0.5 ohm-m. The error in S_w is 11% from Archie's equations.

8.2 The integrated vertical factor, G_{sh}, for the two shoulders is 0.00625.

8.2.1 The apparent resistivity in the center of the bed equals $G_{sh} * C_{sh} + (1 - G_{sh}) * C_t$, which gives 61.8 ohm-m.

8.3 From the D_i given in the figure and from Fig. 8-9, the integrated radial response of the 10 in. curve is 0.96 so that it should read 1.5 ohm-m.

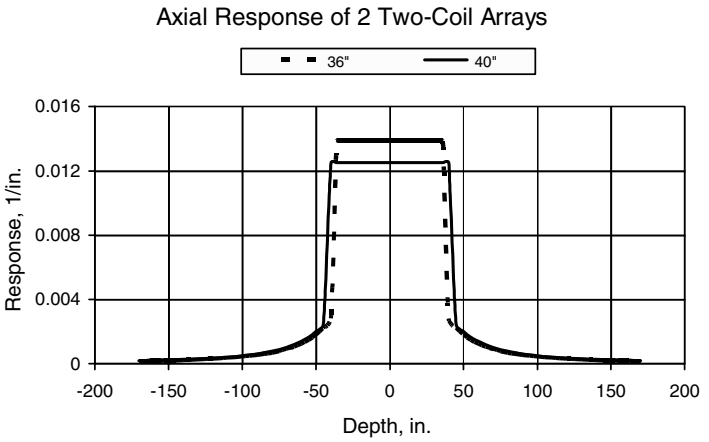
8.3.1 When $R_t << R_t$.

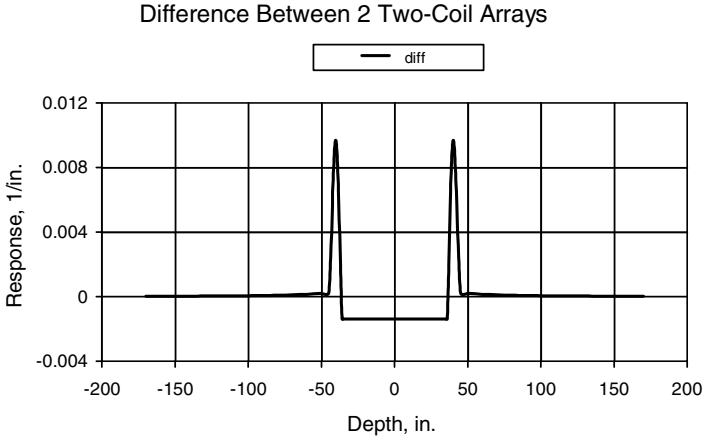


8.4 Radial profile of water saturation and conductivity with an annulus (above).

8.4.1 The maximum possible annulus thickness is 3.6 in. Calculate the volume of formation water originally in the flushed zone up to 48 in., and assume all this water goes into the annulus. Assume also that the original formation water in the annulus remains.

8.4.2 The conductivity is 0.055 S/m, which is higher than that in the flushed zone and the uninvaded zone.





8.5 Vertical (axial) responses above.

8.6 There is an error in Eq. 8.6. in the text: k should be written as k_h. Then:

$$V = K\left[\frac{2i}{\omega\mu L^2} + \sigma_v - \sigma_v\frac{L}{\delta_h}(1-i) - \sigma_v\frac{L\delta_v^2}{3\delta_h^3}(1-i)\,.....\right]$$

8.6.1 6.9 S/m

8.7

Depth, ft	Rv, ohm-m	Rsd, ohm-m	Vsh, %
X420	1.1	2	49
X430	1.1	1.8	42
X440	1.8	2.5	30

8.7.1 $$R_{sd} = \left[(R_v + R_h - 2V_{sh}R_h) +/- \sqrt{\left(R_v^2 - 2R_vR_h\left(1 - 2V_{sh} + 2V_{sh}^2\right) + R_h^2\right)}\right] \Big/ 2\,(1 - V_{sh})$$

R_{sh} can then be written out using Eq. 8.8.

Chapter 9: Propagation Measurements

9.1 Prove by direct comparison of the real and imaginary parts.

9.2 Write ε as (ε' + i$\varepsilon/\omega\varepsilon_0$) from Eq. 9.10 and below, and ignore ε'.

9.3 At induction frequencies e" ranges from 10^3 to 10^7, while e' rarely reaches 10^3. At laterolog frequencies e" ranges from 10^5 to 10^9, while e' rarely reaches 10^5. (see Bona et al., reference 4)

9.4 $R_t = 40$ ohm-m, $\varepsilon' = 40$.

9.4.1 $R_{ps} = 39$ ohm-m, $R_{ad} = 40$ ohm-m from Fig. 9-14.

9.4.2 $R_{ps} = 40$ ohm-m, $R_{ad} = 40$ ohm-m.

9.5

$R_{xo} > R_t$	$R_{ad} > R_{ps}$	Resistive invasion, tool close to resistive boundary
$R_{xo} > R_t$	$R_{ad} < R_{ps}$	Resistive invasion
$R_{xo} < R_t$	$R_{ad} > R_{ps}$	Unlikely
$R_{xo} < R_t$	$R_{ad} < R_{ps}$	Unlikely
$R_{xo} = R_t$	$R_{ad} > R_{ps}$	Tool close to conductive boundary
$R_{xo} = R_t$	$R_{ad} > R_{ps}$	Large dielectric effects

9.5.1 With conductive mud, the uncorrected short-spaced measurements may read too low for both R_{ps} and R_{ad}. The table is still valid except that there could also be resistive invasion for the case of $R_{xo} > R_t$ and $R_{ad} < R_{ps}$.
Oil-base mud can cause the long-spaced measurements of an eccentered tool to read higher than the short-spaced. The effect on the table is therefore similar to that of a conductive mud.

9.5.2 If the uncorrected short-spaced measurements read higher than the long-spaced, then the corrected measurements would read even higher and the same table remains valid.

9.6 Anisotropy. $R_{ps} > R_{ad}$, which could be resistive invasion except that the deeper readings read higher.

Chapter 10: Basic Nuclear Physics for Logging Applications: Gamma Rays

10.1 Hint: use Sterling's approximation.
10.2
10.2.1 $dN/N = -\mu x\, d\rho$
10.2.2 1 p.u. uncertainty corresponds to $\sim\Delta\rho = 0.0155$ g/cm^3. Estimate μ from Fig. 10.8 for Al; dN/N = 4.6%
10.2.3 475 cps
10.3 N(CsCl) $\sim$1.4 x 10^{22}; Vol $\sim$1.8 x 10^{-3} cm^3.
10.4 –
10.5 –
10.6 –

Chapter 11: Gamma Ray Devices

11.1 A/ N_o, where A is atomic weight of isotope and $N_o$is Avogadro's number.
11.2 Use Eq. 11.3 to compute particle flux from U, T, and K. Estimate μ from Fig. 10.8 and average gamma ray energy (1 MeV) to be $\sim$006 cm^2/g. Use Eq. 10.2 and known half-lives to compute partial count rates: K—20.4 cps; U—2.5 cps; Th—1.5 cps.
11.3

Depth, ft	Vcl(GR)	Vcl(SP)
8530	0	0
8549	50%	70%
8560	10%	50%

Thin bed at bottom?
11.4 $\sim$10% & $\sim$60%
11.5 Use only W_4 and W_5 to get two simultaneous equations:
$W_4 = a_{41}Th + a_{42}U$
$W_5 = a_{51}Th + a_{52}U$
after assuming that the K contributions a_{43} and a_{53} are zero.
11.6 Evaluate coefficients of prob. 11.5 using givens.

Chapter 12: Gamma Ray Scattering and Absorption Measurements

12.1 Find porosity =26.2%. Naïve hydrocarbon density =0.32 g/cm^3. Instead, compute electron density of hydrocarbon to be 0.48 g/cm^3. Use data from Table 12.1 to find $\rho_b = 0.87\rho_e$ for CH_2, so $\rho_{HC} = 0.42$ g/cm^3.
12.1.1 $\rho_{log} = 1.07\rho_e - 0.1823$
12.2

12.2.1 Density varies between 2.30 – 2.37 g/cm^3. Formation might be limestone or dolomite so maximum spread of porosity is 21.1 p.u. to 31.2 p.u.
12.2.2 Cross plot density and P_e using chart CP-16 or Fig. 12.19 to find $\phi \sim 24$ p.u.
12.2.3 From crossplot limestone fraction varies between 40% – 95%.
12.3
12.3.1 –
12.3.2 For salt-plugged formation, $\rho_b = 2.73$ g/cm^3 & $P_e = 3.37$. Similar to a 5-6 p.u. water-filled limestone-dolomite mixture.
124 –
12.5.1 2.82 g/cm^3
12.5.2 0.08 v/v (8 p.u.)
12.5.3 7.7% pyrite
12.5.4 1.195 g/cm^3

Chapter 13: Basic Neutron Physics for Logging Applications

13.1
13.1.1 Note from conservation of momentum that He^4 velocity is $1/4$ neutron velocity. 14.08 MeV.
13.1.2 13.2 MeV.
13.2
13.2.1 Use data from Table 13.1 or Table 15.1, and Fig. 13.16. Σ(water) = 22 cu, note that 10^{-3} times capture unit (cu) has dimension of cm^{-1} (it is the probability of being absorbed per cm). So Eq. 13.30 has proper units (4.5 cm).
13.2.2 4.2 cm for 0 p.u. and 3 cm for 20 p.u.
13.3 From data of Table 13.1 and weight fractions of H and Cl, contribution of H is 21 cu and Cl is 33 cu.
13.3.1 See Fig. 13.7
13.3.2 43.7 cu

Chapter 14: Neutron Porosity Devices

14.1
14.1.1 Epithermal tool responds to L_s, so use Fig 13.10 or Fig 14.14 to construct chart.
14.1.2 The correction is not a constant but a function of porosity as found above.
14.2
14.2.1 From Fig. 14.6 deduce a 7 p.u. shift from sand to limestone. Apparent limestone porosity ~33 p.u.
14.2.2 Compute L_m (after computing Σ_{for} to be ~53 cu with inclusion of salt water); ϕ_{lime} ~55 p.u.

14.2.3 After recomputing apparent L_s and combining with the previously determined L_d, the L_m value yields an apparent porosity of 43 p.u.
14.3 See Fig. 14.14
14.4 33 p.u.
14.4.1 Using the data of Fig 14.12 (with a magnifying glass) or a chartbook, estimate that the temperature correction at 33 p.u. is on the order of 11 p.u., so ϕ_n will read 11 p.u. too low, showing cross-over at the two cleanest zones.
14.5 Using data from Reference 7 (Chapter 50) or estimating neutron response on the basis of hydrogen index, the cross-over is found to be ~6-7 pu.
14.6 Hydrocarbon density, for one.
14.7 ~ 26pu, see Section 21.3.2.

Chapter 15: Pulsed Neutron Devices and Spectroscopy

15.1 Solution density increases with addition of NaCl.
15.2 See Eq. 13.5
15.3 Use data of Table 13.1
15.4
15.4.1 Make a S vs ρ_b cross-plot using three end points:
Water: 65 cu, 1.1 g/cm^3
Oil: ~21 cu, ~0.8 g/cm^3
Limestone: ~9 cu, 2.71 g/cm^3
Scale in S_w between water and oil points.
15.4.2 Find R_w @ 100°C. Then S_w from LLD is ~48%. However, from Σ, S_w is ~15%. Fresh water has diluted the formation water.
15.4.3 Iterate on values of salinity, computing S_w from Σ and LLD until values agree. Find salinity ~45 kppm and $S_w \sim 70\%$.
15.5 –
15.5.1 From hydrocarbon zone (not the low-density gas) estimate 12.6 cu.
15.5.2 Putting line from matrix point through the cloud of water points, find $\Sigma \sim 19$ cu. Deduce $\Sigma_w = 34$ cu.
15.6 From Fig. 3.5 or chart book find 0.18 ohm-m @ 115°F implies 30 kppm. From slope of Fig. 15.1 determine $\Sigma_w = 32.2$ cu.
15.6.1 No change. R_w gives consistent estimate.
15.6.2 Invasion must be shallow.
15.7 Use data from Table 13.1
15.7.1 See prob. 13.3.1
15.8 Insufficient data on the log. The value of Σ_{for} is necessary but we can assume a reasonable value. From log at depth X150, $\Sigma = 15$ cu, $\phi g = 20$ pu of which $\phi_{oil} = 3$ pu. From defining equation: $\Sigma = 15 = 0.8 * \Sigma_{ma} + .03 * 21 + 0.17 * \Sigma_{mix}$, the maximum value of 13.2 cu can be determined for the matrix. If Σ_{ma} is assumed to be 5 cu, then show $\Sigma_{mix} = 61$ cu. If connate water volume is 2 pu then its salinity will be 140 kppm from Fig. 15.1.

Chapter 16: Nuclear Magnetic Logging

16.1 5580 Gauss
16.2 5000
16.3 –
16.4 Look at variation of η/T. From Prob 3.6 , η varies as $\eta_o$exp(1825/T). Find that increase of T2 of water with increase in temperature is predicted by η/T when viscosity variation is taken into account. For change from 50–100°C, graph shows x2 increase and η/T predicts x2.5.
16.5 An exercise in applying Eq. 16.32 (and 16.31).
16.6
16.6.1 22 time units
16.6.2 110 x $P_{down} = 11\text{x}P_{up}$ by substitution.
16.7 The position sought is for the same (but unspecified) resonant frequency for the two species.
16.8 Taking T1 to be proportional to correlation time leads to T2 $\propto$ a^2/bD. Show that D = kT/(6π ηa) to confirm the use of η/T to scale the x-axis of Fig. 16.4.

Chapter 17: Introduction to Acoustic Logging

17.1
17.1.1 37°, 17.4°
17.1.2 Neglecting tool diameter, 2.37 ft.
17.2
17.2.1 1.25 μsec/ft
17.2.2 ~66.7 kHz.
17.2.3 ~18 kHz.
17.3 for $\Delta t_{mud} > \Delta t_{for;} \sim 3.9$ ft.
17.4 304.8

Chapter 18: Acoustic Waves in Porous Rocks and Boreholes

18.1 —
18.2 Use compressibility = -1/V(dV/dP)=1/K. For each volume –V_1 C dp = dV_1, to arrive at: $K_t = [V_1/K_1 = V_2/K_2]^{-1}$.
18.3
18.3.1 From Eq. 18.2 use $(k_c)^{-1} = \frac{S_w}{k_w} + \frac{1-S_w}{k_{oil}}$ and substitute into Eq. 18.21.
18.3.2 Use relation $k = \rho(V_p^2 - 4/3V_s^2)$; determine k at two different saturations (and densities)
18.4 From $V_s^2 = 3/4V_c^2 - 3/4B/\rho$, see upper limit is for $\rho \to \infty$; 6.75 km/sec.
18.5

18.5.1 240 μs/ft.

18.5.2 Using Fig. 18.2, ~32 p.u.

18.5.3 Using $V_s = \sqrt{\frac{\mu}{\rho}}$, when density decreases V_s increases, so $V_{s_dry} > V_{s_brine}$. Expect $V_{s_dry}/V_{s_brine} = \sqrt{\frac{\rho_{brine}}{\rho_{air}}} = 1.06$

Chapter 19: Acoustic Logging Methods

19.1 Plot selected values of Δt vs ϕ_d for upper and lower zones using lithology identified from text.

19.2 Assume tube wave can be identified. V_{tube} (Eq. 18.20) can be rewritten in terms of V_{mud}, formation density, ρ, and mud density. Solve for ρ, and combine with V_p and V_s to get elastic constants.

19.3

19.3.1 Average Δt ~100 μs/ft, corresponds to ~33 pu for $Vp_{ma} = 18,000$ ft/sec. Variation is from 95–105 μs/ft corresponding to 29.5 – 36.5 pu.

19.3.2 Correlation between increase in resistivity and Δt increase.

19.3.3 The gas effect may be masked by invasion.

19.3.4 Hole size change inducing cycle skip(?).

19.3.5 Shale.

19.3.6 $\Delta t_{ma} = 45\mu$s/ft, $\Delta t_{fl} = 218\mu$s/ft

19.4 From plotting data on Fig. 18.12, find $\Delta t_{ma} = 49\mu$s/ft, $\Delta t_{fl} = 218$ μs/ft. Middle and lower zones are consistent; upper is shale(?).

19.5 At 25 kHz, $\lambda = 0.48$ ft, so depth of investigation is about one wavelength.

Chapter 20: High Angle and Horizontal Wells

20.1 Taking the transition from sand to shale as 42 ft, and using Fig. 20.2, the dip angle is 3.5°.

20.1.1 9.8°.

20.1.2 Looking downhole the shale is approaching from above.

20.2 See, for example, the website: www.scacompanies.com/publications/newsletters/archives/winter03.html

20.3 Taking the thickness of the sand as 100 ft MD, TVT = 6.47 ft and TST = 6.45 ft.

20.3.1 TVT = 11.73 ft, TST = 11.67 ft.

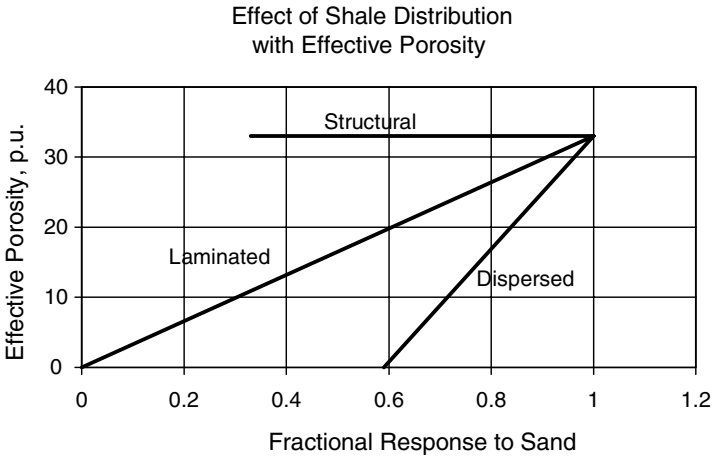
20.4 3 ohm-m. The induction tools.

20.5 88.6°.

20.6 The relative deviation is approximately 88.6°. The beds are thin enough that a density log perpendicular to them would read the average density, 2.25 g/cm^3.

Chapter 21: Clay Quantification

21.1 150 cm^2/cm^3.
21.1 6.9 x $10^4 cm^2/cm^3$.
21.3 2.52 g/cm^3.
21.3.1 $Q_v = 0.02$ meq per pore volume. $V_{cbw} = 0.2\%$.
21.4 –



21.4.1 Above, relationship between effective porosity and fractional sand volume.
21.4.2 Shale volume decreases with depth while total porosity also decreases, indicating structural shale.
21.5 Taking GR_{min} at 1870 ft = 19.5 gapi, and GR_{max} at 1665 ft = 96 gapi, then Vsh at 1700 ft = 5%. (Note: the clay weight % in Fig. 21.8 corresponds to GR_{min} at 1890 ft = 10 gapi, and GR_{max} at 1665 ft = 130 gapi, contrary to the numbers in the text.)
21.6 Expand the partial U_i contribution as $P_{e,i}\rho_{b,i}$. Divide both sides by density, ρ_b. Each terms is $P_{e,i}$ times weight fraction $(\rho_{b,i}/\rho_b)$ and then use $P_{e,i} = (Z_i/10)^{3.6}$.
21.7 Calculate MW of kaolinite as ∼231. Weight fraction Al is 11.7% MW of illite ∼254. K weight fraction is 7.8%.
21.8 From the log the weight % of Al is ∼10% and Fe wt% is 5%. Approximate MW of Illite (using Al) is ∼700. Reduce Al_5 to $\sim Al_{2.5}$. $Fe_{0.6}$ will produce ∼5% Fe by weight.
21.8.1 Limestone from high P_e and low Al and GR.
21.9 ∼0.5%

Chapter 22: Lithology and Porosity Estimation

22.1 Should find (from top to bottom): Anhydrite, dolomite streak, mixed limestone-dolomite, a shale streak, mixed lime-dolomite, dolomite streak and finally limestone at 15380ft.

22.2 Assume ϕ_n in sandstone units, so first correct to limestone to use in cross plotting (correction can be done with charts like Fig. 21.1). Exercise in using Fig. 21.1 and Fig. 21.2. For computation of Δt_{ma}, use $\Delta t_f = 187 \mu$s/ft.

22.3 Compute Pe from U or short-cut of Eq. 21–13.

22.4 At e.g. 9900 ft, $\rho_{maa} = 2.71$ g/cm^3 and $U_{maa} = 12$. The percentages of quartz, calcite and dolomite are 17%, 77% and 6%.

22.5 Density-sonic or density-neutron. For neutron-sonic the ~5 pu lithology shift could be masked by a Δt shift of only 4 μs/ft.

22.6 Weight fraction of Ba in $BaSO_4$ is 58% so mud is 27% Ba by weight. $P_{e,mud} \sim 493x0.27 = 133$. The mud is only 12% of formation density so $P_e \sim 19.9$.

Chapter 23: Saturation and Permeability Estimation

23.1 a. From the cross plot, $S_w = 100\%$ can be drawn through the uppermost points (7, 2, 11,14,9). For construction of graph can show $\sqrt{C_t} = \frac{S_w}{\sqrt{R_w}} \left(\frac{\Delta t - \Delta t_{ma}}{\Delta t_f - \Delta t_{ma}} \right)$. Assuming $\Delta t_f = 187 \mu$s/ft, take a conductivity point off 100% saturation line to compute $R_w = 0.085$ ohm-m.

b. From graphical inspection, 57 μs/ft

c. 16,19,3,5,6

d. 29 p.u.

23.2 First compute porosity from Δt in previous problem, then plot log ϕ vs log R_t.

a. Intercept at $\phi = 100$ gives $R_w \sim 0.88$ ohm-m.

b. From graphical inspection and Eq. 23.6, m = log(90)/log(9) = 2.04.

c. From graphical inspection zone 3–40%; zone 14–50%, zone 17–50%, and zone 19–30%.

23.3 a) F* = 34.5. b) F = 18.5.

23.4 $R_w = 0.017$ ohm-m. C should produce oil (B has gas).

23.5 From Fig. 21–3 the total volume of water is $\phi_t S_{wt} = \phi_t - V_{hyd}$. Similarly the volume of effective water is $\phi_e S_{we} = \phi_e - V_{hyd}$ with V_{hyd} the same in both cases.

23.6 S_w with silt water is 48%, without silt water 25%. From Archie and R_h, $S_w = 49\%$.

23.6.1 $S_w = 44\%$. (Use Eq. 23.16 with silt instead of shale).

23.7 A reasonable approximation for $\log_{10}$K in mD is ($17.1\phi_t - 2.29$).

23.7.1 The Timur relation predicts much higher permeability than the correlation using ϕ_t. If ϕ_e is used the prediction is better, but still high.

23.8 $S_p = S_o \rho_{ma} (1 - \phi) / \phi$

Springer

http://www.springer.com/978-1-4020-3738-2

Well Logging for Earth Scientists
Ellis, D.V.; Singer, J.M.
2007, XX, 708 p. 450 illus., Hardcover
ISBN: 978-1-4020-3738-2